Published in Journals: Agriculture,
International Journal of Environmental Research and Public Health,
Remote Sensing, Sustainability and Water

Topic Reprint

Water Management in the Era of Climatic Change

Volume II

Edited by
Alban Kuriqi and Luis Garrote

mdpi.com/topics

MDPI

Water Management in the Era of Climatic Change—Volume II

Water Management in the Era of Climatic Change—Volume II

Editors

Alban Kuriqi
Luis Garrote

MDPI

Basel • Beijing • Wuhan • Barcelona • Belgrade • Novi Sad • Cluj • Manchester

Editors

Alban Kuriqi
University of Lisbon
Lisbon, Portugal

Luis Garrote
Universidad Politécnica de Madrid
Madrid, Spain

Editorial Office
MDPI
St. Alban-Anlage 66
4052 Basel, Switzerland

This is a reprint of articles from the Topic published online in the open access journals *Water* (ISSN 2073-4441), *Agriculture* (ISSN 2077-0472), *International Journal of Environmental Research and Public Health* (ISSN 1660-4601), *Remote Sensing* (ISSN 2072-4292), and *Sustainability* (ISSN 2071-1050) (available at: https://www.mdpi.com/topics/water).

For citation purposes, cite each article independently as indicated on the article page online and as indicated below:

Lastname, A.A.; Lastname, B.B. Article Title. *Journal Name* **Year**, *Volume Number*, Page Range.

Volume II
ISBN 978-3-0365-9346-3 (Hbk)
ISBN 978-3-0365-9347-0 (PDF)
doi.org/10.3390/books978-3-0365-9347-0

Set
ISBN 978-3-0365-9342-5 (Hbk)
ISBN 978-3-0365-9343-2 (PDF)

Contents

About the Editors

Alban Kuriqi

Alban Kuriqi is a Research Scientist at CERIS–Civil Engineering Research and Innovation for Sustainability, University of Lisbon. He earned his Ph.D. in Civil Engineering from the University of Lisbon, specializing in River Restoration and Management. His extensive research interests and expertise encompass a wide array of areas, including renewable energy, with a particular focus on hydropower and complementary resources, as well as the impacts of hydropower and water resources' management-related issues.

Luis Garrote

Luis Garrote is Full Professor of Hydraulic Engineering at Universidad Politécnica de Madrid. His research focus is the application of hydrological and hydraulic models in water resources' planning and management, including floods, droughts, environmental constraints and reservoir operation, with a special emphasis on dealing with uncertainties, particularly those connected to global change.

Preface

Water is a crucial element on Earth for all living and non-living components. Climate change is an alarming issue for managing and sustaining life on Earth. Given climate change, water resources worldwide have been under drastically stressed conditions, as is evident from the uneven weather patterns, droughts, floods, and cloud bursts. Only three percent of the water resources on Earth are fresh, and two-thirds of the freshwater is locked up in ice caps and glaciers. Of the remaining one percent, a fifth is in remote, inaccessible areas. Much of the seasonal rainfall in monsoonal deluges and floods cannot be easily used. Only about 0.08 percent of all the world's freshwater is exploited by humankind, with an ever-increasing demand for sanitation, drinking, manufacturing, leisure, and agriculture. The ever-increasing water exploitation has intensively degraded freshwater ecosystems, notably rivers.

Furthermore, the climate extremes and water scarcity that are enhanced by climate change induce additional stress on the freshwater ecosystems and may stimulate conflicts among water users. In addition, we know that water is needed for several vital human activities, of which agricultural and industrial activities are the primary water consumers. In the context in which we observe more frequent droughts and incidences of water scarcity in the world, water systems' management requires the most advanced approaches and tools to rigorously address all of the dimensions involved in the sustainability of its development.

Therefore, this Topic Collection's main objective is to contribute to the understanding of water systems' management, and to provide science-based knowledge, new ideas/approaches, and solutions for water resources' management. Water demand for irrigation has been steadily increasing during in recent decades. However, other water users have simultaneously been competing with agricultural sectors for water resources. The conservation of freshwater ecosystems also needs special attention, such as the sufficient allocation of environmental flows. In addition, in terms of the projected climate change caused by warmer temperatures and shifting precipitation patterns, water availability is expected to decrease, and water demand to increase, in many areas of the world.

Consequently, soil productivity and, thus, crop production could be drastically reduced. These trends raise concerns highlighting the role of water and natural resources' management and their conservation to ensure the sustainability of irrigated agriculture. How well-irrigated agriculture adapts to water scarcity scenarios, particularly by increasing water use efficiency and better-estimating evapotranspiration, will directly affect the future and sustainability of the sector. The 89 papers published in this Topic Collection encompass a diverse range of critical issues and potential solutions concerning the sustainable management of water resources. We anticipate that this collection will serve as a source of inspiration for engineers, scientists, policymakers, and decision-makers worldwide, helping them to identify appropriate solutions and make informed decisions regarding their specific water-related challenges.

Alban Kuriqi and Luis Garrote
Editors

water

MDPI

Article

Hydrological Effects of Agricultural Water Supplies on Paddy Fields using Surface–Groundwater Integrated Model

Sanghyun Park [1], Hyeonjun Kim [1,2,*], Choelhee Jang [2] and Deokhwan Kim [2]

[1] Department of Civil and Environmental Engineering, University of Science & Technology, 217, Gajeong-ro, Yuseong-gu, Daejeon 34113, Korea; sanghyun0385@kict.re.kr
[2] Korea Institute of Civil Engineering & Building Technology, 283, Goyang-daero, Ilsanseo-gu, Goyang-si 10223, Korea; chjang@kict.re.kr (C.J.); kimdeokhwan@kict.re.kr (D.K.)
* Correspondence: hjkim@kict.re.kr; Tel.: +82-31-910-0003

Abstract: Agricultural water demands are mainly dependent on the supply from groundwater withdrawals and the supply from agricultural reservoirs. To understand the water cycle of the agricultural catchment, it is necessary to consider the actual situation of the water cycle of paddy fields in catchments through accurate hydrological modeling. In this study, streamflow simulations were implemented in consideration of the levee height of paddy fields and the irrigation period for one sub-catchment of the Boryeong Dam catchment using the integrated surface–groundwater model, CAT (Catchment Hydrologic Cycle Assessment Tool). To consider the agricultural reservoirs in modeling, the catchment was divided into the reservoir sub-catchments, upstream sub-catchments, downstream sub-catchments, and irrigated districts of each sub-catchment. This study aims to analyze the hydrological effects of agricultural reservoirs and groundwater pumping on the hydrological cycle of the catchment and on the soil moisture and groundwater level. As a result of the simulations, we found that the direct flow, baseflow, and groundwater recharge of the catchment increased with the agricultural reservoir supply water. In addition, the effect of drought on soil moisture content and groundwater level in the irrigated paddy fields from agricultural reservoirs was evaluated. The soil moisture increased by about 10% according to the water supply of agricultural reservoirs. The groundwater level rapidly decreased due to the groundwater abstraction during the irrigation period; however, it was analyzed that the water supply from agricultural reservoirs is significantly effective in preventing the decrease in the groundwater level in the irrigation season.

Keywords: hydrological responses; irrigation; paddy fields; groundwater; soil moisture; CAT model

Citation: Park, S.; Kim, H.; Jang, C.; Kim, D. Hydrological Effects of Agricultural Water Supplies on Paddy Fields Using Surface–Groundwater Integrated Model. *Water* **2022**, *14*, 460. https://doi.org/10.3390/w14030460

Academic Editors: Alban Kuriqi and Luis Garrote

Received: 21 December 2021
Accepted: 28 January 2022
Published: 3 February 2022

1. Introduction

Rice paddies in monsoon Asian regions account for 87% of the global paddy rice harvested area and 90% of rice production [1]. Since rice is a staple food in Korea, the agricultural industry is active and paddy fields represent more than 8% of the territory [2]. Generally, agricultural catchments consist of paddy fields, where crops are cultivated and produced, as well as forest areas and residential areas, and nearby water supply facilities artificially supply the water necessary for crop growth [3]. The sources of water supply for agricultural activities can be divided into agricultural reservoirs and groundwater pumping. Water shortages due to the excessive pumping of groundwater in rural areas cause water problems for domestic consumption and can also cause a shortage of water needed for agricultural activities, affecting the amount of streamflow in a catchment [4]. In addition, agricultural water supply is an essential resource for agricultural water consumption, accounting for more than 50% of the total water resource consumption, and it is highly dependent on the water supply of agricultural reservoirs [5]. There are currently 17,629 reservoirs nationwide, of which 17,516 are agricultural purpose reservoirs, accounting for the largest proportion [6]. In addition, as 65% of Korean land is composed

of mountainous areas and the river slopes are steep, runoff occurs in a short period, with a low flow rate during the dry season. As the runoff rate variability is relatively large in Korea [7], it is important to manage water resources through the adequate scale of agricultural reservoirs to meet agricultural water consumption requirements in the catchment. The agricultural reservoir stores the streamflow from the upstream basin and supplies agricultural water to the paddy fields during the irrigation period. A portion of the agricultural water supplied to the paddy fields returns to the stream, and the hydrological cycle in the agricultural catchment works in a complex way with the upstream, the downstream, the irrigation districts, and the reservoirs by the operation of the agricultural reservoirs [3]. Therefore, to understand the hydrological cycle processes of the agricultural catchments, each element should be connected. However, there is a high possibility that they will have difficulties in supplying water during drought because the storage capacity of the agricultural reservoirs is low compared to that of the multi-purpose dams [8]. As the research related to the utilization of water supply is insufficient, the high-accuracy estimation of runoff discharges of reservoir catchment, upstream catchment, and downstream catchment should be preceded for stable water supply and drought response of agricultural catchments. In the agricultural catchments, rice is sensitive to growth periods, the climatic environment, and water content situations. In particular, the soil moisture content is an essential factor in the hydrological modeling of agricultural catchments as crops grow by absorbing soil moisture, the main hydrological component of the agriculture industry [9]. The soil moisture content is the amount of retained water in a soil layer, which could be directly affected by drought. Many drought indices have been developed in the agricultural hydrology field, using variables such as precipitation, evapotranspiration, soil moisture, reservoir, and groundwater level that could directly affect crop growth in drought periods [10]. Representative drought indices indicating agricultural drought include the Reservoir Drought Index, which uses the amount of water stored in agricultural reservoirs; the Soil Moisture Index (SMI), which uses the effective moisture percentage of the soil moisture; and the Integrated Agricultural Drought Index [11]. Bae et al. [12] developed the Agricultural Drought Analysis Model and performed drought analysis on soil moisture and agricultural areas. Shin et al. [13] evaluated daily soil moisture estimation and agricultural drought by linking active- and passive-based soil moisture and a soil moisture data assimilation technique. In this study, the SMI index, often applied for agricultural drought evaluation, and the Standardized Precipitation Index (SPI) and the Standardized Groundwater level Index (SGI), using meteorological data and groundwater level [14], are used to select the drought and normal years within the study period to compare the changes in hydrological components by drought. Research on the hydrological changes of Korean catchments according to agricultural reservoirs has been conducted continuously. Lee et al. [15] analyzed the streamflow changes according to the discharge amount of agricultural reservoirs using the Soil and Water Assessment Tool. Kim et al. [16] evaluated the effect of agricultural reservoirs on streamflow in the Anseong-cheon catchment. Lee et al. [17] evaluated the effect of groundwater consumption and reservoirs on streamflow, and Lee and Noh [18] evaluated the streamflow downstream according to the operation of the agricultural reservoir considering climate change scenarios. In addition, Cho et al. [19] evaluated changes in the river ecological environment and the hydrological environment following the construction of multipurpose dams. However, existing studies on the hydrological changes of catchments according to agricultural reservoirs have been mainly conducted on the streamflow of downstream rivers and ecological changes. Applying the conceptual hydrological model has limitations in considering the infiltration and the streamflow changes by the land use of the catchments. To analyze the water cycle on a catchment scale, hydrologic modeling is required considering streamflow changes in evapotranspiration, direct runoff, and baseflow. In this study, the change in water cycle according to the water supply of the agricultural reservoirs in one sub-catchment of the Boryeong Dam catchment was evaluated, and the changes in the soil moisture content and the groundwater level according to the drought period were analyzed using the integrated

surface–groundwater model, which can consider the actual situation of the paddy fields in Korea. In addition, the sub-catchment where the agricultural reservoirs are located was divided into smaller sub-catchments to analyze the hydrological responses considering the agricultural water supplies. Changes in the soil moisture contents and groundwater elevation in paddy fields according to irrigation and non-irrigation periods were compared and analyzed by considering groundwater withdrawals and agricultural reservoir supplies.

2. Materials and Methods

2.1. Study Area Description

The Boryeong Dam catchment is located in the West Sea basin of the Geum River watershed in Korea. The catchment area is about 162.84 km^2, and the average slope of the catchment is about 29.8%. The catchment has steep and mountainous terrain characteristics, including paddy field areas. Even though this catchment is not a regional-scale catchment, it has complex interactive hydrological cycle processes due to human activities, such as groundwater abstraction, agricultural reservoirs, and water intake supply systems from outside the catchment. Administratively, the Boryeong Dam catchment includes Oesan-myeon of Buyeo-gun and Seongju-myeon and Misan-myeon of Boryeong-si. The Ungcheon Stream flowing through the Boryeong Dam catchment has a separate branch from the Geum River, originating from Oesan-myeon of Buyeo-gun and Seongmyeon of Boryeong-si, respectively; they join together at Misan-myeon of Boryeong-si and flow directly into the west sea of Korea. The total length of the Ungcheon Stream is about 36 km, with 23 km located in the Boryeong Dam catchment. About 8.11% of the total area of the Boryeong Dam catchment comprises paddy fields, about 2.26% is urbanized area, and more than 82% is mountainous area (remaining indicates the area of water surfaces in the catchment) [20]. The average annual precipitation in the catchment is about 1244 mm, and the average monthly temperature during the study period is from −4.5 °C to 27.3 °C [21]. The surface soil texture of the Boryeong Dam catchment is dominated by sandy loam and silty loam, and the subsoil texture is mostly composed of loamy sand. The drainage grade of soil is suitable throughout the catchment [22]. The groundwater is abstracted by public electric pumping stations in the catchment. The amount of water supply of agricultural reservoirs was discharged in the Korean irrigation period between April and September.

The Boryeong Dam, which serves as a major water source in the middle-western region of Korea, recorded its lowest storage volume in 2015 due to the continuous shortage of precipitation since 2014. The water storage volume of the Boryeong Dam in 2015 decreased to 18.87% due to the extreme drought that occurred in the central region of Korea. The drought in the central region continued, and the water storage rate reached 8.29% in 2017, which is the lowest water storage level since the construction of the Boryeong Dam [23,24].

Figure 1a shows the location of the three rainfall gauging stations: one water level station at the outlet of the Boryeong Dam, and two agricultural reservoirs over the catchment [25]. Figure 1b shows the Boryeong Dam catchment divided into three sub-catchments, SC_1, SC_2, and SC_3, according to the previous study [24]. The CAT system for the Boryeong Dam catchment was constructed by dividing the catchment into three sub-catchments and then dividing the paddy field areas of each sub-catchment. The sub-catchments' information, such as the areas, slopes, and impervious area ratio, were calculated as the input data of CAT using the DEM map with 30 × 30 m resolution and of the land use map of the National Geographic Information Institute [26]. Figure 2 shows the Samsan Reservoir and the Hwasung Reservoir, which are agricultural purpose reservoirs located in the upstream of Ungcheon Stream in the Boryeong Dam catchment [25], which are located in the SC_2 sub-catchment according to the catchment division of the previous study [24]. In this study, the SC_2 sub-catchment, in which the agricultural reservoirs are located, is the target area for the streamflow simulation using CAT. The total water storage capacity and the effective water storage capacity of Samsan Reservoir are 546,200 m^3 and 543,200 m^3, respectively. The total water storage capacity and effective water storage ca-

pacity of the Hwasung Reservoir are 724,400 m^3 and 720,900 m^3, respectively [5]. Detailed information on the Samsan and Hwasung reservoirs is shown in Table 1.

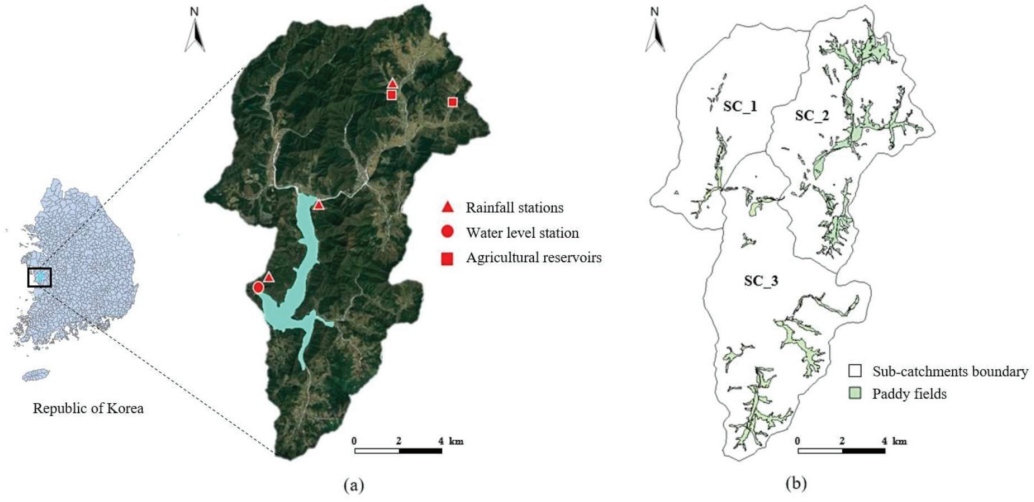

Figure 1. (**a**) Location of the rainfall stations, the water level station, and the agricultural reservoirs; (**b**) sub-catchments and paddy fields of Boryeong Dam catchment.

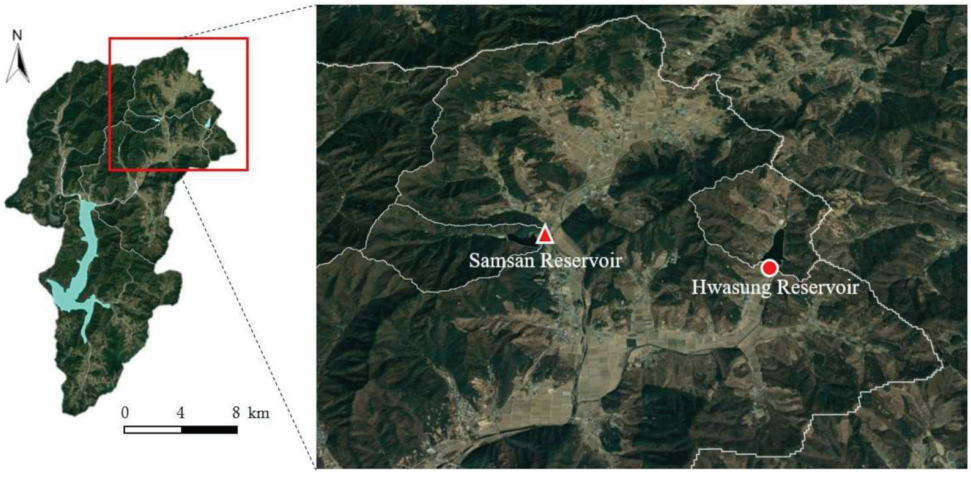

Figure 2. Location of the Samsan reservoir and the Hwasung reservoir in the SC_2 sub-catchment of the Boryeong Dam catchment.

Table 1. Geographic locations, areas, storage capacities, and embankment information of the Samsan and Hwasung reservoirs.

Reservoir	Latitude (DMS)	Longitude (DMS)	Catchment Area (km^2)	Maximum Surface Area (m^2)	Total Storage Capacity (m^3)	Effective Storage Capacity (m^3)	Height of Embankment (m)
Samsan	36°20′14″	126°43′10″	1.8	52,000	546,200	543,200	25.7
Hwasung	36°20′07″	126°45′13″	2.05	85,800	724,400	720,900	24.7

For the streamflow simulation considering the agricultural reservoirs located in the SC_2 sub-catchment, the sub-catchment was divided into 10 smaller sub-catchments according to the Samsan Reservoir catchment, Hwasung Reservoir catchment, upstream catchments, downstream catchment, and the irrigated paddy fields of each sub-catchment. The irrigated districts by two agricultural reservoirs are the target paddy fields for the analysis of soil moisture and groundwater level in this study. The irrigated paddy field by Samsan reservoir is denoted as P_Samsan node; the irrigated paddy field by Hwasung reservoir is denoted as P_Hwasung node in the CAT system. The reservoir nodes each have the upstream sub-catchments (S1 and S2), and paddy fields in S1 and S2 were also created (P1 and P2). In addition, the downstream sub-catchments of the P_Samsan and P_Hwasung were created as S3 and P3, respectively. The CAT system setup considering the division of sub-catchments and paddy fields is shown in Figure 3.

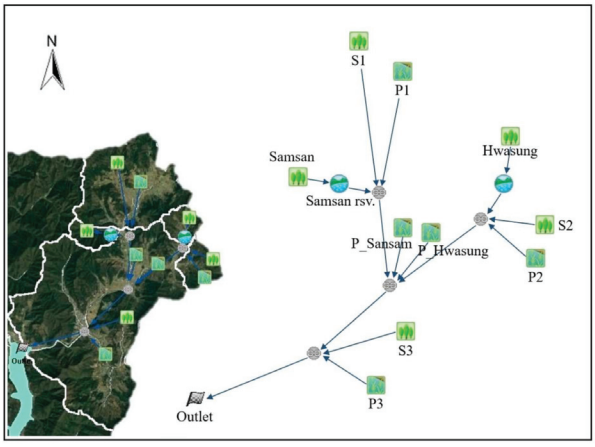

Figure 3. CAT system setup with reservoir sub-catchments, upstream sub-catchments of each reservoirs, downstream sub-catchment, and paddy fields considering Samsan and Hwasung Reservoirs.

The Samsan Reservoir and Hwasung Reservoir nodes were created to input the agricultural water supply data of the reservoirs. The areas, the slopes, and the ratio of impervious area for each sub-catchment were calculated using GIS processes. The paddy fields supplied the agricultural water from the Samsan Reservoir and Hwasung Reservoir are located in the downstream catchment outside each reservoir's sub-catchments. Detailed descriptions of sub-catchments and nodes are shown in Table 2.

Table 2. Description of each node of CAT modeling of SC_2 sub-catchment of Boryeong Dam catchment.

Node	Description	Node	Description
Samsan	Samsan reservoir catchment	S1	Upstream catchment of P_Samsan
Samsan rsv.	Samsan reservoir	P1	Paddy field in C1
P_Samsan	Irrigated paddy field by Samsan reservoir	S2	Upstream catchment of P_Hwasung
Hwasung	Hwasung reservoir catchment	P2	Paddy field in C2
Hwasung_rsv.	Hwasung reservoir	S3	Downstream catchment
P_Hwasung	Irrigated paddy field by Hwasung reservoir	P3	Paddy field in C3

Table 3 shows the areas, slopes, impervious area ratio, and the amount of groundwater withdrawals by pumping in each sub-catchment and paddy field. About 90% of the groundwater withdrawals in the Boryeong Dam catchment is used for agricultural purposes, and the remaining 10% is used for domestic and industrial water demands. Agricultural water consumptions in the sub-catchments were input to the irrigated paddy fields of each sub-catchment, and water consumptions for domestic and industrial demands were input to the remaining forest sub-catchments, except for paddy fields.

Table 3. Area, slope, impervious area ratio, and annual amount of groundwater abstraction in sub-catchments and paddy fields.

Sub-Catchments	**Samsan**	**Hwasung**	**S1**	**S2**	**S3**
Area (km^2)	1.8	2.05	12.25	30.70	2.21
Slope (%)	0.354	0.282	0.281	0.277	0.302
Impv_a (%)	1.02	2.46	5.48	7.84	3.11
GW_pump (m^3/day)	19.58	22.30	133.24	333.93	23.98
Paddy Fields	**P_Samsan**	**P_Hwasung**	**P1**	**P2**	**P3**
Area (km^2)	0.8	0.80	2.5	0.20	3.12
Slope (%)	0.122	0.110	0.095	0.088	0.079
Impv_a (%)	0.00	0.00	0.00	0.00	0.00
GW_pump (m^3/day)	1384.91	1388.37	4327.84	342.77	5401.14

Impv_a refers to the ratio of impervious area; GW_pump refers to observed daily groundwater abstraction.

2.2. CAT Model

CAT is a physical parameter-based and distributed hydrological model that allows the quantitative evaluation of the long- and short-term water cycles of the catchment. CAT is a node- and link-connecting model designed to estimate the hydrological components, such as runoff, infiltration, soil moisture content, evapotranspiration, and baseflow, for each spatial unit. It divides the hydrological cycle process into pervious and impervious areas. The model simulation can be conducted with minute, hour, day, month, and year time step data. The basic concept of the model is based on the unconfined aquifer and single soil layer assumptions. The model categorizes the incoming rainfall into falling on pervious, impervious, and paddy field areas, yielding the surface flow, infiltration, or evapotranspiration (Figure 4). The major physical parameters required for the initial simulation are area, slope, soil type, land use, aquifer, and river information. The basic concept of the model is based on the unconfined aquifer and single soil layer assumptions [27]. In addition, the CAT simulation can be carried out taking into account the actual agriculture situation, such as water supply from agricultural reservoirs, irrigation period, and levee height in the paddy fields of the catchment.

The CAT model has been applied in various hydrological studies for different catchments. Jang et al. [28] analyzed the long-term hydrological responses of agricultural reservoirs in the Idong catchment; Jang et al. [29] assessed the future climate change impacts on the hydrological components in the Gyeongan–Cheon River Basin. Birhanu et al. [30] analyzed and compared the results of five hydrological models, including CAT, applying them in 10 catchments of Korea. Choi et al. [31] carried out a short-term CAT runoff simulation and a sensitivity analysis of soil parameters using three infiltration methods provided in CAT. Lee and Cho [32] analyzed the hydrological cycle in four catchments in Ulsan City using CAT. Miller et al. [33] evaluated stormwater runoff characteristics according to the transformation of rural landscapes into peri-urban areas in the U.K. using CAT.

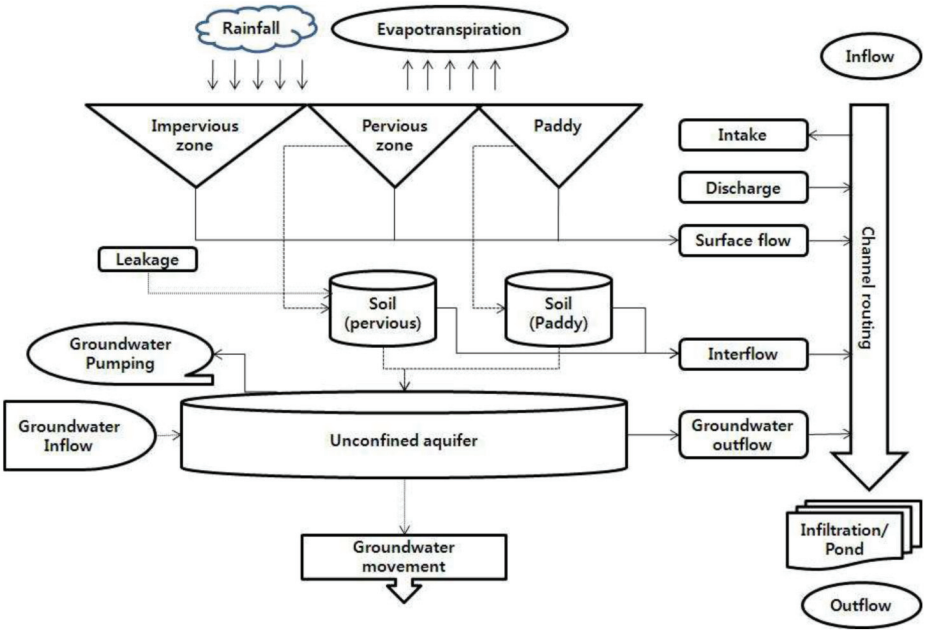

Figure 4. Schematic diagram of water cycle process in CAT model [34].

2.3. Water Cycle Processes of Reservoir and Paddy Field in CAT

In the CAT model, the storage facility node (or reservoir node) can be applied as an online reservoir when the reservoir is located within the stream channel, or as an offline reservoir when the reservoir is located outside the stream channel. In this study, the reservoir node was applied as an online reservoir by reflecting the field situations of the Boryeong Dam catchment. The reservoir node considers the amount of evaporation from the surface of the reservoir and intake amount of water to calculate the amount of outflow discharged through the outlet (Figure 5).

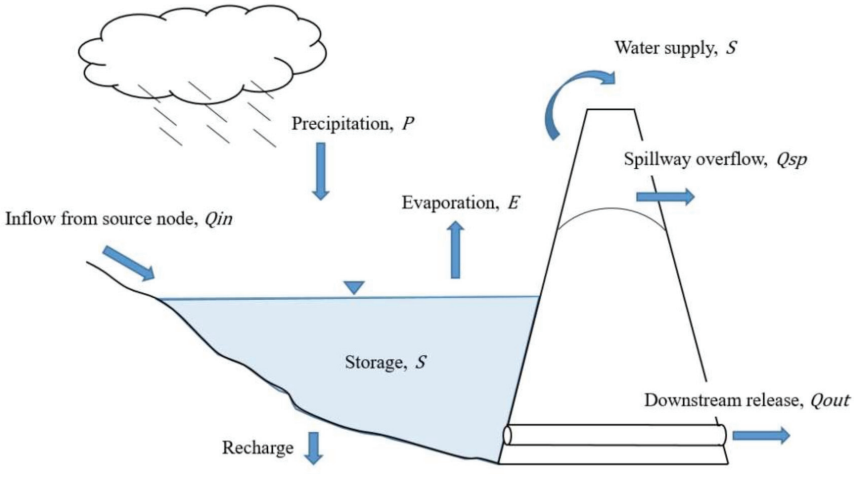

Figure 5. Schematic diagram of hydrological cycle in reservoir in CAT model.

The governing equation is:

$$\frac{dS}{dt} = Qin - Qout - Qsp + P - E \quad (1)$$

where S is the storage volume (m^3), Q_{in} is the inflow to the reservoir (m^3/s), Q_{out} is the outflow of the reservoir (m^3/s), Q_{sp} is the spillway overflow (m^3/s), P is the precipitation to the surface of reservoir (mm), and E is the evaporation from the surface of the reservoir (mm) [34].

To simulate the runoff process in the paddy field (Figure 6), the soil and groundwater layers were divided in the same way as the pervious area of the watershed. Artificial drainage facilities can be included in the soil layer to accommodate underground culvert drainage and pipe drainage; however, only surface drainage by levee height was considered in this study according to the field situation of the catchment. Surface drainage occurs when the ponding depth is greater than the height of the surface drain water threshold.

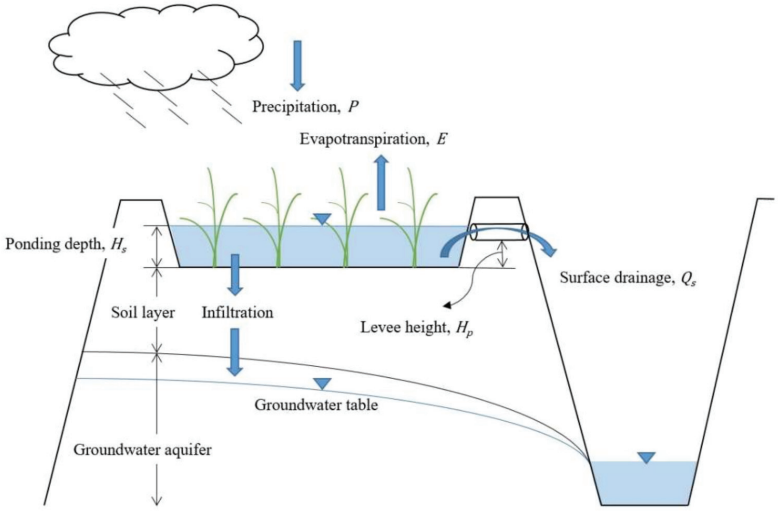

Figure 6. Schematic diagram of the hydrological cycle in the paddy field in CAT model.

The surface drain equations are:

$$Q_s = \alpha\sqrt{H_s - H_p}(H_s > H_p) \quad (2)$$

$$Q_s = 0 \quad (H_s \leq H_p) \quad (3)$$

where Q_s is the discharge from the surface (m^3/s), α is the drainage coefficient of the surface drain levee in the paddy ($mm^{0.5}/h$), H_s is the ponding depth of the paddy (m), and H_p is the height of the surface drain levee of the paddy (m) [34].

The hydrological interrelation between surface water and groundwater was calculated according to Darcy's Law, with flows based on the hydraulic conductivities, river stage, and groundwater level. The interrelation between the river level and the groundwater level was calculated using Equations (4) and (5). Equation (5) was applied when the river level was higher than the groundwater level in the vicinity; otherwise, Equation (4) was applied.

$$Q_r = K_{sr}A_r \quad (4)$$

$$Q_r = K_{sr}\left(\frac{h - H_r}{b_r}\right)A_r \quad (5)$$

$$Q_g = K_{sr} \frac{\partial h}{\partial x} \cdot l \cdot T \tag{6}$$

$$Q_{in} - Q_{out} = A \cdot S \frac{dh}{dt} \tag{7}$$

where Q_r is the inflow into the river or recharge from the river (m^3/s); Q_g is the groundwater flow (m^3/s); Q_{in} and Q_{out} are the inflow and outflow of the aquifer (m^3/s), respectively; K_{sr} is the saturated hydraulic conductivity of the riverbed (m/s); A_r is the area of the riverbed (m^2); b_r is the riverbed thickness (m); h is the groundwater level (m); H_r is the riverbed elevation (m); $\partial h/\partial x$ is the slope of the groundwater level; l is the connected length between catchments (m); T is the average aquifer thickness (m); A is the catchment area (m^2); S is the storage coefficient; and dh/dt is the rate of level change [34].

2.4. Data Collection

The daily precipitation, streamflow, and meteorological data from 2000 to 2019 were already collected for a previous study [24]. The daily precipitation data were gathered from the three rainfall gauging stations operated by K-water [23]. The daily meteorological data used for the Penman–Monteith evapotranspiration estimation, such as minimum and maximum temperature (°C), humidity (%), sunshine hours, and wind speed (m/s), were gathered from the Boryeong Meteorological Station located a relatively short distance from the Boryeong Dam catchment [21]. Evapotranspiration is a critical factor of hydrological processes, especially in arid or semiarid catchments. Generally, to choose the relevant PET (potential evapotranspiration) estimation method for hydrological modeling, researchers often recommend the Penman–Monteith method as the standard for reference the evaporation estimation, which is a physically based combination equation that is able to describe the evaporation processes [35,36]. Therefore, the Penman–Monteith method was applied to estimate PET in this study. Figure 7a shows the observed precipitation and streamflow; Figure 7b shows the simulated actual and potential evapotranspiration in 2000–2019.

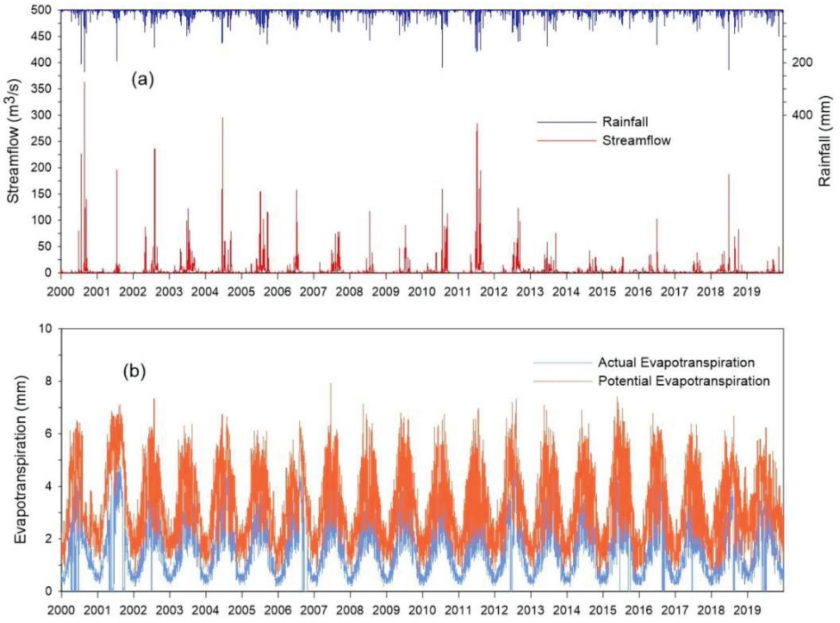

Figure 7. (**a**) Observed rainfall and streamflow data for 2000–2019; (**b**) estimated potential and actual evapotranspiration in the Boryeong Dam catchment.

The monthly agricultural water supply data from 2012 to 2018 were collected [5] as input data for agricultural reservoirs. The daily observed water storage data for Samsan and Hwasung reservoirs [5] were collected from May 2012 to December 2018 to compare with the simulated reservoir storage. For groundwater pumping data, the annual data for 2008–2017 were collected and applied [23]. Water balance analysis of the SC_2 sub-catchment was performed for 2012–2017, which included all data. The soil parameter data were extracted using the 1:25,000 scale soil map provided by the Rural Development Administration [37]. The land use map of the Ministry of Environment [20] was applied to classify forest area and paddy field area of the catchment. All model input data for CAT simulation were input by dividing the catchment into pervious and impervious areas. Most of the agricultural water is supplied during the irrigation period, from April to September. In 2018, both reservoirs supplied agricultural water from May to August. The monthly amount of agricultural water supply usually varies depending on the rice growth process in paddy fields. In the Samsan Reservoir and Hwasung Reservoir, agricultural water supply was the highest in May and lowest in April (Figure 8).

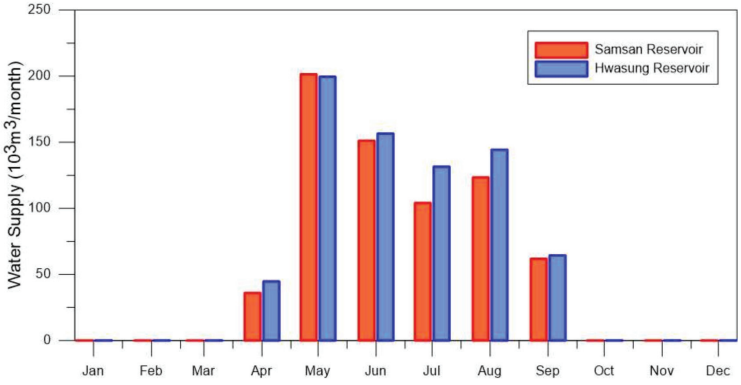

Figure 8. Average monthly amount of agricultural water supply of Samsan Reservoir and Hwasung Reservoir.

In April, the total amounts of agricultural water supply of the Samsan Reservoir and Hwasung Reservoir were 36,007 m^3 and 44,670 m^3, respectively, and the total agricultural water supply amounts in May were 201,431 m^3 and 199,541 m^3, respectively, indicating that the largest consumption of agricultural water is in May when rice planting begins. The total agricultural water supply by year of each reservoir is shown in Table 4.

Table 4. Annual agricultural water supply of the Samsan and Hwasung reservoirs.

					(Unit: 10^3 m^3)
Year	**Samsan Rsv.**	**Hwasung Rsv.**	**Year**	**Samsan Rsv.**	**Hwasung Rsv.**
2012	944.8	953.33	2016	338.63	642.17
2013	814.6	822.8	2017	685.64	415.72
2014	782.6	899.33	2018	625.26	579.79
2015	553.93	873.49	Avg.	677.92	740.95

In the case of Samsan Reservoir, the annual average of 677,920 m^3 of the agricultural water was supplied to the irrigation district from 2012 to 2018; for the Hwasung Reservoir, an annual average of 740,950 m^3 of agricultural water was supplied.

The daily observed storage data, the monthly agricultural water supply data, and the specification of the Samsan and Hwasung reservoirs were collected from the Rural Agricultural Water Resource Information System (RAWRIS) [38] managed by the Korea Rural Community Corporation [5].

2.5. Model Performance Indicators

The multi-objective functions used for evaluating model performances in this study were the Kling–Gupta Efficiency (KGE), Nash–Sutcliffe Efficiency (NSE), LogNSE, the determination coefficient (R^2), and the root mean square error–observations standard deviation ratio (RSR).

NSE is a normalized indicator that determines the relative magnitude of the residual variance compared to the observed data variance; however, it has the disadvantage that the peak value is often overestimated or the valley value is often underestimated by comparing the variance of the error and the variance of the observed values in a relative volume. LogNSE is the logarithm-transformed NSE often applied to put more importance on low flow simulations in hydrological modeling [39]. KGE is an index that aims to overcome the disadvantages of NSE by considering the correlation coefficient and the mean as well as variance. RSR was developed to standardize RMSE using observations in standard deviation, combining the error index and the additional information [40].

The values of the model performance evaluation index closer to 1, excluding RSR, indicate better model performance; in the case of RSR, the closer to 0, the better the model performance. When the NSE > 0.5 and RSR < 0.6, it can be judged as a satisfactory model performance [41].

$$KGE = 1 - \sqrt{(R^2[Q_{obs}, Q_{sim}] - 1)^2 + \left(\frac{SD[Q_{sim}]}{SD[Q_{obs]}} - 1\right)^2 + \left(\frac{M[Q_{sim}]}{M[Q_{obs}]} - 1\right)^2} \quad (8)$$

$$NSE = 1 - \frac{\sum(Q_{obs} - Q_{sim})^2}{\sum(Q_{obs} - Q_{mean})^2} \quad (9)$$

$$R^2 = 1 - \frac{\sum(Q_{obs} - Q_{sim})^2}{\sum(Q_{obs} - \overline{Q_{obs}})^2} \quad (10)$$

$$RSR = \frac{RMSE}{SD[Q_{obs}]} = \frac{\sqrt{\sum(Q_{obs} - Q_{sim})^2}}{\sqrt{\sum(Q_{obs} - Q_{mean})^2}} \quad (11)$$

where Q_{obs}, Q_{sim}, and Q_{mean} are the observed, simulated, and mean observed streamflow, respectively. SD and M are the standard deviation and mean, respectively.

In this study, the daily simulated streamflow was compared to the daily observed streamflow for the CAT model performance evaluation.

3. Results and Discussions

3.1. Model Performance of CAT

The model performance of the CAT simulation for the SC_2 sub-catchment of the Boryeong Dam catchment was evaluated by model performance indicators. As there are no observed streamflow data in the SC_2 sub-catchment, the streamflow data were estimated by dividing the total streamflow from the outlet of the entire Boryeong Dam catchment by the area ratio of the SC_2 sub-catchment according to the drainage area ratio method [42].

The CAT runoff simulation was carried out during the period of 2012–2017, including both the agricultural water supply data and the groundwater abstraction data of Samsan and Hwasung reservoirs. As a result of the daily runoff simulation, the simulated streamflow was well-matched to the observed one (Figure 9a). The KGE, NSE, R^2, and RSR values were 0.88, 0.79, 0.80, and 0.42, respectively, indicating the satisfactory accuracy of the CAT model (Figure 9b). The simulated streamflow tended to be slightly underestimated against the observed one when the streamflow was small, and it tended to be slightly overestimated when the streamflow was large.

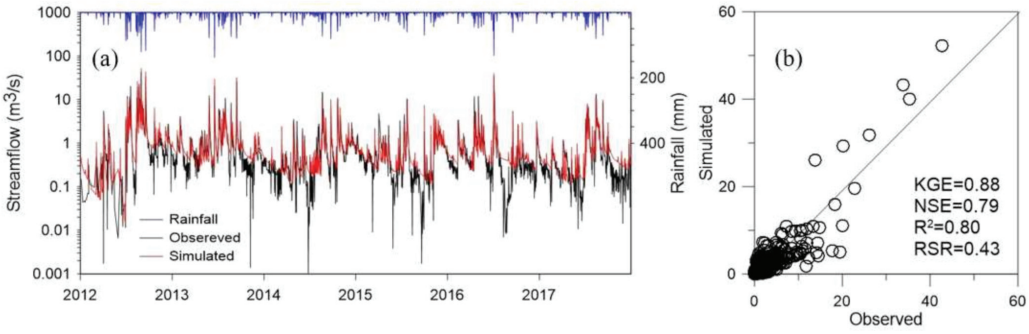

Figure 9. (**a**) Comparison of the estimated observed streamflow and the CAT simulated streamflow. (**b**) Scatter plot of observe and simulated streamflow and the model performances by statistical indicators.

The observed storage data of the Samsan Reservoir and Hwasung Reservoir for May 2012 to December 2018 [5] were compared with the CAT simulated storage (Figure 10). Comparing the sum of observed and simulated daily storages during the study period, the simulated storage of the Samsan Reservoir was 99.84% of the observed storage, and the simulated storage of the Hwasung Reservoir was 99.1% of the observed storage. The CAT simulated storage was underestimated or overestimated by year; however, the annual inflow calibration was not performed in the Samsan and Hwasung nodes, as this study aims to analyze the water balance through long-term runoff simulation and the soil moisture and groundwater level in the paddy fields, according to the agricultural water supply of the reservoir.

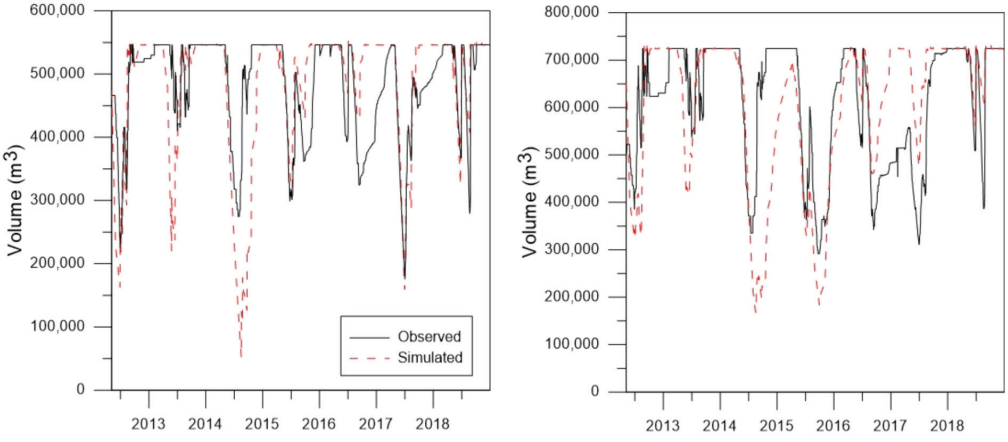

Figure 10. Comparison of the observed and the simulated water storage of Samsan Reservoir and Hwasung Reservoir from May 2012 to December 2018.

3.2. Water Balance Analysis

To analyze the change in water cycle in the catchment according to the presence or absence of the agricultural reservoirs, two models with and without the reservoirs were constructed, and the simulated water balances were compared. The model without reservoirs and the model with reservoirs were constructed with the same conditions, except for the amount of water intake from the agricultural reservoirs.

Figure 11a shows the simulated water balance of the SC_2 sub-catchment to which agricultural reservoirs were applied. Figure 11b shows the simulated water balance to

which agricultural reservoirs were not applied. When the agricultural reservoirs were applied in the CAT simulation, the amount of inflow due to the supply of agricultural water from the reservoirs was considered. The results showed that the total amount of streamflow and the groundwater recharge increase because the reserved water from Samsan and Hwasung reservoirs was supplied to the soil surface of the catchment.

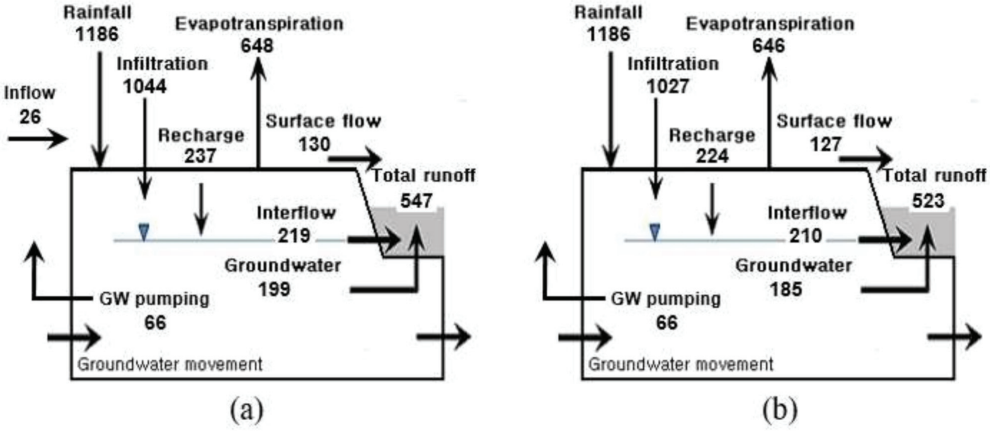

Figure 11. (**a**) Simulated water cycle of the CAT model with application of agricultural reservoirs. (**b**) Simulated water cycle of the CAT model without application of agricultural reservoirs.

By applying the agricultural reservoirs, the total amount of runoff in the Boryeong Dam catchment increased by about 4.72% over the study period due to the supply of agricultural water. The surface runoff, interflow, and baseflow increased by 1.27%, 4.44%, and 6.81%, respectively, and the amount of groundwater recharge increased by about 5.67% (Table 5). Therefore, as the amount of total runoff and groundwater recharge of the catchment increase according to the application of the agricultural reservoirs in the CAT simulation, it can be effective in improving the water cycle soundness of the catchment by proper operation of reservoirs.

Table 5. Increase rate of amount of runoff and groundwater recharge after application of agricultural reservoirs compared to the amount of runoff and groundwater recharge before the application of agricultural reservoirs.

(Unit: %)

Year	Total Runoff	Surface Runoff	Interflow	Baseflow	Recharge
2012	3.71	3.01	2.98	5.57	3.95
2013	4.35	1.84	3.81	6.39	4.95
2014	7.35	0.36	6.91	11.40	8.82
2015	5.48	0.88	5.38	7.48	6.94
2016	2.96	0.61	3.20	4.27	4.13
2017	4.45	0.93	4.37	5.78	5.23
Avg.	4.72	1.27	4.44	6.81	5.67

3.3. Soil Moisture Content of Paddy Fields

As the soil moisture content is a hydrological component that directly affects crop growth, the accurate estimation of soil moisture content in paddy fields should be preceded in the hydrological analysis of agricultural watersheds. In this study, to analyze the effect of drought on the soil moisture content in paddy fields, the representative drought and normal years were divided and analyzed within the study period. Comparing the

drought index in Buyeo-gun [14], where the SC_2 sub-catchment is located, the SGI and SPI drought indices in 2013 were confirmed to be the normal year, and the SMI drought indices indicated frequent dryness. In 2015, SGI indicated the caution drought level, SPI indicated the extreme drought level, and SMI indicated the frequent dry or normal drought level. Therefore, 2013 was selected as the WET period and 2015 as the DRY period, representing the year of severe drought. For soil moisture content analysis, the models with and without the reservoirs were compared according to the WET and DRY periods.

Figure 12a,b show the change in soil moisture content at the P_Samsan node according to the WET and DRY periods when the Samsan Reservoir was applied. Figure 12c,d show the change in soil moisture content at the P_Hwasung node according to the WET and DRY periods when the Hwasung Reservoir was applied. The CAT simulation indicated that the soil moisture content increases during the irrigation period from April to September when the agricultural reservoirs were applied to the CAT model. In the WET period, the difference in soil moisture according to the application of the reservoirs is significant from April, when the irrigation season begins, until the end of June, when the rainy season starts. In the DRY period, the difference in the soil moisture content according to the application of the reservoirs is significantly large until November due to the lack of precipitation. There was no significant difference in the trends of soil moisture content changes in the Samsan Reservoir and Hwasung Reservoir. The analyses of the change in soil moisture content by irrigation and non-irrigation periods are shown in Figure 13.

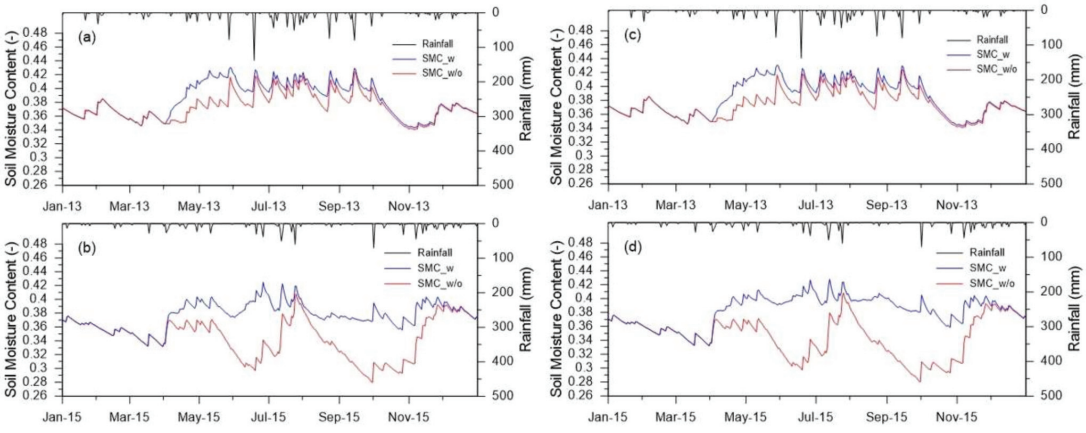

Figure 12. (**a**) Soil moisture content changes of P_Samsan in the WET year by applying reservoir nodes in CAT. (**b**) Soil moisture content changes of P_Samsan in the DRY year by applying reservoir nodes in CAT. (**c**) Soil moisture content changes of P_Hwasung in the WET year by applying reservoir nodes in CAT. (**d**) Soil moisture content changes of P_Hwasung in the DRY year by applying reservoir nodes in CAT.

The increase rate of the soil moisture content according to the application of the agricultural reservoirs was higher in the irrigation period than in the non-irrigation period, and was higher in the DRY period than in the WET period. In the WET period, the average soil moisture content during the irrigation period increased by 5.25% for P_Samsan and by 5.14% for P_Hwasung, according to the operation of the agricultural reservoirs. The average soil moisture content for P_Samsan and P_Hwasung during the non-irrigation period increased by 0.44% and 0.43%, respectively. In the DRY period, the average soil moisture content during the irrigation period increased by 8.91% for P_Samsan and 10.92% for P_Hwasung, according to the operation of the agricultural reservoirs. The average soil moisture content for P_Samsan and P_Hwasung during the non-irrigation period increased by 2.49% and 2.59%, respectively (Table 6).

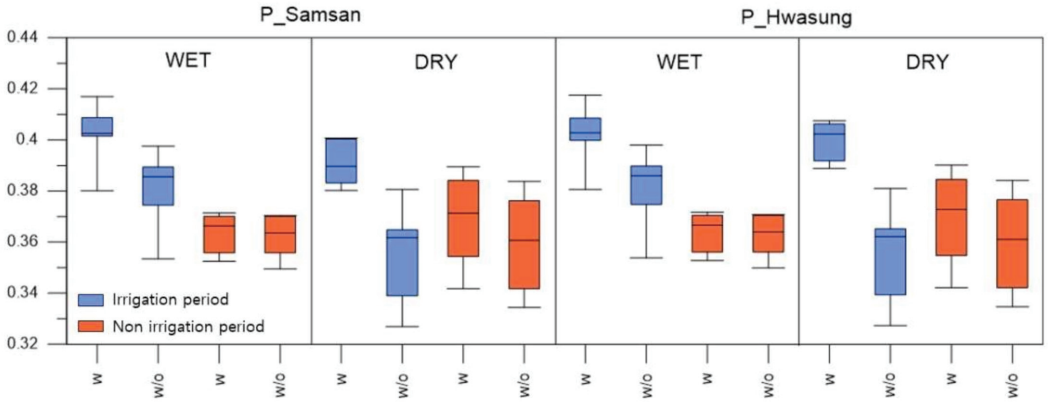

Figure 13. The changes in soil moisture content of P_Samsan and P_Hwasung in the irrigation period and the non-irrigation period by WET and DRY years.

Table 6. Average soil moisture in irrigation and non-irrigation periods and the increase rate by applying agricultural reservoirs.

Period		P_Samsan			P_Hwasung		
		w/o	w	Increase (%)	w/o	w	Increase (%)
WET	Irrig.	0.381	0.402	5.25	0.381	0.402	5.14
	Non irrig.	0.362	0.364	0.44	0.362	0.364	0.43
DRY	Irrig.	0.356	0.391	8.91	0.356	0.400	10.92
	Non irrig.	0.360	0.369	2.49	0.360	0.370	2.59

Irrig. refers to the irrigation period of April to September. Non_irrig. refers to the non-irrigation period. w/o refers to the modeling without the reservoirs, and w refers to the modeling with the reservoirs.

The increase rate of soil moisture content during the DRY period was relatively higher than that during the WET period because the soil layer dried due to drought and lack of precipitation; therefore, it responded sensitively to the reservoir agricultural water supply and absorbed more water. Soil moisture is the retained water in the topsoil layer and has direct effects on the growth of rice during the irrigation period. Analyzing the changes in soil moisture content during the irrigation period in Korea from April to September, we can see that the agricultural water supplies of reservoirs significantly affected the soil moisture increase in the paddy fields, especially in the drought period. Therefore, in order to secure the soil moisture demands for agricultural activities in the paddy catchments, it is necessary to supply sufficient amounts of agricultural water through the installation of agricultural reservoirs.

3.4. The Groundwater Elevation in Paddy Fields

The groundwater elevation changes in P_Samsan and P_Hwasung according to the application of the Samsan Reservoir and Hwasung Reservoir were compared for the WET and DRY periods. Figure 14 indicated that the increase rate of the groundwater elevation due to the operation of the agricultural reservoirs was higher in the WET period than in the DRY period because the rate of groundwater abstraction was lower in the drought period than that in normal period in the catchment [24].

The increase rate of the soil moisture content according to the application of the reservoirs was higher during the DRY period; however, in the case of the groundwater elevation, the increase rate in the WET period was higher than in the DRY period, according to the application of the agricultural reservoirs.

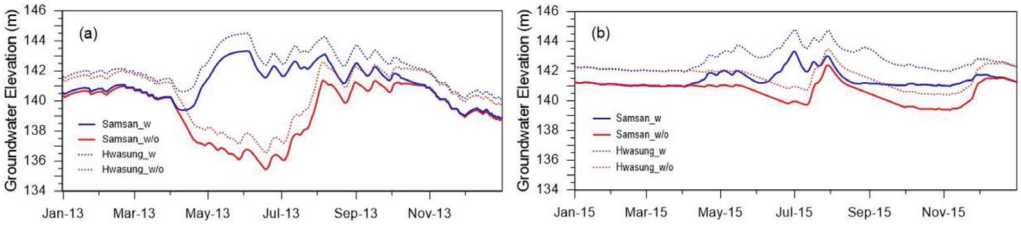

Figure 14. (**a**) Changes in groundwater elevation of P_Samsan and P_Hwasung, according to the application of agricultural reservoirs in the WET period. (**b**) Changes in groundwater elevation of P_Samsan and P_Hwasung, according to the application of agricultural reservoirs in the DRY period.

In the WET period, the difference in groundwater elevation reached 6.11 m in the P_Samsan node and 6.24 m in the P_Hwasung node according to the application of the agricultural reservoirs; the difference in May was the largest of the year. In the DRY period, the difference in groundwater level was 1.77 m in the P_Samsan node and 2.39 m in the P_Hwasung node according to the application of the agricultural reservoirs; the difference in June was analyzed to be the largest of the year (Table 7). During the DRY period, the total amount of groundwater consumption was smaller than in the WET period; therefore, the decrease in the groundwater elevation due to groundwater pumping was not significant in the DRY period. The amount of groundwater abstraction in 2013 was 2255 m^3/day and 2261 m^3/day for P_Samsan and P_Hwasung, respectively; in 2015, it was 457 m^3/day and 458 m^3/day, respectively. Therefore, the difference in groundwater elevation according to the application of the agricultural reservoirs was larger in the WET period than in the DRY period. If the reservoir is not operated, the groundwater level in the paddy field will decrease rapidly as irrigation begins in April. The supply of agricultural water from the reservoirs to the paddy fields seems to prevent the decrease in the groundwater elevation in irrigation period.

Table 7. Increased monthly groundwater elevation of P_Samsan and P_Hwasung after application of agricultural reservoirs compared to monthly groundwater elevation before application of agricultural reservoirs.

				(Unit: m)
Month	**WET**		**DRY**	
	P_Samsan	**P_Hwasung**	**P_Samsan**	**P_Hwasung**
Jan	0.20	0.28	0.00	0.03
Feb	0.15	0.23	0.00	0.02
Mar	0.07	0.19	0.00	0.03
Apr	1.82	2.04	0.43	0.56
May	6.11	6.24	0.83	1.41
Jun	6.09	5.92	1.77	2.39
Jul	4.44	4.19	1.74	2.31
Aug	1.42	1.48	0.40	1.43
Sep	0.94	1.04	1.08	1.74
Oct	0.25	0.29	1.59	1.71
Nov	0.04	0.14	1.41	1.44
Dec	0.12	0.34	0.13	0.17
Avg.	1.81	1.87	0.78	1.11

4. Conclusions

The effect of agricultural reservoirs on improving the water cycle of the SC_2 subcatchment of the Boryeong Dam catchment was evaluated by applying agricultural reservoir nodes in the CAT model, and the soil moisture content and groundwater elevation

changes in paddy fields were compared and analyzed according to the division of normal and drought periods.

As a result of the CAT runoff simulation for the SC_2 sub-catchment, the KGE, NSE, R^2, and RSR indicators were 0.88, 0.79, 0.80, and 0.42, respectively, indicating the satisfactory performance of the CAT model. The observed streamflow was estimated by the area ratio and total discharge at the outlet of the entire Boryeong Dam catchment. Comparing the simulated water storage of the Samsan Reservoir and the Hwasung Reservoir with the observed water storage, there is a match of more than 99% in terms of the total water storage volume during the study period; however, it was either under or overestimated by year. In this paper, as the long-term streamflow simulation for 2012–2017 is performed, the yearly calibration for the reservoirs' storage was not conducted. To analyze the water balance of the SC_2 sub-catchment, the results were compared by simulating the model that applied the agricultural reservoirs in the catchment and the model that did not apply the agricultural reservoirs. As a result of the streamflow simulation, the total amount of streamflow and the groundwater recharge of the catchment increased when considering the agricultural water supply, according to the application of the agricultural reservoirs. The total streamflow increased by 4.92% per year on average, and the groundwater recharge increased by 5.96% per year on average. In addition, to analyze the soil moisture content and groundwater elevation in the reservoirs irrigated districts, WET and DRY periods were selected during the study period according to the SGI, SPI, and SMI drought indices. Analyzing the soil moisture content in WET and DRY periods according to the agricultural reservoirs' application, it is evident that the soil moisture content in the irrigation period from April to September increased when the reservoir was applied. The increase in soil moisture content was significant during the DRY period and was analyzed to be higher during the irrigation period than the non-irrigation period. In particular, the high rate of increase in the soil moisture content during the DRY period is likely due to the sensitive response of the dried soil layer to the water supply of the agricultural reservoirs. On the other hand, it was analyzed that the increase rate of the groundwater elevation with the application of the agricultural reservoirs was higher in the WET period than the DRY period. During the drought period, the groundwater elevation decreased significantly as irrigation began in April, and the groundwater elevation decreased significantly during the drought period due to groundwater pumping. It was analyzed that the reservoir intake prevents the decrease in the groundwater elevation in paddy fields. There were differences in the groundwater elevation of about 6 m depending on the reservoirs during the WET period.

Therefore, the installation of agricultural reservoirs has the effect of improving the water cycle of the catchment by increasing the streamflow and groundwater recharge, the soil moisture content, and the groundwater elevation. In particular, the soil moisture content in paddy fields provides the water necessary for crop growth during the irrigation period; therefore, the increase in soil moisture content according to the supply of agricultural reservoirs is meaningful. Due to the application of the reservoirs, the soil moisture content during the irrigation period in the DRY period increases by about 10%, indicating that the impact of the agricultural reservoir on the irrigated districts is significant. As the agricultural water demands mainly depend on the supply of groundwater pumping and reservoir intake, accurate analyses of the water cycle, soil moisture content, and groundwater level in the watershed through the hydrological model should precede the designing of relevant agricultural reservoirs for the adequate conservation of groundwater.

Author Contributions: Conceptualization, S.P. and H.K.; Methodology, S.P., H.K., C.J., and D.K.; Formal analysis, S.P.; Investigation, S.P. and C.J.; Resources, S.P. and C.J.; Data curation, S.P. and H.K.; Writing—original draft preparation, S.P.; Writing—review and editing, H.K.; Supervision, H.K. and C.J.; Project administration, H.K.; Funding acquisition, H.K. All authors have read and agreed to the published version of the manuscript.

Funding: This research was funded by the Korea Institute of Civil Engineering and Building Technology, grant number 20210194-001.

Institutional Review Board Statement: Not applicable.

Informed Consent Statement: Not applicable.

Data Availability Statement: This study did not include any publicly available datasets.

Conflicts of Interest: The authors declare no conflict of interest.

References

1. Zhang, G.; Xiao, X.; Dong, J.; Xin, F.; Zhang, Y.; Qin, Y.; Doughty, R.B.; Moore, B. Fingerprint of rice paddies in spatial-temporal dynamics of atmospheric methane concentration in monsoon Asia. *Nat. Commun.* **2020**, *11*, 554. [CrossRef] [PubMed]
2. Statistics Korea. Available online: http://kostat.go.kr (accessed on 20 December 2021).
3. Kim, S.; Song, J.; Hwang, S.; Kim, H.; Kang, M. Development of agricultural water circulation rate considering agricultural reservoir and irrigation district. *J. Korean Soc. Agric. Eng.* **2020**, *62*, 83–95. [CrossRef]
4. Kim, N.W.; Lee, J.; Chung, I.M.; Lee, M.H. Combined effects of groundwater abstraction and irrigation reservoir on streamflow. *J. Korea Water Resour. Assoc.* **2013**, *46*, 719–733. [CrossRef]
5. Korea Rural Community Corporation. Available online: https://www.ekr.or.kr/homepage/main.krc (accessed on 20 December 2021).
6. Hong, J.; Choi, Y.; Yi, J. Parameter optimization of agricultural reservoir long-term runoff model based on historical data. *J. Korea Water Resour. Assoc.* **2021**, *54*, 93–104. [CrossRef]
7. Ministry of Land, Infrastructure and Transport. Available online: http://www.molit.go.kr/english/intro.do (accessed on 20 December 2021).
8. Nam, W.; Kwon, H.J.; Choi, K. Reevaluation of design frequency of drought and water supply safety for agricultural reservoirs under changing climate and farming methods in paddy fields. *J. Korean. Soc. Agric. Eng.* **2018**, *60*, 121–131. [CrossRef]
9. Nam, W.H.; Hong, E.M.; Jang, M.W.; Choi, J.Y. Projection of consumptive use and irrigation water for major upland crops using soil moisture model under climate change. *J. Korean Soc. Agric. Eng.* **2014**, *56*, 77–87. [CrossRef]
10. Nam, W.H.; Choi, J.Y.; Jang, M.W.; Hong, E.M. Agricultural drought risk assessment using reservoir drought index. *J. Korean Soc. Agric. Eng.* **2013**, *55*, 41–49. [CrossRef]
11. Kim, J.U.; Lee, J.W.; Kim, S.J. Evaluation of the future agricultural drought severity of South Korea by using reservoir drought index (RDI) and climate change scenarios. *J. Korea Water Resour. Assoc.* **2019**, *52*, 381–395. [CrossRef]
12. Bae, S.J.; Chung, H.W.; Choi, J.Y. Agricultural drought analysis using soil water balance model and geographic information system. *J. Korean Soc. Agric. Eng.* **1999**, *41*, 33–43.
13. Shin, Y.; Lee, T.; Kim, S.; Lee, H.W.; Choi, K.S.; Kim, J.; Lee, G. Development of agricultural drought approach using SMAP soil moisture footprints. *J. Korean Soc. Agric. Eng.* **2017**, *59*, 57–70. [CrossRef]
14. National Drought Information Portal. Available online: https://www.drought.go.kr (accessed on 20 December 2021).
15. Lee, D.G.; Song, J.; Ryu, J.H.; Lee, J.; Choi, S.; Kang, M.S. Integrating the mechanisms of agricultural reservoir and paddy cultivation to the HSPF-MASA-CREAMS-PADDY system. *J. Korean Soc. Agric. Eng.* **2018**, *60*, 60–68. [CrossRef]
16. Kim, B.K.; Kim, B.S.; Kwon, H.H. Impact assessment of agricultural reservoir on streamflow simulation using semi-distributed hydrologic model. *KSCE J. Civ. Eng.* **2008**, *29*, 11–22.
17. Lee, J.; Kim, N.W.; Chung, I.; Lee, J.E. Effects of irrigation reservoirs and groundwater withdrawals on streamflow for the Anseongcheon Upper Watershed. *KSCE J. Civ. Eng.* **2015**, *35*, 835–844. [CrossRef]
18. Lee, J.; Noh, J. Evaluating future stream flow by operation of agricultural reservoir group considering the RCP 8.5 climate change scenario. *J. Korean Soc. Agric. Eng.* **2015**, *57*, 113–122. [CrossRef]
19. Cho, Y.; Park, S.; Na, J.; Kim, T.; Lee, J. Hydrological and ecological alteration of river dynamics due to multipurpose dams. *J. Wetl. Res.* **2019**, *21*, 16–27. [CrossRef]
20. Ministry of Environment. Available online: http://me.go.kr (accessed on 20 December 2021).
21. Korea Meteorological Administration. Available online: http://hydro.kma.go.kr (accessed on 20 December 2021).
22. Korean Soil Information System. Available online: http://soil.rda.go.kr/eng/ (accessed on 20 December 2021).
23. Korea Water Resources Corporation. Available online: https://www.water.or.kr (accessed on 20 December 2021).
24. Park, S.; Kim, H.; Jang, C. Impact of groundwater abstraction on hydrological responses during extreme drought periods in the Boryeong Dam catchment, Korea. *Water* **2021**, *13*, 2132. [CrossRef]
25. Google Earth. Available online: https://earth.google.com/web/ (accessed on 28 January 2022).
26. National Geographic Information Institute. Available online: https://www.ngii.go.kr/eng/main.do (accessed on 20 December 2021).
27. Kim, H.J.; Jang, C.H.; Noh, S.J. Development and application of the catchment hydrologic cycle assessment tool considering urbanization (I)—Model development-. *J. Korea Water Resour. Assoc.* **2012**, *45*, 203–215. [CrossRef]
28. Jang, C.H.; Kim, H.J.; Kim, J.T. Prediction of reservoir water level using CAT. *J. Korean Soc. Agric. Eng.* **2012**, *54*, 27–38. [CrossRef]
29. Jang, C.H.; Kim, H.J.; Ahn, S.R.; Kim, S.J. Assessment of hydrological changes in a river basin as affected by climate change and water management practices, by using the CAT model. *Irrig. Drain.* **2016**, *65*, 26–35. [CrossRef]
30. Birhanu, D.; Kim, H.J.; Jang, C.H.; Park, S.H. Does the complexity of evapotranspiration and hydrological models enhance robustness? *Sustainability* **2018**, *10*, 2837. [CrossRef]

31. Choi, S.W.; Jang, C.H.; Kim, H.J. Analysis of short-term runoff characteristics of CAT-PEST connected model using different infiltration analysis methods. *J. Korea Acad.-Ind. Coop. Soc.* **2016**, *17*, 26–41. [CrossRef]
32. Lee, S.H.; Cho, H.J. Analysis of water cycle at main streams in Ulsan using CAT model. *J. Korea Water Resour. Assoc.* **2014**, *47*, 1–10. [CrossRef]
33. Miller, J.D.; Kim, H.J.; Kjeldsen, T.R.; Packman, J.; Grebby, S.; Dearden, R. Assessing the impact of urbanization on storm runoff in a peri-catchment using historical change in impervious cover. *J. Hydrol.* **2014**, *515*, 59–70. [CrossRef]
34. Catchment Hydrologic Cycle Assessment Tool User's Manual (CAT3.2). Available online: http://watercycle.kict.re.kr/ (accessed on 20 December 2021).
35. McVicar, T.R.; Roderick, M.L.; Donohue, R.J.; Li, L.T.; Van Niel, T.G.; Thomas, A.; Grieser, J.; Jhajharia, D.; Himri, Y.; Mahowald, N.M.; et al. Global review and synthesis of trends in observed terrestrial near-surface wind speeds: Implications for evaporation. *J. Hydrol.* **2012**, *416-417*, 182–205. [CrossRef]
36. Barella-Ortiz, A.; Polcher, J.; Tuzet, A.; Laval, K. Potential evaporation estimation through an unstressed surface-energy balance and its sensitivity to climate change. *Hydrol. Earth Syst. Sci.* **2012**, *17*, 4625–4639. [CrossRef]
37. Rural Development Administration. Available online: http://www.rda.go.kr (accessed on 20 December 2021).
38. Rural Agricultural Water Resource Information System. Available online: https://rawris.ekr.or.kr/main.do (accessed on 20 December 2021).
39. Moussa, R.; Chahinian, N. Comparison of different multi-objective calibration criteria using a conceptual rainfall-runoff model of flood events. *Hydrol. Earth Syst. Sci.* **2009**, *13*, 519–535. [CrossRef]
40. Legate, D.R.; McCabe, G.J., Jr. Evaluating the use of "goodness-of-fit" measures in hydrologic and hydroclimatic model validation. *Water Resour. Res.* **1999**, *35*, 233–241. [CrossRef]
41. Moriasi, D.N.; Arnold, J.G.; Van Liew, M.W.; Bingner, R.L.; Harmel, R.D.; Veith, T.L. Model Evaluation guidelines for systematic quantification of accuracy in watershed simulation. *ASABE* **2007**, *50*, 885–900. [CrossRef]
42. Jung, Y.H.; Jung, C.G.; Jung, S.W.; Park, J.Y.; Kim, S.J. Estimation of upstream ungauged watershed streamflow using downstream discharge data. *J. Korean Soc. Agric. Eng.* **2012**, *54*, 169–176.

water

MDPI

Review

Water Benchmarking in Buildings: A Systematic Review on Methods and Benchmarks for Water Conservation

Rafael A. Flores * and Enedir Ghisi

Laboratory of Energy Efficiency in Buildings, Department of Civil Engineering, Federal University of Santa Catarina, Florianopolis 88040-900, SC, Brazil; enedir.ghisi@ufsc.br
* Correspondence: ralmeidaflores@gmail.com or rafael.flores@posgrad.ufsc.br

Abstract: Water conservation is essential to sustainable development, and among human activities, buildings are responsible for a significant portion of total water consumption. Therefore, we present a systematic review that aims to search for valuable contributions from benchmarking and their potential significance to water conservation. The relevance of performing such a review is to support the research in the field, organise information, and highlight both the lack of data and valuable results in specific building types. Benchmarking highlights best performance buildings, while it also classifies performances, which allows developing interventions for different buildings. Seventy-two documents on the environmental performance of buildings were reviewed, and a variety of methods, metering procedures, and indicators were found as valuable data for water-saving initiatives. In addition to a systematic search in SCOPUS, searches were made in Science Direct and Google Scholar databases. Although the main challenge in this matter lies in the lack of procedures standardisation, it was found that performing benchmarking is relevant for accurately developing water conservation initiatives. Gains of over five million m^3 per year in a set of buildings or above 151 thousand m^3 per year in a single factory were found, which indicate the existing potential for water conservation.

Keywords: benchmarking; water consumption; water conservation; educational buildings; commercial buildings; residential buildings

Citation: Flores, R.A.; Ghisi, E. Water Benchmarking in Buildings: A Systematic Review on Methods and Benchmarks for Water Conservation. *Water* **2022**, *14*, 473. https://doi.org/10.3390/w14030473

Academic Editor: Carmen Teodosiu

Received: 3 November 2021
Accepted: 2 February 2022
Published: 5 February 2022

1. Introduction

Environmentally friendly buildings are essential for sustainable development and require standardisation. In that sense, there are building rating systems, such as LEED (Leadership in Energy and Environmental Design), BREEAM (BRE Environment Assessment Method), and Green Star, which mainly focus on energy efficiency. Although the concern over minimum water supply levels remains, water efficiency is more and more considered in sustainable building assessment.

Due to their high heterogeneity, benchmarking systems could be used to evaluate buildings efficiency, which could be implicated in improving overall resources conservation, such as water and energy. Benchmarking is a methodology that can be used for comparing similar processes of a given activity to highlight the one with the best performance [1], which can be used to assess the management of organisations. Even in presenting slight variations in data acquisition (e.g., sample definition), such practice has its core linked to comparative procedures and optimisations based on knowledge acquired in each organisation [2]. Benchmarking differs from a benchmark, as the first one is a process for comparison, and the other is a reference value of the ideal situation obtained from such a process [3,4].

Benchmarking methods can identify references (benchmarks) and determine systematic manners to compare all data to those references. Thus, benchmarking water consumption allows both highlighting the most efficient building and analysing such performance. Benchmarking is mainly done in three approaches: processes comparison,

performance analysis, and strategies comparison [5]. Such approaches are necessary to establish an efficiency border where each element occupies a relative position compared to others, highlighting differences. A benchmark could be taken as a target, and in some way, it allows users to move from where they are to where is considered the ideal position in terms of sustainable water-use performance [6]. The criteria for sample selection are crucial for these techniques' success [7]. The rules differ in the results and indicators validation. Therefore, benchmarking establishes criteria to represent a given phenomenon with optimal performance, providing indicators and performance goals as optimal references to evaluate similar phenomena [3].

In buildings assessment, benchmarking highlights best performance buildings while it classifies performances, which allows developing interventions for different buildings, and these properties can be used to assess how water is consumed in different types of buildings. Studies on water consumption in buildings generally consider specific indicators for each building type. These indicators could be "litres per inhabitant per day" for residential buildings [6,8]; "litres per guest per night" for hotels and other accommodation sites [9,10]; and "litres per student per day" for educational buildings [11–13]. There is also a dimensionless index ranging from 0 (the lowest performance) to 300 (the highest performance) for measuring water efficiency in dwellings, such as the one developed by Vieira et al. [14]. In addition to developing indicators, several techniques to perform evaluations on water efficiency in buildings have been developed [3,15–18]. Comparison evaluations, such as benchmarking, could use these methods and indicators to identify ideal situations in terms of water efficiency in buildings. Benchmarking systems including strategies such as cluster analysis can overcome such heterogeneity, as buildings can be assessed through their equivalents in resulting clusters. This procedure has been carried out in several studies, such as the study presented by Lara et al. [19], which was performed to assess energy consumption in a set of school buildings in Italy. The authors pointed out that a relevant issue when assessing a set of buildings is its correct definition and argued that a possible solution is the use of data mining techniques, such as the K-means clustering method. According to the authors, this allows the division of a large and heterogeneous sample into more homogenous and small groups, which facilitates finding benchmarks. Although many publications on water benchmarking are on agricultural sciences, as this sector accounts for most of the water consumption globally, the consumption in buildings is a significant portion of total water consumption among human activities. Buildings in non-industrial facilities represent 25.5% of all water withdrawn from nature in developing countries, such as Brazil (529 m^3/s) [20]. In developed countries, water consumption in buildings shows higher values. In Austria, 27% of total withdrawal is consumed in urban buildings (33% of total water consumption) [21]. To assess how efficiently such an important amount of water is consumed in different building types, benchmarking could be used. Thus, this review paper aims to analyse benchmarking methods considering residential, commercial, and educational buildings. These three types compose the most common buildings and should represent the majority of urban facilities that are related to the water consumption mentioned.

As water consumption data are essential to designing sustainable buildings, the literature presents several studies that compare water efficiency levels in commercial, residential, and educational buildings [10,13,15,17,22,23]. Despite that, the development of standardised indicators is still an obstacle to ranking water consumption efficiency in residential buildings, as simple normalisation with a single parameter may not be enough [9]. On the other hand, complicated benchmarking systems may impose difficulties for the user to adapt to novel procedures [6,17]. Therefore, is possible to question whether performing benchmarking could support the development of water-saving measures for increasing water conservation. This question was investigated by reviewing benchmarking methods in buildings to highlight results that could be valuable for water conservation initiatives. Studies on buildings benchmarking focusing not only on water but also on energy and other resources were reviewed.

2. Review Method

The potential of benchmarking methods as a tool for developing water-saving measures and increasing water conservation in buildings was investigated in the literature available. A systematic review was conducted to find as many documents that have used the terms of interest as detailed below. The topics searched were benchmarking techniques to measure environmental performance, including water consumption in residential, commercial, and educational buildings. Buildings were searched as residential, commercial, and educational buildings for the different user behaviour found and water usage in each one. It is far different from how water is consumed in a factory or a dwelling. The same premise is adopted regarding educational buildings, such as universities and schools. For that reason, results from each type of building are categorised in this review.

The initial terms often appeared in exploratory searches on water benchmarking topics. The search on buildings by type (commercial, educational, and residential) comes from the way that buildings appear in publications. Most of the studies do not present "buildings" in their publications but the finality of such buildings instead. Examples are hotels, schools, and dwellings. They are all buildings; however, they are not presented as defined this way but as what those buildings are for. For that reason, buildings were also searched under these forms.

The search on SCOPUS focused on the terms "water consumption", "water use", "benchmarking", and "buildings" found in the title, abstract, or keywords of publications according to the query string below. These four terms refer to the main review objective: how water is consumed in buildings. The final search term was then performed in SCOPUS using Boolean operators as follows:

TITLE-ABS-KEY (("water consumption" OR "water use" OR "water consumption") AND "benchmarking" AND ("buildings" OR "hotel*" OR "school*" OR "household*" OR "dwelling*") AND NOT ("plants" OR "crops" OR "agriculture"))

- OR: finds all the documents that contain any of the terms;
- AND: presents only the documents that contain all the terms;
- AND NOT: excludes the specific terms;
- *: replaces multiple characters (e.g., hotel* = hotel, hotels).

Studies on water consumption in agricultural sciences presenting terms such as agriculture, crops, or plants were excluded, as this review focus on water benchmarking in buildings. The term "benchmarking" maybe be hidden when searched, as many studies on water-use assessment are useful for reviewing water benchmarking but do not mention "benchmarking" in title, abstract, or keywords. This gap was overpassed through supplementary topics and by searching in databases other than SCOPUS. In addition to SCOPUS, Science Direct and Google Scholar were searched. Previous searches showed that in 2000, relevant documents on the field were published. For that reason, this year was taken as the base timeline for the review.

An initial survey on benchmarks led to definitions and performance studies on buildings. These studies concentrate on the energy area, and benchmarking methods there appear more often than in the water efficiency area. Water benchmarking methods were investigated as the main topic of the review alongside supplementary searches, including water consumption drivers, user behaviour, and water efficiency in buildings.

The strategy searched valid results and methods considering commercial, educational, and residential buildings. Based on both results and methods, opportunities for overall water conservation were highlighted. Including documents on supplementary topics, the final number of documents used in this review originated from the searches in the three databases mentioned. This strategy was used to answer two questions: "Which benchmarking methods are used to assess water consumption in buildings?" and mainly "Can benchmarking methods for building performance assessment can support initiatives for improving water conservation?"

The review strategy considered firstly general benchmarking methods to find applicable systems to the water research field. This led to a review of several energy benchmarking systems, as they mainly appear when benchmarking in buildings is searched. Thus, to understand buildings performance was necessary to review several energy benchmarking methods. Then, water benchmarking systems became clearer, as studies suggested that it is possible to use energy benchmarking in water assessment in buildings. This understanding was aided through comprehensive supplementary topics, such as water consumption drivers, user behaviour, and water efficiency in buildings.

The review framework used throughout the study is shown in Figure 1. One can see that performing a systematic review includes reviewing supplementary topics, and that is the reason they appear in the review framework. This helped to build concepts and definitions in such a limited field that presents few studies published.

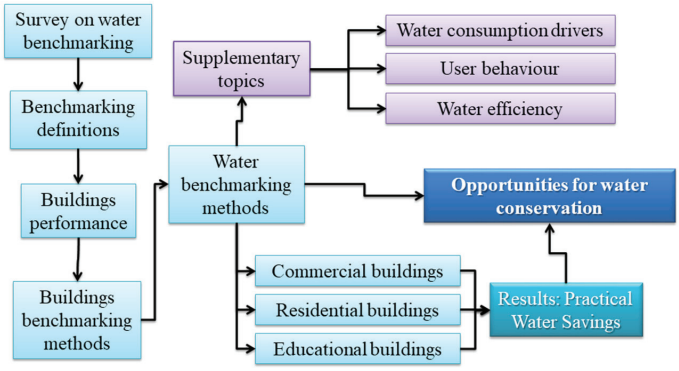

Figure 1. Review framework for the main and supplementary searches.

This review framework is not mandatory to perform this type of review. Nevertheless, it aided the review to explore the field, as the availability of publications is still limited. To divide buildings into three types helped to organize the results as well as the discussions. The supplementary topics supported necessary concepts and definitions. Finally, results from practical research highlighted opportunities for water conservation.

3. Results

The search in SCOPUS alone resulted in 44 documents on benchmarking methods in buildings that could contribute to water conservation from their results. These documents are included in the total number of documents reviewed, which was 72 if searches through the other databases are considered. The documents not included in these results are on studies that do not mention the search terms in their title, abstract, or keywords (e.g., benchmarking, water consumption) but present valuable results on the topic. These results correspond to 28 documents that refer to those valuable results mentioned. Examples of such results are the energy assessment methods for buildings presented in the studies of Dascalaki and Sermpetzoglou [24], Desideri and Proietti [25], Filippín [26], and Santamouris et al. [27]. Other examples are studies with results from which benchmarks for water consumption in school buildings could be extracted, such as the work of Antunes and Ghisi [12] and Melo et al. [15].

The year 2015 presented the most significant number of publications. However, the majority of papers concentrate on recent years. Although the number of publications on this topic is still limited, Figure 2 shows a growing number of published documents since 2000, especially from 2014 onwards. This topic is considered interesting even without a large number of publications, as it could establish novel methodologies and references to support water conservation in buildings.

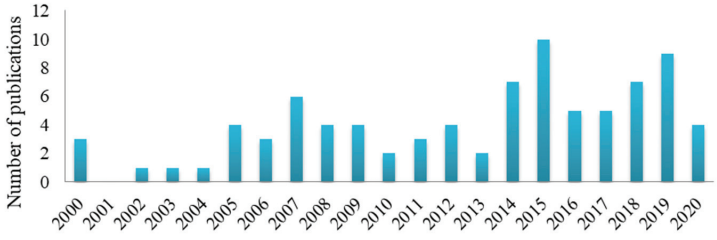

Figure 2. Publications on the topic over 2001–2021.

The areas with the most publications are Engineering and Environmental Sciences, and the majority of papers have been published from studies carried out in Canada and the United States as Figure 3 shows. These numbers could be related to the language spoken in those countries, as benchmarking in English can refer to a comparison between indicators without a deeper search for references. In any case, the normalised values of such numbers could not represent an interest in the topic, as in non-English speaking regions, many documents are published in the local language. As for the type of publication, conference papers (17.6%) and journal papers (73.5%) were the most representative type of publications. Table 1 shows the most relevant documents found in terms of Cite Score, SNIP, and SJR, which could measure their relevance in journal assessment patterns. The journals in which some publications have been published illustrates that, despite their limited number, studies have been published in relevant journals.

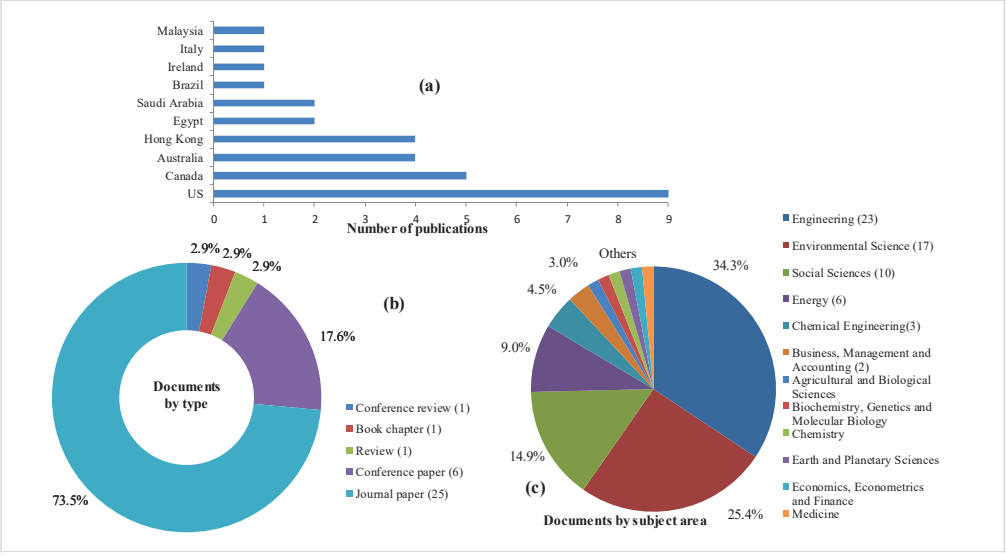

Figure 3. Search results analysis. (**a**) The number of documents by country or territory; (**b**) Documents by type; and (**c**) Documents by subject area.

Table 1. International journals in which the majority of journal papers were published.

Journal	Number of Papers	Cite Score	SNIP [1]	SJR [2]
Energy and Buildings	2	10.7	1.737	2.129
Building and Environment	2	9.7	1.736	2.36
Journal of Water Resources Planning and Management	2	5.1	0.917	1.401
Sustainability	2	3.9	0.612	1.242
Building Services Engineering Research and Technology	2	3.2	0.534	1.004

[1] SNIP, Source Normalised Impact per Paper; [2] SJR, SCImago Journal Rank Indicator.

3.1. Benefits of Performing Benchmarking in Buildings

The literature shows the influence on future projections from data obtained in benchmarking procedures. A relevant water-saving potential through rainwater harvesting systems was highlighted through correlations between water use and variables related to water supply from 62 cities [28]. Benchmarks were found for non-potable water supply alternatives, and their potential impact on water availability was discussed. Rainfall data, roof areas, water demand, and inhabitants per dwelling ratio were surveyed. The comparative assessment showed possible savings ranging from 32–95% of total water use (70–190 L/day). When considering future water availability, there is a significant difference between adopting such a strategy regarding annual per capita water availability [28].

Benchmarking uses measure systems and performance models to compare buildings efficiency using various methods [22,29]. In the construction sector, sustainable benchmarks define the minimum requirements to minimise the environmental impacts that are associated, including energy demand, water use, and emissions during construction, maintenance, and operation [30]. An environmental assessment that manages to isolate a financial analysis achieves better results [31], and benchmarking is shown in the literature as evaluating processes without considering financial aspects that can result from the actions taken. In that sense, benchmarking methods have been performed on energy and water efficiency. Alongside computer simulations, benchmarking is an essential resource performance assessment tool for buildings [8,22,32].

For performance evaluation of buildings with various indicators, measurement procedures require standardising the sample [22]. Benchmarking starts by collecting valuable data, and depending on what information is necessary, surveys are developed for different benchmarking purposes [33], including criteria definition to compose the sample. To evaluate water consumption, Duverge et al. [34] defined aquatic centres to compose their sample as public or community locations with at least one indoor pool and three different services, such as a gym, sauna, and cafe. That is a clear and objective definition to even the sample. The guidelines for benchmarking are the exact definition of sample buildings, which follows previously established criteria, being an essential step for comparative evaluation of buildings. In that sense, standards are suitable to divide the sample into groups for employing clustering analysis to identify representative buildings and parameters for reducing heterogeneity. The work of Lara et al. [19] showed a procedure to find clusters in a heterogeneous sample of school buildings aiming to assess energy consumption in Italy. To overcome an identified issue related to such heterogeneity, authors used data mining techniques to perform clustering analysis. The K-means clustering method was used to find clusters in a sample of 60 school buildings, which allowed to find suitable benchmarks to be compared to other elements. In addition to overcoming heterogeneity in a sample and performing an environmental assessment, benchmarking is also suitable to rank the efficiency of water utilities, whether concessionaires or state agencies. Their benchmarking is an analytical instrument for water conservation and allows obtaining valuable data from institutions [3,7]. Consequently, these organisations may raise their performance to improve indicators and increase water efficiency levels for evaluating both distributors and regulations [29]. In this context, Corton and Berg [3] assessed water services in Central America by surveying indicators, techniques, and cost-efficiency from organisations related to water services. Results showed institutional fragmentation as the main challenge to

achieve better service performance due to inconsistent data from different water utilities operating within the same regions. A similar effort in the United Kingdom showed that many original standards for energy efficiency were inadequate, demanding the sector to be restructured for establishing suitable benchmarks [35].

3.2. Energy Benchmarking

The interest in comparing the performance of buildings on resources consumption comes from energy crises (e.g., the 1979 oil crisis), which led to efforts to design energy-efficient buildings [36,37]. As buildings account for 20−40% of total energy consumption in developed countries [37], their environmental assessment is critical. Human development processes increase water and energy stress due to a closed link between higher development and higher resource demand [38]. As performance benchmarking in buildings first gained prominence in the energy area and then in water conservation studies [37], it is necessary to briefly review energy benchmarking methods to understand their influence over water benchmarking in buildings.

Energy benchmarking methods require consumption forecast and use physical principles to calculate thermal dynamics and energy behaviour in the building, either in its entirety or in its sectors [8]. This procedure is done to compare a sample of buildings with a reference building or indicator [39]. Other methods use physical or thermal dynamic functions to calculate the energy consumption of all building components [40] and use the weather, construction system, building operation, service utilities, and air conditioning systems as inputs of prediction models. Due to rules established to evaluate each element based on performance, benchmarking allows resources consumption assessment even in large heterogeneity samples, such as hotel buildings [9,10,41].

Statistical regression, computer simulations, and score classification systems are the most used performance benchmarking methods [22,33]. The first one uses models developed through existing data to find correlations between several variables, such as the weather and building characteristics (e.g., age, size, number of floors, occupancy rate, and behaviour of occupants) [33]. Computational models calculate benchmarks from the simulated performance of a reference building [39,42]. The scoring classification methods use ranking systems, in which buildings are not compared to each other but assessed against best practice standards instead (e.g., Green Star, LEED, United Kingdom Code for Sustainable Homes—CSH) [6,22]. Alternatively, the hierarchical and end-use metrics method develops performance metrics from the highest level (entire building) to the underlying system performance data [33]. As for water consumption, score systems are found in the environmental performance evaluations of school buildings and are applied to measure the user perception index [13,15,43,44].

Energy efficiency indicators support energy benchmarking and sustainable policies, such as energy codes [22,37], and include the ratio of measured usable area and either use of equipment in hours or the water volume consumed, which is known as energy intensity [45]. Data found for each use are registered in a reference table and then compared with field measurements [37,46] to rank buildings resources consumption. Machine learning has been used to rank buildings and select and analyse specific energy datasets for cities. In that sense, the study of Papadopoulos and Kontocosta [47] cross-validated input normalised data for nearly 7500 buildings in the city of New York with optimal parameters, and then, a clustering algorithm was applied to rank energy use.

Energy benchmarking in buildings allows comparing benchmark residuals from both regression models and evaluated buildings regarding differences instead of similarities [48]. Residuals analysis was also used to develop a suitable model to explain the variability in city-specific energy data compared to the Energy Star benchmarking system [49]. The residuals are, in these cases, a measure of inefficiency, and their quantity should be minimal in the design process. Strategies on benchmarking often require statistical analysis of data collected before the evaluation [11], and alternatively, some methods use actual meter-monitoring data from buildings [8].

According to the transparency in evaluation processes, benchmarking methods are classified into white-box, grey-box, and black-box [50]. Physical constraints exist in white-box modelling, and a large amount of data is required, i.e., there is less empirical knowledge and more modelling processes to perform the assessment. Grey-box and black-box methods grade the amount of available data. Thus, a black-box method presents data adjustment instead of knowledge of physical data and needs a statistical model pre-selected besides data (e.g., Artificial Neural Networks). Reference lines are adopted in four ways: previous performance of similar buildings; current performance of similar buildings; previous performance of the same building; and intended performance of the same building [50].

Although benchmarking supports the understanding of environmental impacts in different building phases, results are limited to that specific building. Nair et al. [51] showed how efficient water conservation measures can save energy at an Irish university building through the assessment of hot water usage, heating water energy, pumping water energy, carbon emissions, and solar power potential. Nonetheless, their findings would be only applicable to similar conditions.

As has been seen, benchmarking not only allows highlighting best practices and results but can also build rankings on efficiency or other characteristics. It also can be applied to evaluate organisations, such as water and energy utilities, rather than only buildings to reach major levels of service quality. Benchmarking methods need data, and any more information represents more accuracy on results. However, not only is the quantity of data important, but mainly quality data are required, as one can see in the work of Duverge et al. [34]. As they can vary on procedures involved, all benchmarking systems so far require particular care on data collection phases.

3.3. Water Benchmarking in Buildings

Although related to high monitoring costs, initiatives in water benchmarking, green buildings, and water-efficient facilities have been encouraged in recent years, as they represent long-term solutions for water and energy savings [52]. Water efficiency has more often been included in key performance indicators for buildings performance assessment alongside energy efficiency [53]. This section focuses on residential, commercial, and educational buildings. A table at the end of each section summarises methods and results for water conservation.

3.3.1. Residential Buildings

Due to the relevance of urban residential water consumption [54], evaluation methods on domestic water efficiency are needed. Such evaluation uses performance assessment functions that include converting state variables (e.g., water flow ratio, volume) in the performance index to be classified in standard water devices. As benchmarking depends on accurate building definition, the existence of alternative water supply systems, such as rainwater harvesting and greywater use systems, could strongly influence results [28,45,55]. In the United Kingdom, the Code for Sustainable Homes (CSH) [51] establishes maximum daily values of 80 L/person for the best-performing benchmarks, 105 L/person for mid-range benchmark levels, and 125 L/person for lowest-performing benchmarks [6,56]. Although domestic consumption is traditionally determined by the per capita approach, it may present high variability due to climate, culture, economy, individual demands, occupation characteristics, and building typology besides water end-uses [18].

Excluding toilet flush, the variation in daily per capita consumption is 65–175 L in Europe, 105–237 L in the United States, and 150–380 L in Asia [17]. Regarding this reality, the study of Wong and Mui [18] assessed 60 flats in Hong Kong with a mean distribution of water consumption as input for the estimative model. Results were compared to regional standards to generate suitable benchmarks. The highest 5% consumption was equal to or higher than 108 m^3 per person per year. Both higher and lowest 5% consumption were used to evaluate consumption. Results showed that according to adjustments to reach benchmarks in different scenarios, the official yearly consumption in Hong Kong (61 m^3

per person per year) could be 43, 47, and 50 m^3 per person per year for the first, second, and third posterior predictions, respectively [18]. For comparison, in 2005, surveys showed 82, 75, and 70 m^3 per person per year, respectively. The third mean found was 50% of Hong Kong total freshwater consumption (140 m^3 per person per year).

In the pursuit of better understanding, researchers have been applying different analysis tools, such as Adaptive Logic Networks (ALN). In the work of Chen et al. [8], ALN has been used with sociodemographic information as input for developing water-use prediction in twenty homes in Sosnowiec, Poland, and ten in Skiathos, Greece. This was done by comparing baseline under two approaches: household water consumption against its consumption over time and comparing several households in the same region. Inputs were the city size, age, the income of inhabitants, and their education level, allowing water consumption prediction in similar cities. This benchmarking system exemplified the use of on-site metering data in addition to statistical procedures, showing that real-world measurements require fewer data to infer useful conclusions. Predicted means can be compared to measurements, and in the case of measurement larger than predicted values, that particular household is using more water than necessary [8].

Performance indicators for individual water-use devices could be dimensionless, ranging from zero to 300 for calculating a general index by weighting each device for the correspondent water use. In the study of Vieira et al. [14], water-use and socioeconomic variables nexuses were analysed in 43 households through dimensionless indicators to highlight measures to enhance water efficiency. In that sense, valuable data for benchmarking can also be obtained from studies that aim to estimate water consumption, as their results highlight the most influential variables. Examples are the influence of building age and its distance to the central city area on the water consumption [57] as well as the number of inhabitants per dwelling, their educational level, building characteristics, number of bathrooms, building age and floor area, the existing water-saving systems, and water conservation habits [58].

In residential buildings, water and finance savings could be reached from benchmarking as the studies of Ghajarkhosravi et al. [33,59] have shown. Water consumption data—among other services (gas, electricity, and waste treatment)—from 2007 to 2011 were used to perform a benchmarking in a set of 105 multi-family residential buildings in Toronto, Canada. Results were classified to identify the top performer, the 25th percentile, the 50th percentile, and the 75th percentile, highlighting the possibility of saving 5,102,089 m^3 of water per year (CAD 12,721,671 based on the 2012 price of water in Canada).

Although studies have shown the benefits of benchmarking techniques, they do not only present positive aspects in the water efficiency context. By highlighting benchmarks, decision makers could impose desired behaviour over regular users in the pursuit of water conservation. Thus, it is critical to understand practical aspects of adopting a benchmarking system in residential buildings by considering the feedback of users related to what is achievable [6]. Reaching benchmarks requires knowing how much it is possible to seek lower consumption without compromising comfort, safety, and hygiene. Therefore, more research on user behaviour in benchmarking the environmental performance of buildings should be carried out [60].

The sensitivity of water indicators is measurable by detecting changes in user behaviour and technology, such as rainwater harvesting, greywater utilisation, and the inclusion of gardening demands [55]. Benchmarking depends on the roof area, gardening area, building location, daily occupancy rates, rainfall parameters, and conventional water supply quality [6]. Available technology and user behaviour, associated with socioeconomic factors, are critical elements in bringing consumption closer to benchmarks. Table 2 summarises findings from benchmarking procedures discussed above that could be applied in sets of buildings for improving their water conservation.

Table 2. Procedures and results related to benchmarking water use in residential buildings.

Reference	Methodology	Findings
Wong and Mui [18]	Comparison between consumption standards and mean distribution analysis in 60 flats in Hong Kong.	Water consumption could be as low as 50% of total consumption if all buildings reached benchmarks.
Chen et al. [8]	Adaptive Logic Networks with drivers for water use in 30 homes.	Water consumption prediction models to be compared with local measurements for controlling water usage.
Vieira et al. [14]	Cluster analysis in 43 households to generate indicators.	Dimensionless indicators with lowest and highest performance.
Dias et al. [57]	Variables analysis for determining drivers and description models.	Water consumption is related to the age of buildings and their distance from the central area.
Garcia et al. [58]	Socioeconomic questionnaires in 108 homes.	Water consumption is related to the number, habits, and education level of inhabitants.
Ghajarkhosravi et al. [33]	Benchmarking in a set of 105 multi-family residential buildings.	Potential savings of 5,102,089 m^3 per year in a set of buildings.
Hunt and Rogers [6]	Band-rating benchmarking system for measuring domestic water-use performance in the United Kingdom.	Discussion on user behaviour imposition by managers to reach water conservation goals.

Benchmarking water use in residential buildings highlights the heterogeneity of this type of building. In general, the number of buildings investigated is low when compared to the actual building number in the cities where the studies have been carried out. It is understandable that researches have limitations, but it is interesting to note that benchmarking procedures can originate useful results from samples. Even the sample results for water conservation are considered a great contribution, such as the potential savings pointed out by Ghajarkhosravi et al. [33]. In addition, from residential buildings come discussions on how the user will react if as a target for low water consumption is imposed. Residential use is far different from factory use or that in a hotel, which is why residential water benchmarking should be addressed separately from other types of buildings.

3.3.2. Commercial Buildings

Benchmarking in non-residential buildings has also been performed, and applications in specific buildings, such as sports centres, hotels, and factories, are found in the literature. In this section, publications were reviewed to assess the relevance of benchmarking on water consumption in high-heterogeneity buildings. An example of a benchmarking system was found in the study of Alkaya and Demirer [61], which was applied to an internal production chain to assess a polyethene terephthalate factory. It was found the possibility of saving 151,428 m^3 of water per year by identifying the most intense water-use processes and implementing suitable measures. Gains in energy consumption were also highlighted in cooling systems due to less heat generation from machines and less CO_2 emitted per year. This shows the potential for water conservation of benchmarking in a particular activity.

In the tourism industry, water scarcity is a primary environmental concern [9,10]. As a highly water-consuming sector, despite driving development for many regions, this activity is also a driver of negative impacts on water resources [62]; i.e., water consumption in hotels is much higher than in dwellings [63]. Consequently, rational water use is a key sustainability challenge for such an industry. Researchers have often focused on direct (on-site) consumption, with tourism water management based almost exclusively on direct water-use benchmarks [9].

As benchmarking supports rational water-use programmes by setting indicators and goals, water efficiency has been surveyed in the accommodation sector. Styles et al. [10] found consumption greater than or equal to 140 L per guest per night at full-service hotels and 94 L per guest per night at camping sites. Suitable benchmarks were then established, and simulations were performed to estimate gains in water efficiency in a 100-room hotel and 60-lot camping site. Potential water savings found was 228 and 127 L per guest

per night in the hotel and the camping site, respectively, representing 16,573 m^3/year (422 million m^3/year if adopted in all Europe) [10].

However, depending on the approach, the use of some indicators can be inappropriate. Although indicators such as "litres per guest per night" could be suitable for benchmarking purposes, they do not indicate whether abstraction levels are sustainable compared to the available renewable water resources [9]. As an example, there is a vast amount of renewable geothermal and heated water in Iceland, and the use of water by tourism is mostly irrelevant. On the other hand, in water-scarcity locations, consumption impacts are highly dependent on the season [62].

Sustainable programmes could be originated from favourable results in benchmarking water use in hotels. The work of Bohdanowicz and Martinac [41] investigated the influence of hotel standards, building area, number of accommodations sold, and number of meals served on water consumption; variable regression analysis was carried out for 184 hotels in Europe. Significant differences in water consumption were observed between Hilton and Scandic hotels, highlighting the need for smaller and more representative classification groups with comparable properties for establishing suitable benchmarks. It was also found that "guest nights" sold was the most influential variable, with each additional guest consuming 0.16 m^3 of water followed by total hotel floor area (0.38 m^3/m^2). Furthermore, the pool facility increases annual consumption by approximately 1000 m^3/year, and each meal sold uses an additional 0.006 m^3 and if irrigation is required, 0.088 m^3/m^2/year. Researchers concluded that the floor area could be more relevant than guest nights for consuming water in water-stressed locations, such as Mediterranean regions, where there is intensive irrigation [41].

A similar effort was made in a hotel in Barbados by correlating the number of accommodations, hotel standard, building size, and employees quantity for developing a unit water consumption model [63]. It was found that in terms of unit consumption (i.e., litres per guest night); there is a high water use when compared to international benchmarks. Another concerning finding is that in a water-stressed place such as Barbados, the daily consumption in hotels was about three times greater than the average consumption of the general population (756 vs. 240 L per capita) [63].

Office buildings are included in benchmarking studies as consumption measures and demand drivers could define a database for their assessment, including guidelines to generate suitable benchmarks. In the benchmarking carried out by Bint et al. [64], the inputs were a letter of acceptance from the manager to survey legal documentation on building characteristics, an information sheet of the history of changes (installations in the last five years and most recent consumption metering), and historical water collection data. On-site surveys were used to validate the information through a generic visiting protocol with all necessary building aspects: number and type of bathroom and kitchen equipment; cooling systems standards; details on the water metering; and building location. Regarding office buildings, flushing toilets and sink taps could be the most contributing pieces of equipment to water consumption, presenting acceptable compatibility between measured consumption and estimates based on user interviews [23]. Such findings could represent useful benchmarks for office buildings.

However, the lack of standardised classification and metering systems is an obstacle to spreading water-saving measures based on benchmarking. Although the efforts to extend such measures increase homogeneity in groups, significant variations in drivers for water-use remain. Energy benchmarking methods could overcome such a gap. They use the principle of the least-squares and multiple linear regressions to enhance simple normalisation, which allows the modelling of numerous use drivers [29]. Thus, it is possible to standardise measurements and increase statistical significance to determine independent variables. Alternatively, data enveloping methods include many observations to set an efficient boundary, from which the deviation measures choose efficiencies of all other elements. Their usability was demonstrated by applying both techniques for studying

water efficiency and generating benchmarks on data from 17,187 commercial, industrial, and institutional facilities in Austin, United States [29].

Benchmarking methods develop suitable indicators for many different situations. However, there is little consensus on which indicator is most appropriate. To overcome this divergence, the initial criteria for choosing the sample could be critical. In that sense, Duverge et al. [34] performed a benchmarking on water use in Australian sports centres and applied pre-established standardised guidelines and procedures. The sample was composed only of sports centres with indoor pools and at least three services, such as a fitness centre or snack bar. Such guidelines allowed sample selection and elements standardisation to compare water consumption in different variables and indicators.

The methods and findings discussed in this section are summarised in Table 3, which also shows different contributions to water conservation. It should be noted that several studies had no intention to explore benchmarking methods but identified benchmarks and drivers.

Table 3. Results from water-use benchmarking in commercial buildings.

Reference	Methodology	Findings
Alkaya and Demirer [61]	Water use processes benchmarking in a polyethene terephthalate factory.	Potential water savings of 151,428 m^3 per year.
Styles et al. [10]	Performance simulations from suitable benchmarks in a hotel and a camping site.	Potential water savings of 16,573 m^3 per year.
Bohdanowicz and Martinac [41]	Variable regression analysis in 184 hotels.	Significant water consumption differences between hotel brands.
Charara et al. [63]	Regression analysis on water consumption drivers in a hotel.	High consumption in Barbados in comparison with international benchmarks.
Bint et al. [64]	Measurements and demand drivers identification to compose a database for buildings assessment.	Guidelines for benchmarking office buildings.
Proença and Ghisi [23]	User interviews and water consumption measurements in office buildings.	Suitable benchmarks with high compatibility between user information and measurements.
Morales and Heaney [29]	Use of methods from energy benchmarking to study water efficiency.	Water efficiency benchmarking in 17,187 buildings.
Duverge et al. [34]	Benchmarking system on sports centres buildings in Australia.	Proper guidelines and criteria for building sample selection.

In commercial buildings, benchmarking could identify references that can be used in simulations that show interest numbers of water-saving potential. Examples are given by Alkaya and Demirer [61] as well as by Styles et al. [10]. In addition, guidelines appear to be more important to benchmark this type of building, as they are generally larger than residential buildings. In larger buildings or facilities, protocols to survey data are important, as such surveys must be equivalent in all buildings for comparison purposes.

3.3.3. Educational Buildings

As buildings in the educational sector are highly heterogeneous, benchmarking methods have been addressed to assess their performance in the energy efficiency area [24–27,42,51,65,66]. The usability of such methods for water efficiency assessment has been demonstrated [29]. In educational buildings, studies have addressed how indicators are produced as well as the influence of both alternative water supply systems and methods for assessing user behaviour [11,12,60,67]. Although benchmarking could support decision making on rational use of water in buildings, the lack of consensus on the most influential drivers for water consumption remains. This reality leads to initiatives that attempt to assign more accurate indicators by multivariate regression and score systems applied to user behaviour [13,44].

Cluster analysis methods, such as Complete Linkage and the Method of Ward, are used to organise benchmarking data. In that sense, Almeida et al. [11] found significant water and energy consumption variability in 23 Portuguese schools with similar phys-

ical characteristics due to non-constant user behaviour in similar environments. Water consumption assessment in schools is within an evaluation system that includes other sustainability variables, such as lectures addressing solid waste production and classification, noise pollution, food waste, and traffic density around the school [43], which could be regarded as drivers for water consumption in benchmarking systems.

Another interesting alternative to rank buildings by their environmental performance is Fuzzy clustering. This approach is useful to overcome uncertainties in evaluation systems [68], such as the definition of where is the efficiency borderline in such buildings. In that sense, higher educational institutions in Canada were ranked regarding water and energy consumption and greenhouse gases emissions [60]. Seventy-one buildings were grouped in three clusters based on their reported energy and water consumption as well as carbon emission: Cluster 2 obtained the best environmental performance (33 buildings, average area 10,051 m^2); Cluster 1 showed a typical performance (30 buildings, average area 11,528 m^2); and Cluster 3 obtained the lowest environmental performance (8 buildings, average area 5843). The average water-use intensity found was 1.01 m^3/m^2 for Cluster 1, 0.80 m^3/m^2 for Cluster 2, and 1.72 m^3/m^2 for Cluster 3 [60]. These findings represent different degrees of membership of each group to the so-considered efficient condition, and the environmental performance was then benchmarked. The results were highlighted as potential realistic targets to concentrate efforts in low-performance buildings.

Heterogeneity tends to be more prominent when drivers for a particular phenomenon are less known. This trend becomes clear in developing countries, where the lack of data is often a reality. In Brazil, daily water consumption in schools varies from 3.79 to 81.1 L per student [13]. A more recent study indicates a disparity between 0.81 and 35.43 L per student per day [12]. Internationally, this variability, through different indicators, can range from 11 L per student per day to 547 L per person (not only student) per day [13,69]. However, the main obstacle to overcoming such disparity, other than the high variability in consumption data, could be the poor standardisation of indicators. Some studies consider only students [12,67], others find general occupants of the school [11,13,44], and even consumer agents per day (water users other than the regular school population, such as parents of students) have been considered [15].

The influence of user perception has been investigated as a driver for improving water efficiency in schools. The analysis of data from 140 schools in Brazil showed 47.14% ranging between 10–20 L/student/day, 25.71% ranging from zero to 10 L/student/day, and 16.43% ranging from 20–30 L/student/day [70]. Using questionnaires, interviews, and on-site observations, this research has also found greater user perception over water consumption in areas inside buildings rather than outside. The study of Melo et al. [15] in twelve public schools distributed in six cities in south-eastern Brazil showed a great variation in water consumption, ranging from 13.6–27.3 L per consumer per day. In another study, a survey of water sanitation facilities was used to calculate a monthly indicator in a technical education building, which found consumption ranging from 6.28–22.78 L/student/day between 2012 and 2015 [71]. An assessment of user perception index applied to different cities revealed that previous studies [44,72] had shown an increase in such index from water users in schools [71]. The variability of water consumption indicators in educational buildings is shown in Table 4.

As for the educational buildings, the main challenge appears to be the lack of standardisation on indicators and information found. This could be linked to education standards around the world, which implicates students as well as the type of buildings where schools and universities are located. Nevertheless, in the same countries, such as Brazil, there are significant differences between such indicators and values, which generates concern about the quality of data available. The availability of data is another concern, as many countries on the globe present a lack of information on water use in educational buildings, as can be seen in Figure 4, which shows the proportion of schools with a basic drinking water service by country, 2016 (%).

Table 4. The water consumption variability in schools.

Reference	Value	Indicator	Location
Keating and Lawson [69]	17.4	L/student·day	The United Kingdom
Cheng and Hong [32]	56.4	L/person·day	Taiwan (Taipei)
Cheng and Hong [32]	59.5	L/person·day	Taiwan (Kau-Shong)
Pedroso [13]	3.79–81.1	L/student·day	Campinas, Brazil
Pedroso [13]	547	L/person·day	Canada
Melo et al. [15]	13.6–26.3	L/consumer·day	Minas Gerais, Brazil
Antunes and Ghisi [12]	0.81–35.43	L/student·day	Florianópolis, Brazil
Moraes et al. [71]	6.28–22.78	L/student·day	Recife, Brazil

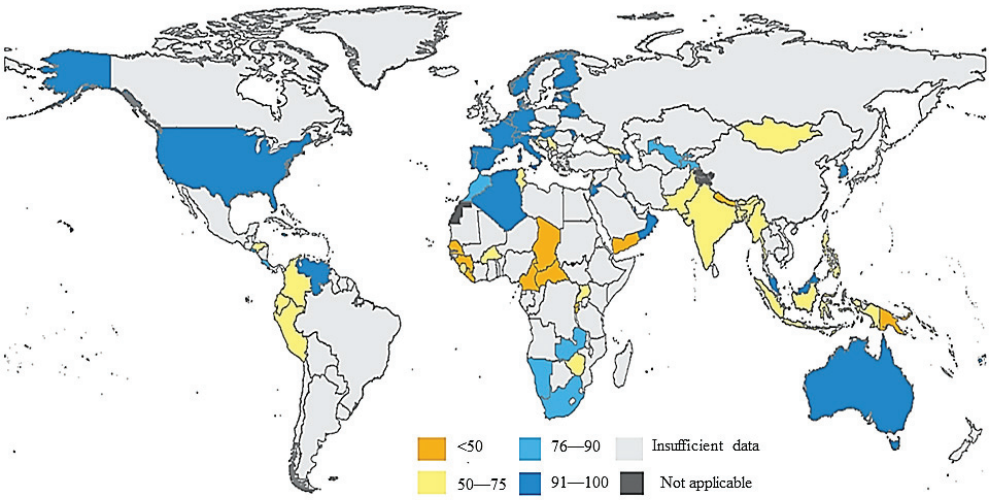

Figure 4. The lack of information on water use in schools [73].

3.4. Potential Water Savings from Initiatives Based on Benchmarking

There are three approaches for water savings in buildings that are more often explored: environmental education for rational use of water programmes, installation of water-saving technologies, and supplementary water supply systems (mainly rainwater harvesting and greywater utilisation). Benchmarking should consider those, as they are increasingly found in current and future building designs. However, it is important to highlight that alternative water supply systems should be considered in buildings design and assessment with concern to the water quality obtained. Moreover, it can complement such approaches by highlighting and organising data so that technologies and programmes can reach better results.

As the review highlights the relevance of benchmarking methods in buildings for water conservation, Table 5 summarises the potential water savings found in each type of building reviewed. The role of benchmarking in promoting overall water conservation shows that relevant amounts of water could be saved even if not adopting best practices but targeting intermediate benchmarks.

Table 5. The potential savings found in studies from water-use benchmarking in buildings.

Research Object	Specific Results						Reference
Performance clusters in 71 educational buildings	Cluster	No. of Buildings	Avg. Area (m^2)	WUI [1] (m^3/m^2)	Relative Water Use	Potential Savings	Alghamdi et al. [60]
	1	33	11,528	1.01	58.72%	11,643 m^3	
	2	30	10,051	0.80	46.51%	8040 m^3	
	3	8	5843	1.72	100%	10,049 m^3	
Per capita water use in multi-family residential buildings	Cluster	Annual water consumption (m^3/capita)			Relative water use	Potential savings	Ghajarkhosravi et al. [33]
	Poor performer set	79–124			64.71–100.00%	Up to 5,102,089 m^3 per year	
	Typical set	58–79			46.77–63.71%		
	Top performer set	28–58			46.77–22.58%		
Hotel (100 rooms) and camping site (60 lots)	Set	Suitable benchmarks	Specific potential savings		Potential water conservation	Potential savings	Styles et al. [10]
	100-room hotel	140 L/guest night	228 L/guest night		22 million m^3/year if adopted in all Europe	16,573 m^3 per year	
	60-lot camping site	94 L/guest night	127 L/guest night				
Water-use processes benchmarking in a factory	Results		Intervention		Secondary results	Potential savings	Alkaya and Demirer [61]
	Most intense identification processes in the production chain		Water-saving policies and technologies		Energy-saving and fewer CO_2 emissions	151,428 m^3 per year	

[1] WUI, water-use intensity.

Clusters found through fuzzy methodology [60] demonstrate that potential water savings could range from 41.28–53.49% if practices adopted in Clusters 1 and 2 were adopted in Cluster 3, which contains the set of buildings with the lowest performance. For Clusters 1, 2, and 3, this represents potential savings of 11,643 m^3, 8040 m^3, and 10,049 m^3, with performance similar to the benchmarks in all buildings. Similar conclusions could be made over the performance groups found for multi-family residential buildings [33], where water savings up to 5,102,089 m^3 per year could be reached. In the accommodation sector, 22 million m^3 per year of water could be saved if benchmarks and best practices were adopted all over Europe [10]. Finally, a single factory showed possible water gains of more than 151 thousand m^3 per year by identifying the most water-intense processes applying water-saving alternatives and optimising such processes [61].

4. Discussion

4.1. Advantages and Disadvantages of Performing Benchmarking to Assess Buildings

Benchmarking is such a great tool to find useful references when assessing water distribution networks. It allows identifying those elements that present high consumption values or those with excessively low consumption. In both cases, these references are useful because they allow the network manager to accurately direct efforts to control network issues, such as issues or under-measuring buildings. In addition, after implementation, benchmarking-based monitoring models are low cost to maintain and make possible remote monitoring of such networks. This is a huge positive aspect and must be pointed out, as they only need to be fed with more and updated data on buildings and network characteristics.

Although benchmarking is useful to identify and compare similar elements to search for best performance references, the lack of indicators and the heterogeneity in procedures could make it difficult to choose the most appropriate method for each evaluation. Benchmarking systems could include clustering analysis, which can overcome heterogeneity, as clusters are similar, and valuable information could be obtained from their internal comparative assessment. This procedure included in benchmarking systems can be used to overcome heterogeneity in a set of buildings. In general, statistical procedures are the most common techniques to build a benchmarking system. On the other hand, some designs use real-world data obtained using smart meters. Both are applicable to assess water consumption, but each one has limitations.

The common benchmarking processes are comparisons between a standard or a benchmark and other elements that can be done using a reference base rule. This common type of benchmarking has limitations related mainly to the specific variables that could be involved. Examples of such variables are climatic conditions, cultural behaviours by users, and technological limitations. This reality could limit average buildings to reach benchmark's water

consumption or even to approximate to an ideal efficiency. Therefore, the results from benchmarking procedures and their limitations should be considered in the process of supporting water-conservation initiatives. This review summarises benchmarking methods that have generated valuable results for promoting water-conservation initiatives. Their use has been increasing in recent years, as water use evaluation requires good-quality data to identify drivers for water consumption. Hence, benchmarking allows researchers to gauge measurements, compare results, and find references of efficiency. Benchmarks can be used as consumption goals for users, which in the very process of trying to approach that level, lower their water consumption.

4.2. Benchmarking and Actual Water Conservation

Even though benchmarking systems present all the advantages mentioned, their contribution to overall water conservation depends on the concrete development of initiatives that promote this benefit. This means that the answer on whether benchmarking systems are capable of promoting water savings would be negative if such concrete terms were considered. However, in indirect terms, it is possible to say that these systems promote water conservation, as they detect issues in distribution networks as well as in industrial production chains and are a tool for setting goals that would help achieve these goals. The gains in water conservation would depend not on benchmarking but on what actions are taken from the information provided by such systems.

In that sense, not performing benchmarking would be the issue, and such an action needs to be discussed. In the absence of benchmarking, rational water-use programmes and water-saving technologies in buildings may show negligible effects due to improper design or, for being applied to an unknown efficient building, not resulting in measurable improvement. This poor initiative implementation is frequent in educational and commercial buildings. Thus, it is important to consider factors that influence the pursuit of benchmarks: socioeconomic, technological, cultural, and climatic aspects. Benchmarking does not directly guarantee lower water consumption rates, as the imposition of consumption targets can have controversial effects on user comfort. However, the assessment of buildings through benchmarks could highlight drivers that should be addressed to improve water efficiency.

4.3. The Relationship between Benchmarking and Regular Water-Saving Initiatives

Water consumption studies results are far from absolute definitions, as indicators may be unsuitable in addition to depending on cultural, socioeconomic, climatic, and technological factors. Benchmarking could be a starting point for an overview of water consumption in buildings by accurately addressing water conservation efforts. Although not being the most water-withdrawing sector or human activity from nature, buildings represent a significant challenge for water conservation due to their high heterogeneity of types and purposes.

Benchmarking water consumption could be as efficient for water conservation as water-saving systems in buildings on a large scale, especially if the implementation of such systems lacks information on which buildings need to be improved. In addition, it has been demonstrated that water-conservation measures supported by benchmarking systems could increase water savings in buildings. In that sense, benchmarking should be performed before installing water-saving systems or implementing educational programmes.

In conclusion, there is less chance of success if such efforts do not have references or benchmarks. Initiatives based on benchmarking are similar to the idea of sustainable development in setting goals that may be challenging or even impossible to achieve. However, the very attempt to improve the indicators leads to improvements in sustainability and water-conservation processes.

Through this review, the potential of benchmarking to support water-saving initiatives becomes clear. This could inspire research on the reasons why such initiatives are less

popular than they should be. Water conservation is critical to a sustainable future, and the application of novel technologies and methodologies is desirable to address it.

As for general environmental concerns, reducing water consumption in buildings is mandatory for sustainable development, as it can significantly contribute to overall water conservation. Buildings are often considered in environmental discussions as a single system. However, regarding many buildings as a single environmental system highlights the massive potential for water conservation. Such procedures could assist in decision making in terms of cities' management.

4.4. Research Opportunities

Alternative water supply systems (rainwater harvesting and greywater utilisation) could be included in the characterisation of buildings for benchmarking systems. The literature does not often address such systems on this topic, which are becoming more popular and promote physical modifications in buildings, making them highly relevant in water-consumption studies. Future research could identify specific conditions in benchmarking systems and define protocols for each technology to be classified according to its influence on the evaluation. It must be pointed out that including alternative water supply systems in future buildings should be done with an awareness of the water quality from these sources, which could be also evaluated in benchmarking procedures.

The literature has not often mentioned the relevance of establishing partial efficiency criteria in water use. Partial efficiency refers to methodologies that are not based on classical logic and do not establish "efficiency" and "not efficiency" conditions for buildings. Fuzzy logic can define efficiency levels that are between those classic logic conditions. This is useful for deeper efficiency evaluations. Determining the relationship between benchmarks and other relative efficiency definition outcomes is essential for establishing efficiency levels that fluctuate between lower- and higher-efficiency scenarios. The establishment of an efficiency ranking could consider such intermediate levels to support decision making and enrich the database on the subject.

Author Contributions: Conceptualization, R.A.F.; methodology, R.A.F. and E.G.; writing—original draft preparation, R.A.F.; writing—review and editing, R.A.F. and E.G.; supervision, E.G.; funding acquisition, E.G. All authors have read and agreed to the published version of the manuscript.

Funding: This research was funded by the Brazilian Council for Scientific and Technological Development—CNPQ, grant number 140878/2018–1.

Institutional Review Board Statement: Not applicable.

Informed Consent Statement: Not applicable.

Data Availability Statement: Data are contained within the article.

Acknowledgments: Authors acknowledge the Brazilian National Council for Scientific and Technological Development—CNPq (Grant no. 140878/2018-1) and the Federal University of Santa Catarina (UFSC) for the support received to carry out this study.

Conflicts of Interest: The authors declare no conflict of interest.

References

1. Camp, R.C. Benchmarking: The search for industry best practices that lead to superior performance. *Qual. Prog.* **1989**, *22*, 62–69.
2. Galindro, B.M.; Zanghelini, G.M.; Soares, S.R. Use of benchmarking techniques to improve communication in life cycle assessment: A general review. *J. Clean. Prod.* **2019**, *213*, 143–157. [CrossRef]
3. Corton, M.L.; Berg, S.V. Benchmarking Central American water utilities. *Util. Policy* **2009**, *17*, 267–275. [CrossRef]
4. Yu, I.; Kim, K.; Jung, Y.; Chin, S. Comparable performance measurement system for construction companies. *J. Manag. Eng.* **2007**, *23*, 131–139. [CrossRef]
5. Lankford, W.M. Benchmarking: Understanding the basics. *Coast. Bus. J.* **2000**, *1*, 57–62.
6. Hunt, D.V.L.; Rogers, C.D.F. A benchmarking system for domestic water use. *Sustainability* **2014**, *6*, 2993–3018. [CrossRef]
7. Corton, M.L. Benchmarking in the Latin American water sector: The case of Peru. *Util. Policy* **2003**, *11*, 133–142. [CrossRef]

8. Chen, X.; Yang, S.H.; Yang, L.; Chen, X. A benchmarking model for household water consumption based on adaptive logic networks. *Procedia Eng.* **2015**, *119*, 1391–1398. [CrossRef]
9. Gössling, S. New performance indicators for water management in tourism. *Tour. Manag.* **2015**, *46*, 233–244. [CrossRef]
10. Styles, D.; Schoenberger, H.; Galvez-Martos, J.L. Water management in the European hospitality sector: Best practice, performance benchmarks and improvement potential. *Tour. Manag.* **2015**, *46*, 187–202. [CrossRef]
11. Almeida, R.M.S.F.; Ramos, N.M.M.; Simões, M.L.; De Freitas, V.P. Energy and water consumption variability in school buildings: Review and application of clustering techniques. *J. Perform. Constr. Facil.* **2015**, *29*, 04014165. [CrossRef]
12. Antunes, L.N.; Ghisi, E. Water and energy consumption in schools: Case studies in Brazil. *Environ. Dev. Sustain.* **2019**, *22*, 4225–4249. [CrossRef]
13. Pedroso, L.P. Estudo das Variaveis Determinantes no Consumo de Agua em Escolas: O Caso das Unidades Municipais de Campinas, São Paulo [Study of the Determinants of Water Consumption in Schools: The Case of Municipal Units in Campinas, Sao Paulo]. Master's Thesis, Faculdade de Engenharia Civil, Universidade Estadual de Campinas, Campinas, Brazil, November 2008.
14. Vieira, P.; Jorge, C.; Covas, D. Assessment of household water use efficiency using performance indices. *Resour. Conserv. Recycl.* **2017**, *116*, 94–106. [CrossRef]
15. De Melo, N.A.; Salla, M.R.; de Oliveira, F.R.G.; Frasson, V.M. Consumo de água e percepção dos usuários sobre o uso racional de água em escolas estaduais do Triângulo Mineiro [Water consumption and User Perception on rational water use in Triangulo Mineiro schools]. *Cienc. Eng. Sci. Eng. J.* **2014**, *23*, 1–9. [CrossRef]
16. Morales, M.A.; Heaney, J.P. Classification, benchmarking, and hydroeconomic modeling of nonresidential water users. *J. Am. Water Work. Assoc.* **2014**, *106*, E550–E560. [CrossRef]
17. Mui, K.W.; Wong, L.T.; Law, L.Y. Domestic water consumption benchmark development for Hong Kong. *Build. Serv. Eng. Res. Technol.* **2007**, *28*, 329–335. [CrossRef]
18. Wong, L.T.; Mui, K.W. Epistemic water consumption benchmarks for residential buildings. *Build. Environ.* **2008**, *43*, 1031–1035. [CrossRef]
19. Lara, R.A.; Pernigotto, G.; Cappelletti, F.; Romagnoni, P.; Gasparella, A. Energy audit of schools by means of cluster analysis. *Energy Build.* **2015**, *95*, 160–171. [CrossRef]
20. ANA (Ed.) *Conjuntura Recursos Hídricos Brasil*; Agência Nacional de Águas: Brasilia, Brazil, 2018.
21. Vanham, D. A holistic water balance of Austria—How does the quantitative proportion of urban water requirements relate to other users? *Water Sci. Technol.* **2012**, *66*, 549–555. [CrossRef]
22. Duverge, J.J.; Rajagopalan, P.; Fuller, R.; Woo, J. Energy and water benchmarks for aquatic centres in Victoria, Australia. *Energy Build.* **2018**, *177*, 246–256. [CrossRef]
23. Proença, L.C.; Ghisi, E. Water end-uses in Brazilian office buildings. *Resour. Conserv. Recycl.* **2010**, *54*, 489–500. [CrossRef]
24. Dascalaki, E.G.; Sermpetzoglou, V.G. Energy performance and indoor environmental quality in Hellenic schools. *Energy Build.* **2011**, *43*, 718–727. [CrossRef]
25. Desideri, U.; Proietti, S. Analysis of energy consumption in the high schools of a province in central Italy. *Energy Build.* **2002**, *34*, 1003–1016. [CrossRef]
26. Filippín, C. Benchmarking the energy efficiency and greenhouse gases emissions of school buildings in central Argentina. *Build. Environ.* **2000**, *35*, 407–414. [CrossRef]
27. Santamouris, M.; Mihalakakou, G.; Patargias, P.; Gaitani, N.; Sfakianaki, K.; Papaglastra, M.; Pavlou, C.; Doukas, P.; Primikiri, E.; Geros, V.; et al. Using intelligent clustering techniques to classify the energy performance of school buildings. *Energy Build.* **2007**, *39*, 45–51. [CrossRef]
28. Ghisi, E.; Montibeller, A.; Schmidt, R.W. Potential for potable water savings by using rainwater: An analysis over 62 cities in southern Brazil. *Build. Environ.* **2006**, *41*, 204–210. [CrossRef]
29. Morales, M.; Heaney, J. Benchmarking nonresidential water use efficiency using parcel-level data. *J. Water Resour. Plan. Manag.* **2016**, *142*, 04015064. [CrossRef]
30. Zimmermann, M.; Althaus, H.-J.; Haas, A. Benchmarks for sustainable construction: A contribution to develop a standard. *Energy Build.* **2005**, *37*, 1147–1157. [CrossRef]
31. Soares, S.R.; Souza, D.M.; Pereira, S.W. A avaliação do ciclo de vida no contexto da construção civil. [Life cycle assessment in the context of civil construction]. *Colet. Habitare* **2006**, *7*, 96–127.
32. Cheng, C.L.; Hong, Y.T. Evaluating water utilization in primary schools. *Build. Environ.* **2004**, *39*, 837–845. [CrossRef]
33. Ghajarkhosravi, M.; Huang, Y.; Fung, A.S.; Kumar, R.; Straka, V. Energy benchmarking analysis of multi-unit residential buildings (MURBs) in Toronto, Canada. *J. Build. Eng.* **2020**, *27*, 100981. [CrossRef]
34. Duverge, J.J.; Rajagopalan, P.; Fuller, R. Defining aquatic centres for energy and water benchmarking purposes. *Sustain. Cities Soc.* **2017**, *31*, 51–61. [CrossRef]
35. Chau, V.S. Benchmarking service quality in UK electricity distribution networks. *Benchmarking* **2009**, *16*, 47–69. [CrossRef]
36. Ilha, M.S.O.; Oliveira, L.H.; Gonçalves, O.M. Environmental assessment of residential buildings with an emphasis on water conservation. *Build. Serv. Eng. Res. Technol.* **2009**, *30*, 15–26. [CrossRef]
37. Pérez-Lombard, L.; Ortiz, J.; González, R.; Maestre, I.R. A review of benchmarking, rating and labelling concepts within the framework of building energy certification schemes. *Energy Build.* **2009**, *41*, 272–278. [CrossRef]
38. Dai, J.; Wu, S.; Han, G.; Weinberg, J.; Xie, X.; Wu, X.; Song, X.; Jia, B.; Xue, W.; Yang, Q. Water-energy nexus: A review of methods and tools for macro-assessment. *Appl. Energy* **2018**, *210*, 393–408. [CrossRef]

39. Capozzoli, A.; Piscitelli, M.S.; Neri, F.; Grassi, D.; Serale, G. A novel methodology for energy performance benchmarking of buildings by means of linear mixed effect model: The case of space and DHW heating of out-patient Healthcare Centres. *Appl. Energy* **2016**, *171*, 592–607. [CrossRef]
40. Zhao, H.X.; Magoulès, F. A review on the prediction of building energy consumption. *Renew. Sustain. Energy Rev.* **2012**, *16*, 3586–3592. [CrossRef]
41. Bohdanowicz, P.; Martinac, I. Determinants and benchmarking of resource consumption in hotels—Case study of Hilton International and Scandic in Europe. *Energy Build.* **2007**, *39*, 82–95. [CrossRef]
42. Bernardo, H.; Antunes, C.H.; Gaspar, A. Exploring the use of indicators for benchmarking the energy performance of Portuguese secondary schools. In Proceedings of the Energy for Sustainability 2015 Sustainable Cities: Designing for People and the Planet, Coimbra, Portugal, 14–15 May 2015; pp. 1–8.
43. Fehr, M.; Andrade, V.S.C.S. Search for objective environmental performance indicators of primary schools. *Benchmarking* **2016**, *23*, 1922–1936. [CrossRef]
44. Ywashima, L.A. Avaliação do Uso de Água em Edifícios Escolares Públicos e Análise de Viabilidade Econômica da Instalação de Tecnologias Economizadoras nos Pontos de Consumo. [Assessment of Water Use in Public School Buildings and Analysis of Economic Feasibility of Installing Water-Saving Technologies at Consumption Points]. Master's Thesis, Faculdade de Engenharia Civil, Universidade Estadual de Campinas, Campinas, Brazil, 2005.
45. Marinoski, A.K.; Vieira, A.S.; Silva, A.S.; Ghisi, E. Water end-uses in low-income houses in Southern Brazil. *Water* **2014**, *6*, 1985–1999. [CrossRef]
46. Sharp, T. Energy benchmarking in commercial office buildings. *ACEEE Summer Study Energy Effic. Build.* **1995**, *4*, 321–329.
47. Papadopoulos, S.; Kontokosta, C.E. Grading buildings on energy performance using city benchmarking data. *Appl. Energy* **2019**, *233–234*, 244–253. [CrossRef]
48. Chung, W.; Hui, Y.V.; Lam, Y.M. Benchmarking the energy efficiency of commercial buildings. *Appl. Energy* **2006**, *83*, 1–14. [CrossRef]
49. *Energy Star® Performance Ratings Technical Methodology*; Environmental Protection Agency, EPA: Washington, DC, USA, 2011.
50. Li, Z.; Han, Y.; Xu, P. Methods for benchmarking building energy consumption against its past or intended performance: An overview. *Appl. Energy* **2014**, *124*, 325–334. [CrossRef]
51. Nair, S.; Hashim, H.; Hannon, L.; Clifford, E. End use level water and energy interactions: A large non-residential building case study. *Water* **2018**, *10*, 810. [CrossRef]
52. Masia, T.; Kajimo-Shakantu, K.; Opawole, A. A case study on the implementation of green building construction in Gauteng province, South Africa. *Manag. Environ. Qual. Int. J.* **2020**, *31*, 602–623. [CrossRef]
53. Li, H.; Hong, T.; Lee, S.H.; Sofos, M. System-level key performance indicators for building performance evaluation. *Energy Build.* **2020**, *209*, 109703. [CrossRef]
54. Cobacho, R.; Arregui, F.; Gascón, L.; Cabrera, E. Low-flow devices in Spain: How efficient are they in fact? An accurate way of calculation. *Water Sci. Technol. Water Supply* **2004**, *4*, 91–102. [CrossRef]
55. Teston, A.; Geraldi, M.S.; Colasio, B.M.; Ghisi, E. Rainwater harvesting in buildings in Brazil: A literature review. *Water* **2018**, *10*, 471. [CrossRef]
56. DCLG. *Code for Sustainable Homes: Technical Guide November 2010*, 1st ed.; Department for Communities and Local Government, DCLG: London, UK, 2010; ISBN 9781859463314.
57. Dias, T.F.; Kalbusch, A.; Henning, E. Factors influencing water consumption in buildings in southern Brazil. *J. Clean. Prod.* **2018**, *184*, 160–167. [CrossRef]
58. Garcia, J.; Salfer, L.R.; Kalbusch, A.; Henning, E. Identifying the drivers of water consumption in single-family households in Joinville, Southern Brazil. *Water* **2019**, *11*, 1990. [CrossRef]
59. Ghajarkhosravi, M.; Huang, Y.; Fung, A.S.; Kumar, R.; Straka, V. Benchmarking of water consumption and waste management in multi-unit residential buildings (MURBs) in Toronto. *Can. J. Civ. Eng.* **2021**, *48*, 628–641. [CrossRef]
60. Alghamdi, A.; Hu, G.; Haider, H.; Hewage, K.; Sadiq, R. Benchmarking of water, energy, and carbon flows in academic buildings: A fuzzy clustering approach. *Sustainability* **2020**, *12*, 4422. [CrossRef]
61. Alkaya, E.; Demirer, G.N. Reducing water and energy consumption in chemical industry by sustainable production approach: A pilot study for polyethylene terephthalate production. *J. Clean. Prod.* **2015**, *99*, 119–128. [CrossRef]
62. Tortella, B.D.; Tirado, D. Hotel water consumption at a seasonal mass tourist destination. The case of the island of Mallorca. *J. Environ. Manag.* **2011**, *92*, 2568–2579. [CrossRef] [PubMed]
63. Charara, N.; Cashman, A.; Bonnell, R.; Gehr, R. Water use efficiency in the hotel sector of barbados. *J. Sustain. Tour.* **2011**, *19*, 231–245. [CrossRef]
64. Bint, L.E.E.; Isaacs, N.; Vale, R. *Water Performance Benchmarks for New Zealand: An Approach to Understanding Water Consumption in Commercial Office Buildings*; Victoria University of Wellington: Wellington, New Zealand, 2010; pp. 1–11.
65. Corgnati, S.P.; Corrado, V.; Filippi, M. A method for heating consumption assessment in existing buildings: A field survey concerning 120 Italian schools. *Energy Build.* **2008**, *40*, 801–809. [CrossRef]
66. Hernandez, P.; Burke, K.; Lewis, J.O. Development of energy performance benchmarks and building energy ratings for non-domestic buildings: An example for Irish primary schools. *Energy Build.* **2008**, *40*, 249–254. [CrossRef]
67. Alghamdi, A.; Haider, H.; Hewage, K.; Sadiq, R. Inter-university sustainability benchmarking for Canadian higher education institutions: Water, energy, and carbon flows for technical-level decision-making. *Sustainability* **2019**, *11*, 2599–2625. [CrossRef]

68. Dubois, D.; Prade, H. What are fuzzy rules and how to use them. *Fuzzy Sets Syst.* **1996**, *84*, 169–185. [CrossRef]
69. Keating, T.; Lawson, R. *The Water Efficiency of Retrofit Dual Flush Toilets*, 1st ed.; Southern Water, A Scottish Power Company: Bristol, UK, 2000.
70. De Oliveira, F.R.G. Consumo de Água e Percepção dos Usuários Para o Uso Racional de Água em Escolas Estaduais de Minas Gerais. [Water Consumption and Users' Perception of Rational Water Use in State Schools in Minas Gerais]. Master's Thesis, Faculdade de Engenharia Civil, Universidade Federal de Uberlândia, Uberlândia, Brazil, August 2013.
71. De Moraes, J.F.S.; Nunes, L.G.C.F.; da Silva, S.R. Estudo de percepções e avaliações do consumo de água em escolas públicas do Recife. [Study of perceptions and assessments of water consumption in public schools in Recife]. *Holos Environ.* **2019**, *19*, 116–130. [CrossRef]
72. Da Silva, S.R.; de Araújo, A.R.B.; da Fonseca, J.M.M.; Nunes, L.G.C.F. Indicadores de uso racional da água em uma escola técnica estadual da cidade de Recife-PE. [Indicators of rational use of water in a state technical school in the city of Recife-PE]. *Rev. Gestão Sustentabilidade Ambient.* **2018**, *7*, 381–396. [CrossRef]
73. UNICEF. *Drinking Water, Sanitation and Hygiene in Schools: Global Baseline Report 2018*; United Nations Children's Fund (UNICEF) and World Health Organization: New York, NY, USA, 2018.

water

MDPI

Article

Delineating MAR Sites Using GIS-MCDA for Nuweiba Alluvial Fan Aquifer, Sinai, Egypt

Karim Soliman [1], Osama M. Sallam [2,*] and Christoph Schüth [3]

[1] Water Resources Research Institute, National Water Research Center, P.O. Box 74, Shubra El-Kheima 13411, Egypt; karim_soliman@nwrc.gov.eg
[2] Research Institute for Groundwater, National Water Research Center, P.O. Box 74, Shubra El-Kheima 13411, Egypt
[3] Institute for Applied Geosciences, Technische Universität Darmstadt, Schnittspahnstraße 9, 64287 Darmstadt, Germany; schueth@geo.tu-darmstadt.de
* Correspondence: sallamosama@hotmail.com

Abstract: In the last few decades, groundwater has been the main water supply to the Nuweiba alluvial fan. However, currently, the main water supply is a desalination plant. The desalination plant might be vulnerable to malfunctions resulting in a severe drought. In addition, the aquifer type in the fan is coastal. Hence, replenishing the groundwater is necessary on a long-term basis to overcome drought events in the case of emergency. To replenish the groundwater using flash-flood water, a Managed Aquifer Recharge (MAR) system could be installed. This study applies the Geo-Information System–Multi-Criteria Decision Analysis (GIS-MCDA) method to delineate the feasible locations for installing a MAR system. To delineate the feasible MAR sites via a potential map, four steps were performed: problem definition, constraint mapping, suitability mapping, and sensitivity analysis. The results show that nearly 52% of the study area is suitable for installing MAR. Additionally, around 6% of the study area shows high potential for installing MAR, whereas nearly 20% falls under the moderate potential class. The potential map shows that the high-potential MAR sites are located at the western portion of the study area, near the ephemeral stream outlet. The map could be utilized as a tool for decision-makers to plan a future sustainable development strategy.

Keywords: water resources sustainability; arid climate coastal aquifer; MAR; GIS-MCDA

Citation: Soliman, K.; Sallam, O.M.; Schüth, C. Delineating MAR Sites Using GIS-MCDA for Nuweiba Alluvial Fan Aquifer, Sinai, Egypt. *Water* **2022**, *14*, 475. https://doi.org/10.3390/w14030475

Academic Editors: Chin H. Wu, Alban Kuriqi and Luis Garrote

Received: 19 December 2021
Accepted: 25 January 2022
Published: 5 February 2022

1. Introduction

The Sinai Peninsula (located in the north-eastern portion of Egypt) has been developed socio-economically in the last four decades [1]. Thus, sufficient sustainable water resources should meet the future water demand in order to cope with this socio-economic development. One of the cities located in Sinai is Nuweiba City. The city was completely dependent on groundwater as a source of drinking water, and limited agriculture for the local population many years ago. Recently, a desalination plant has been constructed to supply the city and touristic resorts with potable water. The city is currently witnessing an accelerating in development in all urban and social fields. Therefore, it is necessary to develop the available water resources (conventional and non-conventional) such as desalinated seawater and storm water, in order to meet the water demand requirements.

The city is located in the Nuweiba alluvial fan between the main ephemeral stream outlet of the Wadi Watir catchment in the west and the Gulf of Aqaba in the east [2] (Figure 1). Various features are present in the city: an international harbor, touristic resorts, and small agricultural farms.

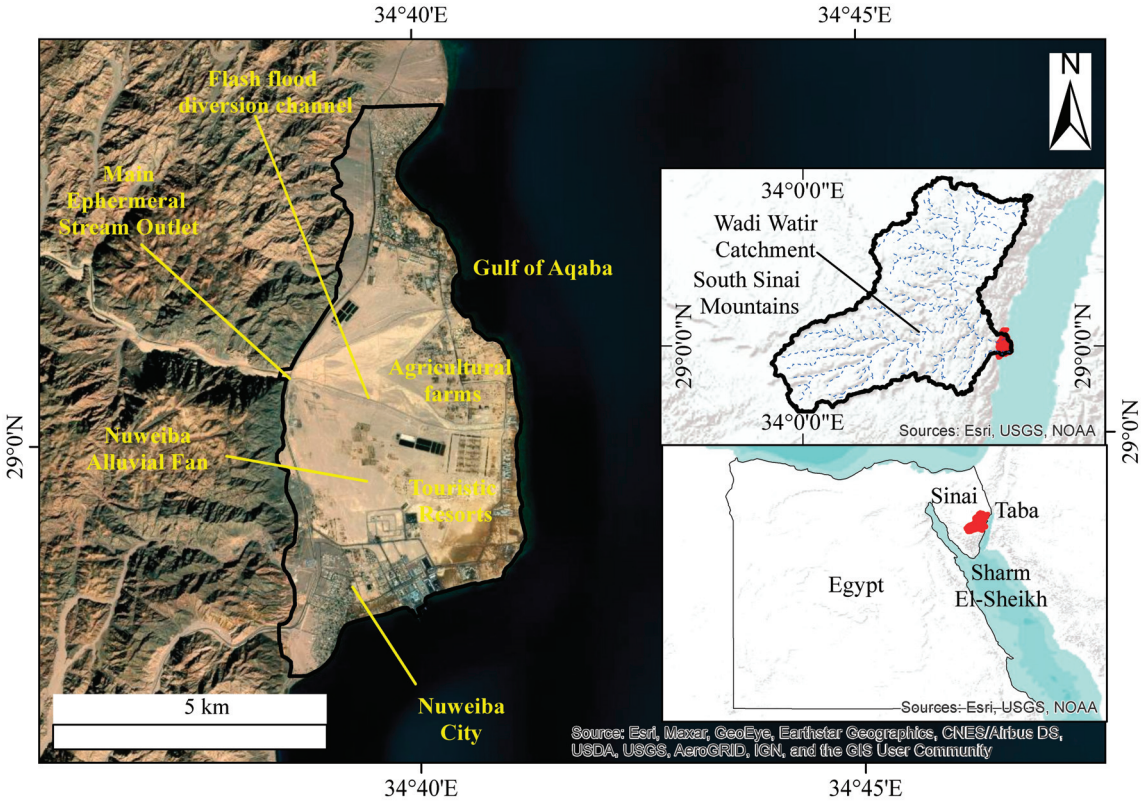

Figure 1. Location map of the Nuweiba alluvial fan. The figure shows the fan location in Wadi Watir catchment and the location of the catchment in Egypt.

In light of the city's rapid growth, desalinated seawater is the main sustainable source that can meet the consumption requirements. However, it is necessary to search for another suitable water source to meet the requirements during drought periods. In other words, it is impossible to rely solely on desalinated seawater to meet the consumption requirements during emergency periods. In addition, the current water supply in the study area is subject to the following risks: desalination plant malfunction, petroleum leakage in the sea, and malfunction of the main intake pipeline to the desalination plant.

Hence, sustainable water resource plans are essential to cope with any future emergent drought. Thus, most previous studies have demonstrated the feasibility of sustaining water resources by focusing on either surface water or groundwater in the future. Previous researchers applied different methods, but most studies lack solutions related to sustaining water resources in the case of emergencies.

Regarding surface water, Masoud [3] quantified the runoff and recharge volumes for the main active catchments using the Soil Conservation Service (SCS) model. Milewski et al. [4] calculated the runoff and recharge volumes for the active catchments in Sinai using the Soil and Water Assessment Tool (SWAT) model via Remote Sensing (RS) data. Zayed et al. [5] evaluated water harvesting potential by imposing Integrated Water Resources Management (IWRM) guidelines based on physical, socioeconomic, environmental, and institutional data analyses.

Regarding groundwater, Abuzied et al. [2] delineated the groundwater potential zones in the study area by creating a groundwater potential map using remote sensing (RS) and geoinformation system (GIS) tools to assess the groundwater resources. Eissa et al. [1]

modeled the groundwater system using Modular Finite Difference Groundwater Flow (MODFLOW), Net Geochemical Reactions Along a Flow Path (NETPATH), and Simulation of Three-Dimensional Variable-Density Groundwater Flow and Transport (SEAWAT) models to understand the recharge sources to the aquifer. Sallam [6] modeled the suitability of Aquifer Storage Recovery (ASR) to the system using the linkage between MODFLOW, MODPATH, and Three-Dimensional Multi-Species Solute Transport (MT3DMS) to evaluate the recovery efficiency when injecting freshwater into the aquifer. Elewa and Qaddah [7] mapped the groundwater potential for Sinai using RS and GIS in order to assess the groundwater resources.

The aforementioned studies focused on sustaining water resources in the future in relation to the current situation; however, the studies did not address the water resources' vulnerability to future droughts. Hence, techniques such as MAR could be applied to act as a back-up system to supply water in the case of emergency. Groundwater management can mitigate the water scarcity problems and sustain water resources supply in the future [8]. As such, MAR has been applied as a groundwater management tool, especially in arid and semi-arid regions [9,10]. MAR is defined according to Dillon et al. [11] as the artificial injection of freshwater into groundwater aquifers to recover water or to gain environmental benefits. It seeks to replenish the aquifer such that the groundwater is the secondary water supply, which could be utilized in the case of emergency. To effectively install MAR, the feasible site locations should be assessed.

Thus, the main objective of this study is to delineate MAR sites. To achieve the objectives, the following steps were taken: (1) reviewing the literature related to the study area and delineation methods; (2) acquiring data from previous studies and field trips; (3) preparing data before applying the delineation method; (4) generating potential maps showing the MAR delineation locations.

2. Materials and Methods

2.1. Nuweiba Alluvial Fan Aquifer

The total area of the Nuweiba alluvial fan is around 30 km^2. The surface elevation ranges from 0 to 48 m above mean sea level (MSL). The fan is characterized by a steep surface; the surface's slope ranges from around 0.3 to 5%, with an arithmetic mean of about 1.4%. Most of the study area is covered by alluvial dunes in the presence of clastic sediments [12], whereas the rest is surrounded by urban buildings, roads, and agricultural sites.

Regarding aquifer geometry and formation, Figure 2 shows the hydrogeological cross-section and the aquifer thickness. The Nuweiba alluvial fan comprises quaternary fine to coarse sands, gravels, and boulders intercalated by a silty and clayey matrix [13]. The quaternary deposits form an unconfined heterogeneous water-bearing aquifer. According to Abbas et al. [12], the aquifer is divided into five layers. The two upper layers consist of fine to coarse alluvial deposits with a thickness lower than 10 m each. The intermediate layer consists of Pleistocene sandy clay with 30 to 45 m thickness. The fourth layer comprises sand and gravel with a thickness ranging from 20 to 40 m. The bottom layer consists of sand with clay intercalation, and is 20 to 50 m thick. A granitic rock basement under-lays the bottom layer. Figure 3 represents the aquifer's geometry.

Regarding aquifer properties, the saturated hydraulic conductivity was determined by different methods (geo-electrical fieldwork, pumping tests, slug tests, and groundwater flow model calibration). The hydraulic conductivity values were estimated by Khalil [14] as 54 m/day by interpreting geo-electrical data, and 1 to 12 m/day by Himida [15] via interpolating the pumping test analysis results. These results were calibrated using groundwater flow models by Eissa et al. [1] and Salam [6] as 4 m/day for the three upper layers, 11 m/day for the fourth layer, and as 0.001 for the lowermost layer. Additionally, Himida [15] calculated the transmissivity parameter such that the value ranged from around 65 to 500 m^2/day.

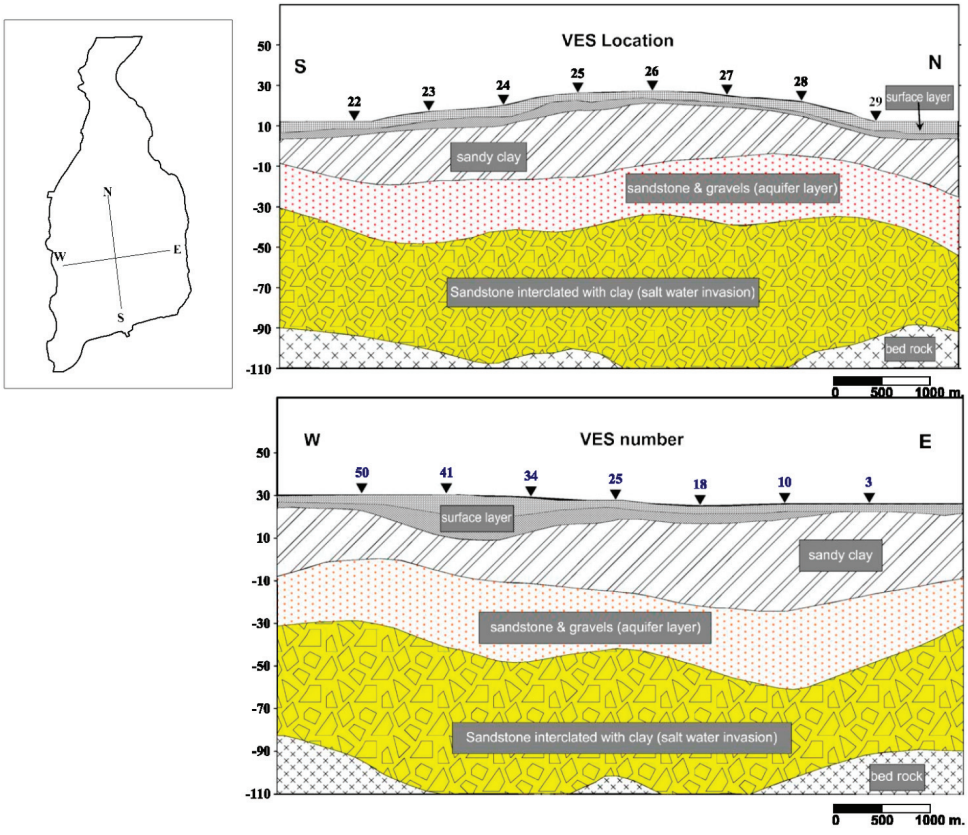

Figure 2. Hydro−geological cross−section of the study area (source: Abbas et al. [12]).

Regarding the unsaturated zone's properties, its vertical permeability was measured and interpolated by Himida [15] by applying infiltration tests at specified points, and this was found to range from approximately 1.75 to 9.18 m/day. Besides this, Eissa et al. [1] measured the vertical permeability at five different locations, with a geometric mean of 0.19 m/day. The porosity and tortuosity were determined by Khalil [14] via geo-electrical analysis as 0.3 and 1.348, respectively. The storativity parameter ranges from around 0.0003 to 0.01 according to field pumping tests [15].

Regarding groundwater recharge and discharge, the aquifer is naturally recharged by rainfall precipitation [16]. The mean annual recharge volume has been estimated, respectively, by Himida [15], Eissa et al. [1], and Eissa et al. [13] as 1.83, 1.58, and 2.16 Mm^3. In addition, groundwater pumping started in the year 1982 with a pumping rate of 870 m^3/day, and increased slightly from the year 1982 to 1998, reaching a rate of 3900 m^3/day, followed by a slight decrease until the year 2013, reaching a rate of 1400 m^3/day [13].

Regarding groundwater characteristics, the groundwater table level was measured, respectively, in 1994 and 2013 by Himida [15] and Eissa et al. [1]. The groundwater level varies from 0.23 to 1.75 m above MSL (Figure 3). Himida [15] calculated the groundwater hydraulic gradient, and found that it varies from 0.00023 to 0.0027, with an arithmetic mean of 0.0015 [15]. Since the aquifer is classified as a coastal aquifer, the Total Dissolved Solids (TDS) concentration of the groundwater is relatively high if it is compared to the fresh groundwater of the in-land aquifers (higher than 1000 mg/L) (Figure 3). The TDS concentration was found to range from around 2000 to 8000 mg/L in 1994 [15], and from about 100 to 14,000 mg/liter in 2009 [1].

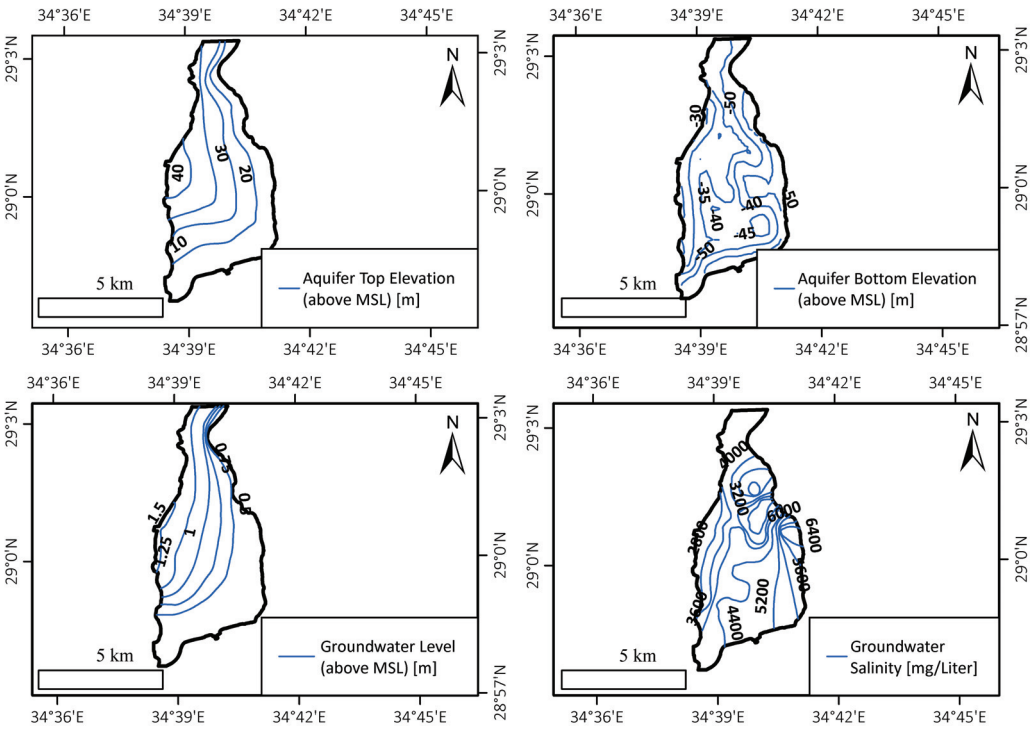

Figure 3. Aquifer and groundwater characteristics.

2.2. Data Acquisition and Preparation

Delineating the MAR sites depends on many factors, such as aquifer hydrogeology, topography, water quality, hydrometeorology, and management (Figure 4) [8]. Thus, data related to the aforementioned fields should be acquired. Our data were collected from the previous studies, except surface water quality, flow discharge hydrographs, and environmental impact assessment, due to the lack of data availability.

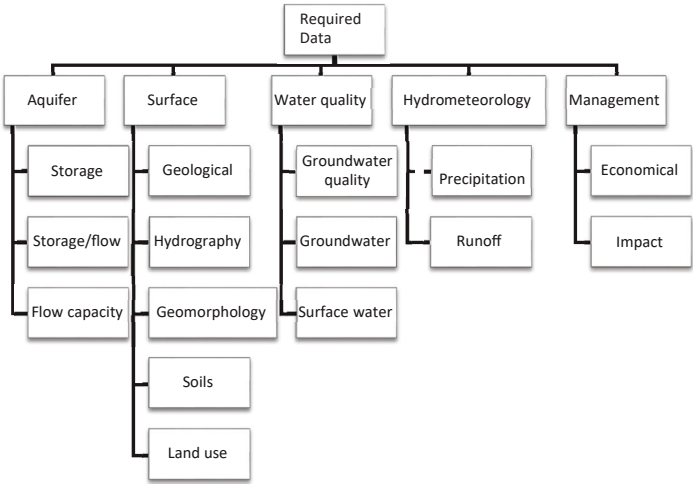

Figure 4. Data required for delineating MAR sites. (Source: Sallwey et al. [8]).

Regarding the aquifer's properties, aquifer geometry data were acquired from geophysical fieldwork and analyses conducted by Abbas et al. [12]. Additionally, aquifer hydrogeology information was collected from Himida [15] in the form of contoured maps based on field measurements. Himida [15] mapped the vertical permeability, groundwater table, transmissivity, and storativity. In addition, hydraulic conductivity data were collected from Eissa et al. [13] and Sallam [6] by calibrating the groundwater flow model. The groundwater hydraulic gradient was processed by ArcGIS 10.7.1 (developed by ESRI (Environmental Systems Research Institute) located in Redlands, California, USA) by using the groundwater table as input data.

Surface topography was prepared by downloading the Digital Elevation Model (DEM) raster file of type Shuttle Radar Topography Mission (SRTM) from the surface elevation data of Consortium for Spatial Information (CGIAR-CSI) geospatial community with a resolution of 30 m. Additionally, the spatial data (surface slope, distance from the shore) were processed by analyzing the acquired DEM data using ArcGIS10.7.1 software. In addition, LULC were classified by downloading Landsat 7 images from USGS, followed by image processing using ArcGIS 10.7.1 software.

The groundwater quality data were acquired from Himida [15] and Eissa et al. [1], taking into account the spatial variability. Regarding hydro-meteorological data, precipitation and runoff data were obtained from Al Zayed et al. [5] and Khalil [14], whereas the groundwater natural recharge was estimated by Himida [15], Eissa et al. [1], and Eissa et al. [13]. However, the hydro-meteorological data are not spatially distributed in the study area. Thus, hydro-meteorological data were excluded from the gathered data.

Since the groundwater level and salinity were last measured in the year 2009, a field trip was performed on 24 July and 25 July 2020 (Appendix A). The main objective of the trip was to check the data collected from the previous studies. Additionally, it was necessary to investigate the current land use and the main water supply in the study area.

2.3. GIS-MCDA Method Set-Up

To apply a MAR system at a specific site, feasibility studies should be carefully conducted to check the suitable elements required for a successful MAR installation. The elements include water source for recharge (surface, storm, reclaimed, potable, desalinated), aquifer for storing and recovering water (geological strata type, hydrogeological characteristics, groundwater hydro-chemistry characteristics, aquifer mineralogy), and a suitable site location for installing MAR (hydrogeology, topography, soil type, land use, climate).

RS and GIS tools have been widely used in the field of hydrogeology. These tools are powerful for use in acquiring, representing, and analyzing thematic layers characterized by spatial variability (topography, hydrogeology, hydro-chemistry, etc.) [16]. Researchers have created potential maps to manage groundwater by applying the aforementioned tools to give the necessary information to decision-makers in order to achieve the following objectives [16]: (i) exploring and assessing the groundwater resources, (ii) delineating artificial recharge sites, (iii) assessing the groundwater's vulnerability to pollution, (iv) estimating natural recharge distribution, (v) analyzing and monitoring hydrogeological properties, (vi) modeling the groundwater flow and pollution.

Therefore, potential maps could be utilized as a tool to delineate the most feasible MAR sites for the decision-makers. Different decision-making methods have been applied to create potential maps: statistical methods [17–19], machine learning [20–22], multi-criteria decision analysis [9,10,23] and groundwater numerical modeling [24].

Most researchers have combined the two methods to delineate feasible MAR sites: GIS and Multi-Criteria Decision Analysis (MCDA). The combination of the aforementioned methods was firstly introduced by Malczewski [25] as GIS-MCDA. It is defined as a group of methods applied by overlaying and aggregating the spatial thematic layers to provide the necessary information for the decision-making process [26]. Despite the presence of several method combinations (as mentioned above) for creating potential MAR site location maps, GIS-MCDA is the most common method among researchers [8].

Most studies applied a specific methodology to select the best MAR sites [27–29]. However, in this study, the locations of the best sites are delineated by classifying the study area into different zones according to site feasibility. This study adopted a GIS-based holistic approach. This approach was introduced by [9] and encompasses the following steps (Figure 5): (i) problem definition (checking the elements and specifying the methods), (ii) constraint mapping (screening out unfeasible sites), (iii) suitability mapping (calculating overall score by combining criteria via a weighting factor), (iv) sensitivity analysis (checking the robustness of the weighting factors).

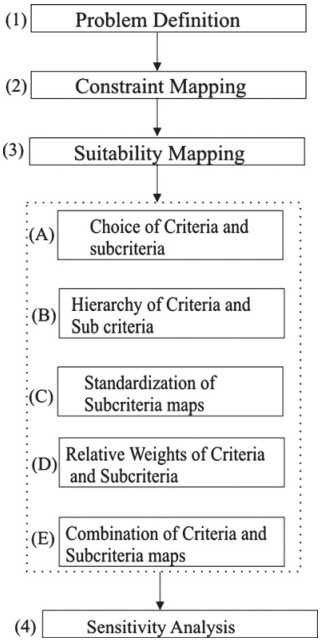

Figure 5. Flowchart showing GIS-MCDS framework (source: Rahman et al. [9]). The figure depicts that 4 major steps should be implemented before delineating the MAR location.

2.3.1. Constraint Mapping

In this study, an intersection operator was chosen for this process. The criterion value of the intersection operator is unity and zero. An intersection operator is practiced by assigning a unity value when the criteria satisfy the logical conditions, and vice versa [9].

Before applying this method, the constraint criteria were validated using the criteria reviewed by Sallwey et al. [8] (Table 1). Afterwards, the chosen criteria were converted from contoured maps to thematic raster layers with a 250 m pixel size using ArcGIS10.7.1 software. The pixel size was assigned based on grain size classification (medium sand in this study), as represented by Lagacherie et al. [30]. Appendix B shows the criterion of thematic layers for the constraint mapping.

Table 1. Validating the criteria reviewed by Sallwey et al. [8] for constraint mapping in the study area.

Constraint Criteria	Validity	Reason
LULC (Land Use Land Cover)	Valid	Presence of different LULC classifications (bare soil, urban areas, Sabkha, and vegetation)
Surface Slope	Valid	High slope values in some areas (>3%)
Geology	Invalid	Homogenous surface layer (medium sand)
Unsaturated Thickness	Valid	Low unsaturated thickness in some areas (<5 m)
Soil Infiltration Rate	Invalid	High vertical permeability in all areas (>0.65 m/day)
Distance from the Pollution Source	Valid	Presence of sea as a pollution source in the study area. Rahman et al. [9] recommended that any area at a distance less than 500 m from the pollution source is unsuitable for installing MAR.

2.3.2. Suitability Mapping

The primary function of suitability mapping is classifying the potential for installing the site at a specific location. During this process, weights are assigned to the criteria and combined to get a score for each area [26]. The assigned weights are estimated by a technical expert or a decision-maker based on field experience [8]. Suitability mapping comprises four steps: (1) choice of criteria, (2) hierarchy of criteria, (3) standardization of criteria, (4) relative weights of criteria and (5) combination of criteria.

Choice of Criteria

Choosing the criteria depends on the problem statement and site conditions [8]. The more complex the problem is, the more criteria are chosen. To determine the criteria to be selected, Sallwey et al. [8] reviewed previous studies to collect all possible criteria that could be applied for this process. We screened out the criteria to choose the most suitable ones for the problem and the case study (Table 2). Appendix B shows the chosen criterion thematic layers for suitability mapping.

Table 2. Validating the criteria for suitability mapping as reviewed by Sallwey et al. [8] in the study area.

Type	Criteria	Validity	Reason
Aquifer hydrogeology	Flow capacity (vertical permeability)	Valid	-
	Storage capacity (unsaturated thickness)	Valid	-
	Storage capacity (saturation thickness)	Valid	-
	Flow capacity (hydraulic gradient)	Valid	-
Hydrological system	Precipitation	Invalid	Small scale area where the spatial distribution of precipitation cannot be applied
	Runoff	Invalid	Lack of data related to the spatial distribution of runoff coefficient
Management	Economic benefits	Invalid	Lack of cost–benefit analysis study
	Environmental impact assessment	Invalid	Lack of environmental impact assessment study
Surface	Geology	Invalid	Homogeneity of the surface layer
	Geomorphology (surface slope)	Valid	-
	Hydrography (drainage density)	Invalid	The study area scale is small
	LULC	Invalid	Unfeasible sites were eliminated in the constraint mapping process
	Soils	Invalid	Homogeneity of the surface layer
Water quality	Groundwater quality (salinity)	Valid	-
	Surface water quality	Invalid	No presence of perennial stream or lake in the study area

Hierarchy of the Criteria

After selecting the criteria, the criteria should be divided into three groups in a hierarchical order. Most of the previous studies adopted the following hierarchy according to the priority of the following criteria: (1) aquifer hydrogeology (unsaturated thickness and vertical permeability), (2) topography (surface slope) and groundwater quality (salinity), and (3) aquifer hydrogeology (saturated thickness and hydraulic gradient).

Standardization of Criteria

To combine the criteria for suitability mapping, the criterion value should be converted to a uniform scale. The method is known as standardization. Standardization is applied by different methods: linear and step functions. In this study, the linear method was practiced. The results range from 0% (assigned for the lowest suitable criterion value) to 100% (assigned for the highest suitable criterion value). Appendix B shows the criterion thematic layers after standardization.

Relative Weights of the Criteria

Relative weights of the criteria were conducted by applying the Analytical Hierarchy Process (AHP) using a pair-wise matrix. AHP was used because it is the most common method in the literature. The matrix was calculated based on the proposal assigned by Saaty [31], as shown in Equations (1) and (2) [21]. Additionally, a consistency check has been performed to verify the assigned relative weights.

$$A = \begin{pmatrix} 1 & \cdots & a_{1n} \\ \vdots & \ddots & \vdots \\ \frac{1}{a_{1n}} & \cdots & 1 \end{pmatrix} \quad (1)$$

where A is the pair comparison matrix, and 1 *to* a_{1n} is the scale of importance determined by an expert [25].

$$W = \sum_{j=1}^{n} w_j a_{ij} / N \quad (2)$$

where W is the vector of weighting factors w_1, w_2, ...w_n, a_{ij} is the normalized scale of importance determined by an expert, and N is the number of the criteria [25].

Combination of Criteria

After assigning weighting and standardizing processes, the overall score is calculated by combining the weighting factors. Weighted Linear Combination (WLC) and weighted average methods were chosen for combining the thematic layers. WLC is an overlay-weighted method applied in most studies before selecting the most suitable MAR site location [27].

2.3.3. Sensitivity Analysis

Sensitivity analysis was conducted to check the results' robustness and determine the uncertainty in the hierarchy and the assignment of relative importance [31]. Ordered Weighted Averaging (OWA) was utilized for the analysis, as OWA is characterized by the presence of a fuzzy linguistic quantifier, which is capable of manipulating the weighting factor. OWA was first proposed by Yager [32] and can be calculated using Equation (3). Table 3 represents the weighting values of weighted average, WLC and the sensitivity analysis.

$$OWA_i = \sum_{j=1}^{n} \left(\left(\sum_{k=1}^{j} u_k \right)^{\alpha} - \left(\sum_{k=1}^{j-1} u_k \right)^{\alpha} \right) W_{ij} \quad (3)$$

where W_{ij} is the weighted factor for the criterion value i, u_k is the criteria weight reordered according to W_{ij}, and α is the parameter linguistic quantifier. α equals 0 when at least one of the criteria is satisfied, resulting in no trade-off, whereas $\alpha = 1$ corresponds to WLC. If $\alpha = \infty$, then most of the criteria are satisfied, resulting in no trade [32].

Table 3. The weighting values at different linguistic quantifier values.

Criteria\α	Weighted Average	WLC	0.50	1.00	2.00	5.00	10.00	20.00
Unsaturated thickness	0.1667	0.32	0.56	0.32	0.10	0.00	0.00	0.00
Vertical permeability	0.1667	0.32	0.23	0.32	0.30	0.10	0.01	0.00
Surface slope	0.1667	0.13	0.08	0.13	0.18	0.16	0.06	0.00
Salinity	0.1667	0.13	0.07	0.13	0.22	0.31	0.26	0.10
Saturated thickness	0.1667	0.05	0.03	0.05	0.10	0.19	0.25	0.23
Hydraulic gradient	0.1667	0.05	0.03	0.05	0.10	0.24	0.42	0.67
Sum	1.00	1.00	1.00	1.00	1.00	1.00	1.00	1.00

3. Results

Constraint mapping, suitability mapping and sensitivity analysis were performed (Figure 6). Suitability mapping was undertaken using two methods: WLC and weighted averaging. High suitability scores indicate high potential for installing MAR and vice versa. WLC involves applying the AHP hierarchy according to its priority based on field experience. Regarding the WLC map, the overall suitability scores are 6.34% (high potential MAR sites), 20.73% (moderate potential MAR site), and 24% (low potential MAR site). The most suitable locations are situated in the western portion of the study area near the ephemeral stream outlet. The most suitable locations are zoned (Zone I). They are characterized by good hydrogeological and groundwater quality conditions (Table 4).

Table 4. The range of aquifer parameters under high potential MAR conditions.

Criteria	Range	Status	Reason
Unsaturated thickness (m)	32.45–42.89	Satisfied	High unsaturated thickness
Vertical permeability (m/day)	6.96–9.17	Satisfied	High vertical permeability
Surface slope (%)	0.94–1.27	Satisfied	Low surface slope
Salinity (mg/L)	2368.22–3443.26	Satisfied	Low salinity
Saturated thickness (m)	31–37.24	Unsatisfied	Low saturated thickness
Hydraulic gradient (%)	0.071–0.05	Satisfied	Low hydraulic gradient

The sensitivity analysis is defined as a change in the overall suitability score due to a change in the weighting factors assigned by the decision-makers or experts. In this study, sensitivity analysis was performed using the OWA method, whereby the weighting factor was changed to determine the effect of changing the criterion's value on the results using quantifier α. Quantifier α ranges from 0.5 to 20. The results show a close agreement between the sensitivity analysis map and the suitability map in the case of a high potential MAR site location (Zone I) (Figure 6).

Table 5 shows the GIS-MCDA results summary. The table represents the fractions of the total area occupied by each potential MAR class.

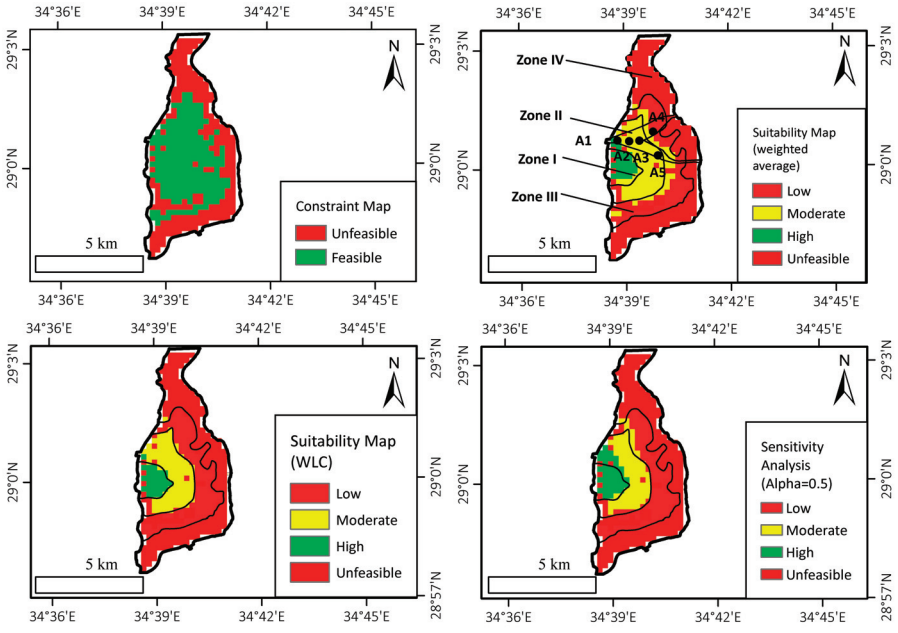

Figure 6. *Cont.*

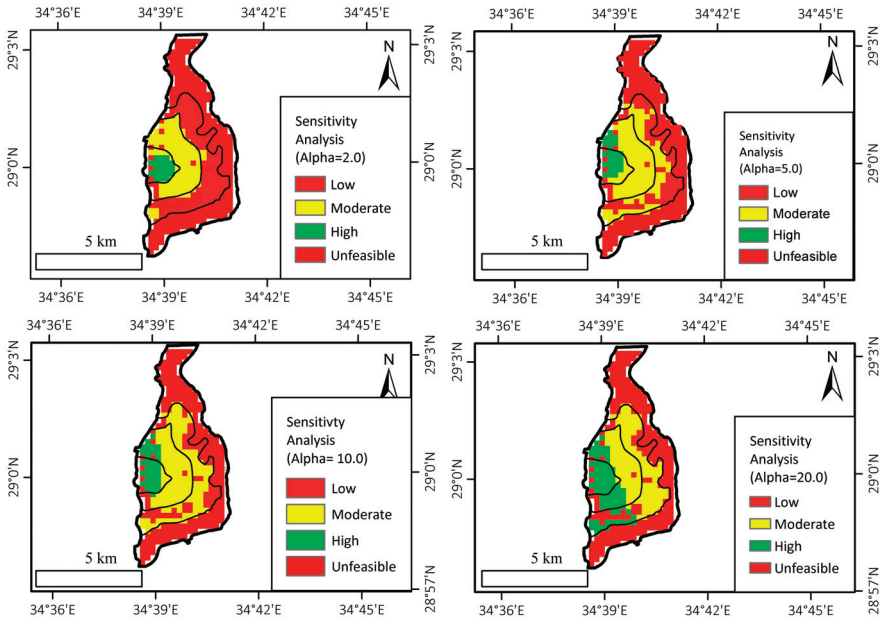

Figure 6. Study results showing the constraint mapping, suitability mapping using weighted averaging, WLC, and sensitivity analysis.

Table 5. GIS-MCDA results summary. (Note: the values represent the area proportion in a percentage).

	High Potential	Moderate Potential	Low Potential	Unfeasible
Constraint mapping		51.21	48.79	
Suitability mapping (weighted average)	5.85	27.56	17.80	48.79
Suitability mapping (WLC)	6.34	20.73	24.14	48.79
Sensitivity analysis (α = 0.5)	9.02	18.04	24.15	48.79
Sensitivity analysis (α = 2.0)	4.87	23.90	22.44	48.79
Sensitivity analysis (α = 5.0)	10.73	34.38	6.10	48.79
Sensitivity analysis (α = 10.0)	15.61	31.82	2.78	48.79
Sensitivity analysis (α = 20.0)	30.73	17.7	2.78	48.79

4. Discussion

Firstly, the study area is suitable for installing the MAR system because MAR elements are satisfied (source of water, adequate aquifer, land for construction). Additionally, the following MAR structures are feasible to use for the study area: infiltration pond, controlled flooding, percolation pond, recharge releases, open wells and shafts, percolation tanks. However, further socio-economic and technical studies are required to decide on the most suitable structure. In addition, environmental studies are necessary to check whether the installed structure positively affects the environment of the hydrogeological system.

The suitability map has indicated that the high potential sites for installing MAR are located in the western portion in the vicinity of the study area, near the ephemeral stream outlet. Additionally, the constraint map has shown that sites near the shoreline are unfeasible.

The suitability map has been compared with the criterion thematic layers, and it has been observed that a close agreement occurs between the suitability map and the criterion thematic layers, except for the saturated thickness, where low criterion values are found in high potential scoring areas, and vice versa. This means that the suitability map reflects not only the potential sites for installing MAR, but also the locations of areas characterized by good aquifer hydrogeological conditions.

The sensitivity analysis indicates that the change in assigned weights does not significantly affect the results at zone I (high potential MAR site), which ensures the robustness of the suitability map at high potential sites.

The suitability map has been compared with the previous study conducted by Sallam [6], who studied the feasibility of installing ASR in the study area. The comparison shows that the highly potential MAR site locations on the suitability map are near to the suggested ASR site locations "A1", "A2" and "A3" proposed by Sallam [6] (Figure 6). Sallam [6] concluded that the "A1", "A2" and "A3" site locations are characterized by a high recovery efficiency at low dispersivity compared to the latter, especially "A1", using the numerical modeling method. This strongly agrees with the results obtained from the GIS-MCDA method in this study.

The suitability map is a tool for decision-makers, and it can be utilized along with other maps in the study area, such as the groundwater potential map, the water allocation map, the flood plain map, etc. Even though the suitability map could contribute to deciding the location of MAR, it has been created without considering the decision rules set by the decision-maker, economic benefits (cost–benefit analysis), risk assessment studies, and environmental benefits (environmental impact assessment). In addition, this study has applied just one approach (GIS-MCDA); however, different methods can identify MAR locations (statistical methods, machine learning, groundwater numerical modeling).

The MAR structure can be applied for the conjunctive use of the surface, groundwater, reclaimed water, and desalinated seawater. Hence, further studies are needed to impose the conjunctive use of water resources using an IWRM framework.

5. Conclusions

The main aim of this research is to delineate the most feasible sites for installing MAR using the GIS-MCDA approach. To delineate the feasible sites, a constraint map and suitability maps have been created. The criteria utilized for screening out the unfeasible sites in the constraint mapping process are as follows: LULC, surface slope, unsaturated thickness, and distance from shore. The constraint map depicts that around 48% of the study area is inappropriate for use as MAR (located mostly in the eastern portion of the study area). Additionally, the criteria utilized to develop a suitability map include vertical permeability, unsaturated thickness, surface slope, salinity, hydraulic gradient, and saturated thickness. The suitability map is divided into four zones according to the feasibility of installing a MAR site: zone I (high), zone II (moderate), zone III (low) and zone IV (infeasible). The suitability map shows that the high and moderate potential areas constitute, respectively, around 6% and 20% of the study area.

To sum up, the suitability map indicates that MAR could be installed at zone I (located in the western portion of the study area near the ephemeral stream outlet), where most conditions for installing MAR are fulfilled, as the zone is characterized by high vertical permeability (6.96–9.17 m/d), high unsaturated thickness (32.45–42.89 m), low surface slope (0.94–1.27%), low salinity (2368.22–3443.26 mg/L), and low hydraulic gradient (0.071–0.05%).

Further studies should be conducted to check the efficiency of replenishing the aquifer after installing the MAR system at the best locations by modeling the groundwater flow and transport. In addition, it is important to identify the risks that may cause MAR malfunction, such as clogging problems and hydro-geochemical reactions during operating MAR. A pilot project should be constructed to perform fieldwork (injection tests, infiltration tests).

Author Contributions: Conceptualization, O.M.S.; methodology, O.M.S.; validation, O.M.S. and C.S.; formal analysis, K.S.; investigation, K.S.; resources, O.M.S.; data curation, O.M.S.; writing—original draft preparation, K.S.; writing—review and editing, O.M.S. and C.S.; visualization, K.S.; supervision, O.M.S. and C.S. All authors have read and agreed to the published version of the manuscript.

Funding: This work was part of a master's thesis conducted by Karim Mohamed Ahmed Soliman via a scholarship awarded by Deutsche Akademischer Austauschdienst (DAAD) (Funding programme/-ID: 57252261), (personal ref. no.: 91708607).

Institutional Review Board Statement: Not applicable.

Informed Consent Statement: Not applicable.

Data Availability Statement: Not applicable.

Acknowledgments: The first author would like to thank Deutsche Akademischer Austauschdienst (DAAD) for awarding him a scholarship to study on a master's program at Technische Universität Darmstadt. The authors would like to thank Water Resources Research Institute (WRRI), National Water Research Center (NWRC), Egypt, for providing the necessary information and support related to the research.

Conflicts of Interest: The authors declare no conflict of interest.

Appendix A

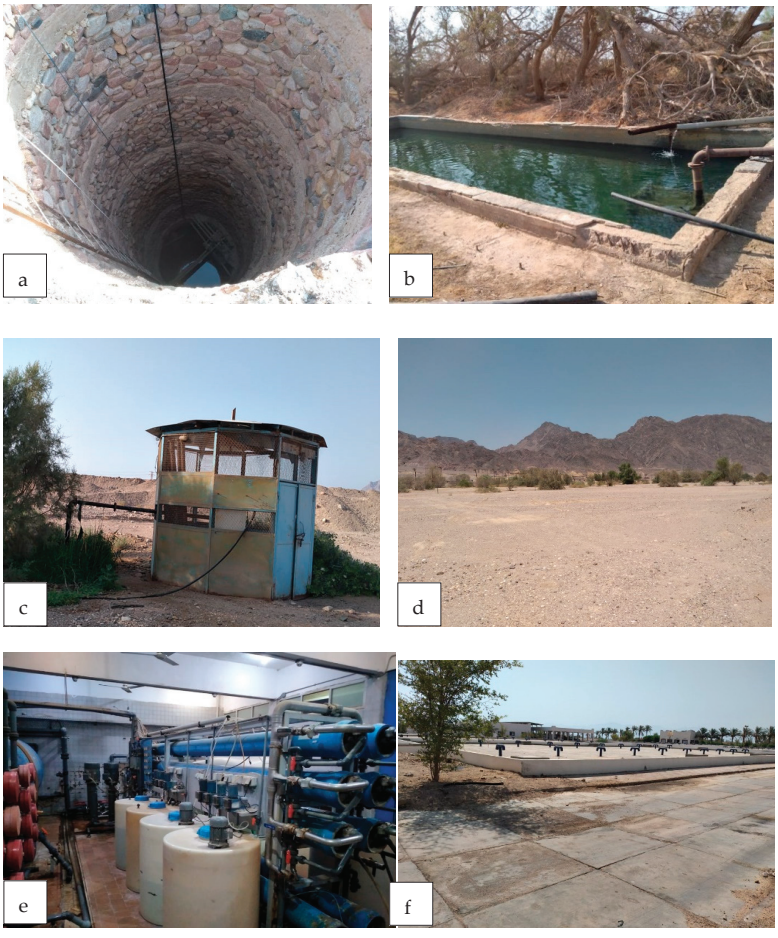

Figure A1. (**a**) Dug wells. (**b**) A basin located beside the hand-dug well for storing the extracted groundwater after the pumping phase. (**c**) Drilled well. (**d**) Forest trees irrigated from groundwater. (**e**) Nuweiba desalination plant. (**f**) Storage tank in Nuweiba desalination plant.

Appendix B

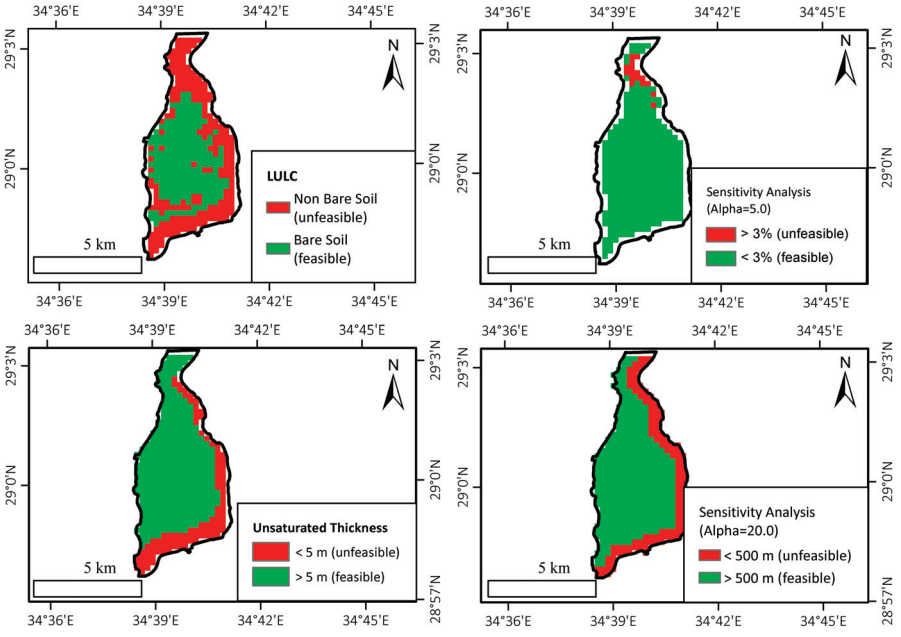

Figure A2. Constraint map criteria thematic layers.

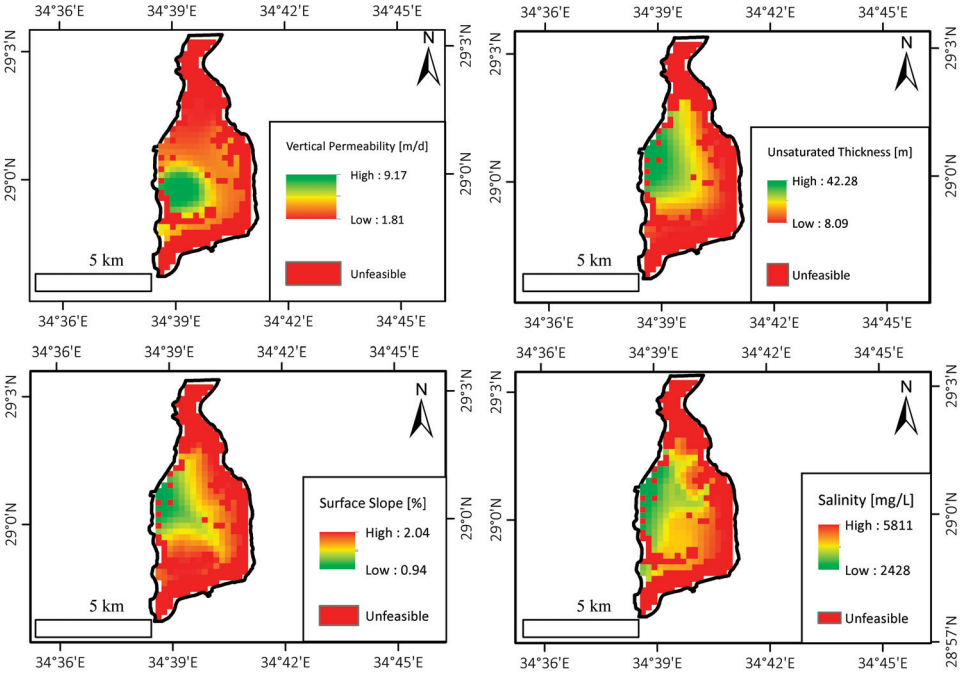

Figure A3. *Cont.*

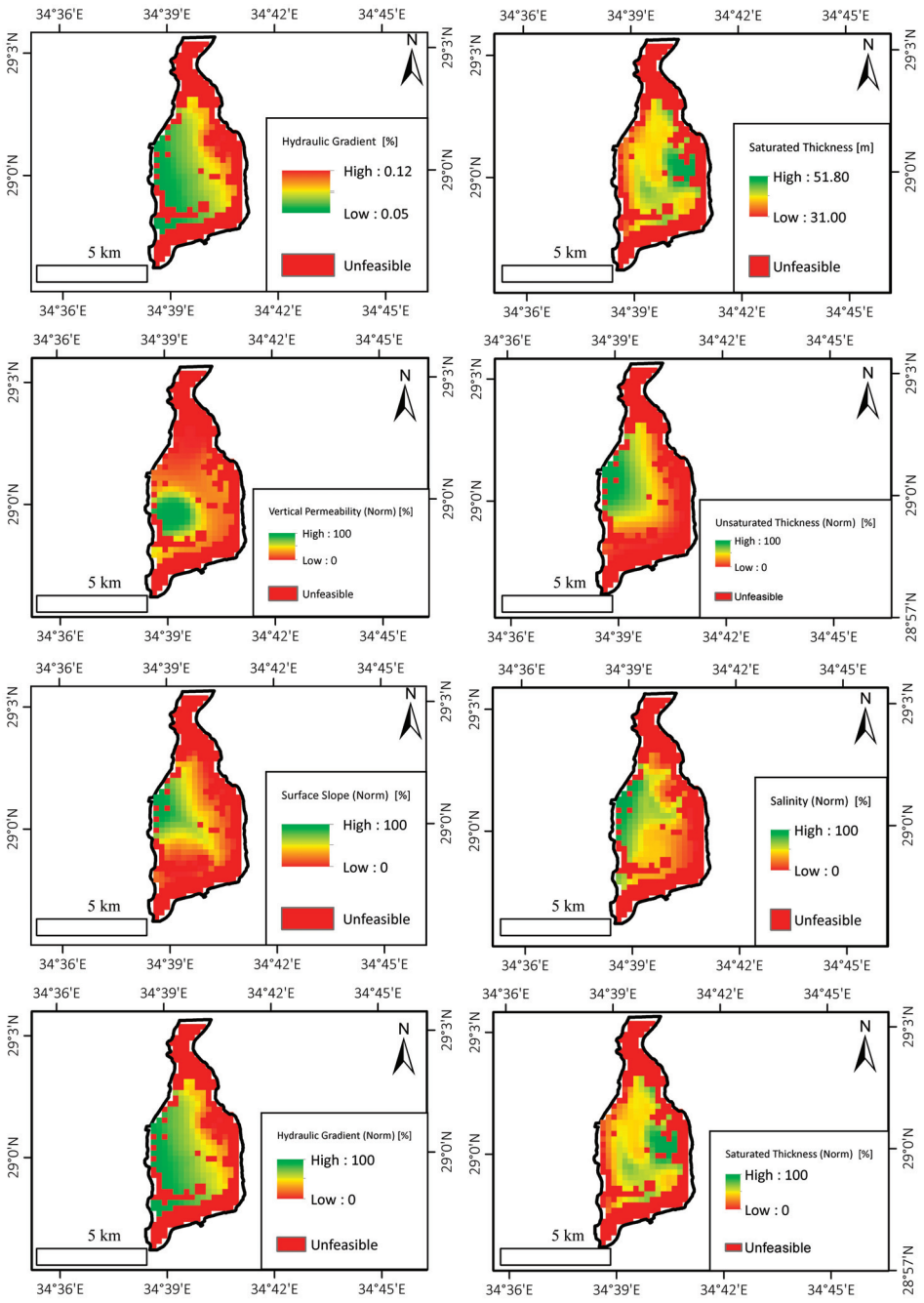

Figure A3. Suitability map criteria thematic layers before and after standardization.

References

1. Eissa, M.A.; Thomas, J.M.; Pohll, G.; Hershey, R.L.; Dahab, K.A.; Dawoud, M.I.; ElShiekh, A.; Gomaa, M.A. Groundwater resource sustainability in the Wadi Watir delta, Gulf of Aqaba, Sinai, Egypt. *Hydrogeol. J.* **2013**, *21*, 1833–1851. [CrossRef]
2. Abuzied, S.M.; Yuan, M.; Ibrahim, S.K.; Kaiser, M.F.; Seleem, T.A. Delineation of Groundwater Potential Zones in Nuweiba Area (Egypt) Using Remote Sensing and GIS Techniques. *Int. J. Signal Process. Syst.* **2015**, *4*, 109–117. [CrossRef]
3. Masoud, A.A. Runoff modeling of the wadi systems for estimating flash flood and groundwater recharge potential in Southern Sinai, Egypt. *Arab. J. Geosci.* **2011**, *4*, 785–801. [CrossRef]
4. Milewski, A.; Sultan, M.; Yan, E.; Becker, R.; Abdeldayem, A.; Soliman, F.; Gelil, K.A. A remote sensing solution for estimating runoff and recharge in arid environments. *J. Hydrol.* **2009**, *373*, 1–14. [CrossRef]
5. Al Zayed, I.; Ribbe, L.; Al Salhi, A. Water Harvesting and Flashflood Mitigation-Wadi Watier Case Study (South Sinai, Egypt). *Int. J. Water Resour. Arid Environ.* **2013**, *2*, 102–109.
6. Sallam, O.M. Use of Numerical Groundwater Modeling to Assess the Feasibility of Aquifer Storage and Recovery (ASR) in the Wadi Watir Delta, Sinai, Egypt. *J. Water Resour. Prot.* **2019**, *11*, 1462–1480. [CrossRef]
7. Elewa, H.H.; Qaddah, A.A. Groundwater potentiality mapping in the Sinai Peninsula, Egypt, using remote sensing and GIS-watershed-based modeling. *Hydrogeol. J.* **2011**, *19*, 613–628. [CrossRef]
8. Sallwey, J.; Valverde, J.P.B.; López, F.V.; Junghanns, R.; Stefan, C. Suitability maps for managed aquifer recharge: A review of multi-criteria decision analysis studies. *Environ. Rev.* **2019**, *27*, 138–150. [CrossRef]
9. Rahman, M.A.; Rusteberg, B.; Gogu, R.; Ferreira, J.L.; Sauter, M. A new spatial multi-criteria decision support tool for site selection for implementation of managed aquifer recharge. *J. Environ. Manag.* **2012**, *99*, 61–75. [CrossRef]
10. Chowdhury, A.; Jha, M.K.; Chowdary, V.M. Delineation of groundwater recharge zones and identification of artificial recharge sites in West Medinipur district, West Bengal, using RS, GIS and MCDM techniques. *Environ. Earth Sci.* **2010**, *59*, 1209–1222. [CrossRef]
11. Dillon, P.; Pavelic, P.; Page, D.; Beringen, H.; Ward, J.R. *Managed Aquifer Recharge: An Introduction. Waterlines Report Series*; National Water Commission: Canberra, Australia, 2009; Volume 13.
12. Abbas, A.M.; Atya, M.A.; Al-Sayed, E.A.; Kamei, H. Assessment of groundwater resources of the Nuweiba area at Sinai Peninsula, Egypt by using geoelectric data corrected for the influence of near surface inhomogeneities. *J. Appl. Geophys.* **2004**, *56*, 107–122. [CrossRef]
13. Eissa, M.; Thomas, J.M.; Pohll, G.; Shouakar-Stash, O.; Hershey, R.L.; Dawoud, M. Groundwater recharge and salinization in the arid coastal plain aquifer of the Wadi Watir delta, Sinai, Egypt. *Appl. Geochem.* **2016**, *71*, 48–62. [CrossRef]
14. Khalil, M.H. Hydro-geophysical Configuration for the Quaternary Aquifer of Nuweiba Alluvial Fan. *J. Environ. Eng. Geophys.* **2010**, *15*, 77–90. [CrossRef]
15. Himida, I.H. *Water Resources in Delta Wadi Watir (Nuweiba Area) and Improvement of the Hydrologic Setting in the Area*; Internal Technical Report; Desert Research Center: Cairo, Egypt, 1994.
16. Jha, M.K.; Chowdhury, A.; Chowdary, V.M.; Peiffer, S. Groundwater management and development by integrated remote sensing and geographic information systems: Prospects and constraints. *Water Resour. Manag.* **2007**, *21*, 427–467. [CrossRef]
17. Razandi, Y.; Pourghasemi, H.R.; Neisani, N.S.; Rahmati, O. Application of analytical hierarchy process, frequency ratio, and certainty factor models for groundwater potential mapping using GIS. *Earth Sci. Inform.* **2015**, *8*, 867–883. [CrossRef]
18. Manap, M.A.; Nampak, H.; Pradhan, B.; Lee, S.; Sulaiman, W.N.A.; Ramli, M.F. Application of probabilistic-based frequency ratio model in groundwater potential mapping using remote sensing data and GIS. *Arab. J. Geosci.* **2014**, *7*, 711–724. [CrossRef]
19. Guru, B.; Seshan, K.; Bera, S. Frequency ratio model for groundwater potential mapping and its sustainable management in cold desert, India. *J. King Saud Univ. Sci.* **2017**, *29*, 333–347. [CrossRef]
20. Naghibi, S.A.; Pourghasemi, H.R.; Dixon, B. GIS-based groundwater potential mapping using boosted regression tree, classification and regression tree, and random forest machine learning models in Iran. *Environ. Monit. Assess.* **2016**, *188*, 1–27. [CrossRef]
21. Kordestani, M.D.; Naghibi, S.A.; Hashemi, H.; Ahmadi, K.; Kalantar, B.; Pradhan, B. Groundwater potential mapping using a novel data-mining ensemble model. *Hydrogeol. J.* **2019**, *27*, 211–224. [CrossRef]
22. Díaz-Alcaide, S.; Martínez-Santos, P. Review: Advances in groundwater potential mapping. *Hydrogeol. J.* **2019**, *27*, 2307–2324. [CrossRef]
23. Valverde, J.P.B.; Blank, C.; Roidt, M.; Schneider, L.; Stefan, C. Application of a GIS Multi-Criteria Decision Analysis for the Identification of Intrinsic Suitable Sites in Costa Rica for the Application of Managed Aquifer Recharge (MAR) through Spreading Methods. *Water* **2016**, *8*, 391. [CrossRef]
24. Russo, T.A.; Fisher, A.T.; Lockwood, B.S. Assessment of Managed Aquifer Recharge Site Suitability Using a GIS and Modeling. *Ground Water* **2015**, *53*, 389–400. [CrossRef] [PubMed]
25. Malczewski, J. *GIS and Multicriteria Decision Analysis*; John Wiley and Sons: New York, NY, USA, 1999.
26. Malczewski, J. GIS-based multicriteria decision analysis: A survey of the literature. *Int. J. Geogr. Inf. Sci.* **2006**, *20*, 703–726. [CrossRef]
27. Saraf, A.K.; Choudary, P.R. Integrated remote sensing and GIS for the groundwater exploration and identification of artificial recharge sites. *Int. J. Remote Sens.* **1998**, *19*, 1825–1841. [CrossRef]

28. Shankar, M.N.R.; Mohan, G. A GIS based hydrogeomorphic approach for identification of site-specific artificial-recharge techniques in the Deccan Volcanic Province. *J. Earth Syst. Sci.* **2005**, *114*, 505–514. [CrossRef]
29. Anbazhagan, S.; Ramasamy, S.M.; Das Gupta, S. Remote sensing and GIS for artificial recharge study, runoff estimation and planning in Ayyar basin, Tamil Nadu, India. *Environ. Earth Sci.* **2005**, *48*, 158–170. [CrossRef]
30. Lagacherie, P.; McBratney, A.B.; Voltz, M. *Digital Soil Mapping: An Introductory Perspective*; Elsevier B.V.: Amsterdam, The Netherlands, 2006.
31. Saaty, T.L. *The Analytical Hierarchy Process*; Mcgraw-Hill: New York, NY, USA, 1980.
32. Yager, R.R. On ordered weighted averaging aggregation operators in multicriteria decision making Systems. *IEEE Trans. Syst. Man Cybern.* **1988**, *18*, 183–190. [CrossRef]

water

MDPI

Article

Characteristic and Attribution of Runoff Variation in the Yanhe River Basin, Loess Plateau, Based on the Budyko Hypothesis

Kun Hou [1], Jiping Wang [2] and Xiuru Wang [1,*]

[1] School of Soil and Water Conservation, Beijing Forestry University, Beijing 100083, China; houkun0822@163.com
[2] Research Center of Saline and Alkali Land of State Forestry Administration, Chinese Academy of Forestry, Beijing 100091, China; wjp_gis@163.com
* Correspondence: wang-xr@163.com; Tel.: +86-10-6233-8044

Abstract: The ecological restoration projects in the Loess Plateau (LP) has significantly altered the underlying surface conditions, coupled with a warming–wetting climate, which has profoundly affected the regional water cycle. Evaluating the response of runoff to external environmental change and quantitatively identifying the contribution of anthropogenic interference and climate change are prerequisites for efficient utilization of water resources in arid/semi-arid regions. Daily recorded data of hydrological and meteorological elements between 1969 and 2019 and the elasticity coefficient method based on Budyko hypothesis were used for attribution analysis of runoff change in the Yanhe River basin. The results show the following: (1) the measured runoff decreased significantly ($p < 0.05$, –0.2845 mm year^{-1}), and suggested substantial difference before and after 2000; (2) the area of woodland and grassland had a sharp increase from 2000, while the elasticity of runoff to precipitation, potential evapotranspiration (ET_0), and vegetation all decreased; (3) the improvement of underlying surface conditions has become the leading factor of runoff reduction with a contribution of 96.78%; (4) the impact of vegetation restoration on runoff reduction is effective within a certain threshold. We consider that more attention should be paid to the afforestation scale and its possible negative eco-hydrological effects in future ecological restoration.

Keywords: Loess Plateau; anthropogenic disturbance; runoff; elasticity coefficient; Budyko hypothesis; warming–wetting

Citation: Hou, K.; Wang, J.; Wang, X. Characteristic and Attribution of Runoff Variation in the Yanhe River Basin, Loess Plateau, Based on the Budyko Hypothesis. *Water* **2022**, *14*, 495. https://doi.org/10.3390/w14030495

Academic Editors: Alban Kuriqi and Luis Garrote

Received: 22 December 2021
Accepted: 5 February 2022
Published: 7 February 2022

1. Introduction

A changing environment strongly influenced by climate and anthropogenic interference can directly affect the land surface process [1] and alter the mechanism of runoff generation and concentration [2]. Decreasing trends in runoff and sediment loads have been observed in approximately 50% of the world's rivers, due to the effects of climate change, when coupled with the impacts of other natural and anthropogenic disturbances [3]. The middle reaches of the Yellow River (YR) in China, which is located in an arid/semi-arid region, have undergone particularly profound declines in runoff, and have gradually become areas of considerable research [4]. Moreover, the sharp reduction of runoff has led to new problems such as the serious shrinkage of the channel in the lower reaches and the reduction of the flood capacity [5].

As one of the common concerns in the field of global water cycle research, runoff dynamic change is particularly sensitive to climate [6,7]. The variation of meteorological elements such as precipitation, temperature, wind speed, and radiation change the cycle and distribution of water resources, and then affect river runoff [8]. China has experienced significant climate change, with the warmest 20 years since the 20th century. Studies have found that the temperature and precipitation have increased in the past 10–15 years in northwest China, exhibiting a trend of warming–wetting [9,10]. In particular, the temperature in the source of the YR [11] and part of the LP [12], showed a faster increase than the

average level for China and the world. The ecological environment and human lives may be adversely affected by extreme climate. Extreme temperature events may lead to glacier melting, reducing ice and snow reserves located upstream, then weakening the ability of glaciers to recharge runoff [13]. Extreme precipitation events may result in infiltration-excess runoff production, causing surface scour and then destroying vegetation roots.

As another important factor, human activities affect hydrological processes mainly through the construction of water conservancy projects [14], the change of underlying surface caused by vegetation restoration [15], etc. Vegetation is an important part of the terrestrial ecosystem and also the most sensitive component of climate change. Since 1999, because of the implementation of ecological restoration projects such as the Grain for Green Project (GGP), the vegetation coverage in arid/semi-arid areas of northwest China has been significantly improved [16], having a profound impact on the underlying surface conditions and hydrological processes in the YR basin. Some scholars believe that the ecological restoration measures have played an absolute leading role in the reduction of runoff and sediment loads in the YR basin [17,18]. However, due to the diversity of the ecosystem, the resources required by vegetation growth cannot be met without limit, while the impact of ecological restoration measures on hydrological processes depends on the scale and coverage of vegetation.

At present, monitoring vegetation dynamics and quantifying the response of vegetation growth to climate has become an important field of global change research in the context of frequent extreme climate events [19,20]. Some scholars have studied the correlation between normalized difference vegetation index (NDVI) variation characteristics of different vegetation types and climate factors at different scales. The results showed that vegetation growth was very sensitive to temperature and precipitation, and climate change has a significant impact on vegetation growth [21], especially in arid/semi-arid areas [22], where extreme climate leads to a decrease in vegetation coverage. In recent years, under the background of large-scale vegetation restoration, have the changes of climate and underlying surface conditions had new effects on runoff in the Loess hilly-gully region with complex geographical conditions? How does the passive remodeling process of hydrological connectivity caused by dramatic changes in underlying surface, affect runoff? The revelation of these concerns will be beneficial in understanding the geographical differentiation of the hydrological effects caused by vegetation and climate change.

Several methods have been applied to quantitatively distinguish the impact of climate and anthropogenic disturbance on runoff, such as the hydrological model [23], the elasticity coefficient [24], the watershed comparative analysis [25], etc. Among them, the elasticity coefficient, based on the Budyko hypothesis, has been widely used in the study of the law of runoff variation, due to its good performance in distinguishing the sensitivity and contribution of the potential factors. For half a century, many scholars have carried out theoretical derivation and empirical research on the Budyko empirical model [26,27].Current studies mainly tend to modify the control parameters in the empirical model, and some research conclusions directly attribute the coupling parameters of precipitation and temperature to the contribution of the underlying surface [28].The research results obtained by using this method have also been widely reported. Zheng et al. [29] analyzed runoff variability in the alpine region (source of the YR) by using the elasticity coefficient method, and found that the contribution of land-use and climate to runoff change were 70% and 30%, respectively. Liu et al. [30] analyzed the variation of the streamflow in a water diversion project in the semi-humid region by using six different elasticity coefficient models based on the Budyko hypothesis, and found that climate change was the main factor leading to the decline of streamflow, contributing 84.1–90.1%. Li et al. [4] analyzed runoff changes in 12 semi-arid basins (the middle reaches of the YR), based on the Choudhury–Yang model and the elastic coefficient, and found that vegetation was the leading factor of runoff decline. However, under the background of climate fluctuation and frequent extreme climate, the application of the Budyko model in the attribution analysis of runoff change in the ecologically fragile

Loess hilly-gully region requires further consideration of the specific conditions of the underlying surface of the study area.

Above all, it is of theoretical and practical significance to quantitatively distinguish the effects of anthropogenic disturbance and climate variation on runoff, so as to deeply appreciate the process of water cycle and improve the management measures of water resources. The main objectives of this paper are to (1) investigate the trends of the main hydrological and meteorological elements in the Yanhe River basin from 1969 to 2019, and study the substantial difference before and after the change point; (2) analyze the transfer of land-use structure caused by the GGP; (3) calculate the elasticity of runoff to precipitation, ET_0, and vegetation; and (4) distinguish the contributions of the above factors to the variation of runoff. This study is structured as follows: In Section 2, the study area, data sources, and methods used in our study are introduced in detail. In Section 3, the trend and elasticity of runoff are evaluated, the land-use transfer processes are identified, and the contributions of climate and anthropogenic interference are calculated. In Section 4, the eco-hydrological effect of vegetation restoration and the uncertainty in attribution analysis of runoff change are discussed. The conclusions are proposed in the final section.

2. Materials and Methods

2.1. Basic Data

This study primarily focuses on the area above the control section of the Ganguyi Hydrological Station in the Yanhe River basin, encompassing an area of 5891.64 km^2 (Figure 1), with a relative altitude difference of 972 m. From 1969 to 2019, the annual average precipitation was 489.79 mm, the maximum precipitation was 844.60 mm, and the minimum was 296.46 mm. The annual precipitation distribution was mostly concentrated in the flood season (from June to September), accounting for more than 70% of the total annual precipitation. The annual average temperature was 9.4 °C, the annual average wind speed was 1.3–3.3 m s^{-1}, the annual average sunshine was 2418 h, the accumulated ≥0 °C annual total temperature was 3878.1 °C, the annual average frost-free period was 172 days, and the annual average evaporation was about 1000 mm.

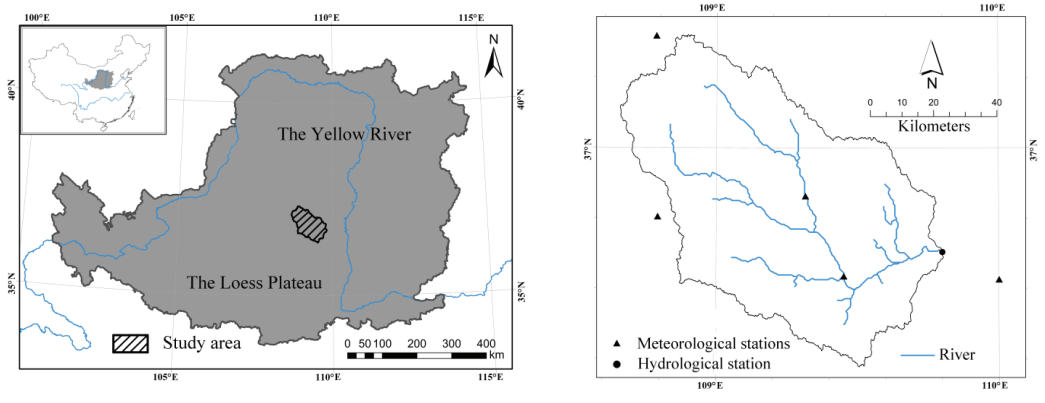

(**a**) (**b**)

Figure 1. Location of the study area: (**a**) location of Yanhe River Basin on the Loess Plateau, (**b**) distribution of hydrological and weather stations.

The daily measured runoff data used in the paper were recorded by the Ganguyi Hydrological Station in the middle reaches of the YR. The meteorological records, such as precipitation, temperature, etc., were obtained from five stations: Ansai, Jingbian, Yan'an, Yanchang, and Zhidan.

Land-use changes were determined using remote sensing images from 1985, 1995, 2000, 2008, and 2015 (resolution 30 m × 30 m). Land-use was mapped by conducting supervised classifications on the images and through manual visual interpretations, using ERDAS 9.2 and ArcGIS 10.2 software.

2.2. Data Processing and Analysis

2.2.1. Potential Evapotranspiration

The ET_0 was calculated according to the following equation [31]:

$$ET_0 = \frac{0.408\Delta(R_n - G) + \gamma \frac{900}{T_\alpha + 273} u_2 VPD}{\Delta + \gamma(1 + 0.34u_2)} \quad (1)$$

where ET_0 is the daily potential evapotranspiration (mm·d^{-1}), Δ is the slope of saturated vapor pressure in relation to air temperature (kPa·°C^{-1}), R_n is the net radiation at the canopy surface (MJ·m^{-2}·d^{-1}), G is the soil heat flux density (MJ·m^{-2}·d^{-1}), γ is the psychrometric constant (kPa·°C^{-1}), T_α is the mean daily air temperature at 2 m height (°C), u_2 is the wind speed at 2 m height (m·s^{-1}), VPD is the vapor pressure deficit (kPa). The annual ET_0 was obtained by the accumulative daily values.

2.2.2. Time-Varying Trends in Hydrological and Meteorological Elements

The daily measured runoff (calculated by dividing the total annual volume of stream flow by the upstream basin area, mm), precipitation, and ET_0 data were collected, sorted and counted on an annual basis from 1969 to 2019. The Mann–Kendall (MK) method [32,33] and a double mass curve were also applied to identify the abrupt change of runoff. The fluctuation of each factor was evaluated by the variation coefficient, calculated according to the following equation:

$$C_v = \sigma / \overline{D} \quad (2)$$

where σ and $\overline{D}$ are the standard deviation and average of time series records, respectively.

2.2.3. Attribution Analysis of Runoff Change

For a closed watershed, the water balance equation at the multi-year scale can be expressed as follows:

$$R = P - ET_a - \Delta S \quad (3)$$

where R is the runoff (mm), P is the precipitation (mm), ET_a is the actual evapotranspiration (mm), ΔS is the change in soil water storage (mm). The variation of soil water storage can be considered constant over a long-time scale (more than 10 years), so Equation (3) can be simplified into the following equation:

$$R = P - ET_a \quad (4)$$

The Budyko hypothesis holds that, there is a coupling equilibrium between water and heat in a watershed under certain climate and vegetation conditions [34]. The relationship between annual mean precipitation, ET_0 and ET_a can be described by an empirical curve. The ET_a over a long-time scale can be estimated by the Budyko models. Among them, the Choudhury–Yang [27] model (as follows), obtained through empirical or analytical methods, was widely used with better application effect.

$$ET_a = \frac{P \times ET_0}{(P^n + ET_0)^{1/n}} \quad (5)$$

where n is the parameter reflecting the characteristics of the underlying surface, including landform, soil, and vegetation. The landform, soil, and other factors in the study area did not change significantly during the study period. Therefore, the parameter n was mainly determined by land-use/vegetation cover change and can be calculated by

Equations (4) and (5). It is generally believed that the increase of n was caused by the improvement of vegetation cover in the basin.

The elasticity coefficient refers to the sensitivity of the dependent variable to independent variable [35]. The elasticity of runoff regarding potential factors can be expressed by the following equation:

$$E_x = \lim_{\Delta x/x \to 0} \left[\frac{\Delta R/R}{\Delta x/x} \right] = \frac{\partial R}{\partial x} \times \frac{x}{R} \tag{6}$$

where R is the runoff (mm) and x is a factor (such as precipitation, ET_0 or vegetation) that can influence the runoff. A positive (negative) elasticity coefficient of the x factor suggests that an increase (decrease) in the x variable will cause an increase (decrease) in runoff. The greater the absolute value of the elasticity coefficient, the higher the sensitivity.

Combining Equations (4)–(6), we can derive:

$$\begin{aligned} \Delta R &= \frac{\partial f}{\partial P} dP + \frac{\partial f}{\partial ET_0} dET_0 + \frac{\partial f}{\partial n} dn \\ &= \left[\frac{\partial R}{\partial P} \frac{P}{R} \right] \frac{\Delta P}{P} R + \left[\frac{\partial R}{\partial ET_0} \frac{ET_0}{R} \right] \frac{\Delta ET_0}{ET_0} R + \left[\frac{\partial R}{\partial n} \frac{n}{R} \right] \frac{\Delta n}{n} R + \delta \\ &= \varepsilon_P \frac{\Delta P}{P} R + \varepsilon_{ET_0} \frac{\Delta ET_0}{ET_0} R + \varepsilon_n \frac{\Delta n}{n} R + \delta \\ &= C_P + C_{ET_0} + C_n + \delta \end{aligned} \tag{7}$$

where C_P, C_{ET_0}, and C_n make up the contribution of precipitation, ET_0 and n to the change of runoff, respectively, ε_P, ε_{ET_0}, and ε_n make up the elasticity of runoff to precipitation, ET_0 and n, respectively, δ is the systematic error.

3. Results

3.1. Identification of Abrupt Change in Runoff

The result of the MK method showed that the UF(k) and UB(k) statistical curves generated for runoff had an intersection in 2000 (Figure 2a). The intersection was within the critical value (α = 0.05, Y = $\pm$1.96), indicating that the temporal sequence abruptly changed in 2000.

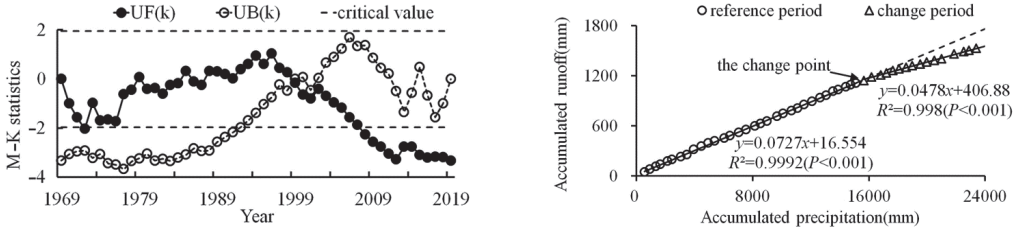

(**a**) (**b**)

Figure 2. Analysis of runoff abrupt change: (**a**) MK mutation test, (**b**) double mass curves of precipitation-runoff.

Based on the result of MK analysis, the study period was divided into a reference period (1969–2000, P_I) and a change period (2001–2019, P_{II}), then a double mass curve was performed on the precipitation-runoff (Figure 2b). As shown, the correlations (R^2) of the fitted trend line of the above cumulative quantities were all relatively high ($p < 0.001$) whether during P_I or P_{II}. The slope of the fitting curve changed significantly in 2000, which was consistent with the conclusion of the MK method.

3.2. Inter-Annual Alteration in Hydrological and Meteorological Elements

Annual hydrological and meteorological records indicated that the observed runoff (Figure 3a) significantly decreased ($p < 0.05$, –0.2845 mm year^{-1}) from 1969 to 2019, while the ET_0 (Figure 3b) exhibited an insignificant upward trend ($p < 0.001$, 4.6696 mm year^{-1}). The

precipitation (Figure 3c) also showed an overall upward trend ($p > 0.05$, 1.3795 mm year^{-1}), but only 3.48% of the total variance can be explained by the timing of the measurement.

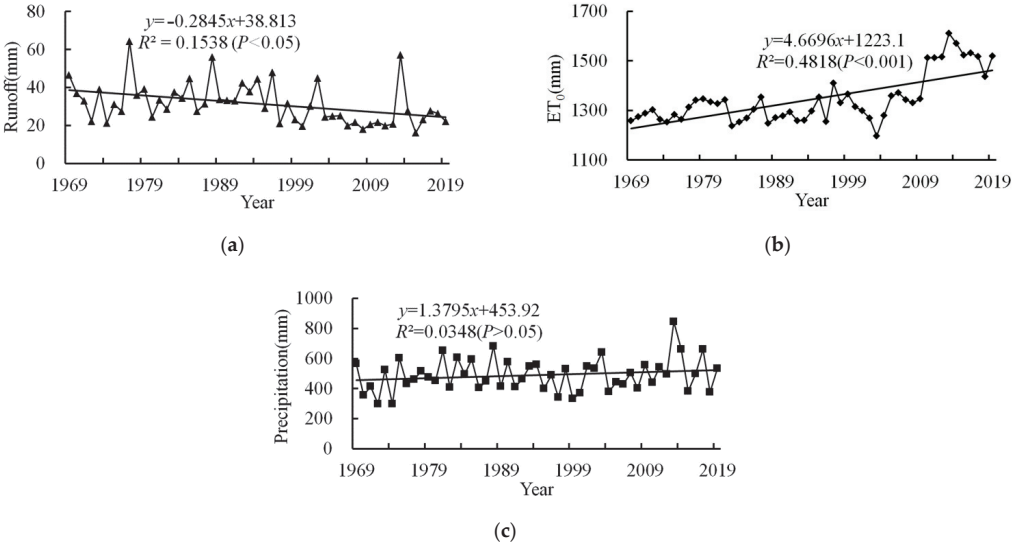

Figure 3. Evolution law of hydrological and meteorological elements: (**a**) runoff; (**b**) ET_0; (**c**) precipitation.

The different performance of hydrological and meteorological elements in P_I and P_{II} are shown in Figure 4. The precipitation increased from 472.27 mm (P_I) to 519.30 mm (P_{II}), with a relative change rate of 9.96% (Figure 4a). The variation range of precipitation narrowed in P_{II}, but the data points were denser away from the median and there were outliers deviating greatly from the box, indicating the frequency of extreme precipitation. The ET_0 increased from 1298.07 mm (P_I) to 1422.79 mm (P_{II}), with a relative change rate of 9.61% (Figure 4b). The variation range of ET_0 expanded considerably in P_{II}, almost all data points were distributed away from the median, close to the extrema. This suggested that the ET_0 fluctuated greatly during P_{II}, which may be related to the surface disturbance caused by the GGP.

Compared with P_I, the runoff in P_{II} decreased by 8.82 mm, with a relative change of –25.42% (Figure 4c). Especially in the early 21st century (2000–2009), the average runoff decreased to 24.90 mm, 28.24% lower than that before 2000, while the decline trend has slowed down since 2010. The variation range of runoff narrowed significantly during P_{II}, but there were many outliers far away from the box, which was considered to be related to the occurrence of extreme precipitation events.

The statistics of the intergenerational level changes of each element (Table 1) showed that the variation coefficient of runoff and precipitation both initially decreased before subsequently increasing, reaching their maximum between 2010 and 2019. The variation coefficient of ET_0 experienced a gradual increase and then decreased slightly, with a maximum between 1990 and 2010.

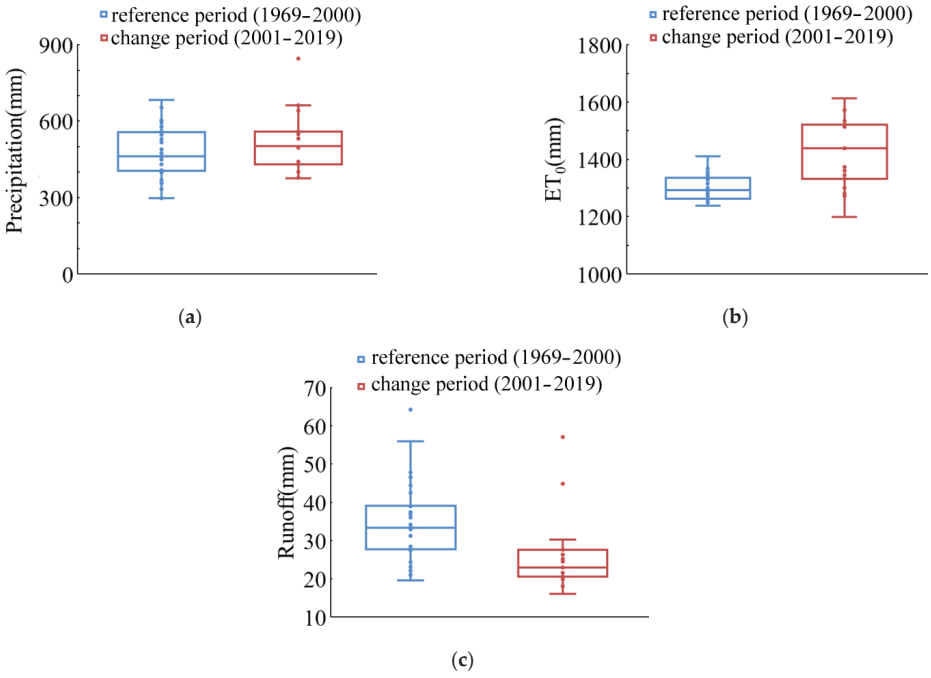

Figure 4. Characteristics of hydrological and meteorological elements during reference period and change period: (**a**) precipitation; (**b**) ET_0; (**c**) runoff.

Table 1. The variation coefficient of hydrological and meteorological elements in the past 50 years.

Period	Runoff	Precipitation	ET_0
1969–1979	0.318	0.217	0.024
1980–1989	0.250	0.198	0.032
1990–1999	0.245	0.184	0.038
2000–2009	0.300	0.177	0.038
2010–2019	0.414	0.253	0.028
1969–2019	0.340	0.074	0.222

3.3. Elasticity of Runoff to Climate and Vegetation

As shown in Table 2, during the whole study period (1969–2019), the elasticity coefficient of runoff to precipitation and ET_0 were 0.166 and –0.039, respectively. This indicates that, when precipitation or ET_0 increased by 10%, runoff would increase by 1.66% or decrease by 0.39%, respectively, and vice versa. The elasticity coefficient of runoff to the underlying surface parameter n, which represented vegetation change, was –1.738, indicating that runoff would be decreased by 17.38% when vegetation coverage increased by 10%.

Parameter n increased from 1.896 (P_I) to 2.244 (P_{II}), with a relative increase of 17.3%, indicating that the vegetation condition experienced a profound change during P_{II}. The elasticity coefficients of runoff to precipitation and ET_0 changed from 0.189 (P_I) to 0.133 (P_{II}), and –0.043(P_I) to –0.033(P_{II}), respectively, indicating that the effect of precipitation and ET_0 on runoff has weakened in the 21st century. Overall, the sensitivity of runoff to precipitation, ET_0, and underlying surface conditions all decreased during the change period.

Table 2. The elasticity of runoff regarding each factor in different periods.

Period	n	ε_P	ε_{ET_0}	ε_n
Reference period (P_I, 1969–2000)	1.896	0.189	–0.043	–2.033
Change period (P_{II}, 2001–2019)	2.244	0.133	–0.033	–1.339
Study period (1969–2019)	2.025	0.166	–0.039	–1.738

3.4. Composition and Transfer of Land-Use

According to the interpretation results (Figure 5) of remote sensing images in 1985, 1995, 2008, 2010, and 2015, the area proportions of each land-use type in the Yanhe River basin were calculated. The area of farmland, woodland, and grassland accounted for 99.29%, 99.22%, 99.16%, 99.05%, and 95.91%, respectively, of the total area in the years above.

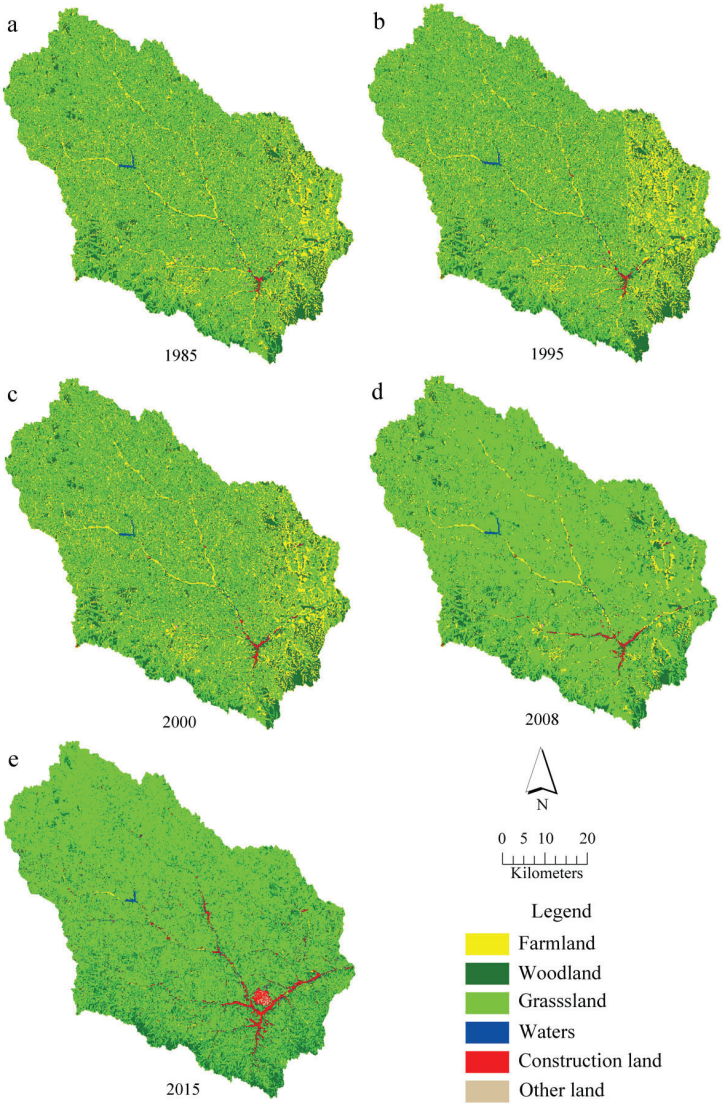

Figure 5. Composition of land-use from 1985 to 2015: (**a**) 1985; (**b**) 1995; (**c**) 2000; (**d**) 2008; (**e**) 2015.

The land-use transfer matrix (Table 3) was constructed based on the spatial analysis toolbox of ArcGIS. It can be found that agriculture was the main mode of production in the study area in 1985–2000, with slow transfer among different land-use types. Since 2000, the balance of original land-use structure fundamentally changed, and the obvious transfer among farmland, woodland, and grassland was the dominant process during this period. The area of farmland in 2015 decreased by 2259.11 km^2 (88.07%) compared with 2000, of which 161.24 km^2 and 2010.58 km^2 were converted to woodland and grassland, respectively. The area proportion of woodland and grassland increased to 91% of the total area, caused by the implementation of the GGP. The increase of grassland and woodland has greatly altered the underlying surface, effectively improving the capacity of the soil to conserve water and maintain a low level of runoff in the watershed.

Table 3. Land-use transfer matrix from 1985 to 2015 (km^2).

Period	Land-Use	Farmland	Construction Land	Other Land	Woodland	Grassland	Waters
1985–1995	Farmland	2513.95	2.72	0.1	13.04	33.95	1.33
	Construction land	0.1	22.18	0	0	0.1	0.05
	Other land	0	0	2.5	0	0	0
	Woodland	14.94	0.38	0	498.69	40.84	0.07
	Grassland	57.83	0.17	0	18.93	2652.82	0.47
	Waters	0.23	0	0	0.15	0.32	15.78
1995–2000	Farmland	2359.47	4.05	0.53	42.67	177.91	2.42
	Construction land	2.09	22.08	0	0.4	0.79	0.09
	Other land	0.75	0	1.75	0.01	0.09	0
	Woodland	24.93	0.33	0.01	479.7	25.6	0.24
	Grassland	156.96	1.79	0.04	47.72	2520.54	0.98
	Waters	1.75	0.15	0.03	0.13	0.75	14.89
2000–2008	Farmland	1023.16	8.13	0	75.28	1438.6	0.78
	Construction land	2.56	25.37	0	0.21	0.21	0.05
	Other land	0.13	0.17	2.06	0	0	0
	Woodland	0	0.26	0	570.37	0	0
	Grassland	0	0.76	0	0	2724.45	0.47
	Waters	0.8	0.86	0	0.03	0.02	16.91
2008–2015	Farmland	295.23	51.66	18.44	85.96	571.98	3.38
	Construction land	0.54	30.7	0.15	0.43	3.62	0.11
	Other land	0.01	0.03	0.04	0.18	1.8	0
	Woodland	1.13	8.54	4.33	437.39	193.81	0.69
	Grassland	8.95	68.25	38.08	753.17	3287.44	7.39
	Waters	0.12	4	0.32	0.53	8.33	4.91

3.5. Attribution Analysis of Runoff Change

The contribution of precipitation, ET_0, and vegetation to runoff change can be obtained by Equation (7), and the results are shown in Table 4. Since runoff was positively correlated with precipitation change, the upward trend of precipitation during P_{II} did not contribute to the decrease of runoff. On the contrary, precipitation increased runoff by 0.461 mm with a contribution of –5.23%. The contribution of ET_0 was 6.15%, which reduced runoff by 0.542 mm during the whole study period.

Table 4. Contribution of hydrological and meteorological elements to runoff change.

	C_P	C_{ET_0}	C_n	δ
Variation/mm	0.461	–0.542	–8.536	–0.203
Contribution/%	–5.23	6.15	96.78	2.30

On the whole, the vegetation contributed the most of runoff decline, reaching 96.78%, and the corresponding runoff variation was –8.536 mm. The change of underlying surface

conditions caused by vegetation restoration resulted in a significant decrease of runoff and offset the effect of precipitation increase.

In addition, we noticed that the systematic error was only 2.30% in the process of attribution analysis, indicating that the elasticity coefficient method was feasible for application in the typical arid/semi-arid region. However, at the same time, it also suggested that there were still one or more unknown factors affecting the change of runoff, besides precipitation, ET_0 and vegetation.

4. Discussion

4.1. Variation of Hydrological and Meteorological Elements in the Yanhe River Basin

Ren et al. [36] found that with the reduction in precipitation, runoff and sediment load in the Yanhe River basin declined between 1961 and 2008. Li et al. [37] reached a similar conclusion by analyzing hydrological records in the Yanhe River basin between 1952 and 2003. Our study found that the decline in runoff ($p < 0.05$) became more significant as the study period was expanded from 1969 to 2019. Additional temporal data, however, showed that the change of precipitation turned into an insignificant upward trend. This finding about precipitation is different from the research conclusions of other scholars. With the ET_0 also showing an extremely significant upward trend ($p < 0.001$), we suggest that the hydrological and meteorological situation within the Yanhe River basin has changed during the past 10 years, and there are also signs of warming–wetting.

The precipitation data points were highly discrete and far away from the median during P_{II}, accompanied by outliers, and the variation coefficient reached its maximum in 2010–2019. All this indicates that, since the 21st century, especially the past 10 years, precipitation has experienced severe fluctuation, with more extreme precipitation events. The variation coefficient of runoff also showed the maximum in 2010–2019, which may have resulted from the extreme precipitation events and long-term accumulation of the GGP.

4.2. Attribution Analysis of Runoff Change

The obvious decrease of runoff in the Loess Plateau has been widely reported, but the dominant factors causing the change have been different in different periods. Zhang et al. [38] analyzed the runoff change and its leading factors in 11 basins of the Loess Plateau since the 1950s and concluded that the change of land use/cover caused by anthropogenic disturbance contributed more than 50% of the runoff reduction in eight basins, and climate factors played a more important role in the remaining three basins. Since the 21st century, it has been recognized that anthropogenic disturbance, represented by ecological restoration measures, have significantly reduced runoff in the Yanhe River basin. However, due to different research periods and methods, the contribution of anthropogenic disturbance has not exactly been the same. Gao et al. [39] believed that the contribution of climate factor to runoff change in the Yanhe River basin was almost equal to that of anthropogenic disturbance, while Wang et al. [40] concluded that the contribution of anthropogenic disturbance was much higher than that of climate factor, reaching 77.4%. We also consider that the change of underlying surface conditions caused by anthropogenic disturbance was the leading factor of runoff reduction in the Yanhe River basin, but its contribution was more than 95%, which is different from previous studies. At the same time, we also found that the frequent occurrence of extreme climate in the last five years has led to a certain recovery of runoff in the basin with time, which has not been reported yet. Whether this trend can continue in the future needs to be tested by more measured data of longer time series.

4.3. The Eco-Hydrological Effects of Vegetation Restoration

In recent years, some scholars have carried out a series of studies on vegetation change and its eco-hydrological effect. Since the 1980s, a significant greening trend has been observed over 25% to 50% of the global area, which has changed the process of the global surface water cycle [41]. The vegetation coverage in China has been also improved

significantly since 2000, due to the impact of climate change and human activities [42]. The vegetation restoration projects have reduced sediment loads (about 90%) and measured runoff in the LP, resulting in an obvious decrease in the runoff coefficient in the middle reaches of the YR. Some scholars suggested that the vegetation restoration should be slowed down, otherwise it will lead to regional shortage of food and water resources.

In order to analyze the impact of the GGP on the eco-hydrological effect of vegetation, the P_{II} was further divided into two periods (2001–2009 and 2010–2019) with a 10-year cycle to compare parameter *n* and its corresponding elasticity coefficient. The parameter *n* decreased in the 2010s, compared with that in 2001–2009 (Table 5), and the sensitivity of runoff to vegetation coverage has been reduced since the 2010s. It can be concluded that, although the area of woodland and grassland has still increased since 2010, it may not achieve the expected effect of vegetation restoration. Xia et al. [43] compared the underlying surface parameters and vegetation coverage in the Yanhe River basin from 2002 to 2016 by using the equation derived from the Budyko hypothesis. They found that the increasing trend of vegetation coverage has slowed significantly since 2010, which was not synchronized with the increase in woodland and grassland area, and the underlying surface parameters obviously showed the same performance. This opinion coincides with the conclusion of this article. In the initial stage, the vegetation restoration measures have a sharp impact on runoff, but with the vegetation restoration reaching a stable period, the impact may tend to moderate. The long-term effects of vegetation restoration on runoff need to be further studied.

Table 5. The change of parameter *n* and elasticity during the change period.

Period	n	ε_n
2001–2009	2.271	–1.398
2010–2019	2.224	–1.215

The GGP would theoretically increase the vegetation coverage, but the planted trees may consume more water, while the poor water resources in arid/semi-arid areas of the LP may aggravate the water shortage in a short period, thus adversely affecting the vegetation diversity. Cao et al. [44] took five demonstration counties as examples in northern Shaanxi Province to study the influence of the GGP on vegetation coverage, and the results showed that the GGP resulted in a 30.5% decrease within vegetation coverage in afforestation areas. Improper selection of tree species or high planting density was considered to be the main cause of the negative effects above. How to increase the survival rate of afforestation is also the focus of further research.

4.4. Uncertainty in Attribution Analysis of Runoff Change

The original study from Budyko did not consider the factors such as underlying surface and watershed area, so the evapotranspiration rate and drought index calculated from measured data could not be fully projected on the Budyko curve in accordance with ideal conditions but were scattered around the curve. The method of interpreting these discrete points is mainly reflected by the control parameters in a series of empirical equations. In this paper, we applied the Choudhury–Yang coupling equation in the Yanhe River basin located in the Loess hilly-gully region, but there might still be some uncertainties resulting in systematic error.

In the process of calculating the contribution of the potential factor, the systematic error was 2.3%, indicating that the uncertainty has a limited influence on the final conclusion. The changes in runoff documented in this study would not be detectable in many humid regions having abundant vegetation, so the approach is likely to be applicable to basins in other arid/semi-arid regions which are sensitive to short-term (decadal scale) climatic shifts.

5. Conclusions

The Chinese government has implemented a number of ecological conservation and protection projects in arid/semi-arid regions to control soil erosion. In this paper, the Yanhe River basin was selected as the study area. We analyzed the variation trends of major measured hydrology and meteorology elements and identified the factors influencing runoff with the elasticity coefficient method based on the Budyko hypothesis. The results showed the following: (1) Between 1969 and 2019, the measured runoff showed an obvious downward trend ($p < 0.05$), with an abrupt change in 2000, and the average runoff in the change period decreased by 25.42% compared with that in the reference period. Precipitation and ET_0 showed an upward trend ($p > 0.05$) and a significant decreasing trend ($p < 0.001$), respectively. The climate condition showed a trend of warming–wetting. (2) Farmland, woodland, and grassland were the three main land-use types, accounting for more than 95% in total. Due to the GGP, the proportion of woodland and grassland has gradually increased to 91% since the 21st century, compared with that in 2000. (3) The underlying surface parameter n increased from 1.896 in the reference period to 2.244 in the change period, with a relative increase of 18.35%. The vegetation was the leading factor resulting in the decline of runoff with a contribution of 96.78%, while the ET_0 followed with a contribution of 6.15%. Precipitation increased runoff with a contribution of 5.23%. (4) By analyzing the periodic change of parameter n and the elasticity coefficient, we suggest that the response of runoff to vegetation restoration measures has a certain threshold effect in an arid/semi-arid area, and the runoff reduction will not remain for a long time. It may be related to the short-term water shortage caused by large-scale vegetation restoration, thus affecting the survival rate of afforestation. Large-scale vegetation restoration needs to be carried out carefully under the premise of assessing a reasonable threshold to avoid an ecological disaster.

Author Contributions: Data curation, J.W.; Methodology, X.W.; Writing—original draft, K.H.; Writing—review and editing, X.W. All authors have read and agreed to the published version of the manuscript.

Funding: This research was funded by [Natural Science Foundation of China] grant number [41871195]. And The APC was also funded by the funder above.

Data Availability Statement: The data used in this study are available from the corresponding author on reasonable request.

Acknowledgments: We thank the two anonymous reviewers for their valuable comments and constructive suggestions on the manuscript.

Conflicts of Interest: The authors declare no conflict of interest.

References

1. Piao, S.; Ciais, P.; Huang, Y.; Shen, Z.; Peng, S.; Li, J.; Zhou, L.; Liu, H.; Ma, Y.; Ding, Y.; et al. The impacts of climate change on water resources and agriculture in China. *Nature* **2010**, *467*, 43–51. [CrossRef] [PubMed]
2. Wang, S.; Fu, B.; Piao, S.; Lü, Y.; Ciais, P.; Feng, X.; Wang, Y. Reduced sediment transport in the Yellow River due to anthropogenic changes. *Nat. Geosci.* **2016**, *9*, 38–41. [CrossRef]
3. Nilsson, C.; Reidy, C.A.; Dynesius, M.; Revenga, C. Fragmentation and flow regulation of the world's large river systems. *Science* **2005**, *308*, 405–408. [CrossRef] [PubMed]
4. Li, Y.; Liu, C.; Zhang, D.; Liang, K.; Li, X.; Dong, G. Reduced runoff due to anthropogenic intervention in the Loess Plateau, China. *Water* **2016**, *8*, 458. [CrossRef]
5. Yao, W.; Xiao, P.; Shen, Z.; Wang, J.; Jiao, P. Analysis of the contribution of multiple factors to the recent decrease in load and sediment yield in the Yellow River basin, China. *J. Geogr. Sci.* **2016**, *26*, 1289–1304. [CrossRef]
6. Milly, P.C.D.; Betancourt, J.; Falkenmark, M.; Hirsch, R.; Kundzewicz, Z.; Lettenmaier, D.; Stouffer, R. Stationarity is dead: Whither water management? *Science* **2008**, *319*, 573–574. [CrossRef]
7. Jaramillo, F.; Destouni, G. Local flow regulation and irrigation raise global human water consumption and footprint. *Science* **2015**, *350*, 1248–1251. [CrossRef]
8. Song, X.; Zhang, J.; Zhan, C.; Liu, C. Review for impacts of climate change and human activities on water cycle. *J. Hydraul. Eng.* **2013**, *44*, 779–790. (In Chinese) [CrossRef]

9. Zhang, X.; Zheng, J.; Hao, Z. Climate change assessments for the main economic zones of China during recent decades. *Prog. Geogr.* **2020**, *39*, 1609–1618. (In Chinese) [CrossRef]
10. Li, M.; Sun, H.; Su, Z. Research progress in dry/wet climate variation in Northwest China. *Geogr. Res.* **2021**, *40*, 1180–1194. (In Chinese) [CrossRef]
11. Liu, C.; Wang, P.; Wen, T.; Yu, D.; Bai, W. Spatio-temporal characteristics of climate change in the Yellow River source area from 1960 to 2019. *Arid Zone Res.* **2021**, *38*, 293–302. (In Chinese) [CrossRef]
12. Gu, C.; Mu, X.; Gao, P.; Sun, W.; Zhao, G. Characteristics of temporal variation in precipitation and temperature in the Loess Plateau from 1961 to 2014. *J. Arid Land Resour. Environ.* **2017**, *31*, 136–143. (In Chinese) [CrossRef]
13. Ding, Y.; Liu, S.; Li, J.; Shangguan, D. The retreat of glaciers in response to recent climate warming in western China. *Ann. Glaciol.* **2006**, *43*, 97–105. [CrossRef]
14. Kingsford, R.T. Ecological impacts of dams, water diversions and river management on floodplain wetlands in Australia. *Austral Ecol.* **2000**, *25*, 109–127. [CrossRef]
15. Li, Z.; Liu, X.; Niu, T.; Kejia, D.; Zhou, Q.; Ma, T.; Gao, Y. Ecological restoration and its effects on a regional climate: The source region of the Yellow River, China. *Environ. Sci. Technol.* **2015**, *49*, 5897–5904. [CrossRef]
16. Jiang, W.; Yuan, L.; Wang, W.; Cao, R.; Zhang, Y.; Shen, W. Spatio-temporal analysis of vegetation variation in the Yellow River Basin. *Ecol. Indic.* **2015**, *51*, 117–126. [CrossRef]
17. Gao, P.; Mu, X.; Wang, F.; Li, R. Changes in streamflow and sediment discharge and the response to human activities in the middle reaches of the Yellow River. *Hydrol. Earth Syst. Sci.* **2011**, *15*, 1–10. [CrossRef]
18. Mu, X.; Zhang, L.; Mcvicar, T.; Chille, B.; Gau, P. Analysis of the impact of conservation measures on stream flow regime in catchments of the Loess Plateau, China. *Hydrol. Process.* **2010**, *21*, 2124–2134. [CrossRef]
19. Chen, P.; Shang, J.; Qian, B.; Jing, Q.; Liu, J. A New Regionalization Scheme for Effective Ecological Restoration on the Loess Plateau in China. *Remote Sens.* **2017**, *9*, 1323. [CrossRef]
20. Mo, K.; Chen, Q.; Chen, C.; Zhang, J.; Wang, L.; Bao, Z. Spatiotemporal variation of correlation between vegetation cover and precipitation in an arid mountain-oasis river basin in northwest China. *J. Hydrol.* **2019**, *574*, 138–147. [CrossRef]
21. Li, C.; Wang, J.; Hu, R.; Shan, Y.; Ayal, D. Relationship between vegetation change and extreme climate indices on the Inner Mongolia Plateau, China, from 1982 to 2013. *Ecol. Indic.* **2018**, *89*, 101–109. [CrossRef]
22. Sun, W.; Song, X.; Mu, X.; Gao, P.; Wang, F.; Zhao, G. Spatiotemporal vegetation cover variations associated with climate change and ecological restoration in the Loess Plateau. *Agric. For. Meteorol.* **2015**, *209–210*, 87–99. [CrossRef]
23. Chang, J.; Wang, Y.; Istanbulluoglu, E.; Bai, T.; Huang, Q.; Yang, D.; Huang, S. Impact of climate change and human activities on runoff in the Weihe River Basin, China. *Quat. Int.* **2015**, *380*, 169–179. [CrossRef]
24. Wang, D.; Hejazi, M. Quantifying the relative contribution of the climate and direct human impacts on mean annual streamflow in the contiguous United States. *Water Resour. Res.* **2011**, *47*, W00J02. [CrossRef]
25. Brown, A.E.; Lu, Z.; Mcmahon, T.A.; Western, A.W.; Vertessy, R.A. A review of paired catchment studies for determining changes in water yield resulting from alterations in vegetation. *J. Hydrol.* **2005**, *310*, 28–61. [CrossRef]
26. Pike, J.G. The estimation of annual run-off from meteorological data in a tropical climate. *J. Hydrol.* **1964**, *2*, 116–123. [CrossRef]
27. Yang, H.; Yang, D.; Lei, Z.; Sun, F. New analytical derivation of the mean annual water-energy balance equation. *Water Resour. Res.* **2008**, *44*, 893–897. [CrossRef]
28. Zhou, G.; Wei, X.; Chen, X.; Zhou, P.; Liu, X.; Xiao, Y.; Sun, G.; Scott, D.; Zhou, S.; Han, L.; et al. Global pattern for the effect of climate and land cover on water yield. *Nat. Commun.* **2015**, *6*, 5918. [CrossRef]
29. Zheng, H.; Zhang, L.; Zhu, R.; Liu, C.; Sato, Y.; Fukushima, Y. Responses of streamflow to climate and land surface change in the headwaters of the Yellow River basin. *Water Resour. Res.* **2009**, *45*, 641–648. [CrossRef]
30. Liu, X.; Liu, C.; Luo, Y.; Zhang, M.; Xia, J. Dramatic decrease in streamflow from the headwater source in the central route of China's water diversion project: Climatic variation or human influence? *J. Geophys. Res. Atmos.* **2012**, *117*, D06113. [CrossRef]
31. Allen, R.G.; Pereira, L.S.; Raes, D.; Smith, M. *Crop Evapotranspiration—Guidelines for Computing Crop Water Requirements*; FAO Irrigation and Drainage Paper 56; FAO: Roma, Italy, 1998.
32. Mann, H.B. Nonparametric test against trend. *Econometrica* **1945**, *13*, 245–259. [CrossRef]
33. Kendall, M.G. Rank correlation methods. Brit. *J. Psychol.* **1990**, *25*, 86–91. [CrossRef]
34. Budyko, M.I. *Evaporation under Natural Conditions, Gidrometeoizdat, Leningrad 1948*; English Translation byIsrael Program for Scientific Translations; IPST: Jerusalem, Israel, 1963.
35. Patterson, L.A.; Lutz, B.; Doyle, M.W. Climate and direct human contributions to changes in mean annual streamflow in the South Atlantic, USA. *Water Resour. Res.* **2013**, *49*, 7278–7291. [CrossRef]
36. Ren, Z.; Zhang, G.; Yang, Q. Characteristics of runoff and sediment variation in Yanhe River basin in last 50 years. *J. China Hydrol.* **2012**, *32*, 81–86. (In Chinese) [CrossRef]
37. Li, C.; Wang, H.; Yu, F.; Yang, A.; Yan, D. Impact of soil and water conservation on runoff and sediment in Yanhe River Basin. *Sci. Soil Water Conserv.* **2011**, *9*, 1–8. (In Chinese) [CrossRef]
38. Zhang, X.; Zhang, L.; Zhao, J.; Rustomji, P.; Hairsine, P. Responses of streamflow to changes in climate and land use/cover in the Loess Plateau, China. *Water Resour. Res.* **2008**, *44*, W00A07. [CrossRef]
39. Gao, P.; Jiang, G.; Wei, Y.; Mu, X.; Wang, F.; Zhao, G.; Sun, W. Streamflow regimes of the Yanhe River under climate and land use change, Loess Plateau, China. *Hydrol. Process.* **2015**, *29*, 2402–2413. [CrossRef]

40. Wang, Y.; Feng, Q. Characteristics of runoff and sediment transport during 1960–2010 and its response to Grain for Green Project in Yanhe River. *Sci. Soil Water Conserv.* **2017**, *15*, 1–7. (In Chinese) [CrossRef]
41. Zhu, Z.; Piao, S.; Myneni, R.; Huang, M.; Zeng, Z.; Canadell, J.; Ciais, P.; Sitch, S.; Friedlingstein, P.; Arneth, A.; et al. Greening of the earth and its drivers. *Nat. Clim. Change* **2016**, *6*, 791–795. [CrossRef]
42. Yang, D.; Shao, W.; Yeh, P.J.F.; Yang, H.; Kanae, S.; Oki, T. Impact of vegetation coverage on regional water balance in the nonhumid regions of China. *Water Resour. Res.* **2009**, *45*, 507–519. [CrossRef]
43. Xia, Y.; Zhang, S.; Gao, W.; Zhang, H.; Guo, L. Influence of greening Loess Plateau on streamflow change in Yanhe River basin of the middle Yellow River, China. *J. Earth Sci. Environ.* **2020**, *42*, 849–860. (In Chinese) [CrossRef]
44. Cao, S.; Chen, L.; Yu, X. Impact of China's Grain for Green Project on the landscape of vulnerable arid and semi–arid agricultural regions: A case study in northern Shaanxi Province. *J. Appl. Ecol.* **2009**, *46*, 536–543. [CrossRef]

sustainability

MDPI

Article

Resilience of a Complex Watershed under Water Variability: A Modeling Study

Kathleen Vazquez and Rachata Muneepeerakul *

Agricultural and Biological Engineering, University of Florida, 1741 Museum Rd, Gainesville, FL 32611, USA; kathleenmvazquez@ufl.edu

* Correspondence: rmuneepe@ufl.edu

Abstract: Understanding how socio-ecological systems respond to environmental variability is an important step in promoting system resilience. In this paper, we asked: How do the frequency and amplitude of water availability variation affect both the social-ecological regimes present and how the system transitions between them? How do these transitions differ under flood-prone and drought-prone conditions? We modified a dynamical systems model of a complex watershed to directly link environmental variability to system-level outcomes, specifically the livelihoods present in the system. The model results suggest that flood-prone systems exhibit more drastic regime shift behavior than drought-prone systems, with abrupt shifts from the complete participation to complete abandonment of livelihood sectors. Drought-prone systems appeared to be more sensitive to the amplitude of water variability, whereas flood-prone systems exhibited more complex relationships with amplitude and frequency, with frequency playing a bigger role compared to drought-prone systems. Lower frequency variations with sufficient amplitudes exposed the system to extended periods of environmental hardship, reducing the system's ability to recover. Our analysis also highlighted the importance of environmental stochasticity: the deterministic version of the model that assumed no stochasticity overestimated system resilience. The model and analysis offer a more systematic framework to investigate the linkages between sustainability of social-ecological systems and environmental variability. This lays the groundwork for future research in systems with significant current or predicted environmental variability due to climate change.

Keywords: regime shifts; resilience; dynamical system modeling; variability; water availability

Citation: Vazquez, K.; Muneepeerakul, R. Resilience of a Complex Watershed under Water Variability: A Modeling Study. *Sustainability* **2022**, *14*, 1948. https://doi.org/10.3390/su14041948

Academic Editors: Alban Kuriqi and Luis Garrote

Received: 14 January 2022
Accepted: 6 February 2022
Published: 9 February 2022

1. Introduction

Understanding how social-ecological systems respond to environmental variability is critical for ensuring their sustainability. Many parts of the world are seeing changes in the frequency and the magnitude of extreme environmental events [1]. Studies in ecological systems have shown that environmental variability can result in changes in the number and nature of system stable states [2–4]. However, few studies in social-ecological systems have explored the effects of variability on such regime shifts, instead focusing on sudden shocks or disturbances and long term trends [5,6]. This work fills this gap by incorporating stochastic fluctuations with a range of frequencies and amplitudes into a dynamical model of a social ecological system and analyzing the effects of such fluctuations on system resilience.

Many existing studies focus on identifying resilience indicators and early warning signs of regime shift [7–10]. These approaches are useful when evaluating social-ecological systems with particular vulnerabilities. For instance, a system experiencing increasingly severe droughts might want to evaluate how close they are to a regime shift, or a region prone to large storms will want to know what the potential outcomes of the next big one are. These approaches are, however, less helpful when investigating the effects of variability. A system may respond to a large storm in one way, but to a series of large storms in another. This work uses dynamical systems modeling to directly link environmental variability to

system-level regimes and examine how the system moves between these regimes under different conditions.

The dynamical systems model was previously developed based on a Northwest Costa Rican watershed (the Tempisque-Bebedero watershed) [11], resulting in the establishment of clearly defined social-ecological regimes. However, it did not incorporate fluctuations in water availability. This paper incorporated these fluctuations and directly related their frequency and amplitude to the system state, examining the transition between system states to answer the following research questions: How do the frequency and amplitude of water availability fluctuations affect both the social-ecological regimes present and how the system transitions between them? How do these transitions differ when induced by water surplus versus water shortage?

2. Materials and Methods

2.1. Model Structure

The model was developed with a goal of capturing the social and eco-hydrologic dynamics in a complex social-ecological system. The model focuses on a type of social-ecological system where human and environmental activities are strongly linked with the possibility for nonlinear dynamics. In this system, residents' livelihoods come from either the agricultural sector or an alternative industry (e.g., tourism), local governance infrastructure reacts to extreme environmental conditions (e.g., flooding), all impacting a downstream wetland. Six dynamical variables were chosen accordingly, with three eco-hydrologic variables and three social variables, summarized in Table 1 and Figure 1 (see [11] for more details on dynamical variable selection). Water in the river (W) represents the available pool of water for industries and the environment. The amount of water (W_{PV}) and invasive cattail (C) in the downstream wetland indicate environmental health. The percent of the population with agricultural livelihoods (U) represents the persistence or collapse of the agricultural sector in the watershed. The water governance capacity indicates the ability of the institutional systems to provide assistance to farmers in times of drought (G_D) or flood (G_F). This model was built on a previous model [11] with the major modification being the inclusion of the negative impact of too much water (flooding) and the governance capacity to deal with flooding (G_F).

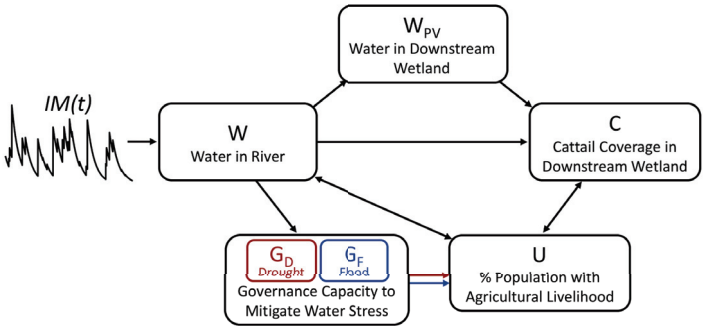

Figure 1. A conceptual diagram of the model. Directed links represent causal effects from one dynamical variable to another. Dynamical variables G_D and G_F are distinct, but interact with the model in essentially the same way depending on if the system is experiencing drought or flood. $IM(t)$ is the variable incoming water, modeled using a marked Poisson process.

Table 1. Dynamical variables and parameters of the model.

Symbol	Unit	Definition
Dynamical Variables		
W	L^3	Water in river
W_{PV}	L^3	Water in downstream wetland
U	-	% of population participating in the agricultural sector
G	-	Governance capacity: the ability to mitigate adverse effects of drought
C	-	Cattail coverage as % of the wetland area
Parameters		
IM	L^3/T	Inflows of water, including the portion transferred/imported into the basin
Ag	$1/NT$	Per capita water allocation rate to farmers
To	$1/T$	Water allocation rate to alternative industry
q	$1/T$	Rate of water leaving the river and entering the wetland
q'	$1/T$	Rate of water leaving the wetland
r	N/\$	Population responsiveness to difference in profit
n	N	Population size in the system
π_T	\$/NT	Per capita income stream for people in alternative industry
π_A	\$/NT	Per capita income stream for people in the agricultural sector
p	$\$/(L^3)^2$	Factor converting agricultural water allocation to profit
b	\$/NT	Base per capita agricultural profit
c	L^3/NT	Per capita farmer allocation threshold, below which drought occurs
f	L^3	flood cutoff
D	$1/T$	Decay rate of governance capacity
β	-	% Damage by birds to agricultural products
m_D	N/L^3	Rate of improvement of governance capacity dependent on severity of drought
m_F	$1/TL^3$	Rate of improvement of governance capacity dependent on severity of flood
g	$1/T$	Natural growth rate of cattail
g_A	$1/([M/L^3]T)$	Additional cattail growth rate induced by increased nutrient concentration due to agricultural activities
k	M/L^3	Nutrient concentration in agricultural runoff
F	$1/T$	Rate of mechanical cattail removal

The symbols for unit/dimension are as follows: L for length; T for time; M for mass (e.g., mg of nutrients); N = number of people; \$ for monetary unit.

The dynamics of W and W_{PV} reflect a simplified mass balance. Water enters the system and exits to the agricultural sector, alternative industry, and the wetland, W_{PV}. The growth of invasive cattail in the wetland, C, is increased by agricultural runoff (determined by W, U, and W_{PV}) and inhibited by management practices. Participation in the agricultural sector, U, is modeled using a replicator equation borrowed from evolutionary game theory [12]: people choose an agricultural livelihood when the payoff is better than the alternative industry. The payoff of agriculture depends on the state of the system: whether there is a flood or a drought (determined by W), whether there is the governance capacity to help when there is a flood or a drought (G_F and G_D), and the severity of the degradation of the wetland (C). Both governance capacity variables, G_F and G_D, operate on an assumption of institutional memory. When the system experiences an event (flood or drought), they gain experience and are thus better equipped to handle the next event that comes along. When an event does not occur for an extended period of time, the capacity drops. This dynamic was incorporated to explore how the frequency as well as magnitude of events can affect the system's resilience. These dynamics are captured in Equations (1)–(6). (Further details can be found in Appendices A and B.)

$$\frac{dW}{dt} = IM(t) - (Ag \cdot n \cdot U + To + q) \cdot W \tag{1}$$

$$\frac{dW_{PV}}{dt} = q \cdot W - q' \cdot W_{PV} \tag{2}$$

$$\frac{dC}{dt} = \left(g + \frac{Ag \cdot n \cdot U \cdot W \cdot k}{q' \cdot W_{PV}} \cdot g_A\right) \cdot C \cdot (1 - C) - F \tag{3}$$

$$\frac{dG_D}{dt} = I_{Ag \cdot W < c} \cdot m_D \cdot (c - Ag \cdot W) \cdot (1 - G_D) - D \cdot G_D \tag{4}$$

$$\frac{dG_F}{dt} = I_{W > f} \cdot m_F \cdot (W - f) \cdot (1 - G_F) - D \cdot G_F \tag{5}$$

$$\frac{dU}{dt} = r \cdot U \cdot (1 - U)(\pi_A - \pi_T) \tag{6}$$

where,

$$\pi_A = [p(1 - G')(Ag \cdot W - c)(f - W) + b](1 - \beta C)$$

$$G' = \begin{cases} G_D & \text{if } Ag \cdot W < c \\ G_F & \text{if } W > f \\ 0 & \text{otw.} \end{cases}$$

2.2. Introducing Variable Water Availability

To investigate system resilience under environmental variability, we incorporated the stochasticity of the incoming water, $IM(t)$. This is a key modification: In the previous deterministic model [11], the incoming water was a constant parameter. For any one value of this parameter, there could be only one model outcome. In this work, incoming water is a stochastic dynamical variable. With the addition of stochasticity, we are able to explore how a single mean value can produce different model outcomes depending on the nature of the fluctuations. To model variations in incoming water, we considered a suite of marked Poisson $IM(t)$. A marked Poisson model of incoming water has been used to capture hydrological fluctuation [13–15] while keeping the simplicity of the original model. To map the model outcomes, parameters of the marked Poisson process were varied to create incoming water signals with an array of frequency and amplitude. For each set of parameters, a marked Poisson process was used to generate $IM(t)$ and the model was run until it reached equilibrium—i.e., when the system no longer exhibited directional changes. This was repeated for 500 realizations. The model outcome of interest is the persistence or collapse of the agricultural sector as defined by a collapse cutoff. When the participation in agriculture (U) was below a collapse cutoff of 2%, the sector was considered to have collapsed. The results, especially those associated with the flood-prone conditions, are quite robust against reasonable choices of the cutoff values (low values to define a collapse). For each parameter set, the percent of the 500 realizations where the agricultural sector collapsed was mapped. To explore the effect of drought-prone and flood-prone conditions, this process was repeated for a range of mean incoming water values, each resulting in a model outcome map (Figure 2). These resilience–amplitude–frequency maps help us understand how both changes in the mean water availability and changes in the occurrence and severity of extreme events can influence how regime shifts occur.

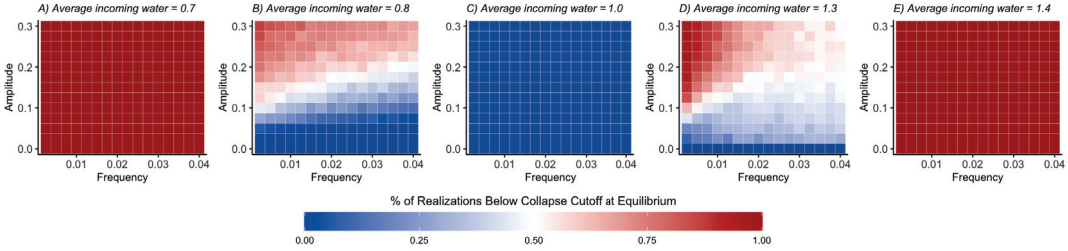

Figure 2. Resilience–amplitude–frequency maps under different hydrological conditions, ranging from drought-prone to flood-prone. The color represents the fraction of realizations where the agricultural system collapsed at equilibrium. In (**A**,**E**), with too low or too high a mean value of $IM(t)$, the agricultural sector cannot support itself at any frequency or amplitude. Between these extremes (**C**), the system survives at all frequencies and intensities. The system transitions between these states of full collapse and full survival with different behavior depending on whether collapse is driven by a shortage of water (**B**) or a surplus of water (**D**).

3. Results and Discussion

Figure 2 includes model results associated with a value of amplitude close to zero, representing the model outcome without fluctuation: These results represent "deterministic benchmarks" that highlight the effects of the environmental variation. In this deterministic case, the agricultural sector survives the mean incoming water in Figure 2B–D. Without taking environmental variation into account, the model overestimates the ability of the system to withstand changes in incoming water—Figure 2B,D allows us to explore system dynamics that would otherwise be overlooked in a deterministic model.

Under drought-prone conditions, the transition from agricultural sector survival to collapse is gradual and largely dependent on the amplitude of variation, with the system surviving low-amplitude variation at any frequency (Figure 2B). The histogram of W (Figure 3A, rightmost panel) is highly concentrated at a value near, but above, the drought cutoff. These values of W correspond to an agriculture payoff competitive with the payoff of alternative industry. When the payoff to agriculture fluctuates between being the more profitable option and the less profitable option, it drives fluctuations in U. The time series of U accordingly fluctuates near, but above, collapse.

Increasing the amplitude (comparing Figure 3B to Figure 3A) resulted in a more dispersed histogram of W, with some values falling below the drought cutoff. The histogram of U exhibits a dramatic shift: it is no longer concentrated around a mean; rather it becomes bimodal, with the primary peak at $U = 0$. While the histogram of U in this case (Figure 3B, second panel from left) may appear similar to those in Figure 3C–F, it is important to note that a mixed strategy ($0 < U < 1$) is still possible, even with a peak at $U = 0$; that is, there are some, although relatively few, realizations with U in the intermediate range. This is not the case with a flood-prone system.

When a drought occurs, the payoff of agriculture becomes less appealing than alternative employment, driving U towards 0. Due to the replicator dynamics of U, the more time U spends approaching 0, the harder it becomes to recover. The higher the amplitude of variation, the more likely it is that the system will encounter a drought. The more time the system spends in a drought, the more likely it is for the agricultural sector to collapse. This leads to the gradient from survival to collapse along the amplitude dimension seen in Figure 2B.

The frequency of variation affects how much time the system has to respond to fluctuations. High frequency oscillations move quickly with respect to other processes, meaning that if a drought occurs, the system may not have time to fully collapse before the drought ends and conditions become more favorable. Low frequency oscillations subject the system to water stress for a more extended period of time. A minor drought that lasts longer gives U more time to decline towards 0, eventually leading to a collapse of the

agricultural sector. This means a lower amplitude of variation is needed to cause a system collapse when the frequency is low, which can be seen in Figure 2B.

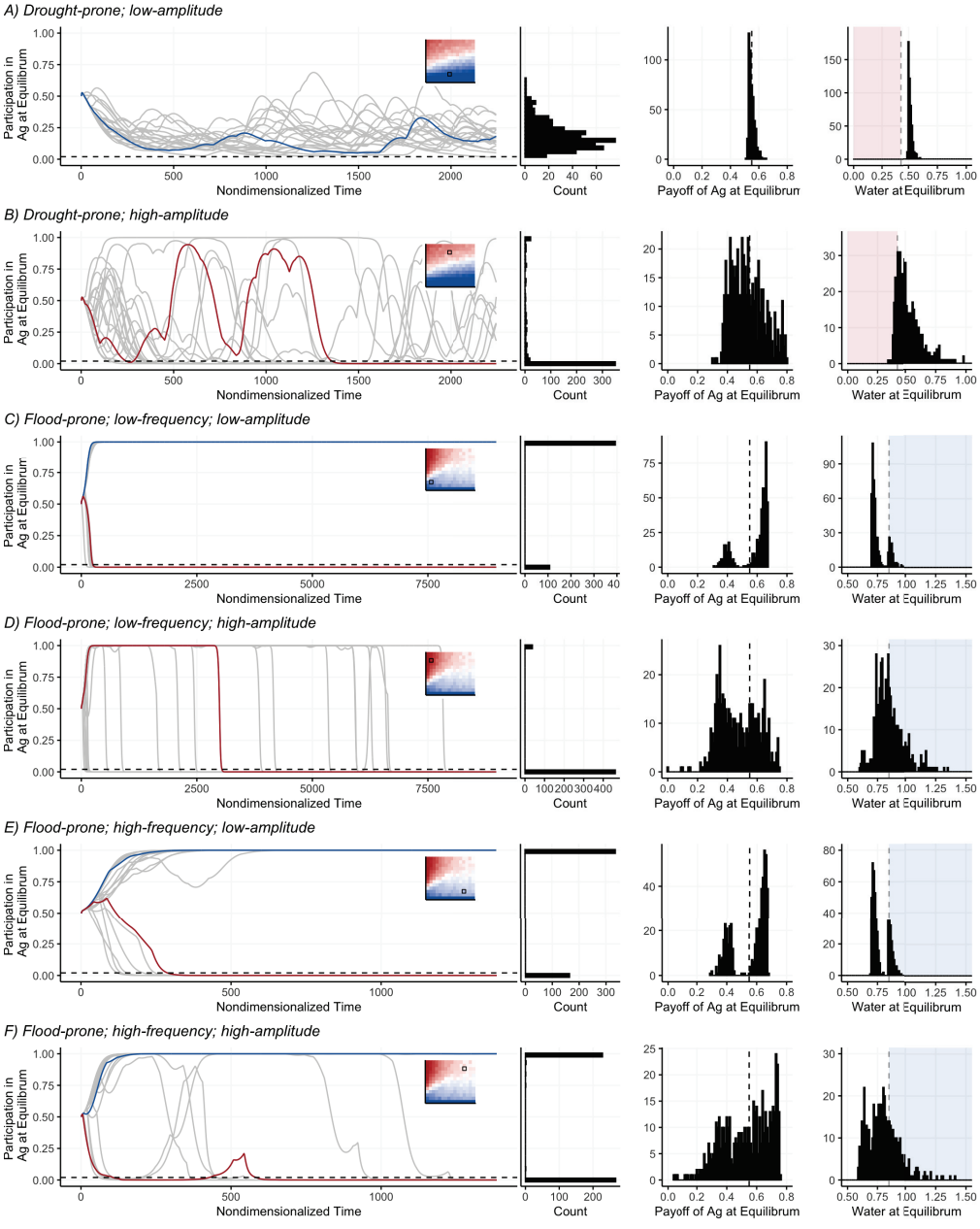

Figure 3. Sample time series of U, and histograms of U, payoff to agriculture, and W values at equilibrium from 500 realizations under different hydrological conditions. The dashed line in the histograms of payoff to agriculture represents payoff to alternative industry—when payoff to agriculture is above this line, it is the more appealing livelihood option. In (**A**,**B**), the dashed line and change in color in the histograms of W represents the drought cutoff; in (**C**–**F**), they represent the flood cutoff.

Frequency plays a bigger role in the transition to collapse under flood-prone conditions (Figure 2D). At lower frequencies, the system experiences either near complete survival (the percentage of realizations below the collapse cutoff is near 0%) or near complete collapse (near 100% below collapse cutoff), with a very sharp transition between the two (compared to the transition under drought-prone conditions). At higher frequencies, the transition is much more gradual and moves between less extreme states. Additionally, from the time series and histograms of U in Figure 3C–F, we see that U demonstrates bimodal behavior under flood-prone conditions. Under any frequency and amplitude, participation in agriculture at equilibrium is concentrated near 0% and 100%.

With low-amplitude variation (Figure 3C,E), the histograms of W display a bimodal distribution—W can be concentrated above or below the flood cutoff. In other words, the system can move to either a flooding or non-flooding regime. When the system moves to a flooding regime, the payoff to agriculture is driven down, and vice versa. Unlike in the drought-prone case, the payoff to agriculture is not fluctuating around the payoff to alternative industry in either flooding or non-flooding regime. Instead, the payoff is fluctuating entirely below or entirely above the payoff to alternative industry. Fluctuations fully below the alternative payoff will not result in fluctuations of U, but will affect how fast U collapses. The time series in Figure 3C and E highlight the "legacy effect": where the system ends up at equilibrium (full collapse or full survival of the agricultural sector), depends on which path was taken at the outset: towards a flooding regime or towards a non-flooding regime.

Higher amplitude variation blurs the lines between flooding and non-flooding regimes: the histograms of W in Figure 3D,F do not display the strong bimodality seen in cases with low-amplitude variation. Higher amplitude variation allows transition between the two system states of collapse and survival. The time series in Figure 3D shows that even if agriculture reaches near full participation, the system can still collapse later on. In Figure 3F, the system can not only collapse later on, but can recover as well. Just as in the water shortage case, lower frequency oscillations subject the system to a more extended period of time with near 0% participation, making it increasingly harder for the system to recover. Higher frequency oscillations allow for more movement between the two alternatives, resulting in less extreme collapse and survival conditions.

4. Conclusions

Changes in the frequency and amplitude of environmental events can have serious impacts on the sustainability of social-ecological systems. In this paper, we asked: How do the frequency and amplitude of water availability variation affect both the social-ecological regimes present and how the system transitions between them? How do these transitions differ under flood-prone and drought-prone conditions? A dynamical systems approach allowed us to explore the qualitative behavior of the system under different conditions, rather than predict the outcome of a particular system. Our analysis resulted in a more systematic framework to investigate the linkages between sustainability of social-ecological systems and environmental variability, e.g., the resilience–amplitude–frequency maps. These maps allowed us to examine system dynamics that would be missed using a deterministic model.

In both flood- and drought- prone systems, resilience was overestimated when variation was not considered. We found that survival or collapse of the agricultural sector is largely determined by the magnitude of the events. Under both flood- and drought-prone conditions, the system survives frequent events better than infrequent, but prolonged, unfavorable conditions. Agricultural sector collapse due to water shortage happens more gradually, with the possibility for a mix of livelihoods. Collapse of the agricultural sector due to water surplus, however, happens more suddenly, and without the possibility of a mix of livelihoods—once conditions become severe enough, the system transitions from fully agricultural to full abandonment.

The frequency of flooding events was found to be more impactful than the frequency of drought events. The agricultural sector could still bounce back after collapse caused by more frequent flooding, whereas less frequent, but longer flooding episodes will lead to a more permanent collapse of the agricultural sector. Low-amplitude variation does not facilitate much transition between the two system outcomes, whereas higher amplitude, higher frequency variation allows the system to move back and forth. High amplitude, low frequency variation allows the system to move from survival to collapse, but it is more difficult to move back once flooding is established.

Incorporating stochastic environmental variation into a dynamical model of a social-ecological system allowed us to directly link the frequencies and severity of environmental events (water surplus and shortage) to system-level outcomes (livelihood choices) in a systematic and quantitative way. This direct link can be difficult to achieve with more highly-parameterized models. Stylized dynamical systems models such as this offer a different perspective on complex problems, with potential to be adapted to similarly interconnected social-ecological systems. Insights and lessons from this approach may be applied to a range of future research, including model development with the goal of predicting social-ecological outcomes. This lays groundwork for future research in systems with significant current or predicted environmental variability due to climate change.

Author Contributions: K.V. and R.M. designed the study. K.V. conducted the analysis. K.V. and R.M. wrote the paper. All authors have read and agreed to the published version of the manuscript.

Funding: The research was supported by the University of Florida's Water Institute through its Fellowship Program (WIGF) under the project: Inducing Resilience for Water-Subsidized Systems. This research was also supported by the Army Research Office/Army Research Laboratory under award W911NF1810267 (Multidisciplinary University Research Initiative). The views and conclusions contained in this document are those of the authors and should not be interpreted as representing the official policies either expressed or implied of the Army Research Office or the U.S. Government.

Institutional Review Board Statement: Not applicable.

Informed Consent Statement: Not applicable.

Data Availability Statement: This study was theoretical in nature and did not use empirical data in its analysis.

Acknowledgments: We wish to thank the WIGF project's participating faculty advisors—Rafael Muñoz-Carpena, Jeffrey Johnson, Christine Angelini, Peter Waylen, Gregory Kiker, and Thomas Ankersen—as well as other WIGF fellows—Stefano Barchiesi, Caroline Huguenin, Oswaldo Medina-Ramirez, and Marco Pazmino for their support and insights.

Conflicts of Interest: The authors declare no conflict of interest.

Appendix A. Site Description

The dynamical model used is based on the The Tempisque-Bebedero watershed in Northwest Costa Rica, a complex social-ecological system: water transfer connects electricity generation, irrigated agriculture, and an internationally recognized migratory bird habitat, in addition to a growing tourism industry [16–18]. Variability of water availability in the Tempisque-Bebedero watershed exists on multiple time scales and for different reasons. The area has well-defined wet and dry seasons that create intra-annual variability [19]. El Niño Southern Oscillation (ENSO) events create inter-annual variability [19]. Climate change trends predict changes in the frequency and severity of extreme events as well as changes in the overall water availability [1,19]. Additionally, in a water subsidized system, management of water transfer can dampen or exacerbate environmental variation.

Appendix B. Nondimensionalized Model

To ease analysis, the model was simplified using nondimensionalization. Dimensionless groups are listed and defined in Table A1 and yield the following model.

$$\frac{dw}{d\tau} = 1 - (\theta_A U + \theta_T + 1) \cdot w \tag{A1}$$

$$\frac{dw_{PV}}{d\tau} = w - \lambda w_{PV} \tag{A2}$$

$$\frac{dC}{d\tau} = (\gamma + \frac{\gamma_A \theta_A w U}{w_{PV}})C(1-C) - \phi \tag{A3}$$

$$\frac{dG_D}{d\tau} = I_{\theta_A \cdot w < \alpha_D} \cdot \mu_D(\alpha_D - \theta_A w)(1 - G_D) - \delta G_D \tag{A4}$$

$$\frac{dG_F}{d\tau} = I_{w > \alpha_F} \cdot \mu_F(w - \alpha_F)(1 - G_F) - \delta G_F \tag{A5}$$

$$\frac{dU}{d\tau} = U(1-U)(\widehat{\pi}_A - \widehat{\pi}_T) \tag{A6}$$

where,

$$\widehat{\pi}_A = [\rho(1-G')(\theta_A w - \alpha_D)(\alpha_F - w) + \psi](1 - \beta C)$$

$$G' = \begin{cases} G_D & \text{if } \theta_A w < \alpha_D \\ G_F & \text{if } w > \alpha_F \\ 0 & \text{otw.} \end{cases}$$

Table A1. Dimensionless group definitions and interpretations.

Symbol	Definition	Interpretation
w	$\frac{W \cdot q}{IM}$	Rescaled water availability in the basin
w_{PV}	$\frac{W_{PV} \cdot q}{IM}$	Rescaled water in downstream wetland
τ	$t \cdot q$	Rescaled time
θ_A	$\frac{Ag \cdot n}{q}$	Relative water allocation rate to agriculture compared to the natural draining rate of the watershed
θ_T	$\frac{To}{q}$	Relative water allocation rate to alternative industry compared to the rate at which water leaves the watershed
λ	$\frac{q'}{q}$	Ratio of water exiting to water entering wetland
$\hat{\pi}_T$	$\frac{r\pi_T}{q}$	Rate of people entering alternative industry relative to the rate at which water leaves the watershed
ρ	$\frac{pr \cdot IM^2}{nq^2}$	Rescaled profit factor for agriculture
α_F	$\frac{fq}{IM}$	Rescaled flood threshold
α_D	$\frac{cn}{IM}$	Rescaled drought threshold
ψ	$\frac{rb}{q}$	Potential rate of people entering the agricultural sector relative to the rate at which water leaves the watershed
μ_D	$\frac{m_D IM}{qn}$	Rescaled maintenance/improvement rate of drought governance capacity
μ_F	$\frac{m_F IM}{q^2}$	Rescaled maintenance/improvement rate of flood governance capacity
δ	$\frac{D}{q}$	Decay rate of governance capacity (due to loss of institutional memory) relative to the rate at which water leaves the watershed
γ	$\frac{g}{q}$	Natural cattail growth rate relative to the rate at which water leaves the watershed
γ_A	$\frac{k g_A}{q'}$	Additional cattail growth due to nutrient pollution relative to the rate at which water leaves the wetland
ϕ	$\frac{F}{q}$	Mechanical cattail removal rate relative to the rate at which water leaves the watershed

References

1. Aghakouchak, A.; Chiang, F.; Huning, L.S.; Love, C.A.; Mallakpour, I.; Mazdiyasni, O.; Moftakhari, H.; Papalexiou, S.M.; Ragno, E.; Sadegh, M. Climate Extremes and Compound Hazards in a Warming World. *Annu. Rev. Earth Planet. Sci.* **2020**, *48*, 519–548. [CrossRef]
2. Guttal, V.; Jayaprakash, C. Impact of noise on bistable ecological systems. *Ecol. Model.* **2007**, *201*, 420–428. [CrossRef]
3. Borgogno, F.; D'Odorico, P.; Laio, F.; Ridolfi, L. Effect of rainfall interannual variability on the stability and resilience of dryland plant ecosystems. *Water Resour. Res.* **2007**, *43*, [CrossRef]
4. Xu, L.; Patterson, D.; Staver, A.C.; Levin, S.A.; Wang, J. Unifying deterministic and stochastic ecological dynamics via a landscape-flux approach. *Proc. Natl. Acad. Sci. USA* **2021**, *118*, e2103779118. [CrossRef] [PubMed]
5. Virapongse, A.; Brooks, S.; Metcalf, E.C.; Zedalis, M.; Gosz, J.; Kliskey, A.; Alessa, L. A social-ecological systems approach for environmental management. *J. Environ. Manag.* **2016**, *178*, 83–91. [CrossRef] [PubMed]
6. Biggs, R.; Schlüter, M.; Biggs, D.; Bohensky, E.L.; Burnsilver, S.; Cundill, G.; Dakos, V.; Daw, T.M.; Evans, L.S.; Kotschy, K.; et al. Toward principles for enhancing the resilience of ecosystem services. *Annu. Rev. Environ. Resour.* **2012**, *37*, 421–448 [CrossRef]
7. Linstädter, A.; Kuhn, A.; Naumann, C.; Rasch, S.; Sandhage-Hofmann, A.; Amelung, W.; Jordaan, J.; Du Preez, C.C.; Bollig, M. Assessing the resilience of a real-world social-ecological system: Lessons from a multidisciplinary evaluation of a South African pastoral system. *Ecol. Soc.* **2016**, *21*, [CrossRef]
8. Nemec, K.T.; Chan, J.; Hoffman, C.; Spanbauer, T.L.; Hamm, J.A.; Allen, C.R.; Hefley, T.; Pan, D.; Shrestha, P. Assessing resilience in stressed watersheds. *Ecol. Soc.* **2014**, *19*, [CrossRef]
9. Lamichhane, P.; Miller, K.K.; Hadjikakou, M.; Bryan, B.A. Resilience of smallholder cropping to climatic variability. *Sci. Total. Environ.* **2020**, *719*, 137464. [CrossRef] [PubMed]
10. Liu, D. Evaluating the dynamic resilience process of a regional water resource system through the nexus approach and resilience routing analysis. *J. Hydrol.* **2019**, *578*, 124028. [CrossRef]
11. Vazquez, K.; Muneepeerakul, R. Modeling resilience and sustainability of water-subsidized systems: An example from northwest Costa Rica. *Sustainability* **2021**, *13*, 2013. [CrossRef]
12. Nowak, M.A. *Evolutionary Dynamics: Exploring the Equations of Life*; Harvard University Press: Chicago, IL, USA, 2006.
13. Botter, G.; Porporato, A.; Rodriguez-Iturbe, I.; Rinaldo, A. Basin-scale soil moisture dynamics and the probabilistic characterization of carrier hydrologic flows: Slow, leaching-prone components of the hydrologic response. *Water Resour. Res.* **2007**, *43*. [CrossRef]
14. Porporato, A.; Daly, E.; Rodriguez-Iturbe, I. Soil water balance and ecosystem response to climate change. *Am. Nat.* **2004**, *164*, 625–632. [CrossRef] [PubMed]
15. Rodriguez-Iturbe, I.; Porporato, A.; Rldolfi, L.; Isham, V.; Cox, D.R. Probabilistic modelling of water balance at a point: The role of climate, soil and vegetation. *Proc. R. Soc. A Math. Phys. Eng. Sci.* **1999**, *455*, 3789–3805. [CrossRef]
16. Guzmán Arias, I.; Calvo Alvarado, J.C. Water resources of the Upper Tempisque River Watershed , Costa Rica (Technical note). *Tecnol. Marcha* **2012**, *25*, 63–70.
17. Guzmán-Arias, I.; Calvo-Alvarado, J. Planning and development of Costa Rica water resources: current status and perspectives. *Tecnol. Marcha* **2013**, *26*, 52–63. [CrossRef]
18. Osland, M.J.; González, E.; Richardson, C.J. Restoring diversity after cattail expansion: Disturbance, resilience, and seasonality in a tropical dry wetland. *Ecol. Appl.* **2011**, *21*, 715–728. [CrossRef] [PubMed]
19. Waylen, P.; Sadí Laporte, M. Flooding and the El Niño-Southern Oscillation phenomenon along the Pacific coast of Costa Rica. *Hydrol. Process.* **1999**, *13*, 2623–2638. [CrossRef]

water

MDPI

Article

Ecological and Health Risk Assessment of Potential Toxic Elements from a Mining Area (Water and Sediments): The San Juan-Taxco River System, Guerrero, Mexico

Edith Rosalba Salcedo Sánchez [1,*], Juan Manuel Esquivel Martínez [1], Manuel Martínez Morales [2], Oscar Talavera Mendoza [1] and María Vicenta Esteller Alberich [3]

[1] Escuela Superior de Ciencias de la Tierra, Universidad Autónoma de Guerrero, Taxco el Viejo 40323, Mexico; jmesquivel@conacyt.mx (J.M.E.M.); otalavera.uagro@gmail.com (O.T.M.)
[2] Instituto Mexicano de Tecnología del Agua, Jiutepec 62550, Mexico; manuelm@tlaloc.imta.mx
[3] Instituto Interamericano de Tecnología y Ciencias del Agua (IITCA), Universidad Autónoma del Estado de Mexico, Toluca 50120, Mexico; mvestellera@uaemex.mx
* Correspondence: edithsalcedos@gmail.com

Abstract: The San Juan-Taxco River system is situated in the Taxco mining district, which is a well-known international producer of silver, jewelry and precious metal handicrafts. The population and biota in the area have been affected by inappropriate disposal of anthropogenic activities that pollute the hydric resources and threaten their health and sustainability, since the inhabitants use the groundwater and river water for human consumption, domestic water supply and irrigation. This study was conducted to assess the pollution in the river system, human health implications and ecological risk in the aquatic environment (groundwater, surface water and superficial sediment). This evaluation was done on the base of hydrochemical, textural, mineralogical and geochemical analysis supported by calculation of human health risk using chronic daily intake (CDI), hazard quotient (HQ) and hazard index (HI) with environmental and geochemical indices for ecological risk evaluation. The health risk assessment indicated increasing non-health carcinogenic risk to the exposed population to the river water and dug wells (HI > 1), and thus, these resources are not recommended for human consumption, domestic activities and prolonged ingestion. The results demonstrated a high degree of pollution due to toxic elements and geochemical indices. The Pollution Load Index indicated potential risk that will cause harmful biological effects in the riverine environment.

Keywords: PTE; water quality; health risk assessment; ecological risk assessment; sediment; contamination factor; pollution load index; enrichment factor

Citation: Salcedo Sánchez, E.R.; Martínez, J.M.E.; Morales, M.M.; Talavera Mendoza, O.; Alberich, M.V.E. Ecological and Health Risk Assessment of Potential Toxic Elements from a Mining Area (Water and Sediments): The San Juan-Taxco River System, Guerrero, Mexico. *Water* **2022**, *14*, 518. https://doi.org/10.3390/w14040518

Academic Editor: Alban Kuriqi

Received: 24 December 2021
Accepted: 30 January 2022
Published: 9 February 2022

1. Introduction

Potential Toxic Elements (PTE) pollution in the fluvial system is one of the major threats for aquatic life and human population due to the abundance, persistence, inherent toxicity, non-degradability, ubiquity, bioaccumulation and biomagnification in the food chain [1–3]. The concentration of these toxic elements as heavy metals has increased in the environment due to their anthropogenic inputs. Numerous rivers and aquifers have been polluted with PTE from industrialization processes and mining activities, especially from the inappropriate disposal of wastewater and mine tailings, resulting in negative effects [4,5]. PTE persist in the environment and can remain for a very long time; they can potentially accumulate and concentrate in aquatic organisms and cause serious harms and finally exhibit high toxicity and bioaccumulation features. A toxic effect is directly linked to human health through the food chain and drinking water resources [6–8].

Risk assessment is a method of evaluate the impacts of pollutants [9] and can be separated into human health risk assessment and ecological risk assessment according to the different protection targets [9,10]. Several studies have developed an integral assessment

of water quality linked to human health and potential risks posed by PTE in aquatic environments [8]. Some PTE, such as Cu, Co, Zn, Fe, Ca, Se, Ni and Mn, are beneficial to humans at low concentrations, but intake of some others, namely As, Cd, Pb and Hg, are highly poisonous to humans, even at a low concentration. Human health risks will be increased due to the intake of excess PTE contents through three pathways: inhalation, oral ingestion and dermal absorption; the ingestion and dermal absorption routes are considered as more common for the accumulation of those toxic metals into the human body [5,11]. Many studies have focused on the ecological risk assessment of PTE in sediments [2–4,6,7,12,13]. Sediments are an appropriate indicator of fluvial ecosystem health due to its main role in transport and storage of pollutants and its peculiarity to release them to the water column [3].

The San Juan-Taxco River system (Guerrero, Mexico) represent a key resource in terms of providing water for drinking supply, agricultural activities and ecosystem services [14–16]. The mining industry, the increase of jewelry and handmade manufacturing workshops and population growth have caused serious pollution in this area [14,17]. Several studies in the region refer the presence PTE as Pb, As, Zn and Fe in the San Juan-Taxco River that exceeded the aquatic life criteria and the presence of Pb concentrations in human blood [14,16–18]. However, these studies have not integrated the effects from sediment, river water and groundwater on human health. There has not been performed a human health risk assessment or an ecological risk assessment and they can be considered diagnostic studies. Therefore, the difference of this investigation is to obtain a complete perspective of ecological and human health risk and impact of mining and jewelry on the San Juan-Taxco River system to improve the hydric management.

The specific objectives of this study are as follows: (1) to analyze the pollution status by PTE in the water and sediments of the San Juan-Taxco River system; (2) to assess the health risk in two population groups (adults and children) using the chronic daily intake, hazard quotient and hazard indices in river water and dug wells; (3) to evaluate the ecological risks using geochemical indices. This study provides a more profound comparison of PTE pollution in this river system for health risk assessment and the basis for better resources management from an ecological health perspective.

2. Study Area

The San Juan-Taxco River system belongs to the Middle Balsas Basin [19]. It is located in the Taxco and Iguala municipalities in the northern part of the state of Guerrero within the mining district of Taxco (Mexico) Figure 1. In Taxco, the climate is warm and subhumid with an annual average temperature of 21.9 °C; the warmest month is April with a mean temperature of 24 °C and the coolest month is December with a mean of 20.3 °C. Precipitation is in the order of 1000 mm/year; the rain is concentrated in the period from June to October with maximum values of 254 mm in September, and the driest month is February, with 7.6 mm [14,19]. The Iguala climate is warm sub-humid. The annual mean temperature is 26.1 °C, with a maximum of 38 °C and a minimum of 14 °C; the warmest months are April and May and the coolest months are December and January. The precipitation is moderate during June to September, with annual mean precipitation of 1100 mm/year, with maximum values of 226 mm in July, and the driest month is March, with 4.2 mm of precipitation [19].

Intensive mining produced large quantities of liquid and solid mining wastes containing EPT [15–17]. Historical solid wastes were buried or re-worked during the 20th century, but modern (1940 to present) wastes are accumulated in tailings dumps (Antonio, El Fraile, La Concha, El Solar, Guerrero I, Guerrero II and Los Jales, etc.), which contain moderately to highly oxidized material, sulfides and PTE, such as lead, barium, cadmium, zinc, iron, arsenic and strontium. These waste dumps were deposited on rocks of the Mexcala and Taxco Schist formations [16]. These formations are considered essentially impermeable units, although secondary porosity can be locally important. These characteristics prevent

the infiltration of large volumes of Acid Mining Drainage (AMD) to aquifers, but enable surface drainage of metal-rich leachates, affecting the quality of effluent water [14,16].

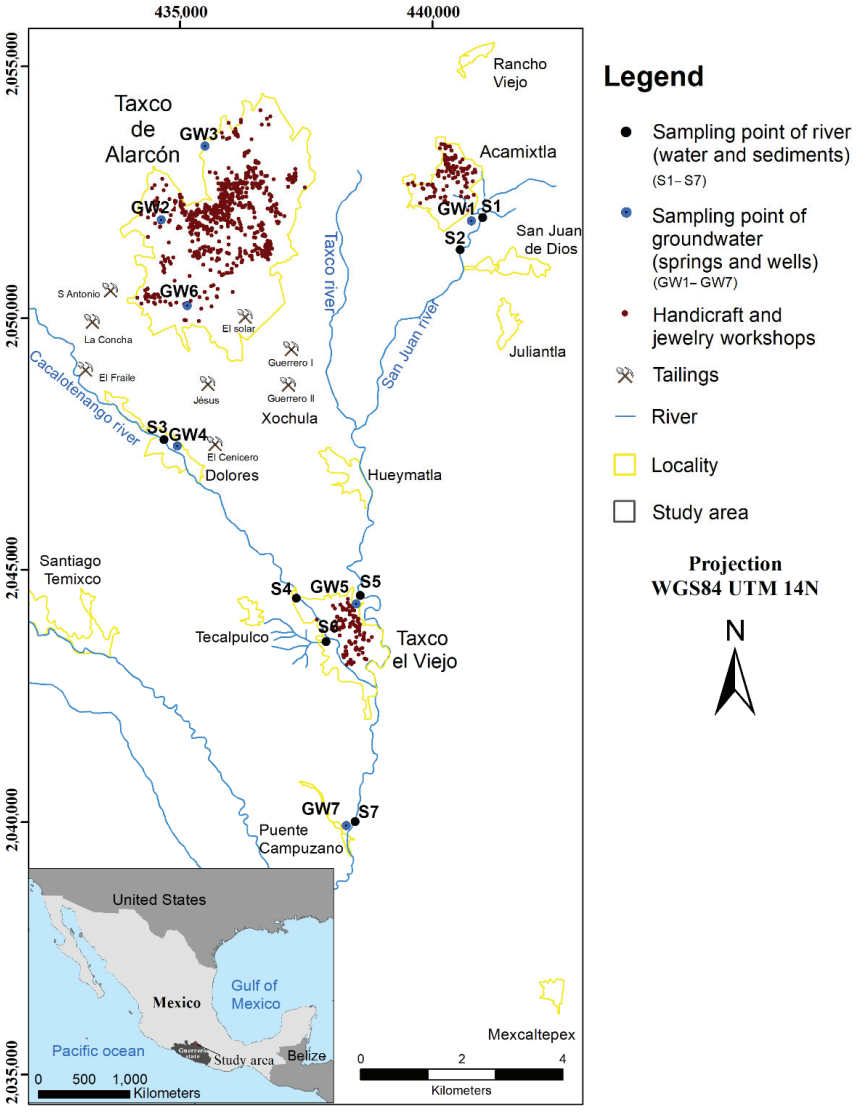

Figure 1. Map of the sampling points (groundwater, river water and fluvial sediment) and location of mining tailings and handicrafts and jewelry workshops in the San Juan-Taxco River system.

This district has been recognized for years of mining and processing of precious metals since pre-Hispanic times until the closure of the mining activities (2009). At present, it is a famous touristic destination and international producer of precious metals handcrafts and jewelry [20]. The extraction of silver was the main activity of Taxco region, leading the inhabitants to undertake the task of working this metal as artisans [20]. The manufacture of jewelry and handicrafts became a key source of income in the region after the closure of the mines; this local industry has been developed through small workshops, which were diversified, including different processes of raw materials besides silver (Ag), such

as alpaca (Zn-Cu-Ni), brass (Cu-Zn), tumbaga (Cu-Au), for local and international trade. In 2019, 1085 workshops were officially recorded in the municipality of Taxco de Alarcon; these are mainly distributed in Taxco, Acamixtla and Taxco el Viejo localities inside the region (Figure 1) [21].

The metal processing has brought negative impacts on natural resources, with rivers being the most affected resources by the waste from these activities [16]. The San Juan-Taxco River system is composed of three rivers. The San Juan (length of 10 km), Cacalotenango (length of 45 km) and Taxco (length of 29.3 km) rivers jointly discharge at the southern portion of the city of Taxco, also in the town of Taxco el Viejo, forming the Iguala or Cocula River (length 75 km), and finally discharge into the Infiernillo reservoir [14,17].

The San Juan River receives wastewater from nearby towns, as well as chemical waste from silversmiths for the manufacture of silver crafts and mining tailings [22]. The Cacalotenango River receives mine waste from La Concha and El Fraile tailings, as well as urban wastewater without treatment [23]. The Taxco River receives mine waste from several tailing piles along its flow, chemical waste from silversmiths and untreated urban wastewater [14,15].

Geological and Hydrogeological Setting

The Figure 2 summarized the geological map of the San Juan-Taxco River system showing the lithology. The bedrock in the area consists of Lower Cretaceous metamorphic rocks of the Taxco Schist Formation, Albian-Cenomanian limestone of the Morelos Formation, Upper Cretaceous sandstone and shale of the Mexcala Formation, Lower Tertiary red beds of the Balsas Formation and Middle Tertiary acidic volcanics of the Tilzapotla Formation [15,16].

Mineralization structures are 1 to 3 m wide, although a few reach 10 m, and 700 to 2000 m long, these structures appear as hydrothermal veins, replacement ores and stockworks hosted in limestones of the Morelos and Mexcala formations, and more rarely in the Taxco Schists and Balsas formations [16]. The San Juan-Taxco River system is part of the recharge zone of the regional aquifer (Buenavista and Iguala aquifers); this zone is immersed in a mountainous region with a rugged in portion of Taxco municipality and the Iguala valley. Therefore, the population uses surface runoff, dug wells and springs that are distributed throughout the region for drinking water, domestic consumption, agriculture and livestock [24].

The regional aquifer is composed by rhyolites from Tilzapotla Formation, gravels and sandstones from Balsas Group and limestones from Morelos Formation. The storage section of the groundwater is made up of the alluvial and fluvial sediments, such as clay, silt, sand and gravels, in the Iguala Valley. The groundwater drains into the lower parts of the study area, a portion of this water discharges into the main streams and another portion is released as a groundwater flow into the Tuxpan Lake [24].

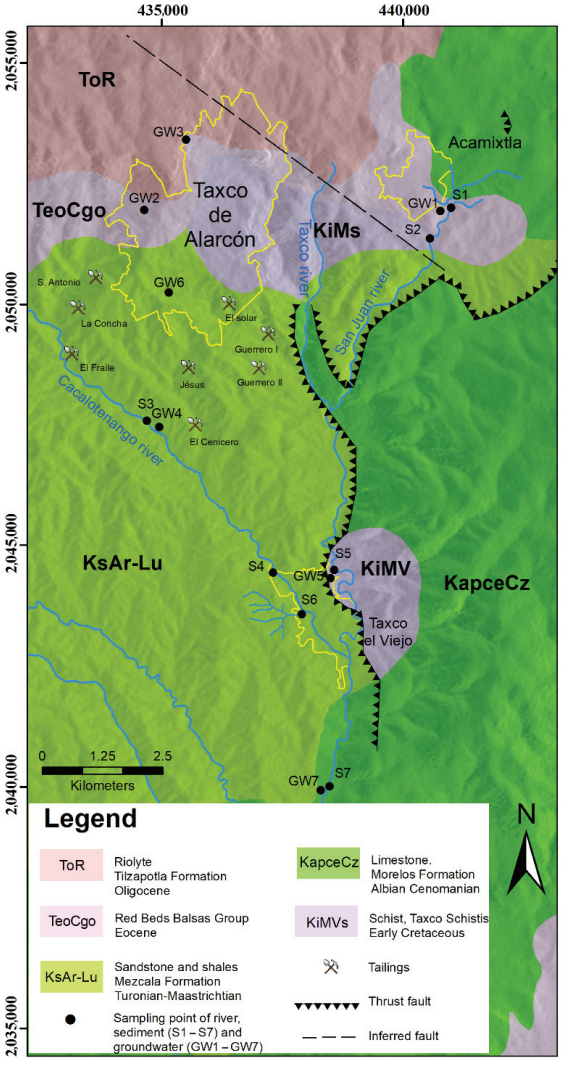

Figure 2. Geological map of the San Juan-Taxco River system.

3. Materials and Methods

3.1. Sample Collection and Analytical Procedure

For this analysis, a total of 21 samples were taken; seven groundwater (two dug wells and five springs), seven river water and seven surface sediment samples were collected in the dry season on May of 2019 to reduce the dilution of the effect of PTE concentrations in the rainy season. These samples were taken from the San Juan River system before its confluence with Taxco River, along the Cacalotenango and Taxco rivers and above and below their confluence, as shown Figure 1. The selection of the sampling points was made considering the spatial and geographical distribution along the river system, the proximity to handicraft and jewelry workshops sites and accessibility of the sites.

Water samples were collected in 1 L polyethylene sampling bottles, pre-cleaned with 10% HNO_3, soaked overnight and rinsed thoroughly with Milli-Q water. The pH, temperature, electrical conductivity (EC) and total dissolved solids (TDS) measurements were performed during sampling using a Hanna multi-parametric sonde. For PTE analysis,

the water samples were filtered using 0.40–0.45 μm membrane, acidified to pH < 2, with HNO_3 at the time of collection to prevent element precipitation and adsorption to the surface of the container during transportation; the samples were then stored at a suitable temperature awaiting analysis (water < 4 °C). The levels of Al, As, Ba, B, Cu, Fe, Pb, Zn, Mn, Ni and Cd in water samples (surface water and groundwater) were analyzed by Inductively Coupled Plasma Emission Spectrometry (ICP-OES) and Liquid Chromatography high performance (HPLC) at the Laboratory of Geosciences at the National Autonomous University of Mexico (UNAM).

The sediment samples were collected using polyethylene spoons and bags to determine physical and geochemical characteristics, kept at 4 °C until further analysis. In the laboratory, sediment samples were air-dried and ground to a fine powder with an agate mortar and then sieved through a 230 ASTM mesh at the Laboratory of Nutrition and Plant Physiology Campus Tuxpan of the Faculty of Agricultural and Environmental Sciences of the Autonomous University of Guerrero (UAGro).

For determining the PTE content (Al, As, Ba, B, Cu, Fe, Pb, Zn, Mn, Ni and Cd), dry-sediment samples were digested in a 1:1 HCl: HNO3 mixture inside a CEM MarxXpress microwave oven [25]. The PTE quantification was conducted using an Inductively Coupled Plasma Optical Emission Spectrometer (ICP-OES) Thermo iCAP 6500 Duo in the Environmental Geosciences Laboratory of UNAM. The grain size analysis was carried out to determine the sediment textural classes according to the Unified Soil Classification System (USCS) [26]. The sediments were classified into gravel, sand, silt and clay. The characterization of mineralogical phases in sediment samples was determined by X-ray diffraction, in a Bruker AXS D8 Advance diffractometer to identify the major minerals; this analysis was performed at the Geochemistry Laboratory of Regional School of Earth Sciences of the UAGro.

3.2. Quality Controls and Calibration Curves for Analytical Equipment

Analytical blanks were implemented throughout the field campaign and analytical process. Replicate samples and standards were processed to determine the precision, and spiked samples were employed to determine accuracy.

The analysis by ICP-OES was made using two calibration curves with six standards, which were prepared from certified mono-elemental standards from the Inorganic Ventures brand and an ICP-200.7 multi-element standard from the High Purity Standards brand. Two types of blanks are analyzed, the calibration blank and the reagent blank, in addition to analyzing three laboratory control samples (MCL), all made from certified standards with traceability to NIST.

HPLC calibration curve is carried out with a standard certificate from Inorganic Ventures IF-FAS-1A, which consists of seven concentrations, and for the drift control of the instrument, it is carried out by means of a Laboratory Control Sample (MCL) prepared from the standard certificate Seven Anion Standard of Dionex, which was analyzed every 10 samples.

The acid digestion of aqueous samples and sediment is carried out with a microwave MARS Xpress CEM, for its calibration, it uses a blank and a sample added with a known concentration of a high purity certified standard (QCS-26) analyzed by ICP-OES.

To establish laboratory accuracy and precision, the limits of the results were calculated from the upper and lower control limits based on the mean and standard deviation of the percent recovery for at least 20 data points.

3.3. Non-Parametric Statistics

All datasets were checked for outliers and assessed for normality (surface water, groundwater and sediments), first objectively using a Shapiro–Wilk test. The calculations were performed using Excel.

3.4. Health Risk Assessment

Risk assessment is a methodology which identifies, characterizes and analyzes the toxic element to qualify the adverse effects in a specified time and estimates risk levels [27]. This approach was applied to identify the exposure and tendency of toxic elements in San Juan-Taxco River system's water with reference to the human body. There are two central ways of metal exposure and pathways in human organism, either through water consumption as ingestion or through dermal absorption [7].

The health risk assessment was computed through the chronic daily intake (CDI; mg kg^{-1}/day). It helps in assessing the health risk caused by exposure to PTE (heavy metals) through different pathways. For this study, ingestion and dermal exposure (CDI) were computed by Equations (1) and (2) [27]. The receptors were categorized into two categories, infants (<6 years old children) and adults (<30 years old).

$$CDI_{ingestion-water} = \frac{EC \cdot IR \cdot EF \cdot ED}{BW \cdot AT} \quad (1)$$

$$CDI_{Dermal} = \frac{EC \cdot SA \cdot AF \cdot ABDS_d \cdot ET \cdot ED \cdot CF}{BW \cdot AT} \quad (2)$$

where EC is the concentration of TEs in the water, IR is the ingestion rate (L day^{-1}), EF is the exposure frequency (days/year), ED is the exposure duration (years), BW is the average body weight (kg), AT is the averaging time (days), SA is the surface area of skin in contact (cm^2), AF is the skin adherence factor, $ABSDS_d$ is the dermal absorption factor ET is the exposure (h day^{-1}), CF is the conversion factor (kg mg^{-1}) and ET is the exposure (h day^{-1}) (Table 1).

Table 1. Exposure factors used in chronic daily intake (CDI) estimation for non-carcinogenic risk.

Symbol	Name	Unit	Recommended Values	Symbol	Name	Unit	Recommended Values (Adult)
Cw	Element concentration	mg L^{-1}		SA	exposed skin area	cm^2	adult 5700, child 28,00 *
IR	Ingestion rate	L day^{-1}	adult 2.5 child: 0.78	AF	adherence factor	-	0.07 *
EF	Exposure frequency	day y^{-1}	350	ABSd	dermal absorption fraction	-	0.03
ED	Total exposure duration	year	adult 30; child 6	ET	exposure time	h day^{-1};	0.58
BW	Average body weight		Adult 52 kg children 15 kg	CF	conversion factor	kg mg^{-1}	10^{-2} +
				RfDingestion			RfDingestion Al = 1, Cu = 0.04, Fe = 0.7, Mn = 0.00096, Pb = 0.00042 Zn = 0.06, As = 0.0003
AT	Average exposure time	day	adult 10,950, child 2190	RfDD	Reference Dose of PTEs	mg kg^{-1} day^{-1}	RfDDerlmal Al = 0.01, Cu = 0.00184, Fe = 0.14, Mn = 0.024, Pb = 0.0035 Zn = 0.3, As = 0.003, Ba = 20

RfDs values from USEPA * [27], + [28].

The hazard quotient (ingestion and dermal) and hazard index (HI) are computed by Equations (3) and (4) [27]:

$$HQ_{ingestion} = \frac{CDI_{ingestion}}{RfD_{ingestion}} \quad (3)$$

$$HQ_{Dermal} = \frac{CDI_{Dermal}}{RfD_{Dermal}} \quad (4)$$

where *RfD* denotes the reference dose (ingestion and dermal) based on the guidelines of the US Environmental Protection Agency [28] and for health risk assessment calculation (*RfD* differs for each PTE). The hazard index (HI) represents the cumulative non-carcinogenic risk. It is the sum of HQs for similar toxic effects and all pathways. It can also be calculated by Equation (5):

$$\mathrm{HI} = \sum HQ_i = HQ(ingestion) + HQ\ (dermal) \quad (5)$$

where *i* is the HQ value of each element. In the context of human health, the *HI* values < 1 are low risk, while the values > 1 are high risk with long-term health hazard effects [5].

3.5. Assessment of PTE in the San Juan-Taxco River System (Water and Sediment)

Water quality was evaluated according to the criteria established for human consumption by the World Health Organization [29]. PTE risk in sediments was assessment using Sediment Quality Guidelines (SQG), probable effect level threshold (PEL), threshold effect concentration (TEC) and probable effect concentration (PEC) [30–32]. These guidelines allowed a simple, comparative mean for assessing the potential risk of pollution in a fluvial aquatic ecosystem.

3.6. Assessment of PTE Enrichment in Sediments

3.6.1. Geoaccumulation Index (Igeo)

The Igeo allows for the assessment of PTE sediment contamination and can be used to evaluate the environmental pollution status compared with background values [13,33,34]. The Igeo is calculated by Equation (6):

$$Igeo = \frac{Log_2(C_n)}{1.5(B_n)} \quad (6)$$

where C_n is the content of elements in the sediment samples, B_n is the concentration of geochemical background for the same elements (n) and factor 1.5 is the background matrix correction factor due to lithological variations. The Igeo, according to Muller [33], includes seven classes, summarized in Table 2 and the background values used are presented in Table 3 [35,36].

3.6.2. Enrichment Factor (EF)

Enrichment factor (EF) is an indicator that reflects the degree of anthropogenic pollution [37]. The EF is calculated using the relationship in Equation (7):

$$EF = \frac{\left(\frac{Metal}{Al}\right) sample}{\left(\frac{Metal}{Al}\right) background} \quad (7)$$

In this case, aluminum (*Al*) was employed as the reference element for geochemical normalization; this element in sediments is useful to eliminate the effect of grain size, since it is a major element and exhibits relatively small content variations and a large distribution. The interpretation provided by Malvandi [2] from the EF values was used for this study and is presented in Table 2 [2,38].

Table 2. Enrichment and contamination categories base don Igeo, EF, CF, PLI and RI.

Geoaccumulation Index (Igeo)		**Enrichment Factor (EF)**		**Contamination Factor (CF)**	
Value	Categorization	Value	Categorization	Value	Categorization
<0	Unpolluted	<1	indicates no enrichment	<1	low contamination
0–1	Pristine to moderately contaminated	3–5	moderate enrichment	1–3	moderate contamination
1–2	Moderately contaminated	5–10	moderately severe enrichment	3–6	considerable contamination
2–3	Moderately to strongly contaminated	10–25	severe enrichment	>6	very high contamination
3–4	Strongly contaminated	25–50	Very severe enrichment		
4–5	Strongly to extremely strongly contaminated	>50	Extremely severe enrichment		
>5	extremely strongly contaminated				
Potential ecological risk factor (E_r^i)		Potential ecological risk index (RI)		Pollution Load Index (PLI)	
Value	Categorization	Value	Categorization	Value	Categorization
<40	low ecological risk	<150	low ecological risk	<1	Unpolluted
40–80	moderate ecological risk	150–300	moderate ecological risk	1–2	Moderately polluted
80–60	appreciable ecological risk	300–600	considerable ecological risk	2–3	Heavily polluted
160–320	high ecological risk	>600	very high ecological risk	>3	Extremely polluted.
>320	serious ecological risk				

3.6.3. Contamination Factor (CF)

Sediment contamination was also assessed by using the contamination factor (CF) and degree of contamination. The CF index values were calculated by dividing the concentration of each PTE in the sediment by the baseline or background values [39]. CF values were explained according to Hakanson [39] in Equation (8) and summarized in Table 2:

$$CF = \frac{C_{heavy\ metal}}{C_{background\ values}} \quad (8)$$

3.6.4. Pollution Load Index (PLI)

Pollution load index (PLI) represents the number of times by which the toxic element concentrations in the sediment exceeds the background concentration, and gives a summative indication of the overall level of PTE toxicity in a particular sample. For the entire sampling site, PLI has been estimated by the n-root from the product of *n* CFs of the studied elements included (Equation (9)):

$$PLI = (CF_1\ x\ CF_2\ x\ CF_3\ x \ldots\ldots\ xCF_n)^n \quad (9)$$

The *PLI* is a multi-elemental index used to assess the degree of PTE pollution and, hence, to evaluate the environmental quality. The PLI for the entire study area (Equation (10)) can be estimated using the same calculation principle for each sampling point; substituting the CF

values for the PLI value of each point, it is determined as the nth root of the product of the *n* CF (Contamination Factors) according to Tomlinson [40]:

$$PLI_{global} = (PLI1 \times PLI2 \times PLI3 \cdots ..x\ PLIn)^{1/n} \quad (10)$$

The index permits a simple, comparative means for assessing PTE pollution levels. A PLI of >1 is contaminated, whereas <1 indicates no contaminated site [39]. Corami et al., (2020) [13] used other evaluation criteria for classifying the degree of contamination for PLI, as shown in Table 2.

Table 3. Potential Toxic Element concentrations (PTE in waters (mg L^{-1}) compared with World Health Organization limits and sediment (mg kg^{-1}) compared with background values [35,36], Sediment Quality Guideline values (SQGs), PEL, TEC and PEC.

	Sites	Nature	pH	Al	As	B	Ba	Cd	Co	Cr	Cu	Fe	Mn	Ni	Pb	Zn
Waters (mg L^{-1})	S1	River water	6.8	0.0071	<l.q.	0.0223	0.0942	<l.q.	<l.q.	<l.q.	<l.q.	0.0137	0.0822	<l.q.	<l.q.	0.0191
	S2		8.1	0.0084	0.0725	0.1173	0.1217	<l.q.	<l.q.	<l.q.	0.0046	0.0755	0.3622	<l.q.	0.0182	0.2335
	S3		7.9	0.0912	0.0291	0.0159	0.1162	<l.q.	<l.q.	<l.q.	0.0044	0.1759	0.1346	<l.q.	0.0149	0.0573
	S4		7.3	0.2525	<l.q.	<l.q.	0.1224	<l.q.	<l.q.	<l.q.	0.0061	0.3164	0.0541	<l.q.	0.0165	0.0858
	S5		7.2	0.0455	<l.q.	0.5284	0.0646	<l.q.	<l.q.	<l.q.	0.0070	0.0396	0.5343	0.0181	<l.q.	0.0843
	S6		7.2	0.0397	<l.q.	<l.q.	0.0722	<l.q.	<l.q.	<l.q.	<l.q.	0.0818	0.0073	<l.q.	<l.q.	0.0069
	S7		8.1	0.0125	<l.q.	0.5791	0.0914	<l.q.	<l.q.	<l.q.	0.0078	0.0175	1.4482	0.0174	<l.q.	0.0503
	GW1	Dug well	7.0	0.0183	<l.q.	<l.q.	0.081	<l.q.	<l.q.	<l.q.	0.004	0.146	0.032	<l.q.	0.0245	0.0770
	GW2	Springs	6.6	<l.q.	<l.q.	<l.q.	0.111	<l.q.	<l.q.	<l.q.	<l.q.	<l.q.	<l.q.	<l.q.	<l.q.	<l.q.
	GW3		6.7	0.0125	<l.q.	<l.q.	0.023	<l.q.	<l.q.	<l.q.	<l.q.	<l.q.	<l.q.	<l.q.	0.0235	0.0053
	GW4		8.2	0.1127	<l.q.	0.017	0.048	<l.q.	<l.q.	<l.q.	<l.c.	0.021	0.009	<l.q.	<l.q.	0.0149
	GW5		7.2	0.0097	<l.q.	0.068	0.081	<l.q.	<l.q.	<l.q.	0.111	0.022	0.006	<l.q.	<l.q.	0.2442
	GW6		6.9	0.0059	<l.q.	<l.q.	0.040	<l.q.	<l.q.	<l.q.	0.010	<l.q.	<l.q.	<l.q.	<l.q.	0.0130
	GW7	Dug well	7.9	0.0135	<l.q.	<l.q.	0.069	<l.q.	<l.q.	<l.q.	<l.q.	<l.q.	<l.q.	<l.q.	<l.q.	0.0277
WHO (2008)			6.5–8.5	0.200	0.025	0.300	0.700			0.050	1.300	0.300	0.400		0.010	3.000
sediment (mg kg^{-1})	S1	River sediment		16,771.0	<l.q.	15.8	154.0	2.1	5.2	5.0	209.0	18,637.0	231.0	18.7	35.6	351.0
	S2			16,610.0	39.3	16.8	151.0	1.8	6.1	2.5	68.3	20,009.0	362.0	16.6	94.2	144.0
	S3			18,313.0	48.8	12.8	173.0	16.2	7.2	<l.q.	78.4	20,526.0	795.0	15.7	265.0	2008.0
	S4			20,303.0	25.5	31.2	278.0	50.4	7.8	5.5	393.0	20,614.0	2710.0	111.0	244.0	4509.0
	S5			19,032.0	24.7	15.9	104.0	5.5	7.2	<l.q.	41.8	23,223.0	334.0	18.6	160.0	967.0
	S6			22,982.0	<l.q.	19.9	143.0	2.0	9.0	9.4	117.0	20,930.0	105.0	24.2	13.9	142.0
	S7			12,086.0	21.3	13.8	88.0	9.4	6.3	<l.q.	55.9	22,301.0	660.0	20.0	189.0	1763.0
PEL a					17 a			3.53 a		90 a	196.6 a			75 a	91.3 a	314.8 a
TEC b					9.79 b			0.99 b		43.4 b	31.6 b			22.7 b	35.8 b	121 b
PEC c					33 c			4.98 c		111 c	149 c			48.6 c	128 c	459 c
Background values				81,500	4.8	17	628	0.09	17.3	92	28	50,400	774	47	17	67

Note: l.q. (limit of quantification).

3.6.5. Potential Ecological Risk Index (RI)

The maximum contamination in sediments caused by PTE is screened by the Potential Environmental Risk Index (PERI or RI); this method is widely used to evaluate quantitatively the level of the ecological risk degree of PTE. This index was proposed by Hankson in 1980 [39] and it is founded on Sedimentation Theory. The RI value is computed following the formula (Equation (11)) [39]:

$$RI = \sum_{i=1}^{n} E_r^i, \quad E_r^i = T_r^i\ x\ CF \quad (11)$$

where E_r^i is the potential ecological risk factor for a given contaminant (i), T_r^i is the toxic response factor of each element, including Cr = 2, Cu = 5, Cd = 30, As = 10 and Pb = 5 [39], and CF are the contamination factors, which have already been described above. This

scheme not only assesses the pollution status in sediment, but also combines ecological and environmental effects with toxicology, providing a better evaluation of the potential risk of PTE contamination with the index level. *RI* is a set of potential risks for each element, is an integrated potential environmental risk index for several PTEs and is classified based on the description summarized in Table 2.

4. Results

4.1. Non-Parametric Statistics

An exploratory analysis with Shapiro–Wilk's method to test the normality was applied to the concentration data. It was found that Ba, Fe and Zn in surface water followed a normal distribution, with R^2 values equal to 0.89, 0.82 and 0.81, respectively; Ba in groundwater had a correlation coefficient of 0.97. For sediments, Al and Ba followed the normal distribution, with R^2 values of 0.97 and 0.87, respectively. For other elements, some outliers were present in the data, which reduced the correlation coefficient. Those outliers were analyzed in the whole context of geographical distribution to correlate them with the presence or absence of an important source of pollution.

4.2. Water

4.2.1. Hydrochemical Characterization

pH is an important factor that influences the solubility of toxic elements (PTE) in water [11]; lower values of pH indicate higher solubility and vice versa. The pH values in the groundwater ranged from 6.75 to 8.1, and that in river water fluctuated from 6.16 to 8.2 (Table 3). In general, the pH varies in water from neutral to slightly alkaline, where the reactivity of PTE was low and their concentration loadings oscillated between low and high concentration. Almost all the collected samples of water (groundwater and river water) have detectable concentrations of PTE.

Water quality was assessed according to criteria established for human use and consumption by the World Health Organization [29]. In case of groundwater, Al, B, Ba, Cu, Fe, Mn, Pb and Zn were measured, and only Pb exceed the criteria (0.03 mgL^{-1}) for human use and consumption of the WHO in samples GW1 and GW3. Al, As, B, Ba, Cu, Fe, Mn, Pb and Zn were detected in the river water (Table 3).

Although Al was measured in all the samples, only S4 showed a concentration above the WHO limit of 0.2 mg L^{-1}; two samples (S2 and S3) showed As concentrations above the WHO limit (0.025 mg L^{-1}). B was present in S1, S2, S3, S5 and S7, but only in S5 and S7 did it exceed the recommended limit for human use and water consumption. Fe and Mn were detected in all the samples; S4 and S5 surpassed the WHO limit of 0.3 mgL^{-1} for Fe and Mn was above the 0.4 mgL^{-1} recommended limit for S7. On the other hand, Ba and Zn were found in all the samples, but were always below the WHO limits (0.7 and 3 mg L^{-1}, respectively).

4.2.2. Health Risk Assessment in Water Samples

The potential health risk to human beings by water for human use and consumption was calculated by assessing the PTE concentration in water (groundwater and river water) and by assessing the pathways through which humans are exposed to these elements. In this study, non-carcinogenic risk was determined by estimating the daily intake index (CDI), which represents the daily exposure of a population to contaminants, hazard quotient (HQ), to estimate the non-carcinogenic risk by toxic elements, and cumulative hazard index (HI), to show the potential health risk possess by multiple elements, considering the additive effect of PTE in HQ were determined. The studied exposure pathways were ingestion and dermal absorption in children and the adult population; the receptors were categorized in children (<6 years old) and adults (>30 years old).

CDI ingestion values for both groups were under limit (<1) and at present poses no serious threat to human health, although Mn values were one of the highest values as

compared with other PTE analyzed for both adults and child (in sample S7), though values of Cu were highest for children in sample GW5 (Figures 3 and 4).

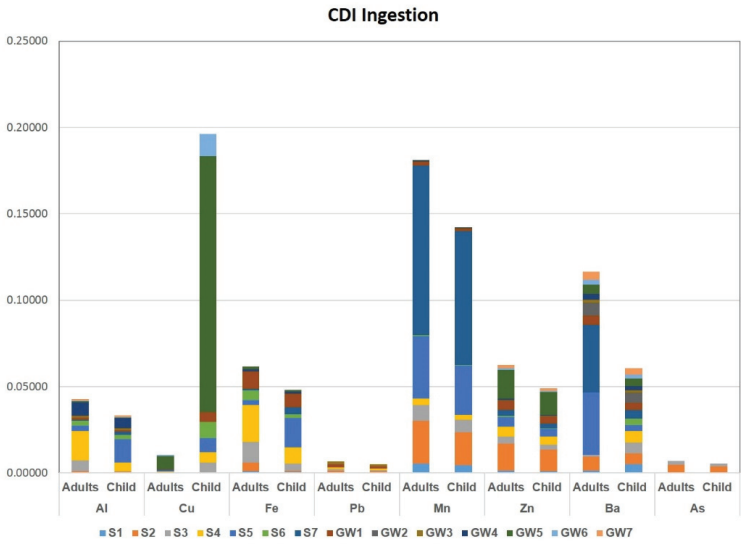

Figure 3. CDI Ingestion values along the sampling sites for each PTE assessed.

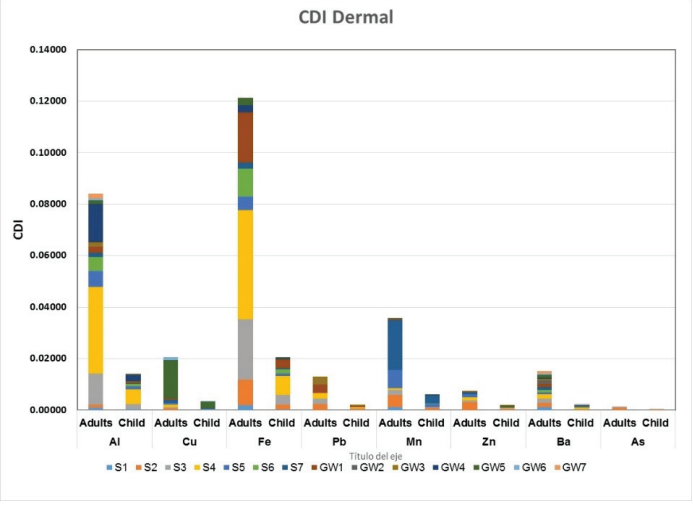

Figure 4. CDI dermal values along the sampling sites for each PTE assessed.

The CDI and HQ dermal values in adults were above the limit 1 for Al, Pb, Mn and As. Specifically, the values with a high impact on the indices for each element and the corresponding samples are as follows: (1) Al in samples S3, S4 and GW4; (2) Pb in samples S2, S3, S4, GW1 and GW3; (3) Mn in samples S1, S2, S3, S5 and S6; and (4) As only in samples S2 and S3. On the other hand, for children the CDI and HQ dermal values were above the limit of 1 for Pb, Mn, and Cu. The samples GW1 and GW3 were above the limit for Pb; whereas for Mn were the samples S5, S7; and finally, for Cu only in the sample GW5 (Table 4 and Figure 4).

Table 4. Chronic daily intake (CDI), hazard quotient (HQ) and hazard index (HI) for adult and child groups for non-carcinogenic risk assessment.

		River Water							Groundwater					
		Oral			Dermal				Oral			Dermal		
		Mean	Min	Max	Mean	Min	Max		Mean	Min	Max	Mean	Min	Max
Adult														
HQ	Al	0.0044	0.0005	0.0171	0.8715	0.0943	3.3710	HQ	0.0017	0.0000	0.0076	0.3290	0.0000	1.5041
	Cu	0.0072	0.0000	0.0132	0.0143	0.0000	0.0259		0.0303	0.0000	0.1883	0.0596	0.0000	0.3702
	Fe	0.0100	0.0013	0.0307	0.0981	0.0130	0.3017		0.0026	0.0000	0.0141	0.0257	0.0000	0.1388
	Pb	0.1375	0.0000	0.3536	2.2537	0.0000	5.7946		0.1330	0.0000	0.4747	2.1805	0.0000	7.7800
	Mn	1.0599	0.0208	4.0964	5.2114	0.1022	20.141		0.0189	0.0000	0.0902	0.0930	0.0000	0.4436
	Zn	0.0174	0.0016	0.0528	0.0165	0.0004	0.0519		0.0123	0.0000	0.0553	0.0012	0.0000	0.0054
	Ba	0.1750	0.0000	0.5616	0.2657	0.1760	0.3334		0.0628	0.0221	0.1078	0.1765	0.0620	0.3029
	As	3.2849	0.0000	16.400	0.6461	0.0000	3.2255							
HI		4.6963	0.0330	17.960	9.3773	0.9090	20.610	HI	0.2617	0.0588	0.6838	2.8656	0.2214	8.8439
Children														
HQ	Al	0.0034	0.0004	0.0135	0.1484	0.0161	0.5741	HQ	0.0013	0.0000	0.0060	0.0560	0.0000	0.2561
	Cu	0.0042	0.0000	0.0094	0.0528	0.0000	0.0959		0.0238	0.0000	0.1479	0.2207	0.0000	1.3706
	Fe	0.0078	0.0010	0.0241	0.0167	0.0022	0.0514		0.0021	0.0000	0.0111	0.0044	0.0000	0.0236
	Pb	0.1080	0.0000	0.2778	0.3838	0.0000	0.9868		0.1045	0.0000	0.3729	0.3713	0.0000	1.3249
	Mn	0.8327	0.0163	3.2183	0.8624	0.0174	3.4299		0.0149	0.0000	0.0709	0.0061	0.0000	0.0214
	Zn	0.0136	0.0012	0.0415	0.0028	0.0001	0.0088		0.0097	0.0000	0.0434	0.0021	0.0003	0.0042
	Ba	0.0743	0.0492	0.0932	0.0396	0.0044	0.0568		0.0494	0.0173	0.0847	0.0021	0.0003	0.0042
	As	2.5808	0.0000	12.884	0.1100	0.0000	0.5493							
HI		3.6249	0.0873	14.102	1.6166	0.0422	3.6014	HI	0.2056	0.0462	0.5372	0.6623	0.0042	1.4523

The hazard index (HI) for ingestion in children ranged from 0.05 to 14.1, with a mean value of 2.04, and for adults 0.03 to 17.96, with mean value 2.48 (Table 4). The HI dermal for adults was more significant than the HI in children. These values demonstrated a health risk for the use and consumption of river water. HI dermal in adults ranged from 0.22 to 20.61 with a mean value of 6.12 and ranged from 0 to 3.61 with mean 1.14 in children (Table 4). HI dermal values suggest that both adult and child population were significantly affected by PTE presence in river water and groundwater by the notable concentrations of Al, Mn, Pb and As.

Based on the USEPA criteria [27], HI ingestion values in adults and children presented a high health risk in S2, S3, S5 and S7. HI dermal values for adults and children presented high risk in river water and groundwater with high values well above the criteria (<1) in samples S1, S2, S3, S4, S5, S7, GW1, GW3 and GW4 for adults and S2, S3, S4, S5, S7, GW1, GW3 and GW5 for children; the samples either have unusual geological enrichment or are under heavy anthropogenic influence (Figure 5).

The results showed that even though there were not much variability in the HI for children and adults, adults generally seem to be at higher non-cancer risks compared with children. In addition, in both children and adults, dermal contact of EPT in river water poses higher non-cancer risks compared to ingestion values.

Similar values of hazard potentials were reported in the literature [41–45]. The results show that Al, Pb, Mn and As pose a non-cancer risk through the dermal pathway to resident adults and children, while Mn and As pose a non-cancer risk to residents that use and consume the river water.

Prassad et al. [11] reported higher HI values for Mn, Zn and Pb in the Ganga River than the reported in the present investigation, suggesting that both the adult and child population were significantly affected.

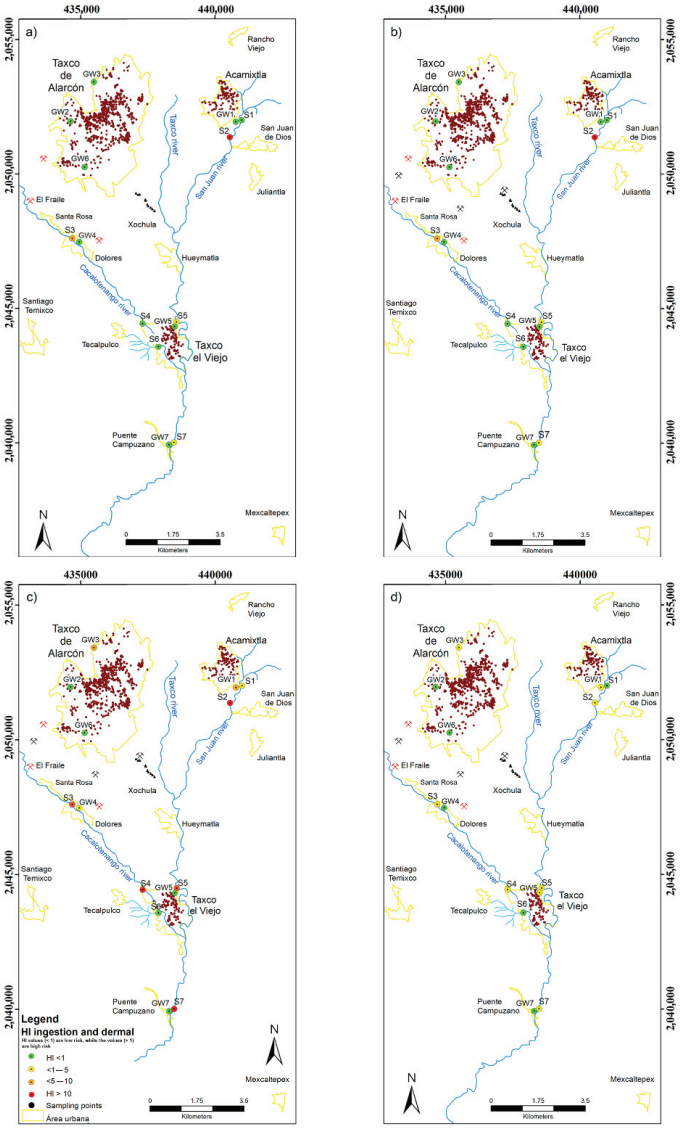

Figure 5. Hazard index (HI) for each site and population group. (**a**) Adult and (**b**) child through the ingestion pathway and (**c**) adult and (**d**) child through the dermal pathway.

The results from Bodrud-Doza et al. [42] are consistent with this study, which also stated, based on the average values of HQ and HI, that the concentration of PTE might pose little health effects to the adults and children of Dhaka city via oral ingestion. They also reported that HQs of metals were lower than the unity via dermal absorption of groundwaters in Dhaka city, which suggests that these pollutants could pose a minimum hazard to the local residents. However, the calculated mean HI dermal value for groundwater was 0.0372, while the same value for surface water was 0.0530. Thus, it can be inferred that surface water possessed more potential non-carcinogenic harmful health risks to the residents compare to groundwater.

PTE toxicity could be acute, while others could be chronic after long-term exposure, which may lead to the damage of several organs in the body, such as the brain, lungs, liver

and kidney, causing diseases in the body. Alternative sources of water supply, including sitting of boreholes (after accurate geochemical surveys) for potable water for the community dwellers, should be facilitated.

4.3. Sediments

4.3.1. PTE Concentrations in Sediments

The concentrations of PTE in sediment samples were contrasted with the TEC, PEC and probable effect level (PEL) values [30–32]. The results are summarized in Table 5. Compared with SQG for aquatic life protection, PTE were above the probable effect level (PEL) for As, Zn and Pb in five samples (71%), for Cd in four samples (57.1%), for Cu in three samples (42%) and for Ni in one sample (14.28). All sites exceeded the TEC levels for As, Cd, Cu, Pb and Zn, demonstrating a high level of pollution; for Pb, only S1 was below the TEC value, while in the case of Ni, two sites exceeded the TEC values (S4 and S6). The concentrations of Ni were below the TEC values for 50% of the samples, indicating that there are no adverse effects in these samples (S1, S2, S3 and S7 samples). For As and Cu, only two samples exceeded the PEC values (S2 and S3 for arsenic and S1 and S4 for copper). The results also showed values higher than PEC for Pb, Zn and Cd in 57% of the samples (S3, S4, S5 and S7), indicating that adverse biological effects often can occur (Table 3).

Table 5. The values of the geoaccumulation indices (Igeo) and enrichment factor (EF) of PTE in fluvial sediments in the San Juan-Taxco River system.

	Geoaccumulation Indices (Igeo)									
	S1	**S2**	**S3**	**S4**	**S5**	**S6**	**S7**	**Mean**	**Max**	**Min**
Al	−2.87	−2.88	−2.7	−2.59	−2.68	−2.41	−3.34	−2.787	−2.41	−3.34
As	-	2.45	2.76	1.82	1.78	-	1.56	2.074	2.76	1.56
B	−0.69	−0.6	−1	0.29	−0.68	−0.36	−0.89	−0.56	0.29	−0.99
Ba	−2.61	−2.64	−2.4	−1.76	−3.18	−2.72	−3.42	−2.681	−1.76	−3.42
Cd	3.96	3.74	6.91	8.54	5.35	3.89	6.12	5.5014	8.54	3.74
Co	−2.32	−2.09	−1.9	−1.73	−1.85	−1.53	−2.04	−1.916	−1.53	−2.32
Cr	−4.79	−5.79	-	−4.65	-	−3.88	-	−4.778	−3.88	−5.79
Cu	2.32	0.7	0.9	3.23	−0.01	1.48	0.41	1.29	3.23	−0.01
Fe	−2.02	−1.92	−1.9	−1.87	−1.7	−1.85	−1.76	−1.857	−1.7	−2.02
Mn	−2.33	−1.68	−0.6	1.22	−1.8	−3.47	−0.81	−1.346	1.22	−3.47
Ni	−1.91	−2.09	−2.2	0.65	−1.92	−1.54	−1.82	−1.543	0.65	−2.17
Pb	0.48	1.89	3.38	3.26	2.65	−0.88	2.89	1.9529	3.38	−0.88
Zn	1.8	0.52	4.32	5.49	3.27	0.5	4.13	2.8614	5.49	0.5
	Enrichment factor (EF)									
Al	1	1	1	1	1	1	1	1	1	1
As	-	40.17	45.3	21.33	22.04	-	29.92	31.742	45.25	21.33
B	4.52	4.85	3.35	7.37	4.01	4.15	5.47	4.8171	7.37	3.35
Ba	1.19	1.18	1.23	1.78	0.71	0.81	0.94	1.12	1.78	0.71
Cd	113.39	98.13	801	2248	261.7	78.81	704.3	615.05	2247.9	78.81
Co	1.46	1.73	1.85	1.81	1.78	1.84	2.46	1.8471	2.46	1.46
Cr	0.26	0.13	-	0.24	-	0.36	-	0.2475	0.36	0.13
Cu	36.27	11.97	12.5	56.34	6.39	14.82	13.46	21.673	56.34	6.39
Fe	1.8	1.95	1.81	1.64	1.97	1.47	2.98	1.9457	2.98	1.47
Mn	1.45	2.29	4.57	14.05	1.85	0.48	5.75	4.3486	14.05	0.48
Ni	1.93	1.73	1.49	9.48	1.69	1.83	2.87	3.0029	9.48	1.49
Pb	10.18	27.19	69.4	57.62	40.3	2.9	74.97	40.366	74.97	2.9
Zn	25.46	10.55	133	270.2	61.81	7.52	177.4	98.044	270.15	7.52

4.3.2. Grain Size

According to the grain size analysis results of the surface sediments in the San Juan-Taxco River system, sand is the overall dominant grain size. At most sites, the sand content exceeds 80%, the contents of gravel and fine particles (clay and silt) were very small

(averaging 6.25 and 2.38%, respectively). The flow rate and flow velocity of the surface water have high influence of grain size; the textural parameters derived from the grain size analysis reflect the energy conditions in the sedimentation environment. In a low-energy environment, the sediments are fine, although in a high-energy environment, the sediments are coarse [46]. In this analysis, the distribution of grain size explains the high-energy in the stream producing the dominance of sand size particles, in which the water flux is high, and the slope is steep, thereby preventing the sedimentation of fine-grained particles along the stream.

4.3.3. Sediment Mineralographic Composition

XRD studies revealed the presence of different minerals as: Quartz, Calcite, Sanidine, Albite, Biotite, Wickenburgite, Lipsconmbite, Phengite, Gypsum and Muscovite. In all the samples, a predominance of Quartz crystals (36 to 51%) and Calcite (6 to 18%) were shown by XRD; Albite was present in four samples (11.5 to 19.2%), while Sanidine was present in three samples (11.8 to 13.9%). In the sediment samples, minerals were found that are composed of aluminum oxide and silicon dioxide, such as Albite, Sanidine, Biotite, Muscovite and Wickenburgite. These minerals are by products of igneous and metamorphic rocks, which are generally unstable in earth-surface due to weathering conditions; these minerals are transformed into stable products (crystalline clay minerals, oxides and hydroxides) that largely conserve aluminum and iron [47]. Therefore, the presence of aluminum and iron in sediments in the study area is associated with an anthropogenic origin.

4.3.4. Degree of PTE Enrichment and Ecological Risk

Geoaccumulation index (Igeo) values are summarized in Table 5. According to the calculation of each sampling point, the order of the TPE from the Igeo assessed is as follows: Cd > Zn > Pb > Cu > As > Mn > Ni > B > Fe > Co > Ba > Al > Cr. S3 and S4 are the most critical points by the Igeo (with four metals in the range of heavily to very heavily contaminated). The Igeo values of Al, B, Ba, Co, Cr and Fe at all sampled were less than zero, suggesting that these sites were not polluted. Cd was the metal that presented the highest contamination in all the sampled sites, the sediment samples were grouped in heavily contaminated for S1, S2 and S6, and heavily and extremely contaminated for S3, S4, S5 and S7. Zn, Pb and Cu are the three PTE that have the greatest influence on the contamination of the river sediments, since they present the highest contamination values of the Igeo. In the case of Zn, these Igeo values were classified as uncontaminated to moderately contaminated (S2 and S6), moderately contaminated (S1), moderately to heavily contaminated (S5), heavily to very contaminated (S3 and S7) and extremely contaminated (S4).

Igeo for Pb were categorized as uncontaminated in S6, uncontaminated to moderately contaminated in S1, moderately contaminated for S2, moderately to heavily contaminated in and S7 and heavily to very contaminated for S3 and S4. For Cu, Igeo values were classified as uncontaminated in S5, uncontaminated to moderately contaminate in S3, S4 and S7, moderately contaminated for S6, moderately to heavily contaminate in S4. The values of Igeo for As were greater than 1 but less than 2 in the samples of S4, S5 and S7, which were classified as moderately contaminated, while the samples S2 and S3 were considered as moderately to heavily contaminated.

The average EF (Table 5) of Cr, Ba, Co, Fe and Ni are found to be less than 3, indicating minor enrichment, although the average enrichment factors of B and Mn are found between 3 and 5, suggesting that contaminations are currently not a major concern, although moderate enrichment is indicated. The average EF of Cu was 21.67, indicating severe enrichment ($10 < EF < 25$). As and Pb presented very severe enrichment ($25 < EF < 50$) and Zn and Cd presented extremely severe enrichment ($EF > 50$); the average enrichment factors for these PTEs were 31.74, 40.36, 98.04 and 615.05, respectively. The Cd presents extremely high enrichment in all the points evaluated.

The results of CFs and individual and global PLI are summarized in Table 6. The level of CF values for each PTE in the sediment was in the order: Cd > Zn > Pb > Cu > As > Mn > Ni > Fe > Co > Ba > Cr. Among all metals, contamination by Cd is the highest in all the sediment samples in a range of CF values from 20 to 560 The CF values for Cd were >6 in all the sediments samples, indicating very high contamination. The CF values for Zn, Pb, Cu and As present very high contamination and considerable contamination. The CF values for Al, Ba, Co, Cr and Fe in all the samples denotes low contamination for all the samples. These results indicated that the contamination is relatively high; there are serious impacts of pollution related to PTE in the Taxco River System coming from abandoned mining tailings, metals processing (jewelry) and untreated sewage.

Table 6. PTE contamination factors (CFs) and pollution load indices (PLIs) for sediments of all sites studied in the San Juan-Taxco River system.

Sites	Contamination Factors (CFs)													PLI
	Al	As	B	Ba	Cd	Co	Cr	Cu	Fe	Mn	Ni	Pb	Zn	
S1	0.21	-	0.93	0.25	23.33	0.3	0.05	7.46	0.37	0.3	0.4	2.09	5.24	0.80
S2	0.2	8.19	0.99	0.24	20	0.35	0.03	2.44	0.4	0.47	0.35	5.54	2.15	0.86
S3	0.22	10.17	0.75	0.28	180	0.42	-	2.8	0.41	1.03	0.33	15.59	29.97	2.08
S4	0.25	5.31	1.84	0.44	560	0.45	0.06	14.04	0.41	3.5	2.36	14.35	67.3	2.83
S5	0.23	5.15	0.94	0.17	61.11	0.42	-	1.49	0.46	0.43	0.4	9.41	14.43	1.43
S6	0.28	-	1.17	0.23	22.22	0.52	0.1	4.18	0.42	0.14	0.51	0.82	2.12	0.72
S7	0.15	4.44	0.81	0.14	104.44	0.36	-	2	0.44	0.85	0.43	11.12	26.31	1.59
Mean	0.22	6.652	1.06	0.25	138.73	0.4	0.06	4.916	0.42	0.96	0.68	8.417	21.07	1.47
Max	0.28	10.17	1.84	0.44	560	0.52	0.1	14.04	0.46	3.5	2.36	15.59	67.3	2.83
Min	0.15	4.44	0.75	0.14	20	0.3	0.03	1.49	0.37	0.14	0.33	0.82	2.12	0.72

In many studies, where the CF index has been calculated, CF values ranged from 0.03 to 2.31 for Cr, As, Fe, Al, Co, Ni, Zn and Mn, CF values in the Zarrin-Gol River ranged from 0.14 to 6.08 for Fe, Mn, ZN, Cr and Ni and CF values in the Yauri River ranged from 0.44 to 2.47 for Cr, Fe, Ni and Zn [2,7].

The PLI values estimated by sampling points ranged from 0.72 to 2.83 (Table 6). These indicate that samples S1, S2 and S6, where PLI was below 1, were unpolluted, the samples S5 and S6 were moderately polluted, while samples S3 and S4 were polluted. For computing the global value, it was necessary to consider all the samples and correct for points S1, S3, S5, S6 and S7, which do not contain As and Cr; therefore, $n = 12$. The global value of PLI for the entire study area was 1.29, which makes it a moderately contaminated area (Figure 6). This indicates that the San Juan, Taxco and Cacalotenango rivers are in a state of contamination due to the influence of the 13 PTEs evaluated, with Cd, Zn, Pb and Cu being the most influential elements.

The ecological risk of PTE in superficial sediments was assessed through the potential ecological risk index (E_r^i and RI) and summarized in Table 7. E_r^i values for Cd in almost all the samples indicated very high ecological risk (666 to 16,800), except for S2, which was classified as considerable ecological risk (600); for As, the values E_r^i were classified as moderate ecological risk in samples S4, S5 and S7 (44.38 to 53.1) to appreciable ecological risk in samples S2 and S3 (81.88 to 101.67). For Cr, all the values of E_r^i in the studied sediments were assessed with low ecological risk.

The E_r^i values for Pb showed low ecological risk in samples S1, S2 and S6, and moderate ecological risk in samples S3, S4, S5 and S7. In the case of Cu, the values in almost all the samples showed a low ecological risk, but S4 showed a moderate ecological risk. The values of RI in all the studied sites were above 600 (RI > 600), which indicated very high ecological risk for the studied area. In summary, the E_r^i and RI indices for the studied elements in the surface sediment at all sites showed that San Juan, Cacalotenango and Taxco river pose considerable to high potential ecological risk with major contribution of As and Cd (Table 7 and Figure 7).

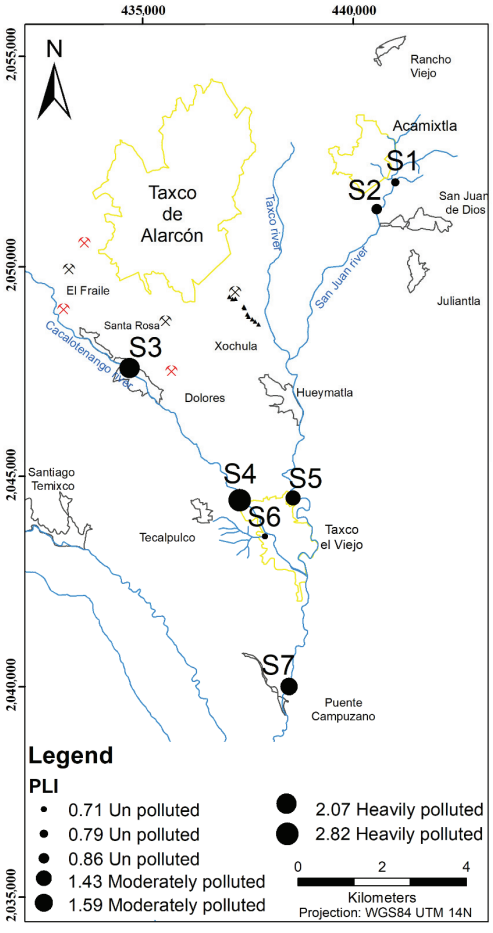

Figure 6. Spatial distribution of the pollution load index (PLI) in fluvial sediments of the San Juan-Taxco River system.

Table 7. Potential ecological risk index in the San Juan-Taxco River system.

Sites	E_r^i					RI	Risk Grade
	As	Cd	Cr	Cu	Pb		
S1		700	0.109	37.32	10.47	747.9	very high
S2	81.88	600	0.054	12.2	27.71	721.83	very high
S3	101.67	5400		14	77.94	5593.61	very high
S4	53.13	16,800	0.12	70.18	71.76	16,995.19	very high
S5	51.46	1833.3		7.46	47.06	1939.31	very high
S6		666.7	0.204	20.89	4.09	691.85	very high
S7	44.38	3133.3		9.98	55.59	3243.28	very high
Mean	66.504	4161.9	0.12175	24.576	42.0886	4276.1386	
Max	101.67	16,800	0.204	70.18	77.94	16,995.19	
Min	44.38	600	0.054	7.46	4.09	691.85	

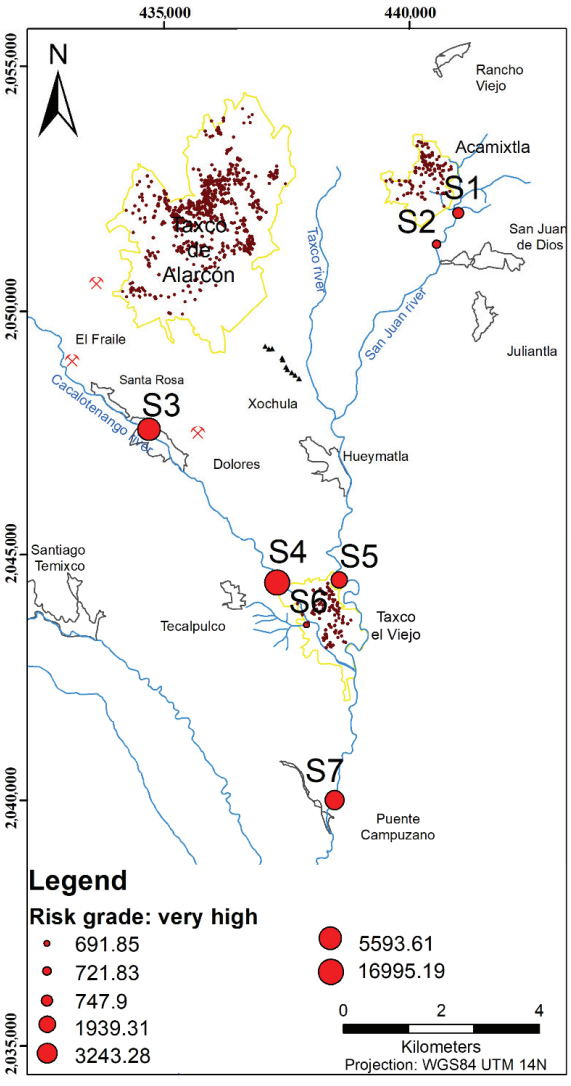

Figure 7. Spatial distribution of the potential ecological risk index in the San Juan-Taxco River system.

Summarizing, the degree of pollution from PTE decreased in the following sequence Cd > Zn > Pb > As > Cu > Mn > Ba > Ni. It is worth noting that the investigations carried out revealed a considerable loading of the surface sediment with Cd. Consequently, Cd, Zn and Pb may originate from mining, jewelry wastes and agricultural sources, such as pesticides and chemical fertilizers (phosphate fertilizer). The indices exhibited very high pollution in S4 and S3, and considerable contamination in S7 and S5. The results revealed the degree of PTE pollution with PLI in the study area is moderately contaminated and RI values demonstrated very high ecological risk for the five metals assessed (As, Cd, Cr, Cu and Pb).

The concentrations of PTEs in the San Juan-Taxco River system were compared with other major polluted rivers in Mexico and worldwide and summarized in the Table 8. The comparison of the PTEs concentrations with other Mexican rivers showed that this system presents higher concentrations of As, Cd, Ni, Fe, Cu and Zn than those reported in the

Atoyac river; Cd, Cu and Zn higher than those reported in the Panuco River and exceeds the concentrations of As, Fe, Cu, Ni and Zn measured in the Coatzacoalcos River [4,48,49].

Table 8. Comparison of PTE concentrations with other riverine environments worldwide.

PTE	As	Ba	Cd	Cr	Cu	Ni	Pb	Zn	Fe
	(mg kg^{-1})								
Present study	17.1–48.8		1.8–50.4	2.5–17.1	4.3–502	15.4–111	2.5–13.9	45.09–142	15,366–23,223
Yangtze River [50]	9.1		0.19	79.1	24.7	31.9	23.8	82.9	-
Yellow River [51]	-		0.1–0.3	61.3–139.5	14.1–30.3	19.3–34.6	15.5–24.6	39.9–74.6	-
Tinto River [52]	1130		2.75	56	805	17	2230	901	11,500
Tigris River [53]			7.9	-	2860		66	1061	-
Ganga River [54]	-		1.7	69.9	29.8	372	26.7	67.8	31,988.60
Euphrates River [55]	-		1.9	58.9	18.9	67.1	22.6	48	2249.50
Zarrin-Gol River [7]	21.91		-	37.67	-	12.39	-	32.68	13,751

4.3.5. Comparison of PTE Concentrations with Other Riverine Environments Worldwide

The worldwide comparison showed higher concentrations, the comparison with Zarrin-Gol River in Iran in As, Ni, Zn and Fe, and the sediment concentrations of Cd, Cu, Ni, Pb and Zn in the present study exceed those reported in the Yantze, Yellow, Ganga and Euphrates Rivers [7,48,55]. The concentration of Fe was found to be higher than the values in the Tinto River and Euphrates River (Table 8). The Fe abundance in sediments has been attributed to weathering, erosion and other natural sources, as well as large-scale human activities (mining release, municipal solid waste and agricultural activities).

Cadmium values are considerably high, compared to the other rivers of Mexico and the world; the results showed concentrations in all study sites to be above the background values, and these vales are associated with wastes from mining and urban and agricultural runoff. The concentration of Pb in this study was found to be lower than the concentration reported in the Atoyac, Panuco, Coatzacoalcos, Yangtze, Yellow, Tinto, Ganga and Euphrates Rivers [7,48–55]. This metal is mainly associated with Fe oxide fraction and shows high retention in sediments. Pb and Zn concentrations is attributed that tailings are being washed down by the action of rain towards the riverbed. Zn is one of the most abundant elements in the sediment of the San Juan-Taxco River system (Table 8). Those values are higher than the values reported in the Atoyac, Panuco, Coatzacoalcos, Yangtze, Yellow, Ganga, Euphrates and Zarrin Rivers [7,48–55].

The results of PTE pollution in surface sediments of the San Juan-Taxco River system indicated that the contamination is relatively high. Several authors have documented the contamination until the closure of the mines and after the abandonment of the mining tailings [14,15,56,57]; the closure of the mines brought with it an increase in formal and informal crafts and jewelry workshops not only made of silver, but also of other alloys, such as alpakar, brass and tumbaga. The results indicate that the concentrations previously reported in the sediments do not coincide in order of abundance or in the same elements; in this work, the toxic elements present in order of abundance are Cd > Zn > Pb > Cu > As and before they were Pb > As > Zn > Fe [17,56].

The manufacturing process of handicrafts and handmade jewelry include refining and alloying with other metals, such as Cd, Zn and Cu, the smelting process, framing the metals, soldering, platinating, polishing or etching the piece. Each task is generally accomplished by the use of some substances and actives of PTEs, such as Cd, Zn and Ni; traditionally, Cd and Zn have been used in jewelry solders or galvanized [20]. The rivers in the mining region of Taxco constantly receive trace amount of PTEs from weathering of rocks. Continuous or intermittent but relatively higher input of heavy metals to rivers and streams is linked to anthropogenic sources [56].

The release of PTE may change between different points depending on the local concentrations and physicochemical conditions and the sources. The contributions of these elements can be from the piles of mining tailings dust, the discharges of the municipal network and water contributions from the jewelry and handicraft workshops, the dust

produced by the metal processing of these workshops and pollution from regular municipal discharges. These toxic elements may be mobilized by rain and air towards the riverbed.

5. Conclusions

PTEs in water resources is a severe threat due to their toxic nature and tendency to bio-accumulate and amplify in higher trophic levels, altering the ecological functions of the river and soil, poisoning the aquatic environment and putting at risk the populations dependent on the river system. This study determined the concentrations of nine PTEs in water samples; the concentrations in water (river water and groundwater) in almost all of the samples were below the standards of the WHO. The concentrations of Mn, As, Al and Pb in water posed health risks based on the CDI, HQ and HI method and USEPA criteria (2005). The human health risk assessment indicated that the water of San Juan-Taxco River system is not recommended for human consumption, domestic activities and prolonged ingestion.

The San Juan-Taxco River system has a potential health risk in both population groups for the two pathways. Non-healthy risk was determined in groundwater; the risk to human health in the river water can be attributed to the dissolution of minerals, trace metals from direct sewage discharge, agricultural runoff, tailings dams and increasing concentration due to bioaccumulation downstream. Therefore, it can be established that the population living in the riverine landscape and using untreated surface water for drinking are vulnerable to the health risk from TPE pollution. Proper monitoring in the area should be implemented to control the pollution and to identify alternative sources of drinking water. It is recommended to implement a proper treatment and management policies of water to reduce the health risk.

Anthropogenic sources have contributed significantly to PTE concentrations in the study area, while natural sources have contributed only small amounts. Cd, Zn and Pb may originate from mining and jewelry wastes, wastewater and agricultural sources, such as pesticides and chemical fertilizers. The analyses also indicate that the main processes that control the pollution are mining tailings erosion with discharge processes and proportional dilution related to grain-size distribution processes (this is a high-energy stream with dominance of sand size particles). Thus, PTE concentrations tend to accumulate in banks and in backwaters with fine sediments with reduced flow rate and flow velocity.

PTE concentration in water and sediments pose a severe threat to the human population due to erratic disposal and rapid discharge of PTE in the river environment by mining tails, numerous jewelry workshops and human settlements in this riverine landscape.

This study provides the environmental knowledge in identifying the contaminants in the sedimentological substrate and locates the sites in need of immediate assistance. In addition, it is necessary to identify the number of handicrafts and jewelry workshops and to know the amount of PTE waste that is generated.

It is also very important to establish the PTE waste concentration in water and the environment to establish regulation, conservation and treatment measures. The information generated from the present study would serve to establish public policies for an effective management of this fluvial system in Mexico. Moreover, sensitization and awareness of the health risk of the consumption of water sources affected with PTE should be carried out intensively.

To reinforce the results of this study, it is recommended to increase the number of samples in those critical areas. Future research should include the risk analysis of the entire population. An isotopic analysis of strontium could provide a more detail source of contaminants.

Author Contributions: E.R.S.S.—sampling collection, data analysis, geochemical assessment and paper writing and editing; M.M.M.—Statistical analysis and paper writing and editing; J.M.E.M.—sampling collection, map editing and paper editing; M.V.E.A.—data analysis, geochemical assessment and paper writing; O.T.M.—laboratory analysis and paper editing. All authors have read and agreed to the published version of the manuscript.

Funding: This research received financial support from the Project Semilla of the Autonomous University of Guerrero (UAGro).

Acknowledgments: We thank the support of the Mexican Institute of Water Technology (IMTA) for the grain size analysis. We thank the Geochemistry and Soil physics laboratories of Autonomous University of Guerrero for the support of the field and laboratory analysis.

Conflicts of Interest: The authors have no conflict of interest to declare.

References

1. Liu, J.; Yin, P.; Chen, B.; Gao, F.; Song, H.; Li, M. Distribution and contamination assessment of heavy metals in surface sediments of the Luanhe River Estuary, northwest of the Bohai Sea. *Mar. Pollut. Bull.* **2016**, *109*, 633–639. [CrossRef] [PubMed]
2. Malvandi, H. Preliminary evaluation of heavy metal contamination in the Zarrin-Gol River sediments, Iran. *Mar. Pollut. Bull.* **2017**, *117*, 547–553. [CrossRef] [PubMed]
3. Rodriguez-Espinosa, P.; Shruti, V.; Jonathan, M.; Tavera, E.M. Metal concentrations and their potential ecological risks in fluvial sediments of Atoyac River basin, Central Mexico: Volcanic and anthropogenic influences. *Ecotoxicol. Environ. Saf.* **2018**, *148*, 1020–1033. [CrossRef]
4. Morales-García, S.; Rodríguez-Espinosa, P.; Shruti, V.; Jonathan, M.; Martínez-Tavera, E. Metal concentrations in aquatic environments of Puebla River basin, Mexico: Natural and industrial influences. *Environ. Sci. Pollut. Res.* **2016**, *24*, 2589–2604. [CrossRef]
5. Singh, U.K.; Kumar, B. Pathways of heavy metals contamination and associated human health risk in Ajay River basin, India. *Chemosphere* **2017**, *174*, 183–199. [CrossRef]
6. Loredo-Portales, R.; Bustamante-Arce, J.; González-Villa, H.N.; Moreno-Rodríguez, V.; Del Rio-Salas, R.; Molina-Freaner, F.; González-Méndez, B.; Archundia-Peralta, D. Mobility and accessibility of Zn, Pb, and As in abandoned mine tailings of northwestern Mexico. *Environ. Sci. Pollut. Res.* **2020**, *27*, 26605–26620. [CrossRef]
7. Hidayati, N.V.; Asia, L.; Khabouchi, I.; Torre, F.; Widowati, I.; Sabdono, A.; Doumenq, P.; Syakti, A.D. Ecological risk assessment of persistent organic pollutants (POPs) in surface sediments from aquaculture system. *Chemosphere* **2020**, *263*, 128372. [CrossRef]
8. Wang, X.; Cui, L.; Li, J.; Zhang, C.; Gao, X.; Fan, B.; Liu, Z. Water quality criteria for the protection of human health of 15 toxic metals and their human risk in surface water, China. *Environ. Pollut.* **2021**, *276*, 116628. [CrossRef]
9. Wang, X.; Fan, B.; Fan, M.; Belanger, S.; Li, J.; Chen, J.; Gao, X.; Liu, Z. Development and use of interspecies correlation estimation models in China for potential application in water quality criteria. *Chemosphere* **2020**, *240*, 124848. [CrossRef]
10. Łuczyńska, J.; Paszczyk, B.; Łuczyński, M.J. Fish as a bioindicator of heavy metals pollution in aquatic ecosystem of Pluszne Lake, Poland, and risk assessment for consumer's health. *Ecotoxicol. Environ. Saf.* **2018**, *153*, 60–67. [CrossRef]
11. Prasad, S.; Saluja, R.; Joshi, V.; Garg, J.K. Heavy metal pollution in surface water of the Upper Ganga River, India: Human health risk assessment. *Environ. Monit. Assess.* **2020**, *192*, 742. [CrossRef] [PubMed]
12. Siddiqui, E.; Pandey, J. Assessment of heavy metal pollution in water and surface sediment and evaluation of ecological risks associated with sediment contamination in the Ganga River: A basin-scale study. *Environ. Sci. Pollut. Res.* **2019**, *26*, 10926–10940. [CrossRef] [PubMed]
13. Corami, F.; Morabito, E.; Gambaro, A.; Cescon, P.; Libralato, G.; Picone, M.; Ghirardini, A.V.; Barbante, C. Geospeciation, toxicological evaluation, and hazard assessment of trace elements in superficial and deep sediments. *Environ. Sci. Pollut. Res. Int.* **2020**, *27*, 15565–15583. [CrossRef] [PubMed]
14. Dótor, A.A.; Armienta, M.A.; Arcega, F.; Talavera, M.O. Procesos de transporte de arsénico y metales en aguas superficiales del distrito minero de Taxco, Mexico: Aplicación de isótopos estables (Transport processes of arsenic and metals in surface waters in the mining district of Taxco, Mexico). *Hidrobiológica* **2014**, *24*, 256.
15. Dótor, A.; Armienta, H.M.; Talavera, M.O.; Ruiz, J. Geochemical behavior of Cu and sulfur isotopes in the tropical mining region of Taxco, Guerrero (southern Mexico). *Chem. Geol.* **2017**, *471*, 1–12. [CrossRef]
16. Talavera, M.O.; Ruiz, J.; Díaz, V.E.; Ramírez, G.A.; Cortés, A.; Salgado SS, A.; Rivera, B.R. Water-rock-tailings interactions and sources of sulfur and metals in the subtropical mining region of Taxco, Guerrero (Southern Mexico): A multi-isotopic approach. *Appl. Geochem.* **2016**, *66*, 73–81. [CrossRef]
17. Árcega–Cabrera, F.; Armienta, M.A.; Daesslé, L.W.; Castillo-Blum, S.E.; Talavera, O.; Dótor, A. Variations of Pb in a mine-impacted tropical river, Taxco, Mexico: Use of geochemical, isotopic and statistical tools. *Appl. Geochem.* **2009**, *24*, 162–171. [CrossRef]
18. Vázquez, B.A.; Talavera, M.O.; Moreno, G.M.; Salgado, S.S.; Ruiz, J.; Huerta, B.G. Source apportionment of lead in the blood of women of reproductive age living near tailings in Taxco, Guerrero, Mexico: An isotopic study. *Sci. Total Environ.* **2017**, *583*, 104–114. [CrossRef]
19. INEGI. *Censo y Conteos de Población y Vivienda of Guerrero*; INEGI: Mexico City, Mexico, 2020.
20. Clausell, A.M. *Historia de la Plata Mexicana*; AAPAUNAM Academia, Ciencia y Cultura: Mexico City, Mexico, 2010; Volume II, pp. 24–34. Available online: https://medigraphic.com/pdfs/aapaunam/pa-2010/pa101f.pdf (accessed on 7 June 2021).
21. INEGI. *La Minería en México*; Serie estadísticas sectoriales No. 24; INEGI: Mexico City, Mexico, 2010.
22. Ramírez, M. *Acuerdos Comunitarios Para la Realización del Programa de Saneamiento de las Aguas Residuales de la Microcuenca del Río San Juan Taxco*; Pueblo Sa-bio AC: San Juan de Dios, Guerrero, Mexico, 2013.

23. Romero, F.M.; Armienta, M.A.; González-Hernández, G. Solid-phase control on the mobility of potentially toxic elements in an abandoned lead/zinc mine tailings impoundment, Taxco, Mexico. *App. Geochem.* **2007**, *22*, 109–127. [CrossRef]
24. CONAGUA. Actualización de la Disponibilidad Media Anual de Agua en el Acuífero de Iguala Estado de Guerrero. México: Comisión Nacional del Agua. *DOF, 20 de abril de 2015.* Available online: https://www.gob.mx/cms/uploads/attachment/file/103668/DR_1205.pdf (accessed on 23 December 2021).
25. Tessier, A.; Campbell, P.G.C.; Bisson, M. Sequential Extraction Procedure for the Speciation of Particulate Trace Metals. *Anal. Chem.* **1979**, *51*, 844–851. [CrossRef]
26. *ASTM D2487-06*; Standard Practice for Classification of Soils for Engineering Purposes (Unified Soil Classification System); ASTM International: West Conshohocken, PA, USA, 2006.
27. USEPA. *Guidelines for Carcinogen Risk Assessment*; EPA/630/P-03/001F; Risk Assessment Forum: Washington, DC, USA, 2005.
28. USEPA. *Exposure Factors Handbook*; EPA/600/R-09/052F; National Center for Environmental Assessment: Washington, DC, USA, 2011. Available online: http://www.epa.gov/ncea/efh (accessed on 15 October 2021).
29. WHO. *Guidelines for Drinking-Water Quality*, 3rd ed.; Incorporating 1st and 2nd Addenda; WHO: Geneva, Switzerland, 2008; Volume 1.
30. Canadian Council of Ministers of the Environment CCME. *Canadian Environmental Quality Guidelines*; CCME: Winnipeg, MB, Canada, 1999.
31. Environmental Protection Agency. 2015. Available online: https://www.epa.gov/sites/production/files/2015-09/documents/r3_btag_fw_sediment_benchmarks_8-06.pdf (accessed on 4 September 2021).
32. Macdonald, D.D.; Ingersoll, C.G.; Berger, T.A. Development and evaluation of Consensus-Based Sediment Quality Guidelines for freshwater ecosystems. *Arch. Environ. Contam. Toxicol* **2000**, *39*, 20–31. [CrossRef] [PubMed]
33. Müller, G. Index of geoaccumulation in sediments of the Rhine River. *Geo. J.* **1969**, *2*, 108–118.
34. Varol, M. Assessment of heavymetal contamination in sediments of the Tigris River (Turkey) using pollution indices and multivariate statistical techniques. *J. Hazard. Mater.* **2011**, *195*, 355–364. [CrossRef] [PubMed]
35. Rudnick, R.L.; Gao, S. Composition of the Continental Crust. *Treatise Geochem.* **2014**, *3*, 1–64. [CrossRef]
36. Barats, A.; Renac, C.; Orani, A.M.; Durrieu, G.; Saint Martin, H.; Esteller, A.M.; Garrido, H.S. Tracing source and mobility of arsenic and trace elements in a hydrosystem impacted by past mining activities (Morelos state, Mexico). *Sci. Total Environ.* **2019**, *712*, 135565. [CrossRef]
37. Sakan, S.M.; Đorđević, D.S.; Manojlović, D.D.; Predrag, P.S. Assessment of heavy metal pollutants accumulation in the Tisza river sediments. *J. Environ. Manag.* **2009**, *90*, 3382–3390. [CrossRef]
38. Al Rashdi, S.; Arabi, A.A.; Howari, F.M.; Siad, A. Distribution of heavy metals in the coastal area of Abu Dhabi in the United Arab Emirates. *Mar. Pollut. Bull.* **2015**, *97*, 494–498. [CrossRef]
39. Hakanson, L. An ecological risk assessment index for aquatic contamination control, a sedimentological approach. *Water Res.* **1980**, *14*, 975–1001. [CrossRef]
40. Tomlinson, D.L.; Wilson, J.G.; Harris, C.R.; Jeffrey, D.W. Problems in the assessment of heavy-metal levels in estuaries and the formation of a pollution index. *Helgol. Meeresunters.* **1980**, *33*, 566–575. [CrossRef]
41. Hadzi, G.Y.; Essumang, D.K.; Ayoko, G.A. Assessment of contamination and health risk of heavy metals in selected water bodies around gold mining areas in Ghana. *Environ. Monit. Assess.* **2018**, *190*, 406. [CrossRef]
42. Bodrud-Doza, M.; Didar-Ul Islam, S.M.; Rume, T.; Quraishi, S.B.; Rahman, M.S.; Bhuiyan, M.A.H. Groundwater quality and human health risk assessment for safe and sustainable water supply of Dhaka City dwellers in Bangladesh Groundw. *Sustain. Dev.* **2020**, *10*, 100374. [CrossRef]
43. Armah, F.A.; Gyeabour, E.K. Health risks to children and adults residing in riverine environments where surficial sediments contain metals generated by active gold mining in Ghana. *Toxicol. Res.* **2013**, *29*, 69–79. [CrossRef] [PubMed]
44. Nkoom, M.; Jerry, S.C.; Michael, K. Assessment of endocrine disrupting trace metals in river Samre at Samreboi in the Wassa Amenfi West District of the western region of Ghana. *J. Water Resour. Prot.* **2013**, *5*, 983–992. [CrossRef]
45. Obasi, P.N.; Akudinobi, B.B. Potential health risk and levels of heavy metals in water resources of lead–zinc mining communities of Abakaliki, southeast Nigeria. *Appl. Water Sci.* **2020**, *10*, 184. [CrossRef]
46. Kim, S.; Lee, K.C.; Kim, J.E.; Jung, K.Y.; Ahn, J.M.; Kim, H.G.; Lee, I.J.; Shin, D.S.; Yang, D.S. Change in geochemical characteristics of surface sediments in the Nakdong river main stream. *J. Environ. Sci. Int.* **2017**, *26*, 311–324. [CrossRef]
47. Farmer, V.C. Sources and speciation of aluminium and silicon in natural waters. *Ciba Found. Symp.* **1986**, *121*, 4–23. [CrossRef]
48. Jonathan, M.P.; Roy, P.D.; Rodríguez-Espinosa, P.F.; Sarkar, S.K.; Muñoz-Sevilla, N.P.; Navarrete-López, M.; Srinivasalu, S.; Thangadurai, N. Evaluation of trace element concentration (acid leachable) in sediments from River Pánuco and its adjacent lagoon areas, NE México. *Environ. Earth Sci.* **2012**, *68*, 2239–2252. [CrossRef]
49. Ruiz-Fernández, A.C.; Sanchez-Cabeza, J.A.; Alonso-Hernández, C.; Martínez-Herrera, V.; Pérez-Bernal, L.H.; Preda, M.; Hillaire-Marcel, C.; Gastaud, J.; Quejido-Cabezas, A.J. Effects of land use change and sediment mobilization on coastal contamination (Coatzacoalcos River, Mexico). *Cont. Shelf Res.* **2012**, *37*, 57–65. [CrossRef]
50. Wang, H.T.; Wang, J.W.; Liu, R.M.; Yu, W.W.; Shen, Z.Y. Spatial variation, environmental risk and biological hazard assessment of heavy metals in surface sediments of the Yangtze River estuary. *Mar. Pollut. Bull.* **2015**, *93*, 250–258. [CrossRef]

51. Ma, X.L.; Zuo, H.; Tian, M.J.; Zhang, L.Y.; Meng, J.; Zhou, X.N.; Min, N.; Chang, X.Y.; Liu, Y. Assessment of heavy metals contamination in sediments from three adjacent regions of the of the Yellow River using metal chemical fractions and multivariate analysis techniques. *Chemosphere* **2015**, *144*, 264–272. [CrossRef]
52. García, J.; Aguado, J.; Morillo, I. Heavy metals in sediments from the Tinto River (Spain). *Mine Water Environ.* **2012**, *1*, 243–246.
53. Varol, M.; Sen, B. Assessment of nutrient and heavy metal contamination in surface water and sediments of the upper Tigris River, Turkey. *Catena* **2012**, *92*, 1–10. [CrossRef]
54. Pandey, J.; Singh, R. Heavy metals in sediments of Ganga River: Up- and downstream urban influences. *Appl. Water Sci.* **2017**, *7*, 669–1678. [CrossRef]
55. Salah, E.A.M.; Zaidan, T.A.; Al-Rawi, A.S. Assessment of heavy metals pollution in the sediments of Euphrates River, Iraq. *J. Water Res. Prot.* **2012**, *4*, 1009–1023. [CrossRef]
56. Armienta, M.A.; Talavera, O.; Villaseñor, G.; Espinosa, E.; Pérez-Martínez, I.; Cruz, O.; Ceniceros, N.; Aguayo, A. Environmental behaviour of metals from tailings in shallow rivers: Taxco, central Mexico. *Appl. Earth Sci.* **2004**, *113*, B76–B82. [CrossRef]
57. Talavera, M.O.; Moreno, T.R.; Dotor-Almazán, A.; Flores-Mundo, N.; Duarte Gutiérrez, C. Mineralogy and geochemistry of sulfide-bearing tailings from silver mines in the Taxco, Mexico Area to evaluate their potential environmental impact. *Geofís. Int.* **2005**, *44*, 49–64. [CrossRef]

water

MDPI

Article

Estimation of Methane Emissions from Reservoirs Based on Country-Specific Trophic State Assessment in Korea

Yongjoo Chung [1], Chunhyun Paik [2] and Young Jin Kim [3,*]

[1] Department of e-Business, Busan University of Foreign Studies, Busan 46234, Korea; chungyj@bufs.ac.kr
[2] Department of Industrial Convergence Systems Engineering, Dongeui University, Busan 47340, Korea; chpaik@deu.ac.kr
[3] Department of Systems Management and Engineering, Pukyong National University, Busan 48513, Korea
* Correspondence: youngk@pknu.ac.kr; Tel.: +82-51-629-6486

Abstract: It has been reported that significant quantities of greenhouse gases are emitted from wetlands, from which emissions and their contributions to global warming have received much less attentions. Thus, a refinement to the previous published guidelines has recently been made to provide an updated and sound scientific basis for the purpose of supporting the preparation of national inventories. This study is aimed at demonstrating the applicability of the refinement for estimating methane emissions from reservoirs in the Republic of Korea. It is desirable to take the direct measurement of total methane fluxes across the reservoir surface, which may require a substantial amount of research efforts though. Alternatively, methane emissions from individual reservoirs may be estimated with relevant parameters accounting for the regional environmental characteristics. The assessment of trophic state has been employed to better represent the emissions behavior of reservoirs, based on which the methane emissions from local reservoirs in Korea are estimated. It is noted that the country has developed its own water quality index with the consideration of environmental characteristics. The seasonal variations in methane emissions are tested for their statistical significance and it is proposed that the emission estimates can be predicted from the trophic state assessment with the application of regression analysis. Following the guidelines prescribed by the refinement and procedures outlined in this study, the results from emissions estimation and prediction can be effectively used for the improvement of national inventories.

Keywords: methane emissions from reservoirs; trophic state assessment; IPCC guideline; emissions estimation; climate change

Citation: Chung, Y.; Paik, C.; Kim, Y.J. Estimation of Methane Emissions from Reservoirs Based on Country-Specific Trophic State Assessment in Korea. *Water* **2022**, *14*, 562. https://doi.org/10.3390/w14040562

Academic Editors: Alban Kuriqi and Luis Garrote

Received: 13 January 2022
Accepted: 11 February 2022
Published: 12 February 2022

1. Introduction

The world's water reservoirs are annually emitting carbon dioxide (CO_2), methane (CH_4), and other greenhouse gases (GHGs) in significant quantities, depending on a variety of different characteristics such as age, land-use prior to flooding, climate, upstream catchment and management practices [1]. It is estimated that the GHG emissions from reservoirs are roughly equivalent to 1.07 gigatons of CO_2 [2], which surprisingly approach to 14% of the annual CO_2 emissions of 7.8 gigatons from fossil fuel combustion [3]. With the exception of CO_2, CH_4 is considered the most important greenhouse gas because its global warming potential is 34 times greater than that of CO_2, though its atmospheric concentration is approximately 200 times less. Especially, wetlands including reservoirs are the largest natural source of methane accounting for roughly one third of total natural and anthropogenic CH_4 emissions. It is argued that the global fossil fuel emissions would have to be reduced by as much as 20% more than previous estimates to achieve the Paris Agreement targets because of the natural GHG emissions from wetlands and permafrost, which is thus critical in the assessment of emission pathways to limit global warming [4]. However, CH_4 emissions from wetlands and their contribution to global warming potential

were poorly assessed before mainly due to the paucity of available data [5–7]. Most attempts are centered on upscaling the GHG emission rates from individual waterbodies to the regional or global estimates and simply multiplying an average emission rate by the total waterbody surface area in the region of interest [8–11]. It is pointed out in [12] that this upscaling approach can be highly biased unless the emission rate measurements come from a representative sample of lakes or reservoirs in the region of interest.

Providing an updated and sound scientific basis to support the preparation and continuous improvement of national inventories, the 2019 Refinement to the 2006 IPCC Guidelines for National Greenhouse Gas Inventories [3] (hereafter referred to as '2019 Refinement') has been adopted to embrace recent scientific advances and technological developments. Scientists recognized the importance of including reservoir emissions in the nation's GHG inventory to better understand their climate impacts, and thus a significant refinement has been made to the estimation of GHG emissions from wetlands, especially from flooded lands, which is described in Chapter 7.3 of Volume 4. An exhaustive collection of related research efforts is well reviewed and presented in [3] emphasizing the urgency of accounting methane emissions from wetlands from the perspective of reporting inventories. The refinement for estimating CO_2 and CH_4 emissions from reservoirs provides the average emission factors for six major climate zones; boreal, cool temperate, warm temperate/dry, warm temperate/moist, tropical dry/montane, and tropical moist/wet. The emission factors for each climate zone are derived from an extensive literature survey and they are multiplied by the total area of water surface to estimate the emissions from reservoirs. Even though the region may be classified as the aggregated climate zone of 'Cool Temperate', it may exhibit different climatic characteristics from season to season due to the noticeable seasonal variations in temperature and precipitation. In addition, the emissions estimation can be adjusted based upon the assessment of trophic state of reservoirs. Even though feasible to obtain the region-specific estimates of emissions from reservoirs by assessing the tropic status of individual reservoirs, there hardly exists such an attempt to adopt the 2019 Refinement for estimating the GHG emissions from wetlands with the consideration of regional climatic characteristics. The objective of this study is to estimate the amount of methane emissions from reservoirs as per the procedure outlined in the 2019 Refinement. Further, it is also proposed to predict the methane emissions based on the country-specific trophic state assessment by employing the statistical regression analysis. For the purpose of this study, selected are six reservoirs in the Republic of Korea, which is recognized as the 9th largest emitter of GHG emissions with more than 700 million tons of carbon emissions in 2019 [13]. It was reported that the methane emissions from wetlands are merely 0.283 million tons equivalent to about 1% of the total methane emissions, which may seem negligible. However, the refinement has not yet been adopted to obtain the emissions estimation in the report and it is extremely probable that the refinement yields a much greater amount of total emissions from wetlands. To the best of authors' knowledge, this study is the first attempt, at least for Korea, to apply the refinement for estimating the methane emissions from individual reservoirs. The defining aspect of this study is that the estimation of methane emissions has been carried out based on the region- or country-specific trophic state assessment method to better account for regional climatic characteristics and the trophic state assessment may also be used to predict the emissions from different reservoirs. The remainder of this manuscript is organized as follows: First, the methodology prescribed in the 2019 Refinement is briefly summarized and the index for country-specific trophic state assessment is introduced in the next section. Section 3 describes the results from the assessment of trophic state of individual reservoirs and their emissions estimation. It is also discussed that the results may be used to predict the methane emissions from reservoirs based on the trophic state assessment. The conclusions will follow in the last section.

2. Methods

2.1. Methodology Based on IPCC Guidelines

The carbon emissions from wetlands are traced from three different source categories: managed peatlands, flooded land, and inland wetland mineral soils. No refinements have been made to the categories of managed peatlands and inland wetland mineral soils. Major developments with regard to the emissions from flooded lands are included in the refinement and described in a greater detail based on the collation of extensive literature survey. The usage of guidelines for the emissions estimation is contingent upon the types of flooded lands; land converted to flooded land, flooded land remaining flooded land, and other constructed water body. All the reservoirs under investigation here can be classified as the type of flooded land remaining flooded land since all of them are more than 20 years old. It is advocated that only methane emissions are estimated in this category to avoid the double counting of CO_2 emissions [3]. Annual total emissions estimation from flooded land remaining flooded land may be obtained by the following as given in [3]: First, the annual emissions from reservoir surface, denoted by $F_{CH_4 res}$, are estimated by

$$F_{CH_4 res} = \sum_{j=1}^{j} \sum_{i=1}^{nres_j} \alpha_i \left(EF_{CH_4 age>20,j} \cdot A_{totj,i} \right) \quad (1)$$

where i and $nres_j$ are the index for individual reservoirs and the number of reservoirs more than 20 years old in climate zone j, respectively. The total area of water surface in hectare is denoted by $A_{totj,i}$ and the CH_4 emission factor from reservoirs more than 20 years old located in climate zone j by $EF_{CH_4 age>20,j}$ measured in kg CH_4/year. The emission factors may be adjusted by α_i, if appropriate, depending upon the trophic state of individual reservoirs. In addition, $F_{CH_4 downstream}$ denotes the annual emissions from CH_4 originating from reservoirs but emitted downstream of corresponding reservoirs, which can be estimated by multiplying the emissions from water surface of individual reservoirs by the ratio R_d of total downstream methane emission to the total flux of methane from the reservoir surface as follows:

$$F_{CH_4 downstream} = \sum_{j=1}^{j} \sum_{i=1}^{nres_j} \alpha_i \left(EF_{CH_4 age>20,j} \cdot A_{totj,i} \right) \cdot R_{d,i} \quad (2)$$

The total annual emissions of CH_4 from all reservoirs under study, denoted by $F_{CH_4 tot}$, is simply the sum of emissions from water surface and downstream, that is,

$$F_{CH_4 tot} = F_{CH_4 res} + F_{CH_4 downstream} \quad (3)$$

If sufficient data are lacking, the default values for parameters, such as R_d and α_i, may be used in a blanket manner even though acknowledged in [3] that it is *good practice* to develop the country-specific emission factors to reduce overall uncertainty. The procedure outlined in [3] is certainly useful to estimate the methane emissions from wetlands, but a certain degree of ambiguity is inevitable without a sufficient amount of data especially related to trophic states. This study uses the default value of 0.09 with the 95% confidence interval (0.05, 0.22) for R_d as recommended in [3] due to the lack of relevant data. On the other hand, the adjustment factor α_i is derived from the seasonal trophic state assessment of individual reservoirs as outlined in the below. It is most desirable to employ the Tier 3 approach by taking the direct measurement of CH_4 diffusion and ebullition fluxes across the reservoir surface or applying Greenhouse Gas Reservoir Tool (G-Res) model [14]. However, it may require a great deal of efforts and resources to capture both the spatial and temporal variability of emissions from a reservoir. As an alternative, the methane emissions from individual reservoirs may be estimated with the relevant parameters adjusted for trophic status and water withdrawal depths of reservoirs. For example, different values of the emission factor adjustment α_i are recommended in [3] depending upon trophic index (TI),

surface concentration of chlorophyll-a (Chl-a), total phosphorus (TP), total nitrogen (TN), Secchi depth (SD), and trophic class. The emission factor adjustment of 10.0 is to be used for a eutrophic reservoir in lieu of its default value of 1.0. It is also noted that the emissions estimation needs to take environmental circumstances as well as properties of individual reservoirs into account. The methane emission factors are highly variable in different climate zones, and it is reasonable to apply different emission factors from season to season where the average temperature and precipitation are greatly fluctuating across the year. The Republic of Korea has four distinct seasons and a significant variation in seasonal weather may be observed. For example, one of the reservoirs investigated here is located near the city of Boryeong where the annual average temperature is 12.7 degrees Celsius and the difference in monthly average temperature between hottest and coldest months is 25.9 degrees Celsius. Further, the annual rainfall total is 1191.4 mm and the precipitation is mainly concentrated in summer with the average rainfall of 652.4 mm. Six reservoirs in the central region of Korea are investigated to demonstrate the applicability of the methodology described above for estimating the methane emissions with the consideration of seasonal climatic characteristics and the trophic state of individual reservoirs.

2.2. Country-Specific Trophic State Assessment

There are about 18,000 reservoirs and dams of various sizes in the Republic of Korea and most of them are more than 20 years old [15]. The country is relatively small in terms of the land area and ranked 109th in the world with the land area of 97,230 km^2. River Act of Korea designates five major river systems as National Rivers, along which a significant number of reservoirs and lakes are located. It is noted that the spatial variations in climatic characteristics are slightly noticeable, if any, compared to the seasonal variations mainly due to the small land area of Korea, and this study rather focuses on the temporal variations in methane emissions. Located in the central region of Korea, the third longest river system from the central region of Korea, called Geumgang, is selected for analysis in this study. From the perspective of data availability and readiness for the country-specific trophic state assessment, six reservoirs of different sizes, from the surface area of 59 to 7419 hectare, along the Geumgang river system are taken as shown in Table 1.

Table 1. Information of Six Reservoirs.

Name (Abbreviation)	Basin Area (ha)	Surface Area (ha)	Water Storage Capacity (10^3 m^3)	Main Use
Bunam (BN)	15,720	3560	21,100	Agriculture
Boryeong (BR)	16,360	217	116,900	Water Supply
Daeho (DH)	31,215	7419	112,000	Agriculture
Sapgyo (SG)	163,950	2017	84,082	Agriculture
Seokmun (SM)	1750	59	975	Agriculture
Tapjeong (TJ)	21,880	636	31,927	Agriculture

As mentioned earlier, the assessment of trophic states is crucial to better estimate the emissions from reservoirs by adjusting the emission factors. Carlson [16] proposed the use of a trophic state index (TSI) based on the measurement of SD, TP, and Chl-a from reservoirs, which is widely adopted for water quality assessment in the literature. On the other hand, it is argued in [17] that the trophic state assessment should be carried out in such a way to better represent environmental characteristics of the region of interest and the trophic state index suitable for Japanese river systems is proposed by modifying Carlson's index. Considering regional environmental characteristics of Korea, NIER [18]

also developed the water quality assessment method and proposed the trophic state index named 'Korean Trophic State Index' (TSI_{KR}), which is basically based on the measurement of chemical oxygen demand (COD), TP, and Chl-a from individual reservoirs [19–23]. It is pointed out in [20,23] that the Korean index adopts the measurement of COD in place of SD used in the Carlson's and Japanese indices with the consideration of Korean river systems characterized by relatively short detention times and a higher intake of organic matters. The index TSI_{KR} separately evaluates the water quality of reservoirs in terms of COD, TP, and Chl-a as shown in Equations (4)–(6), respectively.

$$TSI_{KR\_COD} = 5.8 + 64.4 \log(\text{COD } mg/L) \quad (4)$$

$$TSI_{KR\_TP} = 114.6 + 43.3 \log(\text{TP } mg/L) \quad (5)$$

$$TSI_{KR\_Chl\text{-}a} = 12.2 + 38.6 \log\left(\text{Chl-a } mg/m^3\right) \quad (6)$$

where TSI_{KR_COD}, TSI_{KR_TP}, and $TSI_{KR\_Chl\text{-}a}$ denote the trophic state indices assessed from the measurements of COD, TP, and Chl-a, respectively. Then, the overall TSI_{KR} is derived by taking the weighted average of three sub-indices in the above. The weights of 0.5, 0.25, and 0.25 are assigned to TSI_{KR_COD}, TSI_{KR_TP}, and $TSI_{KR\_Chl\text{-}a}$, respectively, as follows:

$$TSI_{KR} = 0.5(TSI_{KR\_COD}) + 0.25(TSI_{KO\_TP}) + 0.25(TSI_{KR\_Chl\text{-}a}) \quad (7)$$

It should be noted that the trophic state assessment is twice more influenced by TSI_{KR_COD} than the others considering the characteristics of regional reservoirs which are highly affected by allochthonous and autochthonous organic matters [20]. The trophic state of individual reservoirs is to be determined by the value of TSI_{KR} as shown in Table 2. The index has been adopted as the official index for trophic state assessment designated by the Ministry of Environment of Korea in Ministry Notice 2013-134 since 2013. The reasoning behind the development of TSI_{KR} is beyond the scope of this study, and interested readers are referred to [17] for more detailed discussions on TSI_{KR}.

Table 2. Classification of Trophic Class Based on the Value of TSI_{KR}.

Range of TSI_{KR}	Trophic Class	Range (Recommended Value) for Adjustment Factor α_i
0~30	Oligotrophic	0.7 (0.7)
30~50	Mesotrophic	0.7~5.3 (3.0)
50~70	Eutrophic	5.3~14.5 (10.0)
70~100+	Hypertrophic	14.5~39.4 (25.0)

3. Results and Discussion

3.1. Seasonal Trophic State Assessment of Reservoirs

Based on the water quality data on COD, TP, and Chl-a, the trophic state of each reservoir can then be assessed season by season to capture the seasonal variations. The seasonal assessment of trophic state for individual reservoirs has been performed by [18]. Collecting data on the water quality for almost 15 years, the seasonal averages of measurement data are used to determine the trophic state season by season. In addition, the emission factors need to be adjusted for the trophic state to estimate the methane emissions from individual reservoirs. For each trophic class, the range and recommended value for adjustment factor are provided as shown in Table 2 [3]. For example, the range of adjustment factor for mesotrophic state is from 0.7 to 5.3 and it is recommended to use 3.0 when sufficient data are not available. On the other hand, the range of TSI_{KR} value is from 30 to 50 for mesotrophic reservoirs, and it seems reasonable to use the interpolated

adjustment factor. Provided that $TSI_{KR} = 45$, the interpolated adjustment factor can then be calculated as

$$\alpha_i = 0.7 + \frac{(45 - 30)}{(50 - 30)} \times (5.3 - 0.7) = 4.15. \quad (8)$$

Table 3 presents the result of trophic state assessment along with the TSI_{KR} values, their standard errors, and corresponding adjustment factors. As observed from the standard errors of TSI_{KR} values, the trophic state indices do not fluctuate much throughout the data collection period. On the other hand, a relatively large seasonal variations of indices may be observed especially for such reservoirs as DH, SM, and TJ as shown in Figure 1. It is obvious that the trophic state index should be closely related to the adjustment factor, which is depicted in Figure 2. The Pearson's correlation coefficient between them corresponds to 0.98 indicating that there exists a strong positive correlation and the seasonal variations in trophic states are well reflected in the interpolated adjustment factors.

Table 3. Seasonal Assessment of Trophic State and Corresponding Adjustment Factor.

Reservoir	Season	TSI_{KR} Mean (Std. Error)		Trophic Class	Interpolated Adjustment Factor
BN	Spring	68.57	(2.63)	Eutrophic	13.84
	Summer	71.30	(2.91)	Hypertrophic	15.58
	Autumn	70.00	(1.90)	Eutrophic	14.50
	Winter	68.69	(2.14)	Eutrophic	13.90
BR	Spring	26.81	(1.30)	Oligotrophic	0.63
	Summer	31.92	(1.62)	Mesotrophic	1.14
	Autumn	30.68	(0.94)	Mesotrophic	0.86
	Winter	27.07	(0.71)	Oligotrophic	0.63
DH	Spring	50.81	(1.08)	Eutrophic	5.67
	Summer	59.80	(1.13)	Eutrophic	9.81
	Autumn	64.86	(2.80)	Eutrophic	12.14
	Winter	52.49	(1.40)	Eutrophic	6.45
SG	Spring	71.34	(2.01)	Hypertrophic	15.61
	Summer	72.31	(1.88)	Hypertrophic	16.42
	Autumn	70.93	(1.99)	Hypertrophic	15.27
	Winter	70.17	(1.72)	Hypertrophic	14.64
SM	Spring	62.34	(2.46)	Eutrophic	10.98
	Summer	73.74	(6.11)	Hypertrophic	17.60
	Autumn	67.86	(1.88)	Eutrophic	13.52
	Winter	55.60	(0.73)	Eutrophic	7.88
TJ	Spring	39.19	(2.63)	Mesotrophic	2.81
	Summer	50.59	(1.30)	Eutrophic	5.57
	Autumn	51.01	(1.91)	Eutrophic	5.76
	Winter	41.28	(2.06)	Mesotrophic	3.29

3.2. Estimation and Prediction of Methane Emissions from Reservoirs

Derived from the G-Res model, the unadjusted emission factors $EF_{CH_4 age>20,j}$ are provided for each climate zone in [3]. Most of the regions in the Republic of Korea are classified as 'Cool Temperate' zone except for southern and eastern coastal areas, and it is recommended to use the average emissions factor of 54.0 with the 95% confidence interval (48.3, 59.5). The refinement recommends using the default value of 0.09, unless otherwise specified, for the ratio of downstream emissions to the total flux of methane from reservoir surface [3]. Using Equations (1)–(3), the methane emissions from individual reservoirs under investigation can then be estimated with the parameters outlined above. For example, the methane emissions estimation from the reservoir BN over the spring season can be obtained with the following parameters: $EF_{CH_4 age>20,j}$ = 54.0 for the climate

zone of 'Cool Temperate', $A_{totj,i}$ = 3560 for the surface area, α_i = 13.84 for the adjustment factor, and R_d = 0.09 for the ratio of total downstream methane emission to the total flux of methane from the reservoir surface. The surface emissions of methane are 665,150 kg CH_4 and the downstream emissions are simply 59,863 kg CH_4 by adopting the default value 0.09 for R_d due to the lack of data availability, which sums up to 725,013 kg CH_4. Table 4 presents the seasonal methane emissions from individual reservoirs along with the annual per hectare emissions.

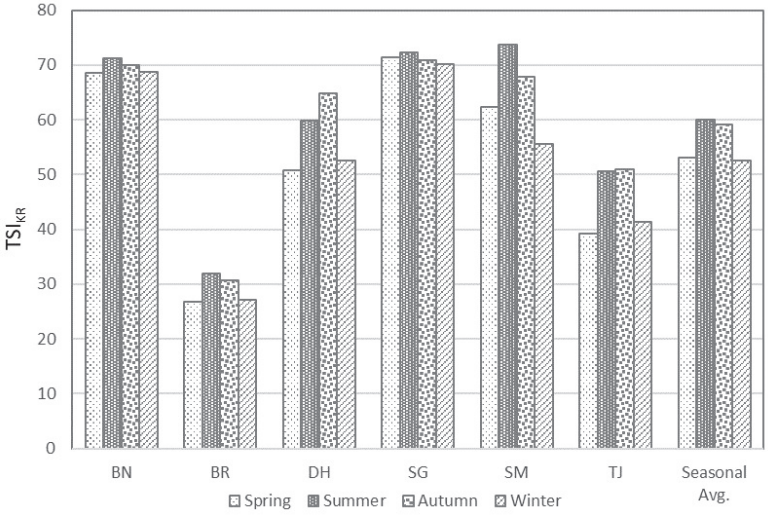

Figure 1. Seasonal Trophic State Assessment of Individual Reservoirs.

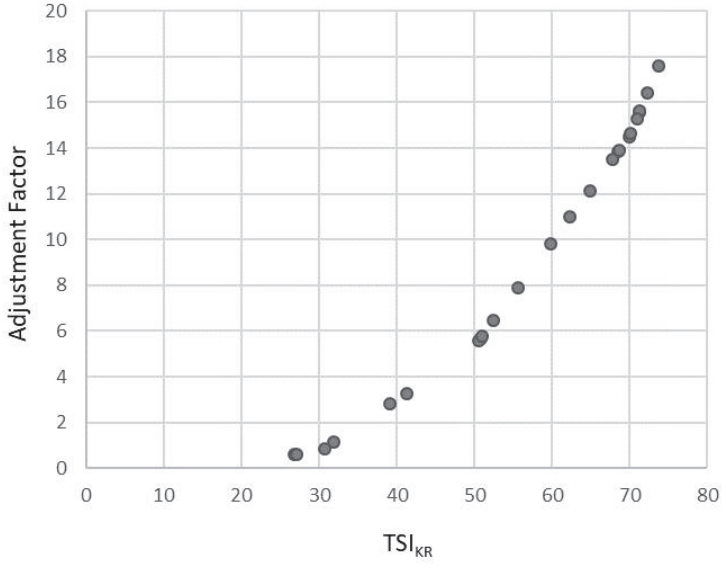

Figure 2. Relationship between Trophic State Index and Adjustment Factor.

Table 4. Estimates of Annual Methane Emissions from Reservoirs (10^3 kg CH_4).

Reservoir	Spring	Summer	Autumn	Winter	Total	Per Hectare
BN	725.0	816.2	759.6	728.2	3028.9	0.851
BR	2.0	3.6	2.7	2.0	10.4	0.048
DH	619.0	1071.0	1325.3	704.2	3719.4	0.501
SG	463.3	487.3	453.2	434.5	1838.4	0.911
SM	9.5	15.3	11.7	6.8	43.3	0.735
TJ	26.3	52.1	53.9	30.8	163.1	0.256

Note that the amount of per hectare methane emissions from the reservoir BR is significantly less than others, which may be contributed to the fact that the reservoir BR is mainly used for drinking water supply and the management of water quality is fairly rigorous. A relatively moderate variation is observed among the other reservoirs mainly used for agriculture. The reservoir SG exhibit the largest per hectare annual emissions of 911 kg CH_4. Rim and Shin [24] pointed out that the water quality of SG is deteriorated because of increased phytoplankton biomass with rich nutrient flowing from the upper stream of watershed. It is also confirmed that the reservoir SG exhibits consistently higher adjustment factors across the year. Since the emissions are affected proportionately to the surface area, the seasonal estimates of per hectare methane emissions from individual reservoirs are compared to reduce the scale differences, which is depicted in Figure 3. Noticeable differences in seasonal estimates can be observed for the reservoirs BR, DH, SM, and TJ whereas the methane emissions from BN and SG do not much differ season by season.

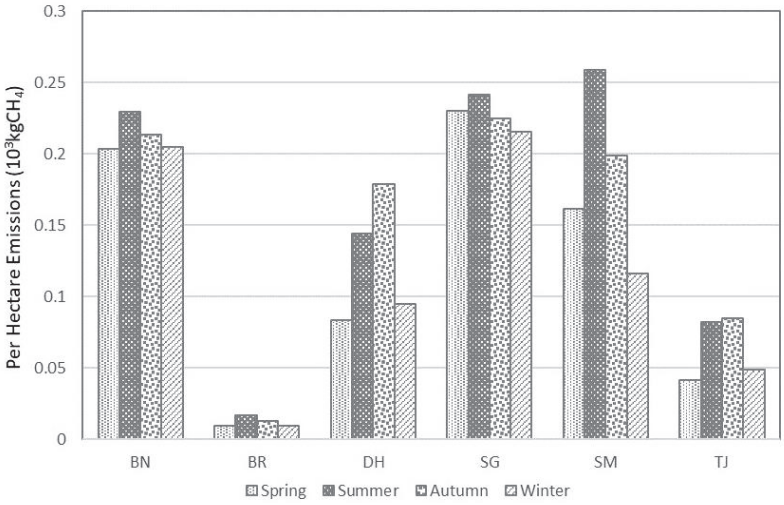

Figure 3. Comparison of Seasonal Estimates of Methane Emissions from Individual Reservoirs.

Statistical analysis can be useful to determine whether there exist statistically significant differences in methane emissions season by season. For the sake of demonstration, the confidence intervals (CIs) of seasonal emissions estimation from DH and SG are derived and depicted in Figure 4. As shown in Figure 4a, the largest amount of methane is emitted in Autumn with mean 1,325,331 kg CH_4 and 95% CI of (1,185,435, 1,460,318). The annual total emissions from DH sum up to 3,719,442 kg CH_4 and its 95% CI is (3,326,834, 4,098,274). It should be noted that the pairwise comparison of CIs reveals the existence of statistically significant differences in seasonal emissions with the significance level of 5%. To the contrary, all the 95% CIs of seasonal estimates of methane emissions from SG overlap with each other, as shown in Figure 4b, implying that the amount of methane emission

does not differ significantly from the statistical point of view with the significance level of 5%. While emissions from DH are fluctuating seasonally to a great extent, a relatively stable amount of methane emissions is observed across the year. It is concluded that the seasonal behavior of methane emissions is quite different from one reservoir to another and it is closely related to the seasonal trophic states of individual reservoirs.

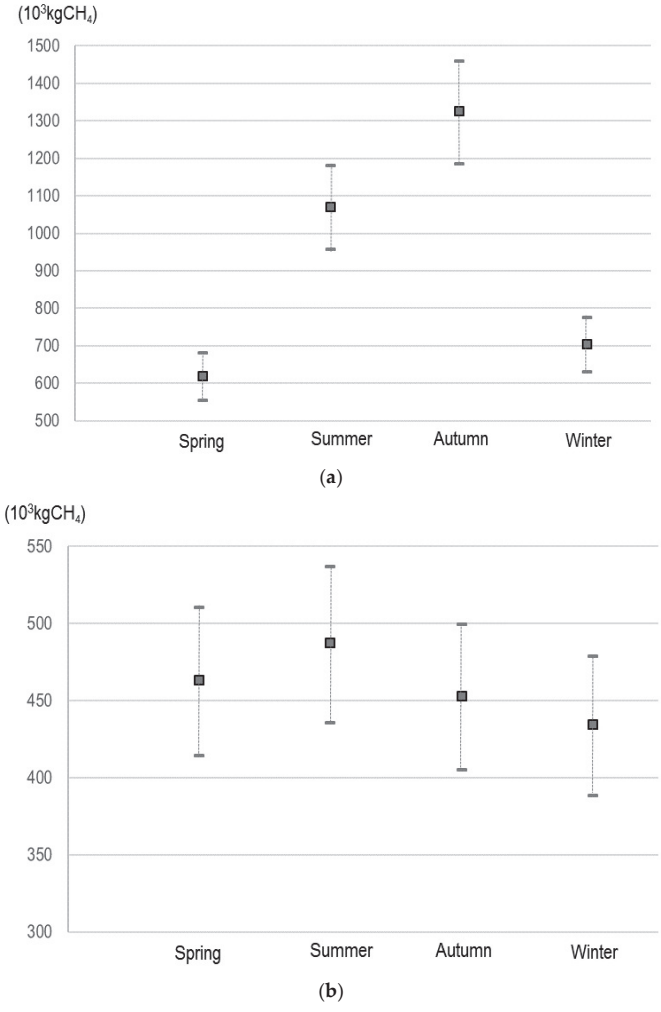

Figure 4. Mean and 95% CI of Methane Emissions by Season. (**a**) Reservoir DH. (**b**) Reservoir SG.

The procedure prescribed in [3] emphasizes the influence of trophic states on emissions estimation from wetland, which is further investigated by way of regression analysis. The estimates of seasonal methane emissions are regressed against surface area and the results from trophic state assessment. It is assumed that the surface area of reservoirs is constant over the years, which seems unreasonable but can be accounted for whenever sufficient data are provided. The omnibus analysis of variance (ANOVA) table and corresponding model coefficients are provided in Tables 5 and 6, respectively, all of which indicate the statistical significance of regression model. The coefficient of determination R^2 is 0.872 implying that 87.2% of variations in the emission estimates can be explained by the model. One of the advantages of regression model is that it can be used for the purpose of prediction.

The marginal means plot with respect to TSI_{KR} is constructed for a reservoir with the average surface area as depicted in Figure 5. The straight line and gray area represent the predictions on emission estimates and their 95% CI, respectively. The estimated marginal means of emission estimates are summarized in Table 7. For example, the emission estimate for a reservoir with average surface area and the mean TSI_{KR} is predicted to be 367 with the 95% CI of (303,430) measured in 10^3 kg CH_4.

Table 5. Omnibus ANOVA Table.

Sources of Variation	Sum of Squares	Degree of Freedom	Mean Square	*F*-Value	*p*-Value
Surface Area	2.22×10^6	1	2.22×10^6	98.7	<0.001
TSI_{KR}	266,863	1	266,863	11.9	0.002
Residuals	472,579	21	22,504		

Table 6. Summary of Regression Model Coefficients.

Predictor	Estimate	Standard Error	95% CI		*t*-Value	*p*-Value
			Lower	Upper		
Intercept	−320.023	115.3802	−559.9692	−80.077	−2.77	0.011
Surface Area	0.123	0.0124	0.0976	0.149	9.94	<0.001
TSI_{KR}	7.127	2.0696	2.8230	11.431	3.44	0.002

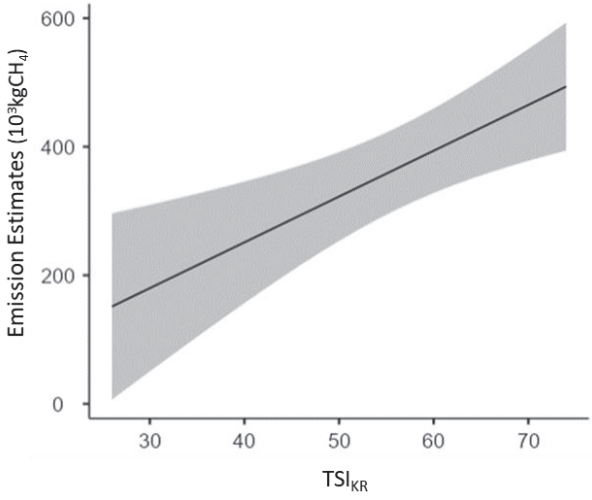

Figure 5. Estimated Marginal Means Plot.

Table 7. Estimated Marginal Means Table.

TSI_{KR}	Marginal Mean	Standard Error	95% CI	
			Lower	Upper
40.4 (1)	254	44.8	161	347
56.2 (2)	367	30.6	303	430
72.1 (3)	480	44.8	386	573

(1) mean (TSI_{KR})–stdev (TSI_{KR}); (2) mean (TSI_{KR}); (3) mean (TSI_{KR}) + stdev (TSI_{KR}).

4. Conclusions

The GHG emissions from wetlands including reservoirs have received less attention from researchers in spite of their enormous impact on global warming mainly because of the low data availability. The 2019 Refinement has been adopted to embrace recent technological development and scientific advances in improving the national GHG inventories. This study is aimed at demonstrating the application of refinement for estimating the methane emissions from reservoirs in Korea. More specifically, the results from tropic state assessment for individual reservoirs are accounted for by deriving the adjusted emission factors. The Korean trophic state index TSI_{KR} is used for identifying the trophic class of reservoirs to take regional environmental characteristics into account. Additionally, the trophic state assessment is performed season by season in an effort to include the seasonal variations in the estimation of methane emissions from reservoirs. It is observed that the magnitude of seasonal variations greatly differs among reservoirs and the emissions are highly dependent upon the main use of reservoirs which affect their management practice for water quality. The differences in methane emissions are tested for their statistical significance by means of confidence intervals, and the statistically significant differences are confirmed for the reservoirs which exhibit greater seasonal variations in the trophic state assessment. Furthermore, it is shown that the emission estimates can effectively be obtained by employing the regression analysis, which may render the functional relationship between emission estimates and trophic state indices. It is thus expected that, given the surface area and seasonal trophic state index, the emission estimates of methane from the reservoir can be predicted from the statistical perspective.

To the best of authors' knowledge, this study is one of the first attempts to apply the refinement for estimating methane emissions from wetlands. However, one of the major limitations of this study comes from the lack of validation procedure for emission estimates. Even though carried out as per the guidelines provided by IPCC, the emissions estimation still needs to be validated against the actual measurement data on the methane emissions from reservoirs. Another limitation of this study is the deficiency of uncertainty assessment to explain the sources of variations in emission estimates except for the trophic states of reservoirs. Further research efforts thus need to be directed towards securing data availability from a wide variety of different geographical contexts. In addition, more accurate estimations and even predictions on methane emissions from wetlands may be enabled by applying advanced analysis methods of statistics and data analytics. Despite unaccounted for uncertainties and opportunities for potential improvement, the procedure outlined above may provide useful tips and guidelines for an effective estimation of methane emissions from reservoirs with the considerations of regional and seasonal variations in emissions behavior.

Author Contributions: Conceptualization, C.P. and Y.J.K.; methodology, Y.C.; formal analysis, Y.C. and Y.J.K.; data curation, Y.C.; writing—original draft preparation, Y.J.K.; writing—review and editing, C.P.; supervision, C.P.; funding acquisition, Y.J.K. All authors have read and agreed to the published version of the manuscript.

Funding: This research was supported by Basic Science Research Program through the National Research Foundation of Korea (NRF) funded by the Ministry of Education (2021R1I1A3047456).

Institutional Review Board Statement: Not Applicable.

Informed Consent Statement: Not Applicable.

Data Availability Statement: Not Applicable.

Conflicts of Interest: The authors declare no conflict of interest. The funders had no role in the design of the study; in the collection, analyses, or interpretation of data; in the writing of the manuscript, or in the decision to publish the results.

Abbreviations

ANOVA	Analysis of Variance
BN	Bunam Reservoir (Name)
BR	Boryeong Reservoir (Name)
Chl-a	Chlorophyll-a
CI	Confidence Interval
COD	Chemical Oxygen Demand
DH	Daeho Reservoir (Name)
GHG	Greenhouse Gas
G-Res	Greenhouse Gas Reservoir Tool
IPCC	Intergovernmental Panel on Climate Change
SD	Secchi Depth
SG	Sapgyo Reservoir (Name)
SM	Seokmum Reservoir (Name)
TI	Trophic Index
TJ	Tapjeong Reservoir (Name)
TN	Total Nitrogen
TP	Total Phosphorus
TSI	Trophic State Index

Nomenclature

α_i	Emission adjustment factor for trophic state in reservoir i within a given climate zone
$A_{totj,i}$	Total area of water surface for reservoir i located in climate zone j (in hectare)
$EF_{CH_4age>20,j}$	Methane emission factor from reservoirs more than 20 years old located in climate zone j (in kg CH_4/year/hectare)
F_{CH_4res}	Annual reservoir surface emissions of methane from all reservoirs more than 20 years old (in kg CH_4/year)
$F_{CH_4downstream}$	Annual emissions of methane originating from all reservoirs but emitted their downstream (in kg CH_4/year)
F_{CH_4tot}	Total annual methane emission from all reservoirs more than 20 years old (in kg CH_4/year)
$nres_j$	Number of reservoirs more than 20 years old in climate zone j
R_d	Ratio of total downstream emission of methane to the total flux of methane from the reservoir surface
TSI_{KR_Chl-a}	Korean Trophic State Sub-Index based on the measurement of Chl-a
TSI_{KR_COD}	Korean Trophic State Sub-Index based on the measurement of COD
TSI_{KR_TP}	Korean Trophic State Sub-Index based on the measurement of TP
TSI_{KR}	Overall Korean Trophic State Index

References

1. IPCC. *2006 IPCC Guidelines for National Greenhouse Gas Inventories, Chapter 7*; Wetlands, Intergovernmental Panel on Climate Change: Geneva, Switzerland, 2006; Volume 4.
2. Harrison, J.A.; Prairie, Y.T.; Mercier-Blais, S.; Soued, C. Year-2020 Global Distribution and Pathways of Reservoir Methane and Carbon Dioxide Emissions According to the Greenhouse Gas from Reservoirs (G-res) Model. *Glob. Biogeochem. Cycles* **2021**, *35*, e2020GB006888. [CrossRef]
3. IPCC. *2019 Refinement to the 2006 IPCC Guidelines for National Greenhouse Inventories, Chapter 7*; Wetlands, Intergovernmental Panel on Climate Change: Geneva, Switzerland, 2019; Volume 4.
4. Comyn-Platt, E.; Hayman, G.; Huntingford, C.; Chadburn, S.E.; Burke, E.J.; Harper, A.B.; Collins, W.J.; Webber, C.P.; Powell, T.; Cox, P.M.; et al. Carbon Budgets for 1.5 and 2 °C Targets Lowered by Natural Wetland and Permafrost Feedbacks. *Nat. Geosci.* **2018**, *11*, 568–573. [CrossRef]
5. Bridgham, S.; Megonigal, P.; Keller, J.K.; Bliss, N.B. The Carbon Balance of North American Wetlands. *Wetlands* **2006**, *26*, 889–916. [CrossRef]
6. Richards, B.; Craft, C.B. Greenhouse Gas Fluxes from Restored Agricultural Wetlands and Natural Wetlands, Northwestern Indiana. In *The Role of Natural and Constructed Wetlands in Nutrient Cycling and Retention on the Landscape*; Vymazal, J., Ed.; Springer: Berlin/Heidelberg, Germany, 2015; pp. 17–32.
7. Zhang, Z.; Zimmermann, N.E.; Stenke, A.; Li, X.; Dodson, E.L.; Zhu, G.; Huang, C.; Poulter, B. Emerging Role of Wetland Methane Emissions in Driving 21st Century Climate Change. *Proc. Natl. Acad. Sci. USA* **2017**, *114*, 9647–9652. [CrossRef] [PubMed]

8. Barros, N.; Cole, J.J.; Tranvik, L.J.; Prairie, Y.T.; Bastviken, D.; Huszar, V.L.M.; del Giorgio, P.; Roland, F. Carbon Emission from Hydroelectric Reservoirs Linked to Reservoir Age and Latitude. *Nat. Geosci.* **2011**, *4*, 593–596. [CrossRef]
9. Bastviken, D.; Tranvik, L.J.; Downing, J.A.; Crill, P.M.; Enrich-Prast, A. Freshwater Methane Emissions Offset the Continental Carbon Sink. *Science* **2011**, *331*, 50. [CrossRef] [PubMed]
10. Cole, J.J.; Prairie, Y.T.; Caraco, N.F.; McDowell, W.H.; Tranvik, L.J.; Striegl, R.G.; Duarte, C.M.; Kortelainen, P.; Downing, J.A.; Middelburg, J.J.; et al. Plumbing the Global Carbon Cycle: Integrating Inland Waters into the Terrestrial Carbon Budget. *Ecosystems* **2007**, *10*, 172–185. [CrossRef]
11. St. Louis, V.L.; Kelly, C.A.; Duchemin, C.A.É.; Rudd, J.W.; Rosenberg, D.M. Reservoir Surfaces as Sources of Greenhouse Gases to the Atmosphere: A Global Estimate. *Bioscience* **2000**, *50*, 766–775. [CrossRef]
12. Beaulieu, J.J.; Waldo, S.; Balz, D.A.; Barnett, W.; Hall, A.; Platz, M.C.; White, K.M. Methane and Carbon Dioxide Emissions from Reservoirs: Controls and Upscaling. *J. Geophys. Res. Biogeosci.* **2019**, *125*, e2019JG005474. [CrossRef] [PubMed]
13. GIR. *2019 National Greenhouse Gas Inventory Report of Korea*; Greenhouse Gas Inventory and Research Center (GIR): Chungbuk, Korea, 2019.
14. Prairie, Y.; Alm, J.; Harby, A.; Mercier-Blais, S.; Nahas, R. *The GHG Reservoir Tool (G-res) Technical Documentation, UNESCO/IHA Research Project on the GHG Status of Freshwater Reservoirs (Version 1.12)*; The International Hydropower Association: London, UK, 2017.
15. Park, H.G.; Jang, B.S. Introduction to Large Dams in Korea. *J. Korean Soc. Civ. Eng.* **2005**, *53*, 206–218.
16. Carlson, R.E. A Trophic State Index for Lakes. *Limnol. Oceanogr.* **1977**, *22*, 361–369. [CrossRef]
17. Aizaki, M.; Otsuki, A.; Fukushima, T.; Kawai, T.; Hosomi, M.; Muraoka, K. *Application of Modified Carlson's Trophic State Index to Japanese Lakes and Its Relationships to Other Parameters Related to Trophic State*; National Institute for Environmental Studies: Tsukuba, Japan, 1981.
18. NIER. *Water Quality Assessment Method and Index Development*; National Institute of Environmental Research: Incheon, Korea, 2006.
19. Kim, E.; Sim, K.; Kim, S.; Choi, H.I. Water Quality Assessment for Reservoirs Using the Korean Trophic State Index. *J. Korean Soc. Water Environ.* **2012**, *28*, 78–83.
20. Ahn, D.H.; Han, S.K.; Jo, S.J.; Lim, M. Water Quality Assessment for Geumgang River Area using the Korean Trophic State Index. *J. Water Treat.* **2013**, *21*, 13–20.
21. Oh, H.J.; Jeong, H.G.; Nam, G.S.; Oda, Y.; Dai, W.; Lee, E.H.; Kong, D.; Hwang, S.J.; Chang, K.H. Comparison of Taxon-Based and Trophi-Based Response Patterns of Rotifer Community to Water Quality: Applicability of the Rotifer Functional Group as an Indicator of Water Quality. *Anim. Cells Syst.* **2017**, *21*, 133–140. [CrossRef]
22. Park, J.B.; Gal, B.S.; Lee, C.K.; Hong, S.H.; Choi, M.J.; Seo, H.S. Analysis of the Trophic Characteristics of the So-Oak River Watershed Using the Korean Trophic State Index. *J. Wetl. Res.* **2018**, *20*, 330–337.
23. Kim, B.C.; Kong, D.S. Examination of the Applicability of TOC to Korean Trophic State Index. *J. Korean Soc. Water Environ.* **2019**, *35*, 271–277.
24. Rim, C.S.; Shin, J.K. Cluster and Factor Analyses Using Water Quality Data in the Sapkyo Reservoir Watershed. *J. Korea Water Resour. Assoc.* **2002**, *35*, 149–159.

water

MDPI

Article

Effect of Different Sowing Methods on Water Use Efficiency and Grain Yield of Wheat in the Loess Plateau, China

Hafeez Noor [1,2], Min Sun [1,2,*], Wen Lin [1,2] and Zhiqiang Gao [1,2]

[1] College of Agriculture, Shanxi Agriculture University, No.1, Minxian South Road, Taiyuan 030006, China; hafeeznoorbaloch@gmail.com (H.N.); slwrdewy@163.com (W.L.); gaosxau@163.com (Z.G.)
[2] State Key Laboratory of Sustainable Dryland Agriculture (In Preparation), Shanxi Agricultural University, Taiyuan 030006, China
* Correspondence: sm_sunmin@126.com

Abstract: Research has revealed that summer fallow sowing improves the water use efficiency (WUE) and grain yield of winter wheat. However, wheat yields differ yearly with crop management. A field experiment over 8 years was established in the Loess Plateau to determine the role of precipitation and soil water storage in wheat yield formation under conservation tillage. The average WUE values were 7.8, 11.0, and 12.6 t·ha^{-1}, while the average evapotranspiration (ET) values were 334.7, 365.5, and 410 mm when the yields were 3.0, 3.0–4.5, and over 4.5 t·ha^{-1}, respectively. Compared to drill sowing (DS), high water consumption during early growth increased the spike number, grain number, and yield. In years of intermediate or low yields, wide-space sowing (WS) and furrow sowing (FS) improved the ET, WUE, spike number, grain number, and yield of wheat compared to (DS) drill sowing. When the wheat yield was 3.0–4.5 t·ha^{-1}, higher soil water intake during jointing, anthesis, and anthesis–maturity increased the tiller number, 1000-grain weight, and yield, related to the use of suitable tillers. Synchronous increases in grain number per spike and 1000-grain weight were observed with increased soil water content at jointing, maturity, and anthesis, as well as consumption of soil water in the latter part during the growing season.

Keywords: evapotranspiration; precipitation; soil water storage; water; wheat yield level

Citation: Noor, H.; Sun, M.; Lin, W.; Gao, Z. Effect of Different Sowing Methods on Water Use Efficiency and Grain Yield of Wheat in the Loess Plateau, China. *Water* **2022**, *14*, 577. https://doi.org/10.3390/w14040577

Academic Editors: Luis Garrote and Alban Kuriqi

Received: 20 December 2021
Accepted: 3 February 2022
Published: 14 February 2022

1. Introduction

The Loess Plateau is the dominant region for cereal crop production in China. In this region, wheat (*Triticum aestivum* L.) covers about 56% of the arable land [1], restricted by the extraordinary variability in precipitation and evaporation during the summer fallow period [2,3]. Agriculture has been exploited in this area to guarantee food security, which has accelerated ecological deterioration, including soil physical structure degradation, water and soil pollution, and reduced crop productivity [4–6].

The production of winter wheat in dryland is important for regional food security [7,8]. In the Loess Plateau dryland, irrigation is not available, and rainfall is the only source of water for the production of wheat. Precipitation levels are low and unevenly distributed, whereby summer rainfall accounts for approximately 60% of the annual precipitation [9,10]. Furthermore, annual precipitation fluctuates considerably [11]. Because of the limited water resources, the main planting approach in this area is to plant one crop (winter wheat) per year and leave the land fallow in the summer [12,13].

Many agricultural management plans have been established in the past few years to improve crop production in dryland regions, with one of the most successful methods being conservation tillage, with permanent organic soil cover and mechanical soil disturbance [7]. Conservation tillage approaches include DS (drill sowing), FS (furrow sowing), and WS (wide-space sowing), and they play an active role in increasing crop yield. FS, which usually includes straw mulching, leads to reduced soil degradation and farmland erosion caused by intensive agriculture [14,15]. Previous studies reported the adverse effects of

FS on soil properties such as improved soil bulk density and reduced total porosity and penetration resistance. Additionally, "reduced tillage" practices, such as WS, whereby soil is usually chisel-plowed to a depth of 25 cm, or DS, in which case soil is frequently chisel-plowed to a complexity of 20 cm, are used to alleviate soil compaction by breaking hardpans [16,17].

These reduced sowing practices have a positive outcome on rain penetration into the soil and water storage, thus improving the soil water content and increasing the tiller number, wheat grain yield, and plant WUE. The excessive use of nitrogen (N) fertilizers can have several negative effects on the environment [18]. A previous study showed that the use of controlled-release nitrogen fertilizers at sowing increased the crop yield, WUE, and economic returns by 8.5%, 10.9%, and 11.3%, respectively [19]. Another study on N fertilizers in the Loess Plateau reported that the application of an appropriate amount of N fertilizer increased the content of total wheat protein and composition of protein, leading to an improvement in the baking quality of wheat flour [20].

With an increase in the N application rate, the investment in N application should be determined to optimize economic return [21]. Soil fertility in the Loess Plateau dryland is low, especially the N level [22]. The application of N fertilizers can significantly increase the grain yield and WUE of wheat [23]. Wheat yield components include the number of tillers, grain number per spike, and 1000-grain weight. Increased coordination among yield components is required to improve crop yield potential [12–14]. However, some studies have shown that the contribution of the various yield components differs with the yield level, and correlation analysis between any single variable and yield does not fully explain the importance of each component [23–25].

Furthermore, some studies have shown a significant correlation influenced by field water consumption between wheat yield and soil moisture status over multiple growth stages from sowing to maturity [26,27]. Apparently, the sowing methods applied by farmers in the area exceed the level of sowing required to achieve high yield. The effects of water on yield, as well as the response of yield to sowing, vary with the annual precipitation level. A study on different sowing approaches in the Loess Plateau for eight consecutive years showed that, when 150 kg N·ha^{-1} was applied, wheat yield in the dry years increased by 14.0% relative to no nitrogen application, whereas it increased by 32.8% in the wet years [18] Therefore, the optimization of sowing methods based on precipitation is important to achieve high wheat yield in dryland while improving grain quality, economic return, and WUE (water use efficiency).

In this study, the main objectives were to determine the correlation between yield and soil water content and water consumption at different yield levels, thereby allowing (1) clarification of the correlation between soil water content at different yield levels and plant growth stages, (2) a comparison of the differences in yield components and WUE, and (3) an evaluation of the relationship between grain yield or yield components and field water consumption during key plant growth stages.

2. Materials and Methods

During the winter, field experiments were conducted for the winter wheat growing seasons in the years 2009–2017 at the experimental station of the Shanxi Agricultural Wenxi region, China. The study area was located in the Wenxi region (34°35′ N; 110°15′ E), Shanxi province, in the southeast of the Loess Plateau is shown in Figure 1.

This region is characterized by a distinctive semiarid, warm temperate continental climate with an annual mean precipitation of 491 mm, annual mean temperature of 12.9 °C, annual sunshine period of 2242 h, and open pan evaporation of 1839 mm. Although the annual precipitation tends to be concentrated in the months of July through September, it displays great annual variability. The precipitation distribution over the years 1981–2017 is shown in Figure 2.

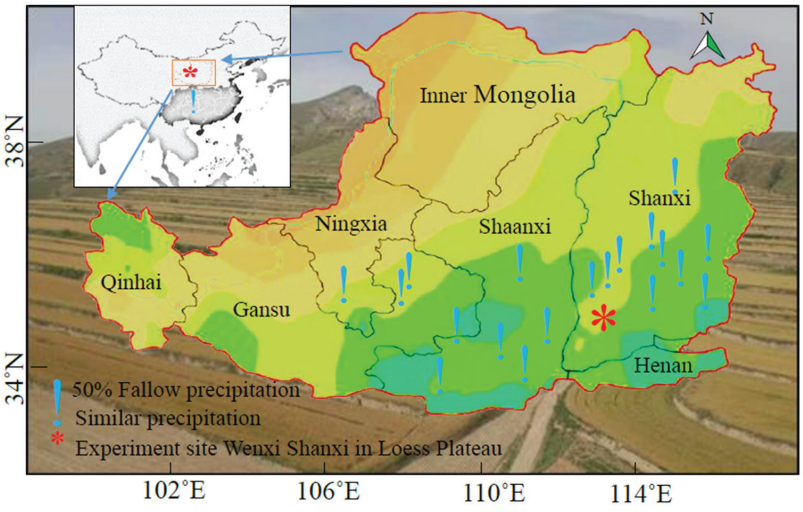

Figure 1. Location of experiment site in the Loess Plateau. The regional distribution of annual precipitation is shown in different colors on the map.

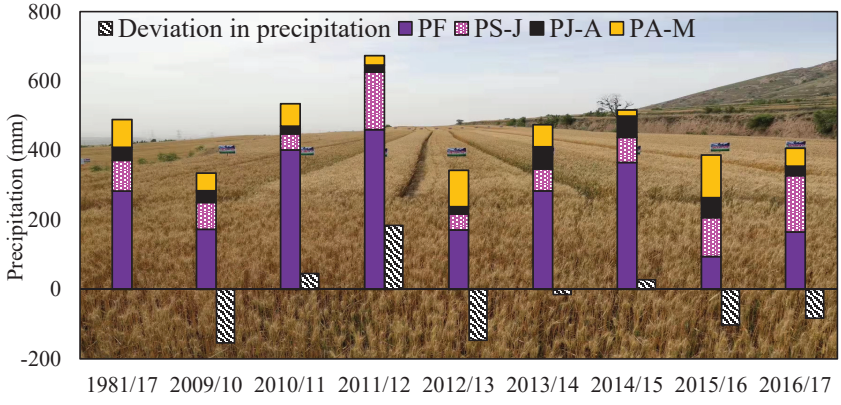

Figure 2. Precipitation distribution in the study area from 2009 to 2017, during the growth stage of winter wheat and the fallow season. P_F, P_S-J, P_J-A, and P_A-M denote the precipitation during the fallow, sowing, anthesis, and maturity stages of wheat, respectively.

2.1. Experimental Design and Field Management

This experiment featured a single-factor randomized block design. Winter wheat (*Triticum aestivum* L.) cultivar 'Yunhan 20410′ was acquired from the Shanxi Agriculture Bureau, Wenxi, China. The trial comprised three different sowing methods: (1) wide-space sowing (WS) (sowing spacing and row spacing of 8 and 25 cm, 2BMF-12/6, with auto-fertilization and tillage), (2) furrow sowing (FS) (ridge height 3/4 cm, furrow depth 6/7 cm, narrow and wide spacing 10/12 cm and 20/25 cm, and 2BMFD-17/14 multi-resolution), and (3) drill sowing (sowing spacing and row spacing of 3 cm and 20 cm, 2BXF-12 seed drill) (Figure 3).

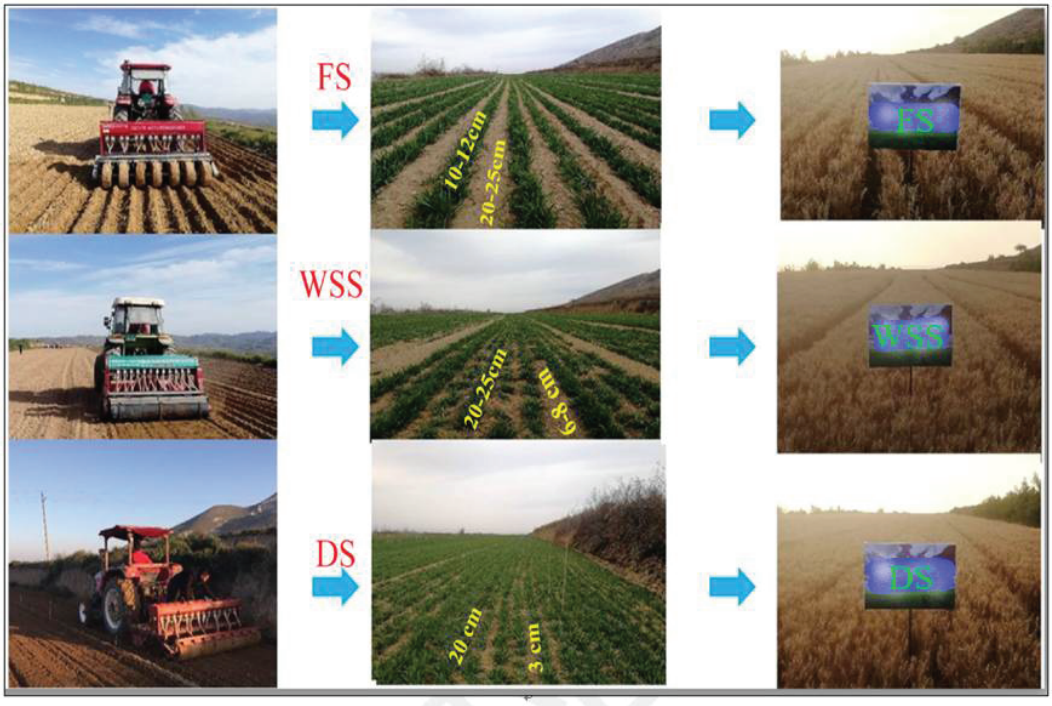

Figure 3. Illustration of sowing methods with row spacing (FS, furrow sowing; WS, wide-space sowing; DS, drill sowing), at different growth stages of wheat in the study area, Shanxi Wenxi, China.

Each plot had an area of 300 m^2 (6 m × 50 m). Before planting, 150 kg N·ha^{-1} (urea 46%), P_2O_5 (38 kg·ha^{-1}), and K_2O (75 kg·ha^{-1}) were applied consistently to the soil is shown in Table 1. During each cropping season, the planting density was 315 × 10^4 plants·ha^{-1}. During each year, all plants were machine-harvested in late June. Throughout the growing season, weeds were manually controlled, and no irrigation was applied at any time during the entire experimental period.

Table 1. Basic soil properties of the 0–20 cm layer in the study area from 2012–2017.

Year	Organic Matter (g·kg^{-1})	Total N (g·kg^{-1})	Alkali-Hydrolysis N (mg·kg^{-1})	Available Phosphorus (mg·kg^{-1})
2012–2013	8.63	0.71	32.89	15.73
2013–2014	9.18	0.70	39.32	16.62
2014–2015	9.55	0.68	37.65	17.64
2015–2016	8.54	0.67	32.79	19.23
2016–2017	9.62	0.69	32.22	15.28
2017–2018	8.07	0.69	33.42	16.26

2.2. Measurements

2.2.1. Soil Moisture

Soil water storage (SWS, mm) and soil gravimetric moisture content (GSW%) were measured gravimetrically at each plant growth stage. Soil samples were collected from a depth of 300 cm at 20 cm intervals [28]. One sample was measured as one replicate. GSW and SWS were obtained using Equations (1) and (2), respectively.

$$GSW(\%) = \frac{Mw\ Md}{Md} \times 100, \quad (1)$$

$$\text{SWS (mm)} = \text{GSW (\%)} \times \rho b \left(\text{g cm}^{-3}\right) \times \text{SD (cm)}, \quad (2)$$

where M_w and M_d are the weights (g) of dry and wet soil, respectively, pb is the soil bulk density of the given soil layer, and SD is the soil depth.

2.2.2. Evapotranspiration (ET), Precipitation, and Water Use Efficiency (WUE)

Precipitation (mm) and consumption of stored soil water (mm) in the 0–300 cm layer were used to calculate the c WUE, PUE, and evapotranspiration (ET) rate for a given cropping season using Equations (3)–(5).

$$ET = SW_0 - SW_1 + P - R - D, \quad (3)$$

$$\text{WUE}\left(\text{kg·ha}^{-1}\text{·mm}^{-1}\right) = \text{grain}\frac{\text{yield}}{\text{ET}}, \quad (4)$$

$$\text{PUE}\left(\text{kg·ha}^{-1}\text{·mm}^{-1}\right) = \text{grain}\frac{\text{yield}}{\text{P}}, \quad (5)$$

where SW_0 is the soil water storage before sowing, and SW_1 is the soil water storage after harvest. P is the precipitation during the wheat growth period, R is the soil surface runoff, D is the deep percolation, and Pt is the total precipitation from tillage to harvest. The experimental field was flat, and the experimental plots were surrounded by ridges to inhibit runoff; in this research, R was estimated to be 0. The ground water table was deeper than 50 m in the study area, and no water was percolated to the deep soil layers; therefore, D was also considered to be 0.

Precipitation (mm) and intake of soil water for storage (mm) in the 0–300 cm layer were used to calculate the crop water consumption during different growth periods. The sum of precipitation (mm) and intake of soil water for storage (mm) in the 0–300 cm layer from sowing to plant maturity was taken as the evapotranspiration (ET) rate for a given cropping season.

2.2.3. Yield and Yield Components

Fifty plants per plot were randomly sampled at maturity from the inner rows to determine yield components including ear number and grain number per ear. Plot grain yield was determined by harvesting all plants in an area of 20 m^2 and shelling them mechanically. Then, the grain was air-dried for determination of grain yield.

2.3. Statistical Analysis

The data of winter wheat growth and yield formation were processed and statistically analyzed using SAS-8.6 (SAS Institute Inc., Cary, NC, USA). In this study, two-way ANOVA was used to determine the main soil water storage and types of yield formation. When there was a significant interaction effect between soil water and yield, the least significant difference (LSD) method was used for differential analysis, while the F-test was used to determine independence; the significance level was set to $\alpha = 0.05$. Differences were considered statistically significant when $p \leq 0.05$.

3. Results

3.1. Soil Water Storage

The association between yield development and soil water storage fluctuated with the yield level (Figure 4). Yield was not significantly related to soil water storage at the jointing or anthesis stages; however, with increasing soil water storage, yield first decreased and then increased. This indicated that soil water storage was higher than 388.2 mm, 331.2 mm, and 258.0 mm at the sowing, jointing, and anthesis stages, respectively (Figure 4A–C). At the intermediate yield level, yields increased with soil water storage, with the maximum soil water storage at the jointing stage (Figure 4B). Lastly, at a high yield level, yields were mostly correlated with soil water storage at the jointing, anthesis, and maturity stages.

This trend was similar to that observed for the intermediate yield level (Figure 4A–C). Our results indicate that higher soil water storage during the late stages of growth is crucial for a higher yield.

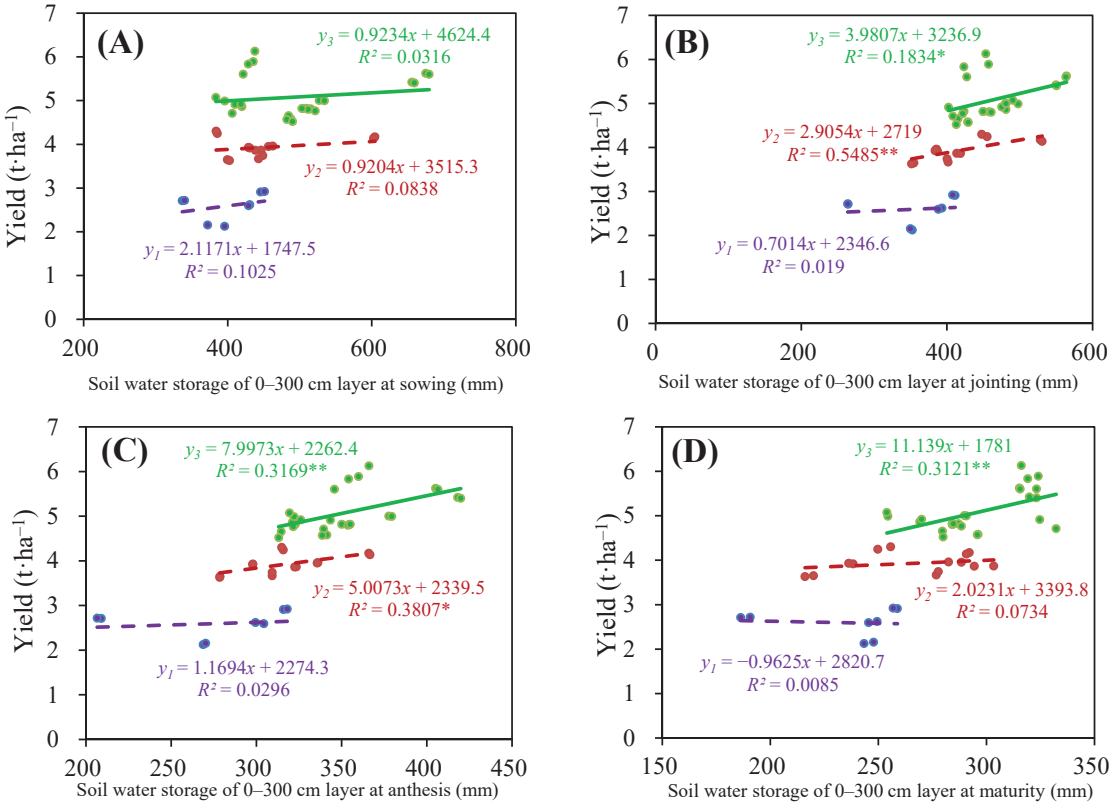

Figure 4. Correlation between soil water storage and sowing stage (y_2 = FS, furrow sowing; y_3 = WS, wide-space sowing; y_1 = DS, drill sowing); * and ** indicate differences at the 0.05 and 0.01 probability levels, respectively. (**A**) Sowing stage soil water storage (**B**) Jointing stage soil water storage (**C**) Anthesis stages soil water storage (**D**) Maturity stages soil water storage.

3.2. Correlation between Yield Formation and Field Water Consumption

During growth, the correlation between water consumption and yield formation was different at each yield level (Figure 5). At a low yield level, yield increased with increasing soil water consumption during each growth stage, although the differences were not significant (Figure 5A–C). Yield increased with field water consumption during the jointing to anthesis stages at the intermediate yield level, as shown in Figure 5B. On other hand, at the high yield level, yield increased with water consumption during the anthesis and maturity stages (Figure 5A–C). These results indicate that higher field water consumption during late growth stages is essential to high yield.

3.3. Water Use Efficiency (WUE) and Yield Components

During the research period from 2009–2017, the lowest yield was recorded under the DS treatment in 2012–2013, while the highest yield was recorded under furrow sowing (FS) in 2015–2016, as shown in Table 2. Moreover, yield composition was different at the different yield levels. In 2012–2013, at a low yield level, the 1000-grain weight and grain number per spike were highest under the WS treatment, while the lowest yield was noted under drill sowing, with values of 300.25 × 104 ha^{-1} and 2.14 kg·ha^{-1} recorded for grain

yield and tiller number, respectively. Meanwhile, at the intermediate yield level, the yield, number of tillers, and grain number per ear were highest under DS in 2016–2017. At the lowest yield recorded in 2015–2016, the tiller number was also lowest. FS and WS treatments increased the number of tillers, grain number per spike, and 1000-grain weight, thereby increasing grain yield by 26.5%, and 24.5%, respectively, compared to DS. At the low yield level, the average field water consumption, WUE, and PUE were 334.7 mm, 7.8 t·ha^{-1}, and 7.6 t·ha^{-1}·mm^{-1}, respectively, while the water consumption was highest in the year with the highest yield, and the WUE was also relatively high. In addition, compared with DS, FS and WS effectively improved the WUE by 11.7% and 11.9% and the PUE by 26.7% and 24.2%, respectively, in the same year.

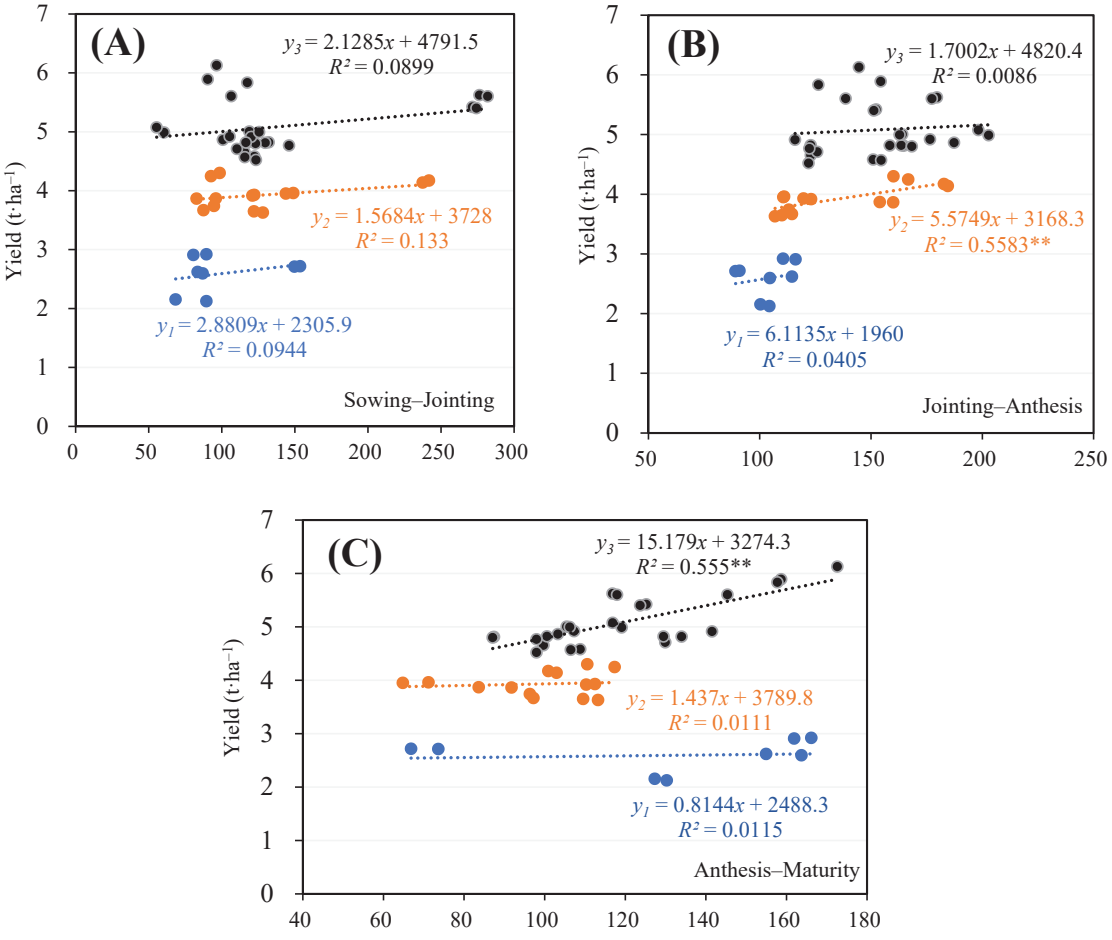

Figure 5. Correspondence between field water intake at different growth stages and yield using different sowing methods (y_1 = DS, drill sowing; y_2 = FS, furrow sowing; y_3 = WS, wide-space sowing); (**A**) Jointing stage soil water storage, (**B**) Jointing stage- anthesis stages soil water storage, (**C**) Anthesis stages-maturity stages soil water storage; * and ** indicate differences at the 0.05 and 0.01 possibility levels, respectively.

Table 2. Differences in yield components and WUE under DS, FS, and WS treatments.

Sowing Methods	Tillers (10^4 ha^{-1})	Grain Number per Spike	1000-Grain Weight (g)	Yield (t·ha^{-1})	Evapotranspiration (mm)	Water Use Efficiency (WUE; kg·h^{-1}·mm^{-1})	Precipitation Use Efficiency (PUE; kg·h^{-1}·mm^{-1})
2009–2010 DS	407.71 ^{a}	20.38 ^{c}	36.14 ^{c}	2714.96 ^{b}	311.98 ^{c}	8.70 ^{a}	8.10 ^{b}
2012–2013 DS	300.25 ^{d}	20.37 ^{c}	36.46 ^{c}	2140.25 ^{d}	310.17 ^{c}	6.90 ^{d}	6.24 ^{d}
2012–2013 FS	341.50 ^{c}	22.29 ^{b}	38.81 ^{b}	2608.30 ^{c}	354.10 ^{b}	7.37 ^{c}	7.61 ^{c}
2012–2013 WS	350.25 ^{b}	23.17 ^{a}	40.67 ^{a}	2915.32 ^{a}	362.43 ^{a}	8.04 ^{b}	8.50 ^{a}
Mean	349.93	21.55	38.02	2594.71	334.67	7.75	7.61
2009–2010 FS	427.18 ^{c}	21.70 ^{f}	39.04 ^{c}	3639.82 ^{f}	344.88 ^{d}	10.55 ^{f}	10.87 ^{b}
2009–2010 WS	453.72 ^{b}	23.78 ^{e}	42.08 ^{a}	3923.57 ^{c}	354.37 ^{c}	11.07 ^{e}	11.71 ^{a}
2010–2011 DS	401.04 ^{e}	26.22 ^{c}	40.51 ^{b}	3705.67 ^{e}	301.65 ^{g}	12.28 ^{a}	6.93 ^{f}
2011–2012 DS	485.50 ^{a}	24.33 ^{d}	35.44 ^{d}	4155.60 ^{b}	525.20 ^{a}	7.91 ^{g}	6.17 ^{g}
2013–2014 DS	386.65 ^{f}	27.55 ^{b}	39.12 ^{c}	3866.73 ^{d}	334.05 ^{e}	11.58 ^{c}	8.15 ^{d}
2014–2015 DS	417.00 ^{d}	27.48 ^{b}	39.14 ^{c}	3956.22 ^{c}	325.22 ^{f}	12.16 ^{b}	7.66 ^{e}
2016–2017 DS	452.12 ^{b}	33.36 ^{a}	35.66 ^{d}	4274.00 ^{a}	373.02 ^{b}	11.46 ^{d}	10.52 ^{c}
Mean	431.89	26.35	38.71	3931.66	365.48	11.00	8.86
2010–2011 FS	446.58 ^{k}	28.24 ^{g}	40.59 ^{c,d}	4588.15 ^{h}	340.81 ^{j}	13.46 ^{c}	8.58 ^{i}
2010–2011 WS	481.08 ^{h}	28.38 ^{f,g}	42.58 ^{a}	4794.56 ^{g}	361.01 ^{i}	13.28 ^{c}	8.97 ^{h}
2011–2012 WS	603.00 ^{b}	26.56 ^{h}	37.15 ^{f}	5412.04 ^{d}	549.04 ^{b}	9.86 ^{h}	8.04 ^{k}
2011–2012 FS	616.50 ^{a}	26.74 ^{h}	38.63 ^{e}	5612.45 ^{c}	575.02 ^{a}	9.76 ^{h}	8.34 ^{j}
2013–2014 FS	454.41 ^{j}	28.31 ^{f,g}	41.04 ^{b,c}	4575.40 ^{h}	379.48 ^{f}	12.06 ^{f}	9.65 ^{f}
2013–2014 WS	466.00 ^{i}	29.63 ^{e}	41.55 ^{b}	4818.74 ^{f,g}	409.82 ^{c}	11.76 ^{g}	10.16 ^{e}
2014–2015 FS	488.33 ^{f,g}	28.79 ^{f}	40.30 ^{d}	4806.55 ^{f,g}	380.16 ^{f}	12.64 ^{e}	9.30 ^{g}
2014–2015 WS	522.98 ^{c}	29.72 ^{e}	41.01 ^{b,c}	4999.96 ^{e}	391.54 ^{e}	12.77 ^{d,e}	9.68 ^{f}
2015–2016 DS	425.75 ^{l}	34.78 ^{d}	39.06 ^{e}	4812.00 ^{f,g}	371.90 ^{h}	12.94 ^{d}	12.44 ^{c}
2015–2016 WS	484.50 ^{g,h}	36.23 ^{b}	39.11 ^{e}	5719.08 ^{b}	396.09 ^{d}	14.44 ^{b}	14.79 ^{b}
2015–2016 FS	493.25 ^{e,f}	37.80 ^{a}	41.26 ^{b}	6009.75 ^{a}	408.60 ^{c}	14.71 ^{a}	15.54 ^{a}
2016–2017 WS	496.25 ^{e}	35.57 ^{c}	33.12 ^{h}	4892.00 ^{f}	390.33 ^{e}	12.53 ^{e}	12.04 ^{d}
2016–2017 FS	503.36 ^{d}	35.54 ^{c}	34.21 ^{g}	5032.00 ^{e}	376.52 ^{g}	13.36 ^{c}	12.38 ^{c}
Mean	498.61	31.25	39.20	5082.51	410.02	12.58	10.76
				ANOVA			
Sowing (S)	<0.001	<0.001	<0.001	<0.001	<0.001	<0.001	<0.001
Year (Y)	<0.001	<0.001	<0.001	<0.001	<0.001	<0.001	<0.001
S × Y	<0.001	<0.001	<0.001	<0.001	<0.001	<0.001	<0.001

Note: DS = drill sowing, FS = furrow Sowing, WS = wide-space sowing. Significant differences between different yield levels are indicated by different letters in the same treatment ($p < 0.05$).

3.4. Correlation Analysis of Yield Components and Contribution of Water Sources

The contribution of the different yield components to yield varied with yield level (Table 3). Thus, at a low yield level, the number of tillers and 1000-grain weight were positively correlated with yield. Meanwhile, at the intermediate yield level, the 1000-grain weight was negatively associated with yield, while the number of tillers and number of grains per spike were the key mechanisms for increasing yield. The association between the 1000-grain weight and yield was nonsignificant, whereas the yield was significantly improved by the number of tillers.

Table 3. Correlation between yield and components.

Sowing Methods	Tillers	Number per Spike	1000-Grain Weight	Simulation Equation
DS	0.676 **	0.661 *	0.634 *	$Y = 5.694 \times Y1 + 111.949 \times Y3 - 3653.974$, $R^2 = 0.999$
FS	0.626 **	0.641 **	−0.700 **	$Y = 4.558 \times Y1 + 42.942 \times Y2 + 831.857$, $R^2 = 0.999$
WS	0.540 **	0.375 *	−0.088	$Y = 8.836 \times Y1 + 111.52 \times Y2 + 93.9 \times Y3 - 6489.48$, $R^2 = 0.999$

Note: DS = drill sowing, FS = furrow sowing, WS = wide-space sowing. * $p < 0.05$. ** $p < 0.01$.

At the low yield level, fallow precipitation and the jointing to anthesis stages were positively correlated with the number of tillers; however, this correlation was negative during the anthesis to maturity stages (Table 4). The number of grains per spike and the 1000-grain weight were negatively correlated with precipitation. Soil water consumption during the sowing to jointing stages was positively correlated with the number of tillers. The grain number per spike and the 1000-grain weight were positively correlated with

soil water consumption during the jointing to anthesis stages and during the anthesis to maturity stages. At the intermediate yield level, precipitation during the sowing to jointing stages was positively correlated with the number of tillers; however, this correlation was negative during the jointing to anthesis stages and during the anthesis to maturity stages. Precipitation during the sowing to jointing stages was negatively correlated with the grain number per spike. Lastly, the correlation between precipitation and the number of tillers at the high yield level was similar to that detected at the low yield level. Furthermore, fallow precipitation and precipitation during the sowing to jointing stages were negatively correlated with the grain number per spike, whereas this correlation was positive during the jointing to anthesis stages and during the anthesis to maturity stages. On the other hand, soil water consumption during the sowing to jointing stages and during the jointing to anthesis stages was positively correlated with the number of tillers, whereas the correlation with water consumption was negative during the anthesis to maturity stages.

The equations in Table 4 show that soil water intake from anthesis to maturity mostly influenced the number of grains per spike and 1000-grain weight under drill sowing. Furthermore, the number of tillers was positively affected by soil water consumption from jointing to maturity, the grain number per ear was affected by soil water consumption from anthesis to maturity, and the 1000-grain weight was affected by precipitation from seeding to jointing and by soil water consumption from anthesis to maturity. Lastly, the number of tillers was positively affected by fallow precipitation from seeding to anthesis at a high yield level, the grain number per spike was affected by water consumption from seeding to anthesis and by precipitation from jointing to maturity, and the 1000-grain weight was affected by fallow precipitation and precipitation during each growth stage.

Table 4. Correlation between yield components and water source contribution.

Sowing Methods	Yield Composition	Fallow Precipitation	Soil Water Consumption Sowing–Jointing	Precipitation Sowing–Jointing	Soil Water Consumption Jointing–Anthesis	Precipitation Jointing–Anthesis	Soil Water Consumption Anthesis–Maturity	Precipitation of Anthesis–Maturity	Simulation Equation
DS	Tillers	0.869 **	0.951 **	0.869 **	−0.698 **	0.869 **	−0.199	−0.869 **	$Y1 = 1.345 \times X6 - 2.108 \times X7 + 489.556$, $R^2 = 0.999$
	Grain number per ear	−0.551 *	−0.338	−0.551 *	0.765 **	−0.551 *	0.949 **	0.551 *	$Y2 = 0.064 \times X6 + 19.014$, $R^2 = 0.999$
	1000-grain weight	−0.585 *	−0.370	−0.585 *	0.779 **	−0.585 *	0.944 **	0.585 *	$Y3 = 0.097 \times X6 + 34.21$, $R^2 = 0.999$
FS	Tillers	0.012	−0.033	0.812 **	0.665 **	−0.611 **	0.939 **	−0.483 *	$Y1 = 0.267 \times X4 + 1.513 \times X6 + 326.621$, $R^2 = 0.999$
	Grain number per ear	−0.112	−0.785 **	0.368	0.242	0.120	−0.167	0.069	$Y2 = 0.01 \times X1 - 0.097 \times X2 - 0.1 \times X6 - 0.131 \times X7 + 38.279$, $R^2 = 0.999$
	1000-grain weight	−0.212	0.360	−0.869 **	−0.730 **	0.259	−0.470 *	0.356	$Y3 = -0.058 \times X3 + 0.051 \times X6 + 41.543$, $R^2 = 0.98$
WS	Tillers	0.345 *	0.630 **	0.819 **	0.524 **	0.629 **	−0.482 **	−0.559 **	$Y1 = 0.375 \times X1 + 0.97 \times X3 + 0.732 \times X5 + 355.131$, $R^2 = 0.999$
	Grain number per ear	−0.872 **	−0.099	−0.478 **	−0.949 **	0.311 *	0.253	0.695 **	$Y2 = 0.053 \times X3 - 0.039 \times X4 - 0.021 \times X5 - 0.077 \times X6 + 44.642$, $R^2 = 0.99$
	1000-grain weight	0.605 **	−0.708 **	−0.211	0.269 *	−0.822 **	0.451 **	0.160	$Y3 = 0.017 \times X1 + 0.061 \times X3 - 0.051 \times X5 + 0.051 \times X7 + 37.26$, $R^2 = 0.999$

Note: DS = drill sowing, FS = furrow sowing, WS = wide-space sowing. * $p < 0.05$. ** $p < 0.01$.

4. Discussion

4.1. Wheat Grain Yield and Yield Components

Precipitation is the only source of water in arid and semiarid areas; therefore, it is the main preventive factor for the production of winter wheat [29]. Field water consumption, precipitation use efficiency, and water use efficiency were affected by the tillage treatment, thereby affecting the winter wheat yield [30]. In addition, wheat yield was significantly correlated with soil water status at numerous developmental stages from sowing to maturity [31]. In a previous study, it was reported that soil water storage from jointing to maturity was the key factor for increasing winter wheat yield in the Loess Plateau region [32], with the main stages for the water demand of winter wheat being sowing, jointing, and anthesis [33].

Soil moisture during the jointing and heading stages is particularly important in determining yield formation. The correlation between yield and soil water storage during each growth stage was different, not only related to regional differences but also to yield level [34]. In a previous study, when yield was lower than 3.00 t·ha^{-1}, it was more strongly related to soil water storage at sowing, jointing, and anthesis [35]. When yield reached between 3.10 and 4.51 t·ha^{-1}, it was more related to soil water storage at jointing, whereas, when it reached over 4.50 kg·ha^{-1}, it was more related to soil water storage at jointing, maturity, and anthesis [36]. In the fallow period, tillage improved the soil water storage and field evapotranspiration, which was conducive to the improvement of yield [37]. Optimizing the spike number per hectare is a key method to maximize yield in most cereal crops because it can increase plant vigor and, hence, plant grain yield [38].

Both the number of tillers and the yield were positively correlated at different yield levels, indicating that a larger number of tillers may guarantee a higher yield from winter wheat. These results are consistent with previous studies [39]. However, the grain number per ear and 1000-grain mass were correlated with yield at different levels of yield. Thus, for example, [39] reported that, at a low yield level (less than 7.50 t·ha^{-1}), yield was positively correlated to grain number per spike ear but negatively correlated with 1000-grain mass, whereas, at a high yield level (i.e., greater than 7.50 t·ha^{-1}), yield was correlated with grain number per ear, but not with 1000-grain weight. In the present study, a significant relationship was found between yield and tiller number. However, when the yield was lower than 3.00 t·ha^{-1}, it was correlated with 1000-grain weight, whereas, when the yield was 3.00 and 4.50 t·ha^{-1}, it was significantly and negatively correlated with 1000-grain weight. In addition to the number of tillers, at low and intermediate yield levels, the 1000-grain mass and the number of grains per spike were the key yield components responsible for increasing crop yield. Similarly, at a high yield level, higher values of grain number per spike, 1000-grain weight, and number of tillers were the key to high crop yield.

4.2. Wheat Yield Formation and Water

The key yield components responsible for the formation of yield are well known to be affected by soil moisture during each growth stage and to influence each other [40]. The early growth stage is conducive to improving the spike number, while the latter growth stage is important for the spike number and 1000-grain weight [41]. The number of tillers was reported to be more closely related to water content at the early stage of growth at different yield levels, and the number of grains per ear and 1000-grain weight were more closely related to growth stage, although the specific correlation varied, especially the relative contribution to the formation of the different yield components [42]. Thus, at low yield levels, the key to improving tiller number and 1000-grain weight was soil water consumption during the period from anthesis to maturity [43]. At the intermediate yield level tested here, tiller number was affected by soil water consumption during jointing, and the effect was positive; the number of grains per spike was positively affected by water consumption during the period from anthesis to maturity [44]. In this study, the fallow period ranged from the last 10 days of June to the last 10 days of September, the

sowing–jointing stage) ranged from the first 10 days of October to the first 10 days of April in the following year, the jointing–anthesis stage ranged from the middle 10 days of April to the first 10 days of May, and the anthesis–maturity stage ranged from the middle 10 days of May to the middle 10 days of June.

Soil erosion has disastrous consequences on local agricultural creation and socioeconomic improvement, thereby affecting people's lives and property, and posing a significant threat to safety. Loess erosion is a main environmental topic that has been addressed in many studies [45–47]. The results of previous studies revealed large differences in soil temperature and moisture across tillage and sowing treatments in wheat [48,49]. In agriculture systems, the method of sowing is an important factor governing the soil microclimate [50,51]. Unlike tillage systems, crop residues are not incorporated in sowing systems [52,53]. The amount of soil water stored at sowing can be used as a guide when applying the basal amount of N. Additional N fertilization as top dressing can be applied when rainfall is higher than expected in the growth season [54,55]. The annual precipitation level fluctuates considerably in the Loess Plateau, as observed in this study [56].

Precipitation is also unevenly distributed within a year. Summer rainfall accounts for approximately 60% of the yearly precipitation [57,58]. The yield increase is largely because optimal sowing promotes tiller and panicle formation, leading to an increased number of spikes per unit area (Table 4). The application of optimal rates of N in years with different precipitation levels can also reduce production cost and environmental pollution [59,60]. In turn, the 1000-grain weight was found to be affected by precipitation from sowing to jointing and by soil water consumption from anthesis to maturity. Lastly, at the high yield level, the number of tillers was positively affected by fallow precipitation during the sowing and anthesis periods, the number of grains per ear was affected by water consumption during the jointing–maturity stages and by precipitation from sowing to anthesis, and the 1000-grain weight was affected by fallow precipitation during each growth stage.

4.3. Water Impact on Wheat Yield

This study showed that sowing method had no significant effect on the grain protein content. Compared to drill sowing, the protein yield of wheat could be significantly increased by wide-space sowing, and the soil moisture could be significantly increased by furrow sowing. Furthermore, the regulation ability of wide-space sowing was higher than that of furrow sowing. The results showed that the difference in protein yield was mainly caused by yield, in contrast to the results in Tai'an, Shadong province [61], where, compared to drill sowing, wide-space sowing could reduce wheat grain protein content and increase protein yield. This may be due to the differences in regional climate and soil type or may be related to wheat genotypes, which need to be verified by years of research. Analysis showed that nitrogen fertilizer could significantly increase grain protein content and yield, and its regulation ability increased with the increase in nitrogen fertilizer. This was consistent with previous studies showing that nitrogen application increased the nitrogen content in grains [62,63], thus increasing the protein content. It was also shown that the sowing method and nitrogen application rate had independent effects on nitrogen accumulation in dryland wheat [64]. This may be due to the different response of grain protein content and yield to the seeding method and nitrogen application rate; thus, further research is needed.

This study showed that the contribution rate of pre-flowering translocation to grains was more than 75%. Compared to drill sowing, the nitrogen accumulation, transshipment volume, and N harvest index of wheat plants were significantly increased by wide-space sowing and trenching tillage sowing, whereas the contribution rate of post-flowering accumulation to grains was significantly decreased by wide-space sowing and trenching tillage sowing, along with a higher regulation ability than trenching tillage sowing. This is consistent with previous studies. The large population [64] produced by wide-space sowing and double-row sowing is accompanied by an increase in plant nitrogen accumulation [65], while the premature aging phenomenon [66,67] results in accelerated filling, high

pre-flowering transshipment volume, transshipment rate [68], and eventually high grain nitrogen content and harvest index [69,70]. The agent quantity of furrow sowing with the buffer effect of temperature [71] is advantageous to plant nitrogen accumulation and delays the grouting by 5–6 months at high temperatures [72]. Additionally, it increases the grain nitrogen content and harvest index [73]; however, of the land utilization rate is low, and the nitrogen accumulation and transportation are lower than under wide refined sowing. In conventional single-row seeding, the lack of seedlings and ridging at the early stage [74] reduces the wheat population, resulting in low nitrogen accumulation in plants and weak resistance to the external environment in smaller groups at the later stages [75]. A high temperature at the filling stage further reduces the transport of nitrogen to grains, resulting in a lower nitrogen content and harvest index in grains. Experimental results in the Loess Plateau showed that soil water storage before sowing was significantly and positively correlated with wheat yield in dryland. In the Weibei region of Shaanxi province and the Jinnan region of Gansu province, soil water storage before sowing showed a significant linear positive correlation with wheat grain yield, especially in dry years. The distribution of precipitation is closely related to wheat yield. If precipitation is insufficient in the early stages of the critical wheat growth period and a soil water deficit occurs, the growth and development of wheat will be significantly affected, resulting in a reduction in yield.

5. Conclusions

It can be concluded from the present study that, compared to the drill sowing method, furrow sowing and wide-space sowing were influenced by field evapotranspiration within the same year. At a low yield level, the average field water consumption, WUE, and PUE were highest in the year with the highest yield. Wide-space sowing in the fallow period improved the precipitation use efficiency, while yield components that were negatively affected by precipitation were also improved. Wide-space sowing was mainly responsible for a reduction in 1000-grain weight and grain number per spike. Therefore, in high-yield years, fallow cultivation can help adjust the relationship among the components, promote a reasonable distribution, and improve yield.

Author Contributions: Conceptualization, M.S.; methodology, H.N., M.S. and Z.G.; software, M.S.; validation, M.S. and H.N.; formal analysis, W.L.; investigation, M.S.; resources, H.N.; data curation, H.N.; writing, H.N., M.S., W.L. and Z.G. All authors read and agreed to the published version of the manuscript.

Funding: The authors are thankful to 'Modern Agriculture Industry Technology System Construction' (No. CARS-3124), the National Key Research and Development Program of China (No. 2018YFD020040105), the Sanjin Scholar Support Special Funds Projects, the National Natural Sci-ence Foundation of China (No. 31771727), and the '1331' Engineering Key Innovation Cultiva-tion Team Organic Dry Cultivation and Cultivation Physiology Innovation Team (No. SXYBKY201733).

Institutional Review Board Statement: Not applicable.

Informed Consent Statement: Not applicable.

Data Availability Statement: The data presented in this study is available on request from the corresponding author.

Acknowledgments: The authors are thankful to 'Modern Agriculture Industry Technology System Construction' (No. CARS-3124), the National Key Research and Development Program of China (No. 2018YFD020040105), the Sanjin Scholar Support Special Funds Projects, the National Natural Science Foundation of China (No. 31771727), and the '1331' Engineering Key Innovation Cultivation Team Organic Dry Cultivation and Cultivation Physiology Innovation Team (No. SXYBKY201733) for financial support of this study.

Conflicts of Interest: The authors declare no conflict of interest.

References

1. Su, Z.; Zhang, J.; Wu, W.; Cai, D.; Lv, J.; Jiang, G.; Huang, J.; Gao, J.; Hartmanne, R.; Gabrielset, D. Effects of conservation tillage practices on winter wheat water-use efficiency and crop yield on the Loess Plateau, China. *Agri. Water Manag.* **2007**, *87*, 307–314. [CrossRef]
2. Qiu, L.; Hao, M.; Wu, Y. Potential impacts of climate change on carbon dynamics in a rain-fed agroecosystem on the Loess Plateau of China. *Sci. Total Environ.* **2017**, *577*, 267–278. [CrossRef] [PubMed]
3. Kang, S.Z.; Zhang, L.; Liang, Y.; Hu, X.; Cai, H.; Gu, B. Effects of limited irrigation on yield and water use efficiency of winter wheat in the Loess Plateau of China. *Agri. Water Manag.* **2002**, *55*, 203–216. [CrossRef]
4. Ren, A.; Sun, M.; Xue, L.; Deng, Y.; Wang, P.; Lei, M.; Lin, W.; Yang, Z.; Gao, Z. Spatio-temporal dynamics in soil water storage reveals effects of nitrogen inputs on soil water consumption at different growth stages of winter wheat. *Agri. Water Manag.* **2019**, *216*, 379–389. [CrossRef]
5. Hungria, M.; Franchini, J.C.; Brandão-Junior, O.; Kaschuk, G.; Souza, R.A. Soil microbial activity and crop sustainability in a long-term experiment with three soil-tillage and two crop-rotation systems. *Appl. Soil Ecology.* **2009**, *42*, 288–296. [CrossRef]
6. Zhang, Q.; Liu, D.; Cheng, S.; Huang, X. Combined effects of runoff and soil erodibility on available nitrogen losses from sloping farmland affected by agricultural practices. *Agric. Water Manag.* **2016**, *176*, 1–8. [CrossRef]
7. Friedrich, T.; Derpsch, R.; Kassam, A. Overview of the global spread of conservation agriculture. In *Sustainable Development of Organic Agriculture*; Apple Academic Press: Palm Bay, FL, USA, 2017; pp. 75–90. Available online: http://journals.openedition.org/factsreports/1941 (accessed on 20 December 2021).
8. Jiang, C.; Wang, F.; Zhang, H.; Dong, X. Quantifying changes in multiple ecosystem ser-vices during 2000–2012 in the Loess Plateau, China, as a result of climate variability and ecological restoration. *Ecol. Eng.* **2016**, *97*, 258–271. [CrossRef]
9. Wang, X.; Wang, B.; Xu, X. Effects of large-scale climate anomalies on trends in seasonal precipitation over the Loess Plateau of China from 1961 to 2016. *Ecol. Indic.* **2019**, *107*, 105643. [CrossRef]
10. Cao, H.; Wang, Z.; He, G.; Dai, J.; Huang, M.; Wang, S.; Luo, L.; Sadras, V.O.; Hoogmoed, M.; Malhi, S.S. Tailoring NPK fertilizer application to precipitation for dryland winter wheat in the Loess Plateau. *Field Crop. Res.* **2017**, *209*, 88–95. [CrossRef]
11. Zhu, Z.; Chen, D. Nitrogen fertilizer use in China—Contributions to food production, impacts on the environment and best management strategies. *Nutr. Cycl. Agroecosyst.* **2002**, *63*, 117–127. [CrossRef]
12. Turner, N.C.; Asseng, S. Productivity, sustainability, and rainfall-use efficiency in Australian rainfed Mediterranean agricultural systems. *Aust. J. Agric. Res.* **2005**, *56*, 1123–1136. [CrossRef]
13. Shi, Z.L.; Li, D.D.; Jing, Q.; Cai, J.; Jiang, D.; Cao, W.X.; Dai, T.B. Effects of nitrogen applications on soil nitrogen balance and nitrogen utilization of winter wheat in a rice-wheat rotation. *Field Crop. Res.* **2012**, *127*, 241–247. [CrossRef]
14. Camarotto, C.; Ferro, N.D.; Piccoli, I.; Polese, R.; Morari, F. Conservation agriculture and cover crop practices to regulate water, carbon and nitrogen cycles in the low-lying Venetian plain. *Catena* **2018**, *167*, 236–249. [CrossRef]
15. Unger, P.W.; Kaspar, T.C. Soil compaction and root growth: A review. *Agron. J.* **1994**, *86*, 759–766. [CrossRef]
16. López-Garrido, R.; Madejón, E.; León-Camacho, M.; Girón, I.; Moreno, F.; Murillo, J.M. Reduced tillage as an alternative to no-tillage under Mediterranean conditions: A case study. *Soil Tillage Res.* **2014**, *140*, 40–47. [CrossRef]
17. Costa, J.L.; Aparicio, V.; Cerda, A. Soil physical quality changes under different management systems after 10 years in the Argentine humid pampa. *Solid Earth* **2015**, *6*, 361–371. [CrossRef]
18. Noor, H.; Wang, Q.; Islam, M.A.; Sun, M.; Lin, W.; Ren, A.X.; Feng, Y.; Yu, S.B.; Fida, N.; Dong, S.F.; et al. Effects of sowing methods and nitrogen rates on photosynthetic characteristics, yield and quality of winter wheat. *Photosynthetica* **2021**, *59*, 277–285. [CrossRef]
19. Xu, X.; He, P.; Wei, J.; Cui, R.; Sun, J.; Qiu, S.; Zhao, S.; Zhou, W. Use of controlled-release urea to improve yield, nitrogen utilization, and economic return and reduce nitrogen loss in wheat-maize crop rotations. *Agronomy* **2021**, *11*, 723. [CrossRef]
20. Raymbek, A.; Saunikov, E.; Kenenbayev, S.; Perovic, V.; Ramazanova, S. Protein content changes in wheat grain as influenced by nitrogen fertilization. *Agrochim. Pisa* **2017**, *61*, 180–189. [CrossRef]
21. Liu, Z.; Yu, N.; Camberato, J.J.; Gao, J.; Liu, P.; Zhao, B.; Zhang, J. Crop production kept stable and sustainable with the decrease of nitrogen rate in North China Plain: An economic and environmental assessment over 8 years. *Sci. Rep.* **2019**, *9*, 19335. [CrossRef]
22. Wang, L.; Palta, J.A.; Chen, W.; Chen, Y.L.; Deng, X.P. Nitrogen fertilization improved water-use efficiency of winter wheat through increasing water use during vegetative rather than grain filling. *Agric. Water Manag.* **2018**, *197*, 41–53. [CrossRef]
23. Guo, S.; Zhu, H.; Dang, T.; Wu, J.; Liu, W.; Hao, M.; Li, Y.; Syers, J.K. Winter wheat grain yield associated with precipitation distribution under long-term nitrogen fertilization in the semiarid Loess Plateau in China. *Geoderma* **2012**, *189*, 442–450. [CrossRef]
24. Qin, X.; Zhang, F.; Liu, C.; Yu, H.; Cao, B.; Tian, S.; Liao, Y.; Siddique, K.H.M. Wheat yield improvements in China: Past trends and future directions. *Field Crop. Res.* **2015**, *177*, 117–124. [CrossRef]
25. Slafer, G.A. Genetic basis of yield as viewed from a crop physiologist's perspective. *Ann. Appl. Biol.* **2003**, *142*, 117–128. [CrossRef]
26. Sadras, V.O.; Slafer, G.A. Environmental modulation of yield components in cereals: Heritabilities reveal a hierarchy of phenotypic plasticities. *Field Crop. Res.* **2012**, *127*, 215–224. [CrossRef]
27. Dewey, D.R.; Lu, K. A correlation and path-coefficient analysis of components of crested wheatgrass seed production. *Agron. J.* **1959**, *51*, 70–74. [CrossRef]
28. Singh, D.; Singh, M.; Sharma, K.C. Correlation and path coefficient analysis among flag leaf area, yield and yield attributes in wheat (*Triticum aestivum* L.). *Cereal Res. Commun.* **1979**, *7*, 145–152.

29. Cao, H.; Li, Y.; Chen, G.; Chen, D.; Qu, H.; Ma, W. Identifying the limiting factors driving the winter wheat yield gap on smallholder farms by agronomic diagnosis in North China Plain. *J. Integr. Agri.* **2019**, *18*, 1701–1703. [CrossRef]
30. Ozturk, A.; Aydin, F. Effect of water stress at various growth stages on some quality characteristics of winter wheat. *J. Agron. Crop. Sci.* **2004**, *190*, 93–99. [CrossRef]
31. Seddaiu, G.; Iocola, I.; Farina, R.; Orsini, R.; Iezzi, G.; Roggero, P.P. Long term effects of tillage practices and N fertilization in rainfed Mediterranean cropping systems: Durum wheat, sunflower and maize grain yield. *Eur. J. Agron.* **2016**, *77*, 166–178. [CrossRef]
32. Wang, Y.; Zhang, Y.; Zhou, S.; Wang, Z. Meta-analysis of no-tillage effect on wheat and maize water use efficiency in China. *Sci. Total Environ.* **2018**, *635*, 1372–1382. [CrossRef] [PubMed]
33. Sun, M.; Ren, A.; Gao, Z.; Wang, P.; Mo, F.; Xue, L.; Lei, M. Long-term evaluation of tillage methods in fallow season for soil water storage, wheat yield and water use efficiency in semiarid southeast of the loess plateau. *Field Crops Res* **2018**, *218*, 24–32. [CrossRef]
34. He, G.; Wang, Z.; Li, F.; Dai, J.; Li, Q. Soil water storage and winter wheat productivity affected by soil surface management and precipitation in dryland of the Loess Plateau. China. *Agric. Water Manag.* **2016**, *171*, 1–9. [CrossRef]
35. Sun, L.; Wang, R.; Li, J.; Wang, Q.; Lyu, W.; Wang, X.; Cheng, K.; Mao, H.; Zhang, X. Reasonable fertilization improves the conservation tillage benefit for soil water use and yield of rain-fed winter wheat: A case study from the Loess Plateau, China. *Field Crops Res.* **2019**, *242*, 107589. [CrossRef]
36. Wang, D. Water use efficiency and optimal supplemental irrigation in a high yield wheat field. *Field Crops Res.* **2017**, *217*, 213–220. [CrossRef]
37. Lin, X.; Wang, D. Effects of supplemental irrigation on water consumption characteristics, grain yield and water use efficiency in winter wheat under different soil moisture conditions at seeding stage. *Acta Agron. Sin.* **2017**, *43*, 1357–1369. [CrossRef]
38. Deng, X.; Shan, L.; Zhang, H.; Turner, N.C. Improving agricultural water use efficiency in arid and semiarid areas of China. *Agric. Water Manag.* **2006**, *80*, 23–40. [CrossRef]
39. Xue, L.; Khan, S.; Sun, M.; Anwar, S.; Ren, A.; Gao, Z.; Lin, W.; Xue, J.; Yang, Z.; Deng, Y. Effects of tillage practices on water consumption and grain yield of dryland winter wheat under different precipitation distribution in the loess plateau of China. *Soil Tillage Res.* **2019**, *191*, 66–74. [CrossRef]
40. Weiner, J.; Griepentrog, H.W.; Kristensen, L. Suppression of weeds by spring wheat Triticum aestivum increases with crop density and spatial uniformity. *J. Appl. Ecol.* **2001**, *38*, 784–790. [CrossRef]
41. Del Blanco, I.A.; Rajaram, S.; Kronstad, W.E. Agronomic potential of synthetic hexaploid wheat-derived populations. *Crop. Sci.* **2001**, *41*, 670–676. [CrossRef]
42. Duan, J.; Wu, Y.; Zhou, Y.; Ren, X.; Shao, Y.; Feng, W.; Zhu, Y.; Wang, Y.; Guo, T. Grain number responses to pre-anthesis dry matter and nitrogen in improving wheat yield in the Huang-Huai Plain. *Sci. Rep.* **2018**, *8*, 1–10. [CrossRef] [PubMed]
43. Dong, Z.; Zhang, X.; Li, J.; Zhang, C.; Wei, T.; Yang, Z.; Cai, T.; Zhang, P.; Ding, R.; Jia, Z. Photosynthetic characteristics and grain yield of winter wheat (*Triticum aestivum* L.) in response to fertilizer, precipitation, and soil water storage before sowing under the ridge and furrow system: A path analysis. *Agric. For. Meteorol.* **2019**, *272*, 12–19. [CrossRef]
44. Hochman, Z. Effect of water stress with phasic development on yield of wheat grown in a semi-arid environment. *Field Crops Res.* **1982**, *5*, 55–67. [CrossRef]
45. Berhe, A.A.; Barnes, R.T.; Six, J.; Marín-Spiotta, E. Role of soil erosion in biogeochemical cycling of essential elements: Carbon, nitrogen, and phosphorus. Annu. *Rev. Earth Planet. Sci.* **2018**, *46*, 521–548. [CrossRef]
46. Jiang, C.; Zhang, H.Y.; Wang, X.C.; Feng, Y.Q.; Labzovskii, L. Challenging the land degradation in China's Loess Plateau: Benefits, limitations, sustainability, and adaptive strategies of soil and water conservation. *Ecol. Eng.* **2019**, *127*, 135–150. [CrossRef]
47. Juang, C.H.; Dijkstra, T.; Wasowski, J.; Meng, X.M. Loess geohazards research in China: Advances and challenges for mega engineering projects. *Eng. Geol.* **2019**, *251*, 1–10. [CrossRef]
48. Johnson, M.D.; Lowery, B. Effect of three conservation tillage practices on soil temperature and thermal properties. *Soil Sci. Soc. Am. J.* **1985**, *49*, 1547–1552. [CrossRef]
49. Amos, B.; Shen, H.; Arkebauer, T.J.; Walters, D.T. Effect of previous crop residue on soil surface carbon dioxide flux in maize. *Soil Sci.* **2007**, *172*, 589–597. [CrossRef]
50. Lueschen, W.E. Tillage, row spacing, and planting date effects on soybean following corn or wheat. *J. Prod. Agric.* **1992**, *5*, 260. [CrossRef]
51. Hatfield, J.L.; Prueger, J.H. Microclimate effects of crop residues on biological processes. *Theor. Appl. Climatol.* **1996**, *54*, 47–59. [CrossRef]
52. Sims, A.L.; Schepers, J.; Olson, R.A.; Power, J.F. Irrigated corn yield and nitrogen accumulation response in a comparison of no-till and conventional till: Tillage and surface-residue variables. *Agron. J.* **1998**, *90*, 630–637. [CrossRef]
53. Zhang, X.; Xin, X.; Zhu, A.; Zhang, J.; Yang, W. Effects of tillage and residue managements on organic C accumulation and soil aggregation in a sandy loam soil of the North China Plain. *CATENA* **2017**, *156*, 176–183. [CrossRef]
54. Wagger, M.G.; Denton, H.P. Crop and tillage rotations: Grain yield, residue cover, and soil water. *Soil Sci. Soc. Am. J.* **1992**, *56*, 1233–1237. [CrossRef]
55. Chen, Y.; McKyes, E. Reflectance of light from the soil surface in relation to tillage practices, crop residues and the growth of corn. *Soil Tillage Res.* **1993**, *26*, 99–114. [CrossRef]

56. Shen, Y.; McLaughlin, N.; Zhang, X.; Xu, M.; Liang, A. Effect of tillage and crop residue on soil temperature following planting for a Black soil in Northeast China. *Sci. Rep.* **2018**, *8*, 1–9. [CrossRef]
57. Van Donk, S.J.; Martin, D.L.; Irmak, S.; Melvin, S.R.; Petersen, J.L.; Davison, D.R. Crop residue cover effects on evaporation, soil water content, and yield of deficit-irrigated corn in west-central Nebraska. *Trans. ASABE* **2010**, *53*, 1787–1797. [CrossRef]
58. Johnson, A.M.; Hoyt, G.D. Changes to the soil environment under conservation tillage. *Horttechnology* **1999**, *9*, 380–393. [CrossRef]
59. Lobell, D.B.; Bala, G.; Duffy, P.B. Biogeophysical impacts of cropland management changes on climate. *Geophys. Res. Lett.* **2006**, *33*, 4–7. [CrossRef]
60. Hirsch, A.L.; Wilhelm, M.; Davin, E.L.; Thiery, W.; Seneviratne, S.I. Can climate-effective land management reduce regional warming? *J. Geophys. Res.* **2017**, *122*, 2269–2288. [CrossRef]
61. Fang, X.; Li, Y.; Nie, J.; Wang, C.; Huang, K.; Zhang, Y.; Zhang, Y.; She, H.; Liu, X.; Ruan, R. Effects of nitrogen fertilizer and planting density on the leaf photosynthetic characteristics, agronomic traits and grain yield in common buckwheat (*Fagopyrum esculentum* M.). *Field Crop. Res.* **2018**, *219*, 160–168. [CrossRef]
62. Noor, H.; Min, S.; Khan, S.; Lin, W.; Ren, A.; Yu, S.; Ullah, S.; Yang, Z.; Gao, Z. Different sowing methods increasing the yield and quality of soil water consumption of dryland winter wheat on the loess plateau of china. *Appl. Ecol. Env. Res.* **2020**, *18*, 8285–8308. [CrossRef]
63. Bijay, S.; Sharma, R.K.; Jaspreet, K.; Jat, M.L.; Martin, K.L.; Yadvinder, S.; Varinderpal, S.; Chandna, P.; Choudhary, O.P.; Gupta, R.K.; et al. Assessment of the nitrogen management strategy using an optical sensor for irrigated wheat. *J. Agron. Sustain. Dev.* **2011**, *31*, 589–603. [CrossRef]
64. Yu, X.; Chen, X.; Wang, L.; Yang, Y.; Zhu, X.; Shao, S.; Cui, W.; Xiong, F. Novel insights into the effect of nitrogen on storage protein biosynthesis and protein body development in wheat caryopsis. *J. Exp. Bot.* **2017**, *68*, 2259–2274. [CrossRef] [PubMed]
65. Zörb, C.; Ludewig, U.; Hawkesford, M.J. Perspective on wheat yield and quality with reduced nitrogen supply. *Trends Plant. Sci.* **2018**, *23*, 1029–1037. [CrossRef] [PubMed]
66. Mullen, R.W.; Freeman, K.W.; Raun, W.R.; Johnson, G.V.; Stone, M.L.; Solie, J.B. Identifying an in-season response index and the potential to increase wheat yield with nitrogen. *Agron. J.* **2003**, *95*, 347–351. [CrossRef]
67. Lu, D.; Lu, F.; Yan, P.; Cui, Z.; Chen, X. Elucidating population establishment associated with N management and cultivars for wheat production in China. *Field Crop. Res.* **2014**, *163*, 81–89. [CrossRef]
68. Li, T.; Zhang, Y.; Dai, J.; Dong, H.; Kong, X. High plant density inhibits vegetative branching in cotton by altering hormone contents and photosynthetic production. *Field Crop. Res.* **2019**, *230*, 121–131. [CrossRef]
69. Gregersen, P.L.; Culetic, A.; Boschian, L.; Krupinska, K. Plant senescence and crop productivity. *Plant Mol. Biol.* **2013**, *82*, 603–622. [CrossRef]
70. Dong, H.; Li, W.; Eneji, A.E.; Zhang, D. Nitrogen rate and plant density effects on yield and late-season leaf senescence of cotton raised on a saline field. *Field Crop. Res.* **2012**, *126*, 137–144. [CrossRef]
71. Su, W.; Kamran, M.; Xie, J.; Meng, X.; Han, Q.; Liu, T.; Han, J. Shoot and root traits of summer maize hybrid varieties with higher grain yields and higher nitrogen use efficiency at low nitrogen application rates. *Peer J.* **2019**, *7*, e7294. [CrossRef]
72. Zhang, X.; Davidson, E.A.; Mauzerall, D.L.; Searchinger, T.D.; Dumas, P.; Shen, Y. Managing nitrogen for sustainable development. *Nature* **2015**, *528*, 51–59. [CrossRef] [PubMed]
73. Kitonyo, O.M.; Sadras, V.O.; Zhou, Y.; Denton, M.D. Nitrogen supply and sink demand modulate the patterns of leaf senescence in maize. *Field Crop. Res.* **2018**, *225*, 92–103. [CrossRef]
74. Luo, Z.; Liu, H.; Li, W.; Zhao, Q.; Dai, J.; Tian, L.; Dong, H. Effects of reduced nitrogen rate on cotton yield and nitrogen use efficiency as mediated by application mode or plant density. *Field Crop. Res.* **2018**, *218*, 150–157. [CrossRef]
75. Shangguan, Z.; Shao, M.; Dyckmans, J. Effects of nitrogen nutrition and water deficit on net photosynthetic rate and chlorophyll fluorescence in winter wheat. *J. Plant Physiol.* **2000**, *156*, 46–51. [CrossRef]

water

MDPI

Article

Systematic Application of Sponge City Facilities at Community Scale Based on SWMM

Yu Jiang [1], Ling Qiu [2], Tian Gao [2] and Shuoxin Zhang [1,*]

[1] College of Forestry, Northwest A&F University, Xianyang 712100, China; rainyery@hotmail.com
[2] College of Landscape Architecture and Arts, Northwest A&F University, Xianyang 712100, China; qiu.ling@nwsuaf.edu.cn (L.Q.); tian.gao@nwsuaf.edu.cn (T.G.)
* Correspondence: sxzhang@nwsuaf.edu.cn; Tel.: +86-29-87082993

Abstract: In the context of global climate change, many countries have taken corresponding measures to cope with the stormwater problems in urbanization. The Chinese government introduced the concept of Sponge City to improve the urban water ecological security, which is a systematic project. Taking the urban community as our research object, we studied the combination application of LID (low-impact development) measures and retention ponds in the community and then discussed the practicability of the systematic application of Sponge City facilities in the construction of community drainage systems. There are four simulation scenarios in SWMM (stormwater management model): traditional drainage scenario, LID scenario, retention pond scenario, and LID-retention pond scenario. By comparing the effects of different facilities on runoff and outflow under the six return periods of 1a, 2a, 5a, 10a, 20a, and 50a, we find that LID measures have evident effects on runoff and outflow reduction. Still, they are greatly affected by the return period. The retention pond has no noticeable impact on runoff, but it reduces the peak value of outflow and is less affected by the return period. The combination of LID and retention pond can combine their advantages, reduce the peak flow rate of the site stably and relieve the pressure of the urban drainage system. This study provides a basis for the graded implementation of Sponge City, especially for community-scale rainwater regulation.

Keywords: Sponge City; urban community; stormwater management; SWMM; LID; retention pond

Citation: Jiang, Y.; Qiu, L.; Gao, T.; Zhang, S. Systematic Application of Sponge City Facilities at Community Scale Based on SWMM. *Water* **2022**, *14*, 591. https://doi.org/10.3390/w14040591

Academic Editors: Alban Kuriqi and Luis Garrote

Received: 19 January 2022
Accepted: 12 February 2022
Published: 15 February 2022

1. Introduction

Urban stormwater management has become a global problem. In the urbanization process, the increase of underlying impervious surfaces has brought water quality and quantity issues exacerbated by extreme rainfall events caused by climate change, complicating urban runoff management [1]. Many countries have taken measures to achieve sustainable stormwater management to deal with urban stormwater problems caused by urbanization. Since the 1970s, many developed countries, such as the United States, Germany, Japan, the United Kingdom, Australia, and other countries, have developed sustainable stormwater management ideas [2]. Some countries have proposed sustainable stormwater management measures, such as the sustainable urban drainage systems (SuDS) in the U.K. [3], the water sensitive urban design (WSUD) in Australia [4], the best management practices (BMPs), the low impact development (LID), and the green infrastructure (G.I.) in the United States [5]. Some countries have put forward regulations on stormwater management to promote the development of sustainable rainwater measures, such as the German Federal Water Act (Wasserhaushaltsgesetz, WHG) that came into force in 2010 (WHG 2009) [6], and the law for promoting rainwater utilization of Japan in 2014 [7]. In general, LID mainly refers to the small, decentralized facilities at the scale before access to municipal pipelines to address the insufficient capacity of traditional channels during heavy storms [8]. On the other hand, from the perspective of urban planning, such as controlling the water permeability of the underlying surface of the city [9], and from the perspective of technology, such as conveying the rainwater to large and deep stilling basins [10], also provide a new direction

for urban stormwater management. In recent years, EPA (U.S. Environmental Protection Agency) has tended to replace LID with G.I. [11]. At the same time, the WSUD in Australia coordinates the relationship between land use, multi-water cycle, and stormwater system from urban planning and urban design to improve urban elasticity.

Since the 1980s, China has experienced large-scale urbanization. In recent years, the problem of waterlogging appeared in Beijing, Wuhan, and other cities, which has got much social attention. How to protect urban water ecological security and improve the resilience and sustainability of the city has become a research hotspot in the relative professional field. To solve the problem of urban waterlogging and protect the safety of people's lives and property, the Chinese government put forward the concept of 'Sponge City' at the end of 2013. It officially launched this project at the end of 2014. The construction of Sponge City takes infiltration, stagnation, storage, purification, utilization, and emission as the "six-words" principle [12], hoping to adapt to climate change and reduce natural disasters through the combination of green infrastructure and gray infrastructure. Therefore, it pays attention to stormwater treatment and site measures and pays more attention to the regional water cycle process, which needs to design large-scale solutions and build undertaking and cooperation between different scales [13].

Since implementing the 'Sponge City' policy, Chinese scholars have made many explorations from the perspectives of hydraulics and hydrology [14], ecology [15], urban planning [16], urban drainage engineering [17], urban landscape [18], and application of materials [19]. Solving complex urban water problems and constructing a multi-objective modern urban stormwater system requires multi-professional collaboration that faces many obstacles and challenges [20]. Therefore, it is necessary to comprehensively recognize the urban ecological relationship and consider landing ecology to obtain the highest economic benefits at a nominal possible ecological cost [21]. Achieving this aim requires integrating urban flood risk assessment, land drainage guidance, climate forecasting methods, and long-term sustainability assessments [22]. The use of stormwater quantity models in simulated urban environments promotes this goal [23], such as SWMM, HEC-HMS, MIKE URBAN. As open-source software, SWMM is widely used for urban stormwater runoff simulation and drainage systems, watershed planning, water-sensitive urban design, and Sponge City construction [24]. At the urban or catchment scale, researchers use SWMM to estimate the surface runoff of urban secondary catchment and evaluate the effectiveness of the urban drainage system [25], or combine with ArcGIS to build an urban waterlogging model for urban waterlogging risk assessment [26]. Other studies have focused on specific projects, such as Sponge City renovation, a residential area [27], an urban road [28], or a waterlogging site [29]. On a smaller scale, SWMM is used to evaluate the effectiveness of single or combined LID measures such as green roofs [30], grassed swales, and permeable pavement [31].

Since the urban water ecological problems are complex, it is necessary to protect the hydrological pattern of the city and improve the efficiency of the regional hydrological cycle in the stage of comprehensive urban planning. Therefore, to relieve the pressure of the urban drainage system and optimize urban stormwater management, it requires systematic planning in the process of the Sponge City construction, including overall planning at the urban scale, comprehensive regulation, and storage at the community scale, and source control at the residential scale. However, most existing studies only focus on one scale [9,24–29] and lack systematic research on two or more scales. To address this shortcoming of previous studies, this study creatively takes the urban community as the research object. This study discusses how to coordinate the source control of a single project and the overall regulation and storage of the community to realize the systematization of the Sponge City construction of urban community.

Taking the Airport Garden Community as an example, this study explores methods of realizing systematic allocation of Sponge City at the community scale to relieve the pressure of the urban drainage system and improve the city's resilience. Using the advantages of the SWMM model in runoff generation and concentration calculation, drainage system

simulation, and LID measures simulation, combining its geographical conditions and functional configuration, the runoff and outfall flow of this community under different scenarios of the layout of facilities in Sponge City are simulated to provide a basis for community-scale Sponge City system construction.

2. Materials and Methods

2.1. Study Area

The Airport Garden Community, located in Xixian New Area of Shaanxi Province, China, between Xi'an City and Xianyang City, is a national development zone and one of China's first Sponge City pilot areas. Under the combined action of atmospheric circulation and topography, this region is hot and rainy in summer and cold and dry in winter. According to the statistical analysis of the maximum daily rainfall from 1960 to 2014 and the monthly average rainfall from 1981 to 2010 recorded by the national benchmark weather station in Qindu District, the annual average rainfall in this area is about 520 mm, of which the rainfall from July to September accounts for 50% of the yearly rainfall. Most of the heavy rain (daily precipitation of 25.0–49.9 mm) and rainstorms (daily precipitation of 50.00–99.9 mm) occurred during this period, which is very easy to cause natural disasters such as floods and soil erosion [32].

The total area of the study area is 54.5 hectares. Located on the loess plateau and in the north of Weihe riverbank, the terrain of the study area is flat, and the overall slope is less than 1%. According to the actual needs of this study, we selected four street areas and four roads connected with them as the research object. The overall terrain of the chosen area is high in the northwest and low in the southeast, including four independent residential areas, a commercial service area, a community service center, a primary school, two kindergartens, and a community park (Figure 1a). The park, located in the south of the community, is an essential prerequisite for undertaking the community's stormwater and flood regulation and storage function. Before development, the land use of the study area was farmland with good hydrological conditions. After completion, the drainage in the site is a separate system that only one of the four blocks and their surrounding facilities introduced LID application, in response to the requirements of Sponge City construction, and other projects, including the park, have adopted traditional gray infrastructure. Therefore, the focus of this study is to reconstruct the local LID facilities combined with the original stormwater pipe network in the study area and how to introduce the regulation and storage tank in the community park to improve the overall elasticity of the community.

2.2. Rainfall Scenario

The rainstorm intensity formula is an essential basic model for rainstorm disaster management. It is a necessary basis for the urban rainwater drainage network design and directly relates to the reliability of urban drainage works [33]. According to The Technical Guide for Sponge City Construction in Xixian New Area, the rainstorm intensity formula in this area is [34]:

$$i = \frac{16.715(1 + 1.16581\lg P)}{(t + 16.813)^{0.9302}}, \quad (1)$$

where i is the average rainfall intensity (mm/min), P is the return period of design rainfall (a); t is the rainfall duration (min). In this study, the Rain-Model-Chicago (Version 2.06) was used to calculate the rainfall time series by rainstorm intensity formula, return period (1a, 2a, 5a, 10a, 20a, and 50a), rainfall duration (t = 120 min), and the time-to-peak ratio r (0.35 [35]). Table 1 shows the design rainfall for different return periods.

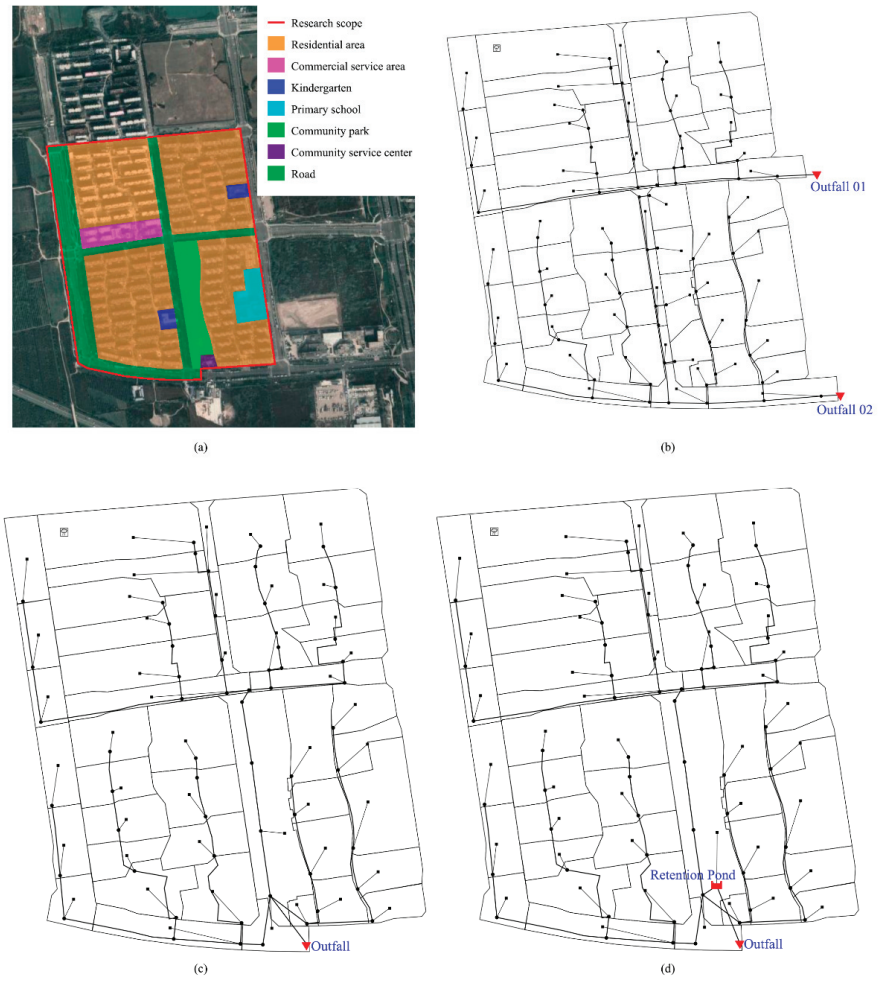

Figure 1. The situation in the study area: (**a**) Overview of the study area (base map from Google Earth); (**b**) The drainage system before the adjustment; (**c**) The drainage system after the adjustment; (**d**) The drainage system including a retention pond.

Table 1. The design rainfall for different return periods.

Return Periods	Rainfall (mm)
1a	20.75
2a	28.03
5a	37.65
10a	44.93
20a	52.21
50a	61.84

2.3. Establishment of the Model

In this study, the drainage network generalization and sub-catchments division is based on the adjusted data to drain more rainwater through the community park. According to the elevation difference of the community, the original drainage design principle is to discharge the rainwater in every block into the drainage network of the nearby road

in the south. This rainwater flows out of the community from west to east along the road stormwater pipeline, forming two outlets in the east of the community (Figure 1b). After the adjustment, we changed the flow direction of some road drainage pipes and took the community park as the main drainage channel. All rainwater in the community flows into the drainage pipes under the community park and then flows out the community from the outlet on the south of the site (Figure 1c). The purpose is to discharge the rainwater into the retention pond in the community park (Figure 1d). That is a more suitable design for the current situation than the existing drainage system in this community.

The sub-catchment areas are divided according to the drainage organization. The pipe network distribution of the site and the drainage network generalization are based on the pipe diameter and slope of the pipe and the branches of the pipe network. Pipe network generalization and sub-catchment division are completed in AutoCAD 2017. The CAD file is exported as a SWMM (Version 5.1.015) model file (.inp) with HS-data (Version 1.2.51) (a CAD plug-in developed by Huishui Technology). The pipe network in the study area is generalized into 58 nodes (57 junctions and one outfall), 57 conduits, and 45 sub-catchments (Figure 1c).

In the AutoCAD, we calculated the area, width of the overland flow path, average surface slope, and percent of impervious area of every sub-catchment, obtained the elevation of junction's invert and maximum water depth of the nodes, the maximum depth of cross-section, and length of the conduit, inlet offset, and outlet offset. Each junction is a rainwater manhole, so the maximum water depth of a node is the depth of the manhole. Since the drains of all projects in this study are circular pipes, the maximum depth of the cross-section of a link is the inner diameter of these pipes. The value of each link's inlet and outlet offset is the altitude difference between the bottom of both ends of the pipeline and the bottom of the manhole at the corresponding locations. The above values can determine the node water storage and the flow of rainwater in the drains. According to the drawing of the projects, the stormwater pipes with a diameter less than 1 m are PVC pipes, and their Manning coefficient is 0.009. The stormwater pipe with a diameter greater than or equal to 1 m is made of concrete, and its Manning coefficient is 0.013. All the above parameters are input into the SWMM model after calculation. According to the previous research results and the characteristics of the study area, the dynamic wave is selected for the flowing routing within a conduit, and Horton's method is used to calculate surface runoff. The parameters of Horton method, Mannings N and Depth of Depression Storage are listed in Table 2.

Table 2. The parameters of Horton method, Mannings N and Depth of Depression Storage.

Name	Property	Value
Horton Parameters	Max. Infil. Rate	76.2
	Min. Infil. Rate	3.81
	Decay Constant	2
	Drying Time	7
	Max. Volume	0
Mannings N *	Mannings N for the impervious area	0.015
	Mannings N for the pervious area	0.21
Depth of Depression Storage *	Depth of depression storage on the impervious area (mm)	2.3
	Depth of depression storage on the pervious area (mm)	3.81

* The values of Mannings N and Depth of Depression Storage are determined according to former studies with cases in Xi'an and Xianyang [35–47]. Mannings N for the impervious area, Mannings N for the pervious area, and Depth of Depression Storage on the impervious area are the average value of these studies [35–47], since these three parameters are inconsistent. Depth of Depression Storage in the pervious area is also based on former studies [44,46].

2.4. Set Simulation Scene

The realization of Sponge City at the community level includes two-level measures: adopting LID measures for source reduction in a single project and using existing conditions in the community to store. To study the role of these two-level measures in stormwater

management, four scenarios were designed in this study: (1) no Sponge City infrastructure in the study area (noted as scenario 1), (2) LID infrastructures in each block and on the roads for source control (noted as scenario 2), (3) no LID infrastructure, and a 5199.3 m^3 retention pond in the community park (noted as scenario 3), (4) LID infrastructure in each project and on roads, and a 4592.7 m^3 retention pond in community park (noted as scenario 4).

On the residential scale, LID measures, which are most commonly used locally, have been selected to modify projects in the site, such as the bio-retention cell, permeable pavement, and vegetation swale. In the scenario without LID measures, runoff from impervious and pervious areas flows directly to the outlet. In the scenario with LID measures, runoff from impervious flows to the pervious area. For the municipal roads with green belt in the center or on both sides, the rainwater is discharged into the bio-retention cell in the green belt and then overflowed. In each block, the rainwater from roofs and green spaces flows into the bio-retention cells, the rainwater from roads and squares flows into the vegetation swales, and the parking spaces and the pavements are transformed into a permeable surface (Figure 2). The bio-retention cells and the vegetative swales areas were correlated with the green land area, accounting for 15% and 25% of the total green land area, respectively. The LID controls module in the SWMM model is applied to the effect evaluation of LID measures. The parameters we used are in Table 3.

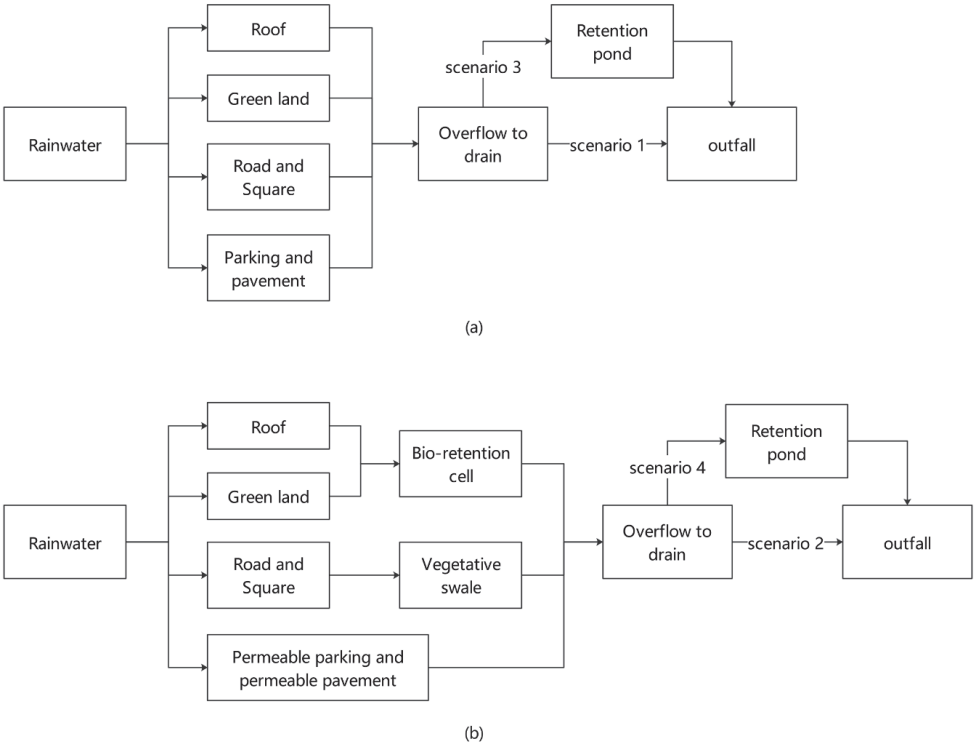

Figure 2. Drainage path in the blocks under different scenarios: (**a**) The drainage path without LID measures; (**b**) The drainage path with LID measures.

Table 3. Parameters of LID measures.

Layer	Parameter	Bio-Retention Cell in Residential Areas	Bio-Retention Cell on Roads	Permeable Pavement	Vegetative Swale
Surface	Berm height (mm)	200	300	0	300
	Vegetation volume fraction	0.2	0.2	0	0.2
	Surface roughness	0.15	0.15	0.013	0.15
	Surface slope (%)	1	1	1	1
	Swale side slope				50
Pavement	Thickness (mm)			100	
	Void ratio (voids/solids)			0.15	
	Impervious surface fraction			0	
	Permeability (mm/h)			360	
	Clogging factor			187.5	
Soil	Thickness (mm)	500	600		
	Porosity	0.43	0.43		
	Field capacity	0.321	0.321		
	Wilting point	0.221	0.221		
	Conductivity (mm/h)	100	100		
	Conductivity slope	10	10		
	Suction head (mm)	90	90		
Storage	Thickness (mm)	300	450	400	
	Void ratio (voids/solids)	0.75	0.75	0.75	
	Seepage rate (mm/h)	250	300	400	
	Clogging factor	0	0		
Drain	Flow coefficient (mm/h, use 0 if there is no drain)	0	20	0	
	Flow exponent		0.5		
	Offset (mm)		0		

At the community level, a retention pond is used to collect rainwater to prevent flooding and erosion. The retention pond is a landscape water body that can combine with green space in the park and other open urban areas, and take the stormwater as the primary water source to make up water. It has the function of stormwater storage and purification and can beautify the landscape and provide a resting place for residents. This study set the retention pond in a community park with a relatively low location in combination with the topography and landform of the community. The rainwater in the community enters the pond and is discharged when the water level reaches a certain height. The storage unites modules expressed in the parameters of the retention pond in the community park. The volume of the retention pond is determined by the volumetric method, and the formula is as follows:

$$V = 10H\varphi F, \quad (2)$$

where H is the design rainfall (mm), φ is the rainfall comprehensive runoff coefficient, F is the catchment area (hm^2). According to the overall goal of the Sponge City construction in the Xixian New Area, the total annual runoff control rate in this area should be 80%, corresponding to 15.9 mm as the design rainfall, which is daily rainfall coming from the statistical data of local multi-year data. According to the Technical Guide for Sponge City Construction (Trial), the comprehensive rainfall-runoff coefficient is calculated by the weighted average method. After calculation, φ is 0.60 when there are no LID measures in the community, and 0.53 when the LID measures are set; the corresponding storage volume is 5199.3 m^3 and 4592.7 m^3, respectively. The storage units in SWMM simulated the operation of the retention pond. However, it has some limitations because it can simulate the water storage capacity of the retention pond and ignores its infiltration capacity.

SWMM simulated the runoff and the outflow of each scenario in the return periods of 1a, 2a, 5a, 10a, 20a, 50a, respectively, and scenario 1 was used as the control group to compare and analyze the runoff generation and outflow of each scenario in different return periods. In the simulation, the rainfall duration is 120 min and the base time of runoff concentration is 240 min.

3. Results and Discussion

3.1. Effect Evaluation of LID Measures and Retention Pond

LID measures can delay the time of runoff generation and reduce runoff peak value and surface runoff, while the retention pond has little effect on runoff (Figure 3).

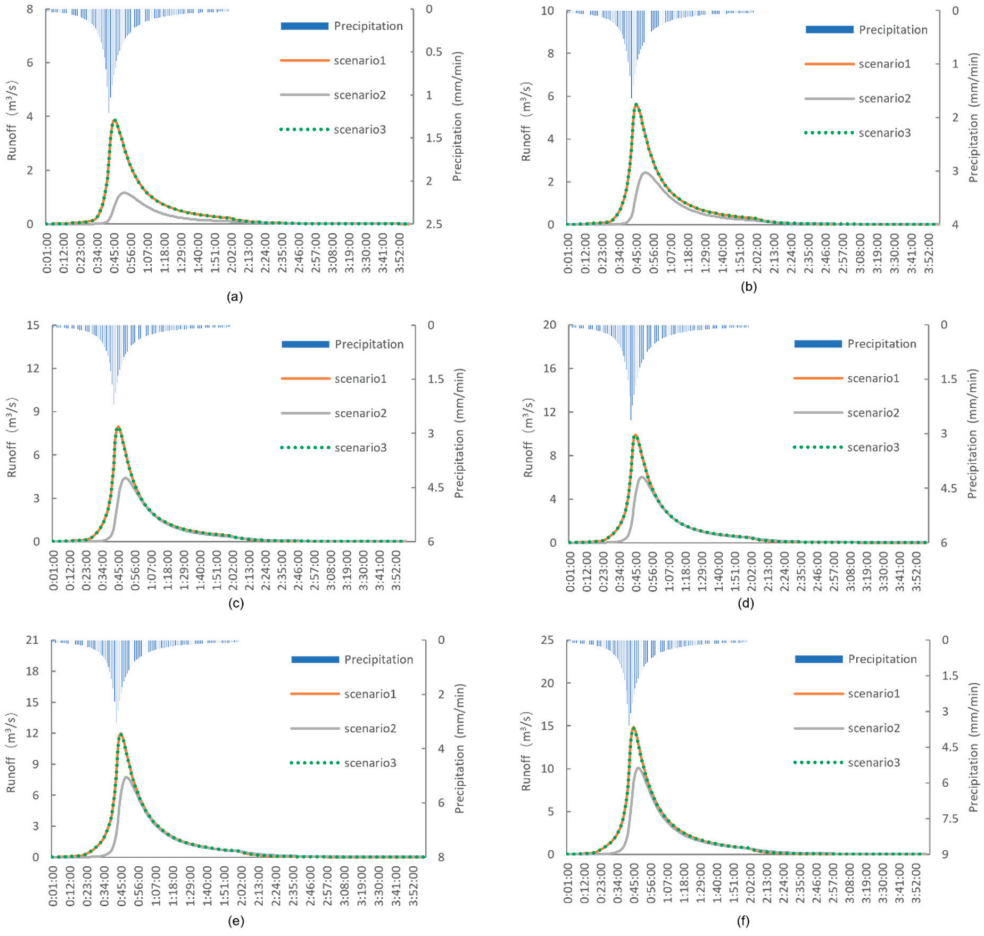

Figure 3. Runoff control effect under different return periods: (**a**) When return period is 1a; (**b**) When return period is 2a; (**c**) When return period is 5a; (**d**) When return period is 10a; (**e**) When return period is 20a; (**f**) When return period is 50a.

In scenario 2 with LID measures, the occurrence time of runoff under six return periods (1a, 2a, 5a, 10a, 20a, 50a) was delayed by 27 min, 24 min, 21 min, 19 min, 17 min, and 15 min, respectively. With the increase of the return period, the surface runoff depth reduced by LID measures was 61.6%, 44.5%, 31.5%, 27.0%, 25.2%, 24.3%, and the peak value of runoff decreased by 69.9%, 56.5%, 44.7%, 39.1%, 35.3%, 31.9%, respectively. The occurrence time of peak runoff was delayed by 6 min, 6 min, 5 min, 4 min, 4 min, and 3 min. LID measures can well reduce the surface runoff and reduce the peak runoff, and delay the generation time of runoff and the peak runoff. However, with the increase of the return period, the ability of LID measures to reduce runoff will be weakened when it reaches saturation. When the return period is 1a and 2a, the runoff of scenario 2 is less than that of scenario 1 (Figure 3a,b) for almost all the production time. Still, when the return period is greater than or equal to

5a, the curves of scenario 2 and scenario 1 gradually coincides after their respective peak (Figure 3c–f). It shows that the effect of LID measures on rainfall storage will decrease with the rise of rainfall intensity. When the return period is about 5a, the capability of LID measures is close to saturation.

Both LID measures and retention ponds can reduce total outflow, reduce peak outflow, and delay the outflow time and the peak outflow time (Figure 4). At the return periods of 1a, 2a, 5a, 10a, 20a, 50a, LID measures can delay the outflow time by 20 min, 20 min, 20 min, 19 min, 18 min, and 17 min, while the outflow time by the retention pond is delayed by 24 min, 24 min, 24 min, 23 min, 22 min, and 21 min. With the return period from low to high, LID measures postponed the peak outflow by 7 min, 7 min, 7 min, 6 min, 6 min, and 4 min, and the peak outflow time by the retention pond was postponed by 8 min, 9 min, 11 min, 12 min, 14 min, and 18 min. Both LID measures and retention ponds can effectively delay the outflow time and peak outflow time, and the regulating effect of the retention pond is better than LID measures. Especially in the regulation of peak outflow time, the retention pond can better postpone peak outflow time with the increase of the return period.

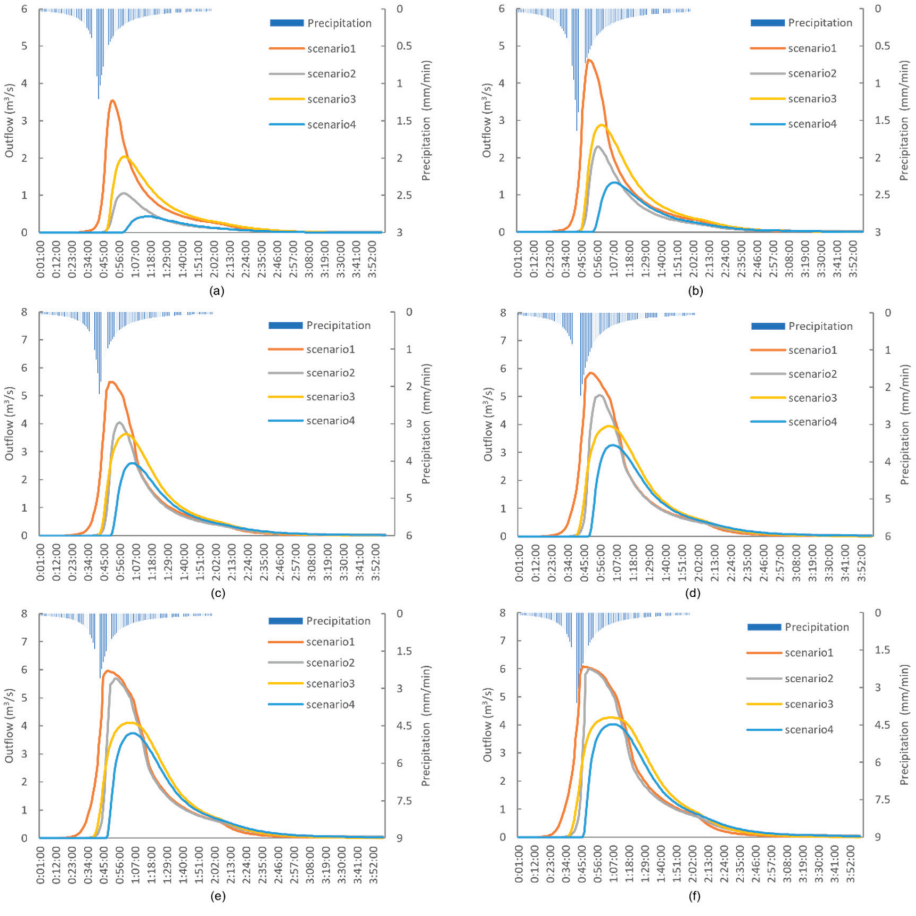

Figure 4. Outflow control effect under different return periods: (**a**) When return period is 1a; (**b**) When return period is 2a; (**c**) When return period is 5a; (**d**) When return period is 10a; (**e**) When return period is 20a; (**f**) When return period is 50a.

The effects of LID measures and retention pond are significantly different in total outflow and peak outflow. Although both of them will decrease with the increase of return period, the reduction of LID measures is much faster than that of the retention pond, and the regulating effect of the retention pond is relatively stable. When the return period is 1a, LID measures can reduce 61.9% of the total outflow, while the retention pond can only reduce 19.8%. LID measures reduced the peak flow by 70.3% at the same return period, while the retention pond was 42.6%. When the return period is 2a, the capability of LID measures is still better than that of the retention pond. However, when the return period is greater than or equal to 5a, the curve of scenario 2 and scenario 1 tends to coincide after the peak flow is reached. After the return period is more than 20a, the peak flow of scenario 2 is close to scenario 1. When the return period is 50a, LID measures can reduce 14.6% of total outflow and 1.3% of peak outflow, while the retention pond can reduce 14.0% of the total outflow and 30.0% of peak outflow.

LID measures improve the infiltration rate of stormwater by increasing the permeable area, and retaining and purifying some stormwater through the bio-retention cells and the vegetation swales. Therefore, LID measures can significantly reduce surface runoff and delay the generation time of runoff peak, thus reducing the total outflow and peak outflow, which better reduces the source. However, when the LID measures are close to saturation, its retention capacity to rainfall decreases significantly, so the adjustment ability of LID measures is limited in high-intensity rainfall.

The retention pond is set before the outlet, which is the secondary regulation of rainwater in the site. Its regulating effect results from the comprehensive influence of the cross-section of the pond, the elevation of inlet and outlet, and the pipe diameter of inlet and outlet. Although the retention pond will not affect the runoff, it can reduce the total outflow and the peak outflow steadily, and delay the outflow time and peak outflow time. The retention pond can further postpone the peak outflow time even in high return period scenarios. Setting the retention pond in the parks at the low point of the community can regulate rainwater, enrich the regional landscape, and increase landscape diversity.

3.2. Effect Evaluation of Comprehensive Measures

Since the retention pond cannot affect the runoff, the runoff curves of scenario 4 with both LID measures and retention, and scenario 2 with only LID measures coincide. However, under the combined action of LID measures and retention pond, the regulating ability of scenario 4 to outflow is further improved. Specifically, compared with scenario 2 and scenario 3, in scenario 4, the outflow time and peak outflow time are further delayed, and the total outflow and peak outflow are further reduced (Figure 4). When the return period is 1a, 2a, 5a, 10a, 20a, and 50a, the outflow time is delayed by 34 min, 33 min, 33 min, 32 min, 32 min, and 31 min, and the total reduction rate of outflow is 79.1%, 58.7%, 41.0%, 33.4%, 29.2%, and 27.1%, far exceeding the adjustment effect of using LID measures or retention pond. In terms of peak flow, with the increase of return period, scenario 4 postpones peak outflow time by 23 min, 17 min, 15 min, 15 min, 17 min, and 20 min, with the reduction rates of 87.6%, 71.2%, 52.9%, 44.1%, and 33.9%, respectively (Table 4). It can be seen that scenario 4 with LID measures and retention pond can reduce the peak value of outflow under different return periods. In terms of time adjustment of outflow peak, due to the combined effect of LID measures and retention pond, the delay of peak outflow time will decrease first and then rise later with the increase of return period. Even in the higher return periods, the peak time occurs later, so the comprehensive measures used in scenario 4 can better reduce the peak outflow and further postpone the peak outflow time, and relieve the overall pressure of the urban pipeline network. Compared with the single measures, the combined LID measures and the retention pond have a better impact on runoff and outflow.

Table 4. The simulation of outfall in different scenarios.

Return Period	Simulated Scenario	Hour of Outflow Generation	Peak Outflow (CMS)	Hour of Max. Outflow	Total Outflow Volume (10^6 L)
1a	scenario 1	0:24:00	3.544	0:52:00	6.101
	scenario 2	0:44:00	1.053	0:59:00	2.326
	scenario 3	0:48:00	2.036	1:00:00	4.89
	scenario 4	0:59:00	0.44	1:15:00	1.276
2a	scenario 1	0:21:00	4.63	0:50:00	8.493
	scenario 2	0:41:00	2.3	0:57:00	4.727
	scenario 3	0:45:00	2.882	0:59:00	7.045
	scenario 4	0:54:00	1.334	1:07:00	3.508
5a	scenario 1	0:18:00	5.5	0:49:00	11.465
	scenario 2	0:38:00	4.036	0:56:00	8.186
	scenario 3	0:42:00	3.63	1:00:00	9.703
	scenario 4	0:51:00	2.591	1:04:00	6.762
10a	scenario 1	0:17:00	5.844	0:49:00	13.56
	scenario 2	0:36:00	5.048	0:55:00	10.774
	scenario 3	0:40:00	3.935	1:01:00	11.547
	scenario 4	0:49:00	3.264	1:04:00	9.031
20a	scenario 1	0:16:00	5.966	0:48:00	15.568
	scenario 2	0:34:00	5.693	0:54:00	13.034
	scenario 3	0:38:00	4.115	1:02:00	13.328
	scenario 4	0:48:00	3.741	1:05:00	11.02
50a	scenario 1	0:15:00	6.089	0:46:00	18.035
	scenario 2	0:32:00	6.011	0:50:00	15.405
	scenario 3	0:36:00	4.26	1:04:00	15.504
	scenario 4	0:46:00	4.024	1:06:00	13.139

4. Conclusions

Since the city is a complex system, the construction and implementation of Sponge City needs to comprehensively consider the effects of the drainage system, the road system, the green space system, the urban geomorphic features, and the water network in the city, etc. More precise and site-specific guidelines are necessary for guiding Sponge City construction in China from local scale, i.e., a residential area; to mesoscale, i.e., a community; to macroscale, i.e., a city.

So far, there are many studies that take a city [9,25,26,35,36], or a district [24,38,41,45], or a single project, i.e., a residential quarter [27,32], a university [14,37,47], or a road [29] as the research objects. However, most of these studies lack systemic measures since they all take a single scale as their research perspective. Furthermore, in studies of urban communities or some local areas, a single block is mostly generalized as a sub-catchment area, and its parameters are set according to their land-use type, which is difficult to meet the diversified needs of Sponge City construction in different regions. For example, in these studies, residential land is often given the same parameter setting; however, the actual runoff and the flow discharging into the drainage network in each residential land are different, determined by the floor area ratio and the greening rate. These neglected differences will have a significant impact on the simulation results. This study has fully considered the characteristics of each block and refined the sub-catchments and drainage networks in the block, which can make the research results closer to reality.

Taking the Airport Garden community as our research area, this study discussed the systematic application of the Sponge City facilities on the community scale. After the reconstruction of the community's current drainage system, the community's SWMM model is established. It should emphasize that if we completely redesign, our transformation scheme may be unrealistic, but as an adjustment to the current situation, this scheme is

more implementable and suitable. Subsequently, the LID measures and a retention pond are applied to the community. The LID measures are applied to each independent residential area and the supporting projects in the community. The retention pond is set before the rainwater outlet of the community to realize further regulation and storage.

The simulation results show that LID measures significantly reduce the source of runoff. However, with the increase of the return period, LID measures tend to be saturated, and the effect of flow regulation decreases significantly. It is difficult to relieve the pressure of the urban drainage network in the high return period. This result is consistent with previous studies [28,32,35,48,49]. Although the retention pond cannot regulate runoff, it can regulate the rainwater to reduce the total outflow and the peak outflow, delay the time of peak outflow, and relieve the overall pressure of the city pipeline network. Although the infiltration function of the retention pond is not considered due to software limitations, this has a weak impact on this study due to the limitation of collapsible loess. However, combining the two can exert their respective advantages and make the community rainwater drainage system more stable and efficient, thus achieving the expected effect of Sponge City construction. Therefore, the research results are of reference value to Sponge City construction in Northern China.

Author Contributions: Funding acquisition, S.Z.; project administration, T.G.; writing—original draft, Y.J.; writing—review and editing, L.Q. All authors have read and agreed to the published version of the manuscript.

Funding: This research was funded by 245 Qinling National Forest Ecosystem Research Station in 2021 financed by the Ministry of Education of China and Ministry of Education of China, grant number 19XJCAH001. The APC was funded by 245 Qinling National Forest Ecosystem Research Station in 2021 financed by the Ministry of Ed-ucation of China.

Institutional Review Board Statement: Not applicable.

Informed Consent Statement: Not applicable.

Data Availability Statement: Data sharing not applicable.

Conflicts of Interest: The authors declare no conflict of interest.

Abbreviations

BMPs	best management practices
CAD	Computer Aided Design
EPA	U.S. Environmental Protection Agency
G.I.	green infrastructure
HEC-HMS	Hydrologic Modeling System
LID	low-impact development
SuDS	sustainable urban drainage systems
SWMM	stormwater management model
WHG	German Federal Water Act
WSUD	water sensitive urban design

References

1. Carlson, C.; Barreteau, O.; Kirshen, P.; Foltz, K. Survey to understand perspectives of low-Impact development for urban storm water management practices under climate change. *J. Water Resour. Plan. Manag.* **2015**, *141*, 4014080. [CrossRef]
2. Che, S.Q.; Xie, C.K.; Chen, D.; Yu, B.Q. Development and constructive approaches for theories and technologies of Sponge City system. *Chin. Landsc. Archit.* **2015**, *31*, 11–15.
3. Melville-Shreeve, P.; Cotterill, S.; Grant, L.; Arahuetes, A.; Stovin, V.; Farmani, R.; Butler, D. State of SuDS delivery in the United Kingdom. *Water Environ. J.* **2018**, *32*, 9–16. [CrossRef]
4. Lloyd, S.D.; Wong, T.H.F.; Chesterfield, C.J. *Water Sensitive Urban Design—A Stormwater Management Perspective*; Cooperative Research Centre for Catchment Hydrology Centre Office: Melbourne, Australia, 2002.
5. Benedict, M.A.; McMahon, E.T. *Green Infrastructure: Linking Landscapes and Communities*; Island Press: Washington, DC, USA, 2006.

6. Walsh, C.J.; Booth, D.B.; Burns, M.J.; Fletcher, T.D.; Hale, R.L.; Hoang, L.N.; Livingston, G.; Rippy, M.A.; Roy, A.H.; Scoggins, M.; et al. Principles for urban stormwater management to protect stream ecosystems. *Freshw. Sci.* **2016**, *35*, 398–411. [CrossRef]
7. Chang, N.B.; Lu, J.W.; Chui, T.F.M.; Hartshorn, N. Global policy analysis of low impact development for stormwater management in urban regions. *Land Use Policy* **2018**, *70*, 368–383. [CrossRef]
8. Che, W.; Zhao, Y.; Li, J.Q.; Wang, W.L.; Wang, J.L.; Wang, S.S.; Gong, Y.W. Explanation of Sponge City development technical guide: Basic concepts and comprehensive goals. *China Water Wastewater* **2015**, *31*, 1–5.
9. Liu, Y.J.; Zhou, Y.; Yu, J.N.; Li, P.C.; Yang, L.Q. Green space optimization strategy to prevent urban flood risk in the city centre of Wuhan. *Water* **2021**, *13*, 1517. [CrossRef]
10. Crispino, G.; Contestabile, P.; Vicinanza, D.; Gisonni, C. Energy head dissipation and flow pressures in vortex drop shafts. *Water* **2021**, *13*, 165. [CrossRef]
11. Che, W.; Yan, P.; Zhao, Y.; Tian, F. Development and analysis of international updated stormwater management systems. *China Water Wastewater* **2014**, *30*, 45–51.
12. Jia, H.F.; Wang, Z.; Zhen, X.Y.; Clar, M.; Yu, S.L. China's sponge city construction: A discussion on technical approaches. *Front. Environ. Sci. Eng.* **2017**, *11*, 18. [CrossRef]
13. Yu, K.J.; LI, D.H.; Yuan, H.; Fu, W.; Qiao, Q.; Wang, S.S. "Sponge City": Theory and practice. *City Plan. Rev.* **2015**, *39*, 26–36.
14. Peng, G.Q. Modelling and Simulation of a Heterogeneous Feature-Based Integrated Hydraulic Model for the Processes of Urban Flooding. Doctoral Dissertation, Nanjing Normal Universtiy, Nanjing, China, 2019.
15. Gong, Y.X.; Cheng, S.S.; Ji, X. Sponge city construction in Xuzhou City from the perspective of ecological security pattern. *J. Fujian Norm. Univ. Nat. Sci. Ed.* **2020**, *36*, 79–89.
16. Yue, B.; Zhuo, X.; Gao, H.G. Summary and outlook of sponge city planning, Sichuan. *Planners* **2017**, *33*, 77–84.
17. Ke, Q.; Wang, L.S.; Tao, T. Resilience assessment of urban rainwater drainage systems. *China Water Wastewater* **2016**, *32*, 6–11.
18. Chen, X.F. Based on biological diversity to explore the design method of sponge urban landscape. *Ecol. Econ.* **2015**, *31*, 194–199.
19. Liang, H.H.; Chen, S.; Zhao, B.; Zhong, Y.T.; Ma, W.J.; Li, Y. A comparative study on inundation tolerance of 7 shrub seedlings under waterlogging stress. *J. Northwest For. Univ.* **2020**, *35*, 61–67.
20. Li, J.Q.; Ren, Y.Z.; Nie, A.H.; Li, X.N.; Gong, Y.W. Sponge city: Cross-disciplinary planning. *Planners* **2016**, *32*, 5–9.
21. Zhai, B.H. Ecological thinking from "Urban Waterlogging" to "Sponge City". *Acta Ecol. Sin.* **2016**, *36*, 4949–4951.
22. Chan, F.K.S.; Griffiths, J.A.; Higgitt, D.; Xu, S.Y.; Zhu, F.F.; Tang, Y.T.; Xu, Y.Y.; Thorne, C.R. "Sponge City" in China—A breakthrough of planning and flood risk management in the urban context. *Land Use Policy* **2018**, *76*, 772–778. [CrossRef]
23. Zoppou, C. Review of urban storm water models. *Environ. Model. Softw.* **2001**, *16*, 195–231. [CrossRef]
24. Kim, H.; Jung, M.; Mallari, K.J.B.; Pak, G.; Kim, S.; Kim, S.; Kim, L.; Yoon, J. Assessment of porous pavement effectiveness on runoff reduction under climate change scenarios. *Desalin. Water Treat.* **2015**, *53*, 3142–3147. [CrossRef]
25. Babaei, S.; Ghazavi, R.; Erfanian, M. Urban flood simulation and prioritization of critical urban sub-catchments using SWMM model and PROMETHEE II approach. *Phys. Chem. Earth* **2018**, *105*, 3–11. [CrossRef]
26. Zhang, J. Research of Rainstorm Water Logging of Zhengzhou City Based on GIS and SWMM. Master's Thesis, Zhengzhou University, Zhengzhou, China, 2012.
27. Zhang, Q.; Su, B.L.; Yuan, J.Y. Simulating rainfall—Runoff in urban residential area based on SWMM. *J. Beijing Norm. Univ. Sci.* **2012**, *48*, 276–281.
28. Hu, A.B.; Ren, X.X.; Pei, G.Z. Simulation of stormwater control effect of LID municipal road based on SWMM. *China Water Wastewater* **2015**, *31*, 130–133.
29. Kou, D.L.; Peng, T.; Liu, Q.L.; Zhao, J.; Liang, Y.H. Cause analysis and modification of waterlogging point in Xianhu Road of Nanning City based on SWMM. *China Water Wastewater* **2018**, *34*, 136–138.
30. Hamouz, V.; Muthanna, T.M. Hydrological modelling of green and grey roofs in cold climate with the SWMM model. *J. Environ. Manag.* **2019**, *249*, 109350. [CrossRef] [PubMed]
31. Xie, J.G.; Wu, C.H.; Li, H.; Chen, G.T. Study on storm-water management of grassed swales and permeable pavement based on SWMM. *Water* **2017**, *9*, 840. [CrossRef]
32. Liu, X.Y.; Jiang, Y.; Ding, X.H.; Zhang, S.X. Evaluation and optimization of low impact development in residential district. *J. Northwest For. Univ.* **2021**, *36*, 266–274.
33. Liu, J.; Zhou, H.; Lu, C.H.; Gao, C. A review on recent advances of urban rainfall intensity-duration-frequency relationships. *Adv. Water Sci.* **2018**, *29*, 898–910.
34. Ma, Y.; Ji, G.Q.; Shi, Z.H.; Ma, X. Reconstruction of rainwater system for low impact development of Qinhuang Avenue in Fengxi new town, Xixian New Area. *Water Wastewater Eng.* **2017**, *53*, 59–67.
35. Ji, B.X. Xi'an Urban Rainwater Catchments Area Division and the Research of Runoff Characteristice Based on Swmm Model. Master's Thesis, Xi'an University of Technology, Xi'an, China, 2017.
36. Ma, L.J. Simulation of Hydrologic Effect of Low Impact Development of Fengxi New City in Xixian New Area Based on SWMM. Master's Thesis, Northwest University, Xi'an, China, 2016.
37. Zhang, T.Y. Research on the Application of Low Impact Development Facilities in Colleges Campus—The Case Analysis of Sponge Campus Construction in Xianyang Vocational Technical College. Master's Thesis, Xi'an University of Architecture and Technology, Xi'an, China, 2018.

38. Li, Y.J. Research on Pollution Control of Combined System Overflow in Old Urban Area of Xi'an Based on SWMM. Master's Thesis, Xi'an University of Technology, Xi'an, China, 2020.
39. Wang, S.R. Simulation of Rainfall Runoff Based on SWMM and Analysis of LID Combination Scheme. Master's Thesis, Xi'an University of Technology, Xi'an, China, 2020.
40. Qu, C. Study on Rainwater Infiltration Efficiency and SWMM Model Simulation of Sunken Green Space and Permeable Pavement—A Case Study of Chang'an Campus in Northwest University. Master's Thesis, Northwest University, Xi'an, China, 2017.
41. Hao, M.Q. Research on the Prevention Technology of Urban Waterlogging. Master's Thesis, Xi'an Technological University, Xi'an, China, 2017.
42. Han, H. Urban Rainstorm Waterlogging Simulation Research Based on Scenario Analysis. Master's Thesis, Xi'an University of Technology, Xi'an, China, 2017.
43. Xia, Z.J. Study on Rainwater Pipe Network with SWMM Model and Sponge City Concept. Master's Thesis, Chang'an University, Xi'an, China, 2017.
44. Deng, C.N. Simulation of Environmental Hydrological Effects of Urban LID in Different Spatial Scales. Master's Thesis, Xi'an University of Technology, Xi'an, China, 2018.
45. Su, H.L. Urban Rain Flood Simulation Research Based on SWMM Model—A Case Study of Xiaozhai District in Xi'an. Master's Thesis, Xi'an University of Technology, Xi'an, China, 2018.
46. Liu, L. Research on Response of LID Runoff Regulation to Rain Type. Master's Thesis, Xi'an University of Technology, Xi'an, China, 2018.
47. Li, J. Study on the Construction of Sponge City Based on SWMM in Collapsible Loess Area—An Example of a Campus in Xixian New Area. Master's Thesis, Chang'an University, Xi'an, China, 2018.
48. Bai, Y.; Zhao, N.; Zhang, R.; Zeng, X. Storm water management of low impact development in urban areas based on SWMM. *Water* **2018**, *11*, 33. [CrossRef]
49. Zhang, Q.; Chen, S.; Cai, S.; Liu, C. Simulation of LID measures combined with stormwater detention tank. *China Water Wastewater* **2018**, *34*, 134–138.

International Journal of
Environmental Research and Public Health

MDPI

Article

Attribution Assessment and Prediction of Runoff Change in the Han River Basin, China

Mengru Wei [1], Zhe Yuan [2,*], Jijun Xu [2], Mengqi Shi [3] and Xin Wen [1]

[1] College of Water Conservancy and Hydropower Engineering, Hohai University, Nanjing 210098, China; 201602010109@hhu.edu.cn (M.W.); njwenxin@163.com (X.W.)
[2] Changjiang River Scientific Research Institute, Changjiang Water Resources Commission of the Ministry of Water Resources of China, Wuhan 430010, China; xujijune@mail.crsri.cn
[3] College of Geomatic, Xi'an University of Science and Technology, Xi'an 710054, China; 20210061026@stu.xust.edu.cn
* Correspondence: yuanzhe@mail.crsri.cn; Tel.: +86-137-1656-5927

Abstract: The ecological environment and water resources of the Han River Basin (HRB) are incredibly susceptible to global warming. Naturally, the analysis of future runoff in HRB is believed to offer a theoretical basis for water resources management and ecological protection in HRB. The purpose of this study is to investigate and forecast the effects of climate change and land use change on runoff in the HRB. This study uses CMIP6 data to simulate three future climate change scenarios (SSP126, SSP245 and SSP585) for changes in precipitation and temperature, a CA-Markov model to simulate future land use change scenarios, and the Budyko framework to predict future runoff changes. The results show that: (1) Between 1974 and 2014, annual runoff (R) and annual precipitation (P) in the HRB decline not so significantly with a rate of 1.3673 mm/a and 1.2709 mm/a, while maximum temperature ($Tmax$) and minimum temperature ($Tmin$) and potential evapotranspiration (E_0) show a non-significantly increasing trend with 0.0296 °C/a, 0.0204 °C/a and 1.3313 mm/a, respectively. Precipitation is considered as main contributor to the decline in Han River runoff, accounting for 54.1%. (2) In the HRB, overall precipitation and temperature are estimated to rise in the coming years, with all other hydrological variables. The comparison of precipitation rise under each scenario is as follows: SSP126 scenario > SSP585 scenario > SSP245 scenario. The comparison of the temperature increase under each scenario is as follows: SSP585 scenario > SSP245 scenario > SSP126 scenario. (3) In the HRB, farmland and grassland land will continue to decline in the future. The amount of forest acreage is projected to decline but not so significantly. (4) The future runoff of the HRB shows an increasing trend, and the future runoff varies in different scenarios and periods. Under the land use scenarios of maintaining LUCC1992–2014 and LUCC2040 and LUCC2060, the R change rates in 2015–2040 are 8.27–25.47% and −8.04–19.35%, respectively, and the R in 2040–2060 are 2.09–13.66% and 19.35–31.52%. At the same time, it is very likely to overestimate the future runoff of the HRB without considering the changes in the land use data of the underlying surface in the future.

Keywords: Han River Basin; Budyko framework; runoff change; land use; cover change

Citation: Wei, M.; Yuan, Z.; Xu, J.; Shi, M.; Wen, X. Attribution Assessment and Prediction of Runoff Change in the Han River Basin, China. *Int. J. Environ. Res. Public Health* **2022**, *19*, 2393. https://doi.org/10.3390/ijerph19042393

Academic Editors: Alban Kuriqi and Luis Garrote

Received: 29 December 2021
Accepted: 16 February 2022
Published: 18 February 2022

1. Introduction

In recent years, global warming has swept through most parts of the world [1]. In some regions, climate change and human activities have induced substantial changes in land use/cover (LUCC), precipitation, and temperature, resulting in significant changes in watershed runoff over the years [2–5]. These changes may probably cause a wide range of natural, environmental, and economical destruction [6]. The spatial and temporal variability in runoff is an essential component of the hydrological cycle [7,8]. Therefore, it is crucial for regional water resources management and planning to analyze the response of watershed hydrology to LUCC changes caused by climate change and human activities, and to assess the impacts of climate change and land use on runoff and water cycle changes [9–11]. In

the context of a changing climatic environment, watershed ecohydrology research and watershed soil and water resources management are facing new challenges [12]. The challenge of predicting and responding to the effects of future climate change and human activities on water resources quantity and ecology in Han River Basin (HRB) of China is particularly prominent [13].

Climate change and LUCC change have essential impacts on precipitation and runoff processes [14,15]. In recent years, a great deal of research has been carried out in China on runoff prediction and attribution analysis in changeable environments [16,17]. There are many quantitative calculations about the contribution of runoff change, such as using the Budyko framework to calculate the elastic coefficient of each driving factor and quantitatively evaluate the contribution rate of climate change and human activities to runoff change [18]. In these studies, precipitation and potential evapotranspiration are the dominant factors influencing runoff, regardless of other factors affected by many watershed characteristics [19,20], such as vegetation and anthropogenic impacts, which have significant regional differences in their effects on runoff variability [21,22]. The current widely used method for predicting the runoff response to climate change is the hydrological model method [23–25], which mainly uses the global climate models (GCMs) model data input into the hydrological model for hydrological simulation [26,27]. Hydrological models can be essentially divided into Newtonian models and Darwinian models. The Darwinian model treats the hydrological system as a whole by identifying spatial and temporal correlations [28]. The Budyko hydrothermal coupling model is one of the Darwinian models. Usually, Budyko assumes that there is a coupled equilibrium relationship between water and energy in the watershed (called the hydrothermal equilibrium relationship) [29]. Therefore, the future runoff can be predicted through the Budyko water balance equation. In addition, its calculation is simple, the data input is small, and its physical meaning is clear. It is equivalent to other hydrological models under certain conditions. It has been widely used to analyze the impact of climate change on runoff for a long time and has been verified in many river basins. It has been widely used for the impact of climate change on runoff [30,31]. Therefore, the future runoff can be predicted through the Budyko water balance equation.

The Han River, China, is the source area of the South-North Water Diversion Project [32], and future changes in water resources in the HRB will directly affect the efficiency of the development and utilization of the South-North Water Diversion Project [33]. The Han River's middle and lower reaches, on the other hand, are hearty grain and cotton production centers in China [34]. Affected by global warming, the trend in annual extreme precipitation at the Han River stations has shown variable performance over the last 50 years [35], but the average annual runoff in the HRB shows a declining trend [36]. Form some experts' perspective, changes in land use in the HRB have a higher impact on runoff throughout the year than during flood season [37]. There have been some previous studies for runoff prediction in the HRB, however, the results are inconsistent due to discrepancies in study indicators, global climate model selection, and other factors. Changes in runoff are actually the result of multiple factors [38]. In previous studies on Budyko, an empirical link between the parameter n and vegetation attributes was created using the Budyko framework [18]. The Budyko parameter n, to a great extent, is influenced by many environmental factors besides vegetation traits (e.g., soil, geology, topography, etc.) [39]. Given these factors, we established an empirical relationship between the Budyko parameter and subsurface land use change, based on which future hydrological changes were predicted.

Therefore, the overall objectives of this study are: (1) analysis of historical hydrological variables in the HRB from 1974–2014, attribution analysis of runoff changes in the HRB using the Budyko framework, and exploration of the causes of runoff changes; (2) a future scenario of the HRB was constructed to establish a semi-empirical relationship between the Budyko parameter n and LUCC, and the Cellular Automata-Markov (CA-Markov) model was used to simulate the land use data in 2040 and 2060 under the current conditions and to calculate the parameter n under the future land use scenario; (3) three shared socioeconomic

pathway (SSP) scenarios (SSP126, SSP245, and SSP585) based on global climate models and the Budyko water balance method were used to predict future runoff. The overview of this paper is as follows: The materials and methods section introduces the Budyko theory, the bias correction method, and the CA-Markov model, and the results section presents the analysis of historical hydro-meteorological elements and attribution analysis, climate and land use change scenario setting, and future runoff prediction of the HRB. Then, the discussion and conclusion are presented in Sections 4 and 5.

2. Materials and Methods

2.1. Study Area

The basin is located within 106°15′~114°3′ E and 30°10′~34°20′ N with an area of about 159,000 km^2. The Han River, as the largest tributary of the Yangtze River, has a total length of 1577 km [26]. The basin's average yearly temperature is 12–16 °C, average yearly precipitation ranges from 600 to 1100 mm, decreasing from southeast to southwest to northwest, while average annual runoff depth in HRB ranges from 100 to 600 mm. The Han River has a subtropical monsoon climate and abundant water resources. The HRB's geography is high in the west and low in the east, high in the north and low in the south. The Qinling Mountains to the north and the Daba Mountains to the south define the rugged upper reaches; the Fuyu Mountains to the north, the Wudang Mountains to the south, and the Nanyang Basin to the center lead to the flat middle reaches [40]. The lower reaches of the Han River are the Jianghan Plain with its flat terrain. The basin's runoff is irregularly distributed throughout the year, with the majority concentrated from May and October, and there will be substantial inter-annual volatility, making it vulnerable to droughts and floods. Figure 1 depicts a schematic representation of the river system and a digital elevation model (DEM) of the HRB.

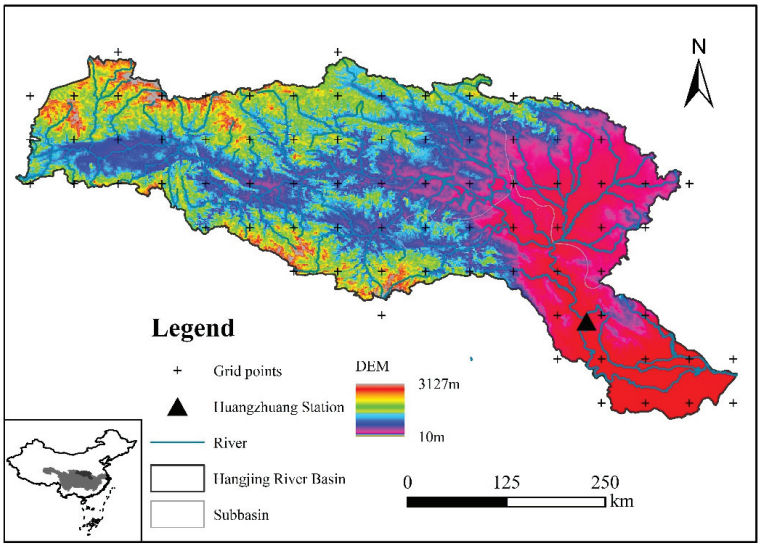

Figure 1. The geographical position of the HRB and meteorological grid points.

2.2. Variables and Data Sources

(1) Huangzhuang hydrological station is the primary control station for the lower sections of the Han River, its geographical location is shown in Figure 1. The Huangzhuang station runoff data utilized in this study were sourced from the Yangtze River Water Resources Commission's Hydrological Bureau (http://www.cjh.com.cn/, accessed on 2 March 2021).

(2) Precipitation and temperature data were obtained from the China Meteorological Science Data Sharing Service (CMSDSS). The 0.5° × 0.5° grid point dataset of daily surface precipitation values in China and the 0.5° × 0.5° grid point dataset of daily surface temperature values in China (http://data.cma.cn/, accessed on 4 January 2021) (1961–2020) were used in this study.

(3) LUCC data were obtained from the Environmental Science Data Centre of the Chinese Academy of Sciences land use remote sensing monitoring data with a resolution of 1 km in years 1980, 1990, 1995, 2000, 2005, 2010, and 2015 (http://www.resdc.cn/, accessed on 5 March 2021). Combined with the actual situation of the study area from 1980–2015, farmland, forestland, grassland, water, built, and unused land were identified as the six land uses in the research region. The DEM data were obtained at a resolution of 1 km from the Chinese Academy of Sciences' Environmental Science Data Centre (http://www.resdc.cn/, accessed on 5 March 2021), and the slope data were generated by processing the DEM with the ArcGIS10.8 toolbox Slope. Referring to the study of Yuan et al. [41], the relevant data were preprocessed in ArcGIS 10.8 software, converted to the same projection and unified at a resolution of 1 km.

(4) The grid data of the mean daily precipitation outputted from 5 global climate models (CanESM5, MRI-ESM2-0, IPSL-CM6A-LR, NESM3, KACE-1-0-G) of CMIP6(Coupled Model Intercomparison Project Phase (6) were used in this paper (https://esgf-node.llnl.gov/search/cmip6/, accessed on 30 May 2021). We have selected these five models to be able to simulate precipitation performance well [42], and provide complete daily climate data (including precipitation, maximum temperature, minimum temperature, etc.) for the future from 2015–2060. Climate models is shown in Table 1. Among the multiple scenarios provided by CMIP6, this study selected the historical (1961–2011) and three shared socioeconomic pathway scenarios (2015–2060): SSP126, SSP245, and SSP585, representing low, medium, and high emission forcing scenarios, respectively. Due to the low spatial resolution of the five selected climate models and the differences between the models, the spatial resolution of all models was standardized to 0.5° × 0.5° using inverse distance weight interpolation, and the interpolated model data were corrected for bias on each grid, the time scale chosen for bias correction in this study is 1961–2011.

Table 1. Basic information on the five global climate models in CMIP6.

Model	Research Institutions	Country	Resolution (Lon × Lat)
CanESM5	Canadian Environment Agency (CCCma)	Canada	2.8125° × 2.8125°
MRI-ESM2-0	Meteorological Research Institute, Japan Meteorological Agency (MRI)	Japan	1.875° × 1.875°
IPSL-CM6A-LR	Pierre-Simon Laplace Institute (IPSL)	France	2.5° × 1.259°
NESM3	Nanjing University of Information Technology (NUIST)	China	1.875° × 1.875°
KACE-1-0-G	Institute of Meteorology, Korea Meteorological Administration (NIMS-KMA)	Korea	1.875° × 1.25°

For ease of reading, the following hydrologic variables are selected in this paper, as you see in Table 2. At the same time, according to the research content, it is divided into two periods, and the specific division is as follows. This study takes 1974–2014 as the historical period to evaluate the historical hydrological variables. The historical period is divided into two sub-periods, 1974–1991 as the base period, and 1992–2014 as the change period, see Section 3.1.1. This study takes 2015–2060 as the future period to evaluate the future hydrological variables. The future period is divided into two sub-periods: the near-term (2015–2040) and the long-term (2040–2060). The historical period of climate model bias correction is 1961–2011, and the future period is 2015–2060.

Table 2. Hydrological variables and definitions.

Abbreviation	Definition	Units
Tmax	Maximum temperature	°C
Tmin	Minimum temperature	°C
E_0	Potential evapotranspiration	mm
P	Precipitation	mm
R	Runoff depth	mm

2.3. Methods

The critical steps in the Budyko-based runoff evolution and prediction in the HRB are as follows: (1) collection of hydro-meteorological data, DEM data, LUCC data, and CMIP6 data. (2) Future climate change scenarios prediction by using statistical downscaling and multi-model ensembles to forecast future climate change sequences. (3) LUCC change prediction by using a CA-Markov model to determine the Budyko parameter *n* in connection to land use under future change scenarios. (4) Prediction of annual runoff in the HRB from 2015 to 2060 under several future change scenarios based on Budyko framework. The specific procedure is shown in Figure 2.

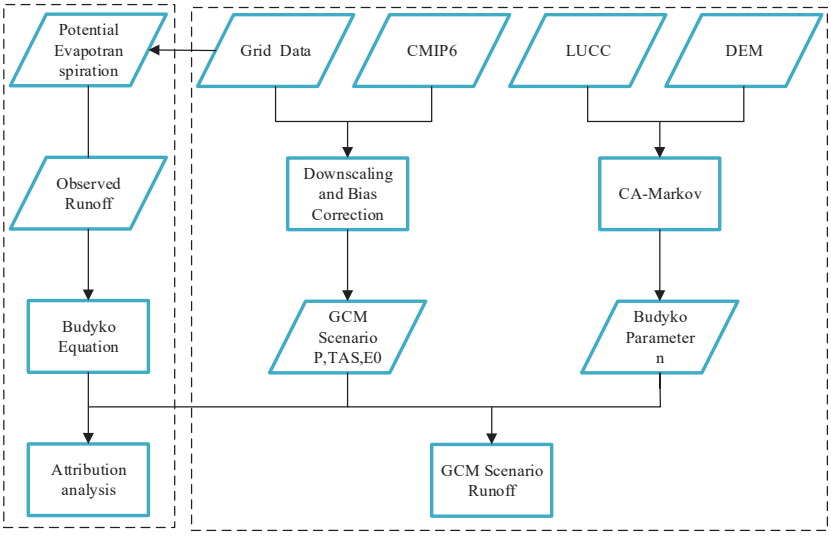

Figure 2. Evolution and prediction of runoff in the HRB based on Budyko hypothesis.

2.3.1. Quantitative Identification of Runoff Changes Based on Budyko's Hypothesis

(1) Budyko hypotheses-based water balance method.

Budyko's theory, based on the hydrothermal equilibrium equation, is commonly utilized in ample watershed water and energy balance investigations [43]. Many scholars have introduced subsurface parameters to characterize the influence on the state of coupled hydrothermal equilibrium in watersheds [39]. The Choudhury–Yang equation is used in this paper and its application is relatively broad [8,44], of which Choudhury–Yang is the hydro-energy equation that contains watershed characteristics (including vegetation changes) and their differences in the equilibrium analytic equation [45]. It can be expressed in the following formula:

$$E = \frac{PE_0}{(P^n + {E_0}^n)^{1/n}} \quad (1)$$

where E is the average annual actual evapotranspiration, n is the subsurface parameter related to the land use type; P is the precipitation, and E_0 is the potential evapotranspiration, which can be calculated according to the Hargreaves formula recommended by FAO56 [46].

Combining the water balance equation:

$$R = P - E \tag{2}$$

A water balance equation such as the following formula can be used to compute the average annual runoff of the basin R:

$$R = P - \frac{PE_0}{\left(P^n + {E_0}^n\right)^{1/n}} \tag{3}$$

where the parameter n can be obtained from the R, P, and E_0 for a given period by Equation (3).

(2) Runoff elasticity based on the Budyko's hypothesis.

Runoff elasticity, defined by Schaake et al. [47] as the degree of change in runoff per unit change in climate factors, was originally presented in 1990. The precipitation elasticity of runoff is expressed as $\varepsilon_P = \frac{dR/R}{dP/P}$, and similarly, we define the potential evapotranspiration elasticity of runoff as $\varepsilon_{E_0} = \frac{dR/R}{dE_0/E_0}$, and the landscape elasticity of runoff as $\varepsilon_n = \frac{dR/R}{dn/n}$. The elasticity coefficients for each variable are calculated as follows:

$$\varepsilon_P = \frac{1 - \left[\frac{(E_0/P)^n}{1+(E_0/P)^n}\right]^{1/n+1}}{1 - \left[\frac{(E_0/P)^n}{1+(E_0/P)^n}\right]^{1/n}} \tag{4}$$

$$\varepsilon_{E_0} = \frac{1}{1+(E_0/P)^n} \frac{1}{1 - \left[\frac{1+(E_0/P)^n}{(E_0/P)^n}\right]^{1/n}} \tag{5}$$

$$\begin{aligned} \varepsilon_n &= \frac{A-B}{\left[1+(P/E_0)^n\right]^{1/n-1}} \\ A &= \frac{P^n \ln(P) + {E_0}^n \ln E_0}{P^n + {E_0}^n} \\ B &= \frac{\ln(P^n + {E_0}^n)}{n} \end{aligned} \tag{6}$$

(3) Runoff attribution based on the Budyko's hypothesis.

In this study, the annual runoff series at Huangzhuang Station (Figure 1) in the HRB was analyzed using the non-parametric Mann–Kendall test and the Pettitt mutation test. The study cycle is divided into two sub-periods based on the mutation points. Changes in runoff computed as a result of changes in precipitation, potential evapotranspiration, and LUCC are stated as:

$$\Delta R_P = \varepsilon_P \frac{R}{P} \Delta P \tag{7}$$

$$\Delta R_{E_0} = \varepsilon_{E_0} \frac{R}{E_0} \Delta E_0 \tag{8}$$

$$\Delta R_l = \varepsilon_n \frac{R}{n} \Delta n \tag{9}$$

where: $\Delta P = P_2 - P_1$, $\Delta E_0 = E_{0,1} - E_{0,2}$, $\Delta n = n_2 - n_1$. The relative contribution of each factor to runoff is calculated as follows.

$$\begin{aligned} \eta_P &= \Delta R_P / \Delta R \times 100\% \\ \eta_{E_0} &= \Delta R_{E_0} / \Delta R \times 100\% \\ \eta_l &= \Delta R_l / \Delta R \times 100\% \end{aligned} \tag{10}$$

where η_P, η_{E_0} and η_l represent the contributions of precipitation, potential evapotranspiration, and landscape change, respectively.

2.3.2. Climate Change Future Scenario Setting

(1) Bias correction.

GCMs output data are often prone to high systematic biases and may not be directly used in basin-scale hydrological simulations [48]. Hence, after inverse distance weight interpolation, the CMIP6 daily data were corrected using two bias correction methods: the local intensity scaling (LOCI) method and the quantile mapping (QM) method. Of which the LOCI can successfully correct precipitation data: the precipitation day frequency and precipitation intensity. The threshold of simulated precipitation occurrence is set at 0.1 mm in this paper to determine that the threshold of simulated precipitation occurrence, so that the frequency of simulated precipitation occurrence in the historical base period is consistent with the measured series. The threshold is used in future periods to correct the frequency of precipitation occurrence in future periods. The QM is a frequency distribution-based method that considers observed and simulated precipitations to be consistent in frequency distribution [49] and uses empirical cumulative distribution functions (ecdfs) to correct precipitation and temperature in future periods, as well as the frequency of precipitation and temperature occurrences [50]. In this paper, two methods, LOCI and QM, were used to correct the frequency and magnitude of occurrence of daily precipitation series in turn, and the QM was used to correct the temperature.

(2) Taylor diagram.

In order to comprehensively evaluate the simulation effects of climate models before and after bias correction, this paper selects the Taylor diagram to evaluate the simulation effects of the five models' annual average precipitation, maximum temperature and minimum temperature. The Taylor diagram can intuitively judge the simulation ability of the five models to the measured precipitation, maximum temperature and minimum temperature. Taylor diagrams are essentially an ingenious combination of the model's correlation coefficient (R), centralized root-mean-square error (RMSE), and standard deviation σ (SD) onto a polar graph. The cosine relationship between the three indicators is based on [51]:

$$R = \frac{\frac{1}{N}\sum_{n=1}^{N}\left(f_n - \overline{f}\right)(r_n - \overline{r})}{\sigma_f \sigma_r} \tag{11}$$

$$\mathrm{RMSE} = \left[\frac{1}{N}\sum_{n=1}^{N}\left[\left(f_n - \overline{f}\right) - (r_n - \overline{r})\right]^2\right]^{1/2} \tag{12}$$

$$\sigma_f = \frac{1}{N}\sum_{n=1}^{N}\left(f_n - \overline{f}\right)^2 \tag{13}$$

$$\sigma_r = \frac{1}{N}\sum_{n=1}^{N}(r_n - \overline{r})^2 \tag{14}$$

where f, r represent the measured and simulated values, respectively, $\overline{f}$ and $\overline{r}$ represent the measured and simulated mean values, respectively. σ_f and σ_r represent the measured and simulated standard deviation, respectively.

2.3.3. Future Land Use Scenario Setting Based on the CA-Markov Model

The ideas behind Markov forecasting come from the work of the mathematician Markov on stochastic processes. The Markov prediction principle is now widely used in studies of the evolution of land patterns. In the study of land cover evolution, a given period's land use category can correspond to the possible conditions in a Markov process that is only related to the previous period's land use category [52,53].

The steps in this article that use CA-Markov are as follows:

(1) Firstly, the measured LUCC 2005 and LUCC 2010 of the HRB were cropped respectively, and the transfer probability matrix and transfer area matrix were obtained based on the Markov module in the IDRISI 17.0 software.

(2) The suitability atlas for different LUCC types is obtained by inputting data information, such as elevation, slope, and the fixed ecological red line to constrain and limit the transformation of different LUCC types, taking into account factors, such as the actual topographical and geomorphological conditions of the watershed and the development of urban areas.

(3) Based on the measured LUCC 2010, the modified transfer probability and area matrices, and the suitability atlas for each LUCC type transfer, 5 × 5 CA filter (a rectangular space within 5 km × 5 km around a cell has a significant effect on the change in the state of the cell) was used for 5 cycles to simulate the LUCC 2015 for the HRB. The CA-Markov model simulates that land use in 2040–2060 will maintain the trend in 2010–2015 and finally get the LUCC 2040–2060 for the HRB.

Typically used in studies on the accuracy of LUCC change simulation and the evaluation of the accuracy of remote sensing image interpretation, the Kappa coefficient can check the consistency of the simulated image results with the observed image data as a whole. The Markov model can extrapolate time series while the CA model can forecast the spatiotemporal dynamic evolution of complex systems, comprehensive utilization of both models may extrapolate the spatial changes of landscape patterns scientifically and reasonably. In this paper, the Kappa coefficient is utilized to assess the precision of land pattern evolution predictions. The calculation formula is as follows [54,55].

$$\text{Kappa} = \frac{(P_0 - P_c)}{(P_p - P_c)} \tag{15}$$

where P_0 is the proportion of correct simulations, P_c is the proportion of correct predictions in the case of random model, P_p is the proportion of correct predictions in the ideal case. Kappa < 0.4 indicates a low degree of similarity between the two images, when $0.4 \leq \text{Kappa} \leq 0.75$, the two images are generally similar, and when Kappa > 0.75, the two images have a significant consistency, indicating a good simulation effect.

Among them, the parameter n, according to the Budyko equation, is mostly related to subsurface circumstances such as land use. An attempt was made to establish the empirical relationship between land use type and model parameter n in the HRB, so as to reveal the quantitative relationship between land use and model parameters and to identify the influence of land use change on runoff. Because forestland, grassland, and farmland occupy more than 95% of the total area of the HRB, this study exclusively considers these three land use types for the empirical equation of the model parameter n.

$$n_t = \beta_1 x_1 + \beta_2 x_2 + \beta_3 x_3 \tag{16}$$

where n_t is the parameter in the Budyko equation at time t; β_i and is the regression parameter of each land use type; x_i is the percentage of land use types (i = 1,..., m). Based on P, R and E_0, the Budyko parameters n (six 5-year periods) were inversed against the HRB during the period 1980–2014, and the β_i was fitted by multiple linear regression.

3. Results

3.1. Historical Hydrometeorological Analysis and Attribution Analysis

3.1.1. Assessment of Climatic and Hydrological Variables during 1974–2014

To better understand the runoff processes during the historical period 1974–2014, linear regression and MK trend tests were used to analyze the trend of hydrometeorological series, as shown in Table 3. Figure 3 shows the linear fitting curves, annual mean lines, and 5-year sliding averages of hydrometeorological variables in the HRB during 1974–2014. From the linear fit curve analysis, it can be seen that temperature and potential evapotranspiration show a non-significant upward trend, which is generally consistent with the results of

the MK trend test, increasing at the rates of 0.0296 °C/a, 0.0204 °C/a and 1.3313 mm/a, respectively. While *P* and *R* show a downward trend, which is generally consistent with the results of the MK trend test, decreasing at the rates of 1.3673 mm/a and 1.2709 mm/a. The maximum values of average annual *P* and *R* from 1974 to 2014 occurred in 1983, at 1255.8 mm and 593.6 mm, respectively. The fluctuations of E_0 were roughly the same as those of temperature. From 1974 to 2014, the average annual *P* was 906.97 mm, the average annual E_0 was 1061.47 mm, and the average annual *R* was 290.47 mm. The potential evapotranspiration is higher than the precipitation in the HRB during the historical period.

Table 3. Results of hydrometeorological trend analysis.

Series	Linear Fitting	Z (MK)	Trend
P	−1.3673	−0.9174	down
E_0	1.3313	1.2489	up
Tmax	0.0296	0.0303	up
Tmin	0.0204	0.0213	up
R	−1.2709	−1.5036	down

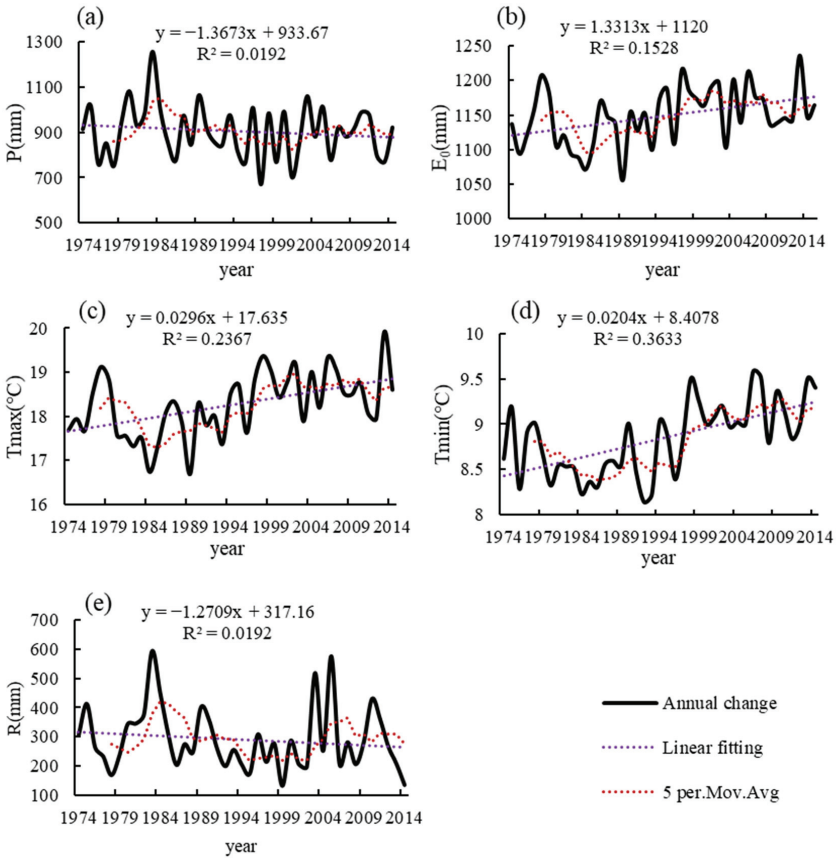

Figure 3. Change trends in climate and hydrology in the HRB 1974–2014: (**a**) average annual precipitation (*P*); (**b**) average annual potential evapotranspiration (E_0); (**c**) average annual maximum temperature (*Tmax*); (**d**) average annual minimum temperature (*Tmin*); (**e**) average annual runoff depth.

The MK test and Pettitt's mutation test were used to determine the mutation years of the HRB runoff, as shown in Figure 4, to better attribute the HRB runoff. The intersection of the MK test UF and UB curves between the two critical levels $\alpha = 0.05$ was first used to determine the year of mutation, and then, the Pettitt test was used to further verify the reasonableness and significance of the MK test for the year of mutation. The UF curve of the average runoff series of the HRB from 1974 to 2014 shows irregular fluctuations, with a decreasing trend from 1984 to 2002, though they are within the confidence interval of the significance level $\alpha = 0.05$ (−1.96). This indicates a decreasing trend in the HRB runoff in these years, but the decrease is not significant. The UF and UB curves in the confidence interval intersected between two significance level lines in 1979, 1991, 2003, 2007, and 2008, preliminarily identifying the year of mutation, while the $U_{t,\,N}$ curve after Pettitt test identified the year of mutation of runoff in the HRB as 1991. Based on the abrupt change test, the study period 1974–2014 can be divided into two segments: the base period 1974–1991 and the change period 1992–2014, both of which provide a foundation for the subsequent attribution analysis.

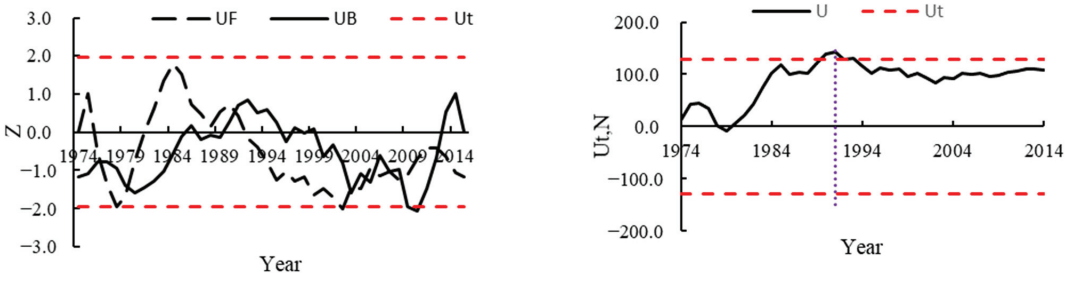

(**a**) (**b**)

Figure 4. Runoff mutation analysis for 1974–2014 in the HRB: (**a**) M-K mutation test (**b**) Pettitt mutation test.

3.1.2. Analysis of Runoff Elastic Coefficient

According to the analysis in Section 3.1.1, it can be determined that the year of a sudden change of runoff in the HRB is 1991, which is consistent with the results of Peng Tao et al. [34]. Based on the results of the mutation analysis, the historical period was divided into the base period (1974–1991) and change period (1991–2014). Based on the average potential evapotranspiration, average runoff depth, and average precipitation of the two periods at Huangzhuang station, the corresponding Budyko parameter n of each period was calculated using Equation (3). Combining Equations (4)–(6) to calculate the elasticity coefficients ε_P, ε_{E_0} and ε_n corresponding to the two periods, we obtained the results as shown in Table 4.

Table 4. Hydroclimatic characteristics of the HRB.

Data Period	Long-Term Mean Value					Elasticity of Runoff		
	Annual P (mm)	Annual E_0 (mm)	Annual R (mm)	E_0/P	n	ε_P	ε_{E_0}	ε_n
1974–1991	932.95	1039.05	319.99	1.11	1.469	1.882	−0.882	−0.900
1992–2014	887.49	1078.29	265.75	1.21	1.554	1.994	−0.994	−1.026
1974–2014	906.97	1061.47	288.98	1.17	1.515	1.942	−0.943	−0.969

The HRB has a subtropical monsoon climate that is both mild and humid. In comparison to previous studies, the E_0 range is 800–1200 mm, the P range is 800–1900 mm, and n primarily ranges from 1.0 to 2.0 in China's humid regions [56]. Comparing the two periods before and after the mutation, P decreased by 4.87% in the change period (1992–2014) compared to the base period (1974–1991), while potential evapotranspiration and n showed an increasing trend compared to the base period (1974–1991), increasing by 3.77% and 5.77%, respectively, or resulting in a 16.95% decrease in the runoff. The precipitation elastic coefficient ε_P, potential evapotranspiration elastic coefficient ε_{E_0} and landscape elastic coefficient ε_n in the change period (1992–2014) are 1.944, −0.944 and −1.026, respectively, indicating that when the P increases by 1%, the runoff will increase by 1.944%, the E_0 will increase by 1%, it will lead to a 0.994% reduction in runoff, and when the Budyko parameter n increases by 1%, it will lead to a 1.026% reduction in runoff. It can be seen that the change in runoff at HRB is positively correlated with precipitation and negatively correlated with potential evapotranspiration and subsurface changes, which reflects the strong influence of climate on the change in the runoff. The absolute magnitude of the elasticity coefficient reflects the sensitivity of runoff to the various influencing factors. The effects of climate change and subsurface on catchment hydrology described above can also be explained by the Budyko curve. With the rise in drying index E_0/P, the precipitation elasticity coefficient of runoff ε_P will increase, while the potential evapotranspiration elasticity coefficient of runoff ε_{E_0} will decrease. In comparison with the base period, $|\varepsilon_P|$ $|\varepsilon_{E_0}|$ and $|\varepsilon_n|$ increase during the change period, demonstrating an increasing susceptibility of runoff to changes in these three factors. Overall, runoff in the HRB is most susceptible to precipitation and least susceptible to changes in potential evapotranspiration.

3.1.3. Runoff Attribution Analysis

Table 5 shows the contribution of each influencing factor to the change in runoff in the HRB. We can learn from Table 5 that the variations of runoff caused by precipitation, potential evapotranspiration and underlying surface are −29.34 mm, −10.66 mm, and −16.66 mm, respectively. Both climate change and human activities contribute to the decrease in the runoff, with precipitation changes accounting for 54.1%, subsurface changes accounting for 30.7%, and potential evapotranspiration accounting for 19.7% for the change in runoff. We can conclude that precipitation is the primary cause of decreased runoff in the HRB.

Table 5. Analysis of runoff attribution in the HRB.

Period		Change from Base Period to Change Period				$P/E_0/n$ Induced Runoff Change (mm)			Contribution to Runoff Change (%)		
Base Period	Change Period	ΔR	ΔP	ΔE_0	Δn	ΔR_P	ΔR_{E_0}	ΔR_l	η_P	η_{E_0}	η_l
1974–1991	1992–2014	−54.24	−45.46	39.2	0.085	−29.34	−10.66	−16.66	54.1%	19.7%	30.7%

3.2. Climate Change Scenario Setting

3.2.1. Evaluation of Statistical Downscaling and Bias Correction Results

Taylor diagrams of simulated P, *Tmax*, and *Tmin* versus observed ones were made to assess the ability of each CMIP6 model to affect measured data after bias correction. Figure 5 illustrates that after bias correction, the correlation coefficients for P are in the range of 0.1–0.6, with MRI-ESM2-0, IPSL-CM6A-LR correlation coefficients more than 0.4, mean squared deviation ratios at 0.98–1.01, and standard deviation ratios at 0.98–1.01. The correlation coefficients for *Tmax* after bias correction ranged from 0.3 to 0.99, with MRI-ESM2-0, IPSL-CM6A-LR and NESM3 having correlation coefficients greater than 0.95, ratios of mean squared deviations between 0.2 and 0.4, and ratios of standard deviations between 0.2 and 4. The correlation coefficients for the *Tmin* after bias correction ranged from 0.3 to 0.99, with MRI-ESM2-0, IPSL-CM6A-LR and NESM3 having correlation coefficients

greater than 0.95, ratios of mean squared deviations between 0 and 0.2, and ratios of standard deviations between 0 and 0.2. By integrating the three indices, we can see that the order of CMIP6 models, after simulation and after bias correction, is *Tmax*, *Tmin*, and *P*, from strongest to worst. MRI-ESM2-0, IPSL-CM6A-LR, and NESM3 are the CMIP6 models offering better simulation ability after bias adjustment. Overall, it is found that the simulation of precipitation and temperature in the HRB by this correction method is better than the simulation of precipitation in the HRB. Nevertheless, the modeled average annual precipitation trends and multi-year averages are reasonably consistent with the observed values. This suggests that the correction method can be applied to future hydrological simulations of the basin and assess future runoff changes in the HRB.

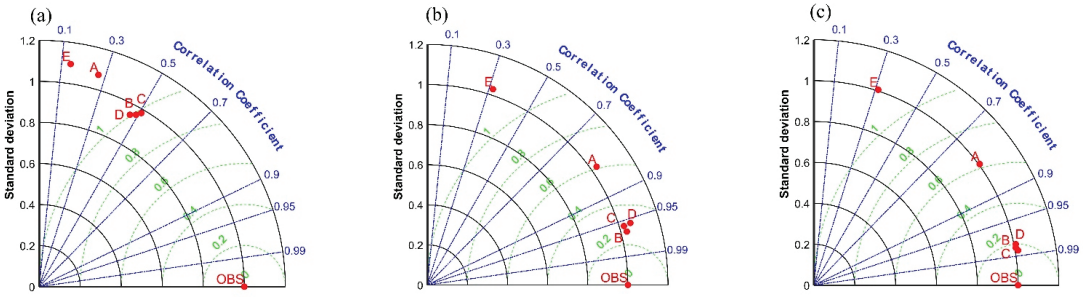

Figure 5. The 1961–2011 mean CMIP6 model-corrected Taylor diagram: (**a**) precipitation (*P*) (**b**) maximum temperature (*Tmax*) (**c**) minimum temperature (*Tmin*); OBS indicates measured values, A, B, C, D, E represent the five models CanESM5, MRI-ESM2-0, IPSL-CM6A-LR, NESM3, KACE-1-0-G, respectively.

The bias-corrected approach has a significant correcting effect on the regional distribution of *P*, *Tmax* and *Tmin*. The multi-model mean can reappear the pattern of decreasing annual mean precipitation and average annual temperature from southeast to northwest in the HRB by comparing bias-corrected simulated data with observed data from 1961 to 2011 (Figure 6). The correction for the multi-year mean values in the basin was good, with the mean *P* deviation reduced from 30.2% to 0.85%, the mean *Tmax* deviation reduced from 53.53% to 0.71%, and the mean *Tmin* deviation reduced from 5.68% to 0.57%. The effect of model bias correction on total annual precipitation and average annual temperature grid point bias correction was also compared. Before and after correction, the model *P* grid point correlation increased from 0.68 to 0.99, the *Tmax* grid point correlation increased from 0.62 to 0.83, and the *Tmin* grid point correlation increased from 0.75 to 0.99. For the simulation of the effect of precipitation and temperature extremes in the basin, it can be seen that the interval correction for *P* is from 1011.7–1430.1 mm to 677.9–1435.8 mm, the interval correction for *Tmax* is from 8.39–8.56 °C to 9.75–23.3 °C, and the interval correction for *Tmin* is from 8.19–8.4 °C to 1.56–13.5 °C, all of which are more in line with the actual values observed in the basin. The bias correction is effective with a good correlation in both space and time, and is anticipated to be applied in subsequent hydrological simulations of the basin.

3.2.2. Analysis of Future Changes in Hydrological Variables

Figure 7 shows the average annual *P*, average annual *Tmax*, and average annual *Tmin* variations of the HRB in the future period under the SSP126, SSP245, and SSP585 scenarios. It can be seen from Figure 7 that the overall *P* is estimated to increase in the coming years, with the increase amplitude under SSP126 scenario > SSP585 scenario > SSP245 scenario, and the increase amplitude of *P* is estimated to enlarge with time. Temperatures are rising, with *Tmax* and *Tmin* increase amplitude under SSP585 scenario>SSP245 scenario >SSP126 scenario, and the increase amplitude is estimated to enlarge with time. The change

rates of hydrological variables in the HRB relative to historical period (1974–2014) under different scenarios are shown in Table 6. Under the SSP126 scenario, *P* in the future period (2015–2040) increases by 22.38%, *Tmax* and *Tmin* decrease by 2.04% and 3.75% compared to the historical period (1974–2014). Under the SSP245 scenario, *P* in the future period (2015–2040) increases by 4.27%, *Tmax* and *Tmin* decrease by 2.25% and 4.89% compared to the historical period (1974–2014). In the SSP585 scenario, the *P* in the future period (2015–2040) increased by 10.64%, *Tmax* and *Tmin* decreased by 3.95% and 7.23% compared to the historical period (1974–2014). However, in the future period (2040–2060), its *P* increases by 22.86%, 10.57% and 16.96%, *Tmax* increases by 2.28%, 2.83% and 5%, and *Tmin* increases by 4.37%, 5.97% and 9.03% for SSP 126, SSP 245 and SSP 585 scenarios, respectively. Compared to the historical period (1974–2014), the increase in average *P* is more pronounced under the SSP126 scenario and the SSP245 scenario has the smallest increase. The SSP585 scenario has the greatest increase in multi-year average temperature, while the SSP126 scenario has the smallest increase.

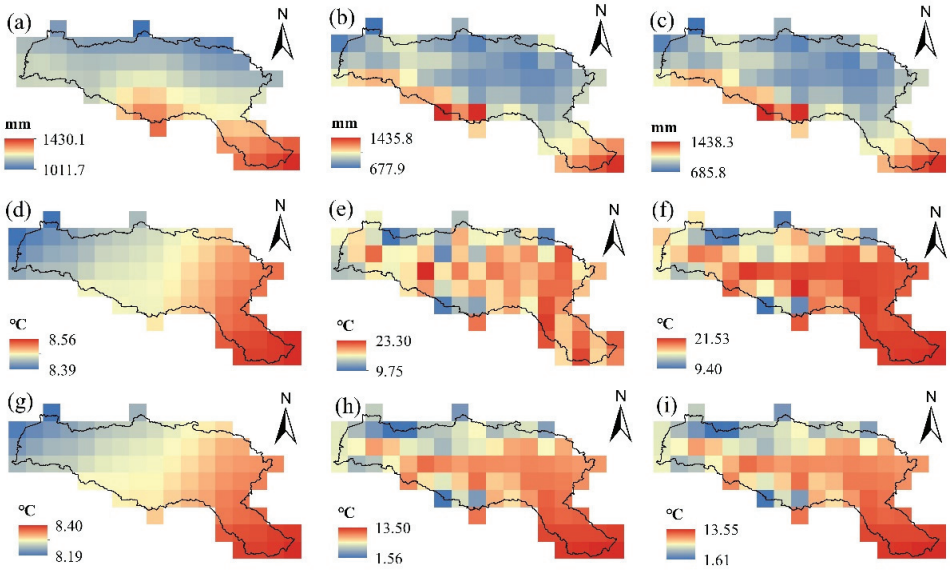

Figure 6. Spatial distribution between multi-model average simulated, corrected and observed values in 1961–2011: (**a**–**c**) pre-corrected multi-model average precipitation (*P*), corrected multi-model mean value, observed value; (**d**–**f**) pre-corrected multi-model average value of maximum temperature (*Tmax*), corrected multi-model average value, observed value; (**g**–**i**) pre-corrected multi-model average value of minimum temperature (*Tmin*), corrected multi-model average value, observed value.

Table 6. Rates of change of hydrological variables in the HRB in future periods under different scenarios.

Period	2015–2040 (%)			2040–2060 (%)		
Variables	126	245	585	126	245	585
P	22.38	4.27	10.64	22.86	10.57	16.96
Tmax	−2.04	−2.25	−3.95	2.28	2.83	5.00
Tmin	−3.75	−4.89	−7.23	4.37	5.97	9.03

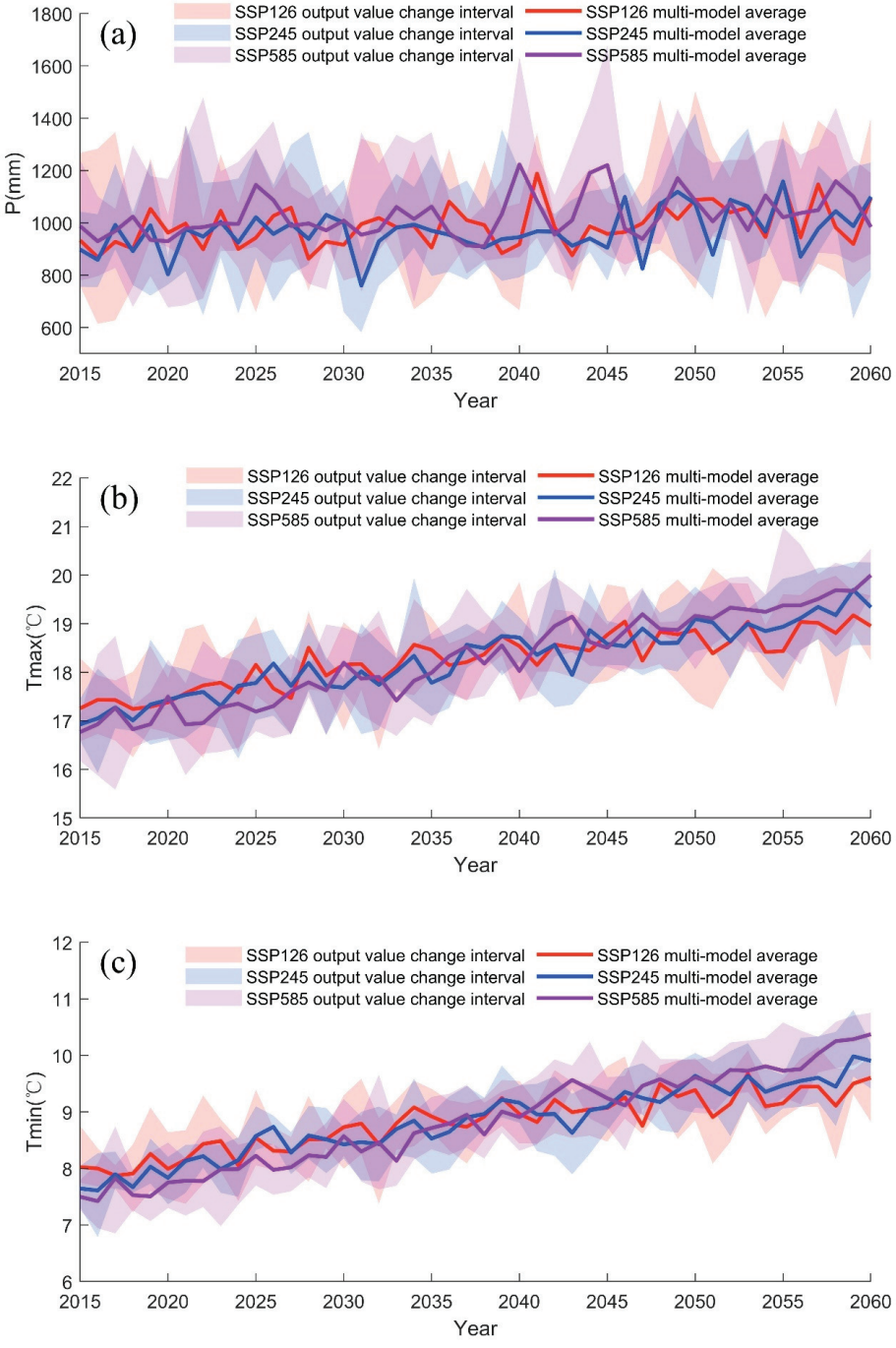

Figure 7. Hydrological variables predicted for 2015–2060 in the HRB: (**a**) average annual precipitation (*P*); (**b**) average annual maximum temperature (*Tmax*) (**c**) average annual minimum temperature (*Tmin*).

3.3. Land Use Change Scenario Setting

Based on LUCC2010 data, the land use transition probability and adaptability atlas of LUCC2005-LUCC2010 were input into the CA-Markov model to predict LUCC2015, LUCC2040 and LUCC2060. The future land use simulation in the HRB is shown in Figure 8. Among them, the actual LUCC2015 (Figure 8a) and the simulated LUCC2015 (Figure 8b) were evaluated by the IDRISI 17.0 software, and the Kappa coefficient of the simulation result was 0.96, which confirmed that the model has a good prediction effect and the prediction results are credible. Based on this, further predictions were made for LUCC2040 (Figure 8c) and LUCC2060 (Figure 8d). According to the analysis of land use types in different periods of the HRB in Table 7, it can be seen that the changes of farmland, grassland and forest land between the measured LUCC2015 and simulated LUCC2015 land use types in the study area are not much different, which can accurately describe the land use situation in the study area and can be used for a follow-up analysis. At the same time, according to the analysis of the proportion of land use in LUCC2015, LUCC2040 and LUCC2060, it can be seen that from 2015 to 2040, the built areas in the study area increased from 3.12% to 7.34%, and the overall change from 2040 to 2060 was not significant. From 2015 to 2040, farmland and grassland will continue to decrease, from 34.95% to 32.78%, and from 19.48% to 17.54%, respectively. From 2015 to 2060, although there is a decreasing trend in forest land, the overall change is insignificant. It is worth noting that there is an increasing trend of unused land, indicating that there may be a trend of land degradation in the future.

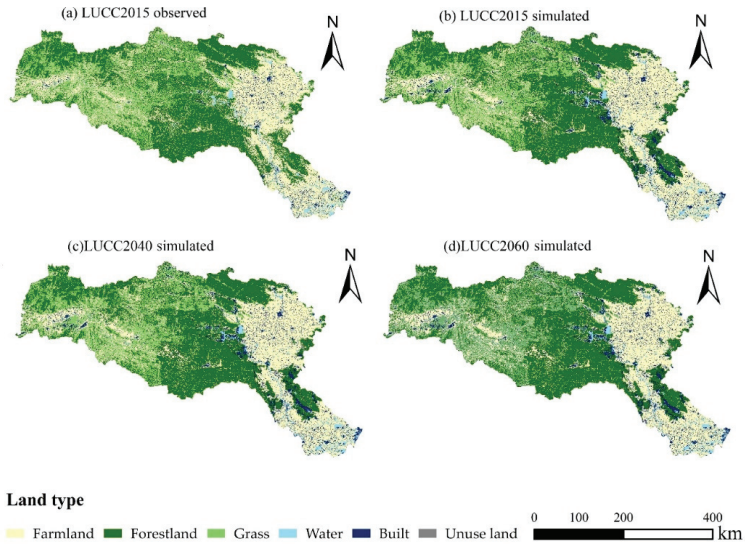

Figure 8. Land use in the HRB: (**a**) LUCC2015 observed; (**b**) LUCC2015 simulated; (**c**) LUCC2040 simulated; (**d**) LUCC2060 simulated.

According to the simulation results of LUCC2040 and LUCC2060 in Table 7 above, inputting the HRB model parameters, land use data into Equation (16), the multiple linear regression method was used to obtain an empirical formula as below, applicable to the study basin.

$$n = -1.693x_1 + 15.602x_2 - 21.290x_3 \quad (17)$$

Substituting future land use data into this equation, it can be determined that the n value is 1.866 for 2015–2040 and the n value is 1.871 for 2040–2060. They are then substituted into the Budyko framework to predict future runoff. After regression analysis, it was found

that in the HRB, farmland and grassland had a negative effect on parameter n, while forestland had a positive impact.

Table 7. Proportion of land use types (%) in the HRB in different periods (%).

Period	Farmland	Forestland	Grassland	Water	Built	Unuse Land
2015 observed	34.95	39.59	19.48	2.82	3.12	0.05
2015 simulated	32.93	39.46	17.53	2.75	7.20	0.13
2040 simulated	32.78	39.46	17.54	2.75	7.34	0.12
2060 simulated	32.76	39.49	17.55	2.75	7.30	0.14

3.4. Future Runoff Forecast

This study uses an ensemble of climate models (multi-model averaging) from five CMIP6 GCMs combined with the Budyko water balance method to predict future runoff. We used Equation (17) to calculate the Budyko parameter n in the future period, see Section 3.3, which represents the land use maintenance LUCC2040 and LUCC2060 land use scenarios. The Budyko parameter n in 1992–2014 was calculated using Equations (1)–(3), shown in Table 3, representing the land use maintenance LUCC1992-2014 land use scenario. Based on Equation (3), the simulation forecast of the future runoff (R) of the HRB from 2015 to 2060 is carried out, as shown in Figure 9. According to Figure 9, it can be seen that the future R of the HRB will increase under the SSP126, SSP245 and SSP585 scenarios. The rate of change for future periods (2015–2040, 2040–2060) relative to historical periods (1974–2014) is shown in Figure 10.

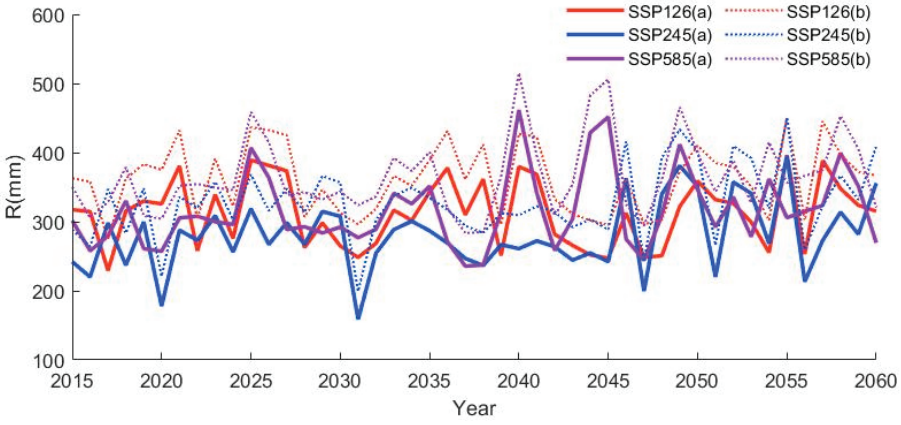

Figure 9. Annual runoff (R) predicted for 2015–2060 in the HRB; (**a**) 2015–2040: n = 1.866, 2040–2060: n = 1.871, (**b**) 2015–2040: n = 1.554, equivalent to the corresponding parameter n in 1992–2014.

To predict future runoff based on the Budyko water balance method, the most important thing is to determine the Budyko parameter n. This study estimates the Budyko parameter n based on land use scenarios. In Figure 10a, it is assumed that the land use maintains the LUCC2040 and LUCC2060 land use scenarios. Figure 10b assumes that the land use maintains the land use in the change period during 2015–2060. That is, the land use maintains LUCC1992-2014. Based on this, the effect of future runoff forecasting in the HRB was compared and analyzed. When the land use maintains the LUCC2040 and LUCC2060 land use scenarios, compared with the historical period (1974–2014), the runoff in the HRB increased by 8.77% under the SSP126 scenario from 2015 to 2040, and under the SSP245 scenario, the runoff in the HRB decreased 8.04%, under the SSP585 scenario, the runoff of the HRB increased by 4.97%, under the SSP126 scenario from 2040 to 2060, the runoff of the HRB increased by 5.79%, under the SSP245 scenario, the HRB runoff increased by 2.09%, under the SSP585 scenario. The runoff of the HRB increased by 13.66%.

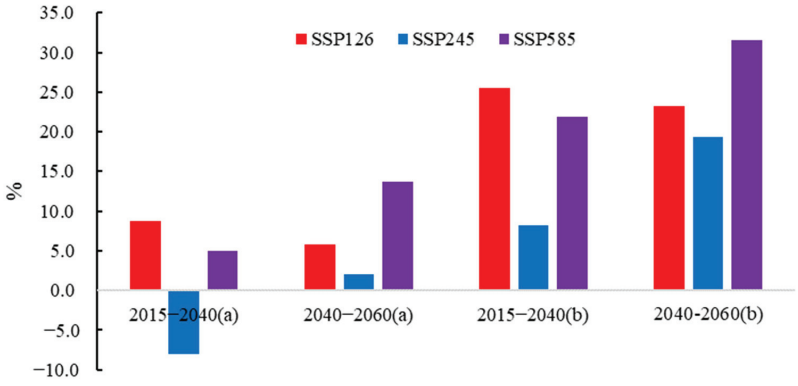

Figure 10. Rate of change of runoff (*R*) in different future periods (2015–2040, 2040–2060) against the historical period; (**a**) 2015–2040: n = 1.866, 2040–2060: n=1.871, (**b**) 2015–2060: n = 1.554, equivalent to the corresponding parameter n in 1992–2014.

When the land use is maintained under the LUCC1992-2014 land use scenario, compared with the historical period (1974–2014), the runoff in the HRB increased by 25.47% under the SSP126 scenario from 2015 to 2040, and under the SSP245 scenario, the HRB runoff increased by 25.47%. 8.27%, under the SSP585 scenario, the runoff of the HRB increased by 21.84%, under the SSP126 scenario from 2040 to 2060, the runoff of the HRB increased by 23.27%, under the SSP245 scenario, the HRB runoff increased by 19.35%, under the SSP585 scenario. The runoff of the HRB increased by 31.52%. When the land use is maintained under the LUCC1992-2014 land use scenario, compared with the historical period (1974–2014), the runoff in the HRB increased by 25.47% under the SSP126 scenario from 2015 to 2040, and under the SSP245 scenario, the HRB runoff increased by 25.47%. 8.27%, under the SSP585 scenario, the runoff of the HRB increased by 21.84%, under the SSP126 scenario from 2040 to 2060, the runoff of the HRB increased by 23.27%, under the SSP245 scenario, the HRB runoff increased by 19.35%, under the SSP585 scenario. The runoff of the HRB increased by 31.52%.

Overall, the future *R* of the HRB will show an increasing trend. Compared with the historical period, under the SSP126 scenario, the *R* increased significantly. Under the SSP585 scenario, the future *R* increase in the HRB is less. Under the SSP245 scenario, the future *R* variation in the HRB ranges from −8.04% to 19.35%. At the same time, by comparing the future *R* under the two ways, it can be found that the estimated future runoff of maintaining LUCC1974-2014 is generally higher than the *R* calculated by maintaining LUCC2040 and LUCC2060. Based on the assumptions in this paper, it is very likely to overestimate the future runoff in the HRB without considering the changes in the land use data of the underlying surface in the future.

4. Discussion

4.1. The Observed Impacts of Climate Change on Water Resources in the HRB

The current study results show that there is a decreasing trend for the annual runoff (*R*) and annual potential evapotranspiration (E_0) in the HRB from 1974 to 2015, while there is an increasing trend for the annual temperature and potential evapotranspiration, overall consistent with the results of other studies [57]. According to the trend analysis in Section 3.1.1, the HRB experienced an extremely dry era following the 1990s, followed by a relatively dry spell in 2014.

Climate change and human activities lead to changes in key elements of the water cycle, such as precipitation, temperature, and substratum, in the future. The current study forecasts an increasing trend in overall precipitation and temperature in the future period. This is generally consistent with the results of other studies [58,59]. It has been shown

that there is a consistent correlation between annual temperature and runoff, with a global temperature increase of 1 °C resulting in a 4% increase in runoff [60]. In this paper, an attribution analysis based on the Budyko equation for the historical period of the HRB can also further corroborate the influence of three factors on the future runoff of the HRB [61].

According to Zhai et al. [62], climate change is the most important risk factor for the hydrological risk of water supply in the South-North Water Transfer Central Line. According to Li et al. [63], climate change leads to a 15% reduction in runoff in the upper Han River. Meanwhile, climate change affects water quality and ecosystems. For example, increased temperature in climate change can lead to algal blooms in the Han River [64], while reduced flow can lead to deterioration of water quality in the middle and lower reaches of the Han River [65]. If this situation continues consistently, it will seriously affect the water transfer and transmission process in the HRB and have a serious impact on the South-North Water Transfer Project in China. This study provides some insights into the development of water resources and water quality management in the South-North Water Diversion by conducting an attribution analysis of the declining runoff in the HRB.

4.2. LUCC Change Impacts on Watershed Water Resources

Regarding the effect of LUCC on runoff variability, this is related to the parameter n in the Choudhury–Yang equation, where LUCC variability changes the vegetation retention, soil water content, and surface evapotranspiration involving hydrological factors [60]. Therefore, in this study, we assume that the change of parameter n is related to LUCC, etc. According to the actual LUCC in the HRB, which is mainly forestland, grassland and farmland, and the area of three land use types accounts for more than 95% of the total area of the HRB, so in this paper, we assume that the Budyko parameter n is related to three land use types in LUCC.

In a previous study, it was found that vegetation cover can weaken the water supply capacity of the South-North Water Transfer to some extent. For example, Zhang et al. [66] found that vegetation greening may exacerbate the degree of hydrological aridity. The increase in forest cover can reduce runoff in the HRB by as much as 0.19%, thus affecting river health to some extent [63]. In addition, the analysis of LUCC effects on water resources in the HRB may provide some suggestions for crop production in the HRB. Vegetation cover can, to some extent, weaken the water supply capacity of the South-North Water Transfer. The greening of vegetation may aggravate the severity of hydrological drought. For example, cotton crops in the HRB are highly dependent on irrigation water and are highly affected by the South-North Water Transfer Project [67].

According to the analysis of land use transfer changes in the HRB in Table 8, the number of transfers of the 3 types of land use, farmland, water and built, was the most obvious from 1980 to 2015. The net transfer out of farmland is 1876 km^2, and the net transfer in water and built is 1092 km^2 and 996 km^2, respectively. The transfer of farmland to water is the highest transfer, 1064 km^2, and built is mainly converted from farmland, 937 km^2. There is a decreasing trend of forestland and grassland, which is not apparent.

Table 8. Land use area transfer matrix for the HRB 1980–2015 (km^2).

Type of Land Use	Farmland	Forestland	Grassland	Water	Built	Unused Land	2015
Farmland	53,191	102	180	98	3	35	53,609
Forestland	136	60,397	169	16		1	60,719
Grassland	148	54	29,648	28		1	29,879
Water	1064	70	25	3057	5	100	4321
Built	937	165	32	29	3610	5	4778
Unuse land	9	1	2	1		64	77
1980	55,485	60,789	30,056	3229	3618	206	153,383

Overall, land use changes will likely lead to significant changes in evapotranspiration in the HRB, which in turn will lead to a decrease in HRB runoff. In this study, there is a trend of decreasing grassland, forested and farmland in the future period, indicating a decrease in future evapotranspiration, further corroborating the increase in future runoff [60]. As future climate warming may lead to an increase in future evapotranspiration, it affects the availability of water resources. Therefore, this study predicts future runoff in the HRB can provide a basis for future water resources management and can also promote benefits such as soil and water conservation and ecological restoration.

4.3. Limitations of This Study

Of course, there are also some limitations in the experiment design. This study, for example, exclusively evaluates the effect of land use change on the subsurface parameter *n*, neglecting the impact of other hydrological variables. The currently available studies assume that the parameter *n* is related to climate change, vegetation, and many other factors, such as mean storm depth, precipitation seasonality, soil, vegetation cover [61,68], etc. In addition to this, there are interactions between various factors, such as the interaction between CA (farmland area as a percentage of total watershed area) and ASD (average storm depth). Many models (e.g., multiple stepwise regression, neural networks) [69] have been proposed to estimate the Budyko parameter *n* under specific conditions. In addition, during the land use simulation, all data were processed to a spatial resolution of 1 km, without considering the scale effect of land use. Further research is needed on how to maximize the mechanisms of natural and human influences on the geospatial system [70]. Therefore, in future studies, the impact of climate change and human activities on runoff should be input into the model to provide a more realistic picture of future runoff predictions in the HRB. The results expected to provide a basis for managing water resources in the changing environment of the HRB.

5. Conclusions

The impact of climate change and land use change on the reduction of runoff in the HRB was first analyzed, followed by an attribution analysis of the HRB based on the Budyko runoff elasticity coefficient method and a prediction for future runoff in the HRB based on the Budyko water balance method in combination with CMIP6 global climate model data. The following conclusions can be derived from the study's findings:

(1) From 1974 to 2014, annual runoff and annual *P* in the HRB decreases non-significantly, with decline rates of 1.3673 mm/a and 1.2709 mm/a, respectively, whereas temperature and potential evapotranspiration increases non-significantly. Based on the mutation test, the year of mutation is confirmed to be 1991. According to the attribution analysis, precipitation is considered as the most critical factor leading to the drop in Han River runoff, with a contribution rate of 54.1%, followed by the lower bedding surface with a contribution rate of 30.7%.

(2) The overall simulation effect of temperature in the HRB after bias correction is better than *P*. The simulated annual average *P* trends and multi-year averages are reasonably consistent with the observed values, indicating a good spatial correlation. For the analysis of the bias-corrected future hydrological data, the overall *P* trend in the future period is increasing, with the increase amplitude under SSP126 scenario > SSP585 scenario > SSP245 scenario, and the precipitation increase amplitude also increases with time. Temperatures are estimated to rise, with *Tmax* and *Tmin* rises in the SSP545 scenario > SSP245 scenario > SSP126 scenario, and the temperature rise amplitude increases with time.

(3) For the future land use evaluation, there is a continuous trend of decreasing farmland and grassland in the future. Forestland has a decreasing trend, though the overall change is not significant. It is worth noting that there is an increasing trend of unused land, indicating that there may be a trend of land degradation in the future. The *n* value is determined to be 1.866 for 2015–2040 and 1.871 for 2041–2060.

(4) The future *R* of the HRB will show an increasing trend. The future runoff of the HRB shows an increasing trend, and the future runoff varies in different scenarios and periods. Under the land use scenarios of maintaining LUCC1992-2014 and LUCC2040 and LUCC2060, the *R* change rates in 2015–2040 are 8.27–25.47% and −8.04–19.35%, respectively, and the *R* in 2040–2060 are 2.09–13.66% and 19.35–31.52%. At the same time, by comparing the future *R* under the two scenarios, it can be found that the estimated future runoff of maintaining LUCC1992-2014 is generally higher than the *R* calculated by maintaining LUCC2040 and LUCC2060. Based on the assumptions in this paper, it is very likely to overestimate the future runoff in the HRB without considering the changes in the land use data of the underlying surface in the future.

Author Contributions: Conceptualization, Z.Y.; methodology, Z.Y.; validation, M.W. and J.X.; data curation, M.W. and M.S.; writing—original draft preparation, M.W. and J.X.; writing—review and editing, M.S.; supervision, X.W. All authors have read and agreed to the published version of the manuscript.

Funding: This research was funded by the National Natural Science Foundation of China, grant number 52079008 U2040212 51909080.

Institutional Review Board Statement: Not applicable.

Informed Consent Statement: Not applicable.

Data Availability Statement: Not applicable.

Conflicts of Interest: The authors declare no conflict of interest.

References

1. Alexander, L.; Allen, S.; Bindoff, N.L. *Working Group I Contribution to the IPCC Fifth Assessment Report Climate Change 2013: The Physical Science Basis Summary for Policymakers*; OPCC: Victoria, BC, Canada, 2013.
2. Xu, X.; Yang, D.; Yang, H.; Lei, H. Attribution analysis based on the Budyko hypothesis for detecting the dominant cause of runoff decline in Haihe basin. *J. Hydrol.* **2014**, *510*, 530–540. [CrossRef]
3. Ype, V.; Nikki, V.; Fernando, J.; Stefan, C.D.; Georgia, D.; Steve, W.L. Exploring hydroclimatic change disparity via the Budyko framework. *Hydrol. Process.* **2014**, *28*, 4110–4118. [CrossRef]
4. Zheng, J.; He, Y.; Jiang, X.I.; Nie, T.; Lei, Y. Attribution analysis of runoff variation in Kuye River Basin based on three Budyko methods. *Land* **2021**, *10*, 1061. [CrossRef]
5. Riad, P.; Graefe, S.; Hussein, H.; Buerkert, A. Landscape transformation processes in two large and two small cities in Egypt and Jordan over the last five decades using remote sensing data. *Landsc. Urban Plan.* **2020**, *197*, 103766. [CrossRef]
6. Kis, A.; Rita, P.; Bartholy, J.; János, A. Projection of runoff characteristics as a response to regional climate change in a central/eastern European catchment. *Hydrol. Sci. J.* **2020**, *65*, 2256–2273. [CrossRef]
7. Xiong, M.; Huang, C.S.; Yang, T. Assessing the impacts of climate change and land use/cover change on runoff based on improved Budyko framework models considering arbitrary partition of the impacts. *Water* **2020**, *12*, 1612. [CrossRef]
8. Yang, H.; Yang, D. Derivation of climate elasticity of runoff to assess the effects of climate change on annual runoff. *Water Resour. Res.* **2011**, *47*, W07526. [CrossRef]
9. Sorg, A.; Bolch, T.; Stoffel, M.; Solomina, O.; Beniston, M. Climate change impacts on glaciers and runoff in Tien Shan (Central Asia). *Nat. Clim. Chang.* **2012**, *2*, 725–731. [CrossRef]
10. Hu, C.; Zhang, L.; Wu, Q.; Jian, S. Response of LUCC on runoff generation process in middle Yellow River Basin: The Gushanchuan Basin. *Water* **2020**, *12*, 1237. [CrossRef]
11. Xing, W.; Wang, W.; Shao, Q.; Yong, B. Identification of dominant interactions between climatic seasonality, catchment characteristics, and agricultural activities on Budyko-type equation parameter estimation. *J. Hydrol.* **2018**, *556*, 585–599. [CrossRef]
12. Pfister, L.; Kwadijk, J.; Musy, A.; Bronstert, A.; Hoffmann, L. Climate change, land use change, and runoff prediction in the Rhine–Meuse basins. *River Res. Appl.* **2004**, *20*, 229–241. [CrossRef]
13. Gebre, S.L. Application of the HEC-HMS model for runoff simulation of Upper Blue Nile River Basin. *Hydrol. Curr. Res.* **2015**, *6*, 199. [CrossRef]
14. Wu, C.; Hu, B.X.; Huang, G.; Wang, P.; Xu, K. Responses of runoff to historical and future climate variability over China. *Hydrol. Earth Syst. Sci.* **2018**, *22*, 1971–1991. [CrossRef]
15. Chen, Q.; Chen, H.; Zhang, J.; Hou, Y.; Shen, M.; Chen, J.; Xu, C. Impacts of climate change and LULC change on runoff in the Jinsha River Basin. *J. Sci.* **2020**, *30*, 85–102. [CrossRef]
16. Ning, T.; Li, Z.; Feng, Q.; Liu, W.; Li, Z. Comparison of the effectiveness of four Budyko-based methods in attributing long-term changes in actual evapotranspiration. *Sci. Rep.* **2018**, *8*, 12665. [CrossRef]

17. Wang, H.; Lv, X.; Zhang, M. Sensitivity and attribution analysis of vegetation changes on evapotranspiration with the Budyko framework in the Baiyangdian catchment, China. *Ecol. Indic.* **2021**, *120*, 106963. [CrossRef]
18. Wang, H.; Lv, X.; Zhang, M. Sensitivity and attribution analysis based on the Budyko hypothesis for streamflow change in the Baiyangdian catchment, China. *Ecol. Indic.* **2021**, *121*, 107221. [CrossRef]
19. Ji, G.; Wu, L.; Wang, L.; Yan, D.; Lai, Z. Attribution analysis of seasonal runoff in the source region of the yellow river using seasonal Budyko hypothesis. *Land* **2021**, *10*, 542. [CrossRef]
20. Liu, J.; Chen, J.; Xu, J.; Lin, Y.; Yuan, Z.; Zhou, M. Attribution of runoff variation in the headwaters of the Yangtze River based on the Budyko hypothesis. *Int. J. Environ. Res. Public Health* **2019**, *16*, 2506. [CrossRef]
21. Liu, J.; You, Y.; Zhang, Q.; Gu, X. Attribution of streamflow changes across the globe based on the Budyko framework. *Sci. Total Environ.* **2019**, *794*, 148662. [CrossRef]
22. Li, H.; Shi, C.; Sun, P.; Zhang, Y.; Collins, A.L. Attribution of runoff changes in the main tributaries of the middle Yellow River, China, based on the Budyko model with a time-varying parameter. *Catena* **2021**, *206*, 105557. [CrossRef]
23. Ahmadi, M.; Moeini, A.; Ahmadi, H.; Motamedvaziri, B.; Zehtabiyan, G.R. Comparison of the performance of SWAT, IHACRES and artificial neural networks models in rainfall-runoff simulation (case study: Kan watershed, Iran). *Phys. Chem. Earth* **2019**, *111*, 65–77. [CrossRef]
24. Hu, J.; Ma, J.; Nie, C.; Xue, L.; Zhang, Y.; Ni, F.; Wang, Z. Attribution Analysis of Runoff change in Min-tuo River Basin based on SWAT model simulations, china. *Sci. Rep.* **2020**, *10*, 2900. [CrossRef]
25. Guo, S.; Guo, L.; Hou, K.; Xiong, H.; Hong, X. Predicting future runoff changes in the Yangtze River basin based on Budyko's hypothesis. *Adv. Water Sci.* **2015**, *26*, 151–160.
26. Chen, H.; Xu, C.Y.; Guo, S. Comparison and evaluation of multiple GCMs, statistical downscaling, and hydrological models in the study of climate change impacts on runoff. *J. Hydrol.* **2012**, *434*, 36–45. [CrossRef]
27. Gardner, L.R. Assessing the effect of climate change on mean annual runoff. *J. Hydrol.* **2009**, *379*, 351–359. [CrossRef]
28. Wang, D.; Tang, Y. A one-parameter budyko model for water balance captures emergent behavior in darwinian hydrologic models. *Geophys. Res. Lett.* **2014**, *41*, 4569–4577. [CrossRef]
29. Li, H.; Shi, C.; Zhang, Y.; Ning, T.; Sun, P.; Liu, X.; Collins, A.L. Using the Budyko hypothesis for detecting and attributing changes in runoff to climate and vegetation change in the soft sandstone area of the middle Yellow River basin, China. *Sci. Total Environ.* **2020**, *703*, 135588. [CrossRef] [PubMed]
30. Xing, W.; Wang, W.; Zou, S.; Deng, C. Projection of future runoff change using climate elasticity method derived from Budyko framework in major basins across China. *Glob. Planet. Chang.* **2018**, *162*, 120–135. [CrossRef]
31. Teng, J.; Chiew, F.H.S.; Vaze, J.; Marvanek, S.; Kirono, D.G.C. Estimation of climate change impact on mean annual runoff across continental Australia using Budyko and Fu equations and hydrological models. *J. Hydrometeorol.* **2012**, *13*, 1094–1106. [CrossRef]
32. Liu, H.; Zheng, L.; Yin, S. Multi-perspective analysis of vegetation cover changes and driving factors of long time series based on climate and terrain data in Hanjiang River Basin, China. *Arab. J. Geosci.* **2018**, *11*, 1–16. [CrossRef]
33. Xia, Z.; Zhou, Y.; Xu, H. Response of water resources to climate change in the Han River basin based on SWAT model. *Y. River Basin Res. Environ.* **2010**, *2010. 19*, 158–163.
34. Peng, T.; Mei, Z.; Dong, X.; Wang, J.; Liu, J.; Chang, W.; Wang, G. Attribution analysis of runoff changes in the Han River basin based on Budyko's hypothesis. *South North. Water Divers. Water Res. Sci. Technol.* **2021**, *19*, 1114–1124.
35. Hao, W.; Hao, Z.; Yuan, F.; Ju, Q.; Hao, J. Regional frequency analysis of precipitation extremes and its Spatio-temporal patterns in the Hanjiang River Basin, China. *Atmosphere* **2019**, *10*, 130. [CrossRef]
36. Chen, H.; Guo, S.; Xu, C.Y.; Singh, V.P. Historical temporal trends of hydro-climatic variables and runoff response to climate variability and their relevance in water resource management in the Hanjiang basin. *J. Hydrol.* **2007**, *344*, 171–184. [CrossRef]
37. Deng, Z.; Zhang, X.; Li, D.; Pan, G. Simulation of land use/land cover change and its effects on the hydrological characteristics of the upper reaches of the Hanjiang Basin. *Environ. Earth Sci.* **2015**, *73*, 1119–1132. [CrossRef]
38. Ji, G.; Lai, Z.; Xia, H.; Liu, H.; Wang, Z. Future Runoff Variation and Flood Disaster Prediction of the Yellow River Basin Based on CA-Markov and SWAT. *Land* **2021**, *10*, 421. [CrossRef]
39. Zhang, S.; Yang, Y.; McVicar, T.R.; Yang, D. An analytical solution for the impact of vegetation changes on hydrological partitioning within the Budyko framework. *Water Resour. Res.* **2018**, *54*, 519–537. [CrossRef]
40. Ma, X.; Wu, T.; Yu, Y. Study on prediction of runoff scenarios in the upper Han River basin based on SWAT model. *Remote Sens. Land Resour.* **2021**, *1*, 174–182.
41. Yuan, T.; Yiping, X.; Lei, Z.; Danqing, L. Land use and cover change simulation and prediction in Hangzhou city based on CA-Markov model. *Int. Proc. Chem. Biol. Environ. Eng.* **2015**, *90*, 108–113.
42. Liao, W.; Liu, X.; Xu, X.; Chen, G.; Liang, X.; Zhang, H.; Li, X. Projections of land use changes under the plant functional type classification in different SSP-RCP scenarios in China. *Sci. Bull.* **2020**, *65*, 1935–1947. [CrossRef]
43. Huang, S.; Chang, J.; Huang, Q.; Chen, Y.; Leng, G. Quantifying the relative contribution of climate and human impacts on runoff change based on the Budyko hypothesis and SVM model. *Water Resour. Manag.* **2016**, *30*, 2377–2390. [CrossRef]
44. Choudhury, B. Evaluation of an empirical equation for annual evaporation using field observations and results from a biophysical model. *J. Hydrol.* **1999**, *216*, 99–110. [CrossRef]
45. Yang, D.; Sun, F.; Liu, Z.; Cong, Z.; Ni, G.; Lei, Z. Analyzing spatial and temporal variability of annual water-energy balance in non-humid regions of China using the Budyko hypothesis. *Water Resour. Res.* **2007**, *43*, W04426. [CrossRef]

46. Zhao, F.; Tang, S.; Zhang, Z.; Zhou, G.; Zhao, L. Analysis of the applicability of the modified Hargreaves-Samani formula for estimating reference crop evapotranspiration in Ningxia. *Flood Drought Control. China* **2021**, *31*, 57–63.
47. Schaake, J.C.; Liu, C. Development and application of simple water balance models to understand the relationship between climate and water resources. *Surf. Water Model. Proc. Baltimore Symp.* **1989**, *181*, 343–352.
48. Gu, L.; Chen, J.; Yin, J.; Guo, Q.; Wang, H.; Zhou, J. Potential risk propagation of meteorological and hydrological droughts in major river basins of China under climate change. *Adv. Water Sci.* **2021**, *32*, 321–333.
49. Lei, H.; Ma, J.; Li, H.; Wang, J.; Shao, D.; Zhao, H. Precipitation error revision of the upper Heihe River climate model based on quantile mapping method. *Highl. Meteorol.* **2020**, *39*, 266–279.
50. Chen, J.; Brissette, F.P.; Chaumont, D.; Braun, M. Performance and uncertainty evaluation of empirical downscaling methods in quantifying the climate change impacts on hydrology over two North American river basins. *J. Hydrol.* **2013**, *479*, 200–214. [CrossRef]
51. Li, X.; Xu, C.; Li, L.; Luo, Y.; Yang, Q.; Yang, Y. Assessment of CMIP5 model's ability to simulate temperature in a typical watershed in the Northwest Arid Zone-taking the Kaidu-Kongchu River as an example. *Resour. Sci.* **2019**, *41*, 1141–1153.
52. Sang, L.; Zhang, C.; Yang, J.; Zhu, D.; Yun, W. Simulation of land uses spatial pattern of towns and villages based on the ca–Markov model. *Math. Comput. Model.* **2011**, *54*, 938–943. [CrossRef]
53. Subedi, P.; Subedi, K.; Thapa, B. Application of a hybrid cellular automaton—Markov (CA-Markov) model in land-use change prediction: A case study of Saddle Creek Drainage Basin, Florida. *Appl. Ecol. Environ. Sci.* **2013**, *1*, 126–132. [CrossRef]
54. Faichia, C.; Tong, Z.; Zhang, J.; Liu, X.; Kazuva, E.; Ullah, K.; Al-Shaibah, B. Using RS data-based CA–Markov model for dynamic simulation of historical and future LUCC in Vientiane, Laos. *Sustainability* **2020**, *12*, 8410. [CrossRef]
55. Zhang, F.; Yushanjiang, A.; Wang, D. Ecological risk assessment due to land use/cover changes (LUCC) in Jinghe County, Xinjiang, China from 1990 to 2014 based on landscape patterns and spatial statistics. *Environ. Earth Sci.* **2018**, *77*, 491. [CrossRef]
56. Yang, H.; Yang, D.; Qingfang, H. An error analysis of the Budyko hypothesis for assessing the contribution of climate change to runoff. *Water Resour. Res.* **2014**, *50*, 9620–9629. [CrossRef]
57. Zhong, H.; Huang, Q.; Yang, Y.; Liu, D.; Ming, B.; Ren, K. Analysis of spatial and temporal evolution patterns of Han River runoff under changing environment. *People Pearl River* **2020**, *5*, 123–131.
58. Xia, J.; Ma, X.; Zou, L.; Wang, Y.; Jing, C. Quantitative study on the impact of climate change and human activities on runoff changes in the upper Han River. *South-North Water Divers. Water Resour. Sci. Technol.* **2017**, *1*, 1–6.
59. Tian, J.; Guo, S.; Liu, D.; Chen, Q.; Wang, Q.; Yin, J.; He, S. Effects of climate and land use change on runoff in the Han River Basin. *J. Geogr.* **2020**, *11*, 2307–2318.
60. Shen, Q.; Cong, Z.; Lei, H. Evaluating the impact of climate and underlying surface change on runoff within the budyko framework: A study across 224 catchments in china. *J. Hydrol.* **2017**, 251–262. [CrossRef]
61. Gentine, P.; D'Odorico, P.; Lintner, B.R.; Sivandran, G.; Salvucci, G. Interdependence of climate, soil, and vegetation as constrained by the budyko curve. *Geophys. Res. Lett.* **2012**, *39*, L19404. [CrossRef]
62. Zhai, J.; Zhao, Y.; Pei, Y. Analysis of hydrological risk factors for water supply in the South-North Water Transfer Central Water Source Area. *South-North Water Divers. Water Sci. Technol.* **2016**, *8*, 13–16.
63. Li, L.; Zhang, L.; Xia, J.; Gippel, C.; Wang, R.; Zeng, S. Implications of modelled climate and land cover changes on runoff in the middle route of the south to north water transfer project in China. *Water Resour. Manag.* **2015**, *29*, 2563–2579. [CrossRef]
64. Rui, X.; Zhi, C.; Yun, Z. Impact assessment of climate change on algal blooms by a parametric modeling study in Han River. *J. Resour. Ecol.* **2012**, *3*, 209–219. [CrossRef]
65. Zhang, J.; Guo, L.; Huang, T.; Zhang, D.; Deng, Z.; Liu, L.; Yan, T. Hydro-environmental response to the inter-basin water resource development in the middle and lower Han River, China. *Hydrol. Res.* **2022**, *53*, 141–155. [CrossRef]
66. Zhang, J.; Zhang, Y.; Sun, G.; Song, C.; Dannenberg, M.P.; Li, J.; Hao, L. Vegetation greening weakened the capacity of water supply to China's South-to-North Water Diversion Project. *Hydrol. Earth Syst. Sci.* **2021**, *25*, 5623–5640. [CrossRef]
67. Wei, Y.; Tang, D.; Ding, Y.; Agoramoorthy, G. Incorporating water consumption into crop water footprint: A case study of China's South–North Water Diversion Project. *Sci. Total Environ.* **2016**, *545*, 601–608. [CrossRef]
68. Zhang, S.; Yang, H.; Yang, D.; Jayawardena, A.W. Quantifying the effect of vegetation change on the regional water balance within the Budyko framework. *Geophy. Res. Lett.* **2016**, *43*, 1140–1148. [CrossRef]
69. Wang, W.; Lu, W.; Wan, L.; Jin, L.; Chang, N. Study on the evolution pattern of parameter n of the budyko equation and its attribution in the Yellow River Basin. *Water Resour. Conserv.* **2018**, *34*, 7.
70. Pontius, R.G., Jr.; Spencer, J. Uncertainty in extrapolations of predictive land-change models. *Environ. Plan. B Plan. Des.* **2005**, *32*, 211–230. [CrossRef]

sustainability

MDPI

Article

Optimal Process Network for Integrated Solid Waste Management in Davao City, Philippines

Kristin Faye Olalo †, Jun Nakatani * and Tsuyoshi Fujita

Department of Urban Engineering, The University of Tokyo, Tokyo 113-8656, Japan; olalo@env.t.u-tokyo.ac.jp (K.F.O.); fujita77@env.t.u-tokyo.ac.jp (T.F.)

* Correspondence: nakatani@env.t.u-tokyo.ac.jp

† Present address: Department of Architecture, University of the Philippines Mindanao, Davao City 8026, Philippines.

Abstract: Municipal solid waste management (MSWM) systems in developing countries adopt practices from developed countries to reduce their environmental burdens. However, several complex issues specific to developing countries hinder the full implementation of these practices. The future of MSWM in Davao City, Philippines, is envisaged as a notable example of the combination of new infrastructure and local MSWM practices. A linear programming model was developed, following material flow analysis and life cycle assessment, to design an optimal system for Davao City. The performance of the system was evaluated in terms of greenhouse gas emissions, energy and revenue generated, and the amount of landfill waste. The results show that the proposed system positively affects the environment compared to the current system, due to additional treatment options. However, the main allocation concern transitions from organic waste in the current system to plastic waste in future scenarios. Furthermore, the mitigation of greenhouse gas emissions and the extension of landfill life will be heavily influenced by trade-offs between sorting operations and the management of incinerated wastes with high calorific values. Therefore, plastic-waste-specific treatment options will be critical for future MSWM systems. The results herein underscore the need for sustainable MSWM in the study area, considering the region-specific conditions.

Keywords: greenhouse gases; integrated solid waste management; life cycle assessment; linear programming; material flow analysis; separation rate

Citation: Olalo, K.F.; Nakatani, J.; Fujita, T. Optimal Process Network for Integrated Solid Waste Management in Davao City, Philippines. *Sustainability* **2022**, *14*, 2419. https://doi.org/10.3390/su14042419

Academic Editor: Luis Garrote

Received: 27 January 2022
Accepted: 15 February 2022
Published: 20 February 2022

1. Introduction

Municipal solid waste management (MSWM) has become an important environmental issue in many developing countries. The threat of global climate change has prompted changes in MSWM systems as one way to reduce greenhouse gas (GHG) emissions. In response, a modernization trend is emerging in the urban areas of developing countries to adopt the experience of developed countries and their integrated solid waste management systems as global best practices [1]. There is also a growing interest in creating environmentally friendly MSWM and resource conservation through improved infrastructure systems, the application of technologies such as incineration, and the use of scientifically derived process networks [2–4].

However, applying current methodologies from developed countries to developing countries presents many obstacles to full implementation, due to the complexity of the situation in developing countries. These complexities include rapid economic growth, high urbanization rates, differences in waste composition, a lack of proper governance, the presence of an informal sector, and a lack of financial resources [1,5–10]. Therefore, MSWM systems need to be adapted to best suit the socio-economic conditions of the region wherein these future improvements will be realized [11,12].

Davao City is a notable example of this current and future waste situation. As the capital of the third-largest metropolitan area in the Philippines, Davao is expected to face

the consequences of rapid waste generation and a lack of waste-related infrastructure. With a projected population of 1.7 million in 2017, the city's waste generation has already reached 991 tons per day (TPD) and is expected to increase further as its population and economy grow. The emergence of this new threat led to a plan to integrate MSWM services, as indicated in the Davao City Ecological Solid Waste Management Plan (ESWMP) for the 10-year period from 2018 to 2027 [13]. Some of the goals identified to support this plan are improving waste separation and reduction at source, increasing waste diversion toward composting and recycling facilities and enhancing MSWM through new waste-to-energy (WTE) and sanitary landfill facilities.

This plan shall follow the waste categorization for separation set forth in the Ecological Solid Waste Management Act of 2000 (RA 9003). These categories are biodegradable waste, recyclable waste, residual waste, and special waste. Biodegradable waste is organic waste that undergoes biological degradation under controlled conditions and can then be converted into compost. On the other hand, recyclable wastes are collected from the waste stream and converted to appropriate beneficial uses. Residual wastes are solid wastes that are neither compostable nor recyclable and that must be disposed of through long-term disposal or sanitary landfilling. Special wastes are hazardous wastes generated by domestic households [14]. In addition, the proposed infrastructure that is needed and targets for MSWM to be implemented within the next 25 years [15] include the expansion of collection areas, the introduction of landfill gas recovery [13], and incineration [16]. Recycling and composting at the barangay (the smallest political unit in the Philippines) or village level will also play an important role in achieving the target waste diversion rates. Therefore, villages without material recovery facilities (MRFs) are encouraged to form market linkages with the nearest and most suitable waste product storage sites to meet their collection and recovery needs [13].

The proposed system relies heavily on the success of source-separated collections, which are as yet not widely practiced in the Philippines. In addition, there are limited studies on the impact of the proposed MSWM system on cities and municipalities. The maximum capacity of each treatment facility and a market for valuable outputs (e.g., recycled materials, compost, and energy generated from waste) is necessary for the proposed MSWM system to function sustainably in the city. Hence, qualitative and quantitative information on current and future MSWM systems will provide valuable supporting resources for policy formulation and appropriate waste treatment, and for the development of disposal facilities in Davao City and other areas with similar conditions.

Material flow analysis (MFA) and life cycle assessment (LCA) are often used to analyze the environmental burdens that need to be considered as part of the decision-making process to better understand current and proposed MSWM systems. In recent studies, LCA has been used to assess the environmental impacts of existing and potential improvements to MSWM systems [2,3]. LCA has also been used to compare different MSWM scenarios regarding mixed MSW [17,18] and individual waste fractions [8,19].

Furthermore, several models have been developed by which to design the ideal MSWM system and waste management system solutions, based on various waste management technologies, most of which are oriented toward economic optimization [4,20–25]. Some have also taken into consideration the GHG emissions of MSWM systems, the limitations of the current treatment technologies, and the demand for MSWM by-products in the respective study area (see Table S1 in the Supporting Information). However, despite the realities of separation, as presented in some system assessment models, most optimization models generally set the waste separation rate at 100%. There is also limited literature published that discusses the impact of local waste separation categories and separation success rates on the proposed systems' functioning. This is especially significant when adding new technologies that require a prescribed amount and quality of waste inputs, such as in the case of incineration.

This study attempts to integrate the proposed treatment/disposal options, taking into account the waste separation categories, local demand for the useful outputs of MSWM,

and the minimization of GHG emissions in the Philippines. Hence, this study aims to assess whether adopting the proposed management system in 2027 will reduce GHG emissions compared to the baseline MSWM system, set in 2017. In addition, the performance of the future system, assuming varying degrees of success in implementing the source separation and collection system, will be evaluated. Therefore, LCA and linear programming (LP) optimization are utilized to determine the ideal MSW treatment network for Davao City. Furthermore, a stepwise approach was used to (1) compare the current MSWM system with future scenarios, (2) examine the environmental performance of future scenarios based on different management priorities, and (3) establish a greener future system for Davao City by changing the existing waste separation categories.

2. Materials and Methods

2.1. Study Area

Davao City is the third-largest city in the Philippines and the most populous city in Mindanao. The total waste generation in the city in 2017 was 991 TPD, 80% of which was from residential sources, followed by public markets at 7%. The per capita waste generation from all sources was 0.58 kg. As shown in Table 1, biodegradable and recyclable components account for 50% and 18% of total waste generation, respectively, while residual and special waste account for 29% and 2%, respectively [13].

Table 1. The physical composition of MSW in Davao City.

Material Composition		Composition (%)	MSW Separation Categorization (%)			
			Biodegradable	Recyclable	Residual	Special
Food		43.40	43.40			
Yard, wood		6.68	6.68			
Glass, ceramic, stone		4.26		3.51	0.75	
Metals	Steel	2.52		2.52		
	Aluminum	0.29		0.29		
Paper		17.29		6.88	10.41	
Plastic, rubber		20.14		5.22	14.92	
Textile		3.11			3.11	
Others		2.31				2.31
Total		100.00	50.08	18.42	29.19	2.31

Data source: 10-year ESWMP of Davao City (2018–2027) [13].

By 2027, total waste generation in the city is projected to reach 1209 TPD, or 441 kilotons (kt), of MSW annually. The 10-year ESWMP assumes that the waste composition in 2027 will be consistent with that in 2017.

2.2. Methodology

MFA and LCA were used to quantify MSW flows and estimate the GHG emissions for MSWM systems in both current and future scenarios. The LCA results were then used to identify the emission factors per ton of waste in processes associated with this study. Finally, these values were used as input data for the LP optimization model, to identify potential improvements or solutions for the 2027 scenario.

2.2.1. MFA

Field visits and interviews were conducted from February 2020 to March 2020, to collect primary and secondary data for the study area. Following these initial studies, a city-level waste flow analysis was conducted to establish a baseline for Business-as-Usual (BAU) practices and future MSW flow upon implementing the local waste diversion plan.

2.2.2. LCA

Following the implementation of MFA, LCA is used as an assessment tool. The technical framework of the LCA methodology is as outlined here. This part of the study

aims to assess GHG emissions from the existing and future MSWM systems in Davao City. The current research has been limited to assessing the emissions of CO_2, CH_4, and N_2O from the studied MSWM systems.

The relevant processes for the current and future scenarios will be included in the MSW management system boundary. However, as shown in Figure 1, the collection and transportation of MSW from the source in each scenario are not included in the system boundary. Apart from the direct processes related to the waste management system, other related processes involved in the waste management system are included. Furthermore, a system expansion or an avoided burden approach (as employed by Nakatani, 2014 [26]) is used to assess whether products recovered from the MSWM system can be used as a substitute for products from virgin resources in other systems.

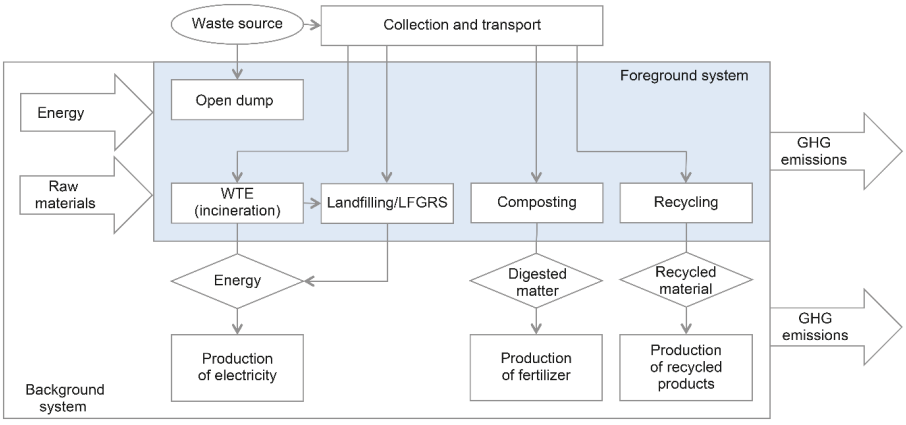

Figure 1. The system boundary of LCA in this study.

This phase was undertaken to compile the input and output data associated with all relevant processes included in the system boundary onto worksheets in Microsoft Excel. Emission factors related to current and future MSW treatment options were calculated using local government information and emission factors drawn from various databases and the literature. Emission factors for open dumping, landfilling, and LFGRS were calculated according to Manfredi et al. (2009) [27], using the Intergovernmental Panel on Climate Change (IPCC) default values for methane emissions and diesel and electricity demand. Emission factors for material recycling were obtained from the work of Friedrich and Trois (2013) [28]. Fossil carbon dioxide emissions from incineration systems were calculated using the lower heating values reported by Dong et al. (2013) [3] and diesel and electricity requirements reported by Astrup et al. (2009) [29]. In the case of composting, the compost produced can be used as a low-quality fertilizer (or soil conditioner). Diesel fuel and electricity requirements for composting were calculated using the values reported by Boldrin et al. (2009) [30].

The emission factors for combined conventional power generation in the Mindanao grid were collected from the Department of Environment and Natural Resources (0.468 kg CO_2-eq/kWh) and were used to calculate the avoided emissions from recovered electricity with waste-to-energy facilities. In addition, the emissions related to diesel combustion were calculated using emission factors reported by Fruergaard et al. (2009) [31].

The GHG emissions calculated in this study are expressed in terms of global warming potential (GWP). The equivalency factors of global warming were obtained from the IPCC [32]. For example, CO_2 has a GWP of 1, whereas CH_4 and N_2O have GWPs of 28 and 265, respectively.

2.2.3. LP Optimization

In this study, an LP model was applied to project the structure of the MSWM system in Davao City in 2027, comprising waste treatment technologies widely implemented in many developing countries. We considered four performance indicators in line with the goals of the 10-year ESWMP for Davao City [13], i.e., environmental (GHG emissions and the amount of landfill waste), economic (revenue), and energy (energy produced from waste) indicators. Moreover, we considered the potential demand for the products recovered from waste as the upper limit constraint, and their sales prices were estimated based on the City Government of Davao (2017) [13] and Asian Development Bank (2013) [33] (see Figure S1 in the Supporting Information).

The objective functions applied in the model correspond to the scenarios analyzed in this part of the study. This includes minimizing the GHG emissions of the system, maximizing the revenue from the system, and minimizing the MSW allocated for final disposal at the sanitary landfill.

System GHG emissions. This refers to the GHG emission of the system (t CO_2-eq/year) shown in Equation (1) as GWP. Here, j is the type of treatment facility, i is the type of waste, q_{ij} is the quantity of waste i (t/year) assigned to treatment process j, and emf_{ij} is the emission factor of waste i for treatment j (t CO_2-eq/t).

$$\text{GWP} = \sum_j \sum_i q_{ij} \cdot \text{emf}_{ij} \tag{1}$$

Energy generated by the system. This refers to the cumulative energy generated by the waste incineration plant and landfill gas recovery system. In Equation (2), ERP_{ij} refers to the energy recoverable from waste, i, in treatment j.

$$\text{Energy} = \sum_j \sum_i q_{ij} \cdot \text{ERP}_{ij} \tag{2}$$

Revenue generated by the system. Revenue shall be limited to the sale of recovered MSWM products, k, such as compost, electricity, and recyclables. Waste disposal costs that are paid to treatment facilities, i.e., revenue from the facilities other than the sales of recovered products, are not considered because we focus on the quantity of the useful outputs that can be obtained from waste in this study.

$$\text{Revenue} = \sum_k q_k \cdot \text{PRICE}_k \tag{3}$$

Furthermore, the model is subject to the constraints described below.

Mass balance constraints. This refers to the amount of waste to be transported to the disposal or treatment process, j. In Equation (4), q_{ij} refers to the amount of waste, i. q_{ij} refers to the amount of waste, i, (t/y) allocated to the treatment facility.

$$\sum_i q_i = \sum_j \sum_i q_{ij} \tag{4}$$

Maximum capacity constraints. The amount of waste resource for each facility should be less than or equal to the maximum allowable amount for that facility. In Equation (5), Z_j refers to the planned capacity (units/y) of facility j.

$$\sum_i q_{ij} \leq Z_j \tag{5}$$

Waste allocation constraints. Each type of waste should be treated only in an appropriate treatment facility. In Equation (6), a_{ij} refers to the waste availability coefficient (%) of

waste i in treatment process j. The waste composition, following the conditions of waste categorization under RA 9003, governs this variable.

$$q_j \leq a_{ij} \cdot \sum_i q_i \tag{6}$$

Recovered product demand. The production rates of electricity, compost, and recycling materials must fulfill the product demands. The demand for compost products should be dictated by the total agricultural area of the study area, where 5 t/ha of compost will be allocated. The electricity demand shall be subject to the design generation capacity of the WTE plant, as defined in the local policy. On the other hand, the demand for recycled materials shall be subject to the capacity of the material recovery/recycling facilities in the study area. In Equation (7), q_k refers to the production rate of product k (units/y), while d_k refers to the demand for product k (units/y).

$$q_k \leq d_k \tag{7}$$

Non-negativity constraints. This constraint means that only positive amounts of MSW will be considered in the solution.

$$q_{ij} \geq 0 \tag{8}$$

The model formulated in this study has been developed and implemented using Excel Solver.

2.3. Description of Alternative Scenarios

This study utilized a stepwise approach to understand the impacts of change on the waste situation in Davao City and identify possible improvements. Various scenarios were proposed and evaluated, as follows.

2.3.1. Examining the Effectiveness of Additional Treatment and Disposal Methods, and Source-Separated Collection

Two scenarios are considered to establish whether a local waste diversion plan can reduce GHG emissions from the existing MSWM system.

Scenario 1. This scenario is defined as the baseline scenario of the MSWM system in 2017. Source-separated collection practices are not considered, and the waste management options are composting, recycling, and landfilling. Due to limited collection compliance, a significant fraction of the waste generated is disposed of by open dumping. Losses in existing collection areas are also assumed to be openly dumped.

Scenario 2. By 2027, source-separated collection will be considered to occur according to the local waste diversion plan. The municipal collection covers all barangays except one because of poor road conditions in the area. Therefore, it is assumed that waste in this excluded barangay is disposed of via open dumping. Waste management options include composting, recycling, landfilling (including gas recovery), incineration, and household hazardous-waste storage.

2.3.2. Establishing an Environmentally Friendly Future MSWM System

In order to improve the MSWM system in Davao City, a 10-year ESWMP was prepared for the period 2018–2027 [13]. The goals outlined in the plan include maximizing the generation of power from waste, extending the life of the sanitary landfill, and minimizing the GHG emissions of the MSWM system. In this section, we evaluate how choosing an optimization goal that corresponds to the goals of the local waste management plan can change the environmental performance of alternative scenarios. The same MSW categories and quantities generated, as in Scenario 2, are considered. The following three scenarios are subject to the upper limit constraints of disposal/treatment options and the estimated demand for valuable outputs in the study area.

Scenario 3. The 2027 system is optimized to minimize GHG emissions.

Scenario 4. The sale of useful outputs is maximized to generate the most revenue. As a result, the power generation capacity of WTE facilities and the recycling and composting processing capacity can be maximized.

Scenario 5. Minimizing landfill waste is a priority when allocating waste to disposal and treatment facilities.

2.3.3. Examining the Effectiveness of Waste Separation

Changes in the local recycling market, such as market standards for recyclable materials, can result in differences in the ratio of recyclable to residual fractions of the waste stream. In this part, the impact of the increase in the recyclable fraction on the performance of the MSWM systems, as described in Scenarios 3 to 5, will be discussed. The same amount of MSW is assumed to be generated as in Scenario 2, taking into account the upper limit constraints of the waste treatment facilities and the demand for useful outputs. Scenarios 3 to 5 are optimized by turning off the upper limit constraints for the recyclable fraction.

2.4. Sensitivity Analysis

The performance of the future MSWM system may be greatly affected by various factors, including the performance of the separation rate in the segregated collection. Hence, a sensitivity analysis was conducted on the change in the separation rate of biodegradable and recyclable wastes in the 2027 system, considering the upper limits of various treatment methods in the study area. In addition, we investigated the sensitivity in GHG emissions of the 2027 scenario to the amount of plastic waste generation, which was considered to be one of the most influential factors on GHG emissions from waste incineration and on the avoided emissions from recycling.

3. Results and Discussion

3.1. MFA of Current and Future Scenarios

3.1.1. MFA of the MSWM System in 2017

In the BAU scenario, municipal collection services are provided to only 65% of the population, most of whom reside in the city's relatively flat and densely populated areas. The estimated waste generation within the collection area was 835 TPD in 2017 [13], of which only 611 TPD (Figure 2) was collected by the local government [34]. The uncollected waste and losses in the collection area are estimated at 156 TPD and 188 TPD, respectively. Out of 182 barangays in the city, there are four barangays with functioning MRFs, of which two barangays have vermiculture composting facilities. The current processing capacity of the MRFs is 1 TPD [15], mainly processing organic waste.

The material flow in the BAU scenario is shown in Figure 3. The collection activities by the private waste sector can be further divided into formal and informal sectors. The material recovery system in the city is mainly established by the informal waste sector (IWS), which supplies the recovered waste as raw materials to the formal private sector. Due to the limited available data, direct flows from non-residential sources to recycling facilities exist but are excluded from this study. The IWS includes roving waste buyers, street collectors, the municipal collection crew, and waste pickers at landfills. The estimated amount of waste recovered for recycling by IWS is about 50 TPD [15,16], 15 TPD of which is contributed by the municipal collection crew. This total value excludes the yield of waste pickers at landfills. As of August 2017, there are 44 registered junk shops in the city, with an estimated total yield of 73 TPD [13]. According to a JICA survey (2008) [35], the recyclables collected in the city comprised 29.1% plastic, 28.5% paper, 25.0% metal, 17.0% glass, and 0.4% other materials. These recyclables were then consolidated in waste product storage facilities and sold to their primary buyers, such as plastic recycling plants, steel mills, and paper mills.

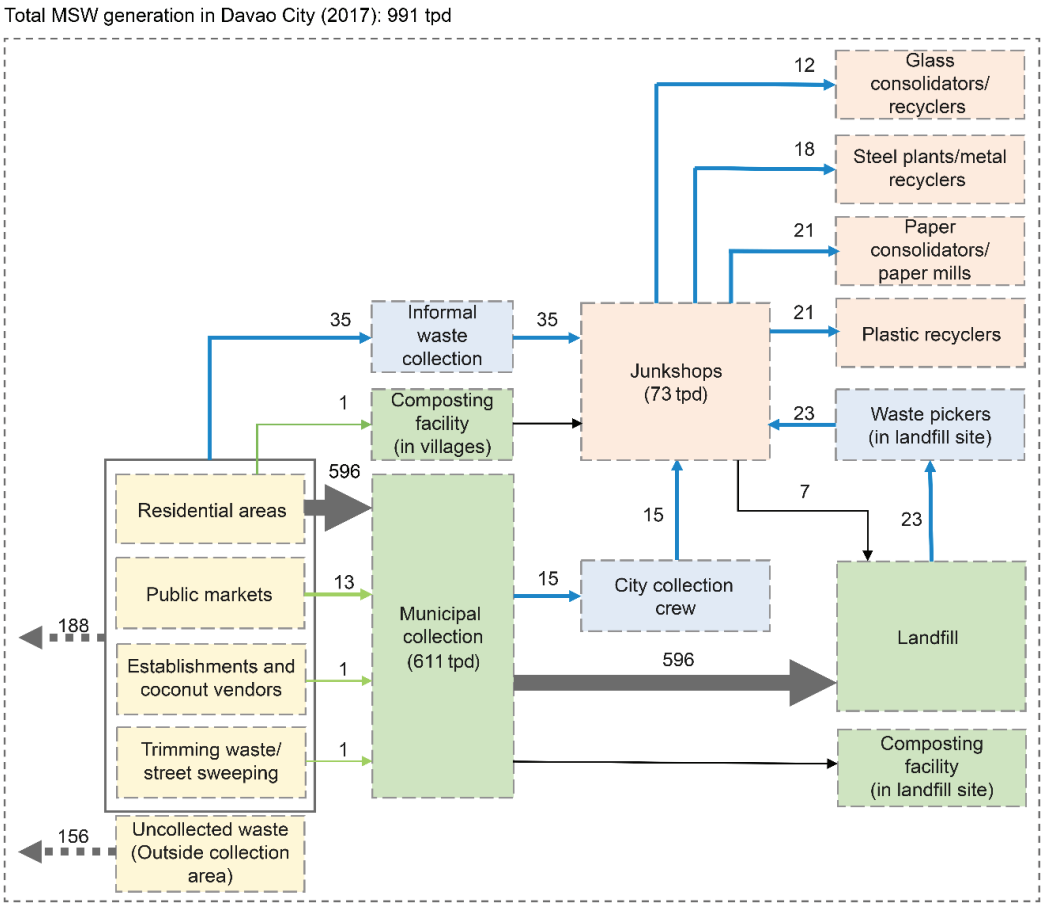

Figure 2. Current status of MSWM in Davao City, Philippines (tons/day: TPD).

There is only one sanitary landfill (SLF) in Davao City, located in Barangay New Carmen. It covers an area of 3.8 ha and has a capacity of 2.85 million m^3 [36]. The landfill started operation in 2010, and the remaining service life of the landfill is estimated to be about 6 years (after the publication of this report in 2018) [34]. The landfill received an estimated amount of 596 TPD in 2017. The landfill site has a composting facility with three rotary composters, which process 3.5 tons per month (TPM) of biodegradable waste to produce 1.5 TPM of compost. The compost generated is used for greening and beautification programs in the city and is distributed free of charge to institutions and small farms upon request [13]. There are also about 200 waste pickers at the landfill. Data on the breakdown of waste recovered by the waste pickers were collected through the receipts used by them to receive payment from buyers. Twenty-two receipts were collected by the researchers. The results showed that the 22 waste pickers collected a total of 3054 kg of waste materials (an average of 139 kg per person), which consisted of plastics (42.22%), metals (28.16%), paper and cardboard (24.82%), glass (4.14%), batteries (0.59%), and coconut shells (0.07%).

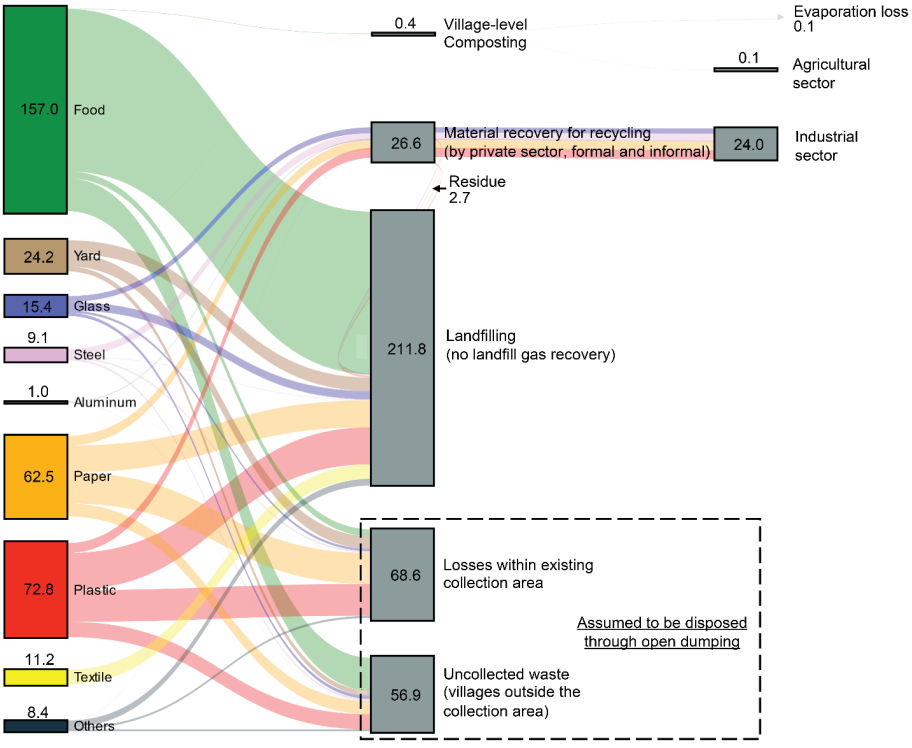

Figure 3. Material flow in the BAU scenario (2017) (unit: kt/yr).

3.1.2. MFA of the MSWM System in 2027

Figure 4 shows the waste flow in the city, according to material composition, for the proposed MSWM system based on the local waste diversion plan. The outline of the proposed MSWM system is shown in Figures S2 and S3 in the Supporting Information.

One of the fundamental changes in the proposed future MSWM system is that the Davao City Environment and Natural Resources Office (CENRO) aims to collect 100% of MSW by 2025 [36]. They intend to implement a segregated collection and transport system by establishing an MRF in each village or a cluster of villages to receive, sort, process, and store compostable and recyclable materials. The following calculations assume that all villages except Barangay Gumitan, which has poor road conditions, will have a village-level MRF capable of receiving and sorting 100% of the waste generated in the village. By 2027, a 50-TPD composting facility and an 18-TPD centralized MRF will also be established. The local waste diversion plan also acknowledges the activities of IWS by allocating recyclable waste diversion by a scavenging crew.

Davao also proposes to operate the Philippines' first WTE facility in 2022 [34,36], which is projected to have a capacity of 600 TPD and to generate 9.7 MW of electricity, or 74,688 MWh/yr [16]. This amount corresponds to about 2% of the demand forecast of the Davao Light and Power Company for 2027 [37]. The city has also acquired land for establishing new sanitary landfills, with an estimated capacity of 3 million tons [34]. In addition, according to the local plan, a private developer has expressed interest in setting up a gas-to-energy project at the New Carmen disposal facility [13]. However, due to the limited information available on this project, details such as the power generation capacity of the proposed project are based on the Payatas disposal facility in Quezon City, which is referenced in the 10-year ESWMP of Davao City (2018–2027) [13].

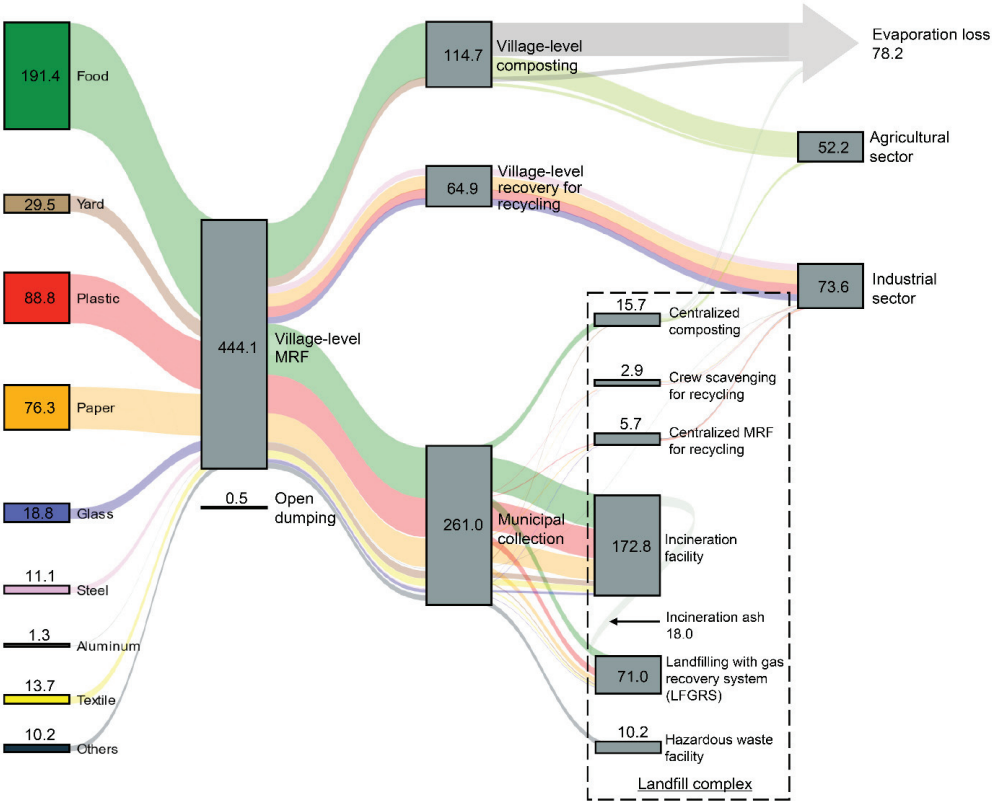

Figure 4. Material flow of the future scenario (2027) (unit: kt/yr).

3.2. Comparison of Current and Future Scenarios

In the BAU scenario, 58.6% of the waste generated was allocated to landfills, 15.7% was uncollected, 6.6% was recovered for recycling by the private formal and informal sectors, and 0.1% was composted. Losses within the existing collection area accounted for 19%, and there was no energy production activity from MSW. The BAU scenario generated an estimated emission amount of 271 kt CO_2-eq/yr (Figure 5). In addition to the emissions shown in Figure 5, diesel consumption for waste collection leads to an estimated 1.2 kt CO_2-eq/yr of GHG emission, which is much smaller than the emissions from landfilling and open dumping. The most significant contributor to GHG emissions in this scenario is the release of methane from landfills and open dumps, due to the degradation of organic waste. It must be noted that the current landfill system is not equipped with a gas collection system.

Future scenarios were designed to anticipate trade-offs between the separation process and additional MSW treatment/disposal options. Based on the local waste diversion plan, 39.2% of the total waste will be allocated to incineration, 29.6% to composting, 12.2% to LFGRS, and 2.3% to hazardous waste storage; only 0.1% will remain uncollected. Therefore, in the 2027 scenario, the system is expected to emit 73 kt CO_2-eq per year, with the incinerated plastic fraction of the residual waste being the main contributor to emissions (Figure 6). Taking this into account, the system's emissions will decrease from 0.75 t CO_2-eq per ton of MSW in the 2017 scenario to 0.17 t CO_2-eq per ton of MSW.

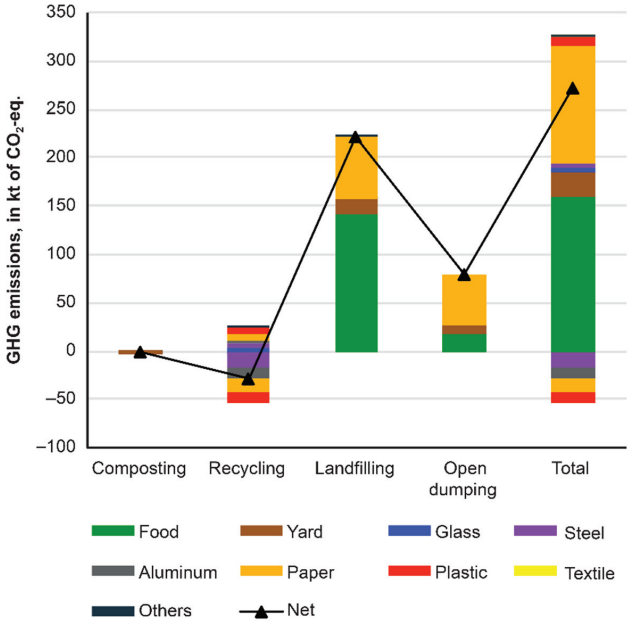

Figure 5. Estimated annual GHG emissions in the 2017 scenario.

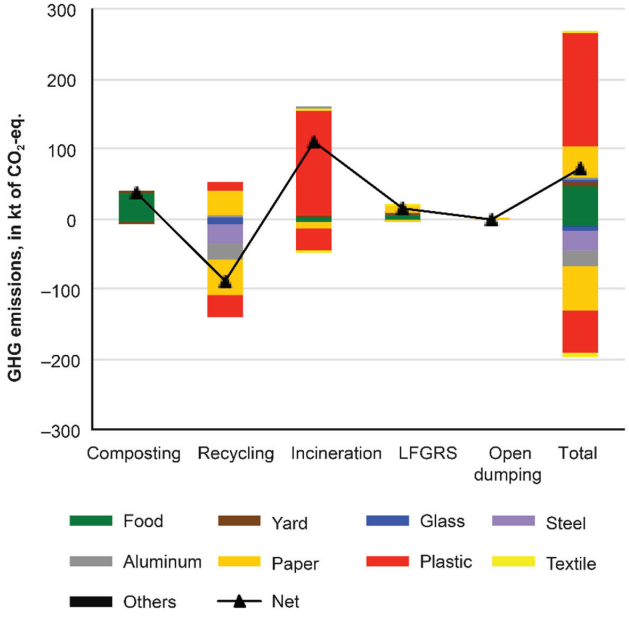

Figure 6. Estimated annual GHG emissions of the 2027 scenario.

However, in the local plan for the 2027 scenario, the challenge is that the maximum power generation of the incineration plant will be reached before the maximum annual throughput of MSW is reached. Furthermore, the upper limit of the local demand for recyclable materials has been estimated. As a result, it is anticipated that a significant amount of MSW will be diverted from the recycling and incineration processes to the sanitary landfill.

Such a change in the allocation of MSW will result in changes in the expected performance of the MSWM system. Here, the net GHG emissions from incineration and landfilling become 46 and 60 kt CO_2-eq/yr, respectively, and the avoided emissions from recycling and composting become −45 kt CO_2-eq/yr. Consequently, the volume of system GHG emissions can decrease to 60 kt CO_2-eq/yr.

3.3. Sensitivity Analysis

The performance of the 2027 MSWM system mentioned earlier is greatly affected by the performance of the separation rate in the segregated collection. As a result of the sensitivity analysis considering the upper limits of various treatment methods in the study area, the target separation rates in the 2027 local plan will be 59% for biodegradable wastes and 91% for recyclable wastes.

3.3.1. Sensitivity Analysis of Landfill Waste to Separation Rate

One of the major impacts of the change in separation rate can be seen in the annual amount of landfill waste. It is assumed that the future landfill facility will have a capacity of 3 million tons and will be operational from 2022 to 2045. Therefore, to achieve sustainable waste management during this 24-year period, it is assumed that the annual amount of landfill waste will not exceed 125 kilotons. Therefore, to prolong the sanitary landfill's life, it is necessary to achieve adequate separation rates for both waste categories in the city (shown in Table 2 as underlined values).

Table 2. Sensitivity of landfill MSW to separation rate (kt/yr).

		Biodegradable Waste Separation Rate										
		0%	**10%**	**20%**	**30%**	**40%**	**50%**	**60%**	**70%**	**80%**	**90%**	**100%**
Recyclable waste separation rate	0%	258	242	226	210	194	178	163	148	133	119	105
	10%	250	233	217	201	186	170	155	140	126	111	98
	20%	240	224	208	193	177	162	147	132	118	104	90
	30%	231	215	200	184	169	154	139	125	110	97	83
	40%	222	206	191	175	160	145	131	117	103	89	76
	50%	213	197	182	167	152	137	123	109	95	82	69
	60%	204	188	173	158	143	129	115	101	88	75	63
	70%	195	179	164	149	135	121	107	93	80	68	56
	80%	185	170	155	140	126	112	99	86	73	61	49
	90%	176	161	146	132	118	104	91	78	66	54	43
	100%	166	151	137	123	109	96	83	70	58	47	36

Note: Underlined values ≤ 125 kt MSW/yr; estimated upper limit of local demand for recyclables at 74%.

This problem is exacerbated by the limited estimated demand for recyclable materials in the study area, requiring higher separation rates for biodegradable waste. In addition, the local waste diversion plan still relies heavily on the support of a network of formal and informal private waste sectors, suggesting the need to promote the capacity-building of these establishments (e.g., waste product storage facilities).

3.3.2. Sensitivity Analysis of System GHG Emissions to Separation Rate

Increasing the separation rate of biodegradable and recyclable wastes will reduce the GHG emissions of the system. However, as shown in Figure 7, a significant decrease in emissions is expected with increasing the biodegradable waste separation rate compared to that of recyclable waste.

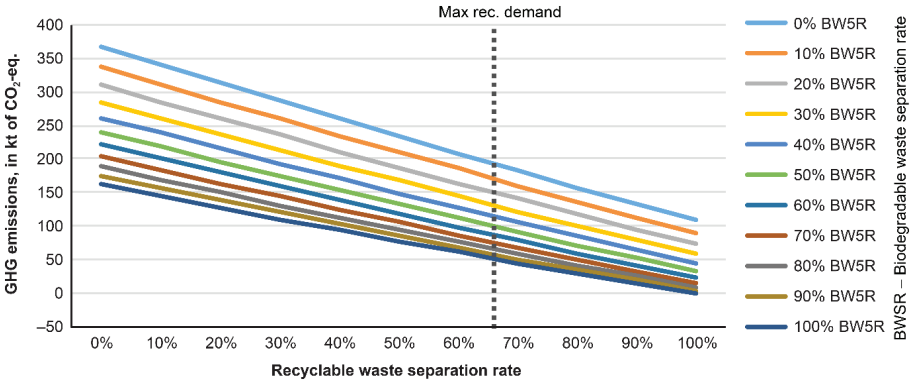

Figure 7. Sensitivity of system's annual GHG emissions to separation rate.

GHG emissions in the 2027 scenario will be heavily affected by the relationship between separation rates and the management of lower calorific value (LCV) of MSW for incineration. Without an efficient source separation of biodegradable and recyclable waste fractions, the maximum power generation of the incineration facility will be reached before the annual amount of processed MSW is capped, leading to an increase in landfill waste. On the other hand, one of the main influencing factors for the high LCV of incinerated MSW is the high percentage of residual plastic waste that is not affected by the improved separation rate. Hence, improving the separation system according to the individual material composition will benefit future MSWM systems, which will be discussed in the following section.

3.3.3. Sensitivity Analysis of System GHG Emissions to Plastic Waste Generation

When the amount of plastic waste generation changes in the range of ±50%, the net GHG emission from incineration in the 2027 scenario, considering the upper limit constraint of the facilities to be 46 kt CO_2-eq/yr, is expected to proportionally vary between 34 and 51 kt CO_2-eq/yr. Similarly, the net GHG emission from landfilling is expected to vary between 16 and 103 kt CO_2-eq/yr, and the avoided emission from recycling and composting also varies between −49 and −27 kt CO_2-eq/yr. As a result, the amount of system GHG emissions can decrease to 1 kt CO_2-eq/yr when the plastic waste generation is halved, whereas it is expected to increase to 127 kt CO_2-eq/yr when the plastic waste generation increases by 50%.

3.4. LP Optimization of the 2027 Scenario

As shown in Figure 8, the optimal solution for organic wastes, such as food and paper, is incineration to minimize the resulting system emissions. This is because the incineration of these components emits biogenic CO_2, while the incineration of textiles and plastics emits fossil-fuel-derived CO_2. Therefore, recyclable plastics, metals, and paper are allocated to recycling. On the other hand, residual plastics, glass, and the remaining unprocessed waste are disposed of in landfills, thus minimizing the use of composting facilities. Furthermore, the energy recovery performance of this scenario is influenced by the avoidance of the incineration of high-calorific-value wastes. Therefore, even though the system emissions are estimated to be about −81 kt CO_2-eq/yr, the amount of landfill waste in this scenario exceeds 125 kilotons, which may shorten the operational life of the sanitary landfill.

As shown in Figure 9, under the maximum revenue scenario, the power generation capacity of the WTE facilities and the processing capacity for recycling are maximized. As a result, the revenue from the sale of MSWM recovered products, including power generation of 82,688 MWh/year, is estimated at PHP 1.49 million. Thirty-nine percent of the total revenue will come from the recycling of plastics, followed by 37% from the sale

of electricity. To achieve this, plastic waste will be used for incineration, increasing the LCV of incinerated waste. As a trade-off, the GHG emissions for this scenario will be 19 kt CO_2-eq/yr. Therefore, landfill waste is reduced to about 84 kt/yr in this scenario.

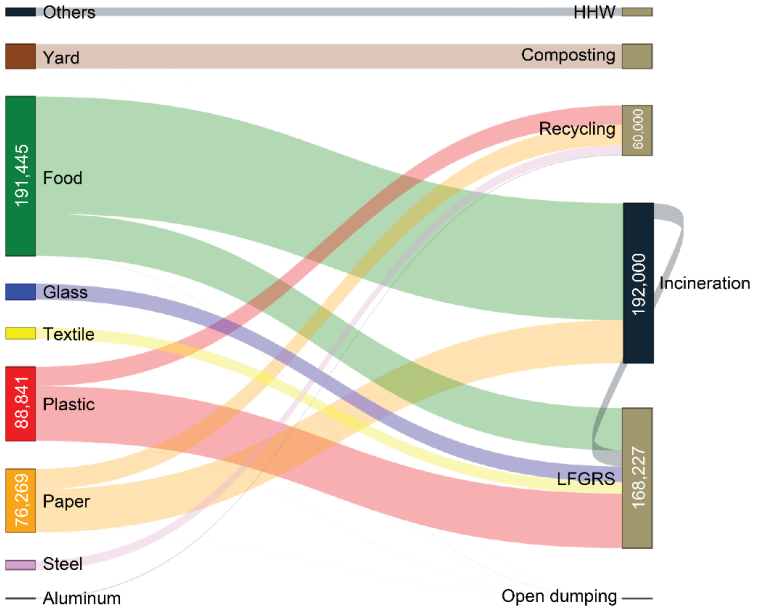

Figure 8. Optimization results: minimization of GHG emissions.

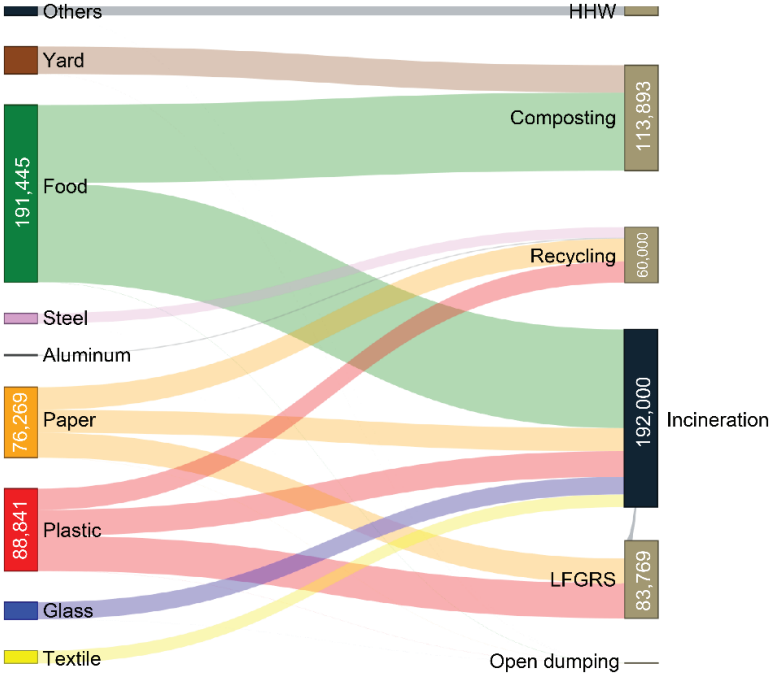

Figure 9. Optimization results: maximization of revenue.

As shown in Figure 10, wastes with high calorific value, such as plastic and paper, are redirected to recycling activities, in line with maximizing food composting to minimize landfill waste. As a result, except for some plastic waste, all the remaining MSW would be incinerated, with an estimated emission of −5 kt CO_2-eq, a revenue of PHP 1.37 million, and landfill waste of 67 kt/yr. This scenario involves minimal landfill gas recovery.

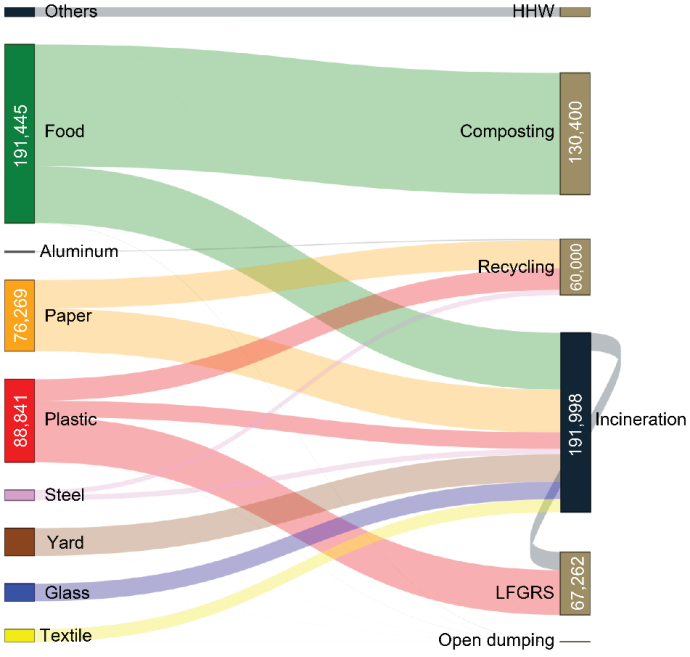

Figure 10. Optimization results: minimization of landfill waste.

3.5. Implications of the Ratio between Recyclable and Residual Fractions of MSW

One of the common MSW allocation procedures observed in the three scenarios is the specific allocation of plastic waste to manage the LCV for incineration. This is achieved either by maximizing recyclable plastics for recovery or by minimizing the residual plastic waste to be incinerated. This is especially noticeable in all three scenarios studied, where landfill plastic is significantly high. Therefore, the recovery or the recycling of this plastic waste with different objective functions is beneficial for revenue generation, the avoidance of emissions, and the diversion of waste from landfills.

As a result, we inputted the data into the LP model and optimized it by turning off the upper limit constraint for the recyclable fraction. This changed the distribution of the conventionally classified recyclable and residual fractions of each material (see Figure S4 in the Supporting Information). All three scenarios prioritized recycling plastic waste, causing a decrease in incinerated plastic and an increase in the incinerated MSW. This causes a decrease not only in the energy generated but also in the system emissions and landfilled waste. The results in Table 3 indicate that prioritizing the collection of waste plastics at the MRFs and expanding the local definition of recyclable plastics will bring additional environmental and economic benefits to future MSWM systems.

Table 3. Summary of the optimization results (the upper limit constraints for the recyclable fraction are disabled).

Performance Indicator	Local Plan	Min GHG	Max Rev	Min LF
GHG emissions (kt CO_2-eq/yr)	73.5	−88.7 (−80.6)	6.1 (19.0)	−19.5 (−5.0)
Recovered energy (GWh/yr)	106.8 *	69.5 (54.5)	82.7 (82.7)	52.0 (67.2)
Revenue (million PHP/yr)	1631 *	1830 (1203)	2274 (1488)	1603 (1366)
Landfill waste (kt/yr)	71.0	163.9 (168.2)	67.3 (83.8)	67.3 (83.8)

Note: The values in parentheses have upper limit constraints. * Exceeds the upper limits of the incineration power generation capacity and local recyclable demand. USD 0.021 = PHP 1.

4. Conclusions

In this study, an LP model was developed to optimize the future MSWM system in Davao City, Philippines. The results indicate that increased MSW treatment options, including incineration, LFGRS, composting, and MRFs, with significant source separation, will offer positive energy and environmental benefits compared to the current MSWM system.

The main emphasis regarding treatment and disposal shifts from organic waste allocation in the BAU scenario to the plastic fraction of MSW in the 2027 scenario. The mitigation of GHG emissions in future scenarios will be heavily influenced by the trade-offs between separation and incineration activities. Without significant separation to manage the LCV of MSW to be incinerated, the capacity of the incineration facility for the annual MSW that is processed will not be maximized. This results in increased landfill waste and a shortened operational life of landfills. Hence, the modified separation scheme may be more beneficial to the future MSWM system, including the specific allocation of plastic waste. This means maximizing the recovery of recyclable plastics and/or minimizing the amount of plastic to be incinerated. Furthermore, the optimization results show that treatment options dedicated to the recovery and recycling of plastics may solve the problems identified so far in the sustainable implementation of the 2027 scenario.

This model could be extended to include additional treatment and disposal options and the related investment, land procurement, and operation and maintenance costs of treatment and disposal facilities. This is because the new MSWM infrastructure, while environmentally beneficial, may be restricted by high transportation costs, local budget constraints, and land availability. Moreover, future MSW processing networks need to improve the circulation of waste materials in the selected study areas, incorporating the capacity and the limitations of other relevant industries.

Supplementary Materials: The following supporting information can be downloaded at: https://www.mdpi.com/article/10.3390/su14042419/s1 [4,13,20–22,24,25,33,37], Figure S1: Process network of MSWM for 2027 in Davao City, Philippines. Figure S2: MSW collection, separation, and treatment/disposal options in the 2027 scenario. Figure S3: Supply and demand for the recovered MSWM products in the 2027 scenario. Figure S4: Changes to the material flow in optimization scenarios when the availability coefficient is disabled. Table S1: Comparison of the optimization models for solid waste management.

Author Contributions: Conceptualization, K.F.O. and J.N.; methodology, K.F.O.; validation, K.F.O., J.N. and T.F.; formal analysis, K.F.O.; investigation, K.F.O.; resources, K.F.O.; data curation, K.F.O.; writing—original draft preparation, K.F.O.; writing—review and editing, J.N.; visualization, K.F.O.; supervision, T.F.; project administration, J.N.; funding acquisition, K.F.O. All authors have read and agreed to the published version of the manuscript.

Funding: This research was funded by the Japan International Cooperation Center, through the Project for Human Resource Development Scholarship, by Japanese Grant Aid (JDS B0012019PHL007) for the graduate studies of Kristin Faye Olalo.

Institutional Review Board Statement: Not applicable.

Informed Consent Statement: Not applicable.

Data Availability Statement: The data presented in this study are available on request from the corresponding author.

Conflicts of Interest: The authors declare no conflict of interest.

References

1. Scheinberg, A.; Spies, S.; Simpson, M.H.; Mol, A.P.J. Assessing urban recycling in low- and middle-income countries: Building on modernized mixtures. *Habitat Int.* **2011**, *35*, 188–198. [CrossRef]
2. Liamsanguan, C.; Gheewala, S.H. The holistic impact of integrated solid waste management on greenhouse gas emissions in Phuket. *J. Clean. Prod.* **2008**, *16*, 1865–1871. [CrossRef]
3. Dong, J.; Ni, M.; Chi, Y.; Zou, D.; Fu, C. Life cycle and economic assessment of source-separated MSW collection with regard to greenhouse gas emissions: A case study in China. *Environ. Sci. Pollut. Res.* **2013**, *20*, 5512–5524. [CrossRef]
4. Tan, S.T.; Lee, C.T.; Hashim, H.; Ho, W.S.; Lim, J.S. Optimal process network for municipal solid waste management in Iskandar Malaysia. *J. Clean. Prod.* **2014**, *71*, 48–58. [CrossRef]
5. Troschinetz, A.M.; Mihelcic, J.R. Sustainable recycling of municipal solid waste in developing countries. *Waste Manag.* **2009**, *29*, 915–923. [CrossRef]
6. Pandyaswargo, A.H.; Onoda, H.; Nagata, K. Energy recovery potential and life cycle impact assessment of municipal solid waste management technologies in Asian countries using ELP model. *Int. J. Energy Environ. Eng.* **2012**, *3*, 28. [CrossRef]
7. Guerrero, L.A.; Maas, G.; Hogland, W. Solid waste management challenges for cities in developing countries. *Waste Manag.* **2013**, *33*, 220–232. [CrossRef] [PubMed]
8. Menikpura, S.N.M.; Gheewala, S.H.; Bonnet, S.; Chiemchaisri, C. Evaluation of the effect of recycling on sustainability of municipal solid waste management in Thailand. *Waste Biomass Valorization* **2013**, *4*, 237–257. [CrossRef]
9. Ferronato, N.; Torretta, V. Waste mismanagement in developing countries: A review of global issues. *Int. J. Environ. Res. Public Health* **2019**, *16*, 1060. [CrossRef]
10. Kazuva, E.; Zhang, J. Analyzing municipal solid waste treatment scenarios in rapidly urbanizing cities in developing countries: The case of Dar es Salaam, Tanzania. *Int. J. Environ. Res. Public Health* **2019**, *16*, 2035. [CrossRef] [PubMed]
11. Oosterveer, P.; Spaargaren, G. Meeting social challenges in developing sustainable environmental infrastructures in East African cities. In *Social Perspectives on the Sanitation Challenge*; Springer: Dordrecht, The Netherlands, 2010; pp. 11–30.
12. Menikpura, S.N.M.; Sang-Arun, J.; Bengtsson, M. Integrated solid waste management: An approach for enhancing climate co-benefits through resource recovery. *J. Clean. Prod.* **2013**, *58*, 34–42. [CrossRef]
13. City Government of Davao. *10-Year Solid Waste Management Plan of Davao City for 2018–2027*; City Government of Davao: Davao City, Philippines, 2017.
14. Republic of the Philippines. Republic Act 9003—The ecological solid waste management act of the Philippines 2000. In Proceedings of the Eleventh Congress of the Philippines, Third Regular Session, Quezon City, Philippines, 26 January 2001.
15. Japan International Cooperation Agency. Davao City Infrastructure Development Plan and Capacity Building Project—Final Report—Summary. 2018. Available online: http://open_jicareport.jica.go.jp/pdf/12308706.pdf (accessed on 1 October 2019).
16. Japan International Cooperation Agency. Collaboration Program with the Private Sector for Disseminating Japanese Technology for Waste to Energy System in Davao City—Final Report. 2016. Available online: http://open_jicareport.jica.go.jp/pdf/12302113.pdf (accessed on 1 October 2019).
17. Gunamantha, M.; Sarto, S. Life cycle assessment of municipal solid waste treatment to energy options: Case study of KARTAMANTUL region, Yogyakarta. *Renew. Energy* **2012**, *41*, 277–284. [CrossRef]
18. Premakumara, D.G.J.; Menikpura, S.N.M.; Singh, R.K.; Hengesbaugh, M.; Magalang, A.A.; Ildefonso, E.T.; Valdez, M.D.C.M.; Silva, L.C. Reduction of greenhouse gases (GHGs) and short-lived climate pollutants (SLCPs) from municipal solid waste management (MSWM) in the Philippines: Rapid review and assessment. *Waste Manag.* **2018**, *80*, 397–405. [CrossRef] [PubMed]
19. Chen, Y.; Cui, Z.; Cui, X.; Liu, W.; Wang, X.; Li, X.; Li, S. Life cycle assessment of end-of-life treatments of waste plastics in China. *Resour. Conserv. Recycl.* **2019**, *146*, 348–357. [CrossRef]
20. Badran, M.F.; El-Haggar, S.M. Optimization of municipal solid waste management in Port Said–Egypt. *Waste Manag.* **2006**, *26*, 534–545. [CrossRef]
21. Dai, C.; Li, Y.P.; Huang, G.H. A two-stage support-vector-regression optimization model for municipal solid waste management—A case study of Beijing, China. *J. Environ. Manag.* **2011**, *92*, 3023–3037. [CrossRef]
22. Ng, W.; Varbanov, P.; Klemeš, J.; Hegyhati, M.; Bertok, B.; Heckl, I.; Lam, H. Waste to energy for small cities: Economics versus carbon footprint. *Chem. Eng. Trans.* **2013**, *35*, 889–894. [CrossRef]
23. Rodionov, M.A.; Nakata, T. Design of an optimal waste utilization system: A case study in St. Petersburg, Russia. *Sustainability* **2011**, *3*, 1486–1509. [CrossRef]
24. Santibañez-Aguilar, J.E.; Ponce-Ortega, J.M.; Betzabe González-Campos, J.B.; Serna-González, M.; El-Halwagi, M.M. Optimal planning for the sustainable utilization of municipal solid waste. *Waste Manag.* **2013**, *33*, 2607–2622. [CrossRef]

25. Yousefloo, A.; Babazadeh, R. Designing an integrated municipal solid waste management network: A case study. *J. Clean. Prod.* **2020**, *244*, 118824. [CrossRef]
26. Nakatani, J. Life-cycle inventory analysis of recycling: Mathematical and graphical frameworks. *Sustainability* **2014**, *6*, 6158–6169. [CrossRef]
27. Manfredi, S.; Tonini, D.; Christensen, T.H.; Scharff, H. Landfilling of waste: Accounting of greenhouse gases and global warming contributions. *Waste Manag. Res.* **2009**, *27*, 825–836. [CrossRef] [PubMed]
28. Friedrich, E.; Trois, C. GHG emission factors developed for the recycling and composting of municipal waste in South African municipalities. *Waste Manag.* **2013**, *33*, 2520–2531. [CrossRef]
29. Astrup, T.; Møller, J.; Fruergaard, T. Incineration and co-combustion of waste: Accounting of greenhouse gases and global warming contributions. *Waste Manag. Res.* **2009**, *27*, 789–799. [CrossRef] [PubMed]
30. Boldrin, A.; Andersen, J.K.; Møller, J.; Christensen, T.H.; Favoino, E. Composting and compost utilization: Accounting of greenhouse gases and global warming contributions. *Waste Manag. Res.* **2009**, *27*, 800–812. [CrossRef] [PubMed]
31. Fruergaard, T.; Astrup, T.; Ekvall, T. Energy use and recovery in waste management and implications for accounting of greenhouse gases and global warming contributions. *Waste Manag. Res.* **2009**, *27*, 724–737. [CrossRef] [PubMed]
32. Pachauri, R.K.; Allen, M.R.; Barros, V.R.; Broome, J.; Cramer, W.; Christ, R.; Church, J.A.; Clarke, L.; Dahe, Q.D.; Dasqupta, P.; et al. *Climate Change 2014: Synthesis Report. Contribution of Working Groups I, II and III to the Fifth Assessment Report of the Intergovernmental Panel on Climate Change*; IPCC: Geneva, Switzerland, 2014; p. 151.
33. Asian Development Bank. *Materials Recovery Facility Tool Kit*; Asian Development Bank: Mandaluyong City, Philippines, 2013. Available online: https://www.adb.org/sites/default/files/publication/30220/materials-recovery-facility-tool-kit.pdf (accessed on 1 December 2020).
34. Japan International Cooperation Agency. Davao City Infrastructure Development Plan and Capacity Building Project Final Report Vol. 1 Part I Present Situation and Annex. 2018. Available online: http://open_jicareport.jica.go.jp/pdf/12308714_01.pdf (accessed on 1 October 2019).
35. Japan International Cooperation Agency. The Study on Recycling Industry Development in the Republic of the Philippines Final Report. 2008. Available online: https://openjicareport.jica.go.jp/pdf/11882404_02.pdf (accessed on 1 November 2019).
36. Japan International Cooperation Agency. Davao City Infrastructure Development Plan and Capacity Building Project Final Report Vol. 2 Part II Development Plan Part III Capacity Development. 2018. Available online: http://open_jicareport.jica.go.jp/pdf/12308722_01.pdf (accessed on 1 October 2019).
37. Department of Energy. Power Supply Procurement Plan. 2019. Available online: https://www.doe.gov.ph/sites/default/files/pdf/du_csp/2019-2028_DLPC_PSPP.pdf (accessed on 1 December 2020).

water

MDPI

Article

Synergistic Effects of PDO and IOD on Water Vapor Transport in the Preflood Season over South China

Junjie Li [1], Lingli Fan [1] and Guangya Zhang [2,*]

[1] South China Sea Institute of Marine Meteorology, College of Ocean and Meteorology, Guangdong Ocean University, Zhanjiang 524088, China; lilidream@outlook.com (J.L.); fanll@gdou.edu.cn (L.F.)
[2] Education Information Center, Guangdong Ocean University, Zhanjiang 524088, China
* Correspondence: zhanggy@gdou.edu.cn; Tel.: +86-759-296-6993

Abstract: It is urgent to improve the prediction accuracy of precipitation in the preflood season (PFS) over South China (SC) under the background of global warming, and thus the research of water vapor conditions is the key. For the period of 1960–2012, using the daily precipitation data from 60 meteorology stations in SC and National Centers for Environmental Prediction (NCEP) reanalysis data, the synergistic effect of PDO (the Pacific Decadal Oscillation) &IOD (the Indian Ocean Dipole Mode) on water vapor transport process to frontal/monsoon precipitation is revealed, based on the Hybrid Single-Particle Lagrangian Integrated Trajectory model (HYSPLIT_4.9). For the frontal precipitation, the positive PDO phase (PDO+) compared with the negative PDO phase (PDO−), there is more water vapor over the West Pacific (WP), the northern South China Sea (SCS), and the Bay of Bengal (BOB). Water vapor for frontal precipitation mainly comes from WP and SCS. When PDO and IOD are in phase resonance, the water vapor transport tracks from the SCS, WP are shorter and westward, so more water vapor is transported to SC, the precipitation efficiency of water vapor to PFS precipitation is higher too. For the summer monsoon precipitation, the tropical Indian Ocean (IO)-BOB is rich in water vapor, especially for PDO−& IOD+. The main water vapor transport tracks are the cross-equatorial flows in the IO, BOB and SCS. The precipitation efficiency of water vapor from the IO-BOB is higher for the positive IOD phase (IOD+) than that for the negative IOD phase (IOD−); however, the precipitation efficiency of water vapor from SCS is higher for the IOD− than that for IOD+. Compared with frontal precipitation, the strong westerly anomaly in the northern IO increases the water vapor transport from the north IO, BOB to SC during monsoon precipitation. For the PDO+&IOD+, the stronger Indian Low and cyclonic anomaly in the WP increases the water vapor transported from the IO-BOB to SC, improving the precipitation efficiency of water vapor. Understanding the synergistic effect of the PDO and IOD on water vapor transport will help to improve the accuracy of precipitation prediction, and reduce the negative impact of drought and flood disasters.

Keywords: preflood season in South China; frontal precipitation; summer monsoon precipitation; PDO; IOD

Citation: Li, J.; Fan, L.; Zhang, G. Synergistic Effects of PDO and IOD on Water Vapor Transport in the Preflood Season over South China. *Water* **2022**, *14*, 722. https://doi.org/10.3390/w14050722

Academic Editors: Alban Kuriqi and Luis Garrote

Received: 25 January 2022
Accepted: 22 February 2022
Published: 24 February 2022

1. Introduction

Precipitation falling over a given area is an aggregation of water molecules over a period of time. Some water molecules may come from the vicinity, some water may be transported from farther sources [1]. There is rich precipitation in the PFS (April–June) over SC, and its variability is enhanced under the background of global warming, but the prediction for PFS precipitation is still a great difficulty for meteorologists [2]. Sufficient water vapor is a necessary condition for the PFS rain formation. The study on the water vapor source of PFS rain, the characteristics of water vapor transport and its formation mechanism, are helpful to deeply understand the occurrence law of drought and

flood disasters over SC, thus providing a reference for government decision-making and precipitation prediction [3–5].

There are two common approaches for analyzing water vapor transport. The Lagrangian method is better than the Eulerian method because it can calculate the air trajectory, and clearly determine the source of water vapor transport [1,6–8].

Thus, based on the HYSPLIT model [9–11], the characteristics of water vapor transport in the PFS over SC can be obtained by statistical and quantitative analysis. The WP, SCS, IO, BOB and Eurasian landmass are the main water vapor sources for rain in SC [12,13].

Studies have also shown that [14,15], before and after the onset of SCSSM, the characteristics of water vapor transport for the PFS over SC are quite different. Before the onset of SCSSM, the WP is the largest source of water vapor contributing to the PFS precipitation, the IO is the largest source of water vapor after its onset. Previous studies have shown [16,17] that the water vapor transport in the PFS also has obvious interdecadal variation characteristics. A further study [18–23] shows that the interdecadal variation of water vapor transport in PFS is closely related to the PDO. By affecting low-level water vapor transport, the IOD has a greater contribution to the variation of precipitation in SC on both interdecadal and interannual scales [24–31].

Multi-factor synergy refers to the combined effect of two or more influencing factors, and the variability of precipitation in SC is the result of multi-factor synergy [32–36]. On the interdecadal scale, the summer precipitation in SC is affected by the tropical IO SST, spring snow cover over the Tibetan Plateau [37], summer intraseasonal oscillation in the Northern Hemisphere [38], and summer convective activity in the SCS [39], a synergistic effect of external forcing factors.

The results of these studies have contributed to a deeper understanding of the complexity of precipitation variability, and also showed that the SST anomaly of the IO and WP has an important impact on the water vapor transport for the PFS. There have been many valuable studies and meaningful results on the relationship between the PFS precipitation variability and SST anomaly of the WP and IO, respectively. On the interdecadal time scale, how does the interdecadal variability of the SST in WP and IO cooperatively affect the water vapor transport for PFS precipitation? In this study, the mechanism of the PDO and IOD synergistically affecting the variability of water vapor transport for the PFS in SC is discussed. Our findings will provide a theoretical basis for an in-depth understanding of the factors governing the PFS precipitation, provide additional information for analyzing drought and flood disasters.

2. Data and Methods

2.1. Data

Our study is based on, daily precipitation data of 60 meteorology stations over SC (20°–26° N,107°–120° E; Figure 1) from 1960 to 2012 provided by CMA. The NCEP reanalysis data available every six hours (00, 06, 12 and 18 UTC), provided by NOAA covers the period from 1960 to 2012, with a resolution of 2.5°∗2.5°, including 17 layers of temperature, wind and relative humidity (1000~10 *hPa*). The definitions and data of PDO and IOD indicators are from the NOAA website (https://psl.noaa.gov/ accessed on 24 February 2022).

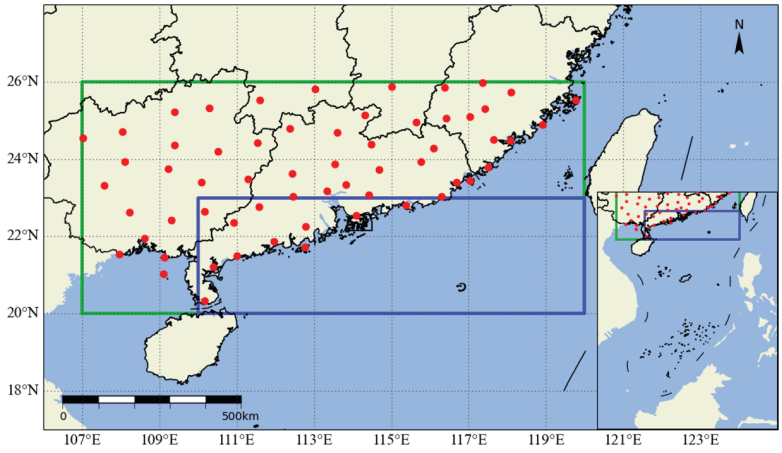

Figure 1. Schematic diagram of the South China (the green box represents the area where the precipitation is studied, the blue box is the judgment area of South China Sea summer monsoon onset, and the red spot is the meteorology stations).

2.2. Methods

The Lagrangian particle dispersion model (HYSPLIT 4.9) developed by Draxler and Hess [9,10] is used to simulate the trajectories of air parcels formed during PFS rain events for the period of 1960–2012. The air parcels at three levels (1000 m, 1500 m, and 3000 m, most water vapor converge) over 60 meteorology stations are selected. The backward trajectory is calculated by taking 02UTC and 14UTC of every day as the starting time point, the position of the trajectory point is output every hour, and the air block specific humidity at the position is obtained by interpolation. Air parcels are traced 240 h into the past, which is the average lifespan of water vapor in the atmosphere [40], to analyze the water vapor sources for SC, 716,416 tracks are selected from 60 stations with rain recording periods. The water vapor trajectories are analyzed by clustering method, to identify the main water vapor channels [41].

2.3. Division of Frontal Precipitation and Monsoon Precipitation for PFS over SC

The atmospheric circulation in PFS over SC is significantly different before and after the establishment of the SCSSM, and the precipitation characteristics are also different [2,42]. It is necessary to determine the beginning date of summer monsoon precipitation in SC, and then divide the water vapor transport process into two stages: frontal precipitation and monsoon precipitation. Climatological mean, SCSSM advances to SC about one week after its onset, when monsoon precipitation begins. According to the definition of Zheng et al. [2], if the 100 *hPa* over the region (20°–23° N, 110°–120° E) changes from westerly to easterly and lasts for more than 5 days, the first day is the beginning day of monsoon precipitation. Based on the NCEP reanalysis data, the mean onset date of monsoon precipitation is May 16 from 1960 to 2012 over SC. In this study, the period from April 1 to May 15 is defined as the frontal precipitation, and the period from May 16 to June 30 is the monsoon precipitation.

3. Results

As previously mentioned, the PDO and IOD are interrelated and have a synergistic effect on precipitation [43,44]. It is necessary to discuss the role of the PDO in detail when paying attention to the impact of the IOD on the water vapor transport in the PFS over SC.

3.1. Cold and Warm Phase of PDO

The PDO index has obvious interdecadal variation characteristics. The monthly PDO index is 12-yr low-pass filtered by the CMA [45]. After filtering, the positive (negative)

PDO index corresponds to the warm (cold) phase. The period of 1960–2012 can be divided into three phases: 1961–1976 (cold), 1977–1998 (warm), and 1999–2012 (cold). When the PDO is in a warm phase, SST in the northern, northeastern and southeastern parts of the North Pacific has a positive anomaly, while the central, western and southern parts have a negative SST anomaly; the PDO cold phase is on the contrary.

3.2. Phase Combinations of PDO and IOD

Using the COBE SST data of NOAA and referring to the definition of Saji et al. [46], the tropical western IO (50–70° E, 10° S–10° N) is called the western IOD region, and the tropical eastern IO (90–110° E, 10° S–0°N) is called the eastern IOD region. The Dipole Mode Index is the west region SST anomaly average minus the IOD East region SST anomaly average. The IOD positive (negative) phase events occur when the index is greater (less) than 0.5 standard deviations in autumn (from September to November). The classification results of phase combinations of PDO and IOD are obtained, as shown in Table 1.

Table 1. Phase combinations of PDO and IOD.

	PDO Positive Phase	**PDO Positive Phase**
IOD positive phase	1977, 1982, 1987, 1994, 1997	1963, 1972, 2006, 2007, 2011, 2012
IOD negative phase	1989, 1992, 1995, 1996, 1998	1964, 1971, 1974, 1975, 1999, 2010

The Pacific Decadal Oscillation (PDO); the Indian Ocean Dipole Mode (IOD).

3.3. Synergistic Effects of PDO and IOD on the Water Vapor Transport Process of Precipitation in PFS over SC

The synergistic effects of PDO and IOD on the water vapor transport process are introduced from three aspects: water vapor distribution, water vapor transport trajectory, and characteristics of atmospheric circulation.

3.3.1. Distribution of Water Vapor

For frontal precipitation, the WP-SCS has rich water vapor from 10 days to 2 days before the water vapor arrives at SC. Water vapor over the WP-SCS-BOB is more for the PDO+ (Figure 2a–f) than that for PDO− (Figure 2m–r). Although the initial position of water vapor transport from the WP is more eastward during the IOD−, the water vapor is more abundant in the WP-SCS-BOB for IOD+ than that of IOD−, and water vapor of PDO+&IOD+ is the most abundant (Figure 2a). For monsoon precipitation, water vapor gathers in IO-BOB (Figure 2m–x), and water vapor maximum covers a larger area in the middle tropical IO for the PDO−&IOD+ (Figure 2s).

3.3.2. Water Vapor Transport Trajectories

The main atmospheric water vapor source regions that involved the PFS rain events over SC are the Mediterranean-Eurasian interior, IO, BOB, SCS, WP, and East China (Figure 3), which is consistent with the previous results presented in the introduction. The differences between clustering water vapor transport tracks for four combinations of the IOD and the PDO phases are shown in Figure 3.

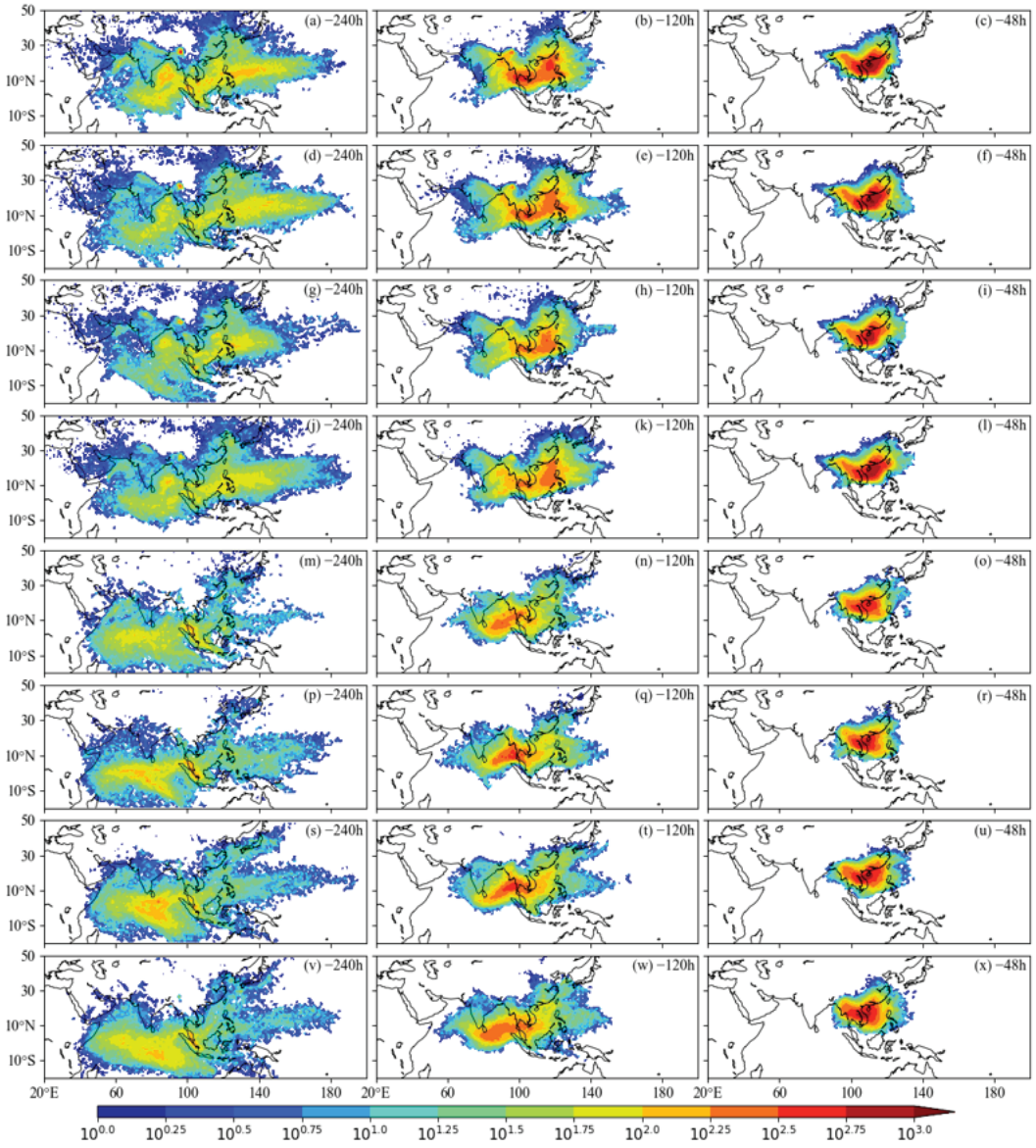

Figure 2. Distribution of cumulative specific humidity of each 1° × 1°grid on the water vapor transport trajectories in the preflood season (1960–2012) 10 days, 5 days, 2 days before the water vapor reaches South China.((**a–l**) for the frontal precipitation, (**m–x**) for the monsoon precipitation; (**a–f**,**m–r**) for PDO positive phase, (**g–l**,**s–x**) for PDO negative phase; (**a–c**,**g–i**,**m–o**,**s–u**) for IOD positive phase, (**d–f**,**j–l**,**p–r**,**v–x**) for IOD negative phase, unit: g/kg/grid).

For the frontal precipitation, when the PDO and IOD are in phase resonance, most water vapor transport tracks from the WP-SCS (trajectories labeled 3 and 4 in Figure 3a) are shorter and westward, so more water vapor is transported to SC, the precipitation efficiency of water vapor is higher (Table 2). The track of the PDO+&IOD+ (blue track 3) is shorter and more westward than that of the PDO+&IOD− (red track 3), the track of PDO−&IOD− (purple track 3) is shorter than that of the PDO−&IOD+ (green track 3). For

water vapor from the WP, the percentages of the PDO+&IOD+ (with 23.97% track number and 25.96% precipitation efficiency) are higher than that of the PDO+&IOD− (with 17.15% track number and 11.91% precipitation efficiency). The percentages of the PDO−&IOD− (with 21.35% track number and 22.67% precipitation efficiency) are higher than that of the PDO−&IOD+ (with 18.22% track number and 17.82% precipitation efficiency).

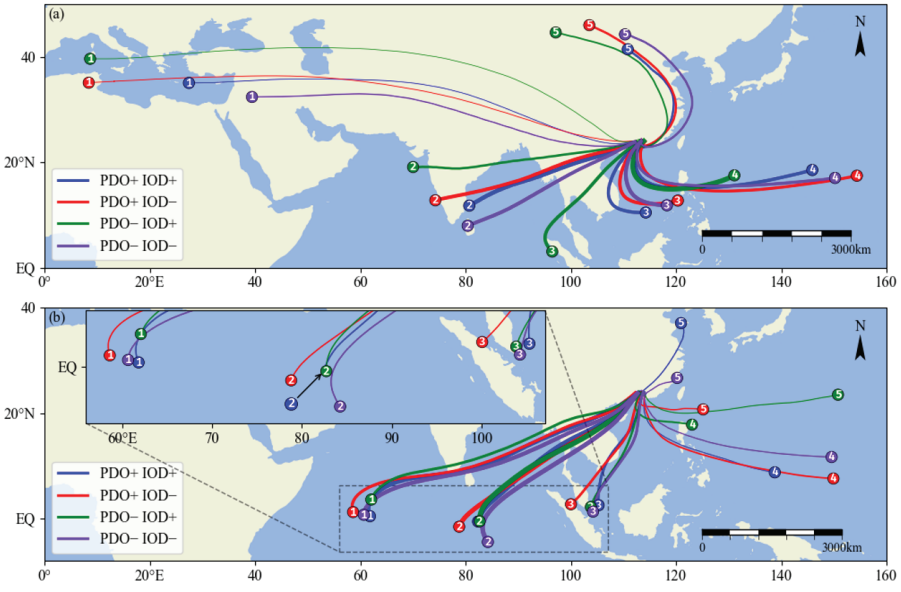

Figure 3. Clustering path of water vapor transport trajectories of precipitation for positive/negative phase of IOD in the preflood season over SC with the synergy of PDO (1960–2012) ((**a**) the frontal precipitation, (**b**) the monsoon precipitation, blue line: clustering trajectories for PDO positive phase and IOD positive phase, red line: clustering trajectories for PDO positive phase and IOD negative phase, green line: clustering trajectories for PDO negative phase and IOD positive phase, purple line: clustering trajectories for PDO negative phase and IOD positive phase, the number at the start of the trace is the trace number).

Table 2. Percentage of track number for clustering path in the total number of water vapor transport tracks and effective precipitation track number for clustering path in its total track number in the preflood season over SC for phase combinations of IOD and PDO (1960–2012) (unit: %).

			PDO Positive Phase					PDO Negative Phase				
		Track Number	**1**	**2**	**3**	**4**	**5**	**1**	**2**	**3**	**4**	**5**
Frontal precipitation	IOD+	Track amount	23.99	15.98	30.52	23.97	5.54	4.94	12.36	26.11	18.22	38.37
		precipitation	23.77	12.90	33.48	25.96	3.9	2.51	8.75	30.07	17.82	40.86
	IOD−	Track amount	26.23	27.9	6.08	17.15	22.63	15.1	28.49	26.28	21.35	8.78
		precipitation	28.91	29.63	2.91	11.91	26.65	12.08	28.52	29.37	22.67	7.36
Monsoon precipitation	IOD+	Track amount	32.00	33.64	19.67	6.30	8.39	20.74	17.25	7.39	13.06	41.56
		precipitation	36.02	35.71	17.03	5.57	5.68	25.64	15.96	4.26	9.52	44.62
	IOD−	Track amount	9.58	11.88	36.12	22.97	19.45	8.26	7.74	19.94	34.16	29.91
		precipitation	5.71	8.37	43.30	25.56	17.06	6.1	6.55	19.26	35.05	33.04

The Pacific Decadal Oscillation (PDO); the Indian Ocean Dipole Mode (IOD); the positive IOD phase (IOD+); the negative IOD phase (IOD−).

For the summer monsoon precipitation, the main water vapor transport tracks are the cross-equatorial flows in the IO, BOB and SCS (trajectories labeled 1, 2 and 3 in Figure 3b), the cluster tracks of four cases for the same region are similar, but the water vapor transport

is quite different. The contribution rate of water vapor from the IO-BOB is higher for the IOD+ than that for the IOD−. For example, for water vapor from the IO, the percentages for the PDO+&IOD+ (with 32.00% track number and 36.02% precipitation efficiency) are higher than that of the PDO+&IOD− (with 9.58% track number and 5.71% precipitation efficiency). However, the contribution rate from the SCS is higher for the IOD− than for the IOD+. For example, the percentages for the PDO+&IOD− (with 36.12% track number and 43.30% precipitation efficiency) are higher than that of the PDO+&IOD+ (with 19.67% track number and 17.03% precipitation efficiency).

3.3.3. Characteristics of Atmospheric Circulation

The differences of 850 *hPa* geopotential height and integrated water vapor flux for the PFS over SC between four PDO&IOD phase combinations are shown in Figure 4. For frontal precipitation (Figure 4a,b), the PDO+&IOD+ compares with the PDO+&IOD−, the western Pacific subtropical high is weaker (Figure 4a), there is a cyclonic anomaly in the WP, which causes a northerly anomaly near South China, and further shortens the length of water vapor transport track from the WP to SC. Similarly, for the PDO−& IOD+ minus PDO−&IOD− (Figure 4b), there is a stronger cyclonic anomaly in the WP, which makes a shorter water vapor transport track from the WP to SC. Compared with frontal precipitation, the strong westerly anomaly in the northern IO increases the water vapor transport from the north IO, BOB to SC during monsoon precipitation (Figure 4c,d). The PDO+&IOD+ compares with the PDO+&IOD−, there are strong westerly anomalies in the north IO and BOB (Figure 4c), which causes abundant water vapor to be transported eastward from the IO and BOB, and the Indian Low is stronger, which makes the path of water vapor transport to move northward, and more water vapor arrives at SC. Meanwhile, SC is located in the west of the cyclonic anomaly of WP, which increases the water vapor transported from the WP to SC. For the PDO−&IOD+ (Figure 4d), there is still a strong westerly anomaly in the IO and BOB, which enhances the water vapor eastward transport. However, the Indian Low is weaker, which makes less water vapor enter the SCS through BOB. At the same time, the cyclonic anomaly in the WP is weaker and more easterly, which makes less water vapor over the WP be transported to the SCS too, resulting in the lowest precipitation efficiency of water vapor from the SCS.

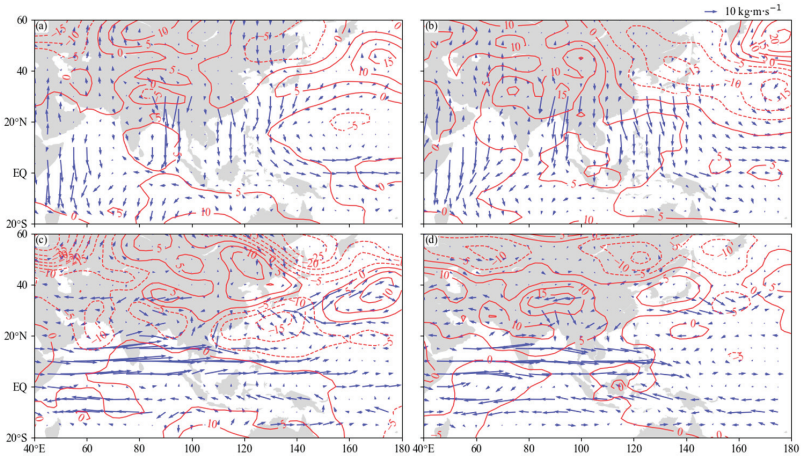

Figure 4. Difference of 850 *hPa* geopotential height field (red contours, unit: gpm), integrated water vapor flux (blue vector, unit: kg·m·s^{-1}) between four PDO&IOD phase combinations in the preflood season over South China during 1960–2012 ((**a**,**b**) for the frontal precipitation, (**c**,**d**) for the monsoon precipitation; (**a**,**c**) for PDO positive phase &IOD positive phase minus PDO positive phase &IOD negative phase, (**b**,**d**) for PDO negative phase &IOD positive phase minus PDO negative phase &IOD negative phase).

4. Conclusions and Discussion

Valuable research on the respective links between SST anomaly of IO, WP and water vapor has provided a framework within which to understand coupled air-sea processes and tropical circulations that produce PFS precipitation variability on different time scales. HYSPLIT 4.9 is used to simulate the trajectories of air parcels formed during PFS precipitation events, cluster analysis is conducted on the trajectories to identify the main water vapor channels. This study reveals some basic facts of the synergistic effect of the PDO and IOD on the water vapor transport process under the background of global warming, to improve the accuracy of precipitation prediction, reduce the negative impact of drought and flood disasters.

For frontal precipitation, the PDO+ compared with PDO−, there is more water vapor over the WP-SCS-BOB, regardless of the PDO phase, the IOD+ has more water vapor over this region than that of the IOD−. Water vapor for frontal precipitation mainly comes from the WP and SCS. When the PDO and IOD are in phase resonance, the water vapor transport tracks from the SCS, the WP is shorter and westward, so more water vapor is transported to SC, the precipitation efficiency of water vapor is higher too. It may be due to the western Pacific subtropical high being weaker, resulting in a northerly anomaly near SC, which shortens the length of the water vapor transport track from the WP to SC but is conducive to the formation of precipitation.

For the summer monsoon precipitation, the tropical IO-BOB is rich in water vapor, the water vapor maximum covers the largest area over the tropical IO for the PDO−& IOD+. The main water vapor transport tracks are the cross-equatorial flows in the IO, BOB and SCS. The precipitation efficiency of water vapor from the IO-BOB is higher for the IOD+ than that for the IOD−; however, the precipitation efficiency of water vapor from the SCS is higher for the IOD−than that for the IOD+. Compared with frontal precipitation, regardless of the phase of the PDO and IOD, the strong westerly anomaly in the northern IO increases the water vapor transport from the north IO, BOB to SC during monsoon precipitation. For the PDO−&IOD+, the Indian Low Pressure is weaker, which causes less water vapor to enter the SCS through the BOB. At the same time, the cyclonic anomaly in the WP is weaker and more easterly, which reduces the water vapor transport from the WP to the SCS, resulting in the lowest precipitation efficiency of water vapor from the SCS.

The results presented in this study are mainly on the interdecadal time scale. Nevertheless, the linkage between the SST anomaly of the Pacific, Indian Ocean and the water vapor transport over SC on an interannual time scale is also an interesting issue and deserves further study in the future.

Author Contributions: Conceptualization, L.F. and J.L.; methodology, G.Z.; software, G.Z.; validation, L.F., G.Z. and J.L.; formal analysis, L.F.; investigation, G.Z.; resources, J.L.; data curation, G.Z.; writing—original draft preparation, L.F. and J.L.; writing—review and editing, L.F.; visualization, G.Z.; supervision, G.Z.; project administration, L.F.; funding acquisition, L.F. All authors have read and agreed to the published version of the manuscript.

Funding: This research was funded by National Key Research and Development Program of China, grant number No. 2018YFC1506002, and by Innovative Experiment Project of Guangdong Ocean University, grant number No.CXXL2020048, No.201710566005, Undergraduate Innovation and Entrepreneurship Team Project of Guangdong Ocean University, grant number No.CCTD201805.

Institutional Review Board Statement: Not applicable.

Informed Consent Statement: Not applicable.

Data Availability Statement: Publicly available datasets are analyzed in this study. All data used in this paper are available in the relevant organizations described in the data section.

Acknowledgments: We would like to acknowledge all data used in this paper, which are available in the relevant organizations described in the data section.

Conflicts of Interest: The authors declare no conflict of interest.

Abbreviations

The preflood season (PFS); South China (SC); the Pacific Decadal Oscillation (PDO); the Indian Ocean Dipole Mode (IOD); the positive PDO phase (PDO+); the negative PDO phase (PDO-); the positive IOD phase (IOD+); the negative IOD phase (IOD-); the West Pacific (WP); the South China Sea (SCS); the Bay of Bengal (BOB); the Indian Ocean (IO); the South China Sea Summer Monsoon (SCSSM); China Meteorological Administration (CMA); National Centers for Environmental Prediction (NCEP); the National Oceanic and Atmospheric Administration (NOAA); the Hybrid Single Particle Lagrangian Integrated Trajectory (HYSPLIT); the sea surface temperature (SST).

References

1. James, P.; Stohl, A.; Spichtinger, N.; Eckhardt, S.; Forster, C. Climatological aspects of the extreme European rainfall of August 2002 and a trajectory method for estimating the associated evaporative source regions. *Nat. Hazards Earth Syst. Sci.* **2004**, *4*, 733–746. [CrossRef]
2. Zheng, B.; Liang, J.Y.; Lin, A.L.; Li, C.H.; Gu, D.J. Frontal Rain and Summer Monsoon Rain During Pre-rainy Season in South China. Part I: Determination of the Division Dates. *Chin. J. Atmos. Sci.* **2006**, *30*, 1207–1210. (In Chinese) [CrossRef]
3. Perry, L.B.; Konrad, C.E.; Schmidlin, T.W. Antecedent upstream air trajectories associated with northwest flow snowfall in the southern Appalachians. *Weather Forecast* **2007**, *22*, 334–352. [CrossRef]
4. Winschall, A.; Pfahl, S.; Sodemann, H.; Wernli, H. Comparison of Eulerian and Lagrangian moisture source diagnostics—the flood event in eastern Europe in May 2010. *Atmos. Chem. Phys.* **2014**, *14*, 29333–29373. [CrossRef]
5. Liu, J.P.; Li, W.J.; Chen, L.J.; Zuo, J.Q.; Zhang, P.Q. Estimation of the Monthly Precipitation Predictability Limit in China Using the Nonlinear Local Lyapunov Exponent. *J. Meteorol. Res.* **2016**, *30*, 93–102. [CrossRef]
6. Brubaker, K.L.; Dirmeyer, P.A.; Sudradjat, A.; Levy, B.S.; Bernal, F. A 36-yr climatological description of the evaporative sources of warm-season precipitation in the Mississippi River basin. *J. Hydrometeorol.* **2001**, *2*, 537. [CrossRef]
7. Stohl, A.; James, P. A Lagrangian analysis of the atmospheric branch of the global water cycle. Part I: Method description, validation, and demonstration for the August 2002 flooding in central Europe. *J. Hydrometeorol.* **2004**, *5*, 656–678. [CrossRef]
8. Drumond, A.; And, R.N.; Gimeno, L. On the contribution of the tropical western hemisphere warm pool source of moisture to the northern hemisphere precipitation through a Lagrangian approach. *J. Geophys. Res. Atmos.* **2011**, *116*, D00Q04. [CrossRef]
9. Draxler, R.R.; Hess, G.D. Description of the HYSPLIT_4 Modeling System. *NOAA Tech. Memo. ERL ARL* **1997**, *224*, 1–25. [CrossRef]
10. Draxler, R.R.; Hess, G.D. An overview of the HYSPLIT_4 modeling system of trajectories, dispersion, and deposition. *Aust. Meteorol. Mag.* **1998**, *47*, 295–308.
11. Jackson, D.R.; Driscoll, S.J.; Highwood, E.J.; Harries, J.E.; Russell, J.M., III. Troposphere to stratosphere transport at low latitudes as studies using HALOE observations of water vapour 1992–1997. *Q. J. R. Meteorol. Soc.* **1998**, *124*, 169–192. [CrossRef]
12. Sun, B.; Wang, H.J. Analysis of the major atmospheric moisture sources affecting three sub-regions of East China. *Int. J. Climatol.* **2015**, *35*, 2243–2257. [CrossRef]
13. Zhou, L.; Cai, R.H.; Lan, M.C.; Yao, R.; Yang, Y.Y. Analysis on the characteristics of low frequency oscillation in precipitation in flood season in Hunan Province. *J. Meteorol. Sci.* **2019**, *39*, 644–653. (In Chinese) [CrossRef]
14. Chen, L.X.; Zhang, B.; Zhang, Y. Progress in research on the East Asian monsoon. *J. Appl. Meteorol. Sci.* **2006**, *17*, 711–724. (In Chinese) [CrossRef]
15. Chi, Y.Z.; He, J.H.; Wu, Z.W. Features Analysis of the Different Precipitation Periods in the Pre-flood Season in South China. *J. Nanjing Inst. Meteorol.* **2005**, *28*, 163–171. (In Chinese) [CrossRef]
16. Li, X.F.; Tang, Z.F.; Yang, T.; Chi, Y.Z. Study on water vapor transport characteristics of low frequency precipitation in South China during pre-flood seasons. *Meteorol. Disaster Reduct. Res.* **2017**, *40*, 83–91. (In Chinese) [CrossRef]
17. Zhao, H.; Zhang, R.H.; Wen, M. Severe rainfalls in south China during May 2013 and its relation to the onset of the south China sea summer monsoon. *Acta Meteorol. Sin.* **2015**, *73*, 442–458. [CrossRef]
18. Mantua, N.J.; Hare, S.R.; Zhang, Y.; Wallace, J.M.; Francis, R.C. A pacific interdecadal climate oscillation with impacts on salmon production. *Bull. Am. Meteorol. Soc.* **1997**, *78*, 1069–1079. [CrossRef]
19. Chu, Q.C.; Wang, Q.G.; Feng, G.L. The roles of moisture transports in intraseasonal precipitation during the preflood season over South China. *Int. J. Climatol.* **2019**, *40*, 2239–2252. [CrossRef]
20. Chen, S.; Gao, J.Y.; Huang, L.N.; You, L.J. Decadal variation characteristics of South China pre-flood season persistent rainstorm and its mechanism. *J. Appl. Meteorol. Sci.* **2017**, *28*, 86–97. [CrossRef]
21. Qian, C.; Zhou, T.J. Multidecadal variability of north China aridity and its relationship to PDO during 1900–2010. *J. Clim.* **2013**, *27*, 1210–1222. [CrossRef]
22. Wu, X.F.; Mao, J.Y. Interdecadal variability of early summer monsoon rainfall over south China in association with the pacific decadal oscillation. *Int. J. Climatol.* **2017**, *37*, 706–721. [CrossRef]

23. Newman, M.; Alexander, M.A.; Ault, T.R.; Cobb, K.M.; Deser, C.; Di Lorenzo, E.; Mantua, N.J.; Miller, A.J.; Minobe, S.; Nakamura, H. The pacific decadal oscillation, revisited. *J. Clim.* **2016**, *29*, 4399–4427. [CrossRef]
24. Jia, X.J.; Zhang, C.; Wu, R.G.; Qian, Q.F. Changes in the relationship between spring precipitation in southern China and tropical Pacific-South Indian Ocean SST. *J. Clim.* **2021**, *34*, 1–37. [CrossRef]
25. Swapna, P.; Krishnan, R.; Wallace, J.M. Indian ocean and monsoon coupled interactions in a warming environment. *Clim. Dyn. Obs. Theor. Comput. Res. Clim. Syst.* **2014**, *42*, 2439–2454. [CrossRef]
26. Cao, J.; Yao, P.; Wang, L.; Liu, K. Summer rainfall variability in low-latitude highlands of China and subtropical Indian Ocean Dipole. *J. Clim.* **2014**, *27*, 880–892. [CrossRef]
27. Zhao, S.S.; Zhou, T.J.; Yang, X.Q.; Zhu, Y.M.; Tan, Y.K.; Sun, X.G. Interdecadal change of the relationship between the tropical Indian Ocean Dipole mode and the summer climate anomaly in China. *J. Meteorol. Res.* **2011**, *25*, 129–141. [CrossRef]
28. Tang, W.Y.; Sun, Z.B.; Tan, G.R. Effect of Indian Ocean Dipole on rainfall anomaly in South of China. *J. Nanjing Inst. Meteorol.* **2008**, *31*, 836–843. [CrossRef]
29. Krishnan, R.; Ramesh, K.V.; Samala, B.K.; Meyers, G.; Slingo, J.M.; Fennessy, M.J. Indian Ocean-monsoon coupled interactions and impending monsoon droughts. *Geophys. Res. Lett.* **2006**, *33*, 153–172. [CrossRef]
30. Zhang, H.Y.; Wen, Z.P.; Wu, R.G.; Chen, Z.S. Inter-decadal changes in the East Asian summer monsoon and associations with sea surface temperature anomaly in the South Indian Ocean. *Clim. Dyn.* **2016**, *48*, 1–15. [CrossRef]
31. Meehl, G.A.; Arblaster, J.M. Decadal variability of Asian-Australian monsoon-ENSO-TBO relationships. *J. Clim.* **2010**, *24*, 4925–4940. [CrossRef]
32. Wu, J.F.; Tan, X.Z.; Chen, X.H.; Lin, K.R. Dynamic changes of the dryness/wetness characteristics in the largest river basin of South China and their possible climate driving factors. *Atmos. Res.* **2020**, *232*, 104685. [CrossRef]
33. Li, W.J.; Zhang, R.N.; Sun, C.H.; Ren, H.L.; Liu, J.P.; Zuo, J.Q.; Li, X. Recent research advances on the interannual-interdecadal variations of drought/flood in South China and associated causes. *J. Appl. Meteorol. Sci.* **2016**, *27*, 577–591. [CrossRef]
34. Li, Y.; Yuan, W.J.; Xu, Q.Q.; Hu, R.J.; Li, J.L.; Mei, X.Y.; Li, X.L. Water vapor transportation characteristics in Pre-rainy season precipitation anomaly of South China. *Plateau Meteorol.* **2017**, *36*, 501–509. [CrossRef]
35. Li, W.J.; Liu, J.P.; Ren, H.L.; Zuo, J.Q. Characteristics and corresponding mechanisms of the leading modes of interdecadal variability of summer rainfall in southern China. *Chin. J. Atmos. Sci. (Chin.)* **2018**, *42*, 859–876. [CrossRef]
36. Fan, L.L.; Zhang, G.Y.; Xu, J.J. Differentiated Effects of Urbanization on Precipitation in South China. *Water* **2021**, *13*, 1386. [CrossRef]
37. Wu, R.G.; Wen, Z.P.; Song, Y.; Li, Y.Q. An Interdecadal change in Southern China summer rainfall around 1992/93. *J. Clim.* **2010**, *23*, 2389–2403. [CrossRef]
38. Wang, L.; Chen, W.; Zhou, W.; Huang, G. Understanding and detecting super-extreme droughts in Southwest China through an integrated approach and index. *Q. J. R. Meteorol. Soc.* **2015**, *142*, 529–535. [CrossRef]
39. Kajikawa, Y.; Yasunari, T.; Wang, B. Decadal change in intraseasonal variability over the South China Sea. *Geophys. Res. Lett.* **2009**, *36*, L06810. [CrossRef]
40. Trenberth, K.E. Atmospheric moisture recycling: Role of advection and local evaporation. *J. Clim.* **1999**, *12*, 1368–1381. [CrossRef]
41. Jiang, Z.H.; Ren, W.; Liu, Z.Y.; Yang, H. Analysis of water vapor transport characteristics during the Meiyu over the Yangtze-Huaihe River valley using the Lagrangian method. *Acta Meteorol. Sin.* **2013**, *71*, 295–304. (In Chinese) [CrossRef]
42. Jian, M.Q.; Qiao, Y.T.; Luo, H.B. The abrupt change of the circulation in Low-Latitudes during the period from April to June. *Clim. Environ. Res.* **2000**, *5*, 356–362. (In Chinese) [CrossRef]
43. Duan, W.S.; Song, L.Y.; Li, Y.; Mao, J.Y. Modulation of PDO on the predictability of the interannual variability of early summer rainfall over south China. *J. Geophys. Res. Atmos.* **2013**, *118*, 13008–13021. [CrossRef]
44. Sun, Z.B.; Xu, Q.Z.; Ni, D.H. Interdecadal variation of spring precipitation in South China and its relationships with atmospheric circulation and SST. *Trans. Atmos. Sci.* **2017**, *40*, 433–442. (In Chinese) [CrossRef]
45. China Meteorological Administration. Available online: http://cmdp.ncc-cma.net/pred/cn_enso.php?product=cn_enso_pdo (accessed on 21 February 2022).
46. Saji, N.H.; Goswami, B.N.; Vinayachandran, P.N.; Yamagata, T. A dipole mode in the tropical Indian ocean. *Nature* **1999**, *401*, 360–363. [CrossRef]

water

MDPI

Article

Simulation and Prediction of the Impact of Climate Change Scenarios on Runoff of Typical Watersheds in Changbai Mountains, China

Zhaoyang Li [1,2,3], Yidan Cao [1,2,3,*], Yucong Duan [1,2,3], Zelin Jiang [1,2,3] and Feihu Sun [1,2,3]

[1] Key Lab of Groundwater Resources and Environment, Ministry of Education, Jilin University, Changchun 130012, China; zhaoyang@jlu.edu.cn (Z.L.); duanyc19@mails.jlu.edu.cn (Y.D.); jiangzl19@mails.jlu.edu.cn (Z.J.); fhsun20@mails.jlu.edu.cn (F.S.)
[2] Key Laboratory of Water Resources and Water Environment, Jilin University, Changchun 130012, China
[3] College of New Energy and Environment, Jilin University, Changchun 130012, China
* Correspondence: caoyd@jlu.edu.cn

Abstract: Simulating the hydrological process of a river basin helps to understand the evolution of water resources in the region and provides scientific guidance for water resources allocation policies between different river basins and water resources management within the river basin. This paper provides a scientific basis for the sustainable development of regional water resources and an accurate grasp of the future change trend of runoff by analyzing the hydrological process response of runoff in typical watersheds in Changbai Mountains, China, to climate change. The applicability of the HEC-HMS (The Hydrologic Engineering Center's-Hydrologic Modeling System) hydrological model in the watershed is verified by calibrating and verifying the daily rainfall-runoff process in the watershed during the wet season from 2006 to 2017. The daily rainfall data of the two scenarios SSP2-4.5 and SSP5-8.5 under the BCC-CSM2-MR model in the 2021–2050 CMIP6 plan were downscaled and interpolated to in-basin stations to generate future daily precipitation series to predict runoff response to future climate change. The daily rainfall data of the two scenarios were downscaled and interpolated to the stations in the basin to generate future daily rainfall series to predict the runoff response under future climate changes. The average certainty coefficient of the HEC-HMS model for daily runoff simulation reached 0.705; the rainfall in the basin under the two climate scenarios of SSP2-4.5 and SSP5-8.5 in the next 30 years (2021–2050) will generally increase, and rainfall will be more evenly distributed in the future; the outlet flow of the basin will increase during the wet season (June–September) in the next 30 years, but it is lower than the historically measured value; the peak flow of the future will appear at most in August and September. The peak flow current time mostly appears in July and August. The time of peak occurrence has been delayed.

Keywords: HEC-HMS model; runoff simulation; future scenarios; Changbai Mountains

Citation: Li, Z.; Cao, Y.; Duan, Y.; Jiang, Z.; Sun, F. Simulation and Prediction of the Impact of Climate Change Scenarios on Runoff of Typical Watersheds in Changbai Mountains, China. *Water* **2022**, *14*, 792. https://doi.org/10.3390/w14050792

Academic Editors: Alban Kuriqi and Luis Garrote

Received: 9 December 2021
Accepted: 14 February 2022
Published: 3 March 2022

1. Introduction

As the foundation of human survival and development, water resources are irreplaceable natural resources for sustainable economic and social development. Global climate change inevitably and significantly affects the water cycle of the river basin, which in turn affects regional water resources security and sustainable development. In the context of continued climate warming in the future, the structure of the water resources system will continue to change. Risks related to freshwater resources, such as water supply and water utilization, will increase significantly. The response to hydrological processes under climate change has become a hot spot in the field of hydrology and water resources research [1–3]. Climate change scenarios are a collection of possible future climate change situations. Simulating the impact of possible climate scenarios on river runoff will help to effectively

reduce floods, droughts, water shortages and pollution through rational and effective use of water resources and adapt the impact of climate change on water resources.

Currently, in making predictions and assessments based on the evolution of the hydrological cycle under different future climate change scenarios [4–8], medium and long-term runoff forecasting has become increasingly important [9,10]. Research usually selects future climate scenarios and climate models or uses mathematical model calculations and downscaling methods to process the data and then analyzes the evolution of future climate and hydrology [11–13], while carrying out prediction and response research on hydrological elements [14,15]. Among them, the uncertain factors of future scenarios and hydrological models are the most difficult points in the research [16]. In recent years, the research on global climate models has made great progress. Among them, the International Coupled Model Comparison Program (CMIP) organized by the World Climate Research Program (WCRP) has been widely used in climate change simulation and projection data. In 2019, WCRP announced the data of the sixth phase of the pilot program (CMIP6), and the analysis results based on these data will form the basis of future climate assessments. Jiang et al. [17] selected five CMIP6 global models including seven combined scenarios (SSP1-1.9, SSP1-2.6, SSP4-3.4, SSP2-4.5, SSP4-6.0, SSP3-7.0 and SSP5-8.5) for downscaling; analyzed the temporal and spatial evolution of the average temperature and precipitation in the Huaihe River Basin from 2021 to 2100; and compared with CMIP5 forecast results; they found that, under the CMIP6 scenario, future temperature growth in the Huaihe River Basin will be faster, and the increase in precipitation will be even greater. Pokhrel et al. [18] used the cumulative distribution function transformation method to correct the deviation of CMIP6 data. Considering future climate scenarios, it predicts the flow of the New River in North Carolina and assesses flood risk. Based on the RBF neural network downscaling model. Wang et al. [19] used two climate scenarios of RCP8.5 and RCP2.6 under the CanESM2 model from 2020 to 2099 to predict runoff in the upper reaches of the Han Jiang River. The results showed that the annual runoff in the upper Han Jiang River did not increase significantly. Based on the HEC-HMS model, Tang et al. [20] predicted that the future runoff in the Lanjiang River Basin will show a significant upward trend, and the increase degree will increase synchronously with the increase in radiative forcing. Li et al. [21] used the Yellow River Water Balance Model (YRWBM) hydrological model to predict future natural runoff and its temporal and spatial changes and used future climate scenarios as input. The forecast results show that the runoff of the Yellow River will decrease in the future.

Hydrological models are considered to be effective tools for water resources utilization and integrated river basin management. They can be used for river management planning; reservoir integrated operation and utilization; and river basin water environmental management in areas with little data. They can be used to simulate the water cycle process of the river basin and changes in climate and human activities. It is an important tool and method to reveal the law of runoff changes in response to water resources [22,23]. The HEC-HMS hydrological model is a basin hydrological simulation system developed by the Hydrological Engineering Center of the U.S. Army Corps of Engineers. It is a distributed hydrological model with a physical concept. Previous studies have shown that the HEC-HMS model can simulate and predict runoff based on data sets and watershed types at different time scales [24]. Most of these studies clearly show that the results of the model simulation are for data at specific locations and at different time scales, because the model contains different combinations of rainfall loss, direct runoff, base flow and channel confluence model sets. The degree of response in different regions is different [25]. Al-Abed et al. [26] used monthly runoff to study the Zhaka Basin in Jordan and showed that the HEC-HMS model has better results than other models. Radmanesh et al. [27] performed the HEC-HMS model in the Yellow River Basin in Southwestern Iran. Calibrated and verified, Sardoii et al. [28] used HEC-HMS and geographic information system GIS to simulate the rainfall-runoff process in the Amirkabir watershed and concluded that the runoff loss method of Green and Ampt can be applied in similar areas and conditions.

Changbai Mountains is the highest mountain system on the eastern edge of Eurasia. Located in the northeast of China and the southeast of Jilin Province, it is the birthplace of the Yalu River, Songhua River and Tumen River in Northeast China. It is also an important water source protection area and ecological function area. Water resources account for 78.6% of Jilin Province. It is an important water conservation area in Jilin province and even the entire Northeast. The Changbai Mountains area has abundant mineral water resources and high quality. It is listed as the world's three major high-quality mineral water production areas alongside the European Alps and the Russian Caucasus. Affected by the climate of the alpine mountainous area, there are about 5 months of the year in the icy period where the temperature is below zero, and rainfall is extremely uneven during the year where it is mainly concentrated in the wet season from June to September. Changbai Mountains is located in the core area of the Northeast China Transect of the Global Change Land Transect. It is significantly affected by global climate change. However, there is a lack of relevant research on the evolution and development trends of regional water resources. Carrying out rainfall and runoff simulation and prediction of typical watersheds in Changbai Mountains during the wet season and studying the response relationship between regional climate and runoff under different climate change scenarios in the future can provide scientific support for water resource management in the watershed to cope with climate change and to maintain regional ecological security.

2. Materials and Methods

2.1. Study Area

Changbai Mountains is located in the southeast of Jilin Province, with geographic coordinates of 127°40′–128°16′ east longitude and 41°35′–42°25′ north latitude, with a total area of 196,400 hectares. The source area of the Three Rivers of Changbai Mountains can be divided into the following: Erdao Songhua River Basin, Toudao Songhua River Basin, etc. The Erdao Songhua River Basin is located at the north source of the Songhua River and northwest slope of Tianchi Lake in Changbai Mountain. The various tributaries, including Toudaobai River, Erdaobai River, Gudong River, Lushui River, etc., account for about 50% of the total area of the source area. In this study, Erdao Songhua River Basin was selected as the study area. The Erdao Songhua River has steep mountains along the two banks, and the terrain is relatively complex. The altitude ranges from about 300 to 2700 m. The terrain has a large amplitude. The river valleys are distributed radially, and flow velocity is turbulent. It has a mid-temperate continental monsoon climate, with a multiyear average temperature of 3.25 °C and a multiyear average rainfall of 655 mm. Rainfall is mainly concentrated in the wet season from June to September. In addition, river floods in the basin are mainly formed by heavy rains. Heavy rains and floods mostly occur from July to August and most often in August, accounting for more than 80% of the total. Figure 1 is an overview map of the basin.

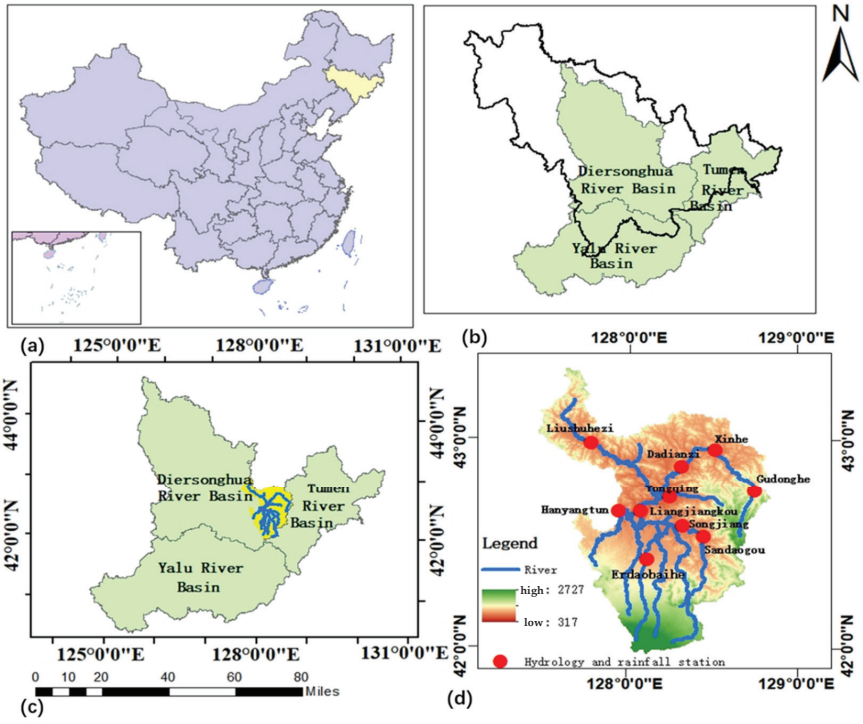

Figure 1. Study area. (**a**) Map of China. (**b**) The Yalu River, the Tumen River, and the Second Songhua River originate from Changbai Mountain, of which the Second Songhua River is located in Jilin Province. (**c**) The location of the study area. (**d**) Elevation map of the study area, as well as a schematic diagram of the site and water system.

2.2. Data Source and Processing

2.2.1. Geospatial Data

Geospatial data include watershed digital elevation, land use and soil distribution data. Digital elevation data comes from the 30-m resolution GDEMV230 M product data set of the geospatial data cloud platform (http://www.gscloud.cn accessed on 8 December 2021). The land use data are the global land use 10 m data set interpreted by Tsinghua University and extracted by the basin vector boundary, and soil distribution data comes from the HWSD data set of the World Soil Database, as shown in Figure 2.

2.2.2. Meteorological and Hydrological Data

The hydrometeorological data for constructing the HEC-HMS (The Hydrologic Engineering Center's-Hydrologic Modeling System) model comes from the China Hydrological Yearbook over the years. Selected actual measurement daily rainfall data from June to September in wet season of 2006–2017 from 10 stations (Hanyangtun Station, Erdaobaihe Station, Dadianzi Station, Liangjiangkou Station, Liushuhezi Station, Yongqing Station, Gudonghe Station, Sandaogou Station, Xinhe Station and Songjiang Station) combined with the daily flow data of the Hanyangtun station of the basin's outlet hydrological station during the wet season simulate rainfall and runoff during the 12-year wet season. In order to predict the future runoff trend in the study area, this paper selected CMIP6 experimental data, which are downloaded from https://pcmdi.llnl.gov/CMIP6/ (accessed on 8 December 2021).What the download obtains is the grid data, and we use the Make NetCDF Feature Layer tool in ArcGIS for downscaling. Then, the desired study area is cut out.

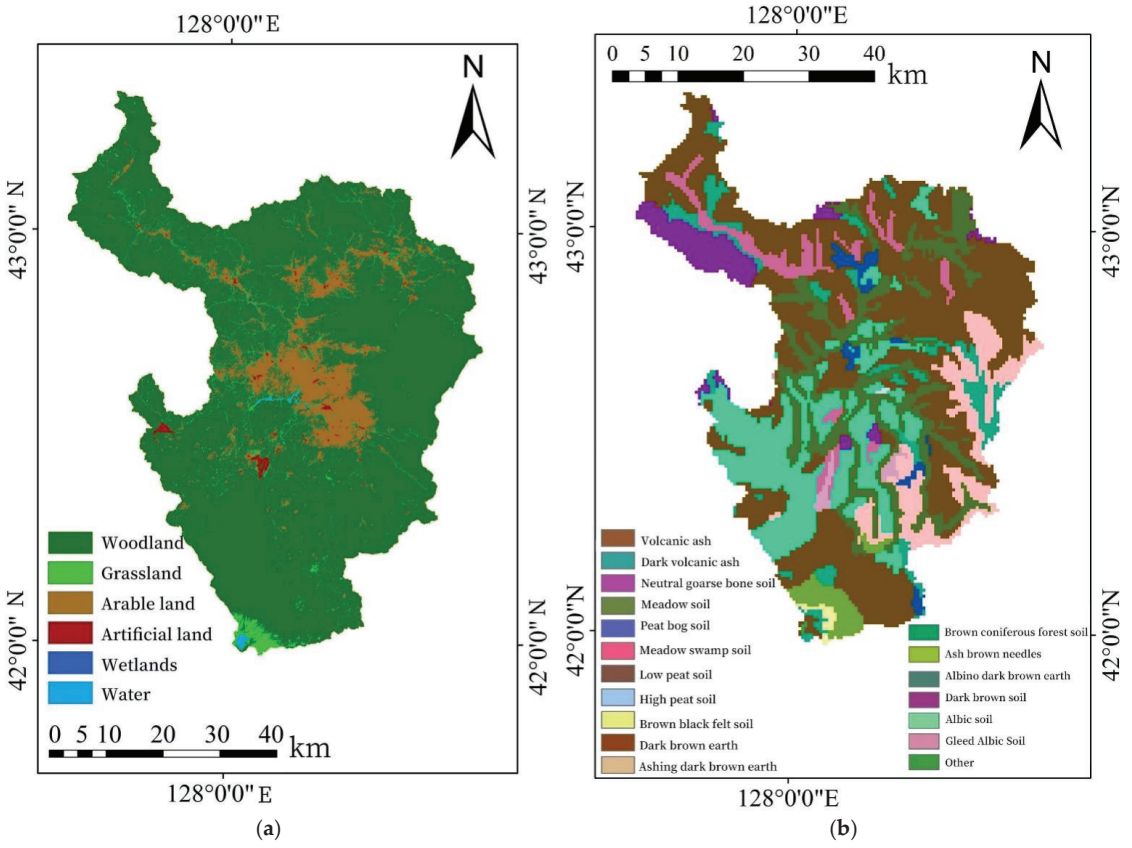

Figure 2. (**a**) Land use map of the study area. (**b**) Soil type map of the study area.

CMIP6 is being organized by the World Climate Research Project (WCRP). As one of the institutes participating in the CMIP6, the National Climate Center, China (Meteorological Administration), has three latest version of models to utilize in the project through model development in recent years. This article applied the middle-resolution climate system model, BCC-CSM2-MR, and the 2021–2050 daily rainfall sequence of two climate scenarios, SSP2-4.5 and SSP5-8.5, was selected. The SSP2-4.5 scenario represents a moderate level of greenhouse gas emissions that is compatible with social and economic development, with the goal of the effective radiative forcing value reaching 4.5 W/m^2 by the end of the 21st century. SSP5-8.5 is the scenario with the highest greenhouse gas concentration, with monotonically increasing greenhouse gas emissions. The trend is to stabilize the effective radiative forcing value at 8.5 W/m^2 by the end of the 21st century. The corresponding social background is a large population, high energy consumption in social development, lag in clean energy technology and lack of measures to deal with climate change. This scenario is less likely to occur.

2.3. Research Methods

HEC-HMS is a distributed rainfall-runoff model with physical concepts. Most of the rainfall in the Changbai Mountains occurs from June to September, and extreme weather such as rainstorms and floods is prone to occur during this period. Thus, this model is suitable for use, and temperature changes have little effect. It includes four parts: a watershed module, a control module, a weather module and a time-series management

module. The operation can use different calculation schemes to simulate hydrological processes of the basin.

In this study, DEM data of the study area were processed by HEC-Geo HMS, and water system characteristics and topographic parameters of the watershed are extracted; the watershed is divided into 15 sub-basins. The Thiessen polygon method is used to calculate the weight of the rainfall station in each sub-basin, and the HEC-HMS project file is generated on this basis. (Figure 3). The runoff generation module uses the SCS curve numerical method, the confluence module uses the SCS unit line method, the base flow module uses the exponential backwater method and the river confluence module uses the Muskingum method. The parameters include CN value, impervious and flow lag. Time (tlag), attenuation coefficient (RC), peak ratio (Ratio), storage constant (K) and flow specific gravity factor (X) are also considered. Considering that the simulation effect of the initial parameters value, input into the model is poor, and the manual trial and error method combined with the built-in peak-weighted root-mean-square objective function method of the model was used to determine the optimal parameters in the parameter calibration process. The verification model uses five indicators, namely, peak-to-current time difference (Δt), peak flow relative error (REp), total flow relative error (REv) and certainty coefficients DC and R^2 to comprehensively evaluate simulation results. We formulate evaluation criteria according to the analysis results of rainfall and runoff forecasting in "Hydrological Information Forecasting Specifications" (GB/T 22482-2008). Among them, the predicted peak flow and the measured value change within 20% are qualified; the predicted peak occurrence time and the measured peak occurrence time interval are within 30%; the predicted total flow and the measured flow value error are within 10%. The assessment of the certainty coefficient DC as DC $\geq$ 0.70 can be used to issue a formal hydrological forecast; that is, forecast is relatively accurate.

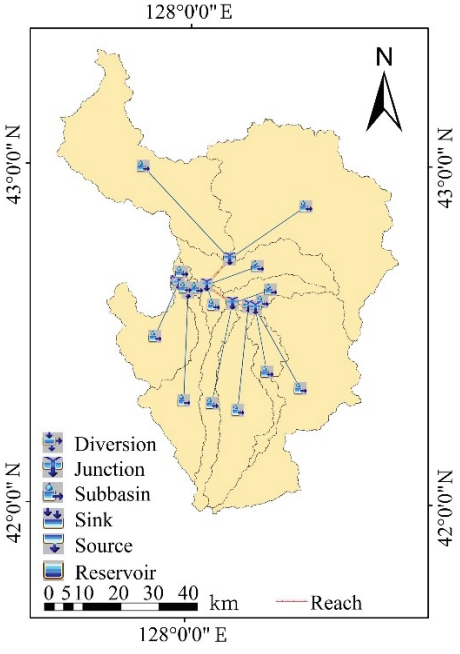

Figure 3. HEC-HMS model construction.

According to the above method, the HEC-HMS model of the typical watershed in Changbai Mountains was constructed. Daily runoff data from 2006 to 2011 were selected to calibrate the model parameters, and daily runoff data from 2012 to 2017 verified the simulation effect of the model.

3. Results and Discussion

3.1. HEC-HMS Hydrological Modeling

The following parameters were determined: CN value, impervious rate (impervious), flow lag (t_{lag}), attenuation coefficient (RC), peak ratio (Ratio), storage constant (K) and flow specific gravity factor (X). The results are shown in Tables 1 and 2.

Table 1. Parameter optimization results of calibration period model.

	CN	Impervious	t_{lag}	RC	Ratio
W280	10	8	450	0.8	0.1
W350	35	8	400	0.8	0.1
W380	28	8	300	0.8	0.1
W390	10	8	60	0.8	0.1
W400	15	8	60	0.8	0.1
W410	20	8	300	0.8	0.1
W420	22	8	60	0.8	0.1
W430	15	8	150	0.8	0.1
W440	15	8	400	0.8	0.1
W450	23	8	200	0.8	0.1
W460	15	8	400	0.8	0.1
W470	28	8	150	0.8	0.1
W480	15	8	400	0.8	0.1
W490	32	8	400	0.8	0.1
W500	20	8	300	0.8	0.1

Table 2. Parameter optimization results of regular channel confluence model.

	R130	R140	R150	R160	R170	R180	R190
K	10	10	10	20	20	30	10
X	0.01	0.5	0.05	0.3	0.25	0.1	0.2

Note: W280–W500 are divided into 15 sub-basins, and R130–R190 are river confluence areas.

Table 3 shows the application of the HEC-HMS model in the evaluation of the daily runoff simulation results of the basin during the wet season. The rate regular qualifying year DC averaged to 0.704, and the average DC of the qualified years of the verification period is 0.71; the simulation effect of peak present time and peak flow is the best. Qualification rate reached 91.7%. In terms of comprehensive evaluation indicators, the total qualification rate was 75%, and the DC average of the qualified year reached 0.705.

From the comparison between simulated and measured flow results (Figure 4), it can be observed that the model simulated rainfall-runoff process in the wet season is basically consistent with the measured process trend. The model simulates extreme runoff simulation values well. There is a large deviation in the peak time in 2011 in the rate period, and all other years are within the allowable error range. The simulated peak present time in 2008 is one day after the actual measured peak present time. The rest of the years are consistent with the actual measured value, which is the regular rate in all years. The absolute value of the relative error of the peak flow rate is within 20% of the allowable error, and the average relative error is 8.2%; the relative error of the total flow at the outlet of the basin during the wet season in 2009 and 2011 is −19.9% and −17.9%, respectively. The absolute value is greater than the allowable error by 10%. During the verification period, the peak times of 2014, 2016 and 2017 are on the same day as the actual situation. The simulated peak times of 2012, 2013 and 2015 are only one day away from actual peak times, and the pass rate is 100%. Except for the relative error of the peak flow rate in 2014, which is 20.2%, the other verification years are all within the allowable error of 20%, and the pass rate is 83.3%; the absolute value of the relative error of the total export flow in 2013 and 2014 exceeds 10% of the flow forecast. In the allowable error range, the pass rate is 66.7%.

Table 3. Simulation results of HEC-HMS model.

Period	Year	Peak Current Time Difference (ΔT)	Relative Error of Peak Flow (REp)	Relative Error of Total Flow (REv)	Coefficient of Certainty (DC)	R^2	Whether It Is Passed
Rate regulation	2006	0	17.8%	−8.2%	0.710	0.763	yes
	2007	0	−5.9%	−4.5%	0.609	0.777	yes
	2008	1	−4.7%	−9.4%	0.660	0.700	yes
	2009	0	−8.5%	−19.9%	0.636	0.706	yes
	2010	0	−4.2%	−4.2%	0.906	0.907	yes
	2011	75	−8.1%	−17.9%	0.303	0.429	no
Verification period	2012	1	15.0%	−9.8%	0.288	0.521	no
	2013	1	−17.4%	−15.1%	0.739	0.749	yes
	2014	0	−20.2%	−12.4%	0.450	0.485	no
	2015	1	−17.0%	1.2%	0.603	0.639	yes
	2016	0	−5.7%	3.6%	0.720	0.824	yes
	2017	0	−18.5%	8.9%	0.760	0.774	yes

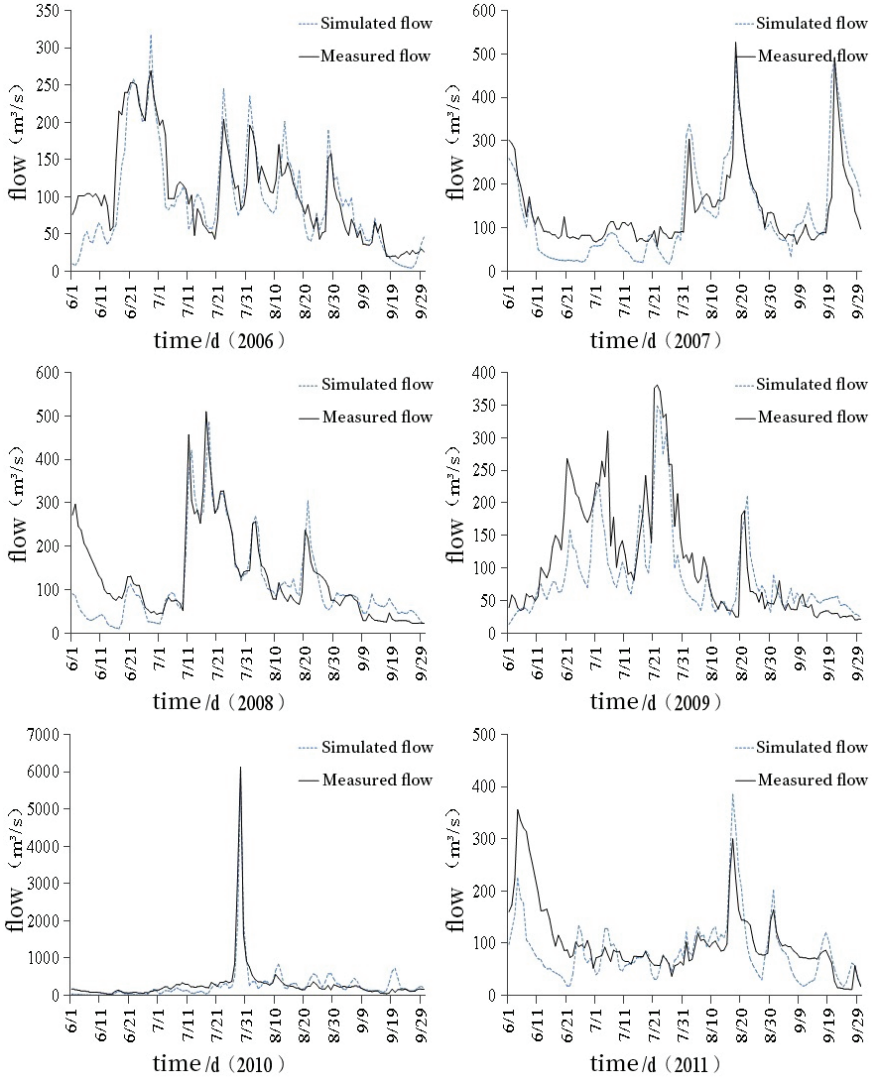

Figure 4. *Cont.*

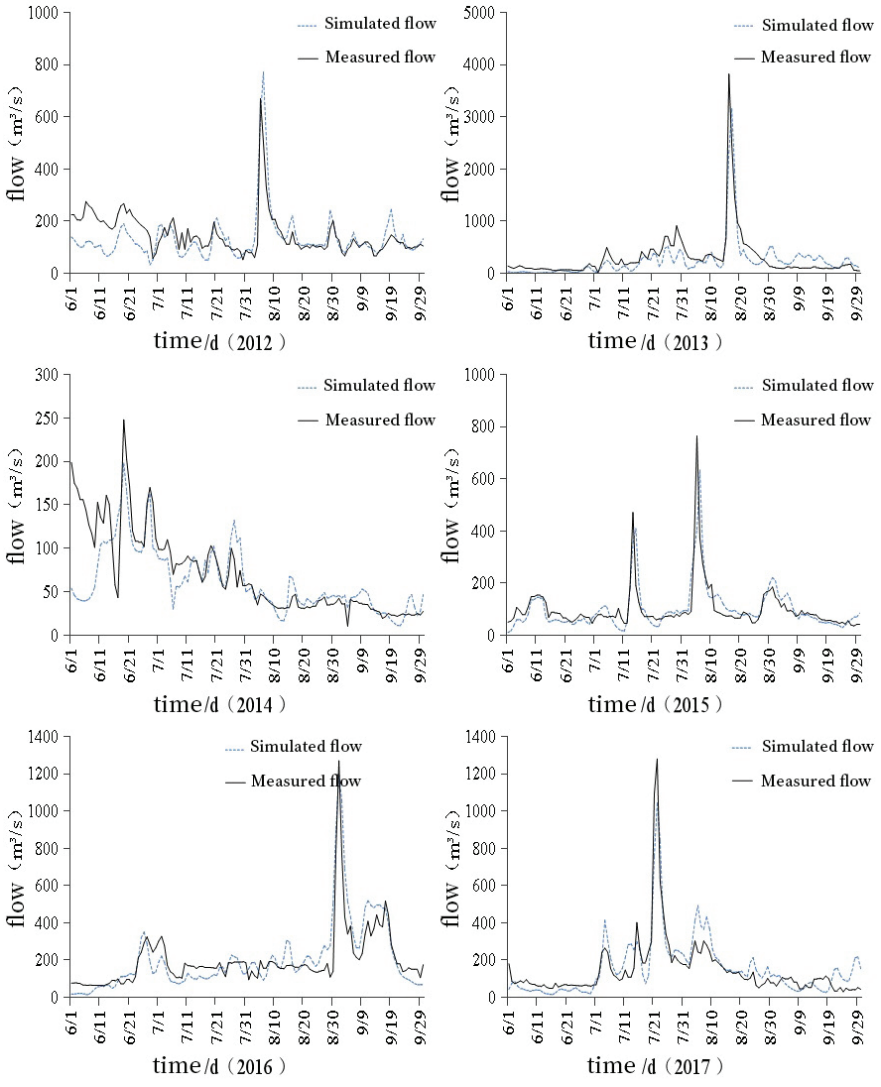

Figure 4. The simulation process of the runoff rate during the wet season and the verification period.

3.2. Future Runoff Simulation

The downloaded CMIP6 future climate scenario data are spatially interpolated to a resolution of 0.25° × 0.25°, and grid point data in the basin are extracted to obtain the rainfall simulation value in the historical period from 1957 to 2014 in the basin, as well as the future under the two climate scenarios. The predicted value of rainfall is taken from 2021 to 2050. As there will be a certain deviations between climate model forecast data and actual weather station data, this paper compares the data of the two historical periods from 1957 to 2014 for verification (since CMIP6 plans to simulate numerical differentiation scenarios from 2015, the simulation values before 2014 are selected for comparison and verification), and the average error is only 7%, which proves that the simulated value can be directly used to predict future rainfall.

The rainfall under the two future climate scenarios is brought into each rainfall station in the basin through spatial interpolation and input into the previously built HEC-HMS

model, and the calibrated parameters are used to simulate and predict future SSP2-4.5 and SSP5-8.5. The flow conditions are at the outlet of the Erdao Songhua River basin during the wet season (June–September) under the two climate scenarios from 2021 to 2050. It is possible to predict changes in the flow during the wet season in the next 30 years in order to effectively prevent flood disasters and fully understand the future runoff of the basin. The change trend and rational management of water resources provide a scientific basis.

Figure 5 shows the change trend of average runoff during the drainage period (June–September) at the outlet of the basin from 2021 to 2050 under SSP2-4.5 climate scenarios and SSP5-8.5 climate scenarios. The runoff presents an insignificant upward trend. Under the SSP2-4.5 climate scenario, it rises at a rate of 1.77 m^3/s per year, and under the SSP5-8.5 climate scenario, it rises at a rate of 1.51 m^3/s per year. The SSP2-4.5 climate scenario is higher than the SSP5-8.5 climate scenario. The scenario rises slightly faster. By calculating the average flow during the wet season from 2021 to 2050, it shows that it is 101.7 m^3/s under the SSP2-4.5 climate scenario and 100.3 m^3/s under the SSP5-8.5 climate scenario, which is the same as the measured average flow during the wet season from 2006 to 2017 during the simulation period of the model to 152.6 m^3/s. Compared with the flow, it has decreased, which is directly related to a decrease in rainfall from June to September in the next 30 years during the wet season compared to the historical period.

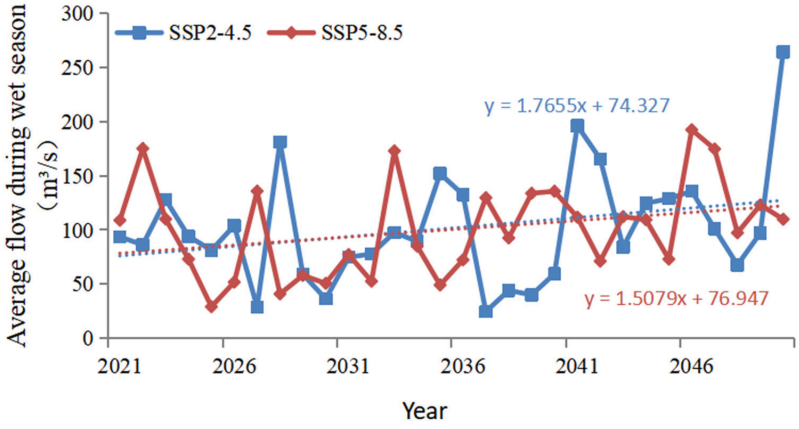

Figure 5. Changes in annual runoff during the wet season under two climate scenarios from 2021 to 2050.

Figure 6 shows the changes in daily average flow during the wet season from 2021 to 2050 under the two scenarios. It can be observed from the graph that the flow from June to August gradually increased, the largest average flow was concentrated in August and gradually decreased in September. The maximum daily average flow under the SSP2-4.5 climate scenario is 7.2% higher than that under the SSP5-8.5 climate scenario, and the maximum overall flow occurs in August.

From the evaluation and analysis of the model simulation results, it can be observed that the model has a good simulation effect on the peak flow rate and the peak present time. Therefore, the two characteristic values of the next 30 years are output. The analysis found that the future peak flow will occur the most in August, accounting for 40% and 46.7% of the two scenarios, followed by September. Compared with the peak time of the historical period, most of them appeared in July and August, both accounting for 33.3%. It was found that the peak time of the next 30 years will be delayed to a certain extent. In the next 30 years, the maximum flow rate under the SSP2-4.5 scenario will be 2130.6 m^3/s in 2050, and the maximum flow rate under the SSP5-8.5 scenario will be 2340.7 m^3/s in 2047.

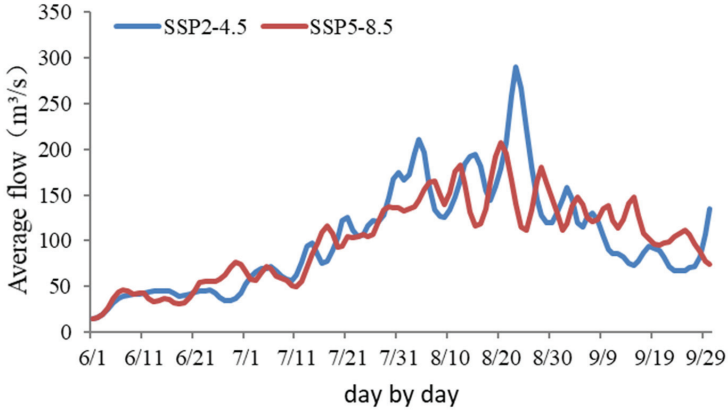

Figure 6. Changes in daily average runoff during the wet season under two climate scenarios from 2021 to 2050.

3.3. Discussion

The Changbai Mountains are affected by the climate of the alpine Mountainsous area. There are about 5 months of the year in the icy period, the temperature is below zero and rainfall is mainly concentrated in the wet season from June to September. The rainfall lasts for a short period of time, intensity is high and rainfall is concentrated; there are many hills and mountains in the basin, the upstream slope of the river is steep, confluence speed is fast and propagation time is short; thus, it is easy to form a flood process of steep ups and downs. Therefore, studying the runoff process in the Changbai Mountains during the wet season, analyzing the historical-future change trend of runoff, establishing a corresponding hydrological model for runoff simulation and improving the accuracy of runoff prediction and the foreseeable period can provide effective theoretical support for the formulation of water resources allocation plans in the basin. In order to improve the water conservation capacity of the regional ecosystem, it is possible to strengthen the temporal regulation of the uneven distribution of water resources of surface runoff during flood and dry periods and spatially regulate the distribution and circulation of surface runoff, soil runoff and underground runoff, etc. At the same time, it is also possible to estimate the situation in response to the synchronization of droughts and floods and other water conditions in the Changbai Mountains Basin or to make an early response to the situation.

On a regional scale, Changbai Mountains constitute a stable snow-covered area in China. Seasonal snow cover can last up to half a year. Therefore, it will be an important source of water supply for river runoff and groundwater during the snowmelt period. The reduction in runoff has suppressed extreme flooding. The occurrence of the incident also reduced the overall water capacity. Therefore, we should pay attention to issues such as global warming. From the perspective of hydrogeological conditions, the lava platform in the Sandaobai River and Songjiang River in the basin contains basalt holes with abundant water. Fissure water provides abundant storage space and good migration channels for groundwater, and it gushes out of the ground in the form of springs where geological faults are exposed. With abundant spring water resources, such as nipple springs, Changbai Mountains springs are the main sources of runoff replenishment. In less rainfall or dry seasons, the replenishment of groundwater and spring water makes a greater contribution to runoff. Therefore, relevant managers should formulate reasonable mineral water mining indicators in this area. Moreover, the relevant thresholds are reasonably calculated to ensure the efficient use of water resources.

In this study, the change trend of runoff in the typical watershed of Changbai Mountains was studied by analyzing future precipitation changes and combined with hydrological models. However, it is difficult to explain that the overall runoff changes in the

watershed have been accurately restored by calibrating and verifying the model only through the single-outlet observation flow rate. With further analysis, the evolution trend of runoff in different regions will be the focus of future research. At the same time, changes in land use types will have a significant impact on runoff in the watershed. Full consideration of the impact of future land use, soil distribution and human activities in the watershed on runoff is a scientific issue worthy of further study.

4. Conclusions

- The HEC-HMS model has good applicability in the Erdao Songhua River Basin of Changbai Mountains. By constructing the HEC-HMS model suitable for the watershed and calibrating the model, the total qualified rate of the daily rainfall runoff simulation in the watershed during the wet season is 75%, and the DC average of the qualified year reaches 0.705. The model can accurately restore hydrological processes in the study area.
- By conducting the analysis of the comparison chart between the simulation and the actual measurement, it can be observed that in the years with better simulation results, such as 2010, 2013 and 2017, the DC value in these years all reached above 0.7, and in 2010, it reached 0.9. The flow changes in these years were relatively gentle, but the peaks were obvious. Statistics on rainfall data found that rainfall in these years was large; it was 688.9 mm in 2010, 652.5 mm in 2013 and 542.3 mm in 2017. During the abundant rainfall period, the river runoff is obviously controlled by the rainfall process. The HEC-HMS hydrological model is mainly driven by precipitation. Thus, the greater the precipitation, the greater the contribution of the surface runoff process to the entire water cycle, and the model's interpretation of runoff flow is more accurate. For the years 2011, 2012 and 2014 with poor simulation results, the simulated value in June was much smaller than the actual flow value, and runoff fluctuated greatly, resulting in inaccurate overall simulation results for that year. Further analysis of the reasons may be related to the geographical location and topographical conditions of the study area. There are many production processes and forms of surface runoff in this area, including melting of ice and snow, and groundwater discharges to river valley runoff in the form of springs. Therefore, when discussing the water cycle process in this region, especially in dry years and dry seasons, various recharge sources such as precipitation, surface water, groundwater and springs should be comprehensively considered.
- In the next 30 years (2021–2050), under the two climate scenarios of SSP2-4.5 and SSP5-8.5, rainfall in the basin will generally increase, and rainfall will be more evenly distributed in the future. The flow of the basin's outlet during the wet season in the next 30 years was simulated, and it was found that the SSP2-4.5 and SSP5-8.5 scenarios have decreased by 33.3% and 34.2%, respectively. This may be related to the decrease in rainfall from June to September during the wet season in the next 30 years compared with the historical period.
- Analysis of the simulated future runoff eigenvalues shows that the peak future runoff occurs most in August, accounting for 40% and 46.7% of the two scenarios, respectively, followed by September. Compared with the peak time in the historical period, most of them appeared in July and August, both accounting for 33.3%, indicating that there will be a certain delay in the peak time in the next 30 years. In the next 30 years, the maximum flow rate under the SSP2-4.5 scenario will be 2130.6 m^3/s in 2050, and the maximum flow rate under the SSP5-8.5 scenario will be 2340.7 m^3/s in 2047.

Author Contributions: Conceptualization, Z.L.; methodology, Z.L. and Y.C.; software, Y.C.; validation, Z.L.; formal analysis, Y.D.; investigation, Y.C.; resources, F.S. and Y.D.; data curation, F.S. and Z.J.; writing—original draft preparation, Y.C.; writing—review and editing, Z.L. and Y.C.; visualization, Z.J.; supervision, Z.L.; project administration, Z.L.; funding acquisition, Z.L. All authors have read and agreed to the published version of the manuscript.

Funding: This research was funded by Evolution Law and Trend Forecast of Water Resources in Changbai Mountains Area under Changing Environment of National Key R & D Project, grant number 2019YFC0409101.

Data Availability Statement: The data presented in this study are available upon request from the corresponding author.

Acknowledgments: We acknowledge the model developed by the U.S. Army Corps of Engineers Hydrology Engineering Center. We are thankful to the United States Geological Survey (USGS) and China Meteorological Data Network for providing free data. At the same time, we would like to thank the reviewers for their helpful suggestions on the improvements of this paper.

Conflicts of Interest: The authors declare no conflict of interest. The funders had no role in the design of the study; in the collection, analyses or interpretation of data; in the writing of the manuscript; or in the decision to publish the results.

References

1. Dong, L.H.; Xiong, L.H.; Yu, K.X. Research progress of climate change and human Activities on hydrology. *Adv. Water Sci.* **2012**, *23*, 278–285. (In Chinese)
2. Chen, S.; Yu, B.; Wu, R.; Chen, W.; Song, L. The dominant North Pacific atmospheric circulation patterns and their relations to Pacific SSTs: Historical simulations and future projections in the IPCC AR6 models. *Clim. Dyn.* **2021**, *56*, 701–725. [CrossRef]
3. Fischer, H.; Broek, K.; Ramisch, K.; Okan, Y. When IPCC graphs can foster or bias understanding: Evidence among decision-makers from governmental and non-governmental institutions. *Environ. Res. Lett.* **2020**, *15*, 114041. [CrossRef]
4. Cao, W.X.; Zhang, Z.Q.; Liu, Y.Q.; Band, L.E.; Wang, S.P.; Xu, H. Seasonal differences in future climate and streamflow variation in a watershed of Northern China. *J. Hydrol. Reg. Stud.* **2021**, *38*, 100959. [CrossRef]
5. Sun, J.Q.; Li, H.Y.; Wang, X.J.; Shahid, S. Water resources response and prediction under climate change in Tao'er River Basin, Northeast China. *J. Mt. Sci.* **2021**, *18*, 2635–2645. [CrossRef]
6. Golmohammadi, G.; Rudra, R.; Prasher, S.; Madani, A.; Mohammadi, K.; Goel, P.; Daggupatti, P. Water Budget in a Tile Drained Watershed under Future Climate Change Using SWATDRAIN Model. *Climate* **2017**, *5*, 39. [CrossRef]
7. Kim, S.; Kim, H.; Kim, K.; Jun, S.M.; Hwang, S.; Kang, M.S. Assessing the Hydroclimatic Movement Under Future Scenarios Including Both Climate and Land Use Changes. *Water* **2021**, *13*, 1120. [CrossRef]
8. Song, P.; Liu, W.; Sun, J.; Wang, C.; Kong, L.; Nong, Z.; Lei, X.; Wang, H. Annual runoff forecasting based on multi-model information fusion and residual error correction in the ganjiang river basin. *Water* **2020**, *12*, 2086. [CrossRef]
9. Yang, M.X. Prediction of annual runoff at the danjiangkou reservoir, china based on forecast domain. *Appl. Ecol. Environ. Res.* **2019**, *17*, 9561–9575. [CrossRef]
10. Liu, Y.; Ye, L.; Qin, H.; Ouyang, S.; Zhang, Z.; Zhou, J. Middle and long-term runoff probabilistic forecasting based on gaussian mixture regression. *Water Resour. Manag.* **2019**, *33*, 1785–1799. [CrossRef]
11. Sun, M.; Kong, X.C.; Geng, W.H. Time series analysis of monthly Precipitation in Shandong Province based on ARIMA Model. *J. Ludong Univ.* **2013**, *29*, 244–249. (In Chinese)
12. Sun, X.T.; Ren, G.H.; Du, K. Monthly rainfall prediction based on grey correlation method. *J. Irrig. Drain.* **2019**, *38*, 90–95. (In Chinese)
13. Yuan, M.; Shen, J.S.; Zhang, Y.; Zhang, R.J.; Zhang, Y.H. Global Temperature Prediction Based on GA-BP Neural Network. *J. Zhengzhou Inst. Aeronaut. Ind. Manag.* **2020**, *38*, 67–75. (In Chinese)
14. Zhou, Y.; Guo, P.; Yang, L. Prediction model of monthly Runoff in wet season based on wavelet analysis. *Shaanxi Water Resour.* **2019**, *10*, 37–39+42. (In Chinese)
15. Sun, D.Y.; Hu, X.Q.; Wang, Z.G.; Lv, H.F. Runoff change and prediction in the Shule River Basin. *Water Resour. Plan. Des.* **2019**, *9*, 1–4+118. (In Chinese)
16. Bao, Z.X.; Zhang, J.Y.; Yan, X.L.; Wang, G.Q.; Jin, J.L.; Liu, Y.; Guan, X.X. Future streamflow assessment in the Haihe River basin located in northern China using a regionalized variable infiltration capacity model based on 18 CMIP5 GCMs. *J. Water Clim. Chang.* **2020**, *11*, 1551–1569. [CrossRef]
17. Jiang, T.; Lu, Y.R.; Huang, J.L.; Wang, Y.J.; Su, B.D. Overview of CMIP6 Model new Scenario (SSP-RCP) and Its Application in Huaihe River Basin. *Prog. Meteorol. Sci. Technol.* **2020**, *10*, 102–109. (In Chinese)
18. Pokhrel, I.; Kalra, A.; Rahaman, M.M.; Thakali, R. Forecasting of Future Flooding and Risk Assessment under CMIP6 Climate Projection in Neuse River, North Carolina. *Forecasting* **2020**, *2*, 323–346. [CrossRef]
19. Wang, L.; Zhai, W.L.; Zhang, J.H.; Cao, H.Q.; Tang, J. Prediction and characteristics of runoff in the upper Han River basin under climate change based on RBF-SWA. *J. Chang. Acad. Sci.* **2022**, *19*, 1–8. (In Chinese)
20. Tang, Z.N.; Yang, G.L.; Liu, P.X. Prediction of Runoff in Lanjiang River Basin Based on HEC-HMS Model. *Soil Water Conserv. Bull.* **2021**, *41*, 137–145. (In Chinese)
21. Zhang, L.; Yang, X.L. Applying a Multi-Model Ensemble Method for Long-Term Runoff Prediction under Climate Change Scenarios for the Yellow River Basin, China. *Water* **2018**, *10*, 301. [CrossRef]

22. Gao, Y.F.; Chen, Y.; Jiang, Y.F.; Peng, T. Effect of DEM data source and resolution on HEC-HMS hydrological modeling. *Adv. Water Sci.* **2015**, *26*, 624–630. (In Chinese)
23. Li, S.; Lai, Z.; Wang, Q.; Wang, Z.; Li, C.; Song, X. Distributed simulation for hydrological process in Plain River network region using SWAT model. *Trans. Chin. Soc. Agric. Eng.* **2013**, *29*, 106–112.
24. Chu, X.; Steinman, A. Event and Continuous Hydrologic Modeling with HEC-HMS. *J. Irrig. Drain. Eng.* **2009**, *135*, 119–124. [CrossRef]
25. Demlie, Z.; Assefa, M. Applicability of a Spatially Semi-Distributed Hydrological Model for Watershed Scale Runoff Estimation in Northwest Ethiopia. *Water* **2018**, *10*, 923.
26. Al-Abed, N.; Abdulla, F.; Khyarah, A.A. GIS-hydrological models for managing water resources in the Zarqa River basin. *Environ. Geol.* **2005**, *47*, 405–411. [CrossRef]
27. Meenu, R.; Rehana, S.; Mujumdar, P.P. Assessment of hydrologic impacts of climate change in Tunga-Bhadra river basin, India with HEC-HMS and SDSM. *Hydrol. Processes* **2013**, *27*, 1572–1589. [CrossRef]
28. Sardoii, E.R.; Rostami, N.; Sigaroudi, S.K.; Taheri, S. Calibration of loss estimation methods in HEC-HMS for simulation of surface runoff (Case Study: Amirkabir Dam Watershed, Iran). *Adv. Environ. Biol.* **2012**, *6*, 343–348.

sustainability

MDPI

Article

Simulation of Freshwater Ecosystem Service Flows under Land-Use Change: A Case Study of Lianshui River Basin, China

Yang Zou and Dehua Mao *

School of Geographical Sciences, Hunan Normal University, Changsha 410081, China; zou_y@hunnu.edu.cn
* Correspondence: maodehua@hunnu.edu.cn

Abstract: The service function of freshwater ecosystem is of great significance for ensuring the water security and the sustainable development of the social economy. However, it is vague how land-use change can influence freshwater ecosystem service flows. In this paper, we analyzed the land-use changes in the Lianshui River Basin from 2000 to 2018, built an ecosystem service flow model, and quantified the supply, demand, and flow of freshwater ecosystems under land-use change. The most intensified shifts of land-use change were the transfer of woodland to arable land and the transfer of arable land to built-up land. Urbanization and deforestation have increased water output by 0.06 billion m^3, but water demand has increased by 2.42 billion m^3, resulting in a 6% reduction in the flow of freshwater ecosystem services. Our study provides detailed information on freshwater ecosystem services flow from providers to beneficiaries within a watershed, showing how land-use change and ecosystem service flows can be integrated at the watershed scale to provide information for land-use management and the availability of freshwater ecosystems. Sustained development provides a scientific basis.

Keywords: ecosystem service flows; land-use change; supply; demand; Lianshui River Basin

Citation: Zou, Y.; Mao, D. Simulation of Freshwater Ecosystem Service Flows under Land-Use Change: A Case Study of Lianshui River Basin, China. *Sustainability* **2022**, *14*, 3270. https://doi.org/10.3390/su14063270

Academic Editors: Alban Kuriqi and Luis Garrote

Received: 24 January 2022
Accepted: 7 March 2022
Published: 10 March 2022

1. Introduction

Life originates from water, and water is also an important component of all living things, and its importance is self-evident. Freshwater supply is closely related to human well-being and is one of the most important ecosystem services [1]. Aquatic ecosystems were the main providers of ecosystem services, especially in the area south of the Yangtze River [2]. Freshwater ecosystem services have great constraints on the sustainable development of many river basins in the south. With the rapid economic development and intensification of land-use, excessive resource development has caused serious damage to the environment. The research on ecosystem services has become a hot spot and frontier, which is of great significance to regional ecology and sustainable development [3,4].

Land-use is one of the most important factors affecting ecosystem services [5,6]. Land-use affects ecosystem services with its type, pattern, and intensity changes [7]. Scientific assessment in the impact of regional land-use changes on the water production function of ecosystems is of great significance to the use of regional water resources [8–11]. The large-scale urban construction activities or conversion of cropland to forest will lead to the change of the underlying surface of the basin, which affects the infiltration process and sink flow process of vegetation evaporation and precipitation entering the soil aquifer and then affects the hydrological cycle interaction process of the whole basin [12,13]. In addition, land-use may also have an impact on the annual runoff, dry season runoff, and flood peak discharge in the basin, which are mainly reflected in the change of water resources in the water cycle and the change of spatial and temporal distribution pattern, which will lead to significant changes in the relationship between water supply and demand in different regions, thus indirectly affecting water ecosystem services [14,15]. Many studies have analyzed the impact of land-use changes on freshwater ecosystem supply, but few studies

have conducted quantitative analysis on the flow of freshwater ecosystem services under land-use changes [16,17].

Land-use changes such as urban sprawl increase the supply of freshwater but also greatly increase the demand for it, which poses new challenges for freshwater resource management [18]. Several attempts have been made to map the spatial dynamics of freshwater ecosystem service supply/demand [19–22]. However, its assessment often has a mismatch between supply and delivery to beneficiaries. Existing studies on quantifying the impact of land-use of ecosystem service flows mostly achieve their goals by scoring land-use cover types or mapping services and benefit areas at the landscape scale [23–25], without knowing the specific information of freshwater ecosystem service flows.

Introducing the flow characteristics of water resources into the evaluation of freshwater ecosystem services can comprehensively analyze the supply, flow path, and demand response mechanism of freshwater ecosystem services to land-use changes, while avoiding the spatial mismatch between supply and demand areas of ecosystem services [26]. The research of ecosystem service flow usually adopts the model method; the Integrated Valuation of Ecosystem Services and Tradeoffs (InVEST) model is applied to quantify the supply of ecosystem service, and the digital elevation model (DEM) can be used to determine the direction of water flow, coupled with the Service Path Attribute Networks (SPANs) model, in which artificial intelligence captures the spatial relationship of ecosystem service flow [17].

The objectives of this study were to map land-use pattern changes, construct a spatial flow model for ecosystem services, and quantify the impact of land-use changes on freshwater ecosystem service flows. For the aim of this study, we used the InVEST model to quantify the supply of freshwater ecosystem services, calculated the water demand of various industries, and combined the SPANs model to construct a spatial watershed model for ecosystem services, quantifying the impact of land-use change in the study area from 2000 to 2018. Impacts on supply, demand, and flow of freshwater ecosystem services. This study can provide a scientific basis for water resources management and ecological protection in the Lianshui River Basin and similar ecosystem basins.

2. Materials and Methods

2.1. Study Area

The Lianshui River Basin is located in the central part of Hunan Province, China, and is a primary tributary on the left bank of the lower Xiangjiang River. The study area is above the Xiangxiang Hydrological station with a catchment area of 5919.03 km^2, including 35 sub-basins, and is located between Shaoyang City, Loudi City, and Xiangtan City (Figure 1). The basin has an average annual temperature of 17.5~18.5 °C and average annual precipitation of 1368 mm. The Shuifumiao reservoir and Baima reservoir are the main sources of freshwater supply [27]. With the rapid economic development, urbanization has led to a series of problems such as water shortages and habitat destruction. Therefore, studying the freshwater ecosystem service flow is of utmost importance to local water security.

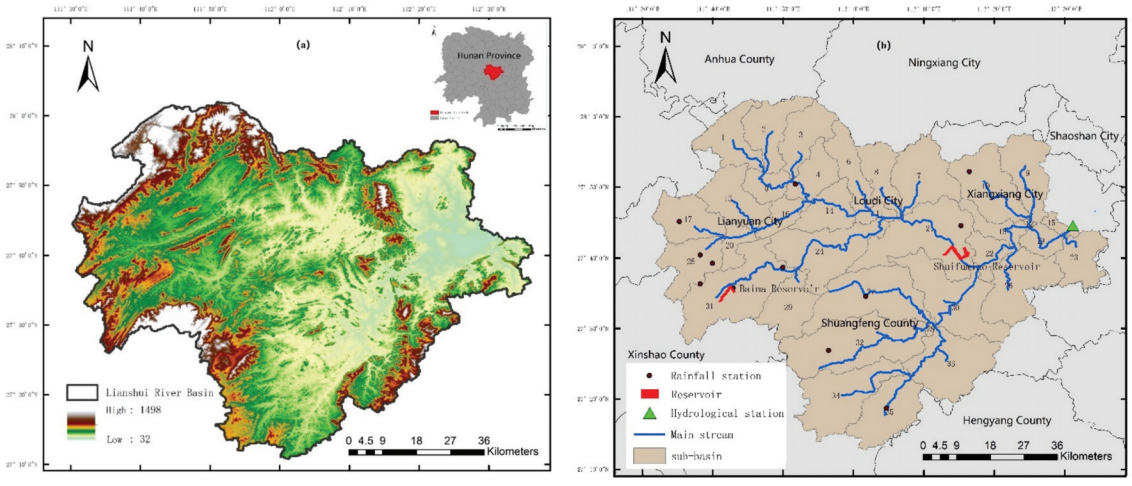

Figure 1. DEM and location (**a**) and river system and sub-basin division (**b**) of the Lianshui River Basin from 2000–2018.

2.2. Data Sources

The digital elevation model (DEM) data were downloaded from the geospatial data cloud website with a resolution of 30 m. The land-use data in 2000 and 2018 were obtained from the Center for Resources and Environment of the Chinese Academy of Sciences with a resolution of 30 m. The soil data were provided by the Harmonized World Soil Database produced by the Food and Agriculture Organization of the United Nations (FAO), and processed by the Institute of Soil Science, Chinese Academy of Sciences. The daily data of five meteorological stations in the research area from 2000 to 2018 were obtained from China Meteorological Data. Due to the sparse distribution of meteorological stations, the Hunan Hydrological Bureau supplemented the daily rainfall data of nine rainfall stations and the continuous hydrological observation data of the Xiangxiang Hydrological Station. The statistical data came from the "Water Resources Bulletin" and the "Statistical Yearbook" (Table 1). All data were resampled to a resolution of 1 km by the Nearest Neighbor Method (NEAREST) in ArcGIS10.5 [28].

Table 1. The data type and data sources.

Type	Data Sources
Digital elevation model (30 m resolution)	Geospatial Data Cloud (https://www.gscloud.cn/) (accessed on 23 January 2022)
Land-use/cover data	Chinese Academy of Sciences Resource and Environmental Science Data Center (http://www.resdc.cn/) (accessed on 23 January 2022)
Meteorological data (precipitation, temperature)	
Hydrological data (runoff)	The Hydrological Bureau of Hunan Province
Water demand data	Water Resources Bulletin of Hunan province
Socioeconomic data (county scale)	Statistical Yearbook(http://slt.hunan.gov.cn/) (accessed on 23 January 2022)

2.3. Analytical Methodology

2.3.1. Land-Use Dynamic Change

The study basin and 35 sub-basins were divided through the processing of depression, flow direction, and flow with the Spatial Analyst in ArcGIS10.5 based on the DEM. Based

on the National Current Land-use Standards (GB/T 21010-2017), land-use in the study area was classified into seven types including woodland, arable land, grassland, water, built-up land, wetland, bare land, and the Kappa coefficient was used to evaluate the results of reclassification [29].

The essence of the land-use transfer matrix is the Markov model [2,30], which can not only quantitatively indicate the conversion between different land-use types but also reveal the transfer rate between different land-use types, so it is widely used in the analysis of land-use changes. The transition matrix model is as follows:

$$A_{ij} = \begin{bmatrix} A_{11} & A_{12} & \cdots & A_{1n} \\ A_{21} & A_{22} & \cdots & A_{2n} \\ \vdots & \vdots & \vdots & \vdots \\ A_{n1} & A_{n2} & \cdots & A_{nn} \end{bmatrix} \quad (1)$$

where A_{ij} represents the area of the land type i before the transfer is converted to the land type j after the transfer; n represents the total number of land-use types; i, j ($i, j = 1, 2, \ldots, n$) is the land-use types before and after the transfer, respectively.

2.3.2. Quantification of Freshwater Ecosystem Service Supply

We used water supply, which is projected by the InVEST model to represent freshwater ES supply [1]. This model was jointly developed by Stanford University, the Nature Conservancy (TNC), and the World Wide Fund for Nature (WWF) [31]. The water production module was based on the water balance formula, ignoring the interactive flow between the surface and groundwater, and calculated the water production through parameters such as precipitation, plant transpiration, surface evaporation, root depth, and soil depth [21]. The main algorithm was as follows:

$$Y_{xj} = \left(1 - \frac{AET_{xj}}{P_x}\right) \cdot P_x \quad (2)$$

where Y_{xj} is the annual water production of the j-th land-use type in the grid x, mm; AET_{xj} is the actual annual evapotranspiration of the j-th land-use type in the grid x, mm; P_x is the average annual precipitationthe in grid x, mm; $\frac{AET_{xj}}{P_x}$ is an approximation of the Budyko curve estimated by [32] as follows:

$$\frac{AET_{xj}}{P_x} = \frac{1 + \omega_x R_{xj}}{1 + \omega_x R_{xj} + \frac{1}{R_{xj}}} \quad (3)$$

$$\omega_x = Z \cdot \frac{AWC_x}{P_x} + 1.25 \quad (4)$$

where ω_x is an unrealistic parameter that describes the soil properties under natural climatic conditions; R_{xj} is the aridity index of the j-th type of land-use type in the grid x, defined as the ratio of potential evaporation to precipitation; AWC_x is the available water content of the vegetation the in grid x, mm, which is used to determine the amount of water provided by the soil for plant growth; Z is the Zhang coefficient, and the more rainfall in the study area, the greater the Zhang coefficient.

Precipitation is first averaged over many years, and then the multi-year average precipitation grid data is obtained through inverse distance-weighted interpolation. Based on daily meteorological data, the FAO-modified Penman–Monteith formula is used to calculate the potential evaporation, and the multi-year average potential evaporation raster data are obtained through the spatial interpolation method [33]. The soil depth data come from the World Soil Database constructed by the FAO. Based on the percentage content of the soil texture, the reference crop evapotranspiration is calculated in the SPAW software using the empirical formula of soil effective water content [34]. The root restricting layer

depth can be replaced by approximate soil depth [35]. The operating parameters of the InVEST water yield model are shown in Table 2.

Table 2. Biophysical table used for the baseline InVEST water yield model run, giving the information about vegetation, plant evapotranspiration coefficient Kc, and root depth for each LULC class.

Lucode	LULC_Desc	Root_Depth	Kc	LULC_Veg
1	arable land	1600	1.055	1
2	woodland	4500	1.008	1
3	grassland	2000	0.865	1
4	wetland	1000	1	1
5	water	10	1.05	0
6	built-up land	0	0.2	0
7	bare land	500	0.15	0

2.3.3. Quantification of Freshwater Ecosystem Service Demand

According to the definition of ecosystem service by the Millennium Ecosystem Assessment [36], we regarded actual water consumption as the demand for freshwater ecosystems, including agricultural water, industrial water, and domestic water (urban resident domestic water and rural resident domestic water). The formula was as follows:

$$W_{dem} = W_{agr} + W_{ind} + W_{dom} = C_{agr} \cdot L_{agr} + C_{ind} \cdot L_{ind} + C_{dom_u} \cdot L_{dom_u} + C_{dom_r} \cdot L_{dom_r} \quad (5)$$

where W_{agr}, W_{ind}, and W_{dom} are agricultural, industrial, and domestic demand for water, respectively. C_{agr} represents water requirement per unit quality of crop products, L_{agr} represents crop yield, C_{ind} is the water indicator per 10,000 yuan of the GDP, L_{ind} is the GDP, C_{dom_u} stands for the domestic water quota of urban residents, L_{dom_u} stands the number of urban residents, C_{dom_r} is dthe omestic water quota for rural residents, and L_{dom_r} is the number of rural residents. Table 3 shows details for these indices of water demand in the study area.

Table 3. Average annual water use of agriculture, residents, and industry.

Year	City	Cagr (m3/ha)	Cind (m3/104 GDP)	Cdomu (L/d·Person)	Cdomr (L/d·Person)
2000	Shaoyang	9015	483	156	114
	Loudi	8209	326	163	118
	Xiangtan	8955	295	163	120
2018	Shaoyang	9044	158	153	92
	Loudi	8544	96	150	95
	Xiangtan	8990	96	150	101

2.3.4. Quantification of Freshwater Ecosystem Service Spatial Flow

Following [37], we defined the freshwater ecosystem flow as the water flowing downstream after the water resources meet the upstream demand by the SPANs [38]. Given the difficulty of obtaining groundwater data, we only consider surface water in the model. The spatial relationship was identified as the path and direction of water flow, which were tracked in ArcGIS10.5 based on the DEM and river water system data. Figure 2 showed the schematic diagram of freshwater ecosystem service flow under land-use change.

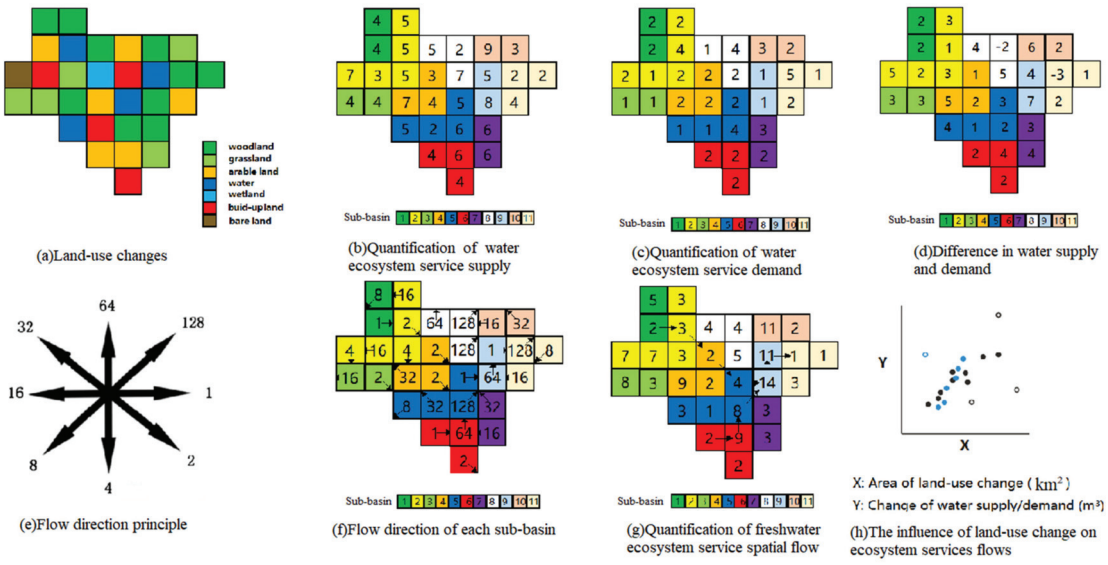

Figure 2. Schematic diagram of freshwater ecosystem service flow model.

2.3.5. Calculation of the Influence of Land-Use Change on Ecosystem Services Flows

We obtained the land-use change matrix during the study period from the 2000–2018 land-use map. In the calculation of the InVEST water supply module, the climatic conditions were fixed and only the land-use data set was changed. Additionally, the slope of the trend line of water supply/demand and land-use area change was used to characterize the response of water supply/demand to land-use change.

3. Results

3.1. Land-Use Change

The Google Earth Quick Bird decimeter-level high resolution images were used as reference for remote sensing interpretation. Among them, 225 and 198 training samples were selected for the data of each year in 2000 and 2018, respectively. All the training samples were greater than 1.8, and the purity of the sample points was higher. The calculated Kappa coefficients were all greater than 0.85 with a good consistency, and the overall classification accuracy was higher than 90%, which met the research requirements.

Table 4 and Figure 3 showed that the land-use types in the study area were mainly arable land and woodland, accounting for about 78% of the basin. From 2000 to 2018, the change in land-use was mainly manifested in the acceleration of urbanization. The built-up area increased from 67.08 to 168.61 km^2, with a growth rate of 151%. At the same time, 4.09 km^2 of bare land appeared in the basin. During the study period, there were 36 types of land-use transfer, among which the transfer of arable land to built-up land and the transfer of woodland to arable land were the most intense (Table 5). Therefore, we focused on the impact of urbanization, deforestation, and reclamation (comprehensive technical process for the regeneration of damaged or degraded land and the restoration of its ecosystem) on the flow of ecosystem services in this study.

Table 4. The structure of land-use in Lianshui River Basin in 2000, 2018.

	2000		2018		2000–2018	
	Area (km^2)	Percentage (%)	Area (km^2)	Percentage (%)	Area (km^2)	Percentage (%)
Arable land	2288.27	38.66	2259.25	38.17	−29.02	−0.49
Woodland	2478.95	41.88	2409.20	40.7	−69.75	−1.18
Grassland	1010.94	17.08	988.41	16.71	−22.53	−0.37
Wetland	2.67	0.05	0.10	0.002	−2.57	−0.048
Water	71.12	1.2	89.36	1.5	+18.24	+0.3
Build-up land	67.08	1.13	168.61	2.85	+101.53	+1.72
Bare land	0.00	0	4.09	0.068	+4.09	+0.068

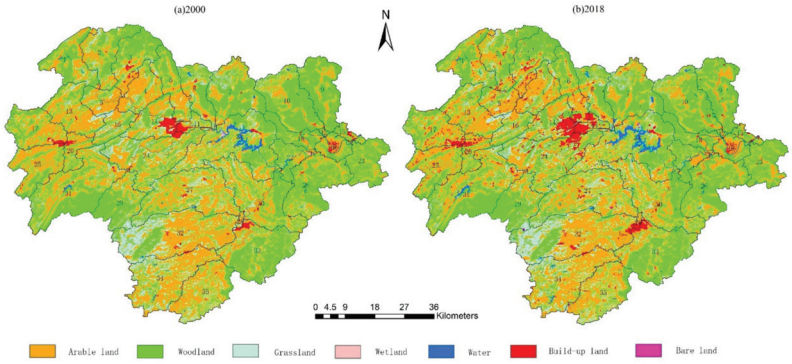

Figure 3. The map of land-use changes in Lianshui River Basin from 2000 to 2018.

Table 5. Land-use transfer matrix in Lianshui River Basin from 2000 to 2018 (km^2).

		2018						
		Arable Land	Woodland	Grassland	Wetland	Water	Build-Up Land	Bare Land
2000	Arable land	2182.47	25.07	3.98	0	28.20	69.58	0.86
	Woodland	70.33	2354.37	21.87	0	2.92	19.82	1.93
	Grassland	11.86	17.35	945.44	0	0.49	19.96	1.29
	Wetland	0.44	0.05	0.04	0.09	2.05	0	0
	Water	9.55	3.36	2.35	0.01	55.13	0.61	0
	Build-up land	4.32	3.09	0.52	0	0.57	58.57	0

3.2. Freshwater Ecosystem Service Supply

We verified the water production of the InVEST model using measured flow data (measured runoff at Xiangxiang Hydrological Station), which proved to be suitable for studying the water production of the basin. The total water supply volumes of the Lianshui River Basin were 4.15 and 4.21 billion m^3 in 2000 and 2018, respectively, and the changes in water production capacity showed a slight upward trend from a numerical point of view. The temporal and spatial heterogeneity of freshwater supply was shown in Figure 4. It can be clearly seen that the water yield capacity of the upper and lower reaches of the Lianshui River Basin was relatively strong, while that of the central region was weak.

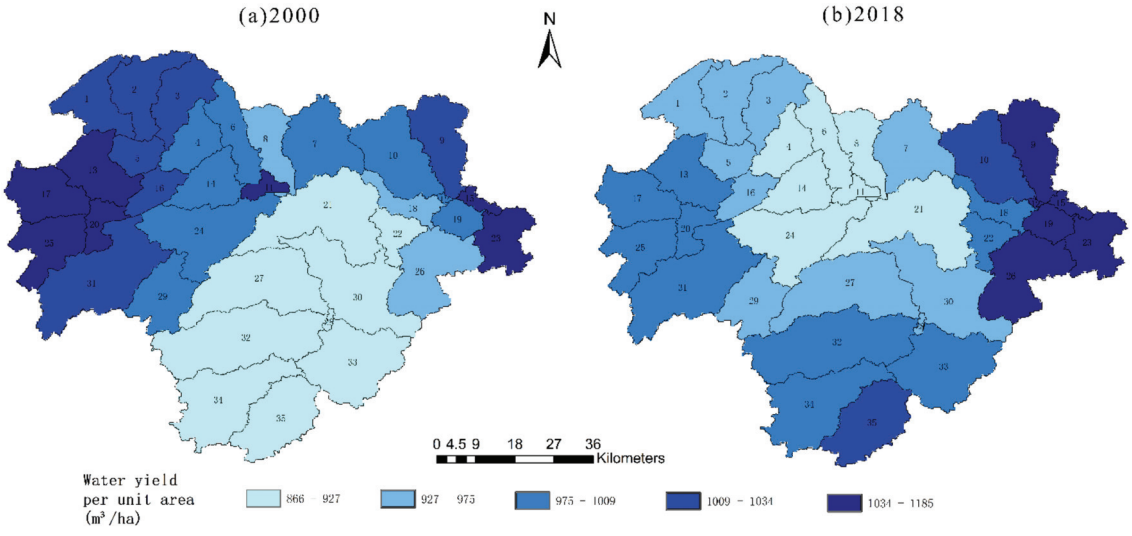

Figure 4. Spatial distribution of water supply.

Keeping climate data fixed at 2000 values and only incorporating the effects of land-use change, we modeled the water supply in 2000 and 2018 (Figure 5). The total water supply changed from 4.15 to 4.20 billion m^3, an increase of 0.05 billion m^3. The increase in the area of arable land, woodland, grassland, wetland, and water area all led to different degrees of reduction in water yield, while the increase in the area of built-up land and bare land increased water supply. The reason was that the impervious layer of construction land was formed, and rainfall infiltration capacity became weaker. Similarly, the water-locking capacity of bare land was weak, and most of the precipitation flowed away directly.

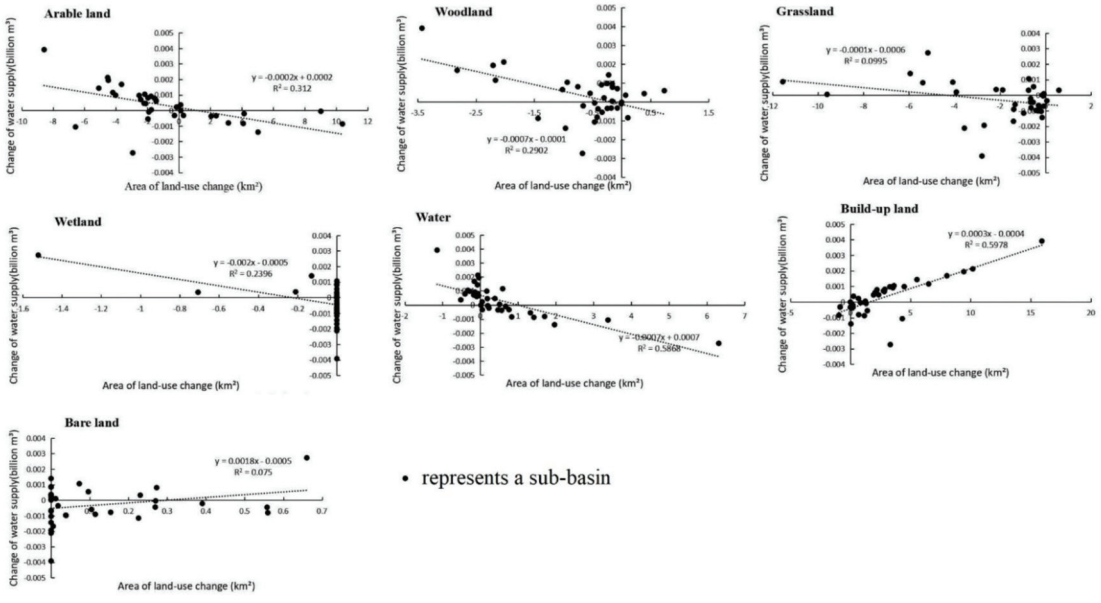

Figure 5. Changes in water supply under land-use changes.

3.3. Freshwater Ecosystem Service Demand

From 2000 to 2018, the total water demand showed an increasing trend, reaching 9.67 and 12.09 billion m^3, respectively. And the spatial distribution has shown in Figure 6. As can be seen in Figure 7, agricultural water demand, industrial water demand, and domestic water demand have increased to varying degrees, and the spatial distribution was different. Agricultural water demand was the largest type of water use in the basin. The high-value areas for agricultural water demand use were located in the lower reaches of the basin, and those for industrial water use were located in the middle and upper reaches of the basin, while domestic water demand was concentrated in several central counties and cities. Various types of water demand were closely related to the local population, socio-economic development, and land-use types.

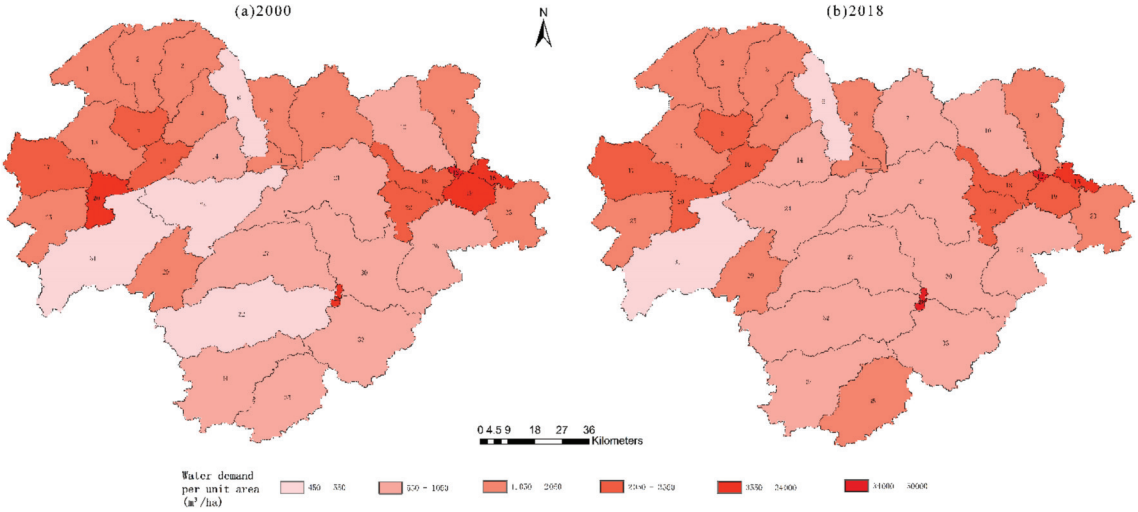

Figure 6. Spatial distribution of water demand.

Different from changes in water supply, all land-use changes and water demand from 2000 to 2018 have a positive correlation, even some small land-use changes, such as wetlands and water. Changes in construction land and grassland have the greatest correlation with water demand, mainly because urbanization has led to an increase in population and a substantial increase in water demand (Figure 8).

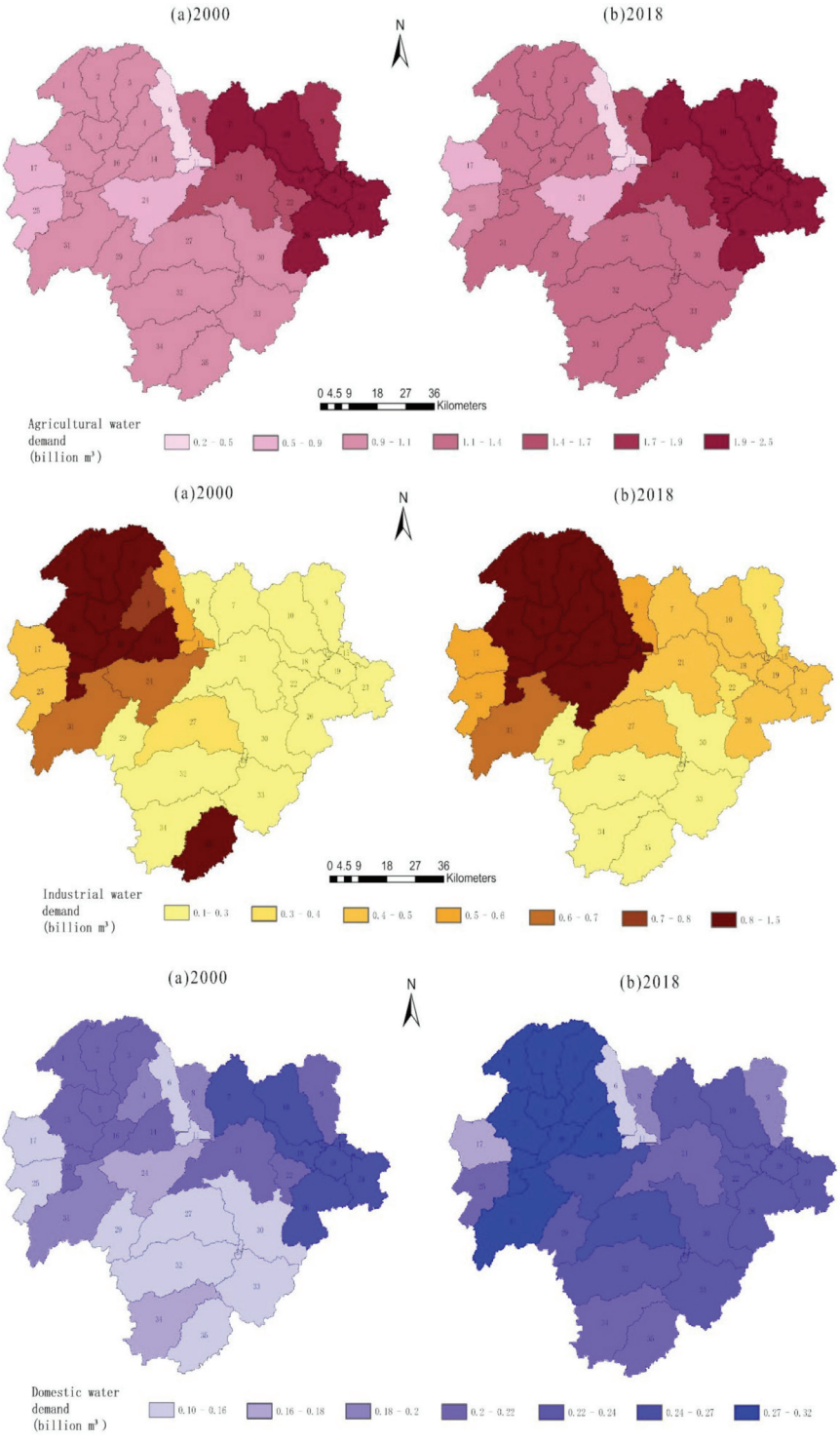

Figure 7. Spatial distribution of water consumption in different industries.

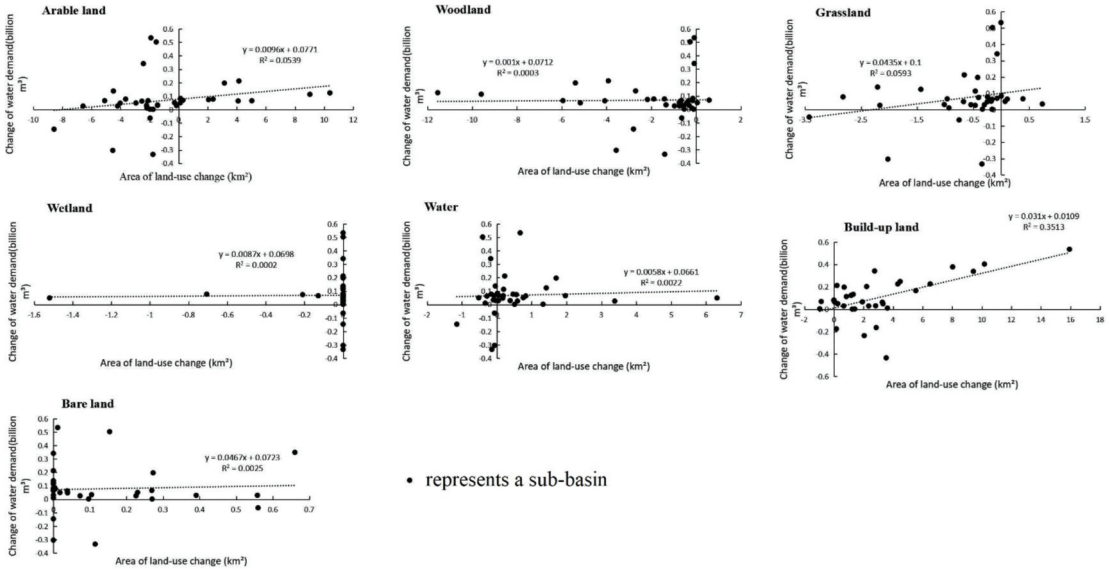

Figure 8. Changes in water demand under land-use changes.

3.4. Freshwater Ecosystem Service Flows

In our research into the freshwater ecosystem service flow based on the flow water security index, the sub-catchment that cannot meet the actual water demand by its water supply and needs to be supplemented by the upstream sub-catchment water was called the beneficiary area; otherwise, it was called the supply area, and the direction of the service flow was consistent with the direction of water flow. In 2000, sub-basins 11, 12, 15, 19, and 28 have all experienced freshwater shortages (Figure 9). This situation intensified in 2018, and the area of freshwater shortages has expanded (sub-basin16). Compared to 2000, freshwater ecosystem service flows decreased by 6% in 2018 under land-use change.

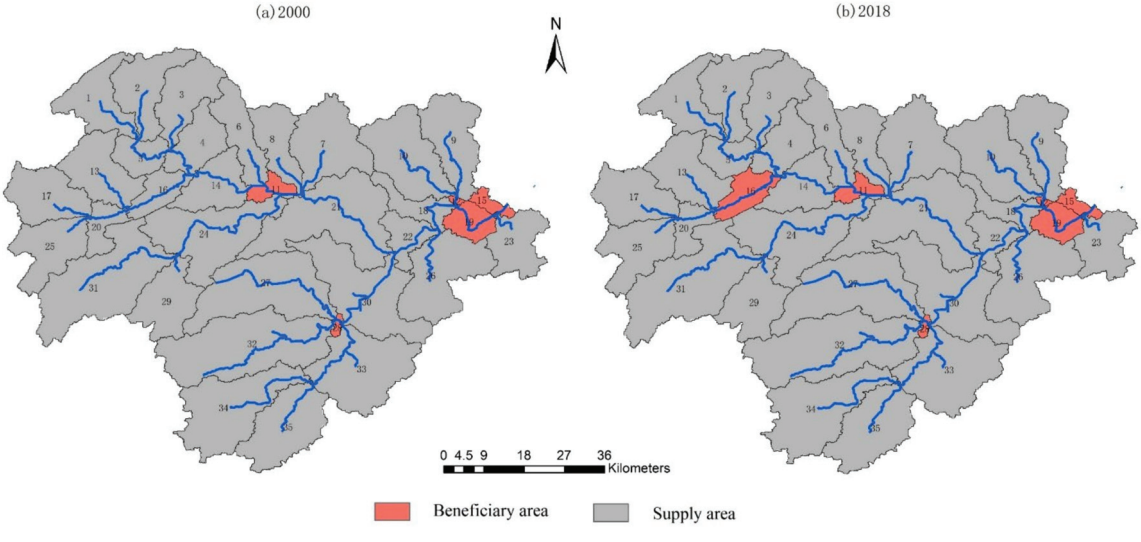

Figure 9. Spatial distribution map of freshwater ecosystem service flow in Lianshui River Basin.

4. Discussion

We quantitatively assessed the impact of land-use change on freshwater ecosystem service flows in the Lianshui River Basin between 2000 and 2018. Deforestation and urban expansion have shifted land-use from cultivated land and forest land to construction land. Changes in land-use had a small positive impact on the supply of freshwater ecosystem services, but the increased industrial and agricultural water demand had a larger impact, resulting in a 6% reduction in the flow of freshwater ecosystem services across the study area. Land-use change influences the flow of freshwater ecosystem services by affecting hydrological processes and human water use. In the past 20 years, China's development speed has been unprecedented, and the trend of urbanization is obvious. Its main manifestation was the decrease of woodland and the increase of built-up land [39]. The land-use change in Lianshui River Basin has this obvious characteristic. Through this research, we found that, from 2000 to 2018, the most intense land-use transfer method in the Lianshui River Basin was the transfer of forest land to cultivated land and cultivated land to construction land, which was related to local urban intensification, deforestation, and other human behaviors. The Louxing District of Loudi City has developed rapidly in recent years, with a GDP growth rate of 4.4%, and the expansion of its surrounding towns was also very obvious. Overall, the supply of freshwater ecosystem services in the Lianshui River Basin increased under land-use changes.

The increase in impervious surface due to urbanization may lead to a decrease in soil water retention and soil moisture. However, additional water supplies caused by changes in more impermeable surfaces were limited, suggesting that land-use change had little positive impact on freshwater supplies. Water demand is strongly influenced by changes in land-use and associated changes in domestic, agricultural, and industrial water use, compared with a slight impact on water supply. During the study period, the area of agricultural land decreased, but the irrigation water demand per mu increased gradually. It was also mentioned before that the rapid economic development of Louxing District of Loudi City is closely related to the increase of its industrial enterprises. From 2016 to 2018 alone, Louxing District added 57 new industrial enterprises above designated size, which greatly increased the demand for industrial water. For domestic water demand, under the control of the water quota policy, the average annual water consumption of residents has declined, but the water demand is related to the population. The population of the study area has been increasing steadily, which also increases the domestic water demand. These combined have resulted in a substantial increase in water demand in the study area. Changes in demand have a far greater impact on the flow of freshwater ecosystem services than changes in water supply due to land-use changes. Therefore, we should pay more attention to the management of water demand, especially in the downstream areas, than the management of the landscape pattern.

At present, the most widely used quantitative methods in the research of ecosystem service flow include the matrix method, the distributed model method, and the ecosystem cascade framework method [40–42]. The InVEST model has obvious advantages in stimulating the supply of freshwater ecosystems, such as few parameters and good adaptability [43,44]. However, the spatial role of water supply services was very complicated. Although measured data were used for model verification, there were still certain uncertainties and limitations. The simulation process ignored the loss of water resources during the flow period and does not consider groundwater, which may underestimate the water supply capacity. At the same time, due to the difficulty of data acquisition, the model simulation process did not consider the impact of man-made infrastructure (such as reservoirs, retaining dam, and water diversion projects) on the regulation and control of water resources. In future research, the uncertainty of the model should be strengthened, and researchers should attempt to integrate more human activities' influencing factors and conduct research on ecosystem service flows at various temporal and spatial scales.

Watershed freshwater supply increases with land-use changes and responds differently to changes in land-use types. This is due to the internal flow and base flow generated

by different land cover surfaces [16]. In the past, there have been many studies on the impact of land-use change on water supply [21,43], but most of them did not distinguish between the impact of climate change and land-use. We fixed the meteorological data in 2000, stripped off the impact of land-use change, and found that the land-use change in the river basin expanded the impervious layer area and increased the water supply by 0.01 billion m^3 from 2000–2018. This conclusion is consistent with the conclusions of [16,45] and others. The increase in construction area has led to an increase in water demand. Compared with the increase in water supply, the water demand has increased more to 2.42 billion m^3. The flow of freshwater ecosystem services varies with the relationship between supply and demand, reducing by 6%.

While urbanization promotes the supply of freshwater ecosystem service flows, the resulting increase in water demand and water pollution problems cannot be ignored [46]. The increase in water consumption means an increase in the amount of sewage. The impervious ground can allow nutrients, chemicals, and other pollutants to enter the waterbody along with the surface runoff, resulting in a decline in water quality. The government should weigh regional development and ecological protection, evaluate the priority of ecological compensation, and carry out targeted ecological compensation. For example, the freshwater ecosystem service beneficiary area should compensate the supply area, and the upstream area should compensate the downstream area for water pollution. The government should also have an in-depth understanding of the characteristics of regional water resources and the structure of water resources development and utilization and conduct key supervision on certain areas with low water efficiency, find out the reasons for the low efficiency, and improve the water security of the river basin.

5. Conclusions

Under rapid economic development and urbanization, land-use changes have a profound impact on the supply, demand, and flow paths of freshwater ecosystem services. The response relationship between changes in different land-use types and changes of freshwater ecosystem services flows are discussed in this paper, which can provide scientific reference and support for basing measures to suit local conditions and strengthen ecological protection and governance. As a study area, the Lianshui River Basin has a unique geographical advantage in the Hengyang-Shaoyang-Loudi Arid Corridor, which can be used for reference. We found that, under the rapid economic development, the urbanization area of the Lianshui River Basin gradually expanded from 2000 to 2018. Changes in land-use types have different impacts on freshwater supply and demand. During the study period, the supply of freshwater ecosystem services increased slightly with the increase of built-up land, but the demand increased significantly, and the spatial distribution was uneven, especially the urban population agglomeration, causing the water demand to greatly exceed the supply. The proportion of benefited areas in the basin increased, which was detrimental to the sustainable development of the watershed. We suggest that the upstream should focus on water conservation in agriculture, and the downstream cities should control the per capita water consumption quota, build a water-saving society in an all-around way, and raise the nation's awareness of water conservation.

Author Contributions: Y.Z. and D.M. designed the research. Y.Z. wrote the article and analyzed the data. Y.Z. and D.M. provided the methods and obtained the results. D.M. provided the basic data and technical support. All authors have read and agreed to the published version of the manuscript.

Funding: This study was supported by the Joint Fund for Regional Innovation and Development of NSFC (U19A2051), the Research Project of Hunan Provincial Water Resources Department (XSKJ 2018179-09), the Key R&D Project of Hunan Province (2017SK2301), and the Construction Program for First-Class Disciplines (Geography) of Hunan Province, China (5010002).

Conflicts of Interest: The authors declare no conflict of interest.

References

1. Li, D.; Wu, S.; Liu, L.; Liang, Z.; Li, S. Evaluating regional water security through a freshwater ecosystem service flow model: A case study in Beijing-Tianjian-Hebei region, China. *Ecol. Indic.* **2017**, *81*, 159–170. [CrossRef]
2. Li, H.; Ye, C.; Hua, J. Impact of Land Use Change on Ecosystem Service Value in Nanchang City. *Res. Soil Water Conserv.* **2020**, *27*, 277–285. [CrossRef]
3. Thomas, A.; Masante, D.; Jackson, B.; Cosby, B.; Emmett, B.; Jones, L. Fragmentation and thresholds in hydrological flow-based ecosystem services. *Ecol. Appl.* **2020**, *30*, e02046. [CrossRef] [PubMed]
4. La Notte, A.; Dalmazzone, S. Sustainability assessment and causality nexus through ecosystem service accounting: The case of water purification in Europe. *J. Env. Manag.* **2018**, *223*, 964–974. [CrossRef]
5. Bujnovský, R. Estimation of benefits from the actual use of inland water ecosystem services in the Slovak Republic. *Ekológia* **2018**, *37*, 201–218. [CrossRef]
6. Kaiser, G.; Burkhard, B.; Römer, H.; Sangkaew, S.; Graterol, R.; Haitook, T.; Sterr, H.; Sakuna-Schwartz, D. Mapping tsunami impacts on land cover and related ecosystem service supply in Phang Nga, Thailand. *Nat. Hazards Earth Syst. Sci.* **2013**, *13*, 3095–3111. [CrossRef]
7. Tong, H.; Shi, P. Using ecosystem service supply and ecosystem sensitivity to identify landscape ecology security patterns in the Lanzhou-Xining urban agglomeration, China. *J. Mt. Sci.* **2020**, *17*, 2758–2773. [CrossRef]
8. Kim, S.; Lee, J.; Jeon, S.; Lee, M.; An, H.; Jung, K.; Park, D. Correlation Analysis between Hydrologic Flow Metrics and Benthic Macroinvertebrates Index (BMI) in the Han River Basin, South Korea. *Sustainability* **2021**, *13*, 11477. [CrossRef]
9. Lee, J.W.; Lee, S.W.; An, K.J.; Hwang, S.J.; Kim, N.Y. An estimated structural equation model to assess the effects of land use on water quality and benthic macroinvertebrates in streams of the Nam-Han River System, South Korea. *Int. J. Environ. Res. Public Health* **2020**, *17*, 2116. [CrossRef]
10. Gao, X.; Huang, B.; Hou, Y.; Xu, W.; Zheng, H.; Ma, D.; Ouyang, Z. Using Ecosystem Service Flows to Inform Ecological Compensation: Theory & Application. *Int. J. Environ. Res. Public Health* **2020**, *17*, 3340.
11. Kim, D.H.; Chon, T.S.; Kwak, G.S.; Lee, S.B.; Park, Y.S. Effects of land use types on community structure patterns of benthic macroinvertebrates in streams of urban areas in the South of the Korea Peninsula. *Water* **2016**, *8*, 187. [CrossRef]
12. Vrebos, D.; Staes, J.; Vandenbroucke, T.; D'Haeyer, T.; Johnston, R.; Muhumuza, M.; Kasabeke, C.; Meire, P. Mapping ecosystem service flows with land cover scoring maps for data-scarce regions. *Ecosyst. Serv.* **2015**, *13*, 28–40. [CrossRef]
13. Brauman, K.A. Hydrologic ecosystem services: Linking ecohydrologic processes to human well-being in water research and watershed management. *Wiley Interdiscip. Rev. Water* **2015**, *2*, 345–358. [CrossRef]
14. Zhang, X.; Fan, J.; Cheng, G. Modelling the effects of land-use change on runoff and sediment yield in the Weicheng River watershed, Southwest China. *J. Mt. Sci.* **2015**, *12*, 434–445. [CrossRef]
15. Liu, Y.; Zhang, X.; Xia, D.; You, J.; Rong, Y.; Bakir, M. Impacts of Land-Use and Climate Changes on Hydrologic Processes in the Qingyi River Watershed, China. *J. Hydrol. Eng.* **2013**, *18*, 1495–1512. [CrossRef]
16. Migliorini, G.H.; Romero, G.Q. Warming and leaf litter functional diversity, not litter quality, drive decomposition in a freshwater ecosystem. *Sci. Rep.* **2020**, *10*, 20333. [CrossRef]
17. Qin, K.; Liu, J.; Yan, L.; Huang, H. Integrating ecosystem services flows into water security simulations in water scarce areas: Present and future. *Sci. Total Environ.* **2019**, *670*, 1037–1048. [CrossRef]
18. Zeng, S.; Liu, Z.; Kaufmann, G.; Zeng, Q.; Chen, B. Seasonal and diurnal variations in DIC, NO_3^- and TOC concentrations in spring-pond ecosystems under different land-uses at the Shawan Karst Test Site, SW China: Carbon limitation of aquatic photosynthesis. *J. Hydrol.* **2019**, *574*, 811–821. [CrossRef]
19. Zhu, Q.; Wang, Y.; Qi, L.; Zhou, W.; Zhou, L.; Yu, D.; Dai, L. A framework of freshwater services flow model into assessment on water security and quantification of transboundary flow: A case study in northeast China. *J. Environ. Manag.* **2022**, *304*, 114318. [CrossRef]
20. Zhang, Z.; Zhang, H.; Feng, J.; Wang, Y.; Liu, K. Evaluation of Social Values for Ecosystem Services in Urban Riverfront Space Based on the SolVES Model: A Case Study of the Fenghe River, Xi'an, China. *Int. J. Environ. Res Public Health* **2021**, *18*, 2765. [CrossRef]
21. Yang, X.; Chen, R.; Meadows, M.E.; Ji, G.; Xu, J. Modelling water yield with the InVEST model in a data scarce region of northwest China. *Water Supply* **2020**, *20*, 1035–1045. [CrossRef]
22. Twisa, S.; Mwabumba, M.; Kurian, M.; Buchroithner, M.F. Impact of Land-Use/Land-Cover Change on Drinking Water Ecosystem Services in Wami River Basin, Tanzania. *Resources* **2020**, *9*, 37. [CrossRef]
23. Parvaiz A, M.B. Fayaz A. Seasonal Spatio-Temporal Variability in Temperature over North Kashmir Himalayas Using Sen Slope and Mann-Kendall Test. *J. Climatol. Weather Forecast.* **2021**, *9*, 1–12.
24. Aneva, I.; Zhelev, P.; Lukanov, S.; Peneva, M.; Vassilev, K.; Zheljazkov, V.D. Influence of the Land Use Type on the Wild Plant Diversity. *Plants* **2020**, *9*, 602. [CrossRef] [PubMed]
25. Campagne, C.S.; Roche, P. May the matrix be with you! Guidelines for the application of expert-based matrix approach for ecosystem services assessment and mapping. *One Ecosyst.* **2018**, *3*, e24134. [CrossRef]
26. Koellner, T.; Bonn, A.; Arnhold, S.; Bagstad, K.J.; Fridman, D.; Guerra, C.A.; Kastner, T.; Kissinger, M.; Kleemann, J.; Kuhlicke, C.; et al. Guidance for assessing interregional ecosystem service flows. *Ecol. Indic.* **2019**, *105*, 92–106. [CrossRef]

27. Feng, C.; Mao, D.; Zhou, H.; Cao, Y.; Hu, G. Game Modeling and Application Analysis of Green Water Management in the River Basin. *Resour. Environ. Yangtze Basin* **2018**, *27*, 2505–2517.
28. Mukhtar, N.N.; Aimrun, W.; Fikri, A.A.; Saufi, M.K.M. Dynamics of potential precipitation under climate change scenarios at Cameron highlands, Malaysia. *SN Appl. Sci.* **2021**, *3*, 1–17. [CrossRef]
29. Esquivel, J.; Echeverría, C.; Saldaña, A.; Fuentes, R. High functional diversity of forest ecosystems is linked to high provision of water flow regulation ecosystem service. *Ecol. Indic.* **2020**, *115*, 106433. [CrossRef]
30. Yu, M.Y.; Meng, F.; Cui, J. Spatial Analysis of Land Use and Land Cover Changes on the Basis of RS and GIS. *Appl. Mech. Mater.* **2011**, *90*, 1711–1714. [CrossRef]
31. Richard, S.; Rebecca, C.-K.; Spencer, W. InVEST 3.2.0 User's Guide. 2015. Available online: https://invest-userguide.readthedocs.io/en/latest/ (accessed on 22 January 2022).
32. Zhang, L.; Dawes, W.R.; Walker, G.R. Response of mean annual evapotranspiration to vegetation changes at catchment scale. *Water Resour. Res.* **2001**, *37*, 701–708. [CrossRef]
33. Gong, X.; Liu, H.; Sun, J.; Gao, Y.; Zhang, X.; Jha, S.K.; Zhang, H.; Ma, X.; Wang, W. A proposed surface resistance model for the Penman-Monteith formula to estimate evapotranspiration in a solar greenhouse. *J. Arid Land* **2017**, *9*, 530–546. [CrossRef]
34. Biao, W.; Xinmin, Z.; Gang, H. Estimation of Reference Crop Evapotranspiration in Northwest China. *Earth Sci.* **2020**, *9*, 89–99.
35. Xu, J.; Xiao, Y.; Li, N.; Wang, H. Spatial and Temporal Patterns of Supply and Demand Balance of Water Supply Services in the Dongjiang Lake Basin and Its Beneficiary Areas. *J. Resour. Ecol.* **2015**, *6*, 386–396.
36. MEA. *Millenium Ecosystem Assessment: Ecosystems and Human Well-Being-Synthesis*; Island Press: Washington, DC, USA, 2005.
37. Johnson, G.W.; Bagstad, K.J.; Snapp, R.R.; Villa, F. Service Path Attribution Networks (SPANs). *Int. J. Agric. Environ. Inf. Syst.* **2012**, *3*, 54–71. [CrossRef]
38. Bagstad, K.J.; Johnson, G.W.; Voigt, B.; Villa, F. Spatial dynamics of ecosystem service flows: A comprehensive approach to quantifying actual services. *Ecosyst. Serv.* **2013**, *4*, 117–125. [CrossRef]
39. Sun, Y.; Liu, S.; Dong, Y.; An, Y.; Shi, F.; Dong, S.; Liu, G. Spatio-temporal evolution scenarios and the coupling analysis of ecosystem services with land use change in China. *Sci. Total Environ.* **2019**, *681*, 211–225. [CrossRef]
40. Smit, I.P.J.; Roux, D.J.; Swemmer, L.K.; Boshoff, N.; Novellie, P. Protected areas as outdoor classrooms and global laboratories: Intellectual ecosystem services flowing to-and-from a National Park. *Ecosyst. Serv.* **2017**, *28*, 238–250. [CrossRef]
41. Owuor, M.A.; Icely, J.; Newton, A.; Nyunja, J.; Otieno, P.; Tuda, A.O.; Oduor, N. Mapping of ecosystem services flow in Mida Creek, Kenya. *Ocean Coast. Manag.* **2017**, *140*, 11–21. [CrossRef]
42. Zank, B.; Bagstad, K.J.; Voigt, B.; Villa, F. Modeling the effects of urban expansion on natural capital stocks and ecosystem service flows: A case study in the Puget Sound, Washington, USA. *Landsc. Urban Plan.* **2016**, *149*, 31–42. [CrossRef]
43. Yang, D.; Liu, W.; Tang, L.; Chen, L.; Li, X.; Xu, X. Estimation of water provision service for monsoon catchments of South China: Applicability of the InVEST model. *Landsc. Urban Plan.* **2019**, *182*, 133–143. [CrossRef]
44. Ke, X.; Wang, L.; Ma, Y.; Pu, K.; Zhou, T.; Xiao, B.; Wang, J. Impacts of Strict Cropland Protection on Water Yield: A Case Study of Wuhan, China. *Sustainability* **2019**, *11*, 184. [CrossRef]
45. Ervinia, A.; Huang, J.L.; Zhang, Z.Y. Land-use changes reinforce the impacts of climate change on annual runoff dynamics in a southeast China coastal watershed. *Hydrol. Earth Syst. Sci.* **2015**, *12*, 6305–6325.
46. Huang, J.L.; Li, Q.S.; Pontius, R.G., Jr.; Klemas, V.; Hong, H.S. Detecting the dynamic linkage between landscape characteristics and water quality in a subtropical coastal watershed, Southeast China. *Environ. Manag.* **2013**, *51*, 32–44. [CrossRef]

agriculture

MDPI

Article

Modelling the Hydrology of an Upland Catchment of Bystra River in 2050 Climate Using RCP 4.5 and RCP 8.5 Emission Scenario Forecasts

Damian Badora *, Rafal Wawer, Anna Nierobca , Aleksandra Krol-Badziak, Jerzy Kozyra, Beata Jurga and Eugeniusz Nowocien

The Institute of Soil Science and Plant Cultivation—State Research Institute, ul. Czartoryskich 8, 24-100 Pulawy, Poland; huwer@iung.pulawy.pl (R.W.); anna.nierobca@iung.pulawy.pl (A.N.); aleksandra.krol@iung.pulawy.pl (A.K.-B.); kozyr@iung.pulawy.pl (J.K.); bjurga@iung.pulawy.pl (B.J.); nowocien@iung.pulawy.pl (E.N.)

* Correspondence: dbadora@iung.pulawy.pl

Abstract: This article presents selected flow modeling indices of the Bystra River catchment area (east Poland) obtained using the SWAT model simulations for three regional climate models driven by the EC-EARTH global climate model for 2021–2050 and both RCP4.5 and RCP 8.5 scenarios. The research area was selected due to the large relief of the terrain, the predominance of soils made of loess and the agricultural nature of the Bystra River catchment area, which is very sensitive to climate change, has very valuable soils, and can be used as a test area for modeling land use-based adaptation measures to climate change. The calibration and validation using the SUFI-2 algorithm in the SWAT CUP program was carried out in order to determine the water balance. After obtaining satisfactory results, the SWAT-CUP program simulated the best parameter values for climate change projections. In analyzed climate projections, the monthly mean sums of actual evapotranspiration and potential evapotranspiration will be higher compared to the simulation period of the 2010–2017 model. The exception is the month of June, where actual evapotranspiration in most climate projections is lower compared to the years 2010–2017. The average monthly total runoff for the Bystra River basin will be lower in most of the 2021–2030 climate change projections for most months compared to the reference period. Also, in the 2031–2040 and 2041–2050 periods, the average monthly total runoff will be lower for the RCP 4.5 scenarios (except for one RCP 4.5 scenario in 2031–2040). Additionally, in the case of the RCP 8.5 for the two scenarios in 2041–2050, the average monthly total runoff will be higher compared to the reference years. We determine that the analysis impact of climate change will result in 31 recognized and different small sub-catchments of the Bystra River, which result from higher precipitation and less evapotranspiration for RCP 8.5 in 2041–2050. All of the above changes in the individual components of the water balance may have a negative impact on the vegetation in the coming decades. The temperature increase and the variable amount of precipitation in individual months may lead to an increased number of extreme phenomena. Increased mean monthly sum of actual and potential evapotranspiration, as well as changes in monthly sums of total runoff, may disturb the vegetation in the studied area at every stage of growth. The above components may also influence changes in the amount of water in the soil (especially during the growing season). Counteracting the effects of future climate change requires various adaptation measures.

Keywords: climate change; water deficit; SWAT; SWAT-CUP

Citation: Badora, D.; Wawer, R.; Nierobca, A.; Krol-Badziak, A.; Kozyra, J.; Jurga, B.; Nowocien, E. Modelling the Hydrology of an Upland Catchment of Bystra River in 2050 Climate Using RCP 4.5 and RCP 8.5 Emission Scenario Forecasts. *Agriculture* **2022**, *12*, 403. https://doi.org/10.3390/agriculture12030403

Academic Editors: Alban Kuriqi and Luis Garrote

Received: 3 December 2021
Accepted: 4 March 2022
Published: 14 March 2022

Publisher's Note: MDPI stays neutral with regard to jurisdictional claims in published maps and institutional affiliations.

1. Introduction

Climate change for the next few decades to come and the related unpredictability of extreme weather phenomena are currently the subject of many studies. This is due to concerns about the environmental, social, and economic risks that may arise in the coming decades. These changes will also apply to agriculture in Poland [1]. The analysis

of the climate for the years 1970–2010 shows a statistically significant increase in the sum of evapotranspiration in the growing season [2]. The increase in evapotranspiration, temperature, and precipitation in the coming decades will also apply to the Vistula basin [3] and Europe as a whole [4,5].

Moreover, the amount of precipitation increases in winter and early spring and decreases in spring and summer. This contributes to the reduction of the climatic water balance (i.e., the increase in the deficit of precipitation in relation to the potential evaporation) [2].

The observed increase in air temperature contributed to the increase in potential evapotranspiration. In particular, in the 2011–2020 period, a large increase in potential evapotranspiration was found and the variability of this indicator increased (Figure 1).

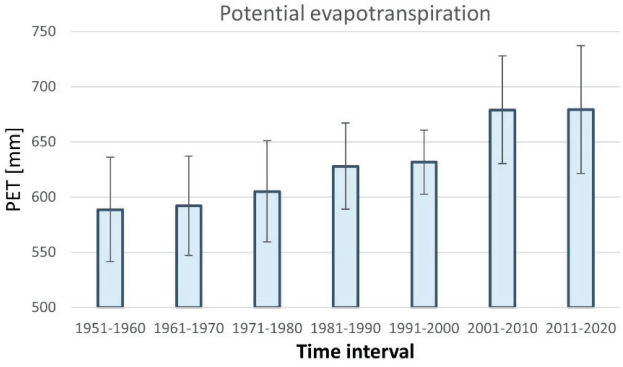

Figure 1. Potential evapotranspiration in Pulawy with error bars calculated according to the Doroszewski formula [6].

In recent decades, changes in the climate have been observed in Poland, resulting from warming, changes in precipitation, and a number of extreme weather events [7–9]. Climate change scenarios developed by the IPCC [10] indicate a 10-fold increase in the occurrence of droughts in Poland in the coming decades [11]. According to NOAA, 2017 was the second warmest year of meteorological recording and analysis (since 1880) in the world [12]. By analyzing the climate scenarios for the years 2021–2050, it has been shown that the growing season in Poland, defined by the number of days with the daily air temperature 5 °C higher in the years 2021–2050, will be longer than in the years 1971–2000 by 16 days. The predicted higher temperature in the growing season of plants will significantly accelerate their development [2]. Therefore, it is necessary to look for solutions to minimize the negative impact of climate change [13], e.g., the occurrence of weather extremes and droughts [6,14–17] in the Bystra catchment areas, in the coming decades. In order to assess the effectiveness of the proposed solutions, it is necessary to develop boundary conditions, indicating a baseline representing the behavior of the Bystra catchment hydrosystem in the 'business as usual scenario' (i.e., taking into account changes in the hydrological cycle caused only by climate change with unchanged conditions of human activity). The above-mentioned boundary conditions for the 2050 horizon must be based on simulation modeling, calibrated on archival data. One of the many mathematical models suitable for the analysis of the water balance of the catchment area and the analysis of the impact of predicted climate changes in the future decades is the SWAT model.

This study uses large scale application SWAT for Vistula and Odra large catchment-based analysis to determine increases of both low and high river flows [18]. It was also shown that soil moisture and soil physical properties add valuable information for the prediction of climate change impact on yield variability [18].

The purpose of this article is to prepare an appropriate SWAT model and to study spatial assessment of hydrological indices obtained in three varied climate projections for two representative concentration pathways (RCPs) in order to analyze differences

in the results of regional climate models based on the same global climate model [19]. These models are characterized by different parameterization of physical processes while running on the same spatial domain, covering the European continent, and benefiting from the boundary and initial conditions of the same global model (EC-EARTH). Such assessment attitudes matter for future research on the effectiveness of agricultural land use change adaptation practices in terms of reducing water erosion and increasing water retention in the landscape, including small retention, introduced in various variants related to land consolidation.

The developed model, after calibration and validation, was used for research related to the prepared projections for the RCP 4.5 and RCP 8.5 scenarios.

The study area was selected due to the large relief and the predominance of soils made of loess. The agricultural nature of the catchment area and loess soils with good retention properties [20] will be used in subsequent publications to assess adaptation scenarios. The Bystra catchment area has been the target of many studies and statutory re-search by IUNG. The results of these studies have been used in this present study.

Due to the observed temperature increase, which also contributes to the increase in potential evapotranspiration in recent years, the years 2010–2017 were adopted for the SWAT model.

The aim of the article is to analyze the hydrology of the Bystra River basin in the 2021–2050 climate projections for the RCP 4.5 and RCP 8.5 climate change scenarios, as well as to provide an assessment against the background of the current state of knowledge related to research covering the European continent and small regional catchments.

2. Study Area

The Bystra River, which is the right tributary of the Vistula River, 33 km long and 306.9 km^2 in area, is located in the Lubelskie Voivodeship (Figure 2). The Bystra River basin is a second order hydrographic unit (Code PLRW2000923899) [21]. According to the generated SWAT model, the lowest point of the catchment area is 123 m above sea level, while the highest point is 246 m above sea level. The catchment area is 296.6 km^2.

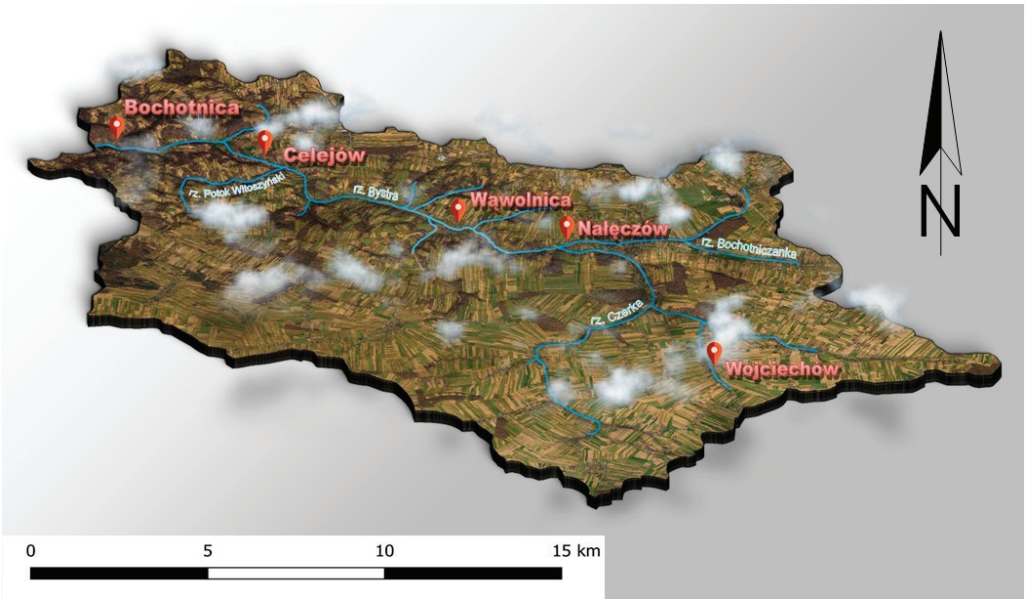

Figure 2. The catchment area of the Bystra River (own study).

The Bystra River basin part of the Lublin Upland [22–24] The relief of the Bystra River valley and its tributaries is very large and consists of many valley forms with a constant or episodic inflow. There are few valleys with a constant tributary. The largest of them, the Bystra valley, is 35 km long. In the section where the Bystra River valley flows into the Vistula, it cuts up to 35 m in marl and rocks [21,25,26].

Virtually the entire catchment area is built of a deep loess (up to 20 m). In the deeper layers there are Quaternary Pleistocene deposits, glacial sands and gravels, and slightly deeper tilts. Paleocene Paleogene deposits lie under the clay (i.e., geoses). On the other hand, under the geezes there are upper Cretaceous deposits (i.e., rocks with limestone inserts) [27].

The upland nature of the catchment area with a predominance of loess soils and the high slopes of the slopes at the mouth of the Bystra River pose a significant threat to the catchment area in terms of medium and very strong water and surface erosion [28].

According to the raster soil map prepared for the SWAT model (Figure 3), the study area consists mainly of podzolic and pseudo-polygonal soils (49%) as well as leached brown soils and acid soils (47%) (Table 1).

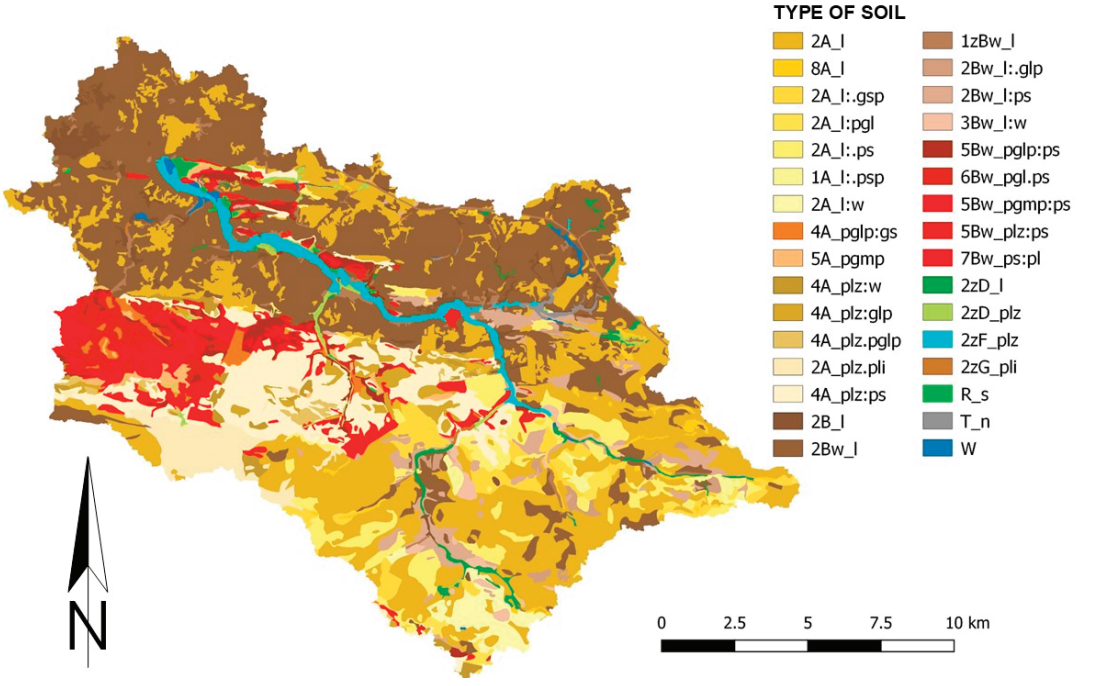

Figure 3. Soil map introduced to the SWAT model with division into soil types (own study).

Overall, 32 grain size groups were separated. Podzolic soils extend mainly in the south-eastern area of the catchment area, while brown soils dominate in the north-west area. Loess (73%) [29–31] and ordinary dust (18%) dominate in the soil cover of the Bystra River catchment area.

According to the map of the cover and land use of the Bystra River catchment area, arable lands (78%) and forests (16%) dominate (Figure 4).

Table 1. Division into soil types and species and the percentage share of soils in the Bystra basin gener-ated in the QSWAT interface (own study).

Soil Agricultural Complex	Type of Soil	Type of Fraction	[%] Part	Soil Agricultural Complex	Type of Soil	Type of Fraction	[%] Part
2	**A**	l	24.8	5	**Bw**	plz:ps	2.7
4	**A**	plz:ps	7.6	7	**Bw**	ps	2.1
2	**A**	l:.ps	4.7	6	**Bw**	pgl.ps	2.0
2	**A**	l:.gsp	2.5	5	**Bw**	pglp:ps	1.8
2	**A**	plz.pli	2.5	1z	**Bw**	l	1.3
4	**A**	plz:glp	1.5	3	**Bw**	l:w	0.7
2	**A**	l:w	1.5	2	**Bw**	l:.glp	0.7
4	**A**	plz	0.9	5	**Bw**	pgmp:ps	0.7
8	**A**	l	0.7	2	**B**	l	1.9
4	**A**	pglp:gs	0.7	2z	**F**	plz	1.7
5	**A**	pgmp	0.6	2z	**D**	l	0.8
2	**A**	l:pgl	0.6	2z	**D**	plz	0.7
1	**A**	l:.psp	0.6	-	**W**		0.3
4	**A**	plz.pglp	0.5	-	**R**	s	0.2
2	**Bw**	l	30.2	-	**T**	n	0.2
2	**Bw**	l:ps	2.9	2z	**G**	pli	0.1
[%] Share of Haplic Podzols and Albic Luvisol soils (A)							49
[%] Share of Haplic Cambisol, Brunic Arenosols and Haplic Cambisol Eutric soils (Bw)							47
[%] Share of loess							73
[%] Share of silt							18

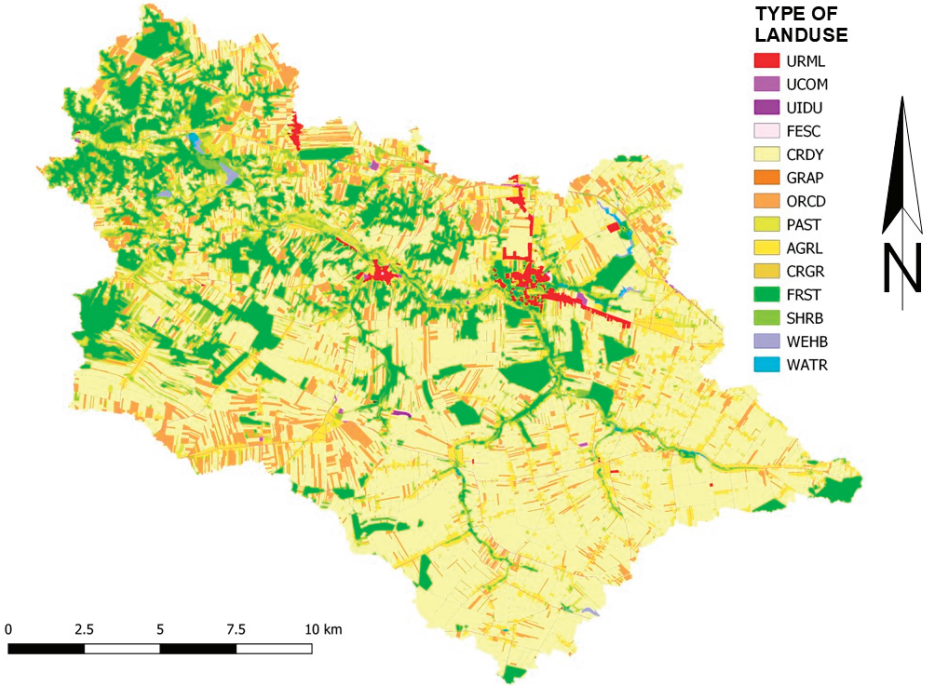

Figure 4. Land cover and use map of Bystra basin (own study).

The largest part of agricultural land is arable land beyond the range of irrigation facilities (52%), a large area is also orchards and plantations (11%), complex systems of cultivating plots (9%) and meadows and pastures (6%) (Table 2).

Table 2. Division of the cover and use as well as the percentage of use in the Bystra basin generated in the QSWAT interface (own study).

Corine Land Cover Legend	CLC	SWAT	[%]
	Code	Code	Part
Discontinuous urban fabric	112	URML	0.9
Industrial or commercial units	121	UCOM	1.6
Mineral extraction sites	131	UIDU	0.1
Sport and leisure facilities	142	FESC	0.1
		SUM=	**3**
Non-irrigated arable land	211	CRDY	52.4
Vineyards	221	GRAP	0.1
Fruit trees and berry plantations	222	ORCD	10.9
Pastures	231	PAST	5.9
Complex cultivation patterns	242	AGRL	9.0
Land principally occupied by agriculture, with signifi-cant areas of natural vegetation	243	CRGR	0.1
		SUM=	**78**
Mixed forest	313	FRST	16.3
Transitional woodland-shrub	324	SHRB	2.4
Inland marshes	411	WEHB	0.3
Water courses	511	WATR	0.3

3. Methods

3.1. SWAT and SWAT-CUP

In order to examine the water balance of the Bystra River catchment area, the soil and water assessment tool (SWAT) model was used [32]. The SWAT model can be used with a variety of computer programs. For the purpose of this article, the QSWAT3 v1.1 model with interface in Quantum GIS 3.10.13 Coruna [33] was used. SWAT Editor 23 October 2012 software [34] was used for model calculations. The SWAT model is a deterministic model developed for the US Department of Agriculture [35] that is based on mapping physical, chemical, and biological processes using mathematical formulas, developed to predict the effects of management practices on water and agricultural chemical yields on a basin scale [36,37].

The water balance is the basis and the driving force behind all of the processes that take place in the catchment area, regardless of the type of analysis performed with the use of the SWAT model [38]. The modeling of the watershed is carried out in two phases: a land phase and routing phase. The land phase of the hydrological cycle [39] controls the amount of water, sediment, nutrients and pesticides entering the main canal in each catchment area. The land phase of the hydrological cycle controls the amount of water, sediment, nutrients, and pesticides introduced into the main canal in each catchment area, covering long periods of time with a time resolution of one year, month, or day (Figure 5).

Routing phase of the hydrologic cycle which can be defined as the movement of water, sediments, etc. through the channel network of the watershed to the outlet. The hydrologic cycle can be defined as the movement of water, sediments, etc. through the channel network of the watershed to the outlet [40]. The simulated processes include the cycles of nitrogen, phosphorus, carbon, pesticides, bacteria, and metals. Above the processes are related in the SWAT model with the plant growth cycle and catchment management practices (e.g., plowing, fertilization, harvesting plants, irrigation of fields, collection and transfer

of water, drainage of water and sewage, use of home sewage treatment plants, and buffer zones along watercourses) [32,41].

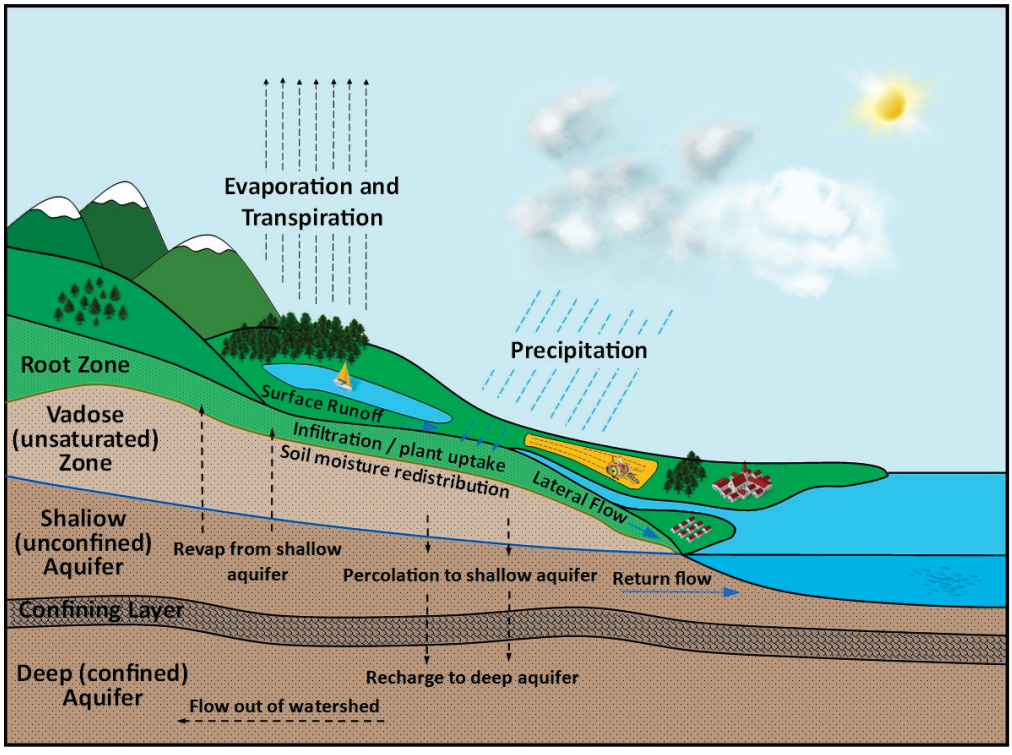

Figure 5. Schematic illustration of the conceptual water balance model in SWAT (own study).

The land phase estimates the runoff for each of these HRUs using the water balance equation:

$$SW_t = SW_0 + \sum_{i=1}^{t=T} (P_d - SURQ - E - w_{seep} - GWQ)$$

where SW_t is the final soil water content (mm); SW_0 is the initial soil water content (mm); t is time in days; P_d is precipitation (mm); $SURQ$ is surface runoff (mm); E is the evapotranspiration (mm); w_{seep} is amount of water entering the vadose zone from the soil profile (mm); and GWQ is groundwater flow (mm) [40].

The SWAT model used the Penman–Monteith method to assess potential evapotranspiration.

To better adjust (calibrate) the SWAT model to the actual conditions in the Bystra river catchment area, SWAT Calibration and Uncertainty Programs 5.2.1 [42] were used. The SWAT-CUP program is an instrument used to calibrate, analyze the uncertainty and sensitivity of the SWAT model [42,43]. The SUFI-2 algorithm was used since it works well for small catchments [44–46].

3.2. Data Used in the SWAT Model

To simulate the water balance in the SWAT model, spatial data were obtained from many sources, including:

- A digital elevation model covering the catchment area with a resolution of 5 m, obtained from the Central Geodetic and Cartographic Documentation Center [47];

- Data on the hydrography of the area (e.g., rivers, lakes, partial catchments), which were obtained from the Polish Hydrological Division Computer Map with descriptions [48];
- Data on sewage treatment plants [49];
- Digital soil and agricultural maps in digital form (scale 1:25,000 and 1:100,000) [50]; which were obtained from the Institute of Soil Science and Plant Cultivation in Puławy [51];
- Geological data describing lithology obtained from the Polish Geological Institute in the form of a Detailed Geological Map of Poland [27];
- Types of land cover and land use, digital data obtained from Corine Land Cover databases [52];
- A high-resolution orthophoto map published on the Geoportal in the form of WMS [53];
- Open Street Map data [54];
- Meteorological data obtained from IUNG in Puławy and the Institute of Meteorology and Water Management [55].

3.3. Adaptation of the SWAT Model for the Study Area

In the first stage, the input data for the precipitation-outflow system was prepared for SWAT modeling. Based on the digital elevation model and the location of the lakes in the studied area and water discharges from the wastewater treatment plant, a division of the Bystra River basin into partial catchments was generated in the SWAT editor. The editor generated 31 partial catchments (Figure 6). According to MPHP, the catchment area of the Bystra River consists of 21 sub-basins. The increased number of partial catchments is related to selecting points representing reservoirs and points source, for which additional data will be entered at a later stage. The above points must be located as close as possible to the line representing the river network. There are also many water reservoirs, ponds, and ponds in the sub-catchments that are not related to the watercourse line. These are the objects for which additional data will also be entered, representing all water reservoirs in the sub-catchment.

In the next stage of creating the SWAT model, hydrologic response unit (HRU) areas had to be generated, HRUs are homogeneous hydrological areas created on the basis of overlapping land cover maps, soil maps and slope maps [40].

For the needs of the SWAT model, a soil map of the Bystra catchment was developed based on digital soil and agricultural maps (scale 1:25,000 and 1:100,000) and geological data describing lithology. Data describing the parameters of the soils in the Bystra river catchment area were obtained as part of the statutory projects of IUNG-PIB [21].

During the preparation of soil data, it was also taken into account that the available water capacity and wilting point values were appropriate for the soils of the Bystra catchment area. These values were obtained from the study "Assessment of Water Retention in Soil and the Risk of Drought Based on the Water Balance for the Area of the Lower Silesia Voivodship", developed in 2013 by the employees of the Department of Soil Science, Erosion, and Land Protection IUNG-PIB in Puławy [20].

Due to the low detail of the Corine Land Cover map, additional vectorization of the cover and land use of the Bystra River catchment area was performed in order to increase the resolution of land use using an orthophoto map and Open Street Map data.

For the Bystra River catchment area, a division was also made due to the decline in the area in the following ranges: 0–6%, 6–10%, 10–18%, 18–27%, >27%. Slope ranges originate from the PWER and AWER indicators [56] for soil erosion risk, remaining as standard in terrain relief visualization in Poland. The Bystra River catchment area is similar to that of the Grodarz catchment area to the south, which has the same slope distribution. [57,58]. The Bystra River basin is similar in relief to the Grodarz River basin. In the studied catchment area, flat and slightly undulating areas with slopes up to 6% (72% of the catchment area) prevail. Steep slopes, from 6% to 10%, account for 11% of the catchment area. A small area of the catchment area is represented by land with falls from 10% to 27% (11%). A total of 6% of the catchment area are falls over 27%.

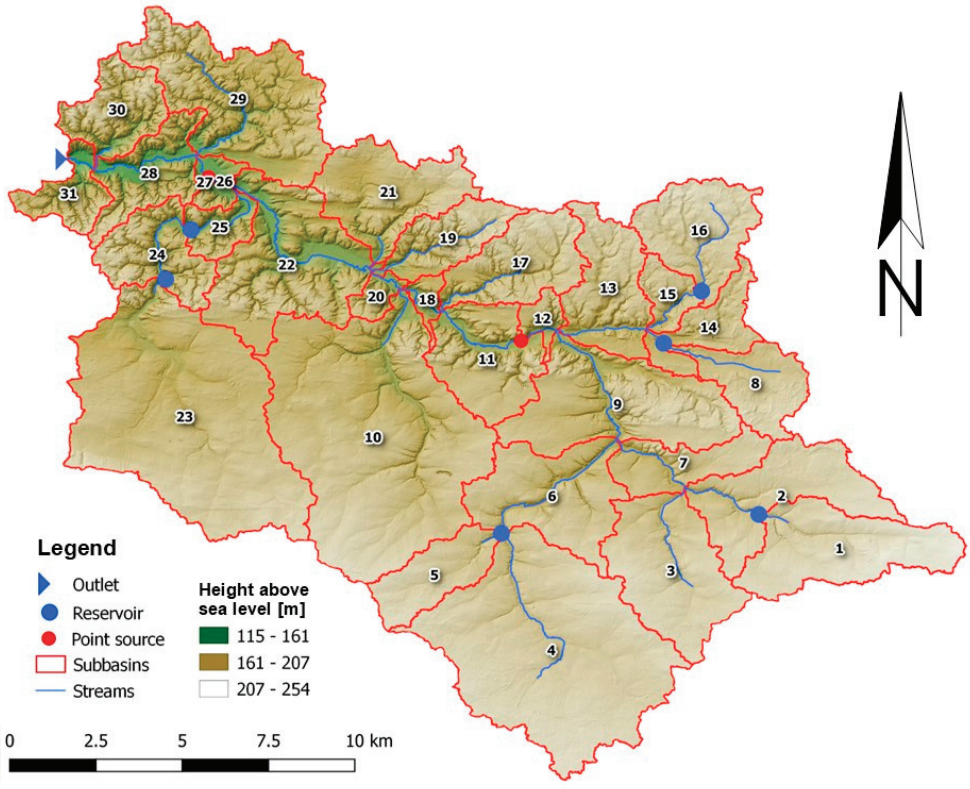

Figure 6. Study area: Bystra River basin with marked main tributaries and their catchments (own study).

After preparing the rasters for soil, land cover, and slopes, the catchment area was divided into HRU areas in the SWAT program.

During the creation of HRU in the SWAT program, the percentage of arable land outside the range of CRDY irrigation devices was separated from winter crops WWHT (43%), spring BARL crops (31%), canola CANP (14%) and other CRDY (12%), based on the publication Agriculture in the Lubelskie Voivodeship in 2019 [59]. From fruit orchards, ORCD was separated on the basis of the above-mentioned APPL apple orchards publication. Forests, on the other hand, were divided into coniferous FRSE forests (49%), deciduous FRSD forests (13%) and mixed FRST forests (38%) according to information obtained from the Regional Directorate of State Forests in Lublin [60].

A total of 484 HRU areas were generated. The HRU areas will be used at a later stage to build the SWAT model.

3.4. Meteorological Data

In the next stage of creating the SWAT model, the following meteorological data had to be loaded: sums of daily precipitation [mm]; daily minimum and maximum air temperature [°C]; average daily wind speed [m/s]; daily mean relative humidity; daily sums of total solar radiation [MJ/m^2]. Meteorological data were obtained from Pulawy weather station (Table 3). The data were prepared in SWAT Weather Database 0.18.03 [61].

Table 3. Meteorological data for the Bystra river basin (own study).

Weather Station	Measurement Period				
	Rainfall [mm]	**Temperature [°C]**	**Wind Speed [m/s]**	**Humidity**	**Solar Total Radiation [MJ/m^2]**
Pulawy	2005–2017	2005–2017	2005–2017	2005–2017	2005–2017
Rogalow	2005–2017	–	–	–	–
Lublin Radawiec	2005–2017	2005–2017	2005–2017	2005–2017	–

In the last stage of the SWAT model construction, some parameters related to point sewage discharges concerning water reservoirs outside the river network, concerning reservoirs, and parameters scheduled management operations for non-irrigated arable land were supplemented and corrected.

The parameters of rivers in the sub catchments were also improved on the basis of data obtained as part of the statutory projects of IUNG-PIB, as the automatically generated parameters of rivers regarding the length, depth, and width of the rivers were overestimated.

The current value of CO_2 concentration was also inserted in the prepared SWAT model.

After entering all of the necessary data into the SWAT model, a simulation of the water cycle in the Bystra River catchment was performed for 2010–2017 with a five-year model start-up period, in a monthly step.

3.5. SWAT CUP Calibration and Validation Results

After the SWAT simulation, the obtained model had to be calibrated in the SWAT-CUP program [62–64] to obtain a more accurate representation of the model with reality. For this purpose, data on average monthly flow velocities [m^3/s] in the vicinity of the estuary of the Bystra River basin to the Vistula for the years 2010–2014 were used, obtained under the statutory projects of IUNG-PIB. After receiving a satisfactory calibration, the model was validated using the data on the monthly average flow velocities [m^3/s] near the mouth of the Bystra River basin to the Vistula for 2015–2017, obtained under the statutory projects of IUNG-PIB. Calibration and validation were performed in a monthly step.

As a result of the calibration in the SWAT-CUP software, the best-fit parameter ranges were obtained that meet the accuracy requirements of calibration and validation [43,65,66].

The figure shows only the months which the water discharge was recorded and compared to the values simulated in 95 Percent Prediction Uncertainty (Figure 7). For the performed calibration and validation, there are data gaps in the measurements covering the periods from December 2010 to March 2013, September 2013 to January 2014, March 2015, July and August 2016, and from October 2016 to February 2017 and September 2017.

In addition to the above-mentioned best fit parameters, there are other parameter sets that can also give a good calibration result [63].

The Nash-Sutclif model efficiency coefficient (NSE) for calibration is in the range of $0.5 < NSE \leq 0.65$ and is a satisfactory result. The coefficient of determination R^2 is also within the acceptable range of $0.5 < NSE \leq 0.65$ [65]. The Nash-Sutclif model efficiency coefficient for the validation is in the range of $0.65 < NSE \leq 0.75$, which is good result. The coefficient of determination R^2 is in the range of $0.5 < NSE \leq 0.65$. This is also a satisfactory result [65].

For the performed calibration and validation, there are data gaps in the measurements covering the periods from December 2010 to March 2013, September 2013 to January 2014, March 2015, July and August 2016, from October 2016 to February 2017 and September 2017.

An important aspect is the appropriate consideration of the flow measurement period for validation and calibration. When preparing the data, the measurement data should be selected so that they cover a homogeneous period of time in terms of constant weather conditions. When preparing the data for the SWAT model, a distinction is made between

the so-called dry and wet years. If there are measurement series covering dry and wet years, then calibration and validation may be difficult [67].

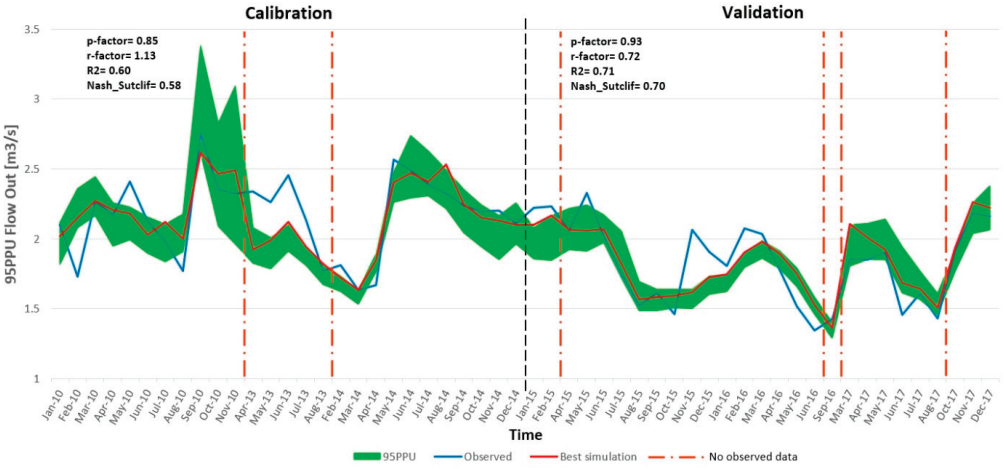

Figure 7. 95ppu plot and observed streamflow during calibration and validation (own study).

During the analysis of the results, the obtained values of potential evapotranspiration were also compared with the results of statutory IUNG-PIB research conducted as part of the Agricultural Drought Monitoring System project [68]. The SWAT model is a good representation of potential evapotranspiration in the studied area. In addition, the results of soil water content were compared with the available water capacity and wilting point values obtained from the study "Assessment of Water Retention in Soil and Drought Risk Based on the Water Balance for the Lower Silesian Voivodeship", developed in 2013 by employees of the Department of Soil Science, Erosion and Land Protection. IUNG-PIB in Pulawy [20].

3.6. Climate Change Scenarios

The daily gridded climate data for the period (2020–2050) with a spatial resolution of 0.11° were obtained from the EURO-CORDEX database that are openly available through the ESGF (Earth System Grid Federation, https://esgf-data.dkrz.de/search/cordex-dkrz, accessed on 10 February 2022) for Europe [69,70]. Climate projections (of daily minimum and maximum air temperature, precipitation, surface downwelling shortwave radiation, wind speed, relative humidity) that were used in SWAT model were extracted from grid cells that corresponds to the weather station's location. The projections are based on three regional climate models (RCMs) and two Representative Concentration Pathways (RCP). The RCMs (Regional Climate Models) were: RACMO22E, HIRHAM5 and RCA4 driven by one GCM (General Circulation Model): EC-EARTH. The RCPs correspond to a radiative forcing value in the year 2100 relative to pre-industrial values of +4.5 W m^{-2} (RCP4.5), while RCP8.5 to + 8.5 W m^{-2} (RCP8.5) [71,72] (Table 4).

In total we used six climate projections (three RCMs × two RCPs). The air temperature and precipitation data were additionally bias adjusted by the SMHI (Swedish Meteorological and Hydrological Institute) using DBS (distribution-based scaling) method [73] and regional reanalysis MESAN (mesoscale analysis) dataset from period 1989–2010 [74]. Since the downloaded data were performed on the rotated polar grid, we applied bilinear interpolation to remap this dataset to regular geographic latitude/longitude grid by using CDO (climate data operators) software [75].

Table 4. Description of the climate scenarios (own study).

Models	Scenario Assumptions		Brief Description of Climate Projections for Radiative Forcing	
GCM/RCM simulation	Increase in the maximum daily temperature	Increase in rainfall	RCP4.5	RCP8.5
			+4.5 W m^{-2}	+8.5 W m^{-2}
EC-EARTH/RACMO22E	+1.3 °C	+9%	RCP 4.5.1	RCP 8.5.1
EC-EARTH/HIRHAM5	+0.6 °C	+3%	RCP 4.5.2	RCP 8.5.2
EC-EARTH/RCA4	+0.9 °C	+5%	RCP 4.5.1	RCP 8.5.3

For the control period of the results of climate projections (RCP 4.5, RCP 8.5), validation was performed with existing observation data of temperature and precipitation (Table 5). The range of differences between the temperatures varies from 0.3 to 0.7 degrees Celsius in the plus. On the other hand, the differences for the climate projections in the control years 2010–2017 are smaller than 11% to 22% percent compared to the observational data.

Table 5. Validation of meteorological data (temperature and precipitation) (own study).

Temperature [°C]								Precipitation [mm]							
Climate model	Observation data	RCP 4.5.1	RCP 4.5.2	RCP 4.5.3	RCP 8.5.1	RCP 8.5.2	RCP 8.5.3	Climate model	Observation data	RCP 4.5.1	RCP 4.5.2	RCP 4.5.3	RCP 8.5.1	RCP 8.5.2	RCP 8.5.3
Time interval		2010–2017						Time interval		2010–2017					
Annual average	9.1	9.5	9.6	9.7	9.6	9.7	9.9	Annual sum	604	543	560	512	549	517	491
		+0.3	+0.5	+0.5	+0.5	+0.5	+0.7			−14%	−11%	−19%	−13%	−18%	−22%

The prepared model, after calibration and validation, was used for research related to the RCP 4.5 and RCP 8.5 climate change scenarios (changes in carbon dioxide concentration in the future decades) [70,76,77] which scenarios have been accepted by the International Panel on Climate Change [78].

For each of the projections, there is a certain confidence interval of the flow result obtained in the SWAT-CUP program. In order to compare the climate change scenarios for individual climate projections (RCP 4.5.1, RCP 8.5.1, RCP 4.5.2, RCP 8.5.2, RCP 4.5.3 and RCP 8.5.3), one iteration was carried out in SWAT-CUP for the best calibration parameters for 2020–2050 for prepared scenarios (Table 4). Additionally, for the RCP 4.5 and RCP 8.5 scenarios, changes in CO_2 concentrations in individual decades were adopted: 2021–2030, 2031–2040 and 2041–2050, developed by the Potsdam Institute for Climate Impact Research [79,80].

4. Average Annual Prospects of Climate Scenarios RCP 4.5 and RCP 8.5 for the Period 2020–2050

The average annual sum of precipitation and the average annual temperature in the years 2000–2050 are different for different projections in the RCP 4.5 and RCP 8.5 climate scenarios (Figure 8). For the projection RCP 4.5.1, RCP 8.5.1, and RCP 8.5.2 the trend of average annual precipitation will be slightly increasing in the following years. On the other hand, for the RCP 4.5.2 projection, the trend of average annual precipitation totals will be slightly decreasing. For the RCP 4.5.3 and RCP 8.5.3 projection, the trend of average annual precipitation totals will be increasing.

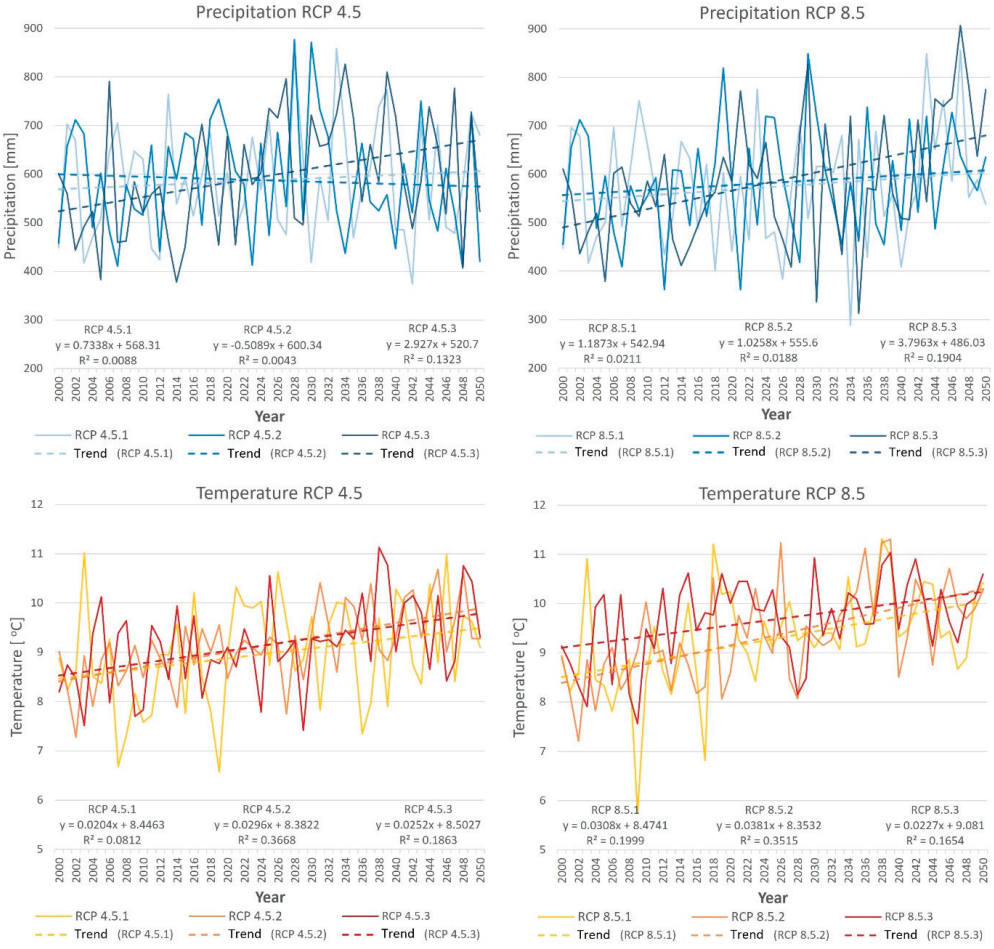

Figure 8. The average annual sum of precipitation and the average annual temperature in the Bystra River catchment area in the years 2000–2050 for individual climate projections in the RCP 4.5 and RCP 8.5 scenarios with trend lines (own study).

For the RCP 4.5 and RCP 8.5 scenarios, all three forecasts will see an increase in the annual mean temperature trend in the coming decades.

The trend of the average annual number of days without precipitation for the RCP 4.5 scenarios for all projections and for the RCP 8.5.2 projection are positive. However, in the case of RCP 8.5.1 and RCP 8.5.3 there is no trend line (Figure 9).

The trend of the average annual number of days with an average temperature above 5 °C in the years 2020–2050 for most climate projections is positive, apart from the RCP 4.5.1 projection.

The average monthly sums of precipitation for the Bystra River basin in the simulation years 2010–2017 and change in the individual climate change projections in the years 2021–2030, 2031–2040, and 2041–2050 are shown in Table 6. These changes are especially visible in March, August, and November, where for most of the projections there is an increase in the average monthly precipitation.

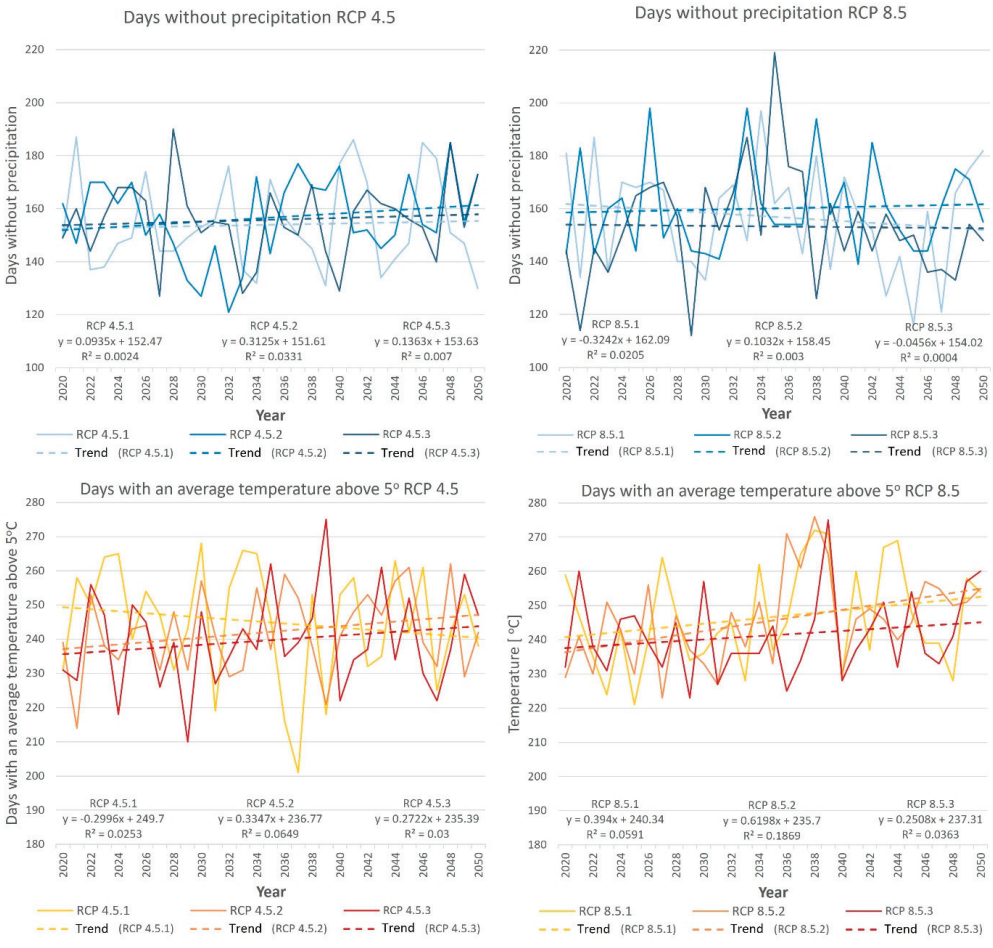

Figure 9. The average annual sum of days without precipitation and the average annual sum of days with temperatures above 5 °C in the Bystra River basin in the years 2020–2050 for individual climate projections in the RCP 4.5 and RCP 8.5 scenarios together (own study).

On the other hand, the decrease in average monthly sums of atmospheric precipitation will occur in most of the projections in January, May, July, and October.

For most of the projections, the average annual precipitation will be lower in the next decades as compared to 2010–2017. Larger annual mean sums will appear in the forecasts RCP5.1 (2031–2040), RCP 4.5.2 (2021–2030), RCP 4.5.3 (2021–2030, 2031–2040, 2041–2050), RCP 8.5.2 (2021–2030, 2041–2050), RCP 8.5.1, and RCP 8.5.3 (2041–2050).

Annual averages for RCP 2041–2050 for RCP 4.5 are lower by 3%, while for RCP 8.5 they are higher by 11% compared to the lower period.

Table 6. Comparison of the average distribution of precipitation in individual months for the SWAT simulation period 2010–2017 with individual projections for the RCP 4.5 and RCP 8.5 climate change scenarios for the periods 2021–2030, 2031–2040, and 2041–2050 (own study).

Climate Model	SWAT	RCP 4.5.1	RCP 4.5.2	RCP 4.5.3	RCP 8.5.1	RCP 8.5.2	RCP 8.5.3	RCP 4.5.1	RCP 4.5.2	RCP 4.5.3	RCP 8.5.1	RCP 8.5.2	RCP 8.5.3	RCP 4.5.1	RCP 4.5.2	RCP 4.5.3	RCP 8.5.1	RCP 8.5.2	RCP 8.5.3
Time Interval	**2010–2017**	**2021–2030**						**2031–2040**						**2041–2050**					
Month	**Average Monthly Precipitation [mm]**																		
January	33	25	30	28	24	27	32	31	44	33	21	29	38	24	33	22	23	41	39
		−25%	−10%	−15%	−25%	−16%	−3%	−5%	+36%	+2%	−36%	−12%	+15%	−27%	+1%	−32%	−31%	+25%	+18%
February	29	22	32	31	27	30	28	20	32	34	21	33	29	16	34	32	27	28	36
		−24%	+11%	+10%	−5%	+6%	−3%	−30%	+12%	+17%	−28%	+16%	+1%	−43%	+19%	+11%	−5%	0%	+26%
March	32	29	44	43	39	37	44	49	46	58	28	41	34	47	41	43	41	59	39
		−11%	+38%	+34%	+22%	+14%	+36%	+51%	+44%	+80%	−13%	+27%	+6%	+46%	+26%	+34%	+28%	+83%	+21%
April	41	46	48	36	32	37	50	30	41	37	46	26	45	36	47	40	47	40	52
		+11%	+15%	−13%	−22%	−10%	+22%	−26%	−1%	−10%	+12%	−38%	+9%	−13%	+13%	−3%	+13%	−3%	+26%
May	82	62	68	75	64	62	61	66	40	66	67	48	69	58	61	75	96	80	74
		−25%	−17%	−9%	−22%	−24%	−25%	−20%	−51%	−19%	−19%	−42%	−16%	−30%	−26%	-8%	+17%	−2%	−10%
June	58	66	81	56	61	72	53	72	53	59	66	74	49	62	52	43	66	69	50
		+14%	+41%	−3%	+6%	+25%	−9%	+25%	−8%	+3%	+14%	+29%	−15%	+8%	−10%	−25%	+14%	+20%	−13%
July	95	114	69	80	83	85	53	130	96	124	62	82	64	96	74	80	62	63	82
		+21%	−27%	−15%	−13%	−10%	−44%	+38%	+1%	+31%	−35%	−14%	−32%	+1%	−22%	−15%	−34%	−33%	−14%
August	55	69	66	87	75	62	59	50	73	73	66	52	76	58	58	59	102	63	75
		+26%	+21%	+58%	+36%	+13%	+7%	−10%	+32%	+33%	+19%	−6%	+37%	+6%	+5%	+7%	+85%	+14%	+35%
September	57	55	47	81	43	51	95	68	52	78	47	43	63	67	65	73	53	70	107
		−3%	−16%	+43%	−23%	−10%	+67%	+21%	−8%	+37%	−16%	−24%	+12%	+18%	+14%	+28%	−6%	+24%	+89%
October	45	38	38	27	46	37	31	41	31	40	46	29	23	41	32	37	44	33	33
		−15%	−14%	−40%	+2%	−17%	−29%	−8%	−31%	−10%	+3%	−34%	−48%	−9%	−28%	−16%	−2%	−25%	−26%
November	34	33	66	42	31	69	41	30	35	45	49	54	35	29	32	58	49	50	68
		−4%	+95%	+24%	−8%	+103%	+22%	−11%	+2%	+31%	+43%	+58%	+3%	−14%	−5%	+71%	+43%	+47%	+99%
December	36	29	30	41	30	33	41	41	23	43	29	35	41	39	32	37	38	26	57
		−20%	−16%	+13%	−18%	−8%	+14%	0%	−36%	+18%	−21%	−4%	+14%	0%	−11%	+2%	+4%	−29%	+59%
Annual sum	596	586	621	627	556	604	588	628	566	690	546	545	566	573	561	600	647	622	712
		−2%	+4%	+5%	−7%	+1%	−1%	+5%	−5%	+16%	−8%	−9%	−5%	−4%	−6%	+1%	+9%	+4%	+19%

By analyzing the spatial distribution of changes in the average annual precipitation total in 31 sub-catchments for the simulation period in 2010–2017 compared to the period 2041–2050 (Figure 10) in the RCP 4.5.1 and RCP 4.5.3 climate projections, the precipitation total will decrease by several percent in north-west and south-east region. In the RCP 4.5.2 projection, a reduced amount of precipitation will occur in the entire catchment area, while in the RCP 8.5.2 projection it will occur only in the northwestern part. In projections 8.5.1 and 8.5.3, an increased amount of precipitation, up to 23%, will be present in the entire area in the period 2041–2050. Most of the RCP 8.5.2 area will also have an increased amount of precipitation.

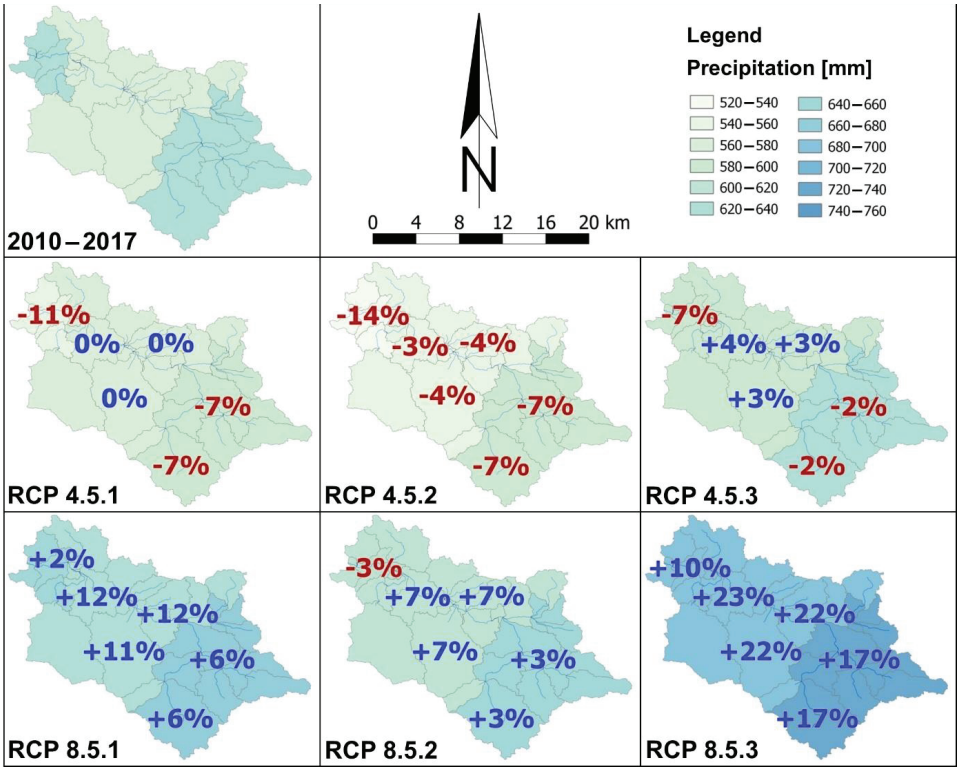

Figure 10. Comparison of the average annual sum of precipitation in 31 sub-catchments for the SWAT simulation period for 2010–2017 and 2041–2050 for individual climate projections in the RCP 4.5 and RCP 8.5 scenarios (own study).

The average monthly temperature distributions for the Bystra River basin in the 2010–2017 simulation years also change compared to the individual climate change projections in 2021–2050 (Table 7). These changes are especially visible in November and December, where for most of the projections the average monthly temperature is lower than in the 2010–2017 simulation period. On the other hand, in January, April, May, September, and October, the average monthly temperatures are higher for most of the projections. For the RCP 8.5.2 (2031–2040, 2041–2050) and RCP 8.5.3 (2041–2050) projections, the average monthly temperatures for most months are higher than in the 2010–2017 simulation years.

The temperature in the 2041–2050 decade for RCP 4.5 will be higher by an average of 0.4 °C, while for RCP 8.5 it will be higher by an average of 0.8 °C compared to the simulation period.

Table 7. Comparison of the average temperature distribution in individual months for the SWAT simulation period 2010–2017 with individual projections for the RCP 4.5 and RCP 8.5 climate change scenarios for the periods 2021–2030, 2031–2040, and 2041–2050 (own study).

Climate Model	SWAT	RCP 4.5.1	RCP 4.5.2	RCP 4.5.3	RCP 8.5.1	RCP 8.5.2	RCP 8.5.3	RCP 4.5.1	RCP 4.5.2	RCP 4.5.3	RCP 8.5.1	RCP 8.5.2	RCP 8.5.3	RCP 4.5.1	RCP 4.5.2	RCP 4.5.3	RCP 8.5.1	RCP 8.5.2	RCP 8.5.3
Time Interval	**2010–2017**	**2021–2030**						**2031–2040**						**2041–2050**					
Month	**Average Monthly Temperature [°C]**																		
January	−2.9	−0.2	0.9	−2.8	−2.9	−2.3	−2.0	−3.0	0.1	0.4	−0.8	−0.4	0.7	−0.9	0.0	−2.3	−2.3	0.6	0.1
		+2.7	+3.7	0.0	−0.1	+0.5	+0.9	−0.1	+2.9	+3.3	+2.0	+2.5	+3.5	+2.0	+2.9	+0.6	+0.6	+3.5	+3.0
February	−0.9	2.1	−2.0	−0.9	−0.3	0.8	0.1	0.3	0.0	0.5	1.8	1.0	3.0	−0.9	0.4	2.3	0.7	0.6	2.9
		+3.0	−1.1	0.0	+0.6	+1.7	+1.0	+1.2	+0.9	+1.4	+2.7	+1.9	+3.9	0.0	+1.3	+3.2	+1.6	+1.5	+3.8
March	4.2	6.3	1.8	5.2	4.3	4.1	3.5	3.6	3.4	4.0	5.9	4.5	4.8	3.8	3.5	4.7	5.0	3.8	5.0
		+2.2	−2.4	+1.1	+0.1	−0.1	−0.7	−0.5	−0.7	−0.1	+1.7	+0.3	+0.7	−0.4	−0.7	+0.6	+0.9	−0.3	+0.9
April	9.4	9.9	8.2	9.1	11.3	9.4	8.3	11.0	8.4	9.8	10.7	9.3	9.8	10.9	9.3	8.3	12.1	9.2	9.8
		+0.5	−1.3	−0.3	+1.9	−0.1	−1.1	+1.6	−1.1	+0.4	+1.3	−0.1	+0.4	+1.5	−0.1	−1.1	+2.7	−0.3	+0.3
May	14.5	15.1	13.8	14.6	16.2	15.0	14.7	14.0	15.1	15.2	16.0	15.7	16.1	16.1	15.6	15.0	14.5	15.0	16.0
		+0.5	−0.8	+0.1	+1.6	+0.4	+0.2	−0.6	+0.5	+0.7	+1.5	+1.2	+1.6	+1.5	+1.0	+0.5	0.0	+0.5	+1.5
June	18.0	17.2	16.8	17.7	16.9	18.0	17.0	17.6	18.3	17.4	16.7	18.6	19.1	18.4	19.1	17.8	17.5	17.6	18.8
		−0.8	−1.2	−0.3	−1.2	−0.1	−1.0	−0.5	+0.3	−0.7	−1.3	+0.5	+1.1	+0.4	+1.0	−0.2	−0.6	−0.4	+0.7
July	20.2	19.8	19.9	20.8	20.0	20.1	20.1	20.2	20.5	20.4	20.6	20.9	20.5	20.1	19.7	21.3	20.4	20.5	20.7
		−0.4	−0.3	+0.6	−0.1	−0.1	−0.1	0.0	+0.3	+0.2	+0.5	+0.7	+0.3	−0.1	−0.4	+1.1	+0.2	+0.4	+0.5
August	19.8	19.2	19.7	19.0	18.4	19.7	20.0	19.7	19.5	19.1	19.4	20.2	20.9	19.1	19.7	19.8	18.9	20.3	19.6
		−0.6	−0.1	−0.8	−1.4	−0.1	+0.2	0.0	−0.3	−0.7	−0.3	+0.4	+1.2	−0.7	−0.1	+0.1	−0.8	+0.5	−0.2
September	14.6	14.0	14.5	13.4	15.1	15.0	14.3	14.8	15.1	14.0	16.0	15.8	16.3	14.7	15.8	15.0	15.1	15.5	14.9
		−0.6	−0.1	−1.2	+0.5	+0.4	−0.3	+0.2	+0.5	−0.6	+1.4	+1.2	+1.7	+0.1	+1.2	+0.4	+0.5	+0.9	+0.3
October	8.6	9.1	10.1	8.7	8.4	9.6	9.6	8.5	10.4	9.4	9.7	9.8	10.7	9.0	10.0	9.8	10.6	11.3	10.4
		+0.5	+1.5	+0.1	−0.2	+1.1	+1.0	0.0	+1.8	+0.8	+1.2	+1.2	+2.2	+0.4	+1.4	+1.2	+2.0	+2.8	+1.9
November	4.9	3.2	4.5	3.8	4.9	3.8	4.5	3.9	3.8	3.8	3.8	4.0	4.3	3.7	3.4	4.3	3.3	4.1	5.0
		−1.6	−0.4	−1.0	0.0	−1.1	−0.4	−0.9	−1.1	−1.1	−1.1	−0.8	−0.6	−1.2	−1.5	−0.5	−1.5	−0.8	+0.1
December	0.4	0.0	−0.6	−1.6	−0.9	0.1	−0.8	−3.0	−0.1	1.4	−1.9	0.8	0.4	−1.2	1.4	−0.3	0.7	0.3	0.9
		−0.4	−1.0	−1.9	−1.2	−0.2	−1.2	−3.4	−0.5	+1.0	−2.2	+0.5	+0.1	−1.6	+1.0	−0.6	+0.3	−0.1	+0.5
Annual averge	9.2	9.6	8.9	8.9	9.3	9.4	9.1	9.0	9.5	9.6	9.8	10.0	10.6	9.4	9.8	9.7	9.7	9.9	10.3
		+0.4	−0.3	−0.3	0.0	+0.2	−0.1	−0.2	+0.3	+0.4	+0.6	+0.8	+1.3	+0.2	+0.6	+0.4	+0.5	+0.7	+1.1

5. Results

The trend of the average annual sum of actual evapotranspiration in the years 2021–2050 in most of the projections (except for RCP 8.5.3) decreases slightly in the coming decades (Figure 11).

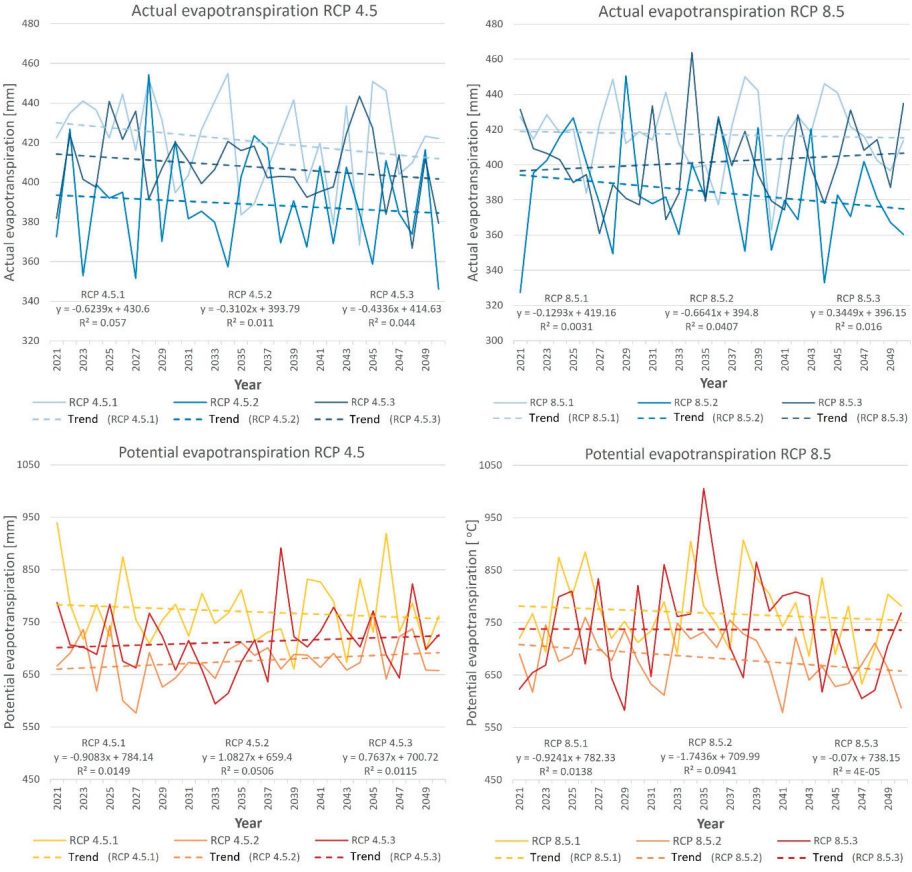

Figure 11. Average annual actual evapotranspiration and potential evapotranspiration in the catchment area of the Bystra River in the years 2021–2050 for individual climate projections in the RCP 4.5 and RCP 8.5 scenarios together with trend lines (own study).

The trend of the average annual sum of potential evapotranspiration in RCP 4.5.1, RCP 8.5.1 and RCP 8.5.2 projections will decrease in the coming decades. However, for the RCP 4.5.2 and RCP 4.5.3 projections, the trend is growing. The trend line for the RCP 8.5.3 projection does not change significantly.

The average monthly sum of actual evapotranspiration increases for all projections for most months compared to the simulation period 2010–2017. In June, for most projections, the average monthly sum of evapotranspiration will be lower than the average for 2010–2017 (Table 8).

The average annual potential evapotranspiration in the 2041–2050 decade for RCP 4.5 will be higher by an average of 8%, while for RCP 8.5 it will be higher by an average of 8% compared to the simulation period.

For potential evapotranspiration, the average monthly sum increases for most of the projections in all months compared to the 2010–2017 simulation period (Table 9).

Table 8. Comparison of the average monthly sum of actual evapotranspiration for the SWAT simulation period 2010–2017 with individual projections for the RCP 4.5 and RCP 8.5 climate change scenarios for the periods 2021–2030, 2031–2040, and 2041–2050 (own study).

Climate Model	SWAT	RCP 4.5.1	RCP 4.5.2	RCP 4.5.3	RCP 8.5.1	RCP 8.5.2	RCP 8.5.3	RCP 4.5.1	RCP 4.5.2	RCP 4.5.3	RCP 8.5.1	RCP 8.5.2	RCP 8.5.3	RCP 4.5.1	RCP 4.5.2	RCP 4.5.3	RCP 8.5.1	RCP 8.5.2	RCP 8.5.3
Time Interval	**2010–2017**	**2021–2030**						**2031–2040**						**2041–2050**					
Month	**Average Monthly Actual Evapotranspiration [mm]**																		
January	4	10	8	10	6	6	9	6	7	10	9	7	10	7	6	9	7	6	10
		+136%	+94%	+143%	+50%	+59%	+114%	+53%	+67%	+152%	+128%	+77%	+142%	+82%	+58%	+116%	+84%	+60%	+156%
February	9	17	11	14	14	12	15	15	9	15	17	12	16	13	12	15	15	10	16
		+91%	+19%	+60%	+55%	+30%	+68%	+69%	+0%	+67%	+88%	+35%	+77%	+45%	+31%	+72%	+70%	+11%	+78%
March	26	36	21	32	32	25	28	30	24	30	34	26	30	31	24	30	33	24	29
		+39%	−19%	+22%	+21%	−4%	+9%	+17%	−9%	+17%	+31%	0%	+16%	+18%	-+6%	+15%	+27%	−9%	+10%
April	44	49	42	40	51	46	44	53	46	42	51	44	46	51	51	41	53	40	43
		+11%	−4%	−9%	+16%	+5%	-1%	+20%	+4%	−4%	+17%	-1%	+4%	+16%	+15%	−7%	+21%	−10%	−2%
May	68	72	73	65	75	71	68	68	70	66	70	68	69	72	74	65	70	72	69
		+6%	+7%	−4%	+10%	+4%	0%	0%	+2%	−3%	+3%	-1%	+2%	+6%	+8%	−4%	+2%	+6%	+1%
June	62	54	64	58	56	60	57	54	58	55	51	58	53	55	56	56	55	59	50
		−12%	+4%	−6%	−10%	−3%	−8%	−12%	−6%	−12%	−18%	−6%	−14%	−11%	−10%	−10%	−12%	−5%	−20%
July	56	59	54	61	62	53	51	61	51	60	56	56	56	58	54	59	56	51	55
		+5%	−4%	+9%	+10%	−6%	−9%	+9%	−8%	+7%	-1%	0%	0%	+4%	−4%	+6%	0%	−9%	−2%
August	49	56	45	57	53	49	48	53	50	53	52	44	52	52	42	53	54	43	54
		+15%	−8%	+16%	+8%	0%	−2%	+7%	+3%	+8%	+6%	−11%	+5%	+7%	−14%	+8%	+10%	−13%	+9%
September	27	34	33	36	33	31	35	39	34	36	35	29	33	36	32	36	36	30	39
		+26%	+22%	+33%	+22%	+15%	+29%	+44%	+26%	+34%	+31%	+6%	+24%	+35%	+19%	+34%	+35%	+13%	+46%
October	16	23	24	20	21	18	21	21	20	19	21	19	22	22	19	22	22	22	21
		+44%	+51%	+31%	+33%	+15%	+35%	+33%	+29%	+24%	+32%	+22%	+38%	+42%	+24%	+42%	+43%	+39%	+35%
November	7	12	13	12	11	13	12	11	12	12	11	14	9	11	10	11	11	13	12
		+65%	+79%	+74%	+58%	+84%	+68%	+60%	+73%	+64%	+58%	+100%	+33%	+60%	+37%	+57%	+62%	+91%	+73%
December	4	8	7	7	7	9	7	6	7	9	4	9	9	7	6	7	6	7	8
		+98%	+72%	+54%	+62%	+107%	+60%	+0%	+66%	+119%	+5%	+101%	+104%	+0%	+48%	+66%	+51%	+60%	+94%
Annual sum	372	430	393	412	420	393	394	417	388	407	412	384	405	416	386	404	420	377	406
		+16%	+6%	+11%	+13%	+6%	+6%	+12%	+4%	+9%	+11%	+3%	+9%	+12%	+4%	+9%	+13%	+1%	+9%

Table 9. Comparison of the average monthly sum of potential evapotranspiration for the SWAT simulation period 2010–2017 with individual projections for the RCP 4.5 and RCP 8.5 climate change scenarios for the periods 2021–2030, 2031–2040, and 2041–2050 (own study).

Climate Model	SWAT	RCP 4.5.1	RCP 4.5.2	RCP 4.5.3	RCP 8.5.1	RCP 8.5.2	RCP 8.5.3	RCP 4.5.1	RCP 4.5.2	RCP 4.5.3	RCP 8.5.1	RCP 8.5.2	RCP 8.5.3	RCP 4.5.1	RCP 4.5.2	RCP 4.5.3	RCP 8.5.1	RCP 8.5.2	RCP 8.5.3
Time Interval	**2010–2017**	**2021–2030**						**2031–2040**						**2041–2050**					
Month	**Average Monthly Potential Evapotranspiration [mm]**																		
January	4	11	9	11	7	7	10	7	8	11	11	8	11	9	7	10	9	7	11
		+154%	+107%	+146%	+65%	+70%	+121%	+60%	+79%	+160%	+152%	+87%	+147%	+99%	+67%	+124%	+98%	+65%	+161%
February	10	22	12	16	16	15	17	18	10	18	22	14	19	17	13	18	18	11	19
		+124%	+21%	+64%	+61%	+48%	+77%	+86%	0%	+77%	+121%	+44%	+91%	+73%	+36%	+85%	+82%	+15%	+92%
March	35	60	27	44	42	34	35	42	30	40	52	36	45	43	31	42	45	30	39
		+70%	−24%	+23%	+19%	−6%	−1%	+19%	−15%	+14%	+46%	+2%	+26%	+22%	−12%	+18%	+26%	−14%	+11%
April	64	81	64	65	90	75	61	92	72	68	86	74	67	87	77	64	91	63	64
		+27%	0%	+2%	+40%	+17%	−4%	+44%	+12%	+6%	+35%	+16%	+5%	+36%	+21%	+1%	+42%	−2%	0%
May	92	111	103	98	114	107	98	102	111	97	110	109	103	115	111	93	95	100	98
		+21%	+12%	+6%	+24%	+15%	+5%	+11%	+20%	+5%	+19%	+18%	+11%	+24%	+20%	+1%	+3%	+8%	+6%
June	112	117	105	110	111	122	106	112	120	110	104	118	125	120	122	114	106	112	116
		+5%	−6%	−1%	−1%	+9%	−6%	0%	+7%	−1%	−7%	+6%	+12%	+7%	+10%	+2%	−5%	0%	+4%
July	119	127	126	135	137	124	137	128	120	121	139	121	136	136	117	133	140	118	127
		+7%	+6%	+13%	+15%	+4%	+15%	+8%	+1%	+2%	+17%	+2%	+15%	+15%	−1%	+12%	+18%	−1%	+6%
August	103	117	94	117	114	100	128	120	94	110	120	102	132	118	96	123	110	96	113
		+14%	−8%	+14%	+11%	−3%	+25%	+16%	−9%	+6%	+16%	0%	+29%	+15%	−7%	+20%	+7%	−7%	+10%
September	51	72	60	61	81	60	63	74	61	64	85	61	84	75	61	76	74	56	70
		+40%	+17%	+20%	+57%	+18%	+23%	+45%	+18%	+24%	+66%	+19%	+63%	+45%	+19%	+47%	+43%	+9%	+37%
October	23	39	36	35	36	30	34	35	34	30	40	32	44	35	32	37	36	34	33
		+70%	+56%	+56%	+60%	+30%	+48%	+54%	+49%	+31%	+74%	+39%	+95%	+53%	+39%	+61%	+60%	+48%	+44%
November	8	14	15	16	15	15	14	15	15	13	15	16	12	14	11	13	13	16	14
		+69%	+77%	+89%	+77%	+77%	+76%	+85%	+81%	+61%	+81%	+95%	+43%	+65%	+37%	+53%	+62%	+92%	+65%
December	5	10	8	7	8	10	7	6	8	10	5	10	9	7	7	8	7	8	9
		+113%	+79%	+55%	+75%	+117%	+62%	0%	+79%	+128%	+12%	+112%	+107%	0%	+60%	+68%	+54%	+69%	+92%
Annual sum	627	782	659	715	771	697	711	753	682	693	789	702	787	775	687	730	744	650	713
		+25%	+5%	+14%	+23%	+11%	+13%	+20%	+9%	+11%	+26%	+12%	+26%	+24%	+10%	+16%	+19%	+4%	+14%

The average annual potential evapotranspiration in the 2041–2050 decade for RCP 4.5 will be higher by an average of 12%, while for RCP 8.5 it will be higher by an average of 17% compared to the simulation period.

By analyzing the spatial distribution of changes in the average annual sum of actual evapotranspiration in 31 sub-catchments for the simulation period in 2010–2017 compared to the period 2041–2050 (Figure 12) for most projections, actual evapotranspiration will increase. Only for the projection of RCP 8.5.2 in the central part of the Bystra catchment area, the sum of actual evapotranspiration will be lower than in the simulation period.

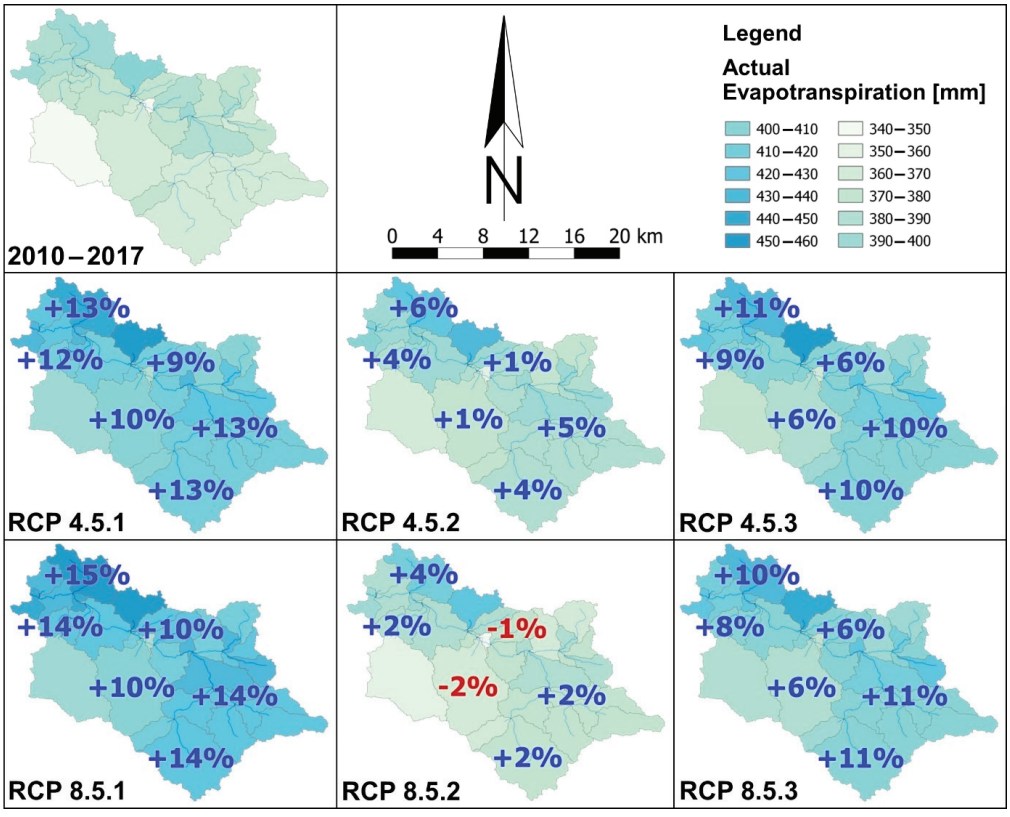

Figure 12. Comparison of the average sum of actual evapotranspiration in 31 sub-catchments for the SWAT simulation period for 2010–2017 and 2041–2050 for individual climate projections in the RCP 4.5 and RCP 8.5 scenarios (own study).

Spatial distribution of changes in the average annual sum of potential evapotranspiration in 31 sub-catchments for the simulation period in 2010–2017 compared to the period 2041–2050 (Figure 13) for all projections, the potential evapotranspiration will increase. The largest increase will be recorded in the RCP 4.5.1 and RCP 8.5.1 projections, reaching even 27% in the north-western part of the catchment area.

The trend of the average annual total runoff consisting of surface runoff, lateral flow and baseline flow in the RCP 8.5.1, RCP 8.5.2, and RCP 8.5.3 projections will increase over the years 2021–2050 (Figure 14). For the RCP 4.5.2 projection, the trend will be downward. However, for the RCP 4.5.1 and RCP 4.5.2 projections, the trend will not change significantly.

The average monthly total runoff for the Bystra River basin will be lower in most climate change projections in the years 2021–2030, 2031–2040, and 2041–2050 (Table 10). The exceptions will be the RCP 4.5.3 (2031–2040) and RCP 8.5.2, RCP 8.5.3 (2041–2050)

projections, where the average total monthly runoff will be higher compared to the 2010–2017 simulation years.

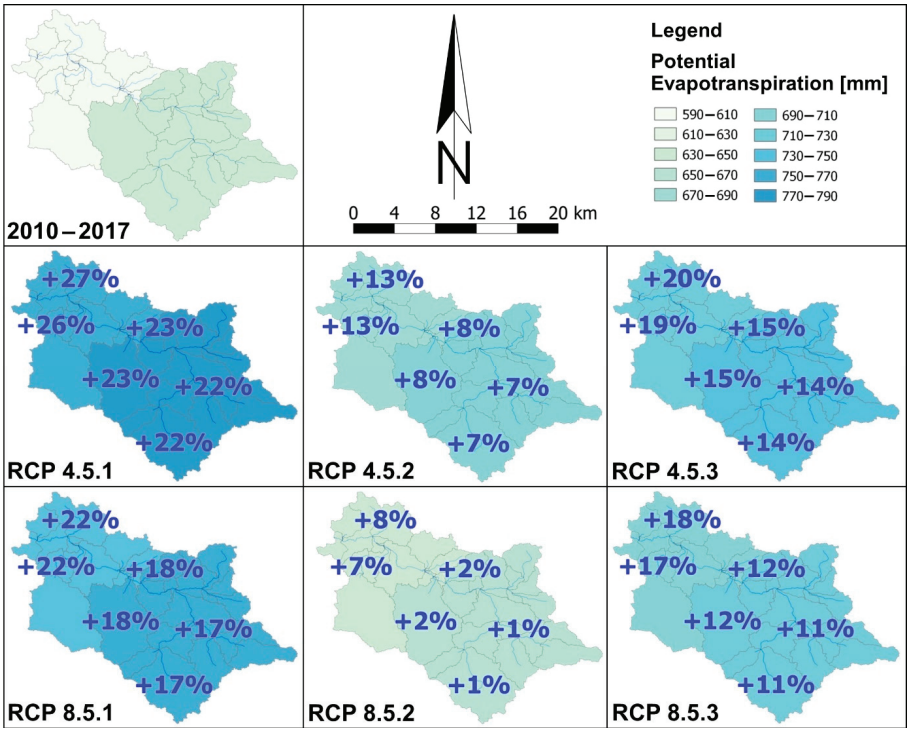

Figure 13. Comparison of the average sum of potential evapotranspiration in 31 sub-catchments for the SWAT simulation period for 2010–2017 and 2041–2050 for individual climate projections in the RCP 4.5 and RCP 8.5 scenarios (own study).

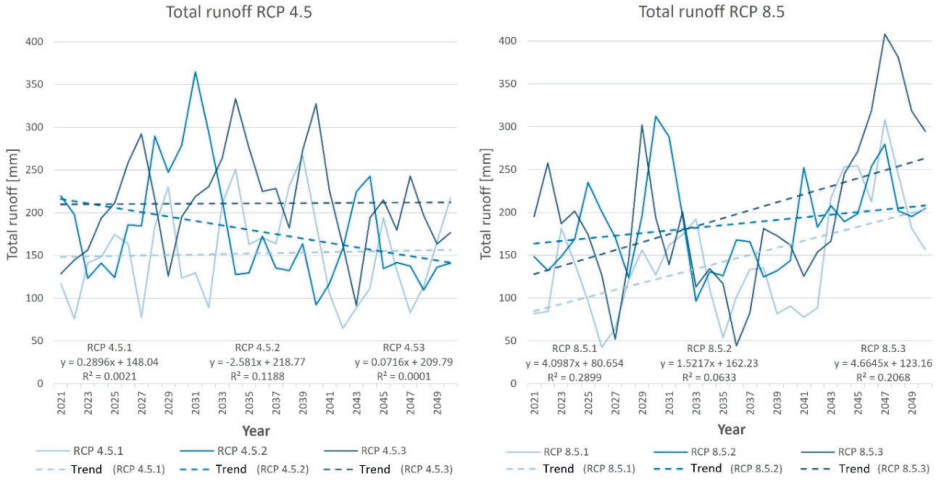

Figure 14. Average annual sum of total runoff in the Bystra River basin in the years 2021–2050 for individual climate projections in the RCP 4.5 and RCP 8.5 scenarios with trend lines (own study).

Table 10. Comparison of the average monthly total runoff for the SWAT simulation period 2010–2017 with individual projections for the RCP 4.5 and RCP 8.5 climate change scenarios for the periods 2021–2030, 2031–2040, and 2041–2050 (own study).

Climate Model	SWAT	RCP 4.5.1	RCP 4.5.2	RCP 4.5.3	RCP 8.5.1	RCP 8.5.2	RCP 8.5.3	RCP 4.5.1	RCP 4.5.2	RCP 4.5.3	RCP 8.5.1	RCP 8.5.2	RCP 8.5.3	RCP 4.5.1	RCP 4.5.2	RCP 4.5.3	RCP 8.5.1	RCP 8.5.2	RCP 8.5.3
Time Interval	**2010–2017**	**2021–2030**						**2031–2040**						**2041–2050**					
Month		**Average Monthly Total Runoff [mm]**																	
January	19	13	17	17	11	15	17	17	18	21	13	14	13	13	14	17	18	18	24
		−32%	−13%	−13%	−45%	−23%	−9%	−12%	−6%	+12%	−32%	−25%	−34%	−31%	−26%	−10%	−7%	−4%	+26%
February	18	12	16	16	9	13	15	14	16	20	11	14	11	10	13	16	16	16	22
		−32%	−7%	−10%	−47%	−24%	−12%	−22%	−10%	+11%	−39%	−20%	−36%	−45%	−28%	−9%	−8%	−8%	+27%
March	18	12	22	17	11	15	16	17	18	22	11	18	12	11	15	17	16	22	23
		−33%	+23%	−3%	−39%	−12%	−7%	−4%	+4%	+26%	−40%	+1%	−29%	−35%	−12%	−2%	−7%	+25%	+29%
April	17	11	17	15	8	14	15	13	18	20	10	14	11	10	14	16	15	20	22
		−38%	+2%	−10%	−50%	−17%	−10%	−21%	+4%	+18%	−41%	−18%	−33%	−39%	−18%	−6%	−14%	+15%	+29%
May	19	10	17	18	8	13	16	14	15	21	9	13	12	9	14	17	16	19	24
		−48%	−13%	−6%	−57%	−33%	−18%	−27%	−23%	+10%	−52%	−34%	−38%	−53%	−27%	−10%	−16%	0%	+23%
June	15	10	16	14	7	11	13	14	13	18	11	13	9	9	12	13	15	18	19
		−33%	+9%	−6%	−54%	−23%	−11%	−3%	−9%	+24%	−28%	−14%	−37%	−37%	−20%	−14%	+1%	+25%	+32%
July	16	16	17	13	8	12	12	22	16	24	9	14	9	12	11	13	15	17	20
		−3%	+3%	−18%	−53%	−30%	−28%	+32%	−2%	+47%	−45%	−17%	−45%	−30%	−34%	−19%	−9%	+3%	+19%
August	15	12	17	16	11	12	12	14	15	23	9	12	12	9	13	13	19	18	21
		−22%	+10%	+5%	−30%	−21%	−20%	−8%	-1%	+52%	−40%	−21%	−23%	−39%	−12%	−11%	+29%	+17%	+38%
September	16	13	15	19	9	12	21	17	15	24	9	11	14	11	13	15	16	18	28
		−23%	−9%	+15%	−45%	−25%	+32%	+3%	−9%	+50%	−43%	−31%	−16%	−31%	−19%	−7%	−2%	+14%	+70%
October	16	12	14	15	9	13	14	15	14	20	10	11	10	11	11	14	15	16	20
		−25%	−12%	−5%	−42%	−23%	−11%	−10%	−17%	+26%	−35%	−34%	−37%	−35%	−29%	−13%	−5%	+1%	+24%
November	16	12	16	15	9	13	14	14	13	20	10	12	10	10	11	15	17	16	22
		−25%	0%	−5%	−40%	−17%	−10%	−10%	−18%	+27%	−33%	−26%	−35%	−34%	−28%	−3%	+10%	+4%	+41%
December	18	12	17	17	10	15	16	17	13	22	12	13	11	12	13	17	21	17	24
		−30%	−6%	−2%	−44%	−16%	−9%	0%	−28%	+23%	−35%	−28%	−36%	0%	−29%	−3%	+16%	−2%	+37%
Annual sum	202	143	199	192	110	158	183	186	183	256	124	157	135	128	154	185	199	217	268
		−29%	−2%	−5%	−46%	−22%	−9%	−8%	−10%	+26%	−39%	−22%	−33%	−37%	−24%	−9%	−1%	+7%	+33%

The average annual total runoff in the decade 2041–2050 for RCP 4.5 will be lower by an average of 23%, while for RCP 8.5 it will be higher by an average of 13% compared to the simulation period.

When analyzing the spatial distribution of changes in the average annual total runoff in 31 sub-catchments for the simulation period in 2010–2017 compared to the period 2041–2050 for the RCP 4.5.1 and RCP 4.5.2 projections, the average annual total runoff amount will be lower in the entire catchment area, even reaching up to 52% (Figure 15). For RCP 4.5.3, total runoff will be lower in the northwest and southeast. It will be higher in the central part. RCP 8.5.1 and RCP 8.5.2 will have runoff volumes varying depending on the catchment area. On the other hand, the projection of RCP 8.5.3 for the whole area will have the average annual total runoff higher than in the simulation period.

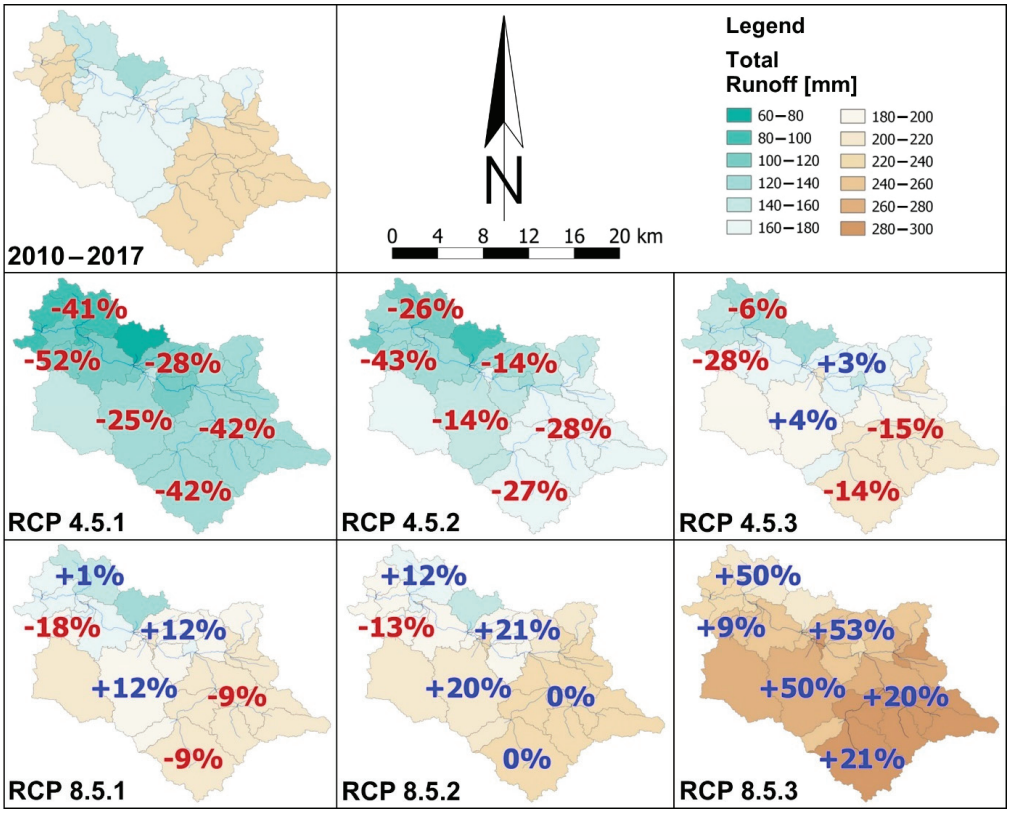

Figure 15. Comparison of the average annual sums of surface runoff in 31 sub-catchments for the SWAT simulation period 2010–2017 and 2041–2050 for individual climate projections in the RCP 4.5 and RCP 8.5 scenarios (own study).

6. Discussion

The analysis of the climate for the years 1970–2004 shows a statistically significant increase in the sum of evapotranspiration in the growing season. In the years 2021–2030, 2031–2040, and 2041–2050, an increase in potential evapotranspiration during the growing season is also shown (Table 8) [81]. Moreover, the amount of precipitation increases in winter and early spring and decreases in spring and summer. Changes in the temporal structure of precipitation may cause an increase in soil moisture in spring, which may affect areas at risk of water erosion where surface runoff should be regulated (especially

on dirt roads). This contributes to lowering the climatic water balance (i.e., increasing the precipitation deficit in relation to potential evaporation) [2,82]. Reducing the amount of precipitation, evapotranspiration, and extending the growing season caused by the temperature increase in the summer period may increase water shortages for plants [1,2].

The climate projection for Poland [82] for the years 2021–2030, 2031–2040, and 2041–2050 shows increased values of precipitation in summer (except for 2041–2050) and in autumn for the RCP 4.5 scenario compared to the period 2011–2020. However, in spring, precipitation will be lower for all decades (Table 11). Similar results were obtained for the average precipitation data in the RCP 4.5 scenario for the years 2021–2030, 2031–2040, and 2041–2050 in the SWAT model compared to the 2010–2017 simulation period. The amount of precipitation in winter is different for the SWAT and KLIMADA models for the RCP 4.5 scenario, except for the period 2031–2040, where changes in precipitation are convergent for all seasons.

The RCP 8.5 scenario for KLIMADA for the years 2021–2030, 2031–2040, and 2041–2050 shows an increased amount of precipitation for most seasons compared to the period 2011–2020. However, in the case of SWAT modeling, the years 2021–2030 and 2031–2040 show a lower amount of precipitation compared to the 2010–2017 simulation period. The exception is the period 2041–2050, where for all seasons there is an increased precipitation, similar to the RCP 8.5 scenario for KLIMADA.

The climate forecast for Poland [82] for the years 2021–2030, 2031–2040, and 2041–2050 shows increased temperatures in winter, spring, summer, and autumn (except for the period 2041–2050 for RCP 8.5). (Table 12). Similar results were obtained for averaged temperature data for winter, spring, and autumn. In summer, however, for most scenarios, temperatures will be lower in the coming decades.

In the work on a small lowland agricultural catchment in Kujawy in central Poland, the results of potential evapotranspiration, precipitation, and total runoff in 2007–2011 were presented [37,83]. The average annual potential evapotranspiration is 679 mm, the average annual precipitation is 558 mm, and the total runoff is 3.2 $L \cdot s^{-1} \cdot km^{-2}$. The above results are similar to the results of the 2010–2017 simulation in this publication, while the total runoff is higher and amounts to 6.3 $L \cdot s^{-1} \cdot km^{-2}$. This is due to the location of the tested objects. According to an academic textbook [84], the runoff value for the highlands ranges from 5 to 10 $L \cdot s^{-1} \cdot km^{-2}$. For the lowlands, it is slightly lower.

Climate change scenarios indicate a 10-fold increase in the occurrence of droughts in Poland in the coming decades [11]. According to NOAA, 2017 was the second warmest year of meteorological recording and analysis (since 1880) in the world [12]. Climate changes in the future will also affect the territory of Poland. By analyzing the climate scenarios for the years 2021–2050, it has been shown that the growing season in Poland defined by the number of days with the daily air temperature 5 °C higher in the years 2021–2050 will be longer than in the years 1971–2000 by 16 days. The predicted higher temperature in the growing season of plants will significantly accelerate their development [2]. The trend of the average annual number of days with an average temperature above 5° Celsius in the years 2020–2050 for most climate projections will be increasing, apart from the 4.5.1 projection (Figure 9).

Another publication describes, among others changes in temperature and precipitation in the near future 2021–2050 and further 2051–2100 for two hydrological models, in different climate projections for eight catchments located in Poland [85], which are similar in size to Bystra. Research shows that in the near future, warming will be ubiquitous and quite uniform spatially. In addition, there is a slight difference between the seasonal temperature increases over the period 2021–2050. In the case of precipitation, changes in the near future depend on the location of the studied catchment. For temperature and precipitation, greater differences in the results are noted for the years 2051–2100. Similar research results were obtained for the Narew River catchment for the years 2040–2069 [86].

Table 11. Comparison of the average distribution of precipitation in seasons for the SWAT simulation period 2010–2017 with individual projections for the RCP 4.5 and RCP 8.5 climate change scenarios for the periods 2021–2030, 2031–2040, and 2041–2050 (own study).

Climate Scenario	SWAT	RCP 4.5	RCP 8.5	RCP 4.5	RCP 8.5	RCP 4.5	RCP 8.5	KLIMADA 2.0 RCP 4.5				KLIMADA 2.0 RCP 8.5			
Time Interval	**2010–2017**	**2021–2030**		**2031–2040**		**2041–2050**		**2011–2020**	**2021–2030**	**2031–2040**	**2041–2050**	**2011–2020**	**2021–2030**	**2031–2040**	**2041–2050**
DJF	98	89	90	100	92	90	105	142	146	154	148	143	141	147	158
		−9%	−8%	+3%	−6%	−8%	+8%		+3%	+9%	+4%		−1%	+3%	+11%
MAM	156	150	142	144	134	149	176	199	182	188	185	180	180	184	192
		−4%	−8%	−7%	−14%	−4%	+13%		−9%	−6%	−7%		0%	+2%	+6%
JJA	207	230	201	243	197	194	210	218	234	234	215	222	228	224	237
		+11%	−3%	+17%	−5%	−6%	+1%		+7%	+7%	−1%		+3%	+1%	+7%
SON	135	142	148	140	130	145	169	155	162	165	165	152	163	165	176
		+5%	+10%	+3%	−4%	+7%	+25%		+4%	+6%	+6%		+7%	+8%	+16%
Annual sum	596	611	581	628	552	578	660	714	723	741	713	697	713	720	763
		+3%	−2%	+5%	−7%	−3%	+11%		+1%	+4%	0%		+2%	+3%	+10%

Table 12. Comparison of the average temperature distribution in the seasons for the SWAT simulation period 2010–2017 with individual forecasts for the RCP 4.5 and RCP 8.5 climate change scenarios for the periods 2021–2030, 2031–2040, and 2041–2050 (own study).

Climate Scenario	**SWAT**	**RCP 4.5**	**RCP 8.5**	**RCP 4.5**	**RCP 8.5**	**RCP 4.5**	**RCP 8.5**	**KLIMADA 2.0 RCP 4.5**				**KLIMADA 2.0 RCP 8.5**			
Time Interval	**2010–2017**	**2021–2030**		**2031–2040**		**2041–2050**		**2011–2020**	**2021–2030**	**2031–2040**	**2041–2050**	**2011–2020**	**2021–2030**	**2031–2040**	**2041–2050**
DJF	−1.1	−0.6	−1.1	−0.4	0.5	−0.2	0.5	−0.8	−0.7	0.4	0.1	−0.4	−0.8	0.0	0.1
		+0.6	+0.1	+0.8	+1.7	+1.0	+1.6		+0.1	+1.2	+0.9		−0.4	+0.4	+0.5
MAM	9.4	9.3	9.6	10.6	10.3	9.7	10.1	8.5	8.5	9.0	8.9	8.7	8.7	9.2	9.5
		0.0	+0.3	+1.2	+1.0	+0.3	+0.7		+0.0	+0.5	+0.4		0.0	+0.5	+0.7
JJA	19.3	18.9	18.9	19.2	19.7	19.4	19.4	18.5	18.6	18.9	19.4	18.8	18.7	19.1	19.3
		−0.4	−0.4	−0.1	+0.3	+0.1	0.0		+0.2	+0.5	+0.9		−0.1	+0.3	+0.5
SON	9.4	9.0	9.5	9.3	10.1	9.5	10.0	9.4	9.5	9.8	9.8	9.5	9.4	10.0	10.3
		−0.3	+0.1	0.0	+0.7	+0.2	+0.7		+0.1	+0.4	+0.4		−0.1	+0.4	+0.7
Annual avearge	9.2	9.2	9.2	9.7	10.1	9.6	10.0	8.9	9.0	9.5	9.5	9.2	9.0	9.6	9.8
		−0.1	0.0	+0.4	+0.9	+0.4	+0.8		+0.1	+0.6	+0.6		−0.2	+0.4	+0.6

Agriculture is strongly related to the prevailing climatic conditions but also has a large impact on them. The risk of an increase in the frequency of unfavorable climatic conditions in agriculture may result in yield variability from year to year. Water shortages during the growing season provided for in climate change scenarios will become more frequent and more severe. Other threats will include: droughts, heavy precipitation, erosion [87], floods, landslides, and strong winds [7]. The decreased precipitation from March to May is shown for most SWAT model projections for 2021–2030, 2031–2040, and 2041–2050 compared to the 2010–2017 simulation period. Increased actual evapotranspiration for the growing season may also contribute to unfavorable phenomena related to plant growth. Total runoff can also disrupt plant growth, both in terms of deficiency (e.g., RCP 4.5.1, RCP 4.5.2, RCP 4.5.3 for 2041–2050) and excess (e.g., RCP 8.5.2, RCP 8.5. 3 for the years 2041–2050).

The changes in the water balance of the Bystra River catchment in the years 2041–2050 were compared to the "Horizon 2050" variant, prepared for the Reda river catchment in the north of Poland, the waters of which flow into the Puck Bay [88]. The average monthly sums of precipitation in the "Horizon 2050" variant will be higher for the following months: February, March, April, July, September, and December compared to the calibration and validation period 1998–2006. On the other hand, the decline will cover May and November. The average monthly sums of precipitation in the remaining months will not change significantly as compared to the simulation results in the "zero" variant. The average monthly increase in precipitation in the Bystra basin in 2041–2050 will be higher in March, August, September, and November for most climate forecasts. The average monthly fall in precipitation will cover May, July and October compared to 2010–2017.

In the publication concerning the Reda catchment area, the total runoff was also analyzed. In the perspective of "Horizon 2050" compared to the calibration and validation period 1998–2006, there was an increase in total runoff for all months. Similar results were obtained for the RCP 8.5.2 and RCP 8.5.3 climate projections for the years 2041–2050, where the total runoff increased for most months, compared to the 2010–2017 simulation period.

Evapotranspiration for the Reda River catchment area in "Horizon 2050" will be higher compared to the zero variant. The increase in evapotranspiration will also occur in the years 2041–2050 compared to 2010–2017 for the Bystra River basin.

Differences between future climate changes in the Reda River basin and in the Bystra River basin may result from the location of both catchments, the calibration and validation period (for Reda it is 1998–2006; for Bystra it is 2010–2017), the climate of a given region, and prepared projections of predicted climate changes.

The publication on hydrological modeling of the Parseta River catchment area calibrated and validated the Parseta catchment area (area 2866 km^2) and two smaller catchments (area 1224 km^2 and 899 km^2) located in the Parseta catchment area [89]. The analysis of the obtained statistical coefficients (R^2, NSE) shows that the smaller the catchment supply area, the worse these coefficients were. The observed relationship between the catchment area and the applied R^2 and NSE statistics was also analyzed in other studies [90,91].

An analysis of the publication on the impact of climate change on the water resources of three Ukrainian catchments in 2040–2071 was also carried out, using the SWIM model [92]. One of the studied catchments is the Bug [93]. The research showed an increase in precipitation in 2040–2071, their seasonal variation for climate scenarios and an increase in temperature for most climate change scenarios, which is also confirmed in this article.

Similar results regarding the increase in precipitation, variation in seasonal precipitation and temperature for the climate change scenarios for the years 2071–2100 were obtained in studies of three catchments in Estonia using the SWAT model [94].

The discrepancies in the results are probably due to the higher resolution IUNG-PIB soil map (1:25,000) and the vectorized land use map used. When preparing the soil data, it was also taken into account that the available water capacity and wilting point values were appropriate for the soils of the Bystra catchment area. These values were obtained for the study titled "Assessment of Water Retention in Soil and the Risk of Drought Based on the Water Balance for the Area of the Lower Silesia" Voivodship", developed in 2013 by the

employees of the Department of Soil Science, Erosion, and Land Protection IUNG-PIB in Pulawy [20].

7. Conclusions

All climate change projections for the RCP 4.5 and RCP 8.5 scenarios show a trend of an increase in temperature.

The temperature for the coming decades will be higher for winter, spring, and autumn compared to the simulation years 2010–2017. In summer, however, temperatures will be lower in most projections in the coming decades.

The number of days with an average temperature above 5 °C will be higher for all projections (except for the RCP 4.5.1 projection).

On the other hand, the trend of the average annual number of days without rainfall for the RCP 4.5 scenario for all projections and for the RCP 8.5.2 and RCP 8.5.3 projections will increase slightly in the coming decades. For RCP 8.5.1, the trend will be downward. In the coming decades, most climate scenarios are projected to have less precipitation in spring and more in fall compared to simulation years 2010–2017. The remaining seasons show mixed results. The trend line of the average annual sum of potential evapotranspiration in the RCP 4.5.1 and RCP 8.5.2 projections will decrease in the next decades. However, in the case of RCP 4.5.2, RCP 4.5.3, RCP 8.5.1 and RCP 8.5.3 projections, the potential evapotranspiration trend line will increase. I The trend line of the average annual total actual evapotranspiration in the projections of RCP 4.5.2, RCP 8.5.3 will slightly change in the next decades. However, in the case of the RCP 4.5.1 projection, the actual evapotranspiration will decrease. For RCP 4.5.3, RCP 8.5.1 and RCP 8.5.3, the trend will be upward. In most climate projections, the monthly mean sums of actual evapotranspiration and potential evapotranspiration will be higher compared to the simulation period of the 2010–2017 model. The exception is the month of June, where actual evapotranspiration in most climate projections is lower compared to the years 2010–2017.

The total runoff will be higher for the RCP 4.5.3 (2031–2040) and RCP 8.5.2, RCP 8.5.3 (2041–2050) projections compared to the 2010–2017 simulation period. For the remaining projections, total runoff will be lower in the coming decades. The size of the total runoff depends on, e.g., climate and anthropogenic changes [88]. The higher total runoff may be due to increased precipitation and lower evapotranspiration in 2041–2050.

All of the above changes in the individual components of the water balance may have an adverse effect on plant vegetation in the 2021–2050 period. The trend of temperature increase and the variable amount of precipitation in individual months may lead to long-term climate changes as well as an increased number of extreme phenomena. Increased average monthly sum of evapotranspiration as well as changes in monthly sums of total runoff may disturb the vegetation of plants grown in the studied region at every stage of its growth, from sowing to harvesting. Probable increase in water deficits in the middle of growing season will foster substantial share of farms to adapt irrigation, which will grow in area compared to Poland's current share of irrigated fields.

Author Contributions: Conceptualization, D.B. and R.W.; methodology, D.B. and R.W.; software, D.B.; validation, D.B., R.W., J.K. and A.N.; formal analysis, B.J. and E.N.; investigation, D.B.; resources, D.B.; data curation, J.K. and A.K.-B.; writing—original draft preparation, D.B.; writing—review and editing, A.N., J.K. and A.K.-B.; visualization, D.B.; supervision, R.W.; project administration, R.W.; funding acquisition, R.W. All authors have read and agreed to the published version of the manuscript.

Funding: Research and ACP was funded by Polish Ministry of Agriculture and Rural Development, DC2.0/2021 Programme.

Institutional Review Board Statement: Not applicable.

Informed Consent Statement: Not applicable.

Data Availability Statement: Not applicable.

Conflicts of Interest: The authors declare no conflict of interest.

References

1. Kozyra, J.; Żyłowska, K.; Nieróbca, A.; Matyka, M.; Smagacz, J.; Jadczyszyn, T.; Wawer, R. *Zmiany Klimatu a Rolnictwo w Polsce Ocena Zagrożeń i Sposoby Adaptacji*; Fundacja Na Rzecz Zrównoważonego Rozwoju: Warsaw, Poland, 2019; p. 59. Available online: https://www.worldcat.org/title/zmiany-klimatu-a-rolnictwo-w-polsce-ocena-zagroe-i-sposoby-adaptacji/oclc/1150352150#borrow (accessed on 3 March 2018).
2. KLIMADA. Adaptacja Do Zmian Klimatu. 2013. Available online: http://klimada.mos.gov.pl/?p=150 (accessed on 22 December 2018).
3. Badora, D.; Wawer, R.; Nieróbca, A.; Król-Badziak, A.; Kozyra, J.; Jurga, B. Hydrological Water Balance in Vistula River Catchment in Climate Projections 2020–2050 for RCP 4.5 and RCP 8.5 Climate Change Scenarios. *Water* 2022, *in press*.
4. Jacob, D.; Kotova, L.; Teichmann, C.; Sobolowski, S.P.; Vautard, R.; Donnelly, C.; Koutroulis, A.G.; Grillakis, M.G.; Tsanis, I.K.; Damm, A.; et al. Climate Impacts in Europe Under +1.5 °C Global W'rming. *Earth's Future.* **2018**, *6*, 264–285. [CrossRef]
5. Kovats, R.S.; Valentini, R.; Bouwer, L.M.; Georgopoulou, E.; Jacob, D.; Martin, E.; Rounsevell, M.; Soussana, J.-F. Europe. In *Climate Change 2014: Impacts, Adaptation, and Vulnerability. Part B: Regional Aspects. Contribution of Working Group II to the Fifth Assessment Report of the Intergovernmental Panel on Climate Change*; Barros, V.R., Field, C.B., Dokken, D.J., Mastrandrea, M.D., Mach, K.J., Bilir, T.E., Chatterjee, M., Ebi, K.L., Estrada, Y.O., Genova, R.C., et al., Eds.; Cambridge University Press: Cambridge, UK; New York, NY, USA, 2014; pp. 1267–1326.
6. Doroszewski, A.; Jadczyszyn, J.; Kozyra, J.; Pudełko, R.; Stuczyński, T.; Mizak, K.; Łopatka, A.; Koza, P.; Górski, T.; Wróblewska, E. Podstawy systemu monitoringu suszy rolniczej. *Woda-Środowisko-Obsz. Wiej.* **2012**, *12*, 78–91.
7. Kundzewicz, Z.; Kozyra, J. Ograniczenie wpływu zagrożeń klimatycznych w odniesieniu do rolnictwa i obszarów wiejskich. *Pol. J. Agron.* **2011**, *7*, 68–81.
8. Kundzewicz, Z. Zmiany klimatu, ich przyczyny i skutki–możliwości przeciwdziałania i adaptacji. *Studia BAS.* **2012**, *1*, 9–30.
9. Zeder, J.; Fischer, E.M. Observed extreme precipitation trends and scaling in Central Europe. *Weather Clim. Extrem.* **2020**, *29*, 100266. [CrossRef]
10. IPCC. *Climate Change 2007: Synthesis Report. Contribution of Working Groups I, II and III to the Fourth Assessment Report of the Intergovernmental Panel on Climate Change*; Core Writing Team, Pachauri, R.K., Reisinger, A., Eds.; IPCC: Geneva, Switzerland, 2007; p. 104.
11. Parry, M.L.; Canziani, O.F.; Palukitof, J.P.; van der Linden, P.J.; Hanson, C.E. *Contribution of Working Group II to the Fourth Assessment Report of the Intergovernmental Panel on Climate Change*; Cambridge University Press: Cambridge, UK; New York, NY, USA, 2007. Available online: https://www.ipcc.ch/publications_and_data/ar4/wg2/en/contents.html (accessed on 12 December 2015).
12. NOAA. National Oceanic and Atmospheric Administration, Global Summary–Informat–on-January 2018. Available online: https://www.ncdc.noaa.gov/sotc/global/201713 (accessed on 3 March 2018).
13. Ministerstwo Środowiska (Ministry of the Environment), Strategiczny Plan Adaptacji dla Sektorów i Obszarów Wrażliwych na Zmiany Klimatu do Roku 2020 z Perspektywą do Roku 2030. Dokument Został Opracowany Przez Ministerstwo Środowiska na Podstawie Analiz Wykonanych Przez Instytut Ochrony Środowiska—Państwowy Instytut Badawczy w Ramach Projektu: "Opracowanie i Wdrożenie Strategicznego Planu Adaptacji dla Sektorów i Obszarów Wrażliwych na Zmiany Klimatu—KLIMADA", Realizowanego na Zlecenie MŚ w Latach 2011–2013 ze Środków Narodowego Funduszu Ochrony Środowiska i Gospodarki Wodnej, Warsaw, Poland. 2013. Available online: https://bip.mos.gov.pl/fileadmin/user_upload/bip/strategie_plany_programy/Strategiczny_plan_adaptacji_2020.pdf (accessed on 15 May 2019).
14. Doroszewski, A.; Jóźwicki, T.; Wróblewska, E.; Kozyra, J. *Susza Rolnicza w Polsce w Latach 1961–2010*; Wyd, IUNG-PIB: Pulawy, Poland, 2014; p. 144. ISBN 978-83-7562-171-6.
15. Doroszewski, A. Lecture: Susza Rolnicza w Polsce w 2015 Roku; Warsaw, Poland. 2016. Available online: https://docplayer.pl/31410328-Susza-rolnicza-w-polsce-w-2015-roku-andrzej-doroszewski.html (accessed on 12 April 2020).
16. Huo, R.; Li, L.; Chen, H.; Xu, C.; Chen, J.; Guo, S. Extreme Precipitation Changes in Europe from the Last Millennium to the End of the Twenty-First Century. *J. Clim.* **2021**, *34*, 567–588. Available online: https://journals.ametsoc.org/view/journals/clim/34/2/JCLI-D-19-0879.1.xml (accessed on 15 December 2021). [CrossRef]
17. Mishra, V.; Cherkauer, K.A.; Shukla, S. Assessment of drought due to *h*istoric *c*limate variability and *p*rojected future climate change in the Midwestern United States. *J. Hydrometeorol.* **2010**, *11*, 46–68. Available online: https://journals.ametsoc.org/view/journals/hydr/11/1/2009jhm1156_1.xml (accessed on 3 February 2022). [CrossRef]
18. Piniewski, M.; Szcześniak, M.; Kundzewicz, Z.W.; Mezghani, A.; Hov, Ø. Changes in low and high flows in the Vistula and the Odra basins: Model projections in the European-scale context. *Hydrol. Process.* **2017**, *31*, 2210–2225. [CrossRef]
19. Brzóska, B.; Jaczewski, A. Przyszłe zmiany wybranych wskaźników klimatycznych dla Polski na podstawie wyników dynamicznego downscalingu, zeszyt. *Pr. Geogr.* **2017**, *149*, 7–14. [CrossRef]
20. IUNG-PIB. *Ocena Retencji Wody w Glebie i Zagrożenia Suszą w Oparciu o Bilans Wodny dla Obszaru Województwa Dolnośląskiego*; Zakład Gleboznawstwa Erozji i Ochrony Gruntów, IUNG-PIB: Pulawy, Poland, 2013.

21. Jurga, B.; Wawer, R.; Kęsik, K. Zlewnia rzeki Bystrej jako przykład wyżynnej zlewni rolniczej o wysokich zdolnościach buforowych względem fosforu- studium przypadku. In *Rolnictwo XXI Wieku–Problemy i Wyzwania*; Łuczyckiej, D., Ed.; Idea Knowledge Future: Wrocław, Poland, 2018; pp. 143–154. ISBN 978-83-945311-9-5.
22. Chałubińska, A.; Wilgat, T. Podział Fizjograficzny Województwa Lubelskiego. In *Przewodnik V Ogólnopolskiego Zjazdu Polskiego Towarzystwa Geograficznego*; Oddział lubelski PTG: Lublin, Poland, 1954; pp. 3–44.
23. Jahn, A. *Wyżyna Lubelska; Rzeźba i Czwartorzęd*; Prace Geograficzne Instytutu Geograficznego, Nr 7, IGiPAN, PWN: Warszawa, Poland, 1956.
24. Sadurska, E. *Charakterystyka Fizycznogeograficzna Dorzecza Bystrej. Z. 29*; IUNG: Puławy, Poland, 1980.
25. Ziemnicki, S.; Pałys, S. Erozja wodna w zlewni rzeki Bystrej. *Zesz. Probl. Postępów Nauk Rol.* **1977**, *193*, 44–71.
26. Wawer, R.; Nowocień, E.; Podolski, B.; Capała, M. Ocena zagrożenia erozją wodną i powierzchniową zlewni rzeki Bystrej z wykorzystaniem modelowania przestrzennego. *Przegląd Naukowy SGGW Inżynieria i Kształtowanie Środowiska.* **2008**, *XVII*, 20–28.
27. SMGP. Szczegółowa Mapa Geologiczna Polski, Arkusz 747–Nałęczów (M-34-33-A). 2006. Available online: http://bazadata.pgi.gov.pl/data/smgp/arkusze_skany/smgp0747.jpg (accessed on 6 September 2018).
28. Wawer, R.; Nowocień, E.; Kozyra, J. Hydrologia i Denudacja w zlewni rzeki Bystrej. In Proceedings of the Konferencja Problemy Gospodarowania Zasobami Środowiska w Dolinach Rzecznych, Wrocław, Poland, 27–29 May 2015.
29. Maruszczak, H. Definicja i klasyfikacja lessów oraz utworów lessopodobnych. *Przegląd Geol.* **2000**, *48*, 580–586.
30. Kalarus, K. *Wpływ Materiału Macierzystego na Właściwości Gleb Wykształconych na Lessie*; Uniwersytet Jagieloński, Wydział Biologii i Nauk o Ziemi: Kraków, Poland, 2009.
31. Piest, R.F.; Ziemnicki, S. Comparative erosion rates of loeass soils in Poland and Iowa. *Trans. ASAE.* **1979**, *22*, 822–827. [CrossRef]
32. Arnold, J.G.; Kiniry, J.R.; Srinivasan, R.; Williams, J.R.; Haney, E.B.; Neitsch, S.L. Soil and Water Assessment Tool Theoretical Documentation. Version 2012. Available online: https://swat.tamu.edu/media/69296/swat-io-documentation-2012.pdf (accessed on 15 December 2021).
33. QGIS. Quantum GIS 3.10.13 Coruna. 2020. Available online: http://www.qgis.org/pl/site/index.html (accessed on 3 March 2020).
34. Winchell, M.; Srinivasan, R. *SWAT Editor for SWAT2012—Documentation*; Blackland Research Center: Temple, TX, USA, 2012; pp. 1–14.
35. USDA. United States Department of Agriculture. 1996. Available online: https://www.usda.gov/ (accessed on 1 December 2020).
36. Arnold, J.G.; Srinivasan, R.; Muttiah, R.; Williams, J. Large area hydrologic modeling and assessment. P. I: Model development. *J. Am. Water Resour. Assoc.* **1998**, *34*, 73–89. [CrossRef]
37. Miatkowski, Z.; Smarzyńska, K. Calibration and validation of SWAT model for estimating water balance and nitrogen losses in a small agricultural watershed in central Poland. *J. Water Land Dev.* **2016**, 31–47. [CrossRef]
38. Neitsch, S.L.; Arnold, J.G.; Kiniry, J.R.; Williams, J.R. Soil and Water Assessment Tool. Theoretical Documentation Version. 2005. Available online: http://swatmodel.tamu.edu/media/1292/swat2005theory.pdf (accessed on 2 January 2020).
39. Bajkiewicz-Grabowska, E.; Mikulski, Z. *Hydrologia Ogólna*; Wojtala, K., Ed.; Polish Scientific Publishers PWN: Warszaw, Poland, 2010; ISBN 978-83-01-14579-8.
40. Neitsch, S.I.; Arnold, J.G.; Kiniry, J.R.; Williams, J.R. *Soil and Water Assessment Tool Theoretical Documentation. Version 2009*; Texas Water Resources Institute: College Station, TX, USA, 2011.
41. Ulańczyk, R. Materiały informacyjne (QSWAT). In Proceedings of the Szkolenie Dotyczące Modelu SWAT (Soil and Water Assessment Tool) Oraz Interfejsu QSWAT, Sosnowiec, Poland, 14–16 May 2018.
42. Abbaspour, K.C. *SWAT-CUP 2012: SWAT Calibration and Uncertainty Programs—A User Manual*; Eawag: Dübendorf, Switzerland, 2012.
43. Abbaspour, K.C.; Vejdani, M.; Haghighat, S. SWAT-CUP calibration and uncertainty programs for SWAT. In Proceedings of the International Congress on Modelling and Simulation (MODSIM'07), Christchurch, New Zealand, 10–13 December 2007; Oxley, L., Kulasiri, D., Eds.; Modelling and Simulation Society of Australia and New Zealand: Melbourne, Australia, 2007; pp. 1603–1609.
44. Abbaspour, K.C.; Yang, J.; Maximov, I.; Siber, R.; Bogner, K.; Mieleitner, J.; Zobrist, J.; Srinivasan, R. Modelling hydrology and water quality in the prealpine/alpine Thur watershed using SWAT. *J. Hydrol.* **2007**, *333*, 413–430. [CrossRef]
45. Bilondi, M.P.; Abbaspour, K.C.; Ghahraman, B. Application of three different calibration-uncertainty analysis methods in a semi-distributed rainfall-runoff model application. *Middle-East J. Sci. Res.* **2013**, *15*, 1255–1263.
46. Yang, W.; Andréasson, J.; Phil Graham, L.; Olsson, J.; Rosberg, J.; Wetterhall, F. Distribution-based scaling to improve usability of regional climate model projections for hydrological climate change impacts studies. *Hydrol. Res.* **2010**, *41*, 211–229. [CrossRef]
47. CODGiK. Centralny Ośrodek Dokumentacji Geodezyjnej I Kartograficznej. 2013. Available online: http://www.codgik.gov.pl/ (accessed on 2 February 2017).
48. MPHP. Komputerowa Mapa Podziału Hydrograficznego Polski. 2017. Available online: https://danepubliczne.gov.pl/dataset?q=zlewnia&sort=metadata_modified+desc (accessed on 4 June 2018).
49. KPOŚK. Krajowy Program Oczyszczania Ścieków Komunalnych. 2017. Available online: https://www.kzgw.gov.pl/index.php/pl/materialy-informacyjne/programy/krajowy-program-oczyszczania-sciekow-komunalnych (accessed on 3 March 2020).
50. Jadczyszyn, J.; Smreczak, B. Mapa glebowo-rolnicza w skali 1:25 000 i jej wykorzystanie na potrzeby współczesnego rolnictwa. *Studia i Reporty IUNG PI.* **2017**, *51*, 9–27. [CrossRef]
51. IUNG-PIB. *Igital s–Il-Agricultural Maps 1:25,000 and 1:100,000*; IUNG-PIB: Pulawy, Poland, 2010.

52. CLC. CORIN–Land Cover-CLC. Główny Inspektorat Ochrony Środowiska. 2018. Available online: http://clc.gios.gov.pl/index.php/clc-2018/o-clc2018 (accessed on 25 June 2018).
53. Geoportal. Instytucja Odpowiedzialna: Główny Urząd Geodezji i Kartografii. 2020. Available online: www.geoportal.gov.pl;https://mapy.geoportal.gov.pl/wss/service/PZGIK/ORTO/WMS/HighResolution (accessed on 5 March 2020).
54. OSM. Open Street Map. 2018. Available online: http://download.geofabrikolandrolandland.html (accessed on 6 September 2019).
55. IMGW. Instytut Meteorologii i Gospodarki Wodnej PIB. 2019. Available online: http://danepubliczne.imgw.pl/data/dane_pomiarowo_obserwacyjne/ (accessed on 3 March 2019).
56. Wawer, R.; Nowocień, E.; Podolski, B. Actual water erosion risk in Poland based upon Corine Land Cover 2006. *EJPAU*. **2010**, *13*, 13. Available online: http://www.ejpau.media.pl/volume13/issue2/art-13.html (accessed on 10 December 2021).
57. Józefaciuk, C.Z.; Józefaciuk, A.; Nowocień, E.; Wawer, R. *Przeciwerozyjne Zagospodarowanie Zlewni Wyżynnej Potoku Grodarz z Uwzględnieniem Ograniczania Występowania Powodzi*; IUNG: Pulawy, Poland, 2002; Volume 4, p. 65. ISBN 83-88031-84-8.
58. Nowocień, E. Wybrane zagadnienia erozji gleb w Polsce–Ocena zagrożenia gleb erozją. *Studia i Raporty IUNG-PIB*. **2008**, *10*, 9–29. [CrossRef]
59. Markowski, K. *Rolnictwo w Województwie Lubelskim w 2019 r*; Urząd Statystyczny w Lublinie: Lublin, Poland, 2020; ISSN 2080-0517.
60. Lasy Regionu (The Forests of the Region), Regionalna Dyrekcja Lasów Państwowych w Lublinie. Available online: https://www.lublin.lasy.gov.pl/lasy-regionu#.yg89jegzzaq (accessed on 5 July 2019).
61. Essenfelder, A.H. SWAT Weather Database—A Quick Guide. 2018. Available online: https://www.researchgate.net/publication/330221011_SWAT_Weather_Database_A_Quick_Guide (accessed on 3 March 2019).
62. Abbaspour, K.C.; Rouholahnejad, E.; Vaghefi, S.; Srinvasan, R.; Yang, H.; Kløve, B. A continental-scale hydrology and water quality model for Europe: Calibration and uncertainty of a high-resolution large-scale SWAT model. *J. Hydrol.* **2015**, *524*, 733–752. [CrossRef]
63. Abbaspour, K.C.; Vaghefi, S.A.; Srinivasan, R.A. Guideline for successful calibration and uncertainty analysis for soil and water assessment: A review of papers from the 2016 International SWAT Conference. *Water* **2018**, *10*, 6. [CrossRef]
64. Arnold, J.G.; Moriasi, D.N.; Gassman, P.W.; Abbaspour, K.C.; White, M.J.; Srinivasan, R.; Santhi, C.; Harmel, R.D.; Griensven, A.; Van Liew, M.W.; et al. Swat: Model use, calibration, and validation. *Trans. ASABE*. **2012**, *55*, 1491–1508. [CrossRef]
65. Kouchi, D.M.; Esmaili, K.; Faridhosseini, A.; Sanaeinejad, S.H.; Khalili, D.; Abbaspour, K.C. Sensitivity of Calibrated Parameters and Water Resource Estimates on Different Objective Functions and Optimization Algorithms, MDPI. *Water* **2017**, *9*, 384. [CrossRef]
66. Abbaspour, K.C. SWAT-CUP Tutorial (2): Introduction to SWAT-CUP program, Parameter Estimator (SPE). 2020. Available online: https://www.youtube.com/watch?v=nNsDPhOI7cc&ab_channel=2w2e,2w2eGmbH (accessed on 15 December 2021).
67. Gao, X.; Chen, X.; Biggs, T.; Yao, H. Separating Wet and Dry Years to Improve Calibration of SWAT in Barrett Watershed, Southern California, MDPI. *Water.* **2018**, *10*, 274. [CrossRef]
68. ADMS. Agricultural Drought Monitoring System. 2013. Available online: https://susza.iung.pulawy.pl/system/ (accessed on 10 February 2022).
69. Hennemuth, T.I.; Jacob, D.; Keup-Thiel, E. Guidance for EURO-CORDEX Climate Projections Data Use. Version1 0-201708. 2017. Available online: https://www.euro-cordex.net/imperia/md/content/csc/cordex/euro-cordex-guidelines-version1.0-2017.08.pdf (accessed on 13 January 2020).
70. Jacob, D.; Petersen, J.; Eggert, B.; Alias, A.; Christensen, O.B.; Bouwer, L.M.; Braun, A.; Colette, A.; Déqué, M.; Georgievski, G. EURO-CORDEX: New high-resolution climate change projections for European impact research. *Reg. Environ. Chang.* **2014**, *14*, 563–578. [CrossRef]
71. Moss, R.H.; Edmonds, J.A.; Hibbard, K.A.; Manning, M.R.; Rose, S.K.; Van Vuuren, D.P.; Carter, T.R.; Emori, S.; Kainuma, M.; Kram, T. The next generation of scenarios for climate change research and assessment. *Nature.* **2010**, *463*, 747–756. [CrossRef]
72. Thomson, A.M.; Calvin, K.V.; Smith, S.J.; Kyle, G.P.; Volke, A.; Patel, P.; Delgado-Arias, S.; Bond-Lamberty, B.; Wise, M.A.; Clarke, L.E. RCP4. 5: A pathway for stabilization of radiative forcing by 2100. *Clim. Chang.* **2011**, *109*, 77–94. [CrossRef]
73. Yang, J.; Reichert, P.; Abbaspour, K.C.; Xia, J.; Yang, H. Comparing uncertainty analysis techniques for a SWAT application to the Chaohe Basin in China. *J. Hydrol.* **2008**, *358*, 1–23. [CrossRef]
74. Landelius, T.; Dahlgren, P.; Gollvik, S.; Jansson, A.; Olsson, E. A high-resolution regional reanalysis for Europe. Part 2: 2D analysis of surface temperature, precipitation and wind. *Q. J. R. Meteorol. Soc.* **2016**, *142*, 2132–2142. [CrossRef]
75. Schulzweida, U.; Kornblueh, L.; Quast, R. CDO 'ser's guide. *Clim. Data Oper. Version* **2006**, *1*, 205–209.
76. Kundzewicz, Z.W.; Piniewski, M.; Mezghani, A.; Okruszko, T.; Pińskwar, I.; Kardel, I.; Hov, Ø.; Szcześniak, M.; Szwed, M.; Benestad, R.E.; et al. Assessment of climate change and associated impact on selected sectors in Poland. *Acta Geophys.* **2018**, *66*, 1509–1523. [CrossRef]
77. Czernecki, B.; Ptak, M. The impact of global warming on lake surface water temperature in Poland–the application of empirical–statistical downscaling, 1971–2100. *J. Limnol.* **2018**, *77*, 330–348. [CrossRef]
78. IPPC. Intergovernmental Panel on Climate Change. 1998. Available online: https://www.ipcc.ch/ (accessed on 7 May 2020).
79. PIK. Potsdam Institute for Climate Impact Research. 2012. Available online: http://www.pik-potsdam.de/~{}mmalte/rcps/ (accessed on 5 August 2021).

80. Meinshausen, M.; Smith, S.J.; Calvin, K.V.; Daniel, J.S.; Kainuma, M.L.T.; Lamarque, J.-F.; Matsumoto, K.; Montzka, S.A.; Raper, S.C.B.; Riahi, K.; et al. The RCP Greenhouse Gas Concentrations and their Extension from 1765 to 2300. *Clim. Chang.* **2011**, *109*, 213–241. [CrossRef]
81. Łabędzki, L.; Bąk, B.; Kanecka-Geszke, E. Wielkość i zmienność ewapotranspirację wskaźnikowej według Penmana-Monteitha w okresie wegetacyjnym w latach 1970–2004 w wybranych rejonach Polski, Instytut Technologiczno-Przyrodniczy, Kujawsko-Pomorski Ośrodek Badawczy w Bydgoszczy. *WODA-Środowisko-OBSZARY WIEJSKIE* **2012**, *2*, 159–170.
82. KLIMADA 2.0. KLIMADA 2.0–Baza Wiedzy o Zmianach Klimatu, Scenariusze Zmian Klimatu. 2019. Available online: https://www.itp.edu.pl/old/wydawnictwo/woda/zeszyt_38_2012/artykuly/Labedzki%20in.pdf (accessed on 2 February 2022).
83. Miatkowski, Z.; Smarzyńska, K. Surface water resources of small agricultural watershed in the Kujawy region, central Poland. *J. Water Land Dev.* **2017**, *33*, 131–140. [CrossRef]
84. Dynowska, I.; Pociask-Karteczka, J. *Obieg Wody [w:] Starkel L. (Red.), Geografia Polski*; Środowisko Przyrodnicze, Wyd, Nauk, PWN: Warszawa, Poland, 1999.
85. Piniewski, M.; Meresa, H.K.; Romanowicz, R. What can we learn from the projections of changes of flow patterns? Results from Polish case studies. *Acta Geophys.* **2017**, *65*, 809–827. [CrossRef]
86. Piniewski, M. *Impacts of Natural and Anthropogenic Conditions on the Hydrological Regime of Rivers: A Narew River Basin Case Study*; Instytut Meteorologii i Gospodarki Wodnej: Warszawa, Poland, 2012.
87. Józefaciuk, A.; Nowocień, E.; Wawer, R. *Erozja Gleb w Polsce–Skutki Środowiskowe i Gospodarcze, Działania Zaradcze*; nr 44; Monografie i Rozprawy Naukowe IUNG-PIB: Pulawy, Poland, 2014; p. 263.
88. Marcinkowski, P.; Piniewski, M.; Kardel, I.; Giełczewski, M.; Okruszko, T. Modelling of discharge, nitrate and phosphate loads from the Reda catchment to the Puck Lagoon using SWAT. *Ann. Warsaw Univ. Life Sci. –SGGW Land Reclam.* **2013**, *45*, 125–141. [CrossRef]
89. Gudowicz, J.; Zwoliński, Z. Kształtowanie się odpływu rzecznego w dorzeczu Parsęty w świetle modelowania hydrologicznego. *Przegląd Geogr.* **2017**, *89*, 45–66. [CrossRef]
90. Piniewski, M.; Okruszko, T. *Multi-Site Calibration and Validation of the Hydrological Component of SWAT in a Large Lowland Catchment, [w:] D. Świątek, T. Okruszko (Red.), Modelling of Hydrological Processes in the Narew Catchment, Geoplanet: Earth and Planetary Sciences*; Springer: Berlin, Germany, 2011; pp. 15–41.
91. Piniewski, M.; Marcinkowski, P.; Kardel, I.; Giełczewski, M.; Izydorczyk, K.; Frątczak, W. Spatial quantifi cation of non-point source pollution in a meso-scale catchment for an assessment of buffer zones effi ciency. *Water* **2015**, *7*, 1889–1920. [CrossRef]
92. Krysanova, V.; Wechsung, F.; Arnold, J.; Ragavan, S.; Williams, J. *SWIM (Soil and Water Integrated Model), User Manual*; Report Nr. 69; Potsdam Institute Climate Impact Research (PIK): Potsdam, Germany, 2000.
93. Didovets, I.; Lobanova, A.; Bronstert, A.; Snizhko, S.; Maule, C.F.; Krysanova, V. Assessment of climate change impacts on water resources in three representative Ukrainian catchments using eco-hydrological modelling. *Water* **2017**, *9*, 204. [CrossRef]
94. Tamm, O.; Luhamaa, A.; Tamm, T. Modeling future changes in the North-Estonian hydropower production by using. *Hydrol. Res.* **2016**, *47*, 835–846. [CrossRef]

sustainability

MDPI

Article

Spatial and Temporal Changes in Wetland in Dongting Lake Basin of China under Long Time Series from 1990 to 2020

Zhi-Min Yang [1,2], Long-Fei Han [1,*], Qing-Ping Liu [3], Chun-Hui Li [2], Zhao-Yi Pan [4] and Ke Xu [1]

[1] School of Geographic Sciences, Hunan Normal University, Changsha 410081, China; yangzm@mail.bnu.edu.cn (Z.-M.Y.); 201830163036@hunnu.edu.cn (K.X.)
[2] School of Environment, Beijing Normal University, Beijing 100875, China; chunhuili@bnu.edu.cn
[3] College of Water Sciences, Beijing Normal University, Beijing 100875, China; 202121470018@mail.bnu.edu.cn
[4] School of Humanities and Social Science, The Chinese University of Hong Kong, Shenzhen 518172, China; zhaoyipan@link.cuhk.edu.cn
* Correspondence: hanlf@hunnu.edu.cn; Tel.: +86-18260086993

Abstract: Wetland plays a pivotal role in sustaining ecosystems and adapting to climate change. This paper used remote sensing images from 1990, 2000, 2010, and 2020 to investigate the changes in wetland in the Dongting Lake Basin (DLB) and their possible causes. The land-use conversion matrix and contribution rate were calculated in 1990–2000, 2000–2010, and 2010–2020, and results showed that the total wetland area displayed an increasing trend, especially the reservoir ponds and channels across DLB from 1990 to 2020. Forest and agricultural land conversion into wetland accounted for the main proportion, with the greatest contribution rate (234.13%) of forest land and the smallest rate (−117.46%) of agricultural land between 1990 and 2000. On the contrary, agricultural land had the highest contribution rate (47.96%) for wetlands compared to other land-cover types from 2000 to 2010, followed by forest land (39.03%). The contribution rates of forest and agricultural lands to wetlands were 60.17% and 39.02% from 2010 to 2020, respectively. Wetlands showed a more significant net gain (a total of 259 km^2) in Central and Southern Hunan Province. More specifically, the wetlands area in North Hunan Province decreased by 45 km^2 from 1990 to 2000. It increased over the next two decades (155 km^2 and 22 km^2, respectively). Southern Hunan Province continued increasing from 1990 to 2010 (a total of 149 km^2) while decreasing from 2010 to 2020 (a total of −297 km^2). Forestation was the principal driving force promoting the continuous increase in wetlands. In addition, agricultural land was mainly related to wetland change in this region, characterized by reclaiming land from lakes in the earlier period and returning agricultural land to wetland in the later period. Built-up land occupied a small area of wetlands over the study period. The study is beneficial to understanding the wetlands' dynamic changes in the past and present, as well as being useful for wetland management, consistent with sustainable development.

Keywords: wetland; temporal and spatial change; land-use change; Dongting lake basin

Citation: Yang, Z.-M.; Han, L.-F.; Liu, Q.-P.; Li, C.-H.; Pan, Z.-Y.; Xu, K. Spatial and Temporal Changes in Wetland in Dongting Lake Basin of China under Long Time Series from 1990 to 2020. *Sustainability* **2022**, *14*, 3620. https://doi.org/10.3390/su14063620

Academic Editors: Alban Kuriqi and Luis Garrote

Received: 16 February 2022
Accepted: 9 March 2022
Published: 19 March 2022

1. Introduction

Wetlands play significant roles in mitigating floods, serving as natural habitats to support biodiversity, safeguarding human welfare, maintaining the regional and global ecological balances, and maintaining carbon sequestration [1–4]. The wetlands ecosystem service value accounts for more than 40% of the global ecosystem's value among all kinds of ecosystems [5,6]. The World Resources Institute produced the Millennium Ecosystem Assessment Report, stating that wetlands provide invaluable ecosystem services and value for human well-being and poverty alleviation [7]. Recently, wetland conservation and restoration have attracted much attention, such as the Ramsar Convention, the wetlands bank program in the United States, and the NWCP (National Wetland Conservation Program) in China.

The loss of global wetlands is currently a priority issue on the international political agenda [8,9]. According to an OECD/IUCN (Organization for Economic Cooperation and Development/International Union for Conservation of Nature) report, the world may have lost 50% of its wetlands, mainly due to the development of agriculture since 1900. It has been estimated that the area of global wetlands decreased by 64% to 71% over the course of the 20th century, and losses and degradation of global wetlands have continued [10,11]. Davidson notes that wetlands have degraded by about 87% worldwide since 1700, and the loss of wetlands has mainly occurred during the 20th and early 21st centuries [12]. China's wetland protection policies and measures have continued to advance in recent years, including returning agricultural land to lakes. Gong et al. [13] reported that the total wetland area ranged from 3.552×10^5 km^2 in 1990 to 3.048×10^5 km^2 in 2000, with a net loss of 5.036×10^4 km^2 in China. Chen et al. [14] pointed out that the change mode of wetland was mainly the increase and decrease in the area and the conversion of types, and the wetlands in the Yangtze River Basin increased by 5.172×10^3 km^2 from 1975 to 2007. Some studies showed that nearly 30% of China's natural wetlands vanished between 1990 and 2000 [15], while Tong et al. [16] proposed that the wetland area of the Yangtze River basin increased from 1990 to 2012. The middle and lower reaches of the Yangtze River were the central region for wetland loss [17], and as the main component of the Yangtze River Basin, the Dongting Lake Basin was a significant area of wetlands in China. Whether the change in the wetlands in the Dongting Lake Basin is consistent with that of the middle and lower reaches of the Yangtze River remains to be studied.

Wetland changes were caused by various factors, such as climate change and severe weather, geological events, agriculture and aquaculture, urbanization, and human intrusions and disturbances [18]. Some research showed that China's wetlands had a total net gain of 1548 km^2 in 2010–2015 due to wetland restoration projects, climate change, dam construction, and other reasons, mainly distributed in the Qinghai Tibet Plateau, the northwest, and the southwest of China [17]. Gong et al. [19] demonstrated that temperature, precipitation, and agricultural production were closely related to the changes in the wetlands of inland China, especially at the end of the 20th century. Food problems and economic benefits encouraged people to reclaim wetlands to expand agricultural land. Lu et al. [20] demonstrated that agricultural encroachment was the most important driving factor for the degradation and loss of wetlands in the Wusuli River Basin in China. Gong et al. [13] proposed that the loss of wetlands in China was mainly due to human activities, and climate warming mainly affected wetlands in Western China due to glaciers melting. Zhao et al. [21] discovered that the wetlands of Dongting Lake decreased by 49.2% from 1930 to 1998 due to human activities, such as extensive land reclamation. Mao et al. [22] pointed out that the acceleration of urbanization was expected to encroach on more wetland, thus exacerbating the degradation of wetlands in China between 1990 and 2010, which contradicts the viewpoint of Xu et al. [17] mentioned above.

Currently, wetland conservation and restoration have become important sustainable development goals of the United Nations. Many countries, including the United States, have adopted "no net loss" of wetlands as a critical indicator for evaluating and measuring wetland change [17]. The Ramsar Convention encouraged academia to quantify wetlands to promote the sustainable development and utilization of regional wetlands, and spatially explicit information became necessary for sustainable wetland management. Therefore, the relevant research on quantifying the net change in wetlands needs to be supplemented. The reasons for wetland change can be divided into wetland transformation and wetland destruction. However, most of the research focuses on wetland destructions and less on the perspective of land transformation to analyze the mechanism of wetland destruction deeply. The Ramsar Convention claimed that wetland management implies the need to understand the past and current human use of wetlands and ways to achieve sustainable utilization of wetlands. This study fills the gap above. On the one hand, this paper can help us understand wetlands' dynamic changes in the past and present to achieve sustainable wetland management better in the future. On the other hand, the study can provide

essential insights to wetland conservation and rational utilization of wetland in the DLB, thereby promoting the sustainable development of wetland and the coordination and stability of the ecosystem. The main objectives of this study were to: (i) characterize the mutual conversion between wetland and other land-use types by using remote sensing image monitoring data from 1990 to 2020; (ii) comprehensively analyze the contribution rate of different land-use types to wetland; and (iii) further reveal the spatial and temporal change in characteristics of wetland and its main driving factors in the past 30 years.

2. Methods and Data

2.1. Study Area

Dongting Lake Basin, once the largest freshwater lake in China, is located in the middle latitude between 24°38′ and 30°26′ N, and between 107°16′ and 114°17′ E. It crosses the second and third gradient terrain of China's terrain, with a subtropical monsoon climate, with various wetland types. As for spatial distribution, it covers most of Hunan Province, the south of Hubei Province, the west of Guizhou Province, the northwest of Guangxi Province, and the north of Guangdong Province (Figure 1).

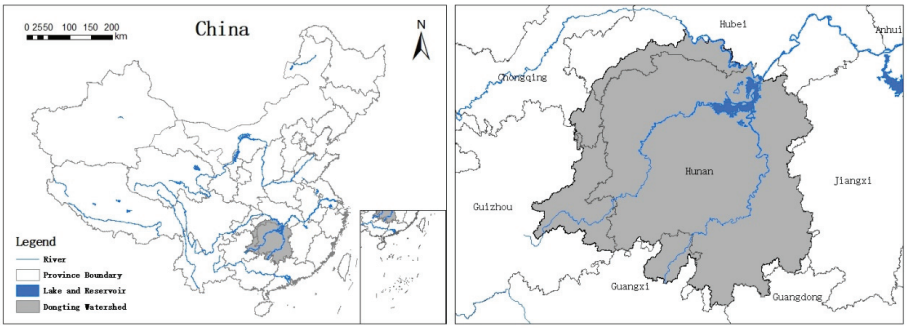

Figure 1. Location of the study area.

Considering that about 80% of the basin area and more than 85% of the wetland area in DLB are distributed in Hunan Province, this paper selected Hunan Province as the vital research object district and further divided it into five partitions: Northern, Western, Central, Eastern, and Southern Hunan (Table 1), to better reveal the spatial differences and the zoning characteristics of wetland changes. A few parts of Changsha, Yueyang, Huaihua, Chenzhou, Yongzhou, and Shaoyang cities are not covered by the DLB. This paper took the basin coverage as the research scope. Given that the DLB does not completely overlay the five subareas, this paper focused on the intersection of Hunan Province and the DLB. It explored the basic spatial pattern and change process of wetland change.

Table 1. Distributions of Hunan Province covered by the DLB.

Research Distribution	Covered Cities
Northern Hunan	Yiyang city, Changde city, Yueyang city
Western Hunan	Zhangjiajie city, Xiangxi autonomous prefecture, Huaihua city
Southern Hunan	Hengyang city, Chenzhou city, Yongzhou city
Central Hunan	Loudi city, Shaoyang city
Eastern Hunan	Zhuzhou city, Xiangtan city, Changsha city

As an essential commodity grain base in China, the wetland area of the DLB shrunk significantly before the 1990s, which seriously limited the function of wetlands in reducing flood peaks, regulating the seasonal runoff, reducing flow variability, and maintaining maintenance biodiversity [23]. Since the 1990s, it has become an urgent issue to restore

the function and value of wetland in the DLB and realize the balance of the wetland ecosystem. The wetlands in the DLB were listed in the National Nature Reserve and the list of internationally important wetlands. In 1998, following the great flood disaster of the Yangtze River, the State Council further clarified returning agricultural land to the lake. At the beginning of the 21st century, aiming at the conservation and sustainable utilization of wetlands, the government promulgated the regulations of Hunan Province on wetland protection, which improved the wetland ecosystem in the basin. The spatial change of wetland reflected the human–land relationship in different regions [24].

2.2. Land-Cover Data

The data of Landsat TM/ETM Remote Sensing Images in 1990, 2000, 2010, and 2020 were acquired from the Resource and Environment Science and Data Center (https://www.resdc.cn/, accessed on 8 May 2020). The study rectified the geometric accuracy of remote sensing images and extracted land-use-type information from remote sensing images by manual visual interpretation to form four-phase 1:100,000-scale vector data of land-use type. The comprehensive evaluation accuracy was more than 85% for the first land-use types and over 90% for the secondary wetland-cover types using the relevant field survey data [25]. The wetland classification used in this paper was derived from the LUCC classification system table of the Institute of Geographical Sciences and Natural Resources Research, CAS. Based on the concept of wetlands and the basic characteristics of the research area, the land surface in the DLB was classified into six types: agricultural land, grassland, forestland, wetlands, built-up land, and unutilized land. This paper classified the wetlands into five categories: river plus canal, lake, reservoir plus pond, beach, and marsh. Supported by remote sensing image data and ArcGIS technology, a grid network of 1 km was created, reducing errors and improving accuracy effectively on the vector graphic of the DLB with a 30 m $\times$ 30 m satellite image (i.e., Landsat TM/ETM). Then, land-use types of the identical blocks in different periods were compared through spatial overlap. Land-change information was obtained by direct interpretation so that land-use-change types in this process had an average qualitative accuracy of more than 90%.

Then, land-use-type conversion matrices of the DLB from 1990 to 2000, 2000 to 2010, and 2010 to 2020 were created using the information of land-use area and transformation status in different periods carried by each grid. Additionally, land-use-type conversion matrices were produced by applying the information on land-use area and conversion situation in different periods of each grid. Eventually, the conversion between wetland and other land-use types was emphatically investigated, and the change direction, extent, and main driving factors of wetland were explored.

2.3. Methods

The study calculated the land-use conversion matrix using the ArcGIS 10.6 software package. The areas converted from wetlands to other land-use types and from others to wetlands were identified, and the conversion patterns were shown in a spatial distribution. The land-transfer matrix could clearly show wetland increase, decrease, and net change. The study defined wetland gain as conversion from other land-cover types to wetlands. In addition, wetland loss was considered a conversion of wetlands to other land-use types. Furthermore, wetland net change was equal to wetland gain minus wetland loss. In order to comprehensively and scientifically reflect the number, direction, magnitude, and distribution of wetland changes, and the contribution of other land-cover types to wetlands in the DLB in the past 30 years, the study introduced three indicators of wetland net increase and net decrease, increase and decrease percentage, and contribution rate.

The contribution rate (C_i) of different land cover types to wetland is a comprehensive and simple index for wetland source and loss quantitatively. It reflects the direction and magnitude of conversion from another land type to wetland and better measures the main driving factors of wetland net change. Therefore, it is beneficial to discuss the

net contribution of a specific type of land use to wetland change, which could help us understand the role of different types of land use in the process clearly and precisely.

$$Ci = \frac{\Delta Si,j}{\Delta Sj} \times 100\% \quad (1)$$

where $\Delta S_{i,j}$ indicates the net change of j converted from land-cover type i. The value is equal to the area of i minus the area of j from the beginning to the end of the study. ΔS_i is the total net change of i converted with all other land-cover types from the beginning to the end of the monitoring period, that is, the total increase in wetlands minus the total decrease during the study period. C_i refers to the contribution rate of land-use type i to j.

3. Result

3.1. Temporal Change in Wetland in the DLB from 1990 to 2020

As shown in Figure 2, there was an apparent increasing trend in the wetland area of 8322 km^2 in 1990, 8448 km^2 in 2000, 8717 km^2 in 2010, and 9006 km^2 in 2020 in the DLB. In total, the net gain in wetlands was 395 km^2 over the 30 years. The wetland increased by 126 km^2, with a growth rate of 1.51% in the first 10 years. Meanwhile, the period between 2000 and 2010 experienced a more apparent increase, with a wetland area expansion of 269 km^2 and a growth rate of 3.18%, the net gain in wetland was 2.14 times that of the first 10 years. The most significant increase in wetland area in the study time frame was from 2010 to 2020. The data showed a total expansion of 289 km^2 and a growth rate of 3.32%. In the first 10 years, the net wetland appreciation was 2.20 and 1.04 times greater than from 2000 to 2010 and 2010 to 2020. The reservoir plus ponds and river plus canal showed an apparent net gain of 58.99% and 31.90% of the total wetland net increase from 1990 to 2010, with the lake and beach areas displaying a slight change. Furthermore, the increase in reservoir-plus-pond and river-plus-canal areas from 2010 to 2020 exceeded the total net increase. The net gains in river plus canal and reservoir plus pond were key survival traits for the first 10 years, which accounted for 89.68% and 81.75% of the total wetland net gain in this period, respectively. In addition, the beaches showed a relatively balanced change. The net loss between 1990 and 2000 was 122 km^2, while the net gain between 2000 and 2020 was 179 km^2. The research documented that the increase in vast wetlands was closely related to the net gain in reservoir plus pond and beach from 2000 to 2010, which accounted for 90.33% of total net wetland increase. The most significant increase occurred in the river-plus-canal area type (540 km^2) from 2010 to 2020, followed by marsh (177 km^2).

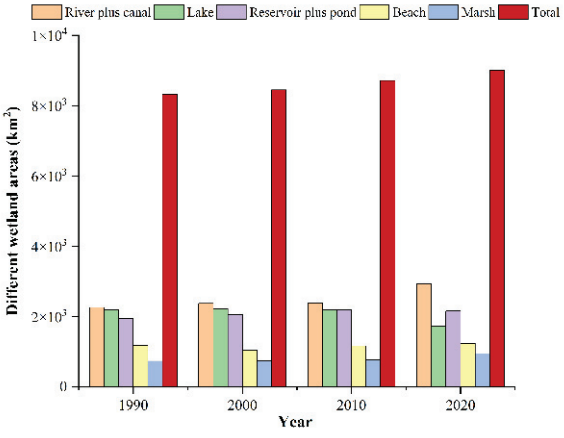

Figure 2. Area (km^2) changes in different wetland categories in DLB from 1990 to 2020.

The conversion of agricultural land and forest land to wetland was the primary change in wetland from 1990 to 2000. Among them, the area of agricultural land converted into wetland was 3480 km^2 (no net increase), while that of wetland converted into agricultural land was 3628 km^2. In comparison, the total net change in wetland was only 126 km^2 during this period. Figure 3 demonstrates that the net gain in wetlands was mainly attributed to forest land, whose contribution rate was 234.13%. However, other land types inevitably encroached on many wetlands, and the contribution rate was negative, especially the agricultural land. The conversion of wetland to agricultural land was the main factor that led to the loss of wetland from 1990 to 2000. Approximately 148 km^2 of the wetlands that disappeared owing to agricultural land were quantified. Ccontribution rate was a minimum of −117.46%. Many forest land areas were converted into wetlands, which, remarkably, made up for the occupation of wetland caused by agricultural land and further drove a significant increase in wetlands in general between 1990 and 2000.

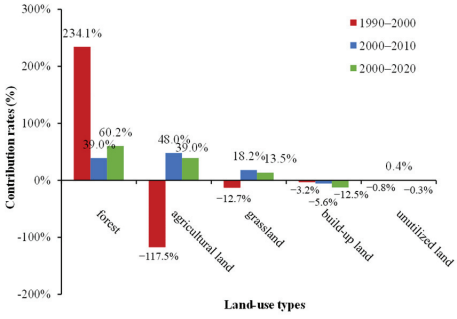

Figure 3. Contribution rates (%) of different land types to wetland changes in DLB from 1990 to 2020.

From 2000 to 2010, the net gain area of wetland was higher than that of the previous period. However, the dynamic degree of wetland decreased from 71.88% to 18.54%, indicating that wetland fluctuation became more stable in the first decade of the 21st century. In this study, built-up land was the only type occupied on wetlands. Furthermore, the net gain in wetlands triggered by agricultural land was the largest, accounting for 47.96% of the total wetland net gain. Secondly, forest land contributed 39.03% to wetlands.

The contribution of other land-use types to wetlands from 2010 to 2020 was relatively balanced compared to the previous 20 years, with the highest contribution from forest land, followed by agricultural land. The conversion of forest land to wetland was the main factor in increasing wetland over the 30 years. Additionally, the conversion direction of agricultural land to wetland in 1990–2000 (negative) was diametrically opposite to that in the next 20 years (positive). During the past 30 years, built-up land showed continuous occupation of wetland, the contribution rates to wetland were −3.17% in 1990–2000, −5.58% in 2000–2010, and −12.46% in 2010–2020, respectively.

3.2. Spatial Change in Wetland Change in DLB

As shown in Figure 4, in Hunan Province of DLB, the wetland areas were 7390, 7485, 7722, and 7844 km^2 in the four periods. Moreover, the net increased wetland areas were 95 km^2 in 1990–2000, 237 km^2 in 2000–2010, and 122 km^2 in 2010–2020. The wetland in Southern Hunan increased significantly in the first 10 years, accounting for 123.2% of the total net change in wetlands in the five zones. The wetland in Northern Hunan increased obviously, accounting for 65.4% of the total net change in wetlands. From 2010 to 2020, the most significant net increase in wetland occurred in Central Hunan, with values of 576 km^2, and was 4.72 times the total net increase. Furthermore, the wetland areas in Eastern Hunan and Southern Hunan decreased significantly, with a net loss of 221 km^2 and 297 km^2 from 2010 to 2020, respectively.

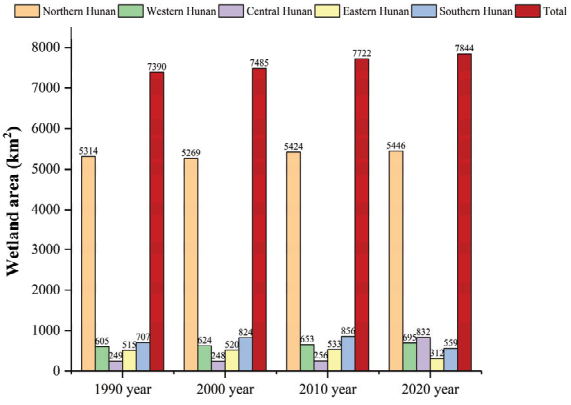

Figure 4. Changes in wetland area (km^2) in research region from 1990 to 2020.

Figure 5 shows the spatial distribution of different wetland changes in Hunan Province covered by the DLB. In Figure 5a, wetland had a net decrease from 1990 to 2000 (−31 km^2) and a net increase from 2000 to 2020 (a total of 223 km^2) due to changes in agricultural land area. Forest land was the primary source of wetland growth and contributed to the net gain in wetlands.

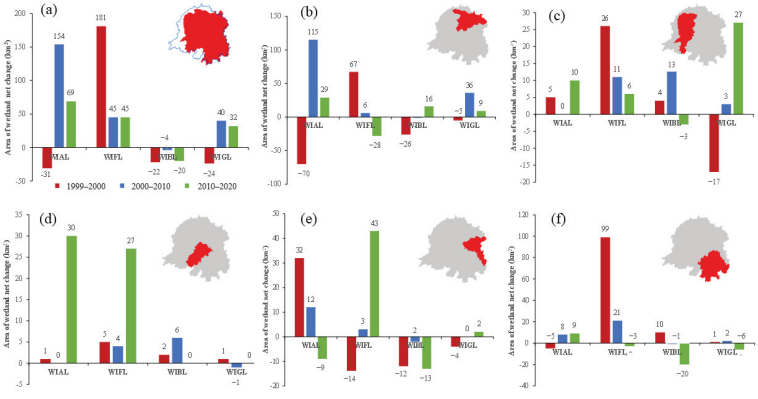

Figure 5. Conversion between wetlands and other land types in each subregion of DLB from 1990 to 2020; (**a**) Hunan Province, (**b**) Northern Hunan, (**c**) Western Hunan, (**d**) Central Hunan, (**e**) Eastern Hunan, (**f**) Southern Hunan; WIAL refers to the net conversion between wetland and agricultural land; WIFL refers to the net conversion between wetland and forestland; WIGL represents the net conversion between wetland and grassland, and WIBL represents the net conversion between wetland and built-up land (km^2).

In Northern Hunan (Figure 5b), the net change in wetlands showed a decreasing trend in the first 10 years and then increased in the next 20 years. From 1990 to 2000, the net reduction in wetland area was 45 km^2, mainly due to the expansion of forest land to invade wetland, resulting in a reduction of 74 km^2 in wetland. The expansion of built-up land was also an important factor in wetland loss. Although agricultural land promoted the restoration of the wetland area of 68 km^2, the surplus did not make up for the deficit, and the wetland showed an evident trend of decrease. From 2000 to 2010, the net increase in wetland area was 155 km^2, of which 73.55% of the increase came from agricultural land. In addition, grassland and forest land changed from the previous encroachment of

wetland into an essential factor in promoting the restoration of wetland areas. Both of them contributed 27% of the total net increase in wetlands. From 2010 to 2020, agricultural land contributed to a net increase in wetlands (29 km^2), with 1.1 times the total net increase in wetlands.

In Western Hunan (Figure 5c), the total net increase in wetland area was 19 km^2 in the first 10 years, and mutual conversion between forest land and wetland was the most frequent. Agricultural land was the primary wetland source, with a net conversion of 20 km^2 of wetland in the interim. Simultaneously, forest land became the second-largest source of wetland increase, with a net change of 16 km^2. From 2000 to 2010, the wetland increase was significantly greater than in the previous period, with a net increase of 29 km^2. Meanwhile, agricultural land, forest land, and grassland all contributed to the wetland, with net increases of 14 km^2, 12 km^2, and 3 km^2 in wetlands, respectively. Similarly, all land-use types contributed to a net increase in wetlands from 2010 to 2020 except for built-up land.

In Central Hunan (Figure 5d), wetlands showed a continuous net gain with the contribution of forest land. Agricultural land contributed more significantly to wetlands from 2010 to 2020 (30 km^2). The wetland change in Eastern Hunan (Figure 5e) was mainly due to the conversion of agricultural land, which led to a net increase of 32 and 12 km^2 in wetlands in the first two decades, but a net decrease of 9 km^2 in wetlands from 2010 to 2020. In Southern Hunan (Figure 5f), forest land contributed 107 km^2 of wetland area, accounting for 91.45% of the newly added wetland from 1990 to 2000. The adjustment of built-up land resulted in a net increase of 9 km^2 in wetland. In the next 10 years, the growth rate of wetlands slowed down. Therein, 65.62% came from the conversion of forest land, 31.25% stemmed from the conversion of agricultural land, and 6.25% derived from the contribution of grassland. Nevertheless, the built-up land showed a weak trend of invading wetlands. From 2010 to 2020, the primary manifestation was the net reduction in wetlands due to the expansion of built-up land (-20 km^2).

4. Discussion

4.1. Wetland Increase Due to Forest Loss

There was a close correlation between wetland and forest land [10]. From 1990 to 2020, forest land was the main reason for the increase in the wetland area, contributing a total of 571 km^2 in the previous three decades. As Figure 6 shows, forest land had different contribution levels to different types of wetlands. Furthermore, the net gain in wetlands in the first 10 years was 2.8 times and 1.7 times that of the next two decades, respectively. The net conversion of forest land to lakes was the most significant, with a net gain of 132 km^2, followed by river plus canal and reservoir plus pond, with a net gain of 101 km^2 and 64 km^2, respectively. From 2000 to 2010, forest land was mainly converted into river plus canal and beach, with a net gain of 48 km^2 and 46 km^2. Generally, in the past 30 years, forest land mainly contributed to the growth of the river plus canal, accounting for 58.49% of the total net increase in wetlands. On the one hand, the river-plus-canal areas were important water conservancy facilities for the development of agriculture [26]. Simultaneously, with the improvement in people's living standards, there was a growing demand for varieties of crop species, which led to the development of suburban agriculture, thus occupying a part of the wetland. Moreover, the construction and matching of river water conservancy facilities could improve agricultural infrastructure and irrigation conditions, thus increasing food production, especially in the 1990s when China's agriculture accounted for a large proportion. On the other hand, because the forestry industry had a long development cycle and low output value, and the importance of forest carbon sequestration was not fully recognized early, the phenomenon of expropriation of forest land to respond to wetland conservation occurred. As the government and academics paid more attention to forest land, society was increasingly aware that forests were the most significant carbon reservoir in terrestrial ecosystems and had a vital and unique role in reducing greenhouse gas

concentrations and mitigating global warming [27], which was an essential reason for the diminishing contribution of forest land to wetland.

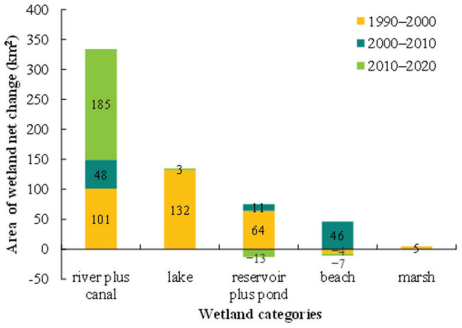

Figure 6. The net conversion area (km^2) of forestlands and wetlands in the DLB from 1990 to 2020.

4.2. Wetland Change Due to Agricultural Land

Over the three decades, the direction of change between agricultural land and wetland was inconsistent. Reclaiming land from lakes was a prominent feature in the early stage from 1990 to 2000. However, returning agricultural land to wetland was the main feature in the later stage from 2000 to 2020. It was indicated that the population increased significantly, leading to a greater demand for grain at the end of the 20th century, which promoted crop cultivation and stimulated the transformation of wetlands [28]. Besides, people in southern China prefer rice, resulting in many wetlands being occupied with growing food. The development of agriculture further accelerated hydraulic engineering construction projects, which interfered with the stability of the wetland ecosystem and aggravated the loss of wetland [29,30]. Although the above alleviated the degree of wetland reduction, there was still a clear trend of agricultural land encroaching on the wetland at the end of the 20th century. As shown in Figure 7, among the various types of wetlands, the main feature was the occupation of agricultural land by lakes. The reduced lakes area accounted for 54.73% of the wetland loss from agricultural land reclamation from 1990 to 2000. In addition, the lakes also showed a clear trend of net loss from 2010 to 2020. The occupation of marsh and beach by agricultural land in the first 10 years was also apparent, accounting for 42.56% and 39.86% of wetland loss, respectively.

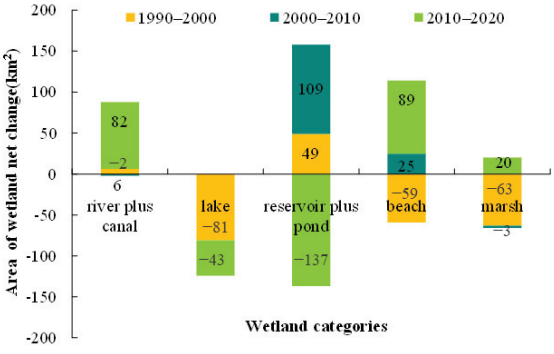

Figure 7. The net conversion area (km^2) of agricultural land and wetland from 1990 to 2020.

At the same time, some agricultural land adjustments led to an increase in wetlands. The area of reservoirs, ponds, and canals was restored under agricultural land conversion to a certain extent, showing an increasing trend. Wetlands such as reservoirs and canals with

the purpose for agriculture irrigation were mainly attributed to economic developments, and the results agreed with Gong et al. [13] and Xu et al. [17]. The main reason for the wetland loss was the transformation of natural wetlands to agricultural land and constructed wetlands.

At the end of the 20th century, the 1998 flood attracted the attention of the government and society. The analysis showed that the "flood of the century" in 1998 in the middle and lower reaches of the Yangtze River brought huge losses to people's lives and production. The State Council pointed out that the destruction of wetland ecological resources was an important cause of frequent flood disasters and further strengthened the implementation of returning agricultural land to wetland. At the same time, Premier Zhu Rongji proposed the "4350 Project" to restore the wetland area of Dongting Lake when he inspected Hunan Province. Consequently, the conservation and restoration of wetlands have risen to the country's strategic height to better realize wetland flood regulation and storage. Moreover, Dongting Lake National Nature Reserves have been established. The national and local governments issued a series of wetland protection and restoration policies [13], such as the National Wetland Conservation Action Plan in 2000 and the National Wetland Conservation Program (NWCP) (2002–2030) in 2003 [31]. In addition, the Ramsar Convention considered water regulation as an important impact factor for wetlands [17]. In addition, agricultural reclamation was an important driving factor for wetland reduction, and the differences in population trends and wetland conservation policies were primary contributors to wetland restoration. These results were consistent with Lu et al. [20].

In the 10 years at the beginning of the 21st century, the reduction in agricultural land resulted in a total restoration of 148 km^2 of wetland; thus, the effect of returning agricultural land to wetland was remarkable. Moreover, in the next 20 years, the total net gain in wetland showed an increasing tendency. However, the increase in wetlands from conservation efforts did not offset the human-caused wetland loss. Although the built-up and restoration promoted the increase in wetlands, high-quality wetlands were taken away and replaced with inferior wetlands whose ecosystem service function was affected [32]. The increased river plus canal may also cause the fragmentation and isolation of wetlands between rivers and lakes, affect hydrological connectivity, threaten aquatic organisms, and lead to the shrinkage and degradation of downstream wetlands [33]. For example, Japan has constructed many artificial wetlands, but 80% of the lakes have limited carrying capacity [34,35]. However, returning agricultural land to wetland has been helping to make up for the wetland losses, which is worthy of our favorable treatment.

At the beginning of the 21st century, our country established a wetland protection system such as the Dongting Lake wetland reserve at all levels and the National Wetland Park, promulgated the "Hunan Province Wetland Protection Regulations" and other legal provisions, and increased the ecological compensation standards for returning agricultural land to lake year by year. These measures have effectively promoted the restoration and stability of the wetland ecosystem.

4.3. Wetland Loss Due to Urbanization

Based on previous studies and the sixth IPCC report, the changes in wetlands were subjected to climate change and agriculture, as well as urbanization and socioeconomic factors (e.g., population, water demand, transportation, gross domestic product, and consumption patterns) and dietary structure [36,37]. With the rapid development of the social economy and the increase in China's population, most cities have experienced unprecedented expansion [38]. The urban population in China increased from 301.95 million in 1990 to 459.06 million in 2000, 669.78 million in 2010, and 902.2 million in 2020 (Figure 8), as well as the rapid growth of population and economy in Hunan Province, the main coverage area of the DLB. Therefore, human settlement, transportation, construction, and industrial development occupied many wetlands. At the same time, with the improvement in people's living standards, there was an increasing demand for the diversification of crop types and suburban agriculture developed, thus occupying part of the wetland.

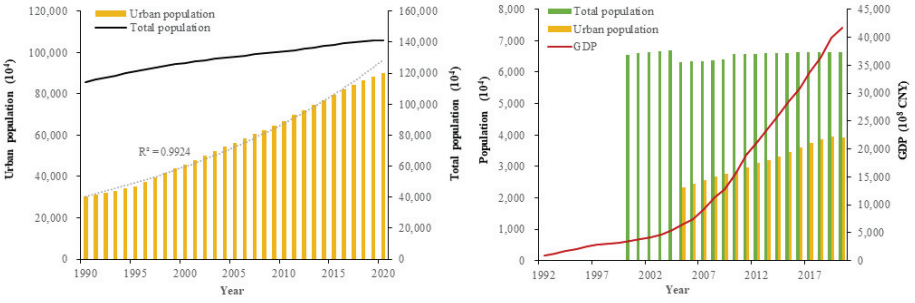

Figure 8. Demographic changes in China (**a**) and Hunan Province (**b**) from 1990 to 2020.

The expansion of built-up land was an important reason for decreasing wetlands (Figure 9). In the next 10 years, from 2000 to 2010, all types of wetlands showed a decreasing trend from built-up land. The loss of reservoir ponds was the most serious, followed by a decrease in marshes. Moreover, the number of canals decreased significantly, and the net change in other wetlands was small. The wetland change may also be affected by aquaculture development because the DLB is the land of fish and rice [17]. Moreover, aquaculture was a critical way to promote regional economic development while destroying the balance of the wetland ecosystem [20]. In this study, the lake area increased by 24 km^2 due to land conversion for construction, alleviating the degree of wetland reduction. This was probably related to the wetland protection policies and other land-conversion types that urban expansion may occupy rather than wetlands. At the same time, with the development of urbanization, the construction of urban landscapes also increased the area of lakes. From the perspective of ecosystem services, the created artificial wetlands could not compensate for and replace the lost natural wetlands [38]. Our country has been committed to rapid economic development since the reform and opening up. With the gradual increase in the number of people and the need to develop production, industrialization and urbanization intensified, resulting in part of the wetland occupied by built-up land. Lu et al. [39] pointed out that human disturbance had a profound impact on the role of wetland carbon sequestration, and the contradiction between people and the wetland remained to be resolved.

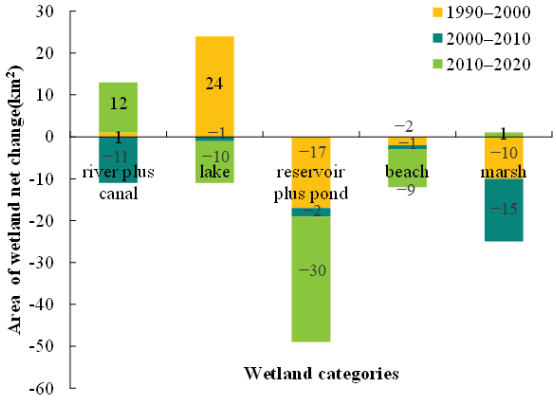

Figure 9. Net conversion of different built-up lands and wetlands in DLB from 1990 to 2020 (km^2).

4.4. Wetland Change Due to Other Factors

Climate change affected the spatial and temporal variability of wetlands in the basin through temperature, precipitation, evaporation, extreme events, etc. The IPCC published

climate change assessment reports in 1990, 1995, 2001, 2007, 2014, and 2021. All six reports noted that the current stage of global climate change was significantly stronger than the normal evolution of history, showing a clear warming trend. This changed the hydrological characteristics of the wetland, increased water consumption, and accelerated the conversion of wetlands to other land-use types [40,41]. In addition, precipitation variability could lead to changes in runoff and water levels, thus affecting the wetland area dynamics.

Under global climate warming, intense human activities greatly influenced the spatial and temporal patterns of wetlands in the basin. With the construction and operation of large water conservancy projects such as Gezhouba Dam and Three Gorges Dam, the river–lake relationship between Dongting Lake and the Yangtze River changed significantly [42], and the hydrological connectivity between rivers and lakes weakened obviously, which had a greater impact on the wetland ecological process and environment in the basin. On the one hand, the water level of the Yangtze River decreased when the Three Gorges Dam was storing water during the flood season, making its top-supporting effect on the water level of Dongting Lake weaker, thus leading to the lower water level in Dongting Lake, which adversely affected water resources and wetland loss in the basin [43]. On the other hand, the construction of water conservancy projects such as the Three Gorges played an important role in reducing the peak and replenishing the dryness, which was conducive to alleviating the flooding in the DLB, improving the hydrological environment for the stability of wetland ecosystems, which was one of the important factors for the increase in wetlands [44].

5. Conclusions

This paper mainly focused on revealing wetland temporal and spatial change characteristics and driving factors by using remote sensing monitoring data to devise the land-use-transfer matrix and calculate the contribution rate in the DLB from 1999 to 2020 at the turn of the century. This study can help understanding of the past changes in wetlands to guide the current work better and promote sustainable development in the future. There were many types of wetlands in the DLB. Temporally, the wetland area continued to increase from 1990 to 2020, with a significant increase in river plus canal (total 666 km^2) and decrease in lakes (total −463 km^2). Comparing the three decades, the growth rate of wetlands increased, with net increase proportions of 1.51%, 3.18%, and 3.32%, respectively. While the conversion frequency between wetlands and other land types decreased, changes stabilized. Spatially, wetlands in the DLB were mainly located in Hunan Province (more than 80%), with the most significant wetlands in Northern Hunan (approximately 70%). The net change in wetlands was inconsistent among subregions. Wetlands in Northern Hunan first decreased and then increased. Western Hunan showed a continuous increase, Central Hunan showed a remarkable net decrease later, and Eastern Hunan decreased in wetlands from 2010 to 2020.

The spatial–temporal change pattern of the wetland in the DLB resulted from the combined effect of human activities and natural factors. Human activities tended to have a more significant impact than climatic conditions in the short term, and their effects were more pronounced. From 1990 to 2020, forest land was a continuous wetland increase source, and agricultural land was a fundamental cause of wetland changes. It was mainly characterized by reclaiming land from lakes in the early stage, and it was mainly characterized by returning agricultural land to wetland later. The expansion of built-up land occupied part of the wetland, yet the total amount was not significant.

In the past 30 years, the wetland area in the DLB was effectively restored. However, due to the complexity and comprehensiveness of the wetland ecological environment, the task of wetland protection and sustainable development still has a long way to go.

Author Contributions: Methodology, Z.-M.Y. and L.-F.H.; resources, L.-F.H. and C.-H.L.; data curation and analysis, Z.-M.Y., Q.-P.L. and K.X.; writing—original draft, Z.-M.Y.; writing—review and editing, L.-F.H.; polish, Z.-M.Y. and Z.-Y.P.; supervision, L.-F.H. and C.-H.L. All authors have read and agreed to the published version of the manuscript.

Funding: This research was financially supported by the Natural Science Foundation of Hunan Province (2020JJ5361), Project of Education Department of Hunan Province (19A311), National Natural Science Foundation of China (52070023; 41807163), and the College students' innovation and entrepreneurship projects (2020109).

Institutional Review Board Statement: Not applicable.

Informed Consent Statement: Not applicable.

Data Availability Statement: The land-use remote sensing monitoring datasets used in the study are available in the Resource and Environment Science and Data Center (https://www.resdc.cn/, accessed on 8 May 2020). Other datasets used in the study are available in the National Bureau of Statistics (http://www.stats.gov.cn/, accessed on 20 February 2021). All data generated or analyzed during this study are included in this paper.

Acknowledgments: We would like to extend special thanks to the editor and the anonymous reviewers for their valuable comments in greatly improving the quality of this paper.

Conflicts of Interest: The authors declare no conflict of interest.

References

1. Hu, S.J.; Niu, Z.G.; Chen, Y.F.; Li, L.F.; Zhang, H.Y. Global wetlands: Potential distribution, wetland loss, and status. *Sci. Total Environ.* **2017**, *586*, 319–327. [CrossRef] [PubMed]
2. Jin, H.; Huang, C.; Lang, M.W.; Yeo, I.Y.; Stehman, S.V. Monitoring of wetland inundation dynamics in the Delmarva Peninsula using Landsat time-series imagery from 1985 to 2011. *Remote Sens. Environ.* **2017**, *190*, 626–641. [CrossRef]
3. D'Odorico, P.; Davis, K.F.; Rosa, L.; Carr, J.A.; Chiarelli, D.; Dell'Angelo, J.; Gephart, J.; MacDonald, G.K.; Seekell, D.A.; Suweis, S.; et al. The global food-energy-water nexus. *Rev. Geophys.* **2018**, *56*, 456–531. [CrossRef]
4. Yang, Q.; Liu, G.; Casazza, M.; Hao, Y.; Giannetti, B.F. Emergy-based accounting method for aquatic ecosystem services valuation: A case of China. *J. Clean. Prod.* **2019**, *230*, 55–68. [CrossRef]
5. Costanza, R.; D'Arge, R.; Groot, R.D.; Farber, S.; Grasso, M.; Hannon, B.; Limburg, K.; Naeem, S.; O'Neill, R.V.; Paruelo, J.; et al. The value of the world' 's ecosystem services and natural capital. *World Environ.* **1997**, *25*, 3–15.
6. Sinclair, M.; Ghermandi, A.; Moses, S.A.; Joseph, S. Recreation and environmental quality of tropical wetlands: A social media based spatial analysis. *Tour. Manag.* **2019**, *71*, 179–186. [CrossRef]
7. Amler, E.; Schmidt, M.; Menz, G. Definitions and mapping of east African wetlands: A review. *Remote Sens.* **2015**, *7*, 5256–5282. [CrossRef]
8. Sica, Y.V.; Quintana, R.D.; Radeloff, V.C.; Gavier-Pizarro, G.I. Wetland loss due to land use change in the Lower Paraná River Delta, Argentina. *Sci. Total Environ.* **2016**, *568*, 967–978. [CrossRef] [PubMed]
9. Serran, J.N.; Creed, I.F.; Ameli, A.A.; Aldred, D.A. Estimating rates of wetland loss using power-law functions. *Wetlands* **2018**, *38*, 109–120. [CrossRef]
10. Bian, H.; Li, W.; Li, Y.; Ren, B.; Niu, Y.; Zeng, Z. Driving forces of changes in China' 's wetland area from the first (1999–2001) to second (2009–2011) National Inventory of Wetland Resources. *Glob. Ecol. Conserv.* **2020**, *21*, e00867. [CrossRef]
11. Cardner, R.C.; Barchiesi, S.; Beltrame, C.; Finlayson, C.; Galewski, T.; Harrison, I.; Paganini, M.; Perennou, C.; Pritchard, D.; Rosenqvist, A.; et al. *State of the World's Wetlands and Their Services to People: A Compilation of Recent Analyses*; Ramsar Briefing Note No. 7; Ramsar Convention Secretariat: Gland, Switzerland, 2015.
12. Davidson, N.C. How much wetland has the world lost? Long-term and recent trends in global wetland area. *Mar. Freshw. Res.* **2014**, *65*, 936–941. [CrossRef]
13. Gong, P.; Niu, Z.; Cheng, X.; Zhao, K.; Zhou, D.; Guo, J.; Liang, L.; Wang, X.; Li, D.; Huang, H.; et al. China' 's wetland change (1990–2000) determined by remote sensing. *Sci. China Earth Sci.* **2010**, *53*, 1036–1042. [CrossRef]
14. Chen, Y.M.; Liu, T.Q.; Huang, Y.; Yang, J.; Li, X.L.; Xiao, Z.H. Remote sensing research of wetland current status and change in the Yangze River Basin. *Resour. Environ. Yangtze Basin* **2014**, *23*, 801–808. (In Chinese)
15. Cyranoski, D. Putting China's wetlands on the map. *Nature* **2009**, *458*, 134. [CrossRef] [PubMed]
16. Tong, L.; Xu, X.; Fu, Y.; Li, S. Wetland changes and their responses to climate change in the "three-river headwaters" region of China since the 1990s. *Energies* **2014**, *7*, 2515–2534. [CrossRef]
17. Xu, W.H.; Fan, X.Y.; Ma, J.G.; Stuart, L.P.; Kong, L.Q.; Zeng, Y.; Li, X.S.; Xiao, Y.; Zheng, H.; Liu, J.G.; et al. *Hidden Loss of Wetlands in China*; Elsevier Ltd.: Amsterdam, The Netherlands, 2019; Volume 29, pp. 3065–3071.
18. Gemechu, G.F.; Rui, X.; Lu, H. Wetland Change Mapping Using Machine Learning Algorithms, and Their Link with Climate Variation and Economic Growth: A Case Study of Guangling County, China. *Sustainability* **2021**, *14*, 439. [CrossRef]
19. Gong, N.; Niu, Z.G.; Qi, W.; Zhang, H.Y. Driving forces of wetland change in China. *J. Remote Sens.* **2016**, *20*, 172–183. (In Chinese)
20. Lu, C.; Ren, C.; Wang, Z.; Zhang, B.; Man, W.; Yu, H.; Gao, Y.; Liu, M. Monitoring and assessment of wetland loss and fragmentation in the Cross-boundary Protected Area: A case study of Wusuli River Basin. *Remote Sens.* **2019**, *11*, 2581. [CrossRef]

21. Zhao, S.; Fang, J.; Miao, S.; Gu, B.; Tao, S.; Peng, C.; Tang, Z. The 7-decade degradation of a large freshwater lake in Central Yangtze River, China. *Environ. Sci. Technol.* **2005**, *39*, 431–436. [CrossRef]
22. Mao, D.H.; Wang, Z.M.; Du, B.J.; Li, L.; Tian, Y.L.; Jia, M.M.; Zeng, Y.; Song, K.S.; Jiang, M.; Wang, Y.Q. National wetland mapping in China: A new product resulting from object-based and hierarchical classification of Landsat 8 OLI images. *ISPRS J. Photogramm. Remote Sens.* **2020**, *164*, 11–25. [CrossRef]
23. Wu, Y.F.; Zhang, G.X.; Rousseau, A.N. Quantitative assessment on watershed-scale hydrological services of wetlands. *Sci. China Earth Sci.* **2020**, *50*, 281–294. (In Chinese)
24. Liu, J.Y.; Kuang, W.H.; Zhang, Z.X.; Xu, X.L.; Qin, Y.W.; Ning, J.; Zhou, W.C.; Zhang, S.W.; Li, R.D.; Yan, C.Z.; et al. Spatiotemporal characteristics, patterns, and causes of land-use changes in China since the late 1980s. *J. Geogr. Sci.* **2014**, *69*, 3–14. (In Chinese) [CrossRef]
25. Liu, M.L.; Tang, X.M.; Liu, J.Y.; Zhuang, D.F. Research on scaling effect based on 1 km grid cell date. *J. Remote Sens.* **2001**, *3*, 183–190. (In Chinese)
26. Yimam, A.Y.; Assefa, T.T.; Sishu, F.K.; Tilahun, S.A.; Reyes, M.R.; Prasad, P.V. Estimating Surface and Groundwater Irrigation Potential under Different Conservation Agricultural Practices and Irrigation Systems in the Ethiopian Highlands. *Water* **2021**, *13*, 1645. [CrossRef]
27. López-Senespleda, E.; Calama, R.; Ruiz-Peinado, R. Estimating forest floor carbon stocks in woodland formations in Spain. *Sci. Total Environ.* **2021**, *788*, 147734. [CrossRef]
28. Grumbine, R.E. Assessing environmental security in China. *Front. Ecol. Environ.* **2014**, *12*, 403–411. [CrossRef]
29. Mao, D.H.; Luo, L.; Wang, Z.M.; Wilson, M.C.; Zeng, Y.; Wu, B.F.; Wu, J.G. Conversions between natural wetlands and farmland in China: A multiscale geospatial analysis. *Sci. Total Environ.* **2018**, *634*, 550–560. [CrossRef] [PubMed]
30. Lu, C.Y.; Wang, Z.M.; Li, L.; Wu, P.Z.; Mao, D.H.; Jia, M.M.; Dong, Z.Y. Assessing the conservation effectiveness of wetland protected areas in Northeast China. *Wetl. Ecol. Manag.* **2016**, *24*, 381–398. [CrossRef]
31. Wang, Z.; Wu, J.; Madden, M.; Mao, D. China's wetlands: Conservation plans and policy impacts. *Ambio* **2012**, *41*, 782–786. [CrossRef]
32. Wong, C.P.; Jiang, B.; Bohn, T.J.; Lee, K.N.; Lettenmaier, D.P.; Ma, D.; Ouyang, Z. Lake and wetland ecosystem services measuring water storage and local climate regulation. *Water Res.* **2017**, *53*, 3197–3223. [CrossRef]
33. Liu, D.; Wang, J.; Li, C.H.; Cai, Y.P.; Liu, Q. Research Progress on the impact of hydrological connectivity on lake ecological environment. *Resour. Environ. Yangtze Basin* **2019**, *28*, 1702–1715. (In Chinese)
34. Xu, T.; Weng, B.; Yan, D.; Wang, K.; Li, X.; Bi, W.; Li, M.; Cheng, X.; Liu, Y. Wetlands of international importance: Status, threats, and future protection. *Int. J. Environ.* **2019**, *16*, 1818. [CrossRef] [PubMed]
35. Yoshimura, C.; Omura, T.; Furumai, H.; Tockner, K. Present state of rivers and streams in Japan. *River Res. Appl.* **2005**, *21*, 93–112. [CrossRef]
36. Alexander, P.; Rounsevell, M.D.A.; Dislich, C.; Dodson, J.R.; Engström, K.; Moran, D. Drivers for global agricultural land use change: The nexus of diet, population, yield and bioenergy. *Glob. Environ. Chang.* **2015**, *35*, 138–147. [CrossRef]
37. Han, L.; Xu, Y.; Lei, C.; Yang, L.; Deng, X.; Hu, C.; Xu, G. Degrading river network due to urbanization in Yangtze River Delta. *J. Geogr. Sci.* **2016**, *26*, 694–706. [CrossRef]
38. Yu, W.; Zang, S.; Wu, C.; Liu, W.; Na, X. Analyzing and modeling land use land cover change (LUCC) in the Daqing City, China. *Appl. Geogr.* **2011**, *31*, 600–608. [CrossRef]
39. Lu, M.Z.; Zou, Y.C.; Xun, Q.L.; Yu, Z.C.; Jiang, M.; Sheng, L.X.; Lu, X.G.; Wang, D.L. Anthropogenic disturbances caused declines in the wetland area and carbon pool in China during the last four decades. *Glob. Chang. Biol.* **2021**, *27*, 3837–3845. [CrossRef] [PubMed]
40. Wang, G.J.; Jiang, T.; Wang, Y.J.; Yu, Z.Y. Characteristics of climate change in Dongting Lake Basin (1961–2003). *J. Lake Sci.* **2006**, *5*, 470–475. (In Chinese)
41. Ahmad, Q.U.A.; Biemans, H.; Moors, E.; Shaheen, N.; Masih, I. The Impacts of Climate Variability on Crop Yields and Irrigation Water Demand in South Asia. *Water* **2021**, *13*, 50. [CrossRef]
42. Yang, M.; Mao, D.H.; Liu, P.L.; Liu, W. Quantitative assessment on influence of runoff and sediment evolution of Dongting Lake and human activities to the runoff in the period of 1951–2015. *Sci. Soil Water Conserv.* **2019**, *1*, 38–43+69. (In Chinese)
43. Xie, Y.H.; Tang, Y.; Chen, X.S.; Li, F.; Deng, Z. The impact of Three Gorges Dam on the downstream eco-hydrological environment and vegetation distribution of East Dongting Lake. *Ecohydrology* **2015**, *8*, 738–746. [CrossRef]
44. Zhou, H.; Mao, D.H.; Liu, P.L. The investigation on water lever of east Dongting Lake affected by Three-Gorge reservoir. *Trans. Oceanol. Limnol.* **2014**, *4*, 180–186. (In Chinese)

remote sensing

MDPI

Technical Note

QDA-System: A Cloud-Based System for Monitoring Water Quality in Brazilian Hydroelectric Reservoirs from Space

Marcelo Curtarelli *, Edmar Neto, Fanny de Siqueira, Felipe Yopan, Gilmar Soares, Gilnei Pauli, João de Souza, Luana Silva, Marcio Sagaz, Miguel Demay, Natália Bortolas, Ricardo Yoshimura and Vitor Guimarães

Fundação CERTI, Florianópolis 88040-970, Brazil; ept@certi.org.br (E.N.); fcs@certi.org.br (F.d.S.); fsy@certi.org.br (F.Y.); ggs@certi.org.br (G.S.); gui@certi.org.br (G.P.); jhb@certi.org.br (J.d.S.); ldv@certi.org.br (L.S.); msg@certi.org.br (M.S.); mbd@certi.org.br (M.D.); nob@certi.org.br (N.B.); rsy@certi.org.br (R.Y.); vsg@certi.org.br (V.G.)

* Correspondence: mei@certi.og.br

Abstract: This article presents the QDA-System (*Sistema Qualidade da Água*, from Portuguese), a system developed to monitor the quality of surface waters in Brazilian hydroelectric reservoirs using satellite images and cloud computing services. The development requirements of the QDA-System considered its use for operational monitoring purposes, with all processing steps automated, and a user-friendly interface to access and query the data generated automatically by the system. A pilot application of the QDA-System was customized and implemented for monitoring the Foz do Chapecó hydroelectric reservoir located in southern Brazil. For the pilot application, the QDA-System was customized to estimate nine water quality parameters,: five were estimated directly from Sentinel-2 multispectral images and four were estimated indirectly. We expect that in the near future the QDA-System can be replicated to monitor other Brazilian reservoirs, bringing benefits and cost reduction related to water quality monitoring, not only for the sector of hydroelectric generation but for other sectors that also need similar monitoring, such as sanitation and aquaculture production.

Keywords: cloud computing; satellite images; bio-optical modeling; reservoirs; lakes

Citation: Curtarelli, M.; Neto, E.; de Siqueira, F.; Yopan, F.; Soares, G.; Pauli, G.; de Souza, J.; Silva, L.; Sagaz, M.; Demay, M.; et al. QDA-System: A Cloud-Based System for Monitoring Water Quality in Brazilian Hydroelectric Reservoirs from Space. *Remote Sens.* **2022**, *14*, 1541. https://doi.org/10.3390/rs14071541

Academic Editor: Teodosio Lacava

Received: 23 February 2022
Accepted: 22 March 2022
Published: 23 March 2022

1. Introduction

The use of remote sensing images for the study of inland water bodies dates back to the 1970s, initially focusing on the development of local models with temporally limited studies [1]. Over the last 50 years, the development of information and image collection technologies has allowed great advances in the field of remote sensing of water, such as the study of multiple parameters [2], the development and the improvement of different approaches for bio-optical modeling [3], the expansion of the temporal and spatial scales of analysis [1], and born of monitoring initiatives such as Satellite earth observations for lake monitoring (OLakeWatch) [4] in Canada and the Cyanobacteria Assessment Network (CyAN) in the USA [5]. All of these advances in terms of basic and applied research have paved the way for us to move forward in the innovation chain through the pilot development of an automatic system for monitoring water quality parameters from space.

Recently, some solutions were developed that combine the use of remote sensing data and cloud computing for the monitoring and the forecasting of different environmental issues. As examples of solutions presented in the literature, we can mention a cloud-based flood warning system [6], a cloud-based system to monitor land use and land cover [7], and an algal bloom alert system [8]. The main advantages of this approach are the use of cloud computing power to process large amounts of data and the absence of a need to download the data to a local server.

Taking into account the need to modernize and to expand the monitoring capacity of Brazilian hydroelectric reservoirs, the CERTI Foundation conducted the Research and

Development (R&D) project "00642-2705/2019-Development of a system for remote monitoring of water quality in water reservoirs based on multispectral images," financed by the Brazilian Electric Energy Agency (ANEEL), with the main objective of developing a system based on cloud computing technology for monitoring inland water bodies. This article aims to present the developed system and its pilot application for monitoring the surface water of the Foz do Chapecó hydroelectric plant reservoir in southern Brazil.

2. QDA-System Design and Development

The monitoring system (hereafter called the QDA-System) was designed using state of the art cloud computing and remote sensing techniques applied to inland water monitoring and bio-optical modeling [3]. The QDA-System was developed to routinely monitor surface water quality in lakes and reservoirs using satellite images and auxiliary data (e.g., residence time, bathymetry, and in situ parameters), allowing the emission of alerts considering rules and thresholds predefined by users. The system was developed in the Python programming language using different computing and cloud storage services offered by Amazon Web Services (AWS), but it can also be deployed and run in other commercial clouds (e.g., Google Cloud or Microsoft® Azure Cloud). For its development, the following requirements were considered:

1. Operational monitoring: A systematic and routine provision of information of various water quality parameters;
2. Automated processing: Achieved without the need for interactions or processing performed by system operators;
3. Customizable: The capacity to use multiple image sources (e.g., Sentinel-2 MSI, Landsat-8 OLI, Planet®) and implementation of different types of water quality models according to site-specific needs;
4. Scalable: The capacity to be easily replicated and parameterized for different water bodies;
5. User-friendly interface with different access levels: developed for accessing via an intuitive web interface, with different access levels, considering specific needs.

Digital Image Processing, Bio-Optical Modeling, and Water Quality Index Computation

The main digital image processing tasks implemented in the pilot version of the QDA-System includes: (1) mosaic images of different tiles (if necessary); (2) resample band images to the same pixel size; (3) the application of scale factors to convert digital number to surface reflectance value; (4) applying a water mask over the target area; and (5) creating and applying a cloud or shadow mask.

The QDA-System supports the implementation of empirical and semi-empirical bio-optical models to estimate optically active and inactive parameters [2,3]. The optically active parameters are those related to the Optically Active Constituents (OAC) that are responsible for the absorption and scattering of electromagnetic energy in the water column and directly related to the satellite measurements. On the other hand, the optically inactive parameters do not interfere in the underwater light field; consequently, they cannot be directly related to measurements taken by satellites. Even so, they can be obtained indirectly from relationships with optically active parameters [2].

The QDA-System also supports the computation of water quality indexes based on estimated parameters combined with in situ measurements that can be entered into the system using spreadsheets. Figure 1 shows the workflow of processing tasks and water quality parameters developed for the first version of the QDA-System based on the use of MSI Sentinel-2 images (detailed in Section 3.2.2).

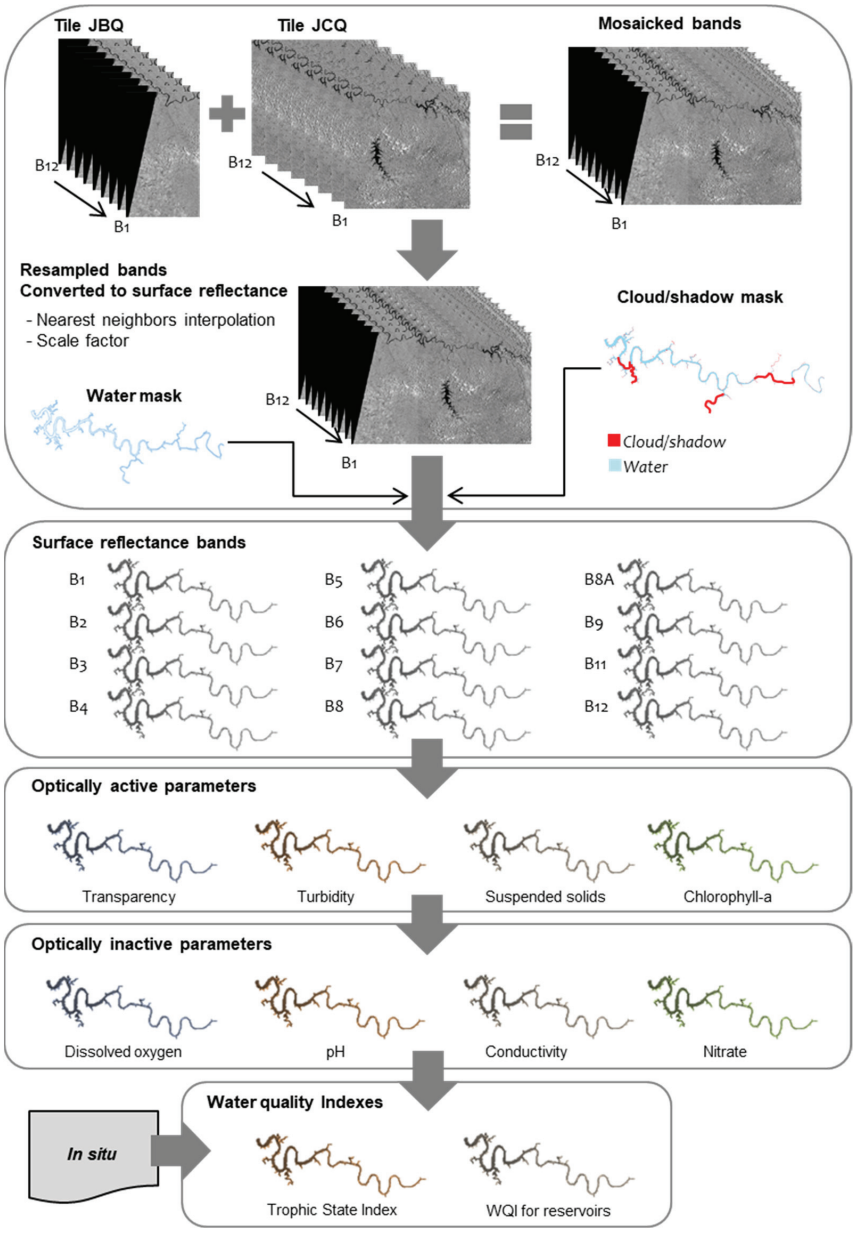

Figure 1. Workflow of processing tasks and water quality parameter retrieval implemented in the QDA-System: example from pilot case. B1 to B12 refers to Sentinel-2 MSI multispectral bands.

3. Study Case—Foz do Chapecó Reservoir

3.1. Site Description

A pilot version of the QDA-System was implemented to monitor the surface water quality of the Foz do Chapecó Hydroelectric Reservoir (FCHR) located in southern Brazil near the city of Chapecó (Figure 2). The FCHR has a latitudinal elongated shape with 79 km^2 of surface area and a mean depth of 18.8 m, covering the area of 12 municipalities [9].

Besides energy production, the FCHR has other uses, such as domestic water supply, irrigation, recreation, fishing, and navigation [10].

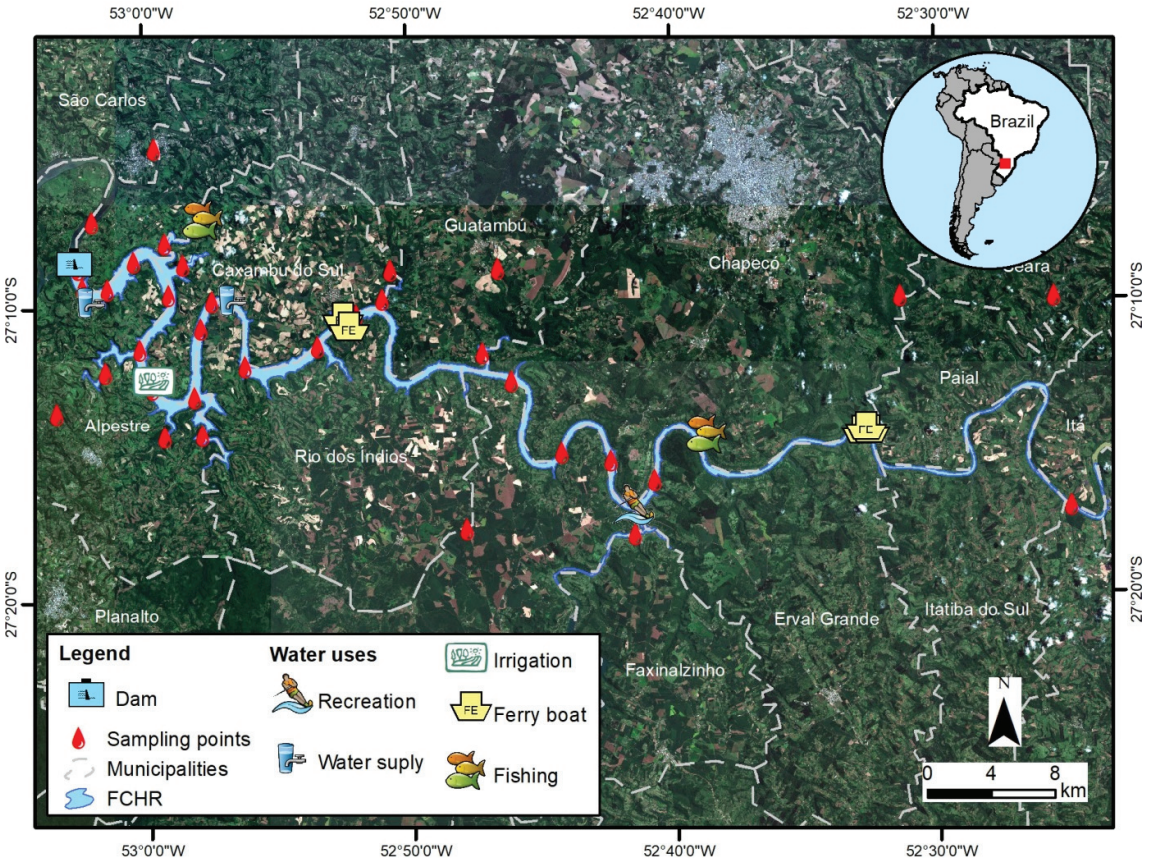

Figure 2. Pilot area location and settings.

3.2. Selected Parameters and Available Dataset

For the pilot application, a set of nine water quality parameters were previously selected, five of which were obtained directly from satellite images (optically active) and four that were obtained indirectly (optically inactive):

1. Optically active: (1) Chlorophyll-*a* (Chla-*a*); (2) Floating macrophytes; (3) Total of Suspended Solids (TSS); (4) Turbidity; and (5) Water transparency (Secchi Disk Depth—SDD);
2. Optically inactive: (1) Conductivity; (2) Dissolved oxygen (DO); (3) Nitrate; and (4) pH.

The dataset available for model calibration and validation included 178 water samples collected during 11 campaigns (see locations in Figure 1), distributed between February 2019 and May 2021, covering all phases of the hydrological cycle and the different operational conditions of the FCHR (Table 1). All campaigns had concurrent passages of Sentinel-2 satellites.

Table 1. Summary of calibration and validation dataset available for FCHR.

Field Campaign	Data	Image Acquisition	Sampling Points
1	22 February 2019	22 February 2019	14
2	18 April 2019	18 April 2019	14
3	8 August 2019	6 August 2019	14
4	11 October 2019	10 October 2019	17
5	20 December 2019	19 December 2019	17
6	12 February 2020	12 February 2020	18
7	12 February 2020	10 February 2020 and 12 February 2020	17
8	27 May 2020	25 May 2020 and 27 May 2020	18
9	23 November 2020	23 November 2020	18
10	10 December 2020	8 December 2020	13
11	27 May 2021	27 May 2021	18

3.2.1. In Situ Data

The water sample collections were conducted by *Aquaeris Engenharia e Soluções Ambientais* LTDA, a third-party company specializing in this type of service. All the field surveys followed the specification and the protocols presented in the Brazilian guide for collection and preservation of samples [11]. Conductivity, dissolved oxygen, pH, and turbidity were measured using a multiparameter probe (Akso www.akso.com.br (accessed on 4 January 2022), model AK88). The water transparency was measured using a Secchi disk. The remaining parameters were analyzed in the laboratory following the Standard Methods for the Examination of Water and Wastewater (SMEWW) [12] and U.S. Environmental Protection Agency [13] procedures.

3.2.2. Satellite Images

The Sentinel-2 mission was chosen for the pilot application [14]. The mission consisted of two satellites, Sentinel-2A and Sentinel-2B, both carrying the Multispectral Instrument (MSI). The joint use of the 2 satellites allowed the acquisition of 73 images of the complete reservoir throughout the year (1 image every 5 days), with spatial resolution ranging from 10 to 60 m depending on the spectral band. The product chosen for the application was the level 2A satellite which provided systematic surface reflectance ortho-images (more information about the 2A algorithm is available at: https://earth.esa.int/web/sentinel/technical-guides/sentinel-2-msi/level-2a/algorithm (accessed on 4 January 2022)).

For this pilot application, the QDA-System was configured to access the Copernicus Open Access Hub (https://scihub.copernicus.eu/ (accessed on 3 January 2022)) using the application programming interface (API) and to download the images to be processed by the QDA-System.

3.3. Model Calibration and Validation

For each modeled water quality parameter, the available dataset was analyzed individually in order to remove samples with values lower than the limit of quantification and detection, outliers and samples located in pixels covered by cloud or shadows, or with low quality. The sample points considered valid for a given parameter were split into two subsets: one was used for model calibration (between 60 and 70% of valid points) and the other was used for model validation (between 30 and 40% of valid points).

The model calibration was performed through adjustments using an ordinary least squares regression method. For the optically active parameter (except for floating macrophytes), we tested different univariate models (empirical and semi-empirical) and different types of adjustments (linear, polynomial, exponential, and power), resulting in more than

1200 regression analyses. For the optically inactive parameters, we tested empirical univariate models relating them to the optically active parameters, resulting in more than 1000 regression analyses. The criteria used to select the best calibrated model for each parameter were the *p*-value and the coefficient of determination (R^2).

The model validation was conducted using the validation subset and the metrics presented by [15] that compare the values estimated by the calibrated models to the in situ measurements:

$$R^2 = 1 - \left(\frac{SS_{res}}{SS_{tot}}\right)$$

where SS_{res} is the residual sum of squares and SS_{tot} is the total sum of squares.

$$MAD = \frac{\sum_{i=1}^{n}|y_i - \overline{y_i}|}{n}$$

where MAD is the mean absolute deviation, y_i is the observed value, $\overline{y_i}$ is the predicted value, and n is the sample size.

$$MSE = \frac{\sum_{i=1}^{n}(y_i - \overline{y_i})^2}{n}$$

where MSE is the mean squared error.

$$RMSE = \sqrt{\frac{\sum_{i=1}^{n}(y_i - \overline{y_i})^2}{n}}$$

where RMSE is the root mean squared error.

$$MAPE = \frac{\sum_{i=1}^{n}\left|\frac{y_i - \overline{y_i}}{y_i}\right|}{n} \times 100$$

where MAPE is the mean absolute percentage error (%).

After the validation procedure, the model with best performance for each parameter was configured in the QDA-System.

Floating Macrophytes

The automatic detection of floating macrophytes is performed by applying thresholds and histogram slicing on a Vegetation Index (VI), which is widely used in the literature. For the pilot application, 4 VI were tested: (1) the Normalized Difference Vegetation Index (NDVI) [16], (2) the Enhanced Vegetation Index (EVI) [17], (3) the Normalized Difference Aquatic Vegetation Index (NDAVI) [18] and (4) the Water Adjusted Vegetation Index (WAVI) [19]. The best VI and threshold to detect floating macrophytes was defined empirically, by comparing values extracted from seven selected images where floating macrophytes were clearly visible. The performance of the VIs and thresholds used to detect floating macrophytes were evaluated based on the superposition of the manually vectored areas and the areas obtained automatically. In addition to the visual assessment, the area automatically mapped and manually obtained for the different macrophyte polygons were compared and the validation metrics were calculated for performance evaluation.

4. Results

4.1. System Overview

The QDA-System architecture (Figure 3) was defined taking into account the concept of micro services. The application was developed considering small services or independent modules that act together to provide system functionalities, communicating with each other through APIs. The main advantages of this approach are that it is highly scalable and easy to develop in the cloud. From a development point of view, it allows parallel development, making the production process and bug fixing more agile.

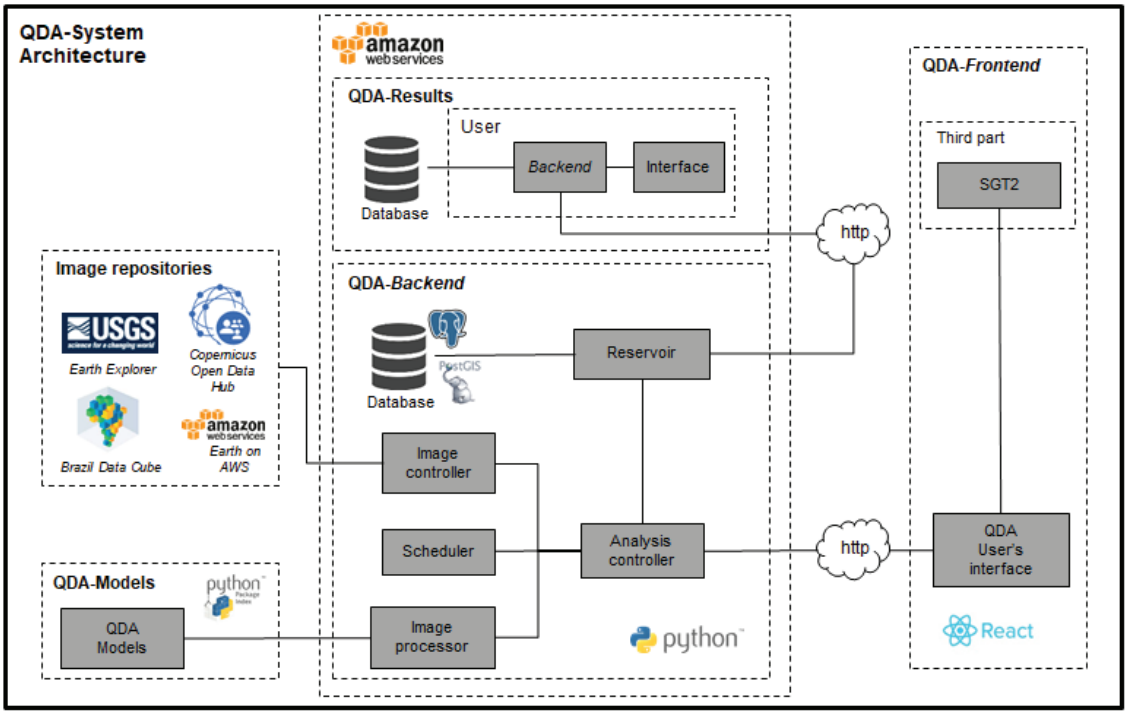

Figure 3. QDA-System architecture.

The architecture of the QDA-System is comprised of substructures each with its respective modules, as described below:

1. QDA-Results: substructure comprised of a backend and a frontend (with Graphics User Interface) so that system users can upload auxiliary data to the system;
2. QDA-Models: this substructure is a module, which has become a public domain project. It has the implementation of bio-optical models found in the literature to assess water quality through the analysis of satellite images. It can be accessed from the Python Package Index (PyPI) package repository https://pypi.org/project/qda-modelos/ (accessed on 5 January 2022);
3. QDA-Backend: substructure comprised of different modules:
    - Analysis controller: It is activated by the scheduler module and it performs the verification and the obtainment of data present in the reservoir module. It performs the described analysis and it manages the image processing modules;
    - Image processor: It performs the pre-processing of images, uses the module imported from the QDA-Models to estimate the parameters, and it manages the life cycle of an execution;
    - Image controller: It abstracts the image source and it stores and retrieves preprocessed images (if necessary);
    - Reservoirs: This is the module for registering a reservoir;
    - Scheduler: It is responsible for activating the analysis controller module and keeping a schedule of executions.
4. QDA-Frontend: This is a frontend substructure responsible for communicating with the backend and for showing the user a graphical interface based on React technology (https://reactjs.org/ (accessed on 20 December 2021)). It is user-friendly and it is easy to interpret when checking the data processed by the system.

4.2. System Interface

The pilot version of the QDA-System interface allows the user access to three views of the monitored water body: (1) dashboard view; (2) alerts view; and (3) analysis view.

The dashboard view allows the user to visualize the current information generated using the last image acquired, with the visualization being segmented by the sub-area of the monitored water body. The screen displays the generated alerts, a water quality map, and a table with a summary of monitored parameters and their trends (worsening, stable, or improving). It also shows the date of the last image processed and its percentage of invalid pixels due to the presence of clouds or shadows.

The alerts view allows the user to view and to manage the alerts generated for the parameters of interest. In this view, it is possible to filter alerts by reservoir sub-area, parameter of interest, period or date, and alert status (recognized and unrecognized). Alerts are displayed with their spatial distribution on the reservoir map, and they are also summarized in a list and a table form. The alerts automatically generated by the QDA-System can be recognized by the user.

The analysis view allows the user to access different functionalities such as querying the space–time history of monitored parameters and indices through thematic maps and time series graphs displayed on the screen, viewing additional layers such as in situ sampling points and points with other uses (e.g., recreation, catchment for public water supply, irrigation), and areas covered by floating macrophytes.

4.3. Pilot Application

4.3.1. Model Calibration

The model calibration was considered satisfactory for the nine water quality parameters selected for the pilot application of the QDA-System (Table 2). The models derived directly from satellite images (optically active parameters) showed results that are corroborated by the literature [3], being the models with the best performance for SDD, TSS, and turbidity based on single band relation (red band corrected for sun glint effect). For the Chl-*a* concentration, the model with the best fit was based on a polynomial relation with the Normalized Difference Chlorophyll Index (NDCI) [20]. The R^2 values obtained for optically active parameter models were higher than those reported in the literature [15], highlighting the turbidity model that showed excellent calibration performance (R^2 = 0.94).

Table 2. Summary of model calibration.

Parameter	Unit	*n*	R^2	Model with Best Calibration Performance
Chl-*a*	µg/L	29	0.89	$Y = 229.95NDCI^2 + 122.58NDCI + 19.964$
SDD	m	62	0.83	$Y = 1.407Ln(B4_{corr}) - 3.1782$
TSS	mg/L	22	0.73	$Y = 3.9215e^{(66.727B4_{corr})}$
Turbidity	NTU	62	0.94	$Y = 9459.9B4_{corr}^2 - 238.53B4_{corr} + 6.0006$
Conductivity	µS/cm	48	0.46	$Y = 1.0144SST + 17.075$
DO	mg/L	30	0.50	$Y = 16.213\left(\frac{1}{SDD}\right)^2 - 3.669\left(\frac{1}{SDD}\right) + 6.861$
Nitrate	mg/L	33	0.69	$Y = 0.205Turibidity + 1.6134$
pH	-	99	0.11	$Y = 0.0073Conductivity + 6.5858$

$B4_{corr}$ refers to Sentinel-2 B4 images corrected for the sun glint effects. The glint effect was removed by subtracting the values of B11 (short wave infrared) from B4 (red) values [21].

As expected the models derived indirectly from satellite images (optically inactive parameters) showed lower performance than the models derived directly, with R^2 values between 0.11 and 0.69. The best calibration performances were obtained for nitrate (R^2 = 0.69) and DO (R^2 = 0.50) parameters. The nitrate model was based on a linear relation with SST, whereas the DO model was based on a polynomial relation with the inverse of

SDD. The electric conductivity and pH models showed the poorest performance during the calibration procedure.

For the detection of floating macrophytes, the model with the best performance during the calibration procedure was based on NDAVI using a detection threshold equal to 0 (R^2 = 0.99). In this case, NDAVI values higher than zero are considered floating macrophytes whereas values equal to or less than zero are considered water.

4.3.2. Model Validation

Regarding the models obtained directly from satellite images, the results of validation (Table 3) indicate an excellent performance of the adjusted model for the estimation of turbidity, showing a strong agreement between the estimated and observed values (R^2 = 0.87), low absolute mean deviation (MAD = 2.87 NTU) and low RMSE (3.05 NTU). The turbidity model adjusted for the FCHR performed better than those presented in other studies (except for the MAPE validation metric), even when compared with more sophisticated models based on neural networks [15].

Table 3. Summary of model validation.

Parameter	*n*	R^2	MAD	MSE	RMSE	MAPE
Floating macrophytes	18	0.99	-	-	0.77	10.13
Chl-*a*	15	0.00	1.670	4.51	2.12	60.00
SDD	49	0.49	0.83	1.00	1.00	50.31
TSS	10	0.70	17.89	401.48	20.04	43.47
Turbidity	47	0.87	2.87	9.33	3.05	125.16
Conductivity	20	0.11	7.52	136.70	11.69	20.51
DO	44	0.10	0.67	1.05	1.02	9.35
Nitrate	14	0.51	0.253	0.095	0.307	11.64
pH	43	0.11	0.611	0.472	0.687	7.892

The adjusted models for estimation of SDD and TSS showed a low performance compared to the turbidity model, but they were also considered very satisfactory. The model for water transparency presented a MAD of 0.83 m and an RMSE of 1 m, whereas the model for TSS presented a MAD of 17.89 mg/L and an RMSE of 20.04 mg/L.

In turn, for the adjusted model to estimate chlorophyll-*a* concentration, the validation results indicated a weak agreement between the estimated and the observed values (R^2 < 0.01). The analysis of the errors obtained with the model adjusted to estimate chlorophyll-*a* concentration showed results considered favorable compared to those presented in the literature [15], with a MAD of 1.84 μg/L and an RMSE of 2.23 μg/L. The historical data from water quality monitoring indicated low concentrations of chlorophyll-*a* in the reservoir, and in 73% of the samples collected between June/2015 and February/2021 the result obtained in the laboratory was less than the quantification limit (1 μg/L).

For the parameters obtained indirectly from images, the best validation performance was obtained for the nitrate model, with low error metrics (e.g., RMSE = 0.3 mg/L) and moderate agreement between the estimated and the observed values (R^2 = 0.51). The DO and pH models also presented low errors but a weak agreement between the estimated and the observed values (R^2 = 0.11). Finally, the model to estimate electric conductivity of water exhibited the poorest performance with a MAPE close to 20% and a weak agreement between the estimated and the observed values (R^2 = 0.10)

The model adjusted to detect floating macrophytes showed a favorable validation performance, with high agreement between detected and vectorized values (R^2 = 0.99) and a MAPE near 10% (0.77 hectares).

4.3.3. User's Interface and Data Access

Figures 4–6 show the three different views developed to access and to query the data through the user's interface of the QDA-System: (1) dashboard view, (2) alert view and (3) analysis view. The dashboard view developed for the pilot application (Figure 4) shows the actual status of the FCHR water quality based on the last MSI image processed by the system. In this case, the information is presented for three different reservoir sectors predefined for the FCHR: "Barramento," "Central," and "Cabeceira".

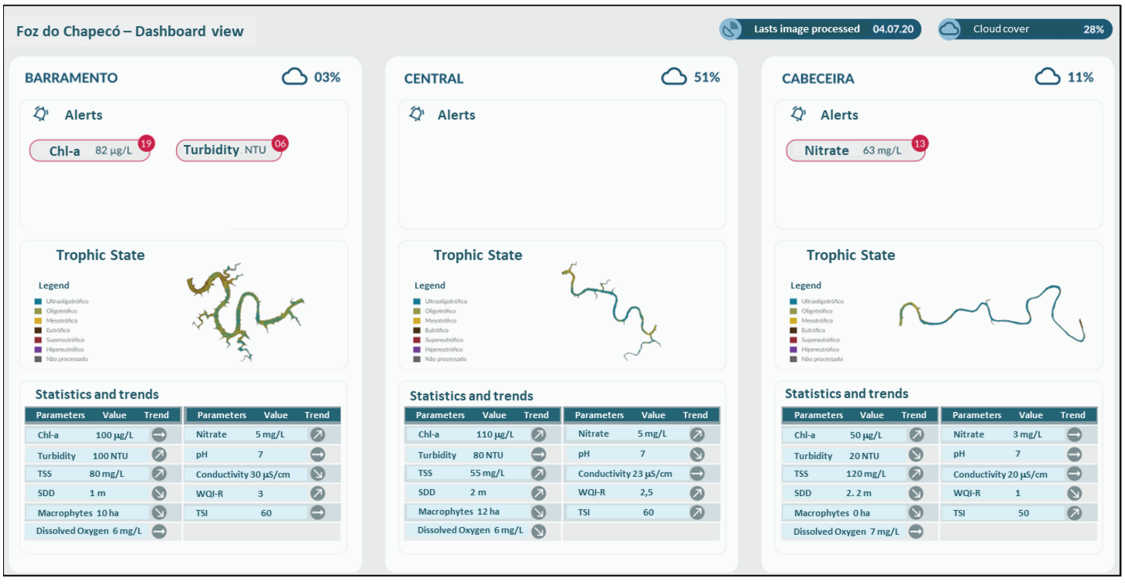

Figure 4. Dashboard view.

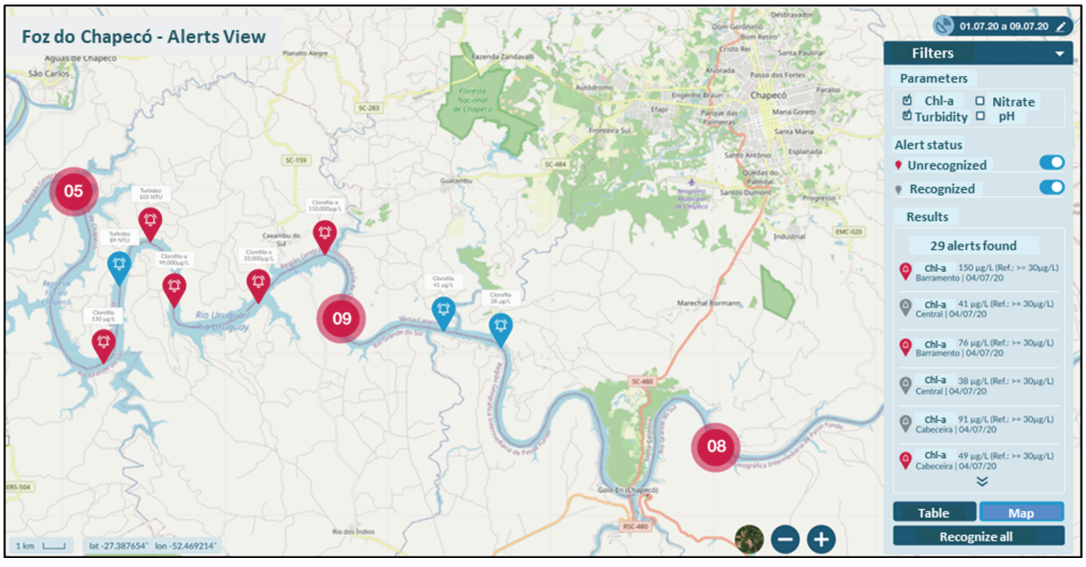

Figure 5. Alerts view.

Figure 6. Analysis view.

For the example shown in Figure 4, the "Barramento" sector presented 19 alerts for chlorophyll-*a* concentration and 6 alerts for turbidity, considering the image processed on 4 July 2020. The "Cabeceira" sector presented 13 alerts for turbidity, while in the "Central" sector no alert was generated by the system. The trophic state presented a steep gradient between the river zone ("Cabeceira") and the dam zone ('Barramento), with low trophic levels (ultra-oligotrophic) observed in the "Cabeceira" sector and high trophic levels observed in the "Barramento" sector (eutrophic).

The alert view (Figure 5) allows the user to consult and to manages alerts generated by the system. The user can filter alerts based on a single or a range of MSI image dates, the reservoir sector, the parameter of interest, and the alert status (recognized or not recognized). The alerts can be displayed on the map or in a table format using a color code for the recognized alerts (blue) and unrecognized alerts (red). For the pilot application, the alerts are generated for four parameters (chlorophyll-*a*, nitrate, turbidity, and pH) based on the water quality standards established for class two freshwaters according to Brazilian regulations [22]. An example of a query, Figure 5, shows the recognized and the unrecognized alerts which were generated for chlorophyll-*a* and turbidity parameters between 1 July 2020 and 9 July 2020.

Finally, Figure 6 shows the analysis view developed for the pilot application at the FCHR.

Figure 6 shows an example of a query for spatial distribution of turbidity retrieved based on the image acquired on 16 February 2022 for the "Barramento" sector. In this case, turbidity presented a homogeneous pattern with values lower than 5 NTU for the entire sector.

5. Conclusions

This paper presents the development and the pilot application of the QDA-System, a cloud-based system to monitor water quality in lakes and reservoirs using remote sensing images. The QDA-System allows the spatial and the temporal monitoring of water quality parameters, emission and management of alerts, and calculation of water quality indexes, such as the trophic state index. The system is an innovative application that combines state of the art remote sensing applied to inland aquatic environments, cloud computing techniques, and software development. Two of the main features of the QDA-System

are its versatility and its scalability, allowing customizations for different areas of interest according to specific monitoring needs and supporting the use of different images (e.g., MSI Sentinel-2 and OLI Landsat-8) and types of models (empirical and semi-empirical).

The pilot application of the QDA-System was implemented to monitor the Foz do Chapecó Hydroelectric Reservoir located in southern Brazil, with the implementation of nine water quality models calibrated and validated specifically for the reservoir. The pilot application is in the initial phase of operation for monitoring the selected reservoir; and, after the testing period, the QDA System will be available to be replicated to other hydroelectric reservoirs, with considerable potential to bring benefits and cost reductions related to water quality monitoring for the entire hydroelectric generation sector in Brazil. In addition, we emphasize that the QDA-System has great potential for application in other areas that also demand routine monitoring of water quality, such as the sanitation sector (public supply reservoirs or monitoring of receiving water bodies) and other industrial applications such as aquaculture.

Author Contributions: Data curation, R.Y.; Formal analysis, V.G.; Funding acquisition, M.C.; Investigation, G.S., G.P., J.d.S. and V.G.; Methodology, M.C., E.N. and M.D.; Project administration, M.C.; Software, F.d.S., F.Y., J.d.S., L.S., M.S. and R.Y.; Supervision, E.N., M.S. and M.D.; Validation, G.S., G.P. and M.D.; Visualization, N.B.; Writing—original draft, M.C. All authors have read and agreed to the published version of the manuscript.

Funding: This work was supported by Foz do Chapecó Energia S.A. and Energética Barra Grande (BAESA) research and technological development programs through the R&D 00642-2705/2019 project, regulated by Brazilian Electricity Regulatory Agency (ANEEL).

Informed Consent Statement: Not applicable.

Data Availability Statement: Not applicable.

Acknowledgments: We would like to thank the Foz do Chapecó S.A. and the Brazilian Electricity Regulatory Agency (ANEEL) for its encouragement, long-term vision, support, and for believing in the local and national capacity to develop innovative systems with a high degree of technological content. We also thank the Fundação CERTI for creating the necessary conditions for the development of the QDA-System.

Conflicts of Interest: The authors declare no conflict of interest.

References

1. Topp, S.N.; Pavelsky, T.M.; Jensen, D.; Simard, M.; Ross, M.R.V. Research trends in the use of remote sensing for inland water quality science: Moving towards multidisciplinary applications. *Water* **2020**, *12*, 169. [CrossRef]
2. Gholizadeh, M.H.; Melesse, A.M.; Reddi, L. A comprehensive review on water quality parameters estimation using remote sensing techniques. *Sensors* **2016**, *16*, 1298. [CrossRef] [PubMed]
3. Mishra, D.R.; Ogashawara, I.; Gitelson, A.A. *Bio-Optical Modeling and Remote Sensing of Inland Waters*; Elsevier: Amsterdam, The Netherlands, 2017.
4. EOLakeWatch: Satellite Earth Observations for Lake Monitoring. Available online: https://www.canada.ca/en/environment-climate-change/services/water-overview/satellite-earth-observations-lake-monitoring.html (accessed on 19 March 2021).
5. U.S. Environmental Protection Agency (EPA). Cyanobacteria Assessment Network (CyAN). Available online: https://www.epa.gov/water-research/cyanobacteria-assessment-network-cyan (accessed on 19 March 2021).
6. Morsy, M.M.; Goodal, J.L.; O'Neil, G.L.; Sadles, J.M.; Voce, D.; Hassan, G.; Huxley, C. A cloud-based flood warning system for forecasting impacts to transportation infrastructure systems. *Environ. Model. Softw.* **2018**, *107*, 231–244. [CrossRef]
7. Ferreira, K.R.; Queiroz, G.R.; Câmara, G.; Souza, R.C.M.; Vinhas, L.; Marujo, R.E.O.; Simões, C.A.F.; Noronha, R.; Costa, W.; Arcanjo, J.S.; et al. Using remote sensing images and cloud services on aws to improve land use and cover monitoring. In Proceedings of the 2020 IEEE Latin American GRSS & ISPRS Remote Sensing Conference (LAGIRS), Santiago, Chile, 22–26 March 2020; pp. 207–211.
8. Malthus, T.J.; Lehmann, E.; Ho, X.; Botha, E.; Anstee, J. Implementation of a satellite based inland water algal bloom alerting system using analysis ready data. *Remote Sens.* **2019**, *11*, 2954. [CrossRef]
9. The Foz do Chapecó Power Plant. Available online: http://www.fozdochapeco.com.br/usina/ (accessed on 2 February 2021).
10. Ecossistêmica Meio Ambiente LTDA (Ecossistêmica). *Foz do Chapecó Reservoir Use Plan*; Ecossistêmica: Porto Alegre, Brazil, 2017.
11. Companhia Ambiental do Estado de São Paulo (CETESB). *Guia Nacional de Coleta e Preservação de Amostras: Água, Sedimento, Comunidades Aquáticas e Efluentes Líquidos*; CETESB: São Paulo, Brazil, 2011.

12. American Public Health Association (APHA). *Standard Methods for the Examination of Water and Waste Water American Public Health Association*; APHA: Washington, DC, USA, 2017.
13. U.S. Environmental Protection Agency (EPA). *Method 300.1: Determination of Inorganic Anions in Drinking Water by Ion Chromatography v. 1.0*; EPA: Cincinnati, OH, USA, 1997.
14. Sentinel-2 Mission. Available online: https://sentinel.esa.int/web/sentinel/missions/sentinel-2 (accessed on 2 March 2021).
15. Sagan, V.; Peterson, K.T.; Maimaitijiang, M.; Sidike, P.; Sloan, J.; Greeling, B.A.; Maalouf, S.; Adams, C. Monitoring inland water quality using remote sensing: Potential and limitations of spectral indices, bio-optical simulations, machine learning, and cloud computing. *Earth-Sci. Rev.* **2020**, *205*, 103–187. [CrossRef]
16. Tucker, C.J. Red and photographic infrared linear combinations for monitoring vegetation. *Remote Sens. Environ.* **1979**, *8*, 127–150. [CrossRef]
17. Huete, A. A comparison of vegetation indices over a global set of TM images for EOS-MODIS. *Remote Sens. Environ.* **1997**, *59*, 440–451. [CrossRef]
18. Villa, P.; Laini, A.; Bresciani, M.; Bolpagni, R. A remote sensing approach to monitor the conservation status of lacustrine Phragmites australis beds. *Wetl. Ecol. Manag.* **2013**, *21*, 399–416. [CrossRef]
19. Villa, P.; Mousivand, A.; Bresciani, M. Aquatic vegetation indices assessment through radiative transfer modeling and linear mixture simulation. *Int. J. Appl. Earth Obs. Geoinf.* **2014**, *30*, 113–127. [CrossRef]
20. Mishra, S.; Mishra, D.R. Normalized difference chlorophyll index: A novel model for remote estimation of chlorophyll-*a* concentration in turbid productive waters. *Remote Sens. Environ.* **2012**, *117*, 394–406. [CrossRef]
21. Curtarelli, V.P.; Barbosa, C.C.F.; Maciel, D.A.; Junior, R.F.; Carlos, F.M.; Novo, E.M.L.M.; Curtarelli, M.P.; da Silva, E.F.F. Diffuse Attenuation of Clear Water Tropical Reservoir: A Remote Sensing Semi-Analytical Approach. *Remote Sens.* **2020**, *12*, 2828. [CrossRef]
22. Conselho Nacional de Meio Ambiente (CONAMA). *Resolução CONAMA n° 357, de 17 de Março de 2005*; CONAMA: Brasília, Brazil, 2005.

agriculture

MDPI

Article

Assessment of BMPs by Estimating Hydrologic and Water Quality Outputs Using SWAT in Yazoo River Watershed

Vivek Venishetty and Prem B. Parajuli *

Department of Agricultural and Biological Engineering, Mississippi State University, Starkville, MS 39762, USA; vv221@msstate.edu

* Correspondence: pparajuli@abe.msstate.edu

Abstract: Water quality is a global concern; it is due to point and non-point source pollution. Non-point sources for pollution are mainly runoff from Agricultural and forest. To decrease nutrient inputs, management practices are implemented. Using Soil and Water Assessment Tool, water quality parameters can be quantified. Yazoo River Watershed is the largest watershed in Mississippi, which have impact on surface water quality due to large scale agriculture and forest lands. Model has been calibrated and validated for streamflow, sediment, Total Nitrogen (TN), Total Phosphorus (TP) for the USGS gauge stations in the watershed. Model efficiency was assessed with Coefficient of Determination (R^2) and Nash-Sutcliffe Efficiency index (NSE). Best Management Practices (BMPs) were implemented throughout the watershed to simulate the impact of BMPs on streamflow, sediment, and nutrient yields. Vegetative Filter Strips (VFS), Riparian Buffer, combination of VFS and Riparian buffer and Cover Crops (CC) were tested for assessing the effective BMP in improving water quality. VFS, Riparian buffer and both (VFS + riparian) have no effect on streamflow, but they were able to decrease sediment, TN, and TP yields. Scenario with both VFS and Riparian buffer had the highest reduction capability as per varying width (5, 10, 15, and 20 m). For CC, Rye grass, Winter Barley and Winter Wheat (WW) were used, of which Rye grass had highest, 5.3% reduction in streamflow. WW has the highest Total Nitrogen reduction that is of 25.4%. CC also has significant reduction ranged between 10% to 11% for TP. This research would assist the Agricultural community to apply appropriate Management practices to improve water quality.

Keywords: water quality; SWAT; BMP; watershed; hydrology

Citation: Venishetty, V.; Parajuli, P.B. Assessment of BMPs by Estimating Hydrologic and Water Quality Outputs Using SWAT in Yazoo River Watershed. *Agriculture* **2022**, *12*, 477. https://doi.org/10.3390/agriculture12040477

Academic Editors: Alban Kuriqi and Luis Garrote

Received: 3 March 2022
Accepted: 27 March 2022
Published: 29 March 2022

1. Introduction

Deterioration of Natural resources due to manmade alternations to land-use and land-cover dates to pre- historic times. Agricultural land-use has first begun in Mesopotamia, that is known to be the host of human civilization [1]. With growing population and advancement in civilization and technology, led to improper use of natural resources which resulted in climate change, sea level rise, water quality impairment, eutrophication, and several impacts of pollution on environment. To meet the needs of current growing population, agriculture producers have ramped the use of fertilizers and pesticides to increase yield. This resulted water quality impairment in several watersheds globally. Agriculture is considered major non-Point source for pollution [2], other point sources for pollutions are sewage treatment plants, industrial effluents etc. Precipitation, soil type and management and slope gradient are the most significant factors in generating runoff from farmlands, which drains into nearby water bodies. This results in excessive inputs of nitrogen and phosphorus into surface water. Water quality impairment due to mineral salts induce the growth of algae that uses N and P as food source, agricultural runoff that is entering into a stream channel is rich in nitrogen and phosphorus, result in abundant food source for phytoplankton in the water; phytoplankton (algae) are harmful for human, aquatic, and other animal species, it also affects other uses of the water bodies such as

drinking water supply, recreation, aesthetic characteristics etc. [3]. About 2.2 billion people of the world population has no access to Safely managed water [4], and about 80 percent of illnesses are caused globally due to consuming impaired water [5]. Impaired water when consumed as drinking water could result in adverse health issues. To mitigate this water quality must be maintained by monitoring practices in the region.

Yazoo river Watershed (YRW) is the largest watershed with almost 50% of the watershed land-use is agriculture, runoff from these fields drain into Yazoo River and ultimately into Mississippi river. There is limited research conducted as a watershed scale analysis for YRW, this study could help in assessing current conditions and projecting for future. Mississippi river carries sediments, nutrients from several parts of the country and drains into Gulf of Mexico. Eutrophication in Gulf of Mexico has been a concern, affecting aquatic life in the area [6].

Inputs such as variety of herbicides, pesticides, and fertilizers are used to maximize yield. Organic manure is one of the inputs that farmers use as fertilizer, to minimize the effect of synthetic ones. Crop management inputs such as irrigation, fertilizer, and pesticide etc. were applied during growing season, although they were applied in prescribed quantities, there is still a significant amount that plants do not use. Residuals after plant uptake will eventually either leach into ground or transported through runoff. This process is quite prominent in parts of the world and in the watershed [7]. Agriculture being a major non-point source pollution [2], to decrease nutrient inputs from agricultural lands, USDA has implemented Best Management Practices in lieu of this concern in several states including Mississippi, but before selecting the appropriate BMP, it is efficient to know the source of pollutant, and the amount of it released into the water.

To assess the efficiency of various management practices, application of modeling tool is essential. Numerous modeling tools are used for the analysis of water quality, they are designed and used based on the applicability of water quality parameters. Soil and Water Assessment Tool (SWAT) is a conceptual model that is used prominently in watershed modelling, there are studies that indicate SWAT model is one of the most efficient models in quantifying hydrologic and water quality parameters at watershed scale [8]. It has also been used in quantifying Nutrient sources in Big sunflower river watershed which is a sub watershed of YRW. Therefore, the objectives of this research were to: (i) calibrate and validate model for streamflow, sediments, total Nitrogen (TN), and total Phosphorus (TP); and (ii) assess Best Management Practices' (BMPs) effects on water quality.

2. Materials and Methods

2.1. Study Area

YRW is the largest watershed in the state of Mississippi, with a drainage area of 5.08 million ha, shown in Figure 1. Located in the north-western region of Mississippi. YRW has two regions that are predominant, the Buff hills where most of the land type is upland, birthplace for many rivers in the state, located in the northeast region of the watershed, and The Delta where most of the land is flat with some of the most fertile soils that are best for Agriculture, located between Yazoo and Mississippi Rivers in the northwest. YRW covers 30 counties of Mississippi with Interstate 55 crossing across the watershed.

Land use characteristics include Agriculture, forest lands, wetlands, lakes, and urban areas. Major crops in agricultural land use are Corn, cotton, Soybean, Pasture lands that accounts to 47.24%. Forest lands are classified as Deciduous, evergreen, and mixed types that cover majority of the watershed to 49.92%, the remainder land that is of 2.84% is covered with lakes, forested and non-forested wetlands, and urban areas as shown in Figure 2. Majority of the soils present in the watershed are Alligator, Dundee, Sharkey, Dowling, Forestdale, Smith-dale. This watershed is divided into 109 smaller watersheds (sub-basins) for ease of analysis in SWAT.

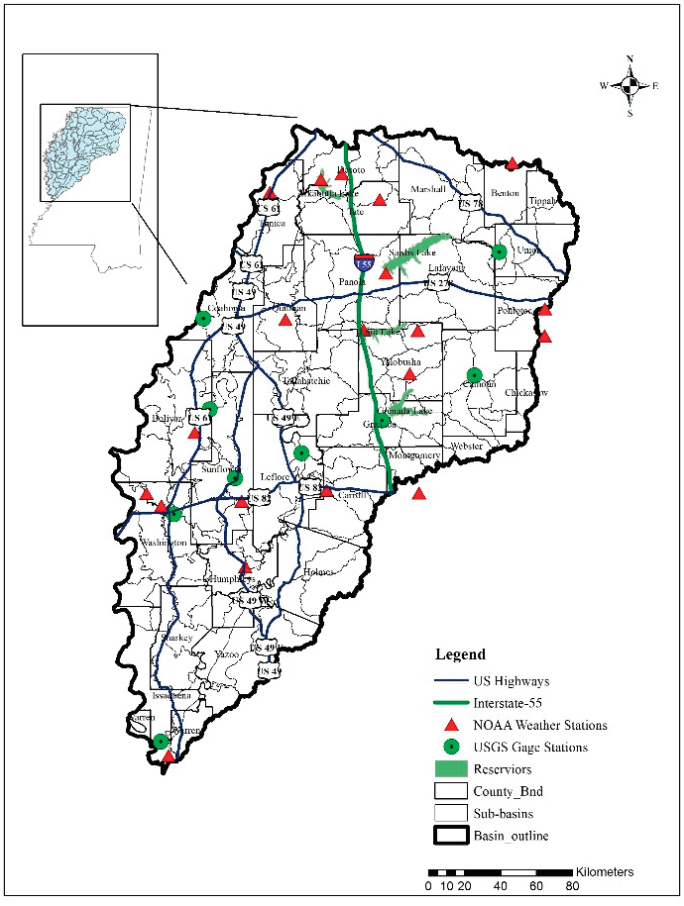

Figure 1. Location of the Yazoo River Watershed showing weather and USGS gage stations.

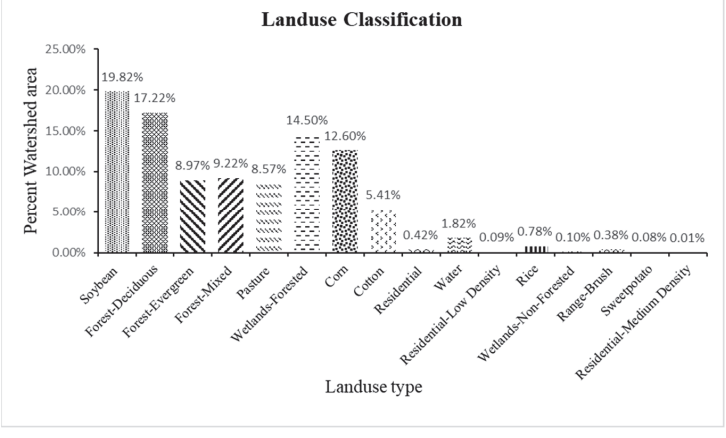

Figure 2. Land use Characteristics in Yazoo River Watershed.

2.2. Model Description

SWAT—Soil and Water Assessment Tool is a continuous daily time-step watershed scale model. SWAT can simulate Hydrologic and water quality parameter outputs such as sediment, total Nitrogen, and total Phosphorus concentrations for each HRU (Hydrologic Response Unit), Sub-basin [9]. Watershed delineation of YRW resulted in 109 sub-basins which are reclassified into HRUs with the help of Digital Elevation Model input, land-use, soil, and slope classifications. This classification helps in applying different crop, soil, and slope parameters for individual HRU for detailed analysis. Output generated from SWAT can also be viewed as per sub-basin and HRU level. Sediment and Nutrient inputs are derived from basin slope, surface lag time etc., for nutrients, Agricultural management inputs such as fertilizer and pesticide application etc., are used. It is one of the efficient hydrological models existing, used for estimating long-term effects caused by agricultural and other management operations. This analysis could be useful in developing management operations. Arc SWAT is an ArcGIS extension, a joint development by USDA-ARS and Texas A&M University.

2.3. Model Inputs

Primary data inputs used were Digital Elevation Models (DEM) for 30 m × 30 m resolution acquired from United States Geological Survey [10], for watershed delineation. Land-use data is acquired from United States Department of Agriculture–National Agricultural Statistics Service (USDA-NASS) [11] that is Crop Land data layer (CDL) of 30 m × 30 m resolution. Soils data was obtained from Soil Survey Geographic (SSURGO) database [12]. Weather inputs such as daily minimum and maximum Temperature and Precipitation data obtained from National Oceanic and Atmospheric Administration [13] from 2000 to 2019 for weather stations in YRW.

Agriculture, since considered as major non-point source of pollution, nutrient inputs in agriculture such as fertilizer, pesticides, animal manure etc. were applied. Mississippi State University Agricultural and Forestry Extension Service [14] keeps the information for different crop, this including Planting date, Fertilizer and Pesticide application date and type used, Irrigation schedule and amounts, Tillage practices and Harvest dates. These dates vary for different crop types, respective dates and types were obtained and applied to the model. Forest Management practices were obtained from Mississippi Forestry Commission [15].

Manure inputs were estimated with the help of revised standards provided by American Society for Agricultural and biological Engineers [16]. Total dry weight produced by cattle is estimated to 2.36 kg/day/animal, similarly, for chicken it is 0.03 kg/day/animal and for swine, it is 0.14 kg/day/animal. Average weight for cattle, chicken and swine are 440 kg, 1.9 kg, and 196 kg respectively. Most of the manure inputs have been given in lieu of timber production for the forested area.

2.4. Model Accuracy Assessment

Accuracy of the model is estimated using two statistical indices, Nash, and Sutcliff Efficiency (NSE) [17] index, and coefficient of determination (R^2) [18] (1) and (2) respectively. For each parameter that is calibrated mainly, Streamflow, sediment, Total Phosphorus and Total Nitrogen both *NSE* and R^2 are evaluated.

$$NSE = 1 - \frac{\sum_{i-1}^{N} (O_i - S_i)^2}{\sum_{i-1}^{N} (O_i - \overline{O})^2} \quad (1)$$

$$R^2 = \left(\frac{\sum_{i-1}^{N} (O_i - \overline{O})(S_i - \overline{S})}{\sqrt{\sum_{i-1}^{N} (O_i - \overline{O})^2} \cdot \sqrt{\sum_{i-1}^{N} (S_i - \overline{S})^2}} \right)^2 \quad (2)$$

where O_i is the Observed data, S_i is simulated data, $\overline{O}$ and $\overline{S}$ are observed and simulated means respectively. Coefficient of Determination helps us in understanding the trend between two sets of data, in this case Observed and Simulated by giving linear relationship between them. R^2 ranges from 0 to 1, if R^2 value is close to 1 then it is perfect relationship between observed and model simulated value. *NSE* ranges $-\infty$ to 1, result close to 1 depicts model is accurate.

2.5. Calibration and Validation

Using R^2 and *NSE* statistics, model accuracy was tested for Streamflow, sediments, total Nitrogen, and total Phosphorus. This is essential, since we are simulating outputs based on limited field collected observations. Once the statistic had shown positive trend, conclusions were based for 20 years.

2.5.1. Streamflow Calibration

Flow parameter calibration is the primary step in calibration and validation process. For a total of 8 USGS Gauge stations in YRW with continuous streamflow data, model was calibrated and validated. Monthly data from these stations is collected and calibrated from year 2008 to 2011 and validated from year 2012 to 2015. By using Auto-Calibration tool, SWAT-CUP (SWAT calibration and Uncertainty Procedures). SWAT_CUP is designed specifically for SWAT calibration procedures, SUFI-2 (Sequential Uncertainty Fitting version 2) algorithm helps in fitting the best parameter value for the given respective range [19]. Flow is affected by numerous parameters; this tool was used so that multiple parameters that are sensitive [8,20–22] that are mentioned in Table 1 for flow were simultaneously changed until best results were obtained.

Table 1. Streamflow sensitive Parameters.

Parameter Name	Fitted Value	Min_Value	Max_Value
R_CN2.mgt	−0.281491	−0.611679	−0.232775
V_ALPHA_BF.gw	0.154628	−0.03763	0.426442
V__GW_DELAY.gw	169.28447	92.200127	278.26578
V__GWQMN.gw	4279.6025	2744.1755	5243.7075
R__ESCO.hru	−0.658654	−0.693971	0.130097
R__SOL_AWC(..).sol	−0.288483	−0.417682	0.278006
V__GW_REVAP.gw	0.038273	−0.041752	0.077434
R__SURLAG.bsn	3.360117	1.552425	7.054097
R__SOL_K(..).sol	0.406588	−0.061624	0.493882

2.5.2. Sediment Calibration

Best Management Practices can limit sediment transport with the runoff; therefore, calibration and validation of Sediment was performed. With the limited available data, model was calibrated and validated for 2 USGS gauge stations, Big Sunflower at Merigold (USGS-07288280) and Bouge Phalia near Leland (USGS-07288650) respectively. Manual calibration approach was used with the help of Manual Calibration helper tool in SWAT. From literature and testing, sensitive parameters [23–26] were selected and used in calibration and validation process, they are mentioned in Table 2 below. Observed suspended sediment data obtained from field collected samples, for the period from 2013 to 2016 that is collected every 15 days for these 4 years. Calibration was performed from 2013 to 2014; and validation was performed from 2015 to 2016.

Table 2. Sensitive Parameters in Sediment Calibration.

Parameter_Name	Fitted_Value
ch_cov1.rte	0.03
ch_cov2.rte	0.035
ERODMO.rte	0.5
PRF.rte	0.57
spcon.rte	0.0006
SLSUBBSN.hru	137.5
ADJ_PKR.bsn	2
USLE_K.sol	0.2
USLE_C.cropdat	0.2
USLE_P.mgt	1

2.5.3. Total Nitrogen

In the process of nutrient quantification, Nitrogen is considered one of the main mineral salts that is deposited in surface water from agricultural runoff. Therefore, Calibration and validation of Total Nitrogen was performed from 2013 to 2014 and 2015 to 2016 respectively. Data collected at 15-day interval was obtained from MDEQ for this process. Manual Calibration approach was chosen due to limited data availability and performed with the help of Manual Calibration Helper tool in SWAT. Sensitive parameters were identified from numerous journals and performed calibration and validation [27,28] that are mentioned in Table 3 below, for Big Sunflower at Merigold (USGS-07288280) and Bouge Phalia near Leland (USGS-07288650) respectively.

Table 3. Sensitive Parameters in Total Nitrogen Calibration.

Parameter Name	Fitted Value
RS3.swq	0.11
RS4.swq	0.0076
BC3.swq	0.305
BC2.swq	1.19
RCN.bsn	0.54
CMN.bsn	0.0011
CDN.bsn	1.1
SSDNCO.bsn	0.85
N_UPDIS.bsn	15
NPERCO	0.25

2.5.4. Total Phosphorus

Phosphorus is one other significant mineral that impacts water quality, therefore, Total phosphorus estimated by the model must be calibrated to achieve accurate results. Calibration and validation for total phosphorus was performed from 2013 to 2014 and 2015 to 2016 respectively. MDEQ collected field samples at an interval of 15 days. This data was obtained and used in the process. With the help of Manual calibration helper tool in SWAT, the model was calibrated for Big Sunflower at Merigold (USGS-07288280) and Bouge Phalia near Leland (USGS-07288650) respectively. Parameters that affect the total phosphorus concentration were identified from the literature, and testing [29–31] had used in the process. They are mentioned in Table 4.

Table 4. Sensitive Parameters in Total Phosphorus Calibration.

Parameter Name	Fitted Value
RS2.swq	0.0965
RS5.swq	0.009
BC4.swq	0.0525
BC2.swq	1.19
RCN.bsn	0.54
PSP.bsn	0.4
PERCOP.bsn	0.8
PHOSKD.bsn	185
P_UPDIS.bsn	1
PPERCO	10.8

2.6. Management Scenarios

After a thorough research, implementation of BMPs is one of the methods to reduce hydrologic and water quality outputs from Agricultural and Forested land-use. There are numerous BMPs that are in practice, for this study Vegetative Filter Strips (VFS), Riparian buffers, Cover Crops were selected.

2.6.1. Vegetative Filter Strips

VFSs are the areas that are located at the edge of Agricultural land and in between these agricultural lands and streams of rivers, bayous, and lakes [32]. They are implemented in such a way that runoff from fields is first passed through VFS before entering the streams. They also provide erosion control locally by trapping sediments, nutrients, and organic matter. VFS widths of 5, 10, 15, 20 m were applied. Water quality outputs were simulated by adjusting.

2.6.2. Riparian Buffer

Riparian Buffer if implemented in forested areas. It is land area alongside surface water streams that is covered with trees, shrubs [33]. For this study, riparian buffer is applied as an edge of field practice [34] in mixed, deciduous, and evergreen forest land use types. Buffer lengths of 5, 10, 15, 20 m were used for simulating the sediment, and nutrient yields.

2.6.3. Cover Crops

Cover Crops (CCs) are considered as BMPs, they provide vegetative cover in agricultural lands, during post-harvest period [35]. CCs are also beneficial in providing organic matter to the field, increasing soil fertility, porosity, and decrease nutrient loss [36]. CCs were added Post harvest of main crop for every agricultural land [14]. CCs are not harvested before the main crop, they are buried in the process of tillage and land preparation for the main crop to avoid more disturbance in the soil, and leaving them in the soil, improves the organic content enrichment. CCs such as Winter wheat, winter barley, Rye grass were used to simulate sediment and nutrient yields.

3. Results and Discussion

3.1. Calibration and Validation

SWAT project for Yazoo River Watershed is created, then calibrated and validated for all the sensitive parameters that affect the water quality. For a total of 109 Sub-basins, streamflow data was obtained for 8 Stations, Total Suspended Solids (TSS), Total Nitrogen (TN), and Total Phosphorus (TP) data were available only for 2 stations in the watershed.

3.1.1. Streamflow (m^3/s)

Streamflow calibration and validation was done for 8 USGS gauge stations, in YRW, they are spread across the watershed with varied sub-basin characteristics. Overall model

performance resulted in good as shown in Figure 3, the values for R^2 and *NSE* ranged from 0.36 to 0.80 and 0.30 to 0.80 respectively for Calibration. Similarly, R^2 and *NSE* ranged from 0.16 to 0.75 and 0.14 to 0.74 for validation. Table 5 shows Statistical results of Calibration and validation of all 8 Stations.

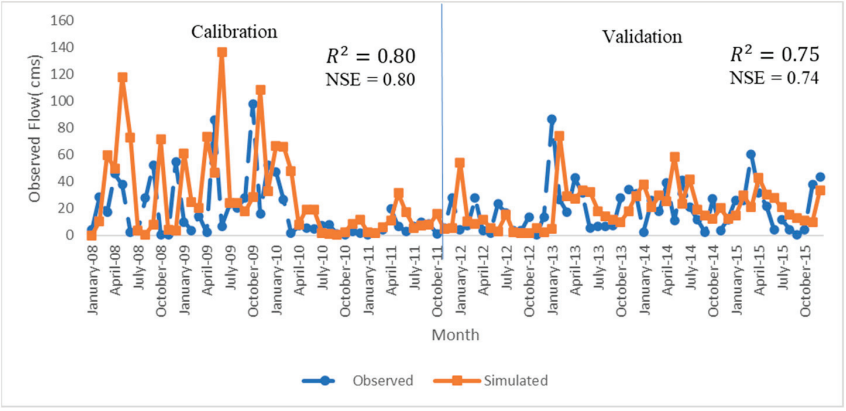

Figure 3. Monthly observed vs. simulated flow during model calibration and validation from Bogue Phalia gauge station.

Table 5. Calibration and Validation Results for Streamflow.

Sc. No.	Gage Station	USGS Gauge Station Number	Subbasin No.	Calibration		Validation	
				R^2	*NSE*	R^2	*NSE*
1	Yazoo River @ Steel Bayou (Vicksburg)	7288955	107	0.36	0.30	0.76	0.74
2	Tallahatchie River @ Money	7281600	61	0.58	0.41	0.68	0.59
3	Bouge Phalia near Leland	7288650	78	0.80	0.80	0.75	0.74
4	Little Tallahatchie @ Etta	7268000	15	0.65	0.62	0.76	0.69
5	Yalobusha @ Grenada	7285500	54	0.47	0.47	0.16	0.12
6	Skuna River	7283000	40	0.62	0.61	0.69	0.57
7	Big Sunflower @ Merigold	7288280	47	0.62	0.60	0.7	0.59
8	Big Sunflower @ Sunflower	7288500	67	0.73	0.69	0.63	0.57

3.1.2. Sediment Concentration

For sediments, due to limited data availability, the model is calibrated and validated from 2013 to 2016 for 2 stations, at Leland (USGS07288650) and Merigold (USGS07288280). Model Performance resulted in Satisfactory, it is due to numerous peaks sediment concentrations due to extreme weather events such as heavy rainfall, snow, hail, and thunderstorms reported in 2014, 2015 in Washington County, Mississippi where the station is located [37]. The slope gradient in this region is very less, close to flat conditions, that are suitable for intense agriculture, resulting nominal flow during normal conditions. But, in the event of extreme weather events, this region is prone to flash floods, and high speed wind gusts during thunderstorms resulting increased sediment concentrations in the stream channel. The R^2 and *NSE* values were 0.12 and 0.17 respectively for calibration and 0.17 and 0.14 respectively for Validation. Calibration of the model was done for Big Sunflower at Merigold (USGS07288280) and validation was done for station Bogue Phalia station (USGS07288650) as mentioned in Table 6. Figures 4 and 5 show the trend plot.

Table 6. Calibration and Validation for Sediment Concentration.

		Sediment		TN		TP	
Process	**Station**	R^2	*NSE*	R^2	*NSE*	R^2	*NSE*
Calibration	Big Sunflower at Merigold	0.17	0.17	0.05	0.10	0.33	0.18
Validation	Bouge Phalia near Leland	0.17	0.14	0.08	0.13	0.41	0.33

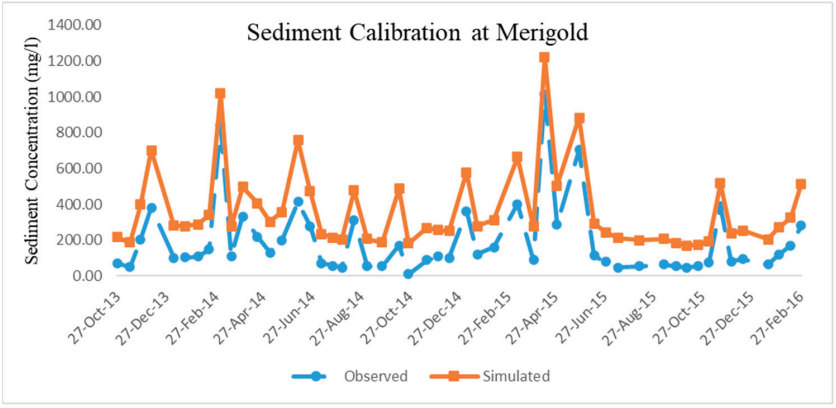

Figure 4. Calibration of Sediment Concentration for station Big Sunflower River at Merigold.

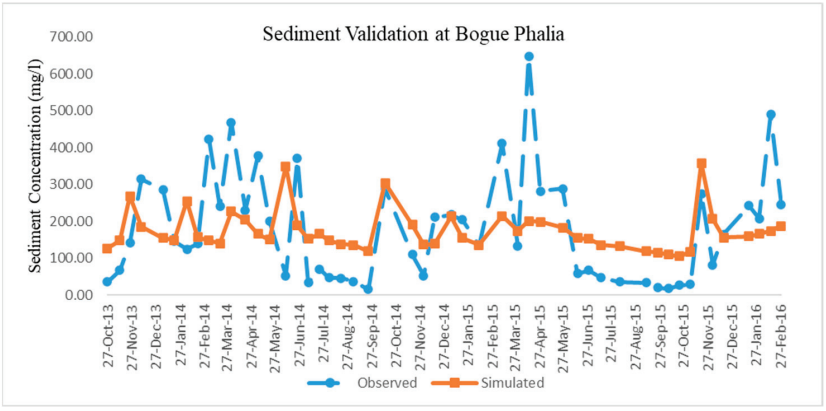

Figure 5. Validation of Sediment Concentration at Bogue Phalia Station near Leland.

3.1.3. Total Nitrogen (TN)

Calibration for Total nitrogen is done for Merigold Station (USGS07288280) and Validation for Leland Station (USGS07288650). As we know, Nitrogen concentrations are extremely difficult to predict, as it is volatile in nature. Model performance was satisfactory. R^2 and *NSE* values for Calibration 0.05 and 0.10 respectively and validation were 0.08 and 0.13 respectively as shown in Table 6. Concentration of Nitrogen is extremely varied from one HRU to the other with in the same sub-basin. These stations are in the area where Agriculture is intensive. Yazoo river watershed is about 50% forest, and field collected data from forested creeks and streams was very sparse and dis-continuous.

3.1.4. Total Phosphorus (TP)

Similar to TN, model was calibrated at Merigold station (USGS07288280) Validated at Leland station (USGS02788650). Model performance resulted poor during calibration, but

the performance was satisfactory in validation. R^2 and *NSE* values for Calibration 0.33 and 0.18 respectively and validation were 0.41 and 0.33 respectively as shown in Table 6.

3.2. Watershed Scale Impact of BMPs

Implementation of BMPs have resulted significant reductions in sediment and Nutrient concentrations in the watershed. Although most of the BMPs does not have impact on flow, Cover crop (CC) BMP has shown about 3–5% reduction, depending on the CC that is used. Results from rest of the BMPs are as following.

3.2.1. Vegetative Filter Strips (VFS)

Sediment and Nutrient trapping from VFS have resulted in proportional to the width of VFS as shown in Figure 6. Sediment and Nutrient yields for varying widths from 5 m to 20 m with 5 m increments have been simulated. When compared with baseline scenario, percentage reduction in Sediment and nutrient concentrations were described in Table 7.

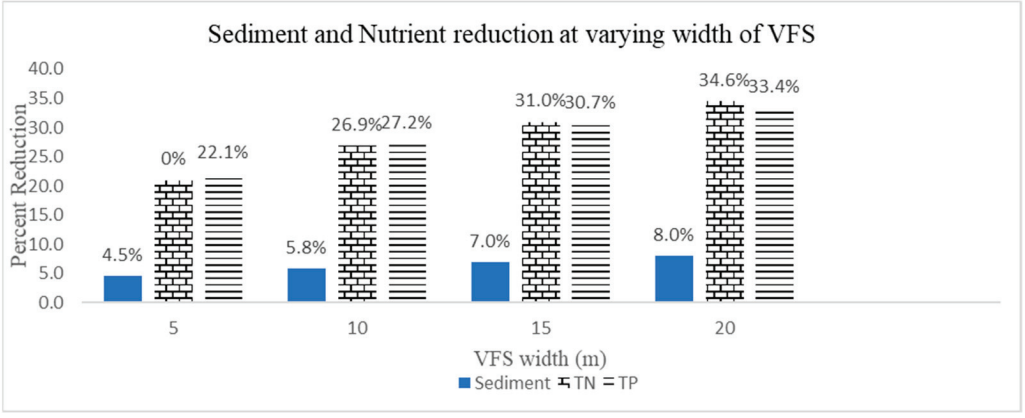

Figure 6. Comparison of different VFS widths based on water quality outputs.

Table 7. Percentage reduction in Sediment and Nutrient Concentrations at varying widths.

Width (m)	VFS			Riparian Buffer Width (m)			VFS + Riparian		
	Sediment	TN	TP	Sediment	TN	TP	Sediment	TN	TP
5	4.5	21.0	22.1	14.5	1.8	8.2	23.7	22.8	30.3
10	5.8	26.9	27.2	26.6	2.3	10.1	36.9	29.0	37.2
15	7.0	31.0	30.7	32.3	2.6	11.4	44.9	33.6	42.0
20	8.0	34.6	33.4	37.0	2.8	12.4	51.8	37.3	45.7

3.2.2. Riparian Buffer

Riparian buffer has been applied as edge of field practice in Forested land-use, with width at baseline conditions 0 m to a maximum of 20 m with 5-m increments. Similar to VFS, increase in buffer width resulted increased reduction in sediment and nutrients concentrations as shown in Figure 7. Percent reduction in Sediment, TN and TP concentrations are listed in Table 7. Although TN and TP reductions were not as good as in case of VFS, it is expected due to no agricultural or silvicultural management for forested land-use.

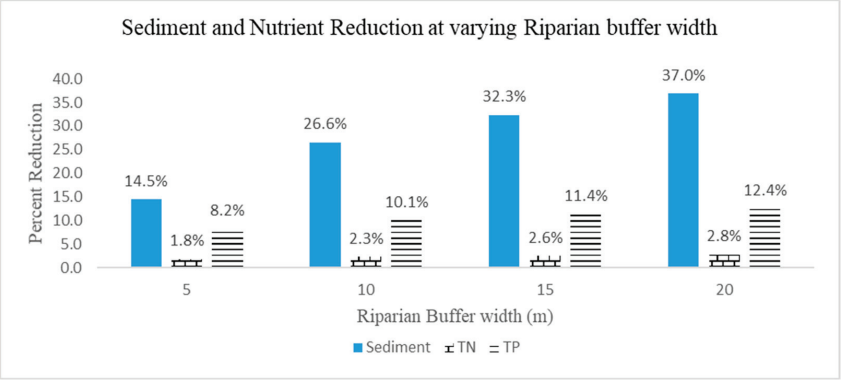

Figure 7. Yield reduction of Sediment and Nutrient due to application Riparian buffer at varying width.

3.2.3. VFS and Riparian Buffer

This scenario is simulated with the combination of two BMPs, VFS and Riparian buffer in Agricultural and forested lands. Implementing both BMPs throughout the watershed has significantly reduced sediment and nutrient yields, shown in Figure 8. Percent reduction varied with respect to width of VFS and buffer. Reduction in sediment concentrations ranged between 23% and 52%, similarly TN ranged between 22% and 37% and TP between 30% and 46%. Percent reductions at varying width are listed in Table 7.

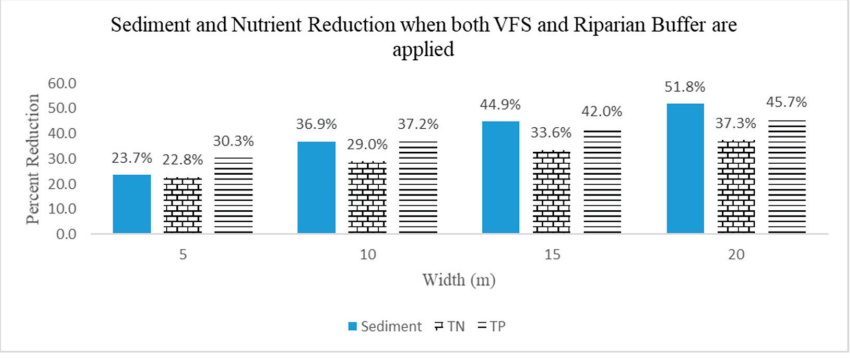

Figure 8. Reduction in sediment and Nutrient yields when both VFS and Riparian buffer are applied.

3.2.4. Cover Crops (CC)

Cover crops (CC) are used to maintain soil nutrient concentrations and provide vegetative cover to minimize impact of rain drop during a storm event. Rye grass, winter barley and winter wheat had different impact in streamflow, TN, and TP concentrations as shown in Figure 9. Although there is no significant impact on sediments, it is observed that reduction in TN is significant, and ranged between 14% to 26%. Reduction in streamflow and Nutrient concentrations is listed in Table 8.

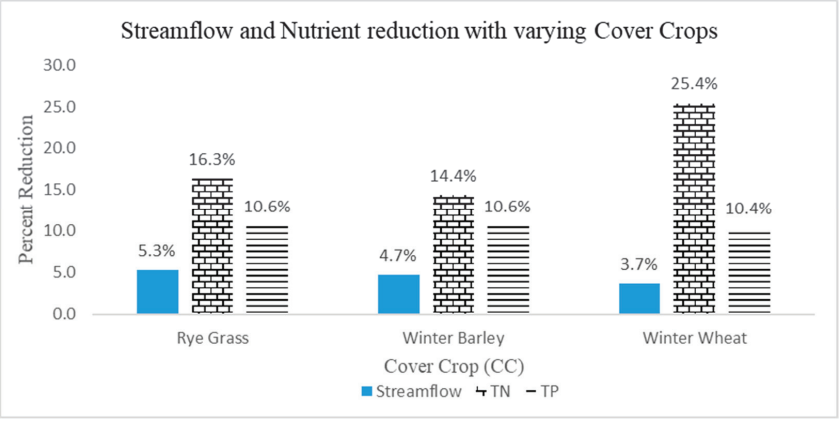

Figure 9. Reductions in Flow and Nutrient concentrations due to CC implementation.

Table 8. Percentage Reductions when CC were implemented.

Cover Crop (CC)	Percent Decrease		
	Streamflow	TN	TP
Rye Grass	5.3	16.3	10.6
Winter Barley	4.7	14.4	10.6
Winter Wheat	3.7	25.4	10.4

4. Conclusions

From this study, it is evident that implementing BMPs in a watershed have significant impact in improving water quality. VFS (in agricultural land), Riparian buffer (forested land) and combination of both have no impact on reducing streamflow, but these BMPs were effective in reducing the sediment concentration, TN, and TP. As both VFS and Riparian buffer are edge of field practices [35], size of the width is directly proportional to extent of reduction. All three scenarios were simulated for five different widths, starting with 0 m, till 20 m with 5-m increments. The highest reduction in sediment and nutrient outputs were at 20 m width for all three scenarios. The results obtained from this study were compared with other studies conducted in Big Sunflower River Watershed, in Mississippi [38], and Alger Creek watershed in Michigan [23] which implemented VFS in their respective watersheds to validate, results from both studies follow similar trend. Combination of VFS and Riparian buffer throughout watershed had the highest reduction of the three, with width of 20 m, it is observed that there is about 52% reduction in sediments, 37% reduction in total nitrogen and 46% reduction in total phosphorus. Therefore, it is recommended to have a combination of VFS and Riparian buffer for highest sediment, nutrient reduction that could result in improving water quality.

Cover Crops (CC) used in this study are planted after the harvest of main crop (Soybean, Corn, Cotton, and Rice). Crop scheduling, and management operations were applied based on the observations from Mississippi Agriculture and Forestry Extension Services [14]. Out of the three crops (Rye grass, winter barley, winter wheat) used as CC, Rye had proved to be reducing streamflow the highest to about 5% compared to other CC, whereas winter wheat had the highest TN reduction, about 25%. TP reduction ranged between 10 to 11% for all three CC. These results were validated by comparing the results from other studies conducted in Alger Creek Watershed in Michigan [23], Eagle creek Watershed in Ohio [39], Smith fry watershed in Indiana [40]. All of them reported the similar trend in application of CC as BMP for Flow, Sediment and Nutrient reductions.

Author Contributions: Model development, data analysis and manuscript draft by V.V. and project supervision, review of manuscript, and funding acquisition by P.B.P. All authors have read and agreed to the published version of the manuscript.

Funding: This research was partially funded by USDA Multi-state Hatch project through Mississippi Agricultural and Forestry Experiment Services (MAFES), MAFES Director's fellowship, position # 7515.

Institutional Review Board Statement: Not applicable.

Informed Consent Statement: Not applicable.

Data Availability Statement: Not applicable.

Acknowledgments: We would like to acknowledge the partial support of USDA's Multi-state Hatch project through Mississippi Agricultural and Forestry Experiment Services (MAFES), MAFES Director's fellowship, position # 7515, NIFA competitive grant award # 2017-67020-26375, Mississippi Agricultural and Forestry Experiment Services (MAFES), and College of Agriculture and Life Sciences at Mississippi State University, United States Geological Survey (USGS), and all our collaborators for providing necessary data for this study.

Conflicts of Interest: The authors declare no conflict of interest.

References

1. Kaplan, J.O.; Krumhardt, K.M.; Zimmermann, N. The prehistoric and preindustrial deforestation of Europe. *Quat. Sci. Rev.* **2009**, *28*, 27–28. [CrossRef]
2. Environment Protection Agency (EPA). Available online: https://www.epa.gov/nps/basic-information-about-nonpoint-source-nps-pollution (accessed on 11 November 2021).
3. Dash, P.; Silwal, S.; Ikenga, J.O.; Pinckney, J.L.; Arslan, Z.; Lizotte, R.E. Water Quality of Four Major Lakes in Mississippi, USA: Impacts on Human and Aquatic Ecosystem Health. *Water* **2015**, *7*, 4999–5030. [CrossRef]
4. World Health Organization (WHO). Available online: https://www.who.int/news-room/fact-sheets/detail/drinking-water#:~{}:text=In%202017%2C%2071%25%20of%20the,at%20least%20a%20basic%20service (accessed on 11 November 2021).
5. United Nations (UN). Available online: https://www.un.org/en/global-issues/water (accessed on 12 November 2021).
6. Rabalais, N.N.; Turner, R.E.; Gupta, B.K.S.; Platon, E.; Parsons, M.L. Sediments tell the history of eutrophication and hypoxia in the northern Gulf of Mexico. *Ecol. Appl.* **2007**, *17*, S129–S143. [CrossRef]
7. Tilman, D.; Balzer, C.; Hill, J.; Befort, B.L. Global food demand and the sustainable intensification of agriculture. *Proc. Natl. Acad. Sci. USA* **2011**, *108*, 20260–20264. [CrossRef] [PubMed]
8. Parajuli, P.B.; Nelson, N.O.; Frees, L.D.; Mankin, K.R. Comparison of AnnAGNPS and SWAT model simulation results in USDA-CEAP agricultural watersheds in south-central Kansas. *Hydrol. Process.* **2009**, *23*, 748–763. [CrossRef]
9. Arnold, J.G.; Srinivasan, R.; Muttiah, R.S.; Williams, J.R. Large area hydrologic modeling and assessment part I: Model development. *J. Am. Water Resour. Assoc.* **1998**, *34*, 73–89. [CrossRef]
10. United States Geological Survey (USGS). Available online: https://apps.nationalmap.gov/downloader/#/productSearch (accessed on 27 August 2020).
11. United States Department of Agriculture—National Agricultural Statistics Service (USDA-NASS) CropScape—Cropland Data Layer. Available online: https://nassgeodata.gmu.edu/CropScape/ (accessed on 10 September 2020).
12. Web Soil Survey (WSS) SSURGO Database. Available online: https://websoilsurvey.sc.egov.usda.gov/App/WebSoilSurvey.aspx (accessed on 10 September 2020).
13. National Oceanic and Atmospheric Administration (NOAA)—Climate Data Online. Available online: https://www.ncdc.noaa.gov/cdo-web/search (accessed on 10 September 2020).
14. Mississippi Agricultural and Forestry Experiment Station (MAFES)—Variety trials. Available online: https://www.mafes.msstate.edu/variety-trials/ (accessed on 5 November 2020).
15. Mississippi Forestry Commission. *Mississippi's BMPs—Best Management Practices for Forestry in Mississippi Handbook*, 4th ed.; Wayback Machine: Jackson, MS, USA, 2008.
16. ASABE. American Society for Agricultural and Biological Engineering (ASABE)—Manure Production and Characteristics. In *ASAE D384.2 MAR2005*; ASABE: St. Joseph, MI, USA, 2019.
17. Nash, J.E.; Sutcliffe, J.V. River flow forecasting through conceptual models. Part I—A discussion of principles. *J. Hydrol.* **1970**, *10*, 282–290. [CrossRef]
18. Wright, S. Correlation and causation. *J. Agric. Res.* **1921**, *20*, 557–585.
19. Abbaspour, K.C.; Rouholahnejad, E.; Vaghefi, S.; Srinivasan, R.; Yang, H.; Kløve, B. A continental-scale hydrology and water quality model for Europe: Calibration and uncertainty of a high-resolution large-scale SWAT model. *J. Hydrol.* **2015**, *524*, 733–752. [CrossRef]

20. Kim, H.K.; Parajuli, P.B.; To, S.F. Assessing impacts of bioenergy crops and climate change on hydrometeorology in the Yazoo River Basin, Mississippi. *Agric. For. Meteorol.* **2013**, *169*, 61–73. [CrossRef]
21. Knouft, J.H.; Botero-Acosta, A.; Wu, C.L.; Charry, B.; Chu, M.L.; Dell, A.I.; Hall, D.M.; Herrington, S.J. Forested riparian buffers as climate adaptation tools for management of riverine flow and thermal regimes: A case study in the Meramec River Basin. *Sustainability* **2021**, *13*, 1877. [CrossRef]
22. Soil and Water Assessment Tool (SWAT)—Input–Output Documentation 2012. Available online: https://swat.tamu.edu/docs/ (accessed on 10 September 2020).
23. Merriman, K.R.; Russell, A.M.; Rachol, C.M.; Daggupati, P.; Srinivasan, R.; Hayhurst, B.A.; Stuntebeck, T.D. Calibration of a field-scale Soil and Water Assessment Tool (SWAT) model with field placement of best management practices in Alger Creek, Michigan. *Sustainability* **2018**, *10*, 851. [CrossRef]
24. Zhang, X.; Zhang, M. Modeling effectiveness of agricultural BMPs to reduce sediment load and organophosphate pesticides in surface runoff. *Sci. Total Environ.* **2011**, *409*, 1949–1958. [CrossRef] [PubMed]
25. Himanshu, S.K.; Pandey, A.; Yadav, B.; Gupta, A. Evaluation of best management practices for sediment and nutrient loss control using SWAT model. *Soil Tillage Res.* **2019**, *192*, 42–58. [CrossRef]
26. Luo, Y.; Zhang, M. Management-oriented sensitivity analysis for pesticide transport in watershed-scale water quality modeling using SWAT. *Environ. Pollut.* **2009**, *15*, 3370–3378. [CrossRef] [PubMed]
27. Risal, A.; Parajuli, P.B. Quantification and simulation of nutrient sources at watershed scale in Mississippi. *Sci. Total Environ.* **2019**, *670*, 633–643. [CrossRef]
28. Jayakody, P.; Parajuli, P.B.; Cathcart, T.P. Impacts of climate variability on water quality with best management practices in sub-tropical climate of USA. *Hydrol. Process.* **2014**, *28*, 5776–5790. [CrossRef]
29. Ni, X.; Parajuli, P.B. Evaluation of the impacts of BMPs and tailwater recovery system on surface and groundwater using satellite imagery and SWAT reservoir function. *Agric. Water Manag.* **2018**, *210*, 78–87. [CrossRef]
30. Parajuli, P.B.; Jayakody, P.; Sassenrath, G.F.; Ouyang, Y. Assessing the impacts of climate change and tillage practices on stream flow, crop and sediment yields from the Mississippi River Basin. *Agric. Water Manag.* **2016**, *168*, 112–124. [CrossRef]
31. Lin, P.; Chen, M.; Guo, L. Speciation and transformation of phosphorus and its mixing behavior in the Bay of St. Louis estuary in the northern Gulf of Mexico. *Geochim. Cosmochim. Acta* **2012**, *87*, 283–298. [CrossRef]
32. United States Department of Agriculture—Natural Resources Conservation Service (USDA-NRCS)—Filter Strips (Code 393, 2016). Available online: https://www.nrcs.usda.gov/Internet/FSE_DOCUMENTS/stelprdb1241319.pdf (accessed on 5 December 2021).
33. United States Department of Agriculture—Natural Resources Conservation Service (USDA-NRCS)—Riparian Forest Buffer (Code 391, 2012). Available online: https://www.nrcs.usda.gov/Internet/FSE_DOCUMENTS/stelprdb1255022.pdf (accessed on 5 December 2021).
34. United States Department of Agriculture—Natural Resources Conservation Service (USDA-NRCS)—Conservation Effects Assessment Project (CEAP). 2013. Available online: https://www.nrcs.usda.gov/Internet/FSE_DOCUMENTS/stelprdb1176978.pdf (accessed on 15 December 2021).
35. United States Department of Agriculture—Natural Resources Conservation Service (USDA-NRCS)—Cover Crops (Code 340, 2021). Available online: file:///C:/Users/vv221/Downloads/340_NHCP_CPS_Cover_Crop_2021%20.pdf (accessed on 20 December 2021).
36. Yeo, I.Y.; Lee, S.; Sadeghi, A.M.; Beeson, P.C.; Hively, W.D.; McCarty, G.W.; Lang, M.W. Assessing winter cover crop nutrient uptake efficiency using a water quality simulation model. *Hydrol. Earth Syst. Sci.* **2014**, *18*, 5239–5253. [CrossRef]
37. National Oceanic and Atmospheric Administration (NOAA)—Storm Events Database. Available online: https://www.ncdc.noaa.gov/stormevents/listevents.jsp?eventType=ALL&beginDate_mm=01&beginDate_dd=01&beginDate_yyyy=2014&endDate_mm=05&endDate_dd=31&endDate_yyyy=2016&county=WASHINGTON%3A151&hailfilter=0.00&tornfilter=0&windfilter=000&sort=DT&submitbutton=Search&statefips=28%2CMISSISSIPPI (accessed on 15 July 2021).
38. Risal, A.; Parajuli, P.B.; Ouyang, Y. Impact of BMPs on water quality: A case study in Big Sunflower River watershed, Mississippi. *Int. J. River Basin Manag.* **2021**, 1–14. [CrossRef]
39. Merriman, K.R.; Daggupati, P.; Srinivasan, R.; Toussant, C.; Russell, A.M.; Hayhurst, B. Assessing the impact of site-specific BMPs using a spatially explicit, field-scale SWAT model with edge-of-field and tile hydrology and water-quality data in the Eagle Creek Watershed, Ohio. *Water.* **2018**, *10*, 1299. [CrossRef]
40. Arabi, M.; Frankenberger, J.R.; Engel, B.A.; Arnold, J.G. Representation of agricultural conservation practices with SWAT. *Hydrol. Process.* **2008**, *22*, 3042–3055. [CrossRef]

sustainability

MDPI

Article

Spatiotemporal Variation of Groundwater Extraction Intensity Based on Geostatistics—Set Pair Analysis in Daxing District of Beijing, China

Chen Li, Baohui Men and Shiyang Yin *

College of Water Resources and Hydropower Engineering, North China Electric Power University, Beijing 102206, China; lichen5969@sina.com (C.L.); menbh@ncepu.edu.cn (B.M.)
* Correspondence: yinshiyang@aliyun.com

Abstract: In this paper, the authors studied the impact of human activities on the groundwater environment to reduce the impacts such activities for sustainable groundwater use. The authors took the monthly water table depth data of 32 long-term observation wells in the Daxing District of Beijing from 1986 to 2016 as samples. The authors used seven interpolation methods in the statistics module of ArcGIS by comparing the average error (ME) and root mean square error (RMSE) between the measured and predicted values so that the authors can select the best interpolation method. Using the geostatistical variogram model variation, the authors analyzed the nugget effect through time in the study area. On the basis of the set pair analysis, the main factors causing the increase in groundwater exploitation intensity were quantitatively evaluated and identified. The results were as follows. (1) After comparing the simulation accuracy of the seven interpolation methods for water table depth, ordinary Kriging interpolation was selected as the best interpolation model for the study area. (2) The spatial correlation of the water table depth gradually weakened, and the nugget effect from 2006 to 2016 was 25.92% (>25%). The data indicated that human groundwater exploitation activities from 2006 to 2016 greatly influenced the spatial correlation of the water table depth. (3) The average mining intensity of groundwater from 2006 to 2016 was medium (Level II), and a bleak gradual deterioration trend was observed. The evaluation results of the subtraction set pair potentials in 2010 and 2013, the years of key regulation of groundwater exploitation intensity, are partial negative potential and negative potential, respectively. In 2010, three indicators had partial negative potential: industrial product, tertiary industry product, and irrigated field area. In 2013, five indicators were in negative potential: irrigated area, vegetable area, facility agricultural area, fruit tree area, and the number of wells. Herein, the spatial and temporal variations in the water table depth of the study area are analyzed using a geostatistical method. Moreover, the influence of each water part on the groundwater exploitation intensity is further diagnosed and evaluated based on set pair analysis. The obtained results can provide a theoretical and methodological reference for the sustainable utilization of groundwater in regions where groundwater is the main water supply source, providing a basis for industrial regulation policies in the region.

Keywords: geostatistical analysis; water table depth; interpolation model; set pair analysis

Citation: Li, C.; Men, B.; Yin, S. Spatiotemporal Variation of Groundwater Extraction Intensity Based on Geostatistics—Set Pair Analysis in Daxing District of Beijing, China. *Sustainability* **2022**, *14*, 4341. https://doi.org/10.3390/su14074341

Academic Editor: Lucio Di Matteo

Received: 10 February 2022
Accepted: 30 March 2022
Published: 6 April 2022

1. Introduction

As an important freshwater resource, groundwater is significant for urban life and industrial and agricultural production. Especially in areas lacking surface water, groundwater may be the only stable water supply source. In Beijing, a city located north of North China Plain, the average annual rainfall is 585 mm. Its average water resource is 165 m^3 per capita, accounting for approximately 8% of China's water resources per capita. Moreover, Beijing is located in a semiarid and semihumid region affected by a continental monsoon climate, and the uncertainty of groundwater exploitable volume increases. These reflect the dire water resources situation in Beijing. In addition, rapid urbanization in the

past 20 years has changed the original natural underlying surface and, consequently, the groundwater recharge and discharge processes. It has caused environmental problems, such as the continuous water table depth decrease in regional groundwater, settling of the ground surface, and deterioration of water quality. Even with the South-to-North Water Diversion Project in Beijing, groundwater still covers a significant proportion of the city's water supply. The exploitable amount of groundwater resources refers to the maximum amount of water that can be obtained from the aquifer without causing deterioration of the ecological environment, which is mainly related to the recharge and consumption of groundwater. According to the relevant research results from 1989 to 2000 [1], the average annual recharge of groundwater in the Beijing plain area was 27.66×10^8 m^3/a, in which rainfall infiltration accounted for 47.92%, lateral recharge in mountainous areas accounted for 24.74%, irrigation recharge accounted for 12.86%, and canal infiltration recharge accounted for 14.48%. More than 92% of the lateral supply in mountainous areas comes from the atmospheric precipitation. Furthermore, atmospheric precipitation accounts for a large proportion of groundwater recharge. According to the Beijing Water Resources Bulletin, the average rainfall in Beijing from 2006 to 2019 was 549.86 mm, and from 1989 to 2000 was 549.92 mm, a minute difference indicating that the overall change in groundwater recharge was not considerable. The average annual groundwater consumption in Beijing plain from 1989 to 2000 was 30.27×10^8 m^3/a, in which groundwater exploitation accounted for 87.64%. The artificial exploitation of groundwater has an absolute advantage over the consumption of groundwater. Therefore, studying the spatiotemporal variability of groundwater exploitation intensity is of great practical significance and theoretical value for reducing the impact of human activities on the groundwater environment and realizing the sustainable utilization of groundwater.

Changes in water table depth significantly correlate with groundwater exploitation intensity [2–4]. Thus, these can reflect the intensity of groundwater extraction in a region by collecting water table depth data from monitoring wells at the water level and establishing a correlation model. However, because water table data around monitoring wells are limited, the authors should choose a spatial interpolation model with the slightest error if the authors must characterize the spatial variation of the water table depth in the whole region. Deterministic and geostatistical interpolation methods are commonly used for this purpose [5–9]. On the basis of similarity or smoothness within the study area, deterministic interpolation methods create surfaces using known points [10,11]. The deterministic interpolation methods can be divided into two types: global and local. Global interpolation methods use the sample data set of a whole study area to calculate predictive values (e.g., global polynomial interpolation [GPI]). In contrast, local interpolation methods use known sample points within a small spatial area of a large study area to calculate predictive values (e.g., inverse distance interpolation [IDW], radial basis interpolation, and local polynomial interpolation [LPI]). Geostatistical interpolation methods mainly include ordinary Kriging interpolation (OK), simple Kriging interpolation (SK), pan-Kriging interpolation, probabilistic Kriging interpolation, disjunctive Kriging interpolation, and collaborative Kriging interpolation. These methods are based on the theory of variation function and structural analysis. These methods are used for the optimal unbiased estimation of regionalized variables in limited regions [12,13].

As a unique function of geostatistical analysis, semi-variation is a quantitative expression of the theorem of close geographic resemblance [14,15]. The strength of the geographical spatial correlation can be reflected by the nugget effect (nugget/sill). The larger the nugget effect, the greater the variation between samples caused by random factors [16,17]. Structural factors can enhance the spatial correlation of the water table depth, such as precipitation, topographic undulations, and water-containing rocks. Contrarily, human exploitation belongs to stochastic factors, which weaken the spatial correlation.

Although the nugget effect can identify the spatial variability of water table depth over time, further diagnosing and evaluating the main factors affecting groundwater exploitation is necessary for controlling it. Some evaluation methods are used in developing

and utilizing groundwater. These include the water balance method [18,19], numerical simulation method [20,21], isotope tracer method [22], principal component analysis, fuzzy comprehensive analysis, risk matrix method, projection pursuit method [23], and set pair analysis method [24,25]. Among these, set pair analysis can reflect the uncertainty relationship between evaluation indexes and evaluation standards from the three aspects of identity, difference, and opposition. Thus, it has unique advantages for treating water resources systems. The adjoint functions of set pair analysis include subtraction set pair potential [26], a partial linkage coefficient [27], and a neighbor-joining coefficient [28].

To reduce the impact of human activities on groundwater environment for the sustainable utilization of groundwater, in this study, the Daxing District in Beijing is used as the research area, and the best interpolation model is selected from the seven interpolation methods in the ArcGIS statistics module. The spatial variability characteristics of groundwater depth are analyzed using the geostatistical function model. The main source of water supply in the study area is groundwater, and the types of water use mainly include agricultural water, industrial water, tertiary industry water and domestic water. Therefore, this paper uses the agricultural irrigation area, industrial output value, tertiary industry output value, population, and the number of wells as the evaluation indexes. Using set pair analysis, the authors quantitatively evaluated and identified the main factors causing the increase in groundwater exploitation intensity. The research results can provide a theoretical and methodological reference for the sustainable utilization of groundwater in areas where groundwater is the main source of water supply, providing a basis for industrial regulation policies in the region.

2. Materials and Methods

2.1. Study Area

The Daxing District is located in the southern plains of Beijing (39°26′–39°51′ N, 116°13′–116°43′ E). It has 14 townships and an area of approximately 1036 km^2. It has a warm, temperate, semihumid, semiarid continental monsoon climate with well-defined seasons: cold and less rainy in winter and spring, hot and rainy in summer, and comfortable in autumn. The average annual rainfall is 510.1 mm, with large annual and interannual rainfall distributions. The annual average temperature is 11.7 °C, and the maximum frozen soil depth is 69 cm. The Daxing District belongs to the Yongding River floodplain, which has a flat topography elevated from 9 to 73 m and a topographic slope of about 0.5–2.0‰. The soil type is predominantly sandy loam with a coarsening gradient from west to east. The Daxing District is an important strategic node for the Beijing–Tianjin–Hebei coordinated development. It has four primary industries: metropolitan industry, modern service industry, cultural creative industry, and urban modern agriculture. With the construction of the Beijing Daxing International Airport, the Daxing District is slated to become one of the fastest-growing regions in Beijing.

2.2. Data Sources

2.2.1. Groundwater Water Level Data

Long-term monthly water table depth monitoring data from 32 observational logs in the study area from 1986 to 2016 were collected to monitor the dynamics of water table depth. The monitored well locations are shown in Figure 1.

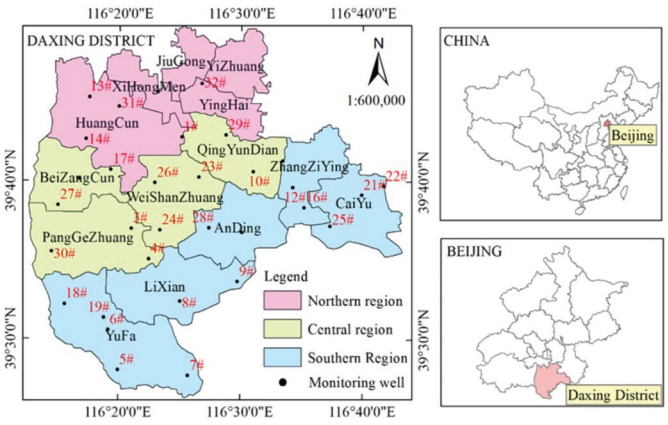

Figure 1. Geographic location map of the study area.

2.2.2. Statistical Information

The annual statistical data used in this paper were collected from relevant data, including the Beijing water service statistical yearbook from 2012 to 2017, the Daxing District statistical yearbook from 2005 to 2017, the groundwater harvest well census results of the Beijing census of water services from 2013, and the third agricultural census data compilation from the Daxing District of Beijing in 2016.

2.3. Research Method

2.3.1. Error Calculation Methods for the Interpolation Model

In this paper, seven methods are used to model the groundwater water level: IDW, GPI, LPI, tension spline interpolation (Tspline), OK, SK, and the universal Kriging method (UK). The advantages and disadvantages of each interpolation method are shown in Table 1. The average errors (MEs), root mean square errors (RMSEs), and Nash–Sutcliffe efficiency coefficient (NSE) of the different methods are compared to select the best model.

Table 1. Advantages and disadvantages of each interpolation method.

Method	Advantages	Disadvantages
IDW	Wide application range and fast calculation speed	IDW can produce bullseyes around data
GPI	Suitable for surface with slow change in spatial data and fast calculation speed	The edge position of data has great influence on the interpolation result
LPI	Suitable for reflecting short-range change of spatial data and medium computing speed	Prone to strip phenomenon
Tspline	Suitable for surfaces with flat spatial data. Compared with GPI, this method provides accurate interpolation and has medium calculation speed	In a short range, when the data change considerably or the sampling point data have great uncertainty, the interpolation results will be greatly affected
OK	The interpolation accuracy is less affected by the sample density and number, and the interpolation effect is good with high accuracy	Intensive calculation and slow operation speed
SK	SK is the same as OK, but also the linear estimation of regionalized variables; the interpolation effect is slightly worse than OK	Intensive calculation and slow operation speed
UK	UK is an extension of OK, which can add explanatory variables to the model	Intensive calculation and slow operation speed

The mean square error, root mean square error, and Nash–Sutcliffe efficiency coefficient (NSE) are calculated as follows:

1. The mean square error

$$\mathrm{ME} = \frac{1}{n}\sum_{i=1}^{n}|z^*(p_i) - z(p_i)| \quad (1)$$

2. Root mean square error

$$\mathrm{RMSE} = \sqrt{\frac{1}{n}\sum_{i=1}^{n}|z^*(p_i) - z(p_i)|^2} \tag{2}$$

3. Nash–Sutcliffe efficiency coefficient

$$\mathrm{NSE} = 1 - \frac{\sum_{i=1}^{n}\left(Z^*(p_i) - Z(p_i)\right)^2}{\sum_{i=1}^{n}\left(Z^*(p_i) - \overline{Z^*}\right)^2} \tag{3}$$

In these equations, ME represents the mean error, RMSE is the root mean square error, NSE represents the Nash–Sutcliffe efficiency coefficient, n represents the sample size, $Z(P_i)$ is the measured value for position P_i, $Z^*(P_i)$ is the predicted value for position P_i, and $\overline{Z^*}$ is the total average of measured values. According to formula (1), formula (2), and formula (3), the average error (ME), root mean square error (RMSE), and Nash–Sutcliffe efficiency coefficient (NSE) of seven interpolation methods were compared. The interpolation method with the smallest ME and RMSE and the closest NSE to one was selected as the best interpolation method.

2.3.2. Calculating the Nugget Effect

The semi-variation coefficient expresses the geographic proximity of similarly quantified expressions [14].

Figure A1 shows that the semi-variation value $r(h)$ increases with distance h because the semi-variation function manifests the spatial correlation coefficient of things. These things are more similar when they are closer to each other and have smaller half mutation values. At greater distances, their similarity weakens, and the half mutation value increases.

When the sampling site distance is 0, the semi-variation function value should be 0. However, when two sampling sites are so close because of measurement error and spatial variation, the semi-variation function value is not 0; that is, these sites form a nugget. The abutment value is when the sampling point increases with the distance h and the semi-variation function $r(h)$ reaches a relatively stable constant from the initial nugget value, called the sill. The spatial correlation does not exist when the variant function value exceeds the abutment value; that is, the functional value does not change with the sampling site interval distance. The variable range is the interval distance between sampling sites when the value of the semi-variation function is taken to reach the abutment value from an initial tuber value.

The nugget effect, which is the ratio of the nugget to the sill, characterizes the strong spatial correlation across samples. The smaller the nugget effect, the smaller the impact of artificial mining on water table depth, and the greater the spatial correlation of water table depth. The greater the nugget effect, the greater the influence of artificial mining on water table depth, and the smaller the spatial correlation of water table depth. A nugget effect <0.25 indicates that the variables are strongly influenced by natural structural factors and have strong spatial correlations. A nugget effect between 0.25 and 0.75 indicates that the variable is influenced by both natural structural and stochastic factors, and the spatial correlation is moderate. When the nugget effect is >0.75, the variables are greatly affected by stochastic factors and have a weak spatial correlation [29].

The nugget effect is calculated as

$$Nugget\ effect = \frac{Nugget}{Sill} \tag{4}$$

2.3.3. Evaluation and Diagnosis of Groundwater Exploitation Intensity Based on Set Pair Analysis

The connection number of set pair analysis is calculated, and the grade of exploitation intensity determined to establish the evaluation and diagnosis model of groundwater exploitation intensity. Then, subtraction sets are used to identify the main factors affecting the intensity of groundwater extraction. The main steps are as follows:

1. Establishment of an evaluation index system and classification of regional groundwater extraction intensity

Because the local natural surface water resources in the study area are insufficient, have low water quality, and cannot be used directly as a water supply, the regional water supply is mainly groundwater and regenerated water. Groundwater composes about 70% of the total water supply. Regenerated water is primarily used for ecological river use, accounting for about 30%. The types of water used in the study area mainly include agricultural water, industrial water, tertiary industry water, domestic water, and ecological water. Agricultural water is used mainly in grain fields, gardens, facility agriculture, and fruit tree irrigation, and the irrigation area of each type is taken as an evaluation indicator. The industrial output is taken as an industrial water evaluation indicator. The tertiary industry output is taken as a tertiary industry water evaluation indicator. The population number is taken as a domestic water evaluation indicator. In addition, the number of wells in the study area is used as a groundwater mining index of groundwater extraction intensity. Therefore, considering practicality, hierarchy, and operability [30], an evaluation index system for evaluating the intensity of groundwater extraction in the township and town areas of the Daxing District and jurisdiction is constructed in this paper. The evaluation indicators of this system are the population (10,000 people), total industrial output (100 million yuan), tertiary industry output (100 million yuan), irrigated area (10,000 mu), vegetable area (10,000 mu), facility agriculture area (10,000 mu), fruit tree area (10,000 mu), and number of machine wells (10,000 eyes).

By referring to the results of previous studies [31] and comprehensively considering economic, social, ecological, and other factors and expert opinions, the intensity of groundwater extraction is classified into three levels, namely, Levels 1, 2, and 3, representing "weak," "medium," and "strong" groundwater extraction intensity, respectively.

2. Calculation of connection numbers for evaluation samples

Equation (5) is used to calculate the connection number of evaluation samples. u_{1i} represents the number of ternary contacts of sample i. n_a, n_b, and n_c indicate the number of evaluation indicators of sample i that are in Levels 1, 2, and 3, respectively. w_j is the weight value of the jth indicator. a_1, b_1, and c_1 respectively denote the sample set pair degrees of identity, divergence, and antagonism, and their values are v_{1i1}, v_{1i2}, and v_{1i3}, respectively. I and J denote the coefficient of difference and the coefficient of opposition, respectively.

$$u_{1i} = \sum_{j=1}^{n_a} w_j + \sum_{j=n_a+1}^{n_a+n_b} w_j I + \sum_{j=n_a+n_b+1}^{n_a+n_b+n_c} w_j J = v_{1i1} + v_{1i2} I + v_{1i3} J = a_1 + b_1 I + c_1 J \quad (5)$$

3. Calculation of the connection number of the evaluation index

The number of contact u_{2ijk} of the evaluation index must be calculated to represent the affiliation degree between the evaluation index x_{ij} and the evaluation standard S_{kj}, where i is the ith sample, j represents the jth indicator, and k represents the rank number.

If the evaluation index is a positive indicator and $S_{0j} < x_{ij} \leq S_{1j}$ or it is a reverse indicator and $S_{0j} > x_{ij} \geq S_{1j}$, the index contact number is calculated using equation (6):

$$\begin{cases} u_{2ij1} = 1 \\ u_{2ij2} = 1 - \frac{2\left(S_{1j} - x_{ij}\right)}{\left(S_{1j} - xi_j\right)} \\ u_{2ij3} = -1 \end{cases} \quad (6)$$

If the evaluation index is a forward indicator and $S_{1j} < x_{ij} \leq S_{2j}$ or it is a reverse indicator and $S_{1j} > x_{ij} \geq S_{2j}$, the index contact number is calculated using Equation (7):

$$\begin{cases} u_{2ij1} = 1 - \frac{2(x_{ij} - S_{1j})}{S_{2j} - S_{1j}} \\ u_{2ij2} = 1 \\ u_{2ij3} = 1 - \frac{2(S_{2j} - x_{ij})}{S_{2j} - S_{1j}} \end{cases} \tag{7}$$

If the evaluation index is a forward indicator and $S_{2j} < x_{ij} \leq S_{3j}$ or it is a reverse indicator and $S_{2j} > x_{ij} \geq S_{3j}$, the index contact number is calculated using Equation (8):

$$\begin{cases} u_{2ij1} = -1 \\ u_{2ij2} = 1 - \frac{2(x_{ij} - S_{2j})}{S_{3j} - S_{2j}} \\ u_{2ij3} = 1 \end{cases} \tag{8}$$

A forward indicator occurs when the rank value increases with the index value; otherwise, it is a reverse indicator. S_{0j}, S_{1j}, S_{2j}, and S_{3j} are the minimum, critical value of Levels 1 and 2, critical value of Levels 2 and 3, and maximum value of index j, respectively.

The degree of membership between the contact number of sample indicators and the evaluation criteria can be expressed as follows:

$$v^*_{2ijk} = 0.5 + 0.5u_{2ijk} \tag{9}$$

In calculating the contact number of sample indicators u_2, Equation (9) is first normalized, and the calculation formula is as follows:

$$v_{2ijk} = \frac{v^*_{2ijk}}{\sum_{k=1}^{3} v^*_{2ijk}} \tag{10}$$

$$u_{2i} = \sum_{j=1}^{n_a} w_j v_{2ij1} + \sum_{j=n_a+1}^{n_a+n_b} w_j v_{2ij2} I + \sum_{j=n_a+n_b+1}^{n_a+n_b+n_c} w_j v_{2ij3} J = v_{2i1} + v_{2i2} I + v_{2i3} J = a_2 + b_2 I + c_2 J \tag{11}$$

In the formula, v_{2ijk} represents the contact number component of the jth indicator in the ith sample. u_{2i} indicates the contact number of sample indicators i. a_2, b_2, and c_2 respectively represent the sample index set pairs' degree of identity, divergence, and antagonism, and their values are v_{2i1}, v_{2i2}, and v_{2i3}, respectively.

4. Calculation of average contact number

The average contact number by sample is obtained by taking the contact number of a sample and the contact number of an index to sufficiently extract sample information [26]:

$$v_{ik} = \frac{(v_{1ik} v_{2ik})^{0.5}}{\sum_{k=1}^{3} (v_{1ik} v_{2ik})^{0.5}} \tag{12}$$

$$u_i = v_{i1} + v_{i2} I + v_{i3} J \tag{13}$$

In the formula, v_{ik} represents the mean number of contact components of the ith sample. u_i indicates the average number of contacts for the ith sample.

5. Determination of the intensity levels of underground extraction

The values of groundwater extraction intensity between sample i and index j are calculated separately using the level eigenvalue method [32], and the calculations are as follows:

$$h(i) = \sum_{k=1}^{3} v_{ik}k \tag{14}$$

$$h(j) = \sum_{k=1}^{3} v_{2ijk}k \tag{15}$$

In the formula, $h(i)$ represents the value of groundwater extraction intensity for the ith sample, and $h(j)$ represents the groundwater extraction intensity value of the jth indicator.

6. Diagnosis of groundwater extraction intensity based on the number of linkages

The identification of key indicators affecting the intensity of groundwater extraction uses subtraction set pair potentials [26].

According to the set pair analysis theory, the subtraction set pair potential for the number of contacts essentially reflects the relative ascertainment status and developmental trends of the study subjects. The subtraction set pair potential $S_f(u)$ is defined as

$$s_f(u) = a - c + ba - bc = (a - c)(1 + b) \tag{16}$$

In the formula, $s_f(u) \in [-1, 1]$. According to the principle of uniformity, the subtraction set pair potentials can be divided into five grades: negative potential, $s_f(u) \in [-1, -0.6)$; partial negative potential, $s_f(u) \in [-0.6, -0.2)$; balanced potential, $s_f(u) \in [-0.2, 0.2]$; partial positive potential, $s_f(u) \in (0.2, 0.6]$; and positive potential, $s_f(u) \in (0.6, 1.0]$. Positive and partial positive potentials illustrate that research subjects favorably develop. Negative and partial negative potentials illustrate that research subjects develop in an unfavorable direction and thus require focusing on and regulating indicators of these negative states. The homogeneous potential is an uncertain state.

The total adjacent subtraction is obtained by calculating the difference between the degree of identity a and the degree of difference b, degree of opposition c, and degree of difference b, which reflects developmental changes of things [33]. The specific calculation procedure is as follows:

$$u_3 = (a - c) + (b - c)(a - b) + (b - a)(c - b) \tag{17}$$

In the formula, $u_3 \in [-2, 1.0625]$, where, when $a = 0$, $b = 1$, and $c = 0$, $u_{3\min} = -2$; when $a = b = 0$, $c = 1$, and $c = 1$, $u_3 = -1$; when $a = 0.875$, $b = 0.125$, and $c = 0$, $u_{3\max} = 1.0625$. When u_3 changed from -2 to 1.0625, the trend of the research object gradually changes from inverse potential to potential, but the critical state cannot be determined.

The potential function can also judge the trend of the set toward the development of events. Its value is also larger, indicating that the research subjects move toward the same potential [28]. The specific calculation is as follows:

$$Shi(u_4) = (a/b)/(b/c) = ac/b^2 \tag{18}$$

3. Results and Discussion

3.1. Results of the Interpolation Calculation of Water Table Depth

The parameters selected for each interpolation method to obtain the spatial distribution characteristics of water table depth in the study area should have minimal errors. The selection of model parameters and error accuracy is shown in Table 2.

Table 2. Interpolation model parameters and interpolation error table of water table depth from 1986 to 2016.

Interpolation Model	Data Conversion	Maximum Number of Predicted Points within the Search Radius	Minimum Number of Predicted Points within the Search Radius	Variation Function	Mean (m)	Root Mean Square (m)	Nash-Sutcliffe Efficiency Coefficient
IDW	no	15	10	/	0.1816	4.5373	0.70
GPI	no	/	/	/	0.0787	5.2072	0.81
LPI	no	20	10	/	0.1309	3.9898	0.83
Tspline	no	25	10	/	0.1348	4.2010	0.80
OK	no	15	5	Globular model	0.0507	3.9577	0.89
SK	no	16	5	Gaussian model	0.0517	4.0492	0.86
UK	no	12	5	Globular model	0.0536	3.9865	0.88

Table 2 shows the deterministic interpolation method is less accurate than the geodesic statistical interpolation method. Among all listed methods, IDW has the largest error and a poor interpolation effect, which may be due to the existence of some extreme points in the interpolation process [5,15]. Tspline, similar to IDW, is susceptible to the influence of extreme value points [7,17], resulting in less effective interpolation, as shown by its ME and RMSE. LPI, which is suitable for local spatial interpolation, shows high simulation accuracy for short-range variations [7,11]. However, it predicts a large fluctuation of results for the analysis of 30 older sequences in the water table depth; thus, its interpolation accuracy is low. GPI is based on the sample data as a whole [5,7,14]. The higher the number of interpolations, the better the interpolation effect. However, the complexity and error are also relatively increased. This high number of interpolations also results in the largest RMSE and a poor prediction effect.

The ME of OK, SK, and UK differ minimally, but the RMSE of the OK method is less than those of SK and UK. Furthermore, the NSE of the geostatistical interpolation method is closer to 1 than that of the deterministic interpolation method, indicating that the geostatistical method is more reliable than the deterministic interpolation method. Among the geostatistical interpolation methods, the NSE of the OK is higher than that of SK and UK, indicating that OK has the highest reliability. Thus, the best interpolation method selected is the OK method.

3.2. The Spatial-Temporal Distribution Rules of Water Table Depth

The water table depth in 1986, 1996, 2006, and 2016 is spatially interpolated using the OK method.

Figure 2 shows that the overall water table depth in the Daxing region constantly decreased. From 1986 to 2016, the water table depth of the regional subsurface decreased from 8.1 to 17.60 m, with an average annual decline rate of 0.30 m. From 1986 to 1996, the water table depth decreased from 8.1 to 10.80 m, with an average annual decline of 0.27 m. From 1996 to 2006, the water table depth decreased from 10.80 to 17.34 m, with an average annual decline of 0.65 m. From 2006 to 2016, the water table depth decreased from 17.34 to 17.60 m, with an average annual decline rate of 0.03 m.

From the above analysis, the period with the most significant decline rate of water table depth in the Daxing District is from 1996 to 2006. This indicates that the groundwater in this period is in a state of overdraft, resulting in a continuous decline of water table depth. From 2006 to 2016, the water table depth was almost flat, although it decreased slightly. This indicates that groundwater is basically in the state of mining–compensation balance, which may be related to the extensive use of regenerated water locally. However, environmental and geological problems caused by groundwater overmining remained serious because of the previous continuous years of overdraft.

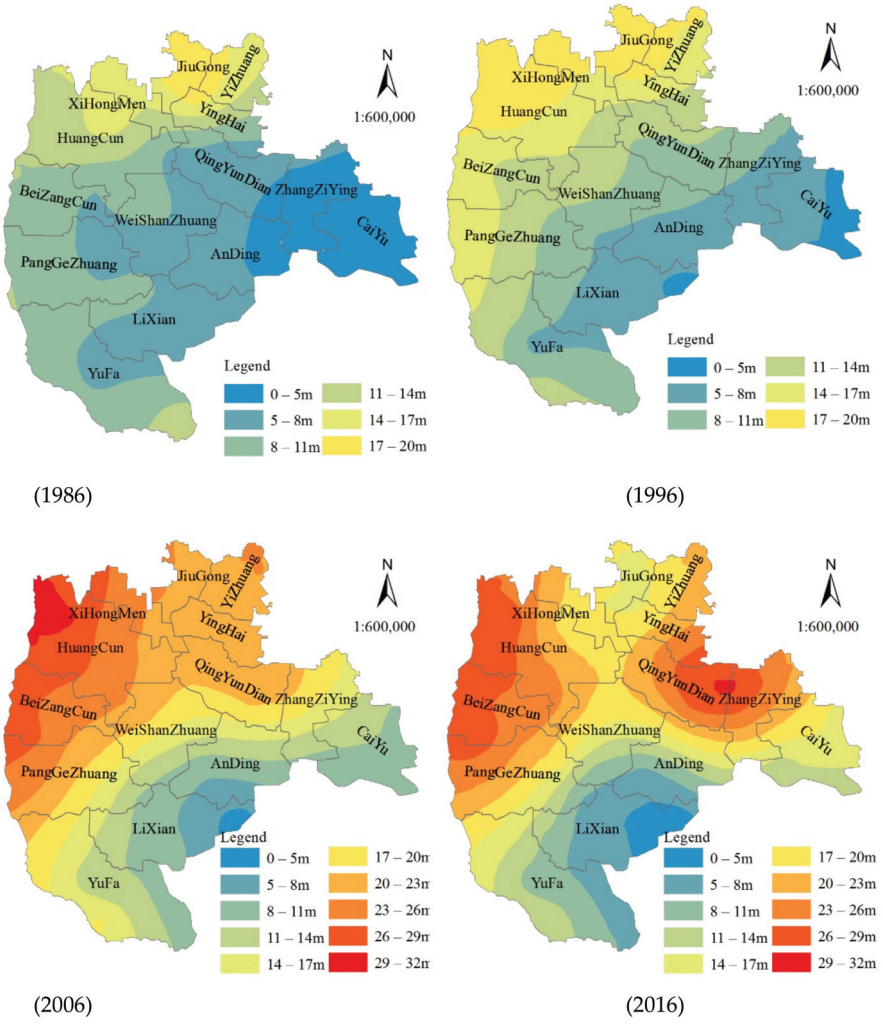

Figure 2. Variation of water table depth from 1986 to 2016.

From 1986 to 2016, the decline rates of water table depth in the northern, central, and southern Daxing District are 0.23, 0.49, and 0.18 m/a, respectively. These indicate that the central region had the largest rate of water table depth decline, followed by the northern and southern regions. Groundwater depression funnels can be found in the Qingyundian and Beizangcun in the central region, with a continuous outward diffusion trend. Thus, groundwater exploitation control in the region should be strengthened. The deepest water table depth in the north is always higher than that in the middle and south, which may be related to population distribution and the industrial layout in the Daxing District. Compared with those in the northern and central regions, the water table depth and water table decline rate in the southern region are relatively small. However, from 1986 to 2006, the water table depth decreased from 6.04 to 11.82 m, and the water table depth continued to decline. Thus, the southern region is also in a state of continuous overextraction.

3.3. Spatial Variability Analysis of Groundwater Depth

In identifying the main factors causing the decline of water table depth, the nugget effects of the three periods from 1986 to 1995, 1996 to 2005, and 2006 to 2016 are calculated to analyze the spatial variability characteristics of water table depth using the OK method.

As shown in Table 3, the nugget effect of water table depth increased from 1986 to 2016, indicating that its spatial correlation gradually weakened and that the influence of human activities on water table depth increased. The nugget effect increased from 0.04 to 0.10 in 1986–1995 and 1996–2005. Compared with that in 1996–2005, the nugget effect increased from 0.10 to 0.26 in 2006–2016 (greater than 0.25), indicating that human extraction activities have become an essential factor affecting water table depth. Therefore, further evaluating and diagnosing the existing groundwater exploitation intensity is necessary to reduce the influence of human mining activities on the water table depth.

Table 3. Semi-variogram model parameters of water table depth from 1986 to 2016.

Name	1986–1995	1996–2005	2006–2016
Nugget value	1.88	5.85	28.03
Partial sill	47.06	45.53	78.95
Sill	48.94	51.38	106.98
Nugget effect	0.04	0.10	0.26

3.4. Determination of Groundwater Exploitation Intensity Levels and Identification of Key Control Years in the Daxing District Using Set Pair Analysis

An index system and an evaluation standard level of groundwater exploitation intensity in the Daxing District are determined according to the calculation method in Section 2.3.3 to analyze the spatiotemporal variation of groundwater exploitation intensity in the Daxing region from 2006 to 2016. The weight of each index is determined using the entropy weight–AHP method, as shown in Table 4.

Table 4. Evaluation index, standard grade, and index weight of groundwater exploitation intensity in the Daxing District.

No.	Subsystem	Evaluation Index	Symbol	Evaluation Index			Index Weight
				Weak (Level I)	Medium (Level II)	Strong (Level III)	
1	Domestic water	Population (10,000)	X1	≤115.90	115.90–150.70	>150.70	0.1480
2	Industrial water	Gross industrial production (100 million yuan)	X2	≤109.28	109.28–202.48	>202.48	0.1476
3	Tertiary industry water	GDP of the tertiary industry (100 million yuan)	X3	≤189.81	189.81–338.37	>338.37	0.1586
4	Agricultural water	Irrigation area (10,000 mu)	X4	≤18.42	18.42–19.35	>19.35	0.1132
5		Vegetable field area (10,000 mu)	X5	≤3.04	3.04–3.15	>3.15	0.1141
6		Facility agricultural area (10,000 mu)	X6	≤7.87	7.87–7.98	>7.98	0.0862
7		Fruit tree area (10,000 mu)	X7	≤6.96	6.96–31.33	>31.33	0.0565
8	Number of underground wells	Number of motorized wells (10,000 eyes)	X8	≤1.17	1.17–1.23	>1.23	0.1788

The subtraction set pair potential, total adjacent subtraction, and the potential function can all reflect the trend of event development. Thus, the potential function values and the total adjacent subtraction of each sample are calculated using Equations (18) and (17), respectively, to verify the rationality of the results of the subtraction set pair potential evaluation.

However, Equation (18) shows that the difference degree b of the potential function cannot be 0; when the difference degree is 0, the potential function method cannot judge the trend of event development. Equation (17) shows that the subtraction of all neighbors

can judge the trend of an event. Still, it cannot judge the critical value of the situation where it is located. Fortunately, the subtraction set pair potential can deal with situations where the difference degree b is 0 and determines the critical value of the development trend of events. Therefore, it is selected for evaluating the potential of groundwater extraction intensity in this paper.

Figure 3 shows that the evaluation results using subtraction set pair potential, evaluation level, potential function, and subtractive full neighbor connection number are basically consistent. However, the evaluation level has a trend opposite to those of the other three methods. With greater development intensity, the evaluation level increased, whereas the other three methods decreased. Figure 3 shows that the groundwater development intensity is largest in 2013 in the Daxing District and smallest in 2008. The groundwater development intensity from 2006 to 2013 had an increasing trend year by year. However, it slightly eased from 2013 to 2016. The average connection number of groundwater development intensities for the whole region in 2010 and 2013 had partial negative potential and negative potential, respectively. In 2006, 2009, 2011–2012, and 2014–2016, they had balanced potential. In 2007–2008, they had partial positive potential. These were consistent with the results of the comprehensive review of the connection numbers. According to the evaluation results, the average mining intensity of groundwater in the Daxing District from 2006 to 2016 was medium (Level II) with a bleak gradual deterioration trend. The evaluation results of the subtraction set pair potential in 2010 and 2013 were partial negative potential and negative potential, respectively, and the comprehensive evaluation results were 2.31 and 2.45. The years 2010 and 2013 were the groundwater exploitation intensity key control years.

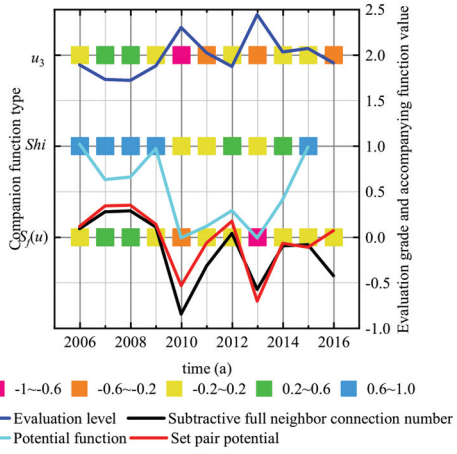

Figure 3. Groundwater exploitation intensity in the Daxing District from 2006 to 2016.

3.5. Identification of Main Factors Affecting Groundwater Exploitation Intensity in the Daxing District Based on Subtraction Set Pair Potential

The authors further identified the main factors affecting the intensity of groundwater extraction and provided technical support for groundwater management and protection. In this paper, the subtraction set of each evaluation index was used to diagnose and analyze the jth index of the ith evaluation sample, which can be obtained as the main index that caused the increase in groundwater extraction from 2006 to 2016 in the Daxing District. As shown in Figure 4, in 2010, three indicators had partial negative potential: industrial GDP, tertiary industry GDP, and irrigation area. In 2013, five indicators had negative potential: irrigated land area, vegetable field area, facility agriculture area, fruit tree area, and the number of wells. In Figs. 4 and 5, the trends of the subtracted set pair potential (evaluation level) of the gross industrial product (X2), gross tertiary industrial product (X3), and irrigation area (X4) are basically consistent between 2006 and 2016. However, the subtraction set pair potentials (evaluation grade) of these indicators significantly decreased

(increased) in 2010, which may be related to the adjustment of the industrial structure in the Daxing District. The Daxing District began vigorous industrial and tertiary industrial developments from 2009 to 2010. Its industrial and tertiary industry output values in 2010 increased by 16.12% and 17.54%, respectively, compared with those in 2009. This rapid development resulted in the rapid increase of industrial water and tertiary industry water consumption.

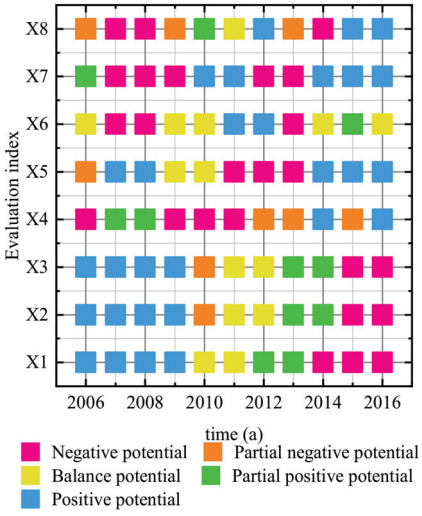

Figure 4. Subtraction set potential of each evaluation index in the Daxing District from 2006 to 2016.

The subtraction set pair potential (evaluation rank) of vegetable area (X5) from 2006 to 2016 had a continued decreasing (rising) trend from 2008 to 2013 (Figure 5). These indicate that the vegetable area (X5) had an increasing trend at this stage, leading to increased water consumption. The subtraction set pair potential (evaluation rank) of the facility agricultural area (X6) continued to increase (decrease) from 2008 to 2012, indicating that it had a decreasing trend at this stage. In 2013, the subtraction set pair potential appeared to increase, indicating that facility agricultural area (X6) had an increasing trend compared with that in 2012. The subtraction set pair potential (evaluation rank) of the fruit tree area (X7) had an increasing (decreasing) trend from 2008 to 2011 and a decreasing (increasing) trend from 2011 to 2013, indicating that it had an increasing trend in 2011–2013 compared with that in the previous stage. From these analyses and from Figs. 2 and 3, the authors can observe that the use of agricultural water has continuously decreased since 2014, which is considerably related to the implementation of agricultural water policies in Beijing. This indicates that the Daxing region has achieved good results in its water-saving social construction practice. The subtraction set pair potential (evaluation grade) of the number of wells (X8) showed an increasing (decreasing) trend from 2008 to 2012 and a decreasing (increasing) trend from 2012 to 2014. This indicates that the number of wells (X8) had a decreasing trend from 2008 to 2012, an increasing trend from 2012 to 2014, and a decreasing trend since 2014. The initial increasing and the ensuing decreasing trends for the number of wells (X8) indicate rapid population growth and the development of three major industries from 2008 to 2014, which continuously increased the demand for groundwater. Conversely, the number of opportunistic wells (X8) tended to decrease since 2014, which may be related to the water-affecting evaluation and approval system implemented in Beijing city and the rigor of new water use. It may additionally be related to the substitution of some subsurface water sources after the north-to-south water diversion into Beijing.

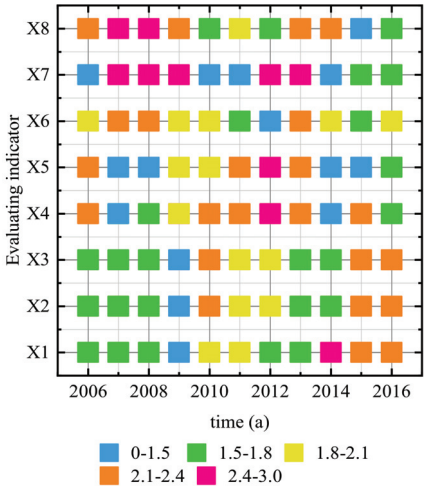

Figure 5. Evaluation grade of each evaluation index in the Daxing District from 2006 to 2016.

3.6. Research Implications and Limitations

The above analysis shows that from 1986 to 2016, the water table depth of the study area has been continuously declining as a whole, indicating that groundwater is in a state of continuous overexploitation and the impact of human exploitation on water table depth is increasing. Through set pair analysis, the main factors causing the increase in the groundwater exploitation intensity were further diagnosed and identified, showing that the groundwater exploitation intensity in this area had a bleak, gradual deterioration trend. The proposed research method can provide a method and theoretical reference for the sustainable utilization of groundwater in the region where the groundwater is the main source of water supply, providing a basis for the industrial regulation policy in this region. However, there are still some limitations in this paper, such as groundwater quality problems caused by the decline in the water table depth. Moreover, the best interpolation method selected in this paper may only be suitable for this area. Therefore, when performing spatial interpolation in other areas, the actual situation must be considered to reselect the optimal method.

4. Conclusions

The spatial variability of groundwater table depth in the study area is combined with the evaluation and diagnosis of groundwater exploitation intensity in this paper. The authors studied the impact of human extraction activities on the water table burial depth and identified the main factors affecting the groundwater extraction intensity. This research can provide theoretical support for sustainable groundwater use and industrial regulation policies in areas with water shortages. The conclusions are as follows:

1. The OK method is selected as the best interpolation model after comparing the prediction accuracies of seven interpolation methods for the water table burial depth in the study area. The OK method had significantly higher accuracy than those of SK and UK. Its ME did not differ much from those of the other methods, but it had a significantly smaller RMSE.
2. The spatial interpolation of groundwater table depth in the study area from 1986 to 2016 is conducted using the OK method. The interpolation results showed that the overall groundwater table depth in the Daxing District increased from 1986 to 2016. The rate of groundwater decline was fastest from 1996 to 2006, with an annual decline rate of 0.65 m. The region with the largest decline rate of groundwater table depth in the Daxing District from 1986 to 2016 is the central area, followed by the northern and

southern areas. Groundwater downwelling funnels occurred in Qingyundian and Beizangcun in the central region, which tended to continuously spread outward.

3. The nugget effect from 1986 to 2016 was calculated using the geostatistical variation function model, which showed that the nugget effect of groundwater table depth increased continuously. The spatial correlation gradually weakened from 1986 to 2016. From 1986 to 2005, the effect of natural structural factors on the burial depth played a dominant role. From 2006 to 2016, human extraction activities have become important factors affecting the burial depth of the water table.
4. The evaluation grade of groundwater exploitation intensity in the Daxing District from 2006 to 2016 was calculated using set pair analysis. The subtraction set pair potential was used to identify the key regulation years and the main factors affecting groundwater exploitation intensity. The results show that the groundwater extraction intensity in the Daxing area is moderate (grade II) with a bleak gradual deterioration trend. The evaluation results in 2010 and 2013, the years of key regulation of groundwater exploitation intensity, are partial negative potential and negative potential, respectively. The comprehensive evaluation results are 2.31 and 2.45, respectively. In 2010, three indicators had partial negative potential: industrial GDP, tertiary industry GDP, and irrigation area. In 2013, five indicators had negative potential: the irrigation area, vegetable area, facility agriculture area, fruit tree area, and number of wells.

To conclude, in the process of urbanization in the study area, the influence of human exploitation on the water table depth is increasing. Therefore, to reduce the impact of human exploitation on the groundwater resources, the regional water table depth monitoring system must be improved to understand the dynamic changes in the water table depth in time. Then, the regional total water consumption and the water consumption of each water-using sector must be analyzed and evaluated to understand the change in the groundwater exploitation intensity in that year and the main water-using sector that caused the change in the groundwater exploitation intensity. Based on the above analysis results of groundwater consumption and groundwater exploitation intensity, it provides the basis for groundwater exploitation planning and industrial regulation policy in the next year. Finally, unconventional water sources should be actively developed, and areas with water diversion conditions should actively strive for external water sources to reduce groundwater exploitation.

Author Contributions: Conceptualization: B.M. and S.Y.; methodology: C.L.; software: C.L.; validation: C.L.; formal analysis: C.L.; investigation: C.L.; resources: C.L.; data curation: C.L.; writing—original draft preparation: C.L.; writing—review and editing: C.L.; visualization: C.L.; supervision: B.M. and S.Y.; project administration: B.M. and S.Y.; funding acquisition: B.M. and S.Y. All authors have read and agreed to the published version of the manuscript.

Funding: This research was funded by the Ministry of Education of the People's Republic of China (2019MS028), Ministry of Science and Technology of the People's Republic of China (2016YFC0401406).

Institutional Review Board Statement: Not applicable.

Informed Consent Statement: Not applicable.

Data Availability Statement: Data can be made available upon request.

Acknowledgments: Thanks for the support of the above funding entities and the Laboratory of College of Water Resources and Hydropower Engineering, North China Electric Power University.

Conflicts of Interest: The authors declare no conflict of interest.

Appendix A

The Appendix is as follows:

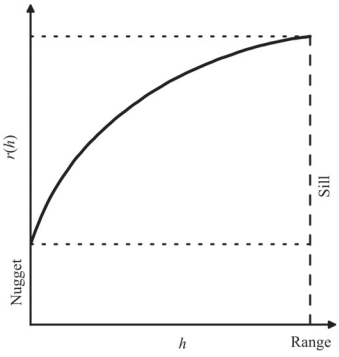

Figure A1. Curve of the semi-variation function.

References

1. Zhang, A.J.; Ye, C. *Beijing Groundwater*, 1st ed.; Geological Publishing House: Beijing, China, 2008; pp. 122–126.
2. Zhang, Z.; Guo, H.; Zhao, W.; Liu, S.; Cao, Y.; Jia, Y. Influences of groundwater extraction on flow dynamics and arsenic levels in the western Hetao Basin, Inner Mongolia, China. *Hydrogeol. J.* **2018**, *26*, 1499–1512. [CrossRef]
3. Sahoo, S.; Russo, T.A.; Elliott, J.; Foster, I. Machine learning algorithms for modeling groundwater level changes in agricultural regions of the U.S. *Water Resour. Res.* **2017**, *53*, 3878–3895. [CrossRef]
4. Chen, M.; Tomás, R.; Li, Z.; Motagh, M.; Li, T.; Hu, L.; Gong, H.; Li, X.; Yu, J.; Gong, X. Imaging Land Subsidence Induced by Groundwater Extraction in Beijing (China) Using Satellite Radar Interferometry. *Remote Sens.* **2016**, *8*, 468. [CrossRef]
5. Pellicone, G.; Caloiero, T.; Modica, G.; Guagliardi, I. Application of several spatial interpolation techniques to monthly rainfall data in the Calabria region (southern Italy). *Int. J. Climatol.* **2018**, *38*, 3651–3666. [CrossRef]
6. Thiesen, S.; Vieira, D.M.; Mälicke, M.; Loritz, R.; Wellmann, J.F.; Ehret, U. Histogram via entropy reduction (HER): An information-theoretic alternative for geostatistics. *Hydrol. Earth Syst. Sci.* **2020**, *24*, 4523–4540. [CrossRef]
7. Ohmer, M.; Liesch, T.; Goeppert, N.; Goldscheider, N. On the optimal selection of interpolation methods for groundwater contouring: An example of propagation of uncertainty regarding inter-aquifer exchange. *Adv. Water Resour.* **2017**, *109*, 121–132. [CrossRef]
8. Adhikary, P.P.; Dash, C. Comparison of deterministic and stochastic methods to predict spatial variation of groundwater depth. *Appl. Water Sci.* **2017**, *7*, 339–348. [CrossRef]
9. Uc Castillo, J.L.; Ramos Leal, J.A.; Martínez Cruz, D.A.; Rodríguez Robles, U.; Cervantes Martínez, A.; Marín Celestino, A.E. Identification of the Dominant Factors in Groundwater Recharge Process, Using Multivariate Statistical Approaches in a Semi-Arid Region. *Sustainability* **2021**, *13*, 11543. [CrossRef]
10. Bronowicka-Mielniczuk, U.; Mielniczuk, J.; Obroślak, R.; Przystupa, W. A Comparison of Some Interpolation Techniques for Deter-mining Spatial Distribution of Nitrogen Compounds in Groundwater. *Int. J. Environ. Res.* **2019**, *13*, 679–687. [CrossRef]
11. Fazeli Sangani, M.; Namdar Khojasteh, D.; Owens, G. Dataset characteristics influence the performance of different inter-polation methods for soil salinity spatial mapping. *Environ. Monit. Assess.* **2019**, *191*, 1–12. [CrossRef]
12. Karami, S.; Madani, H.; Katibeh, H.; Marj, A. Assessment and modeling of the groundwater hydrogeochemical quality param-eters via geostatistical approaches. *Appl. Water Sci.* **2018**, *8*, 1–13. [CrossRef]
13. Zafor, M.A.; Alam, M.J.B.; Rahman, M.A.; Amin, M.N. The analysis of groundwater table variations in Sylhet region, Bangladesh. *Environ. Eng. Res.* **2017**, *22*, 369–376. [CrossRef]
14. Chandan, K.S.; Yashwant, B.K. Optimization of Groundwater Level Monitoring Network Using GIS-based Geostatistical Method and Multi-parameter Analysis: A Case Study in Wainganga Sub-basin, India. *Chin. Geogr. Sci.* **2017**, *27*, 201–215. [CrossRef]
15. Hussain, M.M.; Bari, S.H.; Tarif, M.E.; Rahman, M.T.U.; Hoque, M.A. Temporal and spatial variation of groundwater level in Mymensingh district, Bangladesh. *Int. J. Hydrol. Sci. Technol.* **2016**, *6*, 188. [CrossRef]
16. Zhang, H.; Wang, X.S. The impact of groundwater depth on the spatial variance of vegetation index in the Ordos Plateau, China: A semivariogram analysis. *J. Hydrol.* **2020**, *588*, 125096. [CrossRef]
17. Yin, S.; Gu, X.; Xiao, Y.; Wu, W.; Pan, X.; Shao, J.; Zhang, Q. Geostatistics-based spatial variation characteristics of groundwater levels in a wastewater irrigation area, northern China. *Water Sci. Technol. Water Supply* **2017**, *17*, 1479–1489. [CrossRef]
18. Wakode, H.B.; Baier, K.; Jha, R.; Azzam, R. Impact of urbanization on groundwater recharge and urban water balance for the city of Hyderabad, India. *Int. Soil Water Conserv. Res.* **2018**, *6*, 51–62. [CrossRef]

19. Yue, H.; Liu, Y. Water balance and influence mechanism analysis: A case study of Hongjiannao Lake, China. *Environ. Mental. Monit. Assess.* **2021**, *193*, 1–17. [CrossRef] [PubMed]
20. Mahmoudpour, M.; Khamehchiyan, M.; Nikudel, M.R.; Ghassemi, M.R. Numerical simulation and prediction of regional land subsid-ence caused by groundwater exploitation in the southwest plain of Tehran, Iran. *Eng. Geol.* **2016**, *201*, 6–28. [CrossRef]
21. Dash, C.; Sarangi, A.; Singh, D.K.; Adhikary, P.P. Numerical simulation to assess potential groundwater recharge and net ground-water use in a semi-arid region. *Environ. Monit. Assess.* **2019**, *191*, 1–14. [CrossRef]
22. Négrel, P.; Petelet-Giraud, E.; Widory, D. Strontium isotope geochemistry of alluvial groundwater: A tracer for ground-water resources characterisation. *Hydrol. Earth Syst. Sci.* **2004**, *8*, 959–972. [CrossRef]
23. Yue, C.F.; Wang, Q.J.; Li, Y.Z. Evaluating water resources allocation in arid areas of northwest China using a projection pursuit dynamic cluster model. *Water Supply* **2019**, *19*, 762–770. [CrossRef]
24. Tian, R.; Wu, J. Groundwater quality appraisal by improved set pair analysis with game theory weightage and health risk estimation of contaminants for Xuecha drinking water source in a loess area in Northwest China. *Hum. Ecol. Risk Assess. Int. J.* **2019**, *25*, 132–157. [CrossRef]
25. Giao, N.T.; Nhien, H.T.H.; Anh, P.K.; Van Ni, D. Classification of water quality in low-lying area in Vietnamese Mekong delta using set pair analysis method and Vietnamese water quality index. *Environ. Monit. Assess.* **2021**, *193*, 1–16. [CrossRef] [PubMed]
26. Jin, J.L.; Shen, S.X.; Li, J.Q.; Cui, Y.; Wu, C.G. Assessment and Diagnosis Analysis Method for Regional Water Resources Carrying Capac-ity Based on Connection Number. *J. North China Univ. Water Resour. Electr. Power* **2018**, *39*, 1–9. [CrossRef]
27. Yang, Y.F.; Wang, H.R.; Zhao, W.J.; Yan, G.W. Evaluation Model of Water Resources Carrying Capacity Based on Set Pair Potential and Partial Connection Number. *Adv. Eng. Sci.* **2021**, *53*, 99–105. [CrossRef]
28. Yang, H.M.; Zhao, K.Q. The calculation and application of partical connection numbers. *CAAI Trans. Intell. Syst.* **2019**, *14*, 865–876. [CrossRef]
29. Cambardella, C.A.; Moorman, T.B.; Novak, J.M.; Parkin, T.B.; Karlen, D.L.; Turco, R.F.; Konopka, A.E. Field-Scale Variability of Soil Properties in Central Iowa Soils. *Soil Sci. Soc. Am. J.* **1994**, *58*, 1501–1511. [CrossRef]
30. Gao, F.; Wang, H.X.; Liu, C.M. Variation in groundwater resources carrying capacity in Beijing between 2001 and 2015. *Chin. J. Eco-Agric.* **2019**, *27*, 1088–1096. [CrossRef]
31. Yu, H.Z.; Li, L.J.; Li, J.Y. Evaluation of water resources carrying capacity in the Beijing-Tianjin-Hebei Region based on quantity-quality-water bodies-flow. *Resour. Sci.* **2020**, *42*, 02000358. [CrossRef]
32. Li, Y.L.; Guo, X.N.; Guo, D.Y.; Wang, X.H. An evaluation method of water resources carrying capacity and application. *Prog. Geogr.* **2017**, *36*, 342–349. [CrossRef]
33. Jin, J.L.; He, P.; Zhang, H.Y.; Li, J.Q.; Chen, M.L.; He, J. Subtractive full neighbor connection number and its application in trend analysis of re-gional water resources carrying capacity. *J. Northwest Univ.* **2020**, *50*, 438–446. [CrossRef]

water

MDPI

Hypothesis

Water Footprint Assessment of Rainfed Crops with Critical Irrigation under Different Climate Change Scenarios in SAT Regions

Konda Sreenivas Reddy *, Vegapareddy Maruthi, Prabhat Kumar Pankaj, Manoranjan Kumar, Pushpanjali, Mathyam Prabhakar, Artha Gopal Krishna Reddy, Kotha Sammi Reddy, Vinod Kumar Singh and Ashishkumar Kanjibhai Koradia

ICAR-Central Research Institute for Dryland Agriculture (CRIDA), Santhoshnagar, Hyderabad 500059, India; v.maruthi@icar.gov.in (V.M.); pankaj.pk@icar.gov.in (P.K.P.); manoranjan.kumar@icar.gov.in (M.K.); pushpanjali@icar.gov.in (P.); m.prabhakar@icar.gov.in (M.P.); agk.reddy@icar.gov.in (A.G.K.R.); k.sammireddy@icar.gov.in (K.S.R.); director.crida@icar.gov.in (V.K.S.); akkoradia51@gmail.com (A.K.K.)
* Correspondence: ks.reddy@icar.gov.in

Abstract: Semi-Arid Tropical (SAT) regions are influenced by climate change impacts affecting the rainfed crops in their productivity and production. Water Footprint (WF) assessment for rainfed crops on watershed scale is critical for water resource planning, development, efficient crop planning, and, better water use efficiency. A semi-arid tropical watershed was selected in lower Krishna river basin having a 4700 ha area in Telangana, India. Soil and Water Assessment Tool (SWAT) was used to estimate the water balance components of watershed like runoff, potential evapotranspiration, percolation, and effective rainfall for base period (1994 to 2013) and different climate change scenarios of Representative Concentration Pathways (RCP) 2.6, 4.5 and 8.5 for the time periods of 2020, 2050 and 2080. Green and blue WF of rainfed crops viz., maize, sorghum, groundnut, redgram and cotton were performed by considering rainfed, and two critical irrigations (CI) of 30 mm and 50 mm. It indicated that the effective rainfall (ER) is less than crop evapo-transpiration (ET) during crop growing period under different RCPs, time periods, and base period. The green WF under rainfed condition over different RCPs and time periods had decreasing trend for all crops. The study suggested that in the rainfed agro-ecosystems, the blue WF can significantly reduce the total WF by enhancing the productivity through critical irrigation management using on farm water resources developed through rainwater harvesting structures. The maximum significant reduction in WF over the base period was observed 13–16% under rainfed, 30–32% with 30 mm CI and 40–42% with 50 mm CI by 2080. Development of crop varieties particularly in oilseeds and pulses which have less WF and higher yields for unit of water consumed could be a solution for improving overall WF in the watersheds of SAT regions.

Keywords: green and blue water footprint; crop evapotranspiration; effective rainfall; rainfed crops; climate change; watershed

Citation: Reddy, K.S.; Maruthi, V.; Pankaj, P.K.; Kumar, M.; P.; Prabhakar, M.; Reddy, A.G.K.; Reddy, K.S.; Singh, V.K.; Koradia, A.K. Water Footprint Assessment of Rainfed Crops with Critical Irrigation under Different Climate Change Scenarios in SAT Regions. *Water* **2022**, *14*, 1206. https://doi.org/10.3390/w14081206

Academic Editors: Alban Kuriqi and Luis Garrote

Received: 3 March 2022
Accepted: 6 April 2022
Published: 8 April 2022

1. Introduction

Natural resources, particularly water and food supply, are at tremendous pressure due to global population rise and dynamic changes in the consumption pattern of society, and India, which is projected to be the world's most populated country by 2027, will be one of the most impacted countries [1]. This will have a direct impact on water and land resource availability vis-à-vis agriculture. It is predicted that severe water scarcity is affecting one billion population in India at least for one month of the year which stresses the need for efficient water resource development and management [2]. Rainfed (green water) farming systems in Semi-Arid Tropical (SAT) regions provide diverse food supplies from 51% of net sown area (139.4 mha) in India [3]. SAT regions contribute 60% of nutritive food grains,

although is suffering with 20 to 35% undernourished population [4]. As per IPCC report (AR5), the climate change impacts would lead to global warming by increased temperature from 2 to 5 °C by the end of the century with increased extreme weather events [5]. Indian agriculture is also affected by changes in the rainfall pattern, high intense rainfall, floods, and droughts contributing to the overall reduction in the crop productivity, soil quality, and accelerated land degradation due to erosion, availability of both blue and green water, etc., in the SAT regions. The increase in extreme weather events can affect the crop productivity in the SAT regions of India which contributes to the production of cereals, pulses, oil seeds, cotton, etc., under rainfed farming [6]. Extreme weather events are the greatest global risk in the present climate change [1]. The global requirement of cereals would increase by 55–80% by the year 2050 which can be accomplished through expansion of area under crop or by increasing crop productivity since land and water resources are limited [7].

Agriculture is the highest consumer of global fresh water at 70%. However, India accounts for 80% of fresh water consumption in agriculture [8]. Rainwater harvesting is one of the best options considered in the SAT regions of India for improving the water productivity in the diversified cropping system with improved benefits to the farmer [6]. The Lower Krishna river basin of Telangana, India is of 25.8 million ha, which contributes to a major irrigation project of Nagarjuna Sagar dam. Integrated watershed management programmes are implemented extensively in the region and have the scope for improvement in the water resource development and efficient utilization to manage dry spells [9]. The crop water balance analysis for maize and cotton in the SAT regions indicated that there was decrease in the seasonal rainfall in the normal sowing window and increase in crop water requirements by 2050 for maize and cotton [10]. Water storage on farm provides a mechanism for dealing with the variability in rainfall which, if planned and managed efficiently, increases water security, agricultural productivity, and adaptive capacity to climate change [11].

Water footprint (WF) within the agricultural sector has been extensively studied, mainly focusing on the water footprint of crop production. The WF of domestic, industrial, and agricultural sectors has been calculated and reported at the sub-national region level [12,13] as well as at the national level [14–19] and the global level [20–23]. The green and blue water footprint of crop production are estimated by using a grid-based dynamic water balance model considering local climate and soil conditions after calculating the effective rainfall (ER), potential evapotranspiration (PET), and crop water requirements. Most of these studies pertain irrigated eco systems under major irrigation systems which are different from SAT regions that are critically rainfall dependent. Due to weather aberrations in the SAT region with long dry spells during crop growth stages, there is a need to critically analyse the water supplies for rainwater harvesting on farms and its utilization during dryspells at critical stages of crop growth and its impacts on water footprints for rainfed crops in watersheds [24]. Therefore, a Water footprint assessment would help to make a policy framework for the adaptation of climate-resilient technologies, particularly rainwater harvesting through on-farm reservoirs and efficient use of water resources in the rainfed region on a watershed basis [6,25–27].

The Soil and Water Assessment Tool (SWAT) was used for estimating the runoff, potential evapotranspiration, and percolation apart from other components of groundwater recharge. The rainfall effectiveness (green water use) was evaluated for different crops in the Nagarjuna Sagar canal command area of Andhra Pradesh using SWAT [28]. The spatial optimization of soil and water conservation practices was studied on a watershed scale using SWAT and evolutionary algorithm [27]. The blue and green proportions of crop ET of six important crops were quantified [29] and four major land-use types of Kothakunta sub watershed in Andhra Pradesh for water footprint assessment on a basin scale. The water footprint for 15 different crops was estimated at basin level in the Indo-Gangetic region [30]. The green, blue and grey Water footprint of 126 crops all over the world for the period 1996–2005 was estimated with a high spatial resolution [22]. Various studies on water footprint for different climate change scenarios were reported using different downscaling

models which are region-specific, particularly for irrigated rice [31,32]. Many studies have been reported representing the impacts of climate change the at global and regional levels for irrigated crops on a basin scale. The present study focused on WF assessment for rainfed crops on the watershed scale in SAT regions with adaptation strategies of rainwater harvesting through on-farm reservoirs in a watershed.

2. Material and Methods

2.1. Study Area and Climate

The present study was conducted in a watershed consisting of 8 tribal villages of Padara Mandal, Nagarkurnool district of Telangana state (Figure 1). The area lies between 16°27′ N and 79°1′ E. The watershed has its automatic weather station in PadaraMandal. The watershed having an area of 4700 ha was delineated into several sub watersheds with different land use, soil characteristics and slopes. According to the 20 years observation data, the average annual rainfall in the watershed is 734 mm, of which the average south west seasonal rainfall accounts for 86%. Two-thirds of the rainfall occurs during the period of July to October. The average maximum and minimum temperatures of the area are 33 °C and 12 °C. The elevation of the selected area is 145 m above mean sea level.

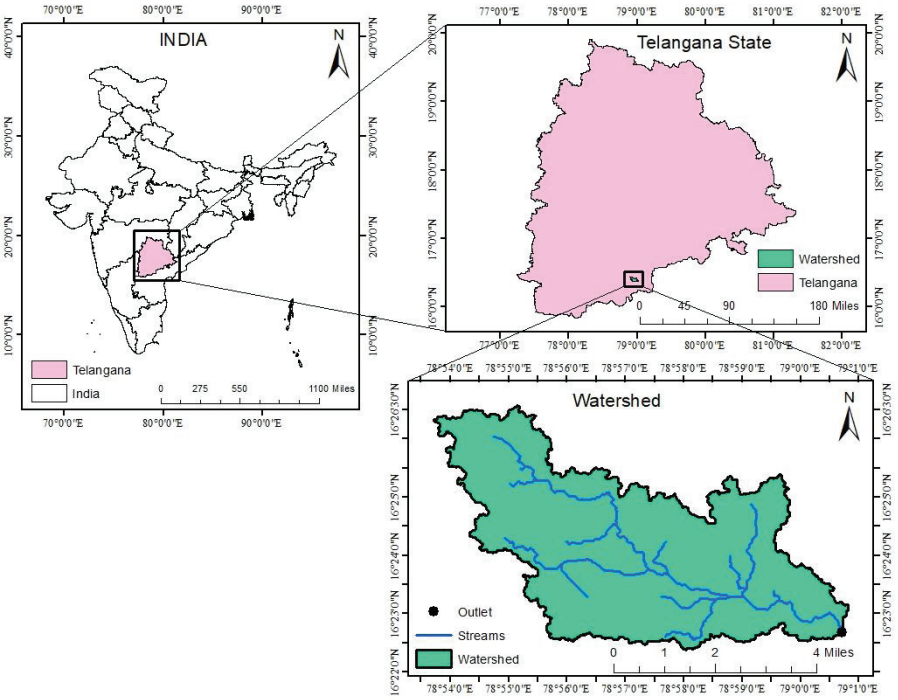

Figure 1. Location map of the watershed.

The area is dominated by sandy clayey loam soils accounting for around 78% with poor soil health. The major land use consists of agriculture (31%) and small bushes (56%) and forest (7.6%). Agriculture in the watershed mainly consists of seasonal rainfed crops like maize, cotton, redgram, groundnut, and sorghum. The watershed has a rolling topography having slopes from 1–11% on average.

2.2. Data Acquisition

Data required for the study were compiled from different sources. Digital elevation map from the ASTER Satellite with an accuracy of 30 m was obtained from USGS. Land

use/land cover map was obtained from IRS-LISS III. Spatial distribution of major soil types and sand, silt, and clay content of these soils were taken from grid-based Harmonized World Soil Database (HWSD-FAO) [33]. Crop coefficients at different crop development stages (initial, middle, and late-stage), were taken from FAO report [34].

Climate Data

The climate data related to monthly average rainfall and temperature of the study area under various RCPs and time periods are presented in Figure 2.

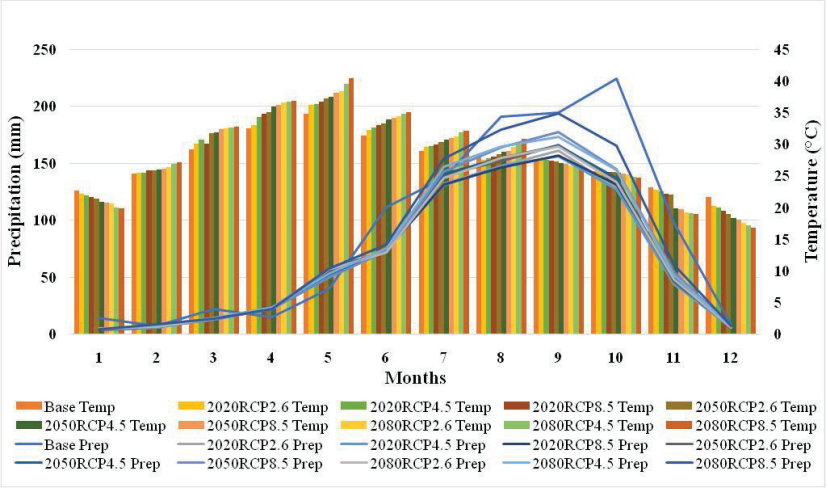

Figure 2. Monthly distribution of average precipitation (Prep) and temperature (Temp) for different RCP, base period, and time periods.

2.3. Estimation of Water Balance in a Watershed Using SWAT

Soil Water Assessment Tool (SWAT) was used to estimate the watershed surface runoff, potential evapotranspiration, and percolation rates, stream flows, etc. In this model, a watershed is divided into multiple sub-watersheds that are then further subdivided into unique soil/land use characteristics called hydrologic response units (HRUs) using ARC-GIS. The input layers of daily rainfall, temperature, relative humidity, radiation, wind, DEM, Land use, Soil cover, etc. were provided to the model (Figure S1). Digital elevation model (DEM) at a resolution of 30 × 30 m was used as input for delineation. In this study, three emission scenarios from the IPCC were used as RCP 2.6, 4.5, and 8.5, representing low, medium, and high radiant energy levels. The long-term data on runoff was generated for three climate change scenarios of 2020, 2050, and 2080. Using these data, effective rainfall of different rainfed crops, PET, and crop ET (ET_c) were calculated.

2.4. Estimation of Crop Yields in Different Climate Change Scenarios

The crop yields for selected crops namely maize, sorghum, groundnut, redgram, and cotton were assessed using the AquaCrop using soil, climate, crop, and water use data under climate change scenarios of RCP 2.6, 4.5, and 8.5 for different time periods of 2020, 2050, and 2080 including base period. The crop yields were estimated for rainfed and two critical irrigation (CI) levels of 30 mm and 50 mm at critical stages of crops for climate change scenarios and base period. Based on the experience, the two levels of 30 mm and 50 mm for both deficit and intensive critical irrigations were found optimum for SAT regions with sandy clay loam soils [6]. These data were used for calculating the WF of selected crops.

2.5. Water Footprint (WF) Assessment

The base data on crops, and existing land productivity in a watershed were taken to calculate both green and blue water footprints. The blue and green *WF* (WF_{blue} and WF_{green}) of rainfed crops were calculated based on the standard methods proposed in the Water Footprint Assessment Manual [23]. Presently, all the crops are grown under rainfed which is primarily rainfall-dependent production. As the scope for runoff water harvesting is seen in the selected watershed, two critical irrigations of 30 mm and 50 mm were taken to provide as a drought management strategy for improving the yields in the existing rainfed cropping systems of the watershed. Using this information, the water footprints were calculated for the existing crops in a watershed. However, the grey water footprint is neglected in the watershed due to the very low application rate of fertilizers in the rainfed agriculture in the watershed by the farmers.

2.5.1. Green Water Footprint

The green crop water use (CWU_{green}) is estimated by considering two parameters namely crop evapotranspiration (ET_c) and Effective rainfall (P_{eff}) during crop growth period. Minimum of these values is considered for calculating the water footprint as given below:

$$CWU_{green} = 10 \times \sum Min\left(P_{eff}, ET_c\right) \quad (1)$$

ET_c was calculated by using crop coefficients at different growth stages of selected crops in the watershed as given below

$$ET_c = ET_0 \times K_c \quad (2)$$

where ET_0 is potential evapotranspiration (mm) and K_c is crop coefficient. Crop coefficients (K_c) were obtained from FAO [35]. Crop planting dates and lengths of cropping seasons were obtained from PJTSAU [36] (Table 1).

Table 1. Crop characteristics of different crops.

Crop	K_{c_Ini}	K_{c_mid}	K_{c_end}	Date of Sowing	Length of Crop Growing Period (Days)
Maize	0.3	1.2	0.5	05-July	120
Sorghum	0.3	1	0.55	05-July	115
Groundnut	0.4	1.15	0.6	10-July	120
Cotton	0.35	1.2	0.6	15-July	180
Redgram	0.3	1	0.5	10-July	120

Source: K_c values: FAO (1988) [35], Sowing dates and length of crop periods: PJTSAU (2019) [36].

Effective rainfall for different crops was calculated by using USDA [37] as given below:

$$P_{eff} = R - SR_0 - PR \quad (3)$$

where R is daily rainfall (mm), SR_0 is surface runoff (mm) and PR is percolation (mm).

2.5.2. Blue Water Footprint

The blue crop water use (CWU_{blue}) is the amount of surface and groundwater used by the crop over the entire crop growing period i.e., the amount of water provided as critical irrigation (I_c) in addition to effective rainfall to the crop during the growing period. The total green crop water use is the summation of ET_c or P_{eff} over the crop growth period.

$$CWU_{blue} = 10 \times \sum I_c \quad (4)$$

The crop water uses over the crop growing period (m^3 ha^{-1}) were obtained by multiplying with factor 10 which converts water depths (mm) into water volumes per unit surface area (m^3 ha^{-1}). The green water footprint (WF_{green}, m^3/t) and blue water footprint (WF_{blue}, m^3/t) were calculated by dividing the green crop water use (CWU_{green}) and the blue crop water use (CWU_{blue}) by the yield of different crops respectively [23] as given below:

$$WF_{green} = CWU_{green}/Y_r \quad (5)$$

$$WF_{blue} = CWU_{blue}/Y_{I_c} \quad (6)$$

The total water footprint of a crop (WF, m^3/t) is the sum of the green and blue components:

$$WF = WF_{green} + WF_{blue} \quad (7)$$

2.5.3. Water Footprints for Climate Change Scenarios

The long-term data on *SRO*, *PET* and *PR* for different RCPs were simulated using SWAT for the periods of 2020, 2050, and 2080. Crop evapotranspiration and effective rainfall were calculated for the scenarios of 2.6, 4.5, and 8.5 for future time periods of 2020, 2050, and 2080. The *WF* for climate change scenarios of RCP 2.6, 4.5 and 8.5 for the periods of 2020, 2050 and 2080 were calculated by providing downscaled rainfall obtained from global climate models (GCM) as input to the calibrated SWAT model. It was assumed that there will be no change in land use for the project area in the future. Climate variables in the future, such as wind speed, relative humidity, and sunshine hours, were also assumed to be the same as that of the base period.

3. Results

3.1. SWAT Calibration and Validation

Calibration and validation were carried out using SWAT-CUP. Sensitive parameters were identified for the selected watershed in the first step. Then the model parameters were calibrated on daily basis comparing the observed and simulated runoff values in the watershed. The validated results are presented in Figure 3 with an R^2 (Coefficient of determination) of 0.87. It indicated that there is a close relationship between observed and simulated runoff in a watershed and the model can be applied to the watershed considered under the present study.

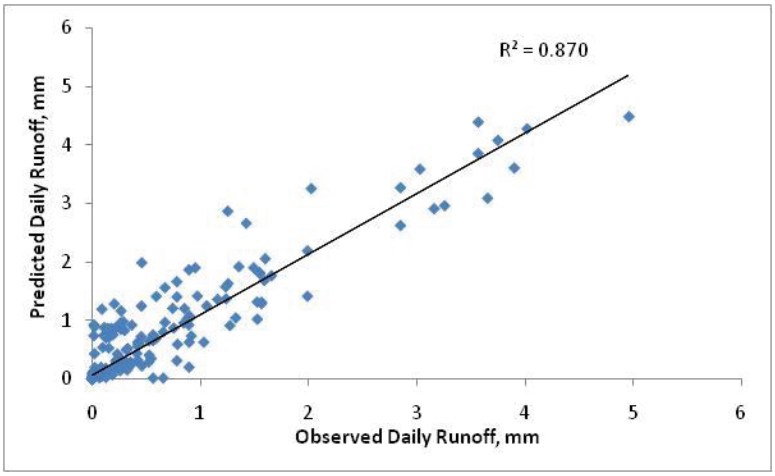

Figure 3. Validation of SWAT model in watershed.

3.2. Water Balance

SWAT outputs of surface runoff, potential evapotranspiration and percolation were taken for calculating effective rainfall (ER), crop evapotranspiration (Et_c) for all selected rainfed crops during their crop growth period. These calculations were made for RCPs (2.6, 4.5 and 8.5) with different time periods (2020, 2050, and 2080). The total rainfall during crop growth stages of different crops has an increasing trend in RCPs and time periods over the base period (Figure 4). The percentage increase in the total rainfall varied from 1.48–2.26% in RCP2.6 in 2020 and 23.5–26.85% in RCP 8.5 in 2080 across the crops over the base period. Accordingly, the surface runoff also increased from 68 mm to 121 mm in maize, 73 mm to 122 mm in sorghum, 74 mm to 124 mm in groundnut, 120 mm to 240 mm in redgram and 119 mm to 200 mm in cotton across the RCPs and time periods. The maximum surface runoff was found under the RCP 8.5 by 2080. During the base period, the surface runoff was found less varying from 68 mm to 114 mm across the crops. The analysis indicated that there was potential for rainwater harvesting through on-farm reservoirs for implementing critical irrigation in watershed for selected crops in both base period and RCPs and time periods of 2020 to 2080. The effective rainfall was found less than ET_c in base period as well as in RCPs for different time periods. The ER was taken for calculating green WF for the respective crops. The percolation varied from 52 mm to 96 mm in different crops and the maximum was noticed in deep-rooted crops like redgram and cotton.

3.3. Water Footprint of Rainfed Crops

3.3.1. Base Period (1994–2013)

The analysis was carried out for five rainfed crops commonly grown in the selected watershed for a base period of 30 years. The crops considered are maize, sorghum, groundnut, redgram and cotton. The crop ET and ER were calculated from SWAT water balance. All the rainfed crops are considered with two critical irrigations during kharif at two critical stages of crops. The average estimated crop ET and effective rainfall for their growing period are presented in Table 2 for base period and for different climate change scenarios. It is observed that the ER was less than crop ET for all the rainfed crops. Green water footprint was calculated by taking a minimum of crop ET and effective rainfall for all the rainfed crops. The average simulated crop yields through AquaCrop are presented in Table 3 for different climate change scenarios and time periods and for the base period.

Table 2. Crop ET and effective rainfall of different crops during crop growth period.

	Maize		**Sorghum**		**Groundnut**		**Redgram**		**Cotton**	
	ET_c (mm)	**ER (mm)**	**ET_c (mm)**	**ER (mm)**	**ET_c (mm)**	**ER (mm)**	**ET_c (mm)**	**ER (mm)**	**ET_c (mm)**	**ER (mm)**
Base period	464.57	321.93	455.20	331.88	508.09	319.74	455.33	352.98	705.55	401.62
2020-2.6	465.63	322.62	462.63	332.14	510.16	319.92	456.82	353.24	707.13	401.70
2020-4.5	466.72	323.90	463.74	333.92	511.09	321.74	457.62	354.84	708.59	402.15
2020-8.5	467.68	325.73	464.25	334.95	512.88	322.61	458.12	356.65	709.14	403.12
2050-2.6	469.87	329.26	467.25	339.32	516.76	326.83	461.58	360.64	713.67	407.80
2050-4.5	473.55	330.54	468.76	340.86	517.61	327.57	462.18	361.62	714.37	408.96
2050-8.5	474.16	332.66	470.47	342.64	521.77	330.44	464.32	364.33	718.95	413.33
2080-2.6	471.59	331.99	469.69	341.02	518.72	328.59	462.07	362.08	715.73	409.46
2080-4.5	475.70	334.16	470.50	345.60	521.09	331.43	463.48	365.68	718.01	413.83
2080-8.5	478.37	339.06	476.18	350.48	532.72	338.06	470.31	370.97	728.29	421.82

ET_c = Crop Evapotranspiration, ER = Effective Rainfall.

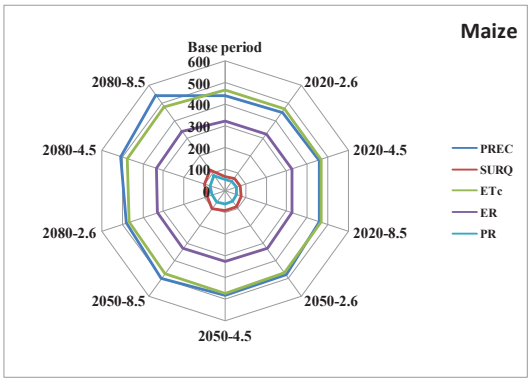

(**a**)

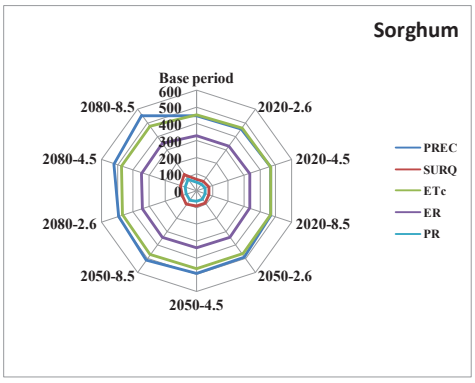

(**b**)

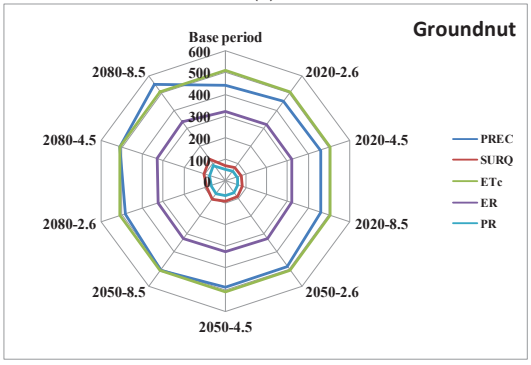

(**c**)

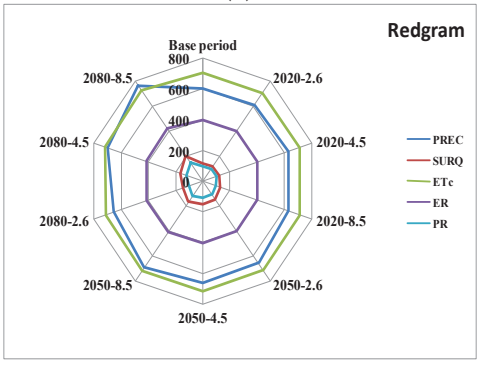

(**d**)

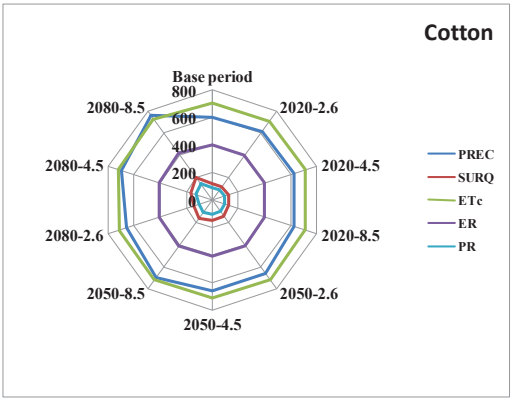

(**e**)

Figure 4. SWAT estimated water balance (mm) for selected crops during their growing period for the base period and climate change scenarios. (PREC, Precipitation; SURQ, Surface runoff; ET_c, Crop evapotranspiration; ER, Effective rainfall; PR, Percolation). (**a**) Maize, (**b**) Sorghum, (**c**) Groundnut, (**d**) Redgram, (**e**) Cotton.

Table 3. Simulated crop yields under rainfed and critical irrigations using AquaCrop.

	Maize (t/ha)			Sorghum (t/ha)			Groundnut (t/ha)			Redgram (t/ha)			Cotton (t/ha)		
	Rainfed	30 mm	50 mm	Rainfed	30 mm	50 mm	Rainfed	30 mm	50 mm	Rainfed	30 mm	50 mm	Rainfed	30 mm	50 mm
Base period	1.50	2.20	4.20	1.00	1.76	2.98	1.30	2.70	4.80	0.80	1.51	2.60	0.90	2.40	4.50
2020-2.6	1.53	2.29	4.51	1.02	1.84	3.17	1.34	2.90	5.19	0.82	1.62	2.80	0.93	2.58	4.87
2020-4.5	1.56	2.39	4.74	1.05	1.91	3.35	1.36	2.99	5.49	0.85	1.66	2.94	0.98	2.66	5.17
2020-8.5	1.60	2.51	4.98	1.09	2.05	3.61	1.39	3.17	5.85	0.87	1.76	3.14	0.99	2.80	5.51
2050-2.6	1.65	2.62	5.25	1.12	2.11	3.92	1.44	3.29	6.27	0.90	1.82	3.39	1.01	2.92	5.91
2050-4.5	1.70	2.76	5.56	1.16	2.21	4.19	1.49	3.41	6.63	0.92	1.89	3.65	1.04	3.04	6.33
2050-8.5	1.74	2.86	6.05	1.18	2.31	4.42	1.52	3.59	7.05	0.94	1.98	3.88	1.06	3.21	6.78
2080-2.6	1.76	2.94	6.42	1.20	2.35	4.73	1.55	3.68	7.58	0.95	2.04	4.09	1.08	3.27	7.09
2080-4.5	1.80	3.05	6.97	1.21	2.46	5.00	1.58	3.84	7.98	0.98	2.11	4.32	1.10	3.39	7.50
2080-8.5	1.83	3.15	7.30	1.24	2.51	5.20	1.61	3.92	8.47	1.00	2.18	4.58	1.13	3.52	8.00

The yields of maize were 1.5 t/ha, 2.2 t/ha and 4.2 t/ha for rainfed, 30 mm and 50 mm critical irrigations in the base period, respectively. The effective rainfall for maize was 321.93 mm as compared to crop ET of 464.6 mm. The green WF for maize was 2146 m^3/t and blue WFs were 273 m^3/t and 238 m^3/t for 30 mm and 50 mm CI, respectively (Figure 5). The yields for the sorghum were 1 t/ha, 1.76 t/ha and 2.98 t/ha under rainfed, with two critical irrigations of 30 mm and 50 mm, respectively. Effective rainfall for the base period was 331.88 mm with a green WF of 3319 m^3/t for sorghum. The blue WFs for sorghum were 341 m^3/t and 336 m^3/t under 30 mm and 50 mm CI, respectively.

The ER calculated during the growing period for groundnut crop was 319.7 mm against crop ET of 508 mm. The yields of groundnut were 1.3 t/ha, 2.7 t/ha and 4.8 t/ha for rainfed, 30 mm, and 50 mm CI, respectively. The green WF for groundnut was 2460 m^3/t and the blue WFs were 222 m^3/t and 208 m^3/t under 30 mm and 50 mm CI's, respectively (Figure 5). The ER during the growing period of redgram was 353 mm against crop ET of 455 mm. The yields of redgram were 0.8 t/ha, 1.5 t/ha and 2.6 t/ha under rainfed, 30 mm, and 50 mm CI's, respectively. The green WF for redgram was 4412.25 m^3/t and blue WF's were 397 m^3/t and 384 m^3/t for 30 mm and 50 mm CI's, respectively. The effective rainfall for cotton during its growth period was 401.6 mm as compared to crop ET of 705.6 mm.

The yields of cotton were 0.9 t/ha, 2.4 t/ha and 4.5 t/ha under rainfed, 30 mm, and 50 mm CI, respectively. The green WF was 4462.5 m^3/t and the blue WFs were 250 m^3/t at 30 mm and 222 m^3/t at 50 mm CI (Figure 5). The strategy of critical irrigations two times during crop season reduced the WF as compared to rainfed which totally depends on the utilization of ER as green water storage in the root zone. ER contribution to the crop yields is rainfall-dependent during the crop growing period. The total WF was minimum for maize as compared to all other crops under rainfed system indicating that the crop has better utilization of water converting into higher yields than the other crops followed by sorghum, groundnut, redgram and cotton.

3.3.2. Green and Blue Water Footprints of Rainfed Crops under Different Climate Change (CC) Scenarios

The green and blue water footprints were calculated for three CC scenarios of RCP 2.6, 4.5 and 8.5 for the time periods of 2020, 2050 and 2080 and the results are presented in Figure 5.

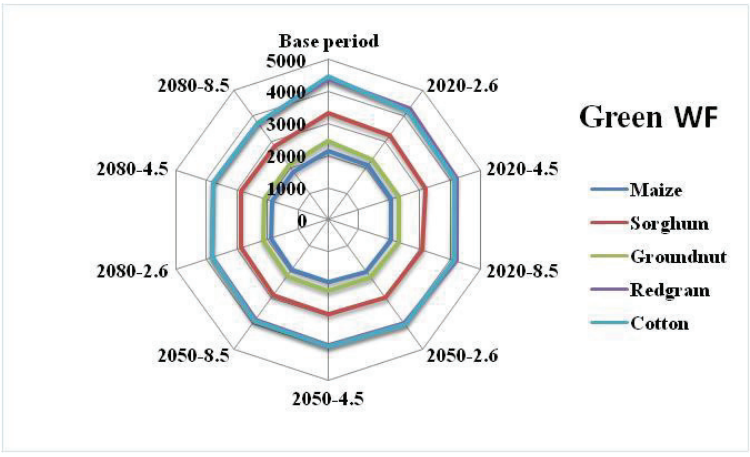

(**a**)

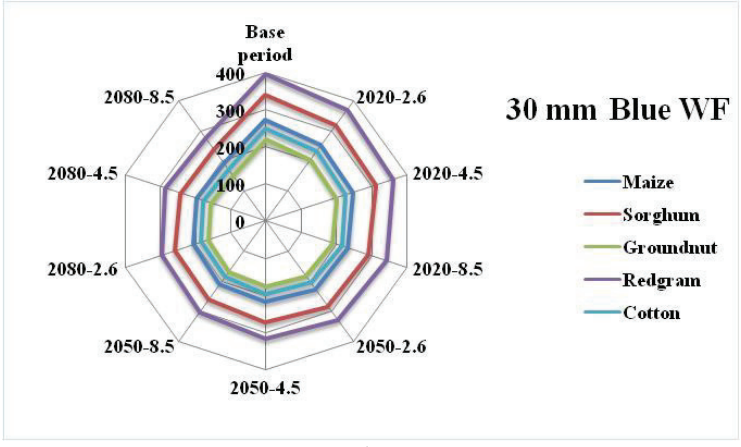

(**b**)

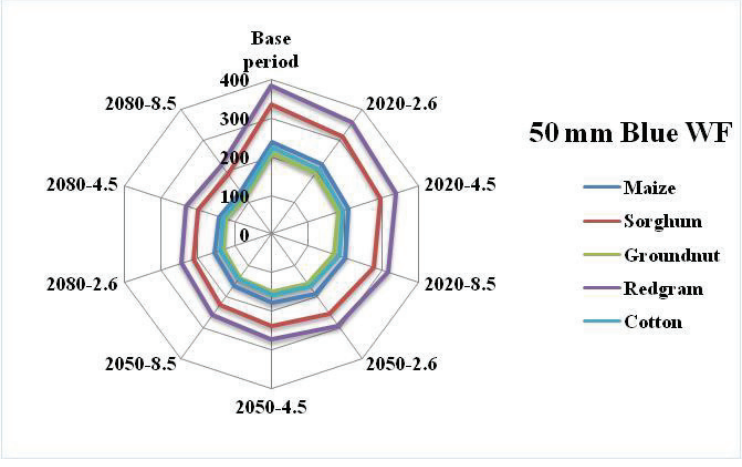

(**c**)

Figure 5. Water Footprint (m^3/t) of rainfed crops with critical irrigation and different RCPs with time periods (**a**) Green WF (**b**) Blue WF CI: 30 mm (**c**) Blue WF CI: 50 mm.

Maize

The crop ET varied from 465.6 mm to 478.4 mm with an increasing trend during its crop growth period of 117 days in different scenarios with a minimum in RCP 2.6 in 2020 and a maximum in RCP 8.5 in 2080. The ER of maize varied from 322.6 mm to 339 mm with an increasing trend in different RCP scenarios. However, the ER observed was less in RCP scenarios for the time periods of 2020 to 2080. Green and blue WF were calculated by taking the yields of 1.5 t/ha, 2.2 t/ha and 4.2 t/ha in rainfed, 30 mm and 50 mm CI's strategies for the base period. There was a slight increase in the maize yield from 1.53 t/ha to 1.76 t/ha in RCP 2.6 for different time periods. Similar trend was observed in RCP 4.5 and 8.5 with a range from 1.56 t/ha to 1.8 t/ha and 1.6 t/ha to 1.83 t/ha under time periods. The green WF of maize reduced from 2106 m^3/t to 1886 m^3/t in RCP 2.6 during the time period of 2020 to 2080 (Figure 5a). In RCP 4.5, it reduced from 2074 m^3/t to 1862 m^3/t from2020 to 2080. In RCP 8.5, green WF varied from 2035 m^3/t to 1853 m^3/t. It was observed that there was a decrease of 1.88%, 7% and 12.1% of green WF in RCP 2.6 for different periods of 2020, 2050 and 2080 respectively over the base period (Figure 6a). In RCP 4.5 green WF was decreased by 3.4%, 9.3%, and 13.3% in different time periods (2020, 2050, and 2080) over the base period. In RCP 8.5, the maximum decrease in green WF (rainfed) was observed varying from 5.2–13.7% in different time periods as compared to the base period.

The WF of maize with two CI of 30 mm and 50 mm as an adaptation strategy to CC, the blue WF with 30 mm CI varied from 255 m^3/t to 204 m^3/t in RCP 2.6, 248 m^3/t to 195 m^3/t in RCP 4.5 and 235 m^3/t to 190.5 m^3/t in RCP 8.5 during the time period of 2020 to 2080 (Figure 5b). Similarly, with a 50 mm CI strategy, the blue WF varied from 222 m^3/t to 156 m^3/t in RCP 2.6, 209 m^3/t to 143 m^3/t in RCP 4.5 and 201 m^3/t to 137 m^3/t in RCP 8.5 during 2020 to 2080 (Figure 5c). Though the blue WF of maize has decreasing trend within RCPs from 2020 to 2080, the WF was decreased over rainfed (green WF). The percentage decrease in blue WF was 6.5–25%, 9–28.4% and 13.7–30.2% in RCP 2.6, 4.5 and 8.5 respectively for different time periods. In 50 mm CI strategy, the blue WF was further reduced by 6.9% to 35%, 12.3–39.7%, and 15.7–42.5% in RCP 2.6, 4.5, and 8.5, respectively (Figure 6a) for different time periods indicating the optimum adaptation strategy for maize in SAT regions.

Sorghum

The crop ET varied from 455 mm to 476.2 mm in different scenarios of climate change (RCP 2.6 to RCP 8.5) during the time periods of 2020 to 2080. Similarly, the ER for the sorghum varied from 332.1 mm to 350.5 mm which is less than crop ET. Therefore, ER is considered for calculating green WF for sorghum in different RCPs and time periods. The yields estimated in different RCPs and time periods varied from 1.02 t/ha to 1.24 t/ha under rainfed, 1.87 t/ha to 2.51 t/ha with 30 mm CI and 3.2 t/ha to 5.2 t/ha with 50 mm CI. The predicted yields had an increasing trend over the RCPs and time periods over the base period (Table 3). The green WF varied from 3253 m^3/t to 2849 m^3/t, 3168 m^3/t to 2849 m^3/t and 3067 m^3/t to 2838 m^3/t in RCP 2.6, 4.5 and 8.5 respectively for different time periods (Figure 5).The green WF decreased from 1.98% to 14.2%, 4.5% to 14.2% and 7.6% to 14.5% over the base period in RCP 2.6, 4.5 and 8.5 respectively over time periods of 2020, 2050 and 2080 (Figure 6b).

With the adaptation strategy of CI's with 30 mm, the blue WF varied from 321 m^3/t to 257.6 m^3/t, 314 m^3/t to 243 m^3/t, 293 m^3/t to 239 m^3/t in RCP 2.6, 4.5 and 8.5, respectively for different time periods (Figure 5b). The percentage decrease in blue WF for 30 mm CI was 5.88–24.4%, 8–28.7%, and 14.1–29.9% over the base period among different RCP and time periods (Figure 6b). In the case of 50 mm CI two times, the blue WF varied from 313.5 m^3/t to211.4 m^3/t, 296 m^3/t to 199.6 m^3/t and 277 m^3/t to 192 m^3/t in RCP 2.6, 4.5 and 8.5, respectively during the time period of 2020 to 2080 (Figure 5c). The maximum decrease was observed with a 50 mm CI strategy varying from 6.58–37%, 11.8–40.5% and 17.5–42.7% (Figure 6b) over the base period in different RCP and time periods. The analysis indicated that the rainfed sorghum when cultivated with effective rainfall, the WF's were

maximum as compared to the adaptation strategy of giving critical irrigations with 30 mm and 50 mm two times during its crop growth period. Among the blue WFs, 50 mm CI reduced maximum WF in all RCP scenarios and time periods. However, it was found that there was a decreasing trend with RCP and time periods in all crops WF.

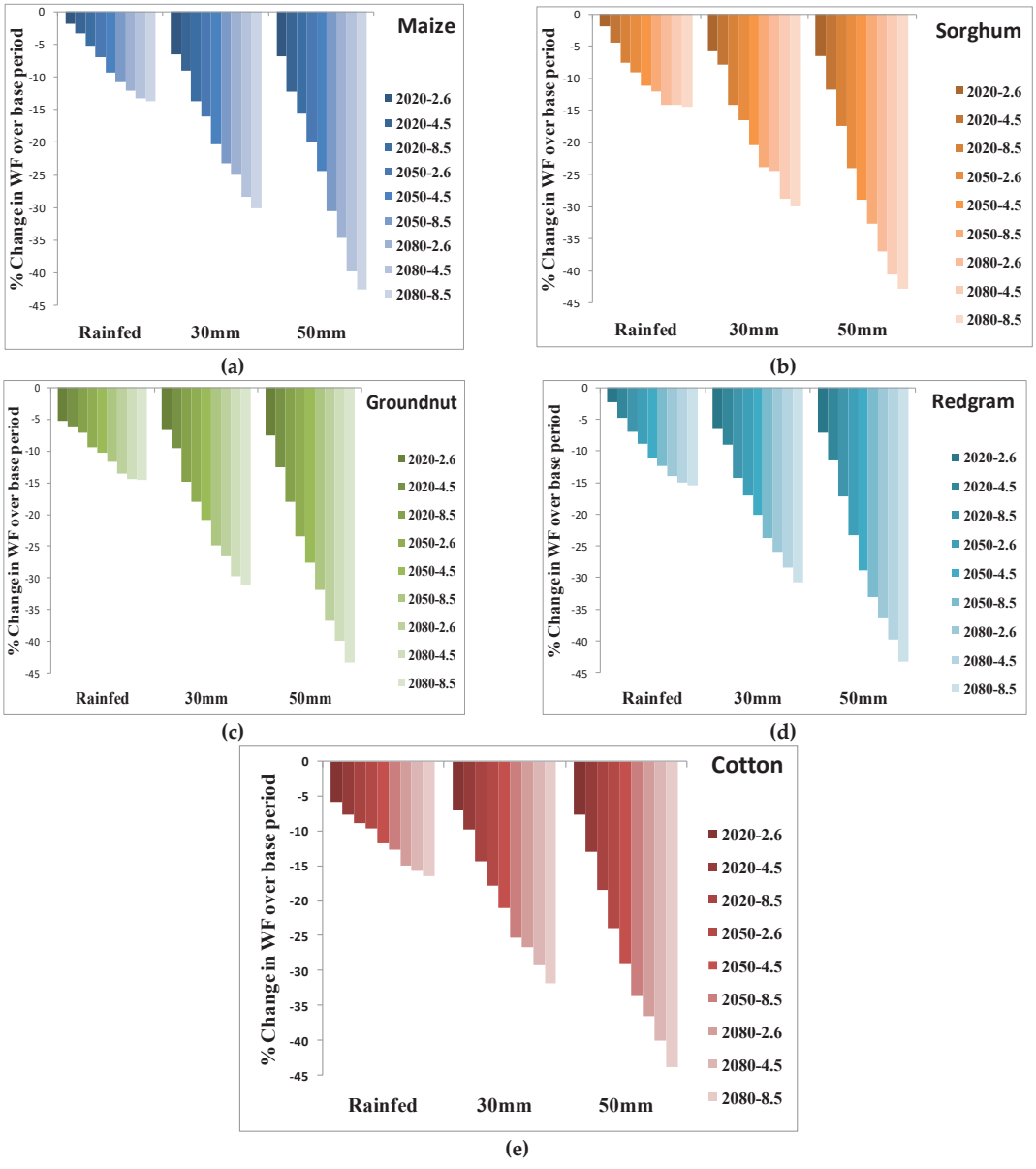

Figure 6. Percentage change in WF of rainfed crops ((**a**) maize (**b**) sorghum (**c**) groundnut (**d**) redgram and (**e**) cotton) with critical irrigation under different RCPs and time periods.

Groundnut

The groundnut yields taken for the WF analysis varied from 1.37 t/ha to 1.61 t/ha, 2.9 t/ha to 3.92 t/ha and 5.19 t/ha to 8.47 t/ha in rainfed, 30 mm and 50 mm CI, respectively,

in different RCPs and time periods (Table 3). The crop ET varied from 510 mm to 519 mm in RCP 2.6, 518 mm to 521 mm in RCP 4.5, and 513 mm to 533 mm in RCP 8.5 during the time period of 2020 to 2080. The ER varied from 320 mm to 329 mm, 322 mm to 331 mm, and 323 mm to 338 mm in RCP 2.6, 4.5, and 8.5, respectively, during the time period of 2020 to 2080 showing the increasing trend (Table 2). However, the ER was observed to be less than crop ET in all RCP and time periods.

The green WF under rainfed with ER contribution in the production varied from 2328 m^3/t to 2125 m^3/t, 2010 m^3/t to 2104.3 m^3/t and 2085 m^3/t to 2100m^3/t in RCP 2.6, 4.5 and 8.5, respectively for different time periods (Figure 5a).The blue WF with 30 mm CI varied from 207 m^3/t to 163 m^3/t, 201 m^3/t to 156 m^3/t and 189 m^3/t to 153 m^3/t in RCP 2.6, 4.5 and 8.5, respectively (Figure 5b). Similarly, with 50 mm CI, the blue WF varied from 193 m^3/t to 132 m^3/t, 182 m^3/t to 125 m^3/t, and 171m^3/t to 118 m^3/t (Figure 5c) in RCP 2.6, 4.5 and 8.5 during the time periods of 2020 to 2080. The percentage decrease in the green WF (rainfed) varied from 5.3–13.5%, 6.1–14.4% and 7.1–14.6% over the base period in different RCP and time periods (Figure 6c). At 30 mm CI, the blue WF varied from 6.7–26.6%, 9.6–29.7% and 14.8–31.1% over the base period in different RPCs and time periods. With a 50 mm CI strategy the blue WF varied from 7.5–36.7%, 12.6–39.9%, and 17.9–43.3% over the base period.

In time periods of 2020 to 2080 in different RCP's both green and blue WFs were decreased with maximum reduction in 50 mm CI strategy. In oilseed crops like groundnut, which is predominantly grown in south-central India is a profitable crop to the farmers with fewer WFs under the adaptation strategy.

Redgram

Redgram is a protein-rich leguminous crop which is commonly grown in rainfed conditions as a pulse crop. The yields of the crop varied from 0.82 t/ha to 1.0 t/ha, 1.6 t/ha to 2.18 t/ha, 2.8 t/ha to 4.58 t/ha in rainfed, 30 mm, and 50 mm CI strategies, respectively under different RCP's and time periods (Table 3). The crop ET varied from 457 mm to 462 mm, 458 mm to 463 mm, and 458 mm to 470 mm in RCP 2.6, 4.5, and 8.5 respectively in time periods of 2020 to 2080 with an increasing trend. The ER varied from 353 mm to 362 mm, 355 mm to 366, mm and 357 mm to 371 mm in different RCPs and time periods (Table 2). The ER was found to be less than ET_c among all RCPs and time periods considered.

The green WF varied from 4308 m^3/t to 3795m^3/t, 4119 m^3/t to 3751m^3/t and 4104 m^3/t to 3728 m^3/t in RCP 2.6, 4.5 and 8.5, respectively during different time periods (Figure 5a). With a 30 mm CI strategy the blue WF varied from 371 m^3/t to 294 m^3/t, 361.5 m^3/t to 284 m^3/t and 341 m^3/t to 275 m^3/t in RCP 2.6, 4.5 and 8.5, respectively in the time period of 2020 to 2080 (Figure 5b). The blue WF with 50 mm CI varied from 357 m^3/t to 244.5 m^3/t, 340 m^3/t to 231.5 m^3/t and 318.5 m^3/t to 218 m^3/t in different RCP and time periods (Figure 5c). The percentage decrease in green WF varied from 2.4–14%, 4.8–15% and 7–15.5%, the percentage decrease in blue WF with 30mn CI varied from 6.6–26%, 9–28% and 14–30.7% by 2080, the percentage decrease in blue WF for 50 mm CI varied from 7.1–36.4%, 11.6–39.8% and 17.2–43.2% (Figure 6d) over the base period in different RCP and time periods.

Cotton

Cotton is grown by the farmers as a commercial crop in rainfed districts of south-central India having a growth period of 180 days. Its yields varied from 0.9 t/ha to 1.13 t/ha, 2.58 t/ha to 3.52 t/ha and 4.87 t/ha to 8.01 t/ha under rainfed, 30 mm CI and 50 mm CI, respectively for different RCP and time periods (Table 3). The crop ET varied from 707 mm to 716 mm, 709 mm to 718 mm, and 709 mm to 728 mm in RCP 2.6, 4.5, and 8.5 respectively in the time periods of 2020 to 2080. The ER varied from 402 mm to 409 mm, 402 mm to 414 mm and 403 mm to 424 mm under different RCPs and time periods. It was observed

that the ER was less than ET_c among all RCPs and time periods (Table 2). Hence, ER was considered for calculating green WF under rainfed.

The green WF of cotton varied from 4202 m^3/t to 3795 m^3/t, 4120.4 m^3/t to 3765.5 m^3/t, and 4067.8 m^3/t to 3733 m^3/t in RCP 2.6, 4.5 and 8.5 for different time periods (Figure 5a). The blue WF with 30 mm CI varied from 233 m^3/t to 183.5 m^3/t, 225.6 m^3/t to 177 m^3/t and 214 m^3/t to 170.5 m^3/t in RCP 2.6, 4.5 and 8.5, respectively during 2020 to 2080 (Figure 5b). Adapting 50 mm CI in cotton reduced the blue WF over the 30 mm CI and rainfed. The blue WF with 50 mm CI varied from 205 m^3/t to 141 m^3/t, 193 m^3/t to 133 m^3/t and 181.5 m^3/t to 124.8 m^3/t (Figure 5c) in different RCP and time periods. The percentage decreases over the base period varied from 5.8% to 15%, 7.7% to 15.6% and 8.8% to 16.4%, with 30 mm CI it varied from 6.9% to 26.6%, 9.8% to 29.2% and 14.3% to 31.8% 1.6%, 2.4% and in 50 mm CI it varied from 7.6% to 36.5%, 13% to 40% and 18.3% to 43.8% (Figure 6e) in different RCP's and time periods. Cotton also has a decreasing trend in WF's over the time periods and climate change scenarios of RCP. However, with adaptation strategy of providing 30 mm and 50 mm CI reduced the WF due to increase in the yields with increased critical water use during the growth period of the crop.

4. Discussion

The commonly grown crops in SAT regions of India are Sorghum, maize, groundnut, redgram and cotton. Sorghum is grown extensively in both Indian and African SAT regions as it is a staple food for poor people. It has localized value additions as well as good fodder value for animals. Though maize is water-intensive crop, it is grown in rainfed regions extensively in most of the SAT regions due to its commercial value, used as feed and fodder to the animals and poultry. Groundnut and redgram are commercial oilseed and pulse crops, respectively that provides protein and in situ nitrogen fixation to the soil. Cotton is long duration commercial crop grown in 67% area in rainfed regions of India having a productivity of 200–275 kg/acre which is very low compared to the other cotton-growing countries. The other crops productivity ranges between 0.8–1.0 t/ha in SAT regions [3]. The above crops suffer from the water supplies during critical stages with long dry spells (30–45 days) due to rainfall breaks. It is seen from Figure 2 that the average temperature increase will be from 1–5 °C having a maximum in RCP8.5. Though rainfall has an increasing trend among RCPs and time periods from 2020–2080, there were more non-rainy days during crop growth period indicating more dryspells happened, calling for a scope of rainwater harvesting on farm for critical irrigation.

Water footprints were studied in SAT regions with critical irrigation strategies applying 30 mm and 50 mm two times during dryspells in the crop-growing period. The available water content for use by the crops in rainfed soils is about 100 mm/m [38]. If the depletion of available water content is not addressed during dryspells at critical stages of rainfed crops, the crop yields are reduced by 30–40% in different crops causing huge losses to the farmers. In order to minimize this loss besides enhancing the crop productivity, critical irrigation of 50 mm was provided by meeting the requirement of the crop during dryspell at 50% depletion and deficit irrigation with 30 mm. Taking these two points into consideration, water footprints of rainfed crops were estimated using both green and blue water. The positive climate effects on crop growth can be adjusted by effective rooting depth and nutrients by providing critical irrigations during dryspells which can improve water productivity by 20–40% [39].

Rainfed crops of maize and groundnut registered the lowest water footprint in all RCP scenarios. Blue water footprint of cotton/redgram was found to be highest in all RCP scenarios with either 30 mm or 50 mm CI while the lowest was recorded for groundnut. It was found that the response of the crop to the CI was positive realizing more yields in the rainfed regions [40].

Deep rootedness, as well as long duration of the crops (redgram and cotton) standing in the field, requires more green water for effective root spread and resource use in the root zone under rainfed conditions. However, the long crop duration/indeterminate nature

of the crop, makes it to survive and recoup from the extreme weather conditions. Crop growth cycle for these crops with a long duration of 180 days in the field suffers from moisture stress during the critical stage of pod/boll development and filling. The green WF was very high for such crops, if they are grown in rainfed conditions and it could be reduced with blue water supplies through CI reducing the WF of these crops. However, if the rain breaks occur immediately after seed germination, the crop suffers affecting the plant density and this stage becomes a critical stage for crop survival. Therefore, CI could be applied at any stage of the crop facing severe moisture stress, resulting in improvement of either crop stand or yields [41]. Under limited soil depths, shallow-rooted crops of groundnut and maize registered the lowest WF as the CI of 30 mm or 50 mm would make water available within root zone to improve crop yields. However, cotton crop, which is deep-rooted also could record lower WF at all RCP scenarios after groundnut which might be due to its deep rootedness and also due to high yields (nearly three times higher) over rainfed cotton crop without CI. Reduction in WF is possible with CI at all RCP scenarios by standardizing timing of irrigation, quantity, and method of irrigation which trigger the crop growth parameters and yield attributes to a greater extent in crops under rainfed SAT regions.

5. Conclusions

Water footprint assessment on watershed basis is required to select the most efficient cropping system per unit of water consumed, which ultimately results in not only conserving water but also economic benefits to the farmers through proper water resource development and use management, particularly in SAT regions. The present study deals with the assessment of water footprints of rainfed crops grown in the watershed with critical irrigation of 30 mm and 50 mm two times as an adaptation strategy to climate change. Out of the water balance of watershed obtained from SWAT, modeling indicated that there was an opportunity for water harvesting through On-Farm Reservoirs for critical irrigation in watersheds, as surface runoff increased due to an increase in the rainfall during the growing period of selected crops across RCP and increasing time periods. The crop yields were simulated using the AquaCrop model for both base period and climate change scenarios with two critical irrigations of 30 mm and 50 mm. The analysis of water footprints for rainfed crops on a watershed basis indicated that the lowest water footprint was observed in maize under the 50 mm CI strategy followed by groundnut, sorghum, redgram, and cotton. The strategy of 50 mm CI during two critical stages of the crops resulted in maximum reduction in the blue WF which is 6.6–37%, 12–40%, and 18–44% for RCP 2.6, 4.5, and 8.5, respectively among the selected crops. In the rainfed system with a green water footprint also resulted in the reduction of green water footprint across the RCP and the time period of 2020 to 2080 which is less than blue water footprint of the crops. It was the result of increasing rainfall in RCPs (1.2–24%) over the base period. Green WF could be reduced further by the application of organics or plastic mulches which needs further investigation and validation under field conditions. The present studies would help to bring a policy framework from governments to effectively use water and develop water-efficient crop plans for enhancing productivity in rainfed SAT regions.

Supplementary Materials: The following supporting information can be downloaded at: https://www.mdpi.com/article/10.3390/w14081206/s1, Figure S1: Input layers to SWAT model.

Author Contributions: K.S.R. (Konda Sreenivas Reddy): conceptualization, methodology and writing manuscript draft; V.M.: conceptualization, methodology; P.K.P.: review and editing; M.K., A.G.K.R. and P.: validation, formal analysis; M.P. and K.S.R. (Kotha Sammi Reddy): validation, data curation and supervision; V.K.S.: project administration, A.K.K.: formal analysis and investigation. All authors have read and agreed to the published version of the manuscript.

Funding: This research was funded by Agri-Consortium Research Platform on Water and National Innovations in Climate Resilient Agriculture (NICRA), Indian Council of Agricultural Research, New Delhi and The APC was funded by NICRA with grant no. 2-2(201)/17-18/NICRA.

Institutional Review Board Statement: Not applicable.

Informed Consent Statement: Not applicable.

Data Availability Statement: Data used in this study are duly available from the first authors on reasonable request.

Acknowledgments: The authors fully acknowledge the financial help received from ACRP-Water, ICAR and the climate data received from NICRA project for undertaking the present research. Also, we acknowledge the help, co-operation, and guidance received from the Directors of ICAR-CRIDA, Hyderabad, and ICAR-IIWM, Bhubaneswar in carrying out this research.

Conflicts of Interest: The authors declare no conflict of interest.

References

1. The World Economical Forum 2021. Available online: https://www.weforum.org/ (accessed on 20 February 2022).
2. Mekonnen, M.M.; Hoekstra, A.Y. Four billion people facing severe water scarcity. *Sci. Adv.* **2016**, *2*, e1500323. [CrossRef] [PubMed]
3. Agricultural Statistics at a Glance 2020. Available online: https://eands.dacnet.nic.in/PDF/Agricultural%20Statistics%20at%20a%20Glance%20-%202020%20(English%20version).pdf (accessed on 20 February 2022).
4. Rockström, J.; Karlberg, L.; Wani, S.P.; Barron, J.; Hatibu, N.; Oweis, T.; Bruggeman, A.; Farahani, J.; Qiang, Z. Managing water in rainfed agriculture—The need for a paradigm shift. *Agric. Water Manag.* **2010**, *97*, 543–550. [CrossRef]
5. IPCC. *Climate Change 2014: Synthesis Report. Contribution of Working Groups I, II and III to the Fifth Assessment Report of the Intergovernmental Panel on Climate Change*; IPCC: Geneva, Switzerland, 2014; p. 151.
6. Reddy, K.S.; Ricart, S.; Maruthi, V.; Pankaj, P.K.; Krishna, T.S.; Reddy, A.A. Economic assessment of water harvesting plus supplemental irrigation for improving water productivity of a pulse–cotton based integrated farming system in Telangana, India. *Irrig. Drain. John Wiley Sons* **2020**, *69*, 25–37. [CrossRef]
7. De Fraiture, C.; Wichelns, D. Satisfying future water demands for agriculture. *Agric. Water Manag.* **2010**, *97*, 502–511. [CrossRef]
8. Hoekstra, A.Y.; Mekonnen, M.M. Reply to Ridoutt and Huang: From water footprint assessment to policy. *Proc. Natl. Acad. Sci. USA* **2012**, *109*, E1425. [CrossRef]
9. Wani, S.P.; Dixin, Y.; Li, Z.; Dar, W.D.; Chander, G. Enhancing agricultural productivity and rural incomes through sustainable use of natural resources in the Semi Arid Tropics. *J. Sci. Food Agric.* **2011**, *92*, 1054–1063. [CrossRef]
10. Reddy, K.S.; Kumar, M.; Maruthi, V.; Ravi Kumar, N.; Maheswari, M.; Sikka, A.K.; Lakshminarayana, P.; Vijayalakshmi, U.B.; Reddy, Y.V.K. *ATLAS on Climate Change Impacts on Crop Water Balance of Cotton (*Gossypium herbaceum*) and Maize (*Zea mays *L.) in Telangana*; ICAR: Hyderabad, India, 2015.
11. McCartney, M.; Smakhtin, V. Water storage in an era of climate change: Addressing the challenge of increasing rainfall variability. *Blue Pap.* **2010**, *11*, 12. [CrossRef]
12. Aldaya, M.M.; Llamas, M. *Water Footprint Analysis for the Guadiana River Basin*; UNESCO-IHE: Delft, The Netherlands, 2008; p. 3.
13. Dong, H.; Geng, Y.; Sarkis, J.; Fujita, T.; Okadera, T.; Xue, B. Regional water footprint evaluation in China: A case of Liaoning. *Sci. Total Environ.* **2012**, *442*, 215–224. [CrossRef]
14. Hoekstra, A.Y.; Chapagain, A.K. The water footprints of Morocco and the Netherlands: Global water use as a result of domestic consumption of agricultural commodities. *Ecol. Econ.* **2007**, *64*, 143–151. [CrossRef]
15. Kampman, D.A.; Hoekstra, A.Y.; Krol, M.S. The water footprint of India. *Value Water Res. Rep. Ser.* **2008**, *32*, 1–152.
16. Van Oel, P.; Mekonnen, M.; Hoekstra, A. The external water footprint of the Netherlands: Geographically-explicit quantification and impact assessment. *Ecol. Econ.* **2009**, *69*, 82–92. [CrossRef]
17. Bulsink, F.; Hoekstra, A.Y.; Booij, M.J. The water footprint of Indonesian provinces related to the consumption of crop products. *Hydrol. Earth Syst. Sci.* **2010**, *14*, 119–128. [CrossRef]
18. Ercin, E.; Mekonnen, M.; Hoekstra, A.Y. The Water Footprint of Switzerland (Value of Water Research Report; No. 57), Unesco-IHE Institute for Water Education. 2012. Available online: https://waterfootprint.org/media/downloads/Report57-WaterFootprintSwitzerland_1.pdf (accessed on 2 March 2022).
19. Shrestha, S.; Pandey, V.P.; Chanamai, C.; Ghosh, D.K. Green, Blue and Grey Water Footprints of Primary Crops Production in Nepal. *Water Resour. Manag.* **2013**, *27*, 5223–5243. [CrossRef]
20. Hoekstra, A.Y.; Chapagain, A.K. Water footprints of nations: Water use by people as a function of their consumption pattern. *Water Resour. Manag.* **2006**, *21*, 35–48. [CrossRef]
21. Liu, J.; Yang, H. Spatially explicit assessment of global consumptive water uses in cropland: Green and blue water. *J. Hydrol.* **2010**, *384*, 187–197. [CrossRef]
22. Mekonnen, M.M.; Hoekstra, A.Y. The green, blue and grey water footprint of crops and derived crop products. *Hydrol. Earth Syst. Sci.* **2011**, *15*, 1577–1600. [CrossRef]
23. Hoekstra, A.Y.; Chapagain, A.K.; Mekonnen, M.M.; Aldaya, M.M. *The Water Footprint Assessment Manual: Setting the Global Standard*; Routledge: London, UK, 2011.
24. Wang, G.; Mang, S.; Cai, H.; Liu, S.; Zhang, Z.; Wang, L.; Innes, J.L. Integrated watershed management: Evolution, development and emerging trends. *J. For. Res.* **2016**, *27*, 967–994. [CrossRef]

25. Thornton, P.K.; Jones, P.G.; Alagarswamy, G.; Andresen, J.; Herrero, M. Adapting to climate change: Agricultural system and household impacts in East Africa. *Agric. Syst.* **2010**, *103*, 73–82. [CrossRef]
26. Cha, K.; Son, M.; Hong, S.; An, S.; Part, S. Method to assess water footprint, a case study for white radishes in Korea. *Int. Soil Water Conserv. Res.* **2017**, *5*, 151–157. [CrossRef]
27. Naseri, F.; Azari, M.; Dastorani, M.T. Spatial optimization of soil and water conservation practices using coupled SWAT model and evolutionary algorithm. *Int. Soil Water Conserv. Res.* **2021**, *9*, 566–577. [CrossRef]
28. Rao, B.K.; Rajput, T.B.S. Rainfall effectiveness for different crops in canal command areas. *J. Agrometeorol.* **2008**, *10*, 328–332.
29. Prasad, A.; Mani, A.; Devi, M.U.; Reddy, M.D. Blue and green water quantification for sustainable water resources management in Kothakunta sub-watershed, Andhra Pradesh. *Indian J. Soil Conserv.* **2013**, *41*, 241–247.
30. Mali, S.S.; Singh, D.; Sarangi, A.; Khanna, M.; Parihar, S.; Das, D. Variability mapping of crop evapotranspiration for water footprint assessment at basin level. *Indian J. Soil Conserv.* **2015**, *43*, 24–32.
31. Bocchiola, D. Impact of potential climate change on crop yield and water footprint of rice in the Po valley of Italy. *Agric. Syst.* **2015**, *139*, 223–237. [CrossRef]
32. Yang, M.; Xiao, W.; Zhao, Y.; Li, X.; Huang, Y.; Lu, F.; Hou, B.; Li, B. Assessment of Potential Climate Change Effects on the Rice Yield and Water Footprint in the Nanliujiang Catchment, China. *Sustainability* **2018**, *10*, 242. [CrossRef]
33. Harmonized World Soil Database Version 1.1 March. 2009. Available online: https://www.fao.org/3/aq361e/aq361e.pdf (accessed on 20 February 2022).
34. Allen, R.G.; Pereira, L.S.; Raes, D.; Smith, M. *Crop Evapotranspiration-Guidelines for Computing Crop Water Requirements*; FAO Irrigation and Drainage Paper-56: Rome, Italy, 1998; p. 300.
35. Doorenbos, J.; Pruitt, W.O. Crop water requirements, FAO irrigation and drainage paper 24. *Land Water Dev. Div. FAO Rome* **1977**, *144*, 214.
36. Venu Gopal, R.C.; Vanishree, K. Telangana Vyavsayam Professor Jayashankar Telangana State Agricultural University 2019. Available online: https://pjtsau.edu.in/Vyavasayam.html (accessed on 21 January 2022).
37. USDA. Irrigation water requirements. *Agr. Soil Manag.* **1967**, *59*, 67–75.
38. Sharma, B.R.; Rao, K.; Vittal, K.; Ramakrishna, Y.; Amarasinghe, U. Estimating the potential of rainfed agriculture in India: Prospects for water productivity improvements. *Agric. Water Manag.* **2010**, *97*, 23–30. [CrossRef]
39. Bazzaz, F.A.; Sombroek, W.G. (Eds.) *Global Climate Change and Agricultural Production: Direct and Indirect Effects of Changing Hydrological, Pedological, and Plant Physiological Processes*; Food & Agriculture Org.: Rome, Italy, 1996.
40. Reddy, K.; Maruthi, V.; Kumar, M.; Pankaj, P.; Reddy, A.; Umesha, B. Enhancing economic water productivity under on farm reservoirs in diversified rainfed cropping systems. *Int. J. Plant Prod.* **2017**, *11*, 193–207. [CrossRef]
41. Gobin, A.; Kersebaum, K.C.; Eitzinger, J.; Trnka, M.; Hlavinka, P.; Takáč, J.; Kroes, J.; Ventrella, D.; Marta, A.D.; Deelstra, J.; et al. Variability in the Water Footprint of Arable Crop Production across European Regions. *Water* **2017**, *9*, 93. [CrossRef]

remote sensing

MDPI

Article

Analysis of Multispectral Drought Indices in Central Tunisia

Nesrine Farhani [1,2,*], Julie Carreau [3], Zeineb Kassouk [1], Michel Le Page [2], Zohra Lili Chabaane [1] and Gilles Boulet [2]

[1] Institut National Agronomique de Tunisie, Université de Carthage, LR17AGR01 (Lr GREEN-TEAM), Tunis 1082, Tunisia; zeineb.kassouk@inat.u-carthage.tn (Z.K.); zohra.lilichabaane@inat.u-carthage.tn (Z.L.C.)
[2] Centre d'Études Spatiales de la Biosphère, Université de Toulouse, CNRS, CNES, IRD, UPS, INRAE, 31400 Toulouse, France; michel.le_page@ird.fr (M.L.P.); gilles.boulet@ird.fr (G.B.)
[3] Department of Mathematics and Industrial Engineering, Polytechnique, Montreal, QC 3453, Canada; julie.carreau@polymtl.ca
* Correspondence: nesrine.farhani@ird.fr; Tel.: +216-20-212-738

Abstract: Surface water stress remote sensing indices can be very helpful to monitor the impact of drought on agro-ecosystems, and serve as early warning indicators to avoid further damages to the crop productivity. In this study, we compare indices from three different spectral domains: the plant water use derived from evapotranspiration retrieved using data from the thermal infrared domain, the root zone soil moisture at low resolution derived from the microwave domain using the Soil Water Index (SWI), and the active vegetation fraction cover deduced from the Normalized Difference Vegetation Index (NDVI) time series. The thermal stress index is computed from a dual-source model Soil Plant Atmosphere and Remote Evapotranspiration (SPARSE) that relies on meteorological variables and remote sensing data. In order to extend in time the available meteorological series, we compare the use of a statistical downscaling method applied to reanalysis data with the use of the unprocessed reanalysis data. Our study shows that thermal indices show comparable performance overall compared to the SWI at better resolution. However, thermal indices are more sensitive for a drought period and tend to react quickly to water stress.

Keywords: indicators; droughts; evapotranspiration; reanalyses

Citation: Farhani, N.; Carreau, J.; Kassouk, Z. ; Le Page, M.; Lili Chabaane, Z.; Boulet, G. Analysis of Multispectral Drought Indices in Central Tunisia. *Remote Sens.* **2022**, *14*, 1813. https://doi.org/10.3390/rs14081813

Academic Editors: Alban Kuriqi and Luis Garrote

Received: 8 March 2022
Accepted: 6 April 2022
Published: 9 April 2022

1. Introduction

Droughts are a recurring natural climate event that result from a reduction in precipitation amount received over an extended period of time, such as a season or a year [1]. In arid and semi-arid areas characterized by a significant temporal and spatial climatic variability, the vulnerability advanced by recurrent droughts is considerable as it makes serious threats to agroecosystem health and productivity [2]. More specifically, in several Mediterranean countries, we observe during the last decade a significant warming trend, more pronounced in summer, and a decrease in rainfall during the wet season [3]. This could have a strong impact on water resources and constitutes the main driver of agricultural droughts which appear as a result of a long-term period of precipitation deficiency and lead to lower soil moisture. Droughts at a sensitive stage of crop development (emergence, pollination, and grain filling) can lead to significant damages [4,5] specifically on rainfed agriculture. Thus, an important issue for rainfed agriculture is to receive adequate rainfall at the appropriate timing. In contrast, drought responses over irrigated areas are related to surface or groundwater resource availability which can also suffer a severe drop during prolonged periods of drought. Therefore, it is crucial to improve the monitoring of agricultural droughts and the prediction of their occurrence in the future [6]. In this work, we are interested in agronomic drought identification.

Several drought indices have been developed to quantify agronomic drought periods. Initial drought indices rely essentially on meteorological variables. Most meteorological

indices use precipitation either on its own or in combination with other meteorological variables [6]. The most commonly used meteorological index is the Standardized Precipitation Index (SPI) [7], which classifies precipitation intensities according to a probability distribution derived from historical records, over different durations (1 month SPI, 3 months SPI, etc.). SPI is particularly useful for drought identification and frequency analysis [7–9]. However, meteorological indices bring information on meteorological droughts defined only in terms of rainfall shortage, but not specifically on their consequences on vegetation for instance, especially for agronomic droughts. On the other hand, remote sensing (RS) is an effective tool to provide information on whether vegetation functioning is optimal or sub-optimal. Indeed, RS has shown high potential to retrieve land surface properties related to plant functionality, such as vegetation cover, from the visible/near infrared domain [10,11], surface soil moisture from the microwave remote sensing using passive or active radiometers [12–15], or surface temperature from the thermal infra-red (TIR) data that exploits surface energy balance components to identify land surface energy interactions [16].

RS observations of green biomass vegetation indices are relevant indicators of year-to-year drought conditions and vegetation greenness, especially over the past few decades thanks to the increasing number of multi and hyperspectral sensors [11,17], such as Advanced Very High Resolution Radiometer (AVHRR), SPOT-Vegetation and Moderate-Resolution Imaging Spectroradiometer (MODIS). These sensors provide spatial resolution ranging from 250 to 1000 m. Historically, the Normalized Difference Vegetation Index (NDVI) [18], built from the normalized difference between near-infrared (NIR) and RED reflectances, has been used for decades to provide information on vegetation health due to its strong correlation with the photosynthetic activity of plant cover. A suite of drought indices based on NDVI were subsequently developed in order to provide more focused information, such as the vegetation condition index (VCI) [19]. VCI uses the NDVI information provided from each pixel normalized with the maximum and minimum statistical range over the available time series of images. It has been tested in several regions of the world, showing a relevant efficiency to characterize periods of droughts [20,21]. The vegetation anomaly index (VAI) developed by [22], also forms a standardization of the NDVI time series. Although RS-based vegetation observation indices have proven their efficiency to assess drought impacts on vegetation growth, they are not able to detect incipient stress because of the time lag needed for the plant to reflect drought-induced physiological changes. Therefore, a delayed response to prolonged stress will be provided using these indices [23]. Response of vegetation to drought is a gradual process altering soil moisture, that leads to a time lag effect [24].

Surface soil moisture (SSM), which is inferred from microwave RS, is another efficient key parameter for agricultural planning and water resource management [12,25]. Nevertheless, for drought monitoring and agricultural modeling, a representation of root-zone soil moisture is needed [26]. A number of soil moisture-based indices have been developed and widely used for drought monitoring, such as the Soil Water Index (SWI) [27]. This index is retrieved from the Advanced SCATterometer (ASCAT) SSM estimates in C band, which was found to be more suitable in bare soils or sparse vegetation cover [28], to determine soil moisture (SM) distributions within the soil profile using an exponential relationship that links surface and subsurface SM via a characteristic time length [29]. SWI is also used on analysis of statistical anomalies over several years to derive the Moisture Anomaly Index (MAI) [15], that has shown a good performance in providing quantitative information on drought periods over the central region of Tunisia. The Soil Moisture Deficit Index (SMDI), developed by [30], was helpful for planning to mitigate drought impacts. This index is calculated from weekly percentage SM deficit or excess using long-term median, maximum and minimum soil water [30]. The main limitation of drought indices based on passive microwave data is their low resolution. Moreover, quantitative soil moisture estimation is still a challenge nowadays, especially under vegetation cover [12,31].

RS maps of land surface temperature (LST) are very informative of water availability and form a good indicator of incipient droughts [32]. Indeed, water stress induces a stomatal closure that generates in turn an elevated canopy temperature [33–37]. Thermal channels of Landsat, AVHRR or MODIS were exploited to retrieve remotely sensed LST estimates. LST can be used as a signature of the land surface energy budget and, in particular, to determine whether the dissipation of available energy is more into sensible (dry conditions) and/or latent heat (wet conditions) [38]. It also enables the computation of evapotranspiration (ET) from latent heat, computed as the residual of the surface energy budget [39,40]. ET is particularly informative about water stress conditions [40,41]. Indeed, the crop water requirements are adjusted to match the water losses from actual evapotranspiration (ETa) [42]. Consequently, in water stress conditions, the plant reduces its transpiration in comparison with unstressed vegetation under the same atmospheric conditions [43]. Thus, the water stress intensity may be inferred from the ratio of actual and potential (unstressed) ET. Several drought indicators that integrate ET have been explored and showed improved drought monitoring. In [44], the authors proposed the so-called Water Deficit Index (WDI) based on the approach Vegetation Index/Temperature Trapezoid (VIT). WDI is estimated for each pixel to retrieve dry/wet conditions based on the fractional vegetation cover and the difference between LST and air temperature (Ta). A good example of TIR indices is the evaporative stress index (ESI) [35] that describes anomalies in the actual and the reference ET ratio. ESI was shown to provide early warning particularly for flash droughts that could produce damaging impacts over short time periods [5]. The stress index (SI) is defined as the ratio between actual and potential evapotranspiration rates.

In summary, several drought indices are commonly used for drought monitoring and impact assessment in agriculture. However, it is hard to assess their respective performance in deciphering stress/non stress and drought/non drought situations. An inter-comparison between the performance of these different drought indicators provided from different wave lengths, in terms of consistency, reliability and ability to detect incipient water plant stress, is thus relevant. Kogan [19] evaluated VCI and the Temperature Condition Index (TCI) in different regions of the world. The analyses show that VCI has an excellent ability to detect each period of stress, the drought onset, intensity, duration, and impact on vegetation. The TCI provides additional information about vegetation stress through LST. In Kogan [19], the authors used VCI and TCI to develop the so-called Vegetation Health Index (VHI), a well known combined stress index that is widely used for drought detection and assessment of drought severity and duration [45]. However, as a simple averaging is performed, there is no real theoretical support for the way to weight the relative impact of stress (through LST) and vegetation development (through NDVI). The relationship between the changes in canopy temperature and the soil water supply in the fields is widely applied as a drought indicator [46]. The Vegetation Supply Water Index (VSWI), which is the ratio between the LST and NDVI, is found reliable to detect vegetation stress, moisture and drought-affected areas [46,47]. However, in this work, we suggest to compare different indices provided from individual biophysical variables (1) the "Normalized difference vegetation index" (NDVI) from the solar (Visible/Near InfraRed spectrum), (2) "Soil Water Index" (SWI) from the microwave domains and, (3) a "Thermal stress Index" (SI) from Thermal InfraRed retrieved from a surface energy budget model. Analyses are carried out in the Kairouan area in central Tunisia which is subject to a semi-arid climate. The thermal stress index used is based on ET simulated from a dual source energy balance model that provides robust estimates of ET when meteorological forcing and vegetation cover are accurately known [48]. A statistical downscaling method [49] combined with reanalysis data is used to generate surrogate series in order to extend the observation period. Then, simulated ET series from the downscaling method or from the unprocessed reanalyses are used to constrain the dual-source model Soil Plant Atmosphere and Remote Evapotranspiration (SPARSE) [50]. In this paper, we address three objectives:

(1) We first assess at a regional scale, the consistency between those indices and a precipitation-based drought index called the "Uniformized Precipitation Index" (UPI)

which is a variant of the SPI without the transformation into Normal quantiles. We assume that a robustness of the indices at very low resolution (12 km) translates into a good accuracy at higher resolution (kilometric).

(2) We assess the reliability of very low (UPI, SWI) and low (SI, NDVI) resolution indices at higher resolution (kilometric) at local scale, by focusing on drought monitoring for pixels either with a high proportion of rainfed wheat or that correspond to the extra large aperture scintillometer (XLAS) transect;

(3) We compare SI when the energy balance model is either forced with the downscaled meteorological data or with the unprocessed reanalysis data, in order to test the applicablity of SI with routinely available data at a global scale.

2. Study Area

The study site, the Merguellil catchment (Figure 1), is located in central Tunisia, which is typical of semi-arid environments. The study area is influenced both by the Mediterranean climate (dry subhumid) and the pre-Saharan climate (arid). It is characterised by the inter-annual irregularity of precipitation, with an average annual rainfall of about 300 mm per year, with a short rainy season mostly between September and May [51] and with a high evaporative demand of about 1600 mm per year. In our study region, the annual mean air temperature did not show considerable variation during the study period. In Figure 2, we observe that this variable is mainly steady during the study period, ranging from about 0 °C and 45 °C with a median of about 20 °C.

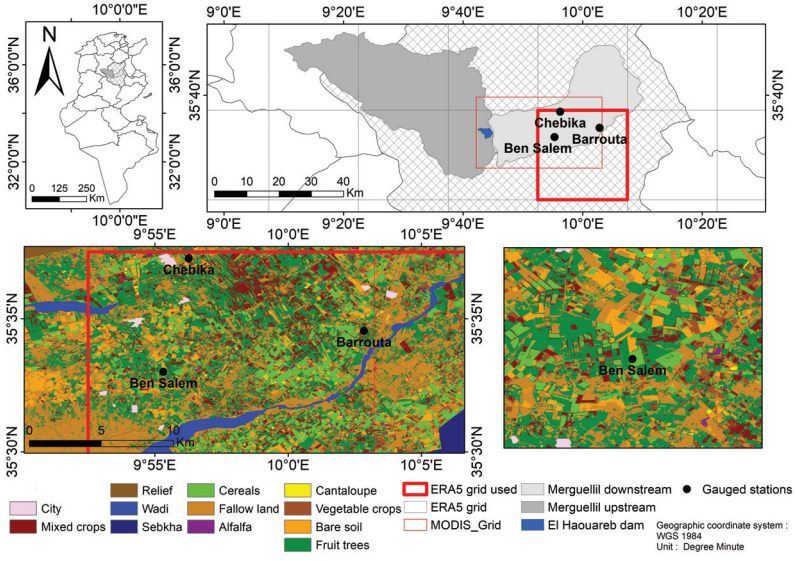

Figure 1. Merguellil catchment in central Tunisia with seasonal (winter–spring) land cover map of 2019–2020.

The upstream and the downstream sub-catchments are separated by El Haouareb dam that protects the village from inundations and provides surface irrigation water for the plain. However, most of the water used for irrigation is extracted from ground water. Merguellil is emblematic of hydrological processes which have been profoundly modified by human activities since the end of the 1960s, by the inclusion of soil and water conservation works, the construction of large and small dams, and intensification of irrigated farming [51,52]. As expected, agriculture is the main water consumer of available water resources in this region (around 80 of the available water%) [53]. Therefore, the aquifer system shows a considerable decrease over time and space due to over-exploitation [52]. This makes

the Merguellil catchment an interesting case study to investigate the ability to monitor agricultural water management in the recent years. In this work, we are interested only by the lower sub-catchment (3000 km^2) which forms an alluvial plain mainly flat with altitude between 50 and 200 m. The plain incorporates mainly small cultivated areas [54], with characteristic vegetation of semi-arid regions: rainfed agriculture (olive trees and cereals) and vegetables (melons, chilis and tomatoes), see Figure 1. The gauged network in the Merguellil plain catchment has three stations (Figure 1), installed since 2012 for the earliest ones.

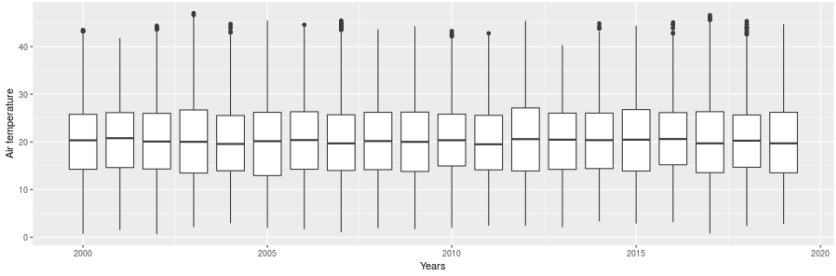

Figure 2. Annual air temperature (using ERA5 data) variation over the study period (2000–2019).

3. Data and Methodology

3.1. Biophysical Indices Derivation

3.1.1. NDVI

We used the MOD13 version 6 product from the Moderate Resolution Imaging Spectroradiometer (MODIS) sensor on board the NASA Terra and Aqua Earth Observation System satellites that provides each 16-day composite at 1 km of spatial resolution. Time series are retrieved between 2000 and 2019 over our study area (see Figure 1). NDVI uses the normalized difference between near-infrared (NIR) and (RED) reflectances.

$$NDVI = \frac{\rho_{NIR} - \rho_{RED}}{\rho_{NIR} + \rho_{RED}}. \quad (1)$$

where ρ_{NIR} and ρ_{Red} are the near-infrared (NIR) and red reflectances, respectively. NDVI increases with the amount of healthy green photosynthetically active vegetation. Uniformized NDVI measures reflect the "current" vegetation conditions according to a longer-term historical average NDVI value over the same study area.

3.1.2. SWI

The soil water index (SWI) data are derived from the surface soil moisture (SSM) using an infiltration model to describe the relation between surface soil moisture and profile soil moisture as a function of time.

$$SWI(t) = \frac{\sum SSM(t_i)e^{-(t-t_i)/T}}{\sum e^{-(t-t_i)/T}}, \quad (2)$$

where SSM is the surface soil moisture estimate from the ASCAT at time t_i. The parameter T, called the characteristic time length, represents the time period to integrate SSM data. T is the most important input parameter to derive the profile soil moisture content from remotely sensed surface time series: a high T value describes a deeper soil layer if the soil diffusivity is constant, and the same T value describes different depths for different soils (texture) [27]. In Ceballos et al. [55], the authors studied a semi-arid region characterized with a similar heterogeneous texture distribution in the soil profiles as our study region, having surface soils of sandy texture and a higher clay concentration to a depth of 2 m [56], and found that T = 60 days is the best choice for the 50–100 cm soil profile, which corresponds to the root layer according to the predominant agricultural use of our study region

(olive trees and cereals). Indeed, the upper part of the profiles promotes high infiltration rates and low water retention forces [55].

The SSM is retrieved from scatterometer observations from the ASCAT instruments on board the MetOP satellites, which measures radar backscatter at C-band in VV polarization, with an initial spatial resolution of 25 km, re-sampled at 12.5 km [57]. SWI product is retrieved from the Copernicus Global Land service and provides global daily information since January 2007 to present [58].

3.1.3. Thermal Infrared Stress Index

We used a stress index (SI) obtained from TIR. The surface temperature (LST) provides indirect estimates of water stress since it enters in the surface energy balance equations and it is thus related to the evapotranspiration rate flux. Daily ET simulation is detailed in Appendix A section. The stress index is defined as the ratio between actual (ET_a) and potential evaporation rates (ET_p) [40].

$$SI = \frac{ET_a}{ET_p} \tag{3}$$

If the actual evaporation value is close to the potential value, the stress index takes values close to one that reflect unstressed conditions. However, if the actual evaporation is low compared to its potential value, the stress index values may reach zero, which represents fully stressed conditions. ET_a and ET_p are simulated from the energy balance model SPARSE [50] using meteorological observations and remote sensing variables.

LST, viewing angle and emissivity data are retrieved from the daily 1-kilometer LST product (MOD11A1) from MODIS VI products on board Terra and Aqua sensors. Quality control (QC) assessment for LST and emissivity product is also provided from the LST product. For stress index retrieval, the Leaf Area Index (LAI) and albedo products are also needed. We used the 8-day of albedo series (MCD43A3) from MODIS at 500 m, resampled to a spatial resolution of 1 km. Finally, the LAI is retrieved from the NDVI time series using an empirical equation [59], defined in the following Equation (4):

$$LAI = -\frac{1}{k} \ln \frac{NDVI_{max} - NDVI_i}{NDVI_{max} - NDVImin} \tag{4}$$

where k is an extinction factor, about 1.13, $NDVI_{max}$ = 0.97 and $NDVI_{min}$ = 0.05 corresponding to the NDVI value of bare soil [48]. The region is characterized by tree-dominant cover with interrow distance of 12 m corresponding to low LAI values (about 0.3 to 0.4) on an image [60].

3.1.4. UPI

We used the Climate Hazards group Infrared Precipitation with Stations (CHIRPS) data which are available from 1981 till now. This product incorporates three types of information: global climatologies, satellite estimates and in situ observations [61]. CHIRPS is available daily and at a spatial resolution of about 5 km. The CHIRPS precipitation data are highly reliable to identify wet and dry periods in our study region [62].

The CHIRPS precipitation time series is used to compute the Uniformized Precipitation Index (UPI), which is constructed following the same steps as the SPI except for the last step that transforms into Normal standard quantiles [7]. SPI maps precipitation amounts to the [0,1] interval by using either the empirical or a parametric cumulative function. Then, a final transformation is applied to obtain values that are normally distributed. UPI is computed with a single transformation: the empirical cumulative function is used to map precipitation amounts derived from historical records, to uniform quantiles in the [0,1] interval, as expressed in Equation (5):

$$\hat{F}_n(x) = \frac{1}{n} \sum_{i=1}^{n} 1_{\{x_i \leq x\}}, \tag{5}$$

where $1_{\{\cdot\}}$ is the indicator function, $x_1, \ldots, x_n$ are rainfall amounts aggregated at different time scales (years, months or decades) and $\hat{F}_n(x)$ is the UPI value with $\hat{F}_n(x) = P(X \leq x) \in [0, 1]$, with X the random variable representing the rainfall amounts at a given time scale. In contrast, SPI is computed as $\Phi^{-1}(\hat{F}_n(x))$ where Φ^{-1} is the quantile function (the inverse of the cumulative function) of the standard normal distribution.

We believe the interpretation in terms of uniform quantiles, which are simply probabilities of non-exceedance, is more straightforward than normal quantiles. For example, if UPI equals 0.1 on a given year, it means that 10% of the yearly precipitation amounts are inferior or equal to the amount observed that year. In other words, that year is among the 10% driest years. The SPI value corresponding to 0.1 is approximately -1.28.

3.2. Thermal Stress Index Derived from Energy Balance Model

3.2.1. SPARSE Model

We rely on the dual source energy balance model SPARSE [50] to simulate evapotranspiration. It estimates evaporation (E) and transpiration (T) separately. This is particularly relevant for arid and semi-arid areas which are characterized by sparse crop canopy and by an uneven relative contribution of evaporation and transpiration [63].

The model can be run in two modes: retrieval and prescribed mode. In retrieval mode, the respective stress levels (between non evaporating/transpiring and fully evaporating/-transpiring, i.e., potential rates) are two unknowns which are determined from the single piece of information provided by $Tsurf$ by assuming at first that the vegetation is not stressed, that allows a simplification to solve the underdetermination problem. $Tsurf$ is used to estimate the latent heat component from the soil (LEs), corresponding to the soil evaporation E. If the vegetation is suffering from water stress, the resulting LEs will decrease to unrealistic levels (negative values). In that case, we assume that the soil surface is stressed and LEs is set to a minimum value close to zero. Then the energy budget equation is solved for the vegetation component of the latent heat flux (LEv), which corresponds to the transpiration T. If LEv is also negative, fully stressed conditions are imposed for both soil and surface components [60]. The prescribed mode provides an estimate of the potential latent flux for the soil and the vegetation (LEs_{pot} and LEv_{pot} respectively). The water stress indice SI is then defined from the actual and unstressed evapotranspiration rates (potential) at the time of the satellite overpass.

The SPARSE model is forced by a series of meteorological observations (air temperature, relative humidity, global radiation and wind speed) and remote sensing variables (NDVI, LAI, albedo and LST). Outputs are derived at meteorological time steps (half-hourly).

3.2.2. Meteorological Forcing

It is important to consider a long meteorological series in order to perform a robust statistical characterization of drought periods. In addition, owing to the temporal and spatial scales of climate variability, evapotranspiration and water stress index must be monitored at high temporal (subdaily to daily scales) and spatial resolution. However, available gauged stations (see Section 2) are scarce with short observation periods and numerous gaps, insufficient to perform a robust statistical analyses and characterization of drought periods. We rely, therefore, on surrogate meteorological series that extend in time the original series in order to be used to constrain the SPARSE energy balance model. In this work, we used two types of surrogate meteorological data:

1. Unprocessed reanalysis data ERA5 extracted at the grid cell closest to the region of interest (see Figure 1): ERA5 reanalyses are available at a 31 km spatial resolution [64]) from 1950 to present at an hourly temporal scale [64]. Reanalysis series that correspond to the four meteorological variables required for the energy balance model to simulate the corresponding index SI_{ERA5} are: the incoming global solar radiation at the surface (bottom of atmosphere), wind speed at 10 m, air temperature at 2 m and the relative humidity that was derived from 2 m air temperature and 2 m dewpoint temperature

ERA5 products, according to the procedures defined in [65]. The specific aim of using unprocessed reanalysis data for our study, is to assess its performance to constrain an energy balance model for regions with no gauged stations.

2. Simulated series from a Stochastic Weather Generator (SWG) called "MetGen" [49]: Its implementation is publicly and freely available as an `R` library. MetGen generates scenarios of meteorological variables at sub-daily temporal resolution in order to extend local observations in the past. It relies on low resolution ERA5 reanalysis data and exploits observations provided by three gauged stations located in our study region (see Figure 1) to simulate regional climatic information. The corresponding index simulated using the SWG meteorological to constrain SPARSE model, is denoted SI_{SWG}.

Inter-comparison between indices will be computed at a daily time scale for a long period in the past from 2000 to 2019. Characteristics of indices used are as follows, see Table 1.

Table 1. Characteristics of indices used.

Wave Lenghts	**Visible/Near Infrared**	**Infrared + Visible + Meteo.**		**Microwave**	**Meteo. + Satellites Data**
Indices	NDVI	SI_{SWG}	SI_{ERA5}	SWI	UPI
Satellites	MODIS	MODIS	MODIS	ASCAT	CHIRPS
Model used	✗	SPARSE	SPARSE	✗	✗
Spatial resolution	1 km	1 km	1 km	12.5 km	5 km
Temporal resolution	daily	daily	daily	daily	daily
Temporal availability	since 2000	since 2000	since 2000	since 2007	since 1981

3.3. Indices Standardization

For added interpretability, the different indices are usually re-scaled or standardized in order (1) to be expressed as frequencies that can be easily interpreted [66] and (2) to statistically characterize the deviation (anomaly) of the index values according to a long series recorded over the study period. For this aim, we standardize each index X with its empirical cumulative density function (ECDF). Let $(x_1, \ldots, x_n)$ be the values taken by the index X for a given data set. Then the ECDF is given by :

$$\hat{F}_n(x) = \frac{1}{n} \sum_{i=1}^{n} 1_{\{x_i \leq x\}}, \tag{6}$$

where $1_{\{\cdot\}}$ is the indicator function, X_i is the index value for time step i and Y_i is the standardized value of the index x. The ECDF standardizes by mapping a value x taken by X to its empirical non exceedance frequency, i.e., the percentage of occurrences of values lesser than or equal to x [67]. This is illustrated in Figure 3 : the ECDF maps the values $x \in [0.1, 0.6]$ to $[0, 1]$. In particular, the value $x_i = 0.31$ is mapped to $y_i = 0.8$ which means that 80% of the values of the index X are expected to be below 0.31.

The advantages of the proposed standardization approach with the ECDF are that (1) it does not rely on the assumption that the raw indices values follow a normal distribution which is implicit in standardization approaches that rely on centering and scaling, (2) it allows for flexibility in the choice of reference sample (depending on seasons for example), and therefore can be used for short scale monitoring, and (3) it produces results that are easily interpreted in terms of non-exceedance probabilities, as for UPI, especially when simultaneous variables are analyzed [67]. Standardization using the empirical cumulative

distribution function is performed over the whole period (20 years). At an annual scale, standardization is performed over each year according to available values observed during the whole study period. At a decadal scale, standardization is performed according to season (winter, autumn, summer and spring).

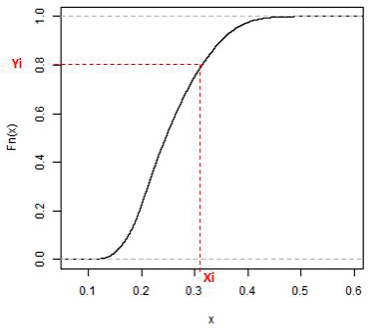

Figure 3. Empirical cumulative density function illustration.

3.4. Evaluation of the Different Drought Indices Performance

3.4.1. At Regional Scale

For comparison at a regional scale, all indices are aggregated at a very low spatial resolution (about 12 km). For this comparison, the CHIRPS precipitation time series is used as a reference to identify water stress conditions at different time scales: annual and decadal scales. In order to assess robustness and consistency between indices, we used for instance time series for visual interpretation and Kendall's τ, which is a rank-based correlation coefficient that measures the strength of the relationship between two indices.

To focus on consistency between the precipitation index and other indices, we assess the ability of the different indices to correctly identify the stress periods defined according to UPI. We define the stress periods based on UPI as follows. We assume that a drought event is a stress period with a probability of occurrence of approximately 20% and that it lasts at least two decades. The threshold of 20% in terms of UPI corresponds to a threshold of about -0.84 in terms of SPI. The drought classes defined in [7] begin when SPI values fall below 0 (this corresponds to 50% in terms of UPI). In our study region, the threshold of 20% corresponds to precipitation amounts inferior to 200 mm, which is approximately the precipitation amount average at a growth season. We transform the decadal standardized indices into Boolean values according to the stress threshold: 0 to denote an unstressed situation ($>$0.2) and 1 for stress conditions ($<$0.2). The second step is to check for each time step (t) how many stress periods are recorded within the period between $(t-1)$ and $(t+1)$, one decade being considered as a buffer (see Figure 4).

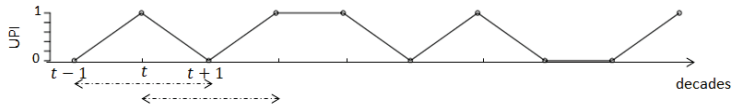

Figure 4. Identification of stress periods using UPI index transformed into Boolean values.

This method allows us to take into account the memory effects for three decades. Moreover, the use of a moving average of UPI allows us to take further consideration of memory effects and delayed responses of the different indices. We consider, therefore, the use of a UPI moving average lagged up to 2, 3 and 4 decades. If the number of stress periods based on UPI or lagged moving averages UPI exceeds two of the three decades

considered, we assign a drought condition for this time step. Then we assess the response stress/unstress of the other drought indices (SI_{SWG}, SI_{ERA5}, SWI and NDVI).

3.4.2. At Local Scale

For comparison at finer spatial resolution, a kilometric scale, we use local precise information based on:

- XLAS in-situ measurements : Sensible heat flux measurements using an extra-large aperture scintillometer (XLAS) are provided as part of the work of [60], for the period ranging between March 2013 and June 2015. The scintillometer (XLAS) was installed close to the Ben Salem village over a 4 km transect above a mixed vegetation canopy: trees (mainly olive orchards) with some annual crops (cereals and market gardening) [60]. For our analyses, pixels enclosed in the mean XLAS are selected in order to compare the different drought indices with the stress index derived from the sensible heat flux measurements, denoted SI_{XLAS}.
- Historical rainfed areas selection : Rainfed crops are more sensitive to rainfall depletion and thus to drought. For our analyses, we identify historical rainfed wheat areas relying on a non-irrigated cereal mask (see Figure 5a), computed for the agricultural year 2011–2012, as part of the work computed by [68]. It is computed using an object-oriented classification technique basing on the Spot image of 31 March 2012. We generate the percentage of non-irrigated cereal fields for this year, over each MODIS pixel, (see Figure 5b). Then, we select pixels that contain more than 40% of rainfed cereal cover. Rainfed cereal pixels selected are used as reference to locate non-irrigated cereal fields in precedent years, in order to assess the response of the different indices over a dry and a wet year.

In order to facilitate interpretation, we define four stress classes that characterize the severity of water stress identified using the different drought indices. The four stress classes are listed in Table 2, "High stress", "Stress", "Moderate stress" and "No stress" according to the values of a given index.

Table 2. Drought indices classification.

Index Values	Drought Class
0–0.15	High stress
0.15–0.3	Stress
0.3–0.7	Moderate stress
0.7–1	No stress

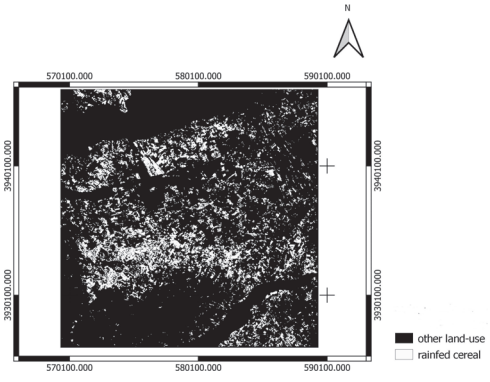

(**a**)

Figure 5. *Cont*.

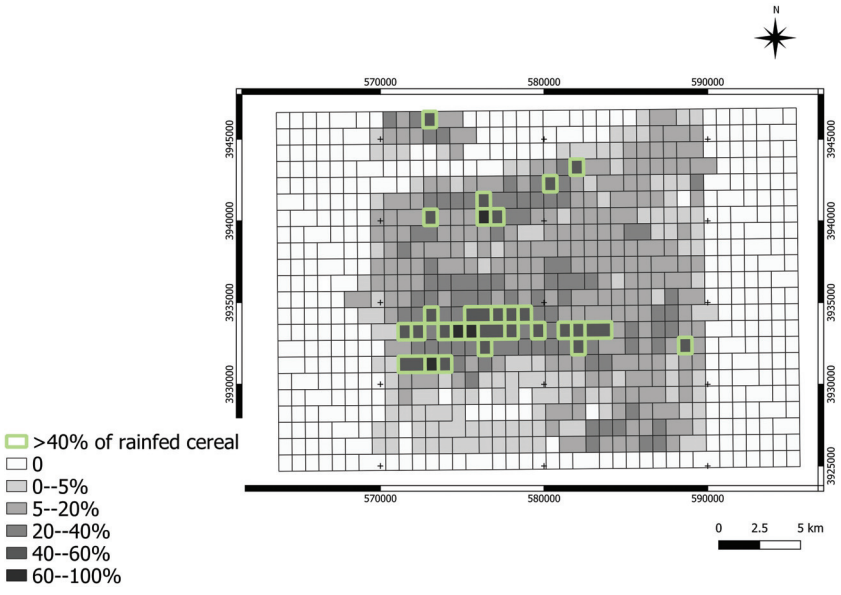

(**b**)

Figure 5. Identification of rainfed cereals in MODIS pixels over the 2011–2012 agricultural season. (**a**) Rainfed cereal mask, produced for the 2011–2012 agricultural season [68]. (**b**) Percentages of rainfed cereal in each Modis pixel of the 2011–2012 agricultural season.

4. Results

4.1. Drought Indices Inter-Comparison at Regional Scale

4.1.1. Annual Scale

Figure 6 presents the cumulative rainfall during the growth season (September to May) with the corresponding NDVI variation for each year (Figure 6a), in order to visually characterize the inter-seasonal variation over the study period. Rainfall data are provided from CHIRPS precipitation time series. The red line in Figure 6a corresponds to 200 mm/growth season of precipitation amount. We assume that a dry year presents a cumulative rainfall below 200 mm during a growth season. The Figure 6b shows the time series of different standardized drought indices: the TIR SI simulated when the SPARSE model is constrained by the SWG or ERA5 meteorological data SI_{SWG} and SI_{ERA5}, the standardized NDVI index, the UPI, and the standardized SWI which is available since 2007. The red line in Figure 6b indicates the drought threshold, fixed in this study at 0.2 which corresponds to a drought event with an approximately 20% non exceedance frequency. The stress threshold is necessary to discuss drought events, as well as their onset, duration and intensity. The farther below the red line a standardized index is, the worse the drought is.

Overall, we see that annual indices show a similar variation. SI_{SWG} and SI_{ERA5} show similar inter-annual variability. Moreover, we observe that they reproduce UPI variability and succeed in identifying wet and dry conditions simultaneously. Dry periods, which correspond to abnormally dry situations that fall below the drought threshold, are well depicted also by a cumulative rainfall less than 200 mm during each growing season, and a low NDVI level. However, we observe in some instances that UPI is not very well correlated with other standardized indices. This is the case for 2004–2005 or 2008–2009 where we observe that UPI is either above the unusual unstressed condition or below the drought threshold while other indices present similar stress level. To better explore the allocation of precipitation intensity along these years, we present in Figure 7, the monthly cumulative precipitation and monthly NDVI variation over these agronomic years. In addition, in

order to facilitate interpretation, we present in Figure 7c, the monthly rainfall and NDVI average over the whole study period between 2000 and 2019. There are in Figure 7a, low cumulative rainfalls in winter and spring in comparison with the monthly rainfall amount mostly observed in our study region during this period (see Figure 7c). However, almost all the largest cumulative rainfall amounts are observed from September to December. Rainfall during this period was sufficient, and coincided with the beginning of the growth season. For this reason, we observe a high level of NDVI in March and May that reflect a good development of vegetation, particularly cereal crops. Consequently, unstressed conditions were also shown by the rest of the standardized indices. We also observe an abnormally unstressed situation depicted by UPI during the agronomic year 2008–2009. However, the other standardized indices indicate a medium stress condition. Indeed, we observe very low rainfall amounts during the whole year, especially in November and December that correspond to seeding and early growth. Then, we observe an abnormally high rainfall amount that exceeds 100 mm/month in January. This high cumulative amount increases the annual cumulative rainfall but it is late for vegetation growth. Indeed, an adequate response of the stress is always dependent on receiving sufficient rainfall at the appropriate moments, with sufficient amounts. In contrast, the agronomic year 2017–2018 shows very low cumulative seasonal rainfall. The TIR SI values succeed to detect the stress period, by presenting low values. However, standardized SWI and NDVI show a medium stress condition. SWI and NDVI did not succeed to detect the drought intensity for this year.

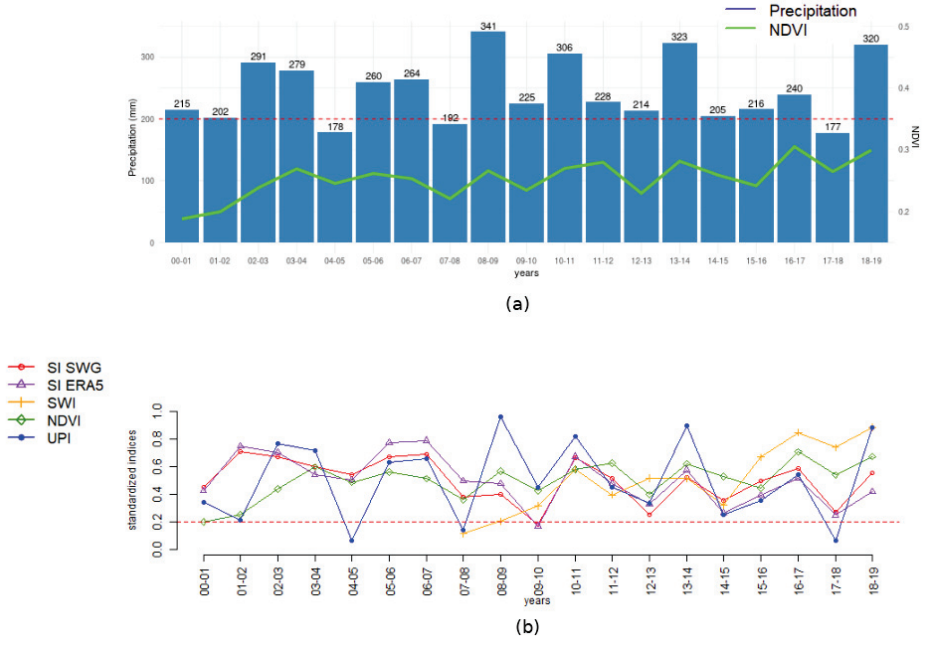

Figure 6. Time-series of seasonal variation of standardized drought indices accumulated in growth season. (**a**) Seasonal cumulative rainfall (September to May) with the corresponding NDVI variation. The red line indicates the 200 mm precipitation amount. (**b**) Drought indices.

To assess the consistency between the various indices at an annual scale, we use Kendall's τ. Kendall's τ is suitable for non-Gaussian distributions, as opposed to the Pearson correlation coefficient [69]. Positive values indicate that both indices tend to increase or decrease simultaneously, while negative values indicate that they tend to vary in an opposite manner. A value near zero signals a lack of dependence. In Figure 8, we see

that all indices present positive correlation coefficients. All indices present high Kendall's coefficients with UPI that exceed 0.35, particularly SI_{ERA5} which presents a Kendall's τ of about 0.46. However, SWI presents a very low correlation coefficient with UPI. This is could be explained by the different responses of these indices to a rainfall supply. UPI presents an instantaneous response to rainfall variation. In contrast, SWI which presents the root zone soil moisture, presents a delayed response to rainfall supply. On the other hand, we observe that SWI presents the highest τ value with NDVI, which reflects a very strong seasonal correlation between them. Furthermore, SI_{SWG} is highly correlated with other indices. It presents a Kendall's τ of about 0.58 with NDVI and with SWI and the highest correlation with SI_{ERA5}, with a Kendall's τ of about 0.64. However, SI_{ERA5} presents low correlation coefficients with NDVI and SWI.

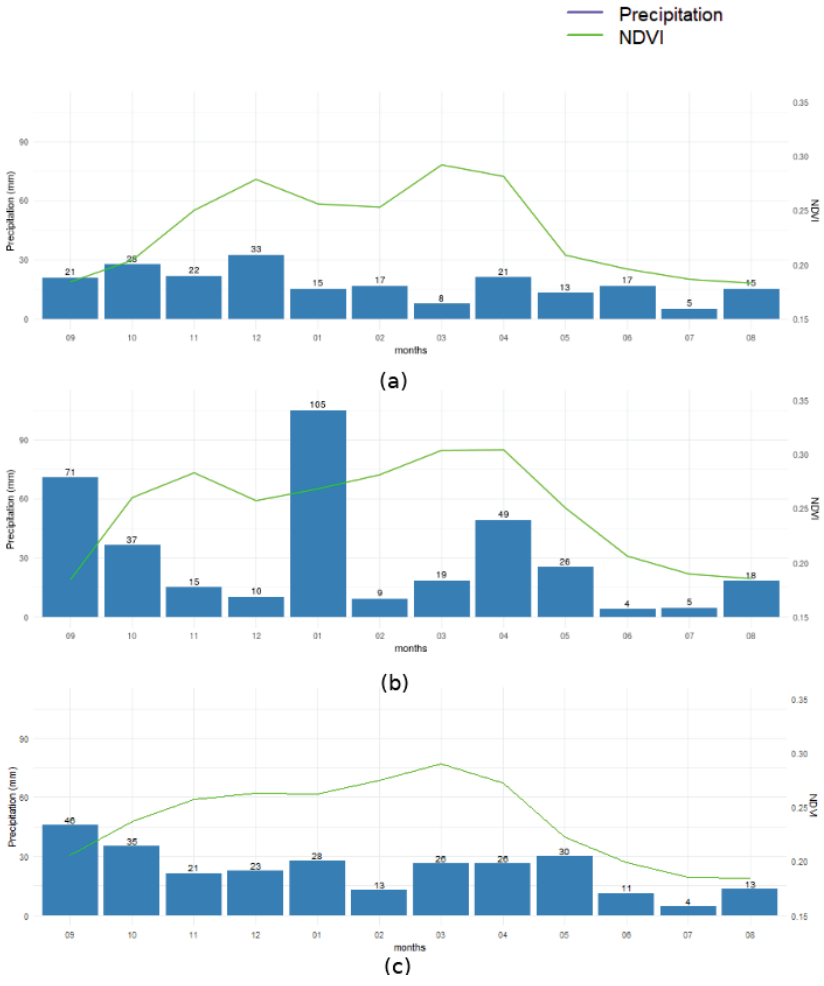

Figure 7. Precipitation and NDVI monthly variation over agronomic years (2004–2005) and (2008–2009). (**a**) 2004–2005. (**b**) 2008–2009. (**c**) Monthly rainfall and NDVI over the study period 2000–2019.

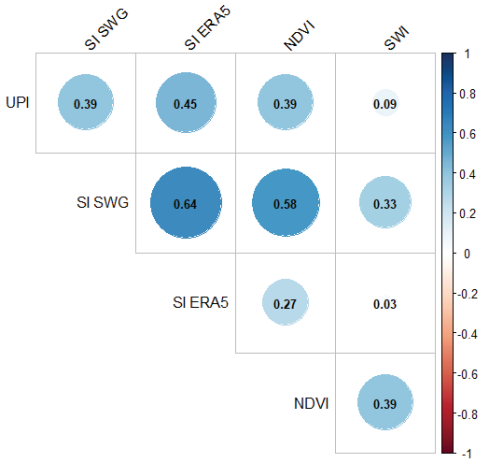

Figure 8. Seasonal Kendall's τ correlation between drought indices.

4.1.2. Decadal Scale

We focus on a finer temporal scale, a decadal scale, in order to assess short term variations. Indeed, a short time scale (monthly or decadal) is more appropriate to provide information on the growing season development over a few months and, therefore, on the water supply, unlike the annual time scale [6].

In Figure 9, we propose a comparison analysis carried out at a decadal scale of the cereal growing season (from September to May) selected from some dry and wet years. We used the values of precipitation index UPI lagged up to five decades rather than the instantaneous value, in order to be more correlated with the aggregated response of the different indices. The agronomic year 2012–2013 (see Figure 9a) is considered as a dry year, based on the cumulative rainfall over the corresponding growth season (Figure 6a). We observe that the standardized NDVI index presents moderate drought conditions (50% of probability of occurrence) at the beginning. Then, it decreases in December to 0.4 and then it reaches 0.2 in the end of the growth season. However, the standardized TIR indices show mainly similar variations, more correlated with lagged UPI variations. UPI shows considerable fluctuations along the whole period. We observe very low values during several decades in September and October and in January until March, that lead to important drops of SI_{SWG}, SI_{ERA5} and extended low values of SWI which fluctuate around 0.2 in the beginning of the growth season.

The period 2013-2014 represents a typical wet growth season. In Figure 9b, we observe that the different drought indices are above the drought threshold over the whole period. The standardized NDVI index present high values in spring that reflect a good vegetation health and a maximum crop development during this period. High NDVI values are observed after an important water supply provided during the growing season. UPI presents abnormally high values that reach 100% probability of non exceedance for several decades. SI_{SWG}, SI_{ERA5} succeed to reproduce the main fluctuation in the lagged UPI: relevant increases in UPI values lead to an important elevation of both the TIR indices and a relevant drop in UPI which falls below the stress threshold mainly in January and February and induces an important rapid decline of both TIR SI values. SWI presents, however, a more delayed response to UPI variations. In fact, we observe a depression in SWI in autumn and spring due to successive drop fluctuations of UPI during these periods.

In Figure 9c, we present another dry growth season. The lack of precipitation observed mainly at the beginning of the growth season induces a decrease in the standardized NDVI and SWI indices at the end of the growing season. The rainfall shortage during this season triggers a relevant depletion of the TIR indices, especially in winter where we observe SI_{SWG}, SI_{ERA5} and UPI are below the stress threshold. However, each lagged UPI value increase leads to an elevation in TIR indices.

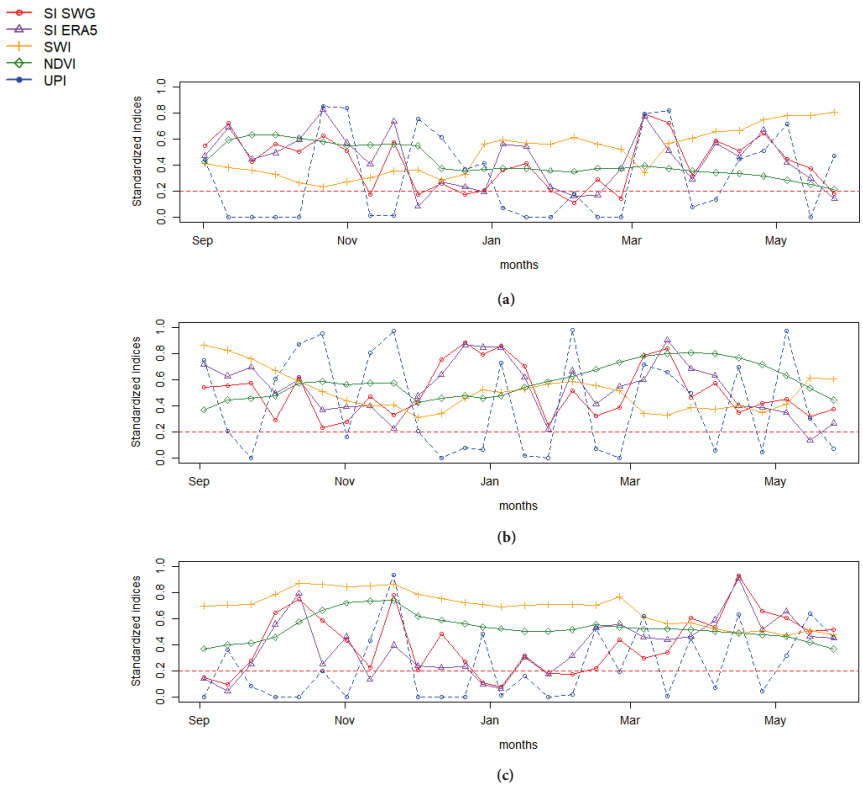

Figure 9. Decadal times series of standardized stress indices derived from different wavelenghts over the growing season of two dry years (2012–2013 and 2017–2018), and a wet year (2013–2014). (**a**) 2012–2013. (**b**) 2013–2014. (**c**) 2017–2018.

A further analysis is carried out to assess more closely the consistency between the different drought indices in identifying stress periods at the decadal timescale according to UPI. As explained in Section 3.4.1, we define stress periods according to the different indices. Besides, we identify three cases: (1) the stress indices correctly reproduce the drought condition identified with UPI (stress period or not stress period), flagged as "Congruent with UPI", (2) the stress indices identify a stress period not confirmed by UPI, called a "Not confirmed by UPI", and the last case, (3) the stress indices do not succeed to identify a stress period detected by the UPI, called a "missed stress". The first case estimates the consistency between the different drought indices and UPI to identify the same stress conditions. Analyses are performed according to seasons, in order to assess drought index responses through different seasons.

In Figure 10, we present the probability to identify these three different cases, according to seasons and UPI values in Figure 10a and lagged moving average UPI to 2, 3 and 4 decades, respectively, for Figure 10b–d. Overall, we observe that the different indices show a good performance to identify the same stress condition in autumn, winter and especially in spring. However, in summer, the probability to detect the same stress conditions using the different stress indices is decreased at the expense of missed stress. Indeed, in summer the probability of rainfall events is extremely low in our study region. Therefore, drought periods identified by UPI increase, but they are not necessarily identified by other drought indices due to the supply of water provided from irrigation as an alternative water supply for this period. The NDVI shows high probability to detect stress status congruent with UPI, especially in spring where we have the maximum of vegetation development. The case of "congruent with UPI" could be related to a stressed or an unstressed period. In this

case, the high level of the "congruent with UPI" performed by NDVI is mainly related to a no stress period over the rainy season and particularly in spring.

Figure 10. Probability of drought detection based on UPI and lagged UPI during the period between 2007 and 2019. (**a**) Stress identification basing on UPI. (**b**) Stress identification based on a UPI 2 decade moving average. (**c**) Stress identification basing on UPI 3 decade moving average. (**d**) Stress identification basing on UPI 4 decade moving average.

Besides, we observe that SI_{SWG} and SI_{ERA5} show a good performance to correctly detect the stress conditions determined from the UPI and it presents a low probability of identifying stress periods not confirmed by UPI, especially using SI_{SWG}. This performance is maintained during different seasons and even enhanced with the comparison with the lagged moving average of the UPI. On the other hand, we observe that SWI shows a better performance in winter and spring. Indeed, during this season, vegetation is well developed with deeper root zones, which could explain the high performance of SWI to identify a stress period or unstressed period according to UPI. Furthermore, this performance is improved incrementally when we increase the lagged moving average value of UPI. The application of a moving average of 4 decades seems to be the best delay period for adequate responses for all drought indices. Beyond this value, too many memory effects are lost.

4.2. Drought Indices Inter-Comparison at Local Scale

4.2.1. Evaluation with XLAS In-Situ Measurements

In Figure 11, we present a decadal time series of the different standardized indices during two growing seasons, where XLAS measurements are available at both local (Figure 11a,c) and regional scale (Figure 11b,d). As mentioned above, we used for this comparison the lagged UPI (up to 5 decades) and SI_{XLAS}, respectively, as regional and local references. The aim of the comparison of indices at a local and a regional scale is to assess if an index found to be robust at low resolution (12 km) maintains its performance at higher resolution (kilometric). For interpretation, we consider two groups of indices according to their spatial resolution: a group with low resolution (kilometric) (SI_{SWG}, SI_{ERA5} and NDVI), and a second group with very low spatial resolution, at dozens of kilometers (SWI and UPI).

In Figure 11a,b, we present a wet year (2013–2014). We see that indices SI_{SWG} and SI_{ERA5} succeed to better reproduce SI_{XLAS} fluctuations in Figure 11a. In addition, we observe that these indices, especially SI_{SWG}, follow the SI_{XLAS} variations more closely, particularly during the rainfall season (from October to February) and the last decades of this growth season. Besides, we observe that stress periods defined by the SI_{XLAS} (under the threshold line), observed in October, December and February, are mostly isolated with SI_{SWG}. Moreover, SI_{SWG} succeed in identifying stress conditions defined by SI_{XLAS}, even using its aggregated values at the regional scale (see Figure 11b). The NDVI, in spite of being defined among higher resolution indices, did not succeed to reproduce SI_{XLAS} decadal variations. However, it brings, as expected, an overall delayed information about stress conditions. We observe, for example, in Figure 11a, which presents a wet year, an elevation in NDVI values in winter and spring that also correspond to several elevated values observed by SI_{XLAS}. On the other hand, we observe a different behavior of the standardized SWI according to the different spatial scale. At a local scale (Figure 11a), SWI did not succeed in correctly reproducing SI_{XLAS} variations. However, at a regional scale (Figure 11b), SWI succeeded in identifying dry or wet conditions, according to the lagged UPI fluctuations. Dry conditions were observed at the beginning of the growth season and in February. Wet conditions were observed in November–December and the end of the growth season.

The 2014–2015 period represents a relatively dry year. We observe that NDVI presents mainly moderate stress values in Figure 11d. In Figure 11c, we observe that TIR stress indices succeed to better reproduce SI_{XLAS} in this growth season, particularly using SI_{SWG}. Indeed, SI_{SWG} succeed to identify a water stress period caught by SI_{XLAS} which persists for several decades during March, as well as an unstressed period observed later in April and May, visible in the same figure. At a local scale (Figure 11c), SWI shows low values observed below the stress threshold during several decades in Autumn and March, which amply testify an overall dry situation during this growth season. Even at a regional scale (Figure 11d), SWI shows moderate stress values. However, SWI was not able to accurately identify stress conditions in comparison with in situ measurements. This could be explained by its very low spatial resolution, inadequate for local stress detection.

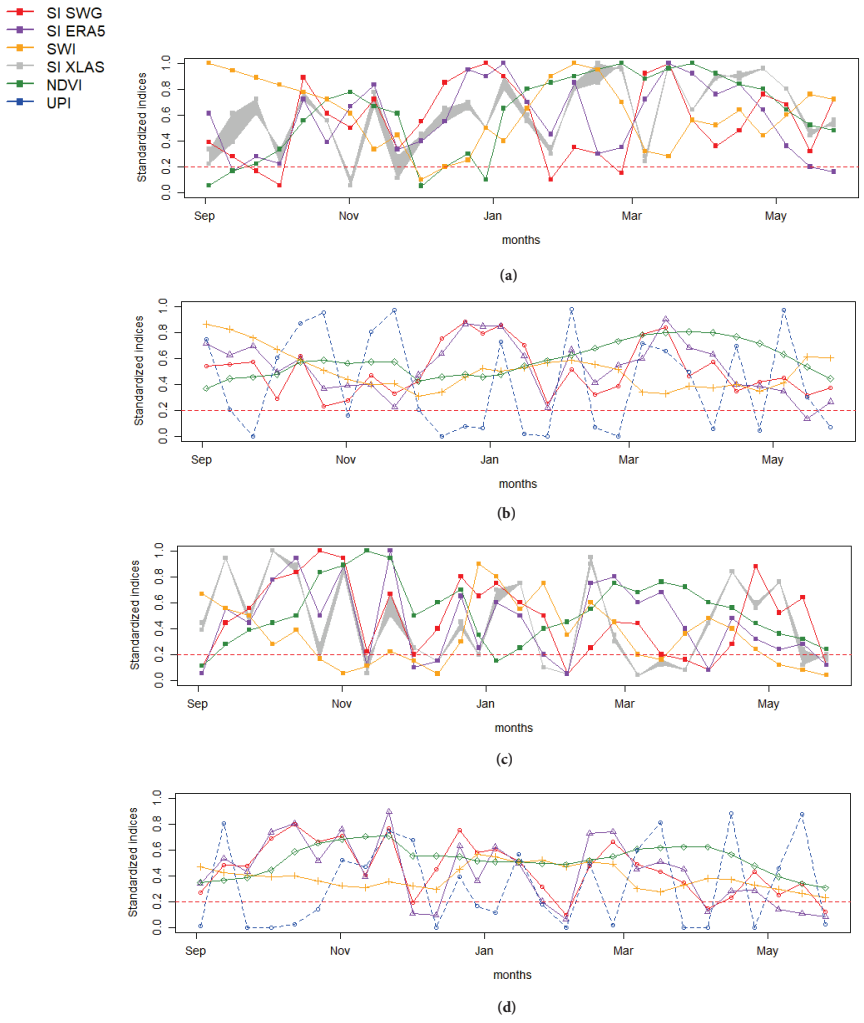

Figure 11. Decadal times series of standardized stress indices derived from different wavelenghts over the growing season of two years (2013–2014) and (2014–2015) at a local scale (**a**,**c**), in comparison with SI_{XLAS} derived from XLAS measurements over pixels containing the scintillometer transect and at a regional scale (**b**,**d**). (**a**) Local scale (2013–2014). (**b**) Regional scale (2013–2014). (**c**) Local scale (2014–2015). (**d**) Regional scale (2014–2015).

4.2.2. Drought Detection in Rainfed Areas

In Figure 12, we present stress class maps of the different indices at the seasonal scale (growth season) of the year 2011–2012: Figure 12a for the standardized thermal index constrained by meteorological SWG data, Figure 12b for the standardized thermal index constrained by meteorological ERA5 data, Figure 12c for standardized NDVI index, Figure 12d for standardized SWI index and Figure 12e for standardized precipitation index. In addition, we present the percentage of stress classes identified by each index using extracted rainfed cereal pixels, as explained in Section 3.4.2 (see Figure 12f). Combined results presented in Figure 12f show that most indices depicted a moderate stress class for this year with the highest percentage. However, we observe that the TIR stress indices and SWI show an elevated percentages of stress class and even a very low percentage of a

high stress class for SI_{SWG} and SI_{ERA5}. This finding is in agreement with the hydrological year characteristics presented in Figure 6a. Indeed, this year characterized by a cumulative seasonal rainfall about 228 mm did not belong to very wet or very dry year. Stress classes depicted by thermal indices and SWI could be more precise than NDVI characterized by a delayed response and than the UPI which is less informative when aggregated at a low temporal scale (seasonal scale).

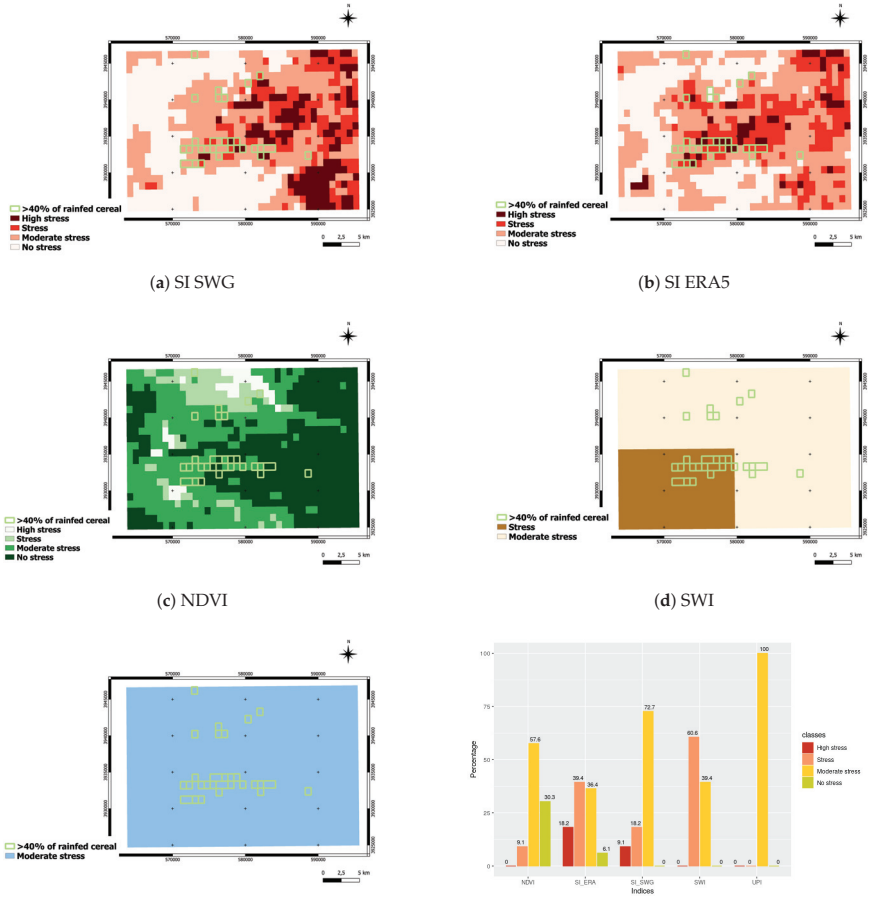

Figure 12. Stress classes for each drought index used over the agronomic year 2011–2012, (**a**) for the standardized thermal index constrained by meteorological SWG data, (**b**) for the standardized thermal index constrained by meteorological ERA5 data, (**c**) for standardized NDVI index (**d**) for standardized SWI index, (**e**) for standardized precipitation index and (**f**) for percentage of the stress class identified by each index.

Then, the same analysis was carried out for a dry year, 2009–2010. In Figure 13, we observe that the rainfed cereal areas selected correspond mainly to high stress or stress classes. More than 80% of rainfed cereal pixels indicate a high stress according to SI_{SWG} and SI_{ERA5} maps. Using the SWI information, we also identify a high stress of more than 50%. However, using the NDVI, we mainly identify stress class and moderate stress, as well as the response of the UPI. Expected results are obtained mostly by the TIR indices and SWI. In fact, these indices are related directly with vegetation water requirement, especially

for the TIR that also depends on atmospheric demand. Precise information concerning vegetation and surface stress should be obtained from these indices. Due to its low spatial resolution, SWI might be less accurate for local analyses.

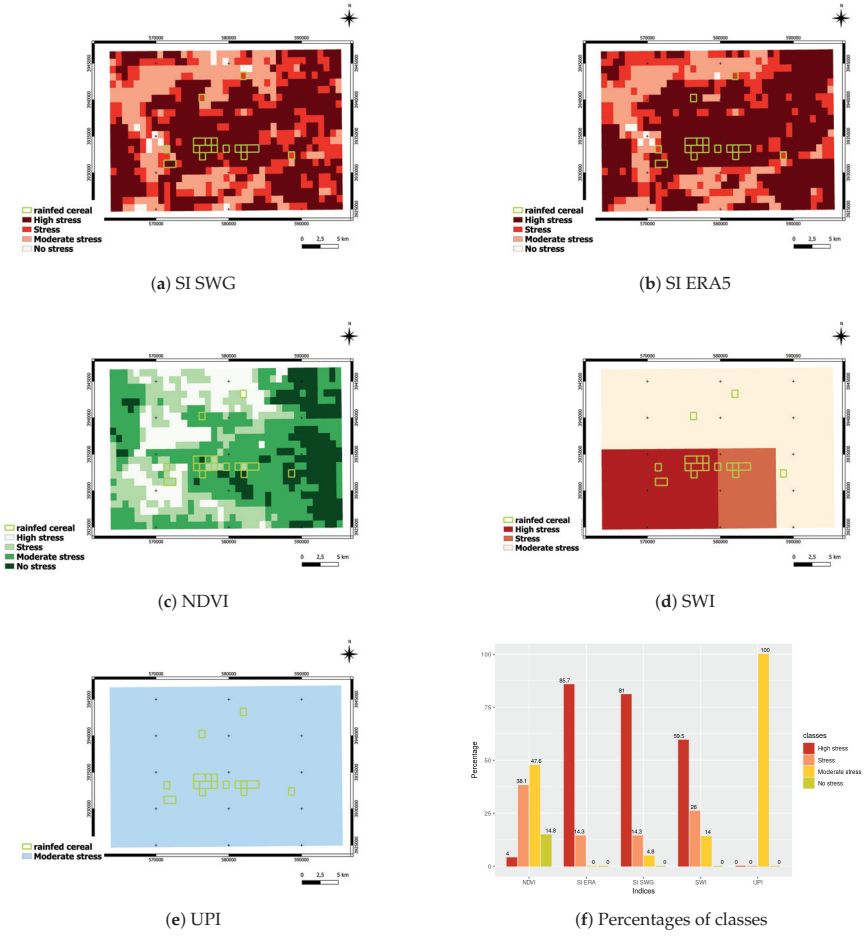

(**a**) SI SWG (**b**) SI ERA5

(**c**) NDVI (**d**) SWI

(**e**) UPI (**f**) Percentages of classes

Figure 13. Stress classes for each drought index used over the agronomic year 2009–2010, (**a**) for the standardized thermal index constrained by meteorological SWG data, (**b**) for the standardized thermal index constrained by meteorological ERA5 data, (**c**) for standardized NDVI index (**d**) for standardized SWI index, (**e**) for standardized precipitation index and (**f**) for percentage of the stress class identified by each index.

5. Discussion

We focused on growing seasons to perform our analysis (from September to May). Indeed, droughts could be damaging for crop health in these periods of the year. Analyses were carried out at different spatial scales: regional and local scale. At the regional scale, UPI is considered as the reference index to characterize the year-to-year water statement, and to assess the response of the aggregated indices used at a large scale (12 km). Overall, we find that drought indices from the different wave lengths show mostly the same variations at the annual time scale. All the indices succeed to reproduce the UPI variations. We also find that thermal stress indices provided by the SPARSE model, when constrained either from SWG or from ERA5 meteorological data, SI_{SWG} and SI_{ERA5}, respectively, are very well

correlated with UPI. However, SI_{ERA5} has a higher Kendall's τ with UPI. Indeed, SI_{ERA5} is simulated using regional climatic information (ERA5 reanalyses) and local remote sensing information. The use of the large scale meteorological data to simulate SI_{ERA5} could explain its high correlation with the UPI also provided by gridded data-sets. Moreover, we observe a very strong seasonal correlation between SI_{SWG} and SI_{ERA5}. This correlation, measured by Kendall's coefficient, was also conserved at the decadal scale (see Figure 9), due to their high spatial resolution. SWI and NDVI also present high correlation due to their aggregated response to a stress condition. Indeed, the NDVI presents a delayed response in comparison with the other indices, and shows less variability because of the time lag needed for vegetation to respond for a supply or a lack of water. On the other hand, SWI, due to the time needed for the water supply to be infiltrated to the root zone soil, also shows a delayed response to water supply in comparison to the other indices.

We assess the consistency between drought indices and UPI as a reference stress index for regional analyses. We find that there is more consistency between UPI and SI_{SWG} to identify the stress condition, especially in autumn, winter and spring. Moreover, this index presents the smallest probability to identify a stress period not confirmed by UPI. SWI shows more consistency with UPI in spring. Indeed, during this season, vegetation presents deeper root zones, which could explain the high performance of this index to identify a stress period or unstressed period according to UPI. Our analyses show also that using a moving average of UPI improves the adequation of drought indices to the hydric status. In fact, all indices need a time lag to respond to a water supply or shortage. This temporal lag depends obviously on the index used.

We can conclude, therefore, that TIR stress indices are more sensitive for a drought period. Indeed, a shortage of water supply will affect the soil (evaporation) and the vegetation (root zone), inducing stomatal closure and a surface temperature elevation detected by thermal sensors. However, SWI, which carries information on the soil moisture in the root zone, did not show immediate response as a result of a lack of precipitation. Indeed, the availability of some water storage in the profile soil after surface soil evaporation could delay the response of SWI to a water stress. For this aim, we need further analyses to identify the optimal parameter for the time infiltration (T) according to the characteristics of our study region. Besides, satellite measurements to estimate soil moisture may not be sufficiently precise because of the low spatial resolution of the SSM product used (see Section 3.1.2). However, SI_{ERA5}, which is derived from very low resolution unprocessed ERA5 reanalyses, shows a good performance in identifying water stress conditions, since it is simulated at kilometric scale with precise satellite information. Analyses at the local scale strengthen our findings. Indeed, comparison of the different drought indices with the index derived from the XLAS measurements over the scintillometer transect show that the thermal stress indices are promising tools for drought identification at low spatial resolution scale (kilometric). In this case, SI_{SWG}, which incorporates information from the local meteorological station close to the XLAS transect, shows better performances than SI_{ERA5} and allows an accurate identification of the stress condition. Moreover, the identification of drought classes in non-irrigated cereal pixels shows, therefore, an ambiguous situation corresponding to SI_{ERA5}. This could be explained by the large spatial resolution of meteorological data (31 km [64]) used to constrain the SPARSE model in order to simulate SI_{ERA5}. For this task, although the SPARSE model allows the retrieval of separate estimates of evaporation and transpiration, vegetation analyses seem to be insufficient to identify plant stress periods, owing to the sparsity of the vegetation cover and the lack of consistent information about rainfed areas.

6. Conclusions

Semi-arid areas are characterized by their high exposure to extreme climatic variability. The occurrence of hot temperatures along with a deficit of rainfall leads to droughts and impacts agricultural production. These trends in drought occurrence could be quantified by a long time series of historical indicators. We rely on RS drought indicators provided by

different wave lengths: the visible/near infrared, the thermal infrared and the microwave domains. These indicators provide information about vegetation health, water requirement and soil moisture that can help us to identify the plant hydric status. We use the SPARSE model, a dual source energy balance model [50], in order to retrieve estimates of evapotranspiration and water stress indices from the thermal infrared domain. SPARSE relies on satellite information and meteorological observation series to characterize vegetation cover and atmospheric demand. As far as we know, not many studies of drought index comparison have been proposed in the literature. Our study shows that NDVI is very informative on the year-to-year water stress conditions. However, in spite of its low resolution (kilometric), its delayed response to water stress forms a major disadvantage. Thermal indices and SWI show consistent information at an annual scale. Nevertheless, SI_{SWG} seems to be more precise for relevant water stress identification, especially at a local scale. Indeed, SWI is not sufficiently reliable to accurately identify stress intensity at finer time scales due to it is large spatial scale. On the other hand, this work highlights the performance of large scale meteorological variables (reanalyses in our case) to identify periods of droughts. We proposed an efficient alternative when local meteorological data are not available, particularly at regional analyses. Perspectives for this work include the simulation of a drought index simulated from transpiration only in order to focus on agronomic droughts. Indeed, information about vegetation water requirements rather than information provided from the "vegetation + soil" composite could be an efficient tool for drought management in semi-arid regions characterized by crop disparity. Moreover, adding mesoscale numerical weather prediction could provide efficient drought prediction. Lastly, the SWG-SPARSE tool will be tested for similar applications but in different climatic conditions (e.g., coastal areas).

Author Contributions: writing original draft preparation, N.F.; data processing, N.F. and M.L.P.; Software, N.F., M.L.P. and J.C.; data analysis, N.F. and G.B.; results interpretation N.F., G.B., Z.L.C. and J.C.; Visualisation, G.B. and M.L.P.; writing review and editing, G.B., M.L.P. and J.C.; ideas and discussions, J.C., M.L.P. and G.B.; data curation, Z.L.C., Z.K. and G.B.; funding acquisition, J.C., Z.L.C. and G.B.; Conceptualisation, N.F. and G.B.; methodology, G.B. and N.F.; supervision, G.B.; validation, G.B. All authors have read and agreed to the published version of the manuscript.

Funding: This work has been supported by the NAILA International Laboratory through a PhD grant, as well as the PHC Utique French-Tunisian bilateral "Amande" project, the H2020 RISE mobility "ACCWA" project, the WaterWorks2017 "FLUXMED", PRIMA 2018 "ALTOS" and ERANETMED "CHAAMS" ERA-NET co-fund projects.

Institutional Review Board Statement: Not applicable.

Informed Consent Statement: Not applicable.

Data Availability Statement: Data are available in Environment Information System of CESBIO site: https://sie.cesbio.omp.eu (generated on 11 October 2021).

Acknowledgments: We extend our warm thanks to all the technical teams of the IRD, GREEN-TEAM, CESBIO and INAT for their strong collaboration and support.

Conflicts of Interest: The authors declare no conflict of interest.

Appendix A. Post-Processing of Instantaneous Evapotranspiration Estimates

Evapotranspiration is simulated at the satellite overpass time and only during days with clear sky. Some post-processing must be performed to reconstruct seasonal evapotranspiration useful for hydrological studies and particularly in agricultural applications. The post-processing involves three steps: fusion, extrapolation and interpolation, that are described below.

Appendix A.1. Extrapolation

ET derived from TIR RS data rely on once-a-day acquisitions. An extrapolation algorithm is used to reconstruct its sub-daily variations using a method based on the evaporative fraction (EF), well described in [70]. EF at the satellite overpass t is defined as the ratio between the latent heat flux (LE) and the available energy (AE), which is derived from the net radiation (Rn) and soil heat flux (G), as defined in the following equation:

$$EF_{obs} = \frac{LE}{AE_t} = \frac{LE}{Rn - G} \tag{A1}$$

According to [71], EF is relatively stable during the daylight hours on clear days. This hypothesis allows the reconstruction of the diurnal behavior (hourly or half-hourly time scale), see Equation (A2), based on the empirical equation of EF defined by [72] (denoted EF_{sim}), see Equation (A3), and observed EF at satellite overpass (Equation (A1)).

$$EF_{(30\ \mathrm{min})} = EFsim_{(30\ \mathrm{min})} * \frac{EF_{obs}}{EF_{sim}} \tag{A2}$$

where,

$$EF_{sim} = [1.2 - (0.4 * \frac{GR_t}{1000} + 0.5 * \frac{RH_t}{100})] \tag{A3}$$

GR and RH are, respectively, the global radiation and relative humidity for a time scale t (semi-hourly or satellite overpass).

Finally, daily evaporation (E_d) can be simply obtained using the Equation (A4):

$$E_d = EF * AE_d, \tag{A4}$$

where AE_d is computed from an equation suggested by [73]: where AE is assumed to present the same diurnal variation as the global radiation, see (A5).

$$AE_d = Rg_d * \frac{AE_t}{Rg_t}, \tag{A5}$$

Appendix A.2. TERRA ET and AQUA ET Merge

ET simulations are derived from TERRA and AQUA satellites. We choose to combine these two sources of data in order to increase the overall temporal availability. Results presented by [60] show that ET derived from these different sensors is potentially biased because of their different overpass time (10:30 a.m. and 13:30 a.m. for Terra and Aqua, respectively) and that TERRA simulations are more correlated with ET derived from measured sensible heat flux (H) from an extra large aperture scintillometer (XLAS). Therefore, in order to take into consideration systematic differences in distributional properties, we perform a bias correction approach for the AQUA simulations (available since 2002) before merging. We considered CDF-t [74], a univariate bias correction method which allows non-linear corrections to reproduce the statistical distributions of the reference time series. Our aim is to keep ET simulations derived from TERRA RS (available since 2000) and to add bias corrected ET derived from AQUA only in days with no TERRA acquisition.

Appendix A.3. Interpolation

to derive seasonal evapotranspiration, we have to fill the gaps between satellite acquisitions in order to reconstruct days with missing ET data. Methods that rely on self preservation or known diurnal shape of the ratio of evapotranspiration to a scale factor are usually used for this aim [70]. Indeed, this scale factor will monitor interpolation between two acquisition dates of successive images. In this work, we used the global radiation as an interpolation reference quantity. Delogu et al. [41] have shown that it is the most robust and best performing scale factor for seasonal timescales.

Appendix B. Daily ET Simulations

Figure A1 shows time series of the ET estimates derived from merging ET Terra and ET Aqua over the agronomic year 2013–2014 (from September to August), for which the residual ET derived from scintillometer (XLAS) measurements are available. We present ET simulations separately when the SPARSE model is constrained by the SWG meteorological data (see Figure A1a) and when the SPARSE model is constrained by the ERA5 reanalyses meteorological data (see Figure A1b). Overall, we observe in both figures that ET constrained from Aqua RS data (ET Aqua) is always biased in comparison with ET constrained from Terra RS data (ET Terra), and that ET Terra present higher values. In Figure A1a, we observe that, in almost all cases, ET derived from XLAS measurements shows similar variation to ET Terra, excepted for summer periods. In addition, ET provided by the merging of Terra and Aqua reproduces more closely ET XLAS and succeeds in removing biases observed originally between ET Terra and Aqua. Using unprocessed ERA5 reanalyses (Figure A1b), ET from merging succeeds as well to reduce biases observed initially between ET Terra and Aqua. However, the three ET series simulated from ERA5 meteorological data are not as close to the ET XLAS variations as the ET series simulated from the SWG meteorological data. Indeed, ERA5 series are always biased in comparison with observations data.

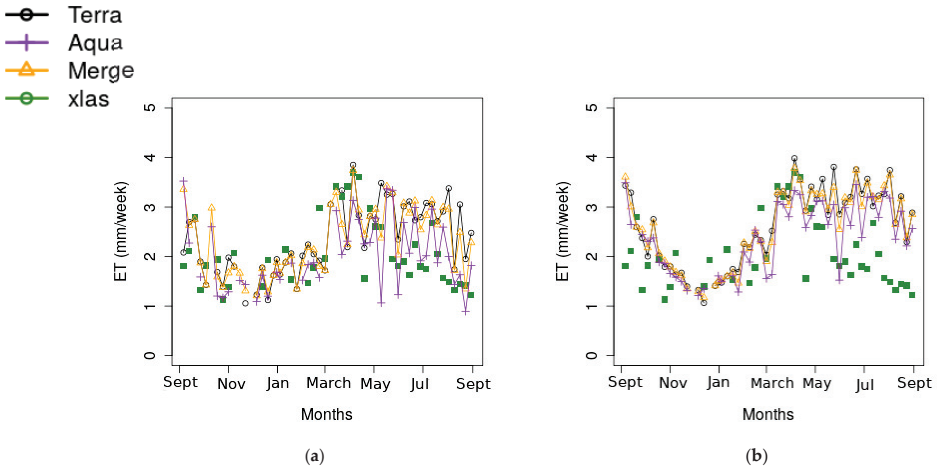

Figure A1. Weekly times series of evapotranspiration simulated initially from TERRA and AQUA satellite data superposed with a time series computed from the merging (Merge) of TERRA and bias corrected AQUA series and ET from XLAS measurements for the agronomic year 2013–2014. (**a**) [ET constrained by SWG meteorological surrogate series. (**b**) ET constrained by ERA5 meteorological surrogate series.

References

1. Wilhite, D.A.; Svoboda, M.D. Drought early warning systems in the context of drought preparedness and mitigation. In *Early Warning Systems for Drought Preparedness and Drought Management*; World Meteorological Organization: Geneva, Switzerland, 2000; pp. 1–21.
2. Schilling, J.; Hertig, E.; Tramblay, Y.; Scheffran, J. Climate change vulnerability, water resources and social implications in North Africa. *Reg. Environ. Chang.* **2020**, *20*, 1–12. [CrossRef]
3. MassonDelmotte, V.; Zhai, P.; Pirani, A.; Connors, S.L.; Péan, C.; Berger, S.; Caud, N.; Chen, Y.; Goldfarb, L.; Gomis, M.I.; et al. (Eds.) Summary for Policymakers. In *Climate Change 2021: The Physical Science Basis. Contribution of Working Group I to the Sixth Assessment Report of the Intergovernmental Panel on Climate Change*; Cambridge University Press: Cambridge, UK, 2021.
4. Anderson, M.C.; Hain, C.; Wardlow, B.; Pimstein, A.; Mecikalski, J.R.; Kustas, W.P. Evaluation of drought indices based on thermal remote sensing of evapotranspiration over the continental United States. *J. Clim.* **2011**, *24*, 2025–2044. [CrossRef]
5. Otkin, J.A.; Anderson, M.C.; Hain, C.; Mladenova, I.E.; Basara, J.B.; Svoboda, M. Examining rapid onset drought development using the thermal infrared–based evaporative stress index. *J. Hydrometeorol.* **2013**, *14*, 1057–1074. [CrossRef]

6. Mishra, A.K.; Singh, V.P. A review of drought concepts. *J. Hydrol.* **2010**, *391*, 202–216. [CrossRef]
7. McKee, T.B.; Doesken, N.J.; Kleist, J. The relationship of drought frequency and duration to time scales. In Proceedings of the 8th Conference on Applied Climatology, Boston, MA, USA, 17-22 January 1993; Volume 17, pp. 179–183.
8. Mishra, A.; Desai, V. Drought forecasting using stochastic models. *Stoch. Environ. Res. Risk Assess.* **2005**, *19*, 326–339. [CrossRef]
9. Mishra, A.; Singh, V.P. Analysis of drought severity-area-frequency curves using a general circulation model and scenario uncertainty. *J. Geophys. Res. Atmos.* **2009**, *114*, *D06120*. [CrossRef]
10. Zhang, J.; Xu, Y.; Yao, F.; Wang, P.; Guo, W.; Li, L.; Yang, L. Advances in estimation methods of vegetation water content based on optical remote sensing techniques. *Sci. China Technol. Sci.* **2010**, *53*, 1159–1167. [CrossRef]
11. AghaKouchak, A. Advancements in Satellite Remote Sensing for Drought Monitoring. In *Drought and Water Crises*; CRC Press: Boca Raton, FL, USA, 2017; pp. 225–258.
12. Dorigo, W.; Wagner, W.; Albergel, C.; Albrecht, F.; Balsamo, G.; Brocca, L.; Chung, D.; Ertl, M.; Forkel, M.; Gruber, A.; et al. ESA CCI Soil Moisture for improved Earth system understanding: State-of-the art and future directions. *Remote Sens. Environ.* **2017**, *203*, 185–215. [CrossRef]
13. Wigneron, J.P.; Chanzy, A.; Calvet, J.C.; Bruguier, N. A simple algorithm to retrieve soil moisture and vegetation biomass using passive microwave measurements over crop fields. *Remote Sens. Environ.* **1995**, *51*, 331–341. [CrossRef]
14. Zribi, M.; Nativel, S.; Le Page, M. Analysis of Agronomic Drought in a Highly Anthropogenic Context Based on Satellite Monitoring of Vegetation and Soil Moisture. *Remote Sens.* **2021**, *13*, 2698. [CrossRef]
15. Amri, R.; Zribi, M.; Lili-Chabaane, Z.; Wagner, W.; Hasenauer, S. Analysis of C-band scatterometer moisture estimations derived over a semiarid region. *IEEE Trans. Geosci. Remote Sens.* **2012**, *50*, 2630–2638. [CrossRef]
16. Zhang, D.; Tang, R.; Zhao, W.; Tang, B.; Wu, H.; Shao, K.; Li, Z.L. Surface soil water content estimation from thermal remote sensing based on the temporal variation of land surface temperature. *Remote Sens.* **2014**, *6*, 3170–3187. [CrossRef]
17. Jiao, W.; Wang, L.; McCabe, M.F. Multi-sensor remote sensing for drought characterization: Current status, opportunities and a roadmap for the future. *Remote Sens. Environ.* **2021**, *256*, 112313. [CrossRef]
18. Tucker, C.J. Red and photographic infrared linear combinations for monitoring vegetation. *Remote Sens. Environ.* **1979**, *8*, 127–150. [CrossRef]
19. Kogan, F.N. Application of vegetation index and brightness temperature for drought detection. *Adv. Space Res.* **1995**, *15*, 91–100. [CrossRef]
20. Quiring, S.M.; Ganesh, S. Evaluating the utility of the Vegetation Condition Index (VCI) for monitoring meteorological drought in Texas. *Agric. For. Meteorol.* **2010**, *150*, 330–339. [CrossRef]
21. Kogan, F.N. Operational space technology for global vegetation assessment. *Bull. Am. Meteorol. Soc.* **2001**, *82*, 1949–1964. [CrossRef]
22. Amri, R.; Zribi, M.; Lili-Chabaane, Z.; Duchemin, B.; Gruhier, C.; Chehbouni, A. Analysis of vegetation behavior in a North African semi-arid region, using SPOT-VEGETATION NDVI data. *Remote Sens.* **2011**, *3*, 2568–2590. [CrossRef]
23. Farrar, T.; Nicholson, S.; Lare, A. The influence of soil type on the relationships between NDVI, rainfall, and soil moisture in semiarid Botswana. II. NDVI response to soil oisture. *Remote Sens. Environ.* **1994**, *50*, 121–133. [CrossRef]
24. Ozelkan, E.; Chen, G.; Ustundag, B.B. Multiscale object-based drought monitoring and comparison in rainfed and irrigated agriculture from Landsat 8 OLI imagery. *Int. J. Appl. Earth Obs. Geoinf.* **2016**, *44*, 159–170. [CrossRef]
25. AghaKouchak, A.; Farahmand, A.; Melton, F.; Teixeira, J.; Anderson, M.; Wardlow, B.D.; Hain, C. Remote sensing of drought: Progress, challenges and opportunities. *Rev. Geophys.* **2015**, *53*, 452–480. [CrossRef]
26. Paulik, C.; Dorigo, W.; Wagner, W.; Kidd, R. Validation of the ASCAT Soil Water Index using in situ data from the International Soil Moisture Network. *Int. J. Appl. Earth Obs. Geoinf.* **2014**, *30*, 1–8. [CrossRef]
27. Paulik, C.; Naeimi, V.; Dorigo, W.; Wagner, W.; Kidd, R. A global validation of the ASCAT Soil Water Index (SWI) with in situ data from the International Soil Moisture Network. In Proceedings of the EGU General Assembly Conference Abstracts, Vienna, Austria, 22–27 April 2012; p. 10189.
28. Baghdadi, N.; Cresson, R.; El Hajj, M.; Ludwig, R.; La Jeunesse, I. Soil parameters estimation over bare agriculture areas from C-band polarimetric SAR data using neural networks. *Hydrol. Earth Syst. Sci. Discuss.* **2012**, *9*, *2897–2933*. [CrossRef]
29. Babaeian, E.; Sadeghi, M.; Jones, S.B.; Montzka, C.; Vereecken, H.; Tuller, M. Ground, proximal, and satellite remote sensing of soil moisture. *Rev. Geophys.* **2019**, *57*, 530–616. [CrossRef]
30. Narasimhan, B.; Srinivasan, R. Development and evaluation of Soil Moisture Deficit Index (SMDI) and Evapotranspiration Deficit Index (ETDI) for agricultural drought monitoring. *Agric. For. Meteorol.* **2005**, *133*, 69–88. [CrossRef]
31. Zhang, N.; Hong, Y.; Qin, Q.; Liu, L. VSDI: A visible and shortwave infrared drought index for monitoring soil and vegetation moisture based on optical remote sensing. *Int. J. Remote Sens.* **2013**, *34*, 4585–4609. [CrossRef]
32. Jackson, R.D.; Idso, S.; Reginato, R.; Pinter, P., Jr. Canopy temperature as a crop water stress indicator. *Water Resour. Res.* **1981**, *17*, 1133–1138. [CrossRef]
33. Wang, X.; Zhao, C.; Guo, N.; Li, Y.; Jian, S.; Yu, K. Determining the canopy water stress for spring wheat using canopy hyperspectral reflectance data in loess plateau semiarid regions. *Spectrosc. Lett.* **2015**, *48*, 492–498. [CrossRef]
34. Jones, H.G.; Serraj, R.; Loveys, B.R.; Xiong, L.; Wheaton, A.; Price, A.H. Thermal infrared imaging of crop canopies for the remote diagnosis and quantification of plant responses to water stress in the field. *Funct. Plant Biol.* **2009**, *36*, 978–989. [CrossRef]

35. Anderson, M.C.; Zolin, C.A.; Sentelhas, P.C.; Hain, C.R.; Semmens, K.; Yilmaz, M.T.; Gao, F.; Otkin, J.A.; Tetrault, R. The Evaporative Stress Index as an indicator of agricultural drought in Brazil: An assessment based on crop yield impacts. *Remote Sens. Environ.* **2016**, *174*, 82–99. [CrossRef]
36. Norman, J.M.; Kustas, W.P.; Humes, K.S. Source approach for estimating soil and vegetation energy fluxes in observations of directional radiometric surface temperature. *Agric. For. Meteorol.* **1995**, *77*, 263–293. [CrossRef]
37. Lili, Z.; Duchesne, J.; Nicolas, H.; Rivoal, R.; de BREGER, P. Détection infrarouge thermique des maladies du blé d'hiver 1. *Eppo Bull.* **1991**, *21*, 659–672. [CrossRef]
38. Sheffield, J.; Wood, E.F. *Drought: Past Problems and Future Scenarios*; Routledge: London, UK, 2012.
39. Lagouarde, J.P.; Boulet, G. Energy balance of continental surfaces and the use of surface temperature. In *Land Surface Remote Sensing in Continental Hydrology*; Elsevier: Amsterdam, The Netherlands, 2016; pp. 323–361.
40. Boulet, G.; Chehbouni, A.; Gentine, P.; Duchemin, B.; Ezzahar, J.; Hadria, R. Monitoring water stress using time series of observed to unstressed surface temperature difference. *Agric. For. Meteorol.* **2007**, *146*, 159–172. [CrossRef]
41. Delogu, E.; Olioso, A.; Alliès, A.; Demarty, J.; Boulet, G. Evaluation of Multiple Methods for the Production of Continuous Evapotranspiration Estimates from TIR Remote Sensing. *Remote Sens.* **2021**, *13*, 1086. [CrossRef]
42. Diarra, A.; Jarlan, L.; Er-Raki, S.; Le Page, M.; Aouade, G.; Tavernier, A.; Boulet, G.; Ezzahar, J.; Merlin, O.; Khabba, S. Performance of the two-source energy budget (TSEB) model for the monitoring of evapotranspiration over irrigated annual crops in North Africa. *Agric. Water Manag.* **2017**, *193*, 71–88. [CrossRef]
43. Moran, M.S. Thermal infrared measurement as an indicator of plant ecosystem health. In *Thermal Remote Sensing in Land Surface Processes*; CRC Press: Boca Raton, FL, USA, 2004; pp. 256–282.
44. Moran, M.; Clarke, T.; Inoue, Y.; Vidal, A. Estimating crop water deficit using the relation between surface-air temperature and spectral vegetation index. *Remote Sens. Environ.* **1994**, *49*, 246–263. [CrossRef]
45. Cunha, A.P.; Zeri, M.; Deusdará Leal, K.; Costa, L.; Cuartas, L.A.; Marengo, J.A.; Tomasella, J.; Vieira, R.M.; Barbosa, A.A.; Cunningham, C.; et al. Extreme drought events over Brazil from 2011 to 2019. *Atmosphere* **2019**, *10*, 642. [CrossRef]
46. Cunha, A.; Alvalá, R.C.; Nobre, C.A.; Carvalho, M.A. Monitoring vegetative drought dynamics in the Brazilian semiarid region. *Agric. For. Meteorol.* **2015**, *214*, 494–505. [CrossRef]
47. Abbas, S.; Nichol, J.E.; Qamer, F.M.; Xu, J. Characterization of drought development through remote sensing: A case study in Central Yunnan, China. *Remote Sens.* **2014**, *6*, 4998–5018. [CrossRef]
48. Chirouze, J.; Boulet, G.; Jarlan, L.; Fieuzal, R.; Rodriguez, J.; Ezzahar, J.; Raki, S.E.; Bigeard, G.; Merlin, O.; Garatuza-Payan, J.; et al. Intercomparison of four remote-sensing-based energy balance methods to retrieve surface evapotranspiration and water stress of irrigated fields in semi-arid climate. *Hydrol. Earth Syst. Sci. Discuss.* **2014**, *18*, 1165–1188. [CrossRef]
49. Farhani, N.; Carreau, J.; Boulet, G.; Kassouk, Z.; Mougenot, B.; Le Page, M.; Lili Chabaane, Z.; Zitouna, R. Scenarios of hydrometeorological variables based on auxiliary data for water stress retrieval in central Tunisia. In Proceedings of the 2020 Mediterranean and Middle-East Geoscience and Remote Sensing Symposium (M2GARSS), Tunis, Tunisia, 9–11 March 2020; pp. 293–296.
50. Boulet, G.; Mougenot, B.; Lhomme, J.; Fanise, P.; Lili-Chabaane, Z.; Olioso, A.; Bahir, M.; Rivalland, V.; Jarlan, L.; Merlin, O.; et al. The SPARSE model for the prediction of water stress and evapotranspiration components from thermal infra-red data and its evaluation over irrigated and rainfed wheat. *Hydrol. Earth Syst. Sci. Discuss.* **2015**, *19*, 4653–4672. [CrossRef]
51. Alazard, M.; Leduc, C.; Travi, Y.; Boulet, G.; Salem, A.B. Estimating evaporation in semi-arid areas facing data scarcity: Example of the El Haouareb dam (Merguellil catchment, Central Tunisia). *J. Hydrol. Reg. Stud.* **2015**, *3*, 265–284. [CrossRef]
52. Massuel, S.; Riaux, J. Groundwater overexploitation: Why is the red flag waved? Case study on the Kairouan plain aquifer (central Tunisia). *Hydrogeol. J.* **2017**, *25*, 1607–1620. [CrossRef]
53. Leduc, C.; Ammar, S.B.; Favreau, G.; Beji, R.; Virrion, R.; Lacombe, G.; Tarhouni, J.; Aouadi, C.; Chelli, B.; Jebnoun, N.; et al. Impacts of hydrological changes in the Mediterranean zone: Environmental modifications and rural development in the Merguellil catchment, central Tunisia / Un exemple d'évolution hydrologique en Méditerranée: Impacts des modifications environnementales et du développement agricole dans le bassin-versant du Merguellil (Tunisie centrale). *Hydrol. Sci. J./J. Des Sci. Hydrol.* **2007**, *52*, 1162–1178.
54. Molle, F.; Wester, P. *River Basin Trajectories: Societies, Environments and Development*; IWMI: Oxford, UK, 2009; Volume 8.
55. Ceballos, A.; Scipal, K.; Wagner, W.; Martínez-Fernández, J. Validation of ERS scatterometer-derived soil moisture data in the central part of the Duero Basin, Spain. *Hydrol. Process. Int. J.* **2005**, *19*, 1549–1566. [CrossRef]
56. Kanzari, S.; Hachicha, M.; Bouhlila, R.; Battle-Sales, J. Characterization and modeling of water movement and salts transfer in a semi-arid region of Tunisia (Bou Hajla, Kairouan)–Salinization risk of soils and aquifers. *Comput. Electron. Agric.* **2012**, *86*, 34–42. [CrossRef]
57. Brocca, L.; Ciabatta, L.; Moramarco, T.; Ponziani, F.; Berni, N.; Wagner, W. Use of satellite soil moisture products for the operational mitigation of landslides risk in central Italy. In *Satellite Soil Moisture Retrieval*; Elsevier: Amsterdam, The Netherlands, 2016; pp. 231–247.
58. C. Paulik. *Copernicus Global Land Operations "Vegetation and Energy"*; TU Wien: Vienna, Austria, 2017.
59. Clevers, J. Application of a weighted infrared-red vegetation index for estimating leaf area index by correcting for soil moisture. *Remote Sens. Environ.* **1989**, *29*, 25–37. [CrossRef]

60. Saadi, S.; Boulet, G.; Bahir, M.; Brut, A.; Delogu, E.; Fanise, P.; Mougenot, B.; Simonneaux, V.; Lili Chabaane, Z. Assessment of actual evapotranspiration over a semi arid heterogeneous land surface by means of coupled low-resolution remote sensing data with an energy balance model: Comparison to extra-large aperture scintillometer measurements. *Hydrol. Earth Syst. Sci.* **2018**, *22*, 2187–2209. [CrossRef]
61. Funk, C.; Peterson, P.; Landsfeld, M.; Pedreros, D.; Verdin, J.; Shukla, S.; Husak, G.; Rowland, J.; Harrison, L.; Hoell, A.; et al. The climate hazards infrared precipitation with stations—a new environmental record for monitoring extremes. *Sci. Data* **2015**, *2*, 1–21. [CrossRef]
62. Bouaziz, M.; Medhioub, E.; Csaplovisc, E. A machine learning model for drought tracking and forecasting using remote precipitation data and a standardized precipitation index from arid regions. *J. Arid. Environ.* **2021**, *189*, 104478. [CrossRef]
63. Massman, W. A surface energy balance method for partitioning evapotranspiration data into plant and soil components for a surface with partial canopy cover. *Water Resour. Res.* **1992**, *28*, 1723–1732. [CrossRef]
64. Hersbach, H.; Bell, B.; Berrisford, P.; Hirahara, S.; Horányi, A.; Muñoz-Sabater, J.; Nicolas, J.; Peubey, C.; Radu, R.; Schepers, D.; et al. The ERA5 global reanalysis. *Q. J. R. Meteorol. Soc.* **2020**, *146*, 1999–2049. [CrossRef]
65. Allen, R.G.; Pereira, L.S.; Raes, D.; Smith, M. Crop evapotranspiration-Guidelines for computing crop water requirements-FAO Irrigation and drainage paper 56. *Fao Rome* **1998**, *300*, D05109.
66. Mega, N.; Medjerab, A. Statistical comparison between the standardized precipitation index and the standardized precipitation drought index. *Model. Earth Syst. Environ.* **2021**, *7*, 373–388. [CrossRef]
67. Hoffman, R.N.; Boukabara, S.A.; Kumar, V.K.; Garrett, K.; Casey, S.P.; Atlas, R. An empirical cumulative density function approach to defining summary NWP forecast assessment metrics. *Mon. Weather. Rev.* **2017**, *145*, 1427–1435. [CrossRef]
68. Chahbi Bellakanji, A.; Zribi, M.; Lili-Chabaane, Z.; Mougenot, B. Forecasting of cereal yields in a semi-arid area using the simple algorithm for yield estimation (SAFY) agro-meteorological model combined with optical SPOT/HRV images. *Sensors* **2018**, *18*, 2138. [CrossRef]
69. Joe, H. *Multivariate Models and Multivariate Dependence Concepts*; CRC Press: Boca Raton, FL, USA, 1997.
70. Delogu, E.; Boulet, G.; Olioso, A.; Coudert, B.; Chirouze, J.; Ceschia, E.; Le Dantec, V.; Marloie, O.; Chehbouni, G.; Lagouarde, J.P. Reconstruction of temporal variations of evapotranspiration using instantaneous estimates at the time of satellite overpass. *Hydrol. Earth Syst. Sci.* **2012**, *16*, 2995–3010. [CrossRef]
71. Lhomme, J.P.; Elguero, E. Examination of evaporative fraction diurnal behaviour using a soil-vegetation model coupled with a mixed-layer model. *Hydrol. Earth Syst. Sci.* **1999**, *3*, 259–270. [CrossRef]
72. Hoedjes, J.; Chehbouni, A.; Jacob, F.; Ezzahar, J.; Boulet, G. Deriving daily evapotranspiration from remotely sensed instantaneous evaporative fraction over olive orchard in semi-arid Morocco. *J. Hydrol.* **2008**, *354*, 53–64. [CrossRef]
73. Jackson, R.D.; Hatfield, J.L.; Reginato, R.; Idso, S.; Pinter, P., Jr. Estimation of daily evapotranspiration from one time-of-day measurements. *Agric. Water Manag.* **1983**, *7*, 351–362. [CrossRef]
74. Michelangeli, P.A.; Vrac, M.; Loukos, H. Probabilistic downscaling approaches: Application to wind cumulative distribution functions. *Geophys. Res. Lett.* **2009**, *36*, *L11708*,. [CrossRef]

water

MDPI

Article

Runoff Reduction Effects at Installation of LID Facilities under Different Climate Change Scenarios

Seungwook Lee [1], Daye Kim [2,*], Seungjin Maeng [2], Muhammad Azam [3] and Bongguk Lee [4]

[1] Chungbuk Research Institute, Cheongju 28517, Korea; swlee@cri.re.kr
[2] Department of Agricultural Rural Engineering, Chungbuk National University, Cheongju 28644, Korea; maeng@chungbuk.ac.kr
[3] Faculty of Agricultural Engineering and Technology, PMAS Arid Agriculture University, Rawalpindi 44000, Pakistan; mazammakram@gmail.com
[4] Water Resources Management Research & Planning Department, Korea Water Resources Corporation, Daejeon 34350, Korea; lbk0206@kwater.or.kr
* Correspondence: kdy8462@naver.com; Tel.: +82-01-5800-1079

Abstract: In order to prepare for floods and droughts that occur as a result of climate change, various studies in water-related fields are being carried out in various countries around the world. Among them, special attention is being paid to the low-impact development (LID) technique. This study measured the annual maximum daily rainfall data from 2019 to 2100 by climate change scenario, which is the annual maximum daily rainfall series observed for rainfall stations, and tested the hydrological data using statistical analysis. After determining whether the data could be analyzed, the probability distribution was selected, and the parameters of the selected probability distribution were calculated using the L-moment method for each rainfall station. The probabilities of rainfall data were derived using GEV distribution, and the United States Environmental Protection Agency Storm Water Management Model (SWMM), a runoff simulation program, was used to compare and analyze the runoff reduction rate before and after the installation of a permeable pavement as an LID facility. The results of the analysis showed that representative concentration pathway (RCP) 4.5 and RCP 8.5 had the effect of reducing the runoff for more than 100 years at a 30% reduction rate compared with before installation.

Keywords: low-impact development (LID); climate change scenarios; SWMM

Citation: Lee, S.; Kim, D.; Maeng, S.; Azam, M.; Lee, B. Runoff Reduction Effects at Installation of LID Facilities under Different Climate Change Scenarios. *Water* **2022**, *14*, 1301. https://doi.org/10.3390/w14081301

Academic Editors: Luis Garrote and Alban Kuriqi

Received: 12 March 2022
Accepted: 14 April 2022
Published: 16 April 2022

1. Introduction

The frequency of typhoons and heavy rains has increased rapidly in Korea due to global warming and abnormal weather conditions, and the scale of flood damage has increased due to climate change and urbanization, resulting in substantial property damage in urban areas. Unlike the flooding of agricultural land, urban flooding amplifies not only economic and human loss, but also the psychological damage and social anxiety of urban residents because, when flooding occurs, many people and a large amount of urban infrastructure are concentrated in a dense space. In Korea, the average temperature recorded in 2016 was the highest since 1973, and there are many signs of a changing climate compared with the past, such as heat waves as well as unexpectedly heavy rains in July and August.

According to the Intergovernmental Panel on Climate Change (IPCC) report [1], the average global temperature will rise by 1 °C in the 2020s, and up to 1.7 billion people worldwide will suffer from water shortages. In the long term, over 30% of coastal areas will be lost due to rising sea level in the 2080s. It has been reported that more than 20% of the world's population will be at risk from flooding [2].

In preparation for many water-related disasters, such as floods and droughts due to climate change, various studies in water-related fields are being conducted in countries

around the world. Among them, much attention is being paid to the low-impact development (LID) technique. LID is a technique that aims to establish water circulation systems similar to those prior to development by installing permeable elements in impervious areas to reduce runoff and improve water quality. Developed countries are responding to the problems caused by climate change and urbanization by applying it to urban areas. LID facilities include bio-retention cells, rain gardens, green roofs, infiltration trenches, permeable pavements, rain barrels, and vegetative swales. Therefore, a permeable pavement is one of the facilities selected to reduce the depletion of groundwater and the impacts of urban flooding.

In this study, by analyzing the changes in the observed rainfall and the probability of rainfall by applying climate change scenarios, by setting the design rainfall for each return period using the probability of rainfall for each scenario, and by simulating the amount of runoff before and after the installation of an LID facility in the object region, we could use the frequency, according to the scenario, to compare and analyze the emission reduction rate. In addition, by comparing the amount of runoff in the return period for each climate change scenario, we sought to show that installing LID facilities has the effect of reducing runoff. Therefore, it is judged that the results analyzed through this study can aid in setting an appropriate design direction when considering an LID facility.

2. Theoretical Analysis

For the case of the current facility design return period, rainfall analysis and return period analysis using rainfall observation data was conducted. However, urban runoff has continued to increase over a short period of time due to the increase in impervious areas, and the return period of damage, accompanied by an irregular climate and locally heavy rainfall, has continued to occur. Therefore, in order to supplement the existing design return period and to design a stable structure, it was necessary to predict the future climate using observational data and utilize the data composed of scenarios, rather than analyze past data only. Therefore, it is suggested that the application of the LID facility in the climate change scenario used in this study be used as the basic premise for disaster prevention standard guidelines, and in measures to respond to climate change in urban areas in the future.

2.1. Climate Change Scenario

For the climate change scenario used in this study, the greenhouse gas concentration is determined as the amount of radiation exerted by human activities on the atmosphere as per the IPCC 5th evaluation report, and the representative concentration pathway (RCP) scenario contains one fixed representative radiative forcing value, with the expression "representative" used in the sense that there can be many socio-economic scenarios. Unlike the existing Special Report on Emission Scenarios (SRES), the RCP scenario reflects the recent trend of changes in greenhouse gas concentrations and has been updated to fit the recent prediction model. The four representative greenhouse gas concentrations in the RCPs are 2.6, 4.5, 6.0, and 8.5. In the process of calculating the greenhouse gas concentrations, the social and economic assumptions were changed from the basis of a future society structure to whether or not to implement climate change response policies.

The Korea Meteorological Administration (KMA) simulated the future climate change scenario by introducing the RCP scenario as forced input data to the Hadley Center Global Environmental Model version 2—Atmosphere and Ocean (HadGEM2-AO) model, a global climate change prediction model, and used the simulated global climate change scenario as input data to the HadGEM3-RA model, a regional climate model. Through epidemiological detailing, regional climate model (RCM) data, a regional climate change scenario that well reflects the effects of complex topography that cannot be expressed by the global model, were calculated. In this study, RCP 4.5 and RCP 8.5 scenarios were selected and analyzed among the four climate change scenarios.

2.2. Return Period Analysis

There are many different probability distribution types for return period analysis according to climate change scenarios, such as Gumbel (GUM), generalized extreme value (GEV), generalized logistic (GLO), generalized Pareto (GPA), generalized normal (GNO), and Pearson type 3 (PT3). The relationship between the probability weighted moment [3] and the L-moment is described by Hosking [4,5], Maeng et al. [6], Maidment [7], and the World Meteorological Organization [8]. Furthermore, Hosking [4] published that the L-moment, which is the linear combination of the statistical characteristics of the probability weight moment (PWM) based probability distribution, enables efficient and safe parameters in smaller samples more than other moment methods and method of maximum likelihood. In addition, the parameter estimation method by L-moment for each probability distribution has been studied and described by Hosking et al. [4,9] and Maidment [7].

2.3. EPA-SWMM for Application of LID Facility

In this study, the Storm Water Management Model (SWMM) was selected and analyzed from among the models for estimating the amount of flooding caused by rainfall in urban watersheds. In 1971, with the support of the United States Environmental Protection Agency (US EPA), the Metcalf & Eddy Corporation, and the University of Florida and Water Resource Engineering (WRE), the model was developed to simulate the flow rate and water quality of the urban watershed sewage system [10]. In addition, in the 1981 SWMM model, the extended transport (EXTRAN) block, designed to calculate the overflow, drainage, and pressure flow of hand structures, was added to the SWMM model to expand and supplement the transport block. Currently, the EPA-SWMM has been developed up to version 5.1.007 (with LID control).

The LID runoff model using the SWMM was mentioned by Lee [11], and the applied model of the study site was selected and analyzed as a permeable pavement.

3. Study Area and Research Method

3.1. Selection of Study Area and Overview

The watershed of the study area was the Eco-Delta City (EDC) located in Busan city in Korea. The location of the study area is shown in Figure 1. The total area was 105.9 ha (1.059 km^2). The West Nakdong River on the west flows from north to south, and the Pyeonggangcheon Stream on the east flows into the West Nakdong River through the Suna sluice gate. The study area was the estuary of the West Nakdong River, which consists of flat land with an elevation of 50 m or less (mostly 0.4 to 4.0 m), and the difference in height between the river and the land is less than 1.0 m, being mostly lowlands. In addition, agricultural water is supplied to the existing irrigation channel in study area through the lower culvert of the Namhae Expressway, but it will be closed due to development of the study area, and there is no external inflow.

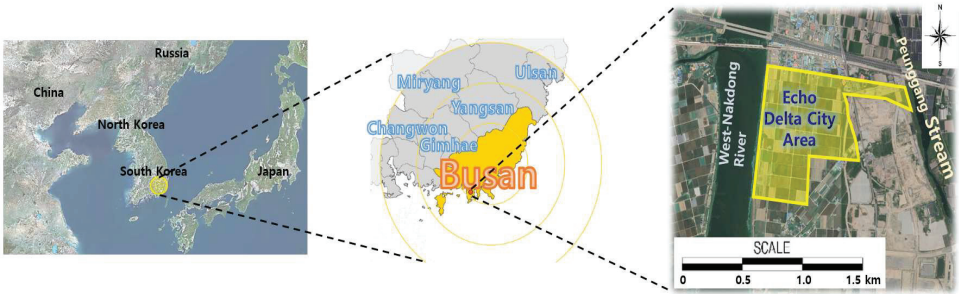

Figure 1. Study area.

Therefore, the study area was selected with regard to the topographical condition of the area and the design stage before the installation of the LID facility, as well as the fact that the permeable pavement will have a large reduction effect on the flat land.

3.2. Collection of Hydrological Data

The rainfall station was selected according to the distance from the study area. Therefore, the Gimhae rainfall station was selected, as it is located close to Gimhae-si, with the data exceeding 30 years. The annual maximum daily rainfall data from the Gimhae rainfall station were used in this study [12]. The location of the Gimhae rainfall station is shown in Figure 2.

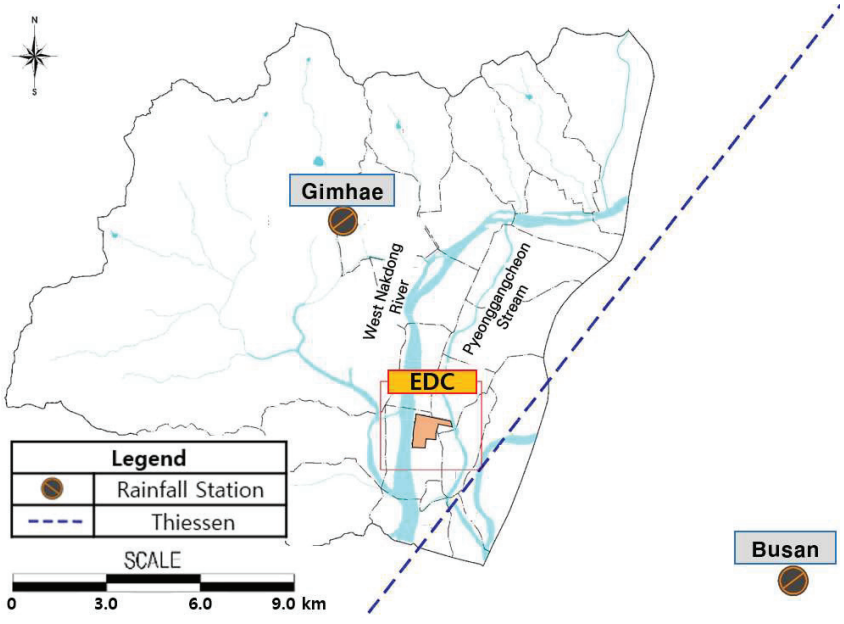

Figure 2. Selection of rainfall station.

In addition, the Korean Peninsula climate change scenario was analyzed using the global climate change scenario data of the HadGEM2-AO model, and was developed in Korea using the HadGEM3-RA model (Hadley Center Global Environment Model version 3 atmosphere regional climate model) at a resolution of 12.5 km.

Production process for climate change scenarios is shown in Figure 3.

In this study, the RCP 4.5 scenario was simulated for the peninsula for 200 years with 12.5 km resolution, and the integral control was based on the RCP 8.5 scenario. The extraction of annual maximum daily rainfall data was based on the past observed time series of daily rainfall (1988–2018) and the climate change scenarios from 2019 to 2100.

The annual maximum daily rainfall for the next 100 years suitable for the EDC, the research study area, was analyzed and used as shown in Table 1.

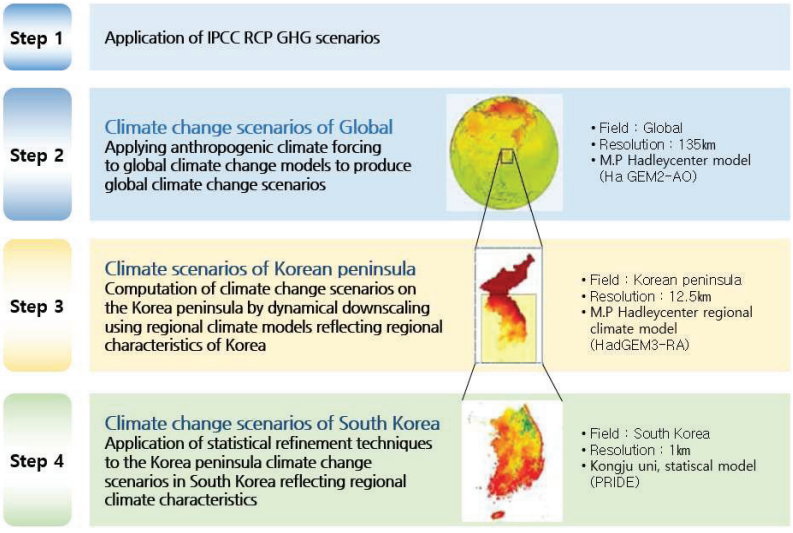

Figure 3. Production process for climate change scenarios [13].

Table 1. Annual maximum daily rainfall according to climate change scenarios.

Year	RCP Scenarios		Year	RCP Scenarios		Year	RCP Scenarios	
	RCP 4.5	RCP 8.5		RCP 4.5	RCP 8.5		RCP 4.5	RCP 8.5
1988	83.0	83.0	2026	145.0	205.8	2064	145.6	87.7
1989	296.0	296.0	2027	93.7	70.0	2065	128.2	106.6
1990	126.0	126.0	2028	134.0	117.3	2066	219.9	109.7
1991	218.0	218.0	2029	85.7	123.9	2067	98.7	65.7
1992	164.0	164.0	2030	117.0	68.0	2068	91.5	112.0
1993	140.0	140.0	2031	113.0	212.1	2069	84.9	101.5
1994	97.0	97.0	2032	50.9	95.4	2070	65.0	134.7
1995	93.0	93.0	2033	66.3	256.1	2071	116.5	91.9
1996	103.0	103.0	2034	189.7	94.0	2072	264.4	120.2
1997	119.0	119.0	2035	124.1	105.8	2073	157.4	187.8
1998	109.0	109.0	2036	168.7	108.7	2074	102.2	68.3
1999	131.0	131.0	2037	57.5	124.8	2075	79.0	71.7
2000	83.0	83.0	2038	82.4	83.4	2076	65.6	97.5
2001	73.0	73.0	2039	229.4	76.1	2077	83.8	163.5
2002	160.0	160.0	2040	85.2	121.6	2078	86.5	80.9
2003	108.0	108.0	2041	113.7	63.5	2079	129.5	82.2
2004	127.0	127.0	2042	133.6	71.9	2080	108.6	123.7
2005	179.0	179.0	2043	80.1	121.1	2081	95.4	128.6
2006	131.0	131.0	2044	130.2	82.7	2082	156.3	127.3
2007	100.0	100.0	2045	80.9	112.8	2083	116.7	171.2
2008	111.0	111.0	2046	216.8	131.9	2084	129.9	101.4
2009	218.0	218.0	2047	86.7	96.9	2085	249.0	89.2
2010	119.0	119.0	2048	156.3	82.0	2086	79.5	72.0
2011	189.0	189.0	2049	93.2	60.0	2087	107.5	122.0
2012	119.0	119.0	2050	110.4	69.1	2088	137.3	403.6
2013	102.0	102.0	2051	111.5	147.9	2089	79.9	83.3
2014	238.0	238.0	2052	157.8	334.9	2090	75.2	97.9
2015	53.0	53.0	2053	176.7	111.8	2091	162.3	81.1
2016	140.0	140.0	2054	114.2	113.3	2092	112.9	269.1
2017	168.0	168.0	2055	140.5	162.6	2093	69.2	142.0
2018	88.0	88.0	2056	99.1	63.4	2094	150.4	121.1
2019	88.9	121.8	2057	355.9	105.8	2095	152.4	124.4
2020	121.1	81.9	2058	108.3	101.7	2096	123.0	141.5
2021	157.2	151.2	2059	189.6	69.5	2097	96.4	181.9
2022	131.6	85.5	2060	75.3	91.7	2098	132.4	151.2
2023	133.2	97.4	2061	152.4	110.9	2099	100.3	105.6
2024	84.7	85.2	2062	81.2	87.0	2100	65.7	74.6
2025	127.6	73.9	2063	103.8	104.6			

3.3. Input Data Composition of SWMM Model

The parameters of the SWMM model are watershed area, permeability, Manning's roughness coefficients, surface storage volume, storage depth, CN value, slope, and sewage pipe data. The rainfall runoff is simulated using these parameters as input data. However, since there is limited observation data to apply all parameters, in this study, watershed area, permeability, Manning's roughness coefficients, slope, and sewage pipe data were used as parameters.

In Korea, the EPA-SWMM is used for flood analysis of LID facilities, and in the case of LID facility effect analysis, the most accurate and ideal result is obtained by performing monitoring under the same conditions before and after installation of the facility and analyzing the effect. In this section, the parameters and data construction before and after LID facility installation are presented. Watershed delineation is the first step in simulating the physical drainage systems. In the EPA-SWMM model, the subwatershed is assumed to be a rectangle with uniform characteristics (slope, roughness, etc.). The shape of the watershed is defined by factors such as area, watershed width, slope, etc. In the case of the EDC area, it flows out through three outlets, and in the case of each watershed, the model was built by unifying the watershed names A, B, and C, as shown in Figure 4, with all three watersheds flowing into the West Nakdong River. The watersheds were divided into subwatersheds according to the pipe network, and there were 133 subwatersheds in A, 171 in B, and 202 in C. The pipe network, according to watershed area, subwatersheds, outlets, nodes, and links, is presented in Table 2 and Figure 4.

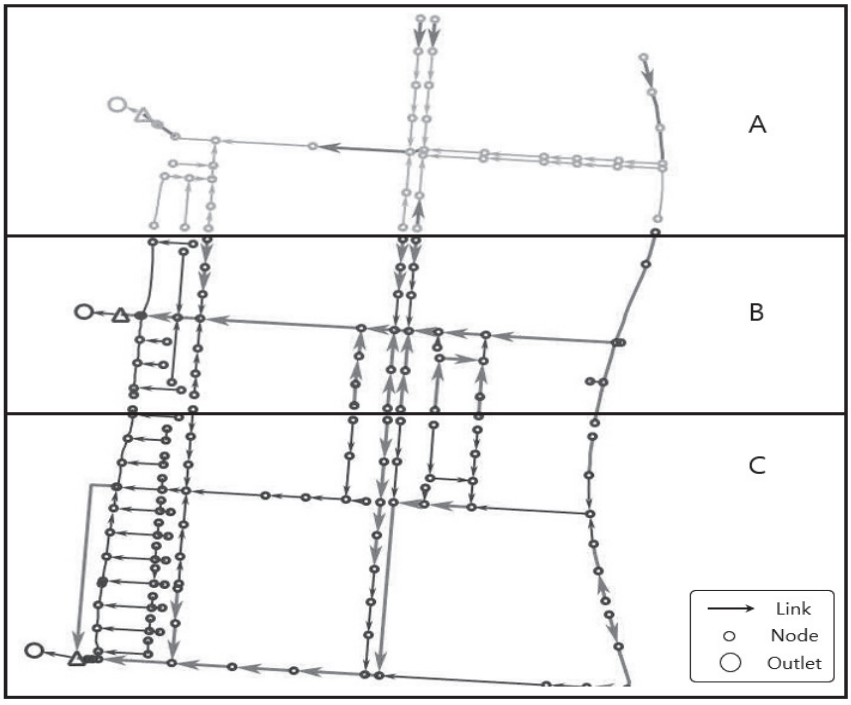

Figure 4. Pipe network of watersheds. (**A**) Outlet of section A; (**B**) Outlet of section B; (**C**) Outlet of section C.

To introduce the LID facilities, variables for each facility were applied. Table 3 shows the designated values of the permeable pavement in this study.

Table 2. Pipe network.

Watershed Area (ha)		Subwatershed (pcs)	Outlet (pcs)	Node (pcs)	Link (pcs)
A	29.4	133	1	43	43
B	32.4	171	1	52	52
C	44.1	202	1	93	93
Total	105.9	506	3	188	188

Table 3. Parameter values of permeable pavement.

Division		Attribute Value
Surface	Berm height (mm)	0
	Vegetation volume fraction	0
	Surface roughness (Manning n)	0.012
	Surface slope (%)	1
Pavement	Thickness (mm)	60
	Void ratio (Voids/Solids)	0.15
	Impervious surface fraction	0.95
	Permeability (mm/h)	360
	Clogging factor	0
Storage	Height (mm)	300
	Void ratio (Voids/Solids)	0.25
	Conductivity (mm/h)	25.9
	Clogging factor	0
Underdrain	Drain coefficient (mm/h)	0
	Drain exponent	0
	Drain offset height	0

In addition, the drainage area of EDC is 52.95 ha, which is 50% of the total watershed area of 105.90 ha. The roughness coefficients among the conduit input data, 0.030 for the permeable area and 0.014 for the impervious area, were applied.

3.4. Research Methodology

The following procedure was followed to analyze the reduction rate of the runoff of the LID facility installed in selected watersheds.

The extraction of annual maximum daily rainfall data was based on the past observed time series of daily rainfall (1988–2018) and the climate change scenarios from 1988 to 2050 and 1988 to 2100. The statistical tests, such as the mean, standard deviation, coefficient of variation, coefficient of skewness, and coefficient of kurtosis, were applied to hydrological data. After calculating the basic statistical values of the annual maximum daily rainfall series, the time series were tested for independence, homogeneity, and outliers. An appropriate distribution was selected for the GUM, PT3, GEV, GLO, GPA, and GNO distributions through the goodness-of-fit test. The parameters of the appropriate distribution were computed according to the study area and the period of analysis using the L-moment method, and the probability of rainfall was estimated using the selected appropriate distribution. Probability of rainfall was computed according to the climate change scenarios.

A rainfall intensity duration equation was derived, and the regression equation was calculated using the precipitation data from the selected rainfall station. The rainfall distribution of the probability of rainfall was constructed using the calculated regression equation. In the EPA-SWMM, the same pipe network data, parameters, and rainfall data before and after the installation of the LID facility were established, and the parameters for the facility after the installation of the LID facility were additionally configured. The effect analysis was presented by estimating the probability of rainfall for each return period of climate change scenario, such as RCP 4.5 and RCP 8.5, by simulating runoff and comparing the reduction rate.

Figure 5 is a schematic diagram of the probability precipitation calculation considering climate change scenarios and LID facilities. The flow chart used in the study based on the procedure introduced in Figure 5 is shown in Figure 6.

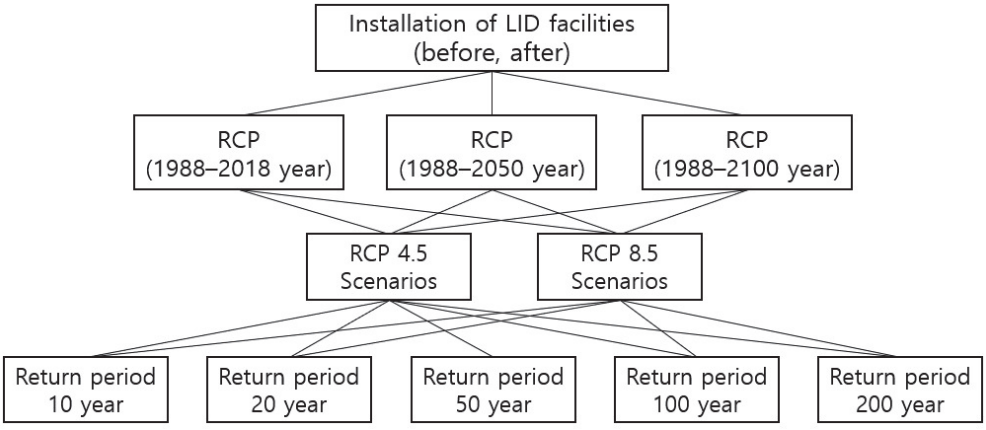

Figure 5. Estimation of probability precipitation by climate change scenario.

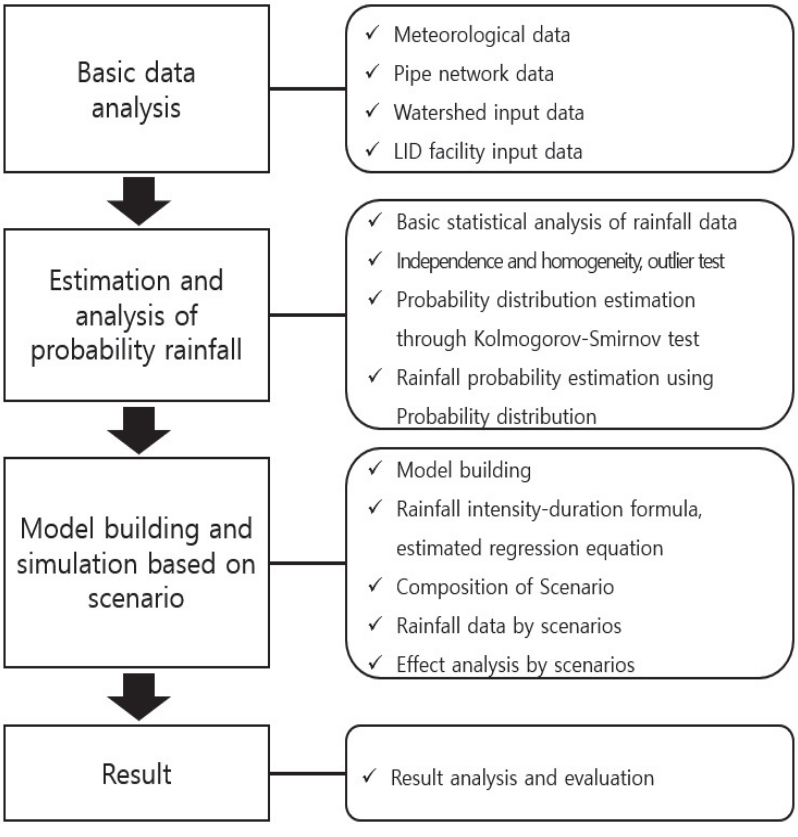

Figure 6. Study flow chart.

4. Results

4.1. Basic Statistical Analysis and Calculation of Probable Rainfall According to Climate Change Scenario

The mean, standard deviation, coefficient of skewness, coefficient of variation, and coefficient of kurtosis for the annual maximum daily rainfall data from the Gimhae rainfall station were calculated. The mean and standard deviation for each period of the RCP 4.5 scenario ranged from 126.2 m^3/day to 135.0 m^3/day and 48.502 to 53.361, respectively, the coefficient of skewness and coefficient of variation were from 1.162 to 1.618 and 0.383 to 0.408, respectively, and the coefficient of kurtosis was from 1.616 to 3.769. This indicated overall that the mean was larger than the range of standard deviation, the coefficient of skewness and the coefficient of variation showed positive values and were biased to the right, and the coefficient of kurtosis was larger than 3, the standard value of normal distribution.

In the RCP 8.5 scenario, the mean and standard deviation ranged from 121.2 to 135.0 and 50.727 to 56.491, respectively, the coefficient of skewness and the coefficient of variation were from 1.231 to 2.255 and 0.395 to 0.461, respectively, and the coefficient of kurtosis was from 1.616 to 6.828.

The basic statistics for RCP 4.5 and RCP 8.5 are shown in Tables 4 and 5.

Table 4. Basic statistics for Gimhae rainfall station using RCP 4.5 scenario.

Duration of Observed Data (Years)	Mean ($\bar{x}$) (m^3/s)	Standard Deviation (S)	Coefficient of Skewness (C_s)	Coefficient of Variation (C_v)	Coefficient of Kurtosis (C_A)
1988–2018	135.0	53.361	1.231	0.395	1.616
1988–2050	126.6	48.502	1.162	0.383	1.646
1988–2100	126.2	51.428	1.618	0.408	3.769

Table 5. Basic statistics for Gimhae rainfall station using RCP 8.5 scenario.

Duration of Observed Data (Years)	Mean ($\bar{x}$) (m^3/s)	Standard Deviation (S)	Coefficient of Skewness (C_s)	Coefficient of Variation (C_v)	Coefficient of Kurtosis (C_A)
1988–2018	135.0	53.361	1.231	0.395	1.616
1988–2050	121.2	50.727	1.421	0.418	1.947
1988–2100	122.4	56.491	2.255	0.461	6.828

4.2. Independence, Homogeneity, and Outlier Detection in Annual Maximum Daily Rainfall

The climate change scenario data were checked to determine the existence of independence, homogeneity, and outliers. The Wald–Wolfowitz test was applied to check the independence, and the Mann–Whitney test was applied to observe the homogeneity of the data. In addition, the Grubbs–Beck test was used for the detection of outliers in the time series data.

For the independence test, the Wald–Wolfowitz test [14], which is a non-parametric test that tests the independence of a population, was performed, and it was found that there were no abnormalities in any of them.

The outlier test induces inappropriate statistical parameters in the case of data that appear far above or below the general balanced distribution of hydrological data, resulting in uncertainty in the presentation of the design hydrologic quantity. Therefore, the presence or absence of outliers was tested using the Grubbs–Beck method for hydrological data of the daily maximum flow series for each analysis in the region to which the climate change scenario was applied. It was confirmed that there were no outliers.

Therefore, the annual maximum daily rainfall in the study area was recognized as valid for analysis as hydrological data.

4.3. Estimation of L-Moment Ratio

L-moment ratios were estimated for goodness-of-fit test evaluation of the probability distributions, such as GUM, PT3, GEV, GLO, GPA, and GNO. L-skewness and L-kurtosis were calculated for the 1988–2018, 1988–2050, and 1988–2100 periods using the annual maximum daily rainfall of RCP 4.5 and RCP 8.5.

In the case of RCP 4.5, L-skewness was 0.2535, 0.2136, and 0.2510, and L-kurtosis was 0.2108, 0.1884, and 0.1999. In the case of RCP 8.5, L-skewness was 0.2535, 0.2822, and 0.3321, and L -kurtosis was 0.2108, 0.2019, and 0.2538.

4.4. Goodness-of-Fit Test

For the goodness-of-fit test, L-moment ratio and Kolmogorov–Smirnov (K–S) tests were performed. First, the selection of an appropriate probability distribution for each period was made by plotting the L-moment ratio, using the L-moment ratio calculated in the previous section. The L-moment ratio diagram was plotted to select the best fitted probability distribution from among GUM, PT3, GEV, GLO, GPA, and GNO. The best fitted probability distribution is the one that follows the observed data.

Therefore, Figure 7 shows the average values of the L-moment ratio for the RCP 4.5 and RCP 8.5 scenarios.

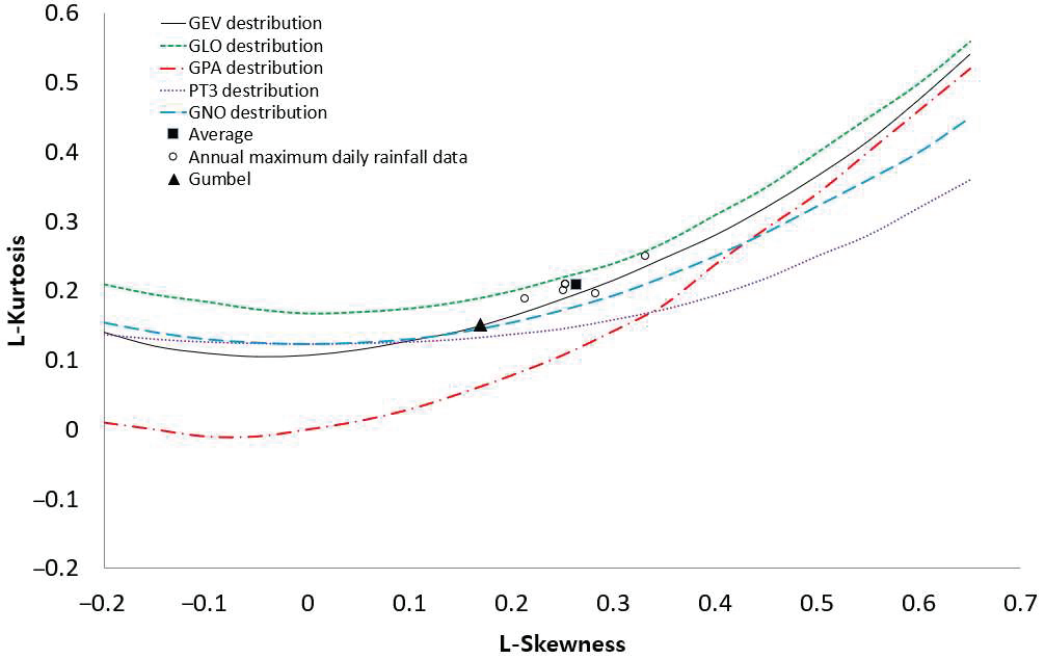

Figure 7. Identification of distributions by L-moment.

The dimensionless L-moment ratios scattered in the diagram are more likely to follow the curve of the GEV distribution, as shown in Figure 7. Therefore, the L-moment method application on the annual maximum daily rainfall for each rainfall station and its plotting in the L-moment ratio diagram showed that the GEV distribution was an appropriate probability distribution compared with GUM, GLO, GPA, GNO and PT3.

Second, the K–S test was applied to choose the best fitted probability distribution for each period of the annual maximum daily rainfall series of the climate change scenario. As a result, at the 5% significance level, data for each period of the annual maximum daily rainfall series were recognized as following the distribution of GEV, GUM, GLO, GPA, GNO, and PT3.

The L-moment ratio diagram and the K–S goodness-of-fit tests showed that the GEV distribution was best fitted probability distribution compared with the other probability distributions. Therefore, the GEV distribution was selected for further analysis.

4.5. Parameter Estimation of Desired Distribution According to L-Moment Method

The parameters of the GEV distribution were estimated by applying it to the annual maximum daily rainfall of the climate change scenarios of RCP 4.5 and RCP 8.5. The parameters of the GEV distribution consist of shape, scale, and location, estimated using the L-moment method for defined periods. The parameters of the GEV distribution that were estimated for the RCP 4.5 and RCP 8.5 scenarios are shown in Tables 6 and 7.

Table 6. Parameters calculated by GEV distribution using L-moment method considering RCP 4.5 scenario at Gimhae rainfall station.

Duration of Observed Data (Years)	Parameter		
	ξ	α	β
1988–2018	108.2442	96.9893	−0.1260
1988–2050	103.4955	35.6241	−0.0668
1988–2100	101.8388	34.1054	−0.1224

Table 7. Parameters calculated by GEV distribution using L-moment method considering RCP 8.5 scenario at Gimhae rainfall station.

Duration of Observed Data (Years)	Parameter		
	ξ	α	β
1988–2018	108.4242	96.9893	−0.1260
1988–2050	96.2268	32.2964	−0.1675
1988–2100	95.8663	30.1751	−0.2377

4.6. Computation of Return Periods Based on Annual Maximum Daily Rainfall

Return periods were computed through the application of GEV distribution on annual maximum daily rainfall of the climate change scenario using the parameters computed in the section above, as shown in Tables 8 and 9.

Table 8. Probable annual maximum daily rainfall at Gimhae rainfall station using RCP 4.5 scenario (unit: mm/day).

Duration of Observed Data (Years)	Return Period (Years)				
	10	20	50	100	200
1988–2018	204.66	241.67	294.83	338.97	386.98
1988–2050	190.00	220.54	262.30	295.35	329.85
1988–2100	190.20	224.00	272.41	312.49	355.98

Table 9. Probable annual maximum daily rainfall at Gimhae rainfall station using RCP 8.5 scenario (unit: mm/day).

Duration of Observed Data (Years)	Return Period (Years)				
	10	20	50	100	200
1988–2018	204.66	241.67	294.83	338.97	386.98
1988–2050	184.50	220.51	274.07	320.05	371.53
1988–2100	185.65	226.10	289.85	347.79	415.92

4.7. Analysis of Runoff before and after Application of LID Facilities by Climate Change Scenario

As a result of the analysis of the reduction rate for RCP 4.5 and RCP 8.5 during the 1988–2018 period, it was found that the reduction rate for the total amount of runoff increases as the return period increases.

In addition, as a result of the analysis of the reduction rate from 1988 to 2050 for the RCP 4.5 scenario, the 10-year return period was 45.4%, the 20-year return period was 45.8%, the 50-year return period was 46.2%, the 100-year return period was 46.5%, and the 200-year return period was 46.7%. It was found that the greater the return period, the greater the reduction rate.

Analyzing the RCP 4.5 scenario as a sample, the reduction rate from 1988 to 2100 decreased from 321.8 m^3/day to 175.7 m^3/day in the 10-year return period of the total runoff, showing a reduction rate of 45.4%. In the 20-year return period, it decreased from 386.8 m^3/day to 209.6 m^3/day, showing a reduction rate of 45.8%; and in the 50-year return period, it decreased from 481.1 m^3/day to 258.4 m^3/day, showing a reduction rate of 46.3%. In the case of the 100-year return period, it decreased from 559.9 m^3/day to 299.0 m^3/day, a reduction rate of 46.6%; and in the 200-year return period, it decreased from 646.2 m^3/day to 343.3 m^3/day, showing a reduction rate of 46.9%.

Table 10 and Figure 8 show the results of the runoff and reduction rates according to the maximum daily rainfall by return period for the 1988–2100 period analysis of the RCP 4.5 scenario.

Table 10. Runoff and reduction rate by return period of maximum daily rainfall (RCP 4.5, 1988–2100).

Return Period (Years)	Watershed Area	Peak Rate of Runoff (m^3/s)		Reduction Efficiency (%)	Runoff (m^3/Day)		Reduction Efficiency (%)
		Before	After		Before	After	
10	A	0.084	0.052	38.5	105.2	54.6	48.1
	B	0.079	0.050	37.1	101.4	57.4	43.4
	C	0.088	0.058	34.6	115.2	63.7	44.7
	Total	0.252	0.159	36.7	321.8	175.7	45.4
20	A	0.104	0.063	39.4	126.0	64.9	48.5
	B	0.097	0.061	37.7	122.2	68.7	43.8
	C	0.109	0.070	35.4	138.5	76.0	45.2
	Total	0.310	0.194	37.4	386.8	209.6	45.8
50	A	0.133	0.080	40.3	156.1	79.7	49.0
	B	0.124	0.077	38.3	152.6	85.1	44.2
	C	0.140	0.089	36.3	172.3	93.6	45.7
	Total	0.397	0.245	38.3	481.1	258.4	46.3
100	A	0.158	0.093	41.0	181.2	92.0	49.2
	B	0.147	0.090	38.7	178.2	98.8	44.5
	C	0.166	0.105	36.9	200.6	108.2	46.0
	Total	0.471	0.288	38.8	559.9	299.0	46.6
200	A	0.186	0.101	45.7	208.6	105.4	49.5
	B	0.172	0.105	39.0	206.2	113.7	44.8
	C	0.196	0.122	37.5	231.4	124.2	46.3
	Total	0.554	0.329	40.6	646.2	343.3	46.9

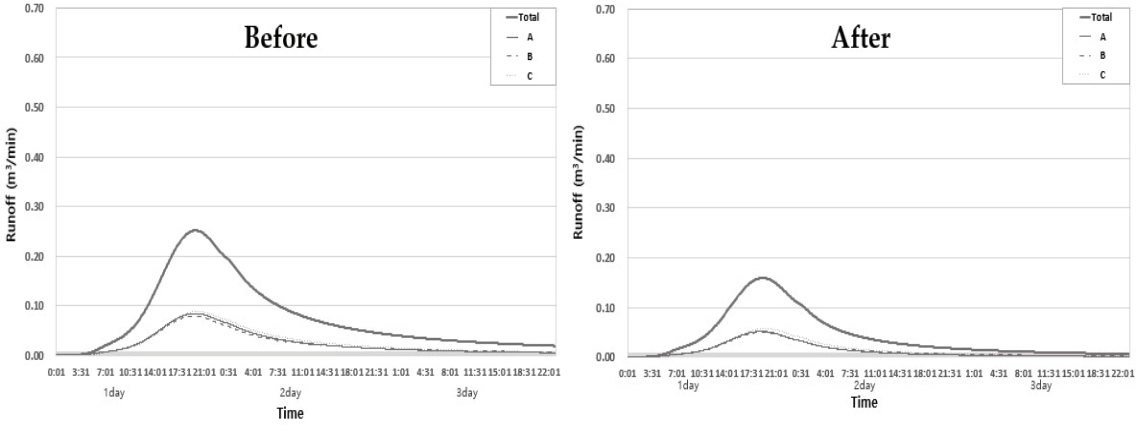

(**a**)

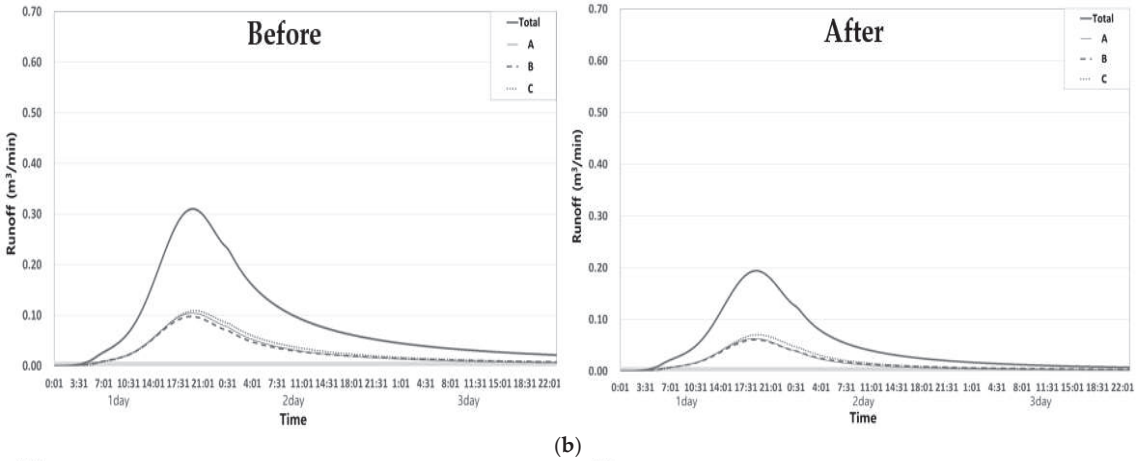

(**b**)

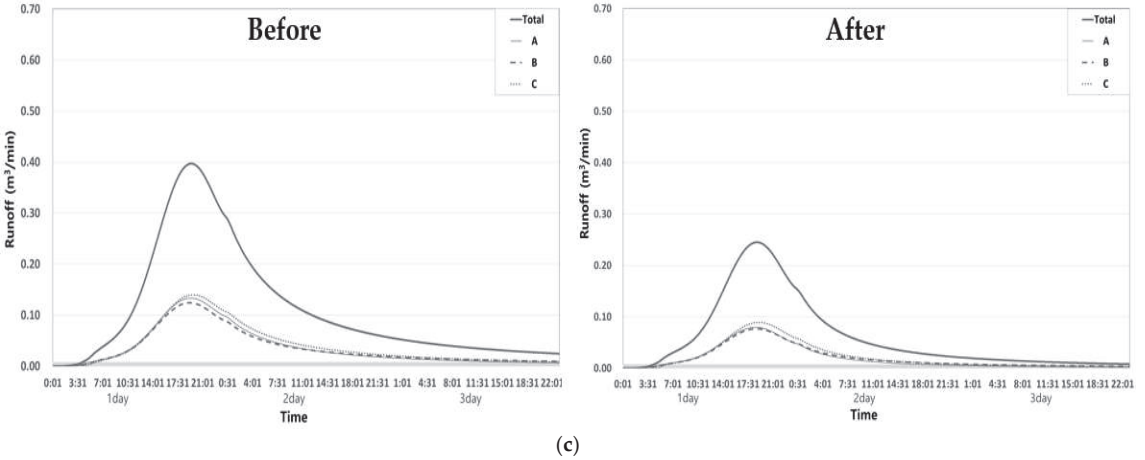

(**c**)

Figure 8. *Cont.*

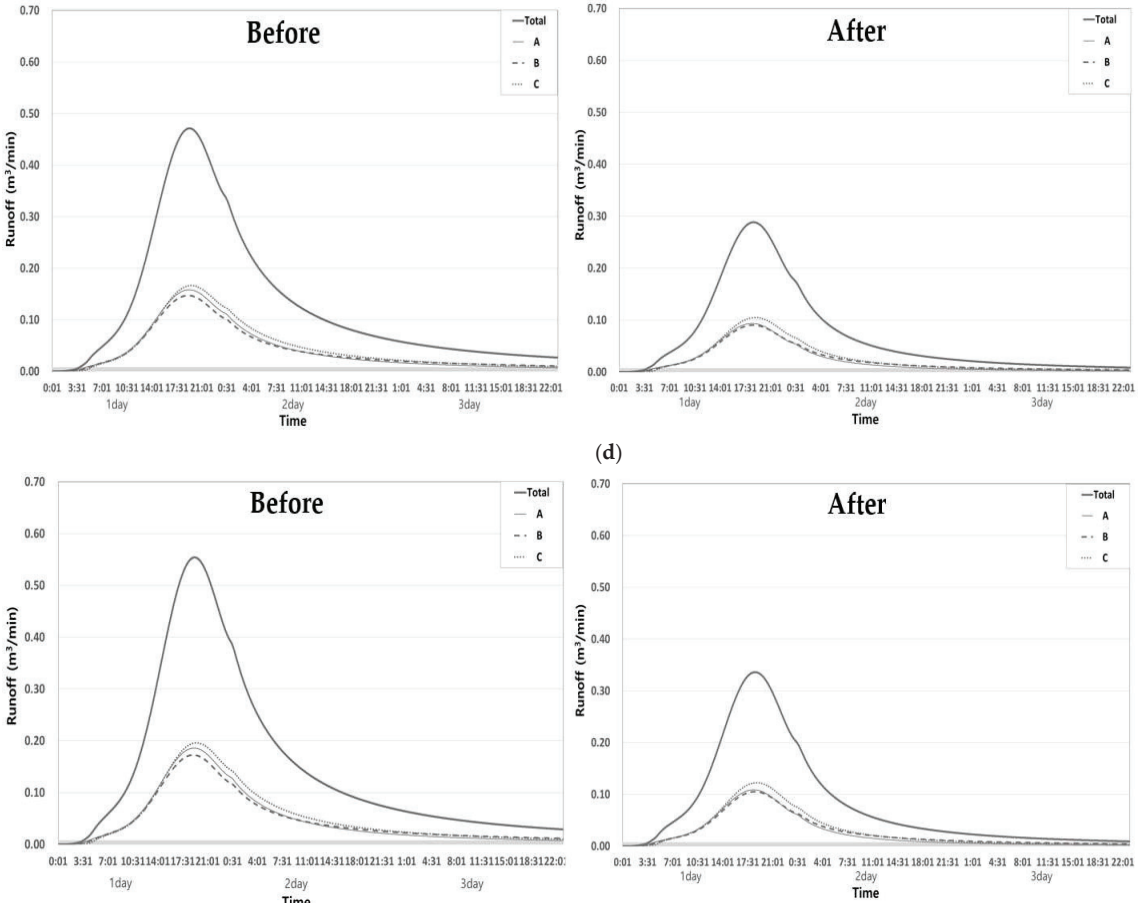

Figure 8. Runoff by return period according to LID facility installation (RCP 4.5, 1988–2100): (**a**) 10-year return period; (**b**) 20-year return period; (**c**) 50-year return period; (**d**) 100-year return period; (**e**) 200-year return period.

As a result of the analysis of the reduction rate for the RCP 8.5 scenario analysis from 2018 to 2050, the 200-year return period decreased from 677.2 m^3/day of the total runoff to 359.1 m^3/day, indicating the largest reduction rate of 47.0%.

Analyzing the RCP 8.5 scenario as a sample, the reduction rate from 1988 to 2100, during the RCP 8.5 scenario analysis period, for the 10-year return period of the total runoff decreased from 313.1 m^3/day to 171.2 m^3/day, showing a reduction rate of 45.3%. In the 20-year return period, it decreased from 390.8 m^3/day to 211.7 m^3/day, showing a reduction rate of 45.8%; and in the 50-year return period, it decreased from 515.3 m^3/day to 276.0 m^3/day, showing a reduction rate of 46.4%. In the case of the 100-year return period, it decreased from 629.9 m^3/day to 334.9 m^3/day, a reduction rate of 46.8%; and in the 200-year return period, it decreased from 766.1 m^3/day to 404.5 m^3/day, showing a reduction rate of 47.2%.

Table 11 and Figure 9 show the results for the runoff and reduction rates according to the maximum daily rainfall by return period for the 1988–2100 period analysis of the RCP 8.5 scenario.

Table 11. Runoff and reduction rate by return period of maximum daily rainfall (RCP 8.5, 1988–2100).

Return Period (Years)	Watershed Area	Peak Rate of Runoff (m^3/s)		Reduction Efficiency (%)	Runoff (m^3/day)		Reduction Efficiency (%)
		Before	After		Before	After	
10	A	0.082	0.050	38.4	102.4	53.2	48.1
	B	0.077	0.048	37.0	98.6	55.9	43.3
	C	0.085	0.056	34.5	112.1	62.1	44.6
	Total	0.244	0.155	36.6	313.1	171.2	45.3
20	A	0.105	0.064	39.4	127.3	65.5	48.5
	B	0.099	0.061	37.7	123.5	69.4	43.8
	C	0.110	0.071	35.4	140.0	76.7	45.2
	Total	0.314	0.196	37.5	390.8	211.7	45.8
50	A	0.144	0.086	40.6	167.0	85.1	49.1
	B	0.134	0.083	38.5	163.7	91.0	44.4
	C	0.151	0.096	36.6	184.6	99.9	45.9
	Total	0.429	0.264	38.5	515.3	276.0	46.4
100	A	0.181	0.106	41.4	203.4	102.9	49.4
	B	0.168	0.102	39.0	200.9	110.9	44.8
	C	0.190	0.119	37.4	225.6	121.2	46.3
	Total	0.538	0.327	39.3	629.9	334.9	46.8
200	A	0.225	0.130	42.2	246.5	123.8	49.8
	B	0.208	0.126	39.4	245.3	134.5	45.2
	C	0.238	0.147	38.2	274.2	146.2	46.7
	Total	0.671	0.403	39.9	766.1	404.5	47.2

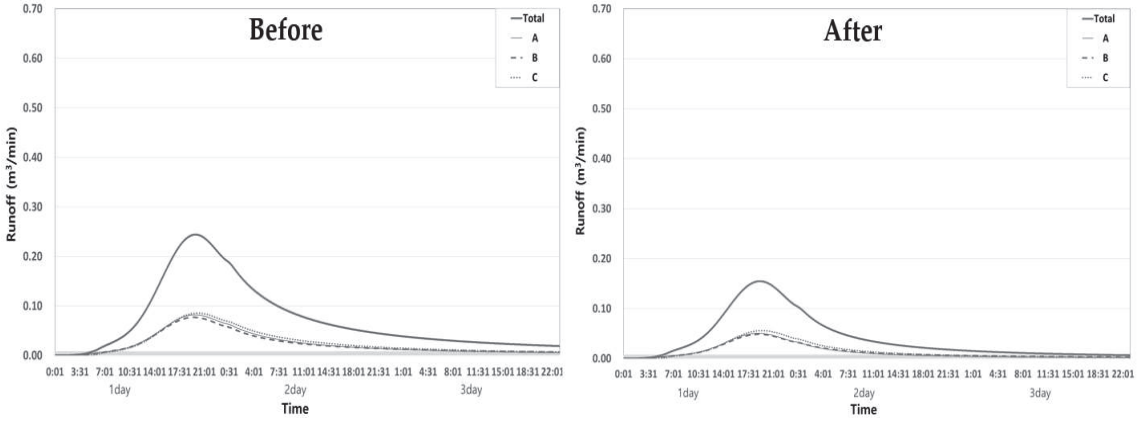

(**a**)

Figure 9. *Cont*.

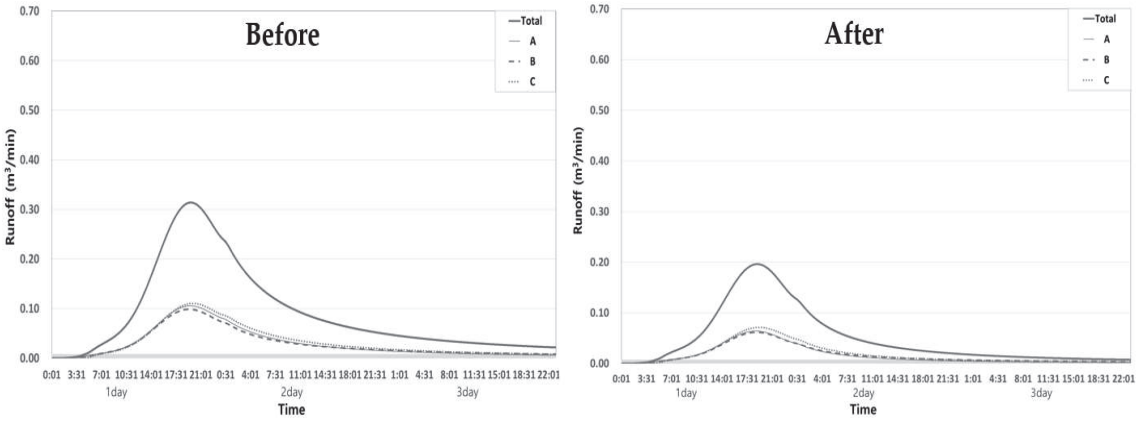

(**b**)

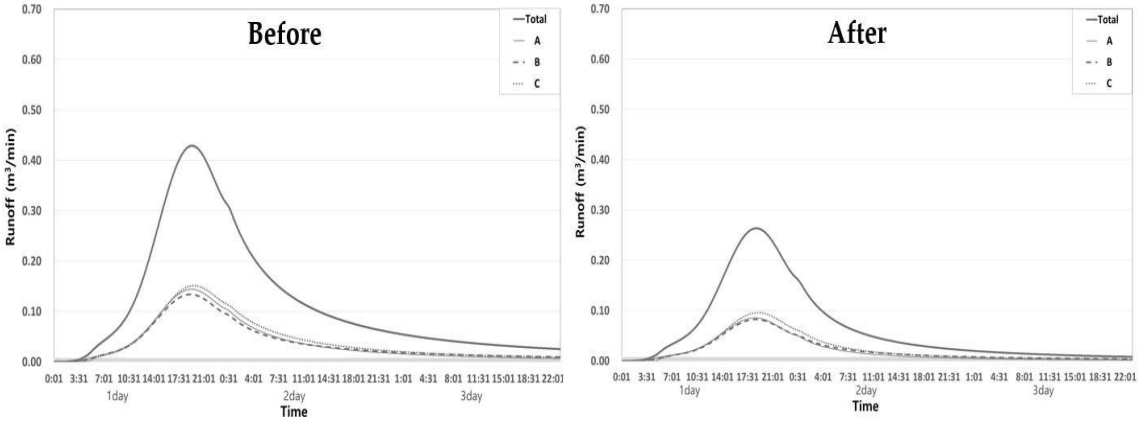

(**c**)

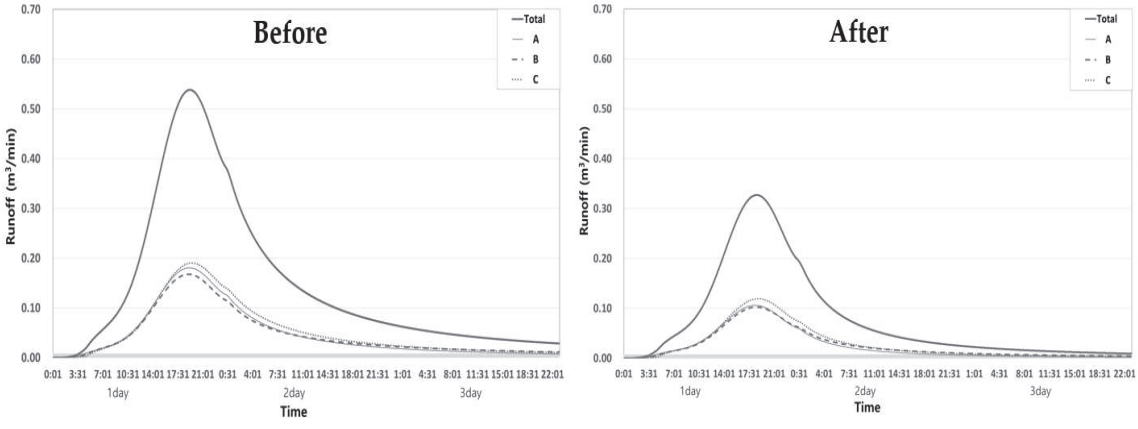

(**d**)

Figure 9. *Cont*.

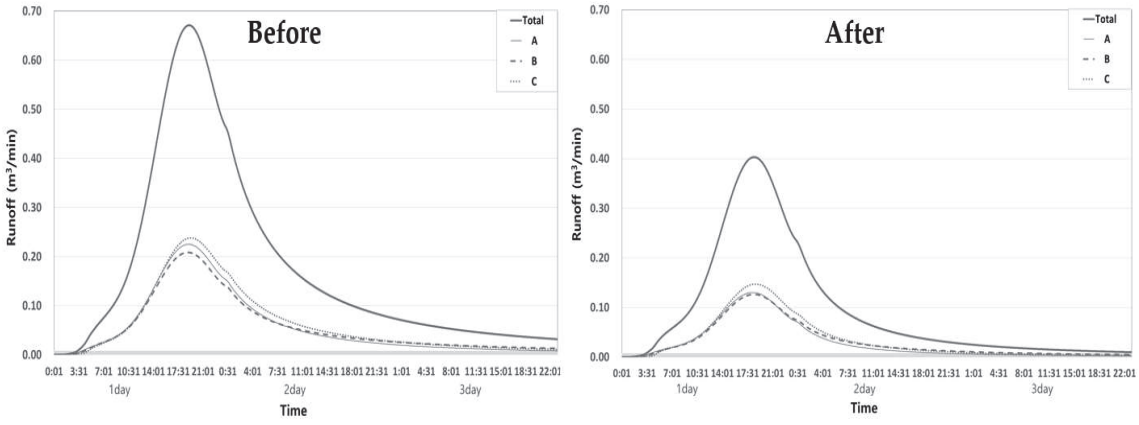

(**e**)

Figure 9. Runoff by return period according to LID facility installation (RCP 8.5, 1988–2100): (**a**) 10-year return period; (**b**) 20-year return period; (**c**) 50-year return period; (**d**) 100-year return period; (**e**) 200-year return period.

4.8. Analysis of Reduction Rate by Climate Change Scenario

To efficiently manage runoff, it is necessary to determine the rainfall (design rainfall) to estimate the size of the reduction potential facility. A pre-disaster impact assessment is recommended [15]. The usual return period used in the design of temporary and permanent facilities is 30 and 50 years, respectively. As a result, a reduction rate return period analysis based on the 20-year runoff was reported in this study for LID facilities. The return period analysis from 1988 to 2018 was the same for the RCP 4.5 and RCP 8.5 scenarios; hence, it is reported only for the RCP 4.5 scenario.

In the RCP 4.5 scenario, as a result of the comparison and analysis of the total runoff from 1988 to 2018, it was found that the runoff on a 20-year return period of 421.1 m^3/day was greater than the 200-year return period of 376.1 m^3/day before and after the LID facility installation, which was predicted to reduce the runoff for up to 200 years, as a result of the LID facility installation, for the 20-year return period, when designing the return period.

In addition, a comparison and analysis of the total runoff from 1988 to 2050 was conducted, and the results showed that 380.1 m^3/day for the 20-year return period before the LID facility installation was higher than 316.7 m^3/day for the 200-year return period after the LID facility installation, which would have the effect of reducing runoff up through the 200-year return period. The results of the comparison and analysis of the total runoff from 1988 to 2100 showed 386.8 m^3/day for the 20-year return period before the LID facility installation, and 343.3 m^3/day for the 200-year return period after the LID facility installation. This showed a value higher than 343.3 m^3/day, and it was predicted that the runoff at the 20-year return period set would be reduced to the 200-year return period as a result of the LID facility installation, when designing the return period.

Table 12 and Figure 10 show the results of the comparison and analysis of the total runoff for the RCP 4.5 scenario by return period before and after the LID facility installation.

Table 12. Runoff by return period using RCP 4.5 scenario (unit: m^3/day).

Year of Analysis	Development	Return Period				
		10-Year	20-Year	50-Year	100-Year	200-Year
1988–2018	Before	349.5	421.1	525.1	612.4	708.1
	After	190.2	227.4	281.1	326.0	376.1
1988–2050	Before	321.4	380.1	461.3	526.1	594.3
	After	175.5	206.1	248.2	281.6	316.7
1988–2100	Before	321.8	386.8	481.1	559.9	646.2
	After	175.7	209.6	258.4	299.0	343.3

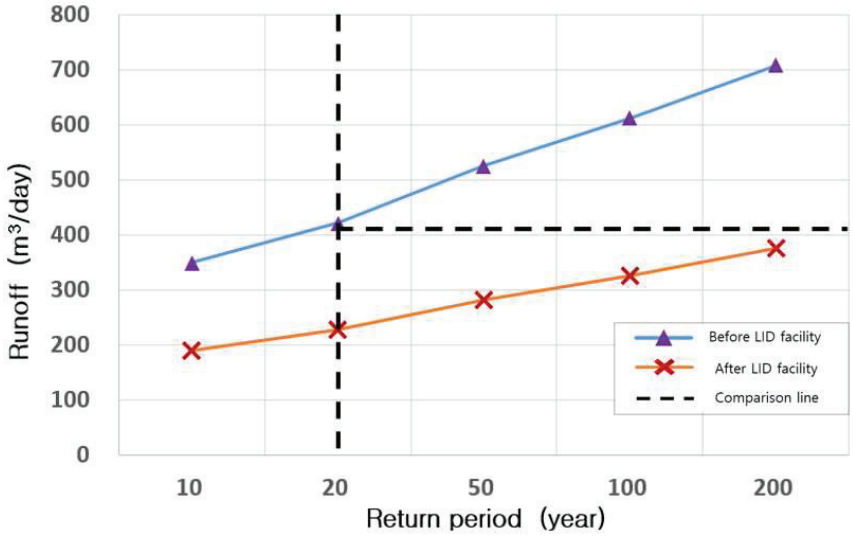

(**a**)

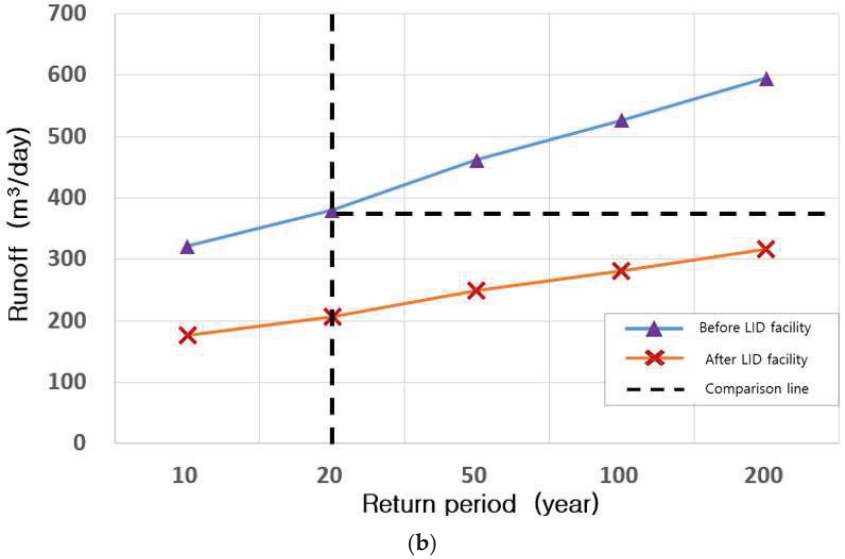

(**b**)

Figure 10. *Cont.*

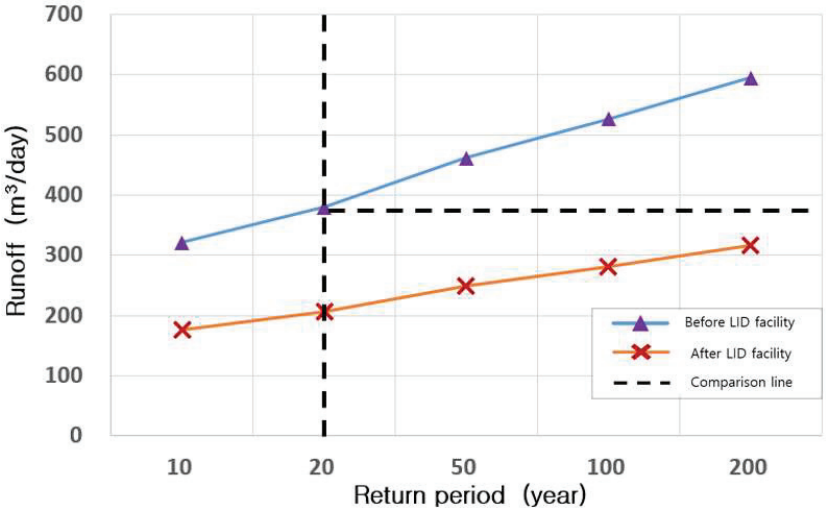

(**c**)

Figure 10. Change in runoff by return period in RCP 4.5 scenario: (**a**) 1988–2018 (year); (**b**) 1988–2050 (year); (**c**) 1988–2100 (year).

In the case of the RCP 8.5 scenario, the analysis of the 20-year return period from 1988 to 2050 before the LID facility installation was based on the comparison and analysis of the total runoff from 1988 to 2050. The return period of 380.0 m^3/day was higher than the return period of 359.1 m^3/day for the 200 years after LID facility installation. When designing the return period, it was found that the amount of runoff, with a return period of 20 years, would be reduced for around 200 years or more due to the LID facility installation.

The analysis of the 20-year return period from 1988 to 2100 before the LID facility installation was based on the comparison and analysis of the total runoff from 1988 to 2100. The return period of 390.8 m^3/day was higher than the return period of 334.9 m^3/day for the 100 years after the LID facility installation, and smaller than the return period of 404.5 m^3/day for 200 years. When designing the return period, it was found that the amount of runoff with a return period of 20 years would be reduced for around 100 years or more due to the LID facility installation.

Table 13 and Figure 11 show the results of the comparison and analysis of total runoff for the RCP 8.5 scenario by return period before and after the installation of the LID facility.

Table 13. Runoff by return period using RCP 8.5 scenario (unit: m^3/day).

Duration of Analysis (Year)	Development	Return Period				
		10-Year	20-Year	50-Year	100-Year	200-Year
1988–2050	Before	310.9	380.0	484.3	574.9	677.2
	After	170.0	206.1	260.1	306.7	359.1
1988–2100	Before	313.1	390.8	515.3	629.9	766.1
	After	171.2	211.7	276.0	334.9	404.5

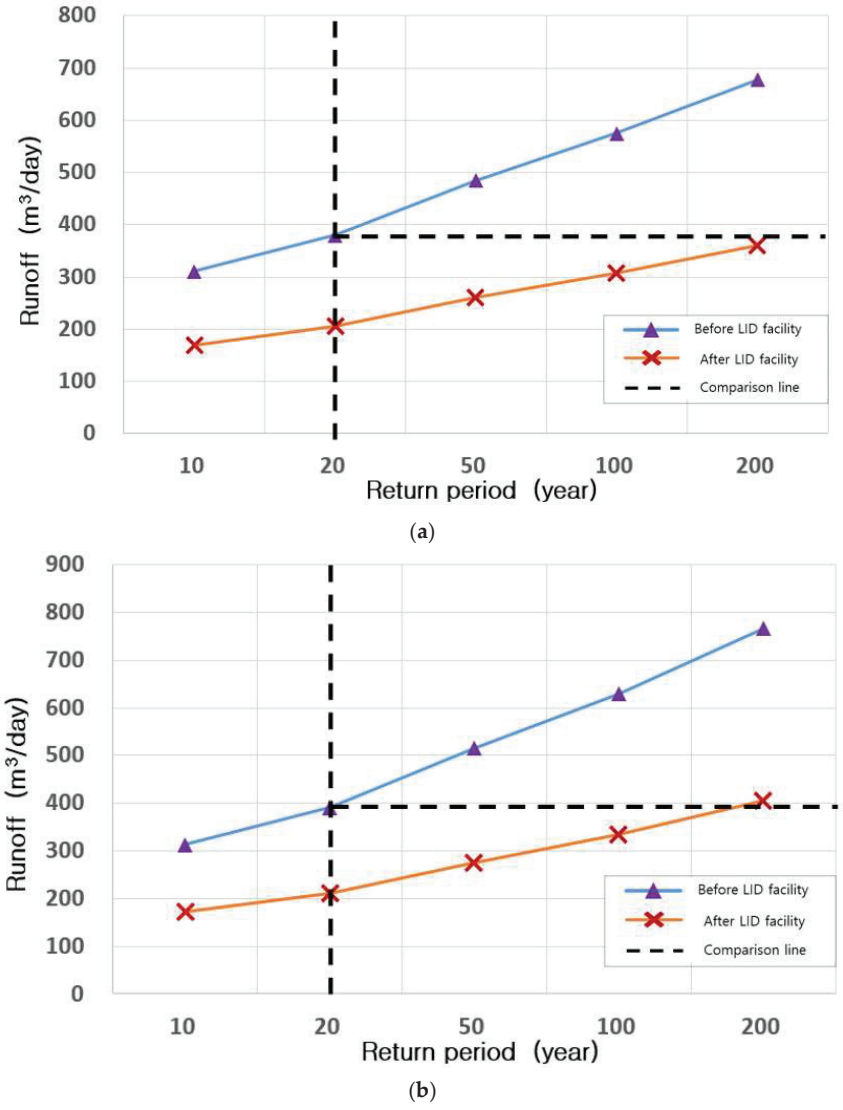

Figure 11. Change in runoff by return period in RCP 8.5 scenario: (**a**) 1988–2050 (year); (**b**) 1988–2100 (year).

5. Conclusions

The runoff reduction rate by return period according to the scenario was compared and decreased in this study by setting the rainfall distribution by return period via an analysis of the change in the probability of rainfall. This was achieved by applying the climate change scenario and the probability of rainfall for each scenario, and simulating the amount of runoff before and after the LID facility installation in the object region.

The above analysis results are summarized as follows:

1. After composing the annual maximum daily rainfall data based on the previously observed annual maximum daily rainfall series (1988–2018) and climate change scenarios from 1988 to 2050 and 1988 to 2100 (provided by the Korea Meteorological

Administration), statistical analysis was undertaken to determine its suitability as hydrological data.

2. The GEV distribution was found to be more appropriate than the other five probability distributions applied to the series of annual maximum daily rainfalls per scenario, according to the analysis after performing the L-moment ratio and K–S tests, which are goodness-of-fit tests.
3. The reduction rate was analyzed by constructing a scenario that considered the same parameters and rainfall data before and after LID facility installation, and the LID parameters after installation. Assuming the same cost aspect in installing the LID, we focused on analyzing and selecting the rainwater reduction rate. Regarding RCP 4.5 and RCP 8.5, we observed a maximum reduction rate of 46.9% for the 200-year return period in the 1988–2100 analysis period for RCP 4.5, and the highest reduction rate of 47.2% for the 200-year return period in the 1988–2100 period for RCP 8.5.
4. As a result of analyzing the reduction rate return period for each scenario, in the case of scenario RCP 4.5, in the analysis of the 1988–2018, 1988–2050 and 1988–2100 periods, the 20-year return period before installation of the LID facility was the same as the amount of runoff after installation of the LID facility. In the analysis of the 1988–2050 period, it was found that the effect of reducing the runoff return period would remain for around 200 years, and that the runoff return period of 20 years before the installation of the LID facility would show the effect of reducing runoff for more than 100 years after the installation.
5. Even in the case of scenario RCP 8.5, in the 1988–2050 analysis period, the amount of runoff with a return period of 20 years before the installation of the LID facility had the effect of reducing the amount of runoff for up to 200 years after installation. In the 1988–2100 analysis period, the amount of runoff with a return period of 20 years before the installation of the LID facility was effective in reducing the amount of runoff for 100 years or more.

This study presented the results of analyzing the reduction rate by return period for the design of LID facilities. In the case of Korea, it is difficult to improve efficiency after the installation of LID facilities due to a lack of basic data on LID specifications and an analysis of their effects. In comparison with other regions, there are many things to consider, such as differences in parameters, rainfall amounts, and land use for each region, and there are limits to construction based only on the related literature. Therefore, analysis through reduction research and actual monitoring data should be continuously undertaken. In addition, this study was limited in that the rate of change in the runoff reduction according to the timing of the permeable pavement and the selected LID facility was not considered.

However, as described in Section 2, the existing studies analyzed only the observational data, but this study considered a new analysis in that the LID facilities used data on climate change scenarios.

Author Contributions: Conceptualization, S.L.; methodology, S.L., S.M.; software, S.L., M.A.; validation, S.L., D.K., M.A.; formal analysis, D.K., B.L.; investigation, D.K., B.L.; resources, M.A., D.K., B.L.; writing—original draft preparation, S.L., S.M.; writing—review and editing, M.A., D.K.; visualization, S.L., D.K.; supervision, S.L., S.M.; project administration, S.L., S.M. All authors have read and agreed to the published version of the manuscript.

Funding: This research was supported by the Korea Agency for Infrastructure Technology Advancement (KAIA) grant funded by the Ministry of Land, Infrastructure and Transport (Grant number 21RITD-C161134-01.

Institutional Review Board Statement: Not applicable.

Informed Consent Statement: Not applicable.

Data Availability Statement: Data sharing is not applicable to this article.

Conflicts of Interest: The authors declare no conflict of interest.

References

1. National Institute of Meteorological Sciences (NIMS), South Korea. *Global Climate Change Report 2012 for IPCC 5th Assessment Report: Climate Change Projections According to RCP 2.6/4.5/6.0/8.5*; National Institute of Meteorological Sciences: Seoul, Korea, 2012. (In Korean)
2. Ministry of Land, Infrastructure and Transport, South Korea. *Plan of Securing for National Water Security against Climate Change*, 1st ed.; Ministry of Construction and Transportation: Seoul, Korea, 2008. (In Korean)
3. Greenwood, J.A.; Landwehr, J.M.; Matalas, N.C.; Wallis, J.R. Probability weighted moments: Definition and relation to parameters of several distributions expressed in inverse form. *Water Resour. Res.* **1979**, *15*, 1049–1054. [CrossRef]
4. Hosking, J.R.M. *The Theory of Probability Weighted Moments*; IBM Research Center Yorktown: Heights, NY, USA, 1986.
5. Hosking, J.R.M. *FORTRAN Routines for Use with the Method of L-moments*; IBM Research Center: Yorktown Height, NY, USA, 1996; pp. 1–43.
6. Maeng, S.J.; Lee, S.H. Estimation of Design Flood by Determination of Best Fitting Order of LH-Moments(II). *J. Korean Soc. Agric. Eng.* **2003**, *45*, 33–44.
7. Maidment, D.R. Handbook of Hydrology, 1st ed.McGraw-Hill Inc.: New York, NY, USA, 1992; pp. 1–55.
8. Cunnane, C. *Statistical Distributions for Flood Frequency Analysis*; World Meteorological Organization (WMO): Geneva, Switzerland, 1989; pp. A4.1–14.
9. Hosking, J.R.M.; Wallis, J.R. *Regional Frequency Analysis*; Cambridge University Press: Cambridge, UK, 1997; p. 240.
10. Environmental Protection Agency (US-EPA). *Protecting Water Quality Urban Runoff*; US-EPA: Washington, DC, USA, 2015. Available online: https://www3.epa.gov/npdes/pubs/nps_urban-facts_final.pdf (accessed on 6 May 2019).
11. Lee, D.C. Runoff Reduction by LID of A Newtown Considering Soil Characteristic. Doctoral Dissertation, Chung-Ang University, Seoul, Korea, 2017.
12. Korea Meteorological Administration. Meteorological Data Open Portal. Available online: https://data.kma.go.kr (accessed on 20 February 2019).
13. Korea Meteorological Administration. Climate Information Portal. Available online: http://www.climate.go.kr (accessed on 7 March 2019).
14. Wald, A.; Wolfowitz, J. On a test whether two samples are from the same population. *Ann. Math. Stat.* **1940**, *11*, 147–162. [CrossRef]
15. National Emergency Management Agency (NEMA), South Korea. *Guideline for Preliminary Disaster Inspection*; National Emergency Management Agency: Seoul, Korea, 2012. (In Korean)

sustainability

MDPI

Article

Benefit Analysis of Economic and Social Water Supply in Xi'an Based on the Emergy Method

Zihan Guo [1], Ni Wang [1,*], Xiaolian Mao [2], Xinyue Ke [1], Shaojiang Luo [2] and Long Yu [2]

[1] State Key Laboratory of Eco-Hydraulics in Northwest Arid Region, Xi'an University of Technology, Xi'an 710048, China; 1200411015@stu.xaut.edu.cn (Z.G.); 1210410008@stu.xaut.edu.cn (X.K.)
[2] Hanjiang-to-Weihe River Valley Water Diversion Project Construction Co., Ltd., Xi'an 710048, China; maoxiaolian@hwrvwd.cn (X.M.); luoshaojiang@hwrvwd.cn (S.L.); yulong@hwrvwd.cn (L.Y.)
* Correspondence: wangni@xaut.edu.cn

Abstract: In order to manage regional water resources efficiently and sustainably and promote the rational utilization of water resources, it is necessary to evaluate the water-supply benefit reasonably. On the basis of emergy theory, this paper constructs the water-supply-benefit model of economic (industry, agriculture, and the tertiary industry) and social (domestic, employment security, entertainment, scientific research) systems. Taking Xi'an from 2014 to 2020 as an example, by analyzing the energy flow of each system and the multisource water transformities, the water contribution rate, the water-supply benefit, and the unit-water-resource value in each system are calculated. For the water-supply benefits: Industry > Agriculture > Domestic > Tertiary industry > Employment Security > Entertainment > Scientific research. For the unit-water-resource values: Industry > Tertiary industry > Agriculture > Domestic > Entertainment > Employment security > Scientific research. In the economic system, the water-supply benefit and the unit-water value of industry were always the largest, followed by agriculture and the tertiary industry. However, the Pearson correlation coefficient between the water contribution rate and the output of the industrial system was only 0.52, which was less than that of other production industries, which indicates that there might be a waste of water and that industrial water conservation needs to be further strengthened. In the social system, the domestic-water-supply benefits and the water-resource value were the largest. This is because water resources, as a basic resource, always affect people's health and quality of life.

Keywords: water-supply benefit; emergy theory; economic system; social system; transformity; water contribution rate; unit-water-resource value

Citation: Guo, Z.; Wang, N.; Mao, X.; Ke, X.; Luo, S.; Yu, L. Benefit Analysis of Economic and Social Water Supply in Xi'an Based on the Emergy Method. *Sustainability* **2022**, *14*, 5001. https://doi.org/10.3390/su14095001

Academic Editors: Alban Kuriqi and Luis Garrote

Received: 24 March 2022
Accepted: 20 April 2022
Published: 21 April 2022

1. Introduction

Nowadays, because of the continuous growth of the population and the economy and the uneven spatial distribution of water resources, the problems of water shortages, uneven supply and demand, and the waste of water resources are becoming increasingly prominent. This not only greatly limits social and economic development, but also stimulates contradictions among different regions and industries [1–3]. In such a severe situation, a reasonable assessment of the water-resource value in different industries is of great significance in order to protect people's livelihoods, promote economic development, and allocate water resources rationally [4,5].

In their study of the quantification of the water-resource value and the water-supply benefits, Qin et al., Tang et al., Bierkens et al., Liu et al., and Shen et al. established a planning, or optimization, model to find the dual solution of the linear programming problem, obtained the shadow price of water, and quantified the value of the water resources [6–10]. Alcon et al., Arena et al., and Arborea et al. measured the economic benefits of reclaimed water for irrigation (including the market and nonmarket benefits) through the CBA model, so as to evaluate the economic sustainability of an irrigation scheme [11–13]. Ward applied the CBA model to water-resource decision making and evaluated the monetary value of

the impact of the decision-making scheme on the overall social environment and economy [14]. Dallman et al. and Zuo et al. evaluated the benefits of rainwater collection from many aspects, established a cost–benefit model, quantified the economic benefits and costs of rainwater collection, and thereby quantified the value of rainwater [15–17]. Sun et al., Downing et al., and Ma et al. analyzed the costs and benefits of soil and water conservation, the benefits brought about by water-quality protection, and the economic value of water in arid and water-shortage areas by using the cost–benefit model [18–20]. Lee et al., Genius et al., Loomis et al., and Mumbi et al. used the dichotomy conditional valuation method (CVM) to measure the economic benefits of tap-water-supply services, the residents' willingness to pay for potable water treatment, the economic value of water treatment, and the residents' willingness to pay for environmental restoration [21–24]. Xu et al. took the Xin'an River Basin as an example, and estimated the water-use benefits of different beneficiaries by analyzing the transformation of the protection costs and benefits in different regions [25]. Van dijk et al. applied linear and spatial hedonic price models to the real estate market in Switzerland, assessed the impact of the water-related environmental factors on the housing sales prices, and analyzed the differences in the contributions of different water-related resources to the housing prices [26]. Chi et al. proposed the comprehensive evaluation index of the social, economic, and environmental benefits of water resources, and analyzed the comprehensive benefits of the water resources in an area by using the multiobjective evaluation model [27]. Wang et al. quantified the ecological and economic benefits brought about by the middle route of the South-to-North Water Transfer Project to the water-receiving area by using the cost–benefit method and an alternative cost method, thereby reflecting the water value [28]. Cheng et al. and Yue et al. analyzed the river ecological service function and quantified the value of the regional ecological base flow through the equivalent factor method [29,30].

The above research has used different analysis methods to fully discuss the water-resource value of different objects, which has provided references for the adaptability of the research methods and the accuracy of the calculation results in this paper. However, because of the complexity of the eco-economic system and the abstractness of the socioeconomic value of water resources [31], the commonly used methods, such as the models of shadow price, marginal benefit, multiobjective evaluation, and cost–benefit, fail to combine the ecological and socioeconomic attributes of water and to quantify the input and output of materials, money, and energy in the eco-economic system uniformly, which may lead to the inaccurate evaluation of the water-resource value [32]. Therefore, in order to break down the original barriers between the different substances in the ecosystem and in the socioeconomic system, to ensure that substances with different attributes have unified measurement standards, and to facilitate unified analysis, statistics, and comparison, emergy theory came into being. Emergy theory is a new scientific system that was first proposed by Odum, a famous American ecologist, in his speech when accepting the Crafoord Prize of the Royal Swedish Academy of Sciences, and in his paper that was published in *Science* in 1987, after his in-depth research on energetics [33]. After further research and demonstration, Odum completed the world's first emergy monograph: "Environmental accounting: Emergy and Environmental Decision Making", in 1996 [34]. The theoretical framework contains a series of new concepts and pioneering viewpoints, including energy systems, energy quality, emergy, and emergy transformity. For the first time, different substances in different systems were connected together, so that they had a unified measurement standard—Emergy—which was a major leap in theory and method. Emergy theory, as a bridge between the natural system and the socioeconomic system, has attracted a lot of attention in academic circles in recent years, and it is widely used in the quantitative research on the value of natural resources and in the sustainability analyses of different systems, such as in the work of Liu et al., who constructed an urban domestic water supplying process metabolism model and accounting framework that is based on emergy theory, and who analyzed the cost and value of the urban domestic water supply [35]. Di et al. constructed the eco-economic value index system, which is based on emergy, and they

analyzed the water-resource values of eight cities in the Yellow River Basin [31]. Wu et al. analyzed the social value of water resources on the basis of the emergy method, which enriched the accounting method of the social value of water resources [32]. Paoli et al. conducted emergy analysis on tourism and cruise tourism in three cities of the Liguria coastal region from the perspective of the environmental costs and economic benefits, and they evaluated the development of tourism in these cities [36]. Kocjancic et al. incorporated the biophysical indicators on the basis of emergy into the socioeconomic optimization model and, through the study of the Slovenian dairy sector, it was confirmed that the inclusion of emergy indicators in the optimization model was conducive to the growth of industrial economic and biophysical benefits [37]. Zhang et al., Zhang et al., and Zhong et al. adopted a series of comprehensive emergy indicators to evaluate the sustainability of China's newly built sewage treatment plant, China's cement industry environment, and the Erhai Lake Basin, respectively [38–40]. Winfrey et al. created the treatment sustainability index on the basis of emergy theory to quantify the sustainability of a waste-treatment system [41]. Shah et al. assessed the sustainability of a regional agricultural production system through the emergy input–output analysis of agricultural production in Pakistan [42]. Peng et al. and Pan et al. quantified the emergy-carrying capacity and emergy ecological footprint of a city on the basis of the emergy ecological footprint framework, and they evaluated the sustainability of the ecological and economic systems of the city [43,44]. Jaklic et al. evaluated the emergy of nine farm types, and they discuss the potential of a multiperspective collaborative evaluation of agricultural activities [45]. Ali et al. evaluated and compared the environmental pressure that is caused by agricultural production on Pakistan and India from the perspective of the emergy index [46]. Viglia et al. used the emergy accounting method to quantify the environmental support that is required by the metabolism of five urban systems with different sizes in Italy in terms of the resource generation and the ecosystem service supply [47].

To sum up, in order to accurately measure the real value of water resources, in view of the existing research results, this paper introduces the concepts of the water-resource eco-economic system and emergy, and it constructs the emergy network of the water-resource ecological and socioeconomic composite system. Taking the economic and social system in Xi'an from 2014 to 2020 as an example, we analyze the emergy flow in each system, and we make a specific analysis of the emergy in the Xi'an economic and social system from three parts, including the original data-processing model, the multisource water-body-transformity model, and the water-supply-benefit model. Thus, the water-resource value and the water-supply benefit of each system are obtained. The purpose is to provide new ideas for improving and perfecting the accounting method of the socioeconomic value of water resources, and to provide a reference for water-resource pricing and water-resource allocation in different industries.

2. Materials and Methods

2.1. Description of the Study Area

Xi'an is located in the middle of the Yellow River Basin in Shaanxi Province, with an area of 9983 km^2; the regional general situation is shown in Figure 1. Xi'an is a major industrial city in Shaanxi Province, as well as a major trade center and manufacturing base in China, with a rich output of industrial products [48]. At the same time, it is also a famous historical and cultural city, and the service industry is developing rapidly. According to the "Xi'an Statistical Yearbook (2014–2020)", Xi'an's resident population and the GDPs of three industries have increased year by year. By the end of 2020, the city's resident population was 12.96 million, and the regional GDP was USD 156.57 billion. According to the "Xi'an Water Resources Bulletin (2014–2020)", from 2014 to 2020, the average annual precipitation of the city was 678.43 mm, the average surface-water resources were 1.904 billion m^3, the average groundwater resources were 1.289 billion m^3, and the average total water consumption was 1813.27 million m^3. The temporal and spatial distribution of the runoffs of the major rivers (Wei River, Jing River, etc.) in Xi'an is uneven [49], and usually only

2% of the annual runoff occurs in February of the dry season, while 45–56% of the annual runoff occurs in the flood season [50]. The natural conditions and the rapid development of the social economy in Xi'an are bound to have a great impact on the development and utilization of the water resources. According to the calculation, in 2020, the per capita water resources of Xi'an were only 213 m^3, which were far lower than the per capita water resources of the whole country and of Shaanxi Province, and much lower than the critical value of 1000 m^3, which is internationally recognized as the standard that must be met for a region to maintain economic and social development. Xi'an is a city with extreme water shortages [48]. In this case, a quantitative analysis of the economic and social value of the water resources and the water-supply benefits in Xi'an will help to comprehensively understand the role of water resources in economic and social development, and to realize the sustainable management of water resources. The research on the economic and social value of water resources and water-supply benefits is not only one of the important means to realize the sustainable utilization of regional water resources, but it is also an important part of the sustainable development strategy.

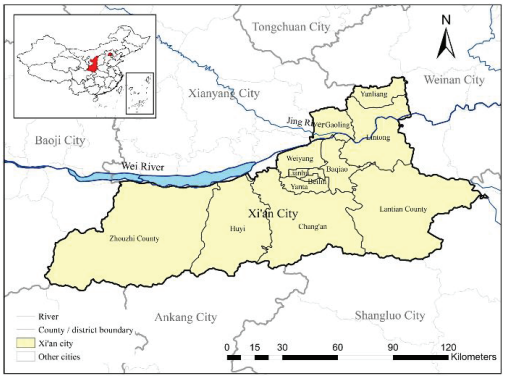

Figure 1. General situation of the study area.

The original data of the natural conditions and the water supply in Xi'an from 2014 to 2020, according to the "Xi'an Water Resources Bulletin (2014–2020)", are shown in Table 1.

Table 1. Raw data of Xi'an city from 2014 to 2020.

Items	2014	2015	2016	2017	2018	2019	2020
Area (10^9 m^2)	9.98 [1]	9.98 [1]	9.98 [1]	9.98 [1]	9.98 [1]	9.98 [1]	9.98 [1]
Rainfall (m)	0.701 [1]	0.691 [1]	0.572 [1]	0.764 [1]	0.583 [1]	0.705 [1]	0.733 [1]
Surface water (10^9 m^3)	1.73 [1]	1.71 [1]	1.42 [1]	2.03 [1]	1.80 [1]	2.36 [1]	2.276 [1]
Groundwater (10^9 m^3)	1.44 [1]	1.43 [1]	1.43 [1]	1.27 [1]	1.12 [1]	1.17 [1]	1.16 [1]
Industrial water supply (10^8 m^3)	4.17 [1]	4.21 [1]	4.24 [1]	4.35 [1]	4.41 [1]	4.45 [1]	2.07 [1]
Agricultural water supply (10^8 m^3)	6.39 [1]	6.59 [1]	6.64 [1]	6.66 [1]	6.49 [1]	5.52 [1]	5.80 [1]
Tertiary-industry water supply (10^8 m^3)	0.87 [1]	0.90 [1]	0.92 [1]	0.97 [1]	1.27 [1]	1.51 [1]	2.33 [1]
Domestic water supply (10^8 m^3)	4.12 [1]	4.25 [1]	4.09 [1]	4.19 [1]	4.32 [1]	4.35 [1]	4.59 [1]
Ecological water supply (10^8 m^3)	1.64 [1]	1.88 [1]	1.98 [1]	2.23 [1]	2.72 [1]	2.64 [1]	3.17 [1]

[1] The data come from the Xi'an Water Resources Bulletin (2014–2020).

2.2. Emergy Theory

Water resources have two attributes, which are, namely, the ecological attribute and the socioeconomic attribute. The water-resource ecosystem and the water-resource socioeconomic system are interrelated and blend with each other. They constitute a complex giant system, which is, namely, the water-resource eco-economic system. Therefore, in order to study the social and economic value of water resources, it is necessary to link the ecosystem with the socioeconomic system where the water resources exist, and to make a compre-

hensive analysis. The water-resource eco-economic system is shown in Figure 2, which describes, in detail, the flow of the different energies in the water-resource eco-economic system: the natural water body in the ecosystem contains the energy of renewable resources, such as solar energy, wind energy, earth-rotation energy, and rainwater energy. In order to make the natural water body flow into the socioeconomic system for use, it must be developed. The energy to be invested into the process of development includes human, material, and financial resources. The energy acts on the natural water and converts it into engineering water, which is then put into the socioeconomic system for production and social life.

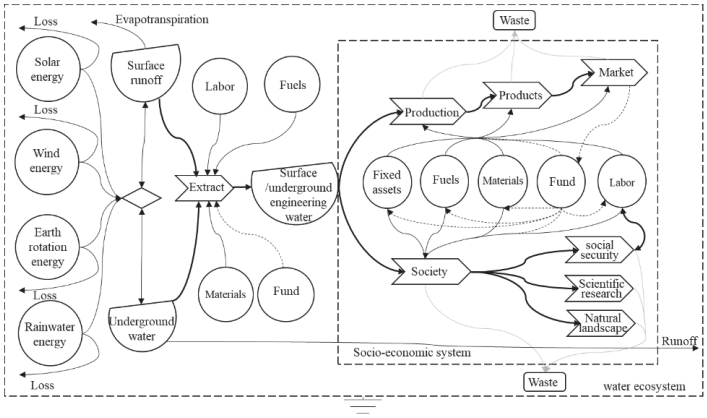

Figure 2. Water-resource eco-economic system.

However, because of the different properties of the different substances in nature and in human society, it is hard to create statistics and to make a comparison between them, which makes it more difficult to accurately measure the contribution value of the water resources to the social economy. Therefore, in order to solve this problem, this paper introduces emergy theory.

Emergy is defined as the amount of another kind of energy that is contained in a flowing or stored energy, which is the emergy of the energy [34]. It is generally believed that all energy comes from solar energy. Therefore, when calculating the emergy of each material, solar energy is often used as the benchmark to convert and measure the energy of other substances. The solar energy that is directly or indirectly needed to form a substance is the solar emergy of the substance, and the unit is solar emjoules (sej).

The calculation of the emergy of substances is shown in Equation (1) [34]:

$$EM = \tau_s \times Q, \tag{1}$$

In the equation, EM is the emergy of the substances, with the unit of sej; τ_s is the solar emergy transformity of the substances, with the unit of sej/j or sej/g; and Q is the energy or quality of the substances, with the unit of J or g.

The core of the conversion from material energy to material solar emergy is to choose the appropriate transformities and convert the raw data into the amount that is based on the solar emergy. Odum, Lan, and other scholars have obtained the solar emergy transformities of the main substances in the eco-economic system through a lot of research [33,34], which provides a solid foundation for the ecological and economic value accounting of water resources and the sustainability analysis of the ecological and economic system.

On the basis of emergy theory, this paper analyzes the emergy of the economic and social system in Xi'an from three parts. The first part is the raw-data-processing model. Through the model, the input and output materials in the economic and social system are transformed into energy for the subsequent calculation of the substances' emergies. The

second part is the multisource water-body-transformity model. For urban water supplies, the emergy transformity of natural water is not enough, and the emergy input in water conservancy projects should also be considered. Therefore, a water body should be divided into a natural water body (including rainfall) and an engineering water body. On this basis, the emergy transformities of the surface, or the underground natural water bodies, and the engineering water bodies are calculated, respectively, which provide a basis for analyzing the emergy input of the water resources in different systems. The third part is the benefit model of the economic and social water supply. The economic benefits of water resources include the water-supply benefits in industry, agriculture, and the tertiary industry, and the social benefits of water resources include social security benefits (domestic and employment security), entertainment benefits, and scientific research benefits. Therefore, by analyzing the input and output of the material emergy in economic and social systems, we can obtain the contribution rate of water resources, and we can further obtain the value of the water resources in each system, as well as the benefits of the urban economic and social water supply.

2.2.1. Raw-Data-Processing Model

The emergy analysis of the economic and social system is the quantitative analysis of the input and output of various material emergies into the economic and social system. The resources that are invested in the economic and social system include renewable resources and nonrenewable resources, and the outputs are mainly industrial products, agricultural products, social-labor-force recovery, scientific research papers, tourism income, etc. The quantity or energy of the inputs and outputs of these resources is the raw data that are needed for the emergy analysis. Then, according to Equation (1), the energy or quantity of the raw data is multiplied by the corresponding emergy transformity to obtain the emergy of the inputs and outputs. In the raw data, the calculations of the amounts of the main substances are shown in Equations (2)–(4):

$$E_s = A \times R_s, \tag{2}$$

In the equation, E_s is the solar energy, in the unit of J; A is the area of the study region, in the unit of m^2; and R_s is the annual average solar radiation, in the unit of J/(m^2·a).

The calculation of wind energy is shown in Equation (3):

$$E_w = H \times \rho_w \times \alpha \times SG \times A, \tag{3}$$

In the equation, E_w is the wind energy, in the unit of J; H is the height, using 1000 m; ρ_w is the wind density, using 1.23 kg/m^3; α is the eddy diffusion coefficient, in the unit of m^2/s; and SG is the wind-speed gradient, using 3.154×10^7 s/a.

The energy calculation of raw materials, fuels, and products is shown in Equation (4):

$$E = C \times \varepsilon, \tag{4}$$

In the equation, E is the energy of the substances, in the unit of J; C is the annual consumption or output of the substances, in the unit of g or t, respectively; and ε is the corresponding energy conversion coefficient [34], in the unit of J/g or J/t, respectively.

2.2.2. Multisource Water-Body-Transformity Model

According to the characteristics of the natural–artificial composite water cycle, the water body is divided into natural water (including rainfall) and engineering water. Natural water is surface water and groundwater that is formed through the precipitation hydrological process. Engineering water is the natural water after considering the investment of water conservancy projects. The specific calculations are as follows:

1. The natural-water-body-transformity model

The main source of natural water is natural rainfall, and its emergy transformity is calculated as shown in Equations (5)–(8):

$$\tau_k^N = EM_p / AW_k, \tag{5}$$

$$EM_p = CE_p \times \tau_p, \tag{6}$$

$$AW_k = W_k / U_k, \tag{7}$$

$$CE_p = P \times G \times A \times \rho, \tag{8}$$

In the equations, τ_k^N is the transformity of the natural water body, in the unit of sej/m^3; k = 1, 2, represent the surface and underground, respectively; EM_p is the annual total emergy of the precipitation in the catchment area, in the unit of sej; AW_k is the annual catchments of the natural water body, in the unit of m^3; CE_p is the chemical energy of the precipitation, in the unit of J; τ_p is the transformity of the chemical energy of the precipitation, using 18,200 sej/J [34]; W_k is the total amount of water, in the unit of m^3; U_k is the renewal period of the water body, using 0.03 a of surface water, and 100 a of groundwater; P is the average annual rainfall, in the unit of m; G is the Gibbs free energy of the rain, using 4.94 J/g [34]; and ρ is the density of the rainfall, using 1×10^6 g/m^3.

2. Engineering-water-body-transformity model

Engineering water is the natural water after considering the investment of water conservancy projects (including capital, labor, operation, and management costs, etc.), and the water body at this time contains the added value of the project investment. The calculation of the emergy transformity of an engineering water body is shown in Equation (9):

$$\tau_k^E = EMI_k / EW_k, \tag{9}$$

In the equation, τ_k^E is the transformity of the engineering water, with the unit of sej/m^3; EMI_k is the total emergy input of the water conservancy project, with the unit of sej; and EW_k is the amount of water that is affected by the project, with the unit of m^3.

2.2.3. Benefit Model of Economic and Social Water Supply

By analyzing the emergy of the input and output in the economic and social system, the contribution rate of water resources can be calculated, and then multiplied by the system output to obtain the water-supply benefit.

In the economic system, the related industries include agriculture, industry, and the tertiary industry. The input of each production system includes all kinds of renewable resources and nonrenewable resources, and the output is mainly the emergy of the products. Among them, according to the "Industry classification of national economy" (GB/T 4754-2011), the tertiary industry includes all kinds of service industries, including tourism, finance, catering, etc. Since the output of the tertiary industry is nonphysical output and cannot be measured by specific products, this paper uses the GDP of the tertiary industry instead for its approximate output.

Talcott Parsons, in his book *The Social System*, defined the social system as the composition of individual or group-interaction behaviors [51], which shows that human beings are the subject in the social system. From the perspective of the Marxist labor value theory, we should understand value in the practical relationship between the subject and the object, and we should regard value as the relationship between the attribute of the object and the needs of the subject, and as a certain meaning of object to subject. Therefore, value can be defined as the meaning of the existence, attribute, and development of the object to the subject's material and spiritual life in social practice [52]. It can be seen that the social value of water resources should be reflected in the satisfaction and benefits of maintaining people's quality of life and their social spiritual needs. This paper abstractly summarizes it as: social security benefits (maintaining people's quality of life), entertainment benefits, and

scientific research benefits (meeting social spiritual needs). Among them, the social security benefits of water resources can be abstracted into the benefits of domestic water supplies and employment security. By analyzing the input and output emergy in the domestic system, the benefits of the domestic water supply can be obtained. Since the inputs of food and nonfood in the domestic system maintain human life and health, the output of the domestic system can be abstracted as the value of the labor-force restoration, which can be calculated by the product of per capita disposable income and the Engel coefficient that can best reflect the people's quality of life [32]. Because the input and output of employment security, entertainment, and scientific research cannot be measured by material objects, the employment security benefits of water resources can be directly calculated by the number of water-related employees and the corresponding transformity. The benefits of entertainment and scientific research can be measured by the annual tourism income that is related to water and the number of relevant papers.

1. Water contribution rate (WCR_i)

The WCR_i is a relative index to measure the contribution of water resources to the total output of the system (i). It is the ratio of the water emergy input to the total emergy input in the system (i). (i = 1, 2, 3, and 4, respectively, represent industry, agriculture, the tertiary industry, and the domestic system. WCR_1, WCR_2, WCR_3, and WCR_4, respectively, represent the water contribution rates of industry, agriculture, the tertiary industry, and the domestic system). The calculations are shown in Equations (10) and (11):

$$WCR_i = WUE_i / EI_i, \tag{10}$$

$$EI_i = EM_i^r + EM_i^n, \tag{11}$$

In the equations, i = 1, 2, 3, and 4, respectively, for industry, agriculture, the tertiary industry, and the domestic system; WCR_i is the water contribution rate in the system (i), with the unit of %; WUE_i is the water emergy input into the system (i), with the unit of sej; EI_i is the total emergy input into the system (i), with the unit of sej; EM_i^r is the emergy input of the renewable resources into the system (i), including solar energy, wind energy, water resources, etc., with the unit of sej; EM_i^n is the emergy input of the nonrenewable resources in the system (i), including fuel, raw materials, fertilizer, labor, investment, food, nonfood household consumption, etc., with the unit of sej.

2. Water-supply-benefit model

The WCR_i is multiplied by the emergy output (EO_i) of the system (i), and it is then combined with the ratio of the emergy to the currency, and the water consumption of the system (i), the water-supply benefit (B_i), and unit-water-resource value (WRV_i) of the system (i) can be obtained, respectively. The calculations are shown in Equations (12)–(14):

$$M_i = WCR_i \times EO_i, \tag{12}$$

$$B_i = M_i / EDR, \tag{13}$$

$$WRV_i = B_i / WU_i, \tag{14}$$

In the equations, i = 1, 2, 3, and 4, respectively, for industry, agriculture, the tertiary industry, and the domestic system; M_i is the emergy value of the water resources in the system (i), with the unit of sej; B_i is the water-supply benefit in the system (i), with the unit of \$; WRV_i is the unit-water-resource value in the system (i), with the unit of \$/m^3; EO_i is the emergy output in the system (i), with the unit of sej; EDR is the ratio of the emergy to the currency, using 3.02×10^{12} sej/\$ [53]; and WU_i is the water consumption in the i system, with the unit of m^3.

As mentioned in Section 2.2.3, because the input and output of the employment security, entertainment, and scientific research cannot be measured by material objects, the employment security benefits of water resources can be directly calculated by the

number of water-related employees and the corresponding transformity. The benefits of entertainment and scientific research can be measured by the annual tourism income that is related to water and the number of relevant papers. The employment security benefits (B_5), entertainment benefits (B_6), and scientific research benefits (B_7) of water resources are shown in Equations (15)–(23):

$$M_5 = (N_1 + N_2) \times \tau_5, \tag{15}$$

$$B_5 = M_5/EDR, \tag{16}$$

$$WRV_5 = B_5/WU, \tag{17}$$

$$M_6 = B_6 \times EDR, \tag{18}$$

$$B_6 = I \times \mu, \tag{19}$$

$$WRV_6 = B_6/WU_5, \tag{20}$$

$$M_7 = T \times P \times \tau_7, \tag{21}$$

$$B_7 = M_7/EDR, \tag{22}$$

$$WRV_7 = B_7/WU, \tag{23}$$

In the equations, M_5 is the employment security value of the water resources, with the unit of sej. B_5 is the employment security benefit of the water resources, with the unit of \$. WRV_5 is the employment security value of the unit water, with the unit of \$/m^3. M_6 is the entertainment value of the water resources, with the unit of sej. B_6 is the entertainment benefit of the water resources, with the unit of \$. WRV_6 is the entertainment value of the unit water, with the unit of \$/m^3. M_7 is the scientific research value of the water resources, with the unit of sej. B_7 is the scientific research benefit of the water resources, with the unit of \$. WRV_7 is the scientific research value of the unit water, with the unit of \$/m^3. N_1 is the number of employees in the agriculture, forestry, animal husbandry, and fishery industries. N_2 is the number of employees in the water conservancy industry. τ_5 is the transformity of the human labor force, using 1.74×10^{15} sej/person/year [33]. WU is the total water consumption of the society's economy and ecology, with the unit of m^3. I is the annual tourism income, with the unit of \$. μ is the proportion of water-related tourism resources in all of the tourism resources in Xi'an, using 1.3%. WU_5 is the ecological water consumption, with the unit of m^3. T is the number of academic papers that are related to water that have been published. P is the average number of pages per paper, using 6 pages. τ_7 is the transformity of the academic papers, using 3.39×10^{15} sej/p [54].

3. Results

3.1. Raw Data Processing

The raw data of the inputs and outputs in the economic and social system in Xi'an from 2014 to 2020 were collected. Most of these data are in tons, but the corresponding transformity unit is usually sej/j. Therefore, it is necessary to convert the units of these data into joules for the subsequent emergy calculation. (The emergy transformity units of some substances are given in sej/t, so the raw data of these substances do not need to be processed.)

Taking the industrial system in 2019 as an example, the energy of the substances in the system can be calculated according to Equations (2)–(4), as is shown in Table 2.

Table 2. Data-processing results.

Items	C [1]	Unit	ε (unit/J) [2]	E (J)
Raw coal and other fuels	1.70×10^7	t	2.09×10^{10}	3.56×10^{17}
Edible oil	3.70×10^{10}	t	2.03×10^5	7.63×10^{15}
Generating capacity	1.55×10^{10}	kw·h	3.60×10^6	5.58×10^{16}
Crude-oil-processing capacity	2.34×10^7	t	4.18×10^{10}	9.79×10^{17}
Gasoline and other fuel oils	2.32×10^7	t	4.18×10^{10}	9.70×10^{17}

[1] The data come from the Xi'an Statistical Yearbook. [2] Adapted with permission from Ref. [34]. 1995, John Wiley and Sons

3.2. Natural- and Engineering-Water-Body Transformities

To facilitate the calculation, the natural water is summarized as the surface water and the groundwater, and the transformity of the natural water and the engineering water from 2014 to 2020 are calculated, respectively.

Taking 2019 as an example, according to Table 1 and Equations (5)–(8), the chemical energy of the rainwater (CE_p), the precipitation emergy (EM_P), the annual catchments of natural water (AW_k), and the transformity of natural water (τ_k^N) can be calculated in turn. (k = 1, 2, represent the surface and underground, respectively).

However, in order to study the engineering-water-body transformity, it is necessary to clarify the emergy input of the water conservancy project. By the end of 2019, 92 reservoirs, 49 hydropower stations, 101 pumping stations, 27 sluice projects, and 133,957 electro-mechanical wells had been built in Xi'an city. Because it is not realistic to calculate the emergy transformity of the engineering water body of each water conservancy project one by one, the surface water and groundwater projects are simplified into reservoirs, pumping stations, and water-diversion works. Because of the lack of information about the construction, operation, and management costs of each project, this paper refers to the analysis in [54] (i.e., the cost of the reservoirs, pumping stations, and water-diversion works are 0.178 \$/m^3, 0.038 \$/m^3, and 0.045 \$/m^3, respectively). The emergy of the cost with the unit of sej/m^3 can be obtained by multiplying the cost by the emergy currency ratio (EDR). Since the engineering water is the natural water after considering the investment of the water conservancy projects, the cost emergy plus the natural water transformity can obtain the engineering water transformity (τ_k^E).

The calculation results of the natural and engineering water transformities in Xi'an from 2014 to 2020 are shown in Table 3.

Table 3. Transformities of natural water and engineering water in Xi'an.

Years	CE_p (10^{16} J)	EM_P (10^{20} sej)	AW_1 (10^{10} m^3)	AW_2 (10^7 m^3)	τ_1^N (10^9 sej/m^3)	τ_2^N (10^{13} sej/m^3)	τ_1^E (10^{11} sej/m^3)	τ_2^E (10^{13} sej/m^3)
2014	3.46	5.34	5.75	1.44	9.29	3.70	7.06	3.72
2015	3.41	5.27	5.68	1.43	9.27	3.69	7.06	3.72
2016	2.82	4.35	4.70	1.43	9.28	3.05	7.06	3.08
2017	3.77	5.82	6.74	1.27	8.64	4.58	7.05	4.60
2018	2.88	4.44	5.97	1.12	7.44	3.97	7.04	3.99
2019	3.48	5.37	7.82	1.17	6.87	4.58	7.03	4.61
2020	3.61	5.58	5.18	1.08	10.78	5.19	6.86	5.21

3.3. Benefits of Economic and Social Water Supply in Xi'an

3.3.1. Benefits of Economic Water Supply in Xi'an

The industrial, agricultural, and tertiary industries are mainly considered for the economic water supply in Xi'an. Taking the industrial system of Xi'an in 2019 as an example, according to Equation (1), the emergy of the substances in the system can be obtained by multiplying the raw data of the substances by the corresponding emergy transformity. The calculation is shown in Table 4.

Table 4. Emergy input and output of Xi'an industrial system in 2019.

	Items	Substances	Raw Data	Unit	Transformity (sej/Unit)	Emergy (sej)	Transformity References
Input	Renewable resources	Solar	6.07×10^{19} [1]	J	1	6.07×10^{19}	Odum [34]
		Wind	8.43×10^{16} [1]	J	623	5.25×10^{19}	Odum [34]
		Industrial water (Surface)	2.50×10^{8} [2]	m^3	6.82×10^{11}	1.70×10^{20}	This study
		Industrial water (Underground)	1.95×10^{8} [2]	m^3	4.61×10^{13}	9.01×10^{21}	This study
	Nonrenewable resources [3]	Raw coal and other fuels	3.56×10^{17} [3]	J	4.00×10^{4}	1.42×10^{22}	Odum [34]
		Raw materials	1.39×10^{10} [3]	$	3.02×10^{12}	4.19×10^{22}	Li [53]
		Labor	1.75×10^{10} [3]	$	3.02×10^{12}	5.29×10^{22}	Li [53]
		Fixed assets	2.20×10^{10} [3]	$	3.02×10^{12}	6.65×10^{22}	Li [53]
	Total input					1.849×10^{23}	
Output	Industrial products [3]	Edible oil	7.63×10^{15} [3]	J	8.60×10^{4}	6.56×10^{20}	Lan [33]
		Generating capacity	5.58×10^{16} [3]	J	1.60×10^{5}	8.93×10^{21}	Odum [34]
		Chemical pesticide	1.30×10^{3} [3]	t	1.62×10^{15}	2.11×10^{18}	Odum [34]
		Plastic	2.76×10^{5} [3]	t	3.80×10^{14}	1.05×10^{20}	Odum [34]
		Steels	3.15×10^{5} [3]	t	1.78×10^{15}	5.61×10^{20}	Lv [54]
		Glass	2.15×10^{4} [3]	t	8.40×10^{14}	1.81×10^{19}	Lv [54]
		Aluminum	2.11×10^{4} [3]	t	1.60×10^{16}	3.38×10^{20}	Lv [54]
		Cement	2.76×10^{6} [3]	t	1.98×10^{15}	5.46×10^{21}	Lv [54]
		Wheatmeal	4.40×10^{5} [3]	t	8.30×10^{4}	3.65×10^{10}	Odum [34]
		Dairy products	7.26×10^{5} [3]	t	1.71×10^{6}	1.24×10^{12}	Lan [33]
		Tap-water production	6.52×10^{8} [3]	m^3	3.89×10^{13}	2.54×10^{22}	Lv [54]
		Meat	7.83×10^{4} [3]	t	1.70×10^{6}	1.33×10^{11}	Lan [33]
		Chemicals and detergents	7.00×10^{5} [3]	t	1.00×10^{15}	7.00×10^{20}	Lv [54]
		Silicon	1.21×10^{4} [3]	t	1.60×10^{16}	1.93×10^{20}	Lv [54]
		Paper Products	1.25×10^{5} [3]	t	3.90×10^{15}	4.86×10^{20}	Wang [55]
		Mechanical products	8.75×10^{4} [3]	t	6.70×10^{15}	5.86×10^{20}	Lv [54]
		Crude-oil-processing capacity	9.79×10^{17} [3]	J	5.40×10^{4}	5.29×10^{22}	Odum [34]
		Gasoline and other fuel oils	9.70×10^{17} [3]	J	6.60×10^{4}	6.40×10^{22}	Odum [34]
		Wood processing and furniture manufacturing	1.01×10^{9} [3]	$	3.02×10^{12}	3.05×10^{21}	Li [55]
		Transportation equipment	1.12×10^{10} [3]	$	3.02×10^{12}	3.38×10^{22}	Li [55]
	Total output					1.972×10^{23}	

[1] The data are calculated according to Equations (2) and (3). [2] The data come from the Xi'an Water Resources Bulletin (2019). [3] The raw data come from the Xi'an Statistical Yearbook (2019).

Similarly, the emergy input and output of the industrial system from 2014 to 2020 can be obtained, as shown in Figures 3 and 4.

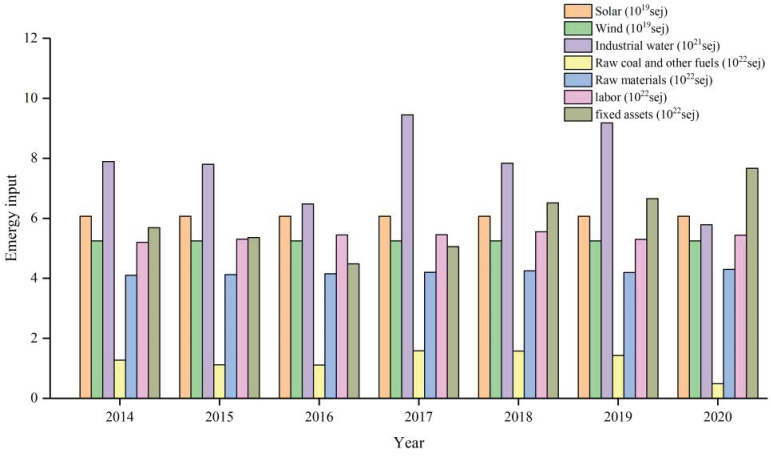

Figure 3. Emergy input of industrial system from 2014 to 2020.

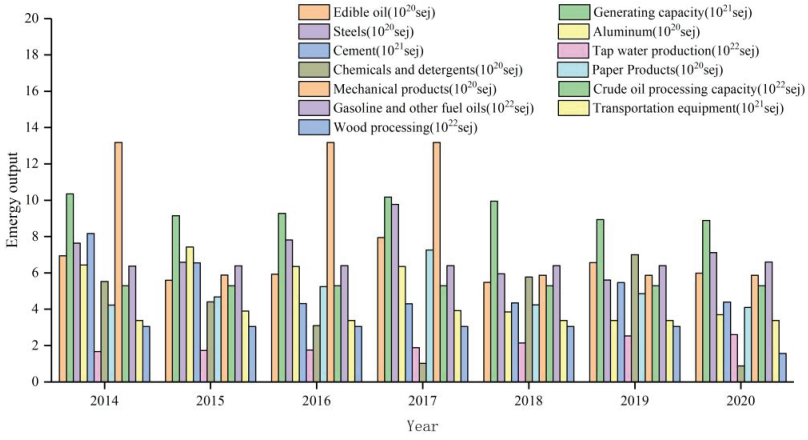

Figure 4. Main emergy output of industrial system from 2014 to 2020.

According to Tables 1 and 4, Figures 3 and 4, and Equations (10)–(13), the EI_1, EO_1, WCR_1, B_1, and WRV_1 in the industrial system from 2014 to 2020 can be calculated, as shown in Table 5.

Table 5. Benefits of industrial water supply in Xi'an from 2014 to 2020.

Item	2014	2015	2016	2017	2018	2019	2020
EI_1 (10^{20} sej)	1724.45	1675.04	1572.9	1708.32	1836.84	1849.15	1822.61
EO_1 (10^{20} sej)	1935.21	1954.67	1892.2	1974.19	1930.67	1971.6	1946.20
WUE_1 (10^{20} sej)	78.96	78.04	64.84	94.52	78.4	91.84	57.85
WCR_1 (%)	4.58	4.66	4.12	5.53	4.26	4.96	3.17
EDR (10^{12} sej/$)	3.02	3.02	3.02	3.02	3.02	3.02	3.02
WU_1 (10^8 m^3)	4.17	4.21	4.24	4.35	4.41	4.45	2.07
B_1 ($10^9$$)	2.93	3.01	2.58	3.61	2.73	3.24	2.05
WRV_1 ($/$m^3$)	7.03	7.16	6.09	8.32	6.18	7.28	9.88

From 2014 to 2020, in the Xi'an agricultural and tertiary industry systems, the emergy input (EI_2, EI_3), the emergy output (EO_2, EO_3), the water contribution rate (WCR_2, WCR_3), the water-supply benefit (B_2, B_3), and the unit-water-resource value (WRV_2, WRV_3) are calculated, in turn, with reference to the industrial system. The results are shown in Tables 6 and 7.

Table 6. Benefits of agricultural water supply in Xi'an from 2014 to 2020.

Item	2014	2015	2016	2017	2018	2019	2020
EI_2 (10^{20} sej)	387.34	410.78	359.98	470.27	437.36	408.45	392.81
EO_2 (10^{20} sej)	99.31	98.80	102.57	113.43	109.96	112.82	117.72
WUE_2 (10^{20} sej)	208.64	214.65	179.40	268.94	227.38	222.86	265.02
WCR_2 (%)	53.87	52.26	49.84	57.19	51.99	54.56	67.47
EDR (10^{12} sej/$)	3.02	3.02	3.02	3.02	3.02	3.02	3.02
WU_2 (10^8 m^3)	6.39	6.59	6.64	6.66	6.49	5.52	5.80
B_2 ($10^9$$)	1.77	1.71	1.69	2.15	1.89	2.04	2.63
WRV_2 ($/$m^3$)	2.77	2.60	2.55	3.22	2.92	3.70	4.53

3.3.2. Benefits of Social Water Supply in Xi'an

In the social system, the WCR_4, B_4, WRV_4, B_5, WRV_5, B_6, WRV_6, B_7, and WRV_7 from 2014 to 2020 in Xi'an are calculated according to Equations (10)–(23). The results are shown in Tables 8 and 9. The raw data required for the calculation are from the Xi'an Statistical Yearbook (2014–2020) and the Water Resources Bulletin (2014–2020).

Table 7. Water-supply benefits of the tertiary industry in Xi'an from 2014 to 2020.

Item	2014	2015	2016	2017	2018	2019	2020
EI_3 (10^{20} sej)	2298.81	1995.00	2157.09	2556.25	2707.13	2761.68	3116.04
EO_3 (10^{20} sej)	1574.46	2198.64	1977.32	2298.57	2619.36	2917.16	3106.75
WUE_3 (10^{20} sej)	17.28	17.70	15.08	22.69	25.02	34.22	54.96
WCR_3 (%)	0.75	0.89	0.70	0.89	0.92	1.24	1.76
EDR (10^{12} sej/$)	3.02	3.02	3.02	3.02	3.02	3.02	3.02
WU_3 (10^8 m^3)	0.87	0.90	0.92	0.97	1.27	1.51	2.33
B_3 ($10^9$$)	0.39	0.65	0.46	0.68	0.80	1.20	1.81
WRV_3 ($/$m^3$)	4.50	7.18	4.97	6.98	6.30	7.95	7.80

Table 8. Benefits of domestic water supply in Xi'an from 2014 to 2020.

Item	2014	2015	2016	2017	2018	2019	2020
EI_4 (10^{15} sej per person)	9.23	10.27	10.65	11.42	11.60	12.56	11.72
Disposable income of residents (10^{16} sej per person)	1.25	1.36	1.46	1.59	1.53	1.66	1.74
Engel coefficient (%)	33.25	32.45	28.10	28.35	25.75	26.10	28.05
WUE_4 (10^{14} sej per person)	9.03	9.05	7.08	9.47	7.82	8.78	8.45
WCR_4 (%)	9.78	8.81	6.65	8.30	6.74	6.99	7.21
EDR (10^{12} sej/$)	3.02	3.02	3.02	3.02	3.02	3.02	3.02
WU_4 (10^8 m^3)	4.12	4.25	4.09	4.19	4.32	4.35	4.59
B_4 ($10^9$$)	1.16	1.12	0.80	1.19	0.88	1.02	1.51
WRV_4 ($/$m^3$)	2.81	2.63	1.95	2.84	2.04	2.35	3.29

Table 9. Employment security, entertainment, scientific research value of water resources in Xi'an from 2014 to 2020.

Item	2014	2015	2016	2017	2018	2019	2020
N_1 (10^4 person)	105.02	107.68	105.13	113.17	101.25	101.37	99.97
N_2 (10^4 person)	3.11	2.61	2.9	3.29	3.64	3.83	3.58
Tourism income ($10^{10}$$)	1.48	1.68	1.90	2.55	3.99	4.92	2.94
μ (%)	1.30	1.30	1.30	1.30	1.30	1.30	1.30
WU_5 (10^8 m^3)	1.64	1.88	1.98	2.23	2.72	2.64	3.17
WU (10^9 m^3)	1.63	1.69	1.70	1.74	1.80	1.70	1.56
EDR (10^{12} sej/$)	3.02	3.02	3.02	3.02	3.02	3.02	3.02
B_5 ($10^8$$)	6.22	6.34	6.21	6.70	6.03	6.05	5.95
B_6 ($10^8$$)	1.93	2.18	2.47	3.32	5.19	6.39	3.82
B_7 ($10^4$$)	12.12	9.43	9.43	14.14	10.78	16.84	33.00
WRV_5 ($/$m^3$)	0.38	0.38	0.37	0.38	0.34	0.36	0.38
WRV_6 ($/$m^3$)	1.18	1.16	1.24	1.49	1.90	2.42	1.21
WRV_7 ($/$m^3$)	0.000074	0.000056	0.000056	0.000081	0.000060	0.000099	0.00021

4. Discussion

4.1. Inputs and Outputs in Economic System

1. Input and output in industrial system

It can be seen from Table 5 that, in the industrial system of Xi'an, from 2014 to 2020, the WCR_1 was the largest in 2017, accounting for 5.53%, and the corresponding EO_1 and B_1 were also the largest, accounting for 1974.19×10^{20} sej and $3.61 \times 10^9$$, respectively. The trend comparison between the WCR_1 and the EO_1 is shown in Figure 5a. The average WCR_1 and the average contribution rates of the other main inputs of the industrial system are shown in Figure 5b.

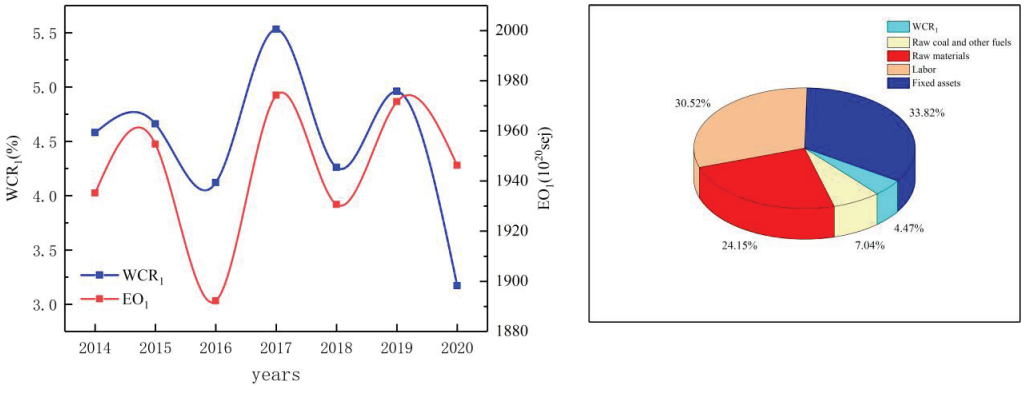

(**a**) (**b**)

Figure 5. (**a**) Trends of WCR_1 and EO_1; (**b**) average contribution rates of main inputs in industrial system.

It can be seen from Figure 5a,b that, in the industrial system, compared to the other inputs, although the WCR_1 was small, the EO_1 was still affected by it, and the two are positively correlated with each other. The Pearson correlation coefficient (ρ) is the most commonly used linear correlation coefficient: $\rho \in [0.4, 0.6]$ is a medium positive correlation, $\rho \in [0.6, 0.8]$ is a strong positive correlation, and $\rho \in [0.8, 1.0]$ is a very strong positive correlation. After calculation, the Pearson correlation coefficient (ρ_1) between the WCR_1 and the EO_1 in the industrial system from 2014 to 2020 is 0.52, which is a medium positive correlation, which indicates that there is a certain degree of waste of water resources in industrial production, and that there is still room for improvement in the water-use efficiency. In order to further improve the utilization efficiency of industrial water resources, we should continue to strengthen the management of industrial water, vigorously develop water-saving technology, and actively streamline the production process.

2. Input and output in agricultural system

It can be seen from Table 6 that, in the agricultural system, from 2014 to 2020, the input of the water resources accounted for a large proportion. Moreover, the WCR_2 reached more than 50% in most years, which is mainly because the growth of the crops largely depended on the water supply. The trend comparison between the WCR_2 and the EO_2 is shown in Figure 6a. The average WCR_2 and the average contribution rates of the other main inputs of the agricultural system are shown in Figure 6b.

It can be seen from Figure 6a,b that, in the agricultural system, compared to the other inputs, the input of the water resources accounted for the largest proportion, and the changing trends of the WCR_2 and the EO_2 were basically the same. After calculation, the Pearson correlation coefficient (ρ_2) between the WCR_2 and the EO_2 is 0.72, which is a strong positive correlation. This shows that the output of agriculture, as the largest water user, is greatly affected by water resources.

3. Input and output in tertiary-industry system

It can be seen from Table 7 that, in the tertiary-industry system, from 2014 to 2020, the input of the water resources was very small, and the WCR_3 in each year was only about 1.0%. The trend comparison of the WCR_3 and the EO_3 is shown in Figure 7a, and the average WCR_3 and the average contribution rates of the other main inputs of the tertiary-industry system are shown in Figure 7b.

It can be seen from Figure 7a,b that, in the tertiary industry, compared to the other inputs, although the WCR_3 was very small, the changes between the WCR_3 and the EO_3 tended to be consistent, and the latter was obviously affected by the former. After calcula-

tion, the Pearson correlation coefficient (ρ_3) between the WCR_3 and the EO_3 is 0.85, which is a very strong positive correlation.

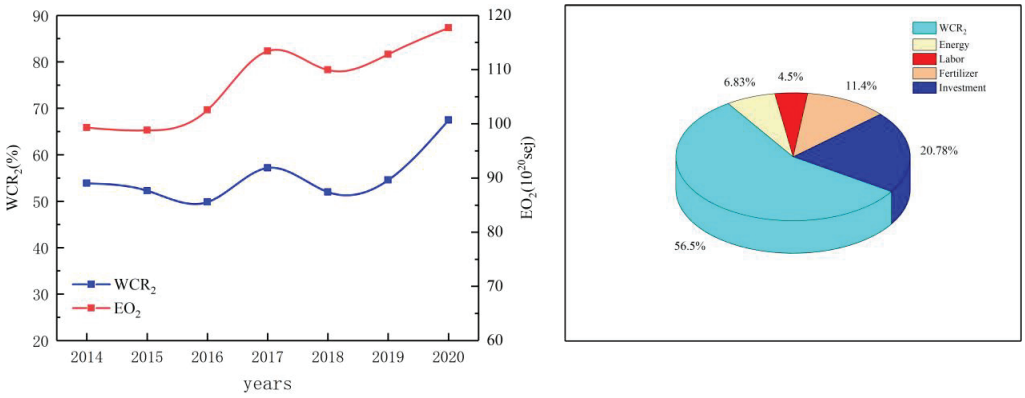

(**a**) (**b**)

Figure 6. (**a**) Trends of WCR_2 and EO_2; (**b**) average contribution rates of main inputs in agricultural system.

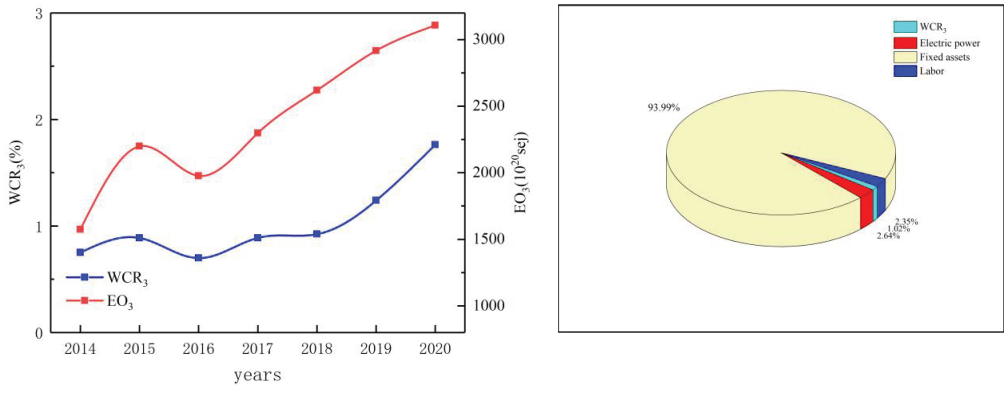

(**a**) (**b**)

Figure 7. (**a**) Trends of WCR_3 and EO_3; (**b**) average contribution rates of main inputs in tertiary industry.

4.2. Inputs and Outputs in Social System

In the social system, the social value generated by water resources is mainly reflected in the satisfaction and benefits in people's lives, health, and spiritual pursuits. The output of the water-resource social system includes the labor-force restoration of the residents, the water-related employees, the water-related tourism income, and scientific research papers. The input of the system mainly includes water resources, food, food services, nonfood consumption, etc. It can be seen from Tables 8 and 9 that, in the social system, the B_4 was greater than the B_5, and far greater than the B_6 and the B_7. This also shows that water resources, as the basic resources for human survival, played a significant role in social security and affected people's life quality, to a large extent. Among the many tourism resources, the investment in water-related tourism resources in Xi'an was very small from 2014 to 2020, accounting for only 1.3% of all the tourism resources, which led to low entertainment benefits from the water resources.

4.3. Differences in Water-Supply Benefits among Industries

The water-supply benefits and the unit-water value in the economic and social system are shown in Figure 8a,b. It can be seen from Figure 8 that there were obvious differences in the water-supply benefits and the unit-water-resource values in different industries in Xi'an from 2014 to 2020. In terms of the water-supply benefits: $B_1 > B_2 > B_4 > B_3 > B_5 > B_6 > B_7$. In terms of the unit-water-resource values: $WRV_1 > WRV_3 > WRV_2 > WRV_4 > WRV_6 > WRV_5 > WRV_7$. This was mainly because the output of the industrial system was much greater than that of other systems, and the socioeconomic value of the water resources mainly came from industrial production. This trend was also in line with the law of the market economy in most cities. It can be seen that the socioeconomic benefits of the water resources mainly came from industrial production. In the economic system and the social system, although the water-supply benefits fluctuated slightly in the study period, they showed an upward trend as a whole. Because of the vigorous development of the tertiary industry in recent years, its market share has become larger and larger, which has far exceeded that of industry and agriculture. Therefore, even if the B_3 was small because of the small WCR_3, the WRV_3 was second only to the WRV_1, and it had an increasing trend year by year.

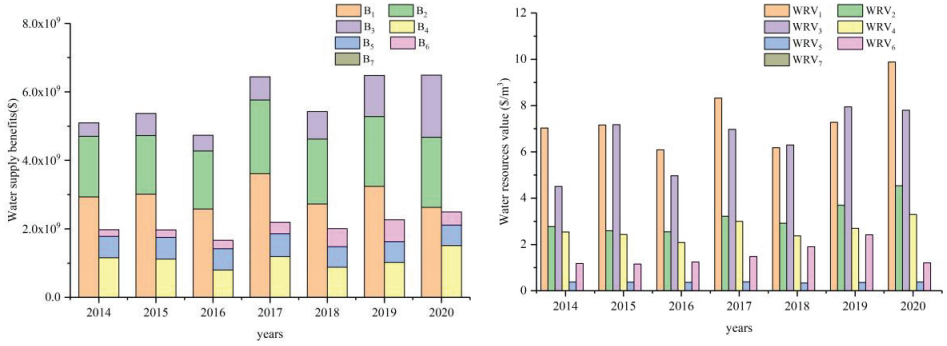

Figure 8. The benefits and values of water resources in economic and social system: (**a**) water-supply benefits among industries; (**b**) unit-water-resource values among industries.

The American scholars D'Odorico and Paolo et al. [56] define the value of irrigation water resources as the added value of the crop yield that is affected by irrigation ($/m^3), and they measured the value of the irrigation water of different crops in the world (0.1 $/m^3–1.2 $/m^3). The Chinese scholars Wei Wang et al. [57] calculated the shadow price of the industrial water resources in China's provinces by using the dual model of the non-radial distance function, and the average price in Shaanxi Province was 3.31 $/m^3. When measuring the value of irrigation water and industrial water, they did not comprehensively consider the value of the natural water and engineering water, and so the result was too small. By using emergy theory, this paper considers both the natural-water value and the engineering-water value, and it considers the sources of the water resources (surface and underground) separately, which are obviously more accurate. In addition, when analyzing the output of the industrial system, Wei Wang et al. only considered the industrial GDP and did not consider the industrial products themselves, which may also lead to the undervaluation of the industrial products. The Korean scholars Won-Seok Lee et al. [22] measured the economic benefits of water for social life through the conditional valuation method (CVM). This method focuses on evaluating the nonmarket value of resources, and it has strong subjectivity, which can easily affect the reliability of the results because of internal deviation. By contrast, the emergy method that is used in this paper takes into account the market value (domestic-water-supply value) and nonmarket value (employment security,

entertainment, and scientific research value) of the social water use, and the evaluation process is more comprehensive and objective.

5. Conclusions

This paper makes up for the defects of the current commonly used water-resource-value evaluation methods, such as the models of shadow price, marginal benefit, and cost–benefit, which fail to combine the ecological and socioeconomic attributes of water resources, and to quantify the input and output of the energy, material, and money in the eco-economic system uniformly. On the basis of emergy theory, this paper analyzes the emergy flow of the economic and social systems in Xi'an from 2014 to 2020, constructs an urban water-supply-benefit model, systematically evaluates the unit-water-resource value and water-supply benefits in various industries, and discusses the results. The conclusions are as follows:

1. The dependence of industrial production on the water resources in Xi'an from 2014 to 2020 was relatively stable. Compared to other industries, the B_1 and the WRV_1 were the largest, and the socioeconomic value of the water resources mainly came from industrial production. In the industrial system, the WCR_1 and the EO_1 have a medium positive correlation with each other, and ρ_1 was 0.52, which still has room for improvement, compared to ρ_2 and ρ_3. It can be seen that there might be a certain degree of waste of industrial water. The government should further strengthen the specification of the industrial water, vigorously develop water-saving technology, and actively streamline the production process, so as to improve the water-use efficiency and obtain greater B_1 and total benefits;
2. Compared to other industries, the input of the water resources into the agricultural system in Xi'an from 2014 to 2020 was the largest, and the agricultural production was extremely dependent on the water supply. However, the B_2 and the WRV_2 were lower than the B_1 and the WRV_1, which were related to the different character of the water-use sector, and this phenomenon was in line with the law of the market economy. There was a strong positive correlation between the WCR_2 and the EO_2 ($\rho_2 = 0.72$), which indicates that, in the agricultural system, the WCR_2 closely affects the EO_2. The more water resources that are input into a certain range, the greater the B_2 and total benefits will be;
3. In the tertiary industry, although the B_3 was small because of the small WCR_3, the WRV_3 was second only to industry and it had an increasing trend year by year, and there was a very strong positive correlation between the WCR_3 and the EO_3 ($\rho_3 = 0.85$); all showed high levels of water-use efficiency;
4. In the social system, the B_4 and the WRV_4 were the largest, mainly because water resources, as an indispensable basic resource for human life, not only affect people's quality of life, to a great extent, but are also the decisive factor for the development of people's lives, and they play a significant role in social security;
5. There were obvious differences in the benefits and the value of the water resources among various industries. The industrial water supply had the greatest benefits and unit-water value, followed by agriculture, the domestic system, the tertiary industry, and others. Therefore, it is very important to accurately evaluate the value and benefits of water resources in industries, which can be used not only as a reference for the government to formulate water prices, but also to help the relevant departments coordinate and alleviate the water contradiction between various industries and allocate water resources reasonably.

The innovation of this paper lies in the following:

1. With regard to the water-resource ecosystem and the socioeconomic system as a whole: building an ecological and socioeconomic composite network of water resources, showing the process of energy circulation and flow, and providing a research basis for the value accounting of water resources;

2. On the basis of emergy theory, the basic framework and model of the urban socioeconomic water-supply-benefit and water-resource-value research are put forward. This enriches the research methods for the water-resource value;
3. On the basis of the basic principle of the emergy transformity calculation, by analyzing the energy change in the process of the water-resource circulation, the water body is divided into the natural water body and the engineering water body, which further refines the emergy calculation process and solves the problem of how to measure the emergy transformity of multisource water bodies in the emergy calculation.

To sum up, at present, the value accounting of the water resources in China is mainly from the perspective of economics, and it uses currency to measure its value. Currency is the product of the social economy. It does not circulate through nature and it cannot reflect the essence and laws of nature. Therefore, the real value of water resources cannot be directly measured by currency. The accounting system of the economic and social water-supply benefits that is based on the emergy theory that is proposed in this paper unifies the dimensions of the different substances in the natural system and in the socioeconomic system, explores the real value of water resources with both socioeconomic and natural attributes, makes up for the defect that the current economic accounting system does not include natural factors, and is of scientific significance to improving the value theory of water resources. It also provides new ideas for the unification of the economic value and the social value of water resources, the rational allocation and pricing of water resources, and the sustainable utilization of regional water resources.

However, because of the interdependence and overlapping between social systems and economic systems, the problem of double calculation may inevitably occur when using emergy theory to analyze the energy flow of each system. How to overcome this problem needs further research.

Author Contributions: Conceptualization, Z.G. and N.W.; methodology, Z.G. and N.W.; software, Z.G. and X.M.; validation, Z.G., S.L. and L.Y.; formal analysis, Z.G.; investigation, Z.G. and X.M.; resources, Z.G.; data curation, X.K.; writing—original draft preparation, Z.G.; writing—review and editing, Z.G.; visualization, Z.G.; supervision, N.W.; project administration, N.W. All authors have read and agreed to the published version of the manuscript.

Funding: This research was funded by the National Natural Science Foundation of China (Grant No. 51979221), by the Natural Science Basic Research Program of Shaanxi (Program No. 2021JLM-45), and by the Natural Science Basic Research Program of Shaanxi Province (Grant No. 2019JLZ-15).

Institutional Review Board Statement: Not applicable.

Informed Consent Statement: Not applicable.

Data Availability Statement: Not applicable.

Conflicts of Interest: The authors declare no conflict of interest.

References

1. Guan, X.; Jiang, P.; Meng, Y.; Qin, H.; Lv, H. Study on Production, Domestic and Ecological Benefits of Reservoir Water Supply Based on Emergy Analysis. *Processes* **2020**, *8*, 1435. [CrossRef]
2. Meng, B.; Liu, J.L.; Bao, K.; Sun, B. Water fluxes of Nenjiang River Basin with ecological network analysis: Conflict and coordination between agricultural development and wetland restoration. *J. Clean. Prod.* **2019**, *213*, 933–943. [CrossRef]
3. Yao, L.M.; Zhao, L.; Pan, L.; Chen, X.D. Optimal water resource allocation based on stability—Considering the correlation between water consumption and output value in different industries. *Water Supply* **2020**, *20*, 2499–2513. [CrossRef]
4. Li, J.Y.; Cui, L.B.; Dou, M.; Ali, A. Water resources allocation model based on ecological priority in the arid region. *Environ. Res.* **2021**, *199*, 111201. [CrossRef]
5. Shen, X.J.; Wu, X.; Xie, X.M.; Wei, C.J.; Li, L.Q.; Zhang, J.J. Synergetic Theory-Based Water Resource Allocation Model. *Water Resour. Manag.* **2021**, *35*, 2053–2078. [CrossRef]
6. Bierkens, M.F.P.; Reinhard, S.; de Bruijn, J.A.; Veninga, W.; Wada, Y. The Shadow Price of Irrigation Water in Major Groundwater-Depleting Countries. *Water Resour. Res.* **2019**, *55*, 4266–4287. [CrossRef]
7. Liu, X.L.; Chen, X.K.; Wang, S.Y. Evaluating and Predicting Shadow Prices of Water Resources in China and Its Nine Major River Basins. *Water Resour. Manag.* **2009**, *23*, 1467–1478. [CrossRef]

8. Qin, C.H.; Gan, H.; Zhang, X.J.; Jia, L. Research on water resources pricing method and practiceII: Analysis of water price in Haihe River Basin. *J. Hydraul. Eng.* **2012**, *43*, 429–436. [CrossRef]
9. Shen, X.B.; Lin, B.Q. The shadow prices and demand elasticities of agricultural water in China: A StoNED-based analysis. *Resour. Conserv. Recycl.* **2017**, *127*, 21–28. [CrossRef]
10. Tang, Y.; Song, X.F.; Ma, Y.; Zhang, Y.H.; Yang, L.H.; Han, D.M.; Pu, H.M. Study on water resources value in the intake area of the South-to-North water diversion project based on water resources optimization. *South North Water Transf. Water Sci. Technol.* **2018**, *16*, 6. [CrossRef]
11. Alcon, F.; Martin-Ortega, J.; Pedrero, F.; Alarcon, J.J.; de Miguel, M.D. Incorporating Non-market Benefits of Reclaimed Water into Cost-Benefit Analysis: A Case Study of Irrigated Mandarin Crops in southern Spain. *Water Resour. Manag.* **2013**, *27*, 1809–1820. [CrossRef]
12. Arborea, S.; Giannoccaro, G.; de Gennaro, B.C.; Iacobellis, V.; Piccinni, A.F. Cost-Benefit Analysis of Wastewater Reuse in Puglia, Southern Italy. *Water* **2017**, *9*, 175. [CrossRef]
13. Arena, C.; Genco, M.; Mazzola, M.R. Environmental Benefits and Economical Sustainability of Urban Wastewater Reuse for Irrigation-A Cost-Benefit Analysis of an Existing Reuse Project in Puglia, Italy. *Water* **2020**, *12*, 2926. [CrossRef]
14. Ward, F.A. Economics in integrated water management. *Environ. Model. Softw.* **2009**, *24*, 948–958. [CrossRef]
15. Dallman, S.; Chaudhry, A.M.; Muleta, M.K.; Lee, J. The Value of Rain: Benefit-Cost Analysis of Rainwater Harvesting Systems. *Water Resour. Manag.* **2016**, *30*, 4415–4428. [CrossRef]
16. Dallman, S.; Chaudhry, A.M.; Muleta, M.K.; Lee, J. Is Rainwater Harvesting Worthwhile? A Benefit-Cost Analysis. *J. Water Resour. Plan. Manag.* **2021**, *147*, 04021011. [CrossRef]
17. Zuo, J.B.; Liu, C.M.; Zheng, H.X. Cost-benefit analysis for urban rainwater harvesting in Beijing. *Water Int.* **2010**, *35*, 195–209. [CrossRef]
18. Downing, J.A.; Polasky, S.; Olmstead, S.M.; Newbold, S.C. Protecting local water quality has global benefits. *Nat. Commun.* **2021**, *12*, 2709. [CrossRef]
19. Ma, M.S.; Zhao, M. Research on an Improved Economic Value Estimation Model for Crop Irrigation Water in Arid Areas: From the Perspective of Water-Crop Sustainable Development. *Sustainability* **2019**, *11*, 1207. [CrossRef]
20. Sun, L.N.; Lu, W.X.; Yang, Q.C.; Martin, J.D.; Li, D. Ecological Compensation Estimation of Soil and Water Conservation Based on Cost-Benefit Analysis. *Water Resour. Manag.* **2013**, *27*, 2709–2727. [CrossRef]
21. Genius, M.; Hatzaki, E.; Kouromichelaki, E.M.; Kouvakis, G.; Nikiforaki, S.; Tsagarakis, K.P. Evaluating Consumers' Willingness to Pay for Improved Potable Water Quality and Quantity. *Water Resour. Manag.* **2008**, *22*, 1825–1834. [CrossRef]
22. Lee, W.S.; Yoo, S.H.; Kim, J. Measuring the Economic Benefits of the Tap Water Supply Service in Urban Areas: The Case of Korea. *Water Resour. Manag.* **2013**, *27*, 619–627. [CrossRef]
23. Loomis, J.; Santiago, L. Economic Valuation of Beach Quality Improvements: Comparing Incremental Attribute Values Estimated from Two Stated Preference Valuation Methods. *Coast. Manag.* **2013**, *41*, 75–86. [CrossRef]
24. Mumbi, A.W.; Watanabe, T. Cost Estimations of Water Pollution for the Adoption of Suitable Water Treatment Technology. *Sustainability* **2022**, *14*, 649. [CrossRef]
25. Xu, F.; Baoligao, B.; Jia, J. Benefits of Xin'an River Water Resources and Ecological Compensation. *Adv. Mater. Res.* **2015**, *1073*, 1660–1663. [CrossRef]
26. Dijk, D.V.; Siber, R.; Brouwer, R.; Logar, I.; Sanadgol, D. Valuing water resources in Switzerland using a hedonic price model. *Water Resour. Res.* **2016**, *52*, 3510–3526. [CrossRef]
27. Chi, Y.; Xue, L.; Zhang, H. Comprehensive benefit analysis of regional water resources based on multi-objective evaluation. *IOP Conf. Ser. Earth Environ. Sci.* **2018**, *108*, 032040. [CrossRef]
28. Wang, Y.X.; Cheng, L.; Tian, H.L.; Liu, X.H. Water supply eco-economic benefit evaluation of middle route of south-to-north water diversion project in Hebei Water-recipient Area. *IOP Conf. Ser. Earth Environ. Sci.* **2018**, *191*, 012064. [CrossRef]
29. Cheng, B.; Li, H.E.; Yue, S.Y.; Huang, K. A conceptual decision-making for the ecological base flow of rivers considering the economic value of ecosystem services of rivers in water shortage area of Northwest China. *J. Hydrol.* **2019**, *578*, 124126. [CrossRef]
30. Yue, S.Y.; Li, H.E.; Cheng, B.; Gao, Z.Y. The Value of Environmental Base Flow in Water-Scarce Basins: A Case Study of Wei River Basin, Northwest China. *Water* **2018**, *10*, 848. [CrossRef]
31. Di, D.; Wu, Z.; Guo, X.; Lv, C.; Wang, H. Value Stream Analysis and Emergy Evaluation of the Water Resource Eco-Economic System in the Yellow River Basin. *Water* **2019**, *11*, 710. [CrossRef]
32. Wu, Z.; Di, D.; Lv, C.; Guo, X.; Wang, H. Defining and evaluating the social value of regional water resources in terms of emergy. *Water Policy* **2018**, *21*, 7390. [CrossRef]
33. Lan, S.F.; Qin, P.; Lu, H.F. *Emergy Analysis of Ecological-Economic System*; Chemical Industry Press: Beijing, China, 2002.
34. Odum, H.T. *Environmental Accounting: Emergy and Environmental Decision Making*; John Wiley & Sons: New York, NY, USA, 1996.
35. Liu, G.Y.; Casazza, M.; Hao, Y.; Zhang, Y.; Ulgiati, S. Emergy analysis of urban domestic water metabolism: A case study in Beijing (China). *J. Clean. Prod.* **2019**, *234*, 714–724. [CrossRef]
36. Paoli, C.; Vassallo, P.; Dapueto, G.; Fanciulli, G.; Massa, F.; Venturini, S.; Povero, P. The economic revenues and the emergy costs of cruise tourism. *J. Clean. Prod.* **2017**, *166*, 1462–1478. [CrossRef]
37. Kocjancic, T.; Debeljak, M.; Zgajnar, J.; Juvancic, L. Incorporation of emergy into multiple-criteria decision analysis for sustainable and resilient structure of dairy farms in Slovenia. *Agric. Syst.* **2018**, *164*, 71–83. [CrossRef]

38. Zhang, J.X.; Ma, L. Environmental Sustainability Assessment of a New Sewage Treatment Plant in China Based on Infrastructure Construction and Operation Phases Emergy Analysis. *Water* **2020**, *12*, 484. [CrossRef]
39. Zhang, X.H.; Shen, J.M.; Wang, Y.Q.; Qi, Y.; Liao, W.J.; Shui, W.; Li, L.; Qi, H.; Yu, X.Y. An environmental sustainability assessment of China's cement industry based on emergy. *Ecol. Indic.* **2017**, *72*, 452–458. [CrossRef]
40. Zhong, S.Z.; Geng, Y.; Kong, H.N.; Liu, B.; Tian, X.; Chen, W.; Qian, Y.Y.; Ulgiati, S. Emergy-based sustainability evaluation of Erhai Lake Basin in China. *J. Clean. Prod.* **2018**, *178*, 142–153. [CrossRef]
41. Winfrey, B.K.; Tilley, D.R. An emergy-based treatment sustainability index for evaluating waste treatment systems. *J. Clean. Prod.* **2016**, *112*, 4485–4496. [CrossRef]
42. Shah, S.M.; Liu, G.Y.; Yang, Q.; Casazza, M.; Agostinho, F.; Giannetti, B.F. Sustainability assessment of agriculture production systems in Pakistan: A provincial-scale energy-based evaluation. *Ecol. Model.* **2021**, *455*, 109654. [CrossRef]
43. Pan, H.Y.; Zhuang, M.F.; Geng, Y.; Wu, F.; Dong, H.J. Emergy-based ecological footprint analysis for a mega-city: The dynamic changes of Shanghai. *J. Clean. Prod.* **2019**, *210*, 552–562. [CrossRef]
44. Peng, W.J.; Wang, X.M.; Li, X.K.; He, C.C. Sustainability evaluation based on the emergy ecological footprint method: A case study of Qingdao, China, from 2004 to 2014. *Ecol. Indic.* **2018**, *85*, 1249–1261. [CrossRef]
45. Jaklic, T.; Juvancic, L.; Kavcic, S.; Debeljak, M. Complementarity of socio-economic and emergy evaluation of agricultural production systems: The case of Slovenian dairy sector. *Ecol. Econ.* **2014**, *107*, 469–481. [CrossRef]
46. Ali, M.; Marvuglia, A.; Geng, Y.; Robins, D.; Pan, H.Y.; Song, X.Q.; Yu, Z.J.; Sun, H.P. Accounting emergy-based sustainability of crops production in India and Pakistan over first decade of the 21st century. *J. Clean. Prod.* **2019**, *207*, 111–122. [CrossRef]
47. Viglia, S.; Civitillo, D.F.; Cacciapuoti, G.; Ulgiati, S. Indicators of environmental loading and sustainability of urban systems. An emergy-based environmental footprint. *Ecol. Indic.* **2018**, *94*, 82–99. [CrossRef]
48. Yang, Z.Y.; Song, J.X.; Cheng, D.D.; Xia, J.; Li, Q.; Ahamad, M.I. Comprehensive evaluation and scenario simulation for the water resources carrying capacity in Xi'an city, China. *J. Environ. Manag.* **2019**, *230*, 221–233. [CrossRef] [PubMed]
49. Wang, B. *Study on the Effective Usage of Urban Water Resources of Xi'an City*; Chang'an University: Xi'an, China, 2015.
50. Liu, J.Y.; Li, J.; Gao, Z.Y.; Yang, M.; Qin, K.Y.; Yang, X.A. Ecosystem Services Insights into Water Resources Management in China: A Case of Xi'an City. *Int. J. Environ. Res. Public Health* **2016**, *13*, 1169. [CrossRef]
51. Parsons, T. *The Social System*; Pyschology Press: New York, NY, USA, 1991.
52. Tang, J.R. *Ecological Economics*; Chemical Industry Press: Beijing, China, 2005.
53. Li, H.E.; Xu, M.M.; Zhao, Y. Study on river ecological base flow value and its changes during the year based on emergy method. *Ecol. Econ.* **2017**, *33*, 160–164.
54. Lv, C.; Wu, Z. Emergy analysis of regional water ecological–economic system. *Ecol. Eng.* **2009**, *35*, 703–710. [CrossRef]
55. Wang, L.F.; Zhou, Y.; Xie, W.T.; Dong, W.G. Emergy Analysis on Contribution of Water Resources to Eco-economic System: A Case Study of Xi'an. *Value Eng.* **2017**, *36*, 10–14. [CrossRef]
56. D'Odorico, P.; Chiarelli, D.D.; Rosa, L.; Bini, A.; Zilberman, D.; Rulli, M.C. The global value of water in agriculture. *Dep. Agric. Resour. Econ. UC Berkeley Work. Pap. Ser.* **2020**, *117*, 21985–21993. [CrossRef] [PubMed]
57. Wang, W.; Xie, H.; Zhang, N.; Xiang, D. Sustainable water use and water shadow price in China's urban industry. *Resour. Conserv. Recycl.* **2016**, *128*, 489–498. [CrossRef]

water

MDPI

Article

A Flood Risk Management Model to Identify Optimal Defence Policies in Coastal Areas Considering Uncertainties in Climate Projections

Francesco Cioffi [1,*], Alessandro De Bonis Trapella [1], Mario Giannini [1] and Upmanu Lall [2]

[1] DICEA—Dipartimento di Ingegneria Civile, Edile ed Ambientale, Università di Roma 'La Sapienza', 00184 Rome, Italy; alessandro.debonistrapella@uniroma1.it (A.D.B.T.); mario.giannini@uniroma1.it (M.G.)
[2] Department of Earth an Environmental al Engineering, Columbia University, New York, NY 10027, USA; ula2@columbia.edu
* Correspondence: francesco.cioffi@uniroma1.it; Tel.: +39-064-991-2228

Abstract: Coastal areas are particularly vulnerable to flooding from heavy rainfall, sea storm surge, or a combination of the two. Recent studies project higher intensity and frequency of heavy rains, and progressive sea level rise continuing over the next decades. Pre-emptive and optimal flood defense policies that adaptively address climate change are needed. However, future climate projections have significant uncertainty due to multiple factors: (a) future CO_2 emission scenarios; (b) uncertainties in climate modelling; (c) discount factor changes due to market fluctuations; (d) uncertain migration and population growth dynamics. Here, a methodology is proposed to identify the optimal design and timing of flood defense structures in which uncertainties in 21st century climate projections are explicitly considered probabilistically. A multi-objective optimization model is developed to minimize both the cost of the flood defence infrastructure system and the flooding hydraulic risk expressed by Expected Annual Damage (EAD). The decision variables of the multi-objective optimization problem are the size of defence system and the timing of implementation. The model accounts for the joint probability density functions of extreme rainfall, storm surge and sea level rise, as well as the damages, which are determined dynamically by the defence system state considering the probability and consequences of system failure, using a water depth–damage curve related to the land use (Corine Land Cover); water depth due to flooding are calculated by hydraulic model. A new dominant sorting genetic algorithm (NSGAII) is used to solve the multi-objective problem optimization. A case study is presented for the Pontina Plain (Lazio Italy), a coastal region, originally a swamp reclaimed about a hundred years ago, that is rich in urban centers and farms. A set of optimal adaptation policies, quantifying size and timing of flood defence constructions for different climate scenarios and belonging to the Pareto curve obtained by the NSGAII are identified for such a case study to mitigate the risk of flooding and to aid decision makers.

Keywords: climate change; multi-objective optimization; coastal region; pumping plant; flooding

Citation: Cioffi, F.; De Bonis Trapella, A.; Giannini, M.; Lall, U. A Flood Risk Management Model to Identify Optimal Defence Policies in Coastal Areas Considering Uncertainties in Climate Projections. *Water* **2022**, *14*, 1481. https://doi.org/10.3390/w14091481

Academic Editors: Alban Kuriqi and Luis Garrote

Received: 8 March 2022
Accepted: 19 April 2022
Published: 5 May 2022

1. Introduction

Flooding due to extreme weather-related events hitting coastal regions has caused devastating damage worldwide in recent decades [1,2]. The negative impacts of these events could worsen in the coming decades due to the rapid anthropogenic development of coastal areas, and due to climate change. The population density in coastal areas is expected to increase by 25% by 2050 [3]. Furthermore, future climate projections indicate that coastal regions will be faced with a general increase in the average sea level, as well as an intensification of extreme meteorological phenomena that can increase the frequency and/or intensity of flooding [4–6]. Thus, flood protection policies to reduce vulnerability and exposition of coastal areas and to adapt to above mentioned future changes [7,8] are necessary. In April 2013, the European Union formally adopted the Adaptation to Climate

Change Strategy, in which the principles, guidelines and objectives of the Community policy on adaptation to climate change were defined. Despite the importance of the issue, methodologies and approaches for long-term planning of adaptation policies are very challenging since they should be able to identify the best adaptation solutions to adopt and their right timing given uncertain future climate scenarios.

1.1. Source of Uncertainty in Climate Projections

There are different sources of uncertainty in future climate projections. First, although different possible mitigation pathways have been hypothesized as Representative Concentration Pathways (RCP) in CMIP5 or Share Social-economic Pathway (SSP) in CMIP6 [9], there is no assessment of the relative likelihood of these scenarios. This is often considered a deep uncertainty. A second source of uncertainty is due to the different characteristics of Global Climate Models (GCMs). Initial condition, parametric and structural uncertainties affect the GCM simulations which represent climate evolution trajectories that can differ significantly even for the same mitigation scenario [10]. To overcome that problem, an ensemble of models is employed to offer a probabilistic representation of climate projections. Third, in order to explore possible adaptation policies at local or regional scales, the trends of the hydrological variables such as temperature, rainfall or sea level rise need to be projected at a finer spatial resolution than that provided by GCMs. Due to the coarse spatial resolution of GCMs, these hydrological variables are usually biased. For instance, in CMIP5 GCMs, oceanographic processes are simulated with a horizontal resolution coarser than 1 degree of latitude and longitude. This resolution is not sufficient to represent bathymetry variation affecting local processes like coastal currents [11], or small-scale processes like eddies [12]. Furthermore, structural errors in models of the sea level components are probable, as well as, systematic bias caused by missing processes and/or feedback. Ref. [13]. Bias correction methods are also usually adopted to correct daily or monthly rainfall amount projections by GCMs and downscaling methods are used to obtain rainfall projections at finer spatial scale. Both methods add further uncertainties that may be unquantifiable [14–16]. Finally, natural variability at decadal or bidecadal scales, could dominate the climate trends and makes the identification of adaptation policies timing very difficult [17]. All these sources of uncertainty are illustrated in Figure 1.

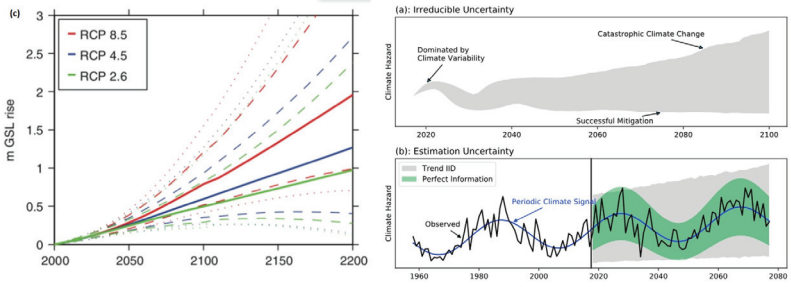

Figure 1. Uncertainties in climate projection due to (**a**) future CO_2 emission scenarios; [18] (**b**) uncertainties in climate modelling; (**c**) long period natural cycle [8].

1.2. Metodology Approaches to Adaptation Action Identification

In the literature, a number of methodologies for the identification and the assessment of adaptive actions and works to cope with hydraulic risks in coastal areas under climate change have been proposed in the past [19–21]. Among the approaches which explicitly take into account the elements of uncertainty due to climate change are the resilience "bottom-up" approach [22] and the predictive "top-down" approach which is the most used.

Bottom-up approaches do not necessary need climate projections by GCMs. Examples of bottom-up approaches include the policy tipping point [23] and the dynamic adaptive policy pathways [24]. The dynamic adaptive policy pathways method developed by [24]

combines some elements of Adaptive Policymaking [25], and Adaptation Pathways [26] methods, like adaptation tipping point, i.e., the point when a particular action is no longer adequate and that triggers a specific condition that requires a new action or plane change. These approaches do not seek to identify the optimal sequence of adaptation actions and their timing.

Top-down methods use climate projections by GCMs as inputs for designing adaptation strategies which might enhance resilience or reduce vulnerability of specific geographic areas to climate change [20,27,28]. Specifically, for coastal areas, [29] developed a top-down type model that integrates multi-objective optimization algorithms and a tree-like decision-making scheme in order to provide the optimal strategy to cope sea level rising. The tree-like scheme coupled with a genetic algorithm evaluates the costs associated with each intervention and the flood risk. The decision tree shows the intervention measures at each planning horizon time step if a threshold value is reached based on the future sea level projections.

The identification of adaptation measure timing provides relevant information which could significantly improve the planning process, and lead to a more efficient use of the economic resource to cope the adverse effects of climate changes. Moreover, approaches should able to schedule the best adaptation actions timing in case of sudden or abrupt climate changes [30].

1.3. The Proposal

In order to address these latter issues, i.e., the need to identify design and timing of defence constructions taking into account the uncertainties in climate projections, including abrupt changes of climate forcing, we propose a multi-objective optimization approach (similar to [29,31]) which integrates hydraulic modelling for simulating flooding and its consequences, in which the timing of the adaptive actions is taken into account among the decision variables of the optimization problem and uncertainties in climate projections are integrated into the definition of objective functions. Multiobjective optimization approach was chosen on the basis of similar considerations as those proposed [29]. Multiobjective optimization methods allows decision makers to choose the preferred solutions among a set (Pareto-optimal set) of trade-off solutions, for example those relative to natural habitat conservation, which can't be easily expressed in monetary terms [32]. In the present paper, the multi-objective optimization model relies on the definition of two optimality criteria: minimizing the cost of the flood defence infrastructure system and the flooding hydraulic risk for the entire period of climate projections. The formalization of the last optimality criteria, i.e., the hydraulic risk associated to flooding events, relies on the definition of the Expected Annual Damage (EAD) [33]. The EAD accounts for the joint probability density functions of extreme rainfall, storm surge and sea level rise, and the corresponding damages, for a given defence system state identified by the water depth–damage curve related to the land use (CORINE Land Cover) [1]).The uncertainties in future climate projections are treated through time varying probability density functions (Pdf) and are used to compute the EAD. A hydraulic model for the assessment of damage is integrated within the multi-objective optimization algorithm (non-dominated sorting genetic algorithm 2, NSGAII [34]). A case study is presented for the Pontina Plain (Lazio Italy), a coastal region, originally a swamp reclaimed about a hundred years ago, that is rich in urban centers and farms. A set of optimal adaptation policies, belonging to the Pareto curve calculated by the NSGAII, to mitigate the risk of flooding and to aid decision makers are identified for such a case study.

2. Methods

A sketch of the model system is shown in Figure 2. Figure 2 synthetized methodology and related algorithms aimed to identify the size and timing of flood defence constructions to cope with sea level rise, as well as, extreme rainfall regime modification due to climate change. The methodology considers a multi-objective optimization problem, in which both hydraulic risk due flooding and construction costs of flood defence system are minimized

for the entire period of climate projections. Hydraulic models are used to calculate the hydraulic variables necessary to the flood damage assessment as a functions of climate forcings and of the state of flood defence systems, taking into account uncertainties in climate projections. Figure 2 also describes decision variables of the multi-objective optimization problem as well as the input ones.

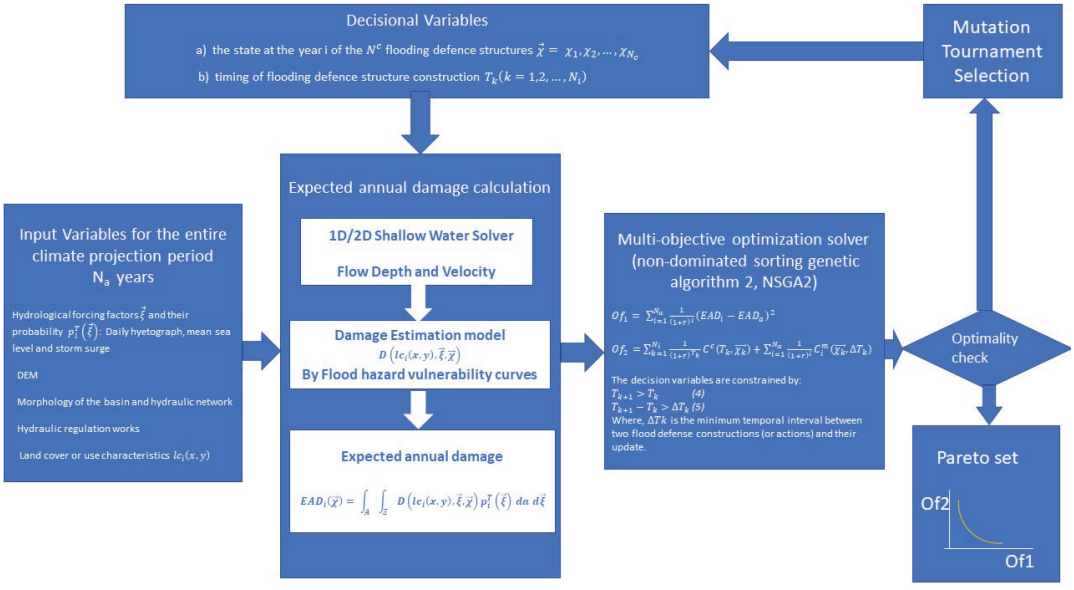

Figure 2. Sketch of model system.

2.1. Multi-Objective Optimization Problem Formalization

Two optimization criteria are defined: (a) minimization of hydraulic risk associated to hydrological extremes for the entire climate projection period; (b) minimization of the cost of the adaptation actions for the same period. Adaptation actions consists of flood defence constructions, as levees, flood retention basins, spillway canals, other actions aimed to reduce exposition to hydraulic risk as for instance retreat strategies [35]. Objective functions for the two optimization criteria are formalized as:

$$Of_1 = \sum_{i=1}^{N_a} \left(\frac{1}{(1+r_d)^i} EAD_i - EAD_a\right)^2 \tag{1}$$

$$Of_2 = \sum_{k=1}^{N_i} \frac{1}{(1+r_c)^{T_k}} C^c + (T_k + \vec{\chi_k}) + \sum_{i=1}^{N_a} \frac{1}{(1+r_c)^i} C_i^m(\vec{\chi_k} + \Delta T_k) \tag{2}$$

The flooding hydraulic risk objective function Equation (1) is constructed with reference to the concept of Expected Annual Damage (EAD). The EAD can be expressed as the integral of the probability of not exceeding certain dangerous events, multiplied by the consequences of the event [36]:

$$EAD_i(\vec{\chi}) = \int_A \int_E D(l_{c_i}(x,y), \vec{\xi}, \vec{\chi}) p_i^T(\vec{\xi})\, da\, d\vec{\xi} \tag{3}$$

where $D(l_{c_i}(x,y), \vec{\xi}, \vec{\chi})$ is the damage depending on: (a) land cover or use characteristics $l_{c_i}(x,y)$ being x, y the coordinate of a generic point of the domain representing the region considered; (b) the probability density $p_i^T(\vec{\xi})$ at the i-th year of the N^c hydrological forcing

factors $\overrightarrow{\xi} = \overrightarrow{\xi_1}, \overrightarrow{\xi_2}, \ldots, \overrightarrow{\xi_{N_c}}$, potentially able to cause flooding; (c) the state at the year i of the N^D flooding defence structures $\overrightarrow{\chi} = \overrightarrow{\chi_1}, \overrightarrow{\chi_2}, \ldots, \overrightarrow{\chi_{N^D}}$. The EAD accounts both the probability density function of the forcing hydrological factors and the damage due to flooding associated with them depending on the intensity of extreme events and of the state of flood defence structures. In Equation (1), EAD_i is Expected Annual Damage ($i = 1, 2, \ldots, N_a$), N_a the number of the years of climate projection, r_d and r_c are discount rates related to the first and second objective function respectively, EAD_a the Acceptable Expected Annual Damage. We define as acceptable EAD_a as the maximum value of EAD that a community can tolerate, in relation to its exposition, vulnerability and hazard. In principle EAD_a should be equal to zero, i.e., a community would not want suffer any kind of damage due to flooding. But since zero risk is unrealistic, a community can bear exceptionally flooding producing limited damage to things or building, no casualties and so on. In this sense the acceptable EAD_a could be thought as a reference acceptable target for the community, not varying in time. The formalization of the Of_1 in Equation (1), therefore is a metric representing the distance from such target. The formalization of Of_1 by Equation (1) is rather general and could also be used for defining other objective functions including those related to assess of intangible damage or related to environmental quality or natural habitat targets which can't easily expressed in monetary terms [31]. In Equation (2) C^c is the cost of the N^D flood defence constructions and other adaptive actions $\overrightarrow{\chi} = \overrightarrow{\chi_1}, \overrightarrow{\chi_2}, \ldots \overrightarrow{\chi_{N_D}}$, at the time $T_k (k = 1, 2, \ldots, N_i)$ where N_i number of horizon times in which the climate projection period is divided , C_m^i is the annual maintenance costs of the flood defense constructions depending on the type of flood defence adopted, and the timing between two succeeding constructions. $\Delta T_k = T_k - T_{k-1}$. In the multi-objective problem formalized in Equations (1)–(3), $\overrightarrow{\chi} = \overrightarrow{\chi}_1, \overrightarrow{\chi}_2, \ldots \overrightarrow{\chi_{N_D}}$ and $T_K (K = 1, 2, \ldots, N_i)$ are the decision variables, $l_{c_i}(x, y)$ are the state variables, $\overrightarrow{\xi}$ and $p_i^T(\overrightarrow{\xi})$ are the input variables. The decision variables are constrained by:

$$T_{k+1} > T_k \tag{4}$$

$$T_{k+1} - T_k > \Delta T_{min} \tag{5}$$

where, ΔT_{min} is the minimum temporal interval between two flood defence constructions (or actions) and their update. We also impose that once a construction is realized at the time T_k it can't remove at the time T_{k+1} but only update if necessary, except for the case in which flood defences can be destroyed by the occurrence of a large event as, for instance, that able to produce an overflow of levees. In the latter case the cost the entire reconstruction of flood defence is taken into account. The other decision variables are also included within an interval of reasonableness, for instance the increase of the embankments will be selected within an predefined range from 0 to a maximum levee crest height.

The probability $p_i^T(\overrightarrow{\xi})$ in Equation (3) is a resulting probability density function that accounts for the probability density of each forcing factor $\xi_j (j = 1, 2, \ldots N_c)$ as well as the changes in probability functions of the forcing factors associated to the ensemble of GCMs simulations within a for each future climate scenarios. If the forcing factors are mutually independent, for a single climate scenario, the probability density function is given by the product of probability of every single event. If the forcing factors are not independent, a different methodology could be used to account for the dependence among the different forcing factors, e.g., bivariate point process method [37]. Furthermore, the probability density function for an ensemble of GCM simulations, as well as the likelihood of different RCP or SSP climatic scenarios have to be taken into account in the definition of $p_i^T(\overrightarrow{\xi})$. This allows one to include the uncertainties of future emission scenarios, as well as those in climate modeling.

2.1.1. Discount Rates

In Equations (1) and (2) two different discount rates r_d and r_c are considered. In the context of climate change policy making, they are very important in understanding how

much society today should invest in trying to protect vulnerable areas, limiting the impacts of climate change later in the future [38]. Depending on the context, discount rates can assume different meanings [39]. In the specific case proposed in the present study, r_d in Equation (1) is as a measure of the relative importance of negative consequences produced by flood events in term of hydraulic risk occurring at different points in time. It therefore can be thought as how we weight risks due to future events within an intergenerational pact. Higher is r_d, lower is our hydraulic risk assessment at future times for the same hydrological event; r_d equal zero is equivalent to assume a temporal independence of hydraulic risk assessment.

The discount rate r_c in Equation (2), that is related to the flood defence construction costs, depends on general condition of economy in a more close relation with the market dynamics. Since our formulation of the multi-objective problem allows to formalize the objective functions in different measurement units, eventually incommensurable, the distinction between the two discount rates appears to be appropriate. Furthermore it allows a more flexible approach to the problem.

2.1.2. Damage Assesment

The term $D(l_{c_i}(x,y), \overrightarrow{\xi}, \overrightarrow{\chi})$ in Equation (3) accounts for the damage due to inundation depending on the state of land cover and the defence constructions, and on the entity of forcing factors. The damage $D(l_{c_i}(x,y), \overrightarrow{\xi}, \overrightarrow{\chi})$ is estimated as follows. The direct damage associated with the physical impacts of a hazard is estimated by unit damage functions or Stage-Damage functions, which are conceptually similar to the fragility curves used in other disciplines. In the event of flooding, the damage functions are determined by the use of a specific relationship between the characteristics of flood and the extent of the economic damage referred to a specific type of asset exposed [40]. The procedure for estimating direct damage has 3 components: (1) The characteristics of the assets exposed through the analysis of the information on land use by satellite data [41]; (2) the characteristics of the flood represented by depth and extension of the flooding: (3) the combination of the (1) and (2) with the depth curve-damage in order to stimulate the extent of the damage with respect to the value of the exposed asset. Vulnerability and exposure of each point of the considered region is featured by the term $l_{c_i}(x,y)$ which is assumed to change from year to year as a consequence of modification of land use or increase/decrease of urbanization or population. The physical characteristics of the territory and the value of vulnerable assets (1) are represented by the digital terrain model (DTM) and by the satellite land use data (CORINE Land Cover), respectively. The extent and depth of the flooding were obtained by numerical hydraulic simulations, for given rainfall intensities and sea levels. The data thus obtained are translated into a damage index or the percentage of the value of the asset that is lost, through the depth-damage curves [42]. Several countries have developed standardized methods for estimating flood damage. An example is the HAZUS methodology developed in the USA [43], the guidelines for cost-benefit analysis (CBA) developed in the UK [44], and Australia (Bureau of Transport Economics, 2001). The model we chose was HAZUS as it provides an estimate of a large variety of damages, direct and indirect. For each calculation cell of 100 m^2, the damage constitutes in the value in Euro of the damage caused by type of asset according to the depth of the flooding.

2.1.3. Hydraulic Models

Flood damage assessment requires knowledge of the hydraulic characteristics of the flooding—water depth, flow velocity, flooding persistence. These are obtained by hydraulic simulations forced by direct application of rainfall, as well as, boundary conditions due to storm surge and sea level rise. In this paper, for the study case, two different hydraulic models are used: (a) a 2D hydraulic model, the USACE Hydrologic Engineering Center's River Analysis System (HEC-RAS 5.0.7); (b) a fast simplified hydraulic model. The first model is a public domain software that meets the minimum requirements of National Flood Insurance Program as required by FEMA (https://www.fema.gov/hydraulic-numerical-models-

meeting-minimum-requirement-national-flood-insurance-program). A recent FEMA report (https://www.fema.gov/media-library-data/1561469561757-6fed6a4fd077673f684920b9ad5a0e53/RapidResponseFloodModelingFinalReport.pdf) shows that the model produces results with higher precision (standard deviation) and predictive value (correlation) than other models.

The equations in HEC-RAS are solved using an implicit Finite Volume algorithm. This algorithm allows the use of a structured or unstructured computational mesh. Local thickening of computational mesh can be applied by breaklines, added along levees, buildings, roads, and in abrupt slope change. One of the advantages of using HEC-RAS is the possibility to simulate the presence of gates, pumping stations, and other hydraulic devices for flow maneuver. For very large domains, the 2D HEC-RAS code can be coupled with HEC-HMS which is a physically based and conceptually semi-distributed model designed to simulate rainfall-runoff processes to provide flood hydrographs generated externally from the 2D integration domain.The fast simplified hydraulic model [45] models the hydraulic network and the flooplain using three elements: the main river hydraulic networks, the storage areas representing the basins, and the ideal channels connecting the storage areas to points of the rivers belonging to the hydraulic network. The 1D Saint-Venant equations are used to simulate the flow along the rivers which belong to the hydraulic networks. The temporal trend of water level over the storage areas is calculated by the continuity equation, which is a function of the flows entering or going out from the ideal channels and of the rainfall amount directly falling over the area.

2.1.4. Flood Defence Construction and Maintenance Costs

To evaluate the objective function expressed by Equation (2) construction and maintenance costs of flood protection structures have to be evaluated. Such costs include the construction of fill, columns, flood walls, levees, and flood shields or closures, as well as, that of auxiliary materials and activities that are required to assure that the primary flood proofing elements function properly. Examples are the cost for providing access to buildings on fill, or interior drainage for areas enclosed by levees or floodwalls. We considered two kind of works: levees in the most critical zones of the hydraulic network, and the creation of flood expansion areas ruled by weirs. In order to estimate the costs of raising the banks, reference is made to the study conducted by [46], which estimate between 4.5–12.4 million Euros per km of length and per meter of raising the embankment in rural areas. In the present study a unit cost of C = 4.5 million Euros/km per meter of embankment elevation will be considered.

For every planning horizon the total cost of the riverbanks rise is calculated using the following equation:

$$C_{arg}(t, l_2) = \delta^t(l_2(t) * C * L) \quad (6)$$

where L is the length of the entire network of embankments, around 35 km. Maintenance costs, €100,000 per kilometer to be spent every 10 years, were provided by the Reclamation Consortium Office. The cost of expansion areas was evaluated as lost space to most productive uses, the amount is €5000 per hectare for each year in which the expansion area is flooded.

2.1.5. NSGAII Genetic Algorithm

The multi-objective optimization problem of Equations (1)–(5) is solved by the NSGA II genetic algorithm. Genetic algorithms mimic the Darwin's theory of natural selection: a population represents a group of solution points. A generation represents algorithm iteration. A chromosome is equivalent to a component of the design vector. In accordance to these definitions genetic algorithm deals with a population of points, and hence multiple Pareto optimal solutions can be obtained from a population in a single run. Random number and information from previous iterations are combined to evaluate and improve a population of points, and then to select non-dominant solutions. In this paper the non-dominant-sorting genetic algorithm II [47], NSGA II, is used, which has been applied

successfully to many optimization problems. This algorithm uses tournament Goldberg and Deb [48], simulated binary crossover (SBX) [49], mutation operator and crowding distance for diversity preservation. The original NSGA II Matlab code has been adapted to the specific multi-objective optimization problem above described.

2.2. Probability Density of Hydrological Forcing Factors

In order to calculate the EAD of Equation (3) it is necessary to estimate the probability density function $p_i^T(\overrightarrow{\xi})$ taking into account the statistical independence or the possible statistical dependence among the different hydrological forcing factors. Generally, heavy daily rainfall amount and storm surge due to wind set-up and low atmospheric pressure are statistically dependent, while the average sea level rise, as a consequence of climate change, can be assumed statistically independent from the above cited forcing factors [50,51]. Therefore, in Equation (3) we express the probability density function as:

$$p_i^T \overrightarrow{\xi} = p_i^T(\xi_1, \xi_2) p_i^T(\xi_3) \tag{7}$$

where $p_i^T(\xi_1, \xi_2)$ and $p_i^T(\xi_3)$ are the probability density functions of the statistical jointly variables heavy rainfall amount ξ_1 and storm surge ξ_2 and of the statistical independent variable sea level rise ξ_3.

2.2.1. Heavy Rain and Storm Surge Joint Probability

The estimation of the joint probability of the occurrence of intense rain and storm surges is extremely important [37] because even a weak dependence can have significant implications in the estimation of the hydraulic risk [52]). Indeed, heavy rainfall and storm surge are often caused by similar atmospheric conditions such as, low atmospheric pressure and strong winds that cause storm surge. Several methods of multivariate statistical analysis exist to estimate the dependence of such events, including the Point Process Method [53,54]. For the estimation of the probability distribution $p(\xi_1, \xi_2)$ the "logistic model" can be applied [37]:

$$p(\xi_1, \xi_2) = exp - (\xi_1^{-1/\alpha} + \xi_2^{-1/\alpha})^{1/\alpha} \qquad 0 < \alpha < 1, \xi_1 > 0, \xi_2 > 0 \tag{8}$$

where ξ_1 and ξ_2 represent the extremes of the bivariate vector consisting respectively of daily rainfall amount and daily storm surge levels, which is assumed to follow the standard Frechet distribution. The parameter α indicates the dependence between the two extremes with $\alpha \to 0$ complete dependence and $\alpha \to 1$ independence. The method used involves identifying the rainfall and storm surge intensity thresholds and estimating the Generalized Pareto Distribution (GPD) of the margins. Then using GPD parameters, the entire dataset is transformed to have the standard Fréchet margins [55]. After the transformation of the Fréchet margins into radial and angular components (r, w), the joint threshold $r0$ is selected. The α parameter is estimated through a likelihood function constructed from the spectral density $h(w)$.

$$h(w) = \frac{1}{2}(\alpha^{-1} - 1)[w(1-w)]^{-1-1/\alpha}[w^{-1/\alpha} + (1-w)^{-1/\alpha}]^{\alpha-2} \tag{9}$$

The inference for the Point Process Method is based on a likelihood function constructed from the spectral density $h(w)$:

$$L(\alpha; (\xi_1, \xi_2) \ldots (\xi_n, \xi_n)) = \prod_{j|r_j > r_0} h(w_j) \tag{10}$$

The joint probability of the events will be considered for each year of the time horizon considered. The model is calibrated using the data relating to the accumulated daily rainfall for 20 years of records of rainfall stations present in the study area.

2.2.2. Mean Sea Level Rise Projections

The future mean sea level until 2200 can be derived from [18,56,57]. Using a model ensemble, ref. [18] provide a method for obtaining probabilistic projections of sea level rise both on the global scale and on the local scale considering the individual contributions due to the melting of both the polar ice caps and glaciers. The projections use 3 RCP scenarios, 8.5, 4.5 and 2.6. In order to obtain local sea level rise projections, the model requires the aggregation of the individual components that influence the sea level change in every site of interest [58]. Those components are respectively the three ice sheet components (Greenland, West Antartic and East Antartic): (a) the global mean thermal expansion and the ocean dynamic effects based upon the CMIP5 [59] and GCM models; (b) the land water storage evaluated following the approach of [60]; (c) the glacier and ice cap surface mass balance and tectonics. The non-climatic effects can be approximated as linear trends over past century and assumed unchanged, using spatiotemporal Gaussian process model [61]. We use the DP16 projections because they included previously omitted processes such as the hydrofracturing of the ice shelf and structural collapse of high ice cliffs ending at sea, which have the potential to drive a higher sea level rise. Projections of ice sheets for the 21st century are generated from IPCC AR5 projections (IPCC, 2014), used to characterize median and likely ranges of sea-level change, while study carried out by [62] is used to calibrate the shape of the tails. For each RCP, the model employ a multivariate t-distribution of ice mass change with a mean and covariance estimated from the model results of [63]. To calculate global and local sea level projections the model uses 10,000 Latin hyper–cube samples from time dependent probability distributions of cumulative contributions of each individual component [18]. To calculate the probability of increasing of the average local sea level at site of interest (ξ_3), taking into account the different RCP scenarios, we estimated the probability linked to each level of increase for each year by calculating the probability distribution function relative to a sample of 30,000 projections, 10,000 for each RCP scenario considered. Each RCP scenario is assumed as independent from others with a different temporal varying density probability function.

3. Case Study

3.1. Site Description

The model developed was tested on the southern area of the Pontine Plain, a recovery area with a surface of 395 km^2, originally a swamp, reclaimed in 1920s and located in the south of Lazio region (Italy). The area is densely populated, with a significant presence of agriculture and industrial activities. A natural park, Circeo National Park, aimed to conserve the biotypes and biodiversity typical of wetland environments covers the areas closer to the coast, with the presence of a long coastal dune and a number of coastal lagoons [64]. These social, economic, naturalistic and ecological characteristics, together with the morphological ones, determine a particular vulnerability and exposition of the zone to extreme hydrological events and sea level rise. In fact, vast areas are below the sea level, furrowed by a dense network of canals that are mostly artificial and subject to periodic flooding phenomena due to the concomitance of meteorological phenomena such as heavy rains and local sea level rises due to storm surge. As shown in Figure 3, the area is kept dry by pumping water that accumulates in the most depressed areas by conveying it into a higher altitude network of canals and then discharged into the sea. In addition, maneuvers are carried out by the network operators, such as opening and closing mechanical sluice gates, to prevent excessive water from accumulating inside the channels during emergency periods.

Figure 3. Hydraulic network of Pontina Plain with maneuvers, pumping stations and gates.

The most important is the Mazzocchio pumping station, which has a maximum capacity of about 30 m^3/s and is used to drain the water that accumulates in the most depressed area of the Pontine plain, with a minimum altitude of up to −3 m above sea level. The area upstream the Mazzocchio pumping station has an extension of about 102 km^2 and due to the lower altitude in respect to surrounding basins it results hydraulically connected with downstream hydraulic network only by the pumping. Therefore changes in flow rates and flow depths in the rivers downstream from the pumping don't affect the flow characteristics of the areas upstream from the pumping station. On contrary the flow rates lifted by Mazzocchio pumping station affects the flow characteristics of the downstream area. A previous study by [45] showed, that during heavy precipitation events, higher pumping flow rates reduce the extension of flooding areas upstream from Mazzocchio pumping station, but it worsens the flooding of those downstream. In the current study case, we explore how to increase the resilience to sea level rise of the drainage network downstream from Mazzoccio pumping station, through both the raising of the embankment elevation along the most vulnerable part of the drainage network and the construction of flood expansion areas ruled by weirs along the channels. In this context an analysis has been conducted with the aim to verify how an increasing of the pumping power of Mazzocchio station could reduce the extension of the flooding in the areas upstream from the station and how such increase could affect the flooding in the downstream zones. Therefore simulation were carried out for two different global pumping power for Mazzocchio station: the current ones with 6 pumps having a 6 m^3/s flowrate and an hypothetical configuration with the same number of pumps but able to lift up to 9 m^3/s.

3.2. Data

The data used in the present study are the amounts of daily rainfall in the study area, the sea level, the ground level, the land use and the channel network morphological characteristics. Above mentioned data can be downloaded at github.com/project.

3.2.1. Rainfall Data

Rainfall data recorded from five rainfall stations present in the study area were used. Four rain gages, whose coordinates are shown in Table 1, provided daily precipitation amount from 1 January 1980 to 31 Decmber 2000. The first station, located in the municipality of Latina (12°58′12″ 41°25′12″) provided hourly rainfall amount time series for a shorter period (since 2009). Using the 10 years long hourly rainfall time series, and applying the method developed by [65], synthetic hyetographs were generated which distribute the total rainfall amount in 24 h according to a statistical distribution obtained from the hourly rainfall data. In fact, a previous study [45] has shown that 24-h-long heavy rainfall (with a daily rainfall amount greater than 100 mm) has, in the past, induced serious flooding in the examined site. Ref. [45] is reported a detailed description of the methodology used to construct the hyetographs for the study case. The daily rainfall amount time series were used to obtain the joint probability between extreme rainfall and storm surge in according to the method described Section 2.2.1.

Table 1. Coordinates Rain Stations.

Rain Gauge	Lon	Lat
Latina	12.8313442	414623368
Lenola	13.4401114	41.4051557
Ponte Ferraioli	13.0958461	41.4643082
Terracina	131255395	41.2848763
Mazzocchio (Pontinia)	13.136856	41.397645

3.2.2. Storm Surge Data

Since direct measurements of storm surge along the coast were not available for the site, we reconstructed the sea level time series from 1 January 1980 to 31 Decmber 2000. using the time series of the wind speed and direction and sea level pressure for the area of interest (Lat 39.75–42, Lon 12–14.25). Sea level is a combination of the component due to the action of the wind (wind set-up), of the astronomical tides (Boon, 2020) and of the atmospheric pressure acting on the sea free surface. Storm surge levels are calculated starting from the pressure data on the mean sea level and zonal and southern wind intensity obtained from the ERA-Interim model [66]. In order to derive the wind set-up, we applied the relationship and coefficient obtained by [67]:

$$S = \frac{K_p L_p U^2}{g(D - h - S)} \ln \frac{D}{h + S} \tag{11}$$

where:

U = wind speed (m/s) at 10 m. over the sea surface;
D = limit depth of the continental shelf (~200 m);
L_p = continental shelf extension (m);
h = depth where storm-surge is calculated (m);
g = gravity acceleration (9.81 m/s^2);
k_p = coefficient equal to 3×10^{-6}.

For the specific coastal zone eastern-southerly winds produce higher storm surges which increase due to the contribution of sea level pressure and astronomic tide. Usually, extreme meteorological events in the considered zones last from one to three days, thus also the maximum tidal amplitude has to be taken into account as a further component to the storm surge. To calculate the height of the sea due to astronomical tides the model developed by [68]. The measurements from which we obtained the trend of the astronomical tides refer to the recordings made by the Gaeta tide gauge (LAT 41°12′35.97″, LON 13°35′23.05″). The range of tidal amplitude in that coastal area result equal to ±200 mm.

3.3. Sea Level Rise Projections

To obtain the projections for raising the local average sea level, we used the data recorded in Civitavecchia tide gauge which is located in a zone close to that of the study case and having very similar morphological characteristics. Two different projections of mean sea levels were calculated referred to [57] (DP16) and [18] (K14). As shown in Figure 4, the two projections show a substantial variation of the median sea level rise ,with regard to the worst-case scenario (RCP 8.5), of more than 1 m in 2100. The two scenarios considered differ mainly in the contribution of the hydro-fracturing of the Arctic ice sheets introduced by [57] in the model developed by [18].

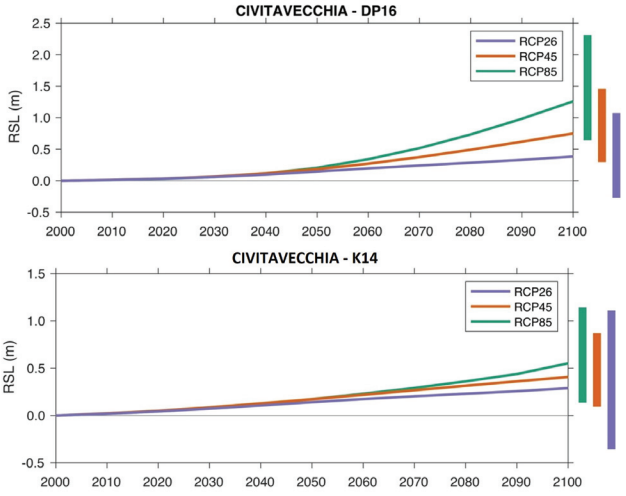

Figure 4. Downscaled projections used to calculate the total probability of sea level rise D16 (**top**) and K14 (**bottom**).

4. Results

4.1. Hydraulic Simulations

In order to analyze the hydraulic response of the hydraulic network and of the surrounding floodplains of the area and to identify the critical zones to flooding 2D hydraulic simulations were carried out. Due to the large dimensions of the catchments feeding the hydraulic network the integration domain was divided as shown in Figure 5.

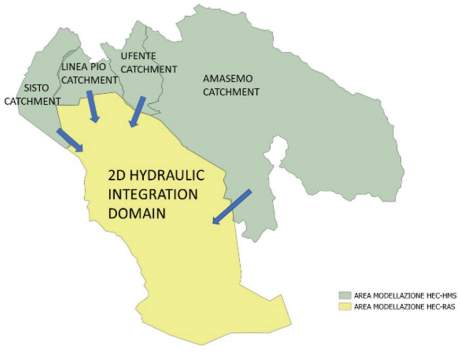

Figure 5. Sketch of integration domain.

Hydrographs at the closing sections of the upstream basins were obtained applying rainfall runoff models. These hydrographs were applied as inputs to the 2D hydraulic model. The rainfall-runoff models as well as the 2D hydraulic model were calibrated using data from the hydrometric and meteorological monitoring system, and Sentinel I satellite image of flooding, recorded during the event of 25 November 2018. The monitoring system consists of eleven hydrometric stations and two meteorological stations, which collect the data and return the hourly averages relating to the water tie, to rainfall, to the wind intensity and direction, atmospheric pressure, etc.

Figure 6a,b show the hyetograph and the sea level trend recorded during the event of 25 November 2018 respectively, and applied as boundary conditions to the rainfall-runoff model as well as to 2D shallow water hydraulic model. Rainfall-runoff models for each of the basins sketched in Figure 5, were calibrated by varying the saturation factor k as defined by Şen (2008)

$$\frac{dR}{dP} = (1 - e^{-kP}) \tag{12}$$

where $\frac{dR}{dP}$ is the runoff rate, being R the runoff and P the precipitation amount. Typically, the value of k ranges between 2.54 to 12.7 (mm^{-1}) depending on the land cover and of hydrologic soil group. In the present study case uniform values of k were assumed for the entire integration domain. Figure 7 shows such comparation.

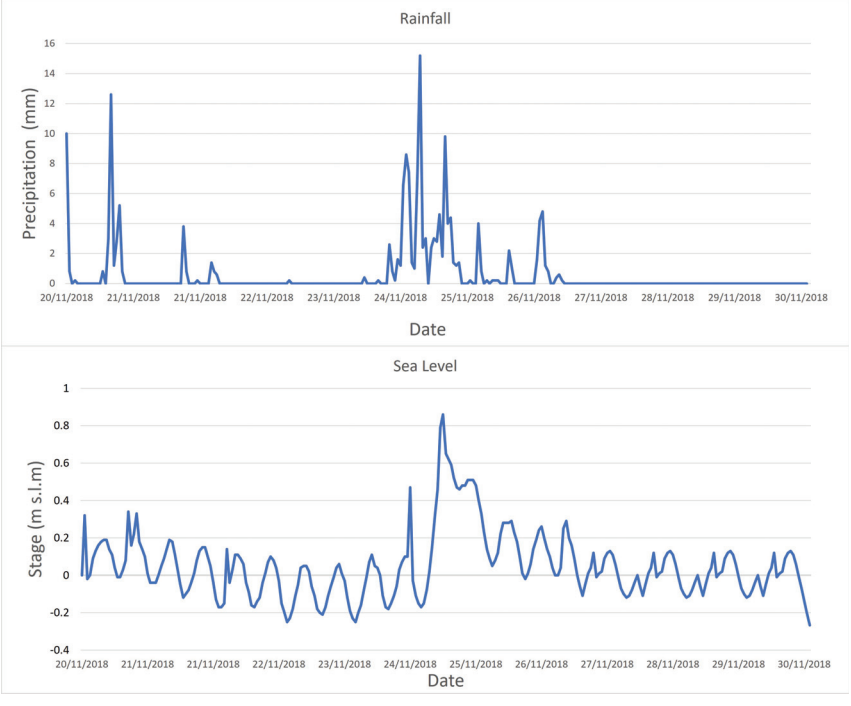

Figure 6. Hyetograph (**top**) and the sea level (**Bottom**) trend recorded during the event of 25 November 2018 respectively.

To calibrate k in the part of the basin simulated by 2D hydraulic model, the fit between the flooding areas detected by satellite images A_{obs} and those obtained by simulations A_{sim} was evaluated by the following index:

$$I(k) = \frac{A_{obs} \cap A_{sim}(k)}{A_{obs} \cup A_{sim}(k)} \tag{13}$$

The best value of the saturation factor k was identified as the one that yields the maximum value of $I(k)$. In Equation (2) refers only to the flooding areas which are detected by satellite. Therefore coastal lakes and other water bodies, as well as, vegetate and dense urbanized areas were removed ([69–71]). After model calibration, a number of simulations were carried out, forced by the same rainfall of the event 25 November 2018, with different values of the pumping rates in Mazzocchio station and of the sea level rise, with the goal to identify the most vulnerable areas to flooding and the type and location of the flood defence constructions, as levees, dikes or flood expansion areas. In order to calculate the damage function $D(l_{c_i}(x,y), \overrightarrow{\xi}, \overrightarrow{\chi})$ of Equation (3), related to flooding in the study area, simulations were carried out using the fast simplified model, which takes into account the entire domain shown in Figure 5, and whose parameters were calibrated with reference to same above mentioned heavy rainfall event used in 2D simulations. Hydraulic simulations were carried out considering rainfall events lasting 24 h. Then, 24 h rainfall amounts were distributed hourly according to the synthetic hytographs. Hydraulic simulations were carried out offline to reduce the computation time. Different hydraulic construction states were considered, raising embarkment level in the range of 0 and 4 m, with longitudinal weir level ruling flood expansion areas varying between 2 and 6 m above mean sea level. The scenarios considered consist of five rainfall intensities, five storm surge levels and five average sea level rise scenarios combined to form 625 different simulations with each combination of boundary conditions. For the simulations, extreme rains of intensity from 30 mm per day to 150 mm per day, storm surge levels from 20 cm per day to 100 cm per day and increases in the average marine level from 20 cm to 200 cm were considered. The most depressed areas of the domain are kept dry by groups of pumping stations whose flow rates were related to the water level in the upstream storage tank.

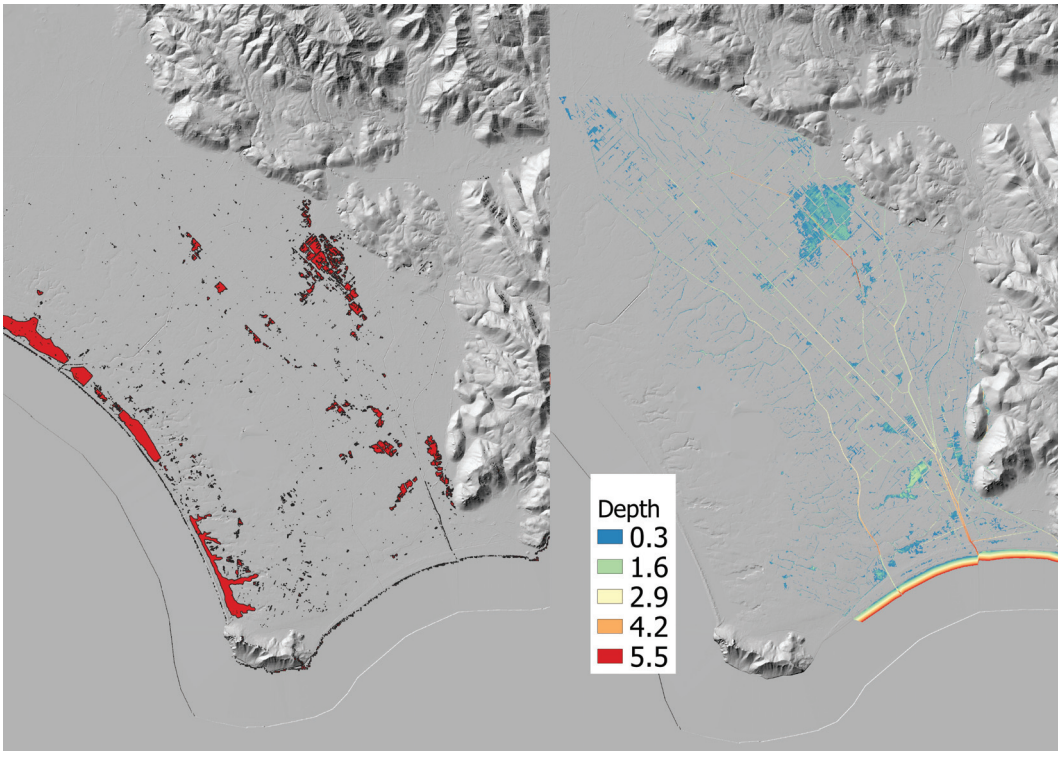

(**a**) (**b**)

Figure 7. Comparison between flooding areas by Sentinel 1 satellite image (**a**) and simulated ones (**b**).

4.2. Effect of the Increase of Pumping Power at Mazzocchio Station and Identification of Flood Defence Constructions by 2D Hydraulic Model Simulations

For the event of 25 November 2018, Figure 8 shows the maximum flow depth difference between the simulated configuration with 9 m^3/s pumping flow rate for each pump of the Mazzocchio Station and with 6 m^3/s ones. In simulations the switch-on and switch off of different group of pumps were considered as a function of different free surface levels in the tank upstream of the Mazzocchio pumping station. The increase of pumping reduces the maximum flow depth of about 0.20 m. in the zones upstream from Mazzocchio Station but increases it in the downstream area up to 0.4 m. in the most depressed zones.

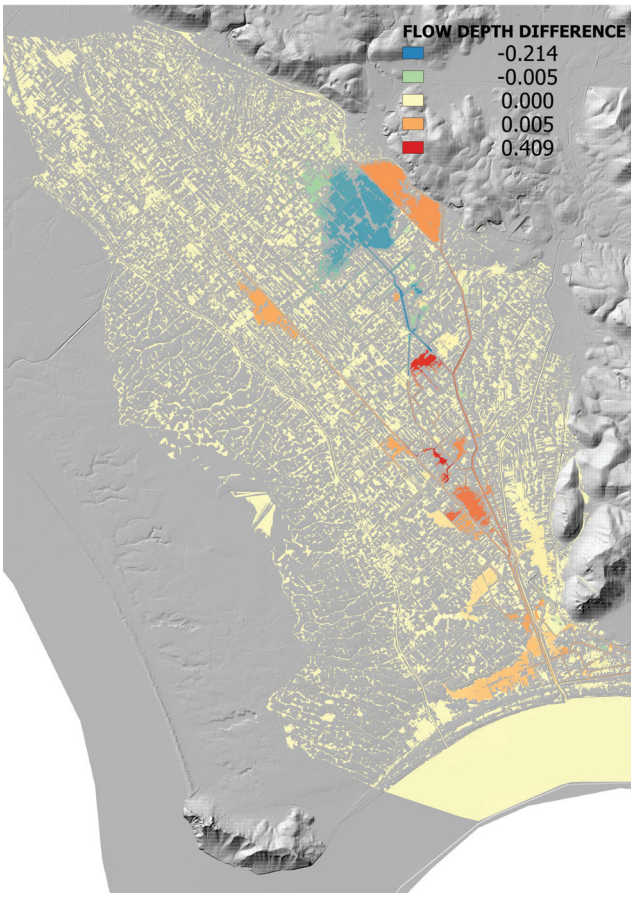

Figure 8. Maximum flow depth difference between configuration with 1.5 increase of pumping flow rate of each single pump (9 m^3/s) at Mazzocchio pumping station and the current one (6 m^3/s).

With the aim to identify the areas most prone to flooding, and to define the type and locations of flood defence constructions, a number of hydraulic simulations for different average sea level rise were carried out, applying the same hyetograph of the event of 25 November 2018, as well as the same storm surge trend. Figure 9a–d shows the comparison between the water depth field at the instant of maximum flooding for the current average sea level and that assuming an average sea level rise equal to m. 0.5. As shown in Figure 9c there is a notable worsening of flooding conditions, especially in the urbanized region closer to the coastal line and where there is the convergence of the main watercourses.

To defend such a region different kinds of flood disaster risk reduction measures could be adopted [72]. Here, as shown in Figure 9d, we consider raising the embankment elevation along the drainage network crossing the most vulnerable areas and the construction of flood expansion areas, upstream from such areas, ruled by the level of weir along the channels.

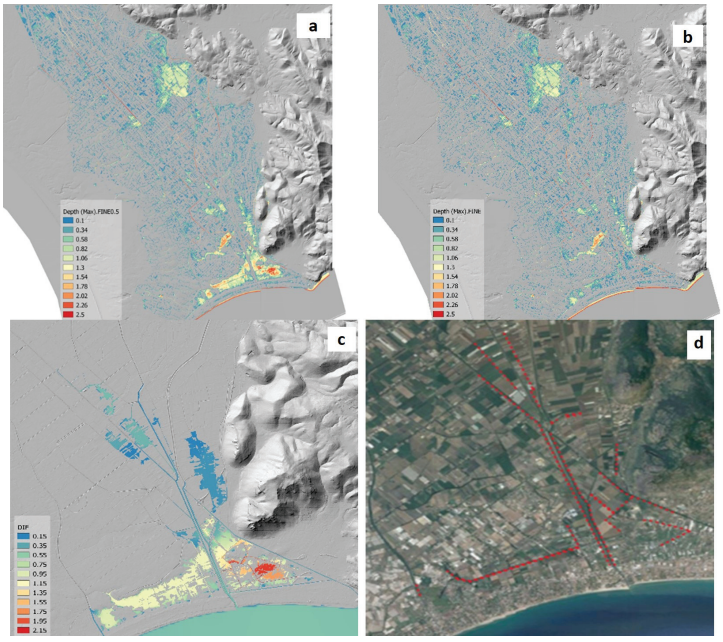

Figure 9. (**a**–**d**) Comparison of the water depth field at the instant of maximum flooding for the current average sea level and that assuming an average sea level rise equal to m. 0.5.

4.3. Probability Density Function for Sea Level Rise Scenarios

To calculate the probability of raising the local sea level, 10,000 simulations were carried out for each RCP emission scenario considered, In the Figure 10a,b the probability density functions at the year 2050 and 2100 for each RCPs,and the total probability density function are shown, for the sea level rise scenarios K14 and DP16 respectively. Figures also show the narrower range of variation of sea level rise in the year 2050 than 2100.

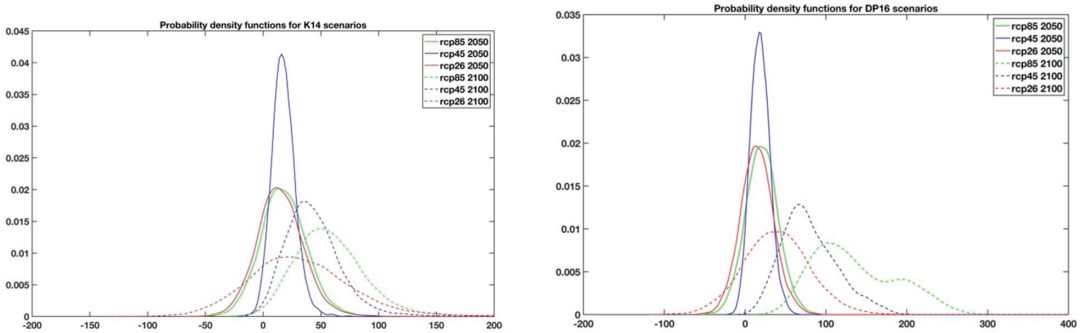

(**a**) (**b**)

Figure 10. Probability density functions at the year 2050 and 2100 for each RCPs, for the sea level rise scenario K14 (**a**) and Dp16 (**b**) respectively.

4.4. Application of Multi-Objective Optimization to Case Study

In order to test the reliability of the multiobjective optimization model for identifying the sizing and the timing of the flood defence constructions, five scenarios with different environmental and economic characteristics were taken into into account. These scenarios are listed in the Table 2. Scenarios refer to: (a) two sea level rise projections previously discussed capitol k14 and D16; (b) different power of the Mazzocchio pumping station; (c) two different spatial domains to calculate the objective function of Equation (1), the one that takes into account both the areas upstream and downstream from the Mazzocchio pumping station and the one that takes into account only the downstream area; (d) different values of the discount rates r_d and r_c. For each of the scenarios considered, Pareto optimal curves were calculated. Each point of Pareto curves identifies the values of decision variables, i.e., the sizing of the flood defence construction and timing.

Table 2. Scenarios description.

	RCPs Considered	Mean Sea Level 2100 Projection	Discount Rate Costs	Discount Rate Damages	Pumping Rate for Each Pump	Selcella Basin's Damages Accounted
Scenario 1	8.5-4.5-2.6	K14	0	0	6 m^3/s	yes
Scenario 2	8.5-4.5-2.6	D16	0	0	6–9 m^3/s	yes
Scenario 3	8.5-2.6	D16	0	0	6 m^3/s	no
Scenario 4	8.5-4.5-2.6	D16	0.02-0.05-0.07	0	6 m^3/s	yes
Scenario 5	8.5-4.5-2.6	D16	0.02	0.02-0.07	6 m^3/s	yes

In the NSGA II algorithm a crowded comparison approach by [47] is used to assure the convergence to the optimal Pareto set and a good spread of solutions. Such approach does not require any user-defined parameter for maintaining diversity among population members. Generally, the algorithm terminates when either a maximum number of generations has been produced, or a satisfactory fitness level has been reached for the population. By performing preliminary runs we selected the minimum number of generations needed to converge to the optimal Pareto set that are reported in Table 3. In carrying out the multiobjective optimization, 50 generations of 1000 individuals each were assumed. The Table 2 shows the parameters used in the multi-objective optimization algorithm.

Table 3. NSGA 2 Parameters.

	NSGA II Parameters
Generations	50
Population	1000
Crossover percentage	0.7
Mutation percentage	0.4
Mutation rate	0.02

The Pareto set obtained solving the multiobjective optimization problem for the scenario 1 of Table 1 is shown in Figure 11. The Pareto curve identifies a set of optimal solutions representing the "best" choices relative to the two objective functions. The curve shows a clear upward concavity: higher costs of flood defence construction reduce the hydraulic risk for the entire period.Each optimal solution belonging to the Pareto set (filled circles) includes the decision variables: size of flood defence works (embankment level and flood expansion area)and timing of their construction. Figure 12 shows the difference among the optimal solutions of Pareto set in term of values of decision variables.

In Figure 12 we explore optimal policy sets by looking at the differences between the safest and most expensive and the most risky and economic ones. The more expensive solutions are characterized by a higher level of banks and time horizons closer to each other (yellow) than the riskier policies (blue) characterized by milder and more distant interventions over time. The solutions (green), positioned in the "elbow" portion of the

Pareto Set, are characterized by height levels of the intermediate banks with respect to the solutions that prefer risk or safety.

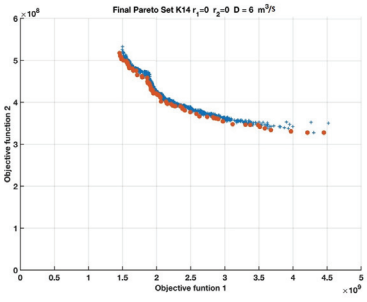

Figure 11. Pareto set for scenario 1. of Table 2.

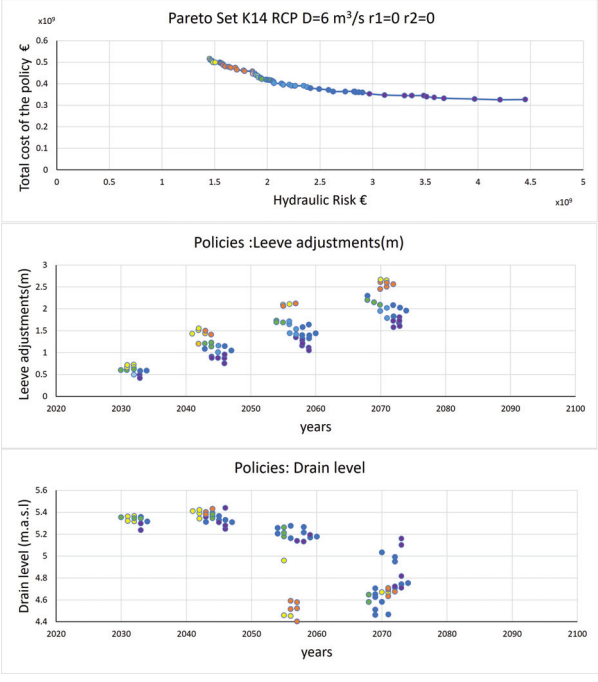

Figure 12. Size and timing of Flood defence constructions for the Pareto set optimal solutions.

The second decision variable, that is the level of the drain, presents solutions characterized by an anticipation over time of the more expensive solutions but little variation in terms of altitude up to 2050; the coincidence of the data is due to the contained rise in the sea level up to that date resulting from the K14 projection. In this case, a lower drain level corresponds to higher costs due to a greater portion of land to be allocated to the expansion area. In Figure 13 the Pareto sets obtained for the scenario 2 of Table 2 are shown. The two curves are obtained for two configurations of Mazzocchio pumping station, single pump power of 6 m^3/s and 9 m^3/s. As evidenced in Section 4.2, the increase in the power of pumps reduces the entity of flooding in the basin upstream of Mazzocchio station but at the same time makes worse the hydraulic risk in downstream areas. As it is evident from Figure 13, due to the low economic values of agriculture production in upstream Mazzocchio region, the reduction of the damages in this part of the watershed

does not compensate the increased damages in the portion of watershed downstream due to the higher pumping flowrates from Figure 13, the increase of hydraulic risk (Objective function 1) at parity of construction costs is made evident from the translation of the curve associated to the higher values of pumping rates.

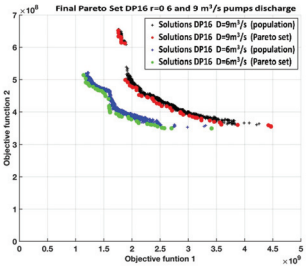

Figure 13. Pareto set for scenario 2 of Table 2.

As shown in Figure 14a,b, coherently with the higher weight of damage (Objective function 1) in the watershed downstream from Mazzocchio station, the optimal solutions belonging to the Pareto set for 9 m^3/s are characterized by higher top level of levees and larger flood expansion areas than those for 6 m^3/s. Furthermore, the construction times of the defence works in the first case are delayed with respect to the second one. This result suggests to limit the pumping power of Mazzocchio station at 6 m^3/s, since further increase of the pumping power does not produce significant reduction of hydraulic risk for the entire domain, but it makes worse the hydraulic risk in the downstream portion of such domain.

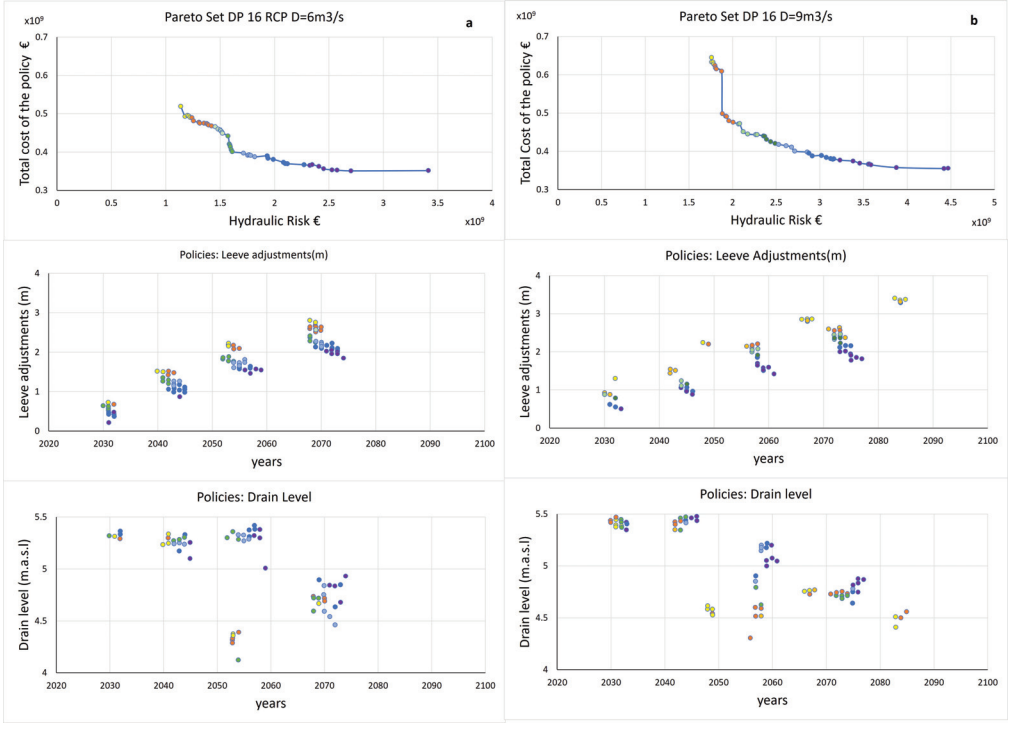

Figure 14. (**a**,**b**) Size and timing of Flood defence constructions for the Pareto set optimal solutions referred to scenario 2 of Table 2.

In Figure 15 the Pareto sets obtained for different sea level rise scenarios, referred to RCP 2.6 and RCP 8.5 respectively, are compared. Even if the RCP 2.6 curve presents lower costs than RCP 8.5 curve at parity of hydraulic risk, as expected, the curves are rather close. This is due to the fact that the trends of SLR for RCP2.6 and RCP 8.5 diverge significantly only starting form the 2060. Despite this, the optimal solutions for the two cases are rather different: for RCP8.5 the levee levels are higher than for RCP 2.6. However, construction timings are rather coincident (see Figure 16a,b).

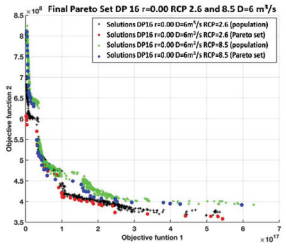

Figure 15. Pareto set for scenario 3 of Table 2.

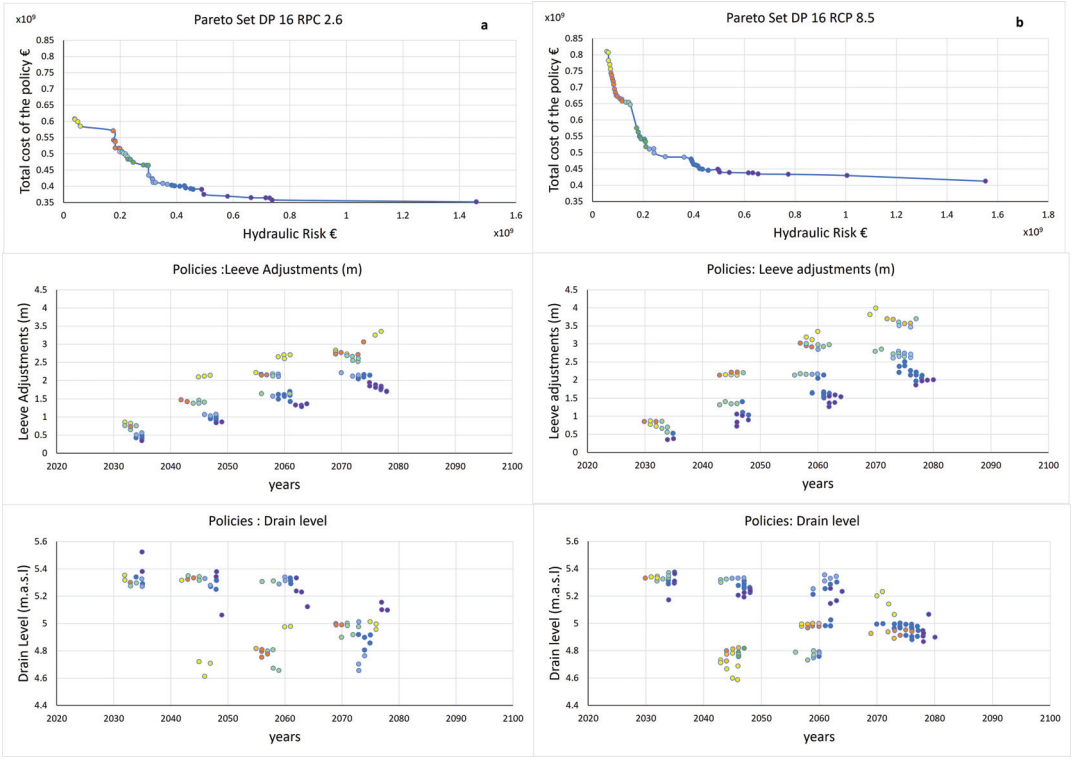

Figure 16. (**a**,**b**) Size and timing of Flood defence constructions for the Pareto set optimal solutions referred to scenario 3 of Table 2.

Thus, the model is able to identify the optimal timing in which to implement the planned intervention. Analyzing Figure 16b, it is possible to observe how the more precautionary policies but also the more expensive ones (yellow) foresee more substantial rises of the embankment summits and closer in time, with a maximum time horizon around 2070. The least expensive policies monetary terms but riskier in terms of potential damage

from flooding (blue) envisage lower river embankments more distant time horizon with a maximum time horizon of around 2080. In the scenarios 4 and 5 in Table 2, a local projection of sea level rise more severe one in which the phenomenon of the detachment of large portions of ice from the Antarctic polar cap takes place was considered (DP16). For this projection of sea level rise, in scenario 4 in Table 1, the results obtained by varying the cost discount rate r_c—equal to 2%, 5% and 7% respectively—were compared. We also assume a damage discount rate equal to zero, i.e., the hydraulic risk does not depend on time. Figure 17a,b shows the Pareto sets relating to such scenario in terms of average sea level rise (DP16) by varying, as said, the discounting of the intervention costs and leaving the actualization of the consequent damages unchanged. The main influence of cost discount rate r_c can be inferred comparing Figure 17a,b: greater the cost discount rate is more delayed the flood construction time horizons are. Indeed defence policies, especially the more expensive ones that involve a greater rise in the level of the levees, tend to be anticipated over time by applying the lower cost discount factor $r_c = 0.02$ than policies in which a greater costal discount factor $r_c = 0.07$ is applied. This is a consequence of the different way in which the cost are weighted in dependence of construction time horizon.

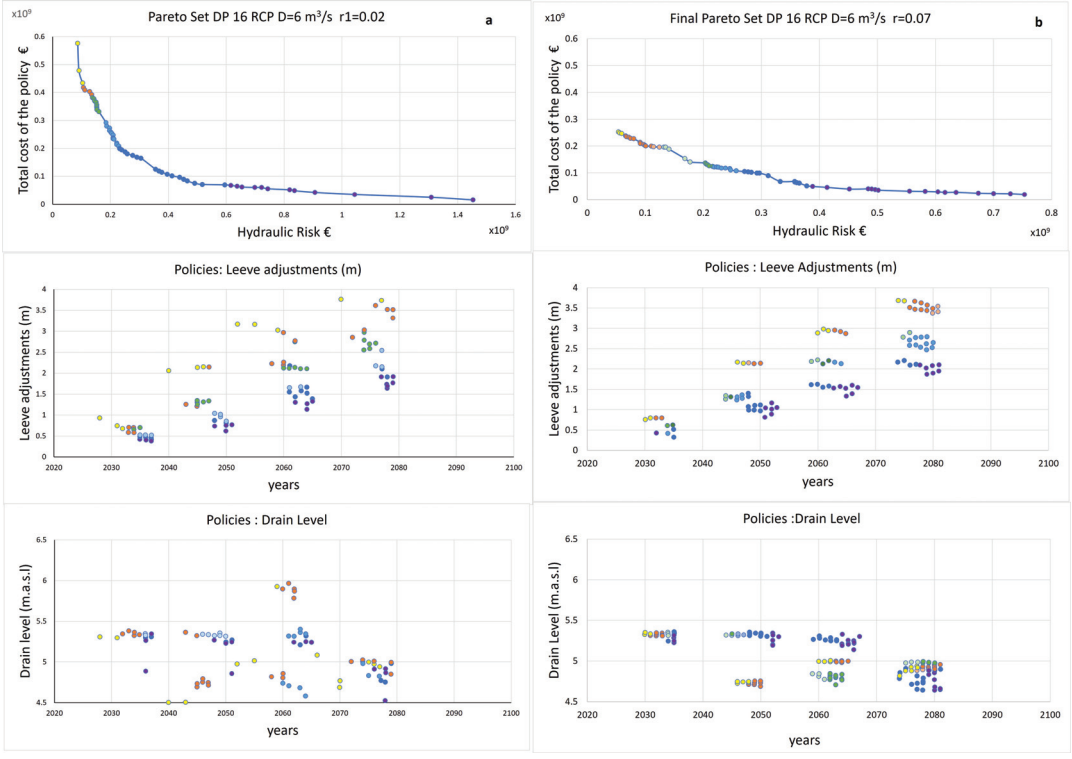

Figure 17. (**a**,**b**) Size and timing of Flood defence constructions for the Pareto set optimal solutions referred to scenario 4 of Table 1.

Figure 18a shows the results of the variation of the social discount rate in the case of the DP16 scenario with $r_c = 0.02$ and $r_d = 0.02$. Comparing with Figure 18b (same case but with $r_d = 0$) we observe that, due to the minor weight of the hydraulic risk in future years, the optimal solutions in the case of $r_d = 0.02$ are characterized by flood defence works of minor size with construction horizon times anticipated in respect to the case in which rd is assumed equal to zero.

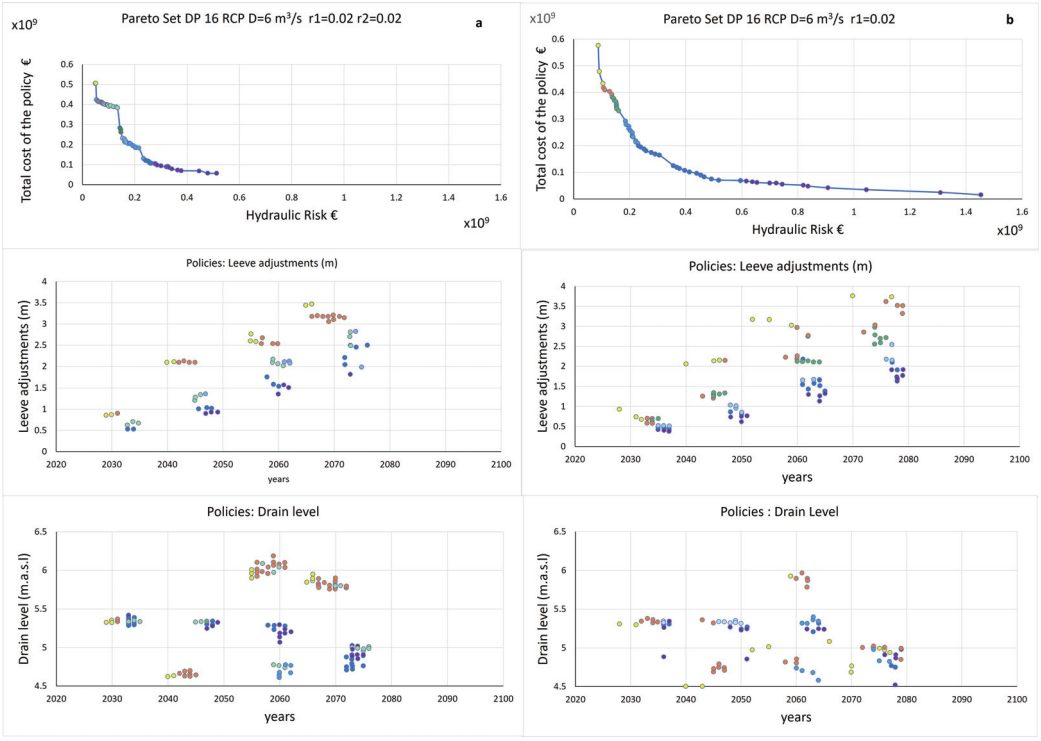

Figure 18. (**a**,**b**) Size and timing of Flood defence constructions for the Pareto set optimal solutions referred to scenario 5 of Table 1.

In conclusion, observing the responses of the model to the variations in the social discount rate, both as regards only the costs of carrying out the works, and as regards the associated damages, we note a tendency to anticipate time horizons for the construction of the defence works DP16. Analogous analysis was conducted also for the projections K14, not shown here since results were substantially similar to those of D16 projections. The results presented are intended to offer a tool that the decision maker can rely on to implement planning based for example on a budget limit or on a long-term goal. The input data can be updated from year to year in order to monitor and, if necessary, modify the chosen policy. This is regardless of the RCP scenario that occurs, as the model considers a total probability for each sea level rise and chooses the optimal policies regardless of the RCP scenario. From the results it is possible to observe the model's ability to grasp differences in the projections of local sea level rise due to a greater contribution from the melting of the Antarctic ice sheet. This difference in the results for the two different projections indicates the model's ability to adapt even to sudden and significant events, such as the rapid rise in the average sea level due to the fracturing of part of the polar caps with the consequent introduction of huge quantities of water into the ocean. The model is able to identify the optimal time in which to implement the planned intervention. Another aspect evident from the results is the influence of uncertainty on the solutions, it is clear that for modest marine rises and less affected by uncertainty, in which the difference between the 95th and the 5th percentile is small, the solutions tend to concentrate in some very precise instants of time (K14), while with increasing uncertainty (DP16) also the solutions tend to be more varied both as regards the geometric characteristics and for the temporal horizons of realization.

5. Summary and Conclusions

We developed a methodology and related algorithms aimed to identify the size and timing of flood defence constructions to cope with sea level rise, as well as, extreme rainfall regime modification due to climate change. The methodology considers a multi-objective optimization problem. The first objective function is related to the hydraulic risk for the entire climate projection period, while the second one refers to the construction and maintenance costs. Two relevant aspects of the multi-objective optimization problem deserve to be highlighted. First, since the construction timing is considered as a decision variable the projected trend of climate variables, whether it corresponds to uncertain abrupt or smooth changes or in the case in which natural variability shadows climate trend, can be addressed. Second, EAD integrates in its definition the uncertainties in climate projections considering the different RCPs postulated by climate community and for each of these RPCs the structural, parametric and initial condition model uncertainties in climate projections. The relative likelihood of each RCP can be specified by the decision maker, including its possible variation in the future. This way optimism or pessimism as to the ability to mitigate future climate risk can be incorporated. The application to the study case has shown the reliability of the proposed approach which has allowed the identification under different forcing factors of a set of optimal solutions belonging to the Pareto Curve, each of them defining sizing and timing of the flood defence constructions along the entire period of climate projections. There are several areas of potential improvement with future research. First we focused our study just on the flooding over the considered coastal region due to the concomitant action of heavy rainfall, storm surge and sea level rise (SLR) for different global warming scenarios. The SLR also has other impacts on coastal regions which can be equally significant. For instance, coastal erosion that threatens the stability of the shore and dune-coastal lake systems, salt intrusion in coastal aquifers, alteration of ecosystem equilibrium as marshes, or lagoons. Further optimality criteria can be added to the proposed multi-objective optimization scheme without loss of generality. These criteria are not necessarily in monetary terms, since the multi-objective optimization problem can be formulated using incommensurable objectives. In the case study we assumed as flood defences only levees and expansion areas controlled by weirs. Different coastal strategies and policies could be hypothesized to cope sea level rise within the three different categories usually considered and referred as retreat, accommodate and protect [72]. More work needs to be done to assess damages due flooding by hydraulic model simulations to capture the entire landscape of possible options also using water quality or eutrophication models [73], groundwater models [74] or coastal erosion models [75]. A further relevant research suggestion is that proposed by [76], who advocates addressing the unintended negative or positive effects of disaster risk reduction measures and strategies on drought risk. To better design disaster risk reduction (DRR) measures and strategies, it is important to consider interactions between flood and drought which are closely linked hydrological phenomena. The mutual interaction of disaster risk reduction (DRR) measures and strategies aimed to cope the two hydrological risk should be investigated and then formalized within the objective functions. Finally, the proposed approach provides an adaptive and flexible way moving forward the temporal window and then time updating climate projections resulting from future improved GCMs. An ideal application would be as part of an adaptive process where the analysis is updated, for instance, every 5 years with new information and assumptions reflecting the evolution of the climate as well as socio-economic systems, and policy variables such as the discount rate.

Author Contributions: F.C.: supervision, methodology, writing; A.D.B.T.: methodology, writing, validation; M.G.: hydraulic simulation, data curation, editing; U.L.: supervision, methodology. All authors have read and agreed to the published version of the manuscript.

Funding: This research received no external funding.

Institutional Review Board Statement: Not applicable.

Informed Consent Statement: Not applicable.

Data Availability Statement: Not applicable.

Conflicts of Interest: The authors declare no conflict of interest.

References

1. Aerts, J.C.; Botzen, W.W.; Emanuel, K.; Lin, N.; De Moel, H.; Michel-Kerjan, E.O. Evaluating flood resilience strategies for coastal megacities. *Science* **2014**, *344*, 473–475. [CrossRef] [PubMed]
2. Kron, W. Coasts: The high-risk areas of the world. *Nat. Hazards* **2013**, *66*, 1363–1382. [CrossRef]
3. Merkens, J.L.; Lincke, D.; Hinkel, J.; Brown, S.; Vafeidis, A.T. Regionalisation of population growth projections in coastal exposure analysis. *Clim. Chang.* **2018**, *151*, 413–426. [CrossRef]
4. Giorgi, F.; Raffaele, F.; Coppola, E. The response of precipitation characteristics to global warming from climate projections. *Earth Syst. Dyn.* **2019**, *10*, 73–89. [CrossRef]
5. Lavell, A.; Oppenheimer, M.; Diop, C.; Hess, J.; Lempert, R.; Li, J.; Myeong, S. Managing the risks of extreme events and disasters to advance climate change adaptation. In *A Special Report of Working Groups I and II of the Intergovernmental Panel on Climate Change (IPCC)*; Cambridge University Press: Cambridge, UK, 2012; pp. 25–64.
6. Kundzewicz, Z.W.; Kanae, S.; Seneviratne, S.I.; Handmer, J.; Nicholls, N.; Peduzzi, P.; Mechler, R.; Bouwer, L.M.; Arnell, N.; Mach, K.; et al. Flood risk and climate change: Global and regional perspectives. *Hydrol. Sci. J.* **2014**, *59*, 1–28. [CrossRef]
7. Milly, P.C.; Betancourt, J.; Falkenmark, M.; Hirsch, R.M.; Kundzewicz, Z.W.; Lettenmaier, D.P.; Stouffer, R.J. Stationarity is dead: Whither water management? *Science* **2008**, *319*, 573–574. [CrossRef] [PubMed]
8. Doss-Gollin, J.; Farnham, D.J.; Steinschneider, S.; Lall, U. Robust adaptation to multiscale climate variability. *Earth Future* **2019**, *7*, 734–747. [CrossRef]
9. Van Vuuren, D.P.; Edmonds, J.; Kainuma, M.; Riahi, K.; Thomson, A.; Hibbard, K.; Hurtt, G.C.; Kram, T.; Krey, V.; Lamarque, J.F.; et al. The representative concentration pathways: An overview. *Clim. Chang.* **2011**, *109*, 5–31. [CrossRef]
10. Parker, W.S. Predicting weather and climate: Uncertainty, ensembles and probability. *Stud. Hist. Philos. Sci. Part B Stud. Hist. Philos. Mod. Phys.* **2010**, *41*, 263–272. [CrossRef]
11. Holt, J.; Harle, J.; Proctor, R.; Michel, S.; Ashworth, M.; Batstone, C.; Allen, I.; Holmes, R.; Smyth, T.; Haines, K.; et al. Modelling the global coastal ocean. *Philos. Trans. R. Soc. A Math. Phys. Eng. Sci.* **2009**, *367*, 939–951. [CrossRef]
12. Penduff, T.; Juza, M.; Barnier, B.; Zika, J.; Dewar, W.K.; Treguier, A.M.; Molines, J.M.; Audiffren, N. Sea level expression of intrinsic and forced ocean variabilities at interannual time scales. *J. Clim.* **2011**, *24*, 5652–5670. [CrossRef]
13. Little, C.M.; Urban, N.M. CMIP5 temperature biases and 21st century warming around the Antarctic coast. *Ann. Glaciol.* **2016**, *57*, 69–78. [CrossRef]
14. Cioffi, F.; Conticello, F.; Lall, U.; Marotta, L.; Telesca, V. Large scale climate and rainfall seasonality in a Mediterranean Area: Insights from a non-homogeneous Markov model applied to the Agro-Pontino plain. *Hydrol. Process.* **2017**, *31*, 668–686. [CrossRef]
15. Conticello, F.; Cioffi, F.; Merz, B.; Lall, U. An event synchronization method to link heavy rainfall events and large-scale atmospheric circulation features. *Int. J. Climatol.* **2018**, *38*, 1421–1437. [CrossRef]
16. Orton, P.; Conticello, F.; Cioffi, F.; Hall, T.; Georgas, N.; Lall, U.; Blumberg, A.; MacManus, K. Flood hazard assessment from storm tides, rain and sea level rise for a tidal river estuary. *Nat. Hazards* **2020**, *102*, 729–757. [CrossRef]
17. Tebaldi, C.; Friedlingstein, P. Delayed detection of climate mitigation benefits due to climate inertia and variability. *Proc. Natl. Acad. Sci. USA* **2013**, *110*, 17229–17234. [CrossRef]
18. Kopp, R.E.; Horton, R.M.; Little, C.M.; Mitrovica, J.X.; Oppenheimer, M.; Rasmussen, D.; Strauss, B.H.; Tebaldi, C. Probabilistic 21st and 22nd century sea-level projections at a global network of tide-gauge sites. *Earth Future* **2014**, *2*, 383–406. [CrossRef]
19. Balica, S.F.; Wright, N.G.; Van der Meulen, F. A flood vulnerability index for coastal cities and its use in assessing climate change impacts. *Nat. Hazards* **2012**, *64*, 73–105. [CrossRef]
20. Muis, S.; Güneralp, B.; Jongman, B.; Aerts, J.C.; Ward, P.J. Flood risk and adaptation strategies under climate change and urban expansion: A probabilistic analysis using global data. *Sci. Total. Environ.* **2015**, *538*, 445–457. [CrossRef]
21. Ramieri, E.; Hartley, A.; Barbanti, A.; Santos, F.D.; Gomes, A.; Hilden, M.; Laihonen, P.; Marinova, N.; Santini, M. Methods for assessing coastal vulnerability to climate change. *ETC CCA Tech. Pap.* **2011**, *1*, 1–93.
22. van der Sluijs, J.P.; Dessai, S. *Uncertainty and Climate Change Adaptation—A Scoping Study*; Copernicus Institute for Sustainable Development and Innovation: Utrecht, The Netherlands, 2007.
23. Kwadijk, J.C.; Haasnoot, M.; Mulder, J.P.; Hoogvliet, M.M.; Jeuken, A.B.; van der Krogt, R.A.; van Oostrom, N.G.; Schelfhout, H.A.; van Velzen, E.H.; van Waveren, H.; et al. Using adaptation tipping points to prepare for climate change and sea level rise: A case study in the Netherlands. *Wiley Interdiscip. Rev. Clim. Chang.* **2010**, *1*, 729–740. [CrossRef]
24. Haasnoot, M.; Kwakkel, J.H.; Walker, W.E.; Ter Maat, J. Dynamic adaptive policy pathways: A method for crafting robust decisions for a deeply uncertain world. *Glob. Environ. Chang.* **2013**, *23*, 485–498. [CrossRef]
25. Walker, W.E.; Rahman, S.A.; Cave, J. Adaptive policies, policy analysis, and policy-making. *Eur. J. Oper. Res.* **2001**, *128*, 282–289. [CrossRef]
26. Kwakkel, J.; Haasnoot, M. *Computer Assisted Dynamic Adaptive Policy Design for Sustainable Water Management in River Deltas in a Changing Environment*; Brigham Young University: Provo, UT, USA, 2012.

27. Parry, M.L.; Canziani, O.; Palutikof, J.; Van der Linden, P.; Hanson, C. *Climate Change 2007-Impacts, Adaptation and Vulnerability: Working Group II Contribution to the Fourth Assessment Report of the IPCC*; Cambridge University Press: Cambridge, UK, 2007; Volume 4.
28. Löwe, R.; Urich, C.; Domingo, N.S.; Mark, O.; Deletic, A.; Arnbjerg-Nielsen, K. Assessment of urban pluvial flood risk and efficiency of adaptation options through simulations—A new generation of urban planning tools. *J. Hydrol.* **2017**, *550*, 355–367. [CrossRef]
29. Woodward, M.; Kapelan, Z.; Gouldby, B. Adaptive flood risk management under climate change uncertainty using real options and optimization. *Risk Anal.* **2014**, *34*, 75–92. [CrossRef]
30. Lenton, T.M.; Rockström, J.; Gaffney, O.; Rahmstorf, S.; Richardson, K.; Steffen, W.; Schellnhuber, H.J. Climate tipping points too risky to bet against. *Nature* **2020**, *575*, 592–595. [CrossRef]
31. Cioffi, F.; Gallerano, F. Multi-objective analysis of dam release flows in rivers downstream from hydropower reservoirs. *Appl. Math. Model.* **2012**, *36*, 2868–2889. [CrossRef]
32. Ngatchou, P.; Zarei, A.; El-Sharkawi, A. Pareto multi objective optimization. In Proceedings of the 13th International Conference on, Intelligent Systems Application to Power Systems, Arlington, VA, USA, 6–10 November 2005; pp. 84–91.
33. Arnell, N.W. Expected annual damages and uncertainties in flood frequency estimation. *J. Water Resour. Plan. Manag.* **1989**, *115*, 94–107. [CrossRef]
34. Deb, K.; Thiele, L.; Laumanns, M.; Zitzler, E. Scalable multi-objective optimization test problems. In Proceedings of the 2002 Congress on Evolutionary Computation—CEC'02 (Cat. No. 02TH8600), Honolulu, HI, USA, 12–17 May 2002; Volume 1, pp. 825–830.
35. Nazarnia, H.; Nazarnia, M.; Sarmasti, H.; Wills, W.O. A systematic review of civil and environmental infrastructures for coastal adaptation to sea level rise. *Civ. Eng. J.* **2020**, *6*, 1375–1399. [CrossRef]
36. Winsemius, H.; Van Beek, L.; Jongman, B.; Ward, P.; Bouwman, A. A framework for global river flood risk assessments. *Hydrol. Earth Syst. Sci.* **2013**, *17*, 1871–1892. [CrossRef]
37. Coles, S.G.; Tawn, J.A. Modelling extreme multivariate events. *J. R. Stat. Soc. Ser. B Methodol.* **1991**, *53*, 377–392. [CrossRef]
38. Johnson, L.T.; Hope, C. The social cost of carbon in US regulatory impact analyses: An introduction and critique. *J. Environ. Stud. Sci.* **2012**, *2*, 205–221. [CrossRef]
39. Gollier, C.; Hammitt, J.K. The long-run discount rate controversy. *Annu. Rev. Resour. Econ.* **2014**, *6*, 273–295. [CrossRef]
40. Jonkman, S.N.; Bočkarjova, M.; Kok, M.; Bernardini, P. Integrated hydrodynamic and economic modelling of flood damage in the Netherlands. *Ecol. Econ.* **2008**, *66*, 77–90. [CrossRef]
41. Bossard, M.; Feranec, J.; Otahel, J. *CORINE Land Cover Technical Guide: Addendum 2000*; European Environment Agency Copenhagen: København, Denmark, 2000; Volume 40.
42. Scawthorn, C.; Flores, P.; Blais, N.; Seligson, H.; Tate, E.; Chang, S.; Mifflin, E.; Thomas, W.; Murphy, J.; Jones, C.; et al. HAZUS-MH Flood loss estimation methodology. II: Damage and loss assessment. *Nat. Hazards Rev.* **2006**, *7*, 72–81. [CrossRef]
43. HAZUS-MH Flood. *Flood Model: Technical Manual*; Federal Emergency Management Agency: Washington, DC, USA, 2003.
44. Riddell, K.; Green, C. Flood and coastal defence project appraisal guidance: Economic appraisal. In *FDCPAG3*; Ministry of Agriculture, Food and Fisheries: Tokyo, Japan, 1999.
45. Cioffi, F.; De Bonis Trapella, A.; Conticello, F.R. Efficiency assessment of existing pumping/hydraulic network systems to mitigate flooding in low-lying coastal regions under different scenarios of sea level rise: The Mazzocchio area study case. *Water* **2018**, *10*, 820. [CrossRef]
46. Jonkman, S.N.; Hillen, M.M.; Nicholls, R.J.; Kanning, W.; van Ledden, M. Costs of adapting coastal defences to sea-level rise—New estimates and their implications. *J. Coast. Res.* **2013**, *29*, 1212–1226. [CrossRef]
47. Deb, K.; Pratap, A.; Agarwal, S.; Meyarivan, T. A fast and elitist multiobjective genetic algorithm: NSGA-II. *IEEE Trans. Evol. Comput.* **2002**, *6*, 182–197. [CrossRef]
48. Goldberg, D.E.; Deb, K. A comparative analysis of selection schemes used in genetic algorithms. In *Foundations of Genetic Algorithms*; Elsevier: Amsterdam, The Netherlands, 1991; Volume 1, pp. 69–93.
49. Deb, K.; Agrawal, R.B. Simulated binary crossover for continuous search space. *Complex Syst.* **1995**, *9*, 115–148.
50. Kemp, A.C.; Horton, B.P.; Donnelly, J.P.; Mann, M.E.; Vermeer, M.; Rahmstorf, S. Climate related sea-level variations over the past two millennia. *Proc. Natl. Acad. Sci. USA* **2011**, *108*, 11017–11022. [CrossRef] [PubMed]
51. Vermeer, M.; Rahmstorf, S. Global sea level linked to global temperature. *Proc. Natl. Acad. Sci. USA* **2009**, *106*, 21527–21532. [CrossRef] [PubMed]
52. Lian, J.; Xu, K.; Ma, C. Joint impact of rainfall and tidal level on flood risk in a coastal city with a complex river network: A case study of Fuzhou City, China. *Hydrol. Earth Syst. Sci.* **2013**, *17*, 679–689. [CrossRef]
53. Coles, S.; Heffernan, J.; Tawn, J. Dependence measures for extreme value analyses. *Extremes* **1999**, *2*, 339–365. [CrossRef]
54. Zheng, F.; Westra, S.; Leonard, M.; Sisson, S.A. Modeling dependence between extreme rainfall and storm surge to estimate coastal flooding risk. *Water Resour. Res.* **2014**, *50*, 2050–2071. [CrossRef]
55. De Haan, L. A spectral representation for max-stable processes. *Ann. Probab.* **1984**, *12*, 1194–1204.
56. Kopp, R.E.; DeConto, R.M.; Bader, D.A.; Hay, C.C.; Horton, R.M.; Kulp, S.; Oppenheimer, M.; Pollard, D.; Strauss, B.H. Evolving understanding of Antarctic ice-sheet physics and ambiguity in probabilistic sea-level projections. *Earth Future* **2017**, *5*, 1217–1233. [CrossRef]

57. DeConto, R.M.; Pollard, D. Contribution of Antarctica to past and future sea-level rise. *Nature* **2016**, *531*, 591–597. [CrossRef]
58. Milne, G.; Gehrels, W.; Hughes, C.; Tamisiea, M. Identifying the causes of sea-level change. *Nat. Geosci.* **2009**, *2*, 471–478. [CrossRef]
59. Taylor, K.E.; Stouffer, R.J.; Meehl, G.A. An overview of CMIP5 and the experiment design. *Bull. Am. Meteorol. Soc.* **2012**, *93*, 485–498. [CrossRef]
60. Rahmstorf, S.; Perrette, M.; Vermeer, M. Testing the robustness of semi-empirical sea level projections. *Clim. Dyn.* **2012**, *39*, 861–875. [CrossRef]
61. Kopp, R.E. Does the mid-Atlantic United States sea level acceleration hot spot reflect ocean dynamic variability? *Geophys. Res. Lett.* **2013**, *40*, 3981–3985. [CrossRef]
62. Bamber, J.L.; Aspinall, W. An expert judgement assessment of future sea level rise from the ice sheets. *Nat. Clim. Chang.* **2013**, *3*, 424–427. [CrossRef]
63. Marzeion, B.; Jarosch, A.; Hofer, M. Past and future sea-level change from the surface mass balance of glaciers. *Cryosphere* **2012**, *6*, 1295–1322. [CrossRef]
64. Cioffi, F.; Gallerano, F. Management strategies for the control of eutrophication processes in Fogliano lagoon (Italy): A long-term analysis using a mathematical model. *Appl. Math. Model.* **2001**, *25*, 385–426. [CrossRef]
65. Kimura, N.; Tai, A.; Chiang, S.; Wei, H.P.; Su, Y.F.; Cheng, C.T.; Kitoh, A. Hydrological flood simulation using a design hyetograph created from extreme weather data of a high-resolution atmospheric general circulation model. *Water* **2014**, *6*, 345–366. [CrossRef]
66. Berrisford, P.; Dee, D.; Poli, P.; Brugge, R.; Fielding, K.; Fuentes, M.; Kallberg, P.; Kobayashi, S.; Uppala, S.; Simmons, A. The ERA-Interim Archive. *Era Rep. Ser.* **2011**, *1*, 1–16.
67. Milano, V. *Idraulica Marittima*; Maggioli Editore: Santarcangelo, Italy, 2008; Volume 152.
68. Pawlowicz, R.; Beardsley, B.; Lentz, S. Classical tidal harmonic analysis including error estimates in MATLAB using T_TIDE. *Comput. Geosci.* **2002**, *28*, 929–937. [CrossRef]
69. Scotti, V.; Giannini, M.; Cioffi, F. Enhanced flood mapping using synthetic aperture radar (SAR) images, hydraulic modelling, and social media: A case study of Hurricane Harvey (Houston, TX). *J. Flood Risk Manag.* **2020**, *13*, e12647. [CrossRef]
70. Farhadi, H.; Najafzadeh, M. Flood Risk Mapping by Remote Sensing Data and Random Forest Technique. *Water* **2021**, *13*, 3115. [CrossRef]
71. Farhadi, H.; Esmaeily, A.; Najafzadeh, M. Flood monitoring by integration of Remote Sensing technique and Multi-Criteria Decision Making method. *Comput. Geosci.* **2022**, *160*, 105045. [CrossRef]
72. Doberstein, B.; Fitzgibbons, J.; Mitchell, C. Protect, accommodate, retreat or avoid (PARA): Canadian community options for flood disaster risk reduction and flood resilience. *Nat. Hazards* **2019**, *98*, 31–50. [CrossRef]
73. Cioffi, F.; Gallerano, F. From rooted to floating vegetal species in lagoons as a consequence of the increases of external nutrient load: An analysis by model of the species selection mechanism. *Appl. Math. Model.* **2006**, *30*, 10–37. [CrossRef]
74. Giambastiani, B.M.; Antonellini, M.; Essink, G.H.O.; Stuurman, R.J. Saltwater intrusion in the unconfined coastal aquifer of Ravenna (Italy): A numerical model. *J. Hydrol.* **2007**, *340*, 91–104. [CrossRef]
75. Gallerano, F.; Cannata, G.; De Gaudenzi, O.; Scarpone, S. Modeling bed evolution using weakly coupled phase-resolving wave model and wave-averaged sediment transport model. *Coast. Eng. J.* **2016**, *58*, 1650011. [CrossRef]
76. Ward, P.J.; de Ruiter, M.C.; Mård, J.; Schröter, K.; Van Loon, A.; Veldkamp, T.; von Uexkull, N.; Wanders, N.; AghaKouchak, A.; Arnbjerg-Nielsen, K.; et al. The need to integrate flood and drought disaster risk reduction strategies. *Water Secur.* **2020**, *11*, 100070. [CrossRef]

sustainability

MDPI

Article

Local-Scale Groundwater Sustainability Assessment Based on the Response to Groundwater Mining (MGSI): A Case Study of Da'an City, Jilin Province, China

Zhang Fang [1,2,*], Xiaofan Ding [1,2,3] and Han Gao [1,2]

[1] Key Laboratory of Groundwater Resources and Environment, Ministry of Education, Jilin University, Changchun 130021, China; dingxf2515@163.com (X.D.); gaohanhan18@163.com (H.G.)
[2] Jilin Provincial Key Laboratory of Water Resources and Environment, Jilin University, Changchun 130021, China
[3] Shenyang Academy of Environmental Sciences, Shenyang 110004, China
* Correspondence: azhang9456@126.com

Abstract: Sustainable groundwater utilization is important for social and economic development. There is a need for groundwater sustainability assessment in small-scale areas lacking detailed mining data. Here, exploiting water level data series, we propose an indicator of groundwater sustainability based on the response to mining (*MGSI*) for better evaluation; it integrates groundwater data and spatio-temporal variability at a local scale. A decomposition coefficient was applied to decompose the pressure exerted by groundwater mining on the groundwater system for each monitoring well. It correlated with the groundwater response state. In Da'an City, Jilin Province, China, the appraised results revealed that the aquifer type exhibiting the greatest risk to groundwater sustainability changed from phreatic to confined during 2008–2017. The spatio-temporal distribution of different sustainability levels between and within the aquifers indicated that adjustment of the groundwater mining layout should be the focus of groundwater management in Da'an City. Additionally, the Mann–Kendall trend test and Sen's slope trend analysis effectively explained the sustainable evolution of groundwater in Da'an City and confirmed the reliability of the *MGSI* method. The proposed method highlights the effects of groundwater mining on sustainability and helps us better understand the interaction between anthropogenic activities and groundwater resources.

Keywords: mining; groundwater response; sustainability assessment

Citation: Fang, Z.; Ding, X.; Gao, H. Local-Scale Groundwater Sustainability Assessment Based on the Response to Groundwater Mining (MGSI): A Case Study of Da'an City, Jilin Province, China. *Sustainability* **2022**, *14*, 5618. https://doi.org/10.3390/su14095618

Academic Editors: Alban Kuriqi and Luis Garrote

Received: 20 March 2022
Accepted: 3 May 2022
Published: 6 May 2022

1. Introduction

Groundwater is one of the most important freshwater resources for maintaining agricultural, economic, and environmental development; it accounts for 35% of global anthropogenic water mining [1–4]. In China, 17.5% of the total water supply is through groundwater mining [5]. The domestic, industrial, and agricultural utilization rates of groundwater are 65%, 50%, and 33%, respectively, as reported by the National Groundwater Pollution and Control Plan (2011–2020) [6]. In particular, the grain-producing areas and commodity grain bases in Northeast China are dominated by groundwater irrigation, with 78% of groundwater mining used for agriculture in 2016 [7]. Consequently, the sustainable mining capacity of groundwater has become crucial to guarantee the steady growth of grain output, promote economic development, maintain the ecological environment, and ensure food security in Northeast China [8]. Accordingly, rigorous assessments of groundwater sustainability are required.

Various methods of groundwater sustainability assessment have been thoroughly investigated; however, none of them are capable of directly and accurately assessing the state of groundwater under the influence of multiple factors such as hydrometeorology, topography, and the extent of anthropogenic activities [9,10]. Thus, several indirect methods are still being applied to assess groundwater sustainability. These indirect methods are

typically based on the following: the theory of water balance and numerical simulation method [11,12], obtaining observational data by remote sensing [13], index evaluation [14], and other techniques such as machine learning [15] and the comprehensive application of multiple methods [16]. Among them, the numerical simulation method can provide effective guidance for groundwater management. However, each numerical model requires abundant datasets and the associated running time to accurately capture the complex relationships between groundwater factors. Moreover, because of the complexity of the model itself, it is difficult for managers to communicate and interact with each other and flexibly adapt to management requirements [17,18]. Remote sensing observation data, such as data obtained from the Gravity Recovery and Climate Experiment (GRACE) program, can indirectly determine the changing trend of groundwater reserves [19–22] in the evaluation of the sustainability of groundwater. However, remote-sensing-based technologies are generally more suitable for larger-scale groundwater research [23,24]. It is difficult to provide sufficient resolution for the acquisition of smaller-scale groundwater information [25]. Moreover, the inappropriate use of such data may lead to erroneous guidance for groundwater management in associated subregions [26]. In contrast, a groundwater sustainability evaluation index system based on monitoring data and statistical data can make better use of surface water data and is more suitable for local-scale assessments. Compared with traditional methods, such an index system can include multiple aspects, such as economic and aquifer variations [27]. It is considerably easier to quantify the influence of each aspect on the entire system. Many such indicators reflecting the current status and future trends of water resources have been used in resource and sustainability evaluations of groundwater and surface water [28–32]. The results have helped to improve our understanding of the spatial and temporal effects of anthropogenic activities and natural processes on water resources [33]. However, owing to the complexity of methodologies, testing, and data acquisition, such an index system is difficult for managers to use.

Long-term variations in groundwater levels reveal natural change processes and disturbances in the water budget related to anthropogenic activities (i.e., groundwater mining). Moreover, in order to describe the dynamic variations in groundwater resources, the groundwater level is more intuitive and is considerably easier to obtain than other indices applied to calculate recharge and discharge. Therefore, the primary aim of this study was to develop a method based on groundwater table data and an indicator system for groundwater sustainability assessment that is suitable for local-scale projects. Therefore, here, we propose the mining-response-based groundwater sustainability index (MGSI). In order to achieve our objective, Da'an City in Jilin Province was selected as the study area. Da'an City is an advanced grain production county (city) in China where crop irrigation is predominantly reliant on groundwater. In recent years, Da'an City has actively promoted the implementation of land consolidation and water-saving irrigation projects in order to improve the current situation of groundwater development and utilization. However, the amount of groundwater withdrawn for irrigation is still increasing (Figure A1). Therefore, a convenient and reliable method to rapidly assess the spatio-temporal distribution of local groundwater sustainability is urgently required to guide future groundwater management in Da'an City.

In this study, groundwater sustainability was quantitatively characterized by combining the pressure index imposed by anthropogenic activities with the groundwater response state. Thereafter, sustainability was classified according to the evaluation results. Subsequently, the nonparametric Mann–Kendall (MK) test [34,35] and Sen's slope trend analysis [36] were applied to analyze the significance and variation degree of the recent long-term trends of groundwater depth to verify the reliability of the index system. The index system reflects the changes in groundwater resource sustainability caused by anthropogenic activities in different locations in the region, providing an assessment method to understand the spatio-temporal evolution of local-scale groundwater sustainability and guide future mining activities.

2. Study Area

Da'an City is a county-level city in Baicheng City in northwestern Jilin Province, China; it experiences one of the most extreme water shortages in western Jilin [37]. The city covers an area of 4879 km^2 (Figure 1) and has a multi-year average precipitation of 389.2 mm and evaporation of 1702.44 mm. It is a county with scarce local surface water resources [38]. The demand for water for daily life, industrial, and agricultural activities predominantly relies on groundwater mining. There is extensive deposition of Neogene mud, sandy rocks, and loose Quaternary materials in the study area, in which several stable and superimposed aquifers have formed. Groundwater mining for industries and agriculture in the study area predominantly involves two Quaternary water aquifers, one phreatic and one confined, which were the target aquifers of this study.

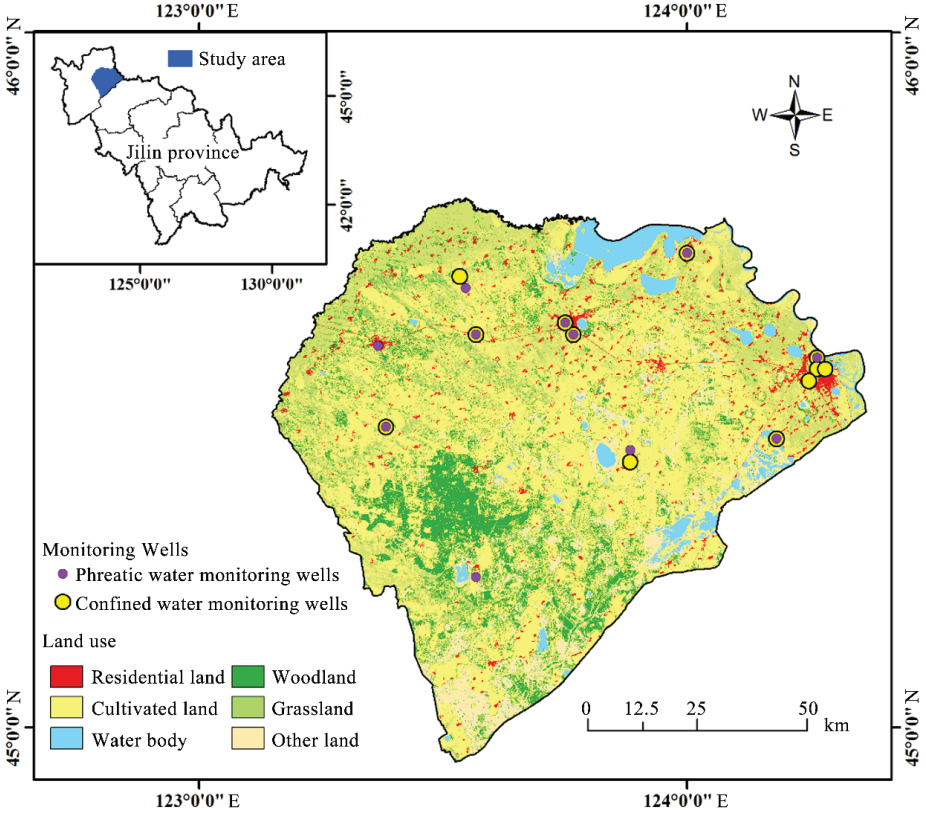

Figure 1. Land use and distribution of monitoring wells in the study area.

Quaternary phreatic aquifers are widely distributed in the study area. The lithology is mainly silty sand and fine sand. The thickness of the aquifer is 1–8 m. The water quality is poor and is generally alkaline. The underlying Quaternary confined aquifers are distributed throughout the area. The lithology is mainly sand and gravel, and the thickness is generally 2–30 m. The water quality is good and the mining value is large.

3. Data Sources

The groundwater depth data of 75 monitoring wells in the study area, collected at five-day intervals between 2000 and 2017, were obtained from the database "Groundwater Dynamic Data (Songyuan and Baicheng volume)" [39]. The monitored horizons, from top to bottom, are as follows: Quaternary phreatic water, Quaternary confined water, and

Neogene confined water. Neogene confined water was not analyzed in this study because it is considered to be a deeper confined water resource and, in principle, can only be used by special industries; therefore, data on mining and monitoring are limited for this horizon.

The data were filtered according to the completeness index (CI, the number of valid data as a percentage of the number of complete data) [40], such that the water level depth data every 5 days in each natural year for each well was greater than 75%. According to this criterion, 23 monitored wells met the requirements (Figure 1), namely, 11 Quaternary phreatic water-monitoring wells and 12 Quaternary confined water-monitoring wells. After filtering, the CI of the water level depth data for each well was 98% for 2008–2017. The groundwater mining data and precipitation data used in this study covered the period from 2000 to 2017 and were obtained from the "Baicheng City Water Resources Bulletin" [41]. The population and economic data used to calculate the degree of mining were collected from the "Jilin Statistical Yearbook" of the Jilin Provincial Bureau of Statistics [42]. The data sharing service system provided a 30 m resolution land-use map of the study area in 2020 [43].

4. Methodology

4.1. Mining-Response-Based Groundwater Sustainability Index (MGSI)

Groundwater sustainability aims to reflect the ability of groundwater to sustain long-term use [18]. Considering this concept, here, we propose the *MGSI*, which reflects both pressure of mining on groundwater sustainability and response of groundwater to mining to indicate how anthropogenic activities affect groundwater sustainability.

After determining the groundwater response state (*RES*) and mining pressure (*PRE*), the *MGSI* can be calculated using Equation (1):

$$MGSI_{ik} = RES_{ik} - PRE_{ik} \quad (1)$$

where i is the year of evaluation and k is the kth monitoring well.

The process of determining the *MGSI* is shown in Figure 2. In ArcGIS, the inverse distance weight method was used to interpolate groundwater sustainability in the study area, and sustainability maps of different aquifers were obtained in accordance with the different monitoring horizons. The mean *MGSI* of the entire aquifer and the *MGSI* at various locations of the aquifer can then be obtained from the *MGSI* grid graph generated by interpolation. The *RES* of each monitoring well can be calculated according to its water level depth data. The *PRE* represents the intensity of mining activities. The degree of mining in the study area is decomposed to each monitoring well through the decomposition coefficient, which indicates whether the groundwater responds sustainably to the pressure of mining activities. In this study, the calculated *MGSI* values of all aquifers were between −0.5660 and 1.938, which were quantified in ArcGIS using the Jenks Natural Breaks Classification method into the following five grades: "Low", "Relatively low", "Medium", "Relatively high", and "High" to describe the sustainability of groundwater, as shown in Table 1. Finally, the spatio-temporal variation in the groundwater sustainability level was analyzed.

Table 1. Classification of groundwater sustainability in the study area.

MGSI Range	Sustainability Level of Groundwater
−0.566 to 0.148	Low
0.148–0.498	Relatively low
0.498–0.776	Medium
0.776–1.145	Relatively high
1.145–1.938	High

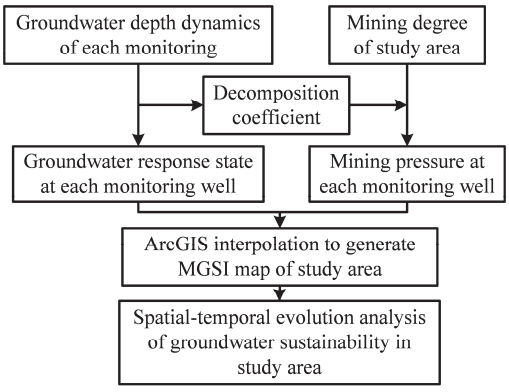

Figure 2. Methodological flowchart for evaluating groundwater sustainability based on artificial mining response.

4.2. Groundwater Response State (RES)

RES refers to the response of groundwater to anthropogenic activities and natural processes and is the sum of the groundwater development potential (*POT*) and groundwater reliability (*REL*), as shown in Equation (2):

$$RES_{ik} = POT_{ik} + REL_{ik} \tag{2}$$

where *POT* describes the relative distance between the groundwater depth in a certain year and the maximum historical depth. The greater the distance, the greater the development potential of the monitoring well location, as shown in Equation (3):

$$POT_{ik} = \frac{max(h_{1k}, h_{2k}, \ldots, h_{mk}) - h_{ik}}{max(h_{1k}, h_{2k}, \ldots, h_{mk}) - min(h_{1k}, h_{2k}, \ldots, h_{mk})} \tag{3}$$

According to the concept of *REL* proposed by Hashimoto et al. [44], this variable indicates the historical possibility that the system is in a satisfactory state; here, the satisfactory state refers to the rise in the water level. As shown in Equations (4) and (5), REL is the ratio of the instances of $\Delta h < 0$ and $m - 1$ in the annual water level series of each monitoring well. Δh was calculated using Equation (5) according to the water level data, and the number of $\Delta h < 0$ indicates the "satisfactory state" in Equation (4). m is the number of years in the water level series, and $m - 1$ is the number of h, which is "all state" in Equation (4). h_{ik} is the average groundwater table depth of hole k in year i:

$$REL_{ik} = \frac{satisfactory\ state}{all\ States} \tag{4}$$

$$\Delta h_{ik} = h_{ik} - h_{i-1,k} \tag{5}$$

4.3. Groundwater Mining Pressure (PRE)

The *PRE* of groundwater at each monitoring well was calculated using Equation (6):

$$PRE_{ik} = DC_{ik} \times MD_i \tag{6}$$

where PRE_{ik} represents the dimensionless value of the groundwater mining pressure at the monitoring well of hole k in year i. DC_{ik} and MD_i indicate decomposition coefficient (*DC*) and degree of mining (*MD*), respectively, which are explained in the following subsections.

4.3.1. Degree of Mining (*MD*)

The technique for order performance by similarity to ideal solution (TOPSIS)-entropy method was used to calculate the comprehensive effect of the amount and intensity of groundwater mining; the selected indexes are listed in Table 2. The entropy weight method can assign weights according to the potential information content of the data, and the TOPSIS method specifically sorts the data according to the relative closeness (C_i) between the evaluation object and the negative ideal solution. The annual mining degree (MD_i) of the study area was replaced by C_i, which was determined using the entropy weight TOPSIS method. Ren [45] describes these calculations in greater detail. However, to avoid a zero value, a different dimensionless method was adopted here, as shown in Equation (7):

$$y_{ij} = \frac{x_{ij}}{\sum_{i=1}^{m} x_{ij}} \quad (7)$$

where i represents the 11 sample years from 2007 to 2017 and j represents the seven indicators in Table 2. In addition, according to the definition of MD_i, the higher the frequency of groundwater mining, the greater the value of y_{ij} and the greater the value of MD_i. The weights of each index and the calculation results of MD_i are listed in Tables 2 and 3, respectively.

Table 2. *MD* index framework and calculation methods.

Target	First-Level Evaluation Index	Serial Number	Secondary Evaluation Index	Data Source/ Calculation Method	Weight Relative to Target
Mining degree	Amount of groundwater mining	1	Total amount of mining	Baicheng City Water Resources Bulletin	0.084
		2	Amount of mining for irrigation	Baicheng City Water Resources Bulletin	0.109
		3	Amount of mining for industry	Baicheng City Water Resources Bulletin	0.122
	Intensity of groundwater mining	4	Groundwater consumption per 10,000 Yuan of GDP	Total amount of mining (10,000 m^3)/GDP (10,000 Yuan)	0.207
		5	Groundwater consumption per capita	Total amount of mining (10,000 m^3)/total population (10,000)	0.099
		6	Intensity of mining for agriculture	Amount of mining for irrigation (10,000 m^3)/total number of agricultural wells	0.228
		7	Groundwater consumption per 10,000 Yuan of industrial production value	Amount of mining for industry (10,000 m^3)/industrial production value (10,000 Yuan)	0.151

Table 3. *MD* calculation results.

i	MD_i	*i*	MD_i	*i*	MD_i
2007	0.126	2008	0.063	2009	0.626
2010	0.789	2011	0.390	2012	0.392
2013	0.140	2014	0.303	2015	0.487
2016	0.971	2017	0.966		

4.3.2. Decomposition Coefficient (*DC*)

As the *MD* can only describe the state of groundwater mining in the entire region, decomposition of *MD* is required to further reflect the *PRE* of the local area and different aquifers. Water level depth dynamics help us understand this groundwater balance as

the difference between the water level depth variation amplitude of different monitoring wells reflecting the magnitude of the production pressure in different locations. Therefore, the *DC*, calculated using Equation (8), was proposed to decompose the *MD* into different spatial locations and closely correlate groundwater mining with the groundwater response. The symbols and subscripts in Equation (8) have the same meaning as those in Equation (5):

$$DC_{ik} = \frac{\Delta h_{ik} - min\left(\Delta h_{i1}, \Delta h_{i2}, \ldots, \Delta h_{iq}\right)}{max\left(\Delta h_{i1}, \Delta h_{i2}, \ldots, \Delta h_{iq}\right) - min\left(\Delta h_{i1}, \Delta h_{i2}, \ldots, \Delta h_{iq}\right)} \quad (8)$$

4.4. Trend Test

The MK trend test method and Sen's slope method were used to detect the trends of time series data and the intensity of trend changes, respectively. These nonparametric methods are widely used in the field of hydrometeorology because they do not require testing of data distribution and the results are considered reliable [46–51]. Here, the two methods were combined to test the annual variation trend of the mean *MGSI* in the study area and the annual average groundwater depth trend of each monitoring well from 2007 to 2017. Details of these methods are not provided here; however, full descriptions can be found in the aforementioned references.

5. Results and Discussion

5.1. Spatio-Temporal Variation in Groundwater Sustainability

The mean *MGSI* of confined water exhibited the same change trend as the amount of mining (Figure 3), indicating that the sustainability of confined water is substantially affected by groundwater mining. Prior to 2015, the *MGSI* of confined water was higher than that of phreatic water; however, later, it became lower than that of phreatic water, although the difference was relatively marginal. This phenomenon was aggravated in 2016–2017, indicating that the rapid increase in mining over the previous years placed a burden on confined water, which is not conducive to groundwater conservation. Therefore, Da'an City should formulate a more reasonable mining plan to ensure the sustainable use of groundwater resources.

In comparison, the phreatic water trend more closely followed that of precipitation, although it was also slightly affected by the amount of mining (Figure 3). For example, during 2012–2014, a decrease in precipitation led to a decrease in the recharge received by phreatic water. However, owing to the simultaneous decrease in the amount of mining during this period, the decreased precipitation did not ultimately lead to a downward trend in the mean *MGSI* of phreatic water. The same situation occurred during 2014–2016, wherein precipitation increased the recharge of phreatic water, but a significant increase in mining ultimately caused a decrease in the mean *MGSI* of phreatic water.

The actual state of groundwater in Da'an City is consistent with the results of this study, that is, poor water quality and low mining are characteristics of phreatic water in the study area and precipitation is the main factor affecting the phreatic water. Although the changes in precipitation affect the leakage recharge of phreatic water to the confined aquifer, confined water is still the main source of water in Da'an City, and it is largely influenced by anthropogenic factors.

The highest mean *MGSI* values for the confined aquifer (1.326) and phreatic aquifer (0.999) occurred in 2008 and 2014, respectively. The lowest mean *MGSI* values for both aquifers occurred in 2010 (0.230 and 0.283 for phreatic and confined water, respectively). The calculation results of the MK trend test and Sen's slope analysis are shown in Table 4. Notably, the average *MGSI* of the phreatic aquifer increased at a rate of 0.01 per year, whereas that of the confined aquifer decreased at a rate of 0.04 per year, which indicates that the risk of groundwater becoming nonsustainable within the study area shifted from the phreatic aquifer to the confined aquifer with time. However, this trend was not significant at the 95% confidence level.

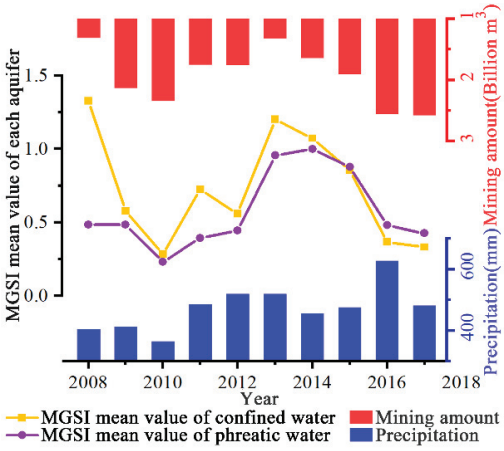

Figure 3. Annual variation trends of the mean *MGSI* for the phreatic and confined aquifers according to the amount of mining and precipitation.

Table 4. Trends of mean *MGSI* for aquifers in the study area.

Aquifer	Mean *MGSI*	Significance (5% Significance Level)	Trend	Sen's Slope (/a)
Phreatic	0.230–0.999	Insignificant	Increasing	0.01
Confined	0.283–1.326	Insignificant	Decreasing	−0.04

This finding is supported by the observation that the zone with the lowest sustainability was the largest in the phreatic aquifer in 2010, representing 45.2% of the study area, but also was the largest in the confined aquifer in 2017, representing 32.5% of the study area (Figure 4). In 2008, the sustainability levels of the two aquifers were highly in contrast. This phenomenon can be explained by the fact that the annual variation in groundwater depth was used to calculate the MGSI; that is, the groundwater depth in 2007 was used to calculate the *MGSI* in 2008. To confirm the validity of the calculation results for 2008, the variation in water level was calculated for 23 monitoring wells from 2007 to 2008. During this period, the groundwater depth of phreatic monitoring wells increased by 0.52 m per year, whereas that of the confined aquifer decreased by 0.03 m per year. This explains the difference in the sustainability levels of the two aquifers in 2008.

During 2009–2012, the sustainability level of the phreatic aquifer was predominantly "Relatively low", whereas that of the confined aquifer was predominantly "Medium". During this period, the depth of the confined aquifer was relatively stable and the overall sustainability was better than that of the phreatic aquifer. Similarly, during 2013–2015, both aquifers showed larger areas of "High" and "Relatively high" sustainability. However, subzones of "High" and "Relatively high" sustainability in the confined and phreatic aquifers gradually decreased after 2013 and 2014, respectively. After 2015, "Low" sustainability subzones gradually expanded, particularly in the confined aquifer.

To understand the changes in the spatio-temporal distribution of the sustainability level of each aquifer, representative years were selected (2008, 2010, 2014, and 2017). Figure 5 shows the spatial changes in the sustainability level subzones of each aquifer throughout the study period (2008–2017). In 2008, "Relatively low" sustainability subzones accounted for a relatively large proportion of the phreatic aquifer (Figure 5a), and they were distributed in the eastern and central regions (Subregion a1 in Figure 5a). This was almost the worst state of phreatic sustainability in 2008, except for a localized "Low" sustainability subzone in the northeast of the study area (Subregion a2 in Figure 5a). By 2010, the

"Medium" sustainability subzone in the east (Subregion a1) had expanded into the middle (Subregion b1 in Figure 5b) of the study area, with some "Relatively high" sustainability subzones appearing in this region. In 2007, in order to secure food and water supplies, the Jilin Provincial Government began to implement the use of water from the Nenjiang River (in the eastern and central parts of the study area) to irrigate the Da'an Irrigation Area. This resolution used part of the confined aquifer area for irrigation and transformed dry and saline land into paddy fields [52]. The expansion of paddy fields would have increased the amount of infiltration into the phreatic aquifer, thereby raising the water level in the area. Dry conditions in 2010 then encouraged evaporation, and high groundwater consumption increased mining, leading to "Low" sustainability levels over a relatively large area of the phreatic aquifer in this year. High precipitation and low mining around 2014 then effectively replenished the groundwater resources, which had an equally large effect on both phreatic and confined aquifers (Figure 5c,g). Continuously increasing mining resulted in the "Relatively low" sustainability subzone again occupying most of the phreatic aquifer (Figure 5d).

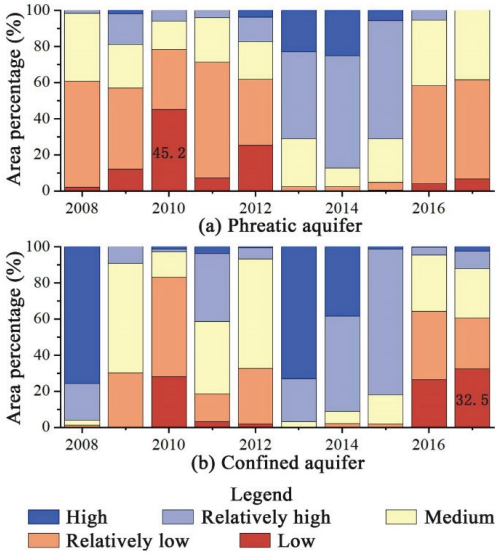

Figure 4. Percentage (by area) of different groundwater sustainability subzones in the study area.

Considering that confined water level recovery in 2008 was relative to the previous year, the sustainability level for the confined aquifer in that year was "High" (Figure 5e). By 2010, under the influence of a more arid climate, almost the entire area exhibited "Relatively low" sustainability, with a large area of "Low" sustainability appearing in the center of the study area (Subregion f1 in Figure 5f). This is because the Da'an Irrigation Area is located in the central region (Subregion f1), which contained a large number of paddy fields that were irrigated by the Nenjiang River in normal years and supplemented by confined water in dry years. Low precipitation in 2010 and crop growth demands led to highly concentrated mining, thereby contributing to the development of a "Low" sustainability subzone in the central region (Subregion f1). To verify the above explanation, the actual amount of groundwater mining was investigated over the entire study area used for agricultural irrigation. The data showed that phreatic water was not used for agricultural irrigation. The amount of confined water extracted for agricultural irrigation was 181.85 million m^3 in 2009, 146.37 million m^3 in 2011, when rainfall was relatively abundant, and 200 million m^3 in 2010, when rainfall was relatively infrequent. The increased mining of confined water in 2010 effectively explain the "Low" sustainability subzone in the central region (Subregion

f1). With this reduction in confined water sustainability, "Low" sustainability subzones became concentrated in the west of the study area by 2017 (Subregion h1 in Figure 5h).

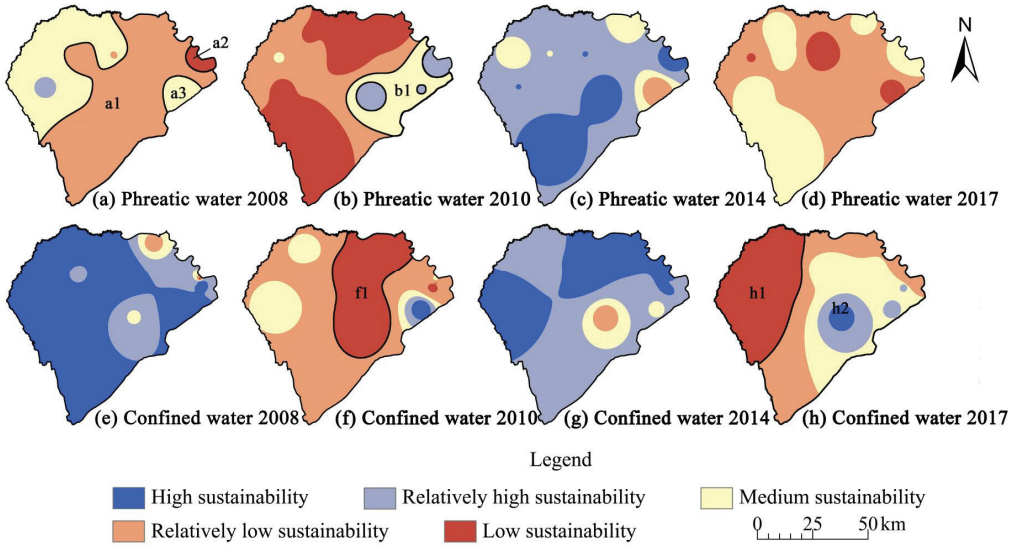

Figure 5. Distribution of sustainability level subzones.

Currently, industrial, agricultural, and domestic water use in Da'an City mainly depend on groundwater, and confined water accounts for a large proportion. Therefore, strengthening the protection of groundwater resources is important for economic development, food security, and water security. In the future, Da'an City should pay close attention to groundwater mining in the western region and improve water use efficiency throughout the region to avoid uncontrolled mining.

5.2. Change Trends of Groundwater Depth

According to the calculation results of the groundwater depth change trend, only a small portion of phreatic monitoring wells (27.3%, three wells) exhibited a decreasing trend during 2007–2017. Phreatic water depth mainly increased in the north, at a typical rate of 0.036–0.083 m/a (Figure 6). The difference in groundwater depth between the north and south verified the results shown in Figure 5, i.e., that the phreatic sustainability level was typically higher in the south than in the north. According to the distribution of Sen's slope values (Figure 6), the trend of rising groundwater depths in southern (−0.009 to 0.036 m/a) and northeastern marginal areas (−0.077 to 0.009 m/a) was consistent with the long-term trends of the distribution of sustainability level subzones for phreatic water. The results for the northeastern marginal area are the most intuitive, that is, the area experienced "Low", then "Relatively high", then "High" sustainability levels during the study period (the subregion corresponding to a2 in Figure 5a–c). By 2017, although the sustainability level of the area had decreased, it was still higher than that of most other areas (Figure 5d). Moreover, Sen's slope value (0.083–0.308 m/a) at Well 9 in Figure 6 verifies the change from "Relatively high" sustainability to "Relatively low" and then "Low" sustainability (Figure 5b–d). In addition, for phreatic water, the number of monitoring wells with significant trends was very small (18.2%). Only two phreatic water-monitoring wells exhibited a significant increase in depth during the study period, namely, Wells 8 and 9 (Figure 6). Of these, Well 9 (southeast of the study area) exhibited the largest Sen's slope value of the entire area (Figure 6), with a significant increase in depth of 0.31 m/a, whereas that for Well 8 (northwest) was 0.15 m/a. These significant increasing trends of groundwater depth indicate that the phreatic water in these subzones has been over-

consumed in recent years. Therefore, long-term monitoring in these subzones is necessary to maintain the sustainable utilization of groundwater.

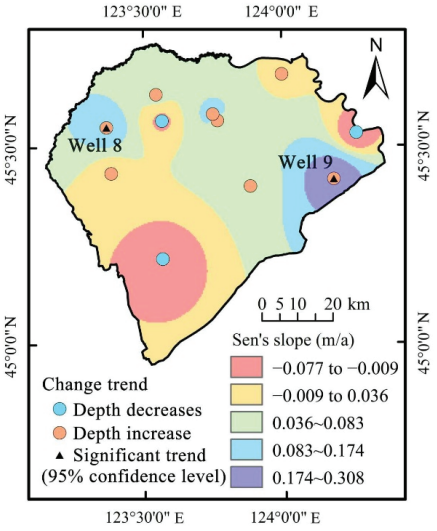

Figure 6. Distribution of Sen's slope values for phreatic water depth and water depth trends in the monitoring wells.

Figure 7 shows the confined water trend analysis and spatial distribution of the Sen's slope calculation results. During the analysis period, six of the twelve confined water-monitoring wells showed an increasing trend, whereas the other six showed a decreasing trend. In contrast to phreatic water, the confined water depth trend differed in the east-west direction, that is, it increased in the west of the study area but generally decreased in the east. The area of increasing groundwater depth (Sen's slope value of 0.015–0.328 m/a in Figure 7) agrees with the reduction in the sustainability level of confined water observed in the west of Da'an City in Figure 5, where the dominant sustainability level in this region changed from "High" to "Low" (subregion corresponding to h1 in Figure 5e,f,h). However, the sustainability level of confined water in the east of the study area (subregion corresponding to h2 in Figure 5e–h) was not consistent with the trend of Sen's slope values (Sen's slope value of −0.316–−0.030 m/a in Figure 7) for the groundwater depth in the monitoring wells. Specifically, the groundwater depth in the monitoring wells in the area characterized by the Sen's slope values of 0.034–0.328 showed a consistent increasing trend, whereas that in the area with the Sen's slope values of −0.316 to 0.034 showed a different trend. Therefore, the spatio-temporal variation in the confined water sustainability level is more complex in the east of the study area than in the west. Regarding the variation in confined water level depths, 16.7% of the monitoring wells (two wells) showed a significant increasing trend. In contrast, 8.3% (one well) showed a significant decreasing trend. Figure 7 shows three confined water-monitoring wells with significant trends in the study area, where Well 5 exhibited the fastest decrease in water depth over the study area (0.32 m/a) and Well 18 exhibited the largest increase in water depth over the study area (0.33 m/a). The significant decrease in water depth in Well 5 indicates that the confined aquifer in this area has the potential for further mining.

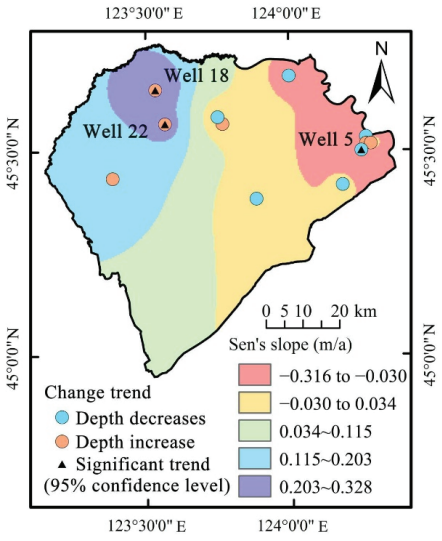

Figure 7. Distribution of Sen's slope values for confined water depth and water depth trends in the monitoring wells.

6. Conclusions

We demonstrated a method developed to assess the sustainability of local-scale groundwater based on the degree of groundwater mining and the subsequent changes in groundwater level, called the mining-response-based groundwater sustainability index (MGSI). This index can be used by water management departments to guide groundwater development and utilization planning. The selection of indicators and evaluation methods is a key aspect of sustainability evaluations. We introduced the following new indicators to construct the evaluation system: (1) the decomposition coefficient (DC) was proposed in order to decompose the degree of mining over the entire study area into mining pressure at each point; (2) an indicator of the development potential of groundwater (POT) was used to describe the relative distance between the current water depth and the maximum historical depth; and (3) an indicator was developed to reflect the reliability of groundwater in terms of the potential groundwater level rise (REL). Long-term variation trends of groundwater depth verified the reliability of the *MGSI* method. The proposed groundwater sustainability index based on groundwater's response to mining can be used to monitor groundwater sustainability and analyze local spatio-temporal variations in groundwater sustainability. Such an analysis can help identify areas of potential groundwater sustainability and areas requiring protection from groundwater mining, as well as to implement effective groundwater resource management.

We demonstrated the potential of the evaluation method by taking Da'an City as an example and made the following conclusions:

(1) The mean *MGSI* of confined water is more significantly affected by groundwater mining than that of phreatic water. During 2013–2017, with the increase in mining, the mean *MGSI* of confined water dropped sharply, and the mean *MGSI* of phreatic water also showed a similar trend. In the future, water resource management should consider replacing groundwater with surface water or other water sources to reduce groundwater exploitation.

(2) The mean *MGSI* of the phreatic aquifer increases at a rate of 0.01 per year, whereas that of the confined aquifer decreases at a rate of 0.04 per year. Therefore, the mining of confined water in Da'an City should be carried out more cautiously in the future.

(3) The sustainability level evaluation using the *MGSI* shows that the continuous increase in mining up to 2017 subsequently led to the "Relatively low" sustainable subzone

occupying most of the submerged aquifer, and the "Low" sustainable subzone of the confined aquifer was concentrated in the west of Da'an City. Reducing mining and the utilization of groundwater is still a challenge that should be overcome in Da'an City, especially in the west of Da'an City. Taking into account the local conditions, developing water-saving agriculture, or replacing paddy fields with dry fields should be considered.

(4) The groundwater depths of Well 8 and Well 9 have increased significantly, indicating that the phreatic water in these areas has been overconsumed during recent years, and management measures should be implemented in the future while continuing to pay attention to the groundwater levels in these areas. The groundwater depth of Well 5 decreased significantly, indicating that the confined water in this area has the potential for further mining.

Author Contributions: Z.F. proposed the indicator of *MGSI* and drafted the manuscript. X.D. appraised the groundwater sustainability. H.G. drew the figures and reviewed the manuscript. All authors have read and agreed to the published version of the manuscript.

Funding: This research was funded by the National Key Research and Development Program of China under Contract No. 2020YFC1808300.

Institutional Review Board Statement: This study did not require ethical approval; all data are available in the public domain.

Data Availability Statement: Authors understand that journal encouraged data sharing and data citation.

Conflicts of Interest: The authors declare no conflict of interest.

Appendix A

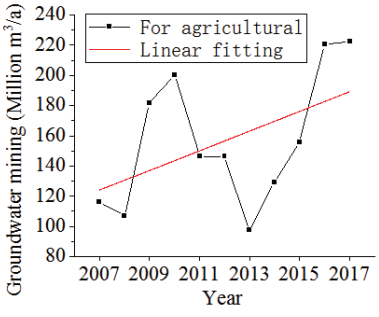

Figure A1. Agricultural exploitation from 2007 to 2017 and linear fitting.

References

1. Döll, P.; Hoffmann-Dobrev, H.; Portmann, F.T.; Siebert, S.; Eicker, A.; Rodell, M.; Strassberg, G.; Scanlon, B.R. Impact of water withdrawals from groundwater and surface water on continental water storage variations(Article). *J. Geodyn.* **2012**, *59–60*, 143–156. [CrossRef]
2. Rahman, A.T.M.S.; Hosono, T.; Kisi, O.; Dennis, B.; Imon, A.H.M.R. A minimalistic approach for evapotranspiration estimation using the Prophet model. *Hydrol. Sci. J.* **2020**, *65*, 1994–2006. [CrossRef]
3. Rahman, A.T.M.S.; Hosono, T.; Quilty, J.M.; Das, J.; Basak, A. Multiscale groundwater level forecasting: Coupling new machine learning approaches with wavelet transforms. *Adv. Water Resour.* **2020**, *141*, 103595. [CrossRef]
4. Rahman, A.T.M.S.; Jahan, C.S.; Mazumder, Q.H.; Kamruzzaman, M.; Hosono, T. Drought analysis and its implication in sustainable water resource management in Barind area, Bangladesh. *J. Geol. Soc. India* **2017**, *89*, 47–56. [CrossRef]
5. Ministry of Water Resources of the People's Republic of China, China Water Resources Bulletin (2015). 2015. Available online: http://www.mwr.gov.cn/sj/tjgb/szygb/201612/t20161229_783348.html (accessed on 21 March 2021).
6. Ministry of Ecology and Environment of the People's Republic of China, 2011, National Groundwater Pollution and Control Plan (2011–2020). Available online: http://www.gov.cn/gongbao/content/2012/content_2121713.htm (accessed on 21 March 2021).

7. Yu, L.; Tang, S.; Ding, Y.; Chen, F.; Yang, Y.; Ding, Y.; He, J. The situation and countermeasures of groundwater overexploitation in northeast China. *Water Resour. Plan. Des.* **2019**, *186*, 37–40. (In Chinese) [CrossRef]
8. Wang, Y.X.; Zheng, C.M.; Ma, R. Review: Safe and Sustainable Groundwater Supply in China. *Hydrogeol. J.* **2018**, *26*, 1301–1324. [CrossRef]
9. Harmancioglu, N.; Barbaros, F.; Cetinkaya, C. Sustainability Issues in Water Management. *Water Resour. Manag.* **2013**, *27*, 1867–1891. [CrossRef]
10. Wable, P.; Jha, M.; Murasingh, S. Evaluation of groundwater resources for sustainable groundwater development in a semiarid river basin of India. *Environ. Earth Sci.* **2017**, *76*, 601. [CrossRef]
11. Pétré, M.-A.; Rivera, A.; Lefebvre, R. Numerical modeling of a regional groundwater flow system to assess groundwater storage loss, capture and sustainable exploitation of the transboundary Milk River Aquifer (Canada–USA). *J. Hydrol.* **2019**, *575*, 656–670. [CrossRef]
12. Zhang, X.; Ren, L.; Kong, X. Estimating spatiotemporal variability and sustainability of shallow groundwater in a well-irrigated plain of the Haihe River basin using SWAT model. *J. Hydrol.* **2016**, *541*, 1221–1240. [CrossRef]
13. Patra, S.; Mishra, P.; Mahapatra, S.C. Delineation of groundwater potential zone for sustainable development: A case study from Ganga Alluvial Plain covering Hooghly district of India using remote sensing, geographic information system and analytic hierarchy process(Article). *J. Clean Prod.* **2018**, *172*, 2485–2502. [CrossRef]
14. Salmoral, G.; Viñarta Carbó, A.; Zegarra, E.; Knox, J.W.; Rey, D. Reconciling irrigation demands for agricultural expansion with environmental sustainability—A preliminary assessment for the Ica Valley, Peru. *J. Clean Prod.* **2020**, *276*, 123544. [CrossRef]
15. Pal, S.; Kundu, S.; Mahato, S. Groundwater potential zones for sustainable management plans in a river basin of India and Bangladesh. *J. Clean Prod.* **2020**, *257*, 120311. [CrossRef]
16. Vu, T.D.; Ni, C.; Li, W.; Truong, M.H.; Hsu, S.M. Predictions of groundwater vulnerability and sustainability by an integrated index-overlay method and physical-based numerical model(Article). *J. Hydrol.* **2021**, *596*, 126082. [CrossRef]
17. Gleeson, T.; Alley, W.M.; Allen, D.M.; Sophocleous, M.A.; Zhou, Y.; Taniguchi, M.; VanderSteen, J. Towards sustainable groundwater use: Setting long-term goals, backcasting, and managing adaptively. *Ground Water* **2012**, *50*, 19–26. [CrossRef]
18. Pandey, V.P.; Shrestha, S.; Chapagain, S.K.; Kazama, F. A framework for measuring groundwater sustainability. *Environ. Sci. Policy* **2011**, *14*, 396–407. [CrossRef]
19. Castle, S.L.; Thomas, B.F.; Reager, J.T.; Rodell, M.; Swenson, S.C.; Famiglietti, J.S. Groundwater depletion during drought threatens future water security of the Colorado River Basin. *Geophys. Res. Lett.* **2014**, *41*, 5904–5911. [CrossRef]
20. Famiglietti, J.S.; Lo, M.; Ho, S.L.; Bethune, J.; Anderson, K.J.; Syed, T.H.; Swenson, S.C.; de Linage, C.R.; Rodell, M. Satellites measure recent rates of groundwater depletion in California's Central Valley. *Geophys. Res. Lett.* **2011**, *38*, L03403–L03406. [CrossRef]
21. Nanteza, J.; de Linage, C.R.; Thomas, B.F.; Famiglietti, J.S. Monitoring groundwater storage changes in complex basement aquifers: An evaluation of the GRACE satellites over East Africa. *Water Resour. Res.* **2016**, *52*, 9542–9564. [CrossRef]
22. Thomas, B.F.; Caineta, J.; Nanteza, J. Global Assessment of Groundwater Sustainability Based On Storage Anomalies. *Geophys. Res. Lett.* **2017**, *44*, 11445–11455. [CrossRef]
23. Chen, J.; Famigliett, J.S.; Scanlon, B.R.; Rodell, M. Groundwater Storage Changes: Present Status from GRACE Observations. *Surv. Geophys.* **2016**, *37*, 397–417. [CrossRef]
24. Di, L.; Pan, Y.; Zhou, J.; Chen, Y.; Hou, X.; Hong, Y.; Scanlon, B.R.; Longuevergne, L. Global analysis of spatiotemporal variability in merged total water storage changes using multiple GRACE products and global hydrological models. *Remote Sens. Environ.* **2017**, *192*, 198–216. [CrossRef]
25. Alley, W.M.; Konikow, L.F. Bringing GRACE Down to Earth. *Ground Water* **2015**, *53*, 826–829. [CrossRef] [PubMed]
26. Thomas, B.; Famiglietti, J. Sustainable Groundwater Management in the Arid Southwestern US: Coachella Valley, California. *Water Resour. Manag.* **2015**, *29*, 4411–4426. [CrossRef]
27. Mays, L.W. Groundwater Resources Sustainability: Past, Present, and Future. *Water Resour. Manag.* **2013**, *27*, 4409–4424. [CrossRef]
28. Gain, A.K.; Giupponi, C.; Wada, Y. Measuring global water security towards sustainable development goals. *Environ. Res. Lett.* **2016**, *11*, 124015. [CrossRef]
29. Chaves, H.M.L.; Alipaz, S. An Integrated Indicator Based on Basin Hydrology, Environment, Life, and Policy: The Watershed Sustainability Index. *Water Resour. Manag.* **2007**, *21*, 883–895. [CrossRef]
30. Lavapuro, M.; Lipponen, A.; Artimo, A.; Katko, T.S. Groundwater sustainability indicators: Testing with Finnish data. *Boreal Environ. Res.* **2009**, *13*, 381–402.
31. Wada, Y.; Van Beek, L.P.; Van Kempen, C.M.; Reckman, J.W.; Vasak, S.; Bierkens, M.F. Global depletion of groundwater resources. *Geophys. Res. Lett.* **2010**, *37*, 1–5. [CrossRef]
32. White, S.D. Framing water sustainability in an environmental decision support system. *Soc. Natur. Resour.* **2013**, *26*, 1365–1373. [CrossRef]
33. Chen, J.; Zhang, Y.; Chen, Z.; Nie, Z. Improving assessment of groundwater sustainability with analytic hierarchy process and information entropy method: A case study of the Hohhot Plain, China. *Environ. Earth Sci.* **2015**, *73*, 2353–2363. [CrossRef]
34. Kendall, M.G. *Rank Auto-Correlation Methods*; Charles Griffin: London, UK, 1975.
35. Mann, H.B. Nonparametric Tests Against Trend. *Econometrica* **1945**, *13*, 245–259. [CrossRef]
36. Sen, P.K. Estimates of the Regression Coefficient Based in Kendall's Tau. *J. Am. Stat. Assoc.* **1968**, *63*, 1379. [CrossRef]

37. Wang, L. Analysis of the main problems existing in the development and utilization of water-saving and grain-increasing water resources in Da'an City, Jilin Province. *Agric. Technol.* **2015**, *35*, 63–64,85. (In Chinese) [CrossRef]
38. Qu, K.; Zhang, Z. Prediction of drawdown cone of groundwater extraction in Da'an City the second water sources. *Jilin Geol.* **2013**, *32*, 133–135. (In Chinese) [CrossRef]
39. Jilin Provincial Water Resources Department. *Groundwater Dynamic Data (Songyuan, Baicheng Volume)*; Jilin Provincial Water Resources Department: Changchun, China, 2007–2017.
40. Manuela, L.; Susanna, M.; Antonio, D.L.D. Groundwater hydrodynamic behaviours based on water table levels to identify natural and anthropic controlling factors in the Piedmont Plain (Italy). *Sci. Total Environ.* **2020**, *716*, 137051. [CrossRef]
41. *Baicheng Water Resources Management Center, 2007–2017*; Baicheng Water Resources Bulletin: Baicheng, China, 2007–2017.
42. Statistic Bureau of Jilin. *Jilin Statistical Yearbook*; Jilin University Audio and Video Press: Jilin, China, 2017. Available online: http://tjj.jl.gov.cn/tjsj/tjnj/ (accessed on 21 March 2021).
43. Liu, L.; Zhang, X. Global 30 m Fine Surface Coverage Products in 2020. 2020. Available online: http://data.casearth.cn/sdo/detail/5fbc7904819aec1ea2dd7061 (accessed on 21 March 2021).
44. Hashimoto, T.; Stedinger, J.R.; Loucks, D.P. Reliability, resiliency, and vulnerability criteria for water resource system performance evaluation. *Water Resour. Res.* **1982**, *18*, 14–20. [CrossRef]
45. Ren, Z. Evaluation Method of Port Enterprise Product Quality Based on Entropy Weight TOPSIS. *J. Coast. Res.* **2020**, *103*, 766–769. [CrossRef]
46. Jayanta, D.; Mandal, T.; Saha, P.I.U.; Bhattacharya, S.K. Variability and trends of rainfall using non-parametric approaches: A case study of semi-arid area. *Mausam* **2020**, *71*, 33–44. [CrossRef]
47. Kamruzzaman, M.; Rahman, A.T.M.; Ahmed, M.; Kabir, M.; Mazumder, Q.H.; Rahman, M.S.; Jahan, C.S. Spatio-temporal analysis of climatic variables in the western part of Bangladesh. *Environ. Dev. Sustain.* **2018**, *20*, 89–108. [CrossRef]
48. Nalley, D.; Adamowski, J.; Khalil, B.; Ozga-Zielinski, B. Trend detection in surface air temperature in Ontario and Quebec, Canada during 1967–2006 using the discrete wavelet transform. *Atmos. Res.* **2013**, *132*, 375–398. [CrossRef]
49. Rahman, A.T.M.S.; Ahmed, M.S.; Adnan, H.M.; Kamruzzaman, M.; Khalek, M.A.; Mazumder, Q.H.; Jahan, C.S. Modeling the changes in water balance components of the highly irrigated western part of Bangladesh. *Hydrol. Earth. Syst. Sci.* **2018**, *22*, 4213–4228. [CrossRef]
50. Rahman, A.T.M.S.; Kamruzzama, M.; Jahan, C.S.; Mazumder, Q.H. Long-term trend analysis of water table using "MAKESENS" model and sustainability of groundwater resources in drought prone Barind area, NW Bangladesh. *J. Geol. Soc. India* **2016**, *87*, 179–193. [CrossRef]
51. Tabari, H.; Nikbakht, J.; Some'e, B.S. Investigation of groundwater level fluctuations in the north of Iran. *Environ. Earth Sci.* **2012**, *66*, 231–243. [CrossRef]
52. Zhang, L. *Study on the Groundwater and Ecological Landscape Influenced by Water Diversion Project in Da'an County*; Jilin University: Changchun, China, 2012.

International Journal of
Environmental Research and Public Health

MDPI

Article

The Economic Impact of Climate Change on Wheat and Maize Yields in the North China Plain

Chunxiao Song [1], Xiao Huang [2], Oxley Les [3], Hengyun Ma [1,*] and Ruifeng Liu [1]

[1] College of Economics and Management, Henan Agricultural University, Zhengzhou 450046, China; scx2011aqr@163.com (C.S.); ruifeng076@163.com (R.L.)
[2] College of Mechanical & Electrical Engineering, Henan Agricultural University, Zhengzhou 450046, China; huangxiao201998@163.com
[3] Department of Economics and Finance, University of Waikato, Hamilton 3240, New Zealand; loxley@waikato.ac.nz
* Correspondence: h.y.ma@163.com

Abstract: Climate change has significantly affected agricultural production. As one of China's most important agricultural production regions, the North China Plain (NCP) is subject to climate change. This paper examines the influence of climate change on the wheat and maize yields at household and village levels, using the multilevel model based on a large panel survey dataset in the NCP. The results show that: (i) Extreme weather events (drought and flood) would significantly reduce the wheat and maize yields. So, the governments should establish and improve the emergency service system of disaster warning and encourage farmers to mitigate the adverse effects of disasters. (ii) Over the past three decades, the NCP has experienced climate change that affects its grain production. Therefore, it is imperative to build the farmers' adaptive capacity to climate change. (iii) Spatial variations in crop yield are significantly influenced by the household characteristics and the heterogeneity of village economic conditions. Therefore, in addition to promoting household production, it is necessary to strengthen and promote China's development of the rural collective economy, especially the construction of rural irrigation and drainage infrastructures.

Keywords: climate change; extreme weather event; multi-level model; grain crop yield; village collective economy

Citation: Song, C.; Huang, X.; Les, O.; Ma, H.; Liu, R. The Economic Impact of Climate Change on Wheat and Maize Yields in the North China Plain. *Int. J. Environ. Res. Public Health* **2022**, *19*, 5707. https://doi.org/10.3390/ijerph19095707

Academic Editors: Alban Kuriqi and Luis Garrote

Received: 9 April 2022
Accepted: 5 May 2022
Published: 7 May 2022

1. Introduction

Climatic conditions have always been an important factor shaping agricultural production. Climate change, especially in terms of extreme weather events, has exacerbated the fluctuations in food production and threatened world food security. In most part of China, increase in temperature is the main climate change issue reducing the major crop (wheat, rice, and maize) yields [1–4]. Increased extreme weather events associated with climate warms have exacerbated the decrease in food production in China. Since the 21st century (2000–2019), the average annual crop area affected by drought and flood were 17,966.6 and 10,011.1 thousand hectares, accounting for 11.3% and 5.3% of the total area, respectively. Crop yield loss due to drought has reached 26.39 million tons, and the crop loss rate has reached 4.7% [5,6]. As one of the most important agricultural production regions in China, the North China Plain (NCP) is subject to climate change and is often hit by extreme weather events, particularly drought [7].

Researchers have used econometric approaches to analyze the impact of climate change on grain production. Mendelsohn et al. [8] first proposed the Ricardian approach to analyze the climate change effect on farmland value (profit or net productivity of land). Liu et al. [9], Wang et al. [10], and Chen et al. [11] also employed the Ricardian approach to study the impact of climate change on China's grain profit. However, the empirical results may be biased due to a few limitations, including the omission of irrigation variables

in the model [10,12,13], the assumption of the unchanged price of grain and production inputs [14–16], and cost-free adaptation and adjustment implied in the models [17].

To address the limitations of the Ricardian approach, the production function approach was used to reveal an empirical relationship between climate factors and grain output in agricultural production, particularly in China [1–3,18–22]. However, most of the existing literature only focuses on long-term climate change such as changes in temperature and precipitation, while the studies on the impact of extreme weather events are scarce [23,24]. Furthermore, most previous literature uses macro data at the provincial or county level, which cannot effectively reflect the farmer's behavioral selection characteristics or the village socio-economic characteristics, and their impact on crop yield. A village composed of farm households is the smallest administrative unit in rural China. The development of village collective economy plays a key role in ensuring food security, and it is an important guarantee for accelerating the building of a moderately prosperous society in all respects in rural areas [25,26]. Therefore, it is essential to capture the impact of climate change on grain yield at both the household and village levels [19,27].

To achieve the above goal, it is necessary to use a multilevel model to analyze large-scale survey data of farm households which typically adopt stratified multistage clustered sampling designs (with household level and village level). The multilevel analysis can model the clusters occurring at different levels of the sampling with nested random effects [28]. This study has shown that there were large spatial and temporal variations in climatic change factors in different growth stages of wheat and maize, and climatic factors in different growth stages have different effects on wheat and maize yield [3,29]. Meanwhile, this paper has also found that village heterogeneity plays a significant role in variation of gain yield, which likely indicates that developing rural village collective economy can reduce the negative effect of climate change on grain crop production in the NCP.

The rest of this paper is organized as follows: Section 2 briefly introduces the theoretical framework of multilevel model. Section 3 describes the sampling procedure and variables. The estimation results are presented in Section 4, and the final section concludes with some policy suggestions.

2. Theoretical Framework of Multilevel Model

The stratified sampling data with clustered characteristics show significant differences between different levels of data and high similarity among data at the same level. In this case, a regular ordinary least squares (OLS) model may result in misspecification by ignoring the average variation between groups. Therefore, a multi-level model (MLM) should be developed to deal with the heteroscedasticity caused by inter-dependent error terms and to estimate group-level averages by both fixed and random effects [30]. MLM decomposes the variance in the outcome into two components, one is attributed to the differences between individuals located in different groups and the other is related to the variation between individuals within the same group. This decomposition of variance into "between groups" and "within groups" corrects parameter estimation errors due to within-level sample similarity. Thus, this study uses the MLM to estimate the influencing factors of wheat and maize yields in the NCP at both household and village levels. The two types of MLM are introduced as follows.

2.1. Unconditional Means Model

The unconditional means model is an "empty model" that does not include any independent variables. It is reasonable to adopt MLM if individual respondents are clustered within groups and the variance of outcome in two levels are significantly different in a data structure. Assuming that Y_{ij} is grain yield measured for the ith farm plot of household in the jth village, the equations are as follows:

$$Y_{ij} = \beta_{0j} + \varepsilon_{ij} \quad (1)$$

$$\beta_{0j} = \gamma_{00} + \mu_{0j} \quad (2)$$

where β_{0j} represents the intercept term (the mean value of Y_{ij}) for village j, and ε_{ij} is the residual for farm household in village j (an individual-level random component) in Equation (1). Equation (2) can be obtained by decomposing β_{0j} into a fixed (γ_{00}) and a village-level random component (μ_{0j}). Then, substituting (2) into (1) obtains Equation (3):

$$Y_{ij} = \gamma_{00} + \mu_{0j} + \varepsilon_{ij} \quad (3)$$

where γ_{00} is the overall intercept or grand mean, μ_{0j} is a village-level random residual component indicating the average deviation from the grand mean for those farm households located in village j, and ε_{ij} remains the farm household-level residual. The usual assumption is that $\mu_{0j} \sim N(0, {\sigma_\mu}^2)$, $\varepsilon_{ij} \sim N(0, {\sigma_\varepsilon}^2)$ and the μ_{0j} are independent from the ε_{ij}. Thus, ${\sigma_\mu}^2$ and ${\sigma_\varepsilon}^2$ represent the between-group variance and the within-group variance, respectively. The intra-class correlation coefficient, $\rho = \frac{{\sigma_\mu}^2}{{\sigma_\varepsilon}^2 + {\sigma_\mu}^2}$, is an indicator of the relative importance of village attributes, with larger values indicating a greater impact of village level on grain yield [31].

2.2. Random Intercept Model

The characteristics of farm households and villages that affect the grain yield remain unmeasured in Equation (3). Therefore, the variables of such characteristics are introduced to determine whether the between and within components of variation can be explained at the household and village levels. The random intercept model can be expressed as:

$$Y_{ij} = (\gamma_{00} + \sum_1^q \beta_{0qj} V_{0qj} + \sum_1^p \beta_{pij} X_{pij}) + (\mu_{0j} + \varepsilon_{ij}) \quad (4)$$

where, X_{pij} represents the independent variable of the farm household level, V_{0qj} represents the independent variable of the village level. Equation (4) consists of two parts: $\gamma_{00} + \sum_1^q \beta_{0qj} V_{0qj} + \sum_1^p \beta_{pij} X_{pij}$ as the fixed effects and $\mu_{0j} + \varepsilon_{ij}$ as the random effects, and it can be expressed as:

$$Y = X\beta + ZU + e \quad (5)$$

Equation (5) is the general model of Equation (4). Where, Y is the observation variable; X is the design matrix of constant parameter β; Z is the design matrix of random effect U; and e is the random error. $\mathrm{cov}(Y) = V(\theta)$. The logarithmic likelihood function of Equation (5) is given as:

$$\ln L(\beta, \theta | Y) = -\ln|V(\theta)| - (Y - X\beta)' V^{-1}(\theta)(Y - X\beta) \quad (6)$$

Maximum likelihood estimation of parameters can be obtained by maximizing Equation (6). That is, $\hat{\beta}(\theta) = \left(X' V^{-1}(\theta) X\right)^{-1} X' V^{-1}(\theta) Y$ by fixing parameter θ. Then, plugging $\hat{\beta}(\theta)$ into $L(\beta, \theta | Y)$ can obtain the maximum likelihood estimation of θ.

3. Data Source and Empirical Model

3.1. Data Source

The NCP is one of China's major grain production areas, accounting for approximately 75% and 35% of China's wheat and maize outputs, respectively [6]. This region only grows winter wheat and summer maize. In recent years, this region has experienced evident climate change such as rising temperature and decreasing precipitation. The frequency of extreme weather events increases as the seasonal variation of precipitation becomes apparent. Specifically, flood often occurs in summer that receives 60% of the annual precipitation. Drought is often a serious threat in spring, autumn, and winter, especially in the areas without irrigation facilities [29,32]. The data used in this study are from a large-scale field survey of five provinces (Henan, Hebei, Shandong, Anhui, and Jiangsu) in the NCP.

To collect the data, stratified multi-stage cluster sampling was implemented. First, three counties were randomly chosen in each province using the following criterion. (i) The counties had experienced at least one episode of either severe drought or flood between 2010 and 2012. China's national standard for natural disasters [33] categorizes the severity of droughts or floods into four levels: most severe, severe, moderate, and mild. A disaster year is when the government declares a warning of the most severe or severe flood or drought. (ii) The counties experienced at least one normal year in the past three years (2010, 2011 or 2012). Grain production usually experiences various weather shocks during any growing season; the term 'normal year' does not refer to a year without any weather shocks, but rather a year with no more than moderate weather shocks. Second, from each of the chosen counties, three townships were randomly selected to represent 'good', 'medium', and 'poor' local irrigation and drainage infrastructure conditions, respectively. Third, three villages were randomly selected from each township, and 10 households were randomly selected from each village for face-to-face interviews. Finally, from each household, two plots with grain production were randomly selected. Meteorological data were provided by National Meteorological Information Center (NMIC) (Data source: The China Meteorological Data Service Center (http://cdc.cma.gov.cn accessed on 15 May 2021), including the daily maximum temperature, minimum temperature, average temperature, and 24 h average precipitation recorded by the meteorological observatory in sample or adjacent counties.

As a result, the samples of winter wheat included 2261 plots of 1216 households, which were distributed in 123 villages (or 41 townships, 14 counties) of five provinces (Table 1). The samples of summer maize covered 1769 plots of 1028 households, distributed in 117 villages (or 40 townships, 14 counties) in five provinces (Table 2). Among the 14 case study counties, 10 suffered from drought disaster, and 4 suffered from flood disaster. The regional (provincial and county) distribution of all samples is shown in Figure 1.

Table 1. The sample distribution of winter ***wheat*** for the NCP.

Province	County	No. of Households	No. of Plots	Disaster Type	Disaster/Normal Year
Henan	Yuanyang	90	167	D	2011/2012
	Huanxian	90	160	D	2011/2012
	Yongcheng	90	176	D	2011/2012
Hebei	Weixian	90	164	D	2011/2012
	Yixian	56	93	F	2012/2011
Shandong	Lingxian	90	167	F	2012/2011
	Yuncheng	90	174	D	2011/2012
	Huishan	90	159	D	2011/2012
Jiangsu	Xinghua	89	160	F	2011/2012
	Xiangshui	90	171	F	2012/2011
	Peixian	81	146	D	2011/2012
Anhui	Yongqiao	90	175	D	2011/2012
	Suixi	90	172	D	2011/2012
	Lixin	90	177	D	2011/2012
Total	14	1216	2261	-	-

Notes: D and F stand for drought and flood, respectively.

Table 2. The sample distribution of summer *maize* for the NCP.

Province	County	No. of Households	No. of Plots	Disaster Type	Disaster/Normal Year
Henan	Yuanyang	72	128	D	2011/2012
	Huanxian	90	159	D	2011/2012
	Yongcheng	62	113	D	2011/2012
Hebei	Weixian	90	164	D	2011/2012
	Yixian	90	162	F	2012/2011
Shandong	Lingxian	90	167	F	2012/2011
	Yuncheng	90	172	D	2011/2012
	Huishan	90	159	D	2011/2012
Jiangsu	Xinghua	11	12	F	2011/2012
	Xiangshui	82	89	F	2012/2011
	Peixian	63	93	D	2011/2012
Anhui	Yongqiao	67	119	D	2011/2012
	Suixi	62	106	D	2011/2012
	Lixin	69	126	D	2011/2012
Total	14	1028	1769	-	-

Notes: D and F stand for drought and flood, respectively.

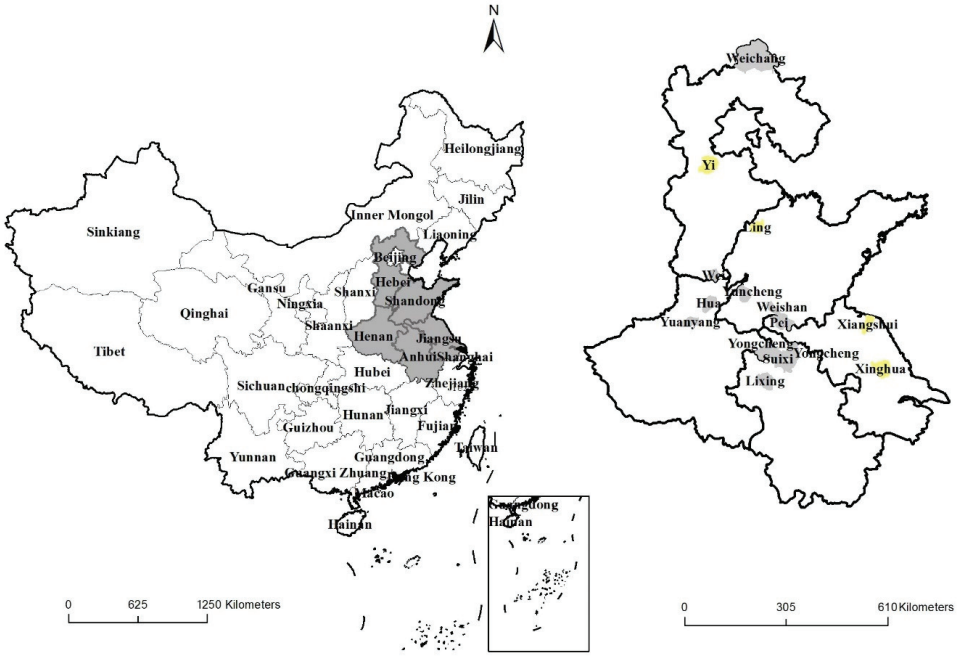

Figure 1. Location of five provinces in the NCP (**left**) and 14 sample counties (**right**).

The 12 main growth stages of winter wheat are seedling emergence, three-leaf, tillering, overwintering, reviving, jointing, booting, heading, anthesis, grain-filling, wax ripeness and mature. This study separated the overwintering stage from the vegetative stage (Firstly, this stage is a special stage of winter wheat to stop growing, which is quite important to store energy; secondly, China boasts the distinctive differences in regions and climate, especially the winter temperature change is more remarkable [18]); it also divided the whole growth period of winter wheat into three major growth stages: the overwintering stage from seedling emergence to reviving (generally from mid-October to mid-February in the following year), the vegetative stage from reviving to heading (generally from

the mid-February to mid-April), and the reproductive stage from anthesis to maturity (generally from mid-April to early June). Similarly, the 12 main growth stages of summer maize include the stages of seedling, three-leaf, jointing, flare opening, tasseling, flowering, silking, filling, milk ripening, wax ripening, and full ripening. They were divided into three major growth stages: the vegetative stage from sowing to jointing (generally from mid-June to mid-July, about 20–30 days), the concurrent stage from jointing to silking (generally from mid-July to mid-August, about 27–30 days), and the reproductive stage from silking to full ripening (generally from mid-August to late September, about 40–60 days) [34].

Table 3 shows the climatic trend of various growth stages of winter wheat and summer maize in the NCP. In general, the overall climate change in the sample area was increasing temperature and precipitation from 1981 to 2010. The rangeability was inconsistent with temperature and precipitation over different grain growth stages. The warming trend during the winter was the most prominent, which further proves that the warming trend is most significant in the winter among the four seasons [35]. Precipitation increased the most during the whole growth period of summer maize, indicating that precipitation increase was most significant in the summer among the four seasons.

Table 3. Climatic trend rate of major crop growth stages in the NCP (1981–2010).

Crop Growth Stages	Daily Average Temperature (°C/10a)	Average Precipitation (cm/10a)
Winter wheat:		
Overwintering stage	0.519	0.115
Vegetative stage	0.675	0.66
Reproductive stage	0.305	1.137
Summer maize:		
Vegetative stage	0.319	1.601
Concurrent stage	0.153	2.25
Reproductive stage	0.229	1.229

The sample data comes from meteorological observation stations in 14 wheat and maize producing counties. Regressed the meteorological variables and time variables of each sample county linearly, and weighted average of all regression coefficients to obtain the annual change rate, which multiply by 10 to obtain climatic trend rate.

3.2. Empirical Model and Variables

Production inputs and economic and social institutional factors should be incorporated into the model; meanwhile, the factors of long-term climate change and extreme weather events should be included in the production function model. The C-D-C production function equation, which is the extension of Equation (4), is specified as:

$$\begin{aligned} \ln(Y_{ij}) = \quad & \beta_0 + \beta_1 C_{ij} + \beta_2 D_{ij} + \beta_3 DL_{ij} + \beta_4 \ln(I_{ij}) + \beta_5 L_{ij} \\ & + \beta_6 H_{ij} + \beta_7 V_{ij} + \beta_8 V_{ij} D_{ij} + \beta_8 V_{ij} DL_{ij} + T + \mu_{0j} + \varepsilon_{ij} \end{aligned} \quad (7)$$

This study independently investigated the effects of climate change and the household and village attributes on the yields of winter wheat and summer maize by Equation (6), respectively. The dependent variable Y_{ij} refers to crop yield, which is measured as the wheat or maize output per hectare. As shown in Table 4, the average yields of wheat and maize in the farm plots were 6400 kg and 6615.1 kg per hectare, respectively.

The variable of long-term climate change C_{ij} examined in this paper includes average daily temperature and precipitation over the past three decades (1981–2010). For winter wheat, the daily average temperature was only 5.2 °C in the over-wintering stage, and it was 20.4 °C in the reproductive stage. For summer maize, the daily average temperature could be above 20 °C, and the precipitation was more than 100 mm at different growth stages (Table 4).

Table 4. Summary statistics of variables used.

Variables	Definition	Winter Wheat		Summer Maize	
		Mean	S.D.	Mean	S.D.
Explained variables:					
Grain yield (Y)	Kg/ha	6400	1176	6615	1535
Explanatory variables:					
The variables of long-run climate change (wheat):					
Daily avg temperature in overwintering stage (T_{wheat1})	°C	5.22	1.19	-	-
Total avg precipitation in overwintering stage (P_{wheat1})	cm	8.40	2.89	-	-
Daily avg temperature in vegetative stage (T_{wheat2})	°C	9.67	1.47	-	-
Total avg precipitation in vegetative stage (P_{wheat2})	cm	7.64	4.05	-	-
Daily avg temperature in reproductive stage (T_{wheat3})	°C	20.38	0.81	-	-
Total avg precipitation in reproductive stage (P_{wheat3})	cm	8.53	2.46	-	-
The variables of long-run climate change (maize):					
Daily avg temperature in vegetative stage (T_{maize1})	°C	-	-	26.13	0.49
Total avg precipitation in vegetative stage (P_{maize1})	cm	-	-	10.73	3.56
Daily avg temperature in concurrent stage (T_{maize2})	°C	-	-	27.12	0.41
Total avg precipitation in concurrent stage (P_{maize2})	cm	-	-	16.95	2.74
Daily avg temperature in reproductive stage (T_{maize3})	°C	-	-	23.33	1.20
Total avg precipitation in reproductive stage (P_{maize3})	cm	-	-	16.93	3.20
Extreme weather events:					
If it occurred drought disaster at the county-level (D_D)	1 = Yes; 0 otherwise	0.25	0.43	0.25	0.43
If it occurred flood disaster at the county-level (D_F)	1 = Yes; 0 otherwise	-	-	0.08	0.27
If it occurred drought disaster on farm plot (DL_D)	1 = Yes; 0 otherwise	0.41	0.49	0.36	0.48
If it occurred flood disaster on the farm plot (DL_F)	1 = Yes; 0 otherwise	0.03	0.16	0.16	0.36
If it occurred continuous rain disaster on farm plot (DL_R)	1 = Yes; 0 otherwise	0.08	0.26	0.04	0.19
If it occurred strong wind disaster on farm plot (DL_w)	1 = Yes; 0 otherwise	0.08	0.27	0.16	0.37
Farmland plot characteristics:					
Farmland area (L_1)	Hectare	0.21	0.18	0.19	0.13
Farmland topography (L_2)	1 = flat land; 0 = otherwise	0.98	0.14	0.06	0.24
Low quality of farmland (L_{31})	1 = Yes; 0 otherwise	0.11	0.31	0.12	0.33
Medium quality of farmland (L_{32})	1 = Yes; 0 otherwise	0.70	0.46	0.67	0.47
High quality of farmland (L_{33})	1 = Yes; 0 otherwise	0.19	0.39	0.21	0.41
Production inputs:					
Fertilizer cost (I_1)	Yuan/ha	2863.29	1246.98	2442.79	1063.44
Pesticide cost (I_2)	Yuan/ha	331.24	263.68	472.71	321.17
Machinery cost (I_3)	Yuan/ha	1678.38	577.16	1248.26	800.56
Labor input (I_4)	Adult days/ha	36.26	34.52	60.90	63.69
Irrigation water (I_5)	m^3/ha	1760.88	1753.53	1730.09	2279.84
Household's characteristics:					
Asset of household (H_1)	Durable goods (10^3 yuan)	9.67	19.24	9.86	19.48
Education of household head (H_2)	Attending year	6.91	3.19	6.93	3.11
Producing/technical training (H_3)	If attending (1 = Yes; 0 otherwise)	0.27	0.45	0.24	0.42
Village's characteristics					
Collective enterprise (V_1)	Number of collective enterprises	0.08	0.55	0.13	0.768

Table 4. *Cont.*

Variables	Definition	Winter Wheat		Summer Maize	
		Mean	S.D.	Mean	S.D.
Ratio of irrigation area to total cultivated area (V_2)	%	83.85	23.71	83.17	27.88
Distance between the village committee and the nearest road above the township level (V_3)	Km	1.36	1.55	1.38	1.58
Year dummy variables:					
2011 (T_{2011})	1 = Yes; 0 otherwise	0.33	0.47	0.33	0.47
2012 (T_{2012})	1 = Yes; 0 otherwise	0.33	0.47	0.33	0.47
Observations	-	6749		5212	

The second climate indicator is extreme weather event, including the variables of county-level disaster D_{ij} and farm plot disaster DL_{ij}. There are two county-level disasters, which are D_D for the severe drought year and D_F for the severe flood year. In the past three years (2010–2012), 24.7% of counties that grew wheat suffered from drought, and 25.1% and only 8.2% of counties that grew maize suffered from drought and flood, respectively. There are four types of farm plot disasters, which are DL_D for farm plots suffering from drought, DL_F for farm plots suffering from flood, DL_R for farm plots suffering from continuous rain, and DL_W for farm plots suffering from strong wind. In the past three years, 40.5% of farm plots growing wheat suffered from drought, 7–8% suffered from continuous rain or strong wind, while 2.7% suffered from flood, indicating that drought was the most frequent disaster during wheat planting. During the same period, 36% of farm plots that grew maize suffered from drought, 16% suffered from strong wind, and 15.5% suffered from flood. This shows that drought was the most frequent disaster during maize planting, and the risk of strong wind and flood should not be underestimated.

Three variables represent farmland plot characteristics. (i) The farmland areas L_1 were relatively small, with an average farm area of only 0.21 ha and 0.19 ha for wheat and maize (Table 4), respectively, which indicates the formation of tiny plots and scattered planting; (ii) Most of the farmland topography L_2 is flat land, and only less than 3% and 5% of farmers chose to grow wheat and maize in the mountains, respectively; (iii) Compared with the overall land quality of village, the farmland quality L_3 is divided into three categories, which are low-quality, middle-quality and high-quality land. The majority of plots (68%) were of medium quality, 10% were of low-quality, and 20% were of high-quality.

I_{ij} is a set of production input variables, covering the fertilizer cost I_1, pesticide cost I_2, machinery cost I_3, labor input I_4, and irrigation water I_5 at the plot level. Table 4 shows that among these costs, the average input costs of fertilizer were the highest with 2863.3 yuan and 2442.8 yuan per hectare, respectively, for wheat and maize. The cost of machinery was the second highest with 1678.4 yuan and 1248.3 yuan per hectare for wheat and maize, respectively, while the labor input costs of wheat and maize were 36.3 and 60.9 adult days per hectare. Thus, there might be a substitution relationship with machinery and labor. The irrigation water reached 1760.9 m^3 and 1730.1 m^3 for wheat and maize, respectively, indicating that the grain grown in the NCP is mainly irrigated rather than rainfed.

Farm household's characteristics (H_{ij}) include variables as follows. (i) The assets possessed by the household (H_1), which are measured as the value of the durable goods. The average value of durable goods of sample households was 9700 yuan; (ii) H_2 represents the education level of the household head, where the average education was 6.9 years. (iii) H_3 represents the production and technical training, and about 25% of household members received such training.

Three variables were used to measure village characteristics. (i) V_1 refers to village collective enterprise. The average village collective enterprise was only about 0.1, which means many villages did not have such enterprises. (ii) V_2 refers to the ratio of irrigation area to total cultivated area in the village, which is more than 80%. (iii) V_3 is the distance

between the village committee and the nearest road above the township level with an average distance of 1.4 km.

In addition, this study used year dummies, T_{2011} (1 = 2011, otherwise = 0) and T_{2012} (1 = 2012, otherwise = 0), to control technological advances or other unobservable factors that change over time.

4. Results and Analyses

4.1. The Unconditional Means Model

Table 5 shows the estimated results of the unconditional means model with maximum likelihood estimation. The intra-class correlation coefficient ρ is 0.384, indicating 38.4% and 61.6% of the variation in wheat yield were caused by the village attributes and household attributes, respectively. Similarly, the inter-class correlation coefficient ρ is 0.238, indicating that 23.8% and 76.2% of the variation in maize yield were caused by the village attributes and household attributes, respectively. Due to the different samples in wheat and maize, the variation was different between villages and households. Moreover, a fairly large part of variation in the wheat and maize yields in the NCP was on the village level. Therefore, it is helpful to adopt a multilevel model to improve the accuracy of parameter estimation results.

Table 5. The estimated results of unconditional means model.

Variance Decomposition	Winter Wheat		Summer Maize	
	Coefficient	S.D.	Coefficient	S.D.
Variance of village level (between-group variance)	0.118	0.008	0.173	0.014
Variance of household level (within-group variance)	0.189	0.002	0.555	0.005
Intra-class correlation coefficient ρ	0.384	-	0.238	-

4.2. The Random Intercept Model

According to Equation (6), the estimated results of the influence of climate factors and other factors on wheat and maize yields are shown in Tables 6 and 7. Model I only included climate change variables and year dummy variables. Then, farmland attributes and production input variables were incorporated into Model II. Finally, village attributes were incorporated into Model III.

Table 6. The estimated results of influencing factors of winter ***wheat*** yield.

Variables	Model I	Model II	Model III
T_{wheat1}	0.080 ** (0.032)	0.079 ** (0.031)	0.088 *** (0.032)
P_{wheat1}	−0.087 *** (0.025)	−0.088 *** (0.025)	−0.097 *** (0.026)
T_{wheat2}	−0.068 * (0.037)	−0.062 * (0.036)	−0.086 ** (0.038)
P_{wheat2}	0.054 *** (0.021)	0.052 ** (0.021)	0.065 *** (0.022)
T_{wheat3}	0.041 (0.032)	0.036 (0.032)	0.051 (0.032)
P_{wheat3}	−0.002 (0.015)	0.005 (0.015)	−0.002 (0.015)
D_D	−0.032 *** (0.011)	−0.033 *** (0.011)	−0.084 *** (0.022)
DL_D	−0.096 *** (0.006)	−0.094 *** (0.006)	−0.197 *** (0.02)
DL_F	−0.057 *** (0.015)	−0.056 *** (0.014)	−0.055 *** (0.014)
DL_R	−0.158 *** (0.01)	−0.161 *** (0.009)	−0.160 *** (0.009)
DL_W	−0.088 *** (0.009)	−0.084 *** (0.009)	−0.086 *** (0.009)
T_{2011}	0.036 *** (0.01)	0.035 *** (0.009)	0.034 *** (0.009)
T_{2012}	−0.033 *** (0.005)	−0.033 *** (0.005)	−0.033 *** (0.005)
L_1	–	0.005 (0.015)	0.003 (0.015)
L_2	–	−0.009 (0.016)	−0.010 (0.016)

Table 6. *Cont.*

Variables	Model I	Model II	Model III
L_{32}	−	0.06 *** (0.007)	0.06 *** (0.007)
L_{33}	−	0.083 *** (0.009)	0.083 *** (0.009)
$\ln(I_1)$	−	0.007 (0.005)	0.006 (0.005)
$\ln(I_2)$	−	−0.002 (0.002)	−0.002 (0.002)
$\ln(I_3)$	−	−0.003 (0.006)	−0.003 (0.006)
$\ln(I_4)$	−	−0.016 *** (0.004)	−0.016 *** (0.004)
$\ln(I_5)$	−	0.004 *** (0.001)	0.004 *** (0.001)
H_1	−	0.0001 (0.0001)	0.0001 (0.0001)
H_2	−	0.002 ** (0.001)	0.002 ** (0.001)
H_3	−	0.012 ** (0.006)	0.012 ** (0.006)
V_1	−	−	0.011 (0.015)
V_2	−	−	−0.0001 (0.0003)
V_3	−	−	0.002 (0.007)
$V_1 \times D_D$	−	−	−0.004 (0.009)
$V_1 \times DL_D$	−	−	0.006 (0.009)
$V_2 \times D_D$	−	−	0.001 *** (0.0002)
$V_2 \times DL_D$	−	−	0.001 *** (0.0002)
$V_3 \times D_D$	−	−	0.001 (0.004)
$V_3 \times DL_D$	−	−	0.01 *** (0.004)
Cons.	8.542 *** (0.421)	8.501 *** (0.418)	8.447 *** (0.415)
Variance ${\sigma_\mu}^2$	0.106 (0.007)	0.105 (0.007)	0.103 (0.007)
Variance ${\sigma_\varepsilon}^2$	0.179 (0.002)	0.177 (0.002)	0.176 (0.002)
Log likelihood	1836.415	1908.163	1935.25
AIC	−3640.829	−3760.326	−3798.5

Notes: *, ** and *** represent significance 10%, 5% and 1% level, respectively.

Table 7. The estimated results of influencing factors of summer ***maize*** yield.

Variables	Model I	Model II	Model III
T_{maize1}	−0.167 (0.111)	−0.158 (0.107)	−0.167 (0.104)
P_{maize1}	−0.023 ** (0.011)	−0.013 (0.01)	−0.011 (0.010)
T_{maize2}	0.533 *** (0.181)	0.427 *** (0.173)	0.453 *** (0.168)
P_{maize2}	−0.016 * (0.009)	−0.012 (0.008)	−0.013 (0.008)
T_{maize3}	−0.083 *** (0.03)	−0.047 (0.03)	−0.047 (0.029)
P_{maize3}	−0.017 (0.012)	−0.013 (0.012)	−0.012 (0.011)
D_D	−0.127 *** (0.041)	−0.13 *** (0.041)	−0.091 (0.080)
D_F	−0.142 *** (0.043)	−0.138 *** (0.043)	−0.165 *** (0.043)
DL_D	−0.136 *** (0.019)	−0.141 *** (0.019)	−0.489 *** (0.056)
DL_F	−0.224 *** (0.027)	−0.219 *** (0.026)	−0.219 *** (0.026)
DL_R	−0.122 *** (0.042)	−0.127 *** (0.042)	−0.133 *** (0.041)
DL_W	−0.098 *** (0.023)	−0.101 *** (0.023)	−0.107 *** (0.023)
T_{2011}	0.149 *** (0.036)	0.149 *** (0.035)	0.137 *** (0.035)
T_{2012}	0.151 *** (0.021)	0.147 *** (0.021)	0.147 *** (0.021)
L_1	−	0.108 (0.069)	0.094 (0.069)
L_2	−	0.001 (0.047)	−0.009 (0.047)
L_{32}	−	0.114 *** (0.024)	0.106 *** (0.024)
L_{33}	−	0.147 *** (0.028)	0.145 *** (0.028)
$\ln(I_1)$	−	−0.006 (0.01)	−0.006 (0.010)
$\ln(I_2)$	−	0.032 *** (0.008)	0.033 *** (0.008)
$\ln(I_3)$	−	0.009 (0.007)	0.011 (0.007)
$\ln(I_4)$	−	−0.036 *** (0.013)	−0.036 *** (0.013)
$\ln(I_5)$	−	0.018 *** (0.003)	0.018 *** (0.003)
H_1	−	0.0008 * (0.0004)	0.001 * (0.000)
H_2	−	0.003 (0.003)	0.003 (0.003)
H_3	−	0.033 (0.021)	−0.033 (0.020)
V_1	−	−	−0.028 (0.023)
V_2	−	−	−0.001 (0.001)

Table 7. *Cont.*

Variables	Model I	Model II	Model III
V_3	–	–	0.004 (0.011)
$V_1 \times D_D$	–	–	0.128 *** (0.022)
$V_1 \times DL_D$	–	–	−0.11 *** (0.021)
$V_2 \times D_D$	–	–	−0.001 (0.001)
$V_2 \times DL_D$	–	–	0.005 *** (0.001)
$V_3 \times D_D$	–	–	0.018 (0.012)
$V_3 \times DL_D$	–	–	−0.018 (0.012)
Cons.	1.449 (2.052)	2.678 (1.977)	2.269 (1.93)
Variance ${\sigma_\mu}^2$	0.152 *** (0.013)	0.141 *** (0.012)	0.133 *** (0.012)
Variance ${\sigma_\varepsilon}^2$	0.541 *** (0.005)	0.537 *** (0.005)	0.532 *** (0.005)
Log likelihood	−4281.319	−4231.07	−4177.54
AIC	8596.638	8520.14	8431.08

Notes: *, ** and *** represent significance 10%, 5% and 1% level, respectively.

4.2.1. The Determinants of Winter Wheat Yield

Table 6 displays the results of the three model for winter wheat yield. The likelihood function ratio, LR = 2[Ln(L_{R2}) − Ln(L_{R1})] = 143.5, is greater than critical $\chi^2_{0.01}(12) = 26.22$, meaning that farmland attributes and production input variables had significant impact on the variation in winter wheat yield. Furthermore, the AIC value is −3760.326 in Model II, which is less than AIC of −3640.829 in Model I, meaning that the better the overall fitting of Model II according to the information criteria, the smaller the AIC value, and the better the overall fitting of the model.

Similarly, Model III shows a better overall fitting than Model II. The likelihood function ratio LR = 2[Ln(L_{R3}) − Ln(L_{R2})] = 54.17 is greater than critical $\chi^2_{0.01}(9) = 21.67$, suggesting that village attributes had significant impact on the variation in winter wheat yield. Meanwhile, AIC of −3798.5 in Model III is smaller than AIC of −3760.326 in Model II. According to Table 6, the following conclusions can be drawn:

Firstly, the heterogeneity of wheat yield was not only caused by household characteristics, but also determined by differences in village economies, except for farmland characteristics and production input factors. For example, the variance of village level is ${\sigma_\mu}^2 = 0.103$ (Table 6, row 36) with introducing explanatory variables (Model III), which is less than the variance of ${\sigma_\mu}^2 = 0.118$ (Table 5, row 1) in the unconditional means model without the introduction of explanatory variables. It indicates that social and economic factors at the village level, such as collective economy (number of collective enterprises), irrigation condition (ratio of irrigation area), and traffic condition (distance between the village committee and the nearest road above the township level), could explain 12.7% ($\frac{{\sigma_\mu}^2(\text{unconditional means model}) - {\sigma_\mu}^2(\text{random intercept model})}{{\sigma_\mu}^2(\text{unconditional means model})} = \frac{0.118-0.103}{0.118} = 0.127$) of the variation in wheat yield at the village level. Household attributes could explain 6.9% ($\frac{{\sigma_\varepsilon}^2(\text{unconditional means model}) - {\sigma_\varepsilon}^2(\text{random intercept model})}{{\sigma_\varepsilon}^2(\text{unconditional means model})} = \frac{0.189-0.176}{0.189} = 0.069$) of variation in wheat yield, which was apparently and substantially smaller than village attributes.

Secondly, the effect of long-term climate change on wheat yield varied across different wheat growth stages. The increase of average temperature significantly promoted wheat production during the overwintering stage. For example, wheat yield would significantly increase by about 8% if temperature increased by 1 °C (row 1, Table 6). However, the increase of average temperature resulted in an obvious decrease in wheat yield during the vegetative stage. Specifically, wheat yield would significantly decline by 6.2–8.6% if average temperature improved by 1 °C (row 3, Table 6). These results indicate that the proper increase in winter temperature has a positive effect on winter wheat yield, while the increase in spring temperature can lead to a decrease of winter wheat yield, which is consistent with some previous studies [36]. This is probably because that the shortened growth period and warming temperature contribute to the increase of productive tiller [37,38].

Thirdly, the occurrence of extreme weather events had significantly negative impact on wheat yield. County-level drought significantly reduced wheat yield. Farm-level disasters also had led to obvious reduction in wheat yield. In particular, drought, flood, continuous rain, and strong wind at the farm level would reduce wheat yield by about 10%, 6%, 16%, and 9%, respectively, holding constant of other variables (rows 8–11, Table 6). Farm-level disasters showed a greater negative impact on wheat yield than county-level disasters.

Fourthly, production input significantly affected the wheat yield. The elasticity of labor is −0.016 with other input factors unchanged (row 21, Table 6). The sign of labor elasticity is negative, which is consistent with previous empirical studies [39]. The possible reasons are two-fold: on the one hand, there is a significant substitution relationship between labor input and machinery input, which leads to multiple collinearities contributing to the unreasonable estimated economic value of labor output elasticity; on the other hand, there is too much surplus labor force in agricultural production in China. The scattered and limited arable farmland will further increase surplus rural labor force, while labor has not fully flowed in the market. Therefore, it is more valuable of focusing on the quality of labor than the quantity of labor to improve grain yield and farmers' income. Moreover, irrigation water could significantly and slightly promote wheat yield (0.004, row 22, Table 6), showing that wheat yield only increased by 0.004% with increasing irrigation water by 1%. The result means that the input of irrigation water is lack of elasticity.

Fifthly, the social and economic characteristics of households had a significant impact on wheat yield. As expected, education and participation in production and technology training programs played an important role in promoting wheat yield. In particular, the wheat yield would significantly increase by 0.2% if the schooling year of the household head increased by one (row 24, Table 6). Similarly, the wheat yield would significantly increase by 1.2% if farmers had previously undertaken a production and technique training (row 25, Table 6).

Finally, the social and economic characteristics of village could mitigate the loss of wheat yield under extreme weather events, especially drought disaster. For example, the wheat yield decreased by 19.7% if farm plot occurred drought disaster, but it only decreased by 1% if the distance shortened by 1 km between the village committee and the nearest township-level road. Moreover, the wheat yield decreased by 8.4% and 19.7%, respectively, when county-level drought and farm plot drought occurred simultaneously. However, in the case of drought, the wheat yield could significantly improve by 0.1% if irrigation proportion rise by 1%.

4.2.2. The Determinants of Summer Maize Yield

Table 7 displays the determinant regression results of summer maize yield using three models. Similarly, according to the likelihood function ratio LR and information criterion AIC, Model III is more preferable than other models. The empirical results of Table 7 are similar to those in Table 6, but there are several differences as follows.

Firstly, the heterogeneity of maize yield was shaped by village attributes. In particular, the village level variance of $\sigma_\mu{}^2 = 0.133$ (row 36, Table 7) with introducing explanatory variables (Model III) is less than the variance of $\sigma_\mu{}^2 = 0.173$ (row 1, Table 5) without introducing explanatory variables (unconditional means model). This indicates that the social and economic characteristics of village, such as the village collective enterprise, the proportion of village irrigation area, and the distance between the village committee and the nearest road above the township level, could explain 23.1% ($\frac{\sigma_\mu{}^2(\text{unconditional means model}) - \sigma_\mu{}^2(\text{random intercept model})}{\sigma_\mu{}^2(\text{unconditional means model})} = \frac{0.173-0.133}{0.173} = 0.231$) of the variation in maize yield at the village level. Household attributes could explain 4.1% ($\frac{\sigma_\varepsilon{}^2(\text{unconditional means model}) - \sigma_\varepsilon{}^2(\text{random intercept model})}{\sigma_\varepsilon{}^2(\text{unconditional means model})} = \frac{0.555-0.532}{0.555} = 0.041$) of variation in maize yield, which was apparently and considerately smaller than village attributes.

Secondly, the occurrence of extreme weather events had a significantly negative impact on maize yield. For example, the maize yield decreased by 12.7% and 14.2% under drought

and flood disasters at the county level, respectively. The disasters occurring on farmland plot led to more loss in maize yield than those at the county level. Specifically, drought, flood, continuous rain, and strong wind reduced maize yield by 13.6%, 22.4%, 12.2%, and 9.8%, respectively.

Thirdly, production input significantly affected the maize yield. The sign of labor elasticity is negative, and the reasons have been mentioned above. Pesticide and irrigation water input could significantly promote maize yield. Specifically, the maize yield would increase by 0.032% and 0.018% for every 1% increase in pesticide input and irrigation water, respectively (rows 20 and 23, Table 7).

Finally, the social and economic characteristics of village could mitigate the loss of maize yield under extreme weather events. The coefficients of the cross term between village collective enterprise and drought disaster reveal that the negative impact of drought disaster on maize yield would decrease dramatically if the village had more collective enterprises. For example, the maize yield declined by 48.9% if drought occurred on the farmland plot, but it only decreased by 11% for one additional collective enterprise. Furthermore, the maize yield could decrease by 9.1% under county-level drought, but it could increase by 12.8% for an additional collective enterprise.

5. Conclusions and Discussion

Based on the data of 6749 wheat plots and 5212 maize plots of farm households over 2010–2012, this paper adopted a multilevel model to analyze the impact of long-term climate change and extreme weather events on the wheat and maize yields in the NCP. It also considered village social and economic conditions, social and economic characteristics of the household, production inputs, and farmland plot characteristics as the influencing factors of wheat and maize yields. The findings of this study suggest the following conclusion and discussion.

5.1. Conclusions

There are three main findings and conclusions in this study.

Firstly, spatial variations in crop yield are significantly influenced by the heterogeneity of village economic conditions. The explained variation in crop yield is much higher at the village level than at the household level. The social and economic characteristics of the village have a positive effect on crop yield and mitigate the loss of crop yield under extreme weather events. Therefore, under China's dual-level management system of integration of unification and separation in rural area, it is necessary to strengthen household production behavior and improve village collective economy.

Secondly, the arid and semi-arid region of NCP has been experiencing climate change, affecting grain production over the past three decades. The effects of long-term climate variables on winter wheat and summer maize yields vary across the growth stages. Therefore, it might be time to think of making agricultural production adapt to climate change. For example, it may need to adjust the planting system, change crop varieties, and build households' adaptive capacity to climate change.

Thirdly, extreme weather events are more likely than long-term climate change to reduce the wheat and maize yields. The negative impact of extreme weather events on crop yield is more serious and immediate. These findings suggest that the governments should establish and improve the disaster service and coping system for grass-roots units. Specifically, it is essential to use modern information technology to improve the monitoring, forecasting, and warning of agricultural disasters and provide and publicize disaster early warning and response information timely. At the same time, agricultural technical guidance and financial support should be provided for disaster prevention and control, enabling farmers to minimize crop production loss. The households also need to prepare for extreme weather events.

5.2. Discussion

In dialogue with the existing literature, we respond to, and confirm, the scholarly view that the role of the village collective economy plays a key role in ensuring food security [25,26]. We have shown that the village collective economy can mitigate the loss of crop yield under extreme weather events. In addition, the impact of extreme weather events on crop yield should be emphasized when revealing an empirical relationship between climate factors and grain output in agricultural production [23,24]. Since the negative impact of extreme weather events on crop yield is more serious and immediate than long-term climate change.

As usual, this paper still has some limitation. Due to data unavailable, for example, the impact of the township or even the county economic levels cannot be taken into consideration; long-term temperature and precipitation at county-level data have to be used for plot-level modelling. For the future study, it be better incorporating long-term plot-level temperature and precipitation into plot-level modelling by taking into consideration of county- and -township-level economic impacts.

Author Contributions: C.S.: making draft, revising, modelling and revising; X.H.: field survey and data processing; O.L.: reviewing and editing; R.L.: field survey and reviewing; H.M.: reviewing, editing, and revising as well as corresponding author. All authors have read and agreed to the published version of the manuscript.

Funding: Financial support from the National Natural Science Foundation of China (Grant No: 72003057, 72173037), Ministry of Education of Humanities and Social Science Research Project of China (Grant No: 21YJA790039), Henan Province Philosophy and Social Science Planning Project (Grant No. 2021BJJ046), Key Scientific Research Project of Henan Provincial Institutions of Higher Learning (Grant No. 21A790011).

Institutional Review Board Statement: Not applicable.

Informed Consent Statement: Not applicable.

Data Availability Statement: Data supporting the conclusions of this article are included within the article. The dataset presented in this study are available on request from the corresponding author.

Conflicts of Interest: The authors declare no conflict of interest.

References

1. Liu, Y.; Li, N.; Zhang, Z.; Huang, C.; Chen, X.; Wang, F. The central trend in crop yields under climate change in China: A systematic review. *Sci. Total Environ.* **2020**, *704*, 135355. [CrossRef] [PubMed]
2. Pickson, R.B.; He, G.; Boateng, E. Impacts of climate change on rice production: Evidence from 30 Chinese provinces. *Environ. Dev. Sustain.* **2022**, *24*, 3907–3925. [CrossRef]
3. Wu, J.; Zhang, J.; Ge, Z.; Xing, L.; Han, S.; Shen, C.; Kong, F. Impact of climate change on maize yield in China from 1979 to 2016. *J. Integr. Agric.* **2021**, *20*, 289–299. [CrossRef]
4. Zhang, T.; Zhu, J.; Wassmann, R. Responses of rice yields to recent climate change in China: An empirical assessment based on long-term observations at different spatial scales (1981–2005). *Agric. For. Meteorol.* **2010**, *150*, 1128–1137. [CrossRef]
5. Ministry of Water Resources of China. *China Flood and Drought Disaster Prevention Bulletin (CFDDPB)*; China Water Conservancy Press: Beijing, China, 2020. (In Chinese)
6. National Bureau of Statistic. *China Statistics Yearbook (CSY)*; China Statistics Press: Beijing, China, 2020. (In Chinese)
7. Wang, J.; Yang, Y.; Huang, J.; Adhikari, B. Adaptive irrigation measures in response to extreme weather events: Empirical evidence from the North China plain. *Reg. Environ. Chang.* **2019**, *19*, 1009–1022. [CrossRef]
8. Mendelsohn, R.; Nordhaus, W.D.; Shaw, D. The Impact of Global Warming on Agriculture: A Ricardian Analysis. *Am. Econ. Rev.* **1994**, *84*, 753–771. [CrossRef]
9. Liu, H.; Li, X.; Fischer, G.; Sun, L. Study on the Impacts of Climate Change on China's Agriculture. *Clim. Chang.* **2004**, *65*, 125–148. [CrossRef]
10. Wang, J.; Mendelsohn, R.; Dinar, A.; Huang, J.; Rozelle, S.; Zhang, L. The impact of climate change on China's agriculture. *Agric. Econ.* **2009**, *40*, 323–337. [CrossRef]
11. Chen, Y.; Wu, Z.; Okamoto, K.; Han, X.; Ma, G.; Chien, H.; Zhao, J. The impacts of climate change on crops in China: A Ricardian analysis. *Glob. Planet. Chang.* **2013**, *104*, 61–74. [CrossRef]
12. Schlenker, W.; Hanemann, W.M.; Fisher, A.C.; Will, U.S. Agriculture Really Benefit from Global Warming? Accounting for Irrigation in the Hedonic Approach. *Am. Econ. Rev.* **2005**, *95*, 395–406. [CrossRef]

13. Schlenker, W.; Hanemann, W.M.; Fisher, A.C. Water Availability, Degree Days, and the Potential Impact of Climate Change on Irrigated Agriculture in California. *Clim. Chang.* **2007**, *81*, 19–38. [CrossRef]
14. Ashenfelter, O.; Storchmann, K. Using hedonic models of solar radiation and weather to assess the economic effect of climate change: The case of Mosel Valley Vineyards. *Rev. Econ. Stat.* **2010**, *92*, 333–349. [CrossRef]
15. Deschênes, O.; Greenstone, M. The Economic Impacts of Climate Change: Evidence from Agricultural Output and Random Fluctuations in Weather. *Am. Econ. Rev.* **2007**, *97*, 354–385. [CrossRef]
16. Kelly, D.L.; Kolstad, C.D.; Mitchell, G.T. Adjustment costs from environmental change. *J. Environ. Econ. Manag.* **2005**, *50*, 468–495. [CrossRef]
17. Schlenker, W.; Roberts, M.J. Nonlinear temperature effects indicate severe damages to U.S. crop yields under climate change. *Proc. Natl. Acad. Sci. USA* **2009**, *106*, 15594–15598. [CrossRef]
18. Chen, S.; Chen, X.G.; Xu, J.T. Impacts of climate change on agriculture: Evidence from China. *J. Environ. Econ. Manag.* **2016**, *76*, 105–124. [CrossRef]
19. Chen, Y.; Han, X.; Si, W.; Wu, Z.; Chien, H.; Okamoto, K. An assessment of climate change impacts on maize yields in Hebei Province of China. *Sci. Total Environ.* **2017**, *581–582*, 507–517. [CrossRef]
20. Wei, T.; Cherry, T.L.; Glomrød, S.; Zhang, T. Climate change impacts on crop yield: Evidence from China. *Sci. Total Environ.* **2014**, *499*, 133–140. [CrossRef]
21. You, L.; Rosegrant, M.W.; Wood, S.; Sun, D. Impact of growing season temperature on wheat productivity in China. *Agric. For. Meteorol.* **2009**, *149*, 1009–1014. [CrossRef]
22. Zhang, P.; Zhang, J.; Chen, M. Economic impacts of climate change on agriculture: The importance of additional climatic variables other than temperature and precipitation. *J. Environ. Econ. Manag.* **2017**, *83*, 8–31. [CrossRef]
23. Song, C.X.; Liu, R.F.; Les Oxley and Ma, H.Y. The adoption and impact of engineering-type measures to address climate change: Evidence from the major grain-producing areas in China. *Aust. J. Agric. Resour. Econ.* **2018**, *62*, 608–635. [CrossRef]
24. Zhang, S.; Tao, F.; Zhang, Z. Changes in extreme temperatures and their impacts on rice yields in southern China from 1981 to 2009. *Field Crops Res.* **2016**, *189*, 43–50. [CrossRef]
25. Kong, X.Z.; Gao, Q. The transition of China's rural collective economy and the urgent problems needed to be solved since reform and opening up. *Theor. Explor.* **2017**, *34*, 116–122. (In Chinese)
26. Liang, H. The development of rural collective economy in China: Problems and countermeasures. *Public Financ. Res.* **2016**, *37*, 68–76. (In Chinese)
27. Ma, J.L.; Chen, Y.F.; Qian, X.P. Climate factors, intermediate inputs and maize yield growth: Based on the empirical analysis of Hebei farmers data with multilevel model. *Chin. Rural Econ.* **2012**, *28*, 11–20. (In Chinese)
28. Graubard, B.I.; Korn, E.L. Modelling the sampling design in the analysis of health surveys. *Stat. Methods Med. Res.* **1996**, *5*, 263–281. [CrossRef] [PubMed]
29. Zhang, L.; Chu, Q.Q.; Jiang, Y.L.; Chen, F.; Lei, Y.D. Impacts of climate change on drought risk of winter wheat in the north China plain. *J. Integr. Agric.* **2021**, *20*, 2601–2612. [CrossRef]
30. Goldstein, H. *Multilevel Statistical Models, Chapter 3*; John Wiley & Sons: Hoboken, NJ, USA, 2010; pp. 64–87.
31. Bryk, A.S.; Raudenbush, S.W. Hierarchical linear models: Applications and data analysis methods. Institute for Social and Economic Research (ISER). *J. Am. Stat. Assoc.* **1992**, *98*, 767–768.
32. Chen, Q.; Liu, Y.; Ge, Q.; Pan, T. Impacts of historic climate variability and land use change on winter wheat climatic productivity in the North China Plain during 1980–2010. *Land Use Policy* **2018**, *76*, 1–9. [CrossRef]
33. China Meteorological Administration (CMA). *Trial Procedures for the Early-Warning Signal Issuance of Unexpected Meteorological Disasters*; China Meteorological Administration: Beijing, China, 2004. (In Chinese)
34. Fu, W. *Effects of Climate Warming of Growth Development Process and Yield of Winter Wheat and Corn in Huang-Huai-Hai Plain Last 20 Years*; Nanjing Agricultural University: Nanjing, China, 2013. (In Chinese)
35. Yao, H.R. *The Spatial Structure of Asian Jet Stream and Its Relation with Winter Climate in China*; Nanjing University of Information Science & Technology: Nanjing, China, 2013. (In Chinese)
36. Xiao, G.; Qiang, Z.; Yu, L.; Wang, R.; Yao, Y.; Hong, Z. Impact of temperature increase on the yield of winter wheat at low and high altitudes in semiarid northwestern China. *Agric. Water Manag.* **2010**, *97*, 1360–1364. [CrossRef]
37. Dofing, S.M.; Knight, C.W. Alternative model for path analysis of small-grain yield. *Crop Sci.* **1992**, *32*, 487–489. [CrossRef]
38. Kobata, T.; Uemuki, N. High temperatures during the Grain-Filling period do not reduce the potential grain dry matter increase of rice. *Agron. J.* **2004**, *96*, 406–414. [CrossRef]
39. Nguyen, T.; Cheng, E.; Findlay, C. Land fragmentation and farm productivity in China in the 1990s. *China Econ. Rev.* **1996**, *7*, 169–180. [CrossRef]

sustainability

MDPI

Review

A Review of On-Site Carwash Wastewater Treatment

Wen-Hui Kuan [1,2], Ching-Yao Hu [3], Li-Wei Ke [1] and Jung-Ming Wu [1,*]

[1] Department of Safety, Health and Environmental Engineering, Ming Chi University of Technology, Taishan, New Taipei City 24301, Taiwan; whkuan@mail.mcut.edu.tw (W.-H.K.); m09168004@o365.mcut.edu.tw (L.-W.K.)
[2] Chronic Disease and Health Promotion Research Center, Chang Gung University of Science and Technology, Chiayi 61363, Taiwan
[3] School of Public Health, Taipei Medical University, 250 Wu-Xing Street, Taipei 11031, Taiwan; cyhu@tmu.edu.tw
* Correspondence: jwu@mail.mcut.edu.tw; Tel.: +886-229-089-899 (ext. 4380); Fax: +886-229-082-201

Abstract: In recent years, people's environmental awareness has increased. The high density of the urban population has caused a considerable increase in the demand for car washing services, which has created large quantities of car wash wastewater. The main pollutants in car wash wastewater are detergents, dirt, oil, and grease. Untreated wastewater released into rainwater sewer systems or other water bodies may pollute the water and generate excessive bubble foams, which negatively affects urban appearance. Car washes are divided into mechanical car washes and manual or self-service car washes. In general, car washes have a small operation and scale, occupy limited land, and cannot afford wastewater treatment costs. Therefore, most car washes are not equipped with wastewater treatment facilities. Consequently, the discharge of wastewater from car washes negatively affects the water quality in the surrounding environment and results in wasteful use of water resources. This study reviewed 68 research papers on the quality, treatment techniques, treatment costs, and treatment effectiveness of car wash wastewater to provide a reference for car wash operators to contribute to the preservation of water resources. We found that there is a higher chance of recycling car wash wastewater when combing two different techniques for car wash wastewater treatment.

Keywords: carwash; SS; COD; NTU; wastewater

Citation: Kuan, W.-H.; Hu, C.-Y.; Ke, L.-W.; Wu, J.-M. A Review of On-Site Carwash Wastewater Treatment. *Sustainability* **2022**, *14*, 5764. https://doi.org/10.3390/su14105764

Academic Editors: Alban Kuriqi and Luis Garrote

Received: 16 April 2022
Accepted: 6 May 2022
Published: 10 May 2022

1. Introduction

The rapid growth in human population has resulted in increased car use, which has increased the demand for car wash services and thereby generated large amounts of car wash wastewater. In metropolitan areas, the foam in the wastewater produced during car washing overflows and spoils the appearance of the city. However, compared with industrial wastewater it is relatively easy to treat car wash wastewater and improve its water quality. In Taiwan, the conditions of the narrow and densely populated area and the small scale of the industry make low-cost and low-space car wash wastewater treatment technology an urgent need, and it is believed that this demand is applicable to other metropolitan areas in Asia as well. The goals of car wash wastewater treatment are to prevent environmental pollution and to reuse water resources. According to one estimation, the world had 1.5 billion cars in 2020 [1]. If each car was washed monthly and each wash consumed 100 L of water [2], the amount of water used for car washing would be 1.8 billion tons/year. At a price of one US dollar per ton of water, the annual total cost of car washing worldwide would be USD 1.8 billion per year [3]. Considering that each person consumes approximately 150 L of water per day, the amount of water used for car washing annually is equal to that used by 33 million people annually [4]. This consumption approximately represents the amount of water used annually by the entire population of Malaysia (33 million), Venezuela (32 million), the Republic of Ghana (30 million), Oceania (including Australia (25 million) and New Zealand (5 million)) or

the combined population of Denmark (5.8 million), Norway (5.4 million), Switzerland (10 million), Finland (5.5 million), and Iceland (360,000). The 2030 Agenda established by the United Nations proposes 17 sustainable development goals as the core objectives for sustainable development among governments and corporations. In particular, goal six is aimed at ensuring access to water and sanitation for all. Access to water is a basic right; thus, the value of water exceeds the price of water. Consequently, the circulation and reuse of water resources is essential. This study reviewed 68 research papers and obtained data on the car wash wastewater produced in 38 cities in 21 countries. These data mainly contained information on the suspended solid (SS, mg/L) concentration, turbidity (Nephelometric Turbidity Unit, NTU), chemical oxygen demand (COD, mg O_2/L), and oil and grease (O&G, mg /L) concentration of car wastewater, as well as on the anionic surfactants (AS, mg /L) used in car wash wastewater treatment. The aforementioned data and the corresponding removal techniques of these pollutants are comprehensively discussed in the following sections.

2. Car Wash Wastewater Quality

Car wash wastewater generally contains suspended particles that originate from the dirt on vehicles, the oil on vehicle exteriors, the oil and grease generated from car wax, and the anionic surfactants caused by detergent use [5,6]. This wastewater has a high COD. Table 1 [2,7–58] presents data on the car wash wastewater quality of each region investigated in the literature review. The SS concentration, turbidity, COD, O&G, and AS values in the collected data ranged from 68 to 1990 mg/L, 60 to 1000 NTU, 85 to 1295 mg O_2/L, 12 to 325 mg/L, and 3 to 68 mg/L, respectively. The median values of the aforementioned parameters were 186 mg/L, 187 NTU, 418 mg O_2/L, 28 mg/L, and 13 mg/L, respectively. The car wash wastewater data of different countries (Table 1) exhibited no significant correlations. In particular, the extreme values of the SS concentration, turbidity, and COD values were 2929 mg/L, 3649 NTU, and 14133 mg O_2/L, respectively [27]. Moreover, the turbidity and COD ranged from 559~733 NTU and from 2640~4160 mg O_2/L, respectively [20,21]. Because the collected data include data on wastewater created when washing garbage trucks, the different water quality parameters were relatively higher in value. If extreme values such as those for the wastewater from washing garbage trucks are eliminated, it is believed that the normal SS, turbidity, COD, O&G and AS values of car wash wastewater would be around level 200 mg/L, 200 NTU, 450 mg O_2/L, 30 mg/L, and 30 mg/L, respectively. The most direct intention of car washing is to remove dust; therefore, Figure 1 shows the NTU data as surveyed from the literature. From Figure 1, it can be seen that the NTU of car washing wastewater is not directly related to the desertification of the urban environment.

Figure 1. NTU data of carwash wastewater surveyed from Table 1.

Table 1. Car wash wastewater characteristics from various literature sources.

Country	Area	Ref.	SS (mg/L)	Turbidity (NTU)	COD (mg/L)	O&G (mg/L)	AS (mg/L)
USA	New Jersey	[2]	115	—	—	—	9.2
USA	Texas	[7]	—	—	260	—	—
Mexico	Toluca	[8]	538	925	1024 t, 541 s	448	—
Mexico	Toluca	[9]	—	898	1295 t, 488 s	369	68.3
Brazil	Porto Alegre	[10]	—	103 ± 57	191~600	—	6.3~21
Brazil	Sao Paulo	[11]	68 ± 19	89 ± 16.5	241 ± 23.5	6 ± 1	11.7 ± 9
Brazil	Sao Paulo	[12]	—	156 ± 45	626 ± 125	—	—
Brazil	Porto Alegre	[13]	112 ± 21	139 ± 45	259 ± 40	12 ± 6	—
Brazil	Porto Alegre	[14]	89 ± 54	103 ± 57	191 ± 22	—	—
Brazil	Natal	[15]	—	—	625 ± 5	—	—
Brazil	Belo Horizonte	[16]	260 ± 20	85 ± 8	85 ± 6	<0.1	—
Brazil	Porto Alegre	[17]	85~279	194~254	249~873	—	11.3~22.3
Belgium	Leuven	[18]	60~140	—	208~382	—	0.7~2.5
Sweden	Goteborg	[19]	—	—	1263~4600	291~550	—
Italy	Genoa	[20,21]	—	—	572	—	95.5
Italy	Brescia	[22]	—	559~733	2640~4160	—	—
France	Toulouse	[23]	46~518	60~152	539~1506	—	~12
Egypt	South of Egypt	[24]	55	28.1	82	—	—
Egypt	Shatby	[25]	—	90.5~386	282~566	—	—
Egypt	Elminia	[26]	—	160	1430~1649	—	—
Ghana	Kumasi	[27]	2929 ± 451	3649 ± 2150	14133 ± 237	—	—
South Africa	Gauteng	[28]	—	109~4000	—	12~43	1.4~5.8
South Africa	Johannesburg	[29]	—	—	750~1864	5~24	—
Syria	Aleppo	[30]	49	—	350~510	20~40	21~35
Turkey	Istanbul	[31]	—	—	314 ± 9.4	—	—
Turkey	Istanbul	[32]	320	—	500	120	290
Turkey	Tekirdag	[33]	—	312~420	7960~8190	—	—
Turkey	Istanbul	[34]	2300	—	560	125	35
Iran	Zahedan	[35]	193 ± 71.5	166.8 ± 51.7	856 ± 217	—	31.2 ± 18.8
Iran	Tehran	[36]	—	118~1400	610~2619	—	—
Iran	Tehran	[37]	—	170 ± 32.5	480~1560	—	—
Iran	Ahvaz	[38]	—	—	480~1560	—	—
Vietnam	Hanoi	[39]	51~110	—	498~808	37~125	—
Malaysia	Johor, Skudai	[40]	—	34.7~86	75~738	—	—
Malaysia	Parit Raja	[41]	—	275.1	220	—	—
Malaysia	Parit Raja	[42]	186 ± 56.6	173.7 ± 58.8	741 ± 316	1.78 ± 0.1	—
Malaysia	Taman University	[43]	202 ± 10	216.3 ± 21.5	893 ± 298	0.004	—
China	Shenyang, Hunan	[44]	—	362~450	—	5.3~13.5	—
China	Shanghai	[45]	—	70~100	100~160	5~25	2~5
China	Zhenjiang	[46]	—	128.7	155.6	—	—
Australia	Melbourne	[47]	1275	522~763	295~471.5	—	—
Australia	Geelong	[48]	4200	1000	433	—	—
Australia	Melbourne	[49]	1200	763	417.5	—	—
Pakistan	Abbottabad	[50]	110~5856	73~772	141~1019	1.3~83.7	—
Pakistan	Peshawar	[51]	1000	253	—	27	—
Pakistan	Hyderabad	[52]	—	82.4~493	—	—	—
Taiwan	Hsinchu	[53]	230	—	67	—	—
Taiwan	Taipei	[54]	30~200	20~40	50~300	—	3~20
Indonesia	Semarang	[55]	—	186.6	700	36	—
India	Bangalore	[56]	970~1020	56.3~195	176.23~246	135~190	—
India	Tasveer Mahal	[57]	242.6	—	79	—	—
India	Trichy	[58]	—	132~140	150~175	—	—

Note: t denotes total, s denotes dissolved.

3. Water Quantities Required to Wash a Car

The quantity required for washing a single car has been measured by different studies as approximately 45~60 L, 130~350 L, 45~60 L, 189~379 L, 400 L, and 151~227 L of water, respectively [2,10,12,18,39,59]. These results indicate that varying amounts of water are required for car washing in different countries. A reasonable amount of water for washing a car is 100~200 L. Several studies have collected data on car wash wastewater for unique vehicles. The car wash water consumption for heavy vehicles and waste container washing vehicles was recorded as approximately 350~900 L and 5000 L, respectively [12,22]. Monney et al. [27] reported that the car wash water consumption of multiple vehicles (e.g., saloon cars, sport utility vehicles or pick-ups, buses or vans, heavy articulators, and graders or loaders) ranged between 105 and 1381 L. The car wash water consumption for washing heavy vehicles, trucks, and trailers ranged between 250 and 1200 L [19]. Germany and Austria have stipulated regulations mandating the recycling of 80% of car wash wastewater. Alternatively, the Netherlands and Scandinavian countries impose restrictions on water consumption for each car wash of 60~70 L [60]. There is a scarce record on car wash water consumption based on what kinds of cars are washed in the literature reviewed, however, it is natural to assume that larger cars require a larger amount of water in a car wash. The amount of water used in a car wash is not highly correlated with the region where the car is washed or the type of car; rather, it is more likely to be related to the culture of water usage. However, there is no significant evidence to support this supposition.

4. Car Wash Wastewater Treatment Technique

Currently, various car wash wastewater treatment techniques are available, as reported in reviewed literatures [61–66]. The scope of this study includes discussion of such techniques as electrocoagulation (EC) [67–69], flocculation flotation (FF) [10,17], filtration (F) [18], coagulation–flocculation (CF) [22,35], biological treatment (Bio) [2,12], adsorption (AD) [70], electro-oxidation (EO) [15,71], and other less-known technologies such as photo-Fenton application [24,72]. In general, the combination of at least two wastewater treatment techniques can enable high treatment efficiency of car wash wastewater [7,20,21,32].

4.1. Electrocoagulation (EC)

Figure 2 depicts the general mechanism of the electrocoagulation process. EC uses metal hydroxides produced by electrolysis to remove pollutants in wastewater. During the electrolysis reaction, a sacrificial anode undergoes an oxidation reaction to release metal ions, while the cathode undergoes a reduction reaction to reduce the metal ions to metal and generate hydrogen. Commonly used metal anodes include aluminum and iron. The EC process has a turbidity removal rate of approximately 90% [8,9,25]. When coupled with adsorption treatment or electro-oxidation treatment, the turbidity removal rate of the EC process can be increased. Moreover, the EC process has a COD removal rate of approximately 80%. When combined with other treatments, the COD removal rate of the EC process can be increased (Table 2). Obviously, it is not efficiently to remove SS by EC.

4.2. Flocculation–Flotation (FF)

Figure 3 presents the mechanism and process of flocculation–flotation (FF). FF combines polymer flocculant addition and air bubble flotation to separate pollutants in carwash wastewater. The SS and turbidity removal rates of the FF process are approximately 85% and 90%, respectively [10,17]. When coupled with other treatments, the SS and turbidity removal rates of this process can reach as high as 96% [11,14]. The FF process has a COD removal rate of approximately 70~80%, which can be increased when this process is coupled with other treatments. Thus, the FF process exhibits a turbidity and COD removal performance comparable to that of the EC process (Table 3).

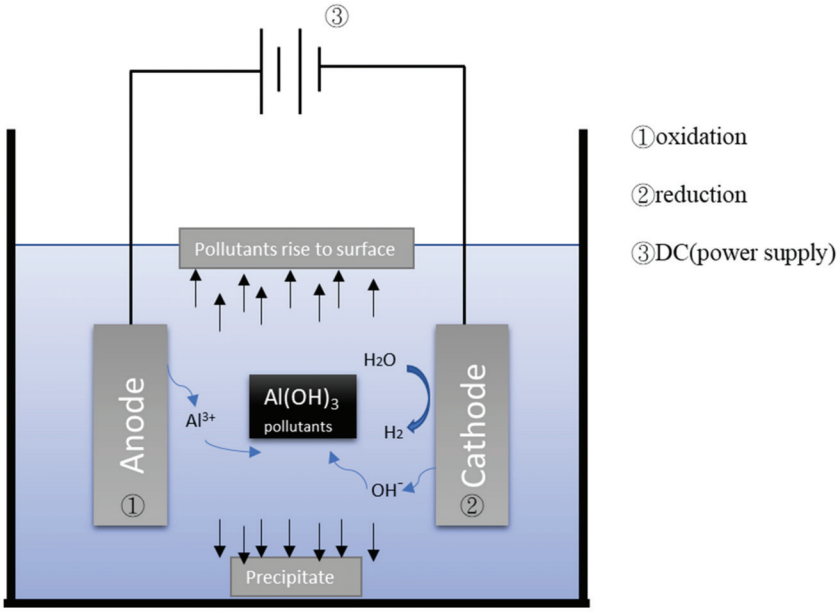

Figure 2. Schematic illustration of electrocoagulation/flotation.

Table 2. Removal rate of various water qualities by EC method.

Country	Area	Ref.	Technique	SS (mg/L)	Turbidity (NTU)	COD (mg/L)	O&G (mg/L)	AS (mg/L)
Mexico	Toluca	[8]	EC + AD	—	92~98%	78~94%	—	—
Mexico	Toluca	[9]	EC + EO	—	98~98.4%	76~96%	92~100%	81~92%
Italy	Genoa	[21]	EC + EO	—	—	75~97%	—	—
Iran	Tehran	[36]	EC	—	85.5%	80.8%	—	—
Iran	Tehran	[38]	EC	—	—	88%	—	—
Iran	Ahvaz	[37]	EC	—	—	90%	—	—
USA	Texas	[7]	EC	—	—	79%	—	—
Egypt	Shatby	[25]	EC	—	~87%	~85%	—	—
Turkey	Istanbul	[34]	EC	—	—	88%	82%	99%
Turkey	Tekirdag	[33]	EC	—	99%	76%	—	—
China	Zhenjiang	[46]	EC + Ultrasound	—	96%	69%	—	—

Table 3. Removal rate of various water qualities by flocculation–flotation method.

Country	Area	Ref.	Technique	SS (mg/L)	Turbidity (NTU)	COD (mg/L)	O&G (mg/L)	AS (mg/L)
Brazil	Porto Alegre	[17]	FF + O	83–99%	89–95% 93–98%	39–85% 81–99%	—	78–89% 81–99%
Brazil	Porto Alegre	[10]	FF	—	91-96%	—	—	40%
Brazil	Sao Paulo	[11]	FF + SF	—	87–91%	—	—	—
Brazil	Porto Alegre	[13]	FF	89%	93%	11%	—	—
Brazil	Porto Alegre	[14]	FF + SC	91–93%	91–96%	63–76%	—	—
Pakistan	Hyderabad, Sindh	[52]	DAF + F	—	97%	—	99%	—

Note: sand filtration (SF), ozonation (O), sand filtration and chlorination (SC), Filtration (F), Dissolved Air Flotation (DAF).

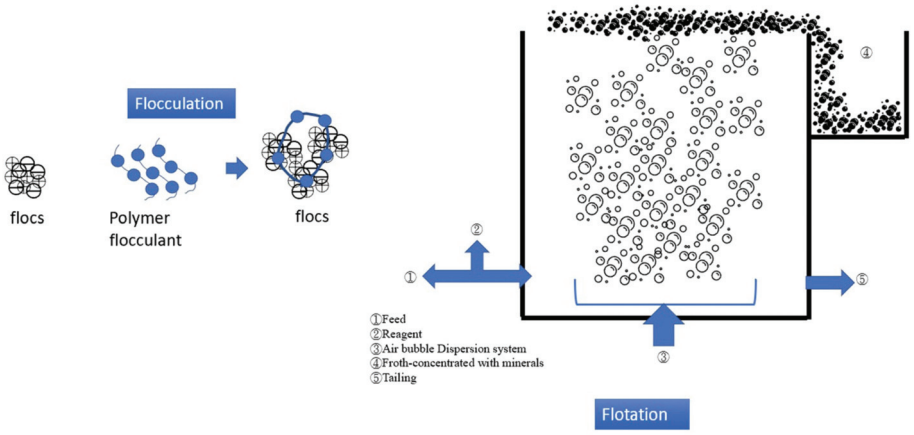

Figure 3. Schematic illustration of flocculation–flotation.

4.3. Filtration (F)

In recent years, filtration has become an excellent method for solid–liquid separation [73], and membrane filtration has especially been used in many fields, for example mineral processing [74], removing surfactants [75], suspension filtration [76], and more. Figure 4 illustrates the mechanism of filtration.

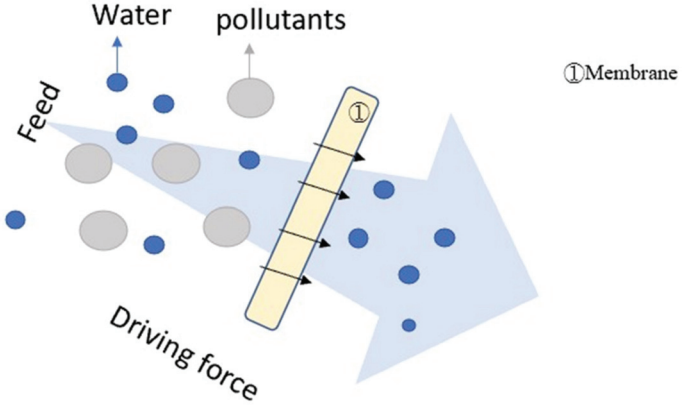

Figure 4. Illustration of filtration.

When the filter element has sufficient selectivity, the flocculation–filtration process can achieve SS and turbidity removal rates over 99%, as presented in [51,55]. However, the filtrate flux of flocculation–ultrafiltration and flocculation–nanofiltration are only approximately 50 and 10 LMH (L/m^2-h), respectively. To provide wastewater treatment for the medium-scale car wash factory discussed in [18], an ultrafiltration plant with a size of approximately 100 m^2 would be required. Such a plant would occupy a large space, and would thus be unsuitable for highly developed urban areas. Despite being able to remove partial COD, the general COD removal rate of the flocculation–filtration process is approximately 60% (Table 3).

The coagulation–filtration process has turbidity and COD removal rates of approximately 90% and 60%, respectively (Table 4).

Table 4. Removal rate of various water qualities by filtration.

Country	Area	Ref.	Technique	SS (mg/L)	Turbidity (NTU)	COD (mg/L)	O&G (mg/L)	AS (mg/L)
Belgium	Leuven	[18]	UF + NF	—	—	60~95%	—	88~95%
Sweden	—	[77]	UF	—	—	60%	—	—
Turkey	Istanbul	[34]	EC + NF	99%	—	88%	90%	91%
Malaysia	Johor, Skudai	[40]	UF + NF	—	—	55~92%	—	—
Brazil	Belo Horizonte	[16]	MF + UF	—	96.2~99.3%	81~85%	—	—
Turkey	Istanbul	[31]	UF + NF	—	—	Negligible~97%	—	—
Indonesia	Semarang	[55]	UF	—	100%	91%	83%	—
Japan	Tokyo	[78]	F + UF	—	75%	50~90%	—	—
China	Shanghai	[45]	C + UF	—	85%	80%	—	
Vietnam	Hanoi	[39]	MBR + F	—	—	90%	88%	—
Australia	Melbourne	[47]	UF + RO	100%	99.9%	96%	—	—
Pakistan	Peshawar	[51]	SED + F	80%	99%	—	49.2%	
India	Aligarh	[57]	SF	89.2%	—	83.5%	—	—
India	Trichy	[58]	UF	—	82%	47–60%	—	—

Note: ultrafiltration (UF), nanofiltration (NF), microfiltration (MF), coagulation (C), sand filtration (SF), sedimentation (SED), reverse osmosis (RO), filtration (F).

When coupled with filtration technology, the biological treatment process achieves turbidity and COD removal rates of approximately 99% and 95%, respectively [48,53].

4.4. Coagulation–Flocculation (CF)

Figure 5 depicts the processes of coagulation–flocculation (CF), which is a two-stage reaction system. In coagulation, a coagulant such as polyaluminum chloride (PAC) or ferric chloride is added to the wastewater to modify the surface charge of the particle pollutants, thereby eliminating the electrostatic repulsion between the particles was. The flocculant (i.e., polymer) is then added to the wastewater to aggregate the near-neutral electrostatic particles and form flocs for easier pollutant removal. Generally speaking, the turbidity removal rate of CF with car wash wastewater is good, generally over 90%; however, the removal rates of COD, O&G, and AS are not as good [22,41]. In addition, CF needs to add a suitable flocculant, which can easily cause cost increases and secondary pollution. Table 5 lists the effects of using CF and its combinations on car wash wastewater treatment as found in the literature.

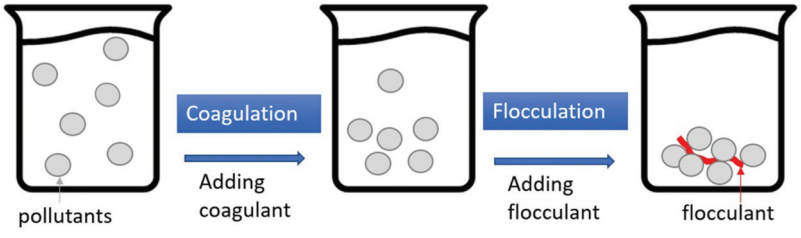

Figure 5. Schematic illustration of coagulation–flocculation (CF).

4.5. Bio-Treatment

Figure 6 illustrates the mechanism of bio-treatment. Aerobic microorganisms in the wastewater degrade the organics into H_2O and CO_2, while the dead biomass of microorganisms forms a sludge in the wastewater. Table 6 lists the effects of biological treatment combined with other technologies on car wash wastewater treatment. For biological treatment followed by filtration treatment, the removal rate of turbidity, COD, and AS can reach more than 95% [2,12,48,49].

Table 5. Removal rate of various water qualities by coagulation–flocculation.

Country	Area	Ref.	Technique	SS (mg/L)	Turbidity (NTU)	COD (mg/L)	O&G (mg/L)	AS (mg/L)
Italy	Brescia	[22]	CF	—	98%	74%	—	—
Iran	Zahedan	[35]	C	37%	—	44%	—	76%
Egypt	Elminia	[26]	CF + SF + O + SF	—	100%	88%	—	—
Malaysia	Parit Raja, Johor	[41]	CF	—	97%	35%	—	—
Malaysia	Parit Raja	[42]	C	—	94%	60%	—	—
Malaysia	Taman University	[43]	C	—	90%	60%	—	—
China	Shenyang	[44]	C + UF	—	94%	—	>40%	—
China	Shanghai	[79]	C + M	—	70%	—	—	—
India	Bangalore	[56]	CF + F	—	—	80–90%	92–93%	—
Pakistan	Abbottabad	[50]	C + H_2O_2	—	97%	93%	96%	—

Note: Chemical coagulation (C), membrane filtration (M).

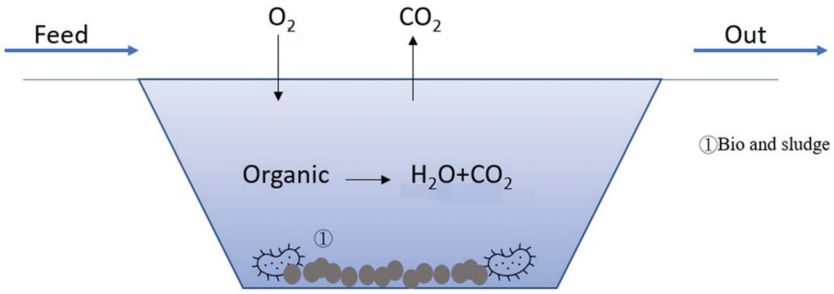

Figure 6. Illustration of bio-treatment.

Table 6. Removal rate of various water qualities by bio-treatment.

Country	Area	Ref.	Technique	SS (mg/L)	Turbidity (NTU)	COD (mg/L)	O&G (mg/L)	AS (mg/L)
Brazil	Sao Paulo	[12]	RBC + F	—	72~97%	56~94%	—	—
USA	New Jersey	[2]	four bioretention mesocosms	84~95%	—	—	—	89~96%
Taiwan	Hsinchu	[53]	Bio + M	95.7%	—	70.2%	—	—
Australia	Geelong	[48]	C + MBR	99.8%	99.6%	—	—	—
Australia	Melbourne	[49]	enhanced MBR (eMBR)	—	99.9%	99.8%	5.9~6.7 LMH	—

Rotating Biological Contactor (RBC).

4.6. Other Methods

A few other single treatment methods, such as the Photo-Fenton's process [24], adsorption [30], electro-oxidation [15], etc., are listed in the table below (Table 7). Except for electro-oxidation, these single-unit processing technologies have a removal rate of less than 90%.

Table 7. Removal rate of various water qualities by other single unit treatment techniques.

Country	Area	Ref.	Technique	SS (mg/L)	Turbidity (NTU)	COD (mg/L)	O&G (mg/L)	AS (mg/L)
Egypt	South of Egypt	[24]	Photo-Fenton's process	—	—	82~93.4%	—	—
Syria	Aleppo	[30]	AD	—	—	81.6%	86.8%	88.3%
Brazil	Natal	[15]	EO	—	—	96%	—	83~96%

Treated water with low turbidity can be obtained by coagulation and flocculation, however, the added chemicals increase the amount of sludge. Treated water with relatively low turbidity can be obtained by ultrafiltration and nanofiltration, as well; however, the filter material is expensive, and a large filtration area is required to obtain a large amount of recycled water. While the electrocoagulation treatment method has a good treatment effect on AS and O&G, it is less effective than filtration in turbidity treatment. Meanwhile, the sacrificial electrode causes additional sludge. Bio-treatment has an excellent effect on COD, although the biological treatment method is relatively slow and unstable. The combination of at least two wastewater treatment techniques can enable the achievement of high treatment efficiency of car wash wastewater treatment.

5. Energy Consumption

The energy consumption rates of the wastewater treatment methods used by EC have been reported by Pinto et al. [16], Kara [33], and Nguegang et al. [29] as 0.14, 1.5, and 2.7 kWh/m^3, respectively. The energy consumption rate based on COD reduction was 66 kWh/kg after 6 h operation [15]. In [35], the energy consumption rate was 10 kWh/m^3; in [67], the energy consumption rate ranged from 1.5 to 2.7 kWh/m^3. In [25], car wash wastewater was subjected to electrocoagulation using a new cell design featuring a horizontal spiral anode placed above a horizontal disk cathode. Excellent treatment results were achieved through electrocoagulation. El-Ashtoukhy et al. [25] used a new EC cell with a spiral tube anode placed above a flat plate cathode resting on the cell bottom; the energy consumption based on COD reduction ranged from 2.3 to 15.1 kWh/kg. In [33], the energy consumption for the treatment of transport container washing wastewater ranged from 3.1 to 46.5 kWh/m^3. The aforementioned electrochemical techniques can have varying flow capacities and involve the use of different types of electrodes. In general, an electricity consumption rate between 0.5 and 2 kWh/m^3 is considered reasonable.

6. Operating Cost

The operating cost depends on the techniques processes used in carwash wastewater treatment, including materials, chemicals, energy consumption, sludge disposal, labor, etc. Table 8 summarizes the operating cost and payback duration for the various techniques. Among the EC methods, the case using a titanium electrode costs substantially more than using an Al and Fe electrode [33,67,68]. In [33], the treatment of transport container washing wastewater is discussed. Because transport container washing wastewater has high COD and turbidity (specifically 8200 mg/L and 420 NTU, respectively), the sludge production rate was 12 kg/m^3. The payback duration was reported as 6 and 15 months for the bio-membrane and electrocoagulation methods when combined with flotation (ECF), respectively [51,53].

Table 8. Comparison of operating costs.

Technique	Operating (US $/$m^3$)	Payback (Month)	Ref.
EC	0.8	-	[33]
EC with Al electrode Fe electrode	- 0.3 0.6	-	[67]
EC with Titanium electrode	9.7	-	[68]
Bio + M	-	7–15	[51]
ECF	-	15	[53]
FF	0.92	-	[10]

The detailed items of operating cost for FF technology have been previously determined; the respective cost for chemicals, sludge disposal, and electricity consumption was USD 0.43/m^3, USD 0.07/m^3, and USD 0.423/m^3 [10]. The market value of a flocculation-column flotation system with a capacity of 1.0 L/h was USD 8687.50 in Brazil. The wastewater treatment system discussed in [51] had a fixed operating cost of USD 2677 and an electricity consumption cost of USD 258.4 kWh/year in filtration, equivalent to USD 51.6/year.

7. Discharge Standards

Table 9 presents the car wash wastewater treatment regulations of various countries. Most countries have imposed the following rigorous regulations on car wash wastewater treatment: SS concentration < 40 mg/L, turbidity < 5 NTU, COD < 50 mg/L, O&G concentration < 5 mg/L, and AS value < 2 mg/L.

Table 9. Discharge standards of different countries.

Country	Criteria	Ref.	SS (mg/L)	Turbidity (NTU)	COD (mg/L)	O&G (mg/L)	AS (mg/L)
China	GB/T 18920-2002	[79]	5	5	50	1	0.5
Iran	Iran Standard	[35]	40	50	60	—	1.5
Australia	Recycled water class A according to EPA	[47]	5	2	—	—	—
Belgium	—	[18]	<60	—	<125	—	3
France	—	[23]	35	—	125	—	—
Malaysia	Environmental quality Act 1974	[41]	—	<5	<50	—	—
Syria	Syrian Standard No. 2752	[30]	50	—	75	5	5
USA	NJDEP	[2]	40	—	—	—	—
Brazil	Local emission standards	[17]	180	—	400	—	2
Mexico	—	[8]	—	—	—	15	—

New Jersey Department of Environmental Protection.

The regulations on suspended solids in China and Australia require less than 5 mg/L, which is stricter. In terms of nephelometric turbidity units, most of the specifications listed in the table are NTU < 5. As the particulate pollution of car wash wastewater is comprehensively reflected in SS and NTU, the regulation of SS < 5 m/L and NTU < 5 is relatively reasonable.

8. Conclusions

This study reviewed the literature on wastewater quality, wastewater treatment technology, the electricity consumption and operating costs of wastewater treatment, and wastewater treatment-related regulations. In summary, car wash wastewater treatment facilities are worth investing in for the reasons described in the text. First, the required filtering, electrochemical, and bioprocessing technologies are relatively mature and able to remove pollutants, i.e., SS, COD, O&G and AS, at rates above ~85%. The operating procedures of the treatment facilities are not complicated, and the operating costs are within a reasonable range, from USD/m^3 0.3–0.92. Second, by selecting and coupling various types of wastewater treatment technologies, operators can treat wastewater in a way that meets government regulations. Third, regions with abundant water resources may experience short- or medium-term droughts under the effects of climate change; thus, water resources are highly valuable. However, whether recycling wastewater yields profit is a valid commercial concern.

Water resources are relatively scarce in the face of frequent droughts and floods in extreme weather. From the second half of 2020 to the first half of 2021, Taiwan has experienced nearly a year of drought (Taiwan is a country with an average annual rainfall of 2500 mm). In Taichung City, water is only available four days a week. While effective and

active treatment of car wash wastewater may not be economical, it is extremely important for the sustainability of precious water resources.

Author Contributions: Data curation, C.-Y.H. and L.-W.K.; Investigation, W.-H.K.; Methodology, C.-Y.H.; Supervision, W.-H.K.; Writing—original draft, J.-M.W.; Writing—review & editing, J.-M.W. All authors have read and agreed to the published version of the manuscript.

Funding: The authors would like to thank the Environmental Protection Administration of the China, Taiwan, for financially supporting this research under Contract No. EPA 109-A339.

Institutional Review Board Statement: Not applicable.

Informed Consent Statement: Not applicable.

Data Availability Statement: Not applicable.

Acknowledgments: The authors would like to thank the Environmental Protection Administration of the Republic of China, Taiwan, for financially supporting this research under Contract No. EPA 109-A339.

Conflicts of Interest: The authors declare that they have no known competing financial interest or personal relationships that could have appeared to influence the work reported in this paper.

Abbreviations

AD	adsorption
AS	anionic surfactant
Bio	biological treatment
COD	chemical oxygen demand
C	chemical coagulation
CF	coagulation-flocculation
DAF	dissolved air flotation
EC	electrocoagulation
EO	electro-oxidation
F	filtration
FF	flocculation flotation
M	membrane filtration
MBR	membrane bio-reactor
MF	microfiltration
NF	nanofiltration
NJDEP	New Jersey Department of Environmental Protection
NTU	nephelometric turbidity units
O&G	oil and grease
O	ozonation
RBC	rotating biological contactor
RO	reverse osmosis
SC	sand filtration and chlorination
SED	sedimentation
SF	sand filtration
SS	suspended solids
UF	ultrafiltration

References

1. Available online: https://www.statista.com/statistics/200002/international-car-sales-since-1990/ (accessed on 18 April 2022).
2. Bakacs, M.E.; Yergeau, S.E.; Obropt, C.C.; ASCE, P.E.M. Assessment of car wash runoff treatment using bioretention mesocosms. *J. Environ. Eng.* **2013**, *139*, 1132–1136. [CrossRef]
3. Available online: https://www.slideshare.net/guest7527d21f/ss-2773696 (accessed on 18 April 2022).
4. Available online: https://kknews.cc/zh-tw/agriculture/xmm99mg.html (accessed on 18 April 2022).
5. Torkashvand, J.; Farzadkia, M.; Younesi, S.; Gholami, M. A systematic review on membrane technology for carwash wastewater treatment: Efficiency and limitations. *Desalin. Water Treat.* **2021**, *210*, 81–90. [CrossRef]
6. Talebzadeh, F.; Valeo, C.; Gupta, R.; Constabel, C.P. Exploring the Potential in LID Technologies for Remediating Heavy Metals in Carwash Wastewater. *Sustainability* **2021**, *13*, 8727. [CrossRef]

7. Gomes, A.J.; Das, K.K.; Jame, S.A.; Cocke, D.L. Treatment of truck wash water using electrocoagulation. *Desalin. Water Treat.* **2016**, *57*, 25991–26002. [CrossRef]
8. Rubi-Juarez, H.; Barrera-Diaz, C.; Uena-Nunez, F. Adsorption-assisted electrocoagulation of real car wash wastewater with equilibrium and kinetic studies. *Pollut. Res.* **2017**, *36*, 175–184.
9. Rubi-Juarez, H.; Barrera-Diaz, C.; Linares-Hernandez, I.; Fall, C.; Bilyeu, B. A combined electrocoagulation-electrooxidation process for carwash wastewater reclamation. *Int. J. Electrochem. Sci.* **2015**, *10*, 6754–6767.
10. Zaneti, R.; Etchepare, R.; Rubio, J. More environmentally friendly vehicle washes: Water reclamation. *J. Clean. Prod.* **2012**, *37*, 115–124. [CrossRef]
11. Zaneti, R.; Etchepare, R.; Rubio, J. Car wash wastewater reclamation. Full-scale application and upcoming features. *Resour. Conserv. Recycl.* **2011**, *55*, 953–959. [CrossRef]
12. Subtil, E.L.; Rodrigues, R.; Hespanhol, I.; Mierzwa, J.C. Water reuse potential at heavy-duty vehicles washing facilities—The mass balance approach for conservative contaminants. *J. Clean. Prod.* **2017**, *166*, 1226–1234. [CrossRef]
13. Rubio, J.; Zaneti, R.N. Treatment of washrack wastewater with water recycling by advanced flocculation–column flotation. *Desalin. Water Treat.* **2009**, *8*, 146–153. [CrossRef]
14. Zaneti, R.N.; Etchepare, R.; Rubio, J. Car wash wastewater treatment and water reuse—A case study. *Water Sci. Technol.* **2013**, *67*, 82–88. [CrossRef] [PubMed]
15. Ganiyu, S.O.; dos Santos, E.V.; de Araújo Costa, E.C.T.; Martínez-Huitle, C.A. Electrochemical advanced oxidation processes (EAOPs) as alternative treatment techniques for carwash wastewater reclamation. *Chemosphere* **2018**, *211*, 998–1006. [CrossRef] [PubMed]
16. Pinto, A.C.S.; de Barros Grossi, L.; de Melo, R.A.C.; de Assis, T.M.; Ribeiro, V.M.; Amaral, M.C.S.; de Souza Figueiredo, K.C. Carwash wastewater treatment by micro and ultrafiltration membranes: Effects of geometry, pore size, pressure difference and feed flow rate in transport properties. *J. Water Process Eng.* **2017**, *17*, 143–148. [CrossRef]
17. Etchepare, R.; Zaneti, R.; Azevedo, A.; Rubio, J. Application of flocculation–flotation followed by ozonation in vehicle wash wastewater treatment/disinfection and water reclamation. *Desalin. Water Treat.* **2015**, *56*, 1728–1736. [CrossRef]
18. Boussu, K.; Kindts, C.; Vandecasteele, C.; van der Bruggen, B. Applicability of nanofiltration in the carwash industry. *Sep. Purif. Technol.* **2007**, *54*, 139–146. [CrossRef]
19. Paxéus, N. Vehicle washing as a source of organic pollutants in municipal wastewater. *Water Sci. Technol.* **1996**, *33*, 1–8. [CrossRef]
20. Panizza, M.; Cerisola, G. Applicability of electrochemical methods to carwash wastewaters for reuse. Part 1: Anodic oxidation with diamond and lead dioxide anodes. *J. Electroanal. Chem.* **2010**, *638*, 28–32. [CrossRef]
21. Panizza, M.; Cerisola, G. Applicability of electrochemical methods to carwash wastewaters for reuse. Part 2: Electrocoagulation and anodic oxidation integrated process. *J. Electroanal. Chem.* **2010**, *638*, 236–240. [CrossRef]
22. Vaccari, M.; Gialdini, F.; Collivignarelli, C. Study of the reuse of treated wastewater on waste container washing vehicles. *Waste Manag.* **2013**, *33*, 262–267. [CrossRef]
23. Sablayrolles, C.; Vialle, C.; Vignoles, C.; Montrejaud-Vignoles, M. Impact of carwash discharge on stormwater quality (Toulouse, France). *Water Sci. Technol.* **2010**, *62*, 2737–2746. [CrossRef]
24. Tony, M.A.; Bedri, Z. Experimental design of photo-Fenton reactions for the treatment of car wash wastewater effluents by response surface methodological analysis. *Adv. Environ. Chem.* **2014**, *2014*, 958134. [CrossRef]
25. El-Ashtoukhy, E.S.Z.; Amin, N.K.; Fouad, Y.O. Treatment of real wastewater produced from Mobil car wash station using electrocoagulation technique. *Environ. Monit. Assess.* **2015**, *187*, 628–638. [CrossRef] [PubMed]
26. Abdelmoez, W.; Barakat, N.A.M.; Moaz, A. Treatment of wastewater contaminated with detergents and mineral oils using effective and scalable technology. *Water Sci. Technol.* **2013**, *68*, 974–981. [CrossRef] [PubMed]
27. Monney, I.; Donkor, E.A.; Buamah, R. Clean vehicles, polluted waters: Empirical estimates of water consumption and pollution loads of the carwash industry. *Heliyon* **2020**, *6*, e03952. [CrossRef]
28. Tekere, M.; Sibanda, T.; Maphangwa, K.W. An assessment of the physicochemical properties and toxicity potential of carwash effluents from professional carwash outlets in Gauteng Province, South Africa. *Environ. Sci. Pollut. Res.* **2016**, *22*, 12816–12828. [CrossRef] [PubMed]
29. Nguegang, B.; Sibanda, T.; Tekere, M. Cultivable bacterial diversity, physicochemical profiles, and toxicity determination of car wash effluents. *Environ. Monit. Assess.* **2019**, *191*, 478. [CrossRef]
30. Baddor, I.M.; Farhoud, N.; Abdel-Magid, I.M.; Alshami, S.; Hassan Ahmad, F.; Olabi, E.A. Study of car wash wastewater treatment by adsorption. In Proceedings of the International Conference of Engineering, Information Technology, and Science, Kuala Lumpur, Malaysia, 1 May 2014; pp. 2–22.
31. Uçar, D. Membrane processes for the reuse of car washing wastewater. *J. Water Reuse Desalin.* **2018**, *8*, 169–175. [CrossRef]
32. Hashim, N.H.; Ibrahim, M.S.S.; Awang, Z. Adsorption of anionic surfactant presence in synthetic car wash wastewater by limestone. *J. Appl. Chem. Nat. Resour.* **2019**, *1*, 1–5.
33. Kara, S. Treatment of transport container washing wastewater by electrocoagulation. *Environ. Prog. Sustain. Energy* **2013**, *32*, 249–256. [CrossRef]
34. Gonder, Z.B.; Balcioglu, G.; Vergili, I.; Kaya, Y. An integrated electrocoagulation-nanofiltration process for carwash wastewater reuse. *Chemosphere* **2020**, *253*, 126713. [CrossRef]
35. Bazrafshan, E.; Mostafapoor, F.K.; Soori, M.M.; Mahvi, A.H. Application of combined chemical coagulation and electrocoagulation process to carwash wastewater treatment. *Fresenius Environ. Bull.* **2012**, *21*, 2694–2701.

36. Mirshahghassemi, S.; Aminzadeh, B.; Torabian, A.; Afshinnia, K. Optimizing electrocoagulation and electro-Fenton process for treating car wash wastewater. *Environ. Health Eng. Manag. J.* **2017**, *4*, 37–43. [CrossRef]
37. Mohammadi, M.J.; Takdastan, A.; Jorfi, S.; Neisi, A.; Farhadi, M.; Yari, A.R.; Dobaradaran, S.; Khaniabadi, Y.O. Electrocoagulation process to Chemical and Biological Oxygen Demand treatment from carwash grey water in Ahvaz megacity, Iran. *Data Brief* **2017**, *11*, 634–639. [CrossRef] [PubMed]
38. Mohammadi, M.J.; Salari, J.; Takdastan, A.; Farhadi, M.; Javanmardi, P.; Yari, A.R.; Dobaradaran, S.; Almasi, H.; Rahimi, S. Removal of turbidity and organic matter from car wash wastewater by electrocoagulation process. *Desalin. Water Treat.* **2017**, *68*, 122–128. [CrossRef]
39. Do, K.U.; Kim, J.H.; Chu, X.Q. Sludge characteristics and performance of a membrane bioreactor for treating oily wastewater from a car wash service station. *Desalin. Water Treat.* **2018**, *120*, 166–172. [CrossRef]
40. Lau, W.J.; Ismail, A.F.; Firdaus, S. Car wash industry in Malaysia: Treatment of car wash effluent using ultrafiltration and nanofiltration membranes. *Sep. Purif. Technol.* **2013**, *104*, 26–31. [CrossRef]
41. Al-Gheethi, A.A.; Mohamed, R.M.S.R.; Rahman, M.A.A.; Johari, M.R.; Kassim, A.H.M. Treatment of wastewater from car washes using natural coagulation and filtration system. *IOP Conf. Ser. Mater. Sci. Eng.* **2016**, *136*, 012046. [CrossRef]
42. Radin Mohamed, R.M.S.; Abdul Rahman, N.; Mohd Kassim, A.H. Moringa Oleifera and Strychnos Potatorum seeds as natural coagulant compared with synthetic common coagulants in treating car wash wastewater: Case study 1. *Asian J. Appl. Sci.* **2014**, *2*, 693–700.
43. Mohamed, R.M.S.R.; Saphira, R.M.; Kutty, A.I.; Mariam, N.; Kassim, M.; Hashim, A. Efficiency of using commercial and natural coagulants in treating car wash wastewater treatment. *Aust. J. Basic Appl. Sci.* **2014**, *8*, 227–234.
44. Zhang, J.K.; Yang, Y.B.; Wang, H.Y.; Dong, Z.B. CFU combined process for the treatment of oily car washing wastewater. *Appl. Mech. Mater.* **2013**, *253–255*, 999–1004. [CrossRef]
45. Tan, X.; Tang, L. Application of enhanced coagulation aided by UF membrane for car wash wastewater treatment. In Proceedings of the 2008 2nd International Conference on Bioinformatics and Biomedical Engineering, Shanghai, China, 16–18 May 2008; pp. 3653–3656. [CrossRef]
46. Chu, J.Y.; Li, Y.R.; Li, N.; Huang, W.H. Treatment of Car-washing Wastewater by Electrocoagulation-Ultrasound Technique for Reuse. *Adv. Mater. Res.* **2012**, *433–440*, 227–232. [CrossRef]
47. Moazzem, S.; Wills, J.; Fan, L.; Roddick, F.; Jegatheesan, V. Performance of ceramic ultrafiltration and reverse osmosis membranes in treating car wash wastewater for reuse. *Environ. Sci. Pollut. Res.* **2018**, *25*, 8654–8668. [CrossRef] [PubMed]
48. Boluarte, I.A.R.; Andersen, M.; Pramanik, B.K.; Chang, C.Y.; Bagshaw, S.; Farago, L.; Jegatheesan, V.; Shu, L. Reuse of car wash wastewater by chemical coagulation and membrane bioreactor treatment processes. *Int. Biodeterior. Biodegrad.* **2016**, *113*, 44–48. [CrossRef]
49. Moazzem, S.; Ravishankar, H.; Fan, L.; Roddick, F.; Jegatheesan, V. Application of enhanced membrane bioreactor (eMBR) for the reuse of carwash wastewater. *J. Environ. Manag.* **2020**, *254*, 109780. [CrossRef]
50. Bhatti, Z.A.; Mahmood, Q.; Raja, I.A.; Malik, A.H.; Khan, M.S.; Wu, D. Chemical oxidation of carwash industry wastewater as an effort to decrease water pollution. *Phys. Chem. Earth Parts A/B/C* **2011**, *36*, 465–469. [CrossRef]
51. Syed, N.H.; Ahmad, J.; Khan, N.A.; Khan, N.; Shafiq, M.A. A low-cost wastewater treatment unit for reducing the usage of fresh water at car wash stations in Pakistan. *Pak. J. Sci. Ind. Res. A Phys. Sci.* **2019**, *62A*, 57–66. [CrossRef]
52. Bhatti, S.; Siddiqui, Z.; Memon, S.; Kandhir, I.; Memon, M.A.; Mahesar, A.W. Analysis and treatment wash off water from vehicular service station in Hyderabad. *Sindh Univ. Res. J. SURJ (Sci. Ser.)* **2017**, *49*, 473–478. [CrossRef]
53. Hsu, S.K.; Chen, C.H.; Chang, W.K. Reclamation of car washing wastewater by a hybrid system combining bio-carriers and non-woven membranes filtration. *Desalin. Water Treat.* **2011**, *34*, 349–353. [CrossRef]
54. Tu, W.K.; Chang, C.C.; Chang, C.Y.; Ji, D.R.; Tseng, J.Y.; Chiu, C.Y.; Chen, Y.H.; Chang, C.F.; Yu, Y.H. Treatment of car wash wastewater via novel technologies for recycling and reutilization. *J. Environ. Eng. Manag.* **2009**, *19*, 49–57.
55. Istirokhatun, T.; Destianti, P.; Hargianintya, A.; Oktiawan, W.; Susanto, H. Treatment of car wash wastewater by UF membranes. In Proceedings of the International Conference of Chemical and Material Engineering, Kyoto, Japan, 29 December 2015; p. 060025.
56. Asha, M.N.; Chandan, K.S.; Harish, H.P.; NikhileswarReddy, S.; Sharath, K.S.; Liza, G.M. Recycling of waste water collected from automobile service station. *Procedia. Environ. Sci.* **2016**, *35*, 289–297. [CrossRef]
57. Alam, J.; Farooqi, I.H. Management of grey water of an automobile workshop—A case study. In Proceedings of the International Workshop on Civil Engineering and Architecture, Istanbul, Turkey, 8–9 August 2014; pp. 133–138.
58. Kiran, S.A.; Arthanareeswaran, G.; Thuyavan, Y.L.; Ismail, A.F. Influence of bentonite in polymer membranes for effective treatment of car wash effluent to protect the ecosystem. *Ecotoxicol. Environmen. Saf.* **2015**, *121*, 186–192. [CrossRef] [PubMed]
59. Al-Odwani, A.; Ahmed, M.; Bou-Hamad, S. Carwash water reclamation in Kuwait. *Desalination* **2007**, *206*, 17–28. [CrossRef]
60. Torkashvand, J.; Pasalari, H.; Gholami, M.; Younesi, S.; Oskoei, V.; Farzadkia, M. On-site carwash wastewater treatment and reuse: A systematic review. *Int. J. Environ. Anal. Chem.* **2020**, *100*, 1–15. [CrossRef]
61. Nadzirah, Z.; Nor Haslina, H.; Rafidah, H. Removal of important parameter from car wash wastewater—A review. *Appl. Mech. Mater.* **2015**, *773–774*, 1153–1157. [CrossRef]
62. Genuino, H.C.; Opembe, N.N.; Njagi, E.C.; McClain, S.; Suib, S.L. A review of hydrofluoric acid and its use in the car wash industry. *J. Ind. Eng. Chem.* **2012**, *18*, 1529–1539. [CrossRef]

63. Kumar, N.S.; Chauhan, M.S. *Water Quality Management*; Treatment of car washing unit wastewater—A review; Springer International Publishing: Singapore, 2018; pp. 247–255.
64. Sarmadi, M.; Foroughi, M.; Saleh, H.N.; Sanaei, D.; Zarei, A.A.; Ghahrchi, M.; Bazrafshan, E. Efficient technologies for carwash wastewater treatment: A systematic review. *Environ. Sci. Pollut. Res.* **2020**, *28*, 34823–34839. [CrossRef]
65. Hassani, A.; Malhotra, M.; Karim, A.V.; Krishnan, S.; Nidheesh, P.V. Recent progress on ultrasound-assisted electrochemical processes: A review on mechanism, reactor strategies, and applications for wastewater treatment. *Environ. Res.* **2022**, *205*, 112463. [CrossRef]
66. Boussu, K.; van Baelen, G.; Colen, W.; Eelen, D.; Vanassche, S.; Vandecasteele, C.; van der Bruggen, B. Technical and economical evaluation of water recycling in the carwash industry with membrane processes. *Water Sci. Technol.* **2008**, *57*, 1131–1135. [CrossRef]
67. Gonder, Z.B.; Balcioglu, G.; Vergili, I.; Kaya, Y. Electrochemical treatment of carwash wastewater using Fe and Al electrode: Techno-economic analysis and sludge characterization. *J. Environ. Manag.* **2017**, *200*, 380–390. [CrossRef]
68. Gonder, Z.B.; Balcıoğlu, G.; Kaya, Y.; Vergili, I. Treatment of carwash wastewater by electrocoagulation using Ti electrode: Optimization of the operating parameters. *Int. J. Environ. Sci. Technol.* **2019**, *16*, 8041–8052. [CrossRef]
69. Ghanbari, F.; Zirrahi, F.; Olfati, D.; Gohari, F.; Hassani, A. TiO_2 nanoparticles removal by electrocoagulation using iron electrodes: Catalytic activity of electrochemical sludge for the degradation of emerging pollutant. *J. Mol. Liq.* **2020**, *310*, 113217. [CrossRef]
70. Enoh, B.S.; Christopher, W. Adsorption of metal ions from carwash wastewater by phosphoric acid modified clay: Kinetics and thermodynamic studies. *Chem. Mater. Res.* **2015**, *7*, 278026770.
71. Ghanbari, F.; Wang, Q.; Hassani, A.; Wacławek, S.; Rodríguez-Chueca, J.; Lin, K.Y.A. Electrochemical activation of peroxides for treatment of contaminated water with landfill leachate: Efficacy, toxicity and biodegradability evaluation. *Chemosphere* **2021**, *279*, 130610. [CrossRef]
72. Ahmadt, A.; Zarei, M.; Hassani, A.; Ebratkhahan, M.; Olad, A. Facile synthesis of iron(II) doped carbonaceous aerogel as a three-dimensional cathode and its excellent performance in electro-Fenton degradation of ceftazidime from water solution. *Sep. Purif. Technol.* **2021**, *278*, 119559. [CrossRef]
73. Zapién Serrano, L.Z.; Ortiz Lara, N.O.; Ríos Vera, R.R.; Cholico-González, D. Removal of Fe(III), Cd(II), and Zn(II) as Hydroxides by Precipitation–Flotation System. *Sustainability* **2021**, *13*, 11913. [CrossRef]
74. Park, J.H.; Han, Y.S.; Ji, S.W. Investigation of Mineral-Processing Wastewater Recycling Processes: A Pilot Study. *Sustainability* **2018**, *10*, 3069. [CrossRef]
75. Siddig, O.; Al-Afnan, S.; Elkatatny, S.; Bahgat, M. Novel Cake Washer for Removing Oil-Based Calcium Carbonate Filter Cake in Horizontal Wells. *Sustainability* **2020**, *12*, 3427. [CrossRef]
76. Mohamed, A.; Basfar, S.; Elkatatny, S.; Al-Majed, A. Prevention of Barite Sag in Oil-Based Drilling Fluids Using a Mixture of Barite and Ilmenite as Weighting Material. *Sustainability* **2019**, *11*, 5617. [CrossRef]
77. Jönsson, C.; Jönsson, A.S. The influence of degreasing agents used at car washes on the performance of ultrafiltration membranes. *Desalination* **1995**, *100*, 115–123. [CrossRef]
78. Hamada, T.; Miyazaki, Y. Reuse of carwash water with a cellulose acetate ultrafiltration membrane aided by flocculation and activated carbon treatments. *Desalination* **2004**, *169*, 257–267. [CrossRef]
79. Tang, L.; Tan, X.J.; Cui, F.Y.; Zhou, Q.; Yin, J. Reuse of carwash wastewater with hollow fiber membrane aided by enhanced coagulation and activated carbon treatments. *Water Sci. Technol.* **2007**, *56*, 111–118.

International Journal of
Environmental Research and Public Health

MDPI

Article

A Bibliometric Analysis of Research on Selenium in Drinking Water during the 1990–2021 Period: Treatment Options for Selenium Removal

Ricardo Abejón

Departamento de Ingeniería Química, Universidad de Santiago de Chile (USACH), Av. Libertador Bernardo O'Higgins 3363, Estación Central, Santiago 9170019, Chile; ricardo.abejon@usach.cl

Abstract: A bibliometric analysis based on the Scopus database was carried out to summarize the global research related to selenium in drinking water from 1990 to 2021 and identify the quantitative characteristics of the research in this period. The results from the analysis revealed that the number of accumulated publications followed a quadratic growth, which confirmed the relevance this research topic is gaining during the last years. High research efforts have been invested to define safe selenium content in drinking water, since the insufficient or excessive intake of selenium and the corresponding effects on human health are only separated by a narrow margin. Some important research features of the four main technologies most frequently used to remove selenium from drinking water (coagulation, flocculation and precipitation followed by filtration; adsorption and ion exchange; membrane-based processes and biological treatments) were compiled in this work. Although the search of technological options to remove selenium from drinking water is less intensive than the search of solutions to reduce and eliminate the presence of other pollutants, adsorption was the alternative that has received the most attention according to the research trends during the studied period, followed by membrane technologies, while biological methods require further research efforts to promote their implementation.

Keywords: selenium; drinking water; treatments; bibliometric analysis; research trends

Citation: Abejón, R. A Bibliometric Analysis of Research on Selenium in Drinking Water during the 1990–2021 Period: Treatment Options for Selenium Removal. *Int. J. Environ. Res. Public Health* **2022**, *19*, 5834. https://doi.org/10.3390/ijerph19105834

Academic Editors: Alban Kuriqi and Luis Garrote

Received: 8 April 2022
Accepted: 4 May 2022
Published: 11 May 2022

1. Introduction

Selenium (Se), with atomic number 34, is a member of group 16 of the periodic table and thus belongs to the chalcogens. The position between the nonmetal sulfur and the metalloid tellurium determines the mainly nonmetallic properties it presents, characterized by high chemical similarity to sulfur. Because of its applications (electronic components, glass additives, metal alloys, etc.) and influence on human and animal health, research related to selenium has gained attention and issues about environmental pollution have become relevant [1].

The speciation of selenium in the natural environment is a key aspect to understanding its mobility, availability and toxicity. This nonmetal can be stable in several oxidation states but the most important ones from the environmental point of view are Se^{-2}, Se^{0}, Se^{+4} and Se^{+6}. Elemental selenium, Se^{0}, normally exists in the hexagonal semimetallic form (gray selenium) at ordinary temperatures, although other allotropic forms, mainly as red monoclinic selenium and different amorphous solids (black and red), can be found [2]. Nevertheless, it rarely occurs in its elemental native state or as pure ore compounds in the Earth's crust. The Se^{-2} valence (selenide) is not frequent in aquatic environments, since it is only present under extreme redox circumstances. The Se^{-2} system includes H_2Se and the corresponding deprotonated derivatives HSe^{-} and Se^{-2} with dissociation constant values of 3.8 and 14.0 for pK_{a1} and pK_{a2}, respectively [3]. Although reduction of other selenium compounds, including insoluble elemental selenium, to selenide may occur due to microbial action [4], reaction between the dissolved selenide and metallic cations

present in natural waters takes place, which results in the precipitation of insoluble metal selenides [5].

Therefore, the two most common oxidation states of selenium in water are Se^{+4} and Se^{+6} as part of the dissolved oxyanions selenite (SeO_3^{-2}) and selenate (SeO_4^{-2}), respectively [6]. Both species can be present in different protonated forms as function of the pH. On the one hand, the Se^{+4} system includes H_2SeO_3 and the corresponding deprotonated derivatives $HSeO_3^-$ and SeO_3^{-2} with dissociation constant values of 2.7 and 8.5 for pK_{a1} and pK_{a2}, respectively. On the other hand, the Se^{+6} system includes H_2SeO_4 and the corresponding deprotonated derivatives $HSeO_4^-$ and SeO_4^{-2}, with dissociation constant values of −2.0 and 1.8 for pK_{a1} and pK_{a2} [3]. According to these data, the prevalent species around neutral conditions (typical pH for natural surface waters and groundwaters ranges from 6.5 to 8.5) are $HSeO_3^-$ (maybe SeO_3^{-2} when the pH is in the upper range) for Se^{+4} and SeO_4^{-2} for Se^{+6}. This fact implies that both valences remain as anions in most water bodies, since the highest pH value compatible with a non-charged molecule is lower than 3 (possible presence of H_2SeO_3).

In addition to pH, the redox potential also plays a relevant role in the definition of the relative abundance of the selenium species. Complete speciation diagrams for selenium in aqueous systems as function of pH and redox potential can be found in bibliography [7,8]. On one hand, under oxidant conditions, the Se^{+6} state becomes clearly dominant over the Se^{+4} one, but, on the other hand, the Se^{+4} species are prevalent under reducing conditions. Nevertheless, in case of extreme reducing conditions, Se^{-2} valence will become dominant. To gain a clearer idea, the redox potentials of selenium in acid and alkaline solutions are included in Figure 1 [3].

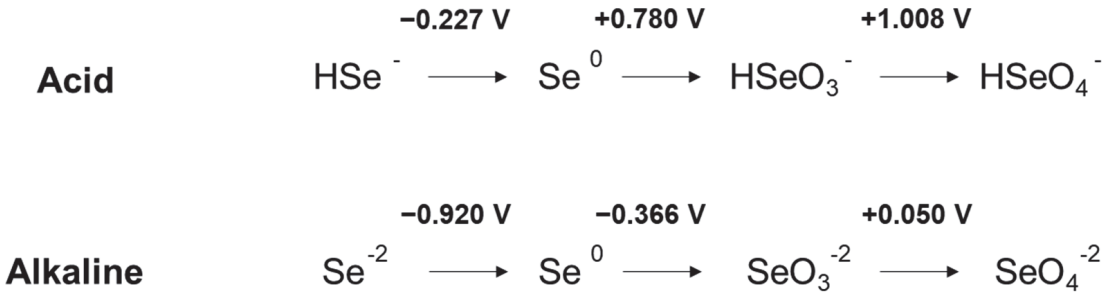

Figure 1. The redox potentials of selenium in acid and alkaline solutions.

Therefore, the selenate system is thermodynamically more stable for surface waters under alkaline conditions, while in acidic waters selenite is predominant. Although selenite in these acid solutions could be reduced at least partially to insoluble elemental selenium under suitable redox conditions, complete removal is often difficult, because the selenium sometimes precipitates as a colloid and further reduction to selenide is very slow [9]. The case of groundwaters is a bit more complex, since both selenite and selenate states can coexist (even selenide can appear under reducing conditions) and the incidence of each specie depends on the total selenium input to the system, the specific chemical conditions and the biological activity.

The effects of selenium on human health have been subject to extensive research. Selenium plays a vital role in different physiological processes and its altered levels have direct impact on human health, since they can be directly related to the development of diseases [10]. Selenium is an essential micronutrient for humans and other animals, since it is important for many cellular processes because it is a component of several selenoproteins and selenoenzymes, such as glutathione peroxidase, with essential biological functions [11]. The biological activity of these selenium biological compounds is mainly related to antioxidant actions, activation and degradation of thyroid hormones and immu-

nity enhancement [12]. Further detailed information about the role of selenium and its functions in the human body can be consulted [13].

Examples of health problems in farm animals caused by both excessive exposure (selenium toxicity) and suboptimal intake (selenium deficiency) have been well-known and the possible impact on human health of these situations has gained great concern [6]. On the one hand, excessive low intake of selenium in humans is directly related to the development of two endemic diseases that mainly occur in China and adjacent countries: a fatal dilated cardiomyopathy called Keshan disease [14–16] and a disabling degenerative disorder of peripheral joints and spine called Kashin–Beck disease [17–20]. On the other hand, a chronic high selenium intake by humans results in selenosis, characterized by symptoms such as hair and fingernails loss, diarrhea, effects on the central nervous system, loss of appetite and hepatic disfunction [21–23]. In addition, early symptoms of acute selenium poisoning include hypotension and tachycardia, vomiting, abdominal pain or diarrhea and neurological signs, such as tremor, muscle spasms, restlessness and confusion. Pulmonary edema develops as a severe complication and in severe cases, death can be reached due to peripheral vasodilatation or direct myocardial depression [24,25].

Consequently, controlled dietary intake of selenium is highly recommended. The World Health Organization (WHO) established the limits for recommended selenium intakes between 25 and 35 μg/d, depending on the genre, with even lower values for infants, children and adolescents [26]. This recommendation clearly reduced previously defined dietary limits, with typical values above 50 μg/d [27]. The uptake and accumulation of selenium by plants define the transference of this element from soils to animals, including humans. Different plant species have different abilities to take selenium from soil, and different plant tissues differ in their selenium contents [28,29]. The bioaccumulation of selenium in food chain components across trophic levels has been investigated for different ecosystems [30,31]. Therefore, the content of Se in different diets varies significantly as a function of both soil and plant and animal species. In addition to food sources, drinking water must be taken into account as a significant source of selenium intake, specifically in regions with selenium-rich soils or waters [32,33].

The simultaneous essentiality and toxicity of selenium for humans have created a great controversy about safe limit values for selenium in drinking water. This debate is not new, since it started in the 1970s and early 1980s, with the scientific discussion related to the justification of a new recommendation of 50 μg/L in the United States, versus the originally proposed 10 μg/L concentration for selenium in drinking water [34–36]. The WHO produces its international norms on water quality and human health in the form of guidelines that are used as the basis for regulation and standard setting. For the particular case of selenium, the standard limit was fixed at 10 μg/L until it was increased to 40 μg/L in 2011 when the fourth edition of the guideline was published [37]. Nevertheless, most jurisdictions nowadays continue applying a threshold value of 10 μg/L in their corresponding legislations [38], including Chile [39] and the European Union. In this last case, even the proposal approved in 2018 to review the European Directive justified the maintenance of the 10 μg/L limit against the new recommended value by the WHO [40]. However, the adopted final Directive defined a 20 μg/L limit, which can be increased until 30 μg/L for regions where geological conditions could lead to high levels of selenium in groundwater [41]. Nevertheless, scientific researchers continue the discussion and propose new limit values below and above the 10 μg/L concentration [42–44].

The presence of selenium in the environment has a highly irregular distribution among the atmospheric, aquatic and terrestrial compartments. The latter one is the most relevant compartment, but natural processes can transfer selenium to groundwaters and surface waterbodies, such as volcanic activity; rock and soil weathering; leaching of soils; transportation by groundwater; uptake and release by plants, animals and microorganisms; adsorption-desorption reactions; or chemically and biologically mediated oxidation-reduction reactions [45]. Although the selenium content of most natural waters does not threaten human health, the aquifers and the related surface water bodies in natural

selenium-rich geological areas can present selenium concentrations that require further treatment to obtain safe drinking water. Chinese, Indian, American and Canadian selenium-rich regions have been deeply investigated [46–48], but other countries with localized areas characterized by high selenium contents can be mentioned, such as Argentina, Brazil, France, Ireland, Israel, Italy or Venezuela [49–56]. Nevertheless, anthropogenic activities account for a widespread selenium contamination as the result of some industrial activities, such as coal mining and combustion; gold, silver and nickel mining; metal smelting (especially pyrometallurgical copper, nickel and zinc production); oil transport, refining and utilization; and agricultural irrigation with selenium-rich waters [57]. Examples of many locations where waterbodies have been polluted by these industrial activities have been deeply identified and investigated [58–70], including the case of Chile, where samples of drinking water with selenium concentration above 10 μg/L have been analyzed [71]. Since no natural geological area rich in selenium has been highlighted in Chile [72,73], the presence of selenium in drinking water can be directly related to the copper mining, smelting and refining activities in most cases [74–76].

Since the management of the high number of published papers about selenium and drinking water that can be found in bibliography is difficult, bibliometric tools are useful to handle all this information. Bibliometrics refers to the research methodology employed in library and information sciences, which applies quantitative analysis and statistics methods to describe the distribution patterns of publications according to some given categories. This methodological approach allows the exploration, organization and analysis of a high number of scientific documents and can be applied to the identification of important research trends, as demonstrated by several works in the environmental and chemical engineering fields [77–92], including water pollution aspects [93–103].

The main purpose of this work was to analyze, from a bibliometric perspective, the scientific literature related to the research on selenium in drinking water published from 1990 to 2021 in the sources compiled in Scopus. These documents were analyzed and evaluated according to several categories (annual outputs, leading countries and institutions, or main journals, subjects and languages) and were used to determine the quantitative characteristics of the research on selenium removal from drinking water worldwide. In addition, a bibliometric network analysis was carried out to contribute to the identification of the most relevant trends related to this topic and possible research gaps.

2. Data Sources and Methodology

The bibliographic search of published scientific literature related to selenium in drinking water was based on the employment of Scopus database. This abstract and indexing database with full-text links is managed by Elsevier and claims to index over 22,800 active titles from more than 5000 international publishers. These figures imply that it is the largest abstract and citation database of peer-reviewed literature and delivers the most comprehensive view of the world's research output in the fields of science and technology [104]. More than 69 million abstracts with references back to 1969 and more than 6 million records before that year are included. Titles from all regions around the world are covered, counting non-English titles when abstracts in English are provided with the documents. In fact, around 20% of titles on Scopus are not published in English, resulting in more than 40 languages. In addition, more than 50% of Scopus content comes from outside North America, with important contributions by European, Latin American and Asian countries. As a result, Scopus offers an extensive coverage of peer-reviewed literature across the sciences, technology, engineering and mathematics (STEM) fields.

The online search within Scopus was completed in April 2022 after the selection of "*selenium*" and "*drinking water*" as keywords in the Article Title, Abstract, Keywords field of the search-engine. The keywords *drinking* and *water* were introduced together with quotations to obtain only the papers that include these two words in the exact sequence. The search was limited from 1990 to 2021 in order to identify the scientific documents

related to the research on this topic published before 2022. The total number of documents recovered was 1117.

The analysis of the scientific literature obtained after a systematic bibliographic search provides a suitable scenario to have a better understanding of the global research situation in such a relevant subject as removal of selenium from drinking water, which can support the identification of present hot topics and the definition of future long-term research strategies. Consequently, the investigated aspects included in this work did not only cover the quantitative description of the publications (annual outputs, leading countries and institutions, or main journals, subject categories and languages), but also the review of the most relevant research topics identified after the study of the corresponding keywords.

3. Results and Discussion

3.1. Bibliometric Analysis of Research Trends on Selenium in Drinking Water (1990–2021)

3.1.1. Publication Year, Document Type and Language of Publications

The distribution of annual publication output identified by Scopus and the total number of accumulated documents are shown in Figure 2. It is obvious that there is a continuously increasing general trend in the number of publications that appears each year, although three different stages can be distinguished. The first one covers the 1990–2002 period and it is characterized by an irregular evolution of the number of publications, where the years 1997 and 2000 must be highlighted because of their prolific production. From 2002 to 2011 a much more regular linear increase can be identified but the year 2007 was especially productive and has the highest value in this period. After 2011, another irregular stage appeared, in this case with a great production rate maintained over time, since only 2018 did not attain 50 annual publications. As a consequence, the references published for the last ten years (from 2012 to 2021) account more than half of the total found publications during the 32-year period (51.3%). Nevertheless, when the accumulated number of publications was observed, the corresponding rise can be considered as a quadratic growth and it was decided to apply a quadratic regression to the data. The obtained equation was $y = 0.995 \cdot x^2 + 2.44 \cdot x + 17.4$, where y represents the number of accumulated documents and x the year (starting at 1 for the year 1990). The result of the regression was a very good fitting, with a R^2 value of 0.9991.

The distribution of document types was analyzed. Eleven different document types were found among the total 1117 publications. Nevertheless, article (967) was the most frequently used document type comprising 86.6% of total production, followed by review (65; 5.8% contribution) and proceedings paper (49; 4.4% contribution). These percentages, and specifically the clear supremacy of articles over other types of publication, are very concordant with the figures obtained by other authors when analyzing the trends on the research about other contaminants in water [93,100,105]. The other less significant categories include book chapter (16), note (7), editorial (5), short survey (3), letter (2), book (1), erratum (1) and retracted (1).

A clear majority (94.0%) of all the publications were published in English. Several other languages were identified, Chinese and Russian being the second and third languages, respectively. The rest of languages represented are compiled in Table 1. English has undoubtedly turned into the global lingua franca and there has never in the past been a language spoken more widely in the world than English is today [106]. Consequently, international communication has moved to a clear pre-eminence of English, especially in the field of scientific research, where more than 75% of the published documents in the social sciences and humanities and well over 90% in the natural sciences are written in English [107]. However, due to China's fast development in research production and its high percentage of national journals published in Chinese, the world is experiencing, for the first time in more than a century, a decrease in the worldwide percentage of active academic journals published in English and an increase in the percentage of documents written in Chinese [108].

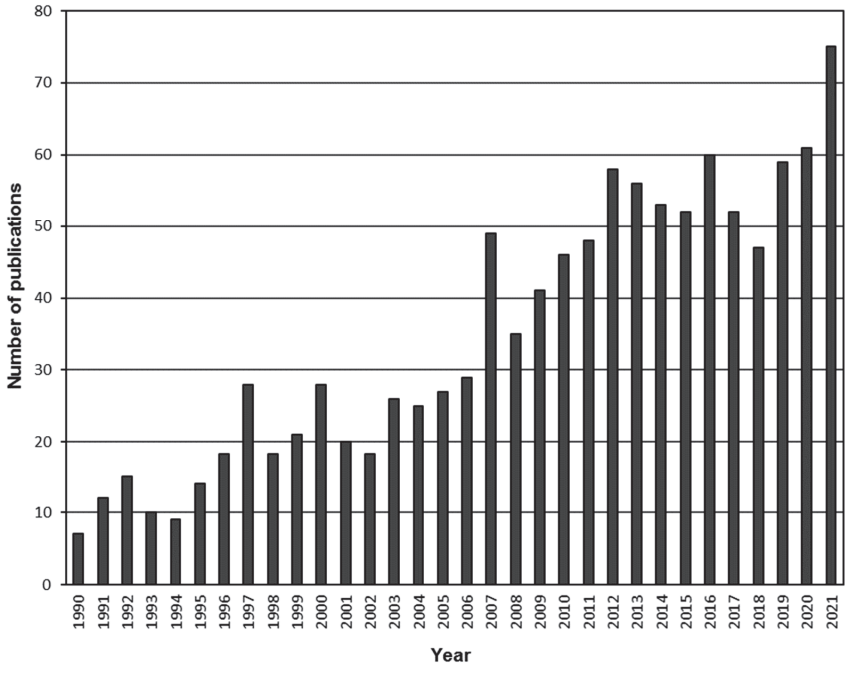

(**a**)

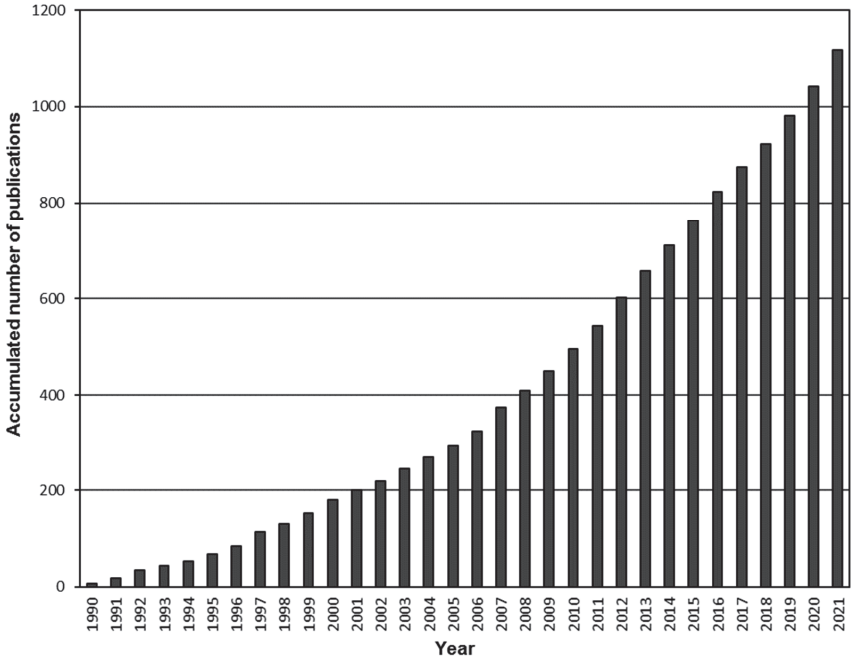

(**b**)

Figure 2. Annual (**a**) and accumulated (**b**) publication output.

Table 1. The languages employed by the publications.

Language	Publications	Contribution (%)
English	1050	94.0
Chinese	33	3.0
Russian	13	1.2
French	7	0.6
Czech	3	0.3
Japanese	3	0.3
Spanish	3	0.3
Bulgarian	2	0.2
German	2	0.2
Hungarian	2	0.2
Moldavian	2	0.2
Romanian	1	0.1
Ukrainian	1	0.1

3.1.2. Publication Distribution of Countries and Institutions

The top 31 countries (the only ones that produced at least 10 documents) ranked by number of total publications are shown in Table 2. Since the country affiliation is not an exclusive category (a document can be contributed by authors from more than one country), some papers may be indexed in more than one country simultaneously. Consequently, the sum of the number of documents in these categories is above the total number. A reduced group of countries usually dominate the global scientific production, as in this case, since the joint contribution of the three first countries in the ranking (USA, China and India) accounts for 47.3% of the total number of documents. USA is the most productive country, with 259 papers, which implies a percentage of 23.2%. This leader country was followed by two Asian countries (China and India) which jointly produce a percentage higher than the one corresponding to USA (24.7%). After Canada and Japan, the top ten positions are completed with European countries: among them Turkey is surprisingly the most prolific country with 44 documents, followed by Italy, Germany, the United Kingdom and France, which are countries with relevant contributions in most research fields. However, the presence of countries with limited scientific production in other topics has been previously identified by other bibliometric studies regarding pollution of drinking water [93]. This fact was explained by the relative importance of the presence of polluted drinking water in these parts of the world and some countries, such as Tunisia, Bangladesh, Egypt or Nigeria, which are included in Table 2, could be mentioned as examples of countries worried by the presence of selenium in drinking water [109–112].

In fact, these countries worried by the presence of polluted waters have deserving contributions when additional indicators that give the possibility of having some benchmarking are analyzed. Besides the total number of publications, two other indicators that take into account the total population and income (GPD) of the countries have been considered in Table 2: the number of publications per million inhabitants and the number of publications per trillion US Dollars (population and income data taken from World Bank database). On the one hand, when the income indicator is observed in detail, Tunisia appeared as the leader with a great difference, since it obtained a value above 600 document/trillion $, which is an order of magnitude higher than the following countries. In this ranking, the second, third and fourth positions corresponded to Bangladesh, Egypt and Pakistan, which are not high-income countries. A group of three European high-income countries occupied the next three positions: Greece, Sweden and Czech Republic in the fifth, sixth and seventh places, respectively. On the other hand, the analysis of the population indicator demonstrated the important research efforts promoted by Scandinavian countries, such as Sweden, Norway and Denmark, are situated in the first, second and fourth positions, respectively. Once again, Tunisia must be highlighted, since it occupied the third position in this ranking, with a contribution above two documents/million inhabitants, a limit only surpassed by four countries.

Table 2. The top 31 most productive countries (at least 10 documents).

Country	Publications	Contribution (%)	Publications/ Million Habitants	Publications/ Trillion US Dollars GPD
United States	259	23.2	0.786	12.4
China	172	15.4	0.122	11.8
India	104	9.3	0.075	41.6
Canada	61	5.5	1.605	37.9
Japan	46	4.1	0.366	10.5
Turkey	44	3.9	0.522	43.1
Italy	37	3.3	0.621	21.3
Germany	36	3.2	0.432	10.5
United Kingdom	36	3.2	0.536	12.5
France	34	3.0	0.505	14.1
Russian Federation	33	3.0	0.229	23.2
Brazil	32	2.9	0.151	18.3
Sweden	31	2.8	2.995	58.2
Spain	30	2.7	0.634	25.4
Egypt	29	2.6	0.283	70.4
Tunisia	27	2.4	2.285	613.6
Saudi Arabia	25	2.2	0.718	38.4
Bangladesh	24	2.1	0.146	88.6
Pakistan	21	1.9	0.095	65.7
Iran	20	1.8	0.238	48.8
Poland	20	1.8	0.527	36.0
Nigeria	18	1.6	0.087	36.4
Australia	17	1.5	0.662	11.4
Norway	14	1.3	2.602	34.7
Austria	12	1.1	1.348	31.1
Belgium	12	1.1	1.038	25.7
Denmark	12	1.1	2.058	36.6
South Africa	12	1.1	0.202	35.7
Switzerland	12	1.1	1.390	16.2
Greece	11	1.0	1.027	59.5
Czech Republic	10	0.9	0.935	49.3

The top 18 institutions (the only ones with at least 10 documents) are compiled in Table 3. Among these top 18 institutions, 5 were in China and 4 in the USA, thus although USA was the most productive country, this production was shared more among different institutions. In the case of China, its production is more concentrated and the leader (Chinese Academy of Sciences with 40 documents) and the second (Institute of Geographical Sciences and Natural Resources Research with 19 documents) institutions were Chinese. Surprisingly, the third position was occupied by a Tunisian university (University of Sfax), which contributed with 16 documents, just two more than the production of the US EPA, a very relevant institution in all the topics related to water pollution. The role of the Panjab University in India, with 14 documents published, the same amount that US EPA, must be highlighted. Moreover, the great concern about the effects of selenium on human health justified the presence of prestigious medical institutions in the ranking, such as the Swedish Karolinska Institute, which is one of Europe's largest and most prestigious medical institutions, or the Columbia Mailman School of Public Health in the USA.

Table 3. The top 18 most productive institutions (at least 10 documents).

Institution	Publications	Contribution (%)
Chinese Academy of Sciences (CHINA)	40	3.6
Institute of Geographical Sciences and Natural Resources Research (CHINA)	19	1.7
University of Sfax (TUNISIA)	16	1.4
Università degli Studi di Modena e Reggio Emilia (ITALY)	15	1.3
University of Chinese Academy of Sciences (CHINA)	15	1.3
Panjab University (INDIA)	14	1.3
Environmental Protection Agency (USA)	14	1.3
Ministry of Education (CHINA)	13	1.2
Northeast Agricultural University (CHINA)	13	1.2
The University of Chicago (USA)	13	1.2
CHU Habib Bourguiba (TUNISIA)	13	1.2
University of Calgary (CANADA)	12	1.1
Karolinska Institutet (SWEDEN)	12	1.1
University of Saskatchewan (CANADA)	12	1.1
Columbia University (USA)	12	1.1
Universidade de São Paulo (BRAZIL)	10	0.9
Columbia Mailman School of Public Health (USA)	10	0.9
Universidade Federal de Santa Maria (BRAZIL)	10	0.9

3.1.3. Distribution of Output in Subject Categories and Journals

The distribution of subject categories defined by Scopus is shown in Table 4, where the 9 most popular categories are compiled (the only ones with at least 40 articles), taking into consideration once again that some documents can be included in more than one subject, since it is not an exclusive category. The ranking indicates that *Environmental Science* was the most common subject, but the role of the biomedical sciences must be highlighted, since *Medicine* occupied the second position and the third position corresponded to *Biochemistry, Genetics* and *Molecular Biology*. Moreover, *Pharmacology, Toxicology and Pharmaceutics* occupied the fifth position of the ranking, just after *Chemistry* in the fourth position. These results are in agreement with those ones obtained by a bibliometric analysis applied to the research trends on lead in drinking water [100], but they do not fit as well with the trends identified in the case of a bibliometric analysis about arsenic in drinking water [93]. The *Engineering* category was very relevant and it occupied the second position in the ranking, while in this case, it occupied the eighth position (49 documents), just two publications more than chemical engineering, which ranked ninth with 47 documents. This fact gives a clear idea about the significant efforts applied to the search of effective technical solutions to the problems caused by the presence of arsenic in drinking water, but in the case of selenium, the efforts are more focused on the identification of the health effects of the intake of selenium.

The distribution of outputs in journals is shown in Table 5. The Scimago Journal Ranking indicator (SJR) of the top 9 journals, which are the only ones that published at least 15 articles, was also included. The two leading journals must be highlighted since their productions more than double the production of the journal in the third position. On the one hand, *Biological Trace Element Research* was the most prolific journal (54 documents) in articles related to selenium and drinking water. This journal is focused on the interdisciplinary field of research on the biological, environmental, and biomedical roles of trace elements. On the other hand, *Science of the Total Environment* occupied the second position in the ranking with 44 documents. It is a multi-disciplinary journal for publication of original research on the whole environment, which includes the atmosphere, hydrosphere, biosphere, lithosphere and anthroposphere. Therefore, these journals confirmed the relevance of the health and environmental aspects of the presence of selenium in the water bodies. A glance at the rest of the journals in the table is enough to discover the importance of the environmental studies regarding selenium, since all these journals con-

tain the word environmental in their title, except the *Journal of Trace Elements in Medicine and Biology*, which covers biomedical issues related to trace elements. The most relevant journals according to the JCR indicators among the top journals are *Environmental Science and Technology* and *Environmental Health Perspectives*, both with JCR values above 2 (2.851 and 2.257, respectively). On the contrary, *Environmental Monitoring and Assessment* was the journal with the lowest JCR value, with a value below 0.6 (0.590).

Table 4. The top 9 most popular subject categories (at least 30 documents).

Ranking	Subject	Publications	Contribution (%)
1	Environmental Science	471	42.2
2	Medicine	359	32.1
3	Biochemistry, Genetics and Molecular Biology	281	25.2
4	Chemistry	226	20.2
5	Pharmacology, Toxicology and Pharmaceutics	164	14.7
6	Agricultural and Biological Sciences	105	9.4
7	Earth and Planetary Sciences	59	5.3
8	Engineering	49	4.4
9	Chemical Engineering	47	4.2

Table 5. The top 8 most popular journals (at least 15 documents).

Source	SJR 2020 (Scopus)	Publications	Contribution (%)
Biological Trace Element Research	0.649	54	4.8
Science of the Total Environment	1.795	44	3.9
Environmental Science and Pollution Research	0.845	19	1.7
Environmental Research	1.460	18	1.6
Environmental Science and Technology	2.851	18	1.6
Environmental Health Perspectives	2.257	16	1.4
Environmental Monitoring and Assessment	0.590	15	1.3
International Journal of Environmental Research and Public Health	0.747	15	1.3
Journal of Trace Elements in Medicine and Biology	0.739	15	1.3

3.1.4. Most Frequently Cited Papers

The top 10 articles according to the number of citations they have received are presented in Table 6. The numbers of citations increased from 226 for the last article to 1278 for the leading article that occupied the first position of the ranking. In addition to the total number of citations, the Field-Weighted Citation Impact (FWCI) was also included. FWCI is the ratio of the total citations actually received by the denominator's output, and the total citations that would be expected based on the average of the subject field. This way, an FWCI value equal to 1 means that the output performs just as expected for the global average. Values above 1 indicate that the output is cited more than expected according to the global average, while values below 1 indicate that the output is cited less than expected according to the global average. Taking into account the FWCI values, the documents in Table 2 present remarkable performance, with values above 3 in most cases; however, the document in the 5th position must be highlighted, since it attains a value above 11, which clearly indicates that this work has achieved a great impact.

Table 6. The top 10 most cited papers.

Ranking	Articles	Times Cited	FWCI
1	Title: **Hepatotoxicity and mechanism of action of haloalkanes: Carbon tetrachloride as a toxicological model** Authors: Weber, L.W.D., Boll, M., Stampfl, A. Source: *Critical Reviews in Toxicology* Published: 2003	1278	3.37
2	Title: **Metals and micronutrients—Food safety issues** Authors: McLaughlin, M.J., Parker, D.R., Clarke, J.M. Source: *Field Crops Research* Published: 1999	729	4.97
3	Title: **Lung cancer in never smokers: Clinical epidemiology and environmental risk factors** Authors: Samet, J.M., Avila-Tang, E., Boffetta, P., (...), Thun, M.J., Rudin, C.M. Source: *Clinical Cancer Research* Published: 2009	348	3.73
4	Title: **Arsenic exposure and cardiovascular disease: A systematic review of the epidemiologic evidence** Authors: Navas-Acien, A., Sharrett, A.R., Silbergeld, E.K., (...), Burke, T.A., Guallar, E. Source: *American Journal of Epidemiology* Published: 2005	300	3.18
5	Title: **The effects of arsenic exposure on neurological and cognitive dysfunction in human and rodent studies: A review** Authors: Tyler, C.R., Allan, A.M. Source: *Current Environmental Health Reports* Published: 2014	274	11.79
6	Title: **Survey of arsenic and other heavy metals in food composites and drinking water and estimation of dietary intake by the villagers from an arsenic-affected area of West Bengal, India** Authors: Roychowdhury, T., Tokunaga, H., Ando, M. Source: *Science of the Total Environment* Published: 2003	251	6.13
7	Title: **Trace elements and cancer risk: A review of the epidemiologic evidence** Authors: Silvera, S.A.N., Rohan, T.E. Source: *Cancer Causes and Control* Published: 2007	248	3.10
8	Title: **Health risks from the exposure of children to As, Se, Pb and other heavy metals near the largest coking plant in China** Authors: Cao, S., Duan, X., Zhao, X., (...), He, B., Wei, F. Source: *Science of the Total Environment* Published: 2014	242	7.48
9	Title: **Antioxidant effect of vitamin E and selenium on lipid peroxidation, enzyme activities and biochemical parameters in rats exposed to aluminium** Authors: El-Demerdash, F.M. Source: *Journal of Trace Elements in Medicine and Biology* Published: 2004	237	2.08
10	Title: **Strategies for safe and effective therapeutic measures for chronic arsenic and lead poisoning** Authors: Kalia, K., Flora, S.J.S. Source: *Journal of Occupational Health* Published: 2005	226	3.72

Although further comments about the most important research trends will be introduced in the next sections after the analysis of the most employed author keywords and the bibliometric network analysis, the reading of the most cited publications gave an initial idea about some relevant issues that have attracted attention from researchers investigating selenium in water. According to this list of top cited papers, health and toxicological as-

pects of selenium have mainly captured the attention of the researchers along the analyzed period. The most cited article was a review that covered the hepatotoxicity and mechanism of action of haloalkanes [113]. It mentioned the antioxidant effects of selenium to mitigate the damage induced by these toxic compounds. Another article in the list (in the ninth position with 237 citations) investigated the role of selenium in alleviating the negative effects of aluminum [114], while other three articles were focused on the interactions between selenium and arsenic in the human body [115–117]. Moreover, the decreased risk of cancer and the preventive effects derived from diets containing adequate levels of selenium have been analyzed by two articles among the most cited [118,119]. Another relevant issue investigated by the other three papers in Table 6 is the identification of the presence of selenium and the quantification of the corresponding concentrations in different water, soil, dust, air and locally produced food samples, including the most important health risks and exposure levels [120–122]. Therefore, none of the 10 most cited documents cover aspects related to treatment alternatives to remove selenium and other metals from water, and, in fact, to find a document regarding this issue, the document in the 12th position in the ranking (216 citations) must be consulted, which explains the removal of some elements, including selenium, just by incorporation into hydrocalumite and ettringite [123]. This fact confirms again that the search of effective technical solutions to the problems caused by the presence of selenium in drinking water has not been a relevant research topic.

3.1.5. Distribution Analysis of Author Keywords and Trending Topics of the Research

The list of the 46 most often used keywords (the only ones that were mentioned at least 100 times) is shown in Figure 3. Obviously, it was clear that "*Selenium*" was the most frequent keyword as it was selected in 879 articles. The second positions of the ranking corresponded to the other expression selected to be introduced in the article title, abstract, keywords field of the search-engine database: "*Drinking water*" appeared 598 times. However, these figures indicated that only 69.6% of all the identified documents used "*Selenium*" as keyword, while the value for "*Drinking water*" decreased to 45.9%. Therefore, the selection of both expressions as keywords did not occur for more than half of the documents analyzed in this study. This fact pointed to the consideration of lower global concern and consequent scarcer research efforts about the presence of selenium in drinking water and the needs of treatment for its removal when compared to other metals or metalloids [124,125]. A further analysis of the keywords revealed a more important interest focused on the health and toxicological effects of selenium. The third position of "*Controlled study*" (444 times) in the keyword ranking underpinned this idea, confirmed also by the presence of other terms directly related to health studies, such as "*Nonhuman*", "*Male*", "*Human*", "*Animal experiment*", "*Female*" or "*Rats*" (all of them selected as keywords more than 220 times).

A further look at the results was enough to find other ten metallic and non-metallic elements in the ranking: "*arsenic*" (340 times), "*zinc*" (233 times), "*cadmium*" (209 times), "*lead*" (197 times), "*manganese*" (184 times), "*copper*" (184 times), "*chromium*" (184 times), "*iron*" (166 times), "*nickel*" (157 times) and "*mercury*" (105 times). On the one hand, the study of the synergistic and antagonistic effects selenium may cause on the toxicity of these other elements is a hot topic under investigation [12,126,127]. On the other hand, the evaluation of the presence and the distribution of these water pollutants implied general water sampling and characterization of the concentrations of all these elements in drinking water, water bodies or in different samples of environmental interest [61,128,129]. Lastly, among the top most frequent keywords, terms directly related to possible technologies for selenium removal in drinking water or wastewater treatments cannot be found.

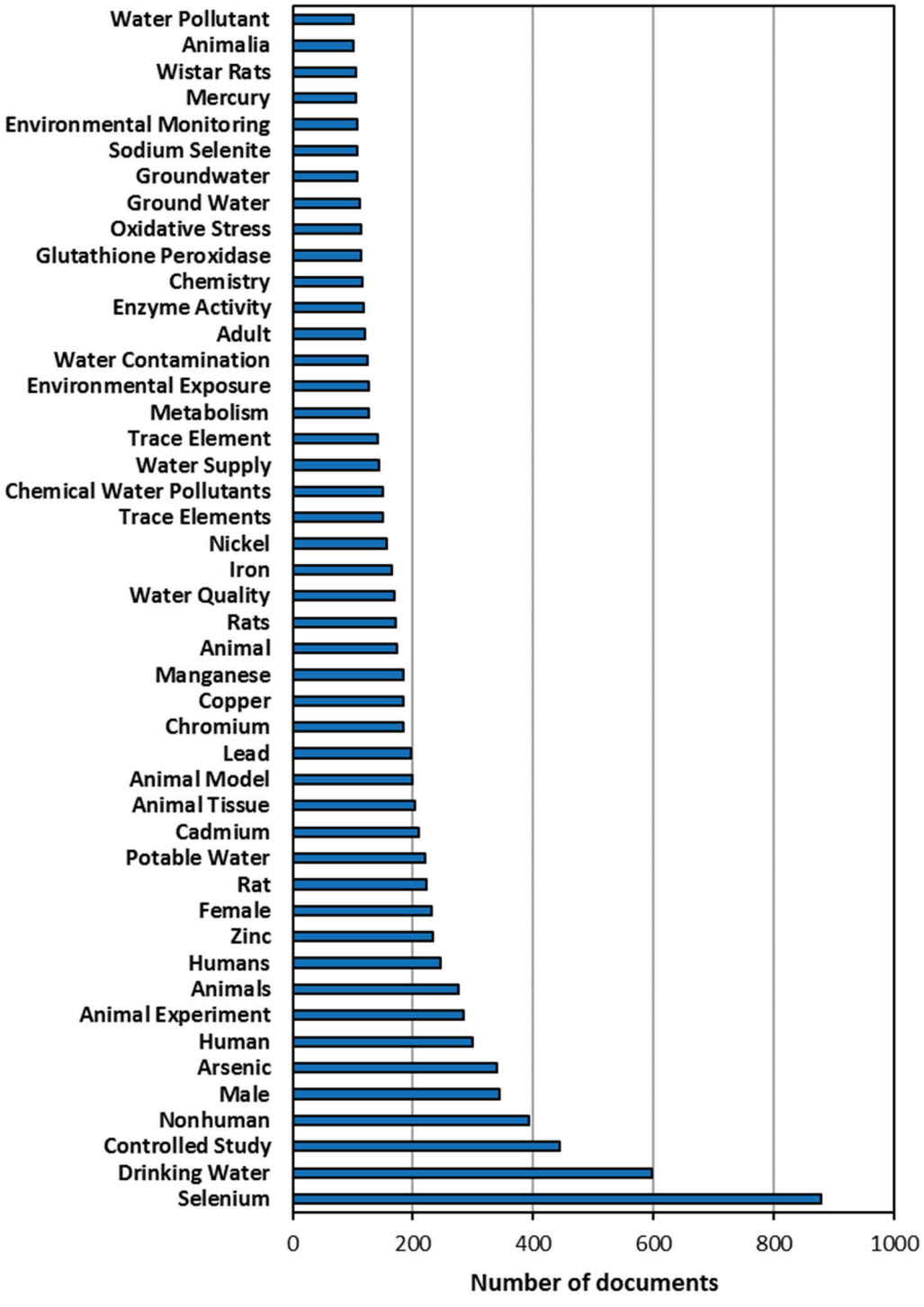

Figure 3. The top 46 most frequently used keywords.

3.1.6. Bibliometric Network Analysis

In order to provide more information about of the most important research topics and their evolution through the studied period, a bibliometric network analysis based on science mapping was applied. This methodology is useful to analyze a field of research, since it allows the identification and visualization of the conceptual subdomains (particular themes or general thematic areas) and provides its thematic evolution throughout time [130]. Although various software tools are available for science mapping analysis, SciMAT software (Universidad de Granada, Granada, Spain) was selected due to its visual and easily understandable strategic diagrams and thematic evolution structure. SciMAT is an open-source science mapping software tool that can be freely downloaded, modified and redistributed according to the terms of the GPLv3 license [131].

The bibliometric network analysis conducted in this paper was based on four phases of analysis within a specified set of 4 periods (1990–2001, 2002–2011, 2012–2019 and 2020–2021). These periods were defined according to the different trends previously identified when the annual production was analyzed. The last period covers the years 2020 and 2021, which have suffered the pandemic lock-down. First, the research themes were identified using a frequency and network reduction of words (the value of the minimal frequency of a word to be considered was 3). The clustering algorithm used was the simple centers algorithm. To normalize data, Salton's cosine was used to create the strategic diagram and the equivalence index was applied to normalize the co-word network of the thematic evolution structure. Secondly, the previously identified themes were then plotted on a bi-dimensional diagram composed of four quadrants, in which the vertical axis characterizes the density and the horizontal axis characterizes the centrality of a theme [132]. Thirdly, the results were organized in thematic network structures of themes as clusters, and the corresponding thematic evolution structure was obtained. These thematic network structures characterize the co-occurrence between the research themes and highlights the number of relationships and internal strength among them, while the thematic evolution structure provides an appropriate image of how the themes preserve a conceptual nexus throughout the defined subperiods. In both cases, the size of the clusters is proportional to the number of core documents and the links indicate cooccurrence among the clusters. Solid lines indicate that clusters share the main theme, and dashed lines represent the shared cluster elements that are not the name of the themes. The thickness of the lines is proportional to the inclusion index, which indicates that the themes have elements in common. Finally, the scientific contribution was measured by analyzing the most important research themes and thematic areas using the h-index, sum of citations, core documents centrality, density and nexus among themes [133].

The strategic diagram of each subperiod is depicted in Figure 4. According to their situation in these strategic diagrams, the themes can be classified into four different categories [134]:

- First quadrant (high centrality and high density): Motor themes. Trending themes for the field of research with high development.
- Second quadrant (high centrality and low density): Basic and transversal themes. Themes that are inclined to become motor themes in the future due to their high centrality.
- Third quadrant (low centrality and low density): Emerging or declining themes. Themes that require a more detailed analysis to define whether they are emerging or declining.
- Fourth quadrant (low centrality and high density): Highly developed and isolated themes. Themes that are no longer trending due to a new concept or technology.

The strategic diagrams present 17 clusters in total, 7 of them are motor themes, 4 are basic and transversal, 2 are emerging or declining themes and 4 are highly developed and isolated themes. The size of the clusters represents the number of total citations (the exact values appear in each cluster). In addition, h-index and absolute centrality and density values are presented for each cluster in Table 7.

The thematic evolution structure is shown in Figure 5, which explains the evolution of the research field over the different subperiods considered in this study. In this way, each individual theme relevance is illustrated through its cluster size as well as with its relationships throughout the different subperiods. Two different continuity lines among clusters that cover all the time periods can be clearly identified. The first one includes the clusters *Rat*, *Selenium* and *Oxidative-stress*, while the second one is formed by the cluster *Drinking-water* and *Trace-element*. The thematic network structures of these two groups can be visualized in Figures 6 and 7, respectively (while the network structures of the rest of clusters are compiled as Supplementary Material), which provide a good representation of the co-occurrence among keywords and allow the depiction of complex patterns.

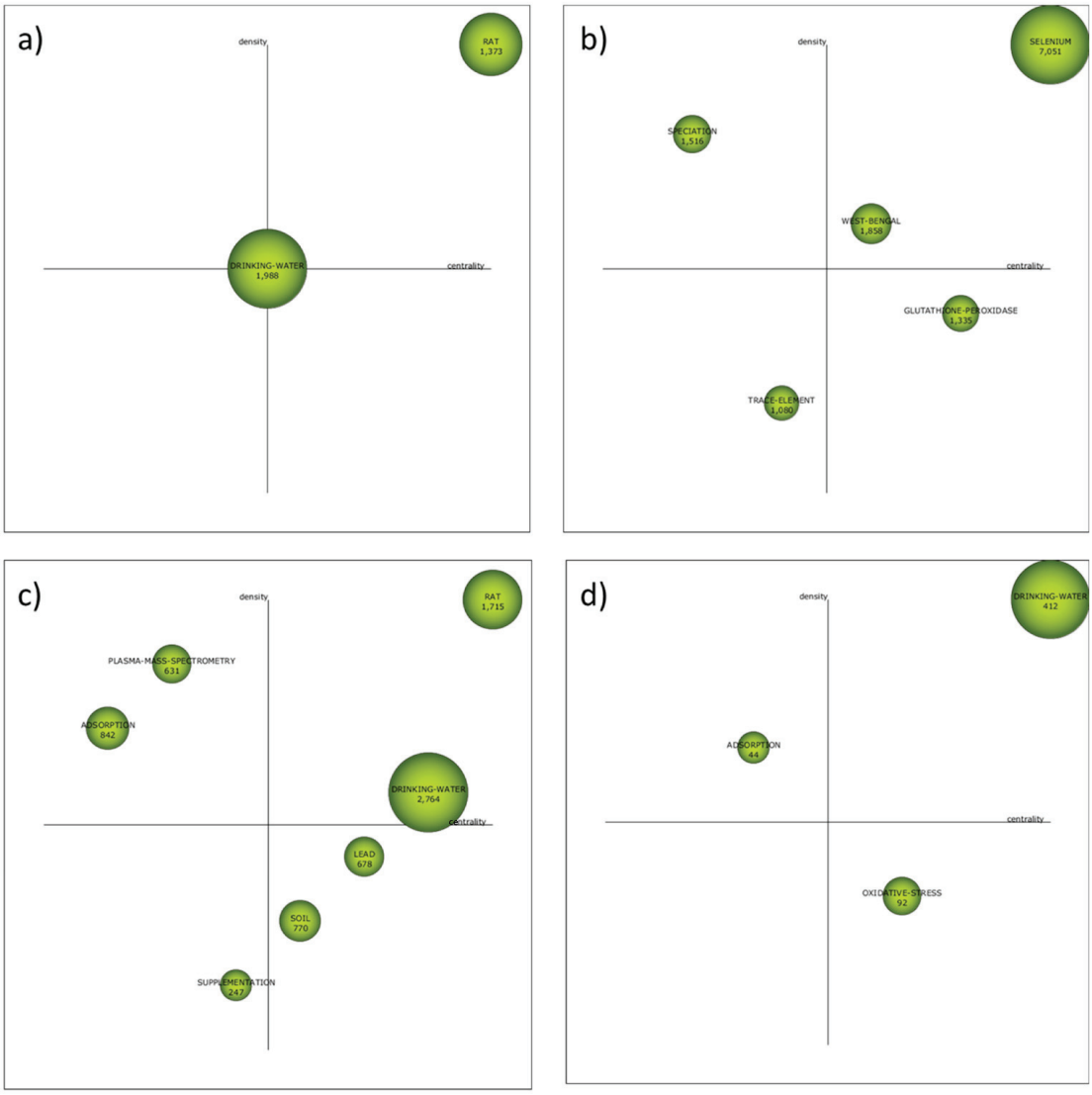

Figure 4. Strategic diagrams of the subperiods: 1990–2001 (**a**), 2002–2011 (**b**), 2012–2019 (**c**) and 2020–2021 (**d**).

Table 7. Citations, h-indexes and centrality and density values of the different clusters identified in the bibliometric network analysis.

Cluster	Citations	h-Index	Centrality	Density
Subperiod 1 (1990–2001)				
Rat	1373	27	49.60	19.06
Drinking-water	1988	16	19.10	13.82
Subperiod 2 (2002–2011)				
Selenium	7051	49	125.8	33.01
West Bengal	1858	35	28.34	17.44
Glutathione-peroxidase	1335	31	54.04	11.51
Speciation	1516	30	16.69	17.80
Trace-element	1080	29	26.05	4.03
Subperiod 3 (2012–2019)				
Rat	1715	30	66.49	34.81
Drinking-water	2764	30	59.20	15.56
Soil	770	26	26.81	10.33
Lead	678	23	30.13	11.80
Supplementation	247	23	17.17	3.23
Plasma-Mass-Spectrometry	631	19	16.83	18.18
Adsorption	842	17	5.14	17.56
Subperiod 4 (2020–2021)				
Drinking-water	412	8	63.42	25.93
Oxidative-stress	92	7	20.11	8.97
Adsorption	44	4	18.96	19.33

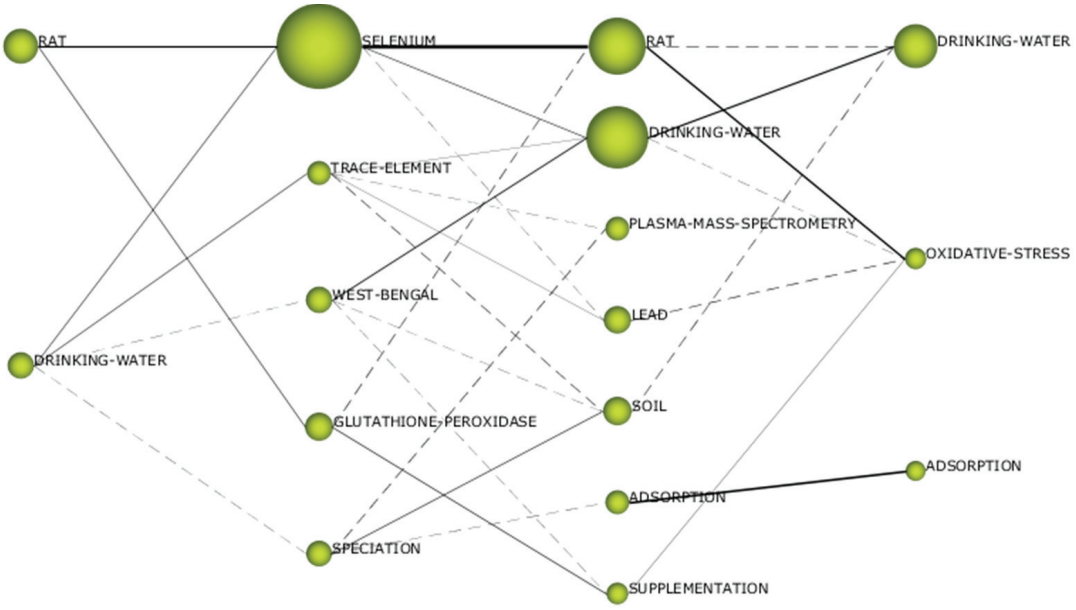

Figure 5. Thematic evolution structure of selenium and drinking water research (1990–2021).

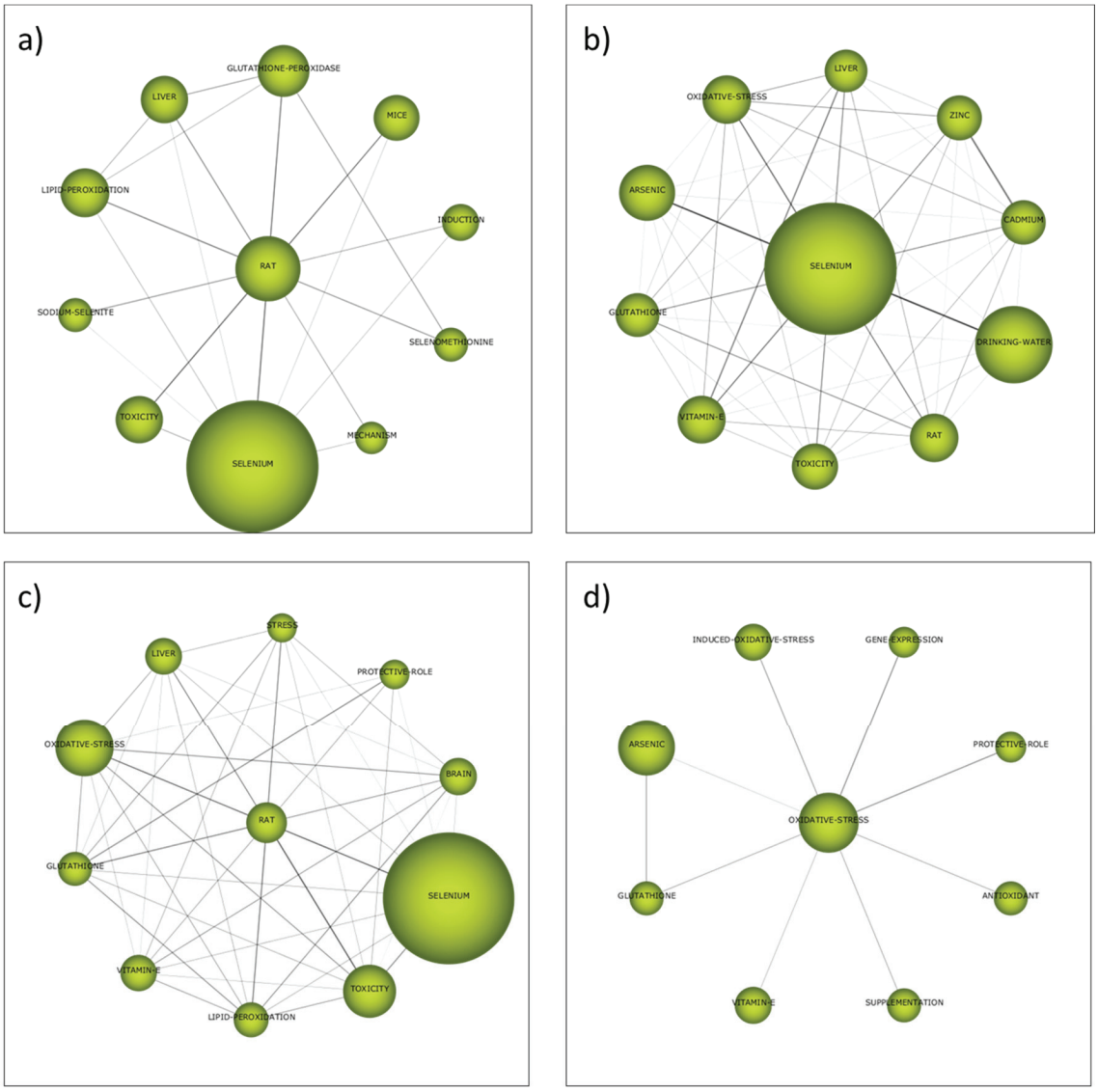

Figure 6. Evolution of the thematic network structure of the clusters *Rat/Selenium/Oxidative-stress*: 1990–2001 (**a**), 2002–2011 (**b**), 2012–2019 (**c**) and 2020–2021 (**d**).

The clusters *Rat* and *Selenium* were motor themes in the three first subperiods, but oxidative-stress was a basic and transversal theme in the last subperiod. The cluster selenium was the most cited one during the second subperiod (2002–2011), but the other clusters were less cited than the cluster *Drinking-water* in the corresponding subperiods. These clusters include the keyword "*Selenium*", but in the case of the last subperiod, complemented with other keywords that give a direct link to health and toxicological aspects and animal testing, such as "*Toxicity*", "*Liver*", "*Rat*" or "*Mice*". Among these topics, the role of selenium and the glutathione system in the context of defense against oxidative agents must be highlighted, since the keywords "*Oxidative-stress*", "*Glutathione*", "*Glutathione-Peroxidase*" and "*Antioxidant*" are included in these clusters. Therefore, the

importance of the health and toxicological effects of selenium that was proposed from the analysis of the most frequent keywords is confirmed by the bibliometric network analysis.

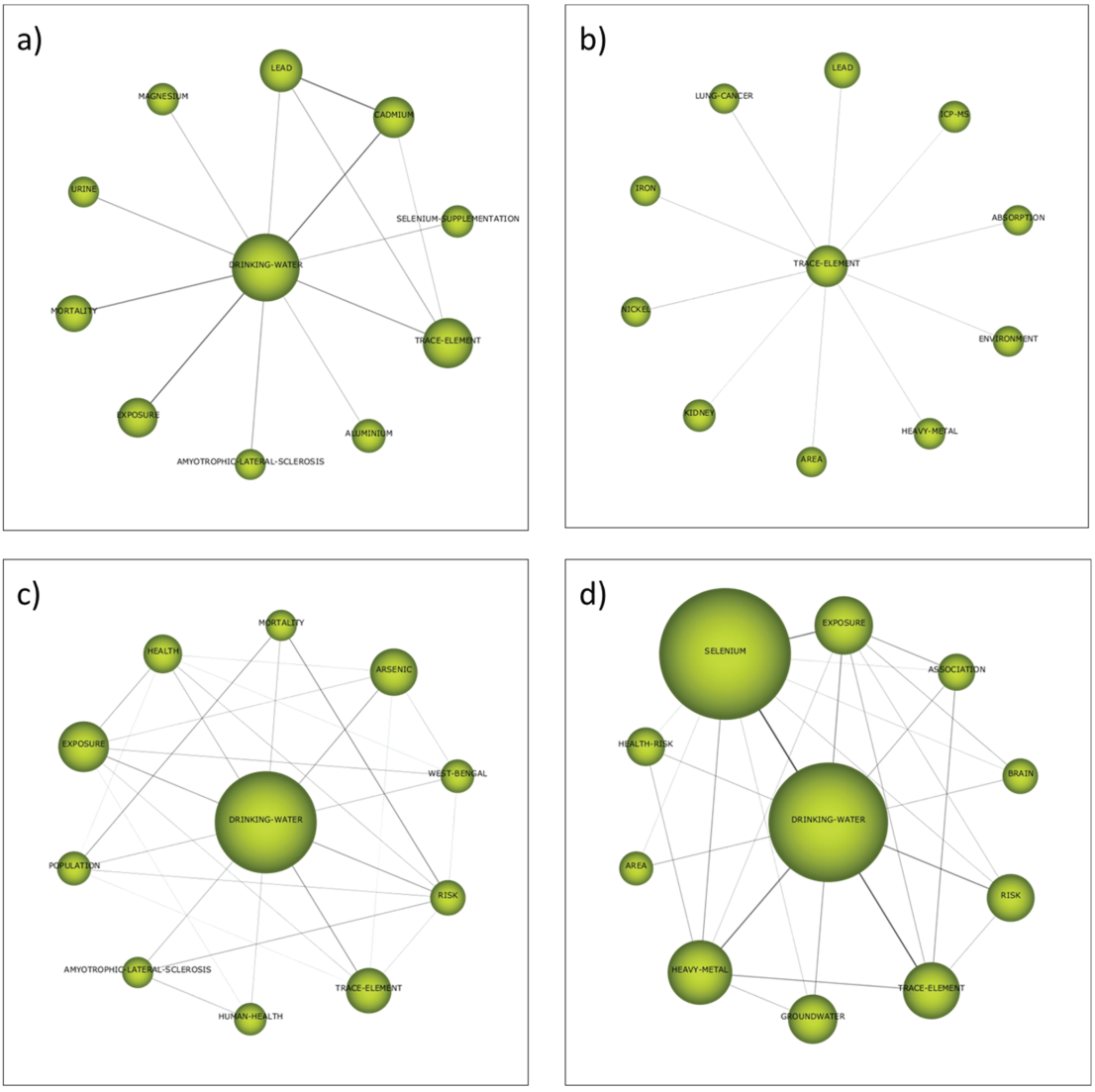

Figure 7. Evolution of the thematic network structure of the clusters *Drinking-water/Trace-element*: 1990–2001 (**a**), 2002–2011 (**b**), 2012–2019 (**c**) and 2020–2021 (**d**).

The cluster *Drinking-water* (renamed *Trace-element* in the second subperiod) started as motor theme in the first subperiod, was an emerging theme in the second subperiod (2002–2011) and it returned to the first quadrant as motor theme in the last two subperiods. The list of keywords that belong to this cluster includes keywords such as "*Heavy-Metal*", "*Lead*", "*Cadmium*", "*Arsenic*", "*Iron*", "*Nickel*" or "*Aluminium*", which were more relevant in the first two subperiods. After the analysis of the most frequent keywords, two different reasons were presented to justify the presence of all these elements as keywords: the study of the synergistic and antagonistic effects selenium may cause on the toxicity of other

elements and the evaluation of the presence and the distribution of these water pollutants in water sampling. The detailed study of the keywords included in the clusters identified in the bibliometric network analysis gave more relative importance to the first reason, the one related to synergistic and antagonistic toxicological effects, due to the presence of keywords such as "*Exposure*", "*Health*", "*Risk*", "*Mortality*", "*Lung*" or "*Kidney*". In fact, keywords more directly related to the second reason, the one related to environmental sampling and measuring of these elements that are pollutants, can be found in other clusters with lower relevance. For instance, in the second subperiod, the cluster *Speciation* (Figure S3) included keywords such as "*Samples*", "*Preconcentration*", "*Water*", "*Soil*" and "*Atomic Absorption Spectrometry*". This cluster was a highly developed and isolated theme, which gives an idea about the well-established technical solutions provided by analytical chemistry for speciation and quantification of selenium in environmental samples. Another cluster in the third subperiod, called "*Plasma-mass-spectrometry*", also considered a highly developed and isolated theme, compiled more keywords regarding these analytical aspects, such as "*Water samples*", "*Speciation Analysis*", "*ICP-MS*", "*HPLC-ICP-MS*", "*Solid-Phase-Extraction*" and "*Atomic Absorption Spectrometry*" (Figure S4).

The lack of terms directly related to possible technologies for selenium removal from water during the analysis of the most frequently used keywords was at least partially solved when the cluster *Adsorption* was examined (Figures S7 and S9). This cluster appeared in the third subperiod (2012–2019) and had continuity until the last subperiod. In both cases it must be considered a highly developed and isolated theme, which was not trending. The list of keywords in this cluster included "*Removal*", "*Arsenic-Removal*", "*Sorption*", "*Membrane*" and "*Selenate*", which gave an idea about the most investigated technologies for selenium removal: the use of adsorbents and membrane-assisted separation processes.

The other cluster identified as motor theme not previously mentioned is *West-Bengal* during the second subperiod from 2002 to 2011 (Figure S1). This keyword in strongly correlated to Bangladesh and both regions suffered similar problems. On the one hand, uncontrolled industrial effluents are an important potential source of selenium pollution in these areas [135]. On the other hand, the dietary status of selenium is adversely affected by a chronic excessive ingestion of arsenic. These high levels of chronic arsenic ingestion from well water by people from these regions accelerate the excretion of selenium lowering the body's content of this essential trace element [136]. Keywords such as "*Exposure*", "*Contamination*", "*Groundwater*", "*Dietary-Selenium*" and "*Metabolism*", which appeared in this cluster, confirmed this double problem that must be solved in these areas.

3.2. Review of Current Treatment Alternatives for Selenium Removal from Drinking Water

Although the health aspects of the presence of selenium in drinking water have been the focus of most research efforts covering this topic, the increasing interest from the scientific community in technical processes for removal of selenium from water has been proved by the publication of some recent reviews that cover this field [137–143]. The list of commercially available and emerging technological options for selenium removal is extensive, but all the alternatives can be included in one of the following main categories:

- Adsorption and ion exchange.
- Coagulation-flocculation-precipitation.
- Membrane-based processes.
- Biological treatments.

Since more detailed reviews are available, the aim of this section is just to mention the most important trending topics identified as a consequence of the bibliometric analysis, without the intention of compiling a concise register of all the scientific bibliography published about technical solutions to remove selenium from water.

3.2.1. Adsorption and Ion Exchange

This treatment category can be considered the most important one according to the number of papers published and the relevance of them. In fact, the unique article included

among the most cited ones in Table 6 that presented results of a technical solution for selenium removal from water was related to the use of anionic clay minerals based on aluminum hydroxides as adsorbents/ion exchangers [123].

Iron compounds have certainly been the most recurrent materials tested as adsorbents for selenium removal from water. Iron oxides, hydroxides and oxyhydroxides, as well as zero-valent iron (ZVI), have frequently been reported as efficient adsorbents for selenium oxyanions [144–154]. The mechanisms that rule selenium oxyanions adsorption on iron compounds have been determined and modelled [155] and the effects that pH, surface loading, and ionic strength have on these mechanisms have been reported [156]. Selenite was more effectively removed that selenate by natural iron oxides (goethite and hematite) under identical conditions [157] and equivalent results were confirmed for other iron compounds derived from corrosion of ZVI [158]. Iron compounds resulted in a cost-effective solution, since they are not expensive and some are even waste materials, such as water treatment residuals, bauxite-processing red mud or fly ashes, can be directly reused as sorbents [159,160]. An innovative approach pointed to the employment of nanoparticles, nanocomposites and other nanomaterials for the intensification of selenium removal [161,162]. ZVI must be considered a very appropriate option for selenium removal, since it is highly reactive and widely available. ZVI can be easily oxidized by dissolved oxygen, contaminants themselves or even just water, resulting in iron oxides, hydroxides and oxyhydroxides as aqueous corrosion products [163]. Enhancing the corrosion of ZVI has been observed as an effective approach to promote its decontamination performance and the role of additional oxidants in this promotion has gained relevance. The addition of chemicals, such as hydrogen peroxide, sodium hypochlorite or potassium permanganate, achieved highly efficient and rapid selenium oxyanion removal [164–166]. Moreover, some treatment proposals have taken advantage of the magnetic properties of some iron-based adsorbents to improve the performance of the process by application of magnetic fields [167–169].

The removal of selenium from water by other metallic compounds, specifically oxides and hydroxides, has been reported. Activated alumina adsorption is known to be an effective and inexpensive technology for the removal of metals from drinking water and has been successfully applied to the case of selenium oxyanions [170–175]. Once again, activated alumina was more effective for selenite adsorption than selenate [176,177]. Other research works have proposed the employment of metallic oxides, such as titania, silica or zirconia, for this same purpose [178–182]. In some cases, the developed adsorbents were highly selective to selenite, even in the presence of selenate or selenide [183,184]. Natural and modified zeolites are high-performance adsorbents that have been implemented in the treatment of drinking water and have demonstrated that the selenium limits for drinking water can be achieved with specific process designs based on these aluminosilicates [185–187].

The removal of toxic oxyanions from water by means of adsorption onto carbon is a well-known process and an increasing number of drinking water treatment plants have installed activated carbon filters as secondary or tertiary treatments for the removal of micropollutants [188]. Both granular activated carbons (GACs) and powdered activated carbons (PACs) have been applied to the removal of selenium and the results revealed practical total removal of selenite (initial 100 μg/L concentration) with contact times not longer than 60 min under acidic or neutral conditions, but worse performance under alkaline pH [189]. However, the results with higher initial concentrations (5–75 mg/L solutions) demonstrated that, although relatively significant removal (87%) was observed for the lowest concentration tested, higher concentrations resulted in reduced removal percentages [171]. Besides, the use of activated carbons as supports to form stable composites loaded with metallic compounds has been reported. This way, the physical sorption that characterized the retention of selenium oxyanions in activated coals can be completed with the chemical adsorption provided by metal oxides and hydroxides, such as iron or cop-

per [190,191]. This combination enhanced the removal of selenium oxyanions, particularly for selenate, which was only partially removed by activated carbons [192].

Layered double hydroxides (LDHs), also called anionic clays, contain positive-charged layers and counter-anions in the interlayer space. They are ordered according to the generic layer sequence $[OHM^2OH\ A\ OHM^3OH]_n$, where M^2 and M^3 represents layers of divalent and trivalent metal cations, respectively, OH are layers of hydroxide anions, and A are layers of counter-anions. These materials have demonstrated effective removal of oxyanions from water due to the combination of adsorption in their large surface area and high anion exchange capacity. For the case of selenium removal, Al^{+3} was clearly the most preferred trivalent cation of the LDHs evaluated [193–195], but examples of Fe^{+3} in combination with Zn^{+2} can be found [196,197]. The tests with Mg/Al and Zn/Al LDHs with intercalated chloride revealed that the oxidation state of selenium was not too relevant, since the adsorption trends for both selenite and selenate on these LDHs were similar under the experimental conditions [198]. The presence of zwitterions instead of the classical anions in the interlayer space can imply a better adsorption capacity and selectivity for the removal of oxyanions. As example, the use of the amino acid glycine replacing nitrate in a Ni/Al LDHs increased the removal of selenate from 34 to 83% [199]. Another innovative approach identified was the loading of ZVI in a Mg/Al LDH, which enhanced the removal of selenate by incorporation of reductive immobilization mechanisms [200]. Nevertheless, the removal of selenium by LDHs can be severely affected and even inhibited by the presence of competitive anions in the water to be treated [201].

The application of commercial ion exchange resins for selenium removal has been reported. Articles describing the performance of strong and weak basic anionic resins in the presence of selenite and selenate are common [202–207], although these ion exchange processes have to deal with two important disadvantages. On the one hand, the occurrence of other oxyanions, such as nitrate or sulfate, implies a strong competition for the sorption sites in the resins. Since typically the concentrations of these competitive anions are several orders of magnitude higher that the selenium concentrations, resin can be exhausted rapidly and selenite and selenate removal inhibited [208]. On the other hand, ion exchange resins do not appear to be the most economical option, especially when compared to alternative adsorbents, which result in being clearly cheaper [197]. Consequently, research efforts have been focused on the search for solutions to improve these two drawbacks that ion exchange resins present. Low-cost ion exchangers derived from waste biomass [209,210] and inorganic ion exchangers based on silicates [211] have been investigated for selenium removal with successful results and can be considered a valid option to reduce the economic costs of the process. In order to improve the selectivity of the resins for selenium oxyanions and avoid the competition of other anions, innovative ligand and chelating resins [212–214] and metal-loaded cationic resins [215] have been proposed. Nevertheless, further research efforts are still required to identify more selective ion exchangers for the removal of selenium from aqueous solutions.

3.2.2. Coagulation-Flocculation-Precipitation Followed by Filtration

The direct precipitation of selenium compounds is not an adequate technology for selenium removal from water. Selenite and selenate oxyanions are the most frequent species of selenium in waters and, in contrast to the low solubility of metallic selenides, most metallic selenites and selenates are soluble in water [3,216]. However, the precipitation of Se^{+4} by sulfide ions is a well-known process, although the nature and characteristics of the solids formed in selenium-sulfide systems are not totally defined. The role of selenium disulfide (SeS_2) is crucial, but sulfur and selenium are miscible in all proportions and can form complex polymer-like molecules, thus the sulfur-selenium solid solutions are composed of cyclic Se–S rings containing a variable number of Se and S atoms [217]. Selenite removal at neutral pH by reductive precipitation using sodium sulfide as reducing agent (with S/Se molar ratios between 1.5 and 11) has been investigated and the precipitation

reaction went to completion with less than 5 μg/L of soluble selenium remaining in solution after 10 min at ambient temperature [218,219].

Ferric coagulants, such as $FeCl_3$ or $Fe_2(SO_4)_3$, are frequently used in water treatments due to their availability and low price. Some metals and metalloids species can co-precipitate or adsorb onto the surface of these ferric coagulants. Selenite behaves in this way and is readily removed through ferric co-precipitation. However, this treatment method is not adequate for selenate [220], but a previous reduction pretreatment, for example with sulfite, has been successfully applied to transform selenate into selenite and remove it by ferric coagulation [221]. Once again, selenium concentration below 5 μg/L in the treated effluent were achieved by ferric coagulants [222]. Aluminum coagulants, such as $AlCl_3$ or poly-aluminum chloride PAC, are very commonly used for water treatment too, since Al cations hydrolyze quickly and form abundant hydroxide precipitates in situ, which can act in a similar way to their homologous ferric compounds. Nevertheless, the research about the use of aluminum coagulants for selenium removal has demonstrated that the use of ferric compounds was preferred, since they were much more efficient [223,224]. Nevertheless, the performance of the coagulation process can be enhanced with the addition of commercially available polymeric flocculants, which enhanced the removal of selenium [225].

In electrocoagulation, an electrical current is used to generate metallic ions from a sacrificial anode immersed in the water to be treated. This way, continuous in situ generation of ions that polymerize rapidly and act as coagulants is possible. Although aluminum sacrificial anodes have been tested with satisfactory results [226], iron has been most frequently selected due to better sedimentability properties of the precipitated particles [227]. Regardless of the applied coagulation and flocculation process, filtration is required to remove the particles and microfiltration membranes [228] or alternative filtration media, such as sand filters [229], must be implemented as post-treatment.

3.2.3. Membrane-Based Processes

The removal of toxic metals and metalloids from environmental aqueous samples with high salinity has been a rising area for membrane separation, because, under these circumstances, they provide a better solution than the technologies explained in the two previous sections, which can suffer worse performance due to elevated ionic contents. Pressure assisted membranes are good candidates for the removal of selenium, but the selection of the most appropriate technology must take into account the balance between high permeate production and efficient selenium rejection.

One the one hand, the strictest membranes, such as reverse osmosis (RO) and tight nanofiltration (NF), produce relatively low permeation fluxes and require high applied pressure, but the rejection percentages are maximal. On the other hand, less restrictive membranes, such as loose NF or ultrafiltration (UF), are characterized by production of larger volumes of permeate, but the removal performances are often considerably lower [230].

Although RO and NF are the most frequent pressure-assisted membrane technologies selected to remove selenium from water because of the small size of the selenium oxyanions, which is around 2.4 Å [137], an example of the application of UF to eliminate selenium was found [231]. This work investigated the potential to remove both Se^{+4} and Se^{+6} states by different polymeric and ceramic membranes. On the one hand, the use of commercial polyamide UF membranes with MWCO values between 2.5 and 3.5 kDa implied high permeate fluxes (more than 5×10^{-5} $m^3/m^2 \cdot s$) and rejection percentages around 90% and 95% for Se^{+4} and Se^{+6}, respectively, with very little influence of the initial selenium concentration. The higher rejection of Se^{+6} can be justified by its stronger electrostatic interactions, since the charge of Se^{+6} oxyanions was higher than the one corresponding to Se^{+4} oxyanions for most pH values. The most extreme case was the rejection at pH 1.5, where neutral H_2SeO_3 is not rejected by the UF membrane while $HSeO_4^-$ showed a rejection value above 40% (similar case when $HseO_3^-$ was compared to SeO_4^{-2}). Even

when the charge of the oxyanions were equal, steric effects favored the rejection of Se^{+6} versus Se^{+4}. The importance of the electrostatic interaction in the rejection of selenium oxyanions was confirmed by the decreased rejection values due to higher ionic strength. On the other hand, the performance of a ceramic UF membrane with MWCO 8 kDa exhibited lower rejection percentages: around 30% and 80% for Se^{+4} and Se^{+6}, respectively (although the permeate flux doubled the values of the polymeric membranes). However, these rejection values were greatly improved by addition of chitosan as chelating agent to improve selenium removal.

The first examples of the application of RO to selenium removal were published in the late 1970s and 1980s [140]. In contrast to arsenic, where the oxidation state of the element highly determined the performance of the membrane process due to the presence of neutral species of As^{+3} [93], selenium appears as negatively charged oxyanions in most environmental water samples and both Se^{+4} and Se^{+6} are efficiently rejected by RO membranes [232]. Several studies have analyzed in detail the permeability of selenium species through RO membranes and the interactions with other ions in aqueous solution [233,234]. Nevertheless, RO can be an inadequate solution to treat streams with excessive salinity, due to the extreme osmotic pressure these types of solutions present. As an example, deep formation water, which is extracted as an undesired byproduct from oil production wells, can be mentioned, since its hypersalinity requires pressure conditions exceeding 200 bars across the RO membrane [235]. Some illustrative case studies of the application of RO to the removal of selenium are compiled in Table 8. The rejection percentages attained by RO membranes are higher than 94%, with some examples around 100%, but the lower rejection values corresponded to initial selenium concentrations below 100 µg/L. However, the permeate fluxes are significantly reduced and due to the balance between simultaneous high water permeability and rejection that NF presents, it can be considered a most adequate technology to achieve this goal [236]. Table 9 introduces some relevant articles that covered the treatment by NF of water samples with high selenium content. An analysis of the results of these works pointed to a more valuable compromise solution by implementation of NF. The rejection of selenium maintained equivalent values to those obtained by RO, but NF provided increased permeate production, with values at least an order of magnitude higher than the case of RO [237].

Table 8. Examples of application of reverse osmosis for selenium removal from water.

Treated Water	Membrane	ΔP (bar)	Permeate Flux ($m^3/m^2 \cdot s$)	Initial [Se] (µg/L)	Removal (%)	Reference
Agricultural drainage water	-	55	1.1×10^{-7}	30,000	99.9	[232]
Mining polluted groundwater	PAC1/TW30 (Ionics/Filmtec)	7	-	550	98	[230]
Synthetic aqueous solution (previous biological treatment)	ESPA (Hydranautics)	8	-	326	99	[238]
Groundwater	BW30 (Filmtec)	13	1.5×10^{-5}	15	94	[239]
Mining polluted groundwater	-	-	-	21	100	[240]
Potabilization inlet water	-	-	-	5	100	[241]
Previously NF treated landfill leachate	BW30 (Filmtec)	76	3.6×10^{-6}	63	94	[242]

Table 9. Examples of application of nanofiltration for selenium removal from water.

Treated Water	Membrane	ΔP (bar)	Permeate Flux ($m^3/m^2 \cdot s$)	Initial [Se] (μg/L)	Removal (%)	Reference
Agricultural drainage water	Unidentified (Filmtec)	-	-	3000	95	[243]
Coal-fired power plant scrubber water	NF3A/PNF2 (SEPRO)	-	-	634	98.6	[148]
Synthetic aqueous solution	POSS-TFN (non-commercial)	10	1.5×10^{-5}	100,000	97.4	[244]
Synthetic aqueous solution	UiO-66-TFN (non-commercial)	10	3.2×10^{-5}	1,000,000	97.4	[236]
Synthetic aqueous solution	Zwitterionic copolymer-TFN (non-commercial)	10	2.4×10^{-5}	1,000,000	99.9	[245]
Synthetic aqueous solution	Carbon quantum dots-TFN (non-commercial)	10	2.9×10^{-5}	1,000,000	98.2	[246]
Synthetic aqueous solution	Polyamide intercalated membrane with biofunctionalized core shell composite (non-commercial)	0.5	1.2×10^{-4}	100	98	[247]
Potabilization inlet water	NF1/NF2/NF20 (SEPRO)	14	3.9×10^{-5}	400–2000	98	[237]

Furthermore, apart from pressure-assisted membrane technologies, other innovative membrane technologies have been investigated for selenium removal. Firstly, supported liquid membranes, which have been successfully applied to the removal of other metals and metalloids from water, have been investigated for the case of selenium. Three different stages and phases are involved in supported liquid membranes: solute extraction from the feed phase, diffusion of solute through the extractant-containing phase and stripping of solute to the acceptor phase. For the particular case of selenium, several investigations have been completed, all based on the use of feed and acceptor aqueous phases, while the extractant is an organic phase. Mafu et al. employed Aliquat 336 supported on PP (polypropylene) hollow fibers to transfer selenium to a 0.8 M NaOH stripping solution [248]. From an initial 100 μg/L concentration, the selenium content was reduced by 78%. Lower removal percentages (around 60%) were achieved by Ambe et al., which selected TBP (tributyl phosphate) as carrier in a decalin phase supported on microporous PTFE (polytetrafluoroethylene) disks [249]. In this case, HCl solution was employed as acceptor phase. Selective removal of selenium compared to other metallic impurities in aqueous solution was demonstrated by Noguerol et al., in this case with NaDDTC (sodium diethyldithiocarbamate) as carrier in kerosene phase supported on PTFE (polytetrafluoroethylene) membrane and with H_2O_2 as stripping agent [250]. Secondly, brackish groundwater was treated by pervaporation to be used for micro-irrigation [251,252]. In pervaporation, the membrane acts as a selective barrier between the two phases: the liquid-phase feed and the vapor-phase permeate. It allows the desired components of the liquid feed to transfer through it by vaporization, and consequently, the separation of the components is based on a difference in transport rate of individual components through the membrane. Among the model compounds selected for these pervaporation studies, Se^{+6} was included. Under optimal configuration of the sweeping gas pervaporation system, the maximal permeate water flux was 5.1×10^{-8} $m^3/m^2 \cdot s$. The removal of selenium from solutions with initial concentrations in the range 56–154 μg/L attained 92% with corrugated sheet membranes made of thermoplastic copolyether esters elastomers. Lastly, electrodialysis was applied to the removal of inorganic trace contaminants (including selenium) from a real brackish groundwater in a remote Australian community [253]. Electrodialysis is based on the transport of salt ions from one solution through ion-exchange membranes to another solution under the influence of an applied electric potential difference. A systematic investigation of the most relevant operation conditions (applied voltage and solution pH) was completed to elucidate removal efficiency. A higher applied voltage enhanced removal of Se^{+6} (from 33 to 48%) at pH 7, but the adjustment of the pH value was a more effective measure to improve the removal. On the one hand, pH below 6 increased the removal percentage above 80%, while,

on the other hand, pH values between 8 and 11 formed insoluble $CaSeO_4$, which eliminated selenium from the water but caused fouling of the membrane.

3.2.4. Biological Treatments

The reactions that are involved in the biogeochemical cycle of selenium have been deeply investigated, including the ones more directly related to microorganisms, which are depicted in Figure 8 [254]. Among all these transformation reactions, dissimilatory reduction pathways must be considered the most interesting option in terms of biological removal of selenium from water [255–258]. Many microorganisms that transform the soluble selenate and selenite oxyanions into insoluble elemental selenium have been identified and isolated from pristine [259–261] and polluted environments [262–265] for better understanding of the metabolic mechanisms involved [143]. A compilation of major cultured selenium-reducing microorganisms and their main properties has been published [4].

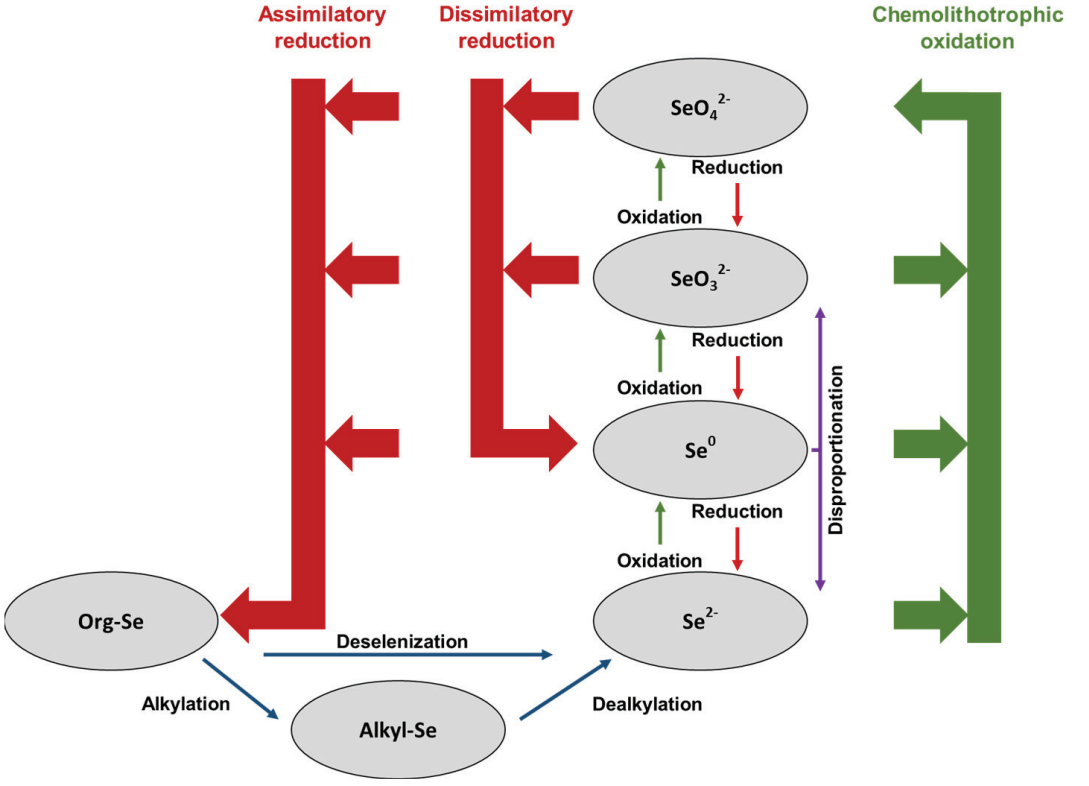

Figure 8. Selenium transformations in nature.

Biological selenium removal by environmentally sustainable technologies is an attractive alternative due to the water characteristics (dilute selenium concentration and high volume to be treated) and low costs. In addition, adequate biological treatment may imply the transformation of dissolved selenium into a recoverable insoluble form. The recovery of the elemental red selenium resulting from dissimilatory reduction is seriously considered to reduce or even compensate the treatment costs. Although several studies have demonstrated that these bacterial selenium nanoparticles can contain impurities, such as heavy metals or organic compounds, the recovery of selenium provides high value for the industrial sectors interested in its applications [266]. Nevertheless, the recovery of the biogenic elemental selenium is challenging, since it exhibits colloidal properties that require

further post-treatment (filtration, centrifugation, coagulation, electrocoagulation, etc.) for separation of the colloidal selenium from the treated water [226,267].

The dissimilatory reduction of selenate and selenite has been investigated under different scenarios and it was successfully applied under methanogenic, sulfate reducing, denitrifying or hydrogenotrophic conditions [268]. All these tests have demonstrated that the dissimilatory reduction to elemental selenium is viable even in presence of high concentrations of other oxyanions, such as sulfate or nitrate [263,269–271]. In addition, the presence of heavy metals did not exert a significant effect on selenite microbial reduction [272]. The biological treatment of selenium-polluted water required the enrichment and retention of microorganisms in bioreactors. Different bioreactor configurations have been analyzed for this purpose. Among all the alternatives tested, which include from basic anaerobic ponds to complex bio-electrochemical systems [273–275], fluidized bed reactors (FBRs), upflow anaerobic sludge blankets (UASBs) and membrane biofilms reactors (MBfRs) must be highlighted [276].

In FBRs, a biofilm is formed on added solid particles, which are fluidized by the movement of the liquid to be treated, avoiding the transport limitations that appear in stationary-bed processes. For the removal of selenium, examples of activated carbon and commercial supports, such as Kaldness-K1 or Extendospheres, as added solid particles have been investigated [277–279]. Optimization of the bioreactor operation conditions resulted in selenium removal percentages above 88% with hydraulic retention times no longer that 0.5 h. Meanwhile, UASBs employ beds of granular sludge developed by the self-aggregation of microorganisms, which are fed from the bottom with water to be treated, while a gas-liquid-solid separator in the upper section of the bioreactor retains the biomass. Different types of granular sludge have been investigated for selenium microbial reduction, with removal values above 90%, even when the selenium concentration in the influent exceeded 3 mg/L [280,281]. Finally, a type of MBfR has been systematically studied in the last decade for the removal of selenium oxyanions: the H_2-based MBfR [282]. These bioreactors consume non-toxic gaseous hydrogen as electron donor for the reduction of dissolved pollutants. The gas is delivered by diffusion through the walls of non-porous hollow fiber membranes and a biofilm is naturally formed on the outer wall of the membranes [283]. Different interactions between selenium oxyanions and other anions present in the influent, such as nitrate or sulfate, have great influence on the performance of MBfRs due to the direct link between the specific microbial community structure in the biofilm and the composition of the aqueous solution medium [284–286]. Once again, the decrease of the selenium content in the water treated in these bioreactors ranged between 90 and 99%, even with initial concentration from 1 to 11 mg/L, values more than one order of magnitude higher than the maximum contaminant level for drinking water [287–289].

Phytoremediation takes advantage of the ability of some plants and their related microbes to take selenium from the environment [290,291]. The design of constructed wetlands is a valuable green option to apply the potential of these plants for improving water quality. The main mechanisms for removal of selenium in constructed wetlands include biosorption, biologically-mediated precipitation, assimilation and accumulation, and volatilization of organic selenium compounds produced via bioalkylation [292]. The relative contribution of each pathway and the precise roles of the plants, the corresponding microorganisms and even the animals that may be present depends on the specific biotic community and the abiotic conditions in the constructed wetland. The identification of the most adequate plant species for selenium removal is a key aspect of the research in this field. Cattails (*Typha* spp.) have demonstrated a satisfactory performance to effectively reduce the selenium concentration in waters, but other species, such as bulrushes (*Cyperus* spp., *Scirpus* spp., *Schoenoplectus* spp.), reeds (*Phragmites* spp.), saltgrass (*Distichlis* spp.), rabbitfoot grasses (*Polypogon* spp.) or trees, such as poplars (*Populus* spp.), must be mentioned too as adequate candidates for selenium removal [293–295].

In addition, microalgae, such as *Chlorella vulgaris*, have been successfully applied to the removal of selenium [296,297]. The percentage of removal of selenium was highly

dependent on the exact conditions of each constructed wetland, but the most frequent values ranged from around 40–50% as minimal values [298,299] to practically complete removal in the most effective cases [297,300,301], with many case studies around 75% removal [302–306].

Biological methods must be considered efficient ways to reduce the selenium concentration in water. These methods allow the recovery of selenium as insoluble forms or selenium-enriched vegetables can be produced, which exhibit interesting antioxidant properties [299]. Therefore, research efforts must be promoted in this field in order to demonstrate the technical and economic viability of real scale processes and pave the way to further implementation.

4. Conclusions

A summary of the research on selenium in drinking water was prepared from the results of a bibliometric analysis (information about annual publications, document types, languages, countries, institutions, categories, journals and keywords). The number of accumulated publications about this subject increased according to a quadratic evolution during the 1990–2019 period. The USA was the leading country in total number of publications, followed by a couple of Asian countries (China and India). In fact, Chinese institutions appeared among the most productive ones. Although *Environmental Science* was the most frequent category, many studies in *Medicine* and *Biochemistry, Genetics and Molecular Biology* have investigated the identification of the health effects of the intake of selenium. In fact, these aspects directly related to the consequences of selenium intake on the human health have been identified as the most deeply investigated. The bibliometric network analysis revealed that the clusters with keywords in this field were more relevant and they were cited a higher number of times than the clusters with keywords more easily related to water treatment.

Although the search of effective technical solutions to solve the problems caused by the presence of selenium in drinking water has been less intensive than the treatments of other pollutants, such as arsenic, many research works have investigated the best practices to remove selenium oxyanions. Adsorption was by far the most investigated treatment alternative. Several metallic compounds, mainly iron and aluminum oxides, hydroxides and oxyhydroxides, are the most relevant sorbents under study. Nevertheless, further research efforts to identify more selective ion exchangers must be recommended. Pressure-assisted membrane technologies (mainly nanofiltration and reverse osmosis) must be considered competitive solutions, but a balance between selenium rejection and permeate production is required. Processes for selenium removal based on coagulation, flocculation and precipitation have not gained too much attention by researchers, although iron and aluminum salts have been successfully employed as coagulants, especially for the retention of colloidal elemental selenium particles. The most relevant biological treatments take advantage of the dissimilatory reduction of selenate and selenite to elemental selenium. Moreover, the recovery of this elemental selenium could be a sustainable option to close the cycle of selenium, thus the investigation related to the biological methods that can close this loop must be promoted, including the production of selenium-enriched vegetables.

Supplementary Materials: The following supporting information can be downloaded at: https://www.mdpi.com/article/10.3390/ijerph19105834/s1, Figure S1: Structure of the cluster *West-Bengal* in the second subperiod (2002–2011), Figure S2: Structure of the cluster *Glutathione-Peroxidase* in the second subperiod (2002–2011), Figure S3: Structure of the cluster *Speciation* in the second subperiod (2002–2011), Figure S4: Structure of the cluster *Plasma-Mass-Spectrometry* in the third subperiod (2012–2019), Figure S5: Structure of the cluster *Lead* in the third subperiod (2012–2019), Figure S6: Structure of the cluster *Soil* in the third subperiod (2012–2019), Figure S7: Structure of the cluster *Adsorption* in the third subperiod (2012–2019), Figure S8: Structure of the cluster *Supplementation* in the third subperiod (2012–2019), Figure S9: Structure of the cluster *Adsorption* in the fourth subperiod (2020–2021).

Funding: The APC was funded by Dirección de Investigación Científica y Tecnológica (DICyT) de la Universidad de Santiago USACH.

Institutional Review Board Statement: Not applicable.

Informed Consent Statement: Not applicable.

Conflicts of Interest: The author declares no conflict of interest.

References

1. Bailey, R.T. Review: Selenium contamination, fate, and reactive transport in groundwater in relation to human health. *Hydrogeol. J.* **2017**, *25*, 1191–1217. [CrossRef]
2. Hoffmann, J.E.; King, M.G. Selenium and selenium compounds. In *Kirk-Othmer Encyclopedia of Chemical Technology*; Wiley: New York, NY, USA, 2002.
3. Seby, F.; Potingautier, M.; Giffaut, E.; Borge, G.; Donard, O.F.X. A critical review of thermodynamic data for selenium species at 25 °C. *Chem. Geol.* **2001**, *171*, 173–194. [CrossRef]
4. Eswayah, A.S.; Smith, T.J.; Gardiner, P.H.E. Microbial Transformations of Selenium Species of Relevance to bioremediation. *Appl. Environ. Microbiol.* **2016**, *82*, 4848–4859. [CrossRef] [PubMed]
5. Ullah, H.; Liu, G.; Yousaf, B.; Ubaid, M.; Irshad, S.; Abbas, Q.; Ahmad, R. A Comprehensive Review on Environmental Transformation of Selenium: Recent Advances and Research Perspectives. *Environ. Geochem. Health* **2019**, *41*, 1003–1035. [CrossRef] [PubMed]
6. Paul, T.; Saha, N.C. Environmental Arsenic and Selenium Contamination and Approaches towards Its Bioremediation Through the Exploration of Microbial Adaptations: A Review. *Pedosphere* **2019**, *29*, 554–568. [CrossRef]
7. Saji, V.S.; Lee, C.W. Selenium electrochemistry. *RSC Adv.* **2013**, *3*, 10058–10077. [CrossRef]
8. Pourbaix, M. *Atlas of Electrochemical Equilibria in Aqueous Solutions*; Pergamon Press: Brussels, Belgium, 1974.
9. Langner, B.E. Selenium and selenium compounds. In *Ullmann's Encyclopedia of Industrial Chemistry*; Wiley-VCH: Weinheim, Germany, 2005.
10. Riaz, M.; Mehmood, K.T. Selenium in human health and disease: A review. *J. Postgrad. Med. Inst.* **2012**, *26*, 120–133.
11. Sun, H.J.; Rathinasabapathi, B.; Wu, B.; Luo, J.; Pu, L.P.; Ma, L.Q. Arsenic and selenium toxicity and their interactive effects in humans. *Environ. Int.* **2014**, *69*, 148–158. [CrossRef]
12. Zwolak, I.; Zaporowska, H. Selenium interactions and toxicity: A review. *Cell Biol. Toxicol.* **2012**, *28*, 31–46. [CrossRef]
13. Fairweather-Tait, S.J.; Bao, Y.; Broadley, M.R.; Collings, R.; Ford, D.; Hesketh, J.E.; Hurst, R. Selenium in human health and disease. *Antioxid. Redox Signal.* **2011**, *14*, 1337–1383. [CrossRef]
14. Zhu, Y.; Wang, X.; Yang, G.; Wei, J.; Tan, W.; Wang, L.; Guo, X.; Lammi, M.J.; Xu, J. Efficacy of Long-term Selenium Supplementation in the Treatment of Chronic Keshan Disease with Congestive Heart Failure. *Curr. Med. Sci.* **2019**, *39*, 237–242. [CrossRef] [PubMed]
15. Zhang, X.; Wang, T.; Li, S.; Ye, C.; Hou, J.; Li, Q.; Liang, H.; Zhou, H.; Guo, Z.; Han, X.; et al. A Spatial Ecology Study of Keshan Disease and Hair Selenium. *Biol. Trace Elem. Res.* **2019**, *189*, 370–378. [CrossRef]
16. Johnson, C.C.; Ge, X.; Green, K.A.; Liu, X. Selenium distribution in the local environment of selected villages of the Keshan disease belt, Zhangjiakou district, Hebei Province, People's Republic of China. *Appl. Geochem.* **2000**, *15*, 385–401. [CrossRef]
17. Xie, D.; Liao, Y.; Yue, J.; Zhang, C.; Wang, Y.; Deng, C.; Chen, L. Effects of five types of selenium supplementation for treatment of Kashin-Beck disease in children: A systematic review and network meta-analysis. *BMJ Open* **2018**, *8*, e017883. [CrossRef] [PubMed]
18. Wang, J.; Li, H.; Li, Y.; Yu, J.; Yang, L.; Feng, F.; Chen, Z. Speciation, distribution, and bioavailability of soil selenium in the tibetan plateau kashin-beck disease area—A case study in Songpan County, Sichuan Province, China. *Biol. Trace Elem. Res.* **2013**, *156*, 367–375. [CrossRef]
19. Shi, Z.; Pan, P.; Feng, Y.; Kan, Z.; Li, Z.; Wei, F. Environmental water chemistry and possible correlation with Kaschin-Beck Disease (KBD) in northwestern Sichuan, China. *Environ. Int.* **2017**, *99*, 282–292. [CrossRef] [PubMed]
20. Lei, R.; Jiang, N.; Zhang, Q.; Hu, S.; Dennis, B.S.; He, S.; Guo, X. Prevalence of Selenium, T-2 Toxin, and Deoxynivalenol in Kashin–Beck Disease Areas in Qinghai Province, Northwest China. *Biol. Trace Elem. Res.* **2016**, *171*, 34–40. [CrossRef]
21. Cui, Z.; Huang, J.; Peng, Q.; Yu, D.; Wang, S.; Liang, D. Risk assessment for human health in a seleniferous area, Shuang'an, China. *Environ. Sci. Pollut. Res.* **2017**, *24*, 17701–17710. [CrossRef]
22. Sutter, M.E.; Thomas, J.D.; Brown, J.; Morgan, B. Selenium toxicity: A case of selenosis caused by a nutritional supplement. *Ann. Intern. Med.* **2008**, *148*, 970–971. [CrossRef]
23. Li, Y.; Wang, W.; Luo, K.; Li, H. Environmental behaviors of selenium in soil of typical selenosis area, China. *J. Environ. Sci.* **2008**, *20*, 859–864. [CrossRef]
24. Yücel, U.M.; Başbuğan, Y.; Uyar, A.; Kömüroğlu, A.U.; Keleş, Ö.F. Use of an antiarrhythmic drug against acute selenium toxicity. *J. Trace Elem. Med. Biol.* **2020**, *59*, 126471. [CrossRef] [PubMed]
25. Hadrup, N.; Ravn-Haren, G. Acute human toxicity and mortality after selenium ingestion: A review. *J. Trace Elem. Med. Biol.* **2020**, *58*, 126435. [CrossRef] [PubMed]
26. WHO. *Vitamin and Mineral Requirements in Human Nutrition*; Organization of the United Nations: Geneva, Switzerland, 2004; ISBN 92 4 154612 3.

27. Jablonska, E.; Vinceti, M. Selenium and Human Health: Witnessing a Copernican Revolution? *J. Environ. Sci. Health-Part C Environ. Carcinog. Ecotoxicol. Rev.* **2015**, *33*, 328–368. [CrossRef]
28. Yu, D.; Liang, D.; Lei, L.; Zhang, R.; Sun, X.; Lin, Z. Selenium geochemical distribution in the environment and predicted human daily dietary intake in northeastern Qinghai, China. *Environ. Sci. Pollut. Res.* **2015**, *22*, 11224–11235. [CrossRef]
29. Miyazaki, Y.; Koyama, H.; Sasada, Y. Dietary Habits and Selenium Intake of Residents Coastal Communities in Japan in Mountain and Masami NOJIRI5 and Shosuke SUZUKI6 of Public Health Nursing, Faculty of Nursing, Jobu Gunma of Public Health of Medicine, Maebashi Junior College of Public Health. *J. Nutr. Sci. Vitaminol.* **2004**, *50*, 309–319. [CrossRef] [PubMed]
30. Cianciolo, T.R.; McLaughlin, D.L.; Zipper, C.E.; Timpano, A.J.; Soucek, D.J.; Whitmore, K.M.; Schoenholtz, S.H. Selenium Bioaccumulation Across Trophic Levels and Along a Longitudinal Gradient in Headwater Streams. *Environ. Toxicol. Chem.* **2020**, *39*, 692–704. [CrossRef] [PubMed]
31. Hamilton, S.J. Review of selenium toxicity in the aquatic food chain. *Sci. Total Environ.* **2004**, *326*, 1–31. [CrossRef] [PubMed]
32. Yang, Y.; Wu, P.; Li, X.-X.; Zha, X.-F. Distribution and ecological risk assessment of heavy metals in selenium-rich soil with high cadmium content of coal mining area in upper reaches of Guancheng river in Zhijin county, Guizhou. *Chin. J. Ecol.* **2018**, *37*, 1797–1806. [CrossRef]
33. Mills, T.J.; Mast, M.A.; Thomas, J.; Keith, G. Controls on selenium distribution and mobilization in an irrigated shallow groundwater system underlain by Mancos Shale, Uncompahgre River Basin, Colorado, USA. *Sci. Total Environ.* **2016**, *566–567*, 1621–1631. [CrossRef]
34. Hammer, M.J. An Assessment of Current Standards for Selenium in Drinking Water. *Groundwater* **1981**, *19*, 366–369. [CrossRef]
35. Pletnikova, I.P. Biological effect and level of safety of selenium in its entry into the organism with drinking water. *Gig. Sanit.* **1970**, *35*, 14–19. [PubMed]
36. Lafond, M.G.; Calabrese, E.J. Is the selenium drinking water standard justified? *Med. Hypotheses* **1979**, *5*, 877–899. [CrossRef]
37. WHO. *Guidelines for Drinking-Water Quality*; Organization of the United Nations: Geneva, Switzerland, 2011.
38. Gilron, G. The selenium drinking water quality guideline in Canada: The case for a re-evaluation. *Integr. Environ. Assess. Manag.* **2012**, *8*, 194–196. [CrossRef]
39. Instituto Nacional de Normalización de Chile. *NCh409/1.Of2005: Agua Potable-Parte 1-Requisitos*; Instituto Nacional de Normalización de Chile: Santiago, Chile, 2005.
40. European Union. *1829/2003 del Parlamento Europeo y del Consejo de 22 de Septiembre de 2003 Reglamento (CE) n*; European Union: Brussels, Belgium, 1998.
41. European Union. *Propuesta de Directiva del Parlamento Europeo y del Consejo Relativa a la Calidad de las Aguas Destinadas al Consumo Humano (Versión Refundida)*; European Union: Brussels, Belgium, 2018; ISBN 1349-7448.
42. Barron, E.; Migeot, V.; Rabouan, S.; Potin-Gautier, M.; Séby, F.; Hartemann, P.; Lévi, Y.; Legube, B. The case for re-evaluating the upper limit value for selenium in drinking water in Europe. *J. Water Health* **2009**, *7*, 630–641. [CrossRef] [PubMed]
43. Vinceti, M.; Crespi, C.M.; Bonvicini, F.; Malagoli, C.; Ferrante, M.; Marmiroli, S.; Stranges, S. The need for a reassessment of the safe upper limit of selenium in drinking water. *Sci. Total Environ.* **2013**, *443*, 633–642. [CrossRef]
44. Gilron, G.; Downie, J. The practical quantitation limit: Implications for regulating selenium in the context of applying aquatic life guidelines in North America. *Integr. Environ. Assess. Manag.* **2016**, *12*, 594–595. [CrossRef]
45. Gore, F.; Fawell, J.; Bartram, J. Too much or too little? A review of the conundrum of selenium. *J. Water Health* **2010**, *8*, 405–416. [CrossRef]
46. Dhillon, K.S.; Dhillon, S.K. Distribution and Management of Seleniferous Soils. *Advances* **2003**, *79*, 119–184.
47. Wadgaonkar, S.L.; Nancharaiah, Y.V.; Esposito, G.; Lens, P.N.L. Environmental impact and bioremediation of seleniferous soils and sediments. *Crit. Rev. Biotechnol.* **2018**, *38*, 941–956. [CrossRef]
48. Paikaray, S. Origin, Mobilization and Distribution of Selenium in a Soil/Water/Air System: A Global Perspective with Special Reference to the Indian Scenario. *Clean-Soil Air Water* **2016**, *44*, 474–487. [CrossRef]
49. Campostrini, I.; Gramaccioli, C.M. Selenium-rich secondary minerals from the Baccu Locci mine (Sardinia, Italy). *Neues Jahrb. Für Mineral.-Abh.* **2001**, *177*, 37–59. [CrossRef]
50. Brätter, P.; De Negretti Brätter, V.E. Influence of high dietary selenium intake on the thyroid hormone level in human serum. *J. Trace Elem. Med. Biol.* **1996**, *10*, 163–166. [CrossRef]
51. Grundmann, G.; Förster, H.-J. The sierra de cacheuta vein-type se mineralization, Mendoza Province, Argentina. *Minerals* **2018**, *8*, 127. [CrossRef]
52. Silva Junior, E.C.; Wadt, L.H.O.; Silva, K.E.; Lima, R.M.B.; Batista, K.D.; Guedes, M.C.; Carvalho, G.S.; Carvalho, T.S.; Reis, A.R.; Lopes, G.; et al. Natural variation of selenium in Brazil nuts and soils from the Amazon region. *Chemosphere* **2017**, *188*, 650–658. [CrossRef]
53. Armstrong, J.G.T.; Parnell, J.; Bullock, L.A.; Boyce, A.J.; Perez, M.; Feldmann, J. Mobilisation of arsenic, selenium and uranium from Carboniferous black shales in west Ireland. *Appl. Geochem.* **2019**, *109*, 104401. [CrossRef]
54. Parnell, J.; Bullock, L.; Armstrong, J.; Perez, M. Liberation of selenium from alteration of the Bowland Shale Formation: Evidence from the Mam Tor landslide. *Q. J. Eng. Geol. Hydrogeol.* **2018**, *51*, 503–508. [CrossRef]
55. Yan, J.; Wang, F.; Qin, H.; Chen, G.; Eviatar, N.; Fahima, T.; Cheng, J. Natural Variation in Grain Selenium Concentration of Wild Barley, Hordeum spontaneum, Populations from Israel. *Biol. Trace Elem. Res.* **2011**, *142*, 773–786. [CrossRef]
56. Koriyama, C.; Campos, F.I.; Yamamoto, M.; Serra, M.; Carrasquilla, G.; Carrascal, E.; Akiba, S. Toenail selenium levels and gastric cancer risk in Cali, Colombia. *J. Toxicol. Sci.* **2008**, *33*, 227–235. [CrossRef]

57. Zhang, H.; Feng, X.; Larssen, T. Selenium speciation, distribution, and transport in a river catchment affected by mercury mining and smelting in Wanshan, China. *Appl. Geochem.* **2014**, *40*, 1–10. [CrossRef]
58. Emmanuelle, B.; Virginie, M.; Fabienne, S.; Isabelle, I.; Martine, P.-G.; Bernard, L.; Sylvie, R. Selenium exposure in subjects living in areas with high selenium concentrated drinking water: Results of a French integrated exposure assessment survey. *Environ. Int.* **2012**, *40*, 155–161. [CrossRef]
59. Barwick, M.; Maher, W. Biotransference and biomagnification of selenium copper, cadmium, zinc, arsenic and lead in a temperate seagrass ecosystem from Lake Macquarie Estuary, NSW, Australia. *Mar. Environ. Res.* **2003**, *56*, 471–502. [CrossRef]
60. Santos, M.D.; da Silva Júnior, F.M.R.; Zurdo, D.V.; Baisch, P.R.M.; Muccillo-Baisch, A.L.; Madrid, Y. Selenium and mercury concentration in drinking water and food samples from a coal mining area in Brazil. *Environ. Sci. Pollut. Res.* **2019**, *26*, 15510–15517. [CrossRef] [PubMed]
61. Wilkin, R.T.; Lee, T.R.; Beak, D.G.; Anderson, R.; Burns, B. Groundwater co-contaminant behavior of arsenic and selenium at a lead and zinc smelting facility. *Appl. Geochem.* **2018**, *89*, 255–264. [CrossRef] [PubMed]
62. YanardaĞ, R.; Orak, H. Total selenium concentration in various waters of turkey. *Environ. Technol.* **2001**, *22*, 237–246. [CrossRef] [PubMed]
63. Chang, Y.; Müller, M.; Wu, Y.; Jiang, S.; Cao, W.W.; Qu, J.G.; Ren, J.L.; Wang, X.N.; Rao, E.M.; Wang, X.L.; et al. Distribution and behaviour of dissolved selenium in tropical peatland-draining rivers and estuaries of Malaysia. *Biogeosciences* **2020**, *17*, 1133–1145. [CrossRef]
64. Conde, J.E.; Sanz Alaejos, M. Selenium concentrations in natural and environmental waters. *Chem. Rev.* **1997**, *97*, 1979–2003. [CrossRef]
65. Ćurković, M.; Sipos, L.; Puntarić, D.; Dodig-Ćurković, K.; Pivac, N.; Kralik, K. Arsenic, copper, molybdenum, and selenium exposure through drinking water in rural eastern Croatia. *Polish J. Environ. Stud.* **2016**, *25*, 981–992. [CrossRef]
66. Dhillon, K.S.; Dhillon, S.K. Selenium in groundwater and its contribution towards daily dietary Se intake under different hydrogeological zones of Punjab, India. *J. Hydrol.* **2016**, *533*, 615–626. [CrossRef]
67. El Haraoui, N.; Tao, T.; Xin, K.; Wang, Q. Analysis of heavy metals and ions in tap water: A case of Shanghai P District. *Fresenius Environ. Bull.* **2014**, *23*, 395–399.
68. Hu, X.; Wang, F.; Hanson, M.L. Selenium concentration, speciation and behavior in surface waters of the Canadian prairies. *Sci. Total Environ.* **2009**, *407*, 5869–5876. [CrossRef]
69. Lemly, A.D. Aquatic selenium pollution is a global environmental safety issue. *Ecotoxicol. Environ. Saf.* **2004**, *59*, 44–56. [CrossRef]
70. Parnell, J.; Brolly, C.; Spinks, S.; Bowden, S. Selenium enrichment in Carboniferous Shales, Britain and Ireland: Problem or opportunity for shale gas extraction? *Appl. Geochem.* **2016**, *66*, 82–87. [CrossRef]
71. Cortés, I.; Ríos, J.; Gaete, L.; Tchernitchin, A.N. Metales pesados en muestras ambientales de la Región de Atacama. Situación postaluviones. In Proceedings of the XIV Congreso Geológico Chileno, La Serena, Chile, 4–8 October 2015; pp. 302–305.
72. Ruz, M.; Codoceo, J.; Hurtado, S.; Muñoz, L.; Gras, N. Characterization of the Regional Distribution of Selenium in Chile Using Selenium in Hens' Eggs as a Monitor. *Top. Catal.* **1995**, *9*, 156–159. [CrossRef]
73. Ceballos, A.; Espíndola, S.; Uslar, D.; Neumann, J.; Quiroz, E.; Chihuailaf, R.; Wittwer, F. Concentración de selenio en leche de estanques de rebaños lecheros del sur de Chile y su relación con indicadores productivos TT-Bulk tank milk selenium concentration in dairy herds from Southern Chile and its relationship to productive performance. *Arch. Med. Vet.* **2013**, *45*, 33–39. [CrossRef]
74. De Gregori, I.; Lobos, M.G.; Pinochet, H. Selenium and its redox speciation in rainwater from sites of Valparaíso region in Chile, impacted by mining activities of copper ores. *Water Res.* **2002**, *36*, 115–122. [CrossRef]
75. De Gregori, I.; Lobos, G.; Lobos, S.; Pinochet, H.; Potin-Gautier, M.; Astruc, M. Comparative study of copper and selenium pollution in agricultural ecosystems from valparaiso region, chile. *Environ. Technol.* **2000**, *21*, 307–316. [CrossRef]
76. Pinochet, H.; De Gregori, I.; Cavieres, M.F. Selenium concentration in compartments of aquatic ecosystems in Central Chile. *Bull. Environ. Contam. Toxicol.* **2002**, *69*, 139–146. [CrossRef]
77. Abejón, R.; Pérez-Acebo, H.; Garea, A. A Bibliometric Analysis of Research on Supported Ionic Liquid Membranes during the 1995–2015 Period: Study of the Main Applications and Trending Topics. *Membranes* **2017**, *7*, 63. [CrossRef]
78. Abejón, R.; Pérez-Acebo, H.; Clavijo, L. Alternatives for Chemical and Biochemical Lignin Valorization: Hot Topics from a Bibliometric Analysis of the Research Published During the 2000–2016 Period. *Processes* **2018**, *6*, 98. [CrossRef]
79. Bhatt, Y.; Ghuman, K.; Dhir, A. Sustainable manufacturing. Bibliometrics and content analysis. *J. Clean. Prod.* **2020**, *260*, 120988. [CrossRef]
80. Mallawaarachchi, H.; Sandanayake, Y.; Karunasena, G.; Liu, C. Unveiling the conceptual development of industrial symbiosis: Bibliometric analysis. *J. Clean. Prod.* **2020**, *258*, 120618. [CrossRef]
81. Colares, G.S.; Dell'Osbel, N.; Wiesel, P.G.; Oliveira, G.A.; Lemos, P.H.Z.; da Silva, F.P.; Lutterbeck, C.A.; Kist, L.T.; Machado, Ê.L. Floating treatment wetlands: A review and bibliometric analysis. *Sci. Total Environ.* **2020**, *714*, 136776. [CrossRef] [PubMed]
82. Andreo-Martínez, P.; Ortiz-Martínez, V.M.; García-Martínez, N.; de los Ríos, A.P.; Hernández-Fernández, F.J.; Quesada-Medina, J. Production of biodiesel under supercritical conditions: State of the art and bibliometric analysis. *Appl. Energy* **2020**, *264*, 114753. [CrossRef]
83. Badassa, B.B.; Sun, B.; Qiao, L. Sustainable transport infrastructure and economic returns: A bibliometric and visualization analysis. *Sustainability* **2020**, *12*, 2033. [CrossRef]
84. Dell'Osbel, N.; Colares, G.S.; de Oliveira, G.A.; de Souza, M.P.; Barbosa, C.V.; Machado, Ê.L. Bibliometric Analysis of Phosphorous Removal Through Constructed Wetlands. *Water. Air. Soil Pollut.* **2020**, *231*, 117. [CrossRef]
85. Li, W.; Dong, H.; Yu, H.; Wang, D.; Yu, H. Global characteristics and trends of research on ceramic membranes from 1998 to 2016: Based on bibliometric analysis combined with information visualization analysis. *Ceram. Int.* **2018**, *44*, 6926–6934. [CrossRef]
86. Md Khudzari, J.; Kurian, J.; Tartakovsky, B.; Raghavan, G.S.V. Bibliometric analysis of global research trends on microbial fuel cells using Scopus database. *Biochem. Eng. J.* **2018**, *136*, 51–60. [CrossRef]

87. Gonçalves, M.C.P.; Kieckbusch, T.G.; Perna, R.F.; Fujimoto, J.T.; Morales, S.A.V.; Romanelli, J.P. Trends on enzyme immobilization researches based on bibliometric analysis. *Process Biochem.* **2019**, *76*, 95–110. [CrossRef]
88. Yang, F.; Qiu, D. Exploring coal spontaneous combustion by bibliometric analysis. *Process Saf. Environ. Prot.* **2019**, *132*, 1–10. [CrossRef]
89. de Miranda, D.M.V.; Dutra, L.D.S.; Way, D.; Amaral, N.; Wegenast, F.; Scaldaferri, M.C.; Jesus, N.; Pinto, J.C. A bibliometric survey of Paraffin/Olefin separation using membranes. *Membranes* **2019**, *9*, 157. [CrossRef]
90. Zhao, L.; Dai, T.; Qiao, Z.; Sun, P.; Hao, J.; Yang, Y. Application of artificial intelligence to wastewater treatment: A bibliometric analysis and systematic review of technology, economy, management, and wastewater reuse. *Process Saf. Environ. Prot.* **2020**, *133*, 169–182. [CrossRef]
91. Tang, Y.; Long, X.; Wu, M.; Yang, S.; Gao, N.; Xu, B.; Dutta, S. Bibliometric review of research trends on disinfection by-products in drinking water during 1975–2018. *Sep. Purif. Technol.* **2020**, *241*, 116741. [CrossRef]
92. Blinova, I.; Muna, M.; Heinlaan, M.; Lukjanova, A.; Kahru, A. Potential hazard of lanthanides and lanthanide-based nanoparticles to aquatic ecosystems: Data gaps, challenges and future research needs derived from bibliometric analysis. *Nanomaterials* **2020**, *10*, 328. [CrossRef] [PubMed]
93. Abejón, R.; Garea, A. A bibliometric analysis of research on arsenic in drinking water during the 1992–2012 period: An outlook to treatment alternatives for arsenic removal. *J. Water Process Eng.* **2015**, *6*, 105–119. [CrossRef]
94. Martinho, V.J.P.D. Best management practices from agricultural economics: Mitigating air, soil and water pollution. *Sci. Total Environ.* **2019**, *688*, 346–360. [CrossRef] [PubMed]
95. Li, W.; Chen, X.; Xie, L.; Liu, Z.; Xiong, X. Bioelectrochemical systems for groundwater remediation: The development trend and research front revealed by bibliometric analysis. *Water* **2019**, *11*, 1532. [CrossRef]
96. Sun, J.; Wang, M.-H.; Ho, Y.-S. A historical review and bibliometric analysis of research on estuary pollution. *Mar. Pollut. Bull.* **2012**, *64*, 13–21. [CrossRef]
97. Blettler, M.C.M.; Abrial, E.; Khan, F.R.; Sivri, N.; Espinola, L.A. Freshwater plastic pollution: Recognizing research biases and identifying knowledge gaps. *Water Res.* **2018**, *143*, 416–424. [CrossRef]
98. Yang, B.; Huang, K.; Sun, D.; Zhang, Y. Mapping the scientific research on non-point source pollution: A bibliometric analysis. *Environ. Sci. Pollut. Res.* **2017**, *24*, 4352–4366. [CrossRef]
99. López-Vicente, M.; Wu, G.-L. Soil and water conservation in agricultural and forestry systems. *Water* **2019**, *11*, 1937. [CrossRef]
100. Hu, J.; Ma, Y.; Zhang, L.; Gan, F.; Ho, Y.S. A historical review and bibliometric analysis of research on lead in drinking water field from 1991 to 2007. *Sci. Total Environ.* **2010**, *408*, 1738–1744. [CrossRef] [PubMed]
101. Fu, H.-Z.; Wang, M.-H.; Ho, Y.-S. Mapping of drinking water research: A bibliometric analysis of research output during 1992–2011. *Sci. Total Environ.* **2013**, *443*, 757–765. [CrossRef] [PubMed]
102. Shi, G.; Zeng, H.; Chang, W.-J. Review on pollution ecological environmental effects of coastal zone in China. *Chin. J. Ecol.* **2019**, *38*, 576–585. [CrossRef]
103. Zhang, S.; Mao, G.; Crittenden, J.; Liu, X.; Du, H. Groundwater remediation from the past to the future: A bibliometric analysis. *Water Res.* **2017**, *119*, 114–125. [CrossRef]
104. *Scopus Content Coverage Guide*; Version 08.17; Scopus: Amsterdam, The Netherlands, 2017.
105. Yi, H.; Jie, W. A bibliometric study of the trend in articles related to eutrophication published in Science Citation Index. *Scientometrics* **2011**, *89*, 919–927. [CrossRef]
106. Melitz, J. English as a lingua franca: Facts, benefits and costs. *World Econ.* **2018**, *41*, 1750–1774. [CrossRef]
107. Hamel, R.E. The dominance of English in the international scientific periodical literature and the future of language use in science. *AILA Rev.* **2007**, *20*, 53–71. [CrossRef]
108. Liu, X.; Chen, X. CJK languages or English: Languages used by academic journals in China, Japan, and Korea. *J. Sch. Publ.* **2019**, *50*, 201–214. [CrossRef]
109. Abdennadher, A.; Ramírez, F.; Romdhane, M.S.; Ruiz, X.; Jover, L.; Sanpera, C. Little Egret (Egretta garzetta) as a bioindicator of trace element pollution in Tunisian aquatic ecosystems. *Environ. Monit. Assess.* **2011**, *175*, 677–684. [CrossRef]
110. Nkono, N.A.; Asubiojo, O.I. Elemental composition of drinking water supplies in three states in Southeastern Nigeria. *J. Radioanal. Nucl. Chem.* **1998**, *227*, 117–119. [CrossRef]
111. Frisbie, S.H.; Mitchell, E.J.; Mastera, L.J.; Maynard, D.M.; Yusuf, A.Z.; Siddiq, M.Y.; Ortega, R.; Dunn, R.K.; Westerman, D.S.; Bacquart, T.; et al. Public health strategies for western Bangladesh that address arsenic manganese, uranium, and other toxic elements in drinking water. *Environ. Health Perspect.* **2009**, *117*, 410–416. [CrossRef] [PubMed]
112. El-Badry, A.E.M.A.; Khalifa, M.M. The occurrence and distribution of high-arsenic, selenium, tin and antimony in bottom sediments of Burullus lagoon and its effects on human health, Egypt. *J. African Earth Sci.* **2017**, *136*, 305–311. [CrossRef]
113. Weber, L.W.D.; Boll, M.; Stampfl, A. Hepatotoxicity and mechanism of action of haloalkanes: Carbon tetrachloride as a toxicological model. *Crit. Rev. Toxicol.* **2003**, *33*, 105–136. [CrossRef] [PubMed]
114. El-Demerdash, F.M. Antioxidant effect of vitamin E and selenium on lipid peroxidation, enzyme activities and biochemical parameters in rats exposed to aluminium. *J. Trace Elem. Med. Biol.* **2004**, *18*, 113–121. [CrossRef] [PubMed]
115. Navas-Acien, A.; Sharrett, A.R.; Silbergeld, E.K.; Schwartz, B.S.; Nachman, K.E.; Burke, T.A.; Guallar, E. Arsenic exposure and cardiovascular disease: A systematic review of the epidemiologic evidence. *Am. J. Epidemiol.* **2005**, *162*, 1037–1049. [CrossRef]
116. Kalia, K.; Flora, S.J.S. Strategies for safe and effective therapeutic measures for chronic arsenic and lead poisoning. *J. Occup. Health* **2005**, *47*, 1–21. [CrossRef]

117. Tyler, C.R.; Allan, A.M. The Effects of Arsenic Exposure on Neurological and Cognitive Dysfunction in Human and Rodent Studies: A Review. *Curr. Environ. Health reports* **2014**, *1*, 132–147. [CrossRef]
118. Samet, J.M.; Avila-Tang, E.; Boffetta, P.; Hannan, L.M.; Olivo-Marston, S.; Thun, M.J.; Rudin, C.M. Lung cancer in never smokers: Clinical epidemiology and environmental risk factors. *Clin. Cancer Res.* **2009**, *15*, 5626–5645. [CrossRef]
119. Silvera, S.A.N.; Rohan, T.E. Trace elements and cancer risk: A review of the epidemiologic evidence. *Cancer Causes Control* **2007**, *18*, 7–27. [CrossRef]
120. McLaughlin, M.J.; Parker, D.R.; Clarke, J.M. Metals and micronutrients—Food safety issues. *Field Crop. Res.* **1999**, *60*, 143–163. [CrossRef]
121. Roychowdhury, T.; Tokunaga, H.; Ando, M. Survey of arsenic and other heavy metals in food composites and drinking water and estimation of dietary intake by the villagers from an arsenic-affected area of West Bengal, India. *Sci. Total Environ.* **2003**, *308*, 15–35. [CrossRef]
122. Cao, S.; Duan, X.; Zhao, X.; Ma, J.; Dong, T.; Huang, N.; Sun, C.; He, B.; Wei, F. Health risks from the exposure of children to As, Se, Pb and other heavy metals near the largest coking plant in China. *Sci. Total Environ.* **2014**, *472*, 1001–1009. [CrossRef] [PubMed]
123. Zhang, M.; Reardon, E.J. Removal of B, Cr, Mo, and Se from wastewater by incorporation into hydrocalumite and ettringite. *Environ. Sci. Technol.* **2003**, *37*, 2947–2952. [CrossRef] [PubMed]
124. Hashim, M.A.; Mukhopadhyay, S.; Sahu, J.N.; Sengupta, B. Remediation technologies for heavy metal contaminated groundwater. *J. Environ. Manag.* **2011**, *92*, 2355–2388. [CrossRef]
125. Järup, L. Hazards of heavy metal contamination. *Br. Med. Bull.* **2003**, *68*, 167–182. [CrossRef]
126. Wang, A.; Barber, D.; Pfeiffer, C.J. Protective effects of selenium against mercury toxicity in cultured Atlantic spotted dolphin (*Stenella plagiodon*) renal cells. *Arch. Environ. Contam. Toxicol.* **2001**, *41*, 403–409. [CrossRef]
127. Cuvin-Aralar, M.L.A.; Furness, R.W. Mercury and selenium interaction: A review. *Ecotoxicol. Environ. Saf.* **1991**, *21*, 348–364. [CrossRef]
128. Frisbie, S.H.; Ortega, R.; Maynard, D.M.; Sarkar, B. The concentrations of arsenic and other toxic elements in Bangladesh's drinking water. *Environ. Health Perspect.* **2002**, *110*, 1147–1153. [CrossRef]
129. Suzuki, J.; Katsuki, Y.; Ogawa, H.; Suzuki, K.; Matsumoto, H.; Yasuda, K. Concentration of trace elements in bottled drinking water. *J. Food Hyg. Soc. Jpn.* **2000**, *41*, 387–396. [CrossRef]
130. Herrera-Viedma, E.; López-Robles, J.R.; Guallar, J.; Cobo, M.J. Global trends in coronavirus research at the time of COVID-19: A general bibliometric approach and content analysis using SciMAT. *Prof. Inf.* **2020**, *29*, 11. [CrossRef]
131. Cobo, M.J.; López-Herrera, A.G.; Herrera-Viedma, E.; Herrera, F. SciMAT: A New Science Mapping Analysis Software Tool. *J. Am. Soc. Inf. Sci. Technol.* **2012**, *63*, 1609–1630. [CrossRef]
132. Furstenau, L.B.; Rabaioli, B.; Sott, M.K.; Cossul, D.; Bender, M.S.; Farina, E.M.J.D.M.; Filho, F.N.B.; Severo, P.P.; Dohan, M.S.; Bragazzi, N.L. A bibliometric network analysis of coronavirus during the first eight months of COVID-19 in 2020. *Int. J. Environ. Res. Public Health* **2021**, *18*, 952. [CrossRef] [PubMed]
133. Kolling, M.L.; Furstenau, L.B.; Sott, M.K.; Rabaioli, B.; Ulmi, P.H.; Bragazzi, N.L.; Tedesco, L.P.C. Data mining in healthcare: Applying strategic intelligence techniques to depict 25 years of research development. *Int. J. Environ. Res. Public Health* **2021**, *18*, 3099. [CrossRef] [PubMed]
134. Cobo, M.J.; López-Herrera, A.G.; Herrera-Viedma, E.; Herrera, F. An approach for detecting, quantifying, and visualizing the evolution of a research field: A practical application to the Fuzzy Sets Theory field. *J. Informetr.* **2011**, *5*, 146–166. [CrossRef]
135. Devi, P.; Singh, P.; Malakar, A.; Snow, D. *Selenium Contamination in Water*; John Wiley and Sons Ltd.: Oxford, UK, 2021.
136. Spallholz, J.E.; Boylan, L.M.; Rhaman, M.M. Environmental hypothesis: Is poor dietary selenium intake an underlying factor for arsenicosis and cancer in Bangladesh and West Bengal, India? *Sci. Total Environ.* **2004**, *323*, 21–32. [CrossRef]
137. Sandy, T.; DiSante, C. *Review of Available Technologies for the Removal of Selenium from Water*; North American Metals Council: Washington, DC, USA, 2010.
138. Frankenberger, W.T.; Amrhein, C.; Fan, T.W.M.; Flaschi, D.; Glater, J.; Kartinen, E.; Kovac, K.; Lee, E.; Ohlendorf, H.M.; Owens, L.; et al. Advanced treatment technologies in the remediation of seleniferous drainage waters and sediments. *Irrig. Drain. Syst.* **2004**, *18*, 19–42. [CrossRef]
139. He, Y.; Xiang, Y.; Zhou, Y.; Yang, Y.; Zhang, J.; Huang, H.; Shang, C.; Luo, L.; Gao, J.; Tang, L. Selenium contamination, consequences and remediation techniques in water and soils: A review. *Environ. Res.* **2018**, *164*, 288–301. [CrossRef]
140. Kapoor, A.; Tanjore, S.; Viraraghavan, T. Removal of selenium from water and waste water. *Int. J. Environ. Stud.* **1995**, *49*, 137–147. [CrossRef]
141. Santos, S.; Ungureanu, G.; Boaventura, R.; Botelho, C. Selenium contaminated waters: An overview of analytical methods, treatment options and recent advances in sorption methods. *Sci. Total Environ.* **2015**, *521–522*, 246–260. [CrossRef]
142. Sharma, V.K.; Sohn, M.; Mcdonald, T.J. *Remediation of Selenium in Water: A Review*; Elsevier: Amsterdam, The Netherlands, 2019; ISBN 9780128147900.
143. Tan, L.C.; Nancharaiah, Y.V.; van Hullebusch, E.D.; Lens, P.N.L. Selenium: Environmental significance, pollution, and biological treatment technologies. *Biotechnol. Adv.* **2016**, *34*, 886–907. [CrossRef]
144. Duc, M.; Lefevre, G.; Fedoroff, M.; Jeanjean, J.; Rouchaud, J.C.; Monteil-Rivera, F.; Dumonceau, J.; Milonjic, S. Sorption of selenium anionic species on apatites and iron oxides from aqueous solutions. *J. Environ. Radioact.* **2003**, *70*, 61–72. [CrossRef]
145. Franzblau, R.E.; Daughney, C.J.; Moreau, M.; Weisener, C.G. Selenate adsorption to composites of Escherichia coli and iron oxide during the addition, oxidation, and hydrolysis of Fe(II). *Chem. Geol.* **2014**, *383*, 180–193. [CrossRef]
146. Yoon, I.H.; Bang, S.; Kim, K.W.; Kim, M.G.; Park, S.Y.; Choi, W.K. Selenate removal by zero-valent iron in oxic condition: The role of Fe(II) and selenate removal mechanism. *Environ. Sci. Pollut. Res.* **2016**, *23*, 1081–1090. [CrossRef]

147. Lo, S.L.; Chen, T.Y. Adsorption of Se(IV) and Se(VI) on an iron-coated sand from water. *Chemosphere* **1997**, *35*, 919–930. [CrossRef]
148. Gui, M.; Papp, J.K.; Colburn, A.S.; Meeks, N.D.; Weaver, B.; Wilf, I.; Bhattacharyya, D. Engineered iron/iron oxide functionalized membranes for selenium and other toxic metal removal from power plant scrubber water. *J. Memb. Sci.* **2015**, *488*, 79–91. [CrossRef] [PubMed]
149. Dong, H.; Chen, Y.; Sheng, G.; Li, J.; Cao, J.; Li, Z.; Li, Y. The roles of a pillared bentonite on enhancing Se(VI) removal by ZVI and the influence of co-existing solutes in groundwater. *J. Hazard. Mater.* **2016**, *304*, 306–312. [CrossRef]
150. Fu, F.; Lu, J.; Cheng, Z.; Tang, B. Removal of selenite by zero-valent iron combined with ultrasound: Se(IV) concentration changes, Se(VI) generation, and reaction mechanism. *Ultrason. Sonochem.* **2016**, *29*, 328–336. [CrossRef]
151. Okibe, N.; Sueishi, K.; Koga, M.; Masaki, Y.; Hirajima, T.; Sasaki, K.; Heguri, S.; Asano, S. Selenium (Se) removal from copper refinery wastewater using a combination of zero-valent iron (ZVI) and Se(VI)-reducing bacterium, thaurea selenatis. *Mater. Trans.* **2015**, *56*, 889–894. [CrossRef]
152. Qin, H.; Sun, Y.; Yang, H.; Fan, P.; Qiao, J.; Guan, X. Unexpected effect of buffer solution on removal of selenite and selenate by zerovalent iron. *Chem. Eng. J.* **2018**, *334*, 296–304. [CrossRef]
153. Qin, H.; Li, J.; Yang, H.; Pan, B.; Zhang, W.; Guan, X. Coupled Effect of Ferrous Ion and Oxygen on the Electron Selectivity of Zerovalent Iron for Selenate Sequestration. *Environ. Sci. Technol.* **2017**, *51*, 5090–5097. [CrossRef]
154. Tang, C.; Huang, Y.H.; Zeng, H.; Zhang, Z. Reductive removal of selenate by zero-valent iron: The roles of aqueous Fe^{2+} and corrosion products, and selenate removal mechanisms. *Water Res.* **2014**, *67*, 166–174. [CrossRef] [PubMed]
155. Fukushi, K.; Sverjensky, D.A. A surface complexation model for sulfate and selenate on iron oxides consistent with spectroscopic and theoretical molecular evidence. *Geochim. Cosmochim. Acta* **2007**, *71*, 1–24. [CrossRef]
156. Peak, D.; Sparks, D.L. Mechanisms of selenate adsorption on iron oxides and hydroxides. *Environ. Sci. Technol.* **2002**, *36*, 1460–1466. [CrossRef]
157. Rovira, M.; Giménez, J.; Martínez, M.; Martínez-Lladó, X.; de Pablo, J.; Martí, V.; Duro, L. Sorption of selenium(IV) and selenium(VI) onto natural iron oxides: Goethite and hematite. *J. Hazard. Mater.* **2008**, *150*, 279–284. [CrossRef] [PubMed]
158. Yang, Z.; Xu, H.; Shan, C.; Jiang, Z.; Pan, B. Effects of brining on the corrosion of ZVI and its subsequent As(III/V) and Se(IV/VI) removal from water. *Chemosphere* **2017**, *170*, 251–259. [CrossRef]
159. Donovan, J.J.; Ziemkiewicz, P.F. Selenium Adsorption onto Iron Oxide Layers beneath Coal-Mine Overburden Spoil. *J. Environ. Qual.* **2013**, *42*, 1402–1411. [CrossRef]
160. Jacukowicz-Sobala, I.; Ociński, D.; Kociołek-Balawejder, E. Iron and aluminium oxides containing industrial wastes as adsorbents of heavy metals: Application possibilities and limitations. *Waste Manag. Res.* **2015**, *33*, 612–629. [CrossRef]
161. Lee, C.G.; Kim, S.B. Removal of arsenic and selenium from aqueous solutions using magnetic iron oxide nanoparticle/multi-walled carbon nanotube adsorbents. *Desalin. Water Treat.* **2016**, *57*, 28323–28339. [CrossRef]
162. Zelmanov, G.; Semiat, R. Selenium removal from water and its recovery using iron (Fe^{3+}) oxide/hydroxide-based nanoparticles sol (NanoFe) as an adsorbent. *Sep. Purif. Technol.* **2013**, *103*, 167–172. [CrossRef]
163. Yang, Z.; Shan, C.; Zhang, W.; Jiang, Z.; Guan, X.; Pan, B. Temporospatial evolution and removal mechanisms of As(V) and Se(VI) in ZVI column with H_2O_2 as corrosion accelerator. *Water Res.* **2016**, *106*, 461–469. [CrossRef]
164. Wu, B.; Jia, H.; Yang, Z.; Shan, C.; Weng, J.; Xu, Z.; Pan, B. Enhanced removal of selenate from mining effluent by H_2O_2 /HCl-pretreated zero-valent iron. *Water Sci. Technol.* **2018**, *78*, 2404–2413. [CrossRef] [PubMed]
165. Shan, C.; Chen, J.; Yang, Z.; Jia, H.; Guan, X.; Zhang, W.; Pan, B. Enhanced removal of Se(VI) from water via pre-corrosion of zero-valent iron using H_2O_2/HCl: Effect of solution chemistry and mechanism investigation. *Water Res.* **2018**, *133*, 173–181. [CrossRef] [PubMed]
166. Li, Y.; Guo, X.; Dong, H.; Luo, X.; Guan, X.; Zhang, X.; Xia, X. Selenite removal from groundwater by zero-valent iron (ZVI) in combination with oxidants. *Chem. Eng. J.* **2018**, *345*, 432–440. [CrossRef]
167. Fan, P.; Li, L.; Sun, Y.; Qiao, J.; Xu, C.; Guan, X. Selenate removal by Fe0 coupled with ferrous iron, hydrogen peroxide, sulfidation, and weak magnetic field: A comparative study. *Water Res.* **2019**, *159*, 375–384. [CrossRef]
168. Liang, L.; Guan, X.; Huang, Y.; Ma, J.; Sun, X.; Qiao, J.; Zhou, G. Efficient selenate removal by zero-valent iron in the presence of weak magnetic field. *Sep. Purif. Technol.* **2015**, *156*, 1064–1072. [CrossRef]
169. Zhang, X.; Li, J.; Sun, Y.; Li, L.; Pan, B.; Zhang, W.; Guan, X. Aging of zerovalent iron in various coexisting solutes: Characteristics, reactivity toward selenite and rejuvenation by weak magnetic field. *Sep. Purif. Technol.* **2018**, *191*, 94–100. [CrossRef]
170. Dynes, J.J.; Huang, P.M. Influence of Organic Acids on Selenite Sorption by Poorly Ordered Aluminum Hydroxides. *Soil Sci. Soc. Am. J.* **1997**, *61*, 772–783. [CrossRef]
171. Jegadeesan, G.; Mondal, K.; Lalvani, S.B. Comparative study of selenite adsorption on carbon based adsorbents and activated alumina. *Environ. Technol.* **2003**, *24*, 1049–1059. [CrossRef]
172. Jordan, N.; Franzen, C.; Lützenkirchen, J.; Foerstendorf, H.; Hering, D.; Weiss, S.; Heim, K.; Brendler, V. Adsorption of selenium(VI) onto nano transition alumina. *Environ. Sci. Nano* **2018**, *5*, 1661–1669. [CrossRef]
173. Papelis, C.; Roberts, P.V.; Leckie, J.O. Modeling the Rate of Cadmium and Selenite Adsorption on Micro- and Mesoporous Transition Aluminas. *Environ. Sci. Technol.* **1995**, *29*, 1099–1108. [CrossRef]
174. Su, T.; Guan, X.; Gu, G.; Wang, J. Adsorption characteristics of As(V), Se(IV), and V(V) onto activated alumina: Effects of pH, surface loading, and ionic strength. *J. Colloid Interface Sci.* **2008**, *326*, 347–353. [CrossRef] [PubMed]

175. Su, T.; Guan, X.; Tang, Y.; Gu, G.; Wang, J. Predicting competitive adsorption behavior of major toxic anionic elements onto activated alumina: A speciation-based approach. *J. Hazard. Mater.* **2010**, *176*, 466–472. [CrossRef] [PubMed]
176. Ji, Y.; Li, L.; Wang, Y. Tin Selenium removal by activated alumina in batch and continuous-flow reactors. *Water Environ. Res.* **2020**, *92*, 51–59. [CrossRef] [PubMed]
177. Ghosh, M.M.; Cox, C.D.; Yuan-Pan, J.R. Adsorption of selenium on hydrous alumina. *Environ. Prog.* **1994**, *13*, 79–88. [CrossRef]
178. Rashad, G.M.; Soliman, M.A.; Mahmoud, M.R. Removal of radioselenium oxyanions from aqueous solutions by adsorption onto hydrous zirconium oxide. *J. Radioanal. Nucl. Chem.* **2018**, *317*, 593–603. [CrossRef]
179. Wu, X.; Guo, X.; Zhang, L. Fabrication of Porous Zirconia Microspheres as an Efficient Adsorbent for Removal and Recovery of Trace Se(IV) and Te(IV). *Ind. Eng. Chem. Res.* **2019**, *58*, 342–349. [CrossRef]
180. Karatchevtseva, I.; Astoux, M.; Cassidy, D.J.; Yee, P.; Bartlett, J.R.; Griffith, C.S. Synthesis and characterization of functionalized silica-based nanohybrid materials for oxyanions adsorption. *Langmuir* **2010**, *26*, 8327–8335. [CrossRef]
181. Labaran, B.A.; Vohra, M.S. Competitive adsorption of selenite [se(Iv)], selenate [se(vi)] and selenocyanate [secn^{-}] species onto TiO_2: Experimental findings and surface complexation modelling. *Desalin. Water Treat.* **2018**, *124*, 267–278. [CrossRef]
182. Zhang, L.; Liu, N.; Yang, L.; Lin, Q. Sorption behavior of nano-TiO_2 for the removal of selenium ions from aqueous solution. *J. Hazard. Mater.* **2009**, *170*, 1197–1203. [CrossRef]
183. Kim, J.; Lim, H.B. Separation of selenite from inorganic selenium ions using TiO_2 magnetic nanoparticles. *Bull. Korean Chem. Soc.* **2013**, *34*, 3362–3366. [CrossRef]
184. Suzuki, T.M.; Tanco, M.L.; Tanaka, D.A.P.; Matsunaga, H.; Yokoyama, T. Adsorption characteristics and removal of oxo-anions of arsenic and selenium on the porous polymers loaded with monoclinic hydrous zirconium oxide adsorption characteristics and removal of oxo-anions of arsenic and seleni. *Sep. Sci. Technol.* **2001**, *36*, 103–111. [CrossRef]
185. Mishra, D. *Characterization Studies of Deccan Zeolites for the Removal of the Selenium from Waste Water*; Elsevier: Amsterdam, The Netherlands, 2008; Volume 174.
186. Yusof, A.M.; Idris, N.H.; Malek, N.A.N.N.; Wood, A.K.H. Use of granulated modified zeolite Y for the removal of inorganic arsenic and selenium species. *J. Radioanal. Nucl. Chem.* **2009**, *281*, 269–272. [CrossRef]
187. Zonkhoeva, E.L.; Sanzhanova, S.S. Infrared Spectroscopy Study of the Sorption of Selenium (IV) on Natural Zeolites. *Russ. J. Phys. Chem.* **2011**, *85*, 1339–1342. [CrossRef]
188. Prieto, J.C.G.; Galende, P.P.; Silverio, J.M.C.; Roig, M.G. A pilot plant study of the processes of filtration and adsorption of drinking water through granular activated carbons: A comparative study. *Water Sci. Technol. Water Supply* **2013**, *13*, 74–88. [CrossRef]
189. Wasewar, K.L.; Prasad, B.; Gulipalli, S. Removal of selenium by adsorption onto granular activated carbon (GAC) and powdered activated carbon (PAC). *Clean-Soil Air Water* **2009**, *37*, 872–883. [CrossRef]
190. Kwon, J.H.; Wilson, L.D.; Sammynaiken, R. Sorptive uptake of selenium with magnetite and its supported materials onto activated carbon. *J. Colloid Interface Sci.* **2015**, *457*, 388–397. [CrossRef]
191. Dobrowolski, R.; Otto, M. Preparation and evaluation of Fe-loaded activated carbon for enrichment of selenium for analytical and environmental purposes. *Chemosphere* **2013**, *90*, 683–690. [CrossRef]
192. Jegadeesan, G.B.; Mondal, K.; Lalvani, S.B. Adsorption of Se (IV) and Se (VI) Using Copper-Impregnated Activated Carbon and Fly Ash-Extracted Char Carbon. *Water. Air. Soil Pollut.* **2015**, *226*, 234. [CrossRef]
193. Das, N.N.; Konar, J.; Mohanta, M.K.; Srivastava, S.C. Adsorption of Cr(VI) and Se(IV) from their aqueous solutions onto Zr^{4+}-substituted ZnAl/MgAl-layered double hydroxides: Effect of Zr^{4+} substitution in the layer. *J. Colloid Interface Sci.* **2004**, *270*, 1–8. [CrossRef]
194. Li, D.; Yan, W.; Guo, X.; Tian, Q.; Xu, Z.; Zhu, L. Removal of selenium from caustic solution by adsorption with Ca[sbnd]Al layered double hydroxides. *Hydrometallurgy* **2020**, *191*, 105231. [CrossRef]
195. Liu, R.; Frost, R.L.; Martens, W.N. Absorption of the selenite anion from aqueous solutions by thermally activated layered double hydroxide. *Water Res.* **2009**, *43*, 1323–1329. [CrossRef] [PubMed]
196. Mandal, S.; Mayadevi, S.; Kulkarni, B.D. Adsorption of aqueous selenite [Se(IV)] species on synthetic layered double Hydroxide Materials. *Ind. Eng. Chem. Res.* **2009**, *48*, 7893–7898. [CrossRef]
197. Hongo, T.; Iemura, T.; Yamazaki, A. Adsorption ability for several harmful anions and thermal behavior of Zn-Fe layered double hydroxide. *J. Ceram. Soc. Japan* **2008**, *116*, 192–197. [CrossRef]
198. You, Y.; Vance, G.F.; Zhao, H. Selenium adsorption on Mg-Al and Zn-Al layered double hydroxides. *Appl. Clay Sci.* **2001**, *20*, 13–25. [CrossRef]
199. Asiabi, H.; Yamini, Y.; Shamsayei, M. Highly selective and efficient removal of arsenic(V), chromium(VI) and selenium(VI) oxyanions by layered double hydroxide intercalated with zwitterionic glycine. *J. Hazard. Mater.* **2017**, *339*, 239–247. [CrossRef]
200. Hu, B.; Ye, F.; Jin, C.; Ma, X.; Huang, C.; Sheng, G.; Ma, J.; Wang, X.; Huang, Y. The enhancement roles of layered double hydroxide on the reductive immobilization of selenate by nanoscale zero valent iron: Macroscopic and microscopic approaches. *Chemosphere* **2017**, *184*, 408–416. [CrossRef]
201. Chubar, N. The influence of sulfate on selenate sorption on Mg-Al-CO_3 layered double hydroxides prepared by fine inorganic sol-gel synthesis studied by X-ray photoelectron spectroscopy. *Appl. Surf. Sci.* **2018**, *459*, 281–291. [CrossRef]
202. Mahmoud, M.R.; Soliman, M.A.; Ali, A.H.; Othman, S.H. Kinetic studies on radio-selenium uptake by ion exchange resin. *Sep. Sci. Technol.* **2016**, *51*, 976–989. [CrossRef]

203. Martins, K.; Johnson, J.; Leber, K.; Srinivasan, R.; Heller, B. Bench- and pilot-scale testing of ion exchange and zero valent iron technologies for selenium removal from a surface coal mine run-off water. In Proceedings of the 85th Annual Water Environment Federation Technical Exhibition and Conference (WEFTEC 2012), New Orleans, LA, USA, 29 September–3 October 2012; Volume 1, pp. 318–338.
204. Nishimura, T.; Hashimoto, H.; Nakayama, M. Removal of selenium(VI) from aqueous solution with polyamine-type weakly basic ion exchange resin. *Sep. Sci. Technol.* **2007**, *42*, 3155–3167. [CrossRef]
205. Shi, Y.; Shi, Y.; Wang, L. Removal of Se(VI) from raw water by ion exchange process. *Adv. Mater. Res.* **2012**, *430–432*, 941–948. [CrossRef]
206. Staicu, L.C.; Morin-Crini, N.; Crini, G. Desulfurization: Critical step towards enhanced selenium removal from industrial effluents. *Chemosphere* **2017**, *172*, 111–119. [CrossRef] [PubMed]
207. Tan, L.C.; Calix, E.M.; Rene, E.R.; Nancharaiah, Y.V.; Van Hullebusch, E.D.; Lens, P.N.L. Amberlite IRA-900 Ion Exchange Resin for the Sorption of Selenate and Sulfate: Equilibrium, Kinetic, and Regeneration Studies. *J. Environ. Eng.* **2018**, *144*, 04018110. [CrossRef]
208. Cálix, E.M.; Tan, L.C.; Rene, E.R.; Nancharaiah, Y.V.; Van Hullebusch, E.D.; Lens, P.N.L. Simultaneous removal of sulfate and selenate from wastewater by process integration of an ion exchange column and upflow anaerobic sludge blanket bioreactor. *Sep. Sci. Technol.* **2019**, *54*, 1387–1399. [CrossRef]
209. Baes, A.U.; Okuda, T.; Nishijima, W.; Shoto, E.; Okada, M. Adsorption and ion exchange of some groundwater anion contaminants in an amine modified coconut coir. *Water Scie* **1997**, *35*, 89–95. [CrossRef]
210. Marshall, W.E.; Wartelle, L.H. An anion exchange resin from soybean hulls. *J. Chem. Technol. Biotechnol.* **2004**, *79*, 1286–1292. [CrossRef]
211. Hamed, M.M.; Holiel, M.; El-Aryan, Y.F. Removal of selenium and iodine radionuclides from waste solutions using synthetic inorganic ion exchanger. *J. Mol. Liq.* **2017**, *242*, 722–731. [CrossRef]
212. Pakzadeh, B.; Batista, J.R. Impacts of cocontaminants on the performances of perchlorate and nitrate specialty ion-exchange resins. *Ind. Eng. Chem. Res.* **2011**, *50*, 7484–7493. [CrossRef]
213. Schilde, U.; Kraudelt, H.; Uhlemann, E. Separation of the oxoanions of germanium, tin, arsenic, antimony, tellurium, molybdenum and tungsten with a special chelating resin containing methylaminoglucitol groups. *React. Polym.* **1994**, *22*, 101–106. [CrossRef]
214. Namara, C.M.; Torroba, J.; Deacon, A. New Smopex® Ion exchange materials for the removal of selenium from industrial effluent streams. *Johns. Matthey Technol. Rev.* **2015**, *59*, 334–352. [CrossRef]
215. Kawamoto, D.; Yamanishi, Y.; Ohashi, H.; Yonezu, K.; Honma, T.; Sugiyama, T.; Kobayashi, Y.; Okaue, Y.; Miyazaki, A.; Yokoyama, T. A new and practical Se(IV) removal method using Fe^{3+} type cation exchange resin. *J. Hazard. Mater.* **2019**, *378*, 120593. [CrossRef]
216. Stefaniak, J.; Dutta, A.; Verbinnen, B.; Shakya, M.; Rene, E.R. Selenium removal from mining and process wastewater: A systematic review of available technologies. *J. Water Supply Res. Technol.-AQUA* **2018**, *67*, 903–918. [CrossRef]
217. Komulainen, J.; Laitinen, R.S.; Suontamo, R.J. A theoretical study of the 77Se NMR and vibrational spectroscopic properties of SenS8-n ring molecules. *Can. J. Chem.* **2002**, *80*, 1435–1443. [CrossRef]
218. Jung, B.; Safan, A.; Batchelor, B.; Abdel-Wahab, A. Spectroscopic study of Se(IV) removal from water by reductive precipitation using sulfide. *Chemosphere* **2016**, *163*, 351–358. [CrossRef] [PubMed]
219. Geoffroy, N.; Demopoulos, G.P. The elimination of selenium(IV) from aqueous solution by precipitation with sodium sulfide. *J. Hazard. Mater.* **2011**, *185*, 148–154. [CrossRef] [PubMed]
220. Littlejohn, P.; Mohamm, F.; Kratochvil, D. Advancement in non-biological selenium removal treatment systems–Results of continuous pilot scale operations. In Proceedings of the Water Environment Federation Technical Exhibition and Conference 2017, Chicago, IL, USA, 2–4 October 2017; Volume 1, pp. 369–393. [CrossRef]
221. Wang, X.; Liu, H.; Shan, C.; Zhang, W.; Pan, B. A novel combined process for efficient removal of Se(VI) from sulfate-rich water: Sulfite/UV/Fe(III) coagulation. *Chemosphere* **2018**, *211*, 867–874. [CrossRef]
222. Shi, Y.; Wang, L.; Chen, Y.; Xu, D. Research on removing selenium from raw water by using Fe/Se co-precipitation system. *J. Water Supply Res. Technol.-AQUA* **2009**, *58*, 51–56. [CrossRef]
223. Hu, C.; Chen, Q.; Chen, G.; Liu, H.; Qu, J. Removal of Se(IV) and Se(VI) from drinking water by coagulation. *Sep. Purif. Technol.* **2015**, *142*, 65–70. [CrossRef]
224. Kalaitzidou, K.; Bakouros, L.; Mitrakas, M. Techno-economic evaluation of iron and aluminum coagulants on Se(IV) removal. *Water* **2020**, *12*, 672. [CrossRef]
225. Sakhi, D.; Rakhila, Y.; Elmchaouri, A.; Abouri, M.; Souabi, S.; Jada, A. *Optimization of Coagulation Flocculation Process for the Removal of Heavy Metals from Real Textile Wastewater*; Springer International Publishing: Berlin/Heidelberg, Germany, 2019; Volume 913, ISBN 9783030118808.
226. Staicu, L.C.; Van Hullebusch, E.D.; Oturan, M.A.; Ackerson, C.J.; Lens, P.N.L. Removal of colloidal biogenic selenium from wastewater. *Chemosphere* **2015**, *125*, 130–138. [CrossRef]
227. Hansen, H.K.; Peña, S.F.; Gutiérrez, C.; Lazo, A.; Lazo, P.; Ottosen, L.M. Selenium removal from petroleum refinery wastewater using an electrocoagulation technique. *J. Hazard. Mater.* **2019**, *364*, 78–81. [CrossRef]
228. Mavrov, V.; Stamenov, S.; Todorova, E.; Chmiel, H.; Erwe, T. New hybrid electrocoagulation membrane process for removing selenium from industrial wastewater. *Desalination* **2006**, *201*, 290–296. [CrossRef]
229. Carlo, P.L.; Owens, L.P.; Hanna, G.P.; Longley, K.E. The removal of selenium from water by slow sand filtration. *Water Sci. Technol.* **1992**, *26*, 2137–2140. [CrossRef]
230. Chellam, S.; Clifford, D.A. Physical-chemical treatment of groundwater contaminated by leachate from surface disposal of uranium tailings. *J. Environ. Eng.* **2002**, *128*, 942–952. [CrossRef]

231. Déon, S.; Deher, J.; Lam, B.; Crini, N.; Crini, G.; Fievet, P. Remediation of Solutions Containing Oxyanions of Selenium by Ultrafiltration: Study of Rejection Performances with and without Chitosan Addition. *Ind. Eng. Chem. Res.* **2017**, *56*, 10461–10471. [CrossRef]
232. Mariñas, B.J.; Selleck, R.E. Reverse osmosis treatment of multicomponent electrolyte solutions. *J. Memb. Sci.* **1992**, *72*, 211–229. [CrossRef]
233. Mariñas, B.J.; Urama, R.I. Modeling concentration-polarization in reverse osmosis spiral-wound elements. *J. Environ. Eng.* **1996**, *122*, 292–298. [CrossRef]
234. Mukherjee, P.; Sengupta, A.K. Ion exchange selectivity as a surrogate indicator of relative permeability of ions in reverse osmosis processes. *Environ. Sci. Technol.* **2003**, *37*, 1432–1440. [CrossRef]
235. Birkle, P.; Cid Vázquez, A.L.; Fong Aguilar, J.L. Legal Aspects and Technical Alternatives for the Treatment of Reservoir Brines at the Activo Luna Oilfield, Mexico. *Water Environ. Res.* **2005**, *77*, 68–77. [CrossRef]
236. He, Y.; Tang, Y.P.; Ma, D.; Chung, T.S. UiO-66 incorporated thin-film nanocomposite membranes for efficient selenium and arsenic removal. *J. Memb. Sci.* **2017**, *541*, 262–270. [CrossRef]
237. Malhotra, M.; Pal, M.; Pal, P. A response surface optimized nanofiltration-based system for efficient removal of selenium from drinking Water. *J. Water Process Eng.* **2020**, *33*, 101007. [CrossRef]
238. Chung, J.; Rittmann, B.E.; Her, N.; Lee, S.H.; Yoon, Y. Integration of H2-based membrane biofilm reactor with RO and NF membranes for removal of chromate and selenate. *Water. Air. Soil Pollut.* **2010**, *207*, 29–37. [CrossRef]
239. Richards, L.A.; Richards, B.S.; Schäfer, A.I. Renewable energy powered membrane technology: Salt and inorganic contaminant removal by nanofiltration/reverse osmosis. *J. Memb. Sci.* **2011**, *369*, 188–195. [CrossRef]
240. Subramani, A.; Cryer, E.; Liu, L.; Lehman, S.; Ning, R.Y.; Jacangelo, J.G. Impact of intermediate concentrate softening on feed water recovery of reverse osmosis process during treatment of mining contaminated groundwater. *Sep. Purif. Technol.* **2012**, *88*, 138–145. [CrossRef]
241. Thirunavukkarasu, O.S.; Phommavong, T.; Jin, Y.C.; Ferris, S.A. Performance of reverse osmosis and manganese greensand plants in removing naturally occurring substances in drinking water. *Water Qual. Res. J. Canada* **2013**, *49*, 72–81. [CrossRef]
242. Cingolani, D.; Fatone, F.; Frison, N.; Spinelli, M.; Eusebi, A.L. Pilot-scale multi-stage reverse osmosis (DT-RO) for water recovery from landfill leachate. *Waste Manag.* **2018**, *76*, 566–574. [CrossRef]
243. Kharaka, Y.K.; Ambats, G.; Presser, T.S.; Davis, R.A. Removal of selenium from contaminated agricultural drainage water by nanofiltration membranes. *Appl. Geochem.* **1996**, *11*, 797–802. [CrossRef]
244. He, Y.; Tang, Y.P.; Chung, T.S. Concurrent removal of selenium and arsenic from water using polyhedral oligomeric silsesquioxane (POSS)-polyamide thin-film nanocomposite nanofiltration membranes. *Ind. Eng. Chem. Res.* **2016**, *55*, 12929–12938. [CrossRef]
245. He, Y.; Liu, J.; Han, G.; Chung, T.S. Novel thin-film composite nanofiltration membranes consisting of a zwitterionic co-polymer for selenium and arsenic removal. *J. Memb. Sci.* **2018**, *555*, 299–306. [CrossRef]
246. He, Y.; Zhao, D.L.; Chung, T.S. Na+ functionalized carbon quantum dot incorporated thin-film nanocomposite membranes for selenium and arsenic removal. *J. Memb. Sci.* **2018**, *564*, 483–491. [CrossRef]
247. Zeeshan, M.H.; Khan, R.U.; Shafiq, M.; Sabir, A. Polyamide intercalated nanofiltration membrane modified with biofunctionalized core shell composite for efficient removal of Arsenic and Selenium from wastewater. *J. Water Process Eng.* **2020**, *34*, 101175. [CrossRef]
248. Mafu, L.D.; Msagati, T.A.M.; Mamba, B.B. The simultaneous stripping of arsenic and selenium from wastewaters using hollow-fibre supported liquid membranes. *Environ. Monit. Assess.* **2014**, *186*, 8865–8874. [CrossRef]
249. Ambe, S.; Katayama, O.; Ambe, F. Multitracer studies on the permeation of various elements through a supported liquid membrane containing TBP. *J. Radioanal. Nucl. Chem.* **2002**, *253*, 351–355. [CrossRef]
250. Noguerol, J.; Palet, C.; Valiente, M. Transport of selenite through a solid supported liquid membrane using sodium diethyldithiocarbamate, Na(DDTC), as carrier between hydrochloric acid solutions. *J. Memb. Sci.* **1997**, *134*, 261–269. [CrossRef]
251. Quiñones-Bolaños, E.; Zhou, H.; Parkin, G. Membrane pervaporation for wastewater reuse in microirrigation. *J. Environ. Eng.* **2005**, *131*, 1633–1643. [CrossRef]
252. Quiñones-Bolaños, E.; Zhou, H.; Soundararajan, R.; Otten, L. Water and solute transport in pervaporation hydrophilic membranes to reclaim contaminated water for micro-irrigation. *J. Memb. Sci.* **2005**, *252*, 19–28. [CrossRef]
253. Onorato, C.; Banasiak, L.J.; Schäfer, A.I. Inorganic trace contaminant removal from real brackish groundwater using electrodialysis. *Sep. Purif. Technol.* **2017**, *187*, 426–435. [CrossRef]
254. Meseck, S.L.; Cutter, G.A. Evaluating the biogeochemical cycle of selenium in San Francisco Bay through modeling. *Limnol. Oceanogr.* **2006**, *51*, 2018–2032. [CrossRef]
255. Bai, Y.N.; Wang, X.N.; Lu, Y.Z.; Fu, L.; Zhang, F.; Lau, T.C.; Zeng, R.J. Microbial selenite reduction coupled to anaerobic oxidation of methane. *Sci. Total Environ.* **2019**, *669*, 168–174. [CrossRef]
256. Bao, P.; Huang, H.; Hu, Z.Y.; Häggblom, M.M.; Zhu, Y.G. Impact of temperature, CO_2 fixation and nitrate reduction on selenium reduction, by a paddy soil Clostridium strain. *J. Appl. Microbiol.* **2013**, *114*, 703–712. [CrossRef]
257. He, Q.; Yao, K. Microbial reduction of selenium oxyanions by Anaeromyxobacter dehalogenans. *Bioresour. Technol.* **2010**, *101*, 3760–3764. [CrossRef]
258. Rosenfeld, C.E.; Kenyon, J.A.; James, B.R.; Santelli, C.M. Selenium (IV,VI) reduction and tolerance by fungi in an oxic environment. *Geobiology* **2017**, *15*, 441–452. [CrossRef] [PubMed]
259. Zhang, X.; Fan, W.Y.; Yao, M.C.; Yang, C.W.; Sheng, G.P. Redox state of microbial extracellular polymeric substances regulates reduction of selenite to elemental selenium accompanying with enhancing microbial detoxification in aquatic environments. *Water Res.* **2020**, *172*, 115538. [CrossRef] [PubMed]

260. Mishra, R.R.; Prajapati, S.; Das, J.; Dangar, T.K.; Das, N.; Thatoi, H. Reduction of selenite to red elemental selenium by moderately halotolerant Bacillus megaterium strains isolated from Bhitarkanika mangrove soil and characterization of reduced product. *Chemosphere* **2011**, *84*, 1231–1237. [CrossRef] [PubMed]
261. Vetchinkina, E.; Loshchinina, E.; Kupryashina, M.; Burov, A.; Nikitina, V. Shape and Size Diversity of Gold, Silver, Selenium, and Silica Nanoparticles Prepared by Green Synthesis Using Fungi and Bacteria. *Ind. Eng. Chem. Res.* **2019**, *58*, 17207–17218. [CrossRef]
262. Khoei, N.S.; Lampis, S.; Zonaro, E.; Yrjälä, K.; Bernardi, P.; Vallini, G. Insights into selenite reduction and biogenesis of elemental selenium nanoparticles by two environmental isolates of Burkholderia fungorum. *New Biotechnol.* **2017**, *34*, 1–11. [CrossRef]
263. Subedi, G.; Taylor, J.; Hatam, I.; Baldwin, S.A. Simultaneous selenate reduction and denitrification by a consortium of enriched mine site bacteria. *Chemosphere* **2017**, *183*, 536–545. [CrossRef] [PubMed]
264. Tan, Y.; Yao, R.; Wang, R.; Wang, D.; Wang, G.; Zheng, S. Reduction of selenite to Se(0) nanoparticles by filamentous bacterium Streptomyces sp. ES2-5 isolated from a selenium mining soil. *Microb. Cell Fact.* **2016**, *15*, 157. [CrossRef]
265. Xia, X.; Wu, S.; Li, N.; Wang, D.; Zheng, S.; Wang, G. Novel bacterial selenite reductase CsrF responsible for Se(IV) and Cr(VI) reduction that produces nanoparticles in Alishewanella sp. WH16-1. *J. Hazard. Mater.* **2018**, *342*, 499–509. [CrossRef]
266. Nancharaiah, Y.V.; Lens, P.N.L. Ecology and Biotechnology of Selenium-Respiring Bacteria. *Microbiol. Mol. Biol. Rev.* **2015**, *79*, 61–80. [CrossRef]
267. Staicu, L.C.; van Hullebusch, E.D.; Lens, P.N.L. Production, recovery and reuse of biogenic elemental selenium. *Environ. Chem. Lett.* **2015**, *13*, 89–96. [CrossRef]
268. Nancharaiah, Y.V.; Lens, P.N.L. Selenium biomineralization for biotechnological applications. *Trends Biotechnol.* **2015**, *33*, 323–330. [CrossRef]
269. Lenz, M.; Hullebusch, E.D.V.; Hommes, G.; Corvini, P.F.X.; Lens, P.N.L. Selenate removal in methanogenic and sulfate-reducing upflow anaerobic sludge bed reactors. *Water Res.* **2008**, *42*, 2184–2194. [CrossRef] [PubMed]
270. Lenz, M.; Enright, A.M.; O'Flaherty, V.; Van Aelst, A.C.; Lens, P.N.L. Bioaugmentation of UASB reactors with immobilized Sulfurospirillum barnesii for simultaneous selenate and nitrate removal. *Appl. Microbiol. Biotechnol.* **2009**, *83*, 377–388. [CrossRef] [PubMed]
271. Hockin, S.; Gadd, G.M. Removal of selenate from sulfate-containing media by sulfate-reducing bacterial biofilms. *Environ. Microbiol.* **2006**, *8*, 816–826. [CrossRef] [PubMed]
272. Mal, J.; Nancharaiah, Y.V.; van Hullebusch, E.D.; Lens, P.N.L. Effect of heavy metal co-contaminants on selenite bioreduction by anaerobic granular sludge. *Bioresour. Technol.* **2016**, *206*, 1–8. [CrossRef]
273. Green, F.B.; Lundquist, T.J.; Quinn, N.W.T.; Zarate, M.A.; Zubieta, I.X.; Oswald, W.J. Selenium and nitrate removal from agricultural drainage using the AIWPS® technology. *Water Sci. Technol.* **2003**, *48*, 299–305. [CrossRef]
274. Zhang, Z.; Chen, G.; Tang, Y. Towards selenium recovery: Biocathode induced selenate reduction to extracellular elemental selenium nanoparticles. *Chem. Eng. J.* **2018**, *351*, 1095–1103. [CrossRef]
275. Nancharaiah, Y.V.; Mohan, S.V.; Lens, P.N.L. Biological and Bioelectrochemical Recovery of Critical and Scarce Metals. *Trends Biotechnol.* **2016**, *34*, 137–155. [CrossRef]
276. Van Hullebusch, E.D. *Bioremediation of Selenium Contaminated Wastewater*; Springer: New York, NY, USA, 2017; ISBN 9783319578316.
277. Cheng, K.Y.; Ginige, M.P.; Kaksonen, A.H. Microbially catalysed selenate removal in an inverse fluidised bed reactor. *Solid State Phenom.* **2017**, *262*, 677–681. [CrossRef]
278. Sinharoy, A.; Saikia, S.; Pakshirajan, K. Biological removal of selenite from wastewater and recovery as selenium nanoparticles using inverse fluidized bed bioreactor. *J. Water Process Eng.* **2019**, *32*, 100988. [CrossRef]
279. Webster, T.S.; Enegess, D.; Frisch, S. Fluidized bed bioreactor technology: Implementation and operation for industrial contaminated water treatment. *WEFTEC 2012-85th Annu. Tech. Exhib. Conf.* **2012**, *9*, 5494–5505. [CrossRef]
280. Soda, S.; Kashiwa, M.; Kagami, T.; Kuroda, M.; Yamashita, M.; Ike, M. Laboratory-scale bioreactors for soluble selenium removal from selenium refinery wastewater using anaerobic sludge. *Desalination* **2011**, *279*, 433–438. [CrossRef]
281. Astratinei, V.; van Hullebusch, E.; Lens, P. Bioconversion of Selenate in Methanogenic Anaerobic Granular Sludge. *J. Environ. Qual.* **2006**, *35*, 1873–1883. [CrossRef] [PubMed]
282. Zhou, C.; Ontiveros-Valencia, A.; Nerenberg, R.; Tang, Y.; Friese, D.; Krajmalnik-Brown, R.; Rittmann, B.E. Hydrogenotrophic microbial reduction of oxyanions with the membrane biofilm reactor. *Front. Microbiol.* **2019**, *9*, 3268. [CrossRef]
283. Van Ginkel, S.W.; Yang, Z.; Kim, B.O.; Sholin, M.; Rittmann, B.E. The removal of selenate to low ppb levels from flue gas desulfurization brine using the H2-based membrane biofilm reactor (MBfR). *Bioresour. Technol.* **2011**, *102*, 6360–6364. [CrossRef]
284. Chen, X.; Lai, C.Y.; Fang, F.; Zhao, H.P.; Dai, X.; Ni, B.J. Model-based evaluation of selenate and nitrate reduction in hydrogen-based membrane biofilm reactor. *Chem. Eng. Sci.* **2019**, *195*, 262–270. [CrossRef]
285. Zhou, L.; Xu, X.; Xia, S. Effects of sulfate on simultaneous nitrate and selenate removal in a hydrogen-based membrane biofilm reactor for groundwater treatment: Performance and biofilm microbial ecology. *Chemosphere* **2018**, *211*, 254–260. [CrossRef]
286. Lai, C.Y.; Yang, X.; Tang, Y.; Rittmann, B.E.; Zhao, H.P. Nitrate shaped the selenate-reducing microbial community in a hydrogen-based biofilm reactor. *Environ. Sci. Technol.* **2014**, *48*, 3395–3402. [CrossRef]
287. Van Ginkel, S.W.; Yang, Z.; Kim, B.O.; Sholin, M.; Rittmann, B.E. Effect of pH on nitrate and selenate reduction in flue gas desulfurization brine using the H 2-based membrane biofilm reactor (MBfR). *Water Sci. Technol.* **2011**, *63*, 2923–2928. [CrossRef]
288. Xia, S.; Xu, X.; Zhou, L. Insights into selenate removal mechanism of hydrogen-based membrane biofilm reactor for nitrate-polluted groundwater treatment based on anaerobic biofilm analysis. *Ecotoxicol. Environ. Saf.* **2019**, *178*, 123–129. [CrossRef]

289. Ontiveros-Valencia, A.; Penton, C.R.; Krajmalnik-Brown, R.; Rittmann, B.E. Hydrogen-fed biofilm reactors reducing selenate and sulfate: Community structure and capture of elemental selenium within the biofilm. *Biotechnol. Bioeng.* **2016**, *113*, 1736–1744. [CrossRef] [PubMed]
290. Bañuelos, G.S. The green technology of selenium phytoremediation. *BioFactors* **2001**, *14*, 255–260. [CrossRef] [PubMed]
291. Wu, Z.; Bañuelos, G.S.; Lin, Z.Q.; Liu, Y.; Yuan, L.; Yin, X.; Li, M. Biofortification and phytoremediation of selenium in China. *Front. Plant Sci.* **2015**, *6*, 136. [CrossRef]
292. Šíma, J.; Svoboda, L.; Pomijová, Z. Removal of Selected Metals from Wastewater Using a Constructed Wetland. *Chem. Biodivers.* **2016**, *13*, 582–590. [CrossRef] [PubMed]
293. Lin, Z.Q.; Terry, N.; Gao, S.; Mohamed, S.; Ye, Z.H. Vegetation changes and partitioning of selenium in 4-year-old constructed wetlands treating agricultural drainage. *Int. J. Phytoremediation* **2010**, *12*, 255–267. [CrossRef]
294. Adhikari, A.R.; Acharya, K.; Shanahan, S.A.; Zhou, X. Removal of nutrients and metals by constructed and naturally created wetlands in the Las Vegas Valley, Nevada. *Environ. Monit. Assess.* **2011**, *180*, 97–113. [CrossRef]
295. Shardendu; Salhani, N.; Boulyga, S.F.; Stengel, E. Phytoremediation of selenium by two helophyte species in subsurface flow constructed wetland. *Chemosphere* **2003**, *50*, 967–973. [CrossRef]
296. Liu, F.; Huang, J.C.; Zhou, C.; Gao, W.; Xia, S.; He, S.; Zhou, W. Development of an algal treatment system for selenium removal: Effects of environmental factors and post-treatment processing of Se-laden algae. *J. Hazard. Mater.* **2019**, *365*, 546–554. [CrossRef]
297. Huang, J.C.; Suárez, M.C.; Yang, S.I.; Lin, Z.Q.; Terry, N. Development of a constructed wetland water treatment system for selenium removal: Incorporation of an algal treatment component. *Environ. Sci. Technol.* **2013**, *47*, 10518–10525. [CrossRef]
298. Thompson, A.; Parker, D.R.; Amrhein, C. Selenate partitioning in field-situated constructed wetland mesocosms. *Ecol. Eng.* **2003**, *20*, 17–30. [CrossRef]
299. Zhu, H.; Bañuelos, G. Evaluation of two hybrid poplar clones as constructed wetland plant species for treating saline water high in boron and selenium, or waters only high in boron. *J. Hazard. Mater.* **2017**, *333*, 319–328. [CrossRef] [PubMed]
300. Azaizeh, H.; Salhani, N.; Sebesvari, Z.; Shardendu, S.; Emons, H. Phytoremediation of selenium using subsurface-flow constructed wetland. *Int. J. Phytoremediation* **2006**, *8*, 187–198. [CrossRef] [PubMed]
301. Zhao, Q.; Huang, J.C.; He, S.; Zhou, W. Enhancement of a constructed wetland water treatment system for selenium removal. *Sci. Total Environ.* **2020**, *714*, 136741. [CrossRef]
302. Chakraborti, R.K.; Bays, J.S.; Ng, T.; Balderrama, L.; Kirsch, T. A pilot study of a subsurface-flow constructed wetland treating membrane concentrate produced from reclaimed water. *Water Sci. Technol.* **2015**, *72*, 260–268. [CrossRef]
303. Hansen, D.; Duda, P.J.; Zayed, A.; Terry, N. Selenium removal by constructed wetlands: Role of biological volatilization. *Environ. Sci. Technol.* **1998**, *32*, 591–597. [CrossRef]
304. Huang, J.C.; Passeport, E.; Terry, N. Development of a constructed wetland water treatment system for selenium removal: Use of mesocosms to evaluate design parameters. *Environ. Sci. Technol.* **2012**, *46*, 12021–12029. [CrossRef]
305. Lin, Z.Q.; Terry, N. Selenium removal by constructed wetlands: Quantitative importance of biological volatilization in the treatment of selenium-laden agricultural drainage water. *Environ. Sci. Technol.* **2003**, *37*, 606–615. [CrossRef]
306. Johnson, P.I.; Gersberg, R.M.; Rigby, M.; Roy, S. The fate of selenium in the Imperial and Brawley constructed wetlands in the Imperial Valley (California). *Ecol. Eng.* **2009**, *35*, 908–913. [CrossRef]

sustainability

MDPI

Article

Stormwater Utilities: A Sustainable Answer to Many Questions

Carlos Novaes * and Rui Marques

CERIS, Instituto Superior Técnico (IST), University of Lisbon, Av. Rovisco Pais, 1049-001 Lisbon, Portugal; rui.marques@tecnico.ulisboa.pt

* Correspondence: cnovaes.augusto@gmail.com

Abstract: One of the most complex and difficult questions to answer concerns how to organize and economically support public services of all kinds. In terms of services that involve a multiplicity of actors and objectives, as is the case with urban stormwater management, the difficulty is magnified and resources never seem to be sufficient. This paper reviews the successful approaches to stormwater management in a number of countries and concludes that it is both feasible and possible to successfully structure stormwater management in cities using a variety of models and incentives. With examples from cases practiced in the USA and Canada, based theoretically on the user-pays principle and on the fair distribution of impacts, the text innovates showing not only a technically and legally viable option, but an opportunity for users to become aware of the importance of reducing environmental impacts. By raising the possibility of delivering services out of the general public budget, reducing the taxation of all in exchange for charging only users and improving the performance, the discussion is directed, in an innovative way, to a very rarely questioned aspect and links the change in mentality from and economic way of thinking towards the new stormwater paradigm shift and SDGs.

Keywords: drainage; fees; financing; stormwater management; sustainability; utilities

Citation: Novaes, C.; Marques, R. Stormwater Utilities: A Sustainable Answer to Many Questions. *Sustainability* **2022**, *14*, 6179. https://doi.org/10.3390/su14106179

Academic Editor: Shervin Hashemi

Received: 9 April 2022
Accepted: 11 May 2022
Published: 19 May 2022

Publisher's Note: MDPI stays neutral with regard to jurisdictional claims in published maps and institutional affiliations.

1. Introduction

The management of urban stormwater evolved with the understanding of its role and the good and bad characteristics that such water brings to society. In each era, water has had different roles, but has always been connected with human activities, and cities were born and developed in close relationship with water. The close presence of water, whether for agriculture, energy production, navigation or consumption, in most cases brought value to the territories, with the exception of urban flooding [1].

Cities continued to grow and man thought wastewater and stormwater were reasons for diseases, and that it was necessary to take it as soon as possible to rivers, lakes, estuaries and the sea. The function of the receiving water bodies was not only transport, but effluent discharge, without treatment, as is still the case in many places today. In the era of 'tout à l'égout' [2], the hygienist phase of the 19th century, the reigning order indicated was to move waste and rainwater away from the cities as quickly as possible, not only to avoid the proliferation of diseases, but also to prevent flooding. The concern was fundamentally hydraulic, with a focus on quantities and mass flows, i.e., the problem was reduced to the sizing of pipes and channels, a matter for engineers. Concerning stormwater drainage, there was an understanding that these were of good quality and free of pollutants [3], reinforcing the idea that only volumes, mass flows, and dilution should be addressed. As for quality, represented by pollution, people said that it was only a matter of diluting polluted volumes into larger volumes, free of pollutants. The issue of sizing structures for drainage and dilution went through the discovery of which rains could be predictable in each region, a problem of hydrology and statistics, the latter helping by informing the probability of occurrence of certain volumes and the associated risks, expressed by determining the so-called return times of the events. Again, problems and issues are more related to engineers. From the possession of this information, the problem of the decision to

choose return periods, or "project rainfall", depended on political decisions, closely linked to investments to be made in physical infrastructure and their respective risks.

With the advances brought by microbiology and epidemiology and Koch's discoveries regarding cholera, the understanding grew that the issue of wastewater quality was of crucial importance allowing sanitary approaches to sanitation and drainage to occupy a prominent place; it was the beginning of the sanitarian phase after the hygienist phase of the 19th century. The first wastewater treatment plants started to be developed at the turn of the century [4]. The decision about the type of treatment and size of the facilities involved the determination of the desired quality levels for effluents, an issue that no longer affected only engineers, but also health professionals, considering the risks that society would be willing to undergo and the alternatives of investments to be made, i.e., again, decisions of a political nature.

Currently, as of the nineties, there is an upsurge in urban flooding problems for several reasons, with two of them more relevant and interconnected: demographic growth, with the consequent territorial expansion of the urban fabric; and climate change, leading to the perception that just draining downstream, ever further and with greater volumes, treating rainwater effluents in a concentrated manner, at the point of discharge ("end of pipe"), in a vision on the one hand hydraulic and on the other hygienist, has not even found physical spaces for the task [5].

Later on, simultaneously with the environmental and right to the city movements, the vision of sustainability took over urban environments that started to understand water not as a problem anymore, but as a solution to old and new issues of quantity and quality, such as scarcity, well-being and comfort, exemplified, respectively, by its use in daily life, embellishment and the fight against "heat islands" [6].

According to this approach, alternative techniques emerge, in opposition to the traditional method of removal, which mainly uses buried pipes. The new mentality is one of harmonious coexistence with water; therefore, in addition to its visible presence on the surface, there must be treatment at the source, that is, as close as possible to the places of origin, where precipitation occurs [7].

In terms of management, what worked before—the centralized management with command and control concentrated in the public power—requires changes, and a change in the traditional management paradigm. With new and multiple actors assuming different roles, disputing and sharing the resource represented by urban stormwater, practices are gradually changing and favoring the decentralization and democratization of decisions [8].

At the same time, the change reaches aspects of service funding, as the understanding had always been that flooding issues, linked to large volumes and flows (hydraulics), were usually borne, at great expense, by general (centralized) public budgets. The feasibility of solutions at the source, or located where precipitation occurs, generally requires potentially lower and decentralized expenditures enabling private sharing and participation in the solution in a distributed manner [9].

Around the world, this paradigm shift is being studied to create the best format for financing and management. The USA and Canada, countries where there have been successful experiences for some time (around three decades [10]), materialized through stormwater programs, are partially or totally based on the collection of tariffs from users. Users became important and stable sources of funds, specifically for the improvement in urban stormwater management systems to comply with legislation. In the USA and Canada, the collection mechanisms for funding the activity are called stormwater utilities (SWUs), with specific characteristics in each place, but which deserve to be observed in order to learn from them.

The contributions of this paper lie in the approach to a subject absent from the literature, despite its importance, exemplified by the number of existing cases and of importance of the countries in which it is presented. Despite this, however, SWUs are financing stormwater management mechanisms that are little used in most countries where funding is required. In this sense, the contribution is to expand the dissemination and discussions around the

subject and its application, so that through its knowledge its use can be expanded and the improvement in stormwater management can be achieved.

Besides this short introduction, the article is structured in four more sections. The Section 2 will focus on issues related to the origin and reason for the emergence of SWUs. In the Section 3, several cases where SWUs exist are presented; in the Section 4 the results and discussions are briefly presented; finally, in Section 5, the conclusions are drawn. Figure 1 presents a flow chart of the study with each chapter, its main aspects, as well as some of its interconnections.

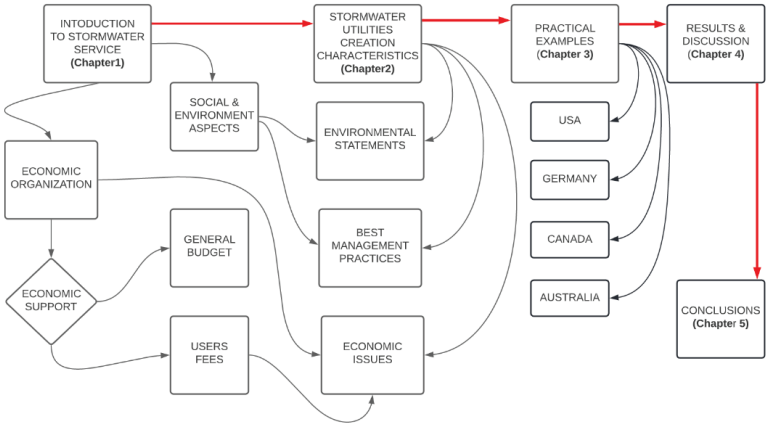

Figure 1. Study flow chart.

2. The Creation of SWUs

In line with the diversity of aspects to be addressed, new demands for resources and management have arisen from the entry into force of legislation and regulations targeted at improving the quality of urban service delivery systems, including stormwater management. Costs expected to result from climate change (increased frequency, intensity, and duration of rainfall with flooding and rising sea levels) have led to a search for alternatives to system funding through the application of the user-pays principle, based on charges levied on users according to their contribution to runoff, supporting, even if sometimes only partially, the new costs to be assimilated by budgets [11]. In each location, these financing methods, often associated with new management practices, have become institutionalized and have been given different names: SWU, stormwater fee, stormwater user fee, and stormwater service fee [12].

Cities support increasing costs, but with no proportionally crescent budgets, of maintenance and replacement of ageing infrastructure, of the new built areas and of quality and quantity costs occurring depending on climate change. In Canada, due to climate change, the stormwater infrastructure is considered in critical condition, but it was built in the last twenty years. With an estimated lifetime of 70–100 years for linear systems, 50–80 years for structures, and 25 years for electrical and mechanical components, this picture is surprising.

The SWUs, mechanisms to obtain resources for financing urban stormwater management, resulted from the perception by the American municipalities of the need to find economic means to cope with the increasing pressure on their budgets to meet socio-economic and environmental demands. These demands were incorporated into the American legislation through water quality control requirements due to diffuse urban stormwater pollution, considered a pollution point source at the point of discharge.

The legal and regulatory framework was developed over the last five decades since 1972, with the Clean Water Act (CWA) aimed at controlling water quality, revised in 1987 through the Water Quality Act (WQA), with provisions added for five categories of stormwater discharge. These provisions, classified under Phase I, established a set of

restrictions for large and medium-sized municipal storm sewer separator systems (MS4). These systems cover populations greater than 100,000 and according to discharge quality permits, bring them into compliance with the National Pollutant Discharge Elimination System (NPDES). In 1990, the final rules were established for Phase I, and later, in 1999, for Phase II. In small MS4, in addition to systems for fewer than 100,000 inhabitants, there are industries and construction areas of 4047 to 20,234 m^2 (1–5 acres). Stormwater eventually carries pollutants such as nutrients, pathogens, sediment, and metals, but must fall within the limits of the Total Maximum Daily Load (TMDL), a pollutant load that can be discharged to a given receiving body, without failing to meet the quality standards established by the states. The TMDL program applies to all MS4 systems, industrial and construction activities, and its limits include both point source and diffuse source loads [13].

Additionally, from the 1980s onwards, partly as a reflection of the taxpayer revolts of the 1970s, and the passage, in 1978, of proposition 13 in California, which placed limits on property taxation, some governments began to consider tariffs as a better source of resources than taxation for urban services. Thus, more favourable conditions were created for the introduction of stormwater utilities, a period considered as the utility model different from the traditional tax-supported public works model, until then predominant [14].

The creation of SWUs in the USA is not mandatory and depends on the perception of their need by the populations, policymakers, and those in charge of state legislations, on which SWUs depend to be implemented. There is no pre-defined size, with small communities such as Indian Creek Village in Florida (only 88 people), according to the 2010 Census population, and Los Angeles (over 4 million inhabitants).

There are nine models for calculating collection rates: dual, flat, tier, square foot, parcel acre, meter, usage, equivalent residential unit (ERU), and residential equivalent factor (REF). Some are based on impervious areas, such as the most widely used, ERU. Others are based on runoff generated, such as REF, or other forms of measurement. ERU is more popular in places with high population density and high property values while flat fee is more popular in places with low population densities and low property values [12].

Thus, in the absence of a general rule, the junction of necessity and opportunity has favored the creation of SWUs. The opportunity often occurred after catastrophic events, such as the hurricanes Katrina, in Louisiana (LA) and Mississippi (MS) fifteen years ago, and Sandy, in Connecticut (CT), New Jersey (NJ), and New York (NY) eight years ago, after which, however, by 2021, there were still no SWUs in place.

In the USA, the coming into force of legislation showed a relationship with the higher number of deployed SWUs [12], as also a clear definition of the legal authority in charge of each city, county, and watershed. In the some way, important was the key role played by the professional organizations, providing information, support, and encouragement to communities interested in the implementation of SWUs.

3. Stormwater Utilities (SWUs)

3.1. The USA

In the US, according to research by the University of Kentucky, there are 1851 distributed SWUs identified, in 41 states and the District of Columbia [15]. While the number of SWUs may seem large, it becomes small when compared to the number of 22,389 communities computed as participants in the National Flood Insurance Program (NFIP), as of June 2019, meaning there are SWUs in less than 10% of this total. Despite a long history of SWU implementation in the US, the main challenges that remain for communities, regardless of their size, are related to adequacy of funding and public support, which are compounded by aging infrastructure [16].

The national average monthly fee paid by single-family homes is USD 5.94, increasing over time according to the consumer price index (CPI), with values varying from USD 0 to 45, although there are situations where reductions may occur and the range may reflect stormwater needs and also political contexts. The most widely used calculation method is based on the impervious areas of the land and on the ERU system, an average of the

single-family residential impervious areas of land, but in some communities, a value can be defined based on the average of all the areas of residential land. The method calculates the amount to be charged based on the impervious areas of the lots, regardless of the total areas. The ERU is calculated through sampling carried out through field research [17], but can also be estimated through aerial or satellite images. Once the total impervious area of residential properties (AI) is obtained, it is divided by the number of properties, giving the ERU value [15].

For non-residential land, the rates are proportional to the ratio of the impervious area of the land to the ERU. The most commonly found average size for ERUs (895 utilities) in the University of Kentucky survey was 3072 square feet of impervious area, so it is important to determine ERUs accurately so that no one pays a disproportionate amount. There are other taxation systems, such as tiered systems (254 utilities) or flat fees (230 utilities). The ERU can be considered a system of infinite levels or steps and the flat fee and dual fee (108 utilities) as systems of a single level or step, the latter considering taxation for residences and another one for non-residential properties.

An example, taken from research conducted in 2021 by the University of Kentucky (Campbell, and Bradshaw 2021) [16], illustrates calculation systematics for a hypothetical area and allows conclusions to be drawn: residential waterproofed area = 15×10^7 sq ft; non-residential waterproofed area = 15×10^7 sq ft; ascertained ERU = 3000 sq ft; annual amount required for the selected level of service = CD$ 12 million and every household pays a fee of 1ERU.

Dividing the total waterproofed area (30×10^7 sq ft) by the standard computed ERU gives a number of 100,000 ERUs, 50% of which are residential areas and 50% of which are non-residential areas; therefore, a monthly fee of CD$ 1 million is required, which when divided by the number of 100,000 ERUs indicates a base amount of CD$ 10 per ERU per month.

If, however, for example for political reasons, it is decided that the assessed value to be used for non-residential areas should be for standard ERUs with 4000 sq ft and not 3000 sq ft, the number of non-residential ERUs becomes no longer 50,000 but 37,500 (1.5×10^7 sq ft divided by 4000 sq ft), totaling no longer 100,000 but 87,500 ERUs in the municipality (50,000 residential and 3700 non-residential), which implies a value no longer of CD$ 10/ERU, but of CD$ 11.43 per ERU (87,500 × 11.43 = CD$ 1 million per month) and, according to the following Equations (1) and (2), the percentage of costs will no longer be 50% between residential and non-residential areas, but 57% for residential and 43% for non-residential.

$$Frac_{res} = ERU_{res}/ERUs_{res} + IA_{nonres}/ERU_{\ used} \quad (1)$$

$$Frac_{nonres} = 1 - Frac_{res} \quad (2)$$

where $Frac_{res}$ corresponds to the fraction of the stormwater program paid by residential customers; ERU_{res} is the total number of residential ERUs in the city; IA_{nonres} is related to the total non-residential impervious areas in town; $ERU_{\ used}$ is the actual ERU used as opposed to the true ERU.

Similarly, if the standard ERU in the non-residential area with the value of 2000 sq ft is used, 125,000 ERUs will be obtained (50,000 residential and 75,000 non-residential), whereby the value of the ERU equals CD$ 8 (125,000 × 8 = 1 million) with the residential area bearing 40 and the non-residential area bearing 60% of the costs. Similarly, for ERU = 1000 sq ft, the percentages of monthly costs borne become 25% for residential areas and 75% for non-residential areas, or for ERU = 5000 sq ft, 62.5% for residential and 37.5% for non-residential users, respectively, according to Equations (1) and (2). From this, it is clear that the determination of the ERU is a very important aspect to have a fair taxation system that reduces the possibility of questioning.

Still, as to the example, it should be highlighted that it does not take into account possible reductions, applied in some municipalities, due to the placement of rainfall retention

devices on lots or even the disconnection from collective drainage systems, besides other aspects that motivate exemptions.

The second most popular model is the REF method, with 133 utility cases; this system is based on the amount of runoff from a unit compared to the amount of runoff by a standard property of a single-family dwelling, considering an event with a determined return time, for example, 2 years and 24 h of rain, calculated by the rational method or the Soil Conservation Service (SCS). Besides relying on hydrological information over time and soils, this system penalizes commercial properties for shorter return times and residential properties for large return times [18].

Thus, building a model for calculating fair taxation, making SWUs accepted by all as a development factor, is still a complex and evolving task that depends on several parameters in addition to policy options in each location and different development context. Nevertheless, some SWUs have made significant capital investments through user fee programs, such as in Fort Collins (CD$ 120 million), Bremerton (CD$ 55 million), and Raleigh (CD$ 100 million), initiated in 1980, 1994, and 2004, respectively, and in the second case the investment is to promote the separation of the existing unitary system [16].

In 2021, most of the 73 participants in the survey, which covered 20 American states, conducted by the consulting firm Black & Veatch, declared to: have a separating system (82%); have a municipality as their area of jurisdiction (97%); carry out the collection of drainage fees on water and sewerage bills (78%); consider a drainage website the most effective means of ensuring approval and support for the fees charged to users; and to fit into Phase II (population under 100,000) of the EPA's Municipal Separate Storm Sewer Systems (MS4s) discharge regulation program.

EPA has 855 participants in Phase I MS4s (population over 100,000) and 6695 in Phase II MS4s which include many cities and regions. In the majority, i.e., in 54% of those locations, where combined systems still exist, the combined systems account for less than 25% of the total system. Despite being the third most important item cited in the survey and that 73% of systems have—according to the survey—aging drainage infrastructure, asset management plans are in place in only 63% of systems falling under MS4s Phase I and 35% falling under MS4s Phase II.

The main percentages of instruments used for funding corresponds to cash (78%) or debts (22%), according to the percentages of answers for each type of instrument. As for the main sources of revenue, 95% of the answers indicate that more than 75% of the amounts are supported by fees received from users and the three main activities described as included in the O&M budget are: illicit discharge detection and elimination (96%), best management practices (90-92%) and public education (92%) [16].

3.2. Germany

In Germany, in several cities since the 1990s, based on the polluter-pays principle, stormwater management charges have been introduced taking into account the impervious area. Since many cities have single systems, i.e., systems that deal with both stormwater and wastewater systems, they are charged jointly through a single fee and the calculation is based on water supply consumption, which is not a fair way of charging. From the idea of changing to a fairer system, based on the mentioned principle, in most states the fee for impervious areas was introduced, but just with a value around only 20–75% of the costs of stormwater and wastewater management [17].

There are two ways to calculate the impervious area: by estimation, according to zoning (Munich, since 1970), or by measurement (Hamburg, since 2012; Dresden, since 1998; and the State of Baden-Wuerttemberg, since 2010). Calculation by estimation is easier to implement but more inaccurate.

The implementation of the levy resulted in: waterproofing area reductions of 4.5 M m^2 or 240,000 m^2/year in Munich with 3000 ML groundwater recharge; 10% reduction in waterproofing area per person in Dresden; and in the state of Baden-Wuerttemberg, 48% of

the cities reported decreases, 11% with high reductions already in the first two years after the levy implementation.

In Munich, maps with colors identify the runoff coefficients, being 0.9 for the blue zone, in the city center; 0.6 for the pink strips, in intermediate regions, between the center and the outskirts; 0.5 for the outer suburban areas (orange); and 0.35 for residential plots in the outer suburbs (green) (Vietz et al. 2018). Additionally, several beneficial effects were noted, such as the reduction in the quantities treated in the combined systems in Munich and Dresden, enabling process optimization and deferring infrastructure upgrades of existing systems [17].

3.3. Canada

In Canada, only 4 out of 48 utilities use the ERU system and eight use property value or "ad valorem" taxation and the average taxation is CD$ 10.67 [15].

In the Victoria Community, located in British Columbia, integration between stormwater management (SWM) and street sweeping has recently been discussed with the latter usually being included in property-related fees [19].

In Victoria, stormwater bills are issued annually to property owners and are determined based on property-specific characteristics such as impervious areas (roofs, car parks, and driveways) measured with the aid of building plans, aerial photography and mapping using georeferencing technology (GIS).

The value, in 2022, is of CD$ 0.654 per square meter and street cleaning is determined by frontage length and street type, charged per meter of lot frontage, varying according to Table 1 below.

Table 1. Victoria charge, according to the type of street.

Street Type	CD$/Meter of Street Frontage
Local streets	1.81
Collector streets	3.84
Arterial streets	4.35
Downtown streets	43.60

The property impact on the stormwater system through a flat portion of the charge, based on the building code is: low density residential—CD$ 0; multi-family residential—CD$ 81.79; civic/institutional—CD$ 72.98, and commercial/industrial—CD$ 148.38. Finally, there is a program in which property can be registered if they have ten or more parking spaces and are self-businesses, recreational facilities, recycling operations, storage yards, or have construction activities on site, paying CD$ 169.70 per year (2022).

In a study conducted in the City of Thunder Bay, comparing the various forms of taxation for stormwater funding, the conclusions were that urban properties subsidize rural areas by approximately CD$ 300.00 annually and that residential properties account for 67% of the contributions to the stormwater program while non-residential properties receive the remaining 33%.

However, the runoff from residential areas is only 58% and the remaining 42% comes from non-residential areas, meaning that a distribution based on contributing areas would lead to a 9% redistribution, i.e., the average residential properties would bear 9% less while the non-residential areas would bear an average of 9% more in levies.

Although this distribution would be fairer, one of the recommendations of the study was that the change would only be worthwhile above 10%, given the high implementation costs of reallocating only CD$ 360,000 per year from residential to non-residential plots, against a budget of CD$ 4 M and minimal apportionment of the difference among the 38,203 existing residential properties.

There are, however, other aspects that should be considered in the long term, such as the observation that property tax encourages urban sprawl while the user fee option encourages densification, and other issues including environmental liabilities [20].

3.4. Stormwater Management in Australia

The changes that occurred in water management in Australia over the past five decades determined its current state, according to a path dependence viewpoint (Otoch et al. 2019) [21].

However, according to Brown and other scholars, moments of tension and alignment existed between six distinct institutional logics (decision making, risk, sustainability, water quality, infrastructure, and demand) that coexisted in permanent evolution. Thus, according to a study conducted in the period between 1970 and 2015, throughout all that time, the urban water management sector in Australia showed great complexity [22].

In this context, the evolution (rather than a revolution) towards the current practices of Sustainable Urban Water Management (SUWM), which emerged in the 1990s, was based on the trajectory traveled by the logic of sustainability, water quality, and demand.

Changes in the idea of sustainability were characterized by the focus on aquatic health and the reorientation of the vision of point source pollution to diffuse, reflected in the logic of water quality that has become more restrictive with standards and monitoring based on aquatic ecology.

The demand was characterized by the emancipation of the end-user and the growth of expectations related to urban amenities and environmental protection. The infrastructure model, identified with engineering expertise, evolved from civil engineering based on forecasting and control to a more significant multidisciplinary approach, in which adaptability and flexibility became important design parameters.

The decision-making logic also evolved from the seventies, when it was characterized by bureaucratic, paternalistic decisions, centralized in powerful, vertically integrated organizations, and focused only on water supply, treatment, and drainage.

As of the 1980s, the government's influence grew, with the private sector participating and the predominance of the economic efficiency viewpoint. Decisions considered economic factors first, causing the user-pays principle to take the place of the tenure principle, which had property as the determining value in pricing decisions.

As of the 1990s, this vision intensified, reflecting free-market competition, with a commercial focus and financial instruments in decision-making. Public–private partnerships, for instance, are considered an alternative, and the user acquires the status of a consumer.

This framework remains from the 2000s with the water markets [23] when, however, due to the "millennium drought" at "a critical juncture", according to the definition of historical institutionalism [24], the logic of risk comes into play, temporarily interrupting decentralization, and the construction of large centralized desalination structures in all major cities [22].

Australia has a federative system of government, commonly referred to as "Commonwealth" or federal, with six states, two territories, a constitution, proclaimed in 1901, which defines the roles of each of the eight federal entities and, according to section 100, water management is the responsibility of each.

In the states and territories, there is another level of local government, which are the municipalities and district councils. In most states, the state governments own the utilities and local governments do the planning and management of stormwater services and the systems are separative.

For over thirty years, Australia has been developing its national water quality management strategy. It includes the use of stormwater for supply and guidelines are available for adoption by the states and territories. There are also guidelines for the evaluation of Water-Sensitive Urban Design (WSUD) options that incorporate an integrated approach to the urban water cycle. This includes the management of water supply, sewerage, groundwater, stormwater, land use, and environmental protection.

3.4.1. The Salisbury Example—South Australia

The city of Salisbury, in the metropolitan area of Adelaide (population 1.3 M), South Australia, developed through rapid urbanization from the 1970s onwards. Today, with around 137,000 inhabitants and an average annual rainfall of around 430 mm, mostly occurring in winter, it adopted WSUD principles to maximize the use of run-off water and reduce the risk of flooding. Aquifer recharge management was introduced to control the low salinity of stormwater by using Aquifer Storage and Recovery (ASR) in a brackish aquifer for subsequent irrigation.

The stormwater is collected in retention basins forming wetlands and lakes and subsequently infiltrated into the aquifers, with retention time around seven to ten days, being recovered through ASRs or Aquifer Storage Transfer and Recovery (ASTRs) allowing the reduction in the demand for water supply used for irrigation of sports fields.

Wetlands now occupy about 200 ha of the catchment area and in 2001 the City of Salisbury expanded the use of urban stormwater as a commercial enterprise through a public–private partnership project. The project focuses on applying AUD 4.5 million to construct wetlands and ASR facilities for stormwater treatment and storage, at Parafield Airport, a secondary airport in Adelaide. In this case, also a purple pipe network was constructed for the Mawson Lakes neighborhood, with recycled water comprised of a combination of stormwater from the Parafield Airport wetlands and wastewater from the Bolivar Sewage Treatment Plant.

The success of this operation led to the formation of a pioneering business that included nine projects in different locations. Providing non-potable water in a volume equal to 5×10^6 m^3 per year showed that stormwater containing contaminants, when stored underground and under control, can be used for uses such as irrigation of public open spaces and, when chlorinated, can be supplied in pipes (third pipe supplies). Its use for potable purposes depends on the additional use of microfiltration, UV disinfection, and chlorination, but the costs of these additional operations to reach the required safety standards are considered to be lower than the costs of laying double distribution pipes. The total cost of supply (capital and operation), for example, in 2012/13 was AUD 1.57/m^3 for non-potable use for irrigation of public spaces and AUD 1.96 to AUD 2.24/m^3 for potable use (excluding distribution network costs), therefore cheaper than the usual AUD 3.45/m^3 for mains water [25]. The costs of providing non-potable water through a new distribution network, however, are similar to or higher than the costs of distributing water from the existing network.

In 2010, a business unit, Salisbury Water Business Unit, participating in the administrative structure, administered by the SWMB and chaired by an external independent member, was established. The unit manages various water collection and supply schemes for non-potable use, being mainly recycled rainwater and native groundwater. Treated to standards, according to the purposes for which they are intended, it is distributed to parks, reserves, schools, industries, and some residential sectors. It serves over 500 users, among them 31 schools, and generated AUD2.8 million in resources in 2015–2016.

3.4.2. Melbourne and Victoria

In Greater Melbourne, 5 million people live in an area of about 10,000 km^2 with an average annual rainfall of around 600 mm [26]. There is a fixed annual charge per household, based on property value, which is paid as part of the Waterways and Drainage Charge, regardless of the amount of waterproofed area and the impact it has on drainage systems. In the Australian state of Victoria, the Water Act governs how the Waterways and Drainage Charge should be implemented, but it is unclear how the level of waterproofing may influence the levy.

The theoretical graph in Figure 2 demonstrates how the fixed charge works and allows a reflection on the greater possibilities for incentives for non-sealing that can exist from a variable charging policy [17], which is fairer, collects more resources to support the systems,

and provides incentives to non-sealing and disconnection. These can alleviate the need for extensions and maintenance on stormwater systems and save resources more efficiently.

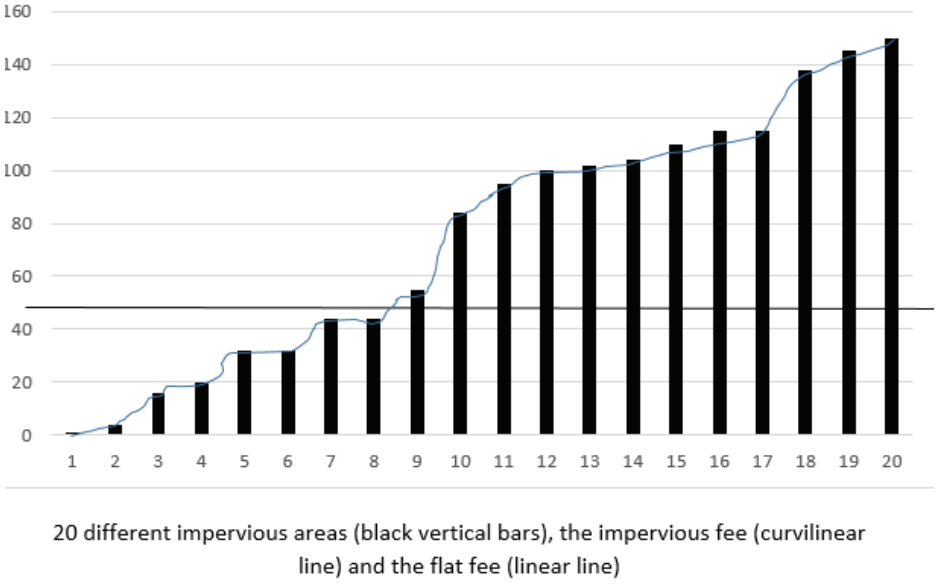

Figure 2. Comparison between fixed and variable rates considering the same total storage for 20 dwellings with different degrees of waterproofing [17].

4. Results and Discussion

Unlike decades ago, when stormwater management was focused only on urban flooding, there was an evolution that, presents differences and similarities in developed and developing countries. The main issues involve multiple aspects and challenges such as water and environmental quality, aquifer recharge, supply and treatment, urban heat islands, urban well-being, street trees [27] aquatic life, landscaping, and leisure, and flood analysis [28], among many others [29].

Although interrelationships between stormwater and wastewater are known, in several countries, especially where the absolute separator system is adopted, at least officially (as is the case for Brazil), management is still focused on wastewater treatment. This is partly due to the significant sanitation deficit [30], and so stormwater is erroneously considered a low priority, except when flooding events occur [19].

Thus, the collection of stormwater fees and the construction of management structures dedicated to urban stormwater management, with or without private sector participation, has been left behind, especially in developing countries. Initiatives for its implementation are the target of many objections, including judicial ones, as was the case in the municipality of Santo André, in the ABC Paulista, metropolitan region of São Paulo. After a period of evolution and success in the use of charging, started in 1998, a setback occurred, with its suspension in 2012 [31].

Experience, however, including in the U.S., has shown the importance of information and disclosure, particularly when on user demand, with the most used channel of communication with the public being the website [16]. The Web aims at the understanding, involvement, and participation of society and the reduction in objections, proposed mainly by non-residential users. The objection questions are mainly of two types: the legality of the authority responsibility for issuing, implementing, and financing the fees and the legality of the charging mechanism [32].

The organization of management through SWUs considers the institutionalization of the application of fees as an economic support strategy for stormwater management. It is based on four criteria: efficiency, equity, adequacy, and feasibility in the collection and use of revenues. It enables long-term planning of capital and operational investments, brings the potential for change in public behavior, and impacts business and management of municipal investments, but at the same time suffers objections from users, including legal ones.

The tariffs, in general, are based on the operating, maintenance, and, when possible, the capital costs of the systems, distributing them among the users according to criteria that, in most cases, correspond to the waterproofed areas. The criteria seek equity not only through proportionality between tariffs and the contribution to runoff and pollution generated, as established by the user-pays principle, but through different payment capacities, expressed, for example, by property values or consumption of services such as water supply.

The issue of stormwater systems' economic support is still quite controversial, even in places such as the USA and Canada, where there are legal challenges, most of them being refused by the courts. Barriers to their implementation also exist, as can be seen in the Canadian example of the City of Thunder Bay, where the conclusion led to the option, even in the short term, of not adopting the fairest method of distributing the burden of waterproofing.

There are several ways of economic viabilization and funding stormwater management services, but they can be summarised in two, especially with regard to fundraising: the traditional model, based on the general budget (payment by all citizens), and the model based on payment just by the users of the service, known as the stormwater utility.

These two different visions on how to obtain resources to economic support public services are part of a larger dispute involving the role that governments should play in the solution of socio-economic-environmental problems. The traditional vision is opposed to the innovative vision of stormwater utilities, the latter responding in part to the population's desire for more fair tariffs and to reduce the burden of general taxes, as occurred in the USA decades ago, when stormwater utilities were implemented. However, decades after their implementation, the thought that they are hidden taxes disguised under another name still survives.

Existing experiences and those under implementation deserve to be observed, as well as examples extracted from them of what may work and what may not work so well in each context. However, there should be no delay, as this is still a subject that deserves practical experimentation, a kind of learning by doing, given the increasing demands that are coming with the growth in urbanization, rising temperatures, increased urban rainfall and rising sea levels, according to climate change forecasts.

For example, in Brazil, where the focus is still very much on the scarcity of public resources, the introduction of management and funding mechanisms such as SWU, based on the user-pays principle, can work. As in other countries, stormwater utilities in Brasil are welcome, as long as they are applied through policies that encourage not only the economic contribution of users, but that consider forms of management with focus on results. Besides that, they may lead to increasing the involvement and participation, bringing the contribution of all actors to the decisions made, including the design of the calculation methods of charging and the legislation. This may mean opening the way to solutions that lead to economic autonomy of stormwater services management and also for disengagement from the general public budget, decreasing taxes, with gains in responsibility distribution efficiency and a permanent flow of resources to the sector, providing sustained continuity to the actions.

The study shows that the use of the stormwater utilities mechanism is more developed in countries where environmental legislation has been fully implemented. Table 2 shows examples of the countries' main approaches, fee criteria and objectives. From the information in Table 2, although it is not possible to verify uniformity in all aspects, there is

a trend in the approach to control environmental effects (reduce pollution of water bodies) and in the criteria for calculating tariffs (sealed areas).

However, there is no definite trend regarding the form of quantification of the objectives, a fact that can be attributed to the experience and reality in each location. From the perspective of the economic efficiency objective, information on collected revenues compared to measurable cost outcomes of avoided environmental impacts (e.g., volumes of treated effluent) can allow for the ranking of stormwater utilities initiatives. Measured economic parameters also enable the comparison with other alternatives such as the overall budget itself.

This is different in countries where there is no legislation incentives or, as in Brazil, where the law has existed for a long time and is broad, but encounters obstacles to application. Utilities with a low level of institutionalization and administrative and economical disorganization tend to relegate environmental issues, postpone the acquisition of economic support and, eventually, adopt the funding and organization structure.

Table 2. Countries, approaches, fee criteria and objectives.

Country	Main Approach	Practical Fee Measures Criteria	Objective's Evaluation Metrics
EUA	Environment Pollution Conttrol	ERU (m^2 of impervious areas); many others (flows, etc)	Pollution and environment statements attendance
Germany	Environment and Equity Polluter-Pays Principle	Impervious area and water supply consumption	Impermeable surface reductions, groundwater recharge and treated quantitative vol. reduction
Canada	Polluter-Pays Principle	ERU (m^2 of impervious area) and "ad valorem" property tax	Impermeable surface reductions
Australia	SUWM—Sustainability Urban Water Management	Fix, based on property values	Groundwater recharge measurements; stormwater and reuse of non-potable supply
Brasil	Flow Control	m^2 of impervious area	Undecided

5. Conclusions

The overview of SWUs presented here provides an update on what has been implemented to ensure the economic sustainability of urban stormwater management systems with the participation not only of the public sector but also of users and private agents, being remunerated as a public service to society as a whole.

The study's contribution comes in the sense of bringing together scattered information and thus allowing the formation of a general picture of the evolution in a certain direction, namely, the economic organization and financial sustainability of urban stormwater drainage and management under a new paradigm, which has been occurring simultaneously in several places around the world.

The perception of this fact as a general trend does more by allowing scholars, researchers, and practitioners to identify it and become aware of what is still missing for its rapid institutionalization, implementation, and experimentation, thus contributing to the evolution and improvement in the sector's actions. This is a small contribution, given what still needs to be done, but with the potential to help transform the reigning mentality, or the business as usual, and in this sense it can be significant.

The institutionalization of charging users for the provision of urban stormwater management services, whether provided by public or private operators, always encounters obstacles, posed by those who believe that they should be compulsorily provided by the public authority and funded by general public budgets, which means the cost is socialized for all the society. Either due to technical reasons, such as methods of quantification of the shares that each one is responsible for (the user-/polluter-pays principle), or to issues of understanding regarding the services to be provided by the state or for various legal

and rights-based reasons (i.e., legal, among others), the fact is that barriers exist to the implementation concept of stormwater utilities.

The reality, however, has shown that in several countries there are feasible ways of charging equitably for the services, relieving public budgets, encouraging the reduction in impervious areas and the disconnection to urban stormwater systems, i.e., saving nature from impacts, taxpayers from unfair costs, and public budgets from unplanned expenses, made to remedy sudden failures after extreme precipitation events, which are increasingly frequent due to the climate.

Based on theoretical knowledge, expressed in various pricing and collection formulas that have been tried in practice in different countries, it is possible to see that economic sustainability, as the economic side of the ongoing paradigm shift in urban stormwater management services already has feasible options and alternatives. Thus, the argument that urban drainage is a public service left "for later" due to a lack of resources or economic organization does not hold. Political will can set in motion policies, institutions, and regulations that, aligned around the objective of solving drainage sector issues, set in motion incentives for economic organisation and financial support.

The novelty is the possibility to make the economic change a viable side of the stormwater paradigm shift, in a win–win manner, with more than economic gains for all actors. There are efficiency gains in terms of environmental, social, institutional, organizational, and political aspects.

This is not all, since society's acceptance of the paradigm shift, through the understanding of the gains that are thus produced, requires an effort of awareness. This is not only motivated by economic–financial gains and reasons, but by others of ideological nature, that is, at the level of ideas and ideals, as is the case for the sustainable development goals. SDG's are present in the paradigm shift, but are not always perceived and require more work from all. A missing economic aspect that is important in ascertaining the speed of the paradigm shift is the quantification of 'green' and 'grey' infrastructure investments made with the revenue raised through SWUs. This is an aspect for study, that is, it is important to know to what extent the mechanism and the collection from users has contributed to the implementation of more infrastructures that favour the paradigm change (e.g., green infrastructures) such as the quantity of street trees and many others leveraging the change. Criteria to measure the achievement of clear objectives make the possibilities of reaching them visible, contribute to adjustments, and can help everything run more quickly towards the change in paradigm.

The study explored the existing publications, information, and data to which it was possible to have access and, by adopting this methodology, it carries with it the limitations arising from it, such as the absence of information that does not exist in the databases studied, or even the form of research used in these bases. Additionally, given the dynamics of the temporal evolution of the experiments, they will continue to occur, often surpassing the ability to become aware of them and analyze them, a fact that is part of the research process.

Author Contributions: Conceptualization, C.N. and R.M.; methodology, C.N. and R.M.; validation, C.N. and R.M.; formal analysis, C.N. and R.M.; investigation, C.N.; resources, C.N. and R.M.; data curation, C.N.; writing—original draft preparation, C.N. and R.M.; writing—review and editing, C.N. and R.M.; visualization, C.N. and R.M.; supervision, R.M.; project administration, R.M.; funding acquisition, C.N. and R.M. All authors have read and agreed to the published version of the manuscript.

Funding: The authors are grateful for the Foundation for Science and Technology's support through funding UIDB/04625/2020 from the research unit CERIS.

Institutional Review Board Statement: Not applicable.

Informed Consent Statement: Not applicable.

Data Availability Statement: Not applicable.

Conflicts of Interest: The authors declare no conflict of interest.

References

1. See, L.S.; Calo, L.; Bannon, B.; Opdyke, A. An open data approach to mapping urban drainage infrastructure in developing communities. *Water* **2020**, *12*, 1880. [CrossRef]
2. Pinheiro, C.B. Políticas Públicas de Manejo de Águas Pluviais em Belo Horizonte: Novos Caminhos em Meio a Velhas Práticas. Master's Thesis, Federal University of Minas Gerais, Belo Horizonte, Brazil, 2019.
3. Imhoff, K.; Imhoff, K.R. *Manual de Tratamento de Águas Residuárias*, 3rd ed.; Edgard Blucher: São Paulo, Brazil, 1985; pp. 1–301.
4. Monte, H.M.; Santos, M.T.; Barreiros, A.M.; Albuquerque, A. *Tratamento de Águas Residuais—Operações e Processos de Tratamento Físico e Químico: Cursos Tecnicos*; ERSAR & ISEL: Lisbon, Portugal, 2016; pp. 1–544.
5. Tucci, C.E.M.; Meller, A. Regulação das águas pluviais urbanas. *REGA* **2007**, *4*, 75–89.
6. Bertrand-Krajewski, J.L. Integrated urban stormwater management: Evolution and multidisciplinary perspective. *J. Hydro-Environ. Res.* **2021**, *38*, 72–83. [CrossRef]
7. Hamel, P.; Daly, E.; Fletcher, T.D. Source-control stormwater management for mitigating the impacts of urbanisation on baseflow: A review. *J. Hydrol.* **2013**, *485*, 201–211. [CrossRef]
8. Novaes, C.A.F.O.; Marques, R.C. Public policy: Urban stormwater in a paradigm shift, is it the end or just the beginning? *Water Sci. Technol.* **2022**, wst2022127. [CrossRef] [PubMed]
9. Braden, J.B.; Ando, A.W. Economic costs, benefits, and achievability of low-impact development-based stormwater regulations. In *Economic Incentives for Stormwater Control*; CRC Press: Boca Raton, FL, USA, 2011; pp. 45–70.
10. Black & Veatch. 2018 Stormwater Utility Survey Black & Veatch. 2018. Available online: https://www.bv.com/resources/2018-stormwater-utility-survey-report (accessed on 15 February 2022).
11. Veiga, M.M.; Feitosa, R.C.; Marques, R.C. Analyzing barriers for stormwater management utilities. *Water Sci. Technol. Water Supply* **2021**, *21*, 1506–1513. [CrossRef]
12. Kea, K.; Dymond, R.; Campbell, W. An analisys of the patterns and trends in United States Stormwater Utility Systems. *J. Am. Water Resour. Assoc.* **2016**, *52*, 1433–1449. [CrossRef]
13. NACWA. *MS4 Stormwater Permitting Guide*; NACWA—National Association of Clean Water Agencies: Washington, DC, USA, 2018; pp. 1–89.
14. Grigg, N.S. Stormwater Programs: Organization, Finance, and Prospects. *Public Works Manag. Policy* **2013**, *18*, 5–22. [CrossRef]
15. Campbell, W.; Bradshaw, J. *Western Kentucky University Stormwater Utility Survey 2021*; Kentucky University: Lexington, KY, USA, 2021; Available online: https://digitalcommons.wku.edu/cgi/viewcontent.cgi?article=1003&context=seas_faculty_pubs (accessed on 15 January 2022).
16. Black and Veatch. *2021 Stormwater Utility Survey Report*; Black & Veach: Overland Park, KS, USA, 2021; Available online: https://www.bv.com/resources/2021-stormwater-survey-report (accessed on 20 February 2022).
17. Vietz, G.; Whiteoak, K.; Ehrenfried, L. Incentivising Stormwater Management in Cities and Suburbs. *Water J.* **2018**, *3*, 1–15. [CrossRef]
18. Campbell, C.W.; Dymond, R.L.; Dritschel, A. *Western Kentucky University Stormwater Utility Survey 2016*; Kentucky University: Lexington, KY, USA, 2016; pp. 1–50. Available online: https://www.wku.edu/seas/documents/swusurvey-2016.pdf (accessed on 18 January 2022).
19. Tasca, F.A.; Assuncão, L.B.; Finotti, A.R. International experiences in stormwater fee. *Water Sci. Technol.* **2017**, *1*, 287–299. [CrossRef] [PubMed]
20. AECOM. *Thunder Bay Stormwater Financing Strategy Report*; AECOM: Gualph, ON, Canada, 2020.
21. Otoch, B.C.C.; Studart, T.M.C.; Campos, J.N.B.; Portela, M.M. Gestão de Recursos Hídricos em Regiões Semiáridas e a Dependência da Trajetória Institucional: Nordeste Brasileiro e Austrália. *Rev. Recur. Hídricos* **2019**, *40*, 43–51. [CrossRef]
22. Brodnik, C.; Brown, R.; Cocklin, C. The Institutional Dynamics of Stability and Practice Change: The Urban Water Management Sector of Australia (1970–2015). *Water Resour. Manag.* **2017**, *31*, 2299–2314. [CrossRef]
23. Fonte, G.M.S. Os Mercados da Água em Operação nos Eua, Chile e Australia: Reflexões para o Brasil. Master's Thesis, Brasília University, Brasília, Brazil, 2020.
24. Monaghan, C. Critical Junctures. *Educ. Durable Solut.* **2021**, *11*, 95–108.
25. Radcliffe, J.C.; Page, D.; Naumann, B.; Dillon, P. Fifty years of water sensitive urban design, Salisbury, South Australia. *Front. Environ. Sci. Eng.* **2017**, *11*, 7. [CrossRef]
26. Australian Government Bureau of Meteorology. Australian Climate Averages—Rainfall (Climatology 1981–2010). 2022. Available online: http://www.bom.gov.au/jsp/ncc/climate_averages/rainfall/index.jsp?period=an&area=vc#maps (accessed on 20 February 2022).
27. Stovin, V.R.; Jorgensen, A.; Clayden, A. Street trees and stormwater management. *Arboric J.* **2008**, *30*, 297–310. [CrossRef]
28. Burgan, H.I.; Icaga, Y. Flood analysis using adaptive hydraulics (ADH) model in the Akarcay basin. *Teknik Dergi Tech. J. Turk. Chamb. Civ. Eng.* **2019**, *30*, 9029–9051. [CrossRef]
29. Barbosa, A.E.; Fernandes, J.N.; David, L.M. Key issues for sustainable urban stormwater management. *Water Res.* **2012**, *46*, 6787–6798. [CrossRef]
30. ANA. *Atlas Esgotos—Despoluição de Bacias Hidrográficas*; Agência Nacional de Águas (ANA): Brasilia, Brazil, 2017; pp. 1–265. Available online: http://arquivos.ana.gov.br/imprensa/publicacoes/ATLASeESGOTOSDespoluicaodeBaciasHidrograficas-ResumoExecutivo_livro.pdf (accessed on 15 February 2022).

31. Tasca, F.A. Simulação de Uma Taxa para Manutenção e Operação de Drenagem Urbana para Municípios de Pequeno Porte. Master's Thesis, Universidade Federal de Santa Catarina (UFSC), Florianópolis, Brazil, 2016.
32. Zhao, J.Z.; Fonseca, C.; Zeerak, R. Stormwater utility fees and credits: A funding strategy for Sustainability. *Sustainability* **2019**, *11*, 1913. [CrossRef]

remote sensing

MDPI

Article

An Extended Watershed-Based AHP Model for Flood Hazard Estimation: Constraining Runoff Converging Indicators via MFD-Derived Sub-Watershed by Maximum Zonal Statistical Method

Hongping Zhang [1,2], Zhenfeng Shao [1,*], Jisong Sun [2], Xiao Huang [3] and Jie Yang [1]

[1] State Key Laboratory of Information Engineering in Surveying, Mapping and Remote Sensing, Wuhan University, Wuhan 430079, China; zhanghongping@whu.edu.cn (H.Z.); yangj@whu.edu.cn (J.Y.)
[2] State Key Laboratory of Severe Weather, Chinese Academy of Meteorological Sciences, Beijing 100081, China; sunjs@cma.gov.cn
[3] Department of Geosciences, University of Arkansas, Fayetteville, AR 72701, USA; xh010@uark.edu
* Correspondence: shaozhenfeng@whu.edu.cn

Abstract: Floods threaten the sustainable development of areas with a high probability of hazard. A typical analytic hierarchy process (pixel-based AHP) based flood hazard estimation method may ignore the similar threat caused by neighborhood cells at the sub-watershed scale. This study proposed an extended watershed-based Zonal Statistical AHP for flood hazard estimation: Constraining converging related indicators by the sub-watersheds (WZSAHP-RC) model to improve this gap. Before calculating the flood hazard index, the proposed model uses the sub-watershed derived by the multiple flow direction method as a based unit to calculate the maximum zonal statistical value of runoff converging indicators. Moreover, taking the Chaohu basin of Anhui in China as the case study, the validation flooding ground-truthing was constructed from GF-3, and Landsat OLI images of the flood event from 20 July to 24 July 2020, which is the biggest flood recorded by the Zhongmiao station, which recorded a new water level, 0.82 m higher than the historical record. Compared with the validation, the results indicated the proposed method could improve the correct ratio by 38% (from 22% to 60%) and the fit ratio by 17% (from 18% to 35%) when considering the predicted flood hazard levels of "High" and "Very High" as flooded areas. Moreover, the flood hazard map derived by WZSAHP-RC demonstrated greater consistency in the flooded districts filtered by Baidu News than the pixel-based AHP. It revealed that considering two- or even multi-dimensional homogeneity may help to improve the accuracy of flood hazard maps on a catchment scale.

Keywords: flood; analytic hierarchy process (AHP); GF-3; Chaohu; watershed; Baidu News

Citation: Zhang, H.; Shao, Z.; Sun, J.; Huang, X.; Yang, J. An Extended Watershed-Based AHP Model for Flood Hazard Estimation: Constraining Runoff Converging Indicators via MFD-Derived Sub-Watershed by Maximum Zonal Statistical Method. *Remote Sens.* **2022**, *14*, 2465. https://doi.org/10.3390/rs14102465

Academic Editors: Luis Garrote and Alban Kuriqi

Received: 27 March 2022
Accepted: 16 May 2022
Published: 20 May 2022

1. Introduction

Flooding is a common phenomenon occurring worldwide, related to climatic conditions, geography, the environment, human activities, and other factors. Flooding is a natural event with great destructive power and a common challenge for human society [1,2]. The underlying surface is a formation environment for floods, and it is also the leading site for human activity. As economic development and urbanization are promoted, more surfaces that were previously natural are being replaced by impermeable surfaces. The increase in impervious surfaces may cause an increase in the surface runoff and a decrease in the time between the start of a flood and the flood peak [3]. These adverse hydrological effects may cause an increase in extreme rainstorm events in the future. Continuous excessive rainfall will cause the water level of rivers, lakes and reservoirs to rise sharply, bringing severe threats to flood-prone areas [4].

China is one of the countries frequently disturbed by flood and waterlogging events. It was reported that 641 out of 654 Chinese cities were exposed to frequent floods [5].

Taking China's third largest catchment—the Yangtze River, as an example, the areas in the middle and lower reaches of this estuary experience plum floods every spring. In 2020, there were five floods whose discharge or water level reached the flood warning level for the Yangtze River. In the flood season of July 2020, seven floods occurred across several provinces. According to the Ministry of Emergency Management of China, as of 13 August 2020, the floods had affected 63.46 million people and caused a direct economic loss of 178.96 billion CNY [6]. Different human settlements might experience an extra loss level in the same hazard [7]. The combination of climate change and increasing urbanization brings tremendous challenges to planning and managing cities for sustainability [4]. Meanwhile, the feedback loop of flood protection and awareness in communities affects their planning and development in the long term [8]. To mitigate urban floods, accurate flood hazard estimation corresponding to patterns of urbanization is a policy objective.

Flood hazard distribution is the dominant factor in flood risk estimation. Compared with the aim of flood risk mapping to identify the exposures of communities and socio-economic places in extreme rainfall events, flood hazard maps focus on the flooded area distribution determined by natural features, such as flow converging, geological permeation, and under-lying surface storage space. AHP is a typical multi-objective-decision-making method widely used in flood hazard estimation. Models, such as analytic hierarchy process (AHP) [9], Bayesian models [10], fuzzy comprehensive evaluation [11,12], and hybrid models between bivariate statistical [13], artificial neural networks and boosting algorithms [14] have been deployed in flood hazard estimation. Bayesian models need measurements and statistical data from historical flood events. Fuzzy methods and swarm intelligence can be supervised classifications, but need samples from historical flood events. Flood hazard estimation via the AHP method does not rely directly on historical records, and it has the advantage of being easy to use and accurate.

The essential flood hazard estimation via AHP describes the individual heterogeneity features of under-lying surface areas [15,16]. As the geology information system (GIS) develops, flood hazard estimation can detail flood hazards involving pixel-scale indicators. For example, Abdouli et al. [17] adopted AHP to map the flooding potential on the Arabian Gulf coast using data that include land use, soil type and antecedent moisture. Wu et al. [18] estimated flood vulnerability via AHP using rainfall intensity and duration, elevation, slope, land use, and population density. However, these pixel-based AHP are difficult, considering terrain connectivity thus leading to the possibility of ignoring flood hazard consistency caused by neighborhood pixels.

A watershed is a natural terrain edge of water converging through the terrain. Sub-watershed reflects a group of pixels with common flow paths to combine rainwater to the same outlet (e.g., rivers, lakes, and wetlands). As in the hydrology and hydrodynamic model, a sub-watershed was usually considered a basic unit, such as SWAT, SWMM, etc. However, these models always rely on detailed input parameters (e.g., rainfall, evaporation, topography, soil, river, and drainage information), are computationally demanding, often simulate the specific rainfall-flood process, and are widely used in flood forecasting. For flood hazard estimation, especially in data-scarce or large-scale areas, the detailed parameters of the hydrology/hydrodynamic model desired cannot be satisfied.

During a flood event, the continuous rainwater converging along the flow path can be considered source flooding, bringing similar threats to pixels at sub-watershed scales [3]. The flood hazard of cells is more dependent on the maximum risk level of neighborhood cells on a sub-watershed scale rather than the individual terrain features or hydrological characteristics of each cell [19]. Therefore, using sub-watershed as a basic unit to estimate flood hazards may consider the hydrological influence introduced by adjacent pixels. Thus, it may increase the estimation accuracy of the flood hazard map.

This study aims to present a new flood hazard estimation method of using the sub-watershed as a constrain unit to express the homogeneity of flood hazards introduced by a group of converging pixels. The proposed model, termed WZSAHP-RC, adopts multiple flow directions (MFD) derived sub-watershed [20] as a basic unit to constrain

runoff, converging related indicators by the maximum zonal statistical method, while other hydrological-formation indicators are also calculated by pixels. Taking the Chaohu basin of Anhui, China, as an example, the flood hazard maps derived from the proposed model were validated by the flooded areas extracted from remote sensing images captured during a real-world flood event in July 2020. Furthermore, the influences of using single flow direction and multiple flow direction algorithms to delimitate a sub-watershed and the adopting minimum area threshold for a sub-watershed were also discussed.

This paper is organized as follows: In Section 2, the primary data sources and the methodology will be described. Subsequently, the results and the significant findings are presented in Section 3. Then, the influence of sub-watershed delimitation methods and function constraining factors of the proposed model will be discussed in Section 4. At last, some conclusions and the limitations of this study are provided in Section 5.

2. Materials and Methods

2.1. Study Area

The Chaohu basin is in the range of Anhui province, China. It is located at the intersection of the Yangtze River catchment and Huaihe River catchment, draining rainwater from the upstream Huaihe River to Chaohu and finally flowing into the Yangtze River. This study selected 11 counties surrounding Chaohu Lake to analyze the flood hazard distribution (Figure 1). These chosen districts implemented a 10-km buffer analysis to avoid the many small-scale sub-watersheds occurring at the edge of specific areas. The boundary was considered the range of the study area.

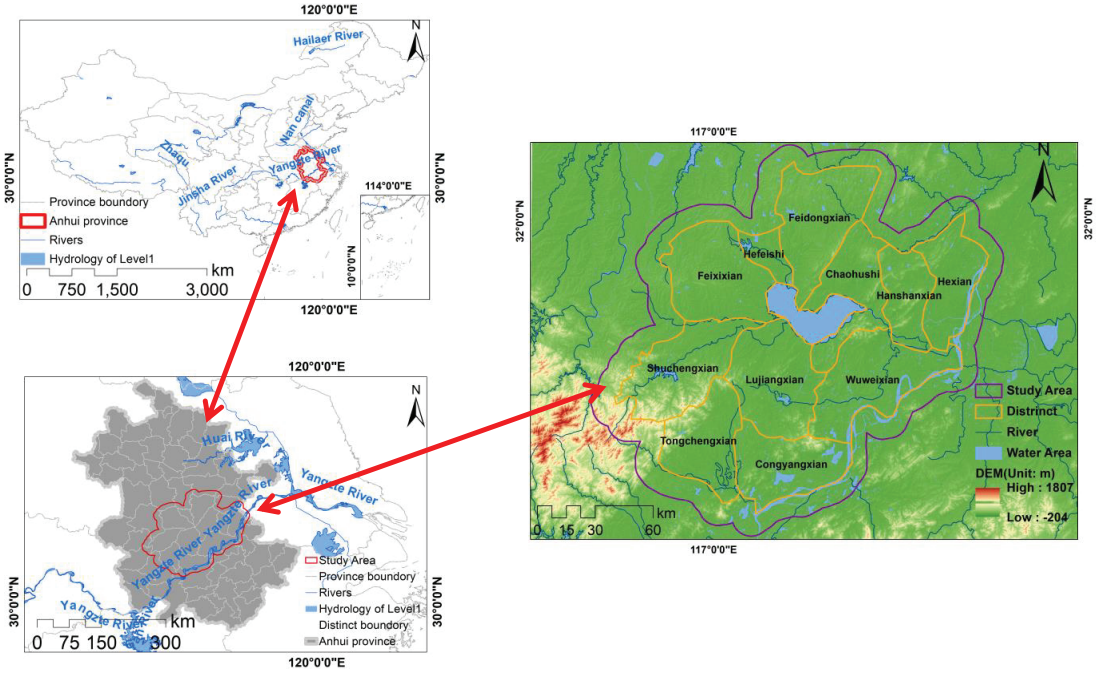

Figure 1. The geographical location of the study area and the DEM of the study area (according to the China basic geographic information, 2008 version).

The terrain surrounding the Chaohu basin is characterized as a "butterfly" pattern, which leads to most areas along with the water system of the Chaohu basin having a high possibility of flooding every flood period. The terrain of the Chaohu basin contains five major terrain types: low mountains, hilly land, hill land, plains (lakeside and wavy plains)

and water areas. The elevation in the northwest and southeast is higher than in other areas of the study area; the middle region has a relatively lower elevation than other areas. Lujiang city and Wuwei city are at relatively lower elevations. Therefore, they are exposed to a high risk of flooding. Improving the accuracy of flood hazard estimation in the Chaohu basin will support future flood risk management and thus help protect the local economy.

2.2. Materials

Primary data sources and their detailed information are presented in Table 1. The geographic information system (GIS) vector map of specific and hydrological information was used in this study. The digital elevation model (DEM) data were used to divide sub-watersheds and calculate slopes. The impermeable surface products were used to extract land-used type and hydrological infiltration information. The images include the SAR (synthetic aperture radar) image of the GF-3 and the optical image of the Landsat 8 OLI image. The GF-3 captured on 24 July 2020, was used to extract flooded areas. The Landsat 8 OLI image shot on 20 July 2020, was used to extract former flood areas. Moreover, the flooding information searched in Baidu News was used to construct the validation of flooded towns and villages. The final used tiles of impervious surface production and the validation dataset were described as in Appendix A.

Table 1. The main data materials used in this study.

Data Sources	Used Data	Detailed Information
Geographic information (1:1 million)	District	The county and town level districts were used. Hydrological layers were utilized to constrain DEM. They were downloaded from the China Science and Technology resources sharing network, Available online: http://www.geodata.cn/data/datadetails.html?dataguid=113730965998632 (accessed on 20 July 2020).
	River and lake	
ASTER GDEM V2 (30 m)	DEM	The DEM divides watersheds and classifies the slope and elevation indicators. The DEM was downloaded from Available online: http://www.gscloud.cn (accessed on 20 July 2020).
China's impermeable surface product (2 m)	Land-use type	Following [21], the water, vegetation, soil, building and road layers were used to classify land use and hydrological indicators. China's impermeable surface production (2 m) dataset is not published on the website. In this study, the involving land use type vector collected from this product can be downloaded according to the detailed description in the Supplementary Material section.
	Hydrological characteristics	
Images for extracting flooding areas	Water bodies	The Landsat 8 OLI on 20 July 2020 and GF-3 on 24 July 2020 were used to extract flooding areas. The Landsat 8 OLI was downloaded from Available online: https://www.usgs.gov (accessed on 20 July 2020). The GaoFen center of Hubei province supports the GF-3 data, and it also can download from the China Science and Technology resources sharing network: Available online: http://39.106.90.21/datashare/newsatelliteset2.html (accessed on 20 July 2020).
Flooding information in Baidu News	Flooding and dam breaks by towns	Baidu News, as a validation source, was searched from Available online: http://news.baidu.com (accessed on 20 July 2020).

1. GIS Vector maps—Geographic information. This study used the vectorized county and town boundaries released in 2008. The administrative districts served as geographic constraints to filter Baidu News flood reports. The hydrological layers, including rivers, streams, and lakes (levels 1 to 5), were compared with water bodies classified from images.
2. DEM—ASTER GDEM V2 dataset. The DEM dataset adopted is ASTER GDEM V2. This study area covers a total of nine scenes. The horizon resolution of the DEM dataset is 30 m, and the vertical resolution is 1 m. The projection is WGS_1984_UTM_Zone_50N. As shown in Figure 1, the range of elevation was −204~1807 m, and they were the original value of DEM in the study area.

3. GRID of Remote sensing production—Land information. This study adopted China's impermeable surface grid product (2 m) [21]. The 18 tiles for Hefei, Luan, Anqing, Wuhu, Maanshan, Chuzhou, and Huainan cities were used to prepare the land use and hydrological indicators.
4. Images—Extracting flooded area. As remote sensing develops, more and more images of multiple spatial resolutions, considerable time, multiple angles, and multiple carrying platforms can be used for urban underlying surface observation [22]. The flooded areas extracted from remote sensing images can construct the flood hazard ground-truthing dataset. This study collected the used optical image of Landsat 8 OLI of 30 m resolution shot on 20 July 2020, and the SAR of GF-3 Fine Stripmap II (FSII) model of 10 m resolution shot on 24 July 2020. The pre-processing of Landsat 8 OLI was performed in ENVI 5.3, and included radiometric calibration, and atmosphere correction; the water bodies were extracted by the maximum likelihood method. The pre-processing of the GF-3 SAR image was implemented in PolSAR Pro 5.2 and GAMMA and included speckle filtering, radiometric calibration, terrain correction and geocoding. The water bodies in GF-3 were classified basing the threshold segmentation method corresponding to the water bodies in Landsat 8 OLI. The validation experiments were constructed to establish the intersecting area's ground truth range considering the temporal differences between these two images. The permanent water bodies extracted from China's impermeable surface product were excluded from the final validation ground truth of the flood areas.
5. Baidu News—Filtering flood and dike rupture information. The damage information from floods and dikes of flood events in July 2020 was used to verify the accuracy of the flood hazard estimation in the Chaohu basin. We used an internet context searching and capturing tool named "Octopus" (Available online: https://www.bazhuayu.com (accessed on 20 July 2020)) to collect information from the Baidu News website (Available online: https://news.baidu.com (accessed on 20 July 2020)). The keywords were used to filter Baidu News, including "flood" and "waterlogging", combined with the names of the county in the range of the study area.

2.3. Methods

The technical workflow used in this study is illustrated in Figure 2. After the primary data sources were pre-processed, the flood hazard criteria were constructed. Moreover, the flood hazard involving indicators grouped by the rainfall-runoff production and the flow converging related indicators were prepared. According to the proposed WZSAHP-RC model, the maximum zonal statistical method will constrain the converging associated indicators. Then, the pixel-based AHP flood hazard index and the sub-watershed-based WZSAHP-RC flood hazard index will be calculated. Then, the two kinds of flood hazard maps will be classified as five levels according to the Nature Break slice method in terms of flood hazard indexes. Finally, the validation process will be implemented.

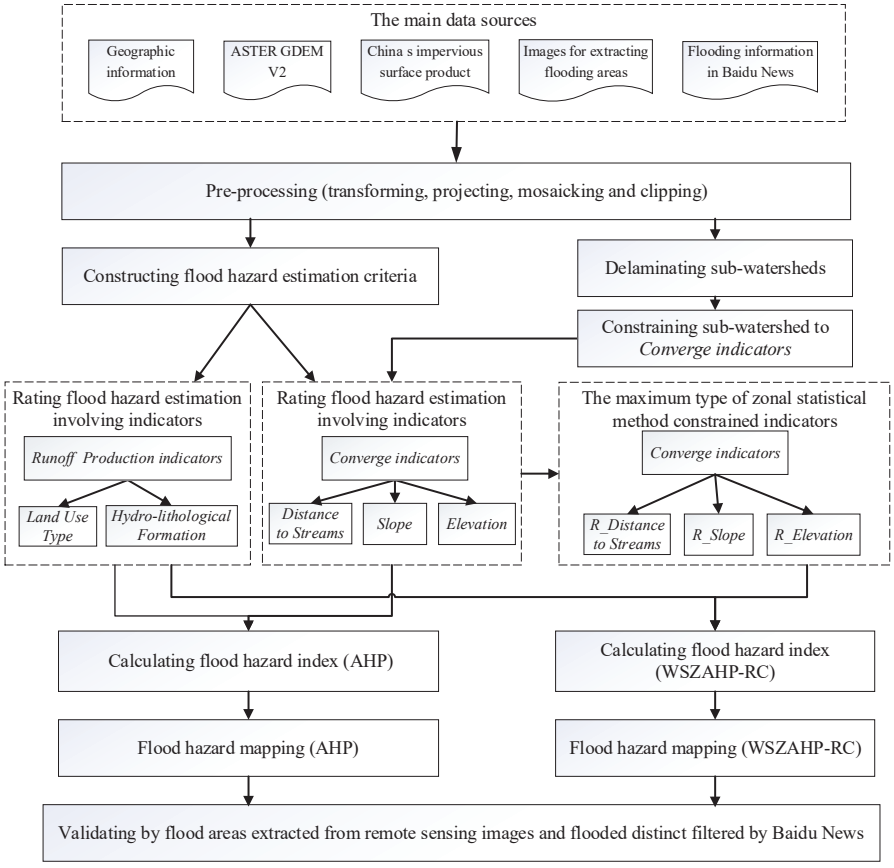

Figure 2. The overall workflow of our study.

The primary data sources and the pre-processing processes were described in Section 2.2. The proposed watershed-based zonal statistic AHP model will be introduced in Section 2.3. Moreover, to further detail the multiple flow direction algorithm and the single flow direction algorithm influence, the sub-watershed division method based on the D8 and MFD algorithms will be introduced in Section 2.4. Finally, the flood hazard validating approach will be supplied in Section 2.5.

2.3.1. Flood Risk Estimating Method

A sub-watershed is a physical range, and it indicates rainwater converging along a section of a digital stream flowing out through the same outlet. The sub-watershed pixels reflect the same runoff outlet along the common converging path. Moreover, the pixels in a sub-watershed can be considered to share the same storage of surface runoff rainwater at the sub-watershed scale. Therefore, in this study, the sub-watershed was adopted as a basic unit to constrain runoff converging related indicators by the maximum zonal statistical method to consider that the spatial connectivity brought similar flood hazards at the sub-watershed scale. The structure of traditional AHP (Figure 3a) and the flood hazard estimation process among pixel-based AHP (Figure 3b) and the proposed WZSAHP-RC (Figure 3c) are shown in Figure 3.

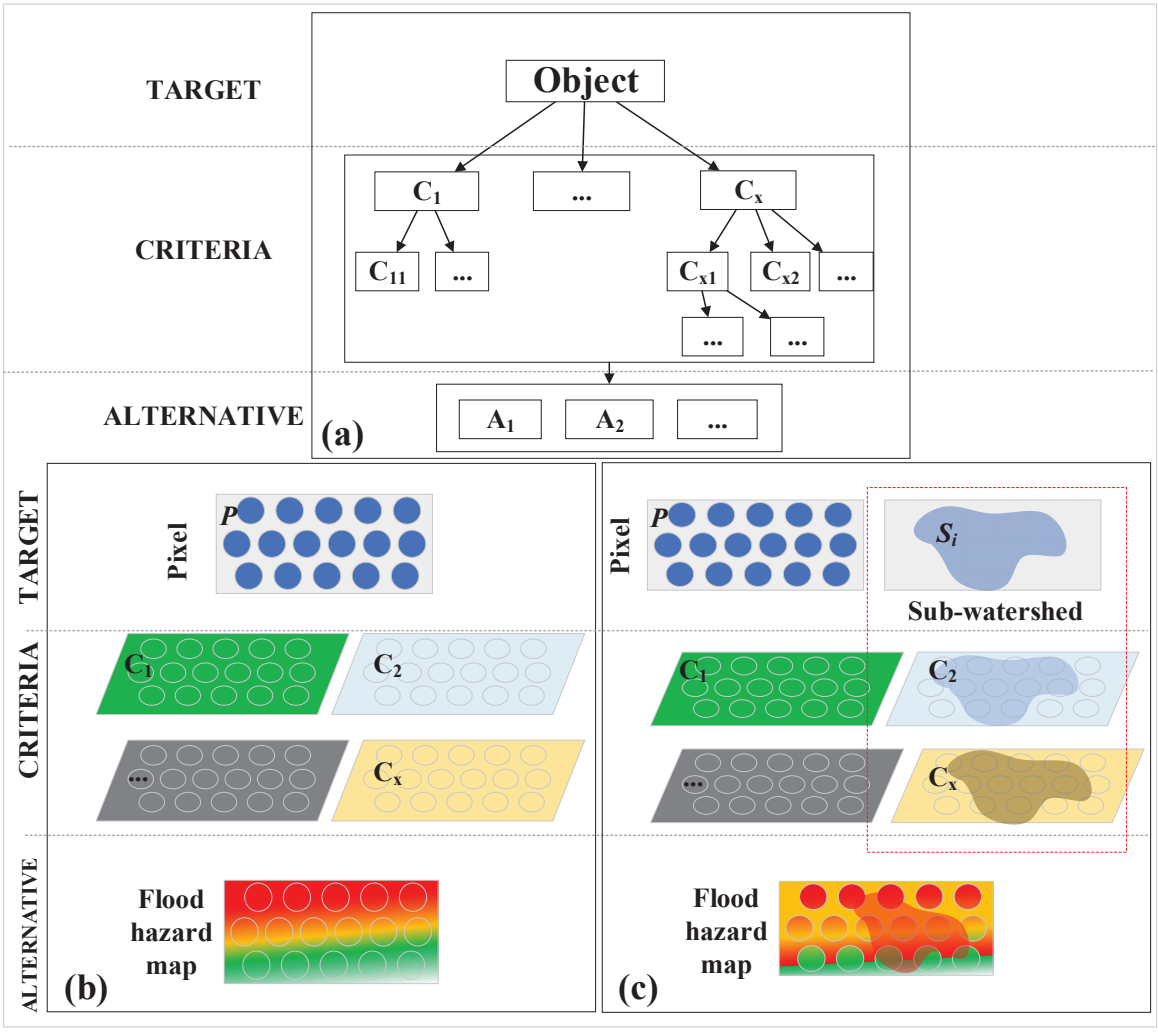

Figure 3. The logical structure of flood hazard estimation methods: (**a**) The general structure of AHP, (**b**,**c**) are diagrams of ordinary AHP and WZSAHP-RC.

Figure 3a shows the structure diagram of the AHP method, its estimation target is recorded as "object", and its criteria are $C = \{C_1, C_2, \ldots, C_x\}$, and the criterion can be constructed in multiple layers as needed. The estimating index can determine its final alternative set $A = \{a_1, a_2, \ldots\}$. The AHP model is widely used in flood hazard estimation to integrate a Geographic Information System (GIS) and remote sensing. AHP is composed of three levels: target, criteria, and alternatives. The target layer refers to the evaluation unit; the criteria (with single or multiple layers) consist of several clusters that reflect different aspects of the target; the alternative is composed of the estimation results set. The AHP-based flood hazard estimation model can be defined as follows:

$$P = \begin{bmatrix} p_{11} & p_{12} & \cdots & p_{1n} \\ p_{21} & p_{22} & \cdots & p_{2n} \\ \cdots & \cdots & \cdots & \cdots \\ p_{m1} & p_{m2} & \cdots & p_{mn} \end{bmatrix}, C = \begin{bmatrix} C_1 \\ C_2 \\ \cdots \\ C_x \end{bmatrix}, C_x = \begin{bmatrix} c_{11} & c_{12} & \cdots & c_{1n} \\ c_{21} & c_{22} & \cdots & c_{2n} \\ \cdots & \cdots & \cdots & \cdots \\ c_{m1} & c_{m2} & \cdots & c_{mn} \end{bmatrix}_x \quad (1)$$

where matrix P represents the pixels in the study area, with a size of $m \times n$, C is the flood hazard estimation indicators, and each of the indicators c_x is a raster layer, with a size of $m \times n$.

A comparative matrix of criteria and calculated weights is constructed. According to the AHP model, the positive pairwise comparison matrix usage value 1 to 9 indicates the relative importance of the two indices. Its largest eigenvalue and corresponding eigenvectors can be used as weight vectors to represent the established hierarchic evaluation structure [23]. The hierarchic evaluation structure can be calculated as follows:

$$J = \begin{bmatrix} j_{11} & j_{12} & \cdots & j_{1x} \\ j_{21} & j_{22} & \cdots & j_{2x} \\ \cdots & \cdots & \cdots & \cdots \\ j_{x1} & j_{x2} & \cdots & j_{xx} \end{bmatrix}_{x \times x}, \; J \bullet X = \lambda_{\max} \bullet X \to \omega_i = \frac{x_i}{\sum_{j=1}^{x} x_j}, \; \omega = \begin{bmatrix} \omega_1 \\ \omega_2 \\ \cdots \\ \omega_x \end{bmatrix} \tag{2}$$

where the comparison matrix J, with a size of $x \times x$, is used to determine the importance order among criteria C (in Equation (1)). X is the eigenvector corresponding to the largest eigenvalue $\lambda_{\max}$ of J, ω is the weight vector corresponding to the normalization value of the eigenvector X.

The consistency ratio was calculated in Equation (3) to calculate the judgment matrix criteria as logically consistent [23]. The pairwise comparison matrix can be accepted if its consistency ratio is less than 0.1 (a consistency ratio of 0 indicates that the judgment matrix is entirely consistent).

$$CI = {}^{\lambda_{\max} - n}/_{n-1}, \; CR = \frac{CI}{RI} \tag{3}$$

where CR is the consistency ratio, CI is the consistency index, RI is a statistic random index, the average CI of randomly generated pairwise comparison matrix of similar size, $\lambda_{\max}$ is the largest eigenvalue of the comparison matrix, and n is the number of indicators used in criteria.

Figure 3b shows that the common AHP model adopts the pixel as a basic unit. The final estimation index can be calculated by accumulating the pairwise cumulative indices and weights.

Figure 3c is a diagram of the proposed WZSAHP-RC model. The constrain runoff converging related indices, such as Slope, Elevation, and Distance from streams, can constrain sub-watersheds and thus help identify neighborhood hazards using the following formulas:

$$S = \begin{bmatrix} \cdots & & & \\ & S_k & S_k & \\ & & S_k & \\ & & & \cdots \end{bmatrix}_{m \times n} \tag{4}$$

$$F(S, c_x) = zonalStatistic(S, c_x, Method) \tag{5}$$

where S is the sub-watershed division raster, $F(S, c_x)$ is the constraint sub-watershed as a statistical zonal unit, to update the corresponding indicator c_x. The size of $F(S, c_x)$ is also $m \times n$; $zonalStatistic$ is calculated using the descriptive statistics of indicator c_x for each sub-watershed S, $Method$ is the statistical method including the majority, maximum and median.

The final flood hazard index is calculated using the pairwise cumulative criteria and weights following Equation (6). As the Natural Break method can maintain slight variance within groups and significant variance among indexes, it is widely used to partition the final flood hazard map [15,16,24–26]. Therefore, the final flood hazard map can be derived by classifying the flood hazard index into {"very low", "low", "moderate", "high", and "very high"} by the Nature Break method.

$$FRI = \; \omega \bullet C = \sum_{i=1}^{i=m} \omega_i \bullet F(S, c_i) + \sum_{j=m+1}^{j=x} \omega_j \bullet c_j, \; (0 \le m \le x) \tag{6}$$

where FRI is the flood hazard index, calculated by the cumulative sum of criteria C and its corresponding weight ω. The criteria can be grouped as the sub-watershed constraint indices $F(S, c_i)$ and the original indices c_j.

2.3.2. Constructing Flood Hazard Estimation Criteria

This study adopted five indices $C = \{C_1, C_2, C_3, C_4, C_5\}$, where C_1 = *Slope*, C_2 = *Elevation*, C_3 = *Distance from streams*, C_4 = *Hydro-lithological formations*, C_5 = *Land use type*, referring to [25] to construct flood hazard estimation criteria. The former three indicators, the "*Slope*", "*Elevation*", and "*Streams*", affect the path of rainwater runoff convergence. They reflect the geological flood hazard factors. The "*Hydro-lithological formations*" and the "*Land-use type*" affect infiltrability and the roughness of the underlying surface. Thus, the "*Hydro-lithological formations*" and the "*Land-use type*" are grouped as runoff production indicators. As in AHP-based flood risk estimation, the weighting definition would influence the accuracy of the final flood hazard distribution. Ekmekcioğlu and Koc et al. [11,12,27] adopted the fuzzy-AHP to increase the reasonable weighting definition. The comparison matrix defined, referred to [25], as shown in Table 2.

Table 2. The judgment matrix of criteria. C_1 = *Slope*, C_2 = *Elevation*, C_3 = *Distance from streams*, C_4 = *Hydro-lithological formations*, C_5 = *Land use type*.

Flood Hazard Potential	C_1	C_2	C_3	C_4	C_5
C_1	1	4	1/2	3	1/2
C_2	1/4	1	1/3	1/2	1/4
C_3	2	3	1	3	1
C_4	1/3	2	1/3	1	1/3
C_5	2	4	1	3	1

In the judgment matrix, the maximum eigenvalue is $\lambda_{\max}$ = 5.133. As the criteria number is 5, the obtain random index value is as RI = 1.12 from a lookup table. Thus, the consistency index of the judgment matrix is: $CI = \frac{\lambda_{\max} - n}{n-1} = \frac{5.133-5}{4} = 0.03325$. Therefore, the final consistency ratio can be calculated as $CR = \frac{CI}{RI} = \frac{0.03325}{1.12} \approx 0.030$. Since the value CR is less than 0.1, the judgment matrix used to derive the weight matrix can be accepted. The process of weighting criteria is calculated as:

$$C = \begin{bmatrix} C_1 \\ C_2 \\ C_3 \\ C_4 \\ C_5 \end{bmatrix} = \begin{bmatrix} FR_{Slope} \\ FR_{Elevation} \\ FR_{Distance\_from\_streams} \\ FR_{Hydro\_lithological\_formations} \\ FR_{Land\_use\_type} \end{bmatrix}, \; A = \begin{bmatrix} 1 & 4 & 1/2 & 3 & 1/2 \\ 1/4 & 1 & 1/3 & 1/2 & 1/4 \\ 2 & 3 & 1 & 3 & 1 \\ 1/3 & 2 & 1/3 & 1 & 1/3 \\ 2 & 4 & 1 & 3 & 1 \end{bmatrix} \quad (7)$$

$$\lambda_{\max} = 5.133, \; \omega = \begin{bmatrix} 0.214 & 0.068 & 0.302 & 0.100 & 0.315 \end{bmatrix}$$

where C is the matrix of used flood hazard estimation criteria. The corresponding indicators are: $\left\{FR_{Slope}, FR_{Elevation}, FR_{Distance\_from\_streams}, FR_{Hydro\_lithological\_formations}, FR_{Land\_use\_type}\right\}^{\tau}$, FRI is the flood risk index, A is the judgment matrix comparing between two indicators, and the weight vector ω is calculated according to Equation (2).

As in the WZSAHP-RC model, the descriptive statistics were calculated based on the value of runoff converging indices, including "*Slope*", "*Elevation*", and "*Distance from streams*". Moreover, the flood hazard index can be expressed as:

$$FRI = \omega_1 \bullet F(S, C_1) + \omega_2 \bullet F(S, C_2) + \omega_3 \bullet F(S, C_3) + \omega_4 \bullet C_4 + \omega_5 \bullet C_5 \quad (8)$$

where FRI is the flood risk index, ω is weight, C is the criteria as defined according to Equation (7), $F(S, C_i)$ is the criterion C_i calculated using the descriptive statistics values of the sub-watershed S, according to Equation (5).

2.3.3. Rating Flood Hazard Estimation Involving Indicators

The original flood hazard estimation involving indicators needs to be rated uniformly. The values of "*Slope*" and "*Elevation*" are numeric, with a natural pattern distribution. Therefore, the natural break method reclassified these two indicators into uniform classes. The value of "*Land-use type*" and "*Hydro-lithological formation*" are category words. They were ranked according to the infiltration and rainfall-runoff production ability corresponding with levels of 1–5. The "*Distance from streams*" adopted specific ranges of Euclidean distance from streams to represent flood hazard levels. The ranked flood hazard estimation indicators are listed in Table 3.

Table 3. The classes and rating of factors in flood hazard estimation.

Factors	Classes	Rating	Factors	Classes	Rating
Slope (°)	0	5	Land use types	Water	5
	0–2	4		Road	4
	2–6	3		Building	3
	6–12	2		Soil	2
	12–20	1		Vegetation	1
	>20	0			
Elevation (m)	−204–12	5	Hydro lithological formations	Water	4
	12–23	4		Impermeable surface	3
	23–46	3		Pervious surface	1
	46–152	2			
	>152	1			

Factors	Classes					Rating
Distance from streams (m)	Rivers, lakes and reservoirs					5
	Level 1	Level 2	Level 3	Level 4	Level 5	
					0–1000	4
			0–500	0–1000	1000–2000	3
		0–500	500–1000	1000–2000	2000–4000	2
	0–500	500–1000	1000–1500	2000–3000	4000–6000	1
	>500	>1000	>1500	>3000	>6000	0

1. Slope. The slope is the main factor influencing the rainwater flow path. The slope range is 0°–81°, classified as six classes by the Natural Break method, the angles (°) of "0", "0–2", "2–6", "6–12", "12–20", and ">20" were labeled as 5, 4, 3, 2, 1 and 0, respectively.
2. Elevation. The elevation influences flood risk distribution. It seems that cells with low elevation are highly likely to suffer flood hazards. The elevation range is −204–1490 m, they were classified into five types by the Natural Break method, the elevations (m) of "−204–12", "12–23", "23–46", "46–152", and ">152" were labeled as 5, 4, 3, 2 and 1, respectively.
3. Distance from streams. Streams are the source of flood risks. The distance from streams reveals the potential risk. In this study, the streams were extracted using the D8 algorithm, and the stream levels were labeled by the STRAHLER method. For specific streams, far away cells had lower flood risks than nearby cells. According to Table 3, six types of distance from streams were defined, including the water bodies ranked into five classes, and the distance from streams of levels 1–5 were classified as 0–4.
4. Land use types. The land-use types determine the rainfall-runoff production. The ranked vegetation, soil, building, road and water were 1, 2, 3, 4 and 5, respectively.
5. Hydro-lithological formations. The hydro-lithological formations influence the infiltration performed by rainfall-runoff production. Hydro-lithological formations were grouped by water, impervious surface, and permeable surface, and they were rated as 4, 3, and 1, respectively.

2.4. Watershed Delaminating

2.4.1. Pre-Processing DEM for Watershed Division

A DEM was the primary data used to derive the watersheds but needed to be enriched with hydrological information before delaminating the sub-watersheds. Kenny et al. [28] found that integrating hydrological streams with a DEM can improve the accuracy of extracting digital drainage. Zhang et al. [29] pointed out that delimiting a watershed and constraining a DEM by water bodies can reduce the uncertainty created when calculating water flow direction. Thus, hydrological features, including streams, rivers, and lakes, were used to update the elevation in a corresponding cell of a DEM.

Hydrological features can be recognized by their shapes. Constructed water bodies, such as rice paddies and ponds always have regular symmetrical shapes. Naturally occurring hydrological elements, such as lakes and even artificial elements, such as reservoirs, always extend along a terrain. The bodies of these hydrological elements are irregular and with long perimeters. Other hydrological features, such as streams, rivers and ditches always have long flow paths, so their shapes appear as long and narrow rectangles. Therefore, the defined natural water body index termed Steady Water Index (SWI) is expressed as Equation (9) to identify hydrological features. For example, since their shapes are like long and narrow rectangles, and river and stream elements, when the value SWI is 200, the ratio of the longer edge and the shorter edge is approximately 10,000. This ratio can represent most rivers and streams.

$$SWI = \frac{Shape\_Length}{\sqrt{Shape\_Area}} \tag{9}$$

where SWI is the steady water index. The $Shape\_Length$ and $Shape\_Area$ are the perimeter and area of the water bodies, respectively. Referring to the study area, it suggests the value of SWI should be set as between 6 to 200. At the same time, the water area threshold is also used to identify hydrological features. As the minimum area of lakes in the study area is about 70,000 m^2, the water polygons with a spatial coverage larger than 78 cells (as pixel resolution is 30 m, this is about 70,200 m^2) were regarded as natural water elements.

2.4.2. Delaminating Sub-Watershed by D8 Algorithm

The D8 algorithm is a typical single flow direction (SFD) method in the watershed division. It is termed via its theory of using the maximum drop of elevation from the neighborhood of eight pixels to obtain the candidate flow outlet of central pixels. Then, the flow accumulation can be determined through the single flow path. Moreover, the sub-watershed was divided by the minimum area threshold according to the accumulation value of flowing pixels.

The hydrology tool in ArcGIS 10.3 is based on the D8 algorithm and was used to segment sub-watersheds in this study. The area threshold of the sub-watershed is a vital parameter in defining watershed schemes. According to Baidu News, the threshold was determined according to the area of flooded parcels. The threshold of 200 hectares (ha) was marked according to the report from the network of China Radio [30], "The Wuwei county released flood water to village parcels with the area of smaller than 30,000 mu (~200 hectares) along dikes". The threshold of 667 ha came from Xinhua news [31], "Hefei city flooded nine village parcels with the area of larger than 100,000 mu (~667 hectares) along dikes". There were six area thresholds defined in the sub-watershed division, as shown in Table 4:

As shown in Table 4, four kinds of area thresholds were defined according to the area threshold of 667. Two types of area thresholds were determined according to 200.

Table 4. Area threshold used in delimitation watersheds via D8 algorithm.

Basic	Area Unit	(1)	(2)	(3)	(4)	(5)	(6)
667	ha	66.7		667.0		3333.0	6667.0
	mu	~10,000		~100,000		~500,000	~1,000,000
200	ha		200.0		2000.0		
	mu		~30,000		~300,000		

2.4.3. Delaminating Sub-Watershed by MFD Algorithm

The multiple flow direction (MFD) algorithm was also used to divide sub-watersheds. Thus, the influence of flood hazard estimation introduced by sub-watershed division derived by SFD and MFD can be compared.

MFD determines the flow direction according to elevation drops between a target cell and adjacent cells. If there are several alternative outflow directions, MFD will choose them as the outlets and distribute the flow accumulation by calculating the average water value of the central cell. The MFD algorithm may reduce the randomness when setting the flow direction as one of the potential outlets in flat areas. The MFD algorithm calculates flow direction as Equation (10) and derives sub-watershed by tracing the flow-in cells.

$$Dir_{flow} += \begin{cases} 2^i, if(Z_0 - Z_i) > 0 \\ 0, if(Z_0 - Z_i) \leq 0 \end{cases}, (0 \leq i \leq 8) \quad (10)$$

where Dir_{flow} is the flow direction of the current cell, it records the potential flow directions in a continuous value between 1–255 by accumulating the potential flow directions; i is the index of the eight adjacent cells, starting from the east, southeast, west, and so on, in a clockwise order; Z_0 is the elevation of the central cell; Z_i is the elevation of the adjacent cells.

The MFD algorithm traces the connected flat cells and sets them as the seed of a new sub-watershed. Searching the seeds from the sink areas, all the pixels flowing into the seed cells will be defined as belonging to the same sub-watershed. The scope of a certain sub-watershed will grow until the size is larger than the area threshold, and then the cells will be recorded as a new sub-watershed. Thus, the algorithm can keep the connected flat cells in the same sub-watershed, while the area threshold will determine the sub-watershed of the in-flowing neighborhood cells. The MFD algorithm was programmed by C#, and the sub-watershed delimitation result by the MFD algorithm is submitted as in Supplementary Materials.

2.5. Flood Risk Validating Method

In this study, the accuracy of flood hazard estimation results derived from the proposed model was quantitatively evaluated by flooded areas extracted from the GF-3 and Landsat 8 OLI images. The flood hazard estimation is always a five classify issue. Each pixel in the study area is ranked as one of the elements in the level set {"very low", "low", "moderate", "high", and "very high"}. Then, the five flood hazard levels were classified into two groups: the positive and the negative groups. Moreover, for each pixel where its flood hazard belongs to the positive group; it will be considered as a predicted flooded pixel. Otherwise, it is regarded as a predicted dry pixel. Following the former literature [32,33], the correct and fit ratios were used to assess flood hazard estimation accuracy. The correct ratio and fit ratio are calculated as follows:

$$Correct(\%) = \frac{FP_p \cap FW_{Flood}}{FW_{Flood}} \times 100 \quad (11)$$

$$Fit(\%) = \frac{FP_p \cap FW_{Flood}}{FP_p \cup FW_{Flood}} \times 100 \quad (12)$$

where $Correct(\%)$ is the correct ratio, and $Fit(\%)$ is the fit ratio. FP_P represents the pixels considered as predicted flood areas. FW_{Flood} represents the ground-truthing flood areas extracted from GF-3 and Landsat 8 OLI images.

The definition of flood hazard positive and negative groups is a critical process for constructing a validation dataset. From the view of classification, this definition means determining the classification threshold. This study defined two kinds of positive group and negative group, as follows:

- Validation 1: {positive group: "very high", "high", "moderate"; negative group: "very low", "low"};
- Validation 2: {positive group: "very high", "high"; negative group: "very low", "low", "moderate"}.

To further distinguish the flood hazard estimation result from the better-matched validation group, the F1-score is additionally used as an indicator. The F1-score is used to distinguish the combined accuracy among the used methods. The F1-score is a comprehensive indicator in binary segmentation problems. More excellent classification usually has a higher value of F1-score in binary segmentation problems. Moreover, the value of the F1-score is expected to be 0.6~0.8 or higher. It can be calculated according to Equation (13):

$$P = \frac{TP}{TP + FP},\ R = \frac{TP}{TP + FN},\ F_1 = \frac{2 \times P \times R}{P + R} \tag{13}$$

where F_1 is the F1-score, P is the precision rate, R is the recall rate, TP is the cells with truthing status predicted as positive in the validation dataset, FP is the cells with false status expected as positive in the validation dataset, and FN is the cells with false status predicted as negative in the validation dataset.

The flood hazard estimation is a five-type classification issue. Its comparison matrix was constructed following Table 5. As in large-scale flood hazard estimation, the ratio of predicted flood area is always small compared with the range of study area. Moreover, in this study, the proposed method considered the flood hazard level of all the water areas (the normal range of transport and storage water, such as rivers, lakes and so on) was "very high". In order to focus on the estimation of the consistency of predicted flood hazard pixels with the ground-truthing flood areas, the validation ground-truthing dataset was constructed by excluding the pixels of normal water body range in rivers, lakes, ponds, and reservoirs. The excluded water bodies were identified according to Equation (9).

Table 5. The classes and rating of factors in flood hazard estimation.

	Validation 1		**Validation 2**	
	Positive Group: "Very High", "High", "Moderate"	**Negative Group: "Very Low", "Low"**	**Positive Group: "Very High", "High"**	**Negative Group: "Very Low", "Low", "Moderate"**
flooded area	*TP*	*FN*	*TP*	*FN*
dry area	*FP*	*TN*	*FP*	*TN*
normal water	/	/	/	/

"*TP*" represents a predicted right result, the predict "Positive" matched the ground-truthing, "*FN*" represents a predicted wrong result, the predict "Negative" does not match the ground-truthing, "*FP*" represents a predicted wrong result, the predict "Positive" does not match the ground-truthing, "*TN*" represents predicted right result, the predict "Negative" matches the ground-truthing.

It is known that the precision, recall, and F1-score indicators in Equation (13) were widely used in the estimation binary segmentation classifier. Moreover, the correct ratio (shown in Equation (11)) and the fit ratio (shown in Equation (12)) were widely used indicators reflecting the flood hazard estimation accuracy. It can be found that both correct ratio and fit ratio focus on the estimation of the consistency of predicted flood areas with the ground-truthing flood pixels. Moreover, the correct ratio is the same as the recall indicator (the R in Equation (13)):

$$Correct(\%) = \frac{FP_p \cap FW_{Flood}}{FW_{Flood}} \times 100 = \frac{TP}{TP + FN} \tag{14}$$

As in flood estimation, precision is important, but the value of recall is more important. Moreover, the fit ratio can be expressed as Equation (15), which can reflect the overestimation of predicting flood pixels.

$$Fit(\%) = \frac{FP_p \cap FW_{Flood}}{FP_p \cup FW_{Flood}} \times 100 = \frac{TP}{TP + FP + FN} \quad (15)$$

3. Results

This session describes the experimental results, including the sub-watershed division results and the flood hazard map derived by the proposed method.

3.1. The Sub-Watershed Derived by DEM Using MFD and D8 Algorithms

In this paper, the hydrology layer collected in geographic information (1:1 million) was used to burn in DEM. Using the hydrology information enforced DEM, the raster of sub-watersheds can be delimitated via the MFD and D8 algorithms (Figure 4).

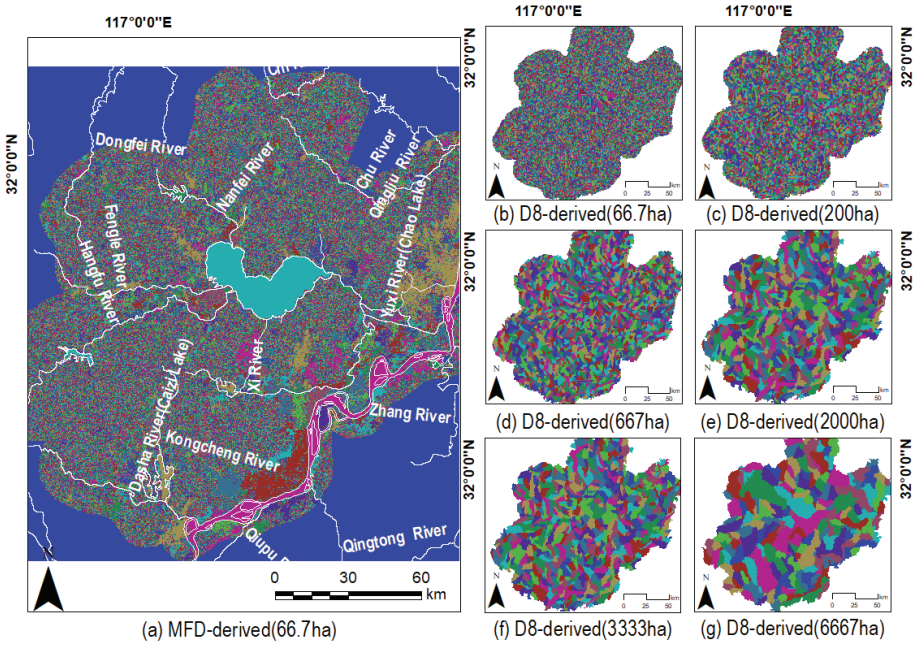

Figure 4. The sub-watersheds derived via MFD (**a**) and D8 (**b**–**g**). The area threshold used in the MFD-derived subwatershed is 66.7 ha, and the area thresholds used in the D8-derived subwatershed as shown in (**b**–**g**) are 66.7 ha, 200.0 ha, 667.0 ha, 2000.0 ha, 3333.0 ha and 6667.0 ha, respectively.

In Figure 4a, the MFD algorithm used to delimitate sub-watersheds was programmed by C#. The MFD algorithm adopts pixels in sink areas as seeds, traces the flow direction raster and identifies all the converging pixels consisting as a whole of sink areas. When delimitating sub-watersheds, all the pixels in the sink area and those pixels in the eight directions flowing towards to sink areas would be kept in the same sub-watershed as the sink area. Otherwise, the converging pixels would be classified as several sub-watersheds according to the flow order adjacent to the labeled sub-watershed in the same sink area. In this study, the maximum area threshold of the MFD algorithm adopted 66.7 ha to delimitate sub-watersheds.

The sub-watersheds produced by the D8 algorithm with different area thresholds were mapped in Figure 4b–g. The hydrological tool of ArcGIS 10.3 is programmed basing the D8 algorithm. The hydrology tool was used to delimitate sub-watersheds. The main

process contained calculating flow direction, calculating flow accumulation, extracting stream, making stream link, and delimitating sub-watersheds. The definition of area threshold determines the process of extracting the stream. Only pixels with an area of flow accumulation larger than the area threshold will be extracted as separate streamlines. The streamline would identify the sub-watersheds derived stream link while considering the stream links as pours. In this study, the used area thresholds in Figure 4b–g were 66.7 ha, 200.0 ha, 667.0 ha, 2000.0 ha, 3333.0 ha and 6667.0 ha, respectively.

As in Figure 4a, the flat area, especially the water bodies, was kept in the same sub-watershed. This indicates that the MFD algorithm can keep connecting flat areas as a whole. While in the D8 algorithm, all the flat areas and water bodies were treated as pixels to divide sub-watershed. The defined area threshold represents the maximum number of pixels converging in upstream water. Thus, as in Figure 4b–g, the flat area, the water areas and corresponding connected neighborhood pixels were sliced as sub-watersheds, and most of the sub-watershed areas seemed to be similar. Moreover, as the area threshold increases from Figure 4b–g, the number of sub-watersheds was reduced.

3.2. The Flood Hazard Map Derived by the Proposed Method

The actual flood areas (Figure 5a), the flood hazard map derived by the proposed method (Figure 5b), and part of the detailed flood area distribution (Figure 5c,d) were shown in Figure 5. Especially for the detailed flood area, the overlayer vector map of flooded towns and villages is filtered from Baidu News. Furthermore, Table 6 listed the comparison matrix of elements corresponding to flood areas, and dry areas with predicted flood hazard pixels.

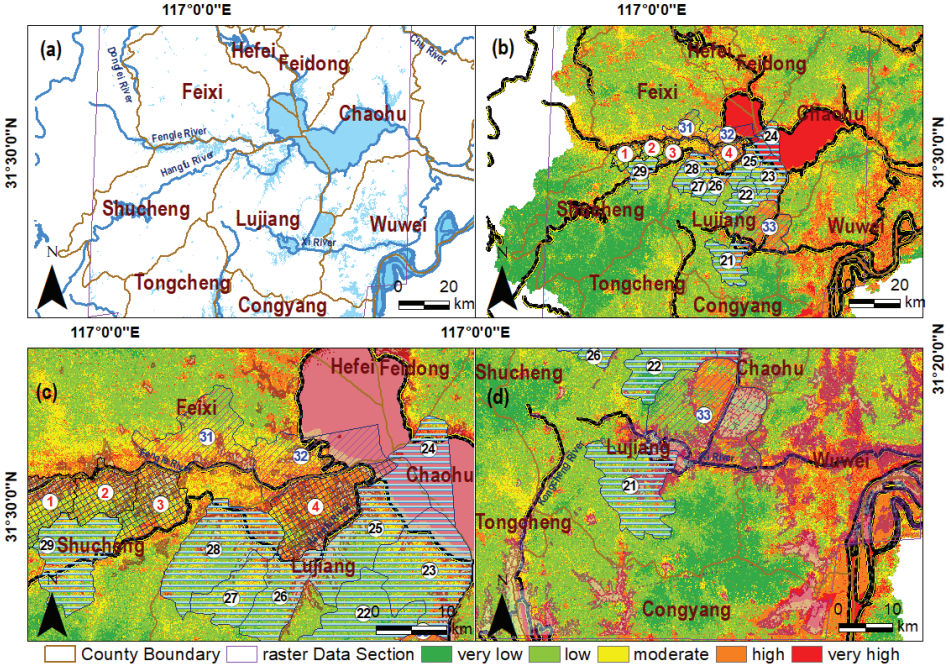

Figure 5. The flood hazard distribution is derived from the proposed method. Subfigure (**a**) was the real-world flooded areas extracted by remote sensing in July 2020 in the Chaohu basin. Subfigure (**b**) was the flood hazard distribution estimated by the proposed model. Subfigure (**c**) was the detailed hazard view of the Fengle river and the Hangfu River, and subfigure (**d**) was the clear hazard view of the Xi River.

Table 6. The comparison matrix and correct ratio, fit ratio, F1-score of flood hazard and flooded areas distribution.

Items	Validation 1		Validation 2	
	Positive Group (P): "Very High", "High", "Moderate"	**Negative Group (N): "Very Low", "Low"**	**Positive Group (P): "Very High", "High"**	**Negative Group (n): "Very Low", "Low", "Moderate"**
Flooded area (T)	842,963	131,230	583,933	390,260
Dry area (F)	1,004,991	302,577	673,359	634,209
Correct ratio (%)	87		60	
Fit ratio (%)	43		35	
F1-Score	0.597		0.523	

Table 6 demonstrated that when considering the flood hazard pixels of {"very high", "high", and "moderate"} derived by the proposed method as Positive results, the *Correct ratio*, *Fit ratio* and *F1-Score* were 87%, 43%, and 0.597, respectively. When considering the flood hazard pixels of {"very high", and "high"} derived by the proposed method as a *Positive* result, the *Correct ratio*, *Fit ratio* and *F1-Score* were 60%, 35%, and 0.523, respectively. Moreover, according to the *F1-score*, the flood hazard estimation result using validation 1 has higher consistency with flood areas extracted by remote sensing images.

As shown in Figure 5a, there were plenty of flooded areas near the north beach of the Fengle River in Feixi city. There were flooded areas distributed at the south beach of the Fengle River and the north beach of the Hangfu River in Shucheng city. Moreover, the flooded regions of Lujiang city were located in the south part of the Hangfu River and Xi River. Moreover, the flood areas of Wuwei city were scattered in the northern region of the Xi River. Moreover, in the northwest of Chaohu, there were some flooded areas near the Nanfei River in Feidong county. In the northeast of Chaohu, there was some flooded area near the Tuohao River in Chaohu city.

Figure 5b–d shows flooding hazard distribution overlayered by breaking points, flooded town/villages, or actively flood areas, which were searched from Baidu News. Moreover, as in Figure 5b–d, the breaking points corresponding to the towns were 1—Taoxi town, 2—Bolin village, 3—Qianrenqiao town, and 4—Tongda town. Moreover, in the area of the flooding point, the related towns were 21—Nihe town, 22—Yefushan town, 23—Shengqiao town, 24—Zhongmiao street, 25—Baishan town, 26—Shitou town, 27—Jinniu town, 28—Guohe town, and 29—Chengguan town. Moreover, in the active flood area, the corresponding towns were 31—Union dike of Shatan, Fengle town, 32—Union dike of Binhe & Union dike of Jiangkouhe, Sanhe town, and 33—Union dike of Peigang, Baihu town.

As shown in Figure 5c,d, the flood hazard map derived by the proposed method almost covered the areas, including the active drainage areas (No. 31, No. 32, and No. 33), the dike broken areas (No. 1, No. 2, No. 3, and No. 4), and the under submerged flooded areas (No. 21~No. 29). The flood hazard map derived by the proposed method contained part of the flooded district. The phenomenon indicated that the proposed method had higher consistency with flooded areas caused by broken and active drainage than natural flooding areas.

3.3. The Flood Hazard Distribution via AHP and the Proposed Models

The flood hazard distribution derived by pixel-based AHP and sub-watershed-based WZSAHP-RC were illustrated in Figure 6.

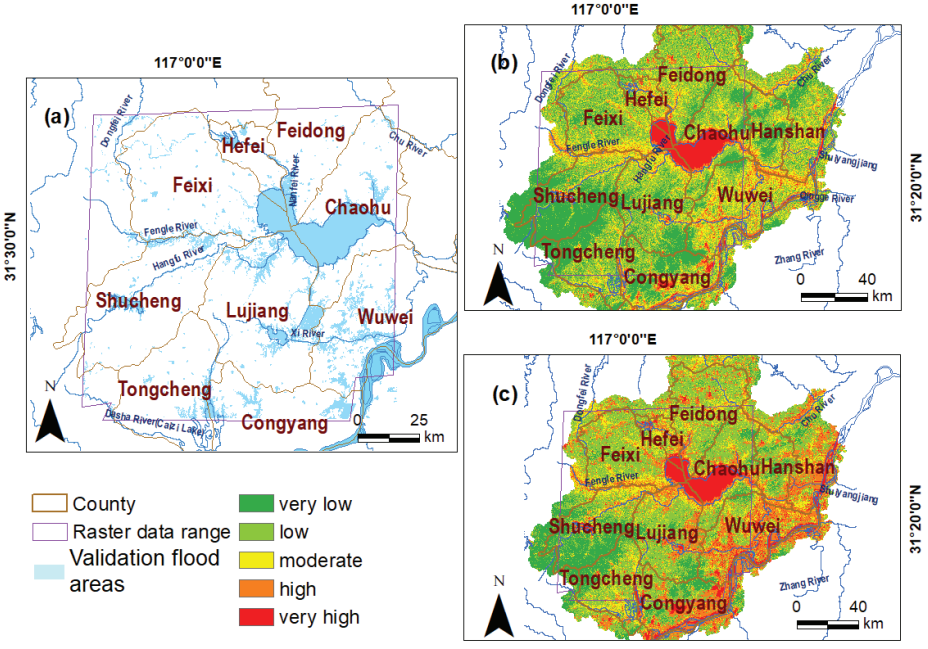

Figure 6. Differences in ground-truthing flooded areas compared with expected flooded areas from the AHP and the proposed model. (**a**) was the distribution of validation flood area, (**b**) was from the original pixel-based AHP, while (**c**) was from the proposed model.

Compared with the flood hazard map derived by AHP (Figure 6c), the areas were classified as higher hazards via the proposed method (Figure 6b), especially those pixels located along the Fengle river, the Hangfu river, the Zhao river, and the Yangtze River. Moreover, in the areas near the north beach of the Yangtze River, the flood hazard levels derived by the proposed model were higher than the AHP model.

Table 7 listed the validation results of *Correct ratio*, *Fit ratio*, and *F1-Score* derived by AHP and WZSAHP-RC models. Compared with the AHP model, when considering pixels of "very high", "high", and "moderate" as predicted flooding areas, the correct ratio and fit ratio calculated by the WZSAHP-RC model increased by 16% and 6%, respectively. Moreover, when considering pixels of "very high" and "high" as predicted flooding areas, the correct ratio and fit ratio calculated by the WZSAHP-RC model were increased by 34% and 17%, respectively.

Table 7. The correct ratio, fit ratio and F1-score were calculated by the pixel-based AHP method and the proposed sub-watershed-based WZSAHP-RC method.

Adopted Method	Base Unit	Validation 1: Positive Group (P): "Very High", "High", "Moderate"; Negative Group (N): "Very Low", "Low"			Validation 2: Positive Group (P): "Very High", "High"; Negative Group (N): "Very Low", "low", "Moderate"		
		Cor.1 (%)	Fit1 (%)	F1-Score	Cor.2 (%)	Fit2 (%)	F1-Score
AHP	Pixel	67	37	0.542	22	18	0.298
WZSAHP-RC	Sub-watershed	83	43	0.597	60	35	0.523
Increasing (%)	/	16	6	/	34	17	/

3.4. The Flood Hazard Results Estimated by Constraining Different Converging Indicators

Figure 7 mapped the flood hazard map derived by AHP (Figure 7a) and WZSAHP-RC using MFD-derived sub-watersheds (Figure 7b–m).

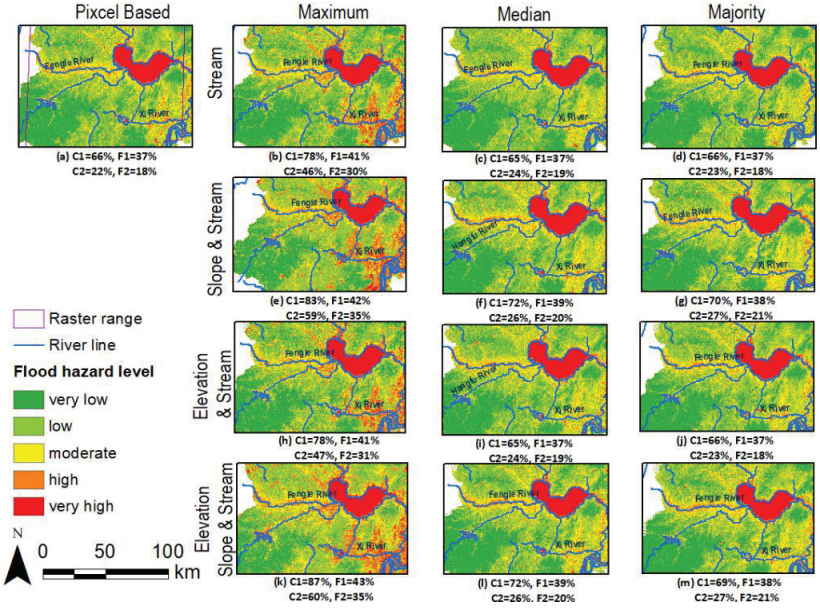

Figure 7. Flood hazard levels from pixel-based AHP (**a**), while (**b**–**m**) show flood hazard levels derived by WZSAHP-RC using different indicators and zonal statistics.

The *C*1 and *F*1 represented the correct ratio and fit ratio considering "very high", "high", and "moderate" as predicted flooded pixels, and the *C*2 and *F*2 represented the correct ratio and fit ratio considering "very high" and "high" as predicted flooded pixels. The range of permanent water bodies was colored blue. The flood hazard levels from low to high were colored with dark green, light green, yellow, orange, and red. For the subfigures of WZSAHP derived flood hazard maps, those in the same row constrained the same kinds of indicators (including {"*Distance from Streams*"}, {"*Slope*", "*Distance from Streams*"}, {"*Elevation*", "*Distance from Streams*"}, {"*Elevation*", "*Slope*", "*Distance from Streams*"}). The sub-figures in the same column adopted the same zonal statistical method (e.g., *maximum*, *median*, *majority*), e.g., Figure 7b–d used the MFD-derived sub-watershed to constrain the "*Distance from Streams*" by the *maximum*, *median*, and *majority* zonal statistical methods, respectively.

As in Figure 7, when using the maximum type of zonal statistical method via the MFD-derived sub-watershed to constrain all kinds of combinations of converging related indicators, the correct ratio and fit ratio could keep being increased, considering {*"high", "very high", "moderate"*} or {"*very high*", "*high*"} as predicted flooding areas.

Using the sub-watershed derived by MFD as a basic unit to constrain different kinds of converging indicators, we obtain the other distribution of the flood hazard index. Figure 8 shows the combined curve plots and bar graphs relating the AHP and the WZSAHP constrained sub-watershed to various converging indicators.

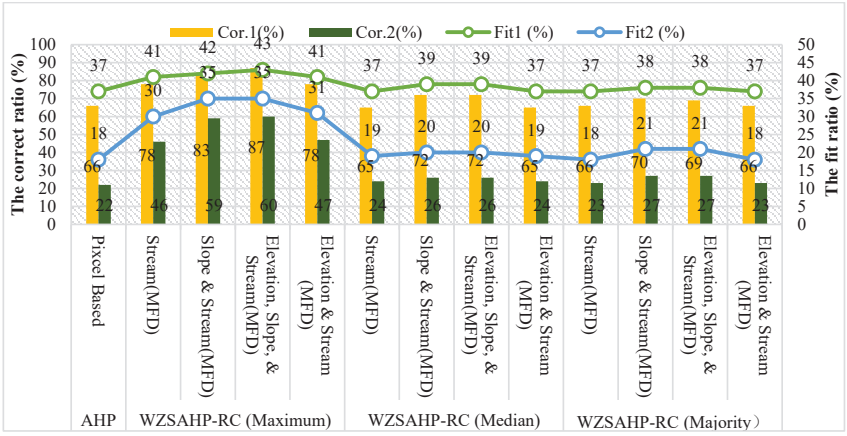

Figure 8. The correct ratio and fit ratio values of pixel-based AHP and sub-watershed-based WZSAHP-RC models constrain different kinds of converging related indicators.

As shown in Figure 8, the quality estimation correct ratio and fit ratio demonstrated that all the used constrain sub-watershed-based indicators via the maximum zonal statistical method could be improved. Moreover, for the *median* and *majority* zonal statistical methods, the correct and fit ratios derived by the WZSAHP-RC model via the constraining sub-watershed to {"*Distance from Streams*"}, {"*Slope*", "*Distance from Streams*"}, {"*Elevation*", "*Distance from Streams*"} or {"*Elevation*", "*Slope*", "*Distance from Streams*"} had a higher value than pixel-based AHP model. As in *maximum*, *median*, and *majority* zonal statistical methods, it could be observed that the correct ratio and fit ratio would be higher as the constraining indicators contain the "*Distance from Streams*" indicator. This phenomenon demonstrated the proposed WZSAHP-RC model—using MFD-derived subwatershed as a basic unit to constrain converging related indicators will steadily improve the flood hazard estimation correct ratio and fit ratio.

Figure 9 demonstrated the distribution of the flood hazard index calculated by pixel-based AHP and sub-watershed-based WZSAHP-RC. All the subfigures in Figure 9 mapped the scatter points (X, Y) in terms of the index of flood hazard indexes $(FRI_{WZSAHP-RC}, FRI_{AHP})$. The $FRI_{WZSAHP-RC}$ represented flood hazard index is calculated by the WZSAHP-RC model, and the FRI_{AHP} represented flood hazard index is derived by the AHP model.

The scatter diagrams used the water areas extracted by remote sensing images as truth values to filter the flood hazard index's raster values. Moreover, the subfigures were sampled using a moving grid window $column \times row$ with a size of 20×30 to obtain the values at the range of the column and row of water areas. Moreover, the unique index points were used to obtain the value of the flood hazard indexes. The scatters diagrams were drawn using a transparent circle with a variable radius $(alpha = 0.1, radius = 2 * Num_{samepoints})$, which adopted 0.1 as the value of transparency and used two times the number of pair points having the same values as the variable radius.

For the influence of the zonal statistical method, as shown in Figure 9 the scatter distribution pattern of using *median* and *majority* types of zonal statistical methods seemed to be similar. The same results could be observed. Only in the subfigures of flood hazards estimated using the *maximum* zonal statistical method (Figure 9a,d,g,j), all the scatter points were distributed on the lower diagonal side, and this indicated that the WZSAHP model using a *maximum* zonal statistical method to constrain converging related indicators would increase the flood hazard index.

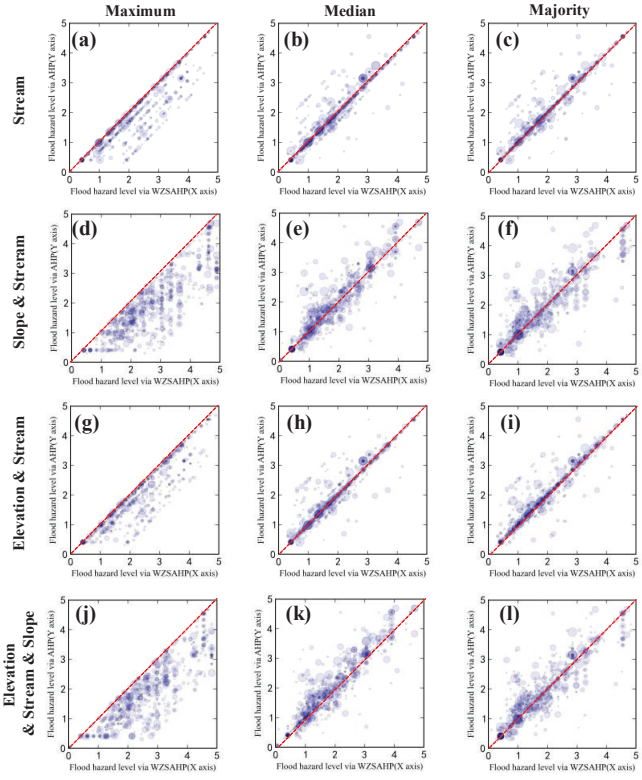

Figure 9. Scatter diagrams of flood hazard index derived by WZSAHP-RC via MFD delimitated sub-watershed as *X*-axis and flood hazard index derived by AHP as *Y*-axis. The converged indicator in (**a–c**), (**d–f**), (**g–i**), and (**j–l**) were the same, and the sub-figures in the same column used the same type of zonal statistical method.

For the influence of constraining indicators, it indicated that as constrained "*Stream* or *Elevation & Stream*", the scatter points distribution in all kinds of zonal statistical methods seemed to be more concentrated than restrained {"*Slope*", "*Distance from Streams*"} or {"*Elevation*", "*Slope*", "*Distance from Streams*"}. Therefore, the spatial distribution of sample points demonstrated that the WZSAHP-RC constrained by {"*Slope*", "*Distance from Streams*"} or {"*Elevation*", "*Slope*", "*Distance from Streams*"} would perform better in distinguishing flood hazard index, which means they might have a higher correct ratio and fit ratio. This phenomenon indicated that the efficient method needs to map a higher flood hazard index and make the flood hazard index distribution a dispersing pattern.

3.5. The Flood Hazard Results Estimated by Using D8-Derived Sub-Watershed with Different Area Thresholds as Basic Units

The flood hazard maps derived by AHP (Figure 10a) and using WZSAHP-RC via D8-derived sub-watersheds using different kinds of area thresholds (as listed in Table 3) were illustrated in Figure 10b–s.

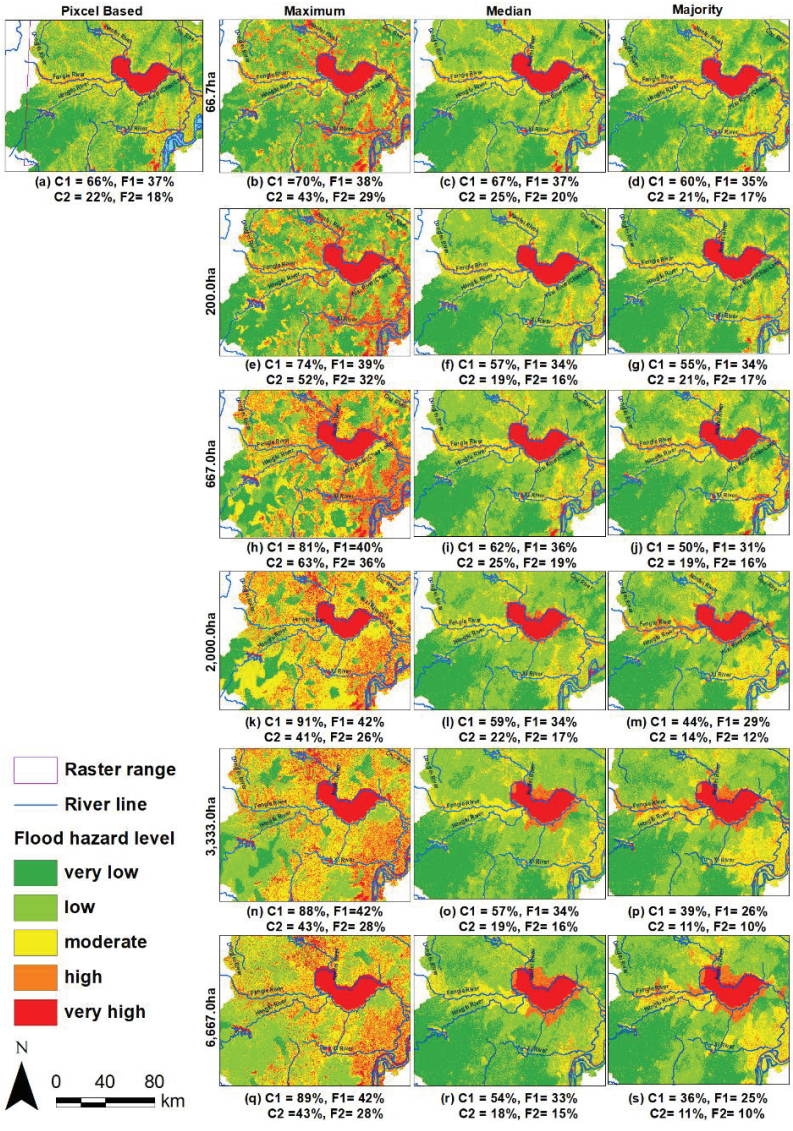

Figure 10. Flood risk levels from pixel-based AHP (**a**) and sub-watershed based AHP using D8-derived sub-watershed to constrain converging related indicators, such as *Elevation*, *Slope* and *Distance from Streams* (**b**–**s**).

The labeled correct ratio and fit ratio corresponding to the validation 1 of {"*very high*", "*high*", "*moderate*"} were recorded as *C*1 and *F*1, and the validation 2 of {"*very high*", "*high*"} were marked as *C*2 and *F*2, respectively. The range of permanent water and the flood hazard levels were colored as same as in Figure 7.

As in Figure 10b–s, subfigures in the same row adopted the same threshold area, and subfigures in the same column used the same statistical method. Moreover, using the maximum type of zonal statistical method to constrain flood converging related indicators, indicated that the correct ratio and fit ratio could keep increasing, considering {"*very high*", "*high*", "*moderate*"} or {"*very high*", "*high*"} as predicted flooding areas.

The flow path and the area threshold determined the final sub-watershed division results. The correct ratio and fit ratio derived by the six kinds of area threshold (as described in Table 4) using the proposed method and D8-derived sub-watershed to constrain "*Slope*" and "*Distance from streams*" were compared in Figure 11.

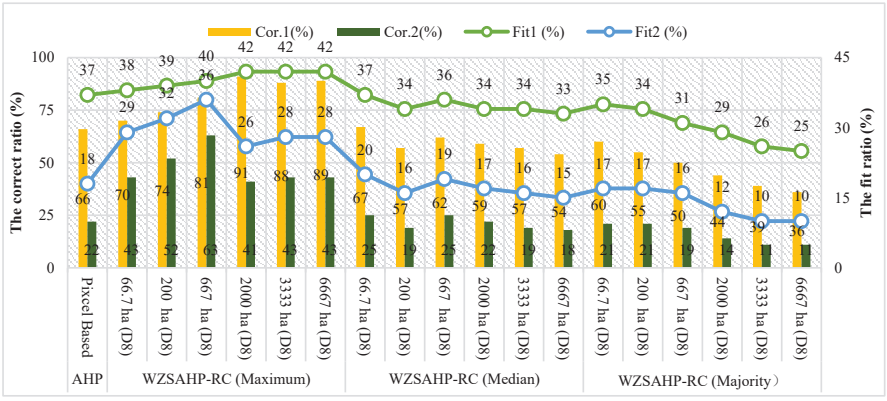

Figure 11. The correct ratio and fit ratio values of pixel-based AHP and the WZSAHP-RC using D8 derived sub-watershed to constrain converging related indicators.

As shown in Figure 11, while in the validation of considering "*high*" and "*very high*" as predicted flooding areas, the inflection point could be observed as the area threshold of 2000 ha. It indicated that the correct ratio and fit ratio derived by D8-based WZSAHP-RC (always using the *maximum* zonal statistical method) were consistently higher than pixel-based AHP, but the increasing of correct ratio and fit ratio derived by D8-based WZSAHP-RC would be influenced by the definition of area threshold for sub-watershed delimitating. For the *median* and *majority* zonal statistical methods, the correct and fit ratios seemed to fluctuate as the area threshold changed.

Figure 12 aimed to distinguish the scatter diagrams of flood hazard index distributions calculated by the AHP and the WZSAHP-RC using the D8 derived sub-watershed as basic units to constrain "*Slope*" and "*Distance from streams*" *by* the *maximum*, *median*, and *majority* zonal statistical methods.

In Figure 12, the scatter point pairs and sampling and mapping methods were the same as in Figure 9. The subfigures in the same row adopted the same area threshold determined sub-watershed as a basic unit. The subfigures in the same column used the same zonal statistical method. For example, as the scatter points $(FRI_{WZSAHP-RC}, FRI_{AHP})$ in Figure 12a, the $FRI_{WZSAHP-RC}$ represented flood hazard index was calculated by the proposed model using a D8-derived sub-watershed with an area threshold of 66.7 ha, and the FRI_{AHP} represented flood hazard index was derived by the AHP model. The scatter was mapped according to the moving sampling grid window of size 20×30 via the flood hazard index raster derived by the AHP and WZSAHP-RC methods. Moreover, the converging related indicators were used to derive $FRI_{WZSAHP-RC}$, which was calculated by the maximum type of zonal statistical method.

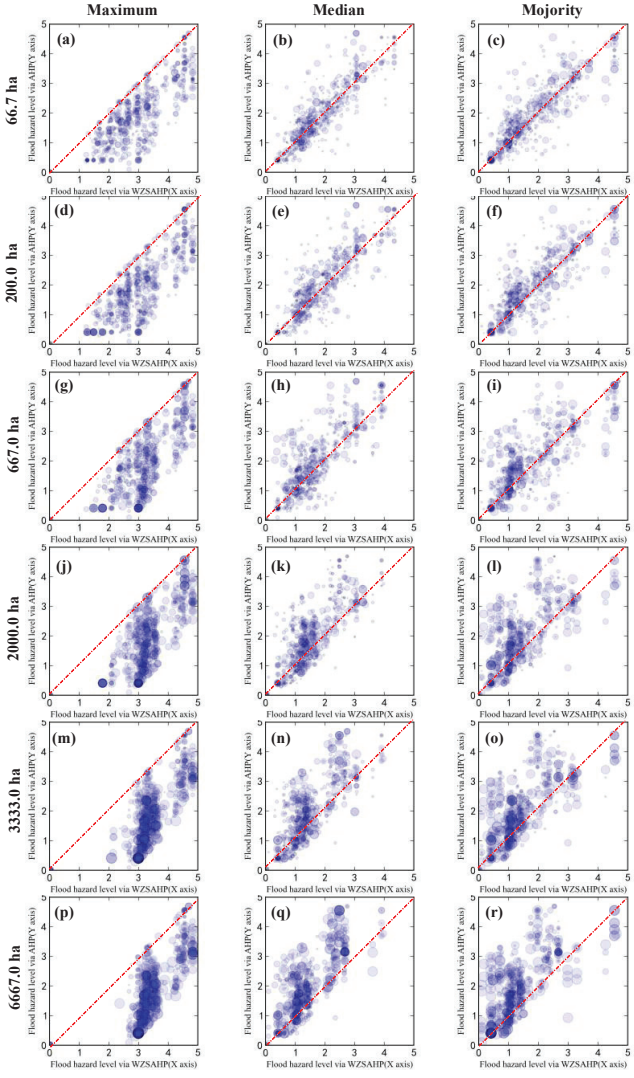

Figure 12. Scatter diagrams of flood hazard indexes distribution sampled by WZSAHP-RC via D8 delimitated sub-watershed a basic unit (WZSAHP-RC-D8) and AHP methods. The subfigures (**a**–**r**) used the flood hazard index derived by WZSAHP-RC-D8 as *X*-axis and using flood hazard index derived by AHP as *Y*-axis.

As in Figure 12a–i, it could be found that the spatial distribution of sampled point pairs was determined by the zonal statistical method. Moreover, the area threshold in the cluster of 66.7 ha, 200 ha and 667 ha were more similar to each other; in the area threshold defined as 2000 ha, 3333 ha, and 6667 ha, their scatter distribution pattern seemed to be more similar. This phenomenon also revealed that the flood hazard index changing trend using the D8-derived sub-watershed as a basic unit would have a point of inflection. Moreover, this suggested that the use of WZSAHP-RC via the D8-based sub-watershed as a basic unit should take care of the proper area threshold for sub-watershed delimitation.

3.6. The Validation of Using the Global River Widths from Landsat (GRWL) as Streams

The Global River Widths from the Landsat (GRWL) database was the first global compilation of river planform geometry at a constant-frequency discharge [34]. It is highly recognized by academics as a worldwide product. In this subsection, the GRWL was used to construct the "*Distance from streams*" indicator (Figure 13); additionally, the flood hazard distribution derived by pixel-based AHP and the proposed WZSAHP-RC method were compared (Figures 14 and 15). Moreover, the WZSAHP-RC uses sub-watershed to constrain the "*Slope*", "*Elevation*", and "*Distance from streams*" indicators. The used "*Slope*" and "*Elevation*" were as same as in Sections 3.4 and 3.5. Only the "*Distance from streams*" was constructed according to the vector stream map supported by the GRWL database.

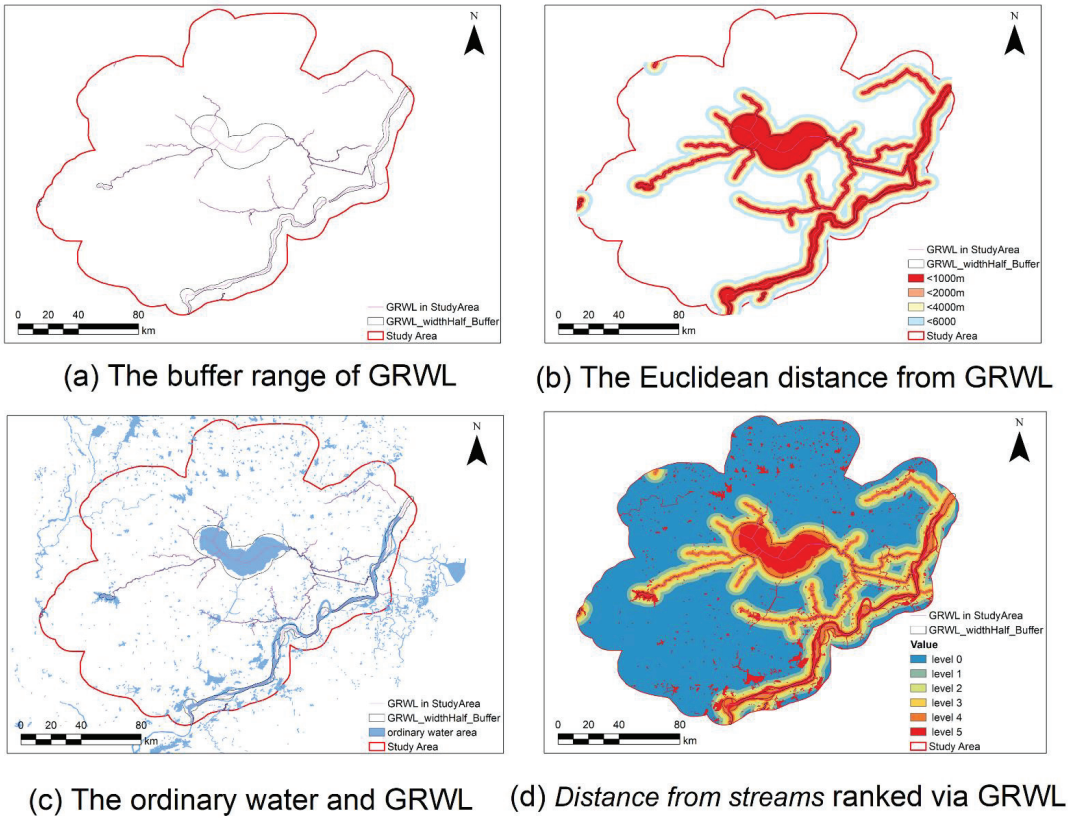

Figure 13. The GRWL distribution and the GRWL-based *Distance from streams* indicator in the study area. Figure (**a**) was the GRWL vectors and corresponding buffer results basing the attribute value of the width, figure (**b**) was the Euclidean distance from the GRWL buffer border, and figure (**c**) was the ordinary water bodies overlying the GRWL buffer layer and the ranked "*Distance from streams*" indicator in figure (**d**) was derived by GRWL and normal water range.

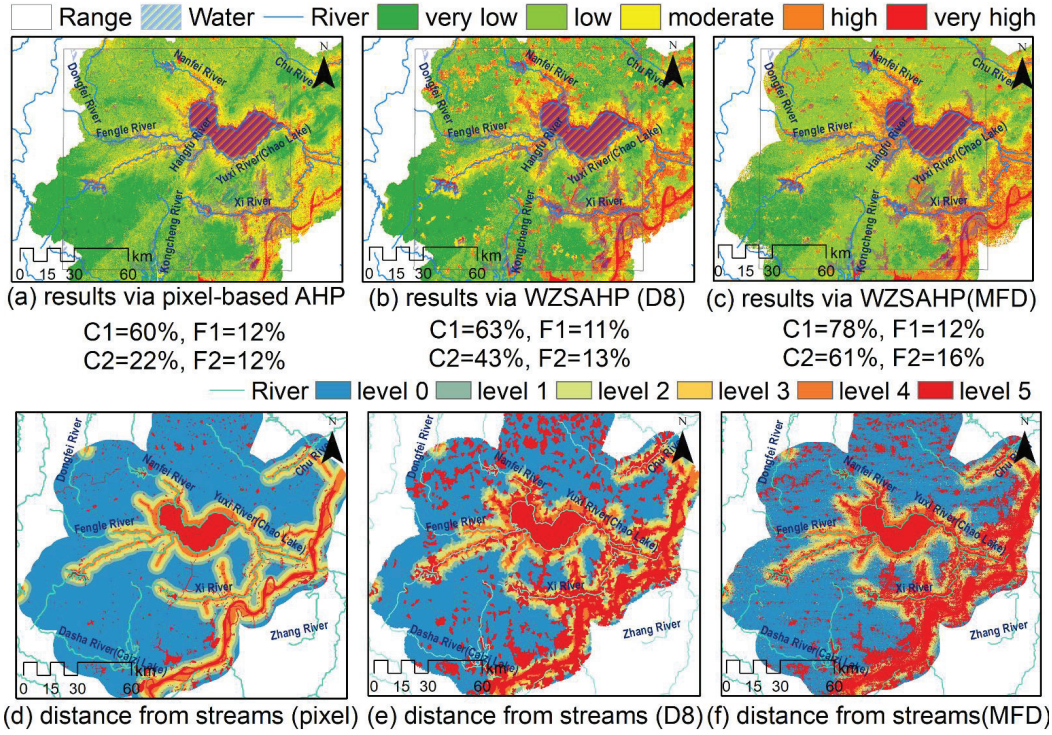

Figure 14. The flood hazard distribution derived by pixel-based AHP, the WZSAHP-RC using D8-derived and MFD to classify sub-watersheds as basic units. (**a**–**c**) were the flood hazard distribution basing pixel-based AHP, WZSAHP via D8-derived sub-watershed, and WZSAHP via MFD derived sub-watershed, respectively. (**d**–**f**) were the GRWL derived distance from streams distribution using pixel-based AHP, WZSAHP via D8-derived sub-watershed, and WZSAHP via MFD derived sub-watershed, respectively.

The GRWL vector is the shape of hydrology lines, and the width was recorded in the attribute table. The hydrology polygon was constructed using the width's value to build buffer areas on both sides of the hydrology lines (Figure 13a). Then, according to the ranking definition of the level 5 digital stream in Table 3, the calculation of Euclidean distance from the GRWL buffer range was implemented using distances of 1000 m, 2000 m, 4000 m, and 6000 m, respectively (Figure 13b). The level "*Distance of streams*" of pixels in the range of regular water areas (Figure 13c) was ranked as 5, and the pixels in the range of Euclidean distance from GRWL of <1000 m, 1000 m~2000 m, 2000 m~4000 m, 4000 m~6000 m, and >60,000 m were classified as 4, 3, 2, 1, 0, respectively (Figure 13d).

Based on the ranked "*Distance from streams*" derived by GRWL, the flood hazard distribution estimated by pixel-based AHP demonstrated the proposed WZSAHP-RC method using the D8-derived and MFD derived sub-watersheds as units (Figure 14). The validation dataset was constructed as in Sections 3.4 and 3.5. The correct ratio and fit ratio indicated that the WZSAHP-RC using the MFD sub-watershed as the basic unit (Figure 14c) performed better than using the pixel-based AHP (Figure 14c) and the WZSAHP-RC using the sub-watershed derived by D8 as units (Figure 14c). Figure 14d–f was the used distance from streams indicator in the pixel-based AHP, WZSAHP-RC using the D8 derived sub-watersheds and MFD derived sub-watershed. As in Figure 14e,f, the neighborhood pixels of those with high levels would be higher, especially using D8-derived sub-watershed as basic units.

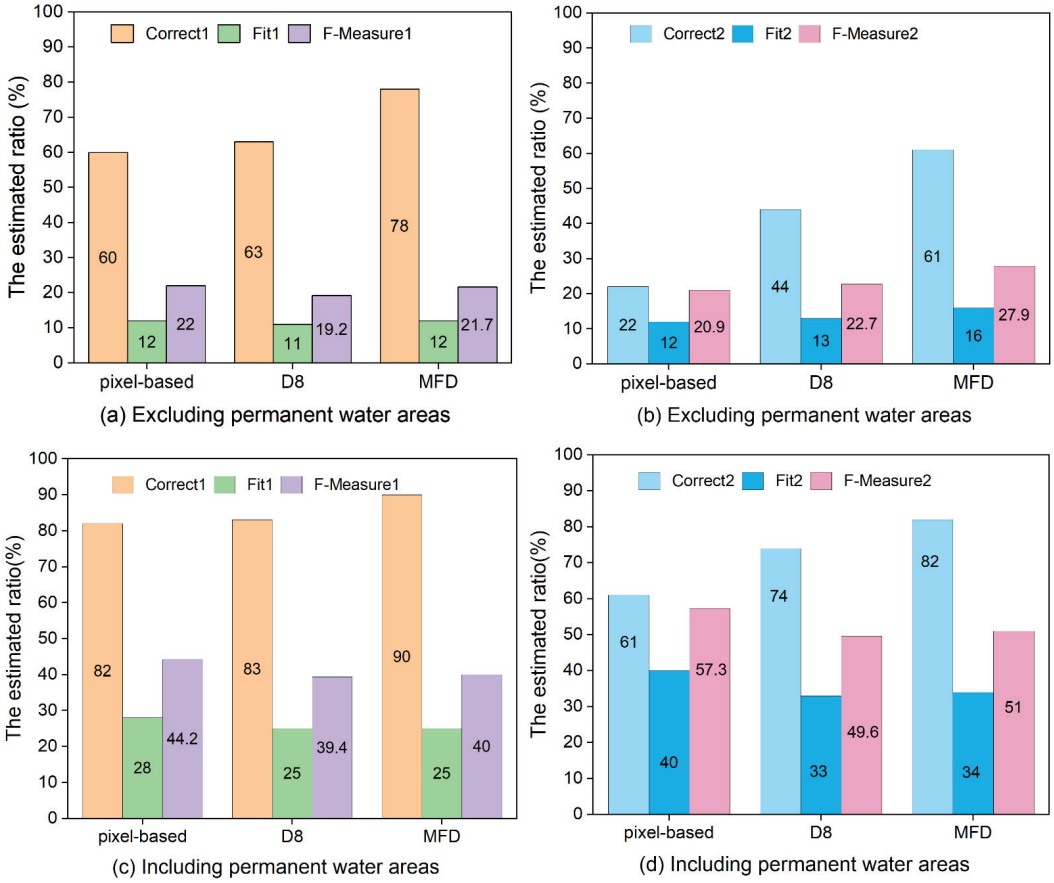

Figure 15. The correct ratio, fit ratio and F-measure basing the validation dataset excluding permanent water areas and including permanent water areas. (**a**,**b**) were the validation ratio using floodwater areas excluding permanent water areas. In contrast, (**c**,**d**) was the validation ratio using all water areas on flood days.

Figure 15 shows the further comparison of statistical results using a different method to construct validation flood areas. There are flood areas on a land surface that use water areas, excluding permanent water areas as a validation range (Figure 15a,b) and flood areas in all regions which contain land surface and common water areas, such as lakes, and rivers (Figure 15c,d). The results indicated that as constructed validation using water areas excluding permanent water areas, the correct ratio and fit ratio of WZSAHP-RC could consistently outperform pixel-based AHP.

As shown in Figure 15b,d, the F1-measures value was higher than in Figure 15a,c). This phenomenon revealed that validation dataset 2 (which adopted "high" and "very high" as predicted flooded areas) was more suitable than validation dataset 1 (which adopted "*moderate*", "*high*", and "*very high*" as indicated flooded areas).

4. Discussion

In this section, the influence and the usage of the proposed WZSAHP-RC model were discussed. The sub-watershed delimitation methods and their influences on the proposed model were discussed in Section 4.1. The converging involving indicator choices

in AHP-based flood hazard related estimation, and the influence on the proposed method is discussed in Section 4.2.

4.1. The Sub-Watershed Delimitation Methods and the Related Influences in the Proposed Model

The contribution of the proposed model revealed using sub-watershed as a basic unit to constrain converging related indicators can improve flood hazard estimation correct ratio and fit ratio. Thus, the sub-watershed delimitation is very important. Usually, the sub-watershed delimitated by DEM could be grouped as SFD and MFD algorithms. The accuracy influence of delimitation methods and the attention points in SFD-based and MFD-based sub-watershed delimitations should be discussed.

Point 1. The influence of DEM accuracy for MFD and SFD methods.

DEM is the primary material for sub-watershed delimitation. The accuracy of DEM is limited by the accuracy of the original captured data quality, the precision of the DEM producing process, and the related resolution format transformation. Therefore, to obtain higher consistency with the real-terrain DEM data, one method is to derive a hydrology data enforced DEM dataset.

Normal water distribution reflected the terrain in low-lying areas and the potential risk locations. The range of normal water can be used to improve the accuracy of DEM and used as auxiliary data to calculate flood hazard estimation involving indicators, such as "*Distance from streams*" and "*Hydro-lithological formations*".

In this study, the SWI index was used to improve the water areas. The essential feature of the SWI was extracting water areas by the defined thresholds to extract those elements with corresponding area and length relations. The RivaMap is a convenient engine to extract river centerlines by Landsat images, a geometric parameter of the multiscale singularity index to distinguish lakes and rivers effectively [35]. Figure 16 revealed the distribution of the normal water range extracted by the SWI and the multiscale singularity index of the RivaMap. Figure 16b,d indicated that the SWI derived water was cleaner than the RivaMap. However, the SWI derived result had a better effect and was beneficial to the accuracy of former potential water bodies supported by the impervious surface production. The RivaMap relay on the input Landsat image derived MNDWI index, and the RivaMap engine might calculate the multiscale singularity index automatically. Then, using the general Natural Break method could distinguish the final water map. Therefore, as in a large area of research, the easily used RivaMap engine might be a good choice to extract the textural characteristics of rivers and lakes.

Moreover, there were some refined river extraction [36] and automatic channel network extraction methods [37]. These methods rely on detailed indicators of remote sensing images and DEM. As in a small area range of study areas, they were using the precise hydrology information extraction method, which might be better to derive more detailed and near real-time water systems than the released geology information.

Point 2. The critical points of the MFD delimitation method.

In this study, the used MFD algorithm [20] adopts pixels in sink areas as seeds, traces the flow direction raster and identifies all the converging pixels consisting of whole sink areas. When delimitating sub-watersheds, all the pixels in the sink area and those in the eight directions totally flowing towards sink areas would be kept in the same sub-watershed as the sink area. Otherwise, the converging pixels would be classified as several sub-watersheds according to the flow order adjacent to the labeled sub-watershed in the same sink area.

Point 3. The critical points of the SFD delimitation method.

The D8 algorithm is one of the classical SFD algorithms. The result (in Section 3.5) indicated that the area threshold of the D8-based sub-watershed would influence the final estimation results. Therefore, for D8-based sub-watershed delimitation, exploring the proper area threshold is very important. In this study, the result indicated that 667 ha is a point of inflection. This might be influenced by some special environment factors, such as the study area scale, the flat terrain features and the special validation event. The proper

area threshold should be further explored in a specific study case. Thus, the high efficiency of sub-watershed delimitation is very important. High-efficient extraction of drainage networks from digital elevation models constrained by enhanced flow enforcement from known river maps proposed a ConstrainedDNE tool to extract drainage networks [38]. It could auto delimitate sub-watershed as several grades of the version, only relying on the given DEM and streamlines.

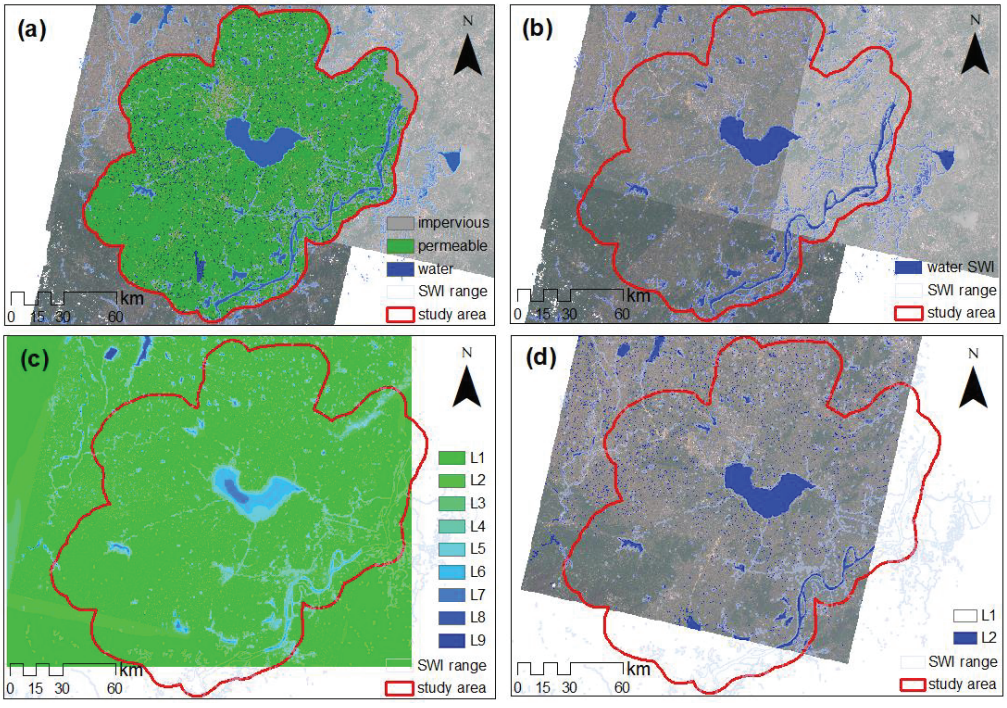

Figure 16. The normal water range extract by the proposed SWI and the RivaMap. (**a**) was the range of water bodies extracted by SWI overlay the distribution of the impervious surface production, (**b**) was the water body and range areas of SWI, and (**c**,**d**) were the distributions of the multiscale singularity index of RivaMap classified by nature break method as nine types and two types.

However, [38] expected to use an outside prepared stream to determine the sub-watershed by back-tracing the outlet of rivers. For one aspect, it is not easy to prepare data. As collecting fully covered stream information in the real world at a sub-watershed scale is relatively easy, the study area may consist of several sub-watersheds. The data requirement of fully covered and high quality makes using the suggested method difficult. For another aspect, it is difficult to fully match the survey streamlines to the used DEM. As in the large-area study case, the public used DEM is always produced by satellite-based InSAR surveying. The production of DEM might not be as high quality as local survey data because the surveyed streamlines are always investigated by local departments. Thus, DEM could use corresponding essential survey points to derive higher accuracy of results.

4.2. The Choice of Converging Indicators and the Related Influences in the Proposed Model

The AHP model is a traditional method used in flood hazard estimation. Thus, it is significant to discuss the possible reasons why and the function of how the converging indicators play a role in the proposed WZSAHP-RC model.

Point 1. The function converging indicators in this study.

In this study, the converging related indicators contain "*Slope*", "*Elevation*", and "*Distance from Streams*". The results in Figures 8 and 9 revealed that when using MFD-derived sub-watershed to constrain indicators {"*Distance from Streams*"}, or {"*Elevation*", "*Distance from Streams*"}, or {"*Slope*", "*Distance from Streams*"}, or {"*Elevation*", "*Slope*", "*Distance from Streams*"}, the proposed WZSAHP-RC model derived correct ratio and fit ratio were demonstrated to be higher than the derived by pixel-based AHP method. Constraining indicators {"*Elevation*", "*Slope*", "*Distance from Streams*"} performed best, and followed by {"*Slope*", "*Distance from Streams*"}, {"*Elevation*", "*Distance from Streams*"}, and {"*Distance from Streams*"}.

The essential of constraining sub-watershed to specific indicators means properly considering the hydrology converging influence on individual pixels. In the research of [39], the similar indicator "*Distance from drainage network*" matched with the "*Distance from streams*" of this study. It explained that the "*Distance from drainage network*" is influenced by the converging indicator "*drainage density*" and the runoff production indicator (such as "*ground water depth*", and "*land use*", etc.). The indicator "*Slope*" also has a significant influence on the indicator "*drainage density*" and "*ground water depth*". Those findings confirmed that the indicator "Distance from streams" could reflect other indicators directly or indirectly. Thus, constraining sub-watershed to "*Distance from streams*" might influence converging and runoff production indicators.

Point 2. The converging indicators are used in the related flood hazard estimation.

In the flood probability estimation based on geo-environment indicators [40], the weight of indicator order is demonstrated as "*slope*", "*distance to rivers*", "*altitude*" (referring to the "*elevation*"), and then followed by the "*terrain ruggedness index*" (TRI) and "*drainage density*". Moreover, in the study of prioritization of sub-watershed flood probability based on *physical*, *hydrological*, and *climatological* parameters [41], the high-risk sub-watersheds have higher "*permeability*" and "*rainfall*" and greater "*drainage network density*" at a shorter "*distance from rivers*". In [42], the flood hazard estimation in the vicinity of the main channels of the Kifisos and Ilisos Rivers indicated that the highest flood hazard areas were total covered "*streams*", expansion of "*impermeable formations*" and "*intense urbanization*". As in the referenced flood probability and flood hazard estimation research, the distance from "*streams*", "*rivers*", or "*drainage networks*" is taken seriously.

In the flood susceptibility mapping research basing the statistical model [43], "*distance from streams*", "*elevation*", and "*slope*" were important indicators in the occurrence of floods, and the "*rainfall*", "*terrain wetness index*" (TWI) and "*land cover type*" also influenced indicators on flood sensitivity. Moreover, the flood susceptibility mapping based machine learning research [44] found the relative importance order of indicators were "*slope angle*", "*distance from rivers*", "*land use*", "*TWI*", "*elevation*", and other indicators. For flash flood susceptibility estimation [45], the *slope* was the essential indicator that occurred and developed floods. Thus, it was assigned the highest weight and followed by the factors of "*land use*", "*lithology*", and "*profile curvature*". Therefore, these works of literature all considered the "*slope*", "*distance from 'streams' or 'rivers'*", "*elevation*" as essential indicators, and some research assigned "*slope*" the highest weight.

Point 3. The choices of digital streams and GRWL to construct "*Distance from streams*".

The choice of using a proper stream also needs to be discussed. DEM can be used to produce digital streams, and there is some mature globe-scale hydrology production, such as GRWL. The digital streams extracted from DEM were used as basic streams to construct "*Distance from streams*" in this study.

The GRWL production contains the width of large-scale lakes and rivers, while the digital streams focus on distinguishing terrain converging characters (Figure 17). As described in Sections 3.4 and 3.6, the proposed WZSAHP-RC method using sub-watershed delimitated by MFD as basic units could improve the correct ratio and fit ratio compared to the pixel-based AHP using both streams to derive the "*Distance from streams*" indicator. Moreover, for WZSAHP-RC method, when using digital streams (Figure 7k), the final estimated flood hazard distribution had a higher correct ratio and fit ratio (*C*1 = 87%,

F1 = 43%, C2 = 60%, F2 = 35%) than using GRWL (C1 = 78%, F1 = 12%, C2 = 61%, F2 = 16%) (Figure 14c). Therefore, it could be concluded that using the DEM derived digital stream was more suitable for constructing "*Distance from streams*" than GRWL at the basin scale. As in the larger scale, such as catchments or regional areas, more experiments should be conducted in the future.

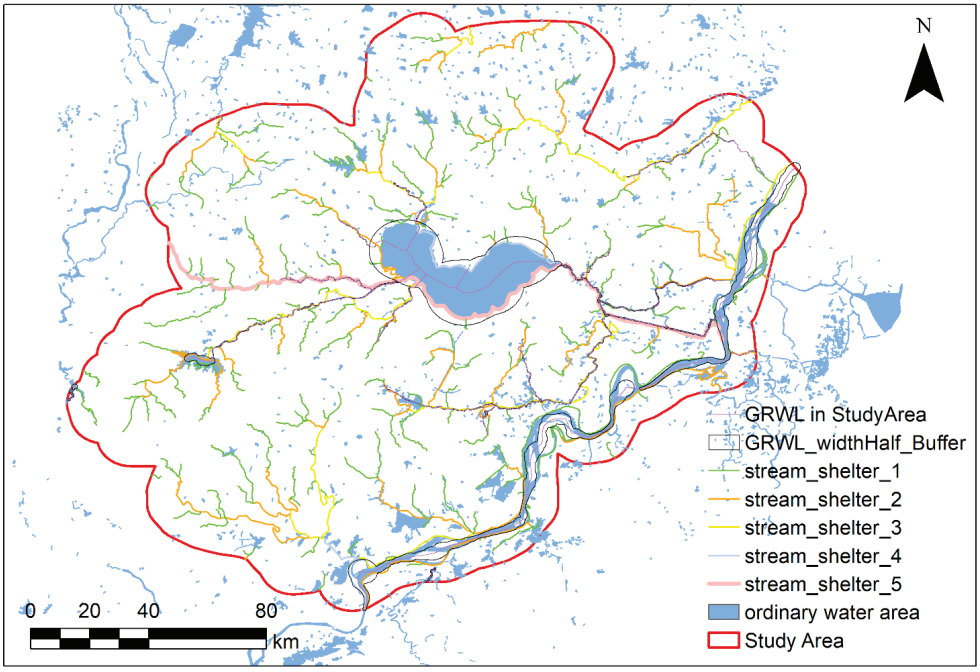

Figure 17. The distribution of GRWL in the study areas, overlaid by the digital streams derived by DEM, and the common water area in the study area.

5. Conclusions

In this study, as the traditional pixel-based AHP method failed to capture the hydrological features caused by neighborhood pixels, a sub-watershed-based extended AHP model named WZSAHP-RC was proposed. Taking the Chaohu Basin of Anhu, China, as an example, the correct ratio and fit ratio of the proposed method were validated using the real-flood areas extracted from remote sensing compared with the pixel-based AHP method. When using {"*very high*", "*high*", "*moderate*"} as predicted in flooded areas, the results indicated that the correct ratio and fit ratio derived by the WZSAHP-RC could improve by 21% (from 66% to 87%) and 6% (from 37% to 43%), respectively. Moreover, when using {"*very high*", and "*high*"} as predicted flooded areas, the correct ratio and fit ratio could increase by 38% (from 22% to 60%) and 17% (from 18% to 35%), respectively. Moreover, in comparison with flood towns filtered by Baidu News, the proposed method had higher consistency with dikes broken and active drainage flooded areas than the pixel-based AHP method.

Furthermore, the correct ratio and fit ratio could be improved using the proposed WZSAHP-RC method to constrain part of converging related indicators by the MFD-derived or D8-derived sub-watershed as a basic unit. When using a D8-derived sub-watershed as a basic unit, the correct ratio and fit ratio were also demonstrated to be increased compared to the pixel-based AHP model. Still, the area threshold of delimitating sub-watershed would influence the increasing value.

Despite the success of the proposed WZSAHP-RC model, we need to acknowledge its limitations. The validation flood is the period from 20 to 24 July 2020 in the Chaohu basin, which is the biggest in recent years, but this is validated by one case, and maybe other places or flood events, would produce different results. Furthermore, it indicated that the area threshold of delimitating sub-watershed would influence the correct ratio and fit ratio increment of WZSAHP-RC. Future research needs to reveal the usability of different terrain character study areas and quantitatively analyze the effective area threshold range of the delimitating sub-watershed for the proposed method. Meanwhile, the potential of flooding and the company risk is a combined effect function by flood hazard, exposure, and vulnerability. Flood hazard estimation needs not only to consider the spatial heterogeneity but also needs to consider the effect of spatial homogeneity. This study demonstrated the space connections between sub-watershed and flood hazard estimation. The flood exposure and vulnerability estimation also need to explore the affiliate effects in horizontal and vertical geological space in detail, even extending to the link affecting the multi-dimensional social-economic environment.

Supplementary Materials: The following supporting information can be downloaded at: https://www.mdpi.com/article/10.3390/rs14102465/s1. These data include the rating dataset of flood risk involve of indicators, the watersheds delimitated by the D8 (with area threshold of 667 ha, 200.0 ha, 667.0 ha, 2000.0 ha, 3333.0 ha, and 6667 ha) and MFD algorithms, and the water body of natural boundary and during validating flood period.

Author Contributions: Conceptualization, H.Z. and Z.S.; methodology, H.Z., Z.S. and J.S.; software, H.Z.; validation, Z.S., J.S. and J.Y.; formal analysis, J.S. and J.Y.; investigation, X.H.; writing—original draft preparation, H.Z.; writing—review and editing, X.H., J.S. and J.Y.; visualization, J.Y. All authors have read and agreed to the published version of the manuscript.

Funding: This research was funded by the National Key R&D Program of China, grant number 2018YFB2100501, the Fundamental Research Funds for the Central Universities, grant number 2042021kf0007, the open grants of the state key laboratory of severe weather, grant number 2021LASW-A17, the Open Fund of Hubei Luojia Laboratory, grant number 220100009, the Shenzhen Science and technology Innovation Key project, grant number JCYJ20200109150833977, in part by the National Natural Science Foundation of China under Grants 42090012, Sichuan Science and Technology Program, grant number 2022YFN0031, Zhuhai industry university research cooperation project of China, grant number ZH22017001210098PWC, 03 special research and 5G project of Jiangxi Province in China, grant number 20212ABC03A09, and Zhizhuo Research Fund on Spatial-Temporal Artificial Intelligence, grant number ZZJJ202202. The authors would like to thank the anonymous reviewers and editors for their comments, which helped us improve this article significantly.

Data Availability Statement: Not applicable.

Acknowledgments: Author thank sincerely to teacher Stephen McClure of Wuhan University for his work in improving this manuscript.

Conflicts of Interest: The authors declare no conflict of interest.

Appendix A. The Used Tiles of Impermeable Surface Product and the Flooded Town Derived from Baidu News

As shown in Section 2.2, the 18 tiles (Table A1) of China's impermeable surface product (2 m) in Hefei, Luan, Anqing, Wuhu, Maanshan, Chuzhou, Huainan cities were used to prepare the land use and hydrological indicators.

Table A1. Tiles of China's impermeable surface product (2 m) were used in the study area.

District	Data Tiles	Districts	Data Tiles
Anqing	R1C1, R1C2	Luan	R1C2, R3C2
Chizhou	R1C1, R1C2	Maanshan	R1C1, R1C2
Chuzhou	R2C1, R2C2	Tongling	R1C1
Hefei	R1C2, R1C2, R2C1, R2C2	Wuhu	R1C1, R2C1
Huainan	R2C1		

As shown in Section 2.2, the retrieved raw flood event-related news were manually cleaned up to derive the final validating dataset of flood town (Table A2) and active breaking dikes for excessive drainage rainwater in the Chaohu basin (Table A3).

Table A2. The flood- and damage-relevant information from Baidu News in the study area.

Date	City	Flooded Town (Village)	Broken Location
19 July 2020	Shuchengxian, Liuan city	Taoxi town Blinding (Bolin, Jiehe village) Qianrenqiao town (Shuxin, Xingfeng, Tonggui, Huangcheng, Wanghe, Sanchahe, Qiandashan etc. villages)	Fengle River (Longtan River) Fenagle (Bolin Reach) Hangfu, Qiandashan rivers
		Chengguan town (Taiping village)	Sanli, Zhanggongdang, Zhucao Rivers
22 July 2020	Lujiangxian, Hefei city	Tongda town (Xuejiayu, Guyu, Lianhe, Yongxing, Shifeng, Changfeng villages) Baishan town (Baishan, Daiqiao, Shilian, Jinsheng, Jiulian, Xingang villages)	Shidayu
Not clear		Shengqiao town, Yefushan town, Shitou town, Jinniu town, Guohe town, Nihe town, Baihu town	

Table A3. Flooding area distribution caused by active dam breaking.

Date	City	Flooded Land	Mitigation Pressure
19 July 2020	Quanjiaoxian, Chuzhou city	Dike of Huangcao district 2 and 3	Chu River
26 July 2020	Feixixian, Hefei city	Union dike of Jiangkouhe, Yandian Xiang Union dike of Binhu, Sanhe Town Union dike of Shatan, Fengle Town	Chaohu
27 July 2020	Lujiangxian, Hefei city	Union dike of Peigang, Baihu Town	Chaohu

References

1. Wheater, H.S. Flood hazard and management: A UK perspective. *Philos. Trans. R. Soc. A Math. Phys. Eng. Sci.* **2006**, *364*, 2135–2145. [CrossRef] [PubMed]
2. Teng, J.; Jakeman, A.J.; Vaze, J.; Croke, B.F.W.; Dutta, D.; Kim, S. Flood inundation modelling: A review of methods, recent advances and uncertainty analysis. *Environ. Model. Softw.* **2017**, *90*, 201–216. [CrossRef]
3. Shao, Z.; Fu, H.; Li, D.; Altan, O.; Cheng, T. Remote sensing monitoring of multi-scale watersheds impermeability for urban hydrological evaluation. *Remote Sens. Environ.* **2019**, *232*, 111338. [CrossRef]
4. Bertilsson, L.; Wiklund, K.; Tebaldi, I.D.M.; Rezende, O.M.; Verol, A.P.; Miguez, M.G. Urban flood resilience—A multi-criteria index to integrate flood resilience into urban planning. *J. Hydrol.* **2019**, *573*, 970–982. [CrossRef]
5. Jiang, Y.; Zevenbergen, C.; Ma, Y. Urban pluvial flooding and stormwater management: A contemporary review of China's challenges and "sponge cities" strategy. *Environ. Sci. Policy* **2018**, *80*, 132–143. [CrossRef]
6. Chinanews. In 2020, the Flood Disaster Caused 63.46 Million People with Direct Economic Losses of 178.96 Billion Yuan. Available online: https://www.chinanews.com.cn/cj/shipin/cns-d/2020/08-13/news865240.shtml (accessed on 30 December 2021).
7. Xu, W.; Zhong, M.; Hong, Y.; Lin, K. Enhancing community resilience to urban floods with a network structuring model. *Saf. Sci.* **2020**, *127*, 104699. [CrossRef]

8. Barendrecht, M.H.; Viglione, A.; Blöschl, G. A dynamic framework for flood risk. *Water Secur.* **2017**, *1*, 3–11. [CrossRef]
9. Haider, H.; Ghumman, A.R.; Al-Salamah, I.S.; Ghazaw, Y.; Abdel-Maguid, R.H. Sustainability evaluation of rainwater harvesting-based flood risk management strategies: A multilevel decision-making framework for arid environments. *Arab. J. Sci. Eng.* **2019**, *44*, 8465–8488. [CrossRef]
10. Han, S.; Coulibaly, P. Bayesian flood forecasting methods: A review. *J. Hydrol.* **2017**, *551*, 340–351. [CrossRef]
11. Ekmekcioğlu, Ö.; Koc, K.; Özger, M. District based flood risk assessment in Istanbul using fuzzy analytical hierarchy process. *Stoch. Environ. Res. Risk Assess.* **2021**, *35*, 617–637. [CrossRef]
12. Ekmekcioğlu, Ö.; Koc, K.; Özger, M. Stakeholder perceptions in flood risk assessment: A hybrid fuzzy AHP-TOPSIS approach for Istanbul, Turkey. *Int. J. Disaster Risk Reduct.* **2021**, *60*, 102327. [CrossRef]
13. Ali, S.A.; Parvin, F.; Pham, Q.B.; Vojtek, M.; Vojteková, J.; Costache, R.; Linh, N.T.T.; Nguyen, H.Q.; Ahmad, A.; Ghorbani, M.A. GIS-based comparative assessment of flood susceptibility mapping using hybrid multi-criteria decision-making approach, naïve Bayes tree, bivariate statistics and logistic regression: A case of Topľa basin, Slovakia. *Ecol. Indic.* **2020**, *117*, 106620. [CrossRef]
14. Costache, R.; Pham, Q.B.; Avand, M.; Thuy Linh, N.T.; Vojtek, M.; Vojteková, J.; Lee, S.; Khoi, D.N.; Thao Nhi, P.T.; Dung, T.D. Novel hybrid models between bivariate statistics, artificial neural networks and boosting algorithms for flood susceptibility assessment. *J. Environ. Manag.* **2020**, *265*, 110485. [CrossRef]
15. Ouma, Y.; Tateishi, R. Urban flood vulnerability and risk mapping using integrated multi-parametric AHP and GIS: Methodological overview and case study assessment. *Water* **2014**, *6*, 1515–1545. [CrossRef]
16. Chakraborty, S.; Mukhopadhyay, S. Assessing flood risk using analytical hierarchy process (AHP) and geographical information system (GIS): Application in Coochbehar district of West Bengal, India. *Nat. Hazards* **2019**, *99*, 189–216. [CrossRef]
17. Abdouli, K.A.; Hussein, K.; Ghebreyesus, D.; Sharif, H.O. Coastal runoff in the United Arab Emirates—The hazard and opportunity. *Sustainability* **2019**, *11*, 5406. [CrossRef]
18. Wu, Z.; Shen, Y.; Wang, H. Assessing urban areas' vulnerability to flood disaster based on text data: A case study in Zhengzhou city. *Sustainability* **2019**, *11*, 4548. [CrossRef]
19. Zhang, H.; Cheng, X.; Jin, L.; Zhao, D.; Zheng, K. A method for estimating urban flood-carrying capacity using the VIS-W underlying surface model: A case study from Wuhan, China. *Water* **2019**, *11*, 2345. [CrossRef]
20. Zhang, H.; Cheng, X.; Jin, L.; Zhao, D.; Feng, T.; Zheng, K. A method for dynamical sub-watershed delimitating by no-fill digital elevation model and defined precipitation: A case study of Wuhan, China. *Water* **2020**, *12*, 486. [CrossRef]
21. Shao, Z.; Pan, Y.; Diao, C.; Cai, J. Cloud detection in remote sensing images based on multiscale features-convolutional neural network. *IEEE Trans. Geosci. Remote Sens.* **2019**, *57*, 4062–4076. [CrossRef]
22. Shao, Z.; Wu, W.; Li, D. Spatio-temporal-spectral observation model for urban remote sensing. *Geo-Spat. Inf. Sci.* **2021**, *24*, 372–386. [CrossRef]
23. Saaty, T.L. Decision making—the analytic hierarchy and network processes (ahp/anp). *J. Syst. Sci. Syst. Eng.* **2004**, *13*, 1–35. [CrossRef]
24. Fernández, D.S.; Lutz, M.A. Urban flood hazard zoning in Tucumán Province, Argentina, using GIS and multicriteria decision analysis. *Eng. Geol.* **2010**, *111*, 90–98. [CrossRef]
25. Bathrellos, G.D.; Skilodimou, H.D.; Chousianitis, K.; Youssef, A.M.; Pradhan, B. Suitability estimation for urban development using multi-hazard assessment map. *Sci. Total Environ.* **2017**, *575*, 119–134. [CrossRef] [PubMed]
26. Papaioannou, G.; Vasiliades, L.; Loukas, A. Multi-criteria analysis framework for potential flood prone areas mapping. *Water Resour. Manag.* **2015**, *29*, 399–418. [CrossRef]
27. Koc, K.; Ekmekcioğlu, Ö.; Özger, M. An integrated framework for the comprehensive evaluation of low impact development strategies. *J. Environ. Manag.* **2021**, *294*, 113023. [CrossRef]
28. Kenny, F.; Matthews, B.; Todd, K. Routing overland flow through sinks and flats in interpolated raster terrain surfaces. *Comput. Geosci.* **2008**, *34*, 1417–1430. [CrossRef]
29. Zhang, H.; Cheng, X.; Zhao, D.; Ma, H. Analyzing the contribution of high resolution water range in dividing catchment based on D8 algorithm. In Proceedings of the IGARSS 2018—2018 IEEE International Geoscience and Remote Sensing Symposium, Valencia, Spain, 23–27 July 2018; IEEE: Valencia, Spain, 2018.
30. Network, C.R. Wuwu Anhui Released Two Orders in the Early Morning: All People Located in Inner River Small Than 200 ha Must Evacuate. Available online: https://baijiahao.baidu.com/s?id=1672632563586115896&wfr=spider&for=pc (accessed on 21 April 2021).
31. XinhuaNews. Chaohu Flood Drainage: Adopt 9 Dikes of Area Larger Than 666 ha and Transfer More Than 140,000 People. Available online: https://baijiahao.baidu.com/s?id=1673508617349741514&wfr=spider&for=pc (accessed on 21 April 2021).
32. Alfieri, L.; Salamon, P.; Bianchi, A.; Neal, J.; Bates, P.; Feyen, L. Advances in pan-European flood hazard mapping. *Hydrol. Process* **2014**, *28*, 4067–4077. [CrossRef]
33. Bates, P.; De Roo, A. A simple raster-based model for flood inundation simulation. *J. Hydrol.* **2000**, *236*, 54–77. [CrossRef]
34. Allen, G.H.; Pavelsky, T.M. Global extent of rivers and streams. *Science* **2018**, *361*, t636. [CrossRef]
35. Isikdogan, F.; Bovik, A.; Passalacqua, P. RivaMap: An automated river analysis and mapping engine. *Remote Sens. Environ.* **2017**, *202*, 88–97. [CrossRef]
36. Li, D.; Wang, G.; Qin, C.; Wu, B. River extraction under bankfull discharge conditions based on sentinel-2 imagery and DEM data. *Remote Sens.* **2021**, *13*, 2650. [CrossRef]

37. Isikdogan, F.; Bovik, A.; Passalacqua, P. Automatic channel network extraction from remotely sensed images by singularity analysis. *IEEE Int. Geosci. Remote Sens. Symp.* **2015**, *12*, 2218–2221. [CrossRef]
38. Wu, T.; Li, J.; Li, T.; Sivakumar, B.; Zhang, G.; Wang, G. High-efficient extraction of drainage networks from digital elevation models constrained by enhanced flow enforcement from known river maps. *Geomorphology* **2019**, *340*, 184–201. [CrossRef]
39. Souissi, D.; Zouhri, L.; Hammami, S.; Msaddek, M.H.; Zghibi, A.; Dlala, M. GIS-based MCDM—AHP modeling for flood susceptibility mapping of arid areas, southeastern Tunisia. *Geocarto. Int.* **2020**, *35*, 991–1017. [CrossRef]
40. Avand, M.; Moradi, H.; Lasboyee, M.R. Spatial modeling of flood probability using geo-environmental variables and machine learning models, case study: Tajan watershed, Iran. *Adv. Space Res.* **2021**, *67*, 3169–3186. [CrossRef]
41. Avand, M.; Khiavi, A.N.; Khazaei, M.; Tiefenbacher, J.P. Determination of flood probability and prioritization of sub-watersheds: A comparison of game theory to machine learning. *J. Environ. Manag.* **2021**, *295*, 113040. [CrossRef]
42. Bathrellos, G.D.; Karymbalis, E.; Skilodimou, H.D.; Gaki-Papanastassiou, K.; Baltas, E.A. Urban flood hazard assessment in the basin of Athens Metropolitan city, Greece. *Environ. Earth Sci.* **2016**, *75*, 319. [CrossRef]
43. Yariyan, P.; Avand, M.; Abbaspour, R.A.; Torabi Haghighi, A.; Costache, R.; Ghorbanzadeh, O.; Janizadeh, S.; Blaschke, T. Flood susceptibility mapping using an improved analytic network process with statistical models. *Geomat. Nat. Hazards Risk* **2020**, *11*, 2282–2314. [CrossRef]
44. Costache, R.; Ţîncu, R.; Elkhrachy, I.; Pham, Q.B.; Popa, M.C.; Diaconu, D.C.; Avand, M.; Costache, I.; Arabameri, A.; Bui, D.T. New neural fuzzy-based machine learning ensemble for enhancing the prediction accuracy of flood susceptibility mapping. *Hydrol. Sci. J.* **2020**, *65*, 2816–2837. [CrossRef]
45. Costache, R.; Pham, Q.B.; Arabameri, A.; Diaconu, D.C.; Costache, I.; Crăciun, A.; Ciobotaru, N.; Pandey, M.; Arora, A.; Ali, S.A.; et al. Flash-flood propagation susceptibility estimation using weights of evidence and their novel ensembles with multicriteria decision making and machine learning. *Geocarto. Int.* **2021**, 1–33. [CrossRef]

MDPI
St. Alban-Anlage 66
4052 Basel
Switzerland
www.mdpi.com

MDPI Books Editorial Office
E-mail: books@mdpi.com
www.mdpi.com/books

Academic Open
Access Publishing

mdpi.com

ISBN 978-3-0365-9347-0